10TH ANNIVERSARY
2015 - 2025

International Journal of BIOPRINTING



ISSN: 2424-7723 (Print)
ISSN: 2424-8002 (Online)
Volume 11·Issue 4
August 2025

ACCSCIENCE PUBLISHING

ACCSCIENCE PUBLISHING

International Journal of Bioprinting

Print ISSN: 2424-7723

Online ISSN: 2424-8002

International Journal of Bioprinting is an international journal covering the technology, science and clinical application of the broadly defined field of Bioprinting. Bioprinting is defined as the use of 3D printing technology with materials that incorporate viable living cells or biological elements to produce tissue or biotechnological products. We are interested in the scientific topics spanning all stages of bioprinting process from concept creation to fabrication and beyond.



Scan to access website:

Scan to submit papers:

About the Publisher

AccScience Publishing is a publishing company based in Singapore. We publish a range of high-quality, open-access, peer-reviewed journals and books from a broad spectrum of disciplines.

Contact Us

Managing Editor
ijb.office@accscience.sg

AccScience Publishing
9 Raffles Place, Republic Plaza 1 #06-00 Singapore 048619.

Volume 11 • Issue 4 • August 2025
ISSN 2424-7723 (print) ISSN 2424-8002 (online)

INTERNATIONAL JOURNAL OF BIOPRINTING

Editor-in-Chief
Chee Kai Chua
Singapore University of Technology and Design, Singapore

ACCSCIENCE PUBLISHING
Access Science Without Barriers

Full issue copyright © 2025 AccScience Publishing
All rights reserved. Without permission in writing from the publisher, this full issue publication in its entirety may not be reproduced or transmitted for commercial purposes in any form or by any means, electronic or mechanical, including photocopying, recording, or any information storage and retrieval system. Permissions may be sought from ijb.office@accscience.sg.

Article copyright © Respective Author(s)
See articles for copyright year. All articles in this full issue publication are open-access. There are no restrictions in the distribution and reproduction of individual articles, provided the original work is properly cited. However, permission to reuse copyrighted materials of an article for commercial purposes is applicable if the article is licensed under Creative Commons Attribution-NonCommercial License. Check the specific license before reusing.

INTERNATIONAL JOURNAL OF BIOPRINTING

ISSN: 2424-7723 (print)
ISSN: 2424-8002 (online)



Editorial and Production Credits

Publisher: AccScience Publishing
Managing Editor: David Wang
Editorial Assistants: Puva Ramakrishnan, Flora Kang
Production Editor: Puva Ramakrishnan
Special Issue Commissioning Editors: Shirley Song, Terra Shi
Article Layout and Typeset: Bsmart Publishing (India)

For all advertising queries, contact ijb.office@accscience.sg.

Supplementary file

Supplementary files of articles can be obtained at https://accscience.com/journal/IJB/11/4.

Disclaimer

AccScience Publishing is not liable to the statements, perspectives, and opinions contained in the publications. The appearance of advertisements in the journal shall not be construed as a warranty, endorsement, or approval of the products or services advertised and/or the safety thereof. AccScience Publishing disclaims responsibility for any injury to persons or property resulting from any ideas or products referred to in the publications or advertisements. AccScience Publishing remains neutral with regard to jurisdictional claims in published maps and institutional affiliations.

International Journal of Bioprinting

Editorial Board

Editor-in-Chief

Chee Kai Chua
Singapore University of Technology and Design, Singapore

Associate Editors

Wai Yee Yeong
Nanyang Technological University, Singapore

Jiankang He
Xi'an Jiaotong University, China

Amit Bandyopadhyay
Washington State University, USA

Liliang Ouyang
Tsinghua University, China

Maling Gou
Sichuan University, China

Yongqiang Hao (Clinician)
Shanghai Jiao Tong University School of Medicine, China

*Editorial Board Members**

Jason A. Burdick, *USA*
Shweta Agarwala, *Denmark*
Eben Alsberg, *USA*
Anthony Atala, *USA*
Douglas B. Chrisey, *USA*
Andrea Barbetta, *Italy*
Mikhael Bechelany, *France*
Martin Birchall, *UK*
Mohd Fauzi Mh Busra, *Malaysia*
Paulo J.D.S. Bártolo, *Singapore*
Christian Celia, *Italy*
Ming-Wei Chang, *UK*
Maria Chatzinikolaidou, *Greece*
Jun Chen, *Australia*
Daniel Chen, *Canada*
Boris Chichkov, *Germany*
Dong-Woo Cho, *Korea*
Gianluca Ciardelli, *Italy*
Jeremy Crook, *Australia*
Cédric Delattre, *France*
Rui Domingues, *Portugal*
Dennis Douroumis, *UK*
Nileshkumar Dubey, *USA*
Tal Dvir, *Israel*
Eleonora Ferraris, *Belgium*
Sanjay Garg, *Australia*
Antonio Gloria, *Italy*
Manuela Gomes, *Portugal*
Brunella Grigolo, *Italy*
Michinao Hashimoto, *Singapore*
Charlotte A. E. Hauser, *Saudi Arabia*
Dong Nyoung Heo, *Korea*
Raymund E. Horch, *Germany*
Geun Hyung Kim, *Korea*
Richard James Bibb, *UK*
Jinah Jang, *South Korea*
Jingchao Jiang, *China*
Qing Jiang, *China*
Hyun-Do Jung, *Korea*
Lifeng Kang, *Australia*
Ali Khademhosseini, *USA*
Moon Suk Kim, *South Korea*
Jangho Kim, *South Korea*
Bahattin Koç, *Turkey*
Dimitrios A. Lamprou, *UK*
Junmin Lee, *South Korea*
Jin Woo Lee, *South Korea*
Shulamit Levenberg, *Israel*
Khoon Lim, *Australia*
Ki-Taek Lim, *South Korea*
Fengyuan Liu, *UK*
Xiao Liu, *Australia*
Veronica MacChi, *Italy*
Carmelo De Maria, *Italy*
Elena Martínez Fraiz, *Spain*
Laurence Meagher, *Australia*
Ferry Melchels, *Australia*
Nikolaos Michailidis, *Greece*
David K. Mills, *USA*
Vladimir Mironov, *Russia*
Mario Moisés Alvarez, *Mexico*
Maurice N Collins, *Ireland*
Makoto Nakamura, *Japan*
Seung Yun Nam, *Korea*
Roger Narayan, *USA*
Insup Noh, *Korea*
Ali Nokhodchi, *UK*

J.M.A.C. de Oliveira, *Portugal*
Aleksandr Ovsianikov, *Austria*
Sang-Hyug Park, *Korea*
Sungsu Park, *South Korea*
Alokesh Pramanik, *Australia*
Aldo R. Boccaccini, *Germany*
Michael Raghunath, *Switzerland*
Anabela Raymundo, *Portugal*
Shinji Sakai, *Japan*
Thomas Scheibel, *Germany*
Cijun Shuai, *China*
Swee Leong Sing, *Singapore*
Kedong Song, *China*
Jie Sun, *China*
Zhonghua Sun, *Australia*
Ergün Süleyman, *Germany*
Ibrahim Tarik Ozbolat, *USA*
Savas Tasoglu, *Turkey*
S. Vijayavenkataraman, *UAE*
Giovanni Vozzi, *Italy*
Liqiang Wang, *China*
Yin Xiao, *Australia*
Seung-Schik Yoo, *USA*
Barbara Zavan, *Italy*
Ioanna Zergioti, *Greece*
Yu Shrike Zhang, *USA*
Yi Zhang, *China*
Hala Zreiqat, *Australia*

Assistant Editor

Jia An, *Singapore*

Youth Editorial Board Members

Tanveer Ahmad, *Saudi Arabia*
Shivesh Anand, *USA*
Gokhan Bahcecioglu, *USA*
Gianluca Cidonio, *Italy*
Wangwang Ding, *China*
Giovanni Falcone, *Italy*
Ruben Foresti, *Italy*
Gabriele Maria Fortunato, *Italy*
Farnaz Ghorbani, *UK*
Paola Serena Ginestra, *Italy*
Xulin Hu, *China*
Anna Jezierski, *Canada*
Yiting Lei, *China*
Lan Li, *China*
Huixin Liang, *China*
Elena Marcello, *Italy*
Wei Long Ng, *Singapore*
Egor Osidak, *Russia*
Chenxi Peng, *Australia*
Rúben Pereira, *Portugal*
Mohammadmajid Sepantafar, *USA*
João Carlos Silva, *Portugal*
Yogendra Pratap Singh, *India*
Thiago Domingues Stocco, *Brazil*
Binbin Sun, *China*
Aitor Tejo-Otero, *Spain*
Danlei Zhao, *China*
Hui Zhu, *China*

*Editorial Board Members as of August 15, 2025

ACCSCIENCE PUBLISHING

Volume 11 | Issue 4 | August 2025 | Page 1 – 461 |

International Journal of Bioprinting

https://accscience.com/journal/IJB

CONTENTS

EDITORIAL

1 **Bioprinting for tissue engineering and modeling**
Xiongbiao Chen, Liqun Ning

REVIEW ARTICLES

4 **Hierarchical 3D-printed scaffolds for osteochondral regeneration: From biomimetic design to functional integration**
Qi Wang, Wei Zhu, Ruoying Wang, Xisheng Weng

32 **Three-dimensional bioprinting technologies and biomaterials for nerve guidance conduits: A review**
Yuexi Zhuang, Miriam Seiti, Eleonora Ferraris

66 **Advances in biomanufacturing and medical applications of three-dimensional-printed organoids: A review**
Lingzi Liao, Qiushi Feng, Xiaofeng Shan, Zhigang Cai, Shang Xie

99 **Three-dimensional bioprinting in human relevant toxicology: Advanced organ models and translational strategies**
Yinpeng Le, Tanqing Long, Qi Wang, Mengcheng Tang, Mingyue Pan, Qingru Song, Wenrui Ma, Yuxin Su, Yutian Feng, Ni An, Wenzhen Yin, Xiangdong Kong, Yunfang Wang, Juan Liu

133 **Advancing sustainability in bioprinting through artificial intelligence**
Hongyi Chen, Jie Huang

RESEARCH ARTICLES

154 **Precise tuning of microstructure for surface bacteriostasis using two-photon polymerization 3D printing technology**
Fang-Yi Huo, Wentao Zhu, Kan Zhou, Enduo Zhou, Lei-Ming Cao, Qian Zhu, Bo Cai, Lin-Lin Bu, Hong He

165 **Innovative design and compression performance of selective laser melting-printed tantalum artificial vertebral bodies**
Yutao Zhang, Wurikaixi Aiyiti, Jintao Li, Yong Huang, Xiaohong Dong

189 **Construction of gelatin–alginate scaffolds containing chondrocytes using 3D bioprinting technology for the study of *in vitro* cartilage senescence**
Hanxiao Qin, Fanqing Xu, Jianfeng Li, Yi Ding

209 **Painting bio: A vector-based method for precise G-code generation across scales in biofabrication**
Zan Lamberger, Camilla Mussoni, Nathaly Chicaiza Cabezas, Florian Heck, Sarah Zwingelberg, Sven Heilig, Taufiq Ahmad, Jürgen Groll, Gregor Lang

225 **High-resolution 3D printing of collagen I-based scaffolds via Schiff-base interaction for enhanced osteogenic differentiation**
Kaixuan Li, Hanxiao Huang, Peng Ge, Cailiang Shen

242 **Rapid 3D reconstruction in fetal ultrasound imaging using artificial intelligence and medical 3D printing**
Wenjuan Zhang, Jiahe Liang, Linbin Lai, Zewen Zhang, Yitong Guo, Na Hou, Zekai Zhang, Zhuojun Mao, Tiesheng Cao, Yu Li, Lijun Yuan, Airong Qian

256 **Neural cell responses to spinal implant biomaterials in a 3D-bioprinted cell culture model**
David J. Wen, Javad Tavakoli, Joanne L. Tipper

278 **Dual-strategy modification for three dimensional-printed silk methacryloyl hydrogels: Nanofiber reinforcement and poly(ethylene oxide)-induced porosity**
Bingxue Xv, Xin An, Ning Zhou, Wenxin Meng, Yvmeng Luo, Guomin Wu

297 **Three-dimensional bioprinted silk fibroin–hydroxypropyl cellulose scaffold loaded with tendon stem/progenitor cells for the prevention of heterotopic ossification following Achilles tendon injury**
Xianzong Ning, Rui Du, Minghao Zhang, Yutao Yang, Fei Yu, Xiaoming Xu, Baoyuan Meng, Kai Yan

315 **Optimizing nozzle design in extrusion-based 3D bioprinting to minimize mechanical stress and enhance cell viability**
Lorenzo Lombardi, Annachiara Scalzone, Chiara Ausilio, Piergiorgio Gentile, Daniele Tammaro

328 **Three-dimensional bioprinting of gelatin methacryloyl hydrogel with a tri-layered vascularized architecture for full-thickness skin regeneration**
Yichen Luo, Dan Li, Cai Lin, Xue Zhou, Jien Ma, Bin Zhang

350 **Immunomodulation and bone repair of 3D-printed SrBG/PCL scaffolds with PDA coating**
Qiping Huang, Xiang Li, Qinghong Fan, Qian Du, Guangquan Zhao, Yuanhao Lv, Yixiao Wang, Weikang Xu, Qingde Wa

378 **Multiscale vascularized tumor-on-a-chip via bioprinting for drug research**
Jing Liu, Ying Zhao, Bihan Ren, Dingming Li, Tianma He, Haizhongshi Zhang, Zhenlei Zhang, Haochen Liu

392 **Fabrication of an *in vitro* three-dimensional tumor model using liver-derived decellularized extracellular matrix/gelatin methacrylate bioink for investigating cancer characteristics and drug resistance**
Chunyang Zhang, Yunze Xu, Hongwei Yu, Xiaochang Lu, Ying Fang, Changyong Li, Weihong Ji, Shibin Wang, Aizheng Chen, Chaoping Fu

409 **Investigation of humidity-driven swelling–shrinking behavior of filaments in material extrusion of medical-grade biodegradable hydrogel**
Kaicheng Yu, Yifeng Yao, Qiang Gao, Le Xu, Wei Zhang, Min Zhu, Peng Zhang, Swee Leong Sing, Lihua Lu

426 **3D-bioprinted osteocytes expressing Wnt7b protect osteoblast differentiation from microgravity**
Jinling Zhang, Pengtao Wang, Xiaoling Chen, Saima Khan, Haiping Ouyang, Yangxi Liu, Bo He, Xian Li, Xing Liu, Xiaolin Tu

446 **3D printing of the keloid scar using tunable GelMA-based bioinks for skin fibrosis modeling**
Laurensia Danis Anggradita, Murugaiyan Manimohan, Sung Sik Hur, Taekyun Kim, Wonjong Seon, Mohamed Aboobucker Sithique, Seung Min Nam, Yongsung Hwang

ACCSCIENCE PUBLISHING

International Journal of Bioprinting

EDITORIAL

Bioprinting for tissue engineering and modeling

Xiongbiao Chen[1] and Liqun Ning[2]

[1]Department of Mechanical Engineering, College of Engineering, University of Saskatchewan, Saskatoon, Saskatchewan, Canada

[2]Department of Mechanical Engineering, Washkewicz College of Engineering, Cleveland State University, Cleveland, Ohio, USA

(This editorial belongs to the *Special Issue*: *Bioprinting for Tissue Engineering and Modeling*)

Bioprinting has emerged as a transformative technology in tissue engineering and regenerative medicine, enabling the precise spatial arrangement of cells, biomaterials, and bioactive molecules to fabricate complex, functional tissue constructs. This Special Issue of the *International Journal of Bioprinting*, titled "Bioprinting for Tissue Engineering and Modeling," presents six original research articles that exemplify the diversity and innovation in this rapidly evolving field. These contributions span applications in ocular drug delivery, bone regeneration, respiratory disease modeling, pluripotent stem cell expansion, bioink optimization, and multi-material printing strategies.

In the first article, Khoshnood et al.[1] developed a 3D-bioprinted gellan gum–polyethyleneimine (GG–PEI) hydrogel system loaded with betamethasone for ocular drug delivery. The constructs demonstrated favorable mechanical properties, high transparency, and sustained drug release, making them suitable for treating ocular inflammation. This study highlights the potential of bioprinting in creating personalized, site-specific drug delivery systems.

Kühl et al.[2] investigated the incorporation of nanosilicates into gelatin methacryloyl (GelMA) bioinks for digital light processing (DLP)-based bioprinting of bone constructs. Their findings revealed enhanced mechanical strength and improved mesenchymal stem cell (MSC) proliferation and osteogenic differentiation. This work underscores the importance of nanomaterial-enhanced bioinks in improving the structural and biological performance of bioprinted bone scaffolds.

Zimmerling et al.[3] presented a 3D-bioprinted respiratory disease model that simulates infection dynamics under various culture conditions. The model incorporates human bronchial epithelial cells and mimics the airway microenvironment, offering a valuable platform for studying host–pathogen interactions and evaluating therapeutic interventions. The study emphasizes the role of controlled release and microenvironmental factors in replicating disease progression.

Komosa et al.[4] addressed the challenge of pluripotent stem cell (PSC) expansion by developing a GelMA-based bioprinted construct that supports robust and reproducible PSC growth. The study systematically evaluates the influence of construct geometry, stiffness, and culture conditions on PSC proliferation and pluripotency maintenance. This work contributes to the development of scalable platforms for stem cell expansion and differentiation.

Lim et al.[5] optimized a composite bioink composed of alginate, gelatin, and dextran-aldehyde for 3D bioprinting and cell engraftment. The study demonstrates that the optimized formulation supports high cell viability, print fidelity, and tissue integration.

Citation: Chen X, Ning L. Bioprinting for tissue engineering and modeling. *Int J Bioprint*. 2025;11(4):1-3. doi: 10.36922/IJB025300302

Received: July 23, 2025
Published online: August 20, 2025

Copyright: © 2025 Author(s). This is an Open Access article distributed under the terms of the Creative Commons Attribution License, permitting distribution, and reproduction in any medium, provided the original work is properly cited.

Publisher's Note: AccScience Publishing remains neutral with regard to jurisdictional claims in published maps and institutional affiliations.

This bioink system holds promise for applications in soft tissue engineering and regenerative therapies.

Finally, Gharraei et al.[6] introduced a novel multi-material bioprinting process using a helical mixer to fabricate fibers with controlled composition. This technique enables the continuous mixing of multiple bioinks during extrusion, allowing for spatially heterogeneous constructs with tunable mechanical and biological properties. The approach opens new avenues for engineering complex tissue interfaces and gradient structures.

The field of bioprinting has witnessed exponential growth over the past decade, driven by advances in biomaterials, printing technologies, and cellular engineering. As researchers continue to refine the resolution, speed, and fidelity of bioprinting systems, the ability to replicate native tissue architecture with increasing complexity becomes more feasible. This progress is not only technological but also conceptual, as interdisciplinary collaborations between engineers, biologists, and clinicians foster innovative approaches to longstanding challenges in tissue engineering.

One of the most promising aspects of bioprinting is its potential to address the shortage of donor organs and tissues. By enabling the fabrication of patient-specific constructs, bioprinting offers a pathway toward personalized regenerative therapies. For instance, the use of patient-derived cells in bioinks can reduce the risk of immune rejection and improve integration with host tissues.[7] Moreover, the ability to customize scaffold geometry and mechanical properties allows for the creation of constructs tailored to the anatomical and functional requirements of individual patients.

In addition to therapeutic applications, bioprinting is revolutionizing the field of *in vitro* modeling. Traditional two-dimensional cell cultures often fail to recapitulate the complex microenvironment of native tissues, limiting their utility in drug discovery and disease research. Bioprinted models, by contrast, can incorporate multiple cell types, extracellular matrix components, and spatial organization, providing more physiologically relevant platforms. These models are particularly valuable for studying diseases such as cancer, fibrosis, and infectious diseases, where cell–cell and cell–matrix interactions play critical roles.[8,9]

The integration of bioprinting with other emerging technologies further expands its capabilities. For example, combining bioprinting with microfluidics enables the creation of organ-on-a-chip systems that mimic the dynamic flow conditions of the human body.[10] Similarly, the use of artificial intelligence and machine learning can optimize printing parameters and predict construct behavior, enhancing reproducibility and efficiency.[11,12] These synergies are paving the way for next-generation biofabrication platforms that are smarter, faster, and more versatile.

Despite these advancements, several challenges remain. Ensuring the long-term viability and functionality of bioprinted tissues, achieving vascularization and innervation, and scaling up production for clinical use are active areas of research. Regulatory considerations also play a crucial role, as the translation of bioprinted products from bench to bedside requires rigorous validation and standardization. Addressing these challenges will require continued investment in research, infrastructure, and interdisciplinary training.

Educational initiatives and workforce development are pivotal to sustaining the rapid advancements in bioprinting. As the field evolves, there is an increasing demand for professionals who possess interdisciplinary expertise in both biological sciences and engineering. Recognizing this need, academic institutions have begun to introduce specialized curricula and training programs in bioprinting and biofabrication. These initiatives aim to equip emerging scientists and engineers with the theoretical knowledge and practical skills necessary to innovate in scaffold design, bioink formulation, and bioprinting technologies.[13,14]

In conclusion, the articles featured in this Special Issue not only highlight the current achievements in bioprinting for tissue engineering and modeling but also point toward a future where engineered tissues and organs become integral components of medical practice. The diversity of approaches and applications presented here reflects the richness of the field and its potential to transform healthcare. We anticipate that continued collaboration, innovation, and investment will accelerate the realization of bioprinting's full potential.

Conflict of interest

Both Dr. Liqun Ning and Dr. Xiongbiao Chen are Guest Editors for this Special Issue. Dr. Xiongbiao Chen is also a co-author for two of the six papers published in this Special Issue. The authors declare they have no competing interests.

References

1. Khoshnood N, Frampton JP, Badri A, Zamanian A. 3D bioprinting of betamethasone-loaded gellan gum–polyethyleneimine composite hydrogels for ocular drug delivery. *Int J Bioprint*. 2024;10(4):3440. doi:10.36922/ijb.3440

2. Kühl J, Krümpelmann SM, Hildebrandt L, Bruhn M, Fuchs S. Nanomaterial-modified bioinks for DLP-based

bioprinting of bone constructs: impact on mechanical properties and mesenchymal stem cell function. *Int J Bioprint*. 2024;10(6):4015.
doi:10.36922/ijb.4015

3. Zimmerling A, Aubrey L, Avery K, *et al*. 3D-bioprinted respiratory disease model: exploring the importance of culture conditions and controlled release in modeling infection. *Int J Bioprint*. 2024;10(6):3895.
doi:10.36922/ijb.3895

4. Komosa ER, Lin W-H, Ogle BM. Toward robust and reproducible pluripotent stem cell expansion in bioprinted GelMA constructs. *Int J Bioprint*. 2025;11(1):363-381.
doi:10.36922/ijb.4633

5. Lim H, Seo D, Park KD, Shim H-E, Kang S-W. Optimization of alginate/gelatin/dextran-aldehyde bioink for 3D bioprinting and cell engraftment. *Int J Bioprint*. 2025;11(3):241-260.
doi:10.36922/ijb.8440

6. Gharraei R, Bergstrom DJ, Chen X. On the multi-material bioprinting process with a helical mixer for printing fibers with controlled composition. *Int J Bioprint*. 2025:025140119.
doi:10.36922/IJB025140119

7. Murphy SV, De Coppi P, Atala A. Opportunities and challenges of translational 3D bioprinting. *Nat Biomed Eng*. 2020;4:370-380.
doi:10.1038/s41551-019-0471-7

8. Avery K, Chen X. Integration of bioprinting advances and biomechanical strategies for in vitro lung modelling. *Biofabrication*. 2024;17:012006.
doi:10.1088/1758-5090/ad91e2

9. Neufeld L, Yeini E, Pozzi S, *et al*. 3D bioprinted cancer models: from basic biology to drug development. *Nat Rev Cancer*. 2022;22:679-692.
doi:10.1038/s41568-022-00514-w

10. Leung CM, de Haan P, Ronaldson-Bouchard K, *et al*. A guide to the organ-on-a-chip. *Nat Rev Methods Primers*. 2022;2:33.
doi:10.1038/s43586-022-00118-6

11. Malekpour A, Chen X. Printability and cell viability in extrusion-based bioprinting from experimental, computational, and machine learning views. *J Funct Biomater*. 2022;13(2):40.
doi:10.3390/jfb13020040

12. Chen Y, Kong M, Zhang T, *et al*. Advancing bioprinting technology utilizing portable bioprinters: from various device designs to dental applications. *Ann Biomed Eng*. 2025.
doi:10.1007/s10439-025-03789-w

13. Chen DXB. Extrusion Bioprinting of Scaffolds for Tissue Engineering, 2nd edition. Switzerland: Springer International Publishing AG; 2025.
doi: 10.1007/978-3-031-72471-8

14. Chen XB, Fazel Anvari-Yazdi A, Duan X, *et al*. Biomaterials / bioinks and extrusion bioprinting. *Bioact Mater*. 2023;28:511-536.
doi:10.1016/j.bioactmat.2023.06.006

ACCSCIENCE PUBLISHING

International Journal of Bioprinting

REVIEW ARTICLE

Hierarchical 3D-printed scaffolds for osteochondral regeneration: From biomimetic design to functional integration

Qi Wang, Wei Zhu, Ruoying Wang, and Xisheng Weng*

Department of Orthopedics, Peking Union Medical College Hospital, Chinese Academy of Medical Sciences & Peking Union Medical College, 100730 Beijing, China

(This article belongs to the *Special Issue: Advances in Bioprinting and Organ-on-a-chip and Applications for Precision Medicine*)

Abstract

Osteochondral defects, characterized by the structural and functional disruption of articular cartilage and subchondral bone, present significant clinical challenges due to the tissue's limited intrinsic regenerative capacity. Scaffold-based tissue engineering has paved the way for osteochondral defect treatment; however, fully restoring the complex structure and composition of native osteochondral tissue remains challenging. Recent advances in three-dimensional (3D) printing have enabled the fabrication of layered, anisotropic scaffolds designed to biomimetically recapitulate the native tissue's zonal properties through precise hierarchical design. High-resolution fabrication techniques facilitate the construction of delicate microarchitectures, while advanced bioprinting methods allow for the incorporation of bioactive factors and cells into the scaffold matrix. This review emphasizes the following four scaffold design paradigms: composite gradients, microarchitectural patterning, biochemical gradients, and cellular heterogeneity. Moreover, key properties of multilayered scaffolds are discussed, including mechanical performance, interfacial strength, and degradation behavior. In addition, several obstacles associated with the *in vivo* scaffold application are discussed, providing insights to guide future clinical translation in osteochondral defects treatment.

Keywords: 3D-printed scaffold; Biomaterials; Osteoarthritis; Osteochondral regeneration; Regenerative medicine; Tissue engineering

***Corresponding author:**
Xisheng Weng
(xshweng@medmail.com.cn)

Citation: Weng X, Wang R, Zhu W, Wang Q. Hierarchical 3D-printed scaffolds for osteochondral regeneration: From biomimetic design to functional integration. *Int J Bioprint*. 2025;11(4):4-31. doi: 10.36922/IJB025120100

Received: March 22, 2025
Revised: April 16, 2025
Accepted: April 28, 2025
Published online: April 28, 2025

Copyright: © 2025 Author(s). This is an Open Access article distributed under the terms of the Creative Commons Attribution License, permitting distribution, and reproduction in any medium, provided the original work is properly cited.

Publisher's Note: AccScience Publishing remains neutral with regard to jurisdictional claims in published maps and institutional affiliations.

1. Introduction

Osteochondral defect, caused by injury or various forms of arthritis including osteoarthritis (OA), imposes a growing global health burden.[1,2] Over 500 million individuals worldwide are suffering from OA,[3] making it the seventh leading cause of disability.[4] Notably, early-onset OA (diagnosed before the age of 55) accounts for over 50% of new cases,[5] indicating a growing trend of osteochondral injuries occurring in younger populations. Unfortunately, osteochondral tissue has limited self-healing capability due to cartilage avascularity.[6] Current therapeutic approaches include the following: (1) palliative treatment, such as topical or oral administration of non-steroidal anti-inflammatory drugs (NSAIDs), corticosteroid intra-articular injections, or physical

therapy for symptom relief[7]; (2) microfracture surgery, a minimally invasive option for defects less than 2 cm^2 via marrow stimulation[8]; (3) autologous or allogeneic grafts, which are limited by insufficient tissue availability and poor integration between the graft and host tissue[9]; and (4) total knee joint arthroplasty (TKA), commonly used to treat end-stage joint degeneration, but in younger patients associated with major drawbacks, including limited lifespan of the prosthesis, restricted physical function and the risk of future revision surgeries.[10-12]

Currently, conventional treatments have proven insufficient to achieve complete bone and cartilage regeneration. In recent years, 3D-printed scaffolds have been increasingly utilized for *in situ* regeneration of joint defects. Considering the layered characteristics of articular cartilage, 3D-printed hierarchical biomimetic scaffolds have garnered significant attention. This paper aims to review the recent advancements in gradient-manufactured strategies based on 3D printing, providing a novel approach for cartilage repair.

2. Natural gradient of osteochondral tissue

Native articular cartilage is a complex hierarchical tissue that transitions from a surface layer of hyaline cartilage, continuing with calcified cartilage in the deep layer, then to the subchondral osseous layer. These layers account for 90%, 5%, and 5% of the total thickness, respectively.[13] Each layer has a distinct composition, along with different microenvironment and mechanical properties. This hierarchical structure enables the joint to bear loads and serves to distribute load, absorb shock, and facilitate motion.[14]

From the surface of the articular cartilage to the subchondral bone, the structure is divided into several distinct layers: the superficial zone (SZ), middle zone (MZ), deep zone (DZ), calcified cartilage zone (CCZ), and subchondral bone (SCB). These layers not only differ in depth but also exhibit gradient features in various aspects, including composition, biochemical properties, mechanical characteristics, and topography gradient.

2.1. Content gradient

Hierarchical compositional gradients emerge across zones from the SZ to the SCB. Collagen types I/II/X, glycosaminoglycans (GAGs), proteoglycans, water, and hydroxyapatite demonstrate depth-dependent gradients, with systematic redistribution patterns.[15]

In the SZ, collagen type II exhibits lower concentration but forms densely packed, surface-parallel fibrillar networks, providing shear resistance to the surface. Progressing to the MZ, fibers adopt a loosely organized configuration, facilitating stress distribution through enhanced deformability. Collagen type II reaches maximal concentration in the DZ, with vertically oriented fibrillar bundles optimized for compressive load-bearing.[16] The CCZ undergoes a compositional shift, replacing collagen type II with type X to establish a calcified matrix for osteochondral integration.[17] This transition reverses abruptly in the SCB, where collagen type I supersedes type X as the predominant isoform. While minimally expressed in the CCZ, collagen type I becomes the dominant organic constituent in the SCB, conferring structural rigidity and tensile strength.[16]

GAGs and proteoglycans increase progressively from the SZ to the DZ, peaking in the DZ. This gradient facilitates water retention and hydrostatic pressure management, critical for load-bearing.[18] Their levels drop sharply in the CCZ as the matrix undergoes mineralization.

Water content is the highest in the SZ,[16] aiding lubrication and reducing friction. It decreases progressively through the MZ and DZ, where lower levels enhance structural strength. In the CCZ, water is nearly absent due to the predominance of mineralized matrix.

Hydroxyapatite concentration increases steadily within the CCZ, reaching its peak in the SCB. This gradient provides hardness and compressive strength to the mineralized regions.[16]

These gradient distributions ensure a seamless mechanical and structural transition between cartilage and bone, supporting the functional integrity of the joint.

2.2. Biochemical gradient

The extracellular matrix (ECM) creates a specialized microenvironment that supports tissue metabolism, repair, and growth, mediated by biomolecular factors such as transcription factors, cytokines, and signaling molecules.[19] Gene expression regulated by these factors varies across osteochondral layers, with zone-specific markers supporting the specialized functions of each region. Articular cartilage and subchondral bone exhibit distinct molecular biology profiles that support their specialized functions. In the SZ, key biomolecular factors such as aggrecan, collagen type II alpha-1 chain (COL2A1), and SOX9 display peak expression levels. Aggrecan and COL2A1 are critical for maintaining cartilage mechanical integrity, while SOX9 regulates chondrocyte differentiation and maturation.[20] Moving to the MZ and DZ, these factors decrease, reflecting a shift from cartilage synthesis to mineralization processes. Concurrently, bone morphogenetic protein-2 (BMP2) and collagen type X alpha-1 chain (COL10A1) are upregulated, driving chondrocyte differentiation into osteoblast-like progenitors[21] and promoting matrix calcification.[22] Alkaline

phosphatase (ALP), a key enzyme in mineralization, is selectively enriched in these zones, underscoring their role in cartilage maintenance and mineralization.[23]

In the CCZ, osteogenesis factors like COL10A1, ALP, and Runx2 are most highly expressed.[24] Runx2, a key osteogenic transcription factor, drives the transition of hypertrophic chondrocytes into osteoblast-like cells, facilitating ossification. Vascular endothelial growth factor (VEGF), a critical angiogenic factor, ensures vascular invasion, necessary for bone formation.[25] These gradients promote the mineralization and ossification of the cartilage matrix, thereby bridging cartilage and bone.

In the SCB, factors like osteocalcin, osteopontin (OPN), Receptor Activator for Nuclear Factor-κ B Ligand (RANKL), and matrix metalloproteinases (MMPs) are concentrated, reflecting bone mineralization, remodeling, and resorption.[26,27] Osteocalcin and OPN are involved in bone matrix formation, while RANKL regulates osteoclast differentiation for bone resorption. MMPs, key for ECM turnover, are highly expressed in the SCB, where active bone remodeling occurs.[28,29] The distribution of osteochondral substances is listed in Table 1.

2.3. Mechanical gradient

The mechanical properties of cartilage layers exhibit a depth-dependent pattern,[30] with each stratum fulfilling specialized biomechanical functions that correlate with the compositional gradients and microstructural organizations described in **Section 2.1**. The SZ, characterized by the lowest compressive modulus, maintains joint flexibility through its unique architecture: fine fibers of collagen types II/IX aligned parallel to the articular surface,[30] coupled with densely packed, flattened disc-shaped chondrocytes arranged horizontally,[2] collectively create a low-friction interface that minimizes shear stress. The MZ exhibits transitional viscoelastic properties, enabled by its randomly oriented thicker collagen bundles forming a porous scaffold, where sparsely distributed spherical chondrocytes facilitate stress redistribution and energy dissipation. The DZ achieves maximal compressive resistance through perpendicularly aligned hypertrophic collagen fibrils relative to the articular surface, accompanied by spherical chondrocytes organized into columnar arrays parallel to the collagen orientation. The CCZ demonstrates ultimate stiffness through mineralized collagen networks, firmly anchoring the cartilage to the SCB while preventing mechanical delamination.[6] This hierarchical mechanical stratification, evolutionarily conserved across mammalian articular cartilage systems, enables efficient stress transmission through depth-specific structural adaptations, ensuring optimal joint functionality and biomechanical stability.

Table 1. Gradient distribution of biochemical factors in articular cartilage

Substance	Function	Distribution
Aggrecan	Enhances cartilage strength and elasticity	High in SZ; low in DZ
COL2A1	Provides cartilage structural integrity	High in SZ; decreases toward CCZ
SOX9	Maintains chondrocyte phenotype	Predominantly active in SZ; reduced in deeper layers
TGF-β	Regulates cell proliferation and ECM synthesis	High in MZ; lower in deeper layers
BMP2	Promotes chondrocyte-to-osteoblast differentiation	Low in SZ and MZ; high in DZ and CCZ
COL10A1	Marker of cartilage mineralization	Present in DZ; high in CCZ
ALP	Promotes mineralization	High in DZ and CCZ
VEGF	Promotes angiogenesis	High in DZ; present in CCZ
Runx2	Promotes cartilage-to-bone conversion	Highest in CCZ
Osteocalcin	Involved in bone mineralization	Present in SCB; high in CCZ
OPN	Involved in bone mineralization and cell adhesion	High in SCB
RANKL	Stimulates osteoclast differentiation	High in SCB
MMPs	Degrades ECM components; aids in tissue remodeling	High in SCB

Abbreviations: ALP, alkaline phosphatase; BMP2, bone morphogenetic protein-2; COL2A1, collagen type II alpha-1 chain; COL10A1, collagen type X alpha-1 chain; CCZ, calcified cartilage zone; DZ, deep zone; ECM, extracellular matrix; MMPs, matrix metalloproteinases; MZ, middle zone; OPN, osteopontin; RANKL, receptor activator of nuclear factor-κB ligand; SCB, subchondral bone; SZ, superficial zone; TGF-β, transforming growth factor β; VEGF, vascular endothelial growth factor.

Niu et al.[31] quantified depth-dependent mechanical gradients in rabbit articular cartilage, reporting Young's modulus progression from the SZ (0.4–0.6 MPa) through the MZ (0.6–1.0 MPa) to the DZ (2.0–3.0 MPa). This mechanical gradient was corroborated in porcine cartilage by Sun et al.,[32] who documented analogous depth-related variations with SZ (0.8 MPa), MZ (2.0 MPa), and DZ (3.6 MPa) Young's modulus values.

The mechanically vulnerable regions within cartilage tissue also correspond to distinct histological microstructural features. A distinct calcified cartilage band, referred to as the "tidemark," separates the DZ from the CCZ, marking the mineralization front of the calcified cartilage. Continuous collagen fibrils pass through the tidemark, hence serving as a transitional interface between calcified and non-calcified cartilage and facilitating the gradual transition of tissue mineralization.[33] The boundary between the CCZ and the SCB is demarcated by the "cement line." The absence of continuous collagenous connections between the CCZ and the SCB renders this region biomechanically vulnerable.[34].Furthermore, the pronounced stiffness changes between the CCZ and SCB are hypothesized to be a key factor underlying the delamination of cartilage from the bone, particularly under shear stress conditions.[35] This steep variation in mechanical properties creates localized stress concentrations, exacerbating the risk of tissue failure at the cartilage–bone interface.[36]

The progression of OA is characterized by progressive reductions in both elastic modulus and stiffness of articular cartilage.[37] Emerging evidence suggests that early-stage OA may involve biomechanical precursors, including stiffening of the DZ and diminished SCB stiffness, prior to overt cartilage degeneration.[38] Furthermore, the elastic modulus of cartilage demonstrates a significant correlation with OA severity grades.[39] Quantitative analyses reveal substantial mechanical degradation in advanced OA, exemplified by the SZ Young's modulus reduction from 26.51 ± 10.63 MPa in healthy cartilage to 18.58 ± 9.61 MPa in severe OA specimens. Concurrently, both aggregate modulus and shear modulus exhibit significant decreases in moderate-to-severe OA, particularly within the SZ and MZ, indicative of compromised load-bearing capacity.[40]

3. Hierarchy establishment strategies for osteochondral regenerating scaffold

Over the past decade, hierarchical 3D-printed scaffolds have emerged as a predominant strategy for osteochondral regeneration. Advances in fabrication technologies have spurred the development of multiphase design strategies to mimic zonal tissue complexity. Hierarchical 3D printing strategies are systematically categorized as follows (Figure 1): (1) composite gradient defined as methodologies that achieve stratified functionality through layer-specific variations in material composition and physicochemical properties; (2) microarchitectural gradient characterized by the implementation of function-specific structural configurations across distinct layers to regulate anisotropic mechanical or nutrient transport behaviors; (3) biochemical gradient entailing spatio-temporal control of biochemical factors within layered constructs to achieve zonal biological responses; and (4) cell heterogeneity involving heterogeneous seed cell populations within discrete strata to emulate native tissue. Recent research efforts have focused on optimizing these hierarchical architectures, with key zone-specific fabrication approaches systematically categorized in Table 2.

3.1. Composite gradient

Composite gradient architectures have become a predominant methodology for engineering scaffold hierarchical organization. This paradigm employs biphasic or multiphasic systems integrating distinct biomaterials, each engineered to address zone-specific mechanical and functional demands. Typical designs incorporate the following: (1) a bioactive, elastomeric, and porous phase for chondral regeneration; and (2) a mechanically reinforced, slow-degrading phase replicating subchondral bone properties.

Materials commonly used for the chondral layer include natural biomaterials such as collagen, hyaluronic acid (HA),[65] sodium alginate (SA),[66] agarose,[67] cellulose,[41] and silk fibroin (SF).[68] These natural materials provide an optimal environment for cell adhesion, proliferation, and growth. However, their mechanical and physicochemical properties may not always be sufficient for tissue engineering applications, leading to the increased use of synthetic materials like polyethylene glycol (PEG),[69] polycaprolactone (PCL), polylactic acid (PLA),[70] gelatin methacrylate (GelMA),[71] and polyethylene glycol diacrylate (PEGDA).[43] These synthetic materials can be modulated during the synthesis process to achieve desired properties. Despite superb mechanical properties, they lack integrin-binding ligands, which limits direct interaction with cells.

Ceramic materials, which are inorganic and non-metallic, are typically characterized by their superb hardness and brittleness. Notable ceramic materials used for osteochondral regeneration include hydroxyapatite (HAp),[72] biphasic calcium phosphate (BCP),[73] tricalcium phosphate (TCP),[57] and bioactive glass (BG).[41] They exhibit favorable biocompatibility and porosity, promoting cell infiltration and tissue integration.[41] Furthermore, inorganic ions released by ceramic materials, such as silicon (Si), lithium (Li), and magnesium (Mg) ions, can

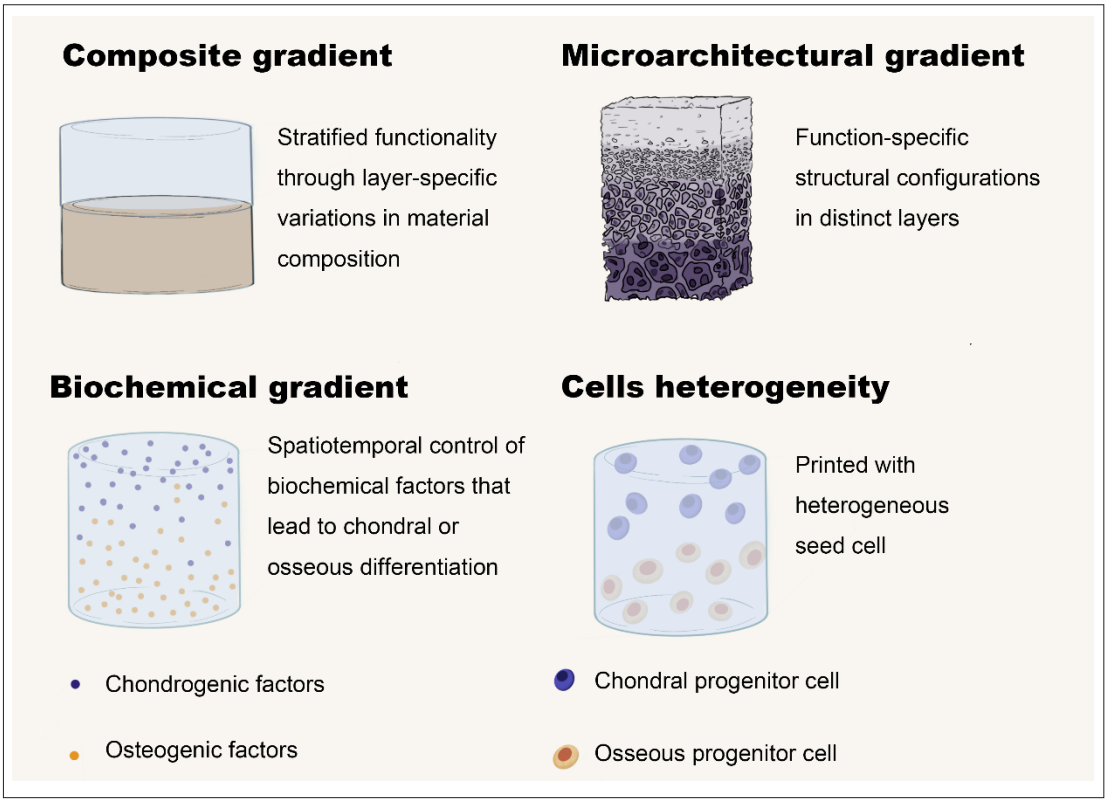

Figure 1. A schematic diagram of natural gradient classification for osteochondral tissue.

promote osteochondral regeneration. Li ions have been shown to stimulate chondrogenesis by upregulating exosomal miR-455-3p in bone marrow mesenchymal stem cells (BMSCs).[74] Mg ions and Mg transporter subtype 1 protein (MagT1) enhance osteogenic differentiation in rBMSCs.[75] Si ions promote angiogenesis by modulating the expression of insulin-like growth factor-1 (IGF-1) and VEGF.[76] However, the use of ceramic materials is limited due to their asynchronized degradation relative to bone regeneration.[77]

Due to the zonal mechanical strength of normal cartilage, which is adapted to different functions, providing layered mechanical support during the repair process and achieving biomimetic repair outcomes are crucial. It has long been established that the growth of both cartilage and bone tissues, both *in vivo* and *in vitro*, is influenced by the surrounding mechanical strength.[78,79] Cells can sense and respond to variations in substrate stiffness, thereby regulating their diffusion, proliferation, and gene expression.[80] Yang et al.[81] fabricated HAp and PEG/SF composites with different stiffness levels and induced osteogenesis in rBMSCs, revealing a positive correlation between stiffness and the expression of osteogenic markers. Cao et al.[82] demonstrated that the matrix stiffness-sensitive miR-99b regulates the osteogenic and adipogenic differentiation of BMSCs by targeting the rapamycin signaling pathway. Similarly, Lai et al.[83] demonstrated that substrate stiffness modulates BMSCs proliferation via exosome-mediated mechanotransduction through Yes-associated protein (YAP) pathways.

Scaffolds with a lower elastic modulus (~10 MPa) inhibit the regeneration of the SCB while promoting the formation of fibrous tissue at the articular interface. In contrast, scaffolds with a higher elastic modulus (~1000 MPa) may compress the opposing cartilage, leading to its degradation.[84] Consequently, scaffolds with biphasic mechanical properties have been extensively studied to improve the healing of both bone and cartilage. Diloksumpan et al.[45] developed a triple-layer scaffold using extrusion-based printing and melt electrospinning writing (MEW). The top chondral layer consists of a PCL mesh infused with GelMA hydrogel, while the middle layer, composed of a PCL mesh and polymer-calcium phosphate (PCaP) composite, is designed to replicate the structure of calcified cartilage for chondral-osseous transition. The osseous layer is fabricated from PCaP. Each layer was designed to adapt to its specific mechanical demand. Gao et al.[47] established a bilayer scaffold based on GelMA, where

the osseous layer was optimized by incorporating HA into the GelMA matrix, thereby enhancing the compressive modulus for bone formation.

3.2. Microarchitectural gradient

Native cartilage exhibits a gradient in microarchitectural patterning, encompassing variations in geometry, porosity, stiffness, and density,[85] which are essential for maintaining its mechanical properties, as described in **Section 3.2**. Meanwhile, the porous structure plays a crucial role in cell adhesion, metabolism, and proliferation, which are critical for spatial organization and tissue regeneration in tissue engineering. Conventional fabrication techniques—such as solvent casting, freeze-drying, electrospinning, and gas foaming—can produce well-structured scaffolds, yet they lack precise microstructural control. Key factors include pore size,[60] shape, distribution,[61] and density.[86] In contrast, 3D printing offers a highly adaptable approach for designing scaffolds that closely replicate the native cartilage microarchitecture.

Previous studies have demonstrated that neo-tissue regeneration predominantly initiates at the defect periphery, whereas central regions often exhibit compromised regeneration capacity due to reliance on cellular migration through the scaffold matrix.[87] Proper microstructures (e.g., pores or channels) provide mechanical support and guidance for cell migration,[88] while simultaneously facilitating nutrient transportation and bioactive factor release. Gu et al.[61] developed a biomimetic bilayer scaffold using digital light processing (DLP)-based 3D printing. The upper cartilage layer features a "lotus and radial" pore distribution that facilitates the transverse migration of chondrocytes and cartilage progenitor cells at superficial layers. The bottom osseous layer exhibits a "lotus" pore structure, guiding BMSCs to vertically migrate to the defect site, thus creating a native tissue-like cell distribution pattern. *In vitro* experiments demonstrated a preference for cell migration along the delicate "lotus and radial" pore structure (Figure 2), resulting in nearly a fourfold increase in cell migration compared to non-porous scaffolds.

Microarchitectural features of biomaterials also regulate cell differentiation.[89,90] Events such as cell–cell interactions, adhesion molecule binding, gap junction formation, and cytoskeletal reorganization, significantly impact chondrogenic differentiation.[91,92] Larger pore sizes promote the aggregation and proliferation of MSCs, facilitating chondrogenic condensation.[60] Li et al.[93] demonstrated that pore sizes in 3D-printed silica hybrid scaffolds critically regulate human BMSCs (hBMSCs) lineage commitment: pores of ~100 μm resulted in poor matrix formation, ~220 μm promoted hyaline cartilage formation through predominant collagen type II deposition, while ~500 μm triggered fibrocartilaginous commitment characterized by collagen type I dominance. Pore sizes around 200 μm promote the maintenance of a spherical cell morphology, facilitating cell–cell interactions, whereas, larger pore sizes encourage cell attachment, reducing intracellular contact. Conversely, smaller pores may not provide sufficient space for ECM production. It has been reported that spherical-shaped BMSCs correlate with higher expression of chondrogenic molecular markers and are more likely to undergo chondrogenic differentiation.[94]

Sun et al.[60] further revealed that pore size modulates BMSCs differentiation by activating the Hypoxia-inducible factor 1α/Focal Adhesion Kinase (HIF1α/FAK) signaling axis. A layered-mesh structured, BMSCs-laden PCL scaffold was fabricated, in which the superficial small-pore zone (SPZ, 150 μm) provides lubrication and shear resistance, while the deep large-pore zone (LPZ, 750 μm) enhances elasticity and maintains structural rigidity. The SPZ exhibited high HIF1α expression, promoting chondrogenesis and maintaining a hyaline cartilage phenotype, whereas the LPZ favored osteogenesis and increased vascularization (Figure 3).

3.3. Biochemical gradient

In scaffold-based osteochondral defect repair, biomimetic strategies for cell-free scaffolds involve *in situ* tissue regeneration through precise coordination of MSC recruitment, differentiation, and maturation. For cell-laden scaffolds, directing cells to undergo specific differentiation at various layers is equally crucial for successful repair. Thus, biochemical factors, functioning as chemoattractants, need to be applied in a spatially distributed manner to regulate cell behavior and optimize tissue regeneration.[95]

Biochemical gradient strategies involve adding growth factors or small molecules to induce cell differentiation. These can be incorporated directly into the material for bioprinting or delivered through carriers such as exosomes or nanoparticles. Additionally, decellularized ECM (dECM) is used to create biochemical gradients.

Growth factors are a large family of cytokines that regulate cell migration, adhesion, proliferation, and differentiation. For cartilage, transforming growth factor (TGF)-β1, IGF-1, fibroblast growth factor-2 (FGF-2), and BMP-2 support maturation and formation, while BMPs, IGF-1/2, TGF-β, and FGFs are primarily involved in bone regeneration.[96] These growth factors are spatially distributed and function in a coordinated manner, working synergistically to promote tissue development and repair. Ding et al.[52] developed a hydrogel scaffold covalently functionalized with bioactive TGF-β1 binding peptides (TBP) to recruit endogenous TGF-β1, thereby

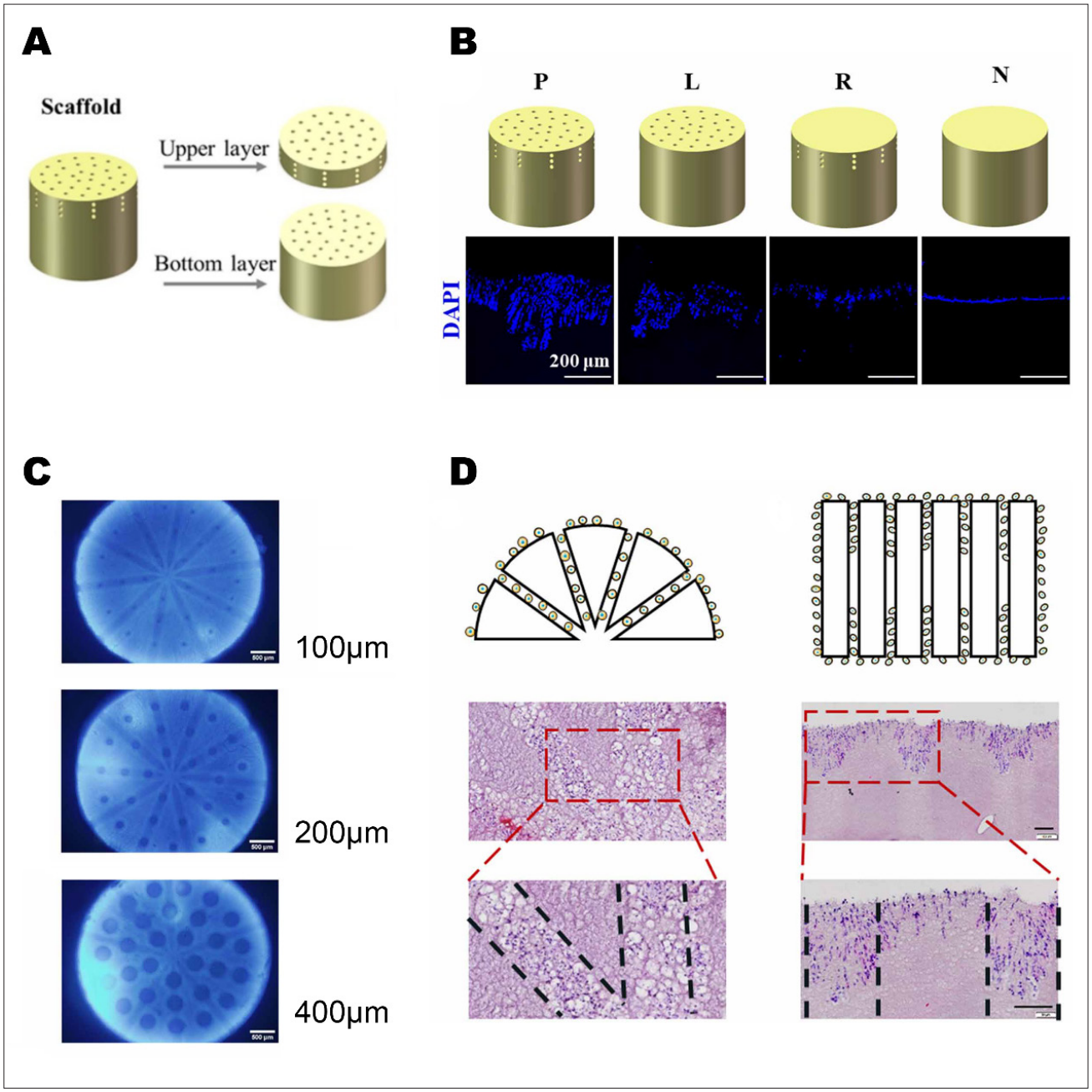

Figure 2. Evaluation of cell infiltration in bilayer scaffolds with different pore architectures. (A) Schematic design of the bilayered scaffold. (B) Representative fluorescent images (DAPI staining) showing cell infiltration into scaffolds 5 days after subcutaneous implantation *in vivo* (scale bar = 200 μm). (C) Fluorescent images of bilayer scaffolds with different longitudinal pore sizes. (D) Schematic illustration and H&E staining images of the P group scaffold in horizontal (left) and vertical (right) sections (scale bar = 100 μm). Black dashed lines indicate pore boundaries in the magnified views. Among all groups, the P group exhibited the greatest cell infiltration depth and the highest number of infiltrating cells, indicating that the combined pore architecture most effectively facilitates cell migration into the scaffold. Group definitions: P = lotus + radial pores; L = lotus pores only; R = radial pores only; N = non-porous scaffold. Reproduced from Ref.[61], Biofabrication (2024), with permission from IOP Publishing.

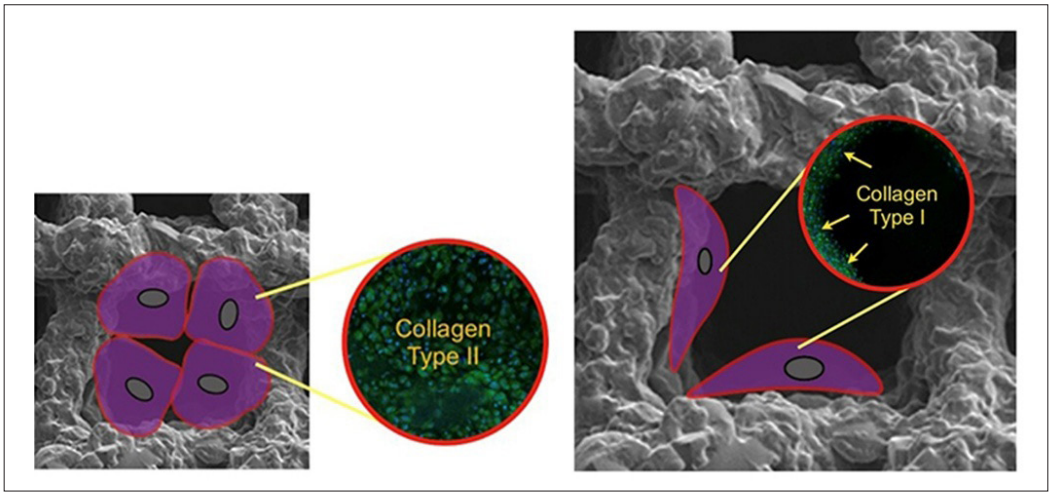

Figure 3. Effect of scaffold pore size on cell morphology and differentiation. hBMSCs cultured in 3D-printed silica hybrid scaffolds exhibited different morphologies depending on the channel size. In scaffolds with smaller channel sizes (~230 μm), cells showed a rounded morphology and underwent chondrogenic differentiation, with widespread expression of type II collagen matrix indicating a hyaline cartilage phenotype. In contrast, in scaffolds with larger pores (~500 μm), cells adopted a spindle-shaped morphology and predominantly expressed type I collagen, suggesting fibrocartilage formation. Reproduced from Ref.[93] with permission from the Royal Society of Chemistry.

enhancing cartilage regeneration. Similarly, Kilian et al.[62] introduced a core-shell bioprinting strategy to fabricate a bilayer scaffold. The chondral layer consists of a human chondrocyte (hChon) shell surrounding a TGF-β3 core, while the osseous layer comprises a human osteoblast (hOB) shell encapsulating a BMP-2 core. This core-shell system enables the spatially controlled delivery of specific cell types and differentiation factors within distinct compartments of the hydrogel strands, promoting targeted tissue regeneration.

The dECM, derived from human or animal tissues, is another biochemical gradient strategy widely used in tissue engineering. It primarily contains ECM macromolecules.[97] The decellularization process preserves the physicochemical signals and biological properties of native tissue, providing a native-like microenvironment that supports the migration, proliferation, and differentiation of BMSCs. Studies have shown that BMSCs embedded in cartilage dECM (DCM) or bone dECM (DBM) hydrogels interact with the adjacent matrix, promoting chondrogenic or osteogenic differentiation and subsequent tissue maturation. However, the mechanical properties of dECM are suboptimal due to the loss of native tissue topography during the decellularization process,[98,99] resulting in delamination, which hinders its application in larger cartilage defect regeneration. Zhang et al.[42] developed a bilayer scaffold using dECM as bioink and enhanced its mechanical properties with SF. The DCM and DBM layers were modified with TGF-β1 and BMP-2, respectively. This scaffold demonstrated promising osteochondral regeneration, exhibiting suitable mechanical strength and degradation rates at the same time. Furthermore, Joyce et al.[100] reinforced an ECM-derived collagen-hyaluronic acid (CHyA) matrix with a 3D-printed PCL framework to enhance mechanical strength to adapt to physiological loads. The PCL reinforcement increased the compressive modulus of the CHyA matrix threefold, which aligned with the physiological range (0.5–2.0 MPa) of healthy cartilage. It also improved the tensile modulus and allowed for suture fixation to the subchondral bone, thereby enhancing scaffold-bone integration. *In vitro* study demonstrated that MSCs were successfully infiltrated the scaffold, leading to significantly higher expression of sGAG.

Small molecules are widely applied in osteochondral engineering to induce cell differentiation, regulate osteoblast/osteoclast function, or exert anti-inflammatory effects. Kartogenin (KGN), which promotes chondrocyte differentiation in a dose-dependent manner,[101] provides a feasible approach to establish biochemical gradients. Wei et al.[55] developed an osteochondral scaffold embedded with BMSCs, exhibiting a high concentration of KGN in the chondral layer and a low concentration of KGN with β-TCP in the osseous layer. Dexamethasone, another small synthesized glucocorticoid molecule,[102] can promote osteogenesis and chondrogenesis by stimulating MSC differentiation into osteoblasts and chondrocytes via Wnt/β-catenin and TGF-β pathways. Its anti-inflammatory properties reduce inflammation, aiding tissue healing. Barrera et al.[103] developed a biomimetic surface coating for implants, applying a layer-by-layer technique to create

Table 2. Hierarchical strategies for 3D-printed osteochondral scaffolds

Scaffold design	Strategy	Seed cell	Manufacturing method	Mechanical properties	*In vivo* model	Reference
wCartilage: Pure cellulose ink Osseous: 58S BG-filled cellulose ink	Composite	Cell-free	Extrusion-based printing	Tensile strength: 5.22 MPa Fracture energy: 1.81 MJ/m^3 Compressive strength: 11.8 MPa	Rabbit	[41]
Cartilage: DCM/SF-TGF-β1 Osseous: PCL + DBM/SF-BMP2	Composite biochemical	BMSCs	Extrusion-based printing	Compressive stress: 44 kPa (cartilage), 47 kPa (osseous without PCL), 310 kPa (osseous with PCL) CM: 9-fold enhancement with PCL applied	Rabbit	[42]
WWCartilage: PCL-HAp Osseous: PHA + PEGDA + DVC	Composite	Cell-free	Extrusion-based printing	YM: 269 ± 20 MPa (PCL), 67% increase in PCL-HAp Flexural stiffness: 206% increase in PCL-HAp (compared to PCL)	Goat	[43]
Cartilage: SA-dNC-$CaCl_2$ Osseous: SA-GelMA-nHA- $CaCl_2$	Composite	Cell-free	Extrusion-based printing	CM: 94.64 ± 5.27 kPa (G-dNC/nHA), 89.12 ± 15.2 kPa (G-nHA control), 70.55 ± 4.29 kPa (G-control) Shear strength: maximum in G-dNC/nHA G: Gradient	Rat	[44]
Cartilage: PCL mesh + GelMA Intermediate: MEW mesh + PCaP Osseous: PCaP	Composite	BMSCs	MEW + extrusion-based printing	CM: 17.7 ± 2.0 kPa *In vivo* interface adhesion strength: 6.6 ± 1.7 kPa (Day 1), 24.4 ± 6.5 kPa (Day 42)	N/A	[45]
Top: MeHA + diclofenac sodium Cartilage: MeHA + BMSCs/PCL + KGN Osseous: PCL + β-TCP	Composite biochemical (KGN)	BMSCs	Layer-by-layer alternate bioprinting	EM: 85 ± 10 MPa (cartilage), 185 ± 15 MPa (osseous) S: 55 ± 5 N/mm (cartilage), 110 ± 8 N/mm (osseous) Maximum stress: 1.5 ± 0.1 MPa (cartilage), 3.0 ± 0.2 MPa (osseous)	Rat	[46]
Cartilage: GelMA Osseous: GelMA-HAp (1% w/t)	Composite	Cell-free	Continuous 3D printing	CM: 300 ± 50 kPa (cartilage), 500 ± 70 kPa (osseous)	Rabbit	[47]
Cartilage: PLGA + fibrin Intermediate: PLCL + CS/BG Osseous: Calcium silicate ceramic	Composite biochemical	BMSCs	Electrospinning + extrusion-based printing	CM: 0.54 ± 0.04 MPa (cartilage), 33.6MPa (osseous) YM: 5.1 ± 0.8 MPa (intermediate)	Rabbit Minipig	[48]
Cartilage: SF Osseous: PEGT/PBT mesh+ porous silk	Composite	Cell-free	FDM + extrusion-based printing	CM: 0.12 ± 0.01 MPa (cartilage), 12.56 ± 1.94 MPa (osseous), 0.113 ± 0.028 MPa (fibrin scaffold)	N/A	[49]
Top: PGS-CS Bottom: Gelatin	Composite	Cell-free	FDM + extrusion-based printing	CM: 0.162 ± 0.005 MPa (PGS, dry); 0.159 ± 0.003 MPa (PGS, wet); 1.139 ± 0.052 MPa (PGS-Gel, dry); 0.195 ± 0.007 MPa (PGS-Gel, wet); 2.443 ± 0.071 MPa (PGS-CS/Gel, dry); 0.315 ± 0.019MPa (PGS-CS/Gel, wet)	Rabbit	[50]
Cartilage: TPU + Gel-Alg Osseous: PLA + HAp	Composite	Cell-free	FDM + extrusion-based printing	CM: 1.079 ± 0.031 MPa (cartilage), 44.369 ± 2.515 MPa (osseous), 21.336 ± 3.683 MPa (total) Shear strength: 0.73 ± 0.027 N YM: 45 MPa (PLA/HAp), 1 MPa (TPU)	Rabbit	[51]

(Continued....)

Table 2. Continued...

Scaffold design	Strategy	Seed cell	Manufacturing method	Mechanical properties	*In vivo* model	Reference
Cartilage: SF Osseous: PEGT/PBT mesh + porous silk	Biochemical (TGF-β1 binding)	Cell-free	UV crosslinking + peptide grafting	CM: 120 kPa (GelMA) TGF-β1 binding peptides reduce the CM.	Rat	[52]
Upper: PGS-CS Bottom: Gelatin	Biochemical (dECM + exosome)	Cell-free	Extrusion-based printing	Reduced modulus: 6.3 ± 0.4 MPa (bilayer hydrogel-exosome), 5.7 ± 0.3 MPa (bilayer hydrogel)	Rat	[53]
Cartilage: TPU + Gel-Alg Osseous: PLA + HAp	Biochemical (thiolated heparin / strontium nanoparticle)	eUCB-MSC	High-throughput microfluidics-based fabrication	CM: approximately 2 MPa of PEGT-PBT scaffold	N/A	[54]
Cartilage: GelMA + KGN (high concentration) Osseous: GelMA + KGN (low concentration)	Biochemical (KGN)	Cell-free	Sequential bioprinting	CM: 190 ± 15 kPa (cartilage), 210 ± 20 kPa (osseous). Interfacial shear strength: 40 kPa.	Rat	[55]
Cartilage: GelMA + DCM Osseous: GelMA + DBM	Biochemical (dECM)	Murine osteoblast/ chondrogenic cell precursors	DLP	CM increased with the incorporation of dECM (data not specified)	N/A	[56]
Cartilage: GelMA + BP + hUMSCs exosome Osseous: GelMA + BP + hUMSCs exosome + β-TCP	Biochemical (phosphate)	Cell-free	Extrusion-based printing	CM: 48.99 ± 15.67 kPa (3% β-TCP-GelMA). YM: 232.86 ± 12.45 kPa (1% β-TCP), 306.17 ± 17.82 kPa (3% β-TCP)	Rabbit	[57]
Cartilage: PEGDA (1MPa) Osseous: PEGDA (7MPa),	Structural (geometry/ porosity)	Cell-free	SLA/ DLP	S: 1 MPa (cartilage), 7 MPa (osseous) Porosity: cartilage 81% (cartilage), 68% (osseous) CM: 11.8 MPa	N/A	[58]
Bi-phasic: Infill density 45% and 60% Tri-phasic: Infill density 30%, 45% and 60% Gradient: Infill density from 30% to 60%; smooth transition in 7 layers	Structural (infill density)	C28/I2 hChon	Concurrent printing + FDM	CM 397.24 ± 41.51 MPa (bi-phasic, 45%); 213.75 ± 32.17 MPa (bi-phasic, 60%); 397.24 ± 41.51 MPa (bi-phasic, total); 228.98 ± 40.84 MPa (tri-phasic, 30%); 140.56 ± 21.73 MPa (tri-phasic, 45%); 118.99 ± 29.13 MPa (tri-phasic, 60%); 228.98 ± 40.84 MPa (tri-phasic, total). Gradient:177.98 ± 44.78 MPa (total)	N/A	[59]
4 layers PCL scaffold with different pore sizes infilled with cell-laden hydrogel	Structural (pore size)	BMSCs	FDM	Pore size of four layers: 150, 350, 550, and 750 μm	Rabbit	[60]

(Continued....)

Table 2. Continued...

Scaffold design	Strategy	Seed cell	Manufacturing method	Mechanical properties	*In vivo* model	Reference
Cartilage: GelMA (lotus/radial pores) + KGN Osseous: GelMA (lotus pores)	Structural (geometry) + biochemical (KGN)	Cell-free	DLP	CM: 388.0 ± 17.52 kPa (15% GelMA, 0 μm porosity); 344.3 ± 16.50 kPa (15% GelMA, 100 μm porosity); 302.0 ± 15.00 kPa (15% GelMA, 200 μm porosity); 203.3 ± 10.41 kPa (15% GelMA, 400 μm porosity); 178.0 ± 7.211 kPa (10% GelMA, 0 μm porosity); 157.3 ± 6.429 kPa (10% GelMA, 100 μm porosity); 139.0 ± 5.568 kPa (10% GelMA, 200 μm porosity); 107.3 ± 3.055 kPa (10% GelMA, 400 μm porosity)	Rabbit	[61]
Cartilage: hChon + Alg-MC + TGF-β3 Osseous: hOB + Alg-MC + BMP-2	Cell heterogeneity + biochemical	hChon, hOB	Extrusion-based printing	N/A	N/A	[62]
Cartilage: ACPCs + GelMA/AlgMA Osseous: BMSCs + GelMA/AlgMA	Cell heterogeneity + biochemical	ACPCs, BMSCs	Extrusion-based printing	YM: ~ 15 kPa.	Rabbit	[63]
Cartilage: PCL/gelatin/fibrin Osseous: PCL/HA nanoparticles	Composite	Cell-free	Extrusion-based printing	Compressive strength: 2.1 MPa (10% fibrin), 0.81 MPa (30% fibrin)	N/A	[64]

Abbreviations: ACPCs, articular cartilage progenitor cells; Alg, alginate; AlgMA, methacrylated alginate; BG, bioactive glass; BMP2, bone morphogenetic protein-2; BMSCs: bone marrow-derived mesenchymal stem cells; CM, compressive modulus; CS, chondroitin sulfate; DBM, decellularized bone matrix; DCM, decellularized cartilage matrix; DLP, digital light processing; dECM, decellularized extracellular matrix; EM, elastic modulus; eUCB-MSC, expanded umbilical cord blood-derived mesenchymal stem cells; FDM, fused deposition modeling; GelMA, gelatin methacrylate; HAp, hydroxyapatite; hChon, human chondrocytes; hOB, human osteoblasts; KGN, Kartogenin; MC, methylcellulose; MEW, melt electrowriting; MeHA, methacrylated hyaluronic acid; PCL, polycaprolactone; PCaP, polymer calcium phosphate; PEGDA, polyethylene glycol diacrylate; PEGT/PBT, poly(ethylene glycol)-terephthalate/poly(butylene terephthalate); PGS, poly(glycerol sebacate); PLA, polylactic acid; PLCL, poly(L-lactide-co-caprolactone); PLGA, poly(lactic-co-glycolic acid); S, stiffness; SA, sodium alginate; SF, silk fibroin; SLA, stereolithography; TCP, tricalcium phosphate; TGF, transforming growth factor; TPU, thermoplastic polyurethane; YM, Young's modulus.

a polyelectrolyte multilayer (PEM) system, which was coated with dexamethasone-loaded liposomes. The study demonstrated that the involvement of dexamethasone-loaded liposomes exhibited more prominent chondrogenic differentiation compared to the baseline PEM system.

Gene therapy offers a promising strategy for osteochondral regeneration by delivering genes essential for cartilage and bone repair or silencing pathological genes associated with joint disease, creating a gene expression gradient to achieve zonal cell differentiation.[104] Commonly used genes include growth factors such as IGF-1,[105] TGF-β,[106,107] BMP,[21] and FGF; transcription factors such as SOX9; and anti-inflammatory molecules like interleukin (IL)-10[108] and IL-1 receptor antagonist (IL-1RA).[109] Traditional gene delivery often relies on viral vectors.[110] Despite their efficiency, viral vectors face limitations, including pre-existing immunity to viruses like adenovirus, which reduces their effectiveness. Additionally, the limited duration of transgene expression, lasting approximately only 1–2 weeks, hinders long-term use *in vivo*.[110] Therefore, non-viral vectors, such as nanoparticle carriers and mRNA delivery, are gaining attention as promising alternatives.

MicroRNAs (miRNAs) have introduced a novel approach to gene therapy due to their ability to precisely regulate the spatial and temporal expression of target genes and associated pathways, which are crucial for chondrogenesis and cartilage development.[111] Notably, reduced levels of miR140-5p have been observed in progenitor/stem cells (CPCs) from OA cartilage, indicating a correlation with OA progression.[112] Exosomes, with low immunogenicity, targeted delivery, and excellent biocompatibility, could serve as a promising carrier for miRNA delivery in gene therapy.[113] Nanoparticles, featuring a porous organosilicon structure, efficiently encapsulate and deliver miRNA with temporal release. Zhu et al.[114] developed a self-healing hydrogel loaded with

Mesoporous organosilicon-Polyethyleneimine (MON-PEI) nanoparticles for stable miRNA140-5p transfection, showing effective cartilage defect repair in a rabbit joint model.

3.4. Cells heterogeneity

Cell-laden hydrogel 3D printing has gradually drawn attention in the last decade. Cells employed for osteochondral regeneration include MSCs, such as BMSCs and adipose-derived stem cells (ADSCs), articular cartilage progenitor cells (ACPCs), and induced pluripotent stem cells (iPSCs).[115] MSCs show low immunogenicity and good *in vivo* safety, becoming the most widely used cell in regenerative medicine.[116] Although technically pluripotent, MSCs rarely repair damaged tissue *in vivo* through direct differentiation and engraftment due to certain limitations, including the reduced capacity of these cells for self-renewal, proliferation, and differentiation in donor sites.[117] Besides, BMSCs are inclined to differentiate into bone tissue rather than cartilage.[118,119] Therefore, scaffolds require the modulation of differentiation through cytokines or drugs. However, the side effects associated with cytokines, combined with their high costs, present significant limitations for their clinical use *in vivo*. For example, although TGF-β is proven to induce chondral differentiation, Zhen et al.[120] reported that overactivation of the TGF-β1 pathway in subchondral bone may lead to pathological changes associated with cartilage degeneration. Furthermore, the release kinetics and half-life of small molecules *in vivo* restrict their long-term therapeutic efficacy.[121] Therefore, a bicellular scaffold could be a promising approach for tissue regeneration. Bicellular scaffolds enable precise spatial cell alignment by delivering the cells during the printing process, rather than relying on intrinsic cell migration. Furthermore, the bicellular system enhances tissue function and structural reconstruction through cell–cell interactions, enabling the synchronous repair of different tissues.[63]

Möller et al. demonstrated that co-encapsulation of hBMSCs and human nasoseptal chondrocytes (hNCs) within GelMA hydrogels for 3D bioprinting resulted in more pronounced ECM deposition compared to hBMSCs alone.[122] Wu et al.[123] developed a bicellular 3D-printed liver lobule-mimetic structure, demonstrating that the HepG2 + NIH/3T3 bicellular system enhanced HepG2 proliferation and function compared to monocellular systems, which can be attributed to crosstalk pathways via NIH/3T3-secreted cytokines and growth factors. The bicellular model better mimics the physiological microenvironment, improving cell–cell/matrix interactions and enhancing functionality.

Zhang et al. developed a bicellular anisotropic hydrogel scaffold using 3D printing. ACPCs were incorporated into the upper hydrogel layer to simulate cartilage, while BMSCs were placed in the lower layer for bone regeneration. The 3D printing technique enabled precise, layer-specific placement of cells, facilitating independent functionality and spatial alignment of cartilage and bone. ACPCs and BMSCs promote cartilage and bone formation through the secretion of specific growth factors and ECM components. Cell–cell interactions simultaneously stabilize the cartilage–bone interface, with BMSCs in the osseous layer driving both bone matrix production and angiogenesis, thus enhancing nutrient supply. Vascular penetration into the cartilage layer is suppressed by the cartilage matrix secreted by ACPCs, maintaining low vascularization within the cartilage.

4. Pivotal properties of scaffolds for *in vivo* application

4.1. Degradation rate

During osteochondral repair, scaffolds must provide temporary and adequate mechanical support to the defect site while degrading at a controlled rate to allow regenerated tissue to replace the scaffold and integrate with surrounding tissue. *In vivo*, osteochondral regeneration typically progresses through the following stages[123]: (1) the inflammatory stage, where immune cells remove dead cells from the damaged tissue to establish a foundation for regeneration; (2) the proliferating stage, lasting approximately 2–6 months, during which endogenous cells migrate to the injury site as the scaffold degrades, proliferate, differentiate, and gradually replace the scaffold; and (3) the remodeling stage, during which the biophysical properties of the newly formed tissue further enhance and replace the scaffold to become the predominant load-bearing component. This stage could last several months. Throughout the process, the biophysical properties of the newly formed tissue improve as the scaffold's mechanical support diminishes, establishing a dynamic balance that preserves the mechanical stability of the osteochondral tissue.[124] Therefore, the degradation kinetics of scaffolds must synchronize with tissue growth.[125] Meanwhile, since bone has higher mechanical support requirements than cartilage, the degradation rate of bone-phase scaffolds is typically slower than that of cartilage-phase. *In vitro* studies reveal that the cartilage phase degrades almost completely within approximately 12 weeks, aligning with cartilage regeneration, while bone-phase scaffolds require a longer degradation period, typically 16–24 weeks or more.[47,48,54]

The degradation rate of scaffolds is influenced by multiple aspects, including chemical composition, geometric structure, porosity, and microenvironment. Blending two or more polymer materials is a common

way to regulate the degradation kinetics. For instance, incorporating HAp[54] and β-TCP nanoparticles[55] into GelMA hydrogels can reduce the degradation rate for bone-phase scaffolds. Gao et al.[54] improved the degradation performance of GelMA scaffolds by adding 1% HAp. *In vitro,* phosphate-buffered saline (PBS) degradation tests showed that scaffolds without HAp exhibited more than 70% weight loss after 4 weeks, while those with HAp degraded by only 50%. dECM can also retard the degradation rate. Li et al.[53] evaluated the residual mass percentage and revealed a significant reduction in the degradation rate with the addition of dECM. Bejarano et al.[126] reported that incorporating BG into the poly(D, L-lactic acid) (PDLLA) polymer could accelerate the degradation rate while simultaneously maintaining the scaffold's dimensional and structural integrity.

Degradation kinetics of scaffolds are influenced by their mesostructure, including factors such as porosity, pore size, pore shape, grain size, and crystallinity. A higher porosity generally leads to an increased degradation rate,[127] as scaffolds with more micropores and a larger surface area facilitate the diffusion of degradation products, thereby accelerating the process. Larger pores also allow better penetration of degradation products and moisture, promoting cell growth and tissue infiltration, which further speeds up degradation.[127,128] Conversely, smaller grain sizes reduce the degradation rate because they increase the grain boundary area, hindering the diffusion of degradation products and enhancing the material's strength.[129]

The inflammatory microenvironment, including cytokines and enzymes, can significantly influence the degradation rate. In the microenvironment of OA, a wide range of enzymes and cytokines undergo significant alterations. Notably, MMP families, which are capable of cleaving collagen type II, play a pivotal role in cartilage degradation.[130] Liu et al.[46] established a triple-layer scaffold consisting of BMSC-laden methacrylated HA (MeHA), PCL, and KGN as the chondral layer, coated with a MeHA plus diclofenac sodium layer, and a PCL plus β-TCP osseous layer. MeHA, a rapidly degradable material, has a tunable degradation rate influenced by enzymes such as MMPs. MMP-sensitive MeHA allows for the modulation of degradation rate and surface drug release in response to disease activity, such as inflammation in arthritis.

To estimate the degradation rate, weight loss is a standard approach for *in vitro* studies, where scaffolds are incubated in simulated body fluid or PBS for 12 weeks, and the remaining mass is measured periodically.[42,48,54,55] *In vivo*, histological evaluation is commonly employed to monitor scaffold degradation and tissue formation at the defect site, providing insights into the material's biological performance over time.[47]

4.2. Interlaminar interface strength

In *in vivo* studies, mechanical stability is considered a critical factor for successful regeneration. Beyond the intrinsic mechanical properties of scaffolds, interface strength—another crucial element—plays a pivotal role in ensuring the efficacy of the repair process. This encompasses two key aspects: the strength of the interlaminar interface (horizontal integration),[131] and integration with native tissue (lateral integration).[132]

During scaffold-based regeneration of osteochondral defects, the interface between the cartilage and bone phases is prone to stress concentration due to the discontinuity in their mechanical properties.[133] Therefore, tissue engineering scaffolds need to achieve an effective integration between cartilage and bone tissue.

However, bilayered or multilayered scaffolds are often ineffective in biomimicking osteochondral tissue due to the potential for delamination between layers.[134] Current strategies for enhancing interlaminar interface strength can be broadly categorized into the following approaches: (1) interlamellar bonding, (2) mechanical interlocking through contact surface topography design, (3) tissue culture with cell seeding, and (4) specified 3D printing techniques.

Bonding is a traditional method to integrate two layers, which can be achieved through chemical bonding or solvent bonding. The dual-phase interface can be modified by introducing reactive group-containing agents that form chemical bonds between components and the biopolymer matrix through chemical interactions. Coyle et al.[56] developed a bilayer dECM-incorporated GelMA scaffold, in which the double layers were chemically bonded using 1-ethyl-3-(3-dimethylaminopropyl) carbodiimide/ N-hydroxysuccinimide (EDC/NHS) coupling. EDC activates the carboxyl groups on the GelMA hydrogels, generating highly reactive O-acylisourea intermediates, which are stabilized by NHS. These intermediates then react with primary amines on the second hydrogel layer, forming amide bonds and effectively conjugating the layers. This method ensures strong covalent bonding, enhancing the structural integrity and interface compatibility of the composite material.

Liuyun et al.[135] designed a method for modifying nano-HAp with the assistance of L-lysine, and incorporated the modified HAp into poly(lactic-co-glycolic acid) (PLGA) to fabricate nanocomposites. L-lysine bonds to the HAp surface through the formation of a calcium-carboxylate linkage between the calcium of HAp and

the carboxylate group of L-lysine, thereby improving the interface compatibility between the HAp particles and the PLGA matrix.

Interlocking is a mechanical bonding method where material surfaces engage through geometric features such as grooves, hooks, or ridges, thereby enhancing adhesion and structural integrity without the need for adhesives or chemical bonding. 3D printing, as a high-precision manufacturing technique, is ideal for creating interlocking surfaces. When utilizing FDM or stereolithography (SLA) to print materials with varying properties, interlocking designs can be incorporated to strengthen the interlayer adhesion.[43] According to the review by Nedrelow et al.[136] focusing on scaffold interface design, interlocking a robust 3D-printed bone phase with a cartilage phase hydrogel is the most effective method for enhancing the interface strength. Diloksumpan et al.[45] created a bilayer scaffold with an interlocking interface design. The bone phase consisted of a bone-biomimetic ceramic ink containing tricalcium phosphate, nanohydroxyapatite, and a custom-synthesized biodegradable poloxamer, while the cartilage phase was composed of MEW-printed PCL microfibers and gelatin-based hydrogel loaded with chondroprogenitor cells. During printing, the PCL microfibers interlaced with the ceramic matrix, protruding into the cartilage region. This spatially organized arrangement enabled mechanical interlocking between the bone and cartilage phases. Compared to non-interlocking designs, the adhesion strength between the composite hydrogel and ceramic increased by over 6.5 times. The fiber within the ceramic scaffold enables more effective lateral constraint of the hydrogel under axial compression, resulting in a stronger mechanical response.

Although interface strength can be enhanced through bonding strategies, it remains inferior to that of native mature bone-cartilage boundaries.[137] Hence, using cell-laden materials to induce *in situ* regeneration at the defect site may offer a promising solution. Current scaffold designs still suffer from uneven cell distribution. The inability to precisely control cell placement and spatial alignment often results in discrepancies in cell density, potentially compromising the efficacy of tissue repair.[138] ECM secretion by cells may help to create a more harmonious interface. Wang et al.[139] designed a cell-based strategy to improve integration and transition between cartilage and osseous layers by sandwiching a human umbilical cord mesenchymal stem cells (hUCMSCs) layer between the constructs before suturing. Histological and immunohistochemical analyses showed more uniform ECM distribution in the cell-loaded constructs, while the control group exhibited V-shaped gaps at the interface due to a lack of cells and ECM.

Co-printing involves the simultaneous or sequential deposition of different materials within a single 3D printing process, enabling the creation of complex, functional structures, and interfaces. This requires 3D printers with multiple print heads, each capable of handling distinct materials.[136] Continuous 3D printing provides another approach to enhance the mechanical properties.[140] In continuous 3D printing, the print head deposits successive material layers without interruption, ensuring seamless integration and smooth transitions between materials. This method effectively eliminates the interface misalignment or gaps often seen in traditional layer-by-layer printing.[47]

4.3. Scaffold-native tissue integration

The mechanical discontinuity at the scaffold-native tissue interface significantly hinders integration. Yodmuang et al.[141] that interface strength before mechanical loading and shear stresses within the scaffold during loading are key determinants of integration. Periodic axial forces of 1 and 6 N were applied to the scaffold to simulate the contact stress experienced by cartilage during daily activities and their effects on scaffold–cartilage interface integration were evaluated. The results indicated that 1 N loading resulted in poor integration between the scaffold and cartilage, whereas 6 N loading significantly enhanced interface strength, demonstrating that higher loading intensity more effectively promotes integration. This effect may be attributed to increased shear and interface stresses, which facilitate scaffold–cartilage cell adhesion and accelerate cell and matrix migration and proliferation. Moreover, high-intensity loading improves mechanical matching between the scaffold and cartilage; simulates physiological loading; and enhances cartilage cell migration, ECM synthesis, and cross-linking. It also activates cellular mechanosensing pathways, promoting cell proliferation, differentiation, and exosome secretion. However, the detailed mechanisms are not yet illustrated; hence, studies devoid of mechanical analysis may lack translational relevance for clinical applications.

Crosslinking of ECM between the scaffold and native tissue can enhance integration. Zhao et al.[142] present a multifunctional scaffold loaded with lysyl oxidase (LOX) plasmid DNA, exosomes, and manganese dioxide nanoparticles (MnO_2 NPs). LOX facilitates ECM crosslinking, strengthening the mechanical bonding between the scaffold and tissue. Concurrently, MnO_2 NPs efficiently scavenge excess ROS at the injury site, preventing ECM degradation and thereby potentiating the crosslinking activity of LOX.

Cell-laden scaffolds offer a promising way to enhance scaffold–tissue integration. Claramunt et al.[143] developed a polyurethane meniscal scaffold coated with fibronectin. The

quality of the newly formed meniscal tissue was assessed *in vivo* by the rabbit model. Compared to scaffolds without MSC loading, the incorporation of MSCs into the scaffold significantly improved scaffold integration, proteoglycan synthesis, and the mechanical properties of the newly formed tissue. Similarly, Chung et al.[144] demonstrated that hUCMSCs-laden 4% HA hydrogel significantly enhanced cartilage quality histologically, achieving a remarkable collagen pattern and cell arrangement that closely resemble the structure of adjacent native cartilage.

4.4. Evaluation assays for interface strength

The interlaminar interface strength can be evaluated mechanically or histologically. For example, in the interface shear test, the osseous phase is fixed while a lateral force is applied to the chondral phase.[36] In contrast, the lap shear test relies on sandwiching the bilayer scaffold between two tabs, with both surfaces of the scaffold being stuck to the tabs with adhesive. The laps are then subjected to tensile loading in opposite directions.[145] Additionally, interface strength can be evaluated using the peel test, in which the chondral phase is gripped and a force perpendicular to the interface is applied to induce delamination from the osteal phase.[146] Compared to the interface shear test, the lap shear test requires extra clamping or adhesive bonding of the scaffold, which may introduce additional artifacts in evaluation.[36] While the peel test provides insight into interface strength, its loading condition failed to replicate *in vivo* scenarios. Given these considerations, the interface shear test is generally regarded as the most appropriate method for evaluating interface strength.[136] Additionally, histological studies can reveal the tissue growth pattern, including cell density, cell alignment, and ECM, which can serve as an important reference for assessing interface integration.[139]

The integration efficacy between the scaffold and native tissue can be quantitatively assessed through mechanical evaluation. Specifically, the push-out test serves as a standardized assay to determine interfacial adhesion strength, in which an axial compressive load is applied parallel to the scaffold–tissue interface until interfacial failure occurs. The maximum load at failure is recorded and normalized to the total surface area of the scaffold's luminal interface, enabling the calculation of the ultimate interfacial shear strength.[141] This parameter provides a quantitative measure of the biomechanical integrity at the scaffold–tissue interface (Figure 4).

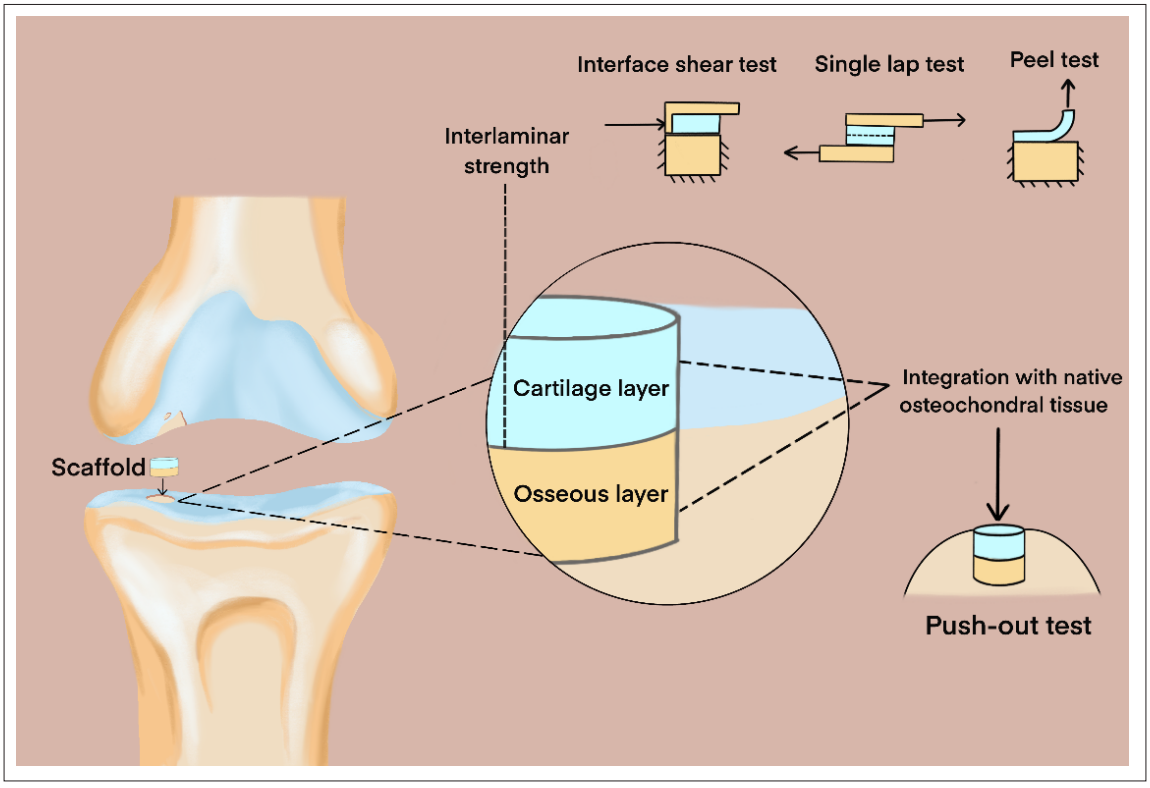

Figure 4. Evaluation assays for interlaminar and integration strength for bilayer scaffold.

5. Discussion

5.1. 3D printing methodology

With the development of bioprinting methods and ink materials compatible with bone engineering, various 3D printing techniques have been applied to fabricate osteochondral scaffolds. Conventional 3D printing, such as SLA, FDM, and selective laser sintering (SLS), involves layer-by-layer deposition of materials. In contrast, 3D bioprinting creates 3D artificial implants or complex tissues through layer-by-layer deposition of living cells, ECM, and other biomaterials. Common techniques for bioprinting include inkjet-based bioprinting, extrusion-based bioprinting, and laser-assisted bioprinting.[147]

As shown in the studies of hierarchical printed scaffolds in Table 2, scaffolds employing different strategies tend to adopt specific 3D printing technologies. Extrusion-based printing is the most commonly used method across all strategies. Extrusion-based bioprinting is compatible with a wide variety of materials and does not involve a heating process, making it particularly suitable for printing materials with high cell densities and biological activity.[147,148] Due to nozzle size limitations, extrusion- and inkjet-based 3D printing can only produce microstructures at a minimum scale of 100 μm.[58] However, the fine strain within the cartilage changes at a length scale ranging from 10 to 100 μm.[149,150]

In contrast, scaffolds designed with a microarchitectural gradient strategy tend to apply SLA and DLP,[60,61,58,59] as these printing methods offer higher resolution and can create finely detailed microstructures.[151,152] In particular, microstereolithography (μSLA) enables layer-by-layer fabrication of high-resolution constructs with spatially programmable mechanical properties. By precisely regulating exposure parameters (e.g., duration, light intensity), this technique achieves *z*-axis control over both microstructure and compressive modulus at 10–50 μm resolution.[58,153] Such precision facilitates the development of biomimetic osteochondral scaffolds replicating native tissue's hierarchical mechanical gradients. The characteristics of various printing technologies are summarized in Table 3.

In addition to manufacturing the structure of the scaffold itself, creating fine micro-structures at the interlayer interfaces using high-precision 3D printing techniques also positively impacts the interfacial bonding strength. **Section 4.2** discusses methods to enhance interface strength through interlocking design. The interlocking features created by high-resolution methods,

Table 3. Comparison of 3D printing technologies for osteochondral scaffold design

Technology	Advantages	Disadvantages	Materials
Inkjet-based printing[147,154,155]	Low cost High cell viability High throughput	Limited resolution Non-continuous printing Nozzle clogging Heat damage to cells	Low-viscosity biomaterials (<20 mPa·s)
Extrusion-based printing[62,148,150,156]	Broad range of bioink selection Short fabrication time High cell density and ≠viability	Limited resolution Shear stress damage to cells	Compatible with a wide range of materials
Laser-based printing[157]	High resolution High cell viability and density Nozzle-free	High cost Long fabrication time Relatively low 3D built-up capability	Photocurable resins/nanocomposites Wide range of viscosities
SLA[158,159]	High resolution Layer thickness adjustable Smooth surface finish	Limited materials High cost Post-processing required	Resins only
FDM[73,151,160,161]	Quick fabrication Low-cost Strong layer bonding	Limited materials Limited resolution	Molten thermoplastic material only
DLP[61,162]	High resolution	Limited materials Slow fabrication	Photopolymers
MEW[45,155]	Ultra-fine fiber production Precise porosity control	Limited materials High cost Slow fabrication	Thermoplastic conductive polymers

Abbreviations: DLP, digital light processing; FDM, fused deposition modeling; MEW, melt electrospinning writing; SLA, stereolithography.

such as MEW,[45,163] enhance the structural stability during both the processing and implantation stages.[145]

5.2. Cell-free versus cell-laden strategies

Over the past decade, notable progress has been achieved in cell-free scaffold-mediated *in situ* osteochondral regeneration. However, critical unresolved challenges persist, including: (1) structural incompatibility between scaffolds and defect topography, (2) inadequate recruitment of endogenous host cells, and (3) suboptimal remodeling of neo-formed tissues.[164] The limited diffusion capacity of oxygen and nutrients within conventional scaffolds, compounded by progressive peripheral mineralization, establishes a diffusion barrier that restricts cellular infiltration to superficial regions.[165] This results in preferential survival of cells localized near the scaffold surface, while deeper regions remain sparsely populated. Bioprinting with cell-laden materials offers a promising alternative by enabling precise spatial deposition of pre-seeded cells within scaffolds. However, a fundamental limitation persists in maintaining the long-term viability and functional persistence of encapsulated cells, particularly under sustained physiological stresses.[166]

Ongoing research should focus on biomaterial optimization to achieve biomimetic cell alignment, density, and ECM patterns to better resemble native tissue.

5.3. Vasculature in osteochondral regeneration

During *in vivo* osteochondral regeneration, angiogenesis serves as a prerequisite for osteogenesis, as neo-vasculature provides indispensable metabolic support for bone-forming cells.[167] Inadequate vascularization results in hypoxic microenvironments and cellular necrosis. Oxygen diffusion constraints restrict metabolically active osteoblasts/osteocytes to within 100–200 μm of functional capillaries to sustain viability and biosynthetic activity.[168] Cartilage, however, must preserve avascularity to avoid pathological ossification and complications, necessitating precise spatial regulation of vascularization in scaffold-based osteochondral regeneration. Current approaches focus on dual-pathway control: pro-angiogenic growth factors such as VEGF and bFGF[169,170] are selectively incorporated into subchondral regions to stimulate vascular infiltration, while anti-angiogenic compounds (e.g., suramin and bevacizumab)[171,172] are embedded within cartilaginous zones to inhibit ectopic vessel formation. Besides this biochemical strategy, a physical barrier—typically a semipermeable membrane engineered to block endothelial cell migration while permitting metabolic exchange—is interposed between osteochondral layers to anatomically restrict vascular encroachment into cartilage layers.[167]

Cell-laden scaffolds can demonstrate dual angiogenic modulation through both direct angiogenic differentiation and paracrine signaling mechanisms. Qin et al.[173] established a pre-vascularized scaffold by encapsulating human umbilical vein endothelial cells (HUVECs) within Li-Mg-Si (LMS) ceramic-incorporated GelMA scaffolds. This design significantly enhanced angiogenic functionality, evidenced by robust neovascularization through both HUVEC-derived capillary network formation and amplified VEGF secretion. Notably, the endothelial paracrine profile concurrently stimulated neurogenic precursor proliferation and bone marrow stromal cell osteogenic differentiation, thereby establishing a multifunctional regenerative microenvironment.

Cellular regulation of angiogenesis demonstrates zonal specificity in osteochondral regeneration. Zhang et al.[63] engineered an anisotropic bilayer scaffold by spatially embedding ACPCs in chondral layers and BMSCs in osseous layers. During regeneration, ACPCs maintained avascularity through paracrine secretion of anti-angiogenic factors (e.g., endostatin, chondromodulin-1) and transcriptional downregulation of pro-angiogenic factors (e.g., VEGF, EGF). Meanwhile, osteogenic-phase BMSCs promoted vascular invasion via sustained release of angiogenic signals (e.g., ANGPT1, VEGFA, endomucin), which stimulated endothelial cell proliferation, chemotaxis, and lumenogenesis through ERK1/2-MMP9 pathway activation. Similarly, Liang et al.[174] engineered GelMA-alginate core-shell microcapsules for dual encapsulation of human dental pulp stem cells (hDPSCs) and HUVECs. Compared to monoculture groups containing either hDPSCs or HUVECs alone, co-cultured groups exhibited elevated proliferation rates. Notably, 3D capillary-like networks formed in all hDPSC-containing co-culture microcapsules, regardless of cell ratio, with significant increases vasculogenesis markers after 14 days of culture (e.g., percentage vascular area, branch length, branch number, and junction points). In contrast, hDPSC-deficient groups showed no vasculogenesis at day 14, demonstrating the essential role of intercellular interactions during vascularization. Given the persistent challenge of vascularizing osteochondral interfaces, scaffolds designed with a cell heterogeneity strategy offer a promising way to address this critical limitation in tissue engineering.

5.4. Inflammatory microenvironment *in vivo*

Osteochondral defects are often accompanied by inflammatory alterations in the local microenvironment. The persistent presence of an inflammatory environment is a major obstacle to cartilage repair, as it may limit the recruitment of endogenous cells to the site, ultimately leading to the failure of *in situ* cartilage regeneration.[175]

Therefore, improving the inflammatory microenvironment at an early stage should be prioritized to achieve better repair outcomes. The alleviation or deterioration of inflammatory markers can reflect the repair status, including the following: (1) pro-inflammatory cytokines, such as IL-1β, IL-6, IL-8, and tumor necrosis factor-alpha (TNF-α); (2) macrophage polarization (M2/M1 ratio) assessed by flow cytometry[176]; (3) immune cell infiltration (e.g., T lymphocytes, neutrophils) assessed by immunostaining[43]; and (4) oxidative stress levels, such as reactive oxygen species (ROS),[177] lipid peroxidation products (e.g., malonaldehyde),[178] and antioxidant enzyme activities (e.g., superoxide dismutase, catalase).[179]

As an implanted foreign material, the inflammatory response induced by scaffolds should be considered. Most studies reviewed in this article did not focus on inflammation-related responses. Nedrelow et al.[43] observed CD4+ T cell infiltration following scaffold implantation; however, this does not necessarily indicate the level of inflammation.[180] Li et al.[86] quantitatively analyzed IL-1β levels after implantation, finding a significant increase in the early stage (1 week), which gradually decreased after 4 weeks, suggesting that scaffold implantation induces a mild inflammatory response during the early phase.

The balance between anti-inflammatory and pro-inflammatory pathways within the microenvironment is closely associated with macrophage phenotypes. M1 phenotype generates ROS and inflammatory cytokines.[181,182] ROS directly degrades the chondral ECM, inducing lipid peroxidation and DNA fragmentation, thereby imposing significant limitations and challenges for scaffold-based tissue regeneration.[183] Hence, the concept of ROS-scavenging hydrogels has been proposed to enhance the efficacy of scaffold-based tissue regeneration. Current strategies for ROS scavenging include: (1) anti-inflammatory small-molecule drugs,[175] such as NSAIDs; (2) integration of antioxidant nanoparticles[184]; (3) incorporation of antioxidant enzymes (e.g., catalase) or nano enzymes[184,185]; and (4) fabrication of scaffolds using bioactive materials with inherent antioxidant properties.[186–189]

Liu et al.[183] incorporated cerium oxide nanoparticles functionalized with cerium bifunctional albumin (CeNPs) into GelMA, which counteracted the toxic effects induced by hydrogen peroxide. 2′,7′-dichlorofluorescein diacetate (DCFH-DA) and dihydroethidium (DHE) staining confirmed a reduction in ROS. Furthermore, the scaffold promoted the activation of the PI3K/Akt/EBV1 pathway, facilitating the polarization of gliogenic cells toward the anti-inflammatory M2 phenotype. Deng et al.[190] utilized human hair-derived antioxidant nanoparticles (HNPs) and microparticles (HMPs). These bioactive nanoparticles protected chondrocytes from oxidative stress-induced damage by scavenging ROS, while simultaneously stimulating the HIF-1α and glucose transporter (GLUT) signaling pathways to promote chondrocyte proliferation and maturation.

Combining ROS-scavenging agents with anti-inflammatory drugs demonstrates synergistic efficacy in alleviating inflammatory progression.[191] Lu et al.[192] developed a dual-layer hydrogel system co-loaded with diclofenac sodium and BMSC-derived exosomes. During the early phase, the ROS-responsive upper layer degrades and releases diclofenac, which rapidly improves the inflammatory microenvironment by suppressing lipoxygenase activity, nuclear factor kappa β (NF-κβ) signaling, and M1 macrophage polarization. Subsequently, the sustained release of exosomes promotes cartilage repair. *In vitro* and *in vivo* analyses confirmed reduced expression of pro-inflammatory M1 markers, inhibition of ECM degradation-related genes, and upregulation of cartilage repair-associated genes.

5.5. *In vivo* animal model verification

Osteochondral repair research utilizes animal models across the following different size categories: small rodents (murine and rat models),[193] intermediate species (rabbits and canines),[42] and large animal models (ovine, caprine, equine, and porcine).[194] Current studies predominantly employ small animal models, particularly rabbits and murines, for *in vivo* experimentation. These models offer practical advantages, including short experimental timelines, low maintenance cost, simplified husbandry, and feasibility for large-scale study.[193]

However, there are notable differences between small animals, large animals, and humans, in terms of joint size, load-bearing capacity, anatomical features, and tissue repair potential, which limits the translational relevance of small animal models. For example, human articular cartilage is typically 2–4 mm thick, whereas rabbit cartilage is only 0.25–0.75 mm,[195] and murine cartilage is even thinner. The area of cartilage defects also varies significantly with body size. Strategies effective in small animals may be inadequate to support larger defects, presenting a major challenge. Furthermore, osteochondral defects in rodent models tend to undergo spontaneous repair,[193] which may lead to an overestimation of scaffold efficacy.

Guinea pigs, which exhibit spontaneous cartilage degeneration similar to humans and lack the ability for spontaneous cartilage repair, are widely used as OA models. However, the anatomical features of their knee joints differ significantly from humans and the medial compartment of their knees bears increasing load during movement.[195]

Generally, the knee joints of small animals are in a highly flexed position, unlike in humans.[196] Additionally, humans engage in a wider range of movements—such as walking, squatting, and stair climbing—that generate different mechanical stress patterns on the knee joint compared to animals. Therefore, while experimental success in small animal models is valuable, a gap remains in clinical translation.

In contrast, large animals such as pigs, goats, and horses exhibit biomechanical features and joint sizes that are more similar to humans.[194,197] Validation in these models can provide more clinically relevant data. Nevertheless, significant interspecies differences persist. For example, only the human knee achieves full extension, a feature not observed in common large animal models.[197] Therefore, clinical translation of osteochondral repair strategies requires careful adaptation to human physiological and biomechanical characteristics.

6. Conclusion

Osteochondral defects remain difficult to repair due to the complex structure and specialized function of osteochondral tissue. Recent advances in 3D printing have enabled the fabrication of hierarchical scaffolds that better mimic native tissue and support zone-specific regeneration. This review has highlighted four key strategies—composite gradients, microarchitectural patterning, biochemical gradient, and cellular heterogeneity—as essential approaches to achieving functional hierarchical design. Despite progress, challenges like degradation mismatch, poor interface integration, and inflammatory responses still limit clinical translation. Future research should prioritize the development of stimuli-responsive biomaterials, validation in large-animal models, and the integration of multi-material bioprinting technologies to further advance scaffold-based osteochondral repair.

Acknowledgment

The graphical abstract was created using BioRender.com.

Funding

This work was supported by the Natural Science Foundation of Beijing, China (Grant No. 7232119), the Beijing Natural Science Foundation (Grant No. L232006), Peking Union Medical College Hospital Talent Cultivation Program (Grant No. UHB11847), the National High Level Hospital Clinical Research Funding (No. 2022-PUMCH-C-036), and the National Natural Science Foundation Youth Fund (Grant No. 82102582).

Conflicts of interest

The authors declare no competing interests.

Authors' Contributions

Conceptualization: Qi Wang, Wei Zhu
Writing-Original Draft: Qi Wang
Writing-Review & Editing: Qi Wang, Wei Zhu
I*nvestigation*: Qi Wang, Ruoying Wang
Resources and supervision: Xisheng Weng

Ethics Approval and Consent to Participate

Not applicable

Consent for Publication

Not applicable

Availability of Data

Not applicable

References

1. Mahmoudian A, Lohmander LS, Mobasheri A, Englund M, Luyten FP. Early-stage symptomatic osteoarthritis of the knee - time for action. *Nat Rev Rheumatol*. 2021;17(10):621-632. doi: 10.1038/s41584-021-00673-4

2. He B, Wu JP, Kirk TB, Carrino JA, Xiang C, Xu J. High-resolution measurements of the multilayer ultra-structure of articular cartilage and their translational potential. *Arthritis Res Ther*. 2014;16(2):205. doi: 10.1186/ar4506

3. Soderquist M, Barnes L. Osteochondral allograft transplantation for articular humeral head defect from ballistic trauma. *JSES Rev Rep Tech*. 2024;4(3):540-546. doi: 10.1016/j.xrrt.2024.04.008

4. GBD 2021 Osteoarthritis Collaborators. Global, regional, and national burden of osteoarthritis, 1990-2020 and projections to 2050: a systematic analysis for the Global Burden of Disease Study 2021. *Lancet Rheumatol*. 2023;5(9):e508-e522. doi: 10.1016/s2665-9913(23)00163-7

5. Weng Q, Chen Q, Jiang T, et al. Global burden of early-onset osteoarthritis, 1990-2019: results from the Global Burden of Disease Study 2019. *Ann Rheum Dis*. 2024;83(7):915-925. doi: 10.1136/ard-2023-225324

6. Abdulghani S, Morouço PG. Biofabrication for osteochondral tissue regeneration: bioink printability requirements. *J Mater Sci Mater Med*. 2019;30(2):20. doi: 10.1007/s10856-019-6218-x

7. Brophy RH, Fillingham YA. AAOS clinical practice guideline summary: management of osteoarthritis of the

knee (nonarthroplasty), third edition. *J Am Acad Orthop Surg*. 2022;30(9):e721-e729.
doi: 10.5435/jaaos-d-21-01233

8. Medina J, Garcia-Mansilla I, Fabricant PD, Kremen TJ, Sherman SL, Jones K. Microfracture for the treatment of symptomatic cartilage lesions of the knee: a survey of International Cartilage Regeneration & Joint Preservation Society. *Cartilage*. 2021;13(1_suppl):1148s-1155s.
doi: 10.1177/1947603520954503

9. Patel S, Caldwell JM, Doty SB, et al. Integrating soft and hard tissues via interface tissue engineering. *J Orthop Res*. 2018;36(4):1069-1077.
doi: 10.1002/jor.23810

10. Lee CH, Cook JL, Mendelson A, Moioli EK, Yao H, Mao JJ. Regeneration of the articular surface of the rabbit synovial joint by cell homing: a proof of concept study. *Lancet*. 2010;376(9739):440-448.
doi: 10.1016/s0140-6736(10)60668-x

11. Patel JM, Merriam AR, Culp BM, Gatt CJ, Jr., Dunn MG. One-year outcomes of total meniscus reconstruction using a novel fiber-reinforced scaffold in an ovine model. *Am J Sports Med*. 2016;44(4):898-907.
doi: 10.1177/0363546515624913

12. Ayers DC. How common is revision for adverse reaction to metal debris after total hip replacement with a metal-on-polyethylene bearing surface?: commentary on an article by Anders Persson, MD, et al.: "Revision for Symptomatic Pseudotumor Following Primary Total Hip Arthroplasty with a Standard Femoral Stem". *J Bone Joint Surg Am*. 2018;100(11):e82.
doi: 10.2106/jbjs.18.00193

13. Ansari S, Khorshidi S, Karkhaneh A. Engineering of gradient osteochondral tissue: from nature to lab. *Acta Biomater*. 2019;87:41-54.
doi: 10.1016/j.actbio.2019.01.071

14. Bedell ML, Wang Z, Hogan KJ, et al. The effect of multi-material architecture on the ex vivo osteochondral integration of bioprinted constructs. *Acta Biomater*. 2023;155:99-112.
doi: 10.1016/j.actbio.2022.11.014

15. McKee TJ, Perlman G, Morris M, Komarova SV. Extracellular matrix composition of connective tissues: a systematic review and meta-analysis. *Sci Rep*. 2019;9(1):10542.
doi: 10.1038/s41598-019-46896-0

16. Di Luca A, Szlazak K, Lorenzo-Moldero I, et al. Influencing chondrogenic differentiation of human mesenchymal stromal cells in scaffolds displaying a structural gradient in pore size. *Acta Biomater*. 2016;36:210-219.
doi: 10.1016/j.actbio.2016.03.014

17. Shen G. The role of type X collagen in facilitating and regulating endochondral ossification of articular cartilage. *Orthod Craniofac Res*. 2005;8(1):11-17.
doi: 10.1111/j.1601-6343.2004.00308.x

18. Horkay F, Basser PJ, Geissler E. Cartilage extracellular matrix polymers: hierarchical structure, osmotic properties, and function. *Soft Matter*. 2024;20(30):6033-6043.
doi: 10.1039/d4sm00617h

19. Rose FR, Oreffo RO. Bone tissue engineering: hope vs hype. *Biochem Biophys Res Commun*. 2002;292(1):1-7.
doi: 10.1006/bbrc.2002.6519

20. Gonzalez-Fernandez T, Rathan S, Hobbs C, et al. Pore-forming bioinks to enable spatio-temporally defined gene delivery in bioprinted tissues. *J Control Release*. 2019;301:13-27.
doi: 10.1016/j.jconrel.2019.03.006

21. Rowland CR, Glass KA, Ettyreddy AR, et al. Regulation of decellularized tissue remodeling via scaffold-mediated lentiviral delivery in anatomically-shaped osteochondral constructs. *Biomaterials*. 2018;177:161-175.
doi: 10.1016/j.biomaterials.2018.04.049

22. Liu Y, Huang C, Bai M, Pi C, Zhang D, Xie J. The roles of Runx1 in skeletal development and osteoarthritis: a concise review. *Heliyon*. 2022;8(12):e12656.
doi: 10.1016/j.heliyon.2022.e12656

23. Li W, Zhang S, Liu J, Liu Y, Liang Q. Vitamin K2 stimulates MC3T3-E1 osteoblast differentiation and mineralization through autophagy induction. *Mol Med Rep*. 2019;19(5):3676-3684.
doi: 10.3892/mmr.2019.10040

24. Grogan SP, Duffy SF, Pauli C, et al. Zone-specific gene expression patterns in articular cartilage. *Arthritis Rheum*. 2013;65(2):418-428.
doi: 10.1002/art.37760

25. Zuscik MJ, Hilton MJ, Zhang X, Chen D, O'Keefe RJ. Regulation of chondrogenesis and chondrocyte differentiation by stress. *J Clin Invest*. 2008;118(2):429-438.
doi: 10.1172/jci34174

26. Ma J, Wang Z, Zhao J, Miao W, Ye T, Chen A. Resveratrol attenuates lipopolysaccharides (LPS)-induced inhibition of osteoblast differentiation in MC3T3-E1 cells. *Med Sci Monit*. 2018;24:2045-2052.
doi: 10.12659/msm.905703

27. Kitaura H, Marahleh A, Ohori F, et al. Osteocyte-related cytokines regulate osteoclast formation and bone resorption. *Int J Mol Sci*. 2020;21(14):5169.
doi: 10.3390/ijms21145169

28. Zhang D, Deng X, Liu Y, et al. MMP-10 deficiency effects differentiation and death of chondrocytes associated with endochondral osteogenesis in an endemic osteoarthritis. *Cartilage*. 2022;13(3):19476035221109226.
doi: 10.1177/19476035221109226

29. Boyce BF, Xing L. Functions of RANKL/RANK/OPG in bone modeling and remodeling. *Arch Biochem Biophys*. 2008;473(2):139-146.
doi: 10.1016/j.abb.2008.03.018

30. Quinn TM, Häuselmann HJ, Shintani N, Hunziker EB. Cell and matrix morphology in articular cartilage from adult human knee and ankle joints suggests depth-associated adaptations to biomechanical and anatomical roles. *Osteoarthritis Cartilage*. 2013;21(12):1904-1912.

31. Niu H, Liu C, Li A, et al. Relationship between triphasic mechanical properties of articular cartilage and osteoarthritic grade. *Sci China Life Sci*. 2012;55(5):444-451. doi: 10.1007/s11427-012-4326-7

32. Sun Y, Zhang K, Dong H, et al. Layered mechanical and electrical properties of porcine articular cartilage. *Med Biol Eng Comput*. 2022;60(10):3019-3028. doi: 10.1007/s11517-022-02653-6

33. Burr DB, Gallant MA. Bone remodelling in osteoarthritis. *Nat Rev Rheumatol*. 2012;8(11):665-673. doi: 10.1038/nrrheum.2012.130

34. Flachsmann ER, Broom ND, Oloyede A. A biomechanical investigation of unconstrained shear failure of the osteochondral region under impact loading. *Clin Biomech (Bristol)*. 1995;10(3):156-165. doi: 10.1016/0268-0033(95)93706-y

35. Madry H, van Dijk CN, Mueller-Gerbl M. The basic science of the subchondral bone. *Knee Surg Sports Traumatol Arthrosc*. 2010;18(4):419-433. doi: 10.1007/s00167-010-1054-z

36. Broom ND, Oloyede A, Flachsmann R, Hows M. Dynamic fracture characteristics of the osteochondral junction undergoing shear deformation. *Med Eng Phys*. 1996;18(5):396-404. doi: 10.1016/1350-4533(95)00067-4

37. Mieloch AA, Richter M, Trzeciak T, Giersig M, Rybka JD. Osteoarthritis severely decreases the elasticity and hardness of knee joint cartilage: a nanoindentation study. *J Clin Med*. 2019;8(11):1865. doi: 10.3390/jcm8111865

38. Davis S, Zekonyte J, Karali A, Roldo M, Blunn G. Early degenerative changes in a spontaneous osteoarthritis model assessed by nanoindentation. *Bioengineering (Basel)*. 2023;10(9):995. doi: 10.3390/bioengineering10090995

39. Peters AE, Akhtar R, Comerford EJ, Bates KT. The effect of ageing and osteoarthritis on the mechanical properties of cartilage and bone in the human knee joint. *Sci Rep*. 2018;8(1):5931. doi: 10.1038/s41598-018-24258-6

40. Hu YJ, Yu YE, Cooper HJ, et al. Mechanical and structural properties of articular cartilage and subchondral bone in human osteoarthritic knees. *J Bone Miner Res*. 2024;39(8):1120-1131. doi: 10.1093/jbmr/zjae094

41. Guo J, Li Q, Zhang R, et al. Loose pre-cross-linking mediating cellulose self-assembly for 3D printing strong and tough biomimetic scaffolds. *Biomacromolecules*. 2022;23(3):877-888. doi: 10.1021/acs.biomac.1c01330

42. Zhang X, Liu Y, Zuo Q, et al. 3D bioprinting of biomimetic bilayered scaffold consisting of decellularized extracellular matrix and silk fibroin for osteochondral repair. *Int J Bioprint*. 2021;7(4):401. doi: 10.18063/ijb.v7i4.401

43. Nedrelow DS, Rassi A, Ajeeb B, et al. Regenerative engineering of a biphasic patient-fitted temporomandibular joint condylar prosthesis. *Tissue Eng Part C Methods*. 2023;29(7):307-320. doi: 10.1089/ten.TEC.2023.0093

44. Wu Z, Yao H, Sun H, et al. Enhanced hyaline cartilage formation and continuous osteochondral regeneration via 3D-Printed heterogeneous hydrogel with multi-crosslinking inks. *Mater Today Bio*. 2024;26:101080. doi: 10.1016/j.mtbio.2024.101080

45. Diloksumpan P, de Ruijter M, Castilho M, et al. Combining multi-scale 3D printing technologies to engineer reinforced hydrogel-ceramic interfaces. *Biofabrication*. 2020;12(2):025014. doi: 10.1088/1758-5090/ab69d9

46. Liu Y, Peng L, Li L, et al. 3D-bioprinted BMSC-laden biomimetic multiphasic scaffolds for efficient repair of osteochondral defects in an osteoarthritic rat model. *Biomaterials*. 2021;279:121216. doi: 10.1016/j.biomaterials.2021.121216

47. Gao J, Ding X, Yu X, et al. Cell-free bilayered porous scaffolds for osteochondral regeneration fabricated by continuous 3d-printing using nascent physical hydrogel as ink. *Adv Healthc Mater*. 2021;10(3):e2001404. doi: 10.1002/adhm.202001404

48. Wang Z, Cao W, Wu F, et al. A triphasic biomimetic BMSC-loaded scaffold for osteochondral integrated regeneration in rabbits and pigs. *Biomater Sci*. 2023;11(8):2924-2934. doi: 10.1039/d2bm02148j

49. Braxton T, Lim K, Alcala-Orozco C, et al. Mechanical and physical characterization of a biphasic 3D printed silk-infilled scaffold for osteochondral tissue engineering. *ACS Biomater Sci Eng*. 2024;10(12):7606-7618. doi: 10.1021/acsbiomaterials.4c01865

50. Wang S, Luo B, Bai B, et al. 3D printed chondrogenic functionalized PGS bioactive scaffold for cartilage regeneration. *Adv Healthc Mater*. 2023;12(27): e2301006. doi: 10.1002/adhm.202301006

51. Wang H, Zhang J, Bai H, et al. 3D printed cell-free bilayer porous scaffold based on alginate with biomimetic microenvironment for osteochondral defect repair. *Biomater Adv*. 2025;167:214092. doi: 10.1016/j.bioadv.2024.214092

52. Ding X, Gao J, Yu X, et al. 3D-printed porous scaffolds of hydrogels modified with TGF-β1 binding peptides to promote in vivo cartilage regeneration and animal gait restoration. *ACS Appl Mater Interfaces*. 2022;14(14):15982-15995. doi: 10.1021/acsami.2c00761

53. Li Q, Yu H, Zhao F, et al. 3D printing of microenvironment-specific bioinspired and exosome-reinforced hydrogel scaffolds for efficient cartilage and subchondral bone regeneration. *Adv Sci (Weinh)*. 2023;10(26):e2303650. doi: 10.1002/advs.202303650

54. Cui X, Alcala-Orozco CR, Baer K, et al. 3D bioassembly of cell-instructive chondrogenic and osteogenic hydrogel microspheres containing allogeneic stem cells for hybrid biofabrication of osteochondral constructs. *Biofabrication*. 2022;14(3):034101. doi: 10.1088/1758-5090/ac61a3

55. Wei W, Liu W, Kang H, et al. A one-stone-two-birds strategy for osteochondral regeneration based on a 3D printable biomimetic scaffold with kartogenin biochemical stimuli gradient. *Adv Healthc Mater*. 2023;12(15):e2300108. doi: 10.1002/adhm.202300108

56. Coyle A, Chakraborty A, Huang J, Shamiya Y, Luo W, Paul A. In vitro engineered ECM-incorporated hydrogels for osteochondral tissue repair: a cell-free approach. *Adv Healthc Mater*. 2025;14(4):e2402701. doi: 10.1002/adhm.202402701

57. Sun T, Feng Z, He W, et al. Novel 3D-printing bilayer GelMA-based hydrogel containing BP,β-TCP and exosomes for cartilage-bone integrated repair. *Biofabrication*. 2023;16(1):015008. doi: 10.1088/1758-5090/ad04fe

58. Eckstein KN, Hergert JE, Uzcategui AC, et al. Controlled mechanical property gradients within a digital light processing printed hydrogel-composite osteochondral scaffold. *Ann Biomed Eng*. 2024;52(8):2162-2177. doi: 10.1007/s10439-024-03516-x

59. Golebiowska A, Nukavarapu SP. Bio-inspired zonal-structured matrices for bone-cartilage interface engineering. *Biofabrication*. 2022;14(2):025016. doi: 10.1088/1758-5090/ac52e1

60. Sun Y, Wu Q, Zhang Y, Dai K, Wei Y. 3D-bioprinted gradient-structured scaffold generates anisotropic cartilage with vascularization by pore-size-dependent activation of HIF1α/FAK signaling axis. *Nanomedicine*. 2021; 37:102426. doi: 10.1016/j.nano.2021.102426

61. Gu Y, Zou Y, Huang Y, et al. 3D-printed biomimetic scaffolds with precisely controlled and tunable structures guide cell migration and promote regeneration of osteochondral defect. *Biofabrication*. 2023;16(1):015003. doi: 10.1088/1758-5090/ad0071

62. Kilian D, Cometta S, Bernhardt A, et al. Core-shell bioprinting as a strategy to apply differentiation factors in a spatially defined manner inside osteochondral tissue substitutes. *Biofabrication*. 2022;14(1):014108. doi: 10.1088/1758-5090/ac457b

63. Zhang Y, Li D, Liu Y, et al. 3D-bioprinted anisotropic bicellular living hydrogels boost osteochondral regeneration via reconstruction of cartilage-bone interface. *Innovation (Camb)*. 2024;5(1):100542. doi: 10.1016/j.xinn.2023.100542

64. Maherani M, Eslami H, Poursamar SA, Ansari M. A modular approach to 3D-printed bilayer composite scaffolds for osteochondral tissue engineering. *J Mater Sci Mater Med*. 2024;35(1):62. doi: 10.1007/s10856-024-06824-9

65. O'Shea DG, Hodgkinson T, Curtin CM, O'Brien FJ. An injectable and 3D printable pro-chondrogenic hyaluronic acid and collagen type II composite hydrogel for the repair of articular cartilage defects. *Biofabrication*. 2023;16(1):015007. doi: 10.1088/1758-5090/ad047a

66. Zineh BR, Roshangar L, Meshgi S, Shabgard M. 3D printing of alginate/thymoquinone/halloysite nanotube bio-scaffolds for cartilage repairs: experimental and numerical study. *Med Biol Eng Comput*. 2022;60(11):3069-3080. doi: 10.1007/s11517-022-02654-5

67. Naranda J, Bračič M, Vogrin M, Maver U. Recent advancements in 3d printing of polysaccharide hydrogels in cartilage tissue engineering. *Materials (Basel)*. 2021;14(14):3977. doi: 10.3390/ma14143977

68. Majumder N, Roy C, Doenges L, Martin I, Barbero A, Ghosh S. Covalent conjugation of small molecule inhibitors and growth factors to a silk fibroin-derived bioink to develop phenotypically stable 3D bioprinted cartilage. *ACS Appl Mater Interfaces*. 2024;16(8):9925-9943. doi: 10.1021/acsami.3c18903

69. Zhang W, Lian Q, Li D, et al. Cartilage repair and subchondral bone migration using 3D printing osteochondral composites: a one-year-period study in rabbit trochlea. *Biomed Res Int*. 2014;2014:746138. doi: 10.1155/2014/746138

70. Golebiowska AA, Nukavarapu SP. Bio-inspired zonal-structured matrices for bone-cartilage interface engineering. *Biofabrication*. 2022;14(2):025016. doi: 10.1088/1758-5090/ac5413

71. Jiang G, Li S, Yu K, et al. A 3D-printed PRP-GelMA hydrogel promotes osteochondral regeneration through M2 macrophage polarization in a rabbit model. *Acta Biomater*. 2021;128:150-162. doi: 10.1016/j.actbio.2021.04.010

72. Parisi C, Salvatore L, Veschini L, et al. Biomimetic gradient scaffold of collagen-hydroxyapatite for osteochondral regeneration. *J Tissue Eng*. 2020;11:2041731419896068. doi: 10.1177/2041731419896068

73. Sa MW, Nguyen BB, Moriarty RA, Kamalitdinov T, Fisher JP, Kim JY. Fabrication and evaluation of 3D printed BCP scaffolds reinforced with ZrO(2) for bone tissue applications. *Biotechnol Bioeng*. 2018;115(4):989-999. doi: 10.1002/bit.26514

74. Liu L, Yu F, Chen L, Xia L, Wu C, Fang B. Lithium-containing biomaterials stimulate cartilage repair through bone marrow stromal cells-derived exosomal miR-455-3p and Histone H3 acetylation. *Adv Healthc Mater*. 2023;12(11):e2202390. doi: 10.1002/adhm.202202390

75. Zheng J, Mao X, Ling J, Chen C, Zhang W. Role of magnesium transporter subtype 1 (MagT1) in the osteogenic differentiation of rat bone marrow stem cells. *Biol Trace Elem Res*. 2016;171(1):131-137. doi: 10.1007/s12011-015-0459-4

76. Wang X, Gao L, Han Y, et al. Silicon-enhanced adipogenesis and angiogenesis for vascularized adipose tissue engineering. *Adv Sci (Weinh)*. 2018;5(11):1800776. doi: 10.1002/advs.201800776

77. Rahaman MN, Day DE, Bal BS, et al. Bioactive glass in tissue engineering. *Acta Biomater*. 2011;7(6):2355-2373. doi: 10.1016/j.actbio.2011.03.016

78. Morgan EF, Salisbury Palomares KT, Gleason RE, et al. Correlations between local strains and tissue phenotypes in an experimental model of skeletal healing. *J Biomech*. 2010;43(12):2418-2424. doi: 10.1016/j.jbiomech.2010.04.019

79. Claes L, Eckert-Hübner K, Augat P. The effect of mechanical stability on local vascularization and tissue differentiation in callus healing. *J Orthop Res*. 2002;20(5):1099-1105. doi: 10.1016/s0736-0266(02)00044-x

80. Chen C, Xie J, Deng L, Yang L. Substrate stiffness together with soluble factors affects chondrocyte mechanoresponses. *ACS Appl Mater Interfaces*. 2014;6(18):16106-16116. doi: 10.1021/am504135b

81. Yang Y, Feng Y, Qu R, et al. Synthesis of aligned porous polyethylene glycol/silk fibroin/hydroxyapatite scaffolds for osteoinduction in bone tissue engineering. *Stem Cell Res Ther*. 2020;11(1):522. doi: 10.1186/s13287-020-02024-8

82. Cao B, Li J, Wang X, et al. Mechanosensitive miR-99b mediates the regulatory effect of matrix stiffness on bone marrow mesenchymal stem cell fate both in vitro and in vivo. *APL Bioeng*. 2023;7(1):016106. doi: 10.1063/5.0131125

83. Lai Q, Li B, Chen L, Zhou Y, Bao H, Li H. Substrate stiffness regulates the proliferation and inflammation of chondrocytes and macrophages through exosomes. *Acta Biomater*. 2025;192:77-89. doi: 10.1016/j.actbio.2024.12.021

84. Tortorici M, Petersen A, Ehrhart K, Duda GN, Checa S. Scaffold-dependent mechanical and architectural cues guide osteochondral defect healing in silico. *Front Bioeng Biotechnol*. 2021;9:642217. doi: 10.3389/fbioe.2021.642217

85. Radhakrishnan J, Manigandan A, Chinnaswamy P, Subramanian A, Sethuraman S. Gradient nano-engineered in situ forming composite hydrogel for osteochondral regeneration. *Biomaterials*. 2018;162:82-98. doi: 10.1016/j.biomaterials.2018.01.056

86. Pattnaik A, Sanket AS, Pradhan S, et al. Designing of gradient scaffolds and their applications in tissue regeneration. *Biomaterials*. 2023;296:122078. doi: doi: 10.1016/j.biomaterials.2023.122078

87. Zhang W, Chen J, Tao J, et al. The use of type 1 collagen scaffold containing stromal cell-derived factor-1 to create a matrix environment conducive to partial-thickness cartilage defects repair. *Biomaterials*. 2013;34(3):713-723. doi: 10.1016/j.biomaterials.2012.10.027

88. Hayashi K, Shimabukuro M, Kishida R, Tsuchiya A, Ishikawa K. Honeycomb scaffolds capable of achieving barrier membrane-free guided bone regeneration. *Mater Adv*. 2021;2(23):7638-7649. doi: 10.1039/D1MA00698C

89. Zhao Y, Liang Y, Ding S, Zhang K, Mao HQ, Yang Y. Application of conductive PPy/SF composite scaffold and electrical stimulation for neural tissue engineering. *Biomaterials*. 2020;255:120164. doi: 10.1016/j.biomaterials.2020.120164

90. He J, Sun C, Gu Z, et al. Morphology, migration, and transcriptome analysis of schwann cell culture on butterfly wings with different surface architectures. *ACS Nano*. 2018;12(10):9660-9668. doi: 10.1021/acsnano.8b00552

91. Zhang J, Wu Y, Thote T, Lee EH, Ge Z, Yang Z. The influence of scaffold microstructure on chondrogenic differentiation of mesenchymal stem cells. *Biomed Mater*. 2014;9(3):035011. doi: 10.1088/1748-6041/9/3/035011

92. DeLise AM, Fischer L, Tuan RS. Cellular interactions and signaling in cartilage development. *Osteoarthritis Cartilage*. 2000;8(5):309-334. doi: 10.1053/joca.1999.0306

93. Li S, Tallia F, Mohammed AA, Stevens MM, Jones JR. Scaffold channel size influences stem cell differentiation pathway in 3-D printed silica hybrid scaffolds for cartilage regeneration. *Biomater Sci*. 2020;8(16):4458-4466. doi: 10.1039/c9bm01829h

94. Zanetti NC, Solursh M. Induction of chondrogenesis in limb mesenchymal cultures by disruption of the actin cytoskeleton. *J Cell Biol*. 1984;99(1 Pt 1):115-123. doi: 10.1083/jcb.99.1.115

95. Vanden Berg-Foels WS. In situ tissue regeneration: chemoattractants for endogenous stem cell recruitment. *Tissue Eng Part B Rev*. 2014;20(1):28-39.

doi: 10.1089/ten.TEB.2013.0100

96. Salgado AJ, Coutinho OP, Reis RL. Bone tissue engineering: state of the art and future trends. *Macromol Biosci*. 2004;4(8):743-765. doi: 10.1002/mabi.200400026

97. Zhang X, Chen X, Hong H, Hu R, Liu J, Liu C. Decellularized extracellular matrix scaffolds: recent trends and emerging strategies in tissue engineering. *Bioact Mater*. 2022;10:15-31. doi: 10.1016/j.bioactmat.2021.09.014

98. Jang J, Kim TG, Kim BS, Kim SW, Kwon SM, Cho DW. Tailoring mechanical properties of decellularized extracellular matrix bioink by vitamin B2-induced photo-crosslinking. *Acta Biomater*. 2016;33:88-95. doi: 10.1016/j.actbio.2016.01.013

99. Zhang X, Liu Y, Luo C, et al. Crosslinker-free silk/decellularized extracellular matrix porous bioink for 3D bioprinting-based cartilage tissue engineering. *Mater Sci Eng C Mater Biol Appl*. 2021;118:111388. doi: 10.1016/j.msec.2020.111388

100. Joyce M, Hodgkinson T, Lemoine M, González-Vázquez A, Kelly DJ, O'Brien FJ. Development of a 3D-printed bioabsorbable composite scaffold with mechanical properties suitable for treating large, load-bearingarticular cartilage defects. *Eur Cell Mater*. 2023;45:158-172. doi: 10.22203/eCM.v045a11

101. Johnson K, Zhu S, Tremblay MS, et al. A stem cell-based approach to cartilage repair. *Science*. 2012;336(6082):717-721. doi: 10.1126/science.1215157

102. Stefani RM, Lee AJ, Tan AR, et al. Sustained low-dose dexamethasone delivery via a PLGA microsphere-embedded agarose implant for enhanced osteochondral repair. *Acta Biomaterialia*. 2020;102:326-340. doi: doi: 10.1016/j.actbio.2019.11.052

103. Brito Barrera YA, Husteden C, Alherz J, Fuhrmann B, Wölk C, Groth T. Extracellular matrix-inspired surface coatings functionalized with dexamethasone-loaded liposomes to induce osteo- and chondrogenic differentiation of multipotent stem cells. *Mater Sci Eng C Mater Biol Appl*. 2021;131:112516. doi: 10.1016/j.msec.2021.112516

104. Yan X, Chen YR, Song YF, et al. Scaffold-based gene therapeutics for osteochondral tissue engineering. *Front Pharmacol*. 2019;10:1534. doi: 10.3389/fphar.2019.01534

105. An C, Cheng Y, Yuan Q, Li J. IGF-1 and BMP-2 induces differentiation of adipose-derived mesenchymal stem cells into chondrocytes-like cells. *Ann Biomed Eng*. 2010;38(4):1647-1654. doi: 10.1007/s10439-009-9892-x

106. Tao K, Frisch J, Rey-Rico A, et al. Co-overexpression of TGF-β and SOX9 via rAAV gene transfer modulates the metabolic and chondrogenic activities of human bone marrow-derived mesenchymal stem cells. *Stem Cell Res Ther*. 2016;7:20. doi: 10.1186/s13287-016-0280-9

107. Lee JM, Im GI. SOX trio-co-transduced adipose stem cells in fibrin gel to enhance cartilage repair and delay the progression of osteoarthritis in the rat. *Biomaterials*. 2012;33(7):2016-2024. doi: 10.1016/j.biomaterials.2011.11.050

108. Vermeij EA, Broeren MG, Bennink MB, et al. Disease-regulated local IL-10 gene therapy diminishes synovitis and cartilage proteoglycan depletion in experimental arthritis. *Ann Rheum Dis*. 2015;74(11):2084-2091. doi: 10.1136/annrheumdis-2014-205223

109. Kay JD, Gouze E, Oligino TJ, et al. Intra-articular gene delivery and expression of interleukin-1Ra mediated by self-complementary adeno-associated virus. *J Gene Med*. 2009;11(7):605-614. doi: 10.1002/jgm.1334

110. Bellavia D, Veronesi F, Carina V, et al. Gene therapy for chondral and osteochondral regeneration: is the future now? *Cell Mol Life Sci*. 2018;75(4):649-667. doi: 10.1007/s00018-017-2637-3

111. Lu H, Wei J, Liu K, et al. Radical-scavenging and subchondral bone-regenerating nanomedicine for osteoarthritis treatment. *ACS Nano*. 2023;17(6):6131-6146. doi: 10.1021/acsnano.3c01789

112. Chen Y, Huang H, Zhong W, Li L, Lu Y, Si HB. miR-140-5p protects cartilage progenitor/stem cells from fate changes in knee osteoarthritis. *Int Immunopharmacol*. 2023;114:109576. doi: 10.1016/j.intimp.2022.109576

113. Xing H, Zhang Z, Mao Q, et al. Injectable exosome-functionalized extracellular matrix hydrogel for metabolism balance and pyroptosis regulation in intervertebral disc degeneration. *J Nanobiotechnol*. 2021;19(1):264. doi: 10.1186/s12951-021-00991-5

114. Zhu W, Wang H, Feng B, et al. Self-healing hyaluronic acid-based hydrogel with miRNA140-5p loaded MON-PEI nanoparticles for chondrocyte regeneration: Schiff base self-assembly approach. *Adv Sci (Weinh)*. 2025;12(1):e2406479. doi: 10.1002/advs.202406479

115. Tuan RS, Chen AF, Klatt BA. Cartilage regeneration. *J Am Acad Orthop Surg*. 2013;21(5):303-311. doi: 10.5435/jaaos-21-05-303

116. Wang LT, Ting CH, Yen ML, et al. Human mesenchymal stem cells (MSCs) for treatment towards immune- and inflammation-mediated diseases: review of current clinical trials. *J Biomed Sci*. 2016;23(1):76. doi: 10.1186/s12929-016-0289-5

117. Bush CJ, Grant JA, Krych AJ, Bedi A. The role of mesenchymal stromal cells in the management of knee chondral defects. *J Bone Joint Surg Am*. 2022;104(3):284-292.

doi: 10.2106/jbjs.20.01800

118. Armiento AR, Alini M, Stoddart MJ. Articular fibrocartilage - why does hyaline cartilage fail to repair? *Adv Drug Deliv Rev*. 2019;146:289-305.
doi: 10.1016/j.addr.2018.12.015

119. Knutsen G, Engebretsen L, Ludvigsen TC, et al. Autologous chondrocyte implantation compared with microfracture in the knee. A randomized trial. *J Bone Joint Surg Am*. 2004;86(3):455-464.
doi: 10.2106/00004623-200403000-00001

120. Zhen G, Wen C, Jia X, et al. Inhibition of TGF-β signaling in mesenchymal stem cells of subchondral bone attenuates osteoarthritis. *Nat Med*. 2013;19(6):704-712.
doi: 10.1038/nm.3143

121. Lam J, Lu S, Kasper FK, Mikos AG. Strategies for controlled delivery of biologics for cartilage repair. *Adv Drug Deliv Rev*. 2015;84:123-134.
doi: doi: 10.1016/j.addr.2014.06.006

122. Möller T, Amoroso M, Hägg D, et al. In vivo chondrogenesis in 3d bioprinted human cell-laden hydrogel constructs. *Plast Reconstr Surg Glob Open*. 2017;5(2):e1227.
doi: 10.1097/gox.0000000000001227

123. Wu H, Wang X, Wang G, et al. Advancing scaffold-assisted modality for in situ osteochondral regeneration: a shift from biodegradable to bioadaptable. *Adv Mater*. 2024;36(47):e2407040.
doi: 10.1002/adma.202407040

124. Karageorgiou V, Kaplan D. Porosity of 3D biomaterial scaffolds and osteogenesis. *Biomaterials*. 2005;26(27): 5474-5491.
doi: 10.1016/j.biomaterials.2005.02.002

125. Brauer DS. Bioactive glasses—structure and properties. *Angew Chem Int Ed Engl*. 2015;54(14):4160-4181.
doi: 10.1002/anie.201405310

126. Bejarano J, Boccaccini AR, Covarrubias C, Palza H. Effect of Cu- and Zn-doped bioactive glasses on the in vitro bioactivity, mechanical and degradation behavior of biodegradable PDLLA scaffolds. *Materials (Basel)*. 2020;13(13):2908.
doi: 10.3390/ma13132908

127. Heiden M, Nauman E, Stanciu L. Bioresorbable Fe–Mn and Fe–Mn–HA materials for orthopedic implantation: enhancing degradation through porosity control. *Adv Healthc Mater*. 2017;6(13):1700120.
doi: doi: 10.1002/adhm.201700120

128. Kim JA, Lim J, Naren R, Yun HS, Park EK. Effect of the biodegradation rate controlled by pore structures in magnesium phosphate ceramic scaffolds on bone tissue regeneration in vivo. *Acta Biomater*. 2016;44:155-167.
doi: 10.1016/j.actbio.2016.08.039

129. Qu Z, Liu L, Deng Y, et al. Relationship between biodegradation rate and grain size itself excluding other structural factors caused by alloying additions and deformation processing for pure Mg. *Materials (Basel)*. 2022;15(15):5295.
doi: 10.3390/ma15155295

130. Hu Q, Ecker M. Overview of MMP-13 as a promising target for the treatment of osteoarthritis. *Int J Mol Sci*. 2021;22(4):1742.
doi: 10.3390/ijms22041742

131. Choe R, Devoy E, Jabari E, Packer JD, Fisher JP. Biomechanical aspects of osteochondral regeneration: implications and strategies for three-dimensional bioprinting. *Tissue Eng Part B Rev*. 2022;28(4):766-788.
doi: 10.1089/ten.TEB.2021.0101

132. Knudson W, Casey B, Nishida Y, Eger W, Kuettner KE, Knudson CB. Hyaluronan oligosaccharides perturb cartilage matrix homeostasis and induce chondrocytic chondrolysis. *Arthritis Rheum*. 2000;43(5):1165-1174.
doi: 10.1002/1529-0131(200005)43:5<1165::Aid-anr27>3.0.Co;2-h

133. Yildirim N, Amanzhanova A, Kulzhanova G, Mukasheva F, Erisken C. Osteochondral interface: regenerative engineering and challenges. *ACS Biomater Sci Eng*. 2023;9(3):1205-1223.
doi: 10.1021/acsbiomaterials.2c01321

134. Kamaraj M, Roopavath UK, Giri PS, Ponnusamy NK, Rath SN. Modulation of 3D printed calcium-deficient apatite constructs with varying mn concentrations for osteochondral regeneration via endochondral differentiation. *ACS Appl Mater Interfaces*. 2022;14(20):23245-23259.
doi: 10.1021/acsami.2c05110

135. Liuyun J, Lixin J, Chengdong X, Lijuan X, Ye L. Effect of l-lysine-assisted surface grafting for nano-hydroxyapatite on mechanical properties and in vitro bioactivity of poly(lactic acid-co-glycolic acid). *J Biomater Appl*. 2016;30(6):750-758.
doi: 10.1177/0885328215584491

136. Nedrelow DS, Townsend JM, Detamore MS. Osteochondral regeneration with anatomical scaffold 3D-printing-design considerations for interface integration. *J Biomed Mater Res A*. 2025;113(1):e37804.
doi: 10.1002/jbm.a.37804

137. Brown WE, Huang BJ, Hu JC, Athanasiou KA. Engineering large, anatomically shaped osteochondral constructs with robust interfacial shear properties. *NPJ Regen Med*. 2021;6(1):42.
doi: 10.1038/s41536-021-00152-0

138. Feng P, He J, Peng S, et al. Characterizations and interfacial reinforcement mechanisms of multicomponent biopolymer based scaffold. *Mater Sci Eng C Mater Biol Appl*. 2019;100:809-825.
doi: 10.1016/j.msec.2019.03.030

139. Wang L, Zhao L, Detamore MS. Human umbilical cord mesenchymal stromal cells in a sandwich approach for osteochondral tissue engineering. *J Tissue Eng Regen Med*. 2011;5(9):712-721.
doi: 10.1002/term.370

140. Li S, Liu C, Zhang Y, et al. Continuous 3D printing of biomimetic beetle mandible structure with long bundles of aramid fiber composites. *Biomimetics (Basel)*. 2023;8(3):283. doi: 10.3390/biomimetics8030283

141. Yodmuang S, Guo H, Brial C, et al. Effect of interface mechanical discontinuities on scaffold-cartilage integration. *J Orthop Res*. 2019;37(4):845-854. doi: 10.1002/jor.24238

142. Zhao R, Han F, Yu Q, et al. A multifunctional scaffold that promotes the scaffold-tissue interface integration and rescues the ROS microenvironment for repair of annulus fibrosus defects. *Bioact Mater*. 2024;41:257-270. doi: 10.1016/j.bioactmat.2024.03.007

143. Torres-Claramunt R, Martínez-Díaz S, Sánchez-Soler JF, et al. Fibronectin-coated polyurethane meniscal scaffolding supplemented with MSCs improves scaffold integration and proteoglycan production in a rabbit model. *Knee Surg Sports Traumatol Arthrosc*. 2023;31(11):5104-5110. doi: 10.1007/s00167-023-07562-1

144. Chung JY, Song M, Ha CW, Kim JA, Lee CH, Park YB. Comparison of articular cartilage repair with different hydrogel-human umbilical cord blood-derived mesenchymal stem cell composites in a rat model. *Stem Cell Res Ther*. 2014;5(2):39. doi: 10.1186/scrt427

145. Romito L, Ameer GA. Mechanical interlocking of engineered cartilage to an underlying polymeric substrate: towards a biohybrid tissue equivalent. *Ann Biomed Eng*. 2006;34(5):737-747. doi: 10.1007/s10439-006-9089-5

146. Scotti C, Wirz D, Wolf F, et al. Engineering human cell-based, functionally integrated osteochondral grafts by biological bonding of engineered cartilage tissues to bony scaffolds. *Biomaterials*. 2010;31(8):2252-2259. doi: 10.1016/j.biomaterials.2009.11.110

147. Ege D, Hasirci V. Is 3D printing promising for osteochondral tissue regeneration? *ACS Appl Bio Mater*. 2023;6(4):1431-1444. doi: 10.1021/acsabm.3c00093

148. Jammalamadaka U, Tappa K. Recent advances in biomaterials for 3d printing and tissue engineering. *J Funct Biomater*. 2018;9(1):22. doi: 10.3390/jfb9010022

149. Steinmetz NJ, Aisenbrey EA, Westbrook KK, Qi HJ, Bryant SJ. Mechanical loading regulates human MSC differentiation in a multi-layer hydrogel for osteochondral tissue engineering. *Acta Biomater*. 2015;21:142-153. doi: 10.1016/j.actbio.2015.04.015

150. Kilian D, Ahlfeld T, Akkineni AR, Bernhardt A, Gelinsky M, Lode A. 3D Bioprinting of osteochondral tissue substitutes - in vitro-chondrogenesis in multi-layered mineralized constructs. *Sci Rep*. 2020;10(1):8277. doi: 10.1038/s41598-020-65050-9

151. Gong L, Li J, Zhang J, et al. An interleukin-4-loaded bi-layer 3D printed scaffold promotes osteochondral regeneration. *Acta Biomater*. 2020;117:246-260. doi: 10.1016/j.actbio.2020.09.039

152. Senior JJ, Cooke ME, Grover LM, Smith AM. Fabrication of complex hydrogel structures using suspended layer additive manufacturing (SLAM). *Adv Funct Mater*. 2019;29(49):1904845. doi: doi: 10.1002/adfm.201904845

153. Uzcategui AC, Muralidharan A, Ferguson VL, Bryant SJ, McLeod RR. Understanding and improving mechanical properties in 3D printed parts using a dual-cure acrylate-based resin for stereolithography. *Adv Eng Mater*. 2018;20(12);1800876. doi: 10.1002/adem.201800876

154. Li X, Liu B, Pei B, et al. Inkjet bioprinting of biomaterials. *Chem Rev*. 2020;120(19):10793-10833. doi: 10.1021/acs.chemrev.0c00008

155. Dufour A, Gallostra XB, O'Keeffe C, et al. Integrating melt electrowriting and inkjet bioprinting for engineering structurally organized articular cartilage. *Biomaterials*. 2022;283:121405. doi: 10.1016/j.biomaterials.2022.121405

156. Li Q, Xu S, Feng Q, et al. 3D printed silk-gelatin hydrogel scaffold with different porous structure and cell seeding strategy for cartilage regeneration. *Bioact Mater*. 2021;6(10):3396-3410. doi: 10.1016/j.bioactmat.2021.03.013

157. Ahn SH, Lee J, Park SA, Kim WD. Three-dimensional bio-printing equipment technologies for tissue engineering and regenerative medicine. *Tissue Eng Regen Med*. 2016;13(6):663-676. doi: 10.1007/s13770-016-0148-1

158. Della Bona A, Cantelli V, Britto VT, Collares KF, Stansbury JW. 3D printing restorative materials using a stereolithographic technique: a systematic review. *Dent Mater*. 2021;37(2):336-350. doi: 10.1016/j.dental.2020.11.030

159. Jeong M, Radomski K, Lopez D, Liu JT, Lee JD, Lee SJ. Materials and applications of 3D printing technology in dentistry: an overview. *Dent J (Basel)*. 2023;12(1):1. doi: 10.3390/dj12010001

160. Wang Y, Ling C, Chen J, et al. 3D-printed composite scaffold with gradient structure and programmed biomolecule delivery to guide stem cell behavior for osteochondral regeneration. *Biomater Adv*. 2022;140:213067. doi: 10.1016/j.bioadv.2022.213067

161. Cailleaux S, Sanchez-Ballester NM, Gueche YA, Bataille B, Soulairol I. Fused Deposition Modeling (FDM), the new asset for the production of tailored medicines. *J Control Release*. 2021;330:821-841. doi: 10.1016/j.jconrel.2020.10.056

162. Jia W, Liu Z, Sun L, et al. A multicrosslinked network composite hydrogel scaffold based on DLP photocuring printing for nasal cartilage repair. *Biotechnol Bioeng*. 2024;121(9):2752-2766. doi: 10.1002/bit.28769

163. Choe R, Devoy E, Kuzemchak B, et al. Computational investigation of interface printing patterns within 3D printed multilayered scaffolds for osteochondral tissue engineering. *Biofabrication*. 2022;14(2):025015. doi: 10.1088/1758-5090/ac5220

164. Tamaddon M, Liu C. Enhancing biological and biomechanical fixation of osteochondral scaffold: a grand challenge. *Adv Exp Med Biol*. 2018;1059:255-298. doi: 10.1007/978-3-319-76735-2_12

165. Tamaddon M, Czernuszka J. The need for hierarchical scaffolds in bone tissue engineering. *Hard Tissue*. 2013;2:37. doi: 10.13172/2050-2303-2-4-773

166. Colosi C, Shin SR, Manoharan V, et al. Microfluidic bioprinting of heterogeneous 3D tissue constructs using low-viscosity bioink. *Adv Mater*. 2016;28(4):677-684. doi: 10.1002/adma.201503310

167. García-Fernández L. Osteochondral angiogenesis and promoted vascularization: new therapeutic target. *Adv Exp Med Biol*. 2018;1059:315-330. doi: 10.1007/978-3-319-76735-2_14

168. Sachlos E, Czernuszka JT. Making tissue engineering scaffolds work. Review: the application of solid freeform fabrication technology to the production of tissue engineering scaffolds. *Eur Cell Mater*. 2003;5:29-39; discussion 39-40. doi: 10.22203/ecm.v005a03

169. Perets A, Baruch Y, Weisbuch F, Shoshany G, Neufeld G, Cohen S. Enhancing the vascularization of three-dimensional porous alginate scaffolds by incorporating controlled release basic fibroblast growth factor microspheres. *J Biomed Mater Res A*. 2003;65(4):489-497. doi: 10.1002/jbm.a.10542

170. Li B, Wang H, Qiu G, Su X, Wu Z. Synergistic effects of vascular endothelial growth factor on bone morphogenetic proteins induced bone formation in vivo: influencing factors and future research directions. *Biomed Res Int*. 2016;2016:2869572. doi: 10.1155/2016/2869572

171. Centola M, Abbruzzese F, Scotti C, et al. Scaffold-based delivery of a clinically relevant anti-angiogenic drug promotes the formation of in vivo stable cartilage. *Tissue Eng Part A*. 2013;19(17-18):1960-1971. doi: 10.1089/ten.TEA.2012.0455

172. Firsching-Hauck A, Nickel P, Yahya C, et al. Angiostatic effects of suramin analogs in vitro. *Anticancer Drugs*. 2000;11(2):69-77. doi: 10.1097/00001813-200002000-00002

173. Qin C, Zhang H, Chen L, et al. Cell-laden scaffolds for vascular-innervated bone regeneration. *Adv Healthc Mater*. 2023;12(13):e2201923. doi: 10.1002/adhm.202201923

174. Liang X, Xie L, Zhang Q, et al. Gelatin methacryloyl-alginate core-shell microcapsules as efficient delivery platforms for prevascularized microtissues in endodontic regeneration. *Acta Biomater*. 2022;144:242-257. doi: 10.1016/j.actbio.2022.03.045

175. Lu X, Dai S, Huang B, et al. Exosomes loaded a smart bilayer-hydrogel scaffold with ROS-scavenging and macrophage-reprogramming properties for repairing cartilage defect. *Bioact Mater*. 2024;38:137-153. doi: 10.1016/j.bioactmat.2024.04.017

176. Xu M, Su T, Jin X, et al. Inflammation-mediated matrix remodeling of extracellular matrix-mimicking biomaterials in tissue engineering and regenerative medicine. *Acta Biomater*. 2022;151:106-117. doi: doi: 10.1016/j.actbio.2022.08.015

177. Shu C, Qin C, Chen L, et al. Metal-organic framework functionalized bioceramic scaffolds with antioxidative activity for enhanced osteochondral regeneration. *Adv Sci (Weinh)*. 2023;10(13):e2206875. doi: 10.1002/advs.202206875

178. Del Rio D, Stewart AJ, Pellegrini N. A review of recent studies on malondialdehyde as toxic molecule and biological marker of oxidative stress. *Nutr Metab Cardiovasc Dis*. 2005;15(4):316-328. doi: 10.1016/j.numecd.2005.05.003

179. Gu T, Zhang Z, Liu J, et al. Chlorogenic acid alleviates LPS-induced inflammation and oxidative stress by modulating CD36/AMPK/PGC-1α in RAW264.7 macrophages. *Int J Mol Sci*. 2023;24(17):13516. doi: 10.3390/ijms241713516

180. Vapniarsky N, Simpson DL, Arzi B, et al. Histological, immunological, and genetic analysis of feline chronic gingivostomatitis. *Front Vet Sci*. 2020;7:310. doi: 10.3389/fvets.2020.00310

181. Mata R, Yao Y, Cao W, et al. The dynamic inflammatory tissue microenvironment: signality and disease therapy by biomaterials. *Research (Wash D C)*. 2021; 2021:4189516. doi: 10.34133/2021/4189516

182. Li S, Niu D, Fang H, et al. Tissue adhesive, ROS scavenging and injectable PRP-based 'plasticine' for promoting cartilage repair. *Regen Biomater*. 2024;11:rbad104. doi: 10.1093/rb/rbad104

183. Liu D, Lu G, Shi B, et al. ROS-scavenging hydrogels synergize with neural stem cells to enhance spinal cord injury repair via regulating microenvironment and facilitating nerve regeneration. *Adv Healthc Mater*. 2023;12(18):e2300123. doi: 10.1002/adhm.202300123

184. Sun H, Xu J, Wang Y, et al. Bone microenvironment regulative hydrogels with ROS scavenging and prolonged oxygen-generating for enhancing bone repair. *Bioact Mater*. 2023;24:477-496.
doi: 10.1016/j.bioactmat.2022.12.021

185. Hu C, Huang R, Xia J, et al. A nanozyme-functionalized bilayer hydrogel scaffold for modulating the inflammatory microenvironment to promote osteochondral regeneration. *J Nanobiotechnol*. 2024;22(1):445.
doi: 10.1186/s12951-024-02723-x

186. Zhao Z, Xia X, Liu J, et al. Cartilage-inspired self-assembly glycopeptide hydrogels for cartilage regeneration via ROS scavenging. *Bioact Mater*. 2024;32:319-332.
doi: 10.1016/j.bioactmat.2023.10.013

187. Liu Z, Wang T, Zhang L, et al. Metal-phenolic networks-reinforced extracellular matrix scaffold for bone regeneration via combining radical-scavenging and photo-responsive regulation of microenvironment. *Adv Healthc Mater*. 2024;13(15):e2304158.
doi: 10.1002/adhm.202304158

188. Zhao LL, Luo JJ, Cui J, et al. Tannic acid-modified decellularized tendon scaffold with antioxidant and anti-inflammatory activities for tendon regeneration. *ACS Appl Mater Interfaces*. 2024;16(13):15879-15892.
doi: 10.1021/acsami.3c19019

189. Xue H, Zhang Z, Lin Z, et al. Enhanced tissue regeneration through immunomodulation of angiogenesis and osteogenesis with a multifaceted nanohybrid modified bioactive scaffold. *Bioact Mater*. 2022;18:552-568.
doi: 10.1016/j.bioactmat.2022.05.023

190. Deng C, Zhou Q, Zhang M, et al. Bioceramic Scaffolds with Antioxidative Functions for ROS scavenging and osteochondral regeneration. *Adv Sci (Weinh)*. 2022;9(12):e2105727.
doi: 10.1002/advs.202105727

191. Zhou T, Xiong H, Wang SQ, et al. An injectable hydrogel dotted with dexamethasone acetate-encapsulated reactive oxygen species-scavenging micelles for combinatorial therapy of osteoarthritis. *Materials Today Nano*. 2022;17:100164.
doi: doi: 10.1016/j.mtnano.2021.100164

192. Pan Y, Cao S, Terker AS, et al. Myeloid cyclooxygenase-2/prostaglandin E2/E-type prostanoid receptor 4 promotes transcription factor MafB-dependent inflammatory resolution in acute kidney injury. *Kidney Int*. 2022;101(1):79-91.
doi: 10.1016/j.kint.2021.09.033

193. da Silva Morais A, Oliveira JM, Reis RL. Small animal models. *Adv Exp Med Biol*. 2018;1059:423-439.
doi: 10.1007/978-3-319-76735-2_19

194. Liu TP, Ha P, Xiao CY, et al. Updates on mesenchymal stem cell therapies for articular cartilage regeneration in large animal models. *Front Cell Dev Biol*. 2022;10:982199.
doi: 10.3389/fcell.2022.982199

195. McIlwraith CW, Frisbie DD, Kawcak CE, Fuller CJ, Hurtig M, Cruz A. The OARSI histopathology initiative - recommendations for histological assessments of osteoarthritis in the horse. *Osteoarthritis Cartilage*. 2010;18(Suppl 3):S93-105.
doi: 10.1016/j.joca.2010.05.031

196. McCoy AM. Animal models of osteoarthritis: comparisons and key considerations. *Vet Pathol*. 2015;52(5):803-818.
doi: 10.1177/0300985815588611

197. Proffen BL, McElfresh M, Fleming BC, Murray MM. A comparative anatomical study of the human knee and six animal species. *Knee*. 2012;19(4):493-499.
doi: 10.1016/j.knee.2011.07.005

ACCSCIENCE PUBLISHING

International Journal of Bioprinting

REVIEW ARTICLE

Three-dimensional bioprinting technologies and biomaterials for nerve guidance conduits: A review

Yuexi Zhuang, Miriam Seiti, and Eleonora Ferraris*

Department of Mechanical Engineering, Faculty of Engineering Technology, KU Leuven, Leuven, Belgium

Abstract

Repairing long peripheral nerve gap injuries and reconstructing corresponding functions remain two major challenges in regenerative medicine. The application of nerve conduits, constructed via neural tissue engineering (NTE) strategies, has emerged as a prominent research focus and an essential tool for nerve repair. Among NTE technologies, additive manufacturing (AM), especially bioprinting, represents one of the most promising fabrication approaches for neural conduits. This review systematically analyzes the current research progress on peripheral nerve conduit fabrication, particularly emphasizing how different conduit structures, biomaterials, and AM techniques synergistically influence nerve regeneration outcomes. The review also summarizes the principles and recommendations for selecting appropriate nerve conduit structures for different defect lengths and injury stages, providing a theoretical basis for the design and practical application of conduit structures. Additionally, it focuses on the role of advanced bioprinting technologies in enhancing conduit complexity, cell guidance, and functional recovery. Furthermore, this review highlights emerging trends and discusses critical future directions for integrating structure design, material selection, and printing strategies toward the next generation of nerve conduits. This review aims to provide a comprehensive perspective for advancing peripheral nerve repair by bridging biomaterial engineering, manufacturing innovations, and regenerative medicine needs.

***Keywords*:** Additive manufacturing; Biofabrication; Nerve conduit; Neural tissue engineering

***Corresponding author:**
Eleonora Ferraris
(eleonora.ferraris@kuleuven.be)

Citation: Zhuang Y, Seiti M, Ferraris E. Three-dimensional bioprinting technologies and biomaterials for nerve guidance conduits: A review. *Int J Bioprint*. 2025;11(4):32-65. doi: 10.36922/IJB025140120

Received: April 2, 2025
Revised: May 16, 2025
Accepted: May 26, 2025
Published Online: June 6, 2025

Copyright: © 2025 Author(s). This is an Open Access article distributed under the terms of the Creative Commons Attribution License, permitting distribution, and reproduction in any medium, provided the original work is properly cited.

Publisher's Note: AccScience Publishing remains neutral with regard to jurisdictional claims in published maps and institutional affiliations.

1. Introduction

Peripheral nerves are characterized by a complex structure and wide distribution, making peripheral nerve injury (PNI) a very common injury in the human body.[1] Once the peripheral nerves are damaged and the nerve conduction pathways are interrupted, the respective target organs are impaired, and bodily functions are hampered. Injured peripheral nerves can self-regenerate under specific microenvironmental conditions,[2] but this repair capacity is limited. Understanding the structural organization and regenerative mechanisms of peripheral nerves is important for elucidating the post-

injury repair process and formulating effective intervention strategies. Nerves are composed of numerous axons that are wrapped and supported by connective tissues, including the endoneurium, perineurium, and epineurium. The anatomy of a healthy peripheral nerve is shown in Figure 1.

The etiology of traumatic PNI usually includes penetrating trauma, traction and compression, ischemia, electrocution, and vibratory injuries. In 1943, British neurosurgeon Herbert Seddon[3] classified nerve injuries into three categories based on the degree of damage to the neural structures: neurapraxia, axonotmesis, and neurotmesis. This is one of the most classic and basic grading systems for nerve injuries. In 1951, Sunderland[4] further refined this classification by dividing PNIs into five classes according to the depth of injury and the degree of structural damage, as shown in Table 1. This classification system helps to describe the damage of nerve structures (e.g., axons, myelin sheaths, nerve endothelium, fasciculus, and ependyma) more accurately from Grade I to V with increasing structural damage and provides a theoretical basis for the subsequent design and selection of different nerve conduits.

It is also important to note that various types of PNI exhibit significant differences in mechanisms, regenerative potential, and clinical manifestations. Studies have demonstrated that peripheral nerve defects with small defects and short gap lengths (usually less than 5 mm) may heal spontaneously under specific conditions.[5] In contrast, when the nerve defects are larger, and the gap length is longer, it is difficult for regenerated nerve axons to accurately bridge the proximal-distal ends of the defective nerves.[6] Consequently, the nerve's self-repair ability is limited. More severe nerve deficits often result in lifelong disability. Therefore, the repair of long-gap peripheral nerve defects and the reconstruction of the corresponding function are major challenges in the field of regenerative medicine.[7]

Autologous nerve grafting is considered the gold standard for the treatment of PNI.[8,9] However, inherent shortcomings, such as limited donor availability and susceptibility to neuroma formation, have prevented autologous nerve grafts from being widely used in clinical practice.[10] Neuroma is a non-malignant neural tissue mass, usually formed due to abnormal proliferation and disordered arrangement of regenerating axons in the absence of effective guidance after PNI.[11] It not only hinders normal nerve regeneration and interferes with the correct connection between axons and target tissues but also may trigger persistent neuropathic pain, which severely affects the patient's sensory and motor functions and even leads to functional reconstruction failure. Therefore, effective prevention of neuroma formation during nerve repair is one of the key objectives to ensure the quality of regeneration.

In recent years, the development of biomedicine and cross-disciplinary interventions, such as biomaterials, biotechnology, and tissue engineering, have provided new solutions for repairing defective nerves. Among

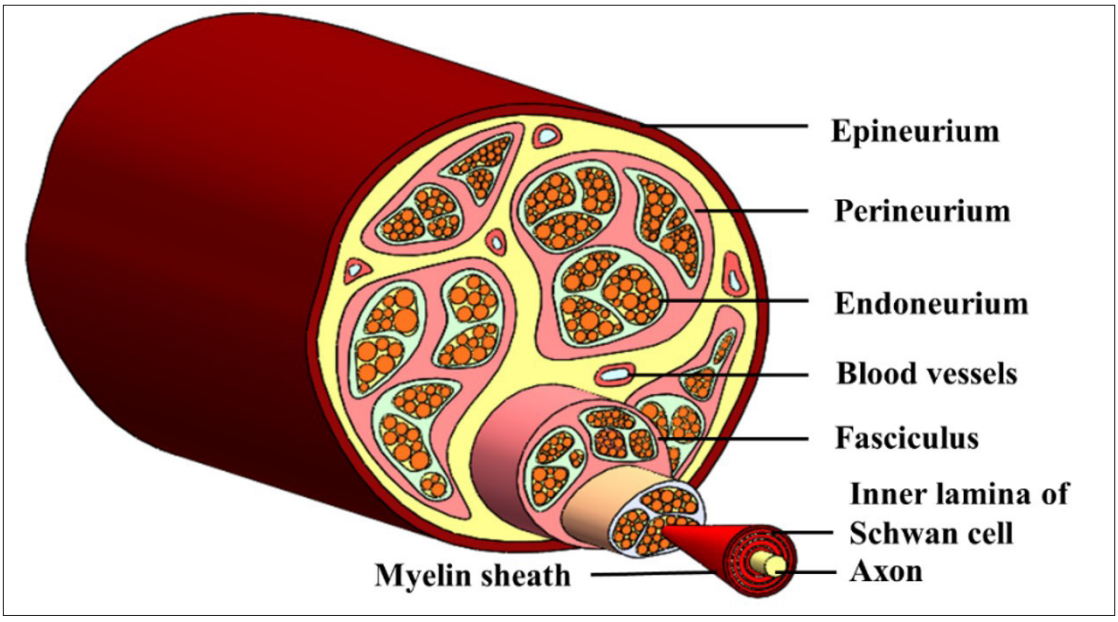

Figure 1. Anatomy of a peripheral nerve in a healthy state.

Table 1. Sunderland's classification of peripheral nerve injuries

Grade	Structural damage	Regeneration potential
I	Local myelin disruption only; axon and connective tissue intact	Complete; recovers in days to weeks
II	Axonal disruption; endoneurium, perineurium, and epineurium intact	Complete; good outcome, about 4–6 weeks
III	Damage to axon, myelin, and endoneurium; perineurium and epineurium intact.	Partial; risk of misdirection
IV	Damage to all structures except epineurium (axon, myelin, endo-, and perineurium)	Poor; surgical repair often required
V	Complete nerve transection, including epineurium	None; requires surgical repair

them, neural tube scaffolds constructed via neural tissue engineering (NTE) approaches have become the main research direction to guide the regeneration of defective nerves.[12] The core of NTE lies in using functionalized biomaterials to construct NTE scaffolds that mimic the natural structure of peripheral nerves, provide a suitable microenvironment for nerve regeneration, and ultimately promote nerve repair.[13] Currently, NTE scaffolds are mostly tubular scaffolds with diameters and lengths matching those of the defective nerves, also known as nerve guidance conduits (NGCs). Studies have shown that such nerve conduits have many advantages in defective nerve repair by serving as: (i) a three-dimensional (3D) specific structure as a suitable microenvironment for migration, proliferation, and functionalization of neural cells, (ii) contact guidance for the directional growth of axons, which in turn improves the accuracy of nerve alignment, and (iii) a sufficient mechanical support for the regenerating nerve fibers, reducing the tension of the surgical suture opening and preventing the growth of scar tissue. Therefore, these advantages make artificial nerve conduits-guided nerve regeneration an ongoing significant research direction.[14]

The main role of the nerve conduit is to bridge injured nerves, provide space and nutrition for axonal growth, and serve as the interface for cell transplantation seeding to treat nerve injuries—guiding cell growth, proliferation, differentiation, migration, apoptosis, and eventually promoting nerve regeneration. Peripheral nerve regeneration is specifically divided into five stages[15] in the presence of nerve conduits, as illustrated in Figure 2: (i) the fluid phase, (ii) the stromal phase, (iii) the cell migration phase, (iv) the axon repair phase, and (v) the myelin formation phase. The fluid phase is within 24 h after implantation. Plasma effluent produced by proximal and distal nerve stumps fills the conduit, leading to the accumulation of neuro-affective factors and extracellular matrix (ECM) molecules. The stromal phase occurs 1–3 days after implantation. ECM precursor molecules emerge from the proximal end and form decellularized fibrin cords between the distal and proximal ends. The cell migration phase occurs 4–7 days after implantation. Schwann cells (SCs), endothelial cells, and fibroblasts migrate from proximal to distal ends, aligning and proliferating along the fibrin cords to form biologic tissue cords, i.e., Bungner bands. The axon repair phase occurs within the 8th to 14th day after implantation. Biological tissue cords provide nutrients and topographical lines for axon repair, and regenerating axon buds reach the distal end using biological tissue cords under the guidance of growth cones. Lastly, the myelin formation phase occurs 15–28 days after implantation, during which SCs transform into a myelin phenotype and form mature myelin with regenerating axons. This is followed by a 1–3-month functional recovery period to restore nerve conduction and tissue integration.

Accordingly, an ideal NGC should meet the following requirements: (i) possesses bioactivity to guide axon growth from proximal to distal stumps, avoiding the formation of neuromas,[16] (ii) has mechanical properties similar to those of human nerve tissue and with enough flexibility to avoid compression of the nerve tissue (tensile strength from 3.39 to 35.93 N and elastic modulus between 8 and 16 MPa), (iii) has good biocompatibility and non-cytotoxicity when in contact with neural cells, without immune reaction,[17] (iv) possess controlled degradation rate to match the one of peripheral nerve regeneration,[18] so that the ideal NGC will gradually break down as the nerve heals, eliminating the need for surgical removal, and (v) has a suitable porous structure, which helps to block scar tissue that hinders nerve regeneration, while allowing essential nutrients and signals to pass through[19] and providing a healthy environment for cellular communication and axonal growth. The basic requirements of these properties are mainly determined by the material and structure of the neural scaffold.[20] Data for this review were obtained from Web of Science, PubMed, and Scopus databases to ensure coverage of high-quality research in the field. To search for studies related to 3D-printed nerve conduits, a combination of the keywords "3D printing" or "3D bioprinting" and "nerve conduit" or "nerve guidance conduit" or "neural regeneration" was used. The search covered 1991–2023

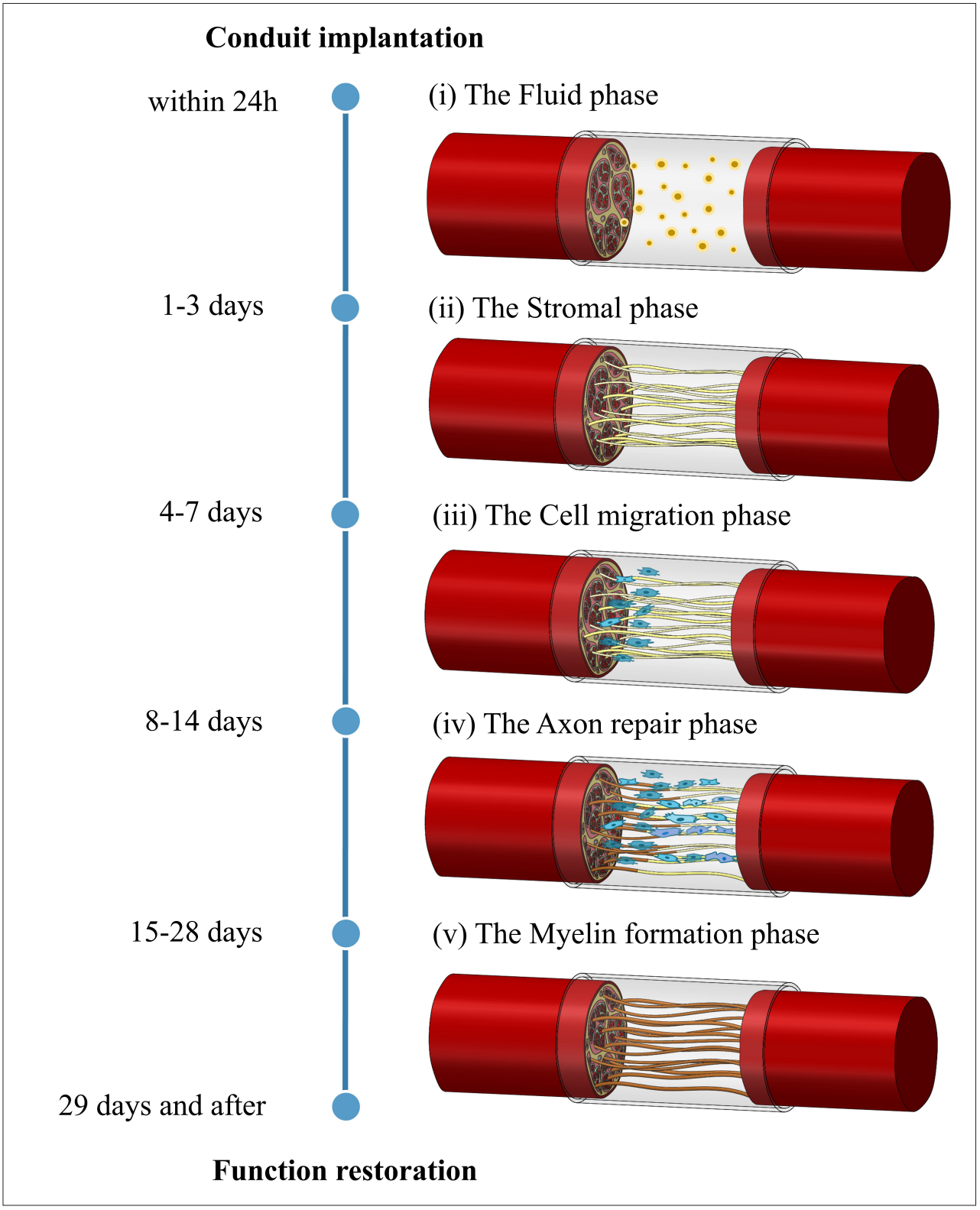

Figure 2. Five stages of peripheral nerve regeneration in the presence of a nerve conduit.

and filtered for topic abstracts and keywords. The statistical data is shown in Figure 3. The statistics include original research, reviews, and conference papers. As shown in Figure 3, research on nerve conduits has increased steadily since the 1990s, with a current focus on the development and study of ideal biomaterials and technologies for nerve conduit biomanufacturing.

Traditional techniques for the preparation of nerve conduits mainly include solvent casting,[21] phase separation,[22] gas foaming,[23] electrospinning,[24] and freeze-drying.[25] These techniques have inherent limitations, such as poor repeatability, low resolution, and limited control of the manufacturable shape, which greatly limit the structure and application of nerve conduits.[26] Additive manufacturing (AM) can effectively overcome (some of) the limitations of these traditional technologies.[27] AM (commonly known as 3D printing) is a manufacturing approach that allows the fabrication of constructs through layer-by-layer (LBL) deposition of materials starting from a digital model file,[28] which is widely used in aerospace,[29] automotive manufacturing,[30] healthcare,[31] construction,[32] textile, and other fields.[33] AM enables the fabrication of complex parts, including scaffolds, lattice structures, and customized patterns, in a wide range of materials, including biopolymers and hydrogels, enabling rapid prototyping of biological conduits with variable designs[34] and providing new solutions for the fabrication of neural conduits.

Since 2011, 3D bioprinting has been increasingly applied to NGC research (Figure 3B). Biofabrication is defined as "the automated generation of biologically functional products with structural organization from living cells, bioactive molecules, biomaterials, cell aggregates, such as micro-tissues, or hybrid cell-material constructs, through bioprinting or bioassembly, and subsequent tissue maturation process".[35(p.5)] This definition includes the fabrication of scaffolds with hierarchical structural properties or smart-surface properties within the realm of bioprinting.[36] The advent of 3D bioprinting has led to more solutions for nerve conduits. Although various biomaterials and preparation strategies have been widely investigated, there are still challenges in achieving good biocompatibility, appropriate mechanical properties, and effective nerve regeneration at the same time. Meanwhile, emerging technologies such as 3D bioprinting offer unprecedented possibilities for constructing NGCs with fine structures, adjustable functions, and individualized features. However, their synergistic integration with applicable biomaterials and bioactive factors is still in its infancy. Therefore, a review of the design principles of nerve conduits, the selection of biomaterials, and the latest advances in 3D bioprinting technologies are needed to identify the current critical issues and provide guidance for future research in this area. Hence, this review will discuss the application of bioprinting technology in the 3D biofabrication of neural conduits, with a focus on its research progress and challenges, specifically divided into three main sections: (i) a discussion of the advantages and limitations of various nerve conduit structures, which provides guidance on selecting appropriate designs under different injury conditions, (ii) introduction of the main biomaterials used in nerve conduit fabrication and their applications in peripheral nerve regeneration, and (iii) summary of current 3D bioprinting technologies for nerve conduits along with relevant fabrication strategies. Finally, the review highlights the key challenges in translating nerve

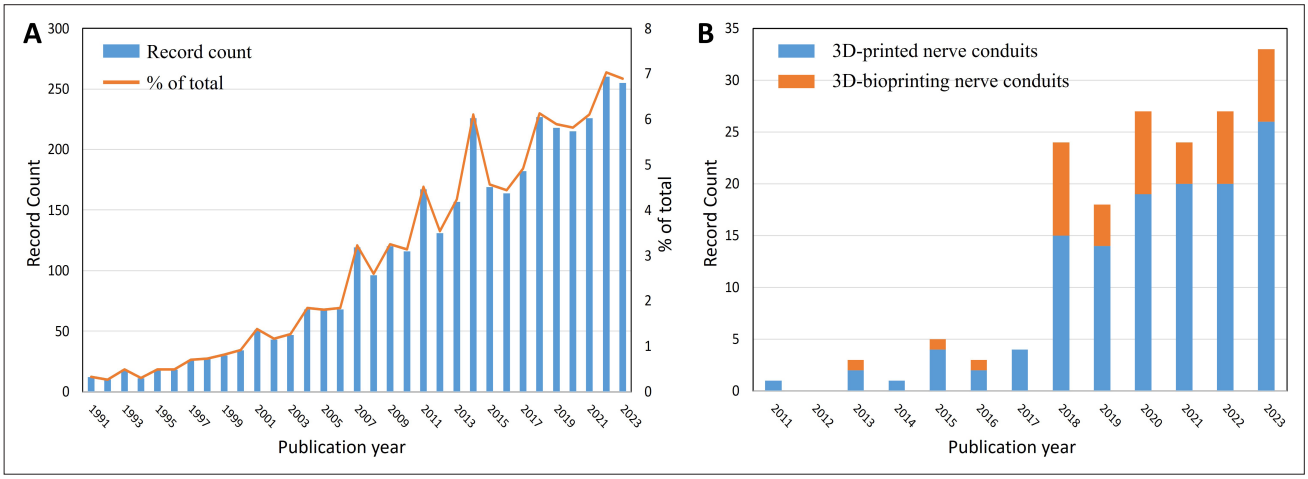

Figure 3. Publication trends in nerve conduit research and 3D printing applications (1991–2023). (A) Number of nerve conduit papers published per year from 1991 to 2023. (B) Number of three-dimensional (3D)-printed nerve conduits and 3D bioprinting nerve conduits papers published per year from 2011 to 2023.

conduits from laboratory research to commercialization and clinical applications and outlines potential future research directions and development trends.

2. Design of a nerve conduit

An ideal nerve conduit should have a rational structural design to provide guidance, support, and a nutrient-rich environment for axonal regeneration. With the advancement of biomaterial science and manufacturing technology, researchers have developed a variety of structural conduits based on the morphological and functional characteristics of natural nerves, such as hollow conduits, multi-channel conduits, porous conduits, conduits with surface microstructures, and bifurcated conduits, as shown in Figure 4. Each structure provides specific solutions for different barriers to nerve regeneration with its own adaptation scenarios and limitations. This chapter systematically introduces the design concepts, key research advances, and experimental performances of different structural nerve conduits.

2.1. Hollow nerve conduit

In preliminary scientific cases, neural conduits were prepared as simple hollow cylinders, commonly known as hollow nerve conduits. This type of conduit has a simple structure that is easily fabricated. It also promotes the formation of fibrin networks during blood coagulation, the migration of various cells (e.g., SCs, endothelial cells, fibroblasts, etc.), and the accumulation of neurotrophic growth factors in the surrounding tissue. This structure is capable of reducing neuromas and scarring and is suitable for repairing short nerve gaps. The first hollow bone bridge for a nerve defect was attempted in a dog model in 1881; however, the results were unsatisfactory.[37] In 1982, Lundborg et al.[38] attempted to bridge a 6 mm nerve defect in rats with a hollow and clear silicone conduit, demonstrating that axonal regeneration begins with the formation of a fibrin clot between the two nerve stumps within the empty conduit, which is subsequently invaded by capillaries, axons, and non-neuronal cells, including SCs. Although the extent and mechanisms by which stump scaffolding promotes cross-gap regeneration were not fully elucidated, the study increased the interest in understanding nerve regeneration. In 1983, Williams et al.[39] further investigated the process of peripheral nerve repair using neural stem cells (NSCs) and impermeable hollow silica nerve conduits by bridging a 10 mm rat sciatic nerve defect. They observed axonal growth reaching the distal stump after 3 weeks.

Although such an NGC structure has been a popular choice for many studies, it presents many drawbacks, such as the lack of morphological and biochemical cues necessary for directional nerve growth,[40] and a very limited effect on the repair of PNI. To better mimic the bundle structure of peripheral nerves, attempts have been made to add fillers, such as fibers, gels, and sponges, as internal filler matrices to reduce the lack of cues required to guide the directional growth of nerves in the hollow conduits and to provide exogenous support for the attachment, migration, and proliferation of SCs. Qin et al.[41] filled the artificial NGC with microfilaments of 80–120 μm in diameter and injected nerve growth factor (NGF) into the conduit to repair sciatic nerve defects in rats. As a result, the number of regenerated axons and myelin maturation were close to those of control autologous nerve grafts. Later,

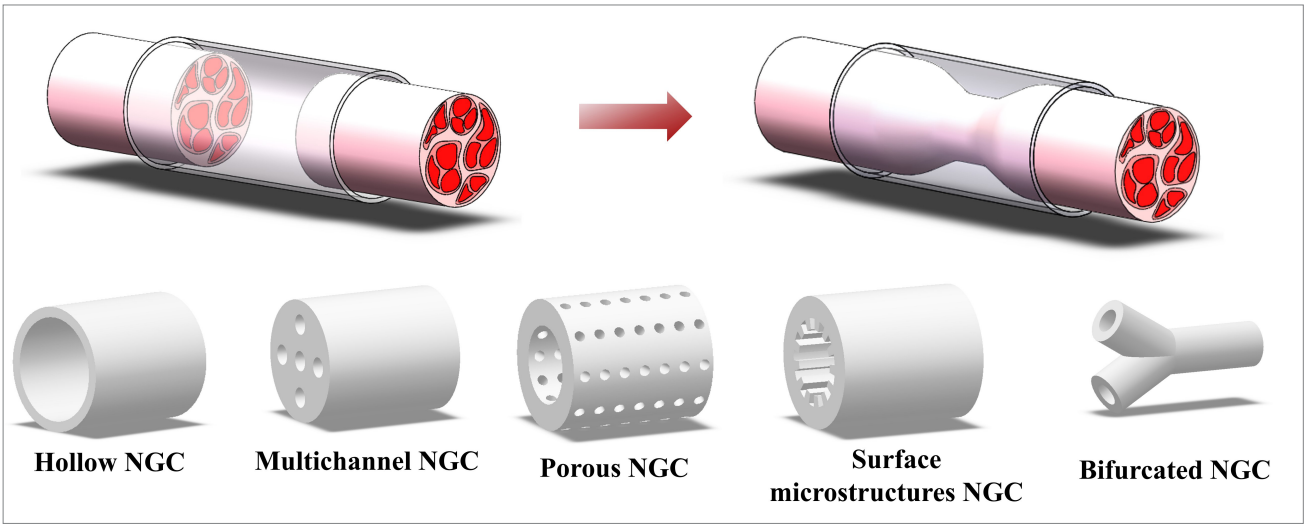

Figure 4. Schematic diagram of various structures of current nerve guidance conduits (NGCs).

Lundborg et al.[42] filled eight longitudinal polyamide fibers into a silicone NGC for the repair of a 15 mm sciatic nerve defect in rats for the first time. Results showed that nerve regeneration was significantly improved compared with that of hollow silicone nerve conduits due to the presence of intraluminal fillers. However, a densely packed lumen matrix was found to hinder axonal regeneration and nerve cell migration. Several studies have demonstrated that the addition of fillers to hollow conduits can compensate for defects and promote nerve repair, but the type, structure, and density of fillers still need further research.

2.2. Multi-channel nerve conduit

Studies have generally shown that multi-channel nerve conduits are more conducive to promoting nerve repair than hollow nerve conduits. First, the longitudinally aligned lumens in multi-channel conduits can act as microtubules with a large surface area required for synthesizing basement membranes, which has a significant positive effect on the attachment, proliferation, and migration of SCs. Moreover, the multiple longitudinal lumens within the nerve conduits reduce axon dispersion and promote the longitudinal extension of axons. This longitudinal arrangement also reduces the rate of axonal misrouting when connecting to distal nerve stumps. However, studies also demonstrated that additional internal structures can affect NGC properties, such as permeability, mechanics, and degradation.[43] In addition, they are also structurally complex and difficult to fabricate.

Over the past few decades, researchers have explored various approaches and fabrication methods to develop microchannels within nerve conduits, which can facilitate nerve repair. In 2004, Moore et al.[44] investigated injection molding and rapid solvent evaporation to fabricate nerve conduits with intraluminal channels. The *in vivo* study on transected adult rat spinal cords further confirmed the presence of regenerating axons 1 month after surgery. Lee et al.[45] also performed an *in vivo* study using arginine–glycine–aspartate (RGD)-functionalized multi-channel nerve conduits in a 10-mm sciatic nerve transection rat model. The results showed that the axon density in the conduit was significantly higher than that in the polycaprolactone (PCL) group after 8 weeks, and the cross-sectional area of gastrocnemius muscle fibers was restored to 80% of that of the healthy control, suggesting that the conduit is close to the autograft in terms of structure, function, and muscle reinnervation. Alternatively, Wang et al.[46] used electrostatic spinning to prepare a multi-channel NGC with directional arrangement of fibers. *In vivo* experiments demonstrated that the conduit had a good guiding effect on nerve repair. Additionally, Jeffries and Wang[24] used electrospinning to fabricate multi-channel nerve conduits. *In vitro* studies show that their high surface area and porosity enhance cell penetration along the nerve-directed channels. The small-sized gaps between the electrostatically spun fibers limited the migration of most of the cells to the channel walls and minimized the influx of inflammatory cells from the surrounding tissues during implantation. The multi-channel NGC, therefore, provided an area of low growth resistance, which is more suitable for guiding axonal growth.

2.3. Porous nerve conduit

Porous structures facilitate the infiltration of cells, the diffusion of nutrients and molecular signals, and the drainage of metabolic waste products. These features promote early adhesion, spreading, proliferation, and differentiation of SCs, as well as the formation of Bungner bands and vascularization, while reducing fibrous scar formation.[47] In addition, studies have shown that the pore structure can alter the degradation rate of nerve conduits by affecting the accumulation of localized monomers and pH.[48] Particularly, Odelius et al.[49] investigated the effect of pore size on the degradability of polylactic acid (PLA) conduits and the release of degradation monomer products. Their study showed that larger pore structures can accelerate degradation through autocatalysis, whereas smaller pore sizes lead to a slower degradation rate. Wu et al.[50] investigated the *in vitro* chemical degradation properties of 3D poly(lactic-co-glycolic acid) (PLGA) porous conduits, revealing that conduits with a higher porosity or a smaller pore size degraded more slowly than the opposite conditions, thus outlasting those with a lower porosity or a larger pore size. The effects are attributed to both wall thickness and surface area size because the scaffolds with lower porosities or larger pores possess thicker pore walls and smaller surface area, which depress the diffusion of acidic degradation products, resulting in stronger acid-catalyzed hydrolysis. Song et al.[51] also investigated the degradation characteristics of porous polyester materials using a mathematical modeling strategy. The increase in porosity slows down the autocatalytic reaction and the degradation process by enhancing the diffusion coefficient of oligomers. The effect of porosity is gradually weakened as further increases in porosity lead to a reduced rate of improvement in diffusion. Numerous experimental results have also confirmed the importance of porous structures on the physicochemical and biological properties of nerve regeneration and repair, leading to their increased widespread application in the design of nerve conduits.

Nonetheless, porous nerve conduits possess certain drawbacks, including the presence of large pore sizes (normally >200 μm) that can result in fibroblast deposition, thereby hindering axonal growth. Ideal

porous nerve conduits usually have a pore size of 20–50 μm and a circular, polygonal, or longitudinal shape with a certain direction to accommodate cell permeation, nutrient exchange, and axonal guidance. However, pore morphology and distribution are usually random due to the limitations of the manufacturing methods, making it difficult to achieve a customized solution. On the contrary, 3D printing can effectively overcome these limitations, generating highly regular and consistent pore structures with a high degree of reproducibility. For instance, Tao et al.[52] developed a low-temperature gelatin porous conduit using a 3D-printed mold to promote functional recovery of transected peripheral nerves after nerve suturing. It was reported that due to its porous structure, the conduit could collapse under mechanical force and return to its original shape after absorbing saline solution. This shape memory property simplifies the conduit installation procedure, demonstrating the potential clinical application of porous NGCs in facilitating nerve sutures.

2.4. Micropatterned nerve conduit

Micropatterns on the inner surface of nerve conduits are widely used to influence cell attachment, migration, orientation, and cellular processes. One of the most used surface microstructures is the microgroove, which provides topological cues to guide cell orientation and migration in a physical model approach. Studies have shown that the *in vitro* nerve sheath can recognize the topological structure of the catheter surface[53] and extend and grow along the length of microgrooves on the plane substrate.[54]

As an example, Schmalenberg et al.[55] evaluated the ability of a microgroove-printed polymer matrix to direct the alignment of SCs. After 4 h of cultivation, more than 47% of SCs on the micro-grooved substrate were arranged within ± 20° of the groove direction, while SCs on the unpatterned substrate showed random arrangements without a clear orientation. This study found that patterned polymer matrices can enhance peripheral nerve regeneration by creating a highly ordered matrix of SCs to guide neurons. Rutkowski et al.[56] used reactive ion etching to fabricate hollow conduit lumens with microgrooves (10 μm width, 4.3 μm depth, 10 μm spacing). Such conduits combine a microfabricated matrix that guides axons at the cellular level with SCs that produce growth factors to promote regeneration. The biodegradable microgroove conduit, pre-implanted with SCs, provided physical, chemical, and biological guiding cues for axon regeneration and offered a better alternative to conventional conduits, especially for repairing sciatic nerve transactions. Davis et al.[57] prepared PLGA films with 10/10 μm and 30/30 μm microgroove structures by microlithography that sustained the release of 3 μg/cm² of FK506 for more than 56 days. In an *in vitro* evaluation of dorsal root ganglion (DRG), the released drug maintained its biological activity and significantly promoted neurite extension (average length up to the level of the positive control 10 ng/mL group). These findings suggest that this structure holds promise as a neuroprosthetic material, offering both topological guidance and sustained drug release. Yu et al.[58] utilized stamping technology to inscribe longitudinally distributed grooves and ridged surfaces of 4–5 μm depth and 5 μm width on porous PCL membranes loaded with artificial peptides. The electrophysiological recovery of the regenerated nerve was significantly enhanced in a rat model of traction sciatic nerve injury, and the compound muscle action potential amplitude was increased by more than 50% at 4 weeks postoperatively. In parallel, *in vitro* experiments showed a significant increase in both the number of SCs adhering to the membrane and their aspect ratio, validating the effectiveness of the structural–functional integration strategy for reconstructing nerve architecture and function.

2.5. Bifurcated nerve conduit

Peripheral nerves are mostly interconnected, branching structures of varying sizes, making a single tubular structure insufficient to meet the needs of complex nerve repair. On the contrary, bifurcated y-shaped nerve conduits can play an important role in inhibiting the formation of traumatic neuromas after PNI, which often leads to long-term functional deficits. Although traditional fabrication methods limit the complexity of NGC structures, AM technology has enabled the fabrication of bifurcated or y-shaped nerve conduits suitable for peripheral nerve bifurcations. Bolleboom et al.[59] 3D printed a customized y-shaped conduit and an autologous nerve graft to create a closed loop that could induce axon regeneration into the y-shaped conduit, which accurately fitted the injured proximal nerve end. This relatively simple combined approach prevented neuroma formation and significantly reduced the number of axons in the middle of the autograft, making it suitable for unilateral PNI. Zhang et al.[60] demonstrated for the first time that individual nerve stumps can form complex branching neural networks in multi-branched nerve conduits. They utilized digital light processing (DLP) 3D technology with gelatin-methacryloyl (GelMA) to construct bifurcated nerve conduits and evaluated their efficacy by transferring them from the tibial nerve to the peroneal nerve in rats. Functional and histologic evaluations showed that the bifurcation of NGC not only promoted the regeneration and functional recovery of the injured peroneal nerve but also preserved a part of the function of the donor's nerve conduit. Alternatively, Hu et al.[61] used an indirect 3D printing technique to prepare bifurcated, multi-

channel cryopolymerized GelMA gel conduits. The results suggested that such conduits could support the attachment, proliferation, and survival of adipose-derived stem cells and upregulate their neurotrophic factor mRNA expression. After implantation in rats, the bioconduits successfully supported reinnervation across a 10 mm sciatic nerve gap. The results, in both functional and histological assessments, were comparable to those of autografts, highlighting its potential clinical utility in peripheral nerve regeneration. AM can also be exploited in combination with nerve image data to successfully produce complex bifurcation nerve injuries. Johnson et al.[62] 3D-printed a rat sciatic nerve bifurcation model by scanning its anatomical structures, and the acquired data were further used to guide the preparation of bifurcated NGCs.

2.6. Selection strategies

Different structural types of nerve conduits offer distinct advantages in terms of functional performance and tissue compatibility. Therefore, selecting the most appropriate conduit type based on the specific characteristics of a nerve injury remains a critical challenge in both current research and clinical practice. A thorough understanding of the structural and functional attributes of each conduit type is essential for evaluating their suitability and developing optimal application strategies across diverse clinical scenarios, thereby enhancing the efficacy of nerve regeneration.

Hollow conduits have significant limitations in guiding directional axonal growth due to the lack of morphological cues and biochemical signals,[63] and are usually applied to short-distance nerve defects (<5 mm). In contrast, multi-channel conduits could help to minimize axonal vagrancy by providing a larger surface area for cell attachment and a more defined growth pathway, making them suitable for the repair of medium-distance (5–8 mm) defects. The porous conduit provides excellent permeability, allowing the free exchange of nutrients and molecular signals inside and outside the conduit and promoting the elimination of metabolic wastes while contributing to the adhesion, migration, and proliferation of SCs. Surface micropatterned conduits provide a significant enhancement of axonal orientation through specific microstructures, such as grooves or gradient arrangements, and are particularly suitable for the repair of larger gap defects.

In addition to the structural characteristics of the conduit, different tissue states, biological responses, and regenerative potentials at various process stages place unique requirements on the nerve conduit's selection strategy.[64] The timing of post-injury treatment can be divided into early stage (<4 weeks) and advanced stage (>4–6 weeks). In the early stage of injury, the distal nerve has not yet undergone severe degeneration. SCs still retain good proliferation and guidance ability, exhibit strong axonal growth, and show no significant local scarring.[65] At this time, excessive support is unnecessary, as a simple structural hollow conduit may be preferred to provide basic mechanical support with axonal guidance. In advanced injury, the distal nerve tissue exhibits significant degeneration and scar deposition, a decline in the number and function of SCs, a deteriorated local regenerative microenvironment, and reduced axonal regenerative potential.[66] In such cases, hollow conduits often struggle to function well, and a conduit that is more supportive, such as multi-channel conduits, porous structure conduits, or micropattern conduits, should be chosen. In addition, in advanced nerve injury, scar tissue formation is one of the key factors hindering regeneration. Massive deposition of collagen with other extracellular matrices leads to tissue sclerosis, which forms a physical barrier, interferes with the direction of axonal growth, and may induce the formation of neuromas. Therefore, the selection of nerve conduits with anti-scarring or pro-regenerative functions is crucial in advanced nerve repair. Micropatterned conduits can effectively guide the directional growth of axons and reduce the obstruction of regeneration by scarring. The characteristics of different conduit structures and their suitability are summarized in Table 2. In summary, the selection of appropriate NGC structures not only facilitates the reconstruction of axonal guidance pathways but also optimizes cellular behavior and promotes the localized accumulation of neurotrophic factors, thereby accelerating nerve regeneration and enhancing functional recovery.

3. Biomaterials for nerve conduit

The structure of the conduit significantly influences the overall outcome of the nerve regeneration process. Nevertheless, structural design alone is insufficient to achieve optimal nerve repair; the choice of materials also plays a critical role. Properties of the conduit material, such as biocompatibility, mechanical performance, degradation rate, and bioactivity, directly impact its functionality during nerve regeneration.[67] Therefore, a synergistic interplay between material and structure is essential. A proper design of the structure provides the necessary space and orientation for nerve repair, while suitable materials ensure that the structure remains stable in the physiological environment to support the growth, proliferation, and differentiation of neural cells. The organic integration of both elements is key to achieving effective nerve regeneration.

The selection of biomaterials for NGCs is based on the following requirements: (i) good processability, (ii)

Table 2. Nerve guidance conduit structures and their advantages and disadvantages

Structure	Structural characteristic	Advantages	Disadvantages	Application
Hollow nerve conduit	Single hollow, no internal filling	Simple structure, easy to manufacture, facilitates the migration of various cells and the accumulation of neurotrophic growth factors	Lack of morphological and biochemical cues; limited regeneration efficiency	Shorter nerve defects, typically less than 5 mm; early damage
Multi-channel nerve conduit	Multiple longitudinal channels, simulated nerve bundle	Provides a larger surface for cell attachment, facilitates migration of Schwann cells, and reduces axonal dispersion	Complex structure, difficult to manufacture, and susceptible to permeability and degradation	Medium length nerve defects, 5–8 mm; advanced injuries
Porous nerve conduit	Porosity in the conduit wall	Allows infiltration of cells, nutrients, and molecular signals, as well as excretion of metabolic wastes	Excessive pore size leads to deposition of fibroblasts and hinders axonal growth; pore distribution is often uneven	Medium length nerve defects, 5–8 mm; advanced injuries
Micropatterned nerve conduit	Microstructure with microgrooves, ridges, etc., on the inner surface	Promotes cell-directed migration and axonal alignment	High manufacturing precision; difficulty in fabricating	5–10 mm; potential to repair longer nerve defects and advanced injuries
Bifurcated nerve conduit	Y-shaped or multi-branch structure	Suitable for complex nerve branch repair; prevents neuroma formation	Difficult to manufacture; requires personalized design	Bifurcated and multi-path nerves

good biocompatibility and bioactivity, and (iii) suitable physicochemical properties, such as mechanical strength and structural stability. The materials for 3D-printed NGCs can be categorized into natural or synthetic polymers based on the type of embedded cells. These biomaterials and representative NGC examples (Table 3) are discussed further.

3.1. Natural polymers

Natural polymers are macromolecular compounds present in living organisms and have re-emerged in the last few decades as major bioactive substances due to the presence of biofunctionalized and bioactive molecules with biomimetic properties and natural recombination. Most natural materials are biocompatible and can be rapidly degraded *in vivo*,[68–70] promoting cell adhesion, migration, growth, and proliferation while avoiding the toxic effects caused by synthetic materials.[71] Excellent biocompatibility, minimal immunogenicity, and the ability to support cell growth make them excellent candidates for the fabrication of NGCs. Chitosan, silk fibroin (SF), gelatin, and collagen are natural polymers commonly used for the 3D printing of nerve conduits.

3.1.1. Chitosan

Chitosan (and derivatives) is a biodegradable linear polysaccharide, obtained from shrimp shells or crustaceans, with excellent biocompatibility and antimicrobial properties. The presence of groups such as amines/aminos and hydroxides on its molecular chain allows cells to better adhere and grow on its surface. In addition, chitosan has good processability and easy degradation in animals.[72] It has been used as an NGC material by controlling its degradation time without the need for secondary surgical removal. Pure chitosan has a tensile modulus of about 20–50 MPa and a modulus of elasticity of 0.5–1.5 GPa.[73] Despite the many advantages, its low strength, the absence of temperature sensitivity, and its shear-thinning behavior limit its applications in the field of biofabrication. Therefore, chitosan is often used in combination with other materials to enhance its mechanical properties and provide a more stable conduit structure. By crosslinking chitosan with high-performance synthetic polymers such as PLA or PCL, the mechanical properties can be significantly enhanced. The resulting composites typically have a tensile strength of 100–150 MPa and a modulus of elasticity of more than 3–4 GPa, making them more suitable for application in scenarios that require high mechanical properties, such as nerve conduits and bone tissue engineering.[73] For instance, Nawrotek et al.[74] prepared chitosan/PCL conduits doped with bioactive agent microspheres using electrodeposition combined with extrusion printing. The structural properties of the conduits did not change significantly during incubation at 37°C in phosphate buffer solution (pH 7.4) for up to 28 days, demonstrating good structural stability. Bianchini et al.[75] prepared porous 3D-printed chitosan/PCL using genipin cross-linking to improve the conduits' physicochemical properties. The results demonstrated that compared to chitosan conduits, the hydration rate of the genipin-cross-linked conduits was significantly reduced, with the equilibrium constant of 470.3 ± 29.7%, which is much smaller than that of the chitosan conduits (642.3

Table 3. Biomaterials and representative examples of nerve guidance conduits

Materials	Method	Conduit structure	*In vitro*/*in vivo*	Model	Culture time	Resolution	Outcomes	References
Chitosan/neurotrophic factor-3	Topography method	Hollow	*In vivo*	15 mm remote nerve defects in rats	12 weeks	10 μm	Effective functional recovery in a rat model of 15 mm sciatic PNI	[76]
Chitosan/PCL	3D melt extrusion	Spiral hollow conduit	*In vitro*	*In vitro* assessment of cell behavior	28 days	1 mm	The structural properties did not change significantly after incubation in phosphate buffer solution, showing good structural stability	[77]
Chitosan/poly-ε-caprolactone	Extrusion-based 3D printing and freeze-drying	Porous	*In vitro*	*In vitro* assessment of cell behavior	3 months	–	Genipin incorporation significantly reduced the degradation rate of the catheter matrix and stabilized the chitosan matrix	[78]
Chitosan/PCL	Extrusion printing	Microstructure modification	*In vivo*	15 mm remote nerve defects in rats	4 months	1 mm	The printed patterns showed excellent flexibility and toughness, capable of withstanding continuous compressive and bending stresses	[164]
Silk fibroin	Electrospinning	–	*In vivo*	10 mm nerve defects in rats	12 weeks	–	Low-molecular filipin composite conduit with good biosafety and degradability; promotion of sciatic nerve regeneration in rats	[83]
PPy/SF	3D electrospinning	–	*In vitro*	*In vitro* assessment of cell behavior	30 days	–	SCs mainly adhered to the surface of the conduits and maintained a normal morphology on the PPy/SF conduit	[84]
SF/dorsal root ganglion/SCs	Injection molding	Hollow	*In vivo*	10 mm nerve defects in rats	12 weeks	–	Enhancement for PNI's repair by incorporating neural equivalents into SF-based conduits	[157]
SF	Electrospinning	Multi-channel		–	–	1 mm	Bionic multi-channel functionalized nerve guidance conduits with comparable mechanical behavior to that of the rat sciatic nerve	[80]
Antheraea pernyi SF/poly(L-lactic acid-co-caprolactone)/graphene oxide nanofibers	Electrospinning	Multi-channel	*In vivo*	10 mm sciatic nerve defect in rats	12 weeks	10 μm	3D biomimetic nerve scaffolds had the ability to offer an effective guiding interface for neuronal cell growth	[173]
PPy/SF	Electrospinning	Double-deck	*In vivo*	10 mm sciatic nerve defect in rats	6 months	0.1 mm	Longitudinally guided PPy/SF electrically conductive composite conduit with good performance for clinical applications	[81]
Collagen/hydrogel/poly(l-lactic acid-co-ε-caprolactone	Electrospinning	–	*In vivo*	8 mm nerve defects in rats	12 weeks	–	Aligned collagen hydrogels are favorable for nerve regeneration as a directional guidance pathway	[85]
Collagen/hyaluronic acid/PCL	Electrospinning	–	*In vitro*	*In vitro* assessment of cell behavior and neuronal differentiation	21 days	–	3D composite conduit with a permissive environment for the proliferation and maturation of SCs, allowing axonal growth	[86]

(*Continued...*)

doi: 10.36922/IJB025140120

Table 3. Continued...

Materials	Method	Conduit structure	*In vitro*/*in vivo*	Model	Culture time	Resolution	Outcomes	References
GelMA/Engelbreth–Holm–Swarm	3D printing	Hollow	*In vitro*	*In vitro* assessment of cell behavior	16 weeks	0.1 mm	Confirming that the Engelbreth–Holm–Swarm hydrogel filling accelerates the repair of nerve defects	[92]
GelMA/methoxy PEG-PCL	Digital light processing	Hollow	*In vivo*	10 mm nerve defects in rats	3 months	–	Gelatin conduit as a physical microenvironment for axonal extension and the promotion of functional recovery after PNI	[93]
GelMA/bone marrow stem cells/PEGDA	Additive lathe 3D bioprinting	Double-deck	*In vitro*	PC12 cell culture *in vitro*	21 days	1 mm	Enhancement of conduit's mechanical properties by adding a biocompatible GelMA/PEGDA hydrogel layer	[94]
Poly(lactic acid)/poly(ε-caprolactone)/graphene	Extrusion printing	porous	*In vitro*	*In vitro* assessment of cell behavior	7 days	300 μm	The stent has a modulus of elasticity of approximately 22.36 MPa and is suitable for peripheral nerve tissue applications	[100]
PLA	Extrusion printing	Hollow	*In vivo*	3 mm nerve defects in rats	56 days	0.1 mm	PLA support for axonal growth as a potential alternative to autografts	[101]
PLA/PCL	Stereolithography	Microgroove	*In vitro*	*In vitro* assessment of cell behavior	7 days	10 μm	PCL/PLA films have higher Young's modulus and cell proliferation trends than PCL films	[102]
PCL/collagen nanofibers/graphene oxide	Electrospinning	Hollow	*In vivo*	10 mm nerve defects in rats	8 weeks	10 μm	Improvement of the mechanical properties of conduits by the addition of graphene oxide doping in PCL	[172]
PCL/decellularized extracellular matrix/PDA	Fused filament fabrication	Hollow	*In vitro*	*In vitro* assessment of cell behavior and neuronal differentiation	7 days	100 μm	Higher mechanical properties of PCL conduit than sciatic nerve; easy surgical manipulation and suturing	[107]
Collagen I/PLGA	Electrospinning	Hollow	*In vivo*	13 mm nerve defects in rats	12 weeks	0.1 mm	Collagen/PLGA conduit for SC proliferation and alignment on nanofiber conduits compared to random orientation	[111]
Poly(l-lactic acid-co-ε-caprolactone/PLGA/PPy	Electrospinning	–	*In vitro*	*In vitro* assessment of cell behavior and neuronal differentiation	7 days	10 μm	High rate of biodegradation for PLGA-based conduits; more suitable for short-distance nerve defects	[112]
Polyurethane/PEG-graphene oxide	Stereolithography	Hollow, porous, and micro-grooved		–	–	0.1 mm	The addition of PEG's functional groups helps to improve the mechanical strength of the conduit	[144]
PEG	Stereolithography	Multi-channel		–	–	0.01 mm	Rigid PEG-fibrinogen constructs have been shown to be better at promoting complete bridging at the injury site compared to fibronectin/PEGDA	[114]

Abbreviations: 3D, three-dimensional; GelMA, gelatin methacryloyl; PCL, polycaprolactone; PEG, polyethylene glycol; PEGDA, poly(ethylene glycol) diacrylate; PLA, polylactic acid; PLGA, poly lactic-co-glycolic acid; PNI, peripheral nerve injury; PPy, polypyrrole; SC, Schwann cell; SF, silk fibroin.

doi: 10.36922/IJB025140120

± 31.6%; $p < 0.01$). The degradation rate of the conduit was significantly reduced, and the structural stability was enhanced. Zhang et al.[76] utilized chitosan/neurotrophic factor-3 for the 3D-printed topology micron track conduit to induce targeted growth of SCs, showing a higher growth density of primary SCs on micron track conduit compared to commercial conduits, which effectively facilitated the functional recovery of a 15 mm gap nerve injury model in rats.

3.1.2. Silk fibroin

SF is obtained from silkworm silk, which is a rich natural source of proteins with outstanding mechanical properties, biodegradability, biocompatibility, and bioabsorbability.[77–79] Silk can be processed in the form of films, gels, nets, etc., having a wide range of applications in NTE, especially using electrospinning. For instance, both Dinis et al.[80] and Zhao et al.[81] electrospun SF-based 3D NGCs. SF-NGCs had an ultimate peak stress of 4.0±0.6 MPa and a corresponding elongation at failure of 156.8±46.7%, demonstrating that the SF-NGCs exhibited a mechanical behavior comparable to that of rat sciatic nerve, good clinical application performance, and potential to promote nerve regeneration and functional recovery. Wang et al.[82] combined electrostatic spinning, braiding, and coating techniques to prepare a composite sericin protein NGC, which was implanted into a 10 mm nerve defect in rats. There was no obvious inflammatory reaction after 8 weeks of implantation. Apparent axonal and myelin tissue appeared inside the conduit group at 12 weeks and directly throughout the conduit tissue, indicating successful regeneration of the rat sciatic nerve within the conduit. Alternatively, Zhao et al.[83] prepared composite polypyrrole (PPy)/SF conduits cultured with SCs by combining 3D bioprinting with electrospinning. The results showed that SCs mainly adhered to the surface of the conduits and maintained normal morphology (full, pike-shaped, and shiny), good interconnection, and good proliferation. This indicated that the composite PPy/SF conduit promoted SC adhesion, differentiation, and proliferation. However, obtaining SF is a complex and expensive process that demands specialized methods and resources. Moreover, variations in silk sources and processing parameters can affect the material's quality and consistency.

3.1.3. Collagen

Collagen is the most abundant protein in mammals, with good biocompatibility, high stability, and the capability to promote axonal regeneration and myelination. Collagen types I and II are the key components of peripheral nerves. Several studies explored collagen and its derivatives as the main material for the biofabrication of NGC. For instance, Fujimaki et al.[84] developed a collagen-based NGC with a guiding effect and bridged a 15 mm peripheral nerve defect in rats; myelinated nerve regeneration was observed at 8 weeks postoperatively, showing good nerve repair. Yoo et al.[85] successfully 3D-printed a natural, unmodified collagen nerve conduit using a dense collagen solution and implanted it into a rat nerve model. 6 weeks after implantation, the 3D-printed NGC showed a denser and more organized pattern of regenerating axons. Morphometric analysis of nerve sections distal to the repair site at 12 weeks showed that myelinated axon counts and myelin thickness were higher in the 3D-printed group than in the control group, confirming the beneficial effects of 3D-printed collagen on axonal regeneration, myelin sheath regeneration, and nerve cells' functional recovery. However, the main drawbacks of collagen are its high cost, poor mechanical properties, and limited stability, as it can only remain liquid at low temperatures. To address this limitation, cross-linking or combining collagen with synthetic materials is often necessary. For instance, Chen et al.[86] fabricated porous 3D-printed collagen/SF (C/S) conduits adsorbed with secretome (ST) derived from human umbilical mesenchymal stem cells (3D-C/S+ST). After co-culture with NSC, 3D-C/S+ST showed good cytocompatibility, and infrared spectroscopy data showed that 3D-C/S+ST had appropriate lipid-soluble and water-soluble chemical bonds suitable for neuronal cell adhesion and growth. From X-ray diffraction analysis, 3D-C/S+ST also showed a desirable crystallinity, hence better control of the rate of degradation. Therefore, the development of collagen-based composites for NGC fabrication is a common procedure to be considered.

3.1.4. Gelatin methacrylate

Gelatin is a natural polymer derived from collagen[87] and has excellent biocompatibility, hemostatic properties, low cytotoxicity, and antigenicity, and promotes cell attachment and growth.[88] However, its mechanical properties and antimicrobial activity are relatively poor, with a tensile strength that is generally 0.05–0.5 MPa.[89,90] Therefore, it often needs to be crosslinked with other polymers to promote its mechanical performance.[91] GelMA is a gelatin-based biomaterial chemically modified to promote cell adhesion, growth, and degradation. GelMA has better mechanical tunability and structural stability than ordinary gelatin. Its mechanical strength and degradation rate are dependent on many factors, such as gelatin concentration, degree of methacrylation, and photo-crosslinking.

Gong et al.[92] proposed a hollow porous GelMA/Engelbreth–Holm–Swarm (EHS) NGC with 89.8% porosity, 167.6 μm pore diameter, 0.489 kPa tensile modulus, and 0.314 kPa compressive modulus. 16 weeks after implantation in rats, hematoxylin and eosin staining

of the gastrocnemius muscle showed that there was no significant difference between the autograft group and the composite conduit group, confirming that the EHS filling accelerated the repair of nerve defects. Tao et al.[93] 3D printed hollow GelMA hydrogels with drug-loaded poly(ethylene glycol)-poly(3-caprolactone) nanoparticles to obtain a physical microenvironment for axon extension and drug release for nerve regeneration. *In vitro* experiments showed that the migration of SCs increased with the drug concentration. The conduit was placed into rats, and the functional recovery of injured peripheral nerves was detected through electrophysiology. The results showed that the efficacy of the 3D-printed conduits was comparable to that of autografts, having a good clinical application value. Liu et al.[94] also repaired a bilayer NGC using GelMA/bone marrow mesenchymal stem cells (BMSCs)/gelatin, which resulted in a high survival rate and extensive morphological expansion of BMSCs encapsulated in the inner layer. The density and value-added rate of PC12 cells attached to the cellularized bilayer NGCs were four and nine times higher than those of the non-cellularized bilayer NGCs, respectively. These results suggested that the 3D bioprinting of BMSCs embedded in bilayer NGCs has great potential to promote peripheral nerve repair. Another example is reported by Ye et al.,[155] which exploited photocurable GelMA to fabricate multi-channel NGCs using DLP technology. Neural crest stem cells cultured on the GelMA NGC showed good survival, proliferation, and migration rates.

In summary, although most natural polymers exhibit low cytotoxicity and possess unique biological advantages, such as the antibacterial activity of chitosan and the neuroregenerative potential of collagen, they still face several challenges in practical applications. Some of these challenges include poor mechanical strength, uncontrollable degradation rates, and complex processing and purification procedures. To overcome these limitations, current research should focus on modifying natural polymers through chemical or physical approaches to enhance mechanical properties and achieve more controllable degradation profiles while preserving inherent biocompatibility and bioactivity. This could help in improving the applicability of natural polymers in nerve conduits and other areas of regenerative medicine.

3.2. Synthetic polymers

Synthetic polymers are artificial polymers with adjustable chemical structures and physical properties, categorized into degradable and non-degradable materials. Degradable materials have been widely used due to their material's inherent plasticity, wide range of sources, lower cost, good biocompatibility, and controllable physicochemical properties.[95] Commonly used biodegradable synthetic polymers include PLA, PCL, PLGA, and polyethylene glycol (PEG). Non-degradable materials are instead less commonly used due to induced chronic foreign body reaction, which inhibits the recovery of peripheral nerve function and requires a secondary surgical procedure to remove them.[4]

3.2.1. Polylactic acid

PLA is a biodegradable thermoplastic aliphatic polyester derived from plants and contains repeating lactic acid units that promote the proliferation, migration, and maturation of myelinated axons.[96,97] The Young's modulus (around 4.1 GPa) and tensile strength (around 62.7 MPa) of PLA are significantly higher than most synthetic conduit materials, implying that PLA-based NGCs can effectively maintain morphology and support nerve regeneration in complex *in vivo* environments. Its degradation product is lactic acid, which can be rapidly metabolized by the body, but its poor cell adhesion and high hydrophobicity limit its application.[98,99] Gerdefaramarzi et al.[100] fabricated PLA/PCL/graphene nanocomposite conduits for peripheral NTE using a fused filament fabrication 3D printing method, which showed porosity and pore sizes in the range of 50– 86% and 300–500 μm, respectively. The elastic modulus of the scaffolds was approximately 22.36 MPa, which is suitable for peripheral nerve tissue applications, and the degradation rate in phosphate buffer solution was 0.14 mm/day, which is very close to the regeneration rate of peripheral nerve tissue. These findings suggest that PLA/PCL/graphene oxide conduits are promising for peripheral NTE. Wang et al.[101] also prepared a composite NGC using chitosan/PLA and used it for bridging long segments of peripheral nerve deficits. The results showed that 6 months after grafting, innervation was restored to the target muscles and limb mobility was improved. Alternatively, Yue et al.[102] prepared film-based surfaces with micro-grooved NGCs on PCL/PLA using micro-stereolithography (SLA). Young's modulus of PCL/PLA films (~109.6 MPa) was higher than that of PCL films (~56.7 MPa), which indicated that the stiffness and deformation resistance of PCL/PLA were improved. PCL/PLA samples showed a higher human neuroblastoma cell proliferation than PCL and longer cellular lengths (~275 μm), which was higher than that of control PCL films (~200 μm). Hence, this facile fabrication method is promising for the fabrication of morphology-guided cues. Zheng et al.[103] developed a combinatorial NGC consisting of longitudinally aligned electrospun nanofibers and porcine decellularized nerve matrix hydrogel. The *in vivo* capacity for facilitating nerve tissue regeneration and functional recovery was evaluated in a rat sciatic nerve defect model. PLA-aligned/0.25% porcine decellularized nerve matrix hydrogel scaffold exhibited the

best performance in facilitating directed axonal extension and SC migration *in vitro* due to the combined effects of the topological cues provided by the aligned nanofibers and the biochemical cues retained in the porcine decellularized nerve matrix hydrogel. Consistent results were obtained in animal experiments with the fabricated NGCs, confirming that PLA is generally a promising approach for NTE and the treatment and diagnosis of PNI.

3.2.2. Polycaprolactone

PCL is a biodegradable aliphatic polyester characterized by a low melting point, ease of processing, high mechanical strength, good biodegradability, and miscibility with various other polymers.[104] However, due to its high plasticity, the physical, chemical, mechanical, and biological properties of PCL can be improved by modifying functional groups or combining it with other materials (e.g., synthetic polymers, metallic materials, etc.).[105] PCL-based NGCs support the adhesion and proliferation of SCs and olfactory sheath cells without causing severe swelling that may locally compress the nerve. Zhu et al.[106] employed electrospinning techniques to fabricate a PCL-based NGC featuring directionally aligned fibers complemented by a concentration-gradient NGF coating on its surface. This innovative design facilitated the directional guidance of DRG neurons toward the high NGF-concentrated region and successfully repaired a 15 mm sciatic nerve defect in rats. Chen et al.[107] tested the mechanical properties of 3D-printed PCL conduits with maximum tensile strength and modulus of elasticity of 21.2 and 142.5 MPa, respectively—values significantly higher than those of native nerves. This enhanced strength offers greater ease of handling and suturing during surgical procedures. Qian et al.[108] innovatively invented an LBL casting method for the fabrication of NGCs, utilizing either single-layer graphene or multi-layer graphene with PCL. Results showed that the higher the number of layers of graphene, the lower the conductivity achieved (8.92×10^{-3} S/cm for a single-layer graphene/PCL conduit, 6.37×10^{-3} S/cm for a multi-layer graphene/PCL conduit). All the above-mentioned studies demonstrate that NGCs made from PCL have great potential for future research and clinical applications. In addition to this, even with synthetic polymers, hybridization with other materials is still an essential way to enhance the performance of conduits.

3.2.3. Poly(lactic-co-glycolic acid)

PLGA is a functional polymeric organic compound formed by the random polymerization of two monomers, lactic acid and hydroxyacetic acid, with a controlled biodegradation rate[109] and good cell adhesion. Although the degradation rate of PLGA reduces with increasing lactic acid content, it remains significantly higher than that of PLA and PCL.[110] Ouyang et al.[111] developed a seamless axial NGC consisting of biocomposite collagen/PLGA nanofibers by electrospinning and evaluated the ability of the conduit to support SC proliferation and axonal growth both *in vitro* and *in vivo*. The aligned NSCs were significantly superior to those composed of randomly aligned collagen/PLGA fibers in facilitating regeneration and functional restoration and were nearly as effective as autologous grafts. Moreover, the collagen/PLGA conduits were mechanically strong enough to suture severed nerve endings and resist collapse *in vivo*, remaining structurally intact for at least 3 months postoperatively. Namhongsa et al.[112] deposited polypyridine particles on 3D-printed poly(l-lactic acid-co-ε-caprolactone)/PLGA conduits to change the electrical conductivity of the conduit surface. Studies have shown that PLGA-based conduits degrade faster and are more suitable for short-gap nerve injuries, and vice versa. By optimizing the structural and surface modifications of the conduits, these materials can provide a favorable option for enhancing cellular biocompatibility. The controlled degradation properties of PLGA are also a valuable factor for achieving multi-phase release of neurotrophic factors. For instance, Lackington et al.[113] developed a PLGA microparticle with encapsulated NGF and glial-derived neurotrophic factor. The factors are sequentially released into the nerve regeneration microenvironment over 28 days, promoting nerve repair. However, PLGA generally exhibits poor hydrophilicity, and its degradation products create an acidic microenvironment, often resulting in limited bioactivity.

3.2.4. Polyethylene glycol

PEG is a linear polyether compound with strong mechanical and degradation properties that can encapsulate cells, good hydrophilicity, and water absorption. However, due to its biological inertness and poor oxidative stability, it may cause cell death during ultraviolet cross-linking. Therefore, it is typically combined with other biomaterials to improve its performance.

Berkovitch et al.[114] sought to evaluate hydrogel assemblies PEG-fibrinogen (Fib) in different formulations for NGCs. Three PEG-Fib hydrogels were prepared and tested: compliant PEG-Fib, rigid PEG-Fib, and micropatterned PEG-Fib with microchannels. All three compositions were implanted into 8 and 12 mm rat sciatic nerve defect models to verify their effectiveness in repairing PNI. Rigid PEG-Fib constructs containing 40 mg/mL of PEG diacrylate (PEGDA) were shown to be better at promoting complete bridging at the injury site compared to fibronectin/PEGDA. The semi-synthetic compositions were superior to fibronectin and fibronectin/PE-DA in bridging nerve injuries. In addition, PEG conduits promoted homeostasis

in vivo by providing cells with an adhesion and degradation substrate. By employing SLA, Farzan et al.[144] used solvent-free polyurethane (PU) and different contents of PEG-graphene oxides (0, 0.5, 1, 3, and 5 wt%) to prepare composites. Among all samples, the composites containing 5 wt% PEG-graphene oxide exhibited the highest tensile stress (3.51±0.54 MPa), tensile rupture strain (~170%), and compressive strength, suggesting that the addition of PEG's functional groups improved the mechanical strength of the conduit.[116] Similarly, Arcaute et al.[142] used SLA-printed multi-lumen PEG-based NGCs, demonstrating that high PEG concentrations, especially from 20 to 30 wt%, were more resistant to suture pullout, with a significant increase in resistance from 0.043±0.0037 to 0.064±0.0090 N/mm.

To summarize, it has been observed that the current choice of conduit materials is shifting toward the utilization of hybrid polymers. By adjusting the composition and mixing ratio of these composite materials, it is possible to achieve a controllable regulation of the biodegradation rate and mechanical strength. These adjustments may be able to meet the different needs of specific types of injuries and injury gaps to promote better PNI repair and regeneration.

3.3. Cells and biomolecules

Assisted by certain advanced technologies, living cell lines and biomolecules can now be directly used as raw materials for 3D printing.[117] The integration of living cells with biomaterials to form bioinks not only enhances the biocompatibility of the printed constructs but also effectively reduces immune rejection and inflammatory responses. In particular, the incorporation of cells can provide structural support derived from the native ECM, thereby promoting the adhesion, growth, and survival of neural cells and ultimately improving the efficiency of nerve regeneration. Moreover, specific biomolecules, such as neurotrophic factors and growth factors, can be co-loaded with cells into the conduit structure, where they play a synergistic role in regulating cellular behavior and enhancing the efficacy of nerve repair during the regeneration process.

3.3.1. Stem cells

Stem cells for NTE mainly include embryonic stem cells, induced pluripotent stem cells, NSCs, and mesenchymal stem cells (MSCs) of different tissue sources.[118] The induction efficiency of NSCs greatly varies due to the heterogeneity of species, age, tissues from which they are derived, and culture conditions.[119] Thus, many studies have focused on the use of MSCs.[120,121] The use of undifferentiated MSCs for *in vivo* studies allows pluripotent cells to differentiate MSCs along multiple pathways by advancing axons and natural SC stimulation. This helps to create a conducive environment for nerve regeneration.[122] In addition, transplanted MSCs have shown the ability to differentiate into other support cells, such as endothelium-like cells, smooth muscle cells, or pericytes.[123] These endothelium-like cells can produce various growth factors, such as vascular endothelial growth factor (VEGF), which have been shown to have synchronous effects on angiogenesis, neurogenesis, and nerve regeneration, with positive effects on *in vivo* nerve regeneration.[124]

Zhang et al.[125] isolated a unique subpopulation of MSCs from human gingival tissue and found that this cell type tends to be induced into neural progenitor cell-like cells. In a rat model of facial segmental defect, gingival MSC spheres were printed as the sole cellular component using 3D bioprinting. Results indicated that axon regeneration and target muscle recovery reached the same level as autogenous nerve transplantation at 12 weeks after implantation. Cui et al.[126] attempted to bridge the 3.5 cm dog sciatic nerve defect with a longitudinally oriented collagen catheter (LOCC) loaded with human umbilical cord mesenchymal stem cells (hUC-MSCs). 9 months after the operation, the connective tissue of the nerve stump at the injured site was collected for tissue chemical analysis. Compared with the control group, the positive signal in the middle ganglia of the LOCC/hUC-MSCs group was more intense. Transmission electron microscopy analysis of the thickness and size of the regenerated myelin fibers showed that the LOCC/hUC-MSC group had a thicker myelin sheath on the nerve fibers regenerated at the midpoint of the ganglia than the LOCC group.

3.3.2. Schwann cells

SCs are non-neuronal cells but provide support and protection to neurons by forming myelin sheaths, constituting supportive factors for maintaining homeostasis within the peripheral nervous system. In PNI, SCs serve as the primary glial cells promoting axonal regeneration.[127] Due to rapid phenotypic changes, they form favorable growth pathways and ultimately generate myelin phospholipids around axons in response to PNI. Therefore, incorporating SCs in conduits is highly encouraged for peripheral nerve repair, and controlling their orientation through 3D bioprinting is expected to effectively guide the directed growth of neurites.

Ning et al.[128] developed a bioprinting process to prepare SC-coated conduits using a novel hydrogel mixture. The observed hydrogel microstructure and cell morphology revealed that the coated SCs exhibited superior performance in environments with high concentrations of fibronectin, as it could provide sufficient micropores and fibers for cell metabolism and adhesion. Although low concentrations of fibronectin could provide cell-binding fibers within the hydrogel, insufficient porosity would

still constrain SC diffusion and phenotype expression. Therefore, an appropriate porosity is a necessary condition for the successful preparation of NGCs encapsulating SCs. Furthermore, Ning et al.[129] researched bioprinting SC-loaded conduits using low-viscosity hydrogel components such as RGD-modified alginate, hyaluronic acid, and fibronectin. Experimental results indicated that bioprinting could induce the alignment of SCs. By controlling the printing speed, the elongation of SCs could be effectively regulated, thereby adjusting the alignment of DRG neurites. As the speed increased from 4 to 9 mm/s, the roundness of SCs increased, and the direction of laminin expression became more apparent. Alternatively, in the study of Summa et al.,[130] SCs were implanted into hollow fibronectin conduits and implanted into a 10 mm rat sciatic nerve model. Compared to control hollow conduits, conduits filled with differentiated BMSCs, or conduits filled with differentiated adipose-derived stem cells, these fibronectin-SC conduits exhibited significantly enhanced nerve regeneration capabilities. All these evidences demonstrate the effective role played by SCs in nerve regeneration.

3.4. Biomolecules

In the process of peripheral nerve repair, various types of biomolecules, especially neurotrophic factors, play an indispensable role in promoting axon guidance, cell migration, SC activation, and nerve regeneration. Integrating these biomolecules into NGCs not only helps to create a microenvironment conducive to regeneration but also serves as a key strategy to enhance the biological activity of the conduits, providing a more precise and efficient intervention for the treatment of nerve injury.

The NGF is one of the earliest neurotrophic factors discovered and mainly promotes the growth of sensory and sympathetic nerves. *In vitro* experiments have demonstrated that NGF promotes the survival, proliferation, and synapse growth of sensory and sympathetic neurons.[131] Histological and morphological studies have shown that NGF treatment significantly increases the number and diameter of myelinated nerve fibers and accelerates the recovery of electrophysiological parameters after sciatic nerve damage.[132] In a 14 mm rat sciatic nerve defect model, researchers utilized NGF gradient immobilization within a nanofiber conduit to significantly guide the directional growth of DRG axons and enhance the recovery of nerve morphology and function, with results comparable to those of autologous nerve grafts.[133] In addition to NGF, other commonly used neurotrophic factors mainly include brain-derived neurotrophic factor, VEGF, and fibroblast growth factor 2 (FGF2). Brain-derived neurotrophic factor has a critical role in the repair of both the central and peripheral nervous systems, especially in the later stages of nerve regeneration, and can significantly promote axon growth and neural network remodeling.[134] VEGF provides the basis for the restoration of nutrient supply to the injured area, mainly by promoting neovascularization. *In vitro* experiments have shown that VEGF promotes the proliferation of SCs by activating signaling pathways. Related *in vivo* studies have shown that the number of regenerated nerve fibers in the VEGF-treated group is almost double that of the hollow conduit control group.[135] FGF2, also known as the basic fibroblast growth factor, is considered to be the most important molecule in promoting nerve regeneration among the 23 members of the fibroblast growth factor family.[136] It has been found that the use of collagen conduits co-modified with FGF2 and ciliary neurotrophic factor significantly improved nerve electrophysiological function and tissue remodeling in a model of long segmental defects in the nerve.[137]

In summary, the integration of neurotrophic factors into nerve conduits provides an important strategy for constructing a functional nerve repair microenvironment. By optimizing the type, dosage, release profile, and spatial distribution of these factors within the conduit structure, it is expected to achieve precise spatial-temporal regulation of the nerve regeneration process, which can significantly enhance the regenerative quality and clinical effects of PNI treatment.

4. Three-dimensional bioprinting technologies for nerve conduits

A significant aspect of NGC research is the optimization of technological approaches to achieve high precision and superior performance in NGC fabrication. In recent years, the application of 3D printing to tissue engineering has revolutionized NGC manufacturing. Among the various NGC biofabrication techniques, 3D bioprinting has been extensively investigated. This method is often combined with 3D imaging tools to develop personalized conduits with micro- or nano-scaled anatomical accuracy tailored to the patient's injury site. In particular, 3D bioprinting allows the assembly of both biological and non-biological elements in a 3D organization to produce bioengineered structures for regenerative medicine, pharmacokinetics, and cell biology research. This technology facilitates the positioning and localization of cells and biomolecules within functionalized biomaterials into inks to replicate the complex nerve ECM and accurately mimic the 3D structure of neural tissue fibers. Consequently, 3D bioprinting can integrate a wide range of components into a single printed structure, making it a powerful tool in nerve regeneration research.

3D bioprinting technologies are divided into three main categories: light-based, extrusion-based, and jet-based printing. Light-based technologies, such as SLA and DLP, are usually not used for bioprinting due to the cytotoxicity of photo-initiators present in the inks. Extrusion-based printing can serve as a 3D bioprinting technique when bioink is incorporated. Other advanced technologies, such as the recently developed Kenzan method, enable bioprinting by constructing fully biological NGCs directly from cells, eliminating the need for biopolymer solutions or hydrogels. The technical principles and main materials utilized for the various technologies are presented in Figure 5, while Table 4 summarizes the advantages and disadvantages of selected 3D bioprinting techniques.

4.1. 3D printed nerve guiding conduit

SLA is an AM technique that constructs 3D components by using a laser beam to scan and cure a photopolymer resin surface in an LBL process. As one of the rapidly developing 3D printing technologies in biomedical engineering, SLA has the advantages of high resolution, smooth surface,[138] and the ability to fabricate complex structures.[139] Although SLA can achieve resolutions up to 30 μm, it is a relatively time-consuming and discontinuous process, which requires additional post-processing steps to fully cure the printed part to obtain mechanically strong and stable building blocks.[140] The main process parameters are laser power, print speed, print layer thickness, and light time. Unlike other applications, SLA in medical contexts mostly uses visible lasers rather than ultraviolet light, as visible wavelengths are less likely to cause cytoplasmic and genomic destruction of printed cells.[141] Several case studies have exploited SLA for the biofabrication of NGC, verifying their feasibility in guiding the regeneration of nerve injuries. Arcaute et al.[142] used SLA to print a multi-channel PEG neural conduit. They found that varying the printing speed and laser intensity impacted the mechanical strength and dimensional accuracy of the conduit. A higher laser speed (~20.5 cm/s) resulted in insufficient mechanical strength post-crosslinking, causing the conduit to deform easily. Gels with good mechanical strength can be crosslinked when using lower laser speeds (3.5 cm/s) (Figure 6A-iii). Conversely, slower laser speeds improved mechanical strength but led to a loss of dimensional accuracy (Figure 6A-iv). An energy level of 65 mJ/cm^2 (laser scanning speed of 10.5 cm/s) was found to crosslink a good pattern with high geometrical precision and adequate strength (Figure 6A-ii). Evangelista et al.[143] also used SLA to test the promotion of single-channel (Figure 6B-i) and multi-channel conduits (Figure 6B-ii) for PNI repair using PEG as the material. It was found that the number of regenerating axons in single-channel NGCs approached that of normal nerves, and that multi-channel conduits showed significantly less nerve regeneration, possibly due to the physical nature of the conduit that inhibits growth. Further studies are needed to evaluate the role of the multi-channel NGCs. Farzan et al.[144] synthesized biodegradable, electrically conductive, solvent-free PU/PEG-graphene oxide composites and successfully printed them into neural conduits with different precise geometries, such as hollow, porous, and microgroove conduits (Figure 6C). It was found that the composites exhibited the highest tensile stress (3.51±0.54 MPa), strain at break (~170%), and electrical conductivity (1.1 × 10^{-3} S/cm) when the graphene oxide content was set at 5 wt%. In addition, 5 wt% PU/PEG-graphene oxide had higher compressive strength

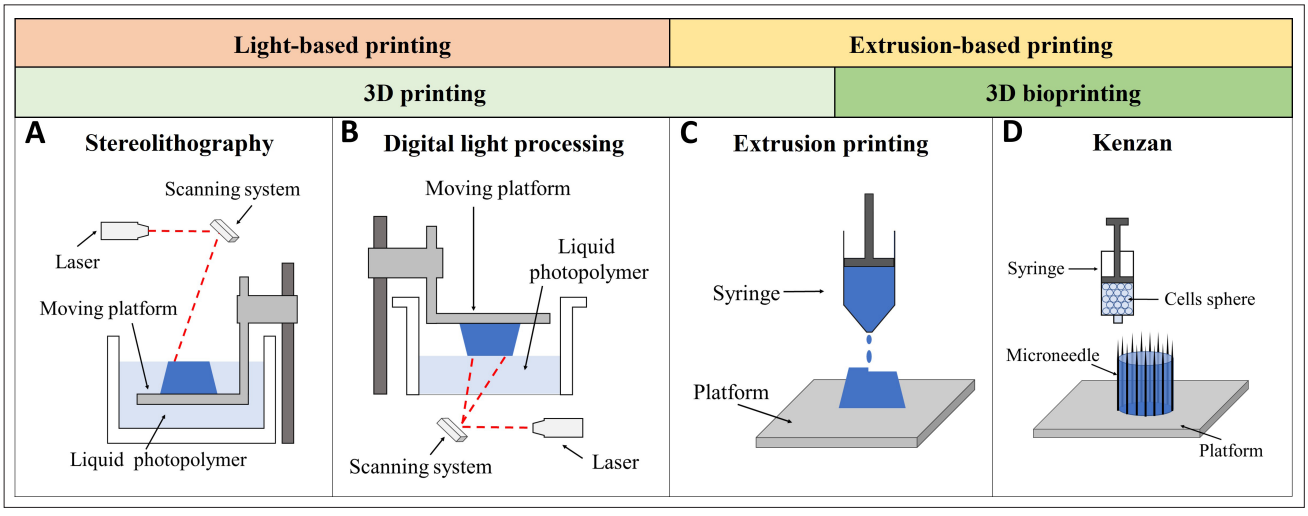

Figure 5. Three-dimensional (3D) bioprinting methods. (A) Stereolithography, (B) Digital light processing, (C) Extrusion printing, and (D) Kenzan.

Table 4. Advantages and disadvantages of three-dimensional bioprinting technologies

Three-dimensional bioprinting technology	Advantages	Disadvantages
Stereolithography	High resolution (~30 μm); ability to manufacture complex structures	Requirement of additional post-processing steps to cure the printed part, a time-consuming printing process, and high material waste; photoinitiators may be toxic
Digital light processing	High resolutions (~25 μm); simultaneous cross-linking within layers for fast production speeds; low viscosity materials; fast light curing capability	Limited selection of photopolymerizable biomaterial resins, photoinitiators may be toxic, and the high price of the printer
Extrusion printing	Suitable for a wide range of materials; printability of bioinks at high viscosity and cell density; low cost and relatively simple printing process	Reduction in cell viability after extrusion; low resolution down to 200 μm
Kenzan	Fully functional biological nerve guidance conduits can be constructed without the need for biopolymer solutions or hydrogels, relying only on cells	Conduit size is vulnerable to change during fusion of cell spheres, with low dimensional accuracy

compared to pure PU and exhibited proper enzymatic degradation after 6 weeks, which is expected to last long enough for effective nerve regeneration. Perez et al.[145] modified a commercial SLA printer with a sterile system to produce clean, particle-free conduits and reduced the laser diameter to increase its micromachining capability for the fabrication of complex conduit structures. Singh et al.[146] prepared hollow, multi-channel, and factor-filled biodegradable NGCs using SLA (Figure 6D), which could bridge a 15 mm nerve injury gap in rats. It was shown that the synthesized NGC was biocompatible and could provide guidance for the migration and proliferation of nerve cells, which improved the rate of nerve regeneration.

4.2. Digital light processing

Similar to SLA technology, DLP uses digital light projection to polymerize or cure the entire photoactive resin for each layer,[147] which in turn enables the layered fabrication of 3D structures. The main advantage of DLP over SLA is the rapid production of 3D structures. The laser source in SLA systems crosslinks the resin at each laser spot,[148] whereas the introduction of digital micromirror devices in DLP promotes the rapid crosslinking of the entire layer. Similar to SLA, c, such as a limited selection of photopolymerizable biomaterial resins, strong odors caused by the polymerization between acrylate groups and photoinitiators, and higher resin waste, which increases the cost of printed parts.[149–151] For DLP, the resolution of the projector determines the accuracy of the print, which is currently up to 25 μm,[152] allowing more detailed microstructures of NGCs to be printed. Numerous scholars have used DLP to conduct experiments on rational NGC printing, and NGCs fabricated using DLP have demonstrated their ability to support peripheral nerve regeneration. Xu et al.[153] established a DLP 3D bioprinting system to fabricate NGCs with oriented and continuous microstructures. The researchers fabricated NGCs with different inner diameters, wall thicknesses (Figure 7A-i), and microfibers (Figure 7A-ii), and tested the effect of functionalized nerve conduits loaded with HDAC3-specific inhibitor (RGFP966) nanoparticles after implantation into 10 mm nerve defects in rats. The results showed that the nerve conduction velocity of the loaded group was 29.83 m/s, which was significantly higher than that of the unloaded group (23.49 m/s), demonstrating the promoting effect of RGFP966 on functional recovery. Tao et al.[154] used DLP to fabricate natural polymers and platelets into NGCs. The compression test showed that the conduit had good mechanical properties and could recover the printed structure after deformation with structural integrity to support peripheral nerve regeneration. In addition, enzymatic degradation studies have shown that the conduit could be degraded *in vitro*, eliminating the requirement of a secondary surgical resection after implantation. As a light-curing technology, exposure time is an important process parameter in the printing process. Ye et al.[155] explored the optimal exposure time for GelMA in the DLP preparation of multi-channel neural conduits. To avoid the potentially harmful effects of ultraviolet light, a 405 nm visible light source was used to cure the biomaterial ink. During printing, the size of the conduit was affected by the layer exposure time, light intensity, and layer thickness. Printability was analyzed by adjusting the layer exposure time while other printing parameters remained constant. Conduits printed with shorter exposure times (<20 s) (Figure 7B-i) exhibited poor mechanical properties and were easily deformed. In contrast, longer exposure times enhanced the mechanical strength (Figure 7B-iii), but resulted in significant blockage at the base of the multi-

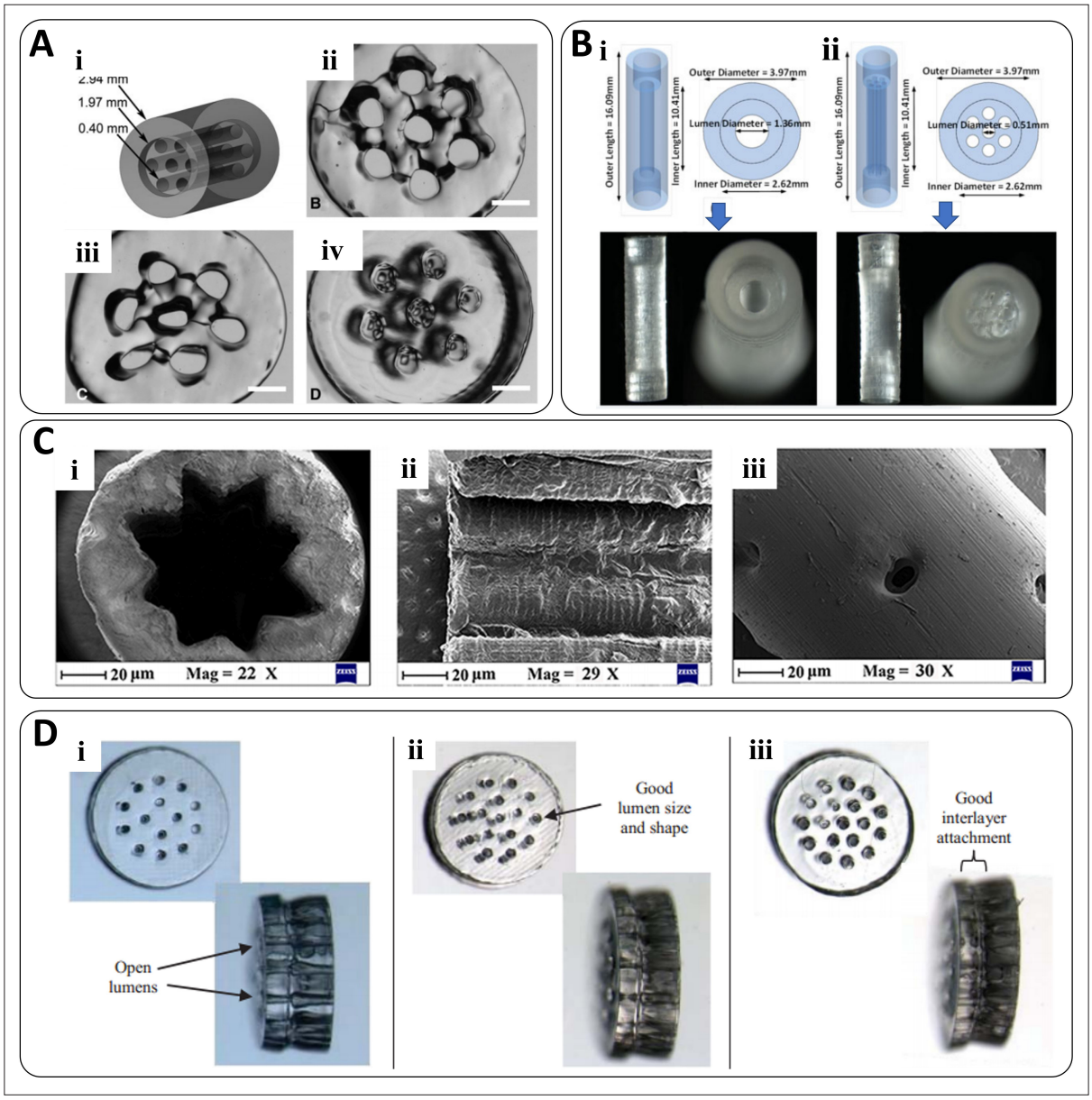

Figure 6. Various conduits prepared using SLA technology. (A) Polyethylene glycol (PEG) nerve guidance conduits. (i) Three-dimensional (3D) design model crosslinked at (ii) appropriate laser scanning speed or energy, (iii) high laser scanning speed or low energy, and (iv) low laser scanning speed or high energy. Scale bar: 500 mm. Reprinted with permission from Ref.[142] Copyright© 2011 Mary Ann Liebert Inc. (B) (i) Single-channel and (ii) multi-channel conduit design dimensions with pre-implantation pictures. Reprinted with permission from Ref.[143] Copyright© 2015 Thieme Medical Publishers. (C) Scanning electron microscopic (SEM) images of (i) transverse section and (ii) longitudinal section of grooved 3D-printed conduits. (iii) SEM images of stereolithography and porous 3D-printed conduit prepared using 5% polyurethane/PEG-graphene oxide. Scale bar: 20 µm, magnifications: 22×, 29×, and 30×. Image adapted from Farzan et al.[144] (D) SEM micrographs of (i) hollow, (ii) 4-pore, and (iii) open pores conduits. Scale bar: 200 µm. Reprinted with permission from Ref.[146] Copyright© 2018 American Chemical Society.

channel structure due to over-curing. An exposure time of 35 s fulfilled the requirements for manufacturing an NGC (Figure 7B-ii) with good mechanical strength and the required dimensions, at a more appropriate exposure time (which is not a generalized duration, but provides a data reference for other experiments). Huang et al.[156] successfully DL-printed NGCs with aligned structures from poly (glycerol sebacate) acrylate (Figure 7C-i) and poly (glycerol sebacate) acrylate-polyvinylpyrrolidone. The aligned microgroove structures could be observed from the NGCs' tomographic view (Figure 7C-iii). The microgroove structure effectively guided the growth

direction of nerve cells, promoting cell proliferation during nerve tissue regeneration. Wu et al.[157] used DLP to prepare an active hydrogel composed of GelMA and SF methacrylate, which had a positive effect on the adhesion, proliferation, and migration of SCs. A 12 mm sciatic nerve defect model was established in rats, and a conduit was implanted. Electrophysiological, morphological, and histological evaluations demonstrated that the conduit could promote axonal regeneration, myelin sheath regeneration, and functional restoration by providing a favorable microenvironment, with strong potential for the treatment of long-gap peripheral nerve injuries.

4.3. Extrusion printing

Extrusion printing is the most widely used 3D printing technique in NTE. The material is loaded and continuously extruded from the print head through a nozzle and selectively deposited LBL according to a pre-generated path,[158,159] with an acceptable resolution between 200 and 2000 μm. Extrusion printing allows the deposition of biomaterials with relatively high viscosity and shear-thinning effect, which withstands during the printing process, preventing any collapse. Therefore, porous conduits with excellent structural integrity, such as neural conduits, can be fabricated. Extrusion 3D printing offers high deposition through (multi) nozzles at high printing speeds and low equipment costs. However, the system is prone to nozzle clogging and pressure drops, which may eventually lead to cell apoptosis.[160,161]

Vijayavenkataraman et al.[162] developed an extrusion-based 3D printing machine to fabricate NGCs using a conductive collagen/PPy-block-PCL hydrogel. The authors investigated the effect of printing speed and material flow rate on the printed path width (Figure 8A), demonstrating that, as the print speed increases, the material is subjected to tension, and the path width narrows or is discontinued. At higher material flow rates, the ink may also aggregate into irregular shapes rather than a continuous line, affecting the structure of the NGC. Although low-viscosity materials are often a good choice for maintaining cell viability during and after printing, high-viscosity materials can provide better support and fidelity during the printing process. Therefore, the right trade-off between printing speed and flow rate was demonstrated to be critical. Kaplan et al.[163] also printed poly(L-lactic acid)/PLGA conduits

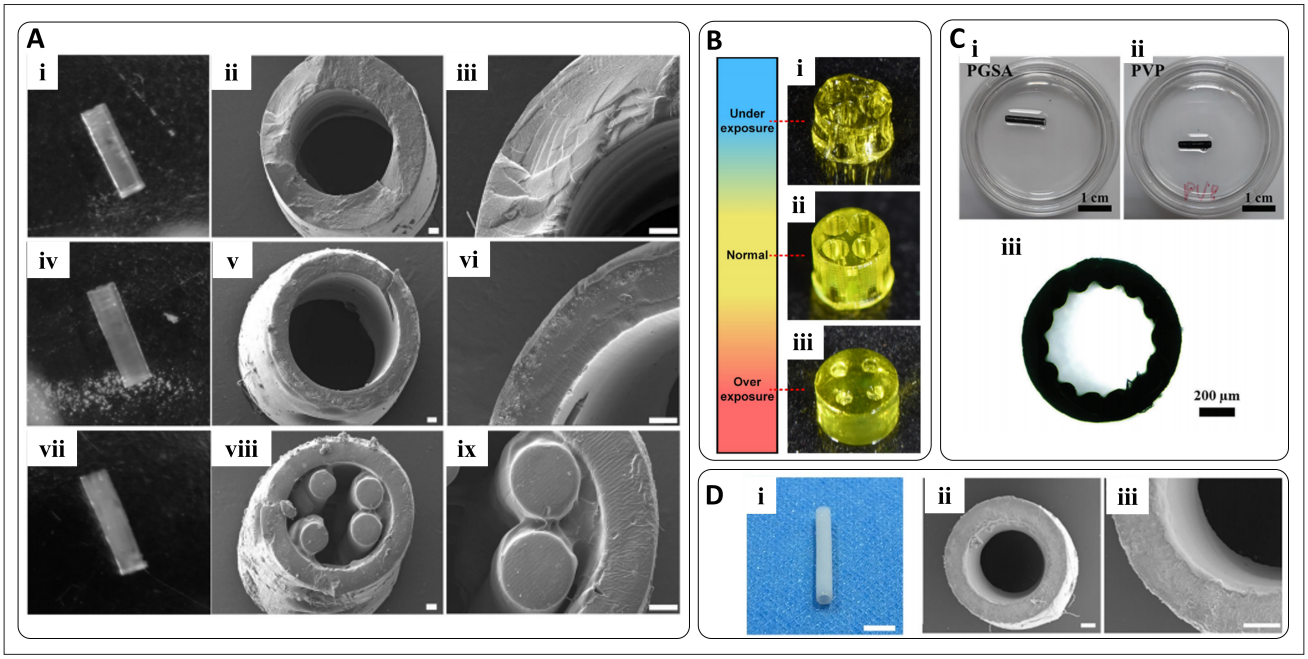

Figure 7. Various conduits prepared using DLP technology. (A) Hydrogel nerve guidance conduits of different structural designs. (i) Thick-walled, (ii) thin-walled, and (iii) microfibers printed using digital light processing technology. Scale bar: 100 μm. Reprinted with permission from Ref.[153] Copyright© 2019 Elsevier. (B) Multi-channel patterned photo crosslinked images at different exposure times. (i) Insufficient exposure time (<20 s), (ii) appropriate exposure time (around 15 s), and (iii) very long exposure time (>50 s). Reprinted with permission from Ref.[155] Copyright© 2020 Elsevier Ltd. (C) Poly(glycerol sebacate) acrylate (PGSA) composite micro-grooved conduits. (i & ii) Images of three-dimensional-printed PGSA and PGSA-polyvinylpyrrolidone (PVP) conduits. (ii) Optical microscope images of the cross-section of PGSA composite micro-grooved conduits. Scale bars: 1 cm and 200 μm. Reprinted with permission from Ref.[156] Copyright© 2023 Wiley. (D) (i) Photographs of the conduit and (ii & iii) scanning electron microscopic images of the conduit. Scale bar: 5 mm. (ii & iii) Scale bar: 200 μm. Reprinted with permission from Ref.[157] Copyright© 2015 Elsevier.

(Figure 8B) with random pore orientations. Stromal cells were implanted onto the fiber-conjugated protein-coated conduits, and after 7 days, the cells had populated the microchannels and exhibited a diffuse morphology, suggesting that the conduits had adequate cell culture and attachment conditions. Redolfi-Riva et al.[164] designed and prepared honeycomb mesh PCLs of different sizes using extrusion printing and embedded them in a chitosan porous matrix (Figure 8C). The hexagonal structural units provided enough space to ensure nutrient exchange and impede the infiltration of fibrotic tissues while constituting the structure of the conduit. As a result, the printed patterns showed excellent flexibility and toughness, capable of withstanding continuous compressive and bending stresses. Histological analysis showed that all rats treated with these grafts had abundant cellularization in the walls and lumens of the tubes as well as in the regenerated axons. Englanda et al.[165] also successfully fabricated fibronectin factor XIII-hyaluronic acid hydrogel conduits (Figure 8D) containing SCs using extrusion bioprinting.

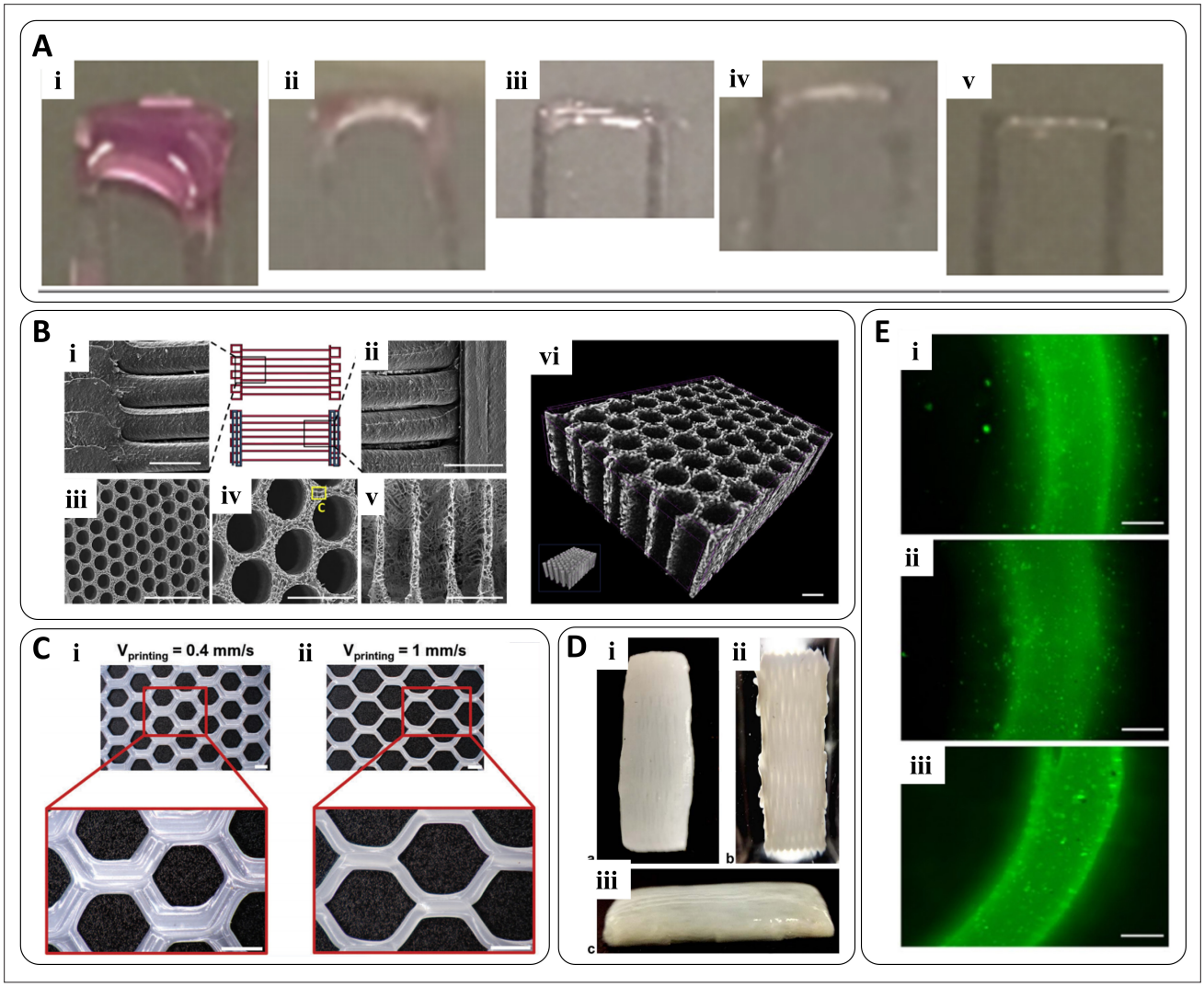

Figure 8. Various conduits prepared using the extrusion printing technique. (A) Effect of printing speed (i) 1 mm/s, (ii) 3 mm/s, (iii) 5 mm/s, (iv) 7 mm/s, and (v) 10 mm/s on fiber angle for printing collagen at a flow rate of 3 mL/min. Reprinted with permission from Vijayavenkataraman et al.[162] Copyright© 2019. (B) (i) Scanning electron microscopic images. (i–v) Scanning electron microscopic images. (i & ii) Scale bar: 200 μm. (iii) Scale bar: 1 mm. (iv) Scale bar: 400 μm. (v) Scale bar: 500 μm. (vi) Computed tomography diagram of poly(L-lactic acid)/PLGA conduit. Scale bar: 200 μm. (ii) Computed tomography diagram of poly(L-lactic acid)/PLGA conduit. Scale bar: 200 μm. Reprinted with permission from Ref.[163] Copyright© 2022 Elsevier Ltd. (C) Conduits at two different printing speeds (i) 0.4 mm/s, (ii)1 mm/s. Scale bar: 1 mm. Image adapted from Redolfi-Riva et al.[164] (D) (i) Frontal, (ii) dorsal, (iii) lateral views of fibrin-factor XIII-hyaluronic acid conduits. Reprinted with permission from Ref.[165] Copyright© 2017 Elsevier BV. Scaffold dimensions: 14 × 5 × 2 mm. (E) LIVE/DEAD staining of N2a-laden three-dimensional bioprinted 7.5G, 7.5G0.1C, and 7.5G7.5P. Images were taken 5 days after bioprinting. The green color represents healthy cells, and the red represents dead cells. Scale bar: 200 μm Reprinted with permission from Ref.[166] Copyright© 2024 American Chemical Society.

During the bioprinting process, SCs were encapsulated within the conduit, promoting the longitudinal alignment of fine fibrin fibers. The physical guidance cues provided by these longitudinally aligned fibrin fibers further directed the SCs to align linearly and facilitated linear neurite elongation along the fibrin factor XIII-hyaluronic acid chain. Finally, Das et al.[166] formulated cell-carrying biobricks with Neuro-2a cell density of 3×10^6 cells/mL into GelMA/carbon nanofiber/PEGDA/gellan gum hydrogels and printed them into two layers of cylindrical conduits (wall thickness of 0.5 mm) using a customized extrusion bioprinter. After 5 days of incubation in a differentiation medium, the Neuro-2a cells showed good cell viability (more than 80%) (Figure 8E).

4.4. Kenzan

The Kenzan method uses pre-designed 3D data and stainless steel microneedle arrays as temporary scaffolds on which multi-cellular spheres are precisely placed. Once these spheroids fuse and produce their own ECM, the microneedles are removed, leaving behind the desired biological structure. This method does not require a biopolymer solution or hydrogel, relying solely on cells to construct fully biological conduits with a certain degree of biomechanical stability. This approach pioneers a new direction in NTE.[167] Needle diameters are typically 100–200 μm with a needle pitch of 300–400 μm. The size of the multi-cellular spheres is determined by the needle spacing. The distribution of cells within the sphere undergoes a continuous rearrangement, with cells exhibiting stronger adhesion migrating toward the core, while those with weaker adhesive properties localize to outer concentric layers in decreasing order of adhesion strength. Inside the sphere, cells move within the available space and limits imposed by intercellular adhesions. This process, combined with ECM deposition, promotes the healing of pinholes. However, since the goal is to print tubes or hollow structures, this contraction may cause them to disappear prematurely, which would require additional stabilization.

Yurie et al.[168] used the Kenzan method to prepare a conduit-free hollow NGC (Figure 9A) from human normal dermal fibroblasts and verified its restorative effect on sciatic nerve defects in rats. Human dermal cells were first aggregated to form homogeneous multi-cellular spheres with a diameter of 750 ± 50 μm, and the spheres were arranged into a 3D shape according to a pre-designed 3D model (Figure 9A-i). After about a week of printing, adjacent spheres were fused together to construct a single tubular shape in a microneedle array, which was then removed (Figure 9A-ii). *In vivo* experiments demonstrated that 3D-bioprinted fibroblast conduits showed a significantly higher number of myelinated axons (Figure 9A-iii) compared to the silicone group (Figure 9A-iv), which could promote nerve regeneration in a rat sciatic nerve defect model. Although there are some limitations, the study confirmed that this new purely biological NGC is effective in promoting nerve regeneration. Alternatively, Takeuchi et al.[169] explored an approach for larger-gap nerve defect repair. A 12 mm NGC (Figure 9B-i & ii) was prepared using the Kenzan method and implanted into a 10 mm sciatic nerve defect in the right hind limbs of rats. A silicone tube implantation group was used as a control. Evaluation was performed 8 weeks after surgery, in the distal region of the suture site, where the number of myelinated axons, myelin sheath diameter, and myelin sheath thickness of regenerated axons were significantly greater in the NGC (Figure 9B-iii) than in the silicone (Figure 9B-iv) groups. It was eventually shown that the NGCs could promote peripheral nerve regeneration, even in a 10 mm nerve defect model. On this basis, Yurie et al.[170] further investigated the promotion of nerve regeneration using NGCs generated from bone marrow stromal cells. NGCs were fabricated with the Kenzan method and transplanted into Lewis rats to bridge the 5 mm right sciatic nerve gap (Figure 9C-i), with two silicone tubes used as control (Figure 9C-ii & iii). Functional and morphological evaluation of nerve regeneration was performed 12 weeks after transplantation. Electrophysiological studies, kinematic analysis, wet muscle weight, and morphological parameters showed that nerve regeneration in the NGC was significantly better than in the silicone tube. Mitsuzawa et al.[171] further investigated the effect of this method on nerve defect regeneration promotion in large mammals. Spheres were extracted from a 96-well plate into a fine nozzle, strung into an array of circular needles (Figure 9D-i & ii), and developed into a tubular structure according to a predesigned pattern (Figure 9D-iii). An NGC (Figure 9D-iv–vi) was used to bridge the ulnar nerve defect in a dog's 5 mm forelimb, and nerve regeneration was observed at 10 weeks postoperatively. Immunohistochemical, histologic, and morphometric assays confirmed the presence of numerous myelinated axons in the NGC. It was shown that the NGC fabricated from canine autologous dermal fibroblasts promoted nerve regeneration even in a 10 mm nerve defect model. This technique is therefore feasible for the preclinical treatment of PNI and segmental nerve defects.

5. Clinical translation and commercial application: moving toward scalable solutions

This review reports the high potential of biofabricating NGCs for nerve tissue repair, focusing on their structure, AM-oriented technology, biomaterials, and cells. The

reported NGC prototypes have all been extensively tested in specific case studies, which validated their efficient use. Nevertheless, their exploitation and clinical translation remain limited. Several key challenges must be addressed before NGCs can be widely adopted in preclinical and clinical studies. These challenges are mainly related to the selection of appropriate biomaterials and technologies, as highlighted in the previous sections. For biomaterials, European Medicines Agency or Food and Drug Administration approval is a critical requirement. Several biomaterials have already been approved for a variety of medical applications, including PLA, PLGA, and collagen. For instance, NeuraGen® and NeuroMatrix® are Food and Drug Administration-approved nerve conduits made from collagen type I and primarily used for small-diameter peripheral nerves with short defects. Particularly, NeuraGen® is a tube filled with chondroitin-6-sulfate, which promotes SC migration and axonal regeneration. Their functionality was demonstrated in rat sciatic nerve gap models to increase nerve fiber density and myelinated axon counts, and was comparable to reversed autografts and superior to hollow or collagen-filled conduits.

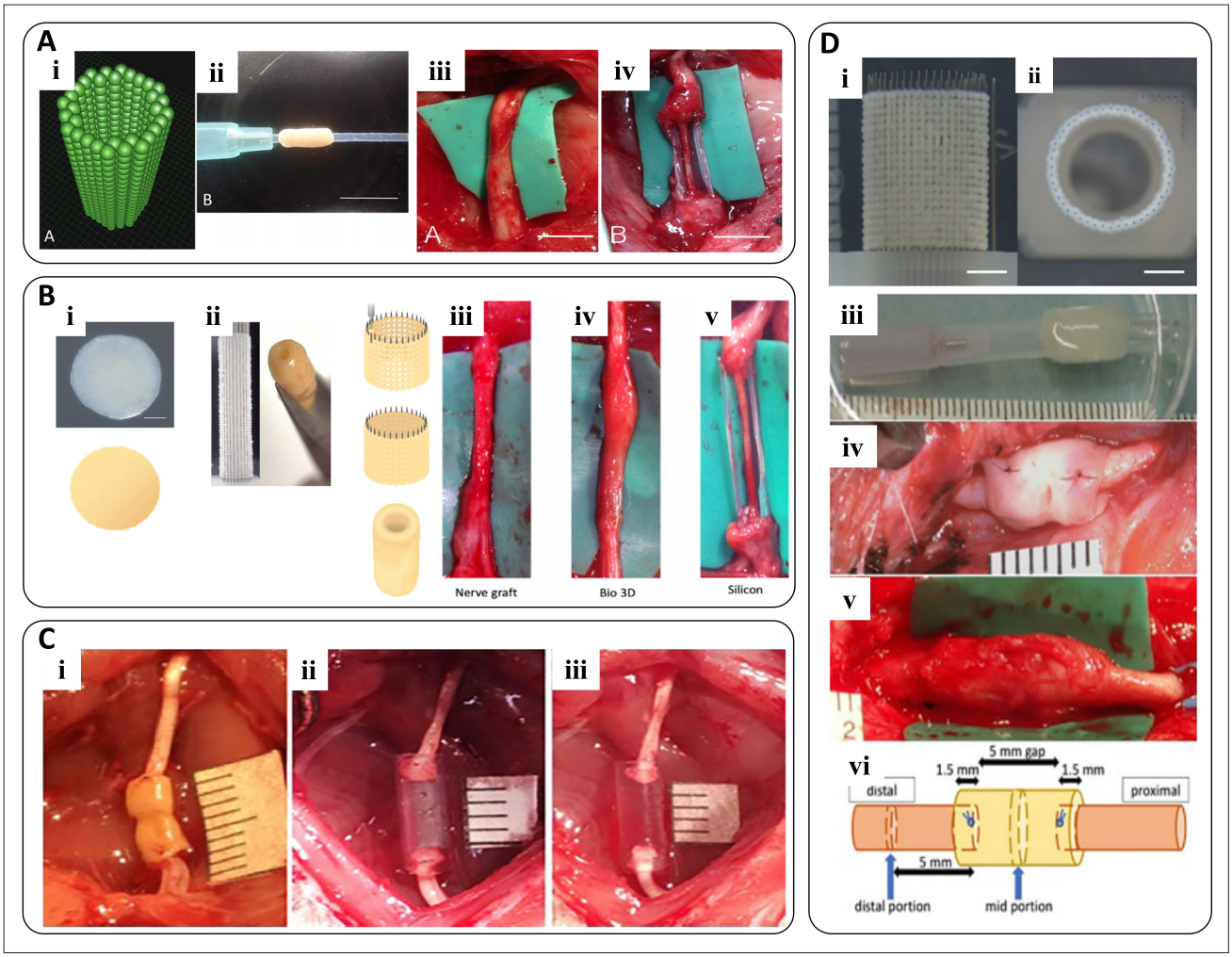

Figure 9. Various conduits prepared using Kenzan technology (A) (i) Pre-designed three-dimensional (3D) tubular structure (green spheres represent homogeneous multi-cellular spheres, cultured only from normal human dermal fibroblasts). (ii) Bio-3D conduit and (iii) bio-3D group regenerates the sciatic nerve 8 weeks after surgery. (iv) Regeneration of the sciatic nerve in the silicone group at 8 weeks postoperatively. Scale bar: (ii) 10 mm. (iii & iv) 5 mm. Adapted from Yurie et al.[168] (B) (i) Fibroblasts aggregate to form spheroids and (ii) fabrication of bio-3D nerve guidance conduits with three types of conduits bridging the 5 mm gap of rat sciatic nerve: (iii) nerve graft group, (iv) bio-3D group, (v) silicon cell group (SC group). Reprinted with permission from Ref.[169] Copyright© 2020 Wiley. (C) (i) Bio-3D group, (ii) silicone group (S group), (iii) (silicone cell group) SC group. Reprinted with permission from Ref.[170] Copyright© 2020 Cognizant Communication Corporation. (D) Stringing of the multi-cellular spheres into circular needle arrays according to a pre-designed pattern (i) from the side, (ii) from above, and (iii) the bio-3D conduit before transplantation. (iv) Insertion of 8 mm bio-3D conduit into nerve defect. (v) Ulnar nerve regeneration at 10 weeks postoperatively. (vi) Schematic of resection and graft dimensions. Scale bar: (i & ii) 2mm Reprinted with permission from Ref.[171] Copyright© 2019 Sage Publications.

However, despite their innovative vision and current implementation in clinical studies, these conduits are still limited to small-diameter nerves and may not be effective for bridging longer nerve gaps. Advancements in biomaterials and 3D bioprinting technologies[115] can therefore offer the potential for developing novel nerve conduits that address such limitations by incorporating bioactive factors to further enhance nerve regeneration, while offering more complex NGC geometrical structures. The use of composite biomaterials functionalized with biomolecules or embedded with SCs or NSCs also inevitably complicates the certification process. The regulatory approval typically focuses on certifying the core biomaterial, such as the scaffold, while the integration of patient-derived cells is subject to separate approval processes. Consequently, one of the biggest obstacles at the moment is regulatory approval. Furthermore, most of the research to date has been based on small animal models, which do not fully capture the complexity of human peripheral nerve regeneration. Validation using large animal models is necessary to accurately mimic human anatomical and physiological conditions. Ultimately, the scalability of such prototypes heavily depends on factors like batch-to-batch variation, long-term sterility, scalability, and rigorous quality control, all of which are crucial for successful product commercialization. For customized or multi-material structures, the scalability of bioprinting platforms remains a significant challenge. Advancements in process automation, closed-loop control systems, and real-time quality assurance technologies will increase their technological availability and market awareness. Within this framework, stronger cooperation between all stakeholders involved, including academic researchers, physicians, regulatory agencies, and business partners, is needed to move forward.

6. Conclusion

NGCs have a broad application prospect in the field of nerve repair for their ability to construct NTE conduits using a combination of designs and biomaterials chosen to mimic the natural structure of peripheral nerves and provide a favorable microenvironment for nerve regeneration. Although there are various current solutions, most of these conduits are still in the experimental stage and have not reached clinical translation. None of them can currently fully substitute autologous nerve grafts to repair peripheral nerve defects. Recently, AM has been exploited for the fabrication of multi-material and multi-functional NGCs. An ideal 3D-bioprinted personalized NGC should mimic the precise structural details of the nerve region to be replaced by guiding tissue regeneration. In this concept, biocomposites of natural and synthetic origins are seen as a promising approach to achieve controlled regulation of the biodegradation rate, mechanical strength, and other properties of the conduit. This customization allows the conduit to meet the specific requirements of different types of injuries and injury gaps, thereby providing superior performance in the repair and regeneration of PNIs.

Although 3D bioprinting has made significant progress in the fabrication of peripheral NGCs, and the prospects are bright, many challenges remain. The biomaterials available for printing are limited, and the performance in terms of degradability, biocompatibility, and mechanical properties needs to be improved. Future research on NGCs should focus more on enhancing their bio-hybridity by controlling the embedment of stem cells with neurotrophic factors and targeted drugs. This strategy aims to further expand the potential for nerve regeneration, addressing the various needs of nerve repair effectively. In addition, future studies of nerve repair mechanisms will provide a better direction for the design of new 3D-printed NGCs. The integration of bioelectronic interfaces, smart biomaterials, and 4D printing is another emerging direction in the field of NGCs that has the potential to completely transform the next generation of NGCs. The development of NGCs that adjust to the physiological conditions of the regenerating nerve is achievable through 4D printing, which involves the generation of dynamic structures capable of responding to environmental stimuli, such as temperature, pH, or electrical signals. The regenerative capacity of NGCs could also be enhanced using smart biomaterials engineered to actively release bioactive molecules or exhibit a controlled degradation profile. In addition, bioelectronic interfaces offer the possibility of integrating electrical stimulation within NGCs to stimulate (and potentially accelerate) *in situ* nerve regeneration. Through regulating neuronal activity, boosting axonal regeneration, and supporting neuroplasticity, electrical stimulation has been demonstrated to stimulate nerve growth. Electrical signals can promote cell proliferation, release neurotrophic factors, and improve the conduit regenerating axon alignment. This controlled stimulation can also support the formation of synaptic connections and improve functional recovery in nerve tissues. Bioelectronic interfaces could be incorporated into NGCs using biocompatible conductive materials, such as poly(3,4-ethylenedioxythiophene) polystyrene sulfonate or graphene, enabling precise control over the electrical signals applied. Therefore, the integration of these technologies promotes the development of highly customizable, multi-functional NGCs that not only provide structural support but also actively participate in the nerve regeneration process.

To further enhance the therapeutic potential of NGCs, developing strategic and personalized conduit selection approaches is essential. Specifically, the structural design of the conduit should be tailored to the length of the nerve defect and the stage of injury. For short-gap defects at an early stage, simple hollow conduits may provide sufficient basic support. In contrast, for long-gap and severe late-stage injuries characterized by scar deposition and reduced SC activity, conduits with stronger guidance capacity and regenerative support, such as multi-channel, porous, or micropatterned designs, are preferred. Moreover, conduit structure should not be considered in isolation, but rather optimized in coordination with material properties, including biocompatibility, mechanical strength, degradation kinetics, and responsiveness to biological signals. Particularly in the context of increasingly functionalized conduit materials, the influence of structural morphology on stem cell differentiation, drug release kinetics, and microenvironment modulation should be given full attention. In terms of fabrication, 3D bioprinting has gradually replaced traditional methods as the mainstream technology for NGC preparation, owing to its capacity for high-resolution and precise reproduction of complex architectures and patient-specific customization. Its advantages are further amplified by the integration of growth factors and bioactive carriers into the printing materials. By leveraging the synergy between structural-material design and the advanced capabilities of 3D bioprinting, next-generation NGCs with multi-functional, intelligent, and personalized features can be developed. Such conduits are not merely passive structural supports, but active participants in modulating the regenerative microenvironment—bridging the gap between structural reconstruction and functional recovery, and moving the field of NTE closer to clinical translation.

In summary, significant progress has been made in the fabrication of NGCs in recent years. As the field of material science and engineering technology continues to innovate, the research and development of NGCs will undoubtedly experience substantial growth. This growth will result in an increasing number of NGCs transitioning from animal experimentation to clinical translation. We believe that by combining the right design, fabrication, materials, and biological factors, the development of NGCs that can effectively repair peripheral nerve deficits is possible within the next decade.

Acknowledgments

The authors would like to gratefully acknowledge De Nayer Stichting for supporting the Advanced Manufacturing Lab.

Funding

The research is funded by the Research Foundation Flanders (FWO) for the doctoral fellowship (1S47325N) granted to Yuexi Zhuang.

Conflict of interest

Eleonora Ferraris is an Editorial Board Member of this journal, but was not in any way involved in the editorial and peer-review process conducted for this paper, directly or indirectly. Separately, other authors declared that they have no known competing financial interests or personal relationships that could have influenced the work reported in this paper.

Author contributions

Conceptualization: Yuexi Zhuang
Visualization: Yuexi Zhuang
Writing–original draft: Yuexi Zhuang
Writing–review & editing: Miriam Seiti, Eleonora Ferraris

Ethics approval and consent to participate

Not applicable.

Consent for publication

Not applicable.

Availability of data

Not applicable.

References

1. Pan, D, Mackinnon, SE, Wood MD. Advances in the repair of segmental nerve injuries and trends in reconstruction. *Muscle Nerve*. 2020;61(6):726-739. doi: 10.1002/mus.26797

2. Joung D, Lavoie NS, Guo SZ, Park SH, Parr AM, McAlpine MC. 3D printed neural regeneration devices. *Adv Funct Mater*. 2020;30(1):1906237. doi: 10.1002/adfm.201906237

3. Seddon HJ. Three types of nerve injury. *Brain*. 1943;66(4):237-288. doi: 10.1093/brain/66.4.237

4. Sunderland S. A classification of peripheral nerve injuries producing loss of function. *Brain*. 1951;74(4):491-516. doi: 10.1093/brain/74.4.491

5. Johnson EO, Soucacos PN. Nerve repair: experimental and clinical evaluation of biodegradable artificial nerve guides. *Injury-Int J Care Inj*. 2008;39(3):30-36. doi: 10.1016/j.injury.2008.05.018

6. Daly W, Yao L, Zeugolis D, Windebank A, Pandit A. A biomaterials approach to peripheral nerve regeneration: bridging the peripheral nerve gap and enhancing functional recovery. *J R Soc Interface*. 2011;9(67):202-221. doi: 10.1098/rsif.2011.0438

7. Scheib J, HoKe A. Advances in peripheral nerve regeneration. *Nat Rev Neurol*. 2013;9(12):668-676. doi: 10.1038/nrneurol.2013.227

8. Yi S, Zhang Y, Gu XK, et al. Application of stem cells in peripheral nerve regeneration. *Burns Trauma*. 2020;8:tkaa002. doi: 10.1093/burnst/tkaa002

9. Han Y, Yin J. Industry news: the additive manufacturing of nerve conduits for the treatment of peripheral nerve injury. *Bio-Des Manuf*. 2021;5(1):6-8. doi: 10.1007/s42242-021-00166-z

10. Ray WZ, Mackinnon S.E. Management of nerve gaps: autografts, allografts, nerve transfers, and end-to-side neurorrhaphy. *Exp Neurol*. 2010;223(1):77-85. doi: 10.1016/j.expneurol.2009.03.031

11. Neumeister MW, Winters JN. Neuroma. *Clin Plast Surg*. 2020;47(2):279-283. doi: 10.1016/j.cps.2019.12.008

12. Stocco E, Barbon S, Emmi A, et al. Bridging gaps in peripheral nerves: from current strategies to future perspectives in conduit design. *Int. J. Mol. Sci.* 2023;24(11):9170. doi: 10.3390/ijms24119170

13. Zhou WX, Rahman MSU, Sun CM, et al. Perspectives on the novel multifunctional nerve guidance conduits: from specific regenerative procedures to motor function rebuilding. *Adv Mater*. 2023;36(4):2307805. doi: 10.1002/adma.202307805

14. Wang SF, Yaszemski MJ, Knight AM, Gruetzmacher JA, Windebank AJ, Lu LC. Photo-crosslinked poly (ε-caprolactone fumarate) networks for guided peripheral nerve regeneration: material properties and preliminary biological evaluations. *Acta Biomater*. 2009;5(5): 1531-1542. doi: 10.1016/j.actbio.2008.12.015

15. Liu XY, Duan XC. Mechanisms and treatments of peripheral nerve injury. *Ann Plast Surg*. 2023;91(2):313-318. doi: 10.1097/SAP.0000000000003480

16. Yang XQ, Huang L, Yi XZY, Huang SY, Duan B, Yu AX. Multifunctional chitin-based hollow nerve conduit for peripheral nerve regeneration and neuroma inhibition. *Carbohydr Polym*. 2020;289:119443. doi: 10.1016/j.carbpol.2022.119443.

17. Homaeigohar S, Tsai TY, Young TH, Yang HJ, Ji YR. An electroactive alginate hydrogel nanocomposite reinforced by functionalized graphite nanofilaments for neural tissue engineering. *Carbohydr Polym*. 2019; 224:115112. doi: 10.1016/j.carbpol.2019.115112

18. Dong Q, Yang XD, Liang X, et al. Composite hydrogel conduit incorporated with platelet-rich plasma improved the regenerative microenvironment for peripheral nerve repair. *ACS Appl Mater Interfaces*. 2023;15(20): 24120-24133. doi: 10.1021/acsami.3c02548

19. Zhang SJ, Wang J, Zheng ZZ, et al. Porous nerve guidance conduits reinforced with braided composite structures of silk/magnesium filaments for peripheral nerve repair. *Acta Biomater*. 2021;134(15):116-130. doi: 10.1016/j.actbio.2021.07.028

20. Gu XS, Ding F, Williams DF. Neural tissue engineering options for peripheral nerve regeneration. *Biomaterials*. 2014;35(24):6143-6156. doi: 10.1016/j.biomaterials.2014.04.064

21. Fregnan F, Ciglieri E, Tos P, et al. Chitosan crosslinked flat scaffolds for peripheral nerve regeneration. *Biomed Mater*. 2016;11(4):045010. doi: 10.1088/1748-6041/11/4/045010

22. Yang F, Murugan R, Ramakrishna S, Wang X, Ma YX, Wang S. Fabrication of nano-structured porous PLLA scaffold intended for nerve tissue engineering. *Biomaterials*. 2004;25(10):1891. doi: 10.1016/j.biomaterials.2003.08.062

23. Yang Y, De Laporte L, Rives CB, et al. Neurotrophin releasing single and multiple lumen nerve conduits. *J Control Release*. 2005;104(3):433. doi: 10.1016/j.jconrel.2005.02.022

24. Jeffries EM, Wang YD. Biomimetic micropatterned multi-channel nerve guides by templated electrospinning. *Biotechnol Bioeng*. 2012;109(6):1571-1582. doi: 10.1002/bit.24412

25. Bozkurt A, Brook GA, Moellers S, et al. In vitro assessment of axonal growth using dorsal root ganglia explants in a novel three-dimensional collagen matrix. *Tissue Eng*. 2007;13(12):2971. doi: 10.1089/ten.2007.0116

26. Vijayavenkataraman S, Zhang S, Thaharah S, Sriram G, Lu WF, Fuh JYH. Electrohydrodynamic jet 3D printed nerve guide conduits (NGCs) for peripheral nerve injury repair. *Polymers*. 2018;10(7):753. doi: 10.3390/polym10070753

27. Wasti S, Adhikari S. Use of biomaterials for 3D printing by fused deposition modeling technique: a review. *Front Chem*. 2020;8:315. doi: 10.3389/fchem.2020.00315

28. O'Brien CM, Holmes B, Faucett S, Zhang LG. Three-dimensional printing of nanomaterial scaffolds for complex tissue regeneration. *Tissue Eng. Part B-Rev*. 2015;21(1):103-114. doi: 10.1089/ten.teb.2014.0168

29. Wang G, Zhao W, Liu YF, Cheng TJ. Review of space manufacturing technique and developments. *Sci Sin-Phys Mech Astron*. 2020;50(4):0416.
doi: 10.1360/SSPMA-2019-0416

30. Schmitt M, Mehta RM, Kim IY. Additive manufacturing infill optimization for automotive 3D-printed ABS components. *Rapid Prototyp. J.* 2020;26(1):89-99.
doi: 10.1108/RPJ-01-2019-0007

31. Alhnan MA, Okwuosa TC, Sadia M, Wan KW, Ahmed W, Arafat B. Emergence of 3D printed dosage forms: opportunities and challenges. *Pharma Res*. 2016;33(8):1817-1832.
doi: 10.1007/s11095-016-1933-1

32. Alexander P, Stefan K, Ernst R. Additive manufacturing in construction: a review on processes, applications, and digital planning methods. *Addit Manuf.* 2019;30:100894.
doi: 10.1016/j.addma.2019.100894

33. Chakraborty S, Biswas MC. 3D printing technology of polymer-fiber composites in textile and fashion industry: a potential roadmap of concept to consumer. *Compos Struct*. 2020;248:112562.
doi: 10.1016/j.compstruct.2020.112562

34. Qian Y, Han QX, Zhao XT, Li H, Yuan WE, Fan CY. Asymmetrical 3d nanoceria channel for severe neurological defect regeneration. *iScience*. 2019;12:216-231.
doi: 10.1016/j.isci.2019.01.013

35. Groll J, Boland T, Blunk T, et al. Biofabrication: reappraising the definition of an evolving field. *Biofabrication*. 2016;8(1):013001.
doi: 10.1088/1758-5090/8/1/013001

36. Moroni L, Boland T, Burdick JA, et al. Biofabrication: a guide to technology and terminology. *Trends Biotechnol.* 2018;36(4):384-402.
doi: 10.1016/j.tibtech.2017.10.015

37. Ijpma FFA, De Graaf RCV, Meek MF. The early history of tubulation in nerve repair. *J Hand Surg-Eur. Vol.* 2008;33E(5):581-586.
doi: 10.1177/1753193408091349

38. Lundborg G, Longo FM, Varón S. Nerve regeneration model and trophic factors in vivo. *Brain Res*. 1982;232(1): 157-161.
doi: 10.1016/0006-8993(82)90618-7

39. Williams LR, Longo FM, Powell HC, Lundborg G, Varón S. Spatial-temporal progress of peripheral nerve regeneration within a silicone chamber: parameters for a bioassay. *J Comp Neurol.* 1983;218(4):460-70.
doi: 10.1002/cne.902180409

40. Ruiter GCW, Malessy MJA, Yaszemski MJ, Windebank AJ, Spinner RJ. Designing ideal conduits for peripheral nerve repair. *Neurosurg Focus*. 2009;26(2):E5.
doi: 10.3171/FOC.2009.26.2.E5

41. Qin JZ, Wang PJ, Wang Y. An experimental study on the repair of peripheral nerve defects by using polylactic-glycolic acid microfilaments wrapped in muscle flap and prefabricated in amniotic tube to simulate peripheral nerve regeneration microenvironment. *Chin J Tissue Eng Res*. 2009;13(16):3093-3096.
doi: 10.3969/j.issn.3093-3096.2009.13.16.

42. Lundborg G, Kanje M. Bioartificial nerve grafts: a prototype. *Scand J Plast Reconstr Surg Hand Surg.* 1996;30(2):105-110.
doi: 10.3109/02844319609056391

43. Wang SF, Cai L. Polymers for fabricating nerve conduits. *Int J Polym Sci*. 2010;2010:1-20.
doi: 10.1155/2010/138686

44. Moore MJ, Friedman JA, Lewellyn EB, et al. Multiple-channel scaffolds to promote spinal cord axon regeneration. *Biomaterials*. 2006;27(3):419-429.
doi: 10.1016/j.biomaterials.2005.07.045

45. Lee DJ, Fontaine A, Meng XZ, Park D. Biomimetic nerve guidance conduit containing intraluminal microchannels with aligned nanofibers markedly facilitates in nerve regeneration. *ACS Biomater Sci Eng.* 2016;2(8):1403-1410.
doi: 10.1021/acsbiomaterials.6b00344

46. Wang YM, WangWJ, Wo Y, et al. Orientated guidance of peripheral nerve regeneration using conduits with a microtube array sheet (MTAS). *ACS Appl Mater Interfaces.* 2015;7(16):8437-8450.
doi: 10.1021/acsami.5b00215

47. Apablaza JA, Lezcano MF, Marquez AL, Sánchez KG, Oporto GH, Dias FJ. Main morphological characteristics of tubular polymeric scaffolds to promote peripheral nerve regeneration-a scoping review. *Polymers*. 2021;13(15):2563.
doi: 10.3390/polym13152563

48. Wan Y, Zhang J, Luo Y, Zhou T, Wu H. Preparation and degradation of chitosan-poly(p-dioxanone)/silk fibroin porous conduits. *Polym Degrad Stabil*. 2015;119:46-55.
doi: 10.1016/j.polymdegradstab.2015.05.004

49. Odelius K, Höglund A, Kumar S, et al. Porosity and pore size regulate the degradation product profile of polylactide. *Biomacromolecules*. 2011;12(4):1250-1258.
doi: 10.1021/bm1015464

50. Wu LB, Ding JD. Effects of porosity and pore size on in vitro degradation of three-dimensional porous poly(D,L-lactide-coglycolide) scaffolds for tissue engineering. *J Biomed Mater Res Part A*. 2005;75(4):767-777.
doi: 10.1002/jbm.a.30487

51. Song CB, Zhang JP, Cen L, Xi ZH, Zhao L, Yuan WK. Modeling strategies for the degradation behavior of porous polyester materials based on their key structural features. *Ind Eng Chem Res*. 2020;59(33):14806-14816.
doi: 10.1021/acs.iecr.0c02694

52. Tao J, Hu Y, Wang SJ, et al. A 3D-engineered porous conduit for peripheral nerve repair. *Sci Rep*. 2017;7:46038.

doi: 10.1038/srep46038

53. Clark P, Connolly P, Curtis SG, Dow JAT, Wilkinson CDW. Topographical control of cell behavior: I. Simple step cues. *Development*. 1987;99(3):439-448. doi: 10.1242/dev.99.3.439. https://webofscience.clarivate.cn/wos/alldb/full-record/WOS:A1987G384800014

54. Miller C, Jeftinija S, Mallapragada S. Synergistic effects of physical and chemical guidance cues on neurite alignment and outgrowth on biodegradable polymer substrates. *Tissue Eng*. 2002;8(3):367-378. doi: 10.1089/107632702760184646

55. Schmalenberg KE, Uhrich KE. Micropatterned polymer substrates control alignment of proliferating Schwann cells to direct neuronal regeneration. *Biomaterials*. 2005;26(12):1423-1430. doi: 10.1016/j.biomaterials.2004.04.046

56. Rutkowski GE, Miller CA, Jeftinija S, Mallapragada SK. Synergistic effects of micropatterned biodegradable conduits and Schwann cells on sciatic nerve regeneration. *J Neural Eng*. 2004;1(3):151-157. doi: 10.1088/1741-2560/1/3/004

57. Davis B, Wojtalewicz S, Labroo P, et al. Controlled release of FK506 from micropatterned PLGA films: potential for application in peripheral nerve repair. *Neural Regen Res*. 2018;13(7):1247-1252. doi: 10.4103/1673-5374.235063

58. Yu X, Zhang DT, Liu C, et al. Micropatterned poly(D, L-lactide-co-caprolactone) conduits with KHI-peptide and NGF promote peripheral nerve repair after severe traction injury. *Front Bioeng Biotechnol*. 2021;9:744230. doi: 10.3389/fbioe.2021.744230

59. Bolleboom A, de Ruiter GCW, Coert JH, Tuk B, Holstege JC, van Neck JW. Novel experimental surgical strategy to prevent traumatic neuroma formation by combining a 3D-printed Y-tube with an autograft. *Lab Invest*. 2019;130(1):184-196. doi: 10.3171/2017.8.JNS17276

60. Zhang J, Tao J, Cheng H, et al. Nerve transfer with 3D-printed branch nerve Conduits. *Burns Trauma*. 2022;10:tkac010. doi: 10.1093/burnst/tkac010

61. Hu Y, Wu Y, Gou ZY, et al. 3D-engineering of cellularized conduits for peripheral nerve regeneration. *Sci Rep*. 2016;6:32184. doi: 10.1038/srep32184

62. Johnson BN, Lancaster KZ, Zhen GH, et al. 3D printed anatomical nerve regeneration pathways. *Adv Funct Mater*. 2015;25(39):6205-6217. doi: 10.1002/adfm.201501760

63. Carvalho CR, Oliveira JM, Reis RL. Modern trends for peripheral nerve repair and regeneration: beyond the hollow nerve guidance conduit. *Front Bioeng Biotechnol*. 2019;7:337. doi: 10.3389/fbioe.2019.00337

64. Wang EG, Inaba K, Byerly S, et al. Optimal timing for repair of peripheral nerve injuries. *J Trauma Acute Care Surg*. 2017;83(5):875-881. doi: 10.1097/TA.0000000000001570

65. Wu GG, Wen XY, Kuang R, et al. Roles of macrophages and their interactions with schwann cells after peripheral nerve injury. *Cell Mol Neurobiol*. 2023;44(1):11. doi: 10.1007/s10571-023-01442-5

66. Gezercan Y, Menekse G, Ökten AI, et al. The outcomes of late term surgical treatment of penetrating peripheral nerve injuries. *Turk Neurosurg*. 2026;26(1):146-152. doi: 10.5137/1019-5149.JTN.14094-15.1

67. Vijayavenkataraman S. Nerve guide conduits for peripheral nerve injury repair: A review on design, materials and fabrication methods. *Acta Biomaterialia*. 2020;106:54-69, doi: 10.1016/j.actbio.2020.02.003

68. Satchanska G, Davidova S, Petrov PD. Natural and synthetic polymers for biomedical and environmental applications. *Polymer*. 2024;16(8):1159. doi: 10.3390/polym16081159

69. Ciardelli G, Chiono V. Materials for peripheral nerve regeneration. *Macromol Biosci*. 2006;6(1):13-26. doi: 10.1002/mabi.200500151

70. Chiono V, Tonda-Turo C, Ciardelli G. Artificial scaffolds for peripheral nerve reconstruction. *Int Rev Neurobiol*. 2009;87:173-198. doi: 10.1016/S0074-7742(09)87009-8

71. Gu XS, Ding F, Yang YM, Liu J. Construction of tissue engineered nerve grafts and their application in peripheral nerve regeneration. *Prog Neurobiol*. 2011;93(2):204-230. doi: 10.1016/j.pneurobio.2010.11.002

72. Benowitz LI, Popovich PG. Inflammation and axon regeneration. *Curr Opin Neurol*. 2011;24(6):577-583. doi: 10.1097/WCO.0b013e32834c208d

73. Zhao YH, Wang YJ, Gong JH, et al. Chitosan degradation products facilitate peripheral nerve regeneration by improving macrophage-constructed microenvironments. *Biomaterials*. 2017;134:64-77. doi: 10.1016/j.biomaterials.2017.02.026

74. Nawrotek K, Kubicka M, Gatkowska J, et. al. Controlling the spatiotemporal release of nerve growth factor by chitosan/polycaprolactone conduits for use in peripheral nerve regeneration. *Int J Mol Sci*. 2022;23(5):2852. doi: 10.3390/ijms23052852.

75. Bianchini M, Zinno C, Micera S, Riva ER. Improved physiochemical properties of chitosan@PCL nerve conduits by natural molecule crosslinking. *Biomolecules*. 2023;13(12):1712. doi: 10.3390/biom13121712.

76. Zhang M, An H, Wan T, et al. Micron track chitosan conduit fabricated by 3D-printed model topography provides bionic

microenvironment for peripheral nerve regeneration. *Int J Bioprinting*. 2023;9(5):770.
doi: 10.18063/ijb.770

77. Yi BC, Zhang HL, Yu ZP, Yuan HH, Wang XL, Zhang YZ. Fabrication of high performance silk fibroin fibers via stable jet electrospinning for potential use in anisotropic tissue regeneration. *J Mater Chem B*. 2018;6(23):3934-3945.
doi: 10.1039/c8tb00535d

78. Chen ZY, Zhang Q, Li HM, Wei Q, Zhao X, Chen FL. Elastin-like polypeptide modified silk fibroin porous scaffold promotes osteochondral repair. *Bioact Mater*. 2021;6(3):589-601.
doi: 10.1016/j.bioactmat.2020.09.003

79. Nguyen TP, Nguyen QV, Nguyen VH, et al. Silk fibroin-based biomaterials for biomedical applications: a review. *Polymers*. 2019;11(12):1933.
doi: 10.3390/polym11121933

80. Dinis TM, Elia R, Vidal G, et al. 3D multi-channel bi-functionalized silk electrospun conduits for peripheral nerve regeneration. *J Mech Behav Biomed Mater*. 2015;41:43-55.
doi: 10.1016/j.jmbbm.2014.09.029

81. Zhao YH, Liang YY, Ding SP, Zhang KY, Mao HQ, Yang YM. Application of conductive PPy/SF composite scaffold and electrical stimulation for neural tissue engineering. *Biomaterials*. 2020;255:120164.
doi: 1016/j.biomaterials.2020.120164

82. Wang Y, Ge Y, Yao K, Zhang L, Yang Y. Repair of sciatic nerve injury in rats by composite filipin conduit. *J Nantong Univ Med Ed*. 2021;41(03):207-211.
https://caod.oriprobe.com/articles/61847006/Repair_study_of_sciatic_nerve_injury_in_rats_with_combined_silk_fibroi.htm

83. Zhao YH, Niu CM, Shi JQ, Wang YY, Yang YM, Wang HB. Novel conductive polypyrrole/silk fibroin scaffold for neural tissue repair. *Neural Regen Res*. 2018;13(8):1455-1464.
doi: 10.4103/1673-5374.235303

84. Fujimaki H, Uchida K, Inoue G, et al. Oriented collagen tubes combined with basic fibroblast growth factor promote peripheral nerve regeneration in a 15 mm sciatic nerve defect rat model. *J Biomed Mater Res Part A*. 2017;105(1):8-14.
doi: 10.1002/jbm.a.35866

85. Yoo J, Park JH, Kwon YW, et al. Augmented peripheral nerve regeneration through elastic nerve guidance conduits prepared using a porous PLCL membrane with a 3D printed collagen hydrogel. *Biomater Sci*. 2020;8(22):6261.
doi: 10.1039/d0bm00847h.

86. Chen C, Xu HH, Liu XY, et al. 3D printed collagen/silk fibroin scaffolds carrying the secretome of human umbilical mesenchymal stemcells ameliorated neurological dysfunction after spinal cord injury in rats. *Regen Biomater*. 2022;9:rbac014.
doi: 10.1093/rb/rbac014

87. Gaspar-Pintiliescu A, Stanciuc AM, Craciunescu O. Natural composite dressings based on collagen, gelatin and plant bioactive compounds for wound healing: A review. *Int J Biol Macromol*. 2019;138:854-865.
doi: 10.1016/j.ijbiomac.2019.07.155

88. Ulubayram K, Aksu E, Gurhan SID, Serbetci K, Hasirci N. Cytotoxicity evaluation of gelatin sponges prepared with different cross-linking agents. *J Biomater Sci-Polym Ed*. 2022;13(11):1203-1219.
doi: 10.1163/156856202320892966

89. Sultana S, Khan RA, Shahruzzaman M, Khan MA, Mustafa AI, Gafur MA. Effect of gamma radiation on the physico- and thermo-mechanical properties of gelatin-based films using 2-hydroxyethyl methacrylate (HEMA). *Polym Plast Technol Eng*. 2010;49(7):662-671.
doi: 10.1080/03602551003681804

90. Le HR, Natesan K, Pranti-Haran S. Mechanical property and biocompatibility of co-precipitated nano hydroxyapatite-gelatine composites. *J Adv Ceram*. 2015;4(3):237-243.
doi: 10.1007/s40145-015-0155-z

91. Sergi R, Bellucci D, Cannillo V. A review of bioactive glass/natural polymer composites: state of the art. *Materials*. 2020;13(23):13235560.
doi: 10.3390/ma13235560

92. Gong H, Fei H, Xu Q, Guo M, Chen HH. 3D-engineered GelMA conduit filled with ECM promotes regeneration of peripheral nerve. *J Biomed Mater Res Part A*. 2020;108A:3.
doi: 10.1002/jbm.a.36859

93. Tao J, Zhang JM, Du T, et al. Rapid 3D printing of functional nanoparticle-enhanced conduits for effective nerve repair. *Acta Biomater*. 2019;90:49-59.
doi: 10.1016/j.actbio.2019.03.047

94. Liu JY, Zhang B, Li L, Yin J, Fu JZ. Additive-lathe 3D bioprinting of bilayered nerve conduits incorporated with supportive cells. *Bioact Mater*. 2021;6(1):219-229.
doi: 10.1016/j.bioactmat.2020.08.010

95. Kuperkar K, Atanase LI, Bahadur A, Crivei IC, Bahadur P. Degradable polymeric bio(nano)materials and their biomedical applications: a comprehensive overview and recent updates. *Polymers*. 2024;16(2):206.
doi: 10.3390/polym16020206

96. Evans GRD, Brandt K, Widmer MS, et al. In vivo evaluation of poly(L-lactic acid) porous conduits for peripheral nerve regeneration. *Biomaterials*. 1999;20(12):1109-1115.
doi: 10.1016/S0142-9612(99)00010-1

97. Cai J, Peng XJ, Nelson KD, Nelson KD, Eberhart R, Smith GM. Permeable guidance channels containing microfilament scaffolds enhance axon growth and maturation. *J Biomed Mater Res Part A*. 2005;75A(2):374-386.
doi: 10.1002/jbm.a.30432

98. Jahromi HK, Farzin A, Hasanzadeh E, et al. Enhanced sciatic nerve regeneration by poly-L-lactic acid/multi-wall carbon

nanotube neural guidance conduit containing Schwann cells and curcumin encapsulated chitosan nanoparticles in rat. *Mater Sci Eng C-Mater Biol Appl*. 2020;109:110564. doi: 10.1016/j.msec.2019.110564

99. Lasprilla AJR, Martinez GAR, Lunelli BH, Jardini AL, Maciel R. Poly-lactic acid synthesis for application in biomedical devices—a review. *Biotechnol Adv.* 2012;30(1):321-328. doi: 10.1016/j.biotechadv.2011.06.019

100. Gerdefaramarzi RS, Ebrahimian-Hosseinabadi M, Khodaei M. 3D printed poly(lactic acid)/poly(ε-caprolactone)/graphene nanocomposite scaffolds for peripheral nerve tissue engineering. *Arab J Chem*. 2024; 17(9):105927. doi: 10.1016/j.arabjc.2024.105927

101. Wang XD, Hu W, Cao Y, Yao J, Wu J, Gu XS. Dog sciatic nerve regeneration across a 30-mm defect bridged by a chitosan/PGA artificial nerve graft. *Brain*. 2005;128(8):1897-1910. doi: 10.1093/brain/awh517

102. Yue HX, Liu XZ, Hou KJ, Vyas C, Bartolo P. Stereolithography 3D printing of microgroove master moulds for topography-induced nerve guidance conduits. *Int J Bioprinting*. 2024;10(3):2725. doi: 10.36922/ijb.2725

103. Zheng CS, Yang ZH, Chen SH, et al. Nanofibrous nerve guidance conduits decorated with decellularized matrix hydrogel facilitate peripheral nerve injury repair. *Theranostics*. 2021;11(6):2917-2931. doi: 10.7150/thno.50825

104. Sachan R, Warkar SG, Purwar R. An overview on synthesis, properties and applications of polycaprolactone copolymers, blends & composites. *Polym Plast Technol Mater.* 2022;62(3):327-358. doi: 10.1080/25740881.2022.2113890

105. Xu PW, Tan S, Niu DY, et al. Effect of temperatures on stress-induced structural evolution and mechanical behaviors of polyglycolic acid/polycaprolactone blends. *Polymer*. 2023;283:126239. doi: 10.1016/j.polymer.2023.126239

106. Zhu L, Jia SJ, Liu TJ, et al. Aligned PCL fiber conduits immobilized with nerve growth factor gradients enhance and direct sciatic nerve regeneration. *Adv Funct Mater*. 2020;30(39):2002610. doi: 10.1002/adfm.202002610

107. Chen CC, Yu J, Ng HY, et al. The physicochemical properties of decellularized extracellular matrix coated 3D printed poly(ε-caprolactone) nerve conduits for promoting schwann cells proliferation and differentiation. *Materials*. 2018;11(9):1665. doi: 10.3390/ma11091665

108. Qian Y, Zhao XT, Han QX, Chen W, Li H, Yuan WE. An integrated multi-layer 3D-fabrication of PDA/RGD coated graphene loaded PCL nanoscaffold for peripheral nerve restoration. *Nat Commun*. 2018;9(1):323. doi: 10.1038/s41467-017-02598-7

109. Luis AL, Rodrigues JM, Amado S, et al. PLGA 90/10 and caprolactone biodegradable nerve guides for the reconstruction of the rat sciatic nerve. *Microsurgery*. 2007;27(2):125-137. doi: 10.1002/micr.20317

110. Makadia HK, Siegel SJ. Poly lactic-co-glycolic acid (PLGA) as biodegradable controlled drug delivery carrier. *Polymers*. 2011;3(3):1377-1397. doi: 10.3390/polym3031377

111. Ouyang YM, Huang C, Zhu Y, Fen CY, Ke QF. fabrication of seamless electrospun collagen/PLGA conduits whose walls comprise highly longitudinal aligned nanofibers for nerve regeneration. *J Biomed Nanotechnol*. 2013;9(6):931-943. doi: 10.1166/jbn.2013.1605

112. Namhongsa M, Daranarong D, Sriyai M, et al. Surface-modified polypyrrole-coated PLCL and PLGA nerve guide conduits fabricated by 3D printing and electrospinning. *Biomacromolecules*. 2022;23(11):4532-4546. doi: 10.1021/acs.biomac.2c00626

113. Lackington WA, Kocí Z, Alekseeva T, et al. Controlling the dose-dependent, synergistic and temporal effects of NGF and GDNF by encapsulation in PLGA microparticles for use in nerve guidance conduits for the repair of large peripheral nerve defects. *J Control Release*. 2019;304:51-64. doi: 10.1016/j.jconrel.2019.05.001

114. Berkovitch Y, Cohen T, Peled E, et al. Hydrogel composition and laser micropatterning to regulate sciatic nerve regeneration. *Tissue Eng Regen Med*. 2017;12(4):1049-1061. doi: 10.1002/term.2606

115. Seiti M, Degryse O, Ferraro RM, Giliani S, Bloemen V, et al. 3D Aerosol Jet® printing for microstructuring: Advantages and limitations. *Int J Bioprinting*. 2023;9(6): 0257. doi: 10.36922/ijb.0257

116. Berkovitch Y, Yelin D, Seliktar D. Photo-patterning PEG-based hydrogels for neuronal engineering. *Eur Polym J*. 2015;72:473-483. doi: 10.1016/j.eurpolymj.2015.07.014

117. Zhu H, Yao C, Wei BY, et al. 3D printing of functional bioengineered constructs for neural regeneration: a review. *Int J Extreme Manuf*. 2023;5(4):042004. doi: 10.1088/2631-7990/ace56c.

118. Li JX, Wu ZW, Zhao L, et al. The heterogeneity of mesenchymal stem cells: an important issue to be addressed in cell therapy. *Stem Cell Res Ther*. 2023;14(1):381. doi: 10.1186/s13287-023-03587-y

119. Andreotti JP, Silva WN, Costa AC, et al. Neural stem cell niche heterogeneity. *Semin Cell Dev Biol*. 2019;14(95):42-53. doi: 10.1016/j.semcdb.2019.01.005

120. Ding F, Wu JA, Yang YM, et al. Use of tissue-engineered nerve grafts consisting of a chitosan/poly(lactic-co-glycolic acid)-based scaffold included with bone marrow mesenchymal

cells for bridging 50-mm dog sciatic nerve gaps. *Tissue Eng Part A*. 2010;16(12):3779-3790.
doi: 10.1089/ten.tea.2010.0299

121. Santiago LY, Clavijo-Alvarez J, Brayfield C, Rubin JP, Marra KG. Delivery of adipose-derived precursor cells for peripheral nerve repair. *Cell Transplant*. 2009; 18(2):145-158.
doi: 10.3727/096368909788341289

122. Jiang LF, Jones S, Jia XF. Stem cell transplantation for peripheral nerve regeneration: current options and opportunities. *Int J Mol Sci*. 2017;18(1):94.
doi: 10.3390/ijms18010094

123. Oliveira JT, Almeida FM, Biancalana A, et al. Mesenchymal stem cells in a polycaprolactone conduit enhance median-nerve regeneration, prevent decrease of creatine phosphokinase levels in muscle, and improve functional recovery in mice. *Neuroscience*. 2010;170(4):1295-1303.
doi: 10.1016/j.neuroscience.2010.08.042

124. Greenberg DA, Jin KL. From angiogenesis to neuropathology. *Nature*. 2015;438(7070):954-959.
doi: 10.1038/nature04481

125. Zhang QZ, Nguyen PD, Shi SH, Burrell JC, Cullen DK, Le AD. 3D bio-printed scaffold-free nerve constructs with human gingiva derived mesenchymal stem cells promote rat facial nerve regeneration. *Sci Rep*. 2018;8:6634.
doi: 10.1038/s41598-018-24888-w

126. Cui Y, Yao Y, Zhao YN, et al. Functional collagen conduits combined with human mesenchymal stem cells promote regeneration after sciatic nerve transection in dogs. *J Tissue Eng Regen Med*. 2018;12(5):1285-1296.
doi: 10.1002/term.2660

127. Endo T, Kadoya K, Suzuki T, et al. Mature but not developing Schwann cells promote axon regeneration after peripheral nerve injury. *NJP Regen Med*. 2022;7:12.
doi: 10.1038/s41536-022-00205-y

128. Ning LQ, Mehta R, Cao C, et al. Embedded 3D bioprinting of gelatin methacryloyl-based constructs with highly tunable structural fidelity. *ACS Appl Mater Interfaces*. 2020;12(40):44563-44577.
doi: 10.1021/acsami.0c15078

129. Ning LQ, Zhu N, Mohabatpour F, Sarker MD, Schreyer DJ, Chen XB. Bioprinting Schwann cell-laden scaffolds from low-viscosity hydrogel compositions. *J Mater Chem*. 2019;7(29):4538-4551.
doi: 10.1039/c9tb00669a

130. Summa PG, Kingham PJ, Raffoul W, Wiberg M, Terenghi G, Kalbermatten DF. Adipose-derived stem cells enhance peripheral nerve regeneration. *J Plast Reconstr Aesthet Surg*. 2010;63(9):1544-1552.
doi: 10.1016/j.bjps.2009.09.012

131. Mesentier-Louro LA, Rosso P, Carito V, et al. Nerve growth factor role on retinal ganglion cell survival and axon regrowth: effects of ocular administration in experimental model of optic nerve injury. *Mol Neurobiol*. 2019;56(2):1056-69.
doi: 10.1007/s12035-018-1154-1

132. Chen ZW, Wang MS. Effects of nerve growth factor on crushed sciatic nerve regeneration in rats. *Microsurgery*. 1995;16(8):547-551.
doi: 10.1002/micr.1920160808

133. Tang S, Zhu JX, Xu YB, Xiang AP, Jiang MH, Quan DP. The effects of gradients of nerve growth factor immobilized PCLA scaffolds on neurite outgrowth in vitro and peripheral nerve regeneration in rats. *Biomaterials*. 2013; 34(29):7086-7096.
doi: 10.1016/j.biomaterials.2013.05.080

134. Xu F, Su GB. *Calendula officinalis* extract-loaded conduits improved sciatic nerve injury repair through upregulation of BDNF and GFAP. *J Bioact Compat Polym*. 2024;39(4):217-235.
doi: 10.1177/08839115241258150

135. Rao F, Wang YH, Zhang DY, et al. Aligned chitosan nanofiber hydrogel grafted with peptides mimicking bioactive brain-derived neurotrophic factor and vascular endothelial growth factor repair long-distance sciatic nerve defects in rats. *Theranostics*. 2020; 10(4):1590-1603.
doi: 10.7150/thno.36272

136. Grothe C, Nikkhah G. The role of basic fibroblast growth factor in peripheral nerve regeneration. *Anat Embryol*. 2001;204(3):171-177.
doi: 10.1007/s004290100205

137. Cui Y, Lu C, Meng DQ, et al. Collagen scaffolds modified with CNTF and bFGF promote facial nerve regeneration in minipigs. *Biomaterials*. 2014;35(27):7819-7827.
doi: 10.1016/j.biomaterials.2014.05.065

138. Mobasseri SA, Terenghi G, Downes S. Micro-structural geometry of thin films intended for the inner lumen of nerve conduits affects nerve repair. *J Mater Sci-Mater Med*. 2013;24(7):1639-1647.
doi: 10.1007/s10856-013-4922-5

139. Melchels FPW, Feijen J, Grijpma DW. A review on stereolithography and its applications in biomedical engineering. *Biomaterials*. 2010;31(4):6121-6130.
doi: 10.1016/j.biomaterials.2010.04.050.

140. Schmidleithner C, Malferarri S, Palgrave R, Bomze D, Schwentenwein M, Kalaskar DM. Application of high resolution DLP stereolithography for fabrication of tricalcium phosphate scaffolds for bone regeneration. *Biomed Mater*. 2018;14(4):045018.
doi: 10.1088/1748-605X/ab279d

141. Zennifer A, Manivannan S, Sethuraman S, Kumbar SG, Sundaramurthi D. 3D bioprinting and photocrosslinking: emerging strategies & future perspectives. *Biomater Adv*. 2021;134:112576.
doi: 10.1016/j.msec.2021.112576

142. Arcaute K, Mann BK, Wicker RB. Fabrication of off-the-shelf multilumen poly(ethylene glycol) nerve guidance conduits using stereolithography. *Tissue Eng Part C-Methods*. 2010;17(1):27-38.
doi: 10.1089/ten.tec.2010.0011

143. Evangelista MS, Perez M, Salibian AA, et al. Single-lumen and multi-lumen poly(ethylene glycol) nerve conduits fabricated by stereolithography for peripheral nerve regeneration in vivo. *J Reconstr Microsurg*. 2015;31(5):327-335.
doi: 10.1055/s-0034-1395415

144. Farzan A, Borandeh S, Seppälä J. Conductive polyurethane/PEGylated graphene oxide composite for 3D-printed nerve guidance conduits. *Eur Polym J*. 2022;167:111068.
doi: 10.1016/j.eurpolymj.2022.111068

145. Perez MA. Manufacturing nerve guidance conduits by stereolithography for use in peripheral nerve regeneration. *The University of Texas at El Paso ProQuest Dissertations & Theses*. 2013;1551240
https://scholarworks.utep.edu/dissertations/AAI1551240

146. Singh A, Asikainen S, Teotia AK, et al. Biomimetic photocurable three-dimensional printed nerve guidance channels with aligned cryomatrix lumen for peripheral nerve regeneration. *ACS Appl Mater Interfaces*. 2018;10(50):43327-43342.
doi: 10.1021/acsami.8b11677

147. Ligon SC, Liska R, Stampfl J, Gurr M, Mülhaupt R. Polymers for 3D printing and customized additive manufacturing. *Chem Rev*. 2017;117(15):10212-10290.
doi: 10.1021/acs.chemrev.7b00074

148. Wu Y, Su H, Li M, Xing HY. Digital light processing-based multi-material bioprinting: processes, applications, and perspectives. *J Biomed Mater Res Part A*. 2023;111(4):527-542.
doi: 10.1002/jbm.a.37473

149. Zhang JM, Hu QP, Wang S, Tao J, Gou ML. Digital light processing based three-dimensional printing for medical applications. *Int J Bioprinting*. 2020;6(1):12-27.
doi: 10.18063/ijb.v6i1.242

150. Wajdi F, Tontowi AE. 3D printed stent from graphene-polyethylene glycol diacrylate using digital light processing technique. *Manag Syst Prod Eng*. 2024;32(4):555-562.
doi: 10.2478/mspe-2024-0053.

151. Li H, Dai J, Wang Z, Zheng H, Li W, Wang M. Digital light processing (DLP)-based (bio)printing strategies for tissue modeling and regeneration. *Aggregate*. 2023;4(2):270.
doi: 10.1002/agt2.270

152. Lee SJ, Esworthy T, Stake S, et al. Advances in 3D bioprinting for neural tissue engineering. *Adv Biosyst*. 2018;2(4):1700213.
doi: 10.1002/adbi.201700213

153. Xu X, Tao J, Wang S, et al. 3D printing of nerve conduits with nanoparticle-encapsulated RGFP966. *Appl Mater Today*. 2019;16:247-256.
doi: 10.1016/j.apmt.2019.05.014

154. Tao J, Liu HF, Wu WB, et al. 3D-printed nerve conduits with live platelets for effective peripheral nerve repair. *Adv Funct Mater*. 2020;30(42):2004272.
doi: 10.1002/adfm.202004272

155. Ye WS, Li HB, Yu K, et al. 3D printing of gelatin methacrylate-based nerve guidance conduits with multiple channels. *Mater Des*. 2020;192:108757.
doi: 10.1016/j.matdes.2020.108757

156. Huang WJ, Wang JE. Development of 3D-printed, biodegradable, conductive PGSA composites for nerve tissue regeneration. *Macromol Biosci*. 2023;23(3):2200470.
doi: 10.1002/mabi.202200470

157. Wu WB, Dong YC, Liu HF, et al. 3D printed elastic hydrogel conduits with 7,8-dihydroxyflavone release for peripheral nerve repair. *Mater Today Bio*. 2023;20:100652.
doi: 10.1016/j.mtbio.2023.100652

158. Bedir T, Ulag S, Ustundag CB, Gunduz O. 3D bioprinting applications in neural tissue engineering for spinal cord injury repair. *Mater Sci Eng C-Mater Biol Appl*. 2020;110:110741.
doi: 10.1016/j.msec.2020.110741

159. Cadena M, Ning LQ, King A, et al. 3D bioprinting of neural tissues. *Adv Healthc Mater*. 2020;10(15):2001600.
doi: 10.1002/adhm.202001600

160. Zhuang P, Ng WL, An J, Chua CK, Tan LP. Layer-by-layer ultraviolet assisted extrusion-based (UAE) bioprinting of hydrogel constructs with high aspect ratio for soft tissue engineering applications. *PloS One*. 2019;14(6):0216776.
doi: 10.1371/journal.pone.0216776

161. Zhu W, Qu X, Zhu J, et al. Direct 3D bioprinting of prevascularized tissue constructs with complex microarchitecture. *Biomaterials*. 2017;124:106-115.
doi: 10.1016/j.biomaterials.2017.01.042

162. Vijayavenkataraman S, Vialli N, Fuh JYH, Lu WF. Conductive collagen/polypyrrole-b-polycaprolactone hydrogel for bioprinting of neural tissue constructs. *Int J Bioprinting*. 2020;6(4):309.
doi: 10.18063/ijb.v5i2.1.229

163. Kaplan B, Merdler U, Szklanny AA, et al. Rapid prototyping fabrication of soft and oriented polyester scaffolds for axonal guidance. *Biomaterials*. 2020;251:120062.
doi: 10.1016/j.biomaterials.2020.120062

164. Redolfi-Riva E, Pérez-Izquierdo M, Zinno C, et al. A novel 3D-printed/porous conduit with tunable properties to enhance nerve regeneration over the limiting gap length. *Adv Mater Technol*. 2023;8(17):2300136.
doi: 10.1002/admt.202300136

165. Englanda S, Rajaramb A, Schreyer DJ, Chen XB. Bioprinted fibrin-factor XIII-hyaluronate hydrogel scaffolds with encapsulated Schwann cells and their in vitro

characterization for use in nerve regeneration. *Bioprinting*. 2017;5:1-9.
doi: 10.1016/j.bprint.2016.12.001

166. Das S, Jegadeesan JT, Basu B. Advancing peripheral nerve regeneration: 3D bioprinting of gelma-based cell-laden electroactive bioinks for nerve conduits. *ACS Biomater Sci Eng*. 2024;10(3):1620-1645.
doi: 10.1021/acsbiomaterials.3c01226

167. Moldovan NI, Hibino N, Nakayama K. Principles of the Kenzan method for robotic cell spheroid-based three-dimensional bioprinting. *Tissue Eng Part B-Rev*. 2017;23(3):237-244.
doi: 10.1089/ten.teb.2016.0322

168. Yurie H, Ikeguchi R, Aoyama T, et al. The efficacy of a scaffold-free Bio 3D conduit developed from human fibroblasts on peripheral nerve regeneration in a rat sciatic nerve model. *PloS One*. 2017;12(2):e0171448.
doi: 10.1371/journal.pone.0171448

169. Takeuchi H, Ikeguchi R, Aoyama T, et al. A scaffold-free bio 3D nerve conduit for repair of a 10-mm peripheral nerve defect in the rats. *Microsurgery*. 2020;40(2):207-216.
doi: 10.1002/micr.30533

170. Yurie H, Ikeguchi R, Aoyama T, et al. Bio 3D conduits derived from bone marrow stromal cells promote peripheral nerve regeneration. *Cell Transplant*. 2020;29: 0963689720951551.
doi: 10.1177/0963689720951551

171. Mitsuzawa S, Ikeguchi R, Aoyama T, et al. The efficacy of a scaffold-free bio 3D conduit developed from autologous dermal fibroblasts on peripheral nerve regeneration in a canine ulnar nerve injury model: a preclinical proof-of concept study. *Cell Transplant*. 2019;28(9-10):1231-1241.
doi: 10.1177/0963689719855346

172. Fang YC, Wang CJ, Liu ZB, et al. 3D printed conductive multiscale nerve guidance conduit with hierarchical fibers for peripheral nerve regeneration. *Adv Sci*. 2023;10(12):202205744.
doi: 10.1002/advs.202205744

173. Wang J, Cheng Y, Wang HY, et al. Biomimetic and hierarchical nerve conduits from multifunctional nanofibers for guided peripheral nerve regeneration. *Acta Biomater*. 2020;117:180-191.
doi: 10.1016/j.actbio.2020.09.037

ACCSCIENCE PUBLISHING

International Journal of Bioprinting

REVIEW ARTICLE

Advances in biomanufacturing and medical applications of three-dimensional-printed organoids: A review

Lingzi Liao[1, 2, 3†], Qiushi Feng[1, 2, 3†], Xiaofeng Shan[1, 2, 3], Zhigang Cai[1, 2, 3*], and Shang Xie[1, 2, 3*]

[1]Department of Oral and Maxillofacial Surgery, Peking University School and Hospital of Stomatology, Beijing, China

[2]National Center for Stomatology, Beijing, China

[3]National Clinical Research Center for Oral Diseases, Beijing, China

Abstract

The emergence of organoid technology has bridged critical gaps between conventional two-dimensional cell cultures and *in vivo* systems by offering self-organized three-dimensional (3D) microtissues that recapitulate organ-specific architecture, cellular heterogeneity, and functional dynamics. However, traditional organoid models face inherent limitations in structural precision, scalability, and physiological relevance, particularly in replicating vascular networks, mechanical microenvironments, and multicellular interactions. Recent advancements in 3D bioprinting have enabled unprecedented spatial control over cellular and extracellular matrix organization, unlocking new frontiers in engineering organoids with enhanced biomimicry and functionality. This review systematically examines the integration of bioprinting technologies with organoid science, spanning biomaterial innovations, vascularization strategies, and dynamic microenvironmental cues that drive functional maturation. By synthesizing interdisciplinary advances in stem cell biology, materials science, and computational modeling, the work highlights applications across regenerative medicine, disease pathophysiology, and personalized drug screening. Key challenges, including immunogenicity, long-term stability, and clinical scalability, are critically evaluated alongside emerging solutions such as four-dimensional bioprinting, organ-on-chip integration, and artificial intelligence-driven bioink optimization. Through a comprehensive analysis of bioprinted organoids for physiology and 3D disease modeling, this review aims to establish a translational roadmap for leveraging spatially programmed organoids to address unmet clinical needs, revolutionize therapeutic development, and advance precision medicine.

Keywords: High-throughput screening; Patient-derived organoids; Regenerative medicine; Spatiotemporal control; Three-dimensional-bioprinting; Vascularization

†These authors contributed equally to this work.

***Corresponding authors:**
Zhigang Cai
(c2013xs@163.com)

Shang Xie
(xs2013@hsc.pku.edu.cn)

Citation: Liao L, Feng Q, Shan X, Cai Z, Xie S. Advances in biomanufacturing and medical applications of three-dimensional-printed organoids: A review. *Int J Bioprint*. 2025;11(4):66-98. doi: 10.36922/IJB025190184

Received: May 7, 2025
Revised: May 20, 2025
Accepted: May 28, 2025
Published Online: June 10, 2025

Copyright: © 2025 Author(s). This is an Open Access article distributed under the terms of the Creative Commons Attribution License, permitting distribution and reproduction in any medium, provided the original work is properly cited.

Publisher's Note: AccScience Publishing remains neutral with regard to jurisdictional claims in published maps and institutional affiliations.

1. Introduction

Organoid technology has emerged as a paradigm-shifting innovation in biomedical research, enabling the *in vitro* reconstruction of self-organized three-dimensional (3D) microtissues that recapitulate structural, functional, and developmental features of native organs.[1] Originating from breakthroughs in stem cell biology and developmental signaling pathways, organoids are typically derived from induced pluripotent stem cells (iPSCs) or various tissue-derived cells, including adult stem cells, differentiated cells, or cancer cells, through spatially controlled differentiation protocols. These models have transcended the limitations of conventional two-dimensional (2D) cultures by preserving cell polarity, cell–cell interactions, and tissue-specific functionality, which are critical for modeling organogenesis, disease progression, and therapeutic responses.[2,3] Additionally, they are particularly useful in cancer research due to their ability to preserve genetic and phenotypic stability, as well as their compatibility with cryopreservation techniques.[4,5] Despite being a relatively nascent field, organoid technology continues to face considerable challenges in both construction and cultivation. For instance, the processes of manual passaging and cultivation are both labor-intensive and financially burdensome.[6] Organoids exhibit a lower level of complexity compared to native tissues, primarily due to the absence of immune and vascular systems. Meanwhile, the integration of organoids with tissue engineering scaffolds and the mass production of organoids, along with their application in drug development, remains a complex endeavor. In response to these challenges, researchers have been actively exploring various biofabrication techniques, including 3D bioprinting, to enhance the development of organoids.

Concurrently, 3D bioprinting has evolved from prototyping tools into a sophisticated biofabrication platform, enabling precise deposition of cell-laden bioinks with microscale resolution. This technology leverages additive manufacturing principles to construct spatially organized tissues through layer-by-layer assembly of living cells, biomaterials, and bioactive cues.[7,8] Modern bioprinting modalities, including extrusion-based, laser-assisted bioprinting, and digital light processing systems, offer unparalleled control over tissue architecture, permitting the engineering of vascular channels, heterogeneous cellular zonation, and mechanically graded matrices (Figure 1).[6] Unlike traditional organoid culture, which relies on self-organization within undefined matrices like Matrigel, bioprinting imposes engineered self-organization, a hybrid approach combining bottom–up biological principles with top–down spatial guidance. This synergy addresses critical gaps in organoid technology. Bioprinting provides structural fidelity and reproducibility, while organoids contribute physiological relevance through inherent cellular differentiation programs.

The strategic combination of these modalities creates a transformative framework for precision tissue engineering. On that basis, bioprinting can spatially arrange organoid-forming progenitors within vascularized scaffolds, overcoming the diffusion-limited growth of conventional organoids.[9] Advanced bioinks functionalized with decellularized extracellular matrix (dECM) components or synthetic mimetic peptides further enhance organoid maturation by replicating tissue-specific biochemical niche. From a translational perspective, automated bioprinting platforms enable scalable production of standardized organoid arrays, facilitating their integration into high-throughput drug screening pipelines and personalized disease modeling. Recent demonstrations include bioprinted hepatorganoids with zonated metabolic activity for toxicity testing, and patient-derived tumor organoids incorporating immune cells for immunotherapy evaluation.

This review examines how the strategic integration of 3D bioprinting and organoid technologies is redefining the frontiers in regenerative medicine and pathophysiological modeling. It analyzes the technological synergies that resolve historical limitations of both fields: the capacity of bioprinting to impose architectural control on organoid self-organization and the ability of organoids to confer innate biological complexity to bioprinted constructs. Emerging applications in multiscale vascularization, neurovascular interface engineering, and immune-competent tumor modeling are critically evaluated. By delineating current achievements and persistent challenges, this work aims to chart a roadmap for next-generation biofabricated organoid systems that bridge the gap between *in vitro* models and clinical translation.

2. Functional bioprinted organoids for physiology and regenerative medicine

Bioprinted organoids hold transformative potential for regenerative medicine. However, clinical translation requires addressing vascularization deficits, functional maturation, and standardization of bioink formulations.

2.1. Engineered hard-tissue organoids

Bone defects are frequently observed in orthopedic clinical research. Traditional treatment strategies often fall short of expectations, due to the distinctive architecture of hard tissue. Bone organoids—3D tissue constructs cultivated *in vitro*—aim to mimic the structure and function of native bone tissue for research and regenerative purposes.[10] The integration of cutting-edge biomaterials and additive manufacturing techniques enables the creation of 3D

Bioprinting technology	Advantages	Disadvantages	Types of organoid
Extrusion bioprinting 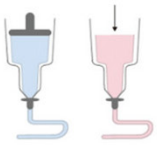	• Versatility • Large-scale printing • High cell survival rate • Lower cost	• Lower resolution • Slower printing speed • Material limitations • Post-processing requirements	• Bone • Liver • Cardiac • Kidney • Cancer
Droplet-based bioprinting 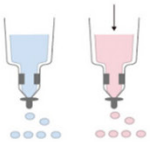	• High resolution • High controllability • Low cost • Rapid prototyping	• Material limitations • Low cell viability • Limited printing speed • Nozzle clogging	• Bone • Intestinal • Kidney • Assembloids
Stereolithography (SLA) 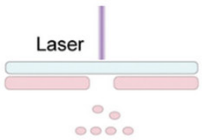	• High resolution • Materials options • Smooth surface • High precision	• Material limitations • Low cell survival rate • Printing speed • Complex post-processing	• Cancer
Digital light processing (DLP) 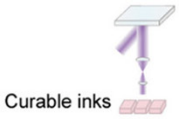	• High resolution • High speed • Good surface quality • High flexibility	• Material limitations • Cell viability • High equipment cost • Resin processing	• Bone • Intestinal
Volumetric bioprinting 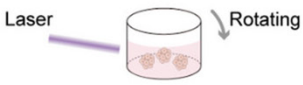	• Fast speed • High resolution • Cell-friendly • Uniformity	• Material complexity • Equipment complexity • Technology maturity • Light scattering issues	• Liver
Magnetic-assisted bioprinting 	• Contactless printing • High precision • Good compatibility • Strong repeatability	• Magnetic particle influence • Complicated equipment • Material limitations • Early stage of technology	• Assembloids • Cancer
Aspiration-assisted bioprinting (AAB) 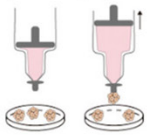	• High precision • Cell-friendly • Material diversity • High flexibility	• Slower speed • Technology maturity • Equipment complexity • High material consumption	• Assembloids

Figure 1. Organoid three-dimensional bioprinting technologies and their advantages, disadvantages, and applications. Adapted with permission from Hu et al.[6] Copyright© Wiley 2025.

tissues that can self-assemble into cell aggregates and organoids in response to physiological and induced signals.[11,12] They also help in evaluating the effectiveness of pharmacological treatments aimed at improving bone density and reducing fracture risk.

Bioprinting has been instrumental in engineering hard tissue, where the fabrication of a bone extracellular matrix (ECM) analog has been achieved to properly mimic the 3D-mineralized ECM components. This approach enables precise spatial control over osteogenic cell populations, thereby inducing specific cell fates and functions[13,14] and facilitating the maturation of bone organoids.[15] Bioprinting enables precise manipulation of biophysical properties, including organoid size, cell number, and conformation, with modifications in organoid conformation substantially increasing secreted yield per initial cell number.[16] Rooted in synthetic biology, recent advancements in light-based 3D printing of DNA hydrogels offer promising potential to revolutionize current ECM-assembling approaches. These hydrogels offer key advantages, including resistance to enzymatic degradation, programmability, precise structural control, and desirable mechanical properties.[17]

Recent advances in bioink design, including gelatin methacrylate/alginate methacrylate/hydroxyapatite (GelMA/AlgMA/HAP) composites, have facilitated the creation of self-mineralizing scaffolds that support long-term maturation of bone organoids.[18] Utilizing cutting-edge 3D bioprinting technology and bone matrix-inspired bioink formulations, researchers have developed a platform for generating bone organoids from bone marrow-derived mesenchymal stem cells.[19] This method involves combining bone marrow-derived mesenchymal stem cells with hydrogels to create bioinks, which are then employed in light-curing 3D bioprinting to produce bone organoids (Figure 2A). Upon implantation into an animal model, these organoids exhibited spontaneous mineralization and maturation processes, leading to the formation of fully developed and vascularized bone tissue (Figure 2B).[20,21] Li et al.[22] added hydroxyapatite nanowires to osteoblast precursor cell spheroids, providing numerous material exchange channels for internal cells by interpenetrating them into cell spheroids. The incorporation of nanowires enhanced the osteogenic phenotype and effectively improved the biological activity of core cells in spheroids, which can potentially be used as building blocks for the construction of large, high-density biomimetic tissues and organoids using 3D bioprinting technology (Figure 2C).[22] Fang et al.[23] successfully printed highly vascularized bone organoid tissues using a granular aggregate-pre-vascularized bioink and found that the pre-vascularized mesenchymal spheroids developed an interconnected vascular network through angiogenic sprouting.[23] These constructs promote osteogenic differentiation and support fracture repair mechanisms.

However, challenges persist in replicating the hierarchical mechanical properties of native hard tissues, particularly in achieving stiffness values that match those of human bones (10–30 GPa) while maintaining cell viability.[24] Innovations in nozzle-free bioprinting techniques, which eliminate shear stress on encapsulated cells, have improved organoid post-printing viability (>95%) and preserved multicellular polarization.[25,26] De Leeuw et al.[27] found that elevated cellular density increases the rates of mineralization and enhances the mechanical stiffness of 3D-bioprinted patient-derived bone organoids when exposed to dynamic loading conditions.[27] The present research on bone organoids is in its early developmental phase. These organoids currently emulate only limited aspects of bone tissue functionality. Beyond the standard functionalities and essential characteristics of organoids, bone organoids must replicate both the micro- and macro-architectures of bone tissue. They should also offer sufficient mechanical support and incorporate a bone marrow microenvironment capable of hematopoietic activity. Furthermore, bone organoids are expected to produce immune cells and establish functional interactions with the nervous, immune, lymphatic, and vascular systems. These attributes will facilitate the ability of bone organoids to more accurately replicate the physiological functions of native bone tissue.[28] Other directions include integrating patient-specific stem cells, osteogenesis under compressive stimulation, and computational modeling to optimize printed scaffold porosity and load-bearing capacity for clinical translation.[10,29–31]

2.2. 3D reconstruction of biomimetic cardiovascular organoids

A 3D culture system for cardiomyocytes can replicate physiological and dynamic conditions effectively for cardiovascular assessment.[32,33] The 3D system addresses limitations seen in 2D monolayer setups, such as inadequate spreading size, excitation-contraction coupling (T-tubules), mature calcium ion channels for active force stimuli, and efficient energy conversion through oxidative metabolism.[34] Cardiomyocytes and other cardiac cells are cultured within solid biomaterials (like scaffolds or hydrogels) in this microenvironment to enhance cardiac tissue formation and simulate the heart's physiological conditions.[35,36] The geometric morphology of cardiomyocytes, myofibril expression, and junction protein formation differ significantly between 3D and 2D cell cultures.[37] Furthermore, 3D culture offers cardiomyocytes protection against drug-induced mechanical stress and apoptosis.[38] Recently, organoids have been developed

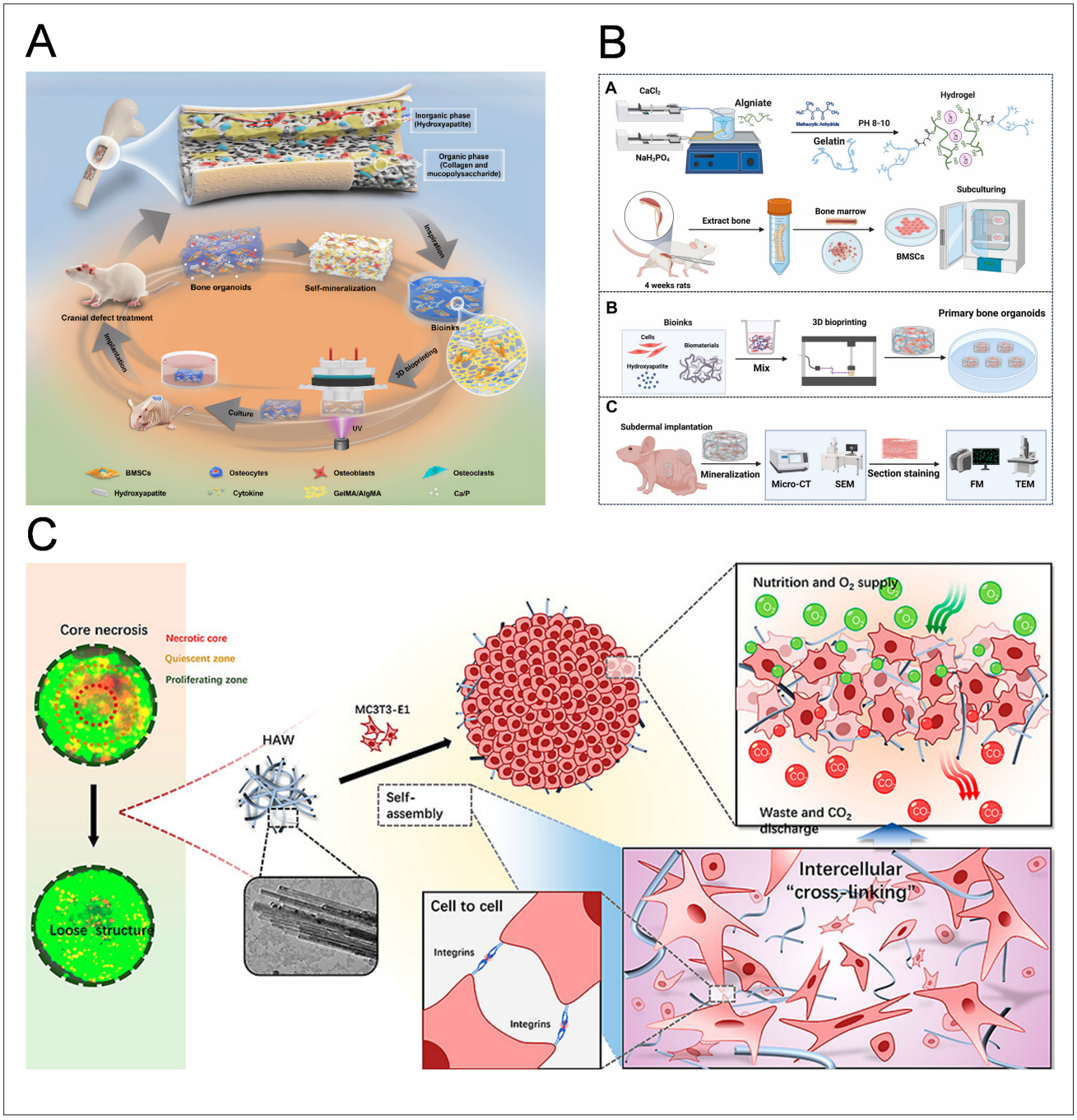

Figure 2. Representative advances in bioprinted bone organoids. (A) Large-scale bioengineered self-mineralizing bone organoid platform printed by bone matrix-inspired hydroxyapatite hybrid bioinks. Adapted with permission from Wang et al.[19] Copyright© Wiley 2024. (B) Bioprinted bone organoids exhibit great mineralization and vascularization properties *in vivo* without external stimuli. Adapted with permission from Wang et al.[21] Copyright© Elsevier 2025. (C) Bioprinted bone organoids exhibit great mineralization and vascularization properties *in vivo* without external stimuli. Adapted with permission from Li et al.[22] Copyright© American Chemical Society 2024.

as artificial cardiac tissues to mimic cardiac structures and functions by adjusting their size, shape, and configuration. The reconstruction of functional cardiac organoids requires biomimetic architectures that emulate the electromechanical coupling and vascularization of native heart tissue.[39] Human cardiac organoids are created through the self-assembly of differentiating cardiomyocytes from human pluripotent stem cells.[40] Consequently, cardiac organoids serve as promising models for replicating native cardiac elements, including inflow-outflow territories, cardiac chamber architecture, and heart-related regulation.[41]

Recent breakthroughs in multi-material bioprinting have allowed for the recreation of complex cardiac structures, enabling the fabrication of ventricle models with perfusable vascular networks, a feat unattainable with traditional 3D printing methods.[42] Fang et al.[42] have successfully developed Sequential Printing in a Reversible Ink Template technology, enabling the fabrication of ventricle models with hierarchical vascular networks by combining sacrificial ink printing with microgel-enhanced bioinks.[42] This approach allows sequential deposition of structural bioinks to form cardiac chambers, followed by sacrificial ink removal to create perfusable channels. The resulting constructs exhibit synchronized contractions and action potential propagation, mimicking the helical fiber orientation critical for ventricular ejection dynamics (Figure 3A). Despite structural progress, achieving electrophysiological maturity comparable to adult myocardium remains challenging. Current cardiac organoids often lack the ion channel density and calcium handling capacity required for sustained rhythmic activity. To overcome this obstacle, 4D bioprinting with shape-memory hydrogels has been employed to spatiotemporally align cardiomyocytes into anisotropic architectures in response to physiological stimuli, enhancing action potential propagation velocity by 2.3-fold compared to static cultures.[43] Additionally, the incorporation of organoid-derived pacemaker cells into bioprinted patches has enabled arrhythmia modeling, demonstrating abnormal conduction patterns under β-adrenergic stimulation.

Intriguingly, Zhang et al.[44] have further advanced vascular integration using six-axis robotic bioprinters, which enable omnidirectional cell deposition on complex arterial scaffolds. By employing a mineral oil-based suspension system, endothelial cells adhere to vascular scaffolds without shear stress, forming confluent monolayers that subsequently sprout capillaries under angiogenic factors. This "print-culture" iterative strategy, where alternating layers of cardiomyocytes and endothelial cells are cultured to promote vascular network maturation, has yielded myocardial tissues that maintain rhythmic contractions for over 6 months *in vitro* (Figure 3B). By combining cardiomyocytes, endothelial cells, and conductive bioinks, researchers have achieved synchronized contractions and action potential propagation in bioprinted cardiac patches. These models replicate the helical myocardial fiber orientation critical for ventricular ejection dynamics.[45]

Nevertheless, limitations in scalability and electrophysiological maturity remain, as current cardiac organoids lack the structural complexity of adult myocardium. Emerging strategies, such as 4D bioprinting with shape-memory hydrogels, aim to dynamically align cells into anisotropic tissue geometries under physiological stimuli.[46,47] Additionally, the integration of organoid-derived pacemaker cells could advance arrhythmia modeling and personalized drug testing.[48] This synthesis of bioprinting and organoid technologies represents a paradigm shift in cardiovascular research, offering unprecedented opportunities to model congenital heart defects, ischemic injury, and pharmacogenomic responses with physiological fidelity.

2.3. Brain organoids

Conventional self-assembly methods often yield structurally inconsistent neural spheroids with limited vascularization and incomplete regional specification.[49,50] Pioneered in 2009, early cerebral organoids derived from embryonic stem cells and iPSCs demonstrated self-organized cortical regions, neural progenitor zones, and rudimentary laminar organization.[51] These primitive models laid the groundwork for investigating neurodevelopmental trajectories, interspecies divergence, and pathological mechanisms.[52] The convergence of 3D bioprinting with cerebral organoid technology has revolutionized our capacity to replicate human neurodevelopment *in vitro*. Cadena et al.[53] printed a high-throughput, adjustable, and repeatable scaffold for precisely controlling the development and patterns of brain organoids, achieving real-time monitoring of calcium signaling and synaptic plasticity.[53] It was confirmed that the fabricated scaffold exhibited stiffness values comparable to the developing human brain. The organoids cultured long-term within the bioprinted scaffold remain healthy and exhibit expected neuroectodermal differentiation. In addition, the endothelial cells within the printed channel structures demonstrated the ability to migrate and infiltrate the embedded brain organoids. Advanced bioprinting strategies enable the spatial orchestration of neural progenitor cells within tunable ECMs, achieving unprecedented control over cortical layering and synaptic connectivity patterns.[54,55] Innovative bioink formulations combining decellularized brain ECM with thermo-responsive hydrogels have demonstrated enhanced neurite outgrowth (2.3-fold increase versus Matrigel

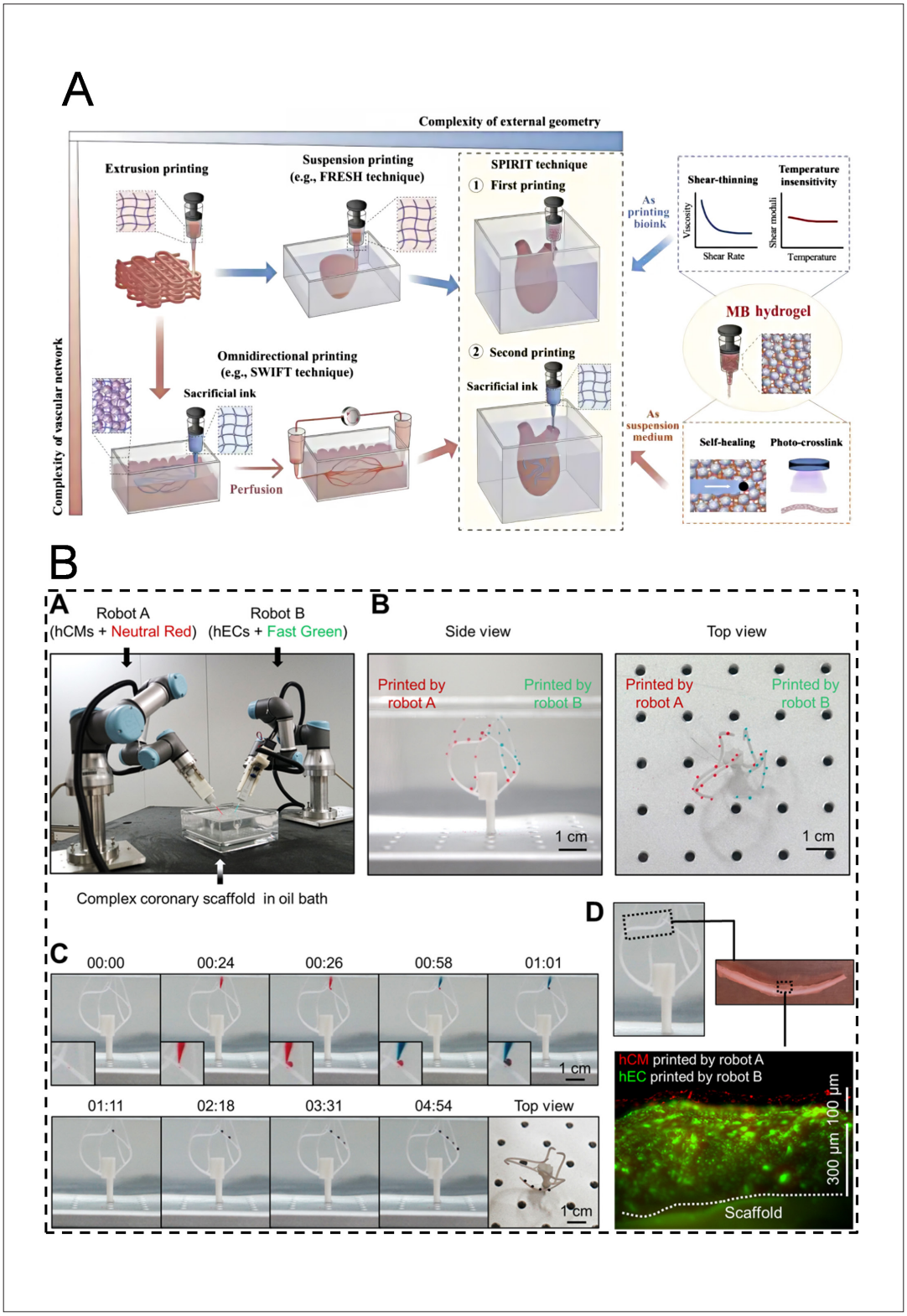

Figure 3. Recent advancements in bioprinting technologies for vascularized organ construction. (A) Expanding embedded three-dimensional bioprinting capability for engineering complex organs with freeform vascular networks. Adapted with permission from Fang et al.[42] Copyright© Wiley 2023. (B) Two-robot platforms, enabling cooperative bioprinting of different bioinks onto complex-shaped scaffolds, are jointly bioprinting on a vascular scaffold resembling major coronary vessels using two bioinks. Scale bar: 1 cm. Adapted with permission from Zhang et al.[44] Copyright© Elsevier 2022.

controls) while maintaining stem cell pluripotency during the printing process.[56] Such matrices permit dynamic stiffness modulation from 0.5 kPa (emulating embryonic neuroepithelium) to 8 kPa (mimicking adult parenchyma), guiding targeted differentiation into specialized subtypes, including dopaminergic neurons and Bergmann glia.[50,57] Yan et al.[58] engineered functional neural tissues using iPSC-laden viscoelastic bioinks, demonstrating synaptically active neuronal networks with electrophysiological signal propagation.[58] Furthermore, hierarchical cell assembly strategies permit the integration of differentially matured neural populations, thereby enhancing functional maturation beyond conventional culture constraints.[59]

Cutting-edge protocols now incorporate vasculature-mimicking channels within organoids, addressing limitations in nutrient diffusion and long-term viability.[60] Recent breakthroughs employ multi-material extrusion systems to co-print endothelial cells alongside iPSC-derived neuroectodermal populations, generating perfusable vascular networks that sustain organoids beyond 150 days *in vitro*.[59] This vascularization breakthrough addresses the critical limitation of necrosis in traditional models, allowing the maturation of functional gamma-aminobutyric acidergic and glutamatergic circuits detectable through calcium imaging and patch-clamp electrophysiology.[54,61]

While bioprinted organoids exhibit basic electrophysiological activity, they lack the cytoarchitectural sophistication (e.g., six-layered neocortex, glial diversity) of native cerebral tissue. Additionally, challenges center on achieving single-cell resolution printing for accurate synaptic connectivity and integrating optogenetic components for real-time circuit modulation.[55] Generative artificial intelligence-assisted optimization of bioink rheology and machine learning-driven printing parameterization could enhance structural fidelity. Microfluidic organ-on-chip systems may further simulate interregional brain connectivity. The emergence of clustered regularly interspaced short palindromic repeats (CRISPR)-edited reporter cell lines promises to overcome these limitations, paving the way for clinically transplantable neural constructs.[62] The development of immunoevasive bioinks with tunable mechanical properties and neuroimmunomodulatory functions will be pivotal for transitioning from investigational models to implantable therapeutics.

2.4. Bioprinting for hepatorganoids

Liver diseases represent a leading cause of global morbidity and mortality. Due to the scarcity of donor organs and complications like immune rejection, liver failure remains a critical challenge. 3D bioprinting offers a transformative approach, surpassing traditional 2D cell cultures, animal models, and organoids by enabling the fabrication of vascularized tissues and organs in terms of hepato–pancreato–biliary models.[63,64] Vascularized hepatorganoids generated via high-throughput bioprinting systems exhibit improved metabolic activity and drug response compared to static cultures.[65–67] Shrestha et al.[68] separately differentiated epithelial cell adhesion molecule^{+} endodermal progenitor cells and mesoderm-derived vascular progenitor cells from the same human iPSC line, which were then mixed in a 2-mercaptoethanol matrix on a pillar plate platform and concurrently differentiated into vascular human hepatorganoids.[68] Remarkably, this 3D-bioprinted expandable model exhibited significantly superior maturity than vasculature-free hepatorganoids, as demonstrated by increased coagulation factor secretion, albumin secretion, drug-metabolizing enzyme expression, and bile acid transportation, likely due to enhanced nutrient and signaling molecule diffusion. Scientists developed a 3D bioprinting technique using GelMA hydrogel to create hepatorganoids resembling hepatic lobules, exhibiting reduced hypoxia, increased albumin and urea secretion *in vitro*, and supporting angiogenesis post-implantation. By incorporating vascular endothelial growth factor and human umbilical vein endothelial cells, vascularized hepatorganoids with enhanced vascularization were produced.[69,70] Upregulation of growth arrest-specific protein 6/AXL and laminin beta 3/integrin subunit alpha 3 pathways in vascularized hepatorganoids promoted vascularization and proliferation. Orthotopic implantation of vascularized hepatorganoids showed prolonged survival, elevated biomarkers, and increased vascularization in grafts. These studies highlight the efficacy of orthotopic implantation of hepatorganoids for enhanced vascularization, benefiting transplantation, drug screening, and therapy.[70]

Bioinks, typically hydrogel-cell composites, serve as a foundational material.[71,72] A key innovation is the use of spheroid-based bioinks, which preserve hepatic polarity and zonation patterns during printing.[25,73] This technology encompasses four principal methods: inkjet-based, extrusion-based, laser-assisted, and vat photopolymerization bioprinting. In hepatorganoids, hepatocytes are often combined with non-parenchymal cells such as hepatic stellate cells, sinusoidal endothelial cells, and Kupffer cells.[74] Hydrogels derived from dECM are commonly utilized in bioprinted hepatorganoids due to their ability to mimic the native tissue microenvironment and retain essential growth factors and cytokines.[71,75] This characteristic renders them highly biocompatible for 3D bioprinting applications. In the field of hepatorganoids bioprinting, these hydrogels, in combination with liver-

derived cell types, can serve as suitable *in vitro* hepatic models for drug efficacy testing and studies on liver metabolism.[76] Moreover, these hydrogels can be viewed as compliant with good manufacturing practices for expanding liver cells and organoids, offering a safer alternative to basement membrane extracts derived from tumorigenic cell lines commonly used in research. Despite challenges such as weak mechanical properties and limited printability that impede the direct use of dECM hydrogels as bioinks, various modifications to both the dECM and the bioprinting process have been implemented to address these issues. Challenges in scaling up and manufacturing dECM hydrogels include undefined manufacturing standards, variable production methods affecting reproducibility, and considerations for animal-derived sources, such as variability, harvesting conditions, and bioburden reduction.

Bioprinted hepatorganoids have demonstrated remarkable progress in recapitulating hepatocytic functions, including albumin secretion, cytochrome P450 activity, and bile canaliculi formation.[77,78] These advancements hold significant potential for disease modeling, pharmaceutical development, and regenerative therapies.[79,80] Nevertheless, challenges persist, including the need for diverse fabrication techniques, real-time monitoring of drug responses in perfusion cultures, the ability to replicate intricate microenvironments of live sinusoids, and the achievement of long-term functional stability (>30 days) *in vitro*. Despite these hurdles, 3D bioprinting remains a groundbreaking strategy for hepatorganoid engineering. Advances in machine learning-guided parameter optimization and perfusion bioreactors are addressing these limitations, enhancing the scalability of hepatorganoids for transplantation.[78,81,82]

2.5. Recapitulation of glandular properties via bioprinting

Glandular organoids, such as pancreatic islets and salivary glands, demand precise biomaterial cues to maintain secretory functions and ductal morphogenesis. The ability of 3D bioprinting to spatially define cellular architectures and ECM microenvironments has revolutionized the engineering of glandular tissues, enabling precise replication of secretory epithelia, ductal networks, and functional polarization.[83] In parallel, bioprinting technology has successfully recreated branching ductal networks in mammary and prostate organoids using hyaluronic acid-based bioinks functionalized with growth factor gradients.[6,84] Recent advances highlight its potential in reconstructing salivary, pancreatic, and mammary gland models with native-like secretory functions and structural hierarchies.

2.5.1. Structural recapitulation of glandular units

Glandular tissues, characterized by intricate acinar-ductal networks, demand bioprinting strategies that mimic their branched morphology. For salivary glands, magnetically guided 3D bioprinting enables precise assembly of epithelial spheroids using iron oxide nanoparticles, replicating acinar-ductal polarity and neural responsiveness.[85,86] Similarly, coaxial microfluidic bioprinting generates cell-laden microfibers and tubules, bypassing xenogeneic matrices like Matrigel to create hierarchical ductal systems.[85] In sweat gland regeneration, GelMA-printed pore-structured matrices (300 μm diameter) guide epidermal progenitors to self-organize into lumenized glands, a process absent in non-printed controls.[87] These findings underscore the critical role of bioprinted scaffolds in dictating morphogenesis through topographical and mechanical cues.

2.5.2. Functional maturation and secretory capacity

Functional maturation of bioprinted glands relies on dynamic biochemical signaling and perfusion. For endocrine glands, the encapsulation of stem cell-derived β-cells within alginate/gelatin scaffolds has been shown to restore glucose-responsive insulin secretion in diabetic models.[88] Another pancreatic organoid demonstrated that mouse insulinoma 6 β-cell constructs, printed using the freeform reversible embedding of suspended hydrogels technique and embedded in vascularized hydrogels, exhibited glucose-stimulated insulin secretion under perfusion, achieving a 4.6-fold increase in insulin output compared to static cultures.[89] In salivary glands, magnetically assembled organoids demonstrate acetylcholine-responsive fluid secretion, mirroring native neuroepithelial interactions.[85]

Bioink design is pivotal for maintaining cell viability and glandular functionality. Chitosan-based bioinks blended with polycaprolactone or glycine methacrylate enhance printability and mechanical strength while supporting acinar cell proliferation.[90] Shear-thinning nanocellulose-alginate composites enable high-resolution printing of cartilage-like structures, with chondrocyte viability exceeding 86% after 7 days, a principle adaptable to glandular applications.[91] These advancements highlight the interplay between bioink rheology, crosslinking kinetics, and glandular morphogenesis.

A critical challenge lies in mimicking the dynamic ECM remodeling of native glands, which regulate cell differentiation through stiffness gradients and protease-sensitive linkages.[92] Recent work leveraging 4D bioprinting with enzyme-responsive polymers has enabled time-dependent ECM degradation, guiding self-organization of acinar and ductal structures.[46,93] Notably, 4D bioprinting

with light-responsive bioinks (e.g., GelMA/poly[ethylene glycol] dimethacrylate) introduces temporal control over scaffold remodeling, enabling post-printing structural anisotropy to support secretory epithelial polarization.[12] Such innovations bridge the gap between structural fidelity and functional integration.

2.5.3. Vascularization and nutrient transport

Vascularization poses a key hurdle for glandular bioprinting, with strategies such as multi-material bioprinting integrating endothelial cells with glandular parenchyma to establish perfusable networks. Evidence shows that pancreatic constructs combining mouse insulinoma 6 cells and vascular bioinks develop anastomosed capillaries under bioreactor perfusion, enhancing nutrient delivery and insulin secretion.[89] A novel tissue-specific bioink was formulated by blending pancreatic ECM with hyaluronic acid methacrylate.[94] The 3D-printed islet organoids created using this bioink can replicate the pancreatic microenvironment, preserving islet cell adhesion and morphology via the Ras-related C3 botulinum toxin substrate 1/rho-associated protein kinase/myosin light chain kinase signaling pathway (Figure 4A). This approach enhances islet function and activity. Moreover, the 3D-printed structures enhance the formation of vascular networks, while the hyaluronic acid methacrylate/pancreatic ECM hydrogel supports the adhesion and proliferation of new blood vessels, thereby augmenting the density of vascular structures. Nanocellulose-alginate bioinks further improve mechanical stability and osteogenic differentiation, suggesting adaptability for vascularized glandular models.[91] Emerging platforms like the Human Islet-like Cellular Aggregates and Vasculature platform simulate native pancreatic vascular niches, promoting β-cell survival and functional maturation.[95]

Traditional organoids lack precise structure and scalability, whereas bioprinting overcomes these limitations by facilitating the efficient production of millimeter-scale constructs with specific geometries. Bioprinted mammary tumor models incorporate cancer-associated fibroblasts (CAFs) and endothelial cells, recapitulating chemoresistance mechanisms absent in 2D cultures (Figure 4B & C).[96,97] Despite advancements, several challenges remain. Functional longevity is a concern as printed glands often display temporary secretory activity due to inadequate innervation or vascular integration. Co-printing with neuronal progenitors or utilizing optogenetic stimulation could potentially improve sustained functionality. Immunogenicity is another obstacle, which can be addressed by employing patient-specific iPSC-derived cells and dECM bioinks to reduce the risk of immune rejection. Achieving multi-scale resolution is crucial, and this can be accomplished by integrating microfluidic bioprinting with two-photon polymerization to replicate sub-10 μm ductal features.

Future applications should include patient-specific glandular models for autoimmune disease studies and hormone replacement therapies.[98,99] As bioink formulations and multi-omics validation evolve, bioprinted glands will likely transition from disease modeling to clinical transplantation, addressing critical shortages in organ replacement therapies.

3. Disease modeling based on three-dimensional bioprinted organoids

3D bioprinted organoids offer a unique advantage in disease modeling due to their ability to replicate the heterotypic organization of multicellular solid organs and the nanoscale precision of pathological processes. It provides a platform for studying the complex microenvironments that regulate cell behavior in various diseases, offering insights into fundamental biological processes and potential therapeutic strategies. A significant advantage of organoids in disease modeling and drug development is the ability to create personalized models using patient-derived cells, which has been studied extensively. Early in 2015, Freedman et al.[100] developed kidney tubular organoids from human pluripotent stem cells with drug responses similar to those found in clinical settings.[100] The model was also amenable to CRISPR/Cas9-based genome editing, which was used to induce polycystic kidney disease characteristics in the organoid. Votanopoulos et al.[101] conducted a study using patient-specific immune-enhanced tumor/node organoids for immunotherapy screening. The responses of the organoids to various immunotherapy drugs were very similar to the clinical response, showing the feasibility of these organoids for patient-specific drug testing.[101] However, further studies are needed to fully understand and widen the applications of organoids. This section discusses advancements in modeling inflammatory, genetic, metabolic, immune, and neurodegenerative disorders using bioprinted organoids.[4]

3.1. Inflammatory-related disorders

Chronic inflammatory conditions like rheumatoid arthritis, inflammatory bowel disease, neuroinflammation, liver inflammation, and osteoarthritis (OA) are intricate disorders characterized by persistent inflammation and tissue damage.[14,102,103] The pathophysiology of these ailments involves a blend of genetic, environmental, and immunological factors, leading to diverse patient responses to conventional therapies, necessitating a more personalized treatment approach.[104,105] Recently, the fusion of 3D bioprinting technologies with patient-

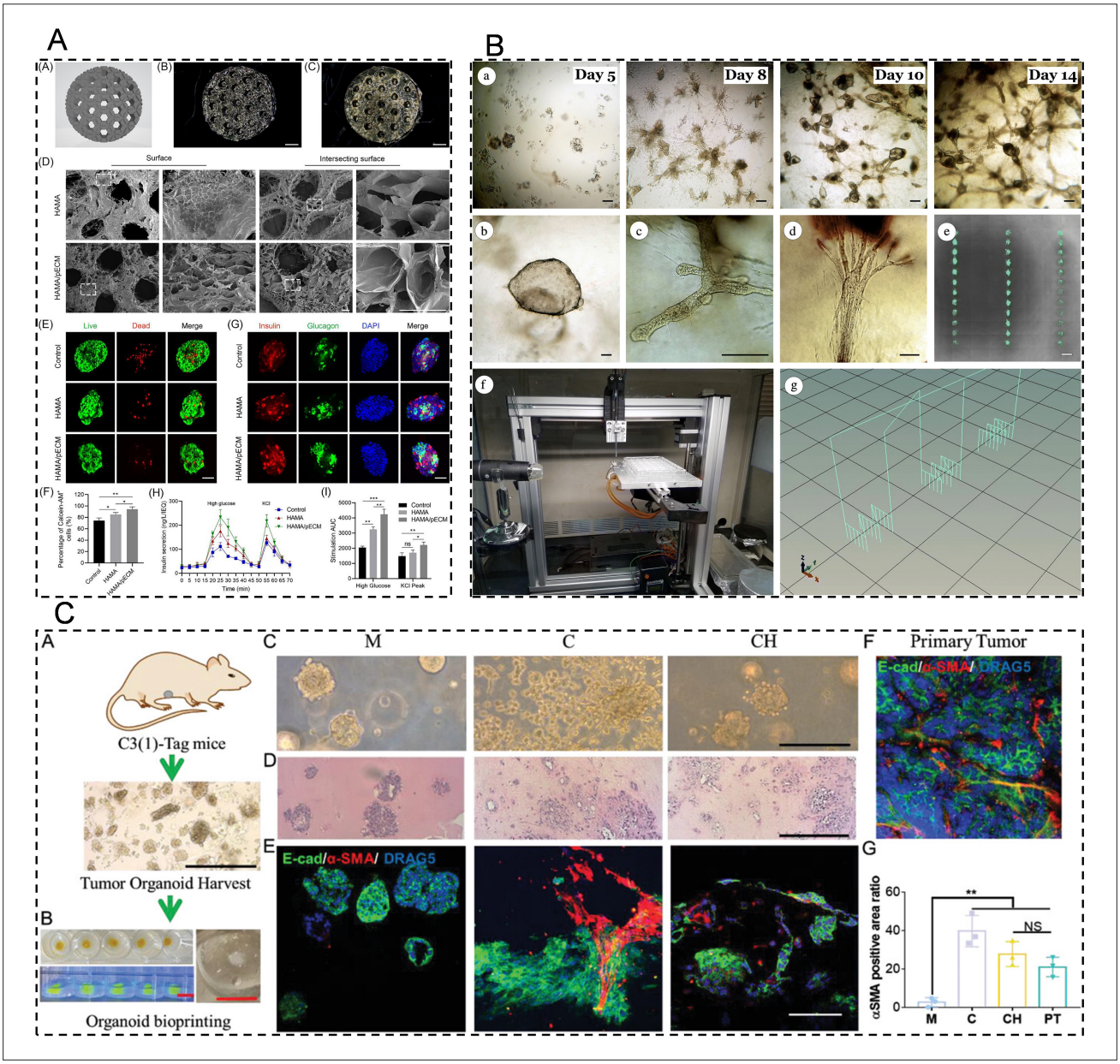

Figure 4. Bioprinting strategies for engineering functional and disease-specific organoids. (A) Design and construction of three-dimensional (3D)-printed hyaluronic acid methacrylate/pancreatic extracellular matrix islet organoids. (B) Scale bar = 2 mm, (C) Scale bar = 2 mm, (D) Scale bar = 300 μm, (E) Scale bar = 50 μm, (G) Scale bar = 50 μm. 4A: (B) Scale bar = 2 mm, (C) Scale bar = 2 mm, (D) Scale bar = 300 μm, (E) Scale bar = 50 μm, (G) Scale bar = 50 μm. Adapted with permission from Wang et al.[94] Copyright© Elsevier 2023. (B) Low-cost and computer numerical control-driven 3D bioprinting for mammary epithelial organoid, including "sphere-like," "duct-like," and "star-like" cells. Scale bar = 200 μm. Adapted with permission from Reid et al.[96] Copyright© BMC 2018. (C) The embedded bioprinted breast tumor organoids in low-concentration collagen-based bioink recapitulated *in vivo* tumor morphology. Scale bar = 200 μm. Adapted with permission from Shi et al.[97] Copyright© Wiley 2022.

derived organoids has revolutionized precision medicine by facilitating the creation of personalized disease models and advancing therapeutic research.[98,103] By incorporating immune cells, stromal cells, and other pertinent cell types as well as vascular networks into organoid models, the ability to embed organoids within customizable bioprinted geometries allows researchers to simulate the spatial heterogeneity of inflammatory microenvironments, including immune cell infiltration and cytokine gradients, and delve into the exploration of disease mechanisms, such as the impact of specific genes and signaling pathways in inflammation, and facilitate the screening of potential therapeutic interventions.[106,107] Bioprinted organoids offer valuable insights into the pathogenesis of rheumatoid arthritis, characterized by persistent joint inflammation and cartilage degradation. By mimicking interactions between synovial tissue and immune cells, these models facilitate the investigation of inflammatory mediators and genetic determinants. Furthermore, they enhance the optimization of pharmacological interventions that target inflammatory pathways, holding promise for personalized medicine.[108]

Intestinal organoids incorporating patient-derived cells have been leveraged to study gut inflammation and epithelial barrier dysfunction, providing insights into inflammatory bowel disease pathogenesis.[109,110] 3D bioprinting is notably applied in generating gastrointestinal organoids, which demonstrate distinctive transcriptomic and secretomic signatures in patients with Crohn's disease, elucidating disease-specific mechanisms and responses.[111] The quest to replicate the small intestine's intricate architecture and physiology *in vitro* has driven innovations in 3D bioprinting. Conventional planar epithelial monolayers lack the 3D villi topography essential for mimicking native absorption and barrier dynamics. Stereolithographic 3D printing now addresses this gap through THE precision fabrication of villus-like micropillar arrays using tunable poly(ethylene glycol) diacrylate hydrogels.[112] These scaffolds sustain month-long Caco-2 cultures, inducing apicobasal polarization akin to *in vivo* epithelial organization, which serves as a critical advance for physiologically relevant transport and metabolic studies (Figure 5A). A key innovation lies in dual-material printing strategies that integrate diffusion-open villus microstructures with diffusion-closed hydrogel walls. This compartmentalization isolates epithelial transport processes, emulating the luminal-interstitial interface while enabling high-throughput analysis. Functionally, Caco-2 cells on these platforms form confluent barriers with tight junctions, validated by transepithelial electrical resistance and fluorescent tracer assays (Figure 5B). The compatibility with compound screening allows real-time evaluation of barrier integrity under pharmacological challenges, offering a scalable tool for drug permeability and toxicity studies. Similarly, Jonathan et al.[113] have developed the BATE technique to create centimeter-sized gastrointestinal tissues with self-organizing features, enhancing the scalability and applicability of bioprinted organoids in various research areas.[113] By merging microstructural fidelity with functional compartmentalization, these approaches transcend the limitations of traditional models.[114] Their scalability and adaptability pave the way for advanced intestinal niches incorporating dynamic cues or microbial interactions, promising transformative applications in drug discovery and gut pathophysiology research.

3.2. Genetic diseases

Genetic disorders such as cystic fibrosis and hereditary metabolic defects have been modeled using bioprinted organoids derived from iPSCs. Bioprinting enables the precise arrangement of wild-type and mutant cells within organoids, facilitating the analysis of cell-autonomous versus non-cell-autonomous disease mechanisms. Human iPSC-derived neural organoids with patterned differentiation have been used to study neurodevelopmental disorders caused by genetic mutations.[84] Organoids offer valuable insights into the cellular mechanisms involved in such disorders and the effectiveness of gene editing tools such as CRISPR/Cas9 for potential therapeutic applications.[115] The integration of CRISPR genome editing techniques (including knockout, base editing, and prime editing) with 3D organoid cultures has enabled the modeling of disease progression and the investigation of genetic disorders. This approach effectively bridges the gap between patient-derived cells and our understanding of diseases.[116] Schene et al.[117] demonstrated the utility of prime editing in repairing genetic defects within patient-derived organoids, showcasing the precision and therapeutic potential of this gene editing strategy.[117] Leigh syndrome, an untreatable mitochondrial disorder associated with a *SURF1* mutation, has been addressed using Cas9 genome editing to rectify the mutated *SURF1* gene in patient-derived organoids.[118] This approach has provided insights into the physiological correlation between *SURF1* and Leigh syndrome. Additionally, patient-specific iPSCs have been utilized to replicate macrocephaly/autism phenotypes, demonstrating the adaptability of patient-derived organoids in investigating intricate genetic conditions. Furthermore, the CRISPR-Cas9 system has been employed in brain organoid models to induce models of congenital nervous system malformation diseases, facilitating the exploration of these intricate disorders.[119,120] Additionally, bone organoids bioprinted with GelMA bioinks have replicated genetic bone disorders, like osteogenesis

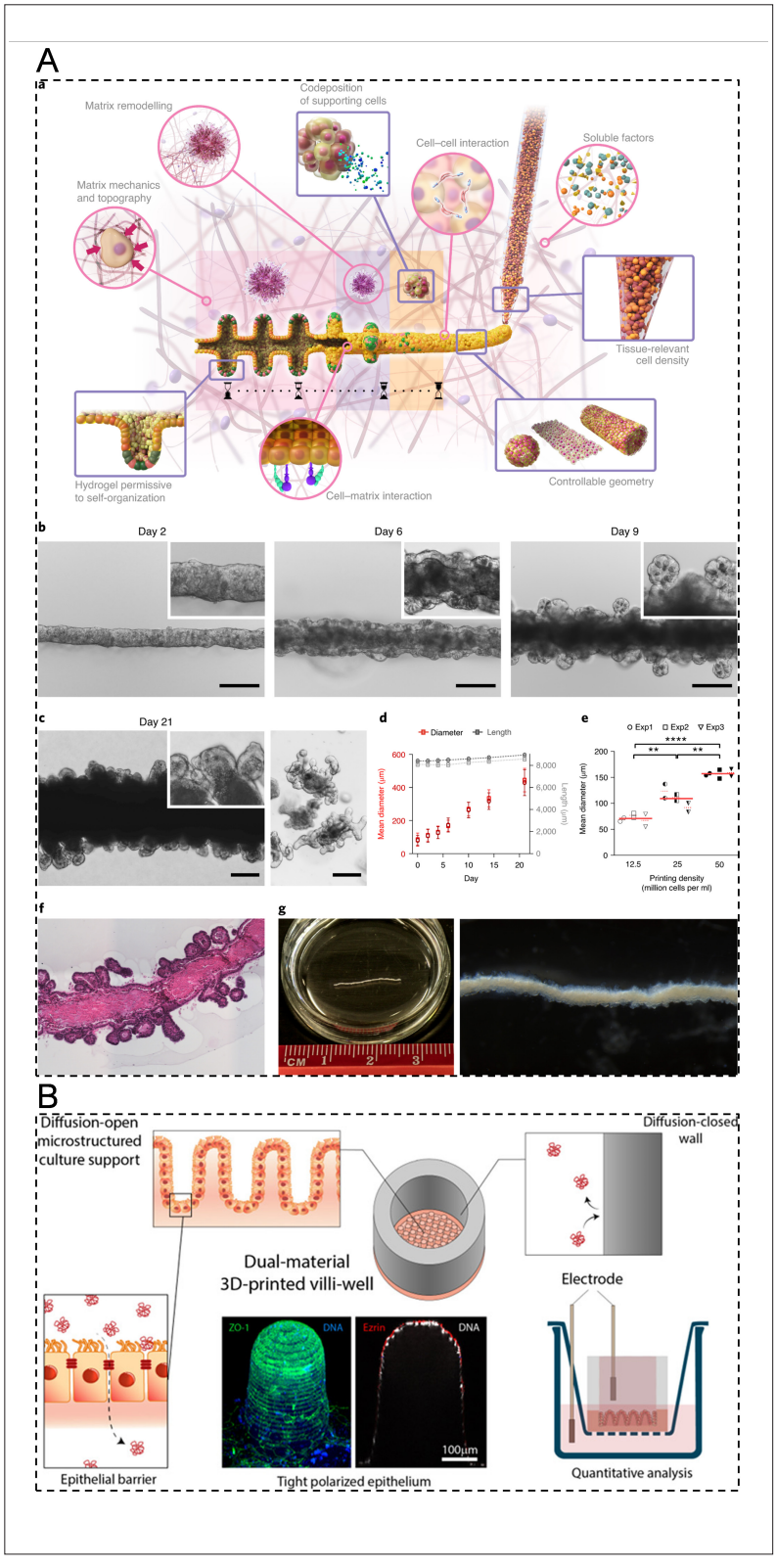

Figure 5. Bioprinted models for engineering functional intestinal structures and analysis platforms. (A) Macroscopic intestinal tube printing. Scale bar: 200 μm. Adapted with permission from Brassard et al.[113] Copyright© Nature 2021. (B) Engineering monolithic transport analysis devices with villi-like surface microstructures. Adapted with permission from Taebnia et al.[112] Copyright© American Chemical Society 2021.

imperfecta, characterized by brittle bones, enabling the study of mutations in collagen-producing genes and their impact on bone structure and strength.[121]

3.3. Metabolic diseases

Metabolic diseases, including diabetes and non-alcoholic fatty liver disease, have been modeled using bioprinted hepatic and pancreatic organoids. Bioprinted liver organoids with perfusable vascular networks mimic the zonated metabolism of hepatocytes, enabling the study of lipid accumulation and insulin resistance.[78] Recent advances in nozzle-free bioprinting have preserved organoid polarization and liver-specific enzyme activity, which are critical for replicating metabolic dysfunction.[25] Breakthroughs in bioprinted pancreatic organoids have demonstrated transformative potential for diabetes research and β-cell regeneration. A seminal study by Ahn et al.[122] has achieved functional restoration in diabetic murine models through extrusion-based bioprinting of human iPSC-derived β-cells co-encapsulated with endothelial progenitors in a tunable alginate matrix. These constructs exhibited glucose-responsive insulin secretion and sustained normoglycemia post-implantation, attributed to the integration of pre-vascular networks via co-printed endothelial cells. This enabled perfusable microvasculature formation within 7 days and an immunoprotective hydrogel design balancing crosslinking density to permit metabolic exchange while evading immune detection.[122] Furthermore, vascularized pancreatic organoids have been employed to investigate β-cell dysfunction and insulin secretion dynamics under hyperglycemic conditions.[123] Bone/cartilage organoids enable the study of metabolic pathways in cartilage development and pathologies. Analyzing the metabolomic profiles of these organoids reveals insights into metabolic changes linked to conditions such as OA. Understanding these alterations is vital for designing therapies targeting specific metabolic pathways to manage cartilage degradation. Integrating metabolomics with organoid technology offers new research opportunities in bone and cartilage biology, disease mechanisms, biomaterials, and pharmacology. This approach lays the groundwork for future research utilizing metabolomics for enhanced diagnostics, treatments, and regenerative approaches.[124]

3.4. Immune diseases

Bioprinted organoids are increasingly used to model autoimmune and immune-mediated disorders. The incorporation of endothelial and immune cells into bioprinted constructs allows the recapitulation of immune cell trafficking and vascular inflammation.[123,125] For example, vascularized skin organoids with hierarchical structures have been developed to study dermatological and lupus-related vasculopathy.[39,125] Parallel advancements in psoriatic modeling have been achieved through laser-assisted bioprinting of stratified skin organoids by Michael et al.[126] Their multilayered architecture, incorporating patient-derived keratinocytes, fibroblasts, and immune cells, recapitulated hallmarks of disease pathogenesis, including hyperproliferative epidermis, interleukin-23/interleukin-17 axis dysregulation, and T-cell infiltration dynamics visualized via integrated microfluidics.[127,128] The platform's dual utility in mechanistic interrogation and therapeutic screening was evidenced by the successful suppression of inflammatory markers using anti-tumor necrosis factor alpha biologics.[129] Nevertheless, the absence of neural components limits its capacity to model neuroimmune crosstalk, which is particularly relevant to pruritus mechanisms.[130] Future iterations incorporating sensory neurons and Schwann cells could bridge this gap, enabling a comprehensive study of itch pathways while preserving the strength in real-time immune monitoring and high-content drug evaluation.[131]

Additionally, lymph node organoids with spatially organized stromal and immune cell populations provide platforms to investigate antigen presentation and T-cell activation in autoimmune contexts.[132] The translational challenge for immune organoid research lies in modeling sensitivity and resistance to immunotherapies, encompassing checkpoint inhibition, novel pathways, and adoptive cell transfer strategies. The identification of underlying resistance pathways also holds considerable promise for human tumor immunotherapy.[133] Together, these studies exemplify how spatial precision in bioprinting accelerates both disease deconstruction and regenerative strategy development.[134] Furthermore, combining organoids with advanced imaging techniques and multi-omics approaches can enhance our understanding of immune responses and disease progression, paving the way for more effective therapeutic interventions.

While significant progress has been made in modeling metabolic and immune diseases using bioprinted organoids, further research is needed to overcome technical challenges and translate these models into clinical applications. The integration of organ-on-a-chip technology with metabolomics and advanced imaging techniques will undoubtedly continue to drive innovation in disease modeling and therapy development.

3.5. Neurodegenerative diseases

Neurodegenerative disorders such as Alzheimer's and Parkinson's diseases have been modeled using bioprinted neural organoids. Multi-material bioprinting of human iPSC-derived neural stem cells and endothelial progenitors has generated cortical organoids with layered regions and

perfusable microvasculature, mimicking the blood–brain barrier and neuronal degeneration.[84] These models enable the study of amyloid-β aggregation and tauopathy in a 3D microenvironment. Moreover, bioprinted midbrain organoids containing dopaminergic neurons have been used to evaluate mitochondrial dysfunction and oxidative stress in Parkinson's disease.[84,123] Wang et al.[135] aimed to create a Corti organoid using 3D bioprinting, integrating a "3D culture scaffold + multiple induction signals + inner ear stem cells." This approach addressed the limitation of regenerated hair cells in forming functional ciliary bundles and establishing synaptic connections with spiral ganglion cells in a 2D system, hindering the achievement of effective physiological repair of hearing. Their study demonstrated that the organoids facilitated the adhesion and proliferation of inner ear stem cells, leading to the generation of both hair cells and nerve cells. This work presents a promising avenue for investigating auditory cell regeneration and repairing hearing loss.[135]

3D bioprinting of organoids has significantly advanced disease modeling by combining stem cell self-organization with engineered architectures. While challenges remain in replicating the full complexity of human tissues, recent innovations in vascularization,[123,125] multicellular patterning,[84] and biomaterial design are bridging these gaps.[25,121] Future efforts should focus on integrating dynamic stimuli, such as mechanical forces and immune cues, to further enhance pathophysiological relevance.[106]

4. Bioprinting tumor organoids: simulacrum or throughput

Bioprinting technology can recreate the spatial topological relationships between different cellular components within tumor organoids, including immune cells, CAFs, and vascular and lymphatic structures, thus reproducing the heterogeneous structure of the primary tumor.[136] Emerging platforms such as organ-on-a-chip, organoids, and bioprinting within micro-physiological systems are increasingly employed to elucidate these interactions. These systems accurately recapitulate key features of tumor microenvironments (TMEs) and immune responses, offering physiologically relevant platforms for investigating cancer progression, immune evasion, and therapeutic interventions.[137] In addition, the application of bioprinting technology has been extended to high-throughput screening in tumor model systems.[138] Tumor organoids, which can be produced at scale and tested systematically through automated bioprinting processes, play a pivotal role in drug development and personalized treatment strategy optimization. The advancement of this technology has facilitated more rapid and precise evaluation of anticancer drug efficacy while also enabling the exploration of personalized cancer therapies.

4.1. Tumor biology-based bioprinting of tumor-like organoids

3D printing enables the reconstruction of quasi-native spatial topological relationships among different cell types within tumor tissue components. This primarily involves the first-level tumor cell components and specific structures, particularly those located on the periphery of the tumor cells, such as immune cells, blood vessels, lymphatic vessels, nerves, and paracancerous cells. Using 3D printing technology, a complex co-culture model with three or even multiple components can be established based on predefined spatial positioning and cell composition ratios. Additionally, the spatial arrangement of different clones between tumor cells and their biological interactions warrants further emphasis. Such intricate constructs of tumor-induced organs or organoids cannot be achieved by conventional methods and necessitate the use of 3D bioprinting. Bioprinting technologies have revolutionized the fabrication of tumor organoids by enabling precise spatial control over cellular and extracellular components, thereby recapitulating the heterogeneous architecture of native tumors. This approach addresses the critical limitations of conventional organoid models, which often fail to mimic the multicellular complexity and spatial organization of TMEs.[25,99]

4.1.1. Spatial arrangement of tumor niche

The spatial heterogeneity of tumor subclones and their dynamic crosstalk with stromal components, driven by genetic and epigenetic variations, constitute a hallmark of cancer progression and therapeutic resistance. Single-cell and spatial transcriptomic analyses reveal that intra-tumoral heterogeneity in gastric cancer arises not only from genetic diversity but also from spatially organized interactions between proliferative/invasive cancer cells and tumor-associated fibroblasts,[139,140] among which CAFs emerge as central orchestrators. CAFs secrete transforming growth factor-beta and matrix metalloproteinases to remodel the ECM, thereby creating biomechanical niches that promote immune evasion and chemoresistance.[141] Multi-material bioprinting strategies enable the integration of tumor cells, patient-derived CAFs, and immune cells into predefined geometries, mimicking the *in vivo* spatial hierarchy observed in solid tumors.[42,99,142,143] Studies have elucidated how CAF-secreted interleukin-6 and C-X-C motif chemokine ligand 12 gradients drive epithelial-mesenchymal transition in breast cancer organoids, while nanoparticle-mediated targeting of fibroblast activation protein enhances T-cell infiltration in murine models.[144,145] Such models have captured dynamic

feedback loops between transforming growth factor-beta-mediated matrix remodeling and tumor cell migration, offering unprecedented resolution of microenvironmental regulation.

Advanced 3D bioprinting platforms have achieved precise reconstruction of spatial topology to organize triple-negative breast cancer cells (MDA-MB-231) alongside stromal fibroblasts and endothelial cells by extrusion-based multi-nozzle bioprinting. This approach replicates the cellular and TME diversity observed in native tumors, preserving subclone viability and minimizing mechanical stress during printing.[25,84] Stratified deposition of *KRAS*-mutated and wild-type cells recapitulates *in vivo* spatial competition dynamics, mirroring the clonal hierarchy observed in native tumors.[146] Complementary approaches, such as magnetic levitation 3D culture systems, have successfully replicated the radial distribution of $CD133^+$ glioblastoma stem cells and non-stem counterparts, mimicking their *in situ* spatial organization.[147] Similarly, bioprinted pancreatic ductal adenocarcinoma models demonstrated the self-organization of cancer cells into heterogeneous aggregates, reflecting the clonal dynamics and spatial complexity of human tumors.[148] Microfluidic-integrated bioprinting systems permit the spatial embedding of vascular endothelial cells, CAFs, and immune cells within biomimetic matrices, thus establishing oxygen/nutrient gradients that emulate tumor ecological heterogeneity.[149] Notably, in GelMA hydrogels containing 10% Matrigel, CAFs self-organize into 50–100 μm fibrous bundles, guiding tumor cells along defined invasion trajectories. These engineered architectures provide a physiologically relevant platform to investigate paracrine signaling networks among sub-clonal niches.

Integration of fluorescent barcoding with 3D bioprinting allows real-time tracking of sub-clonal spatial dynamics, which enables the quantitative profiling of spatial heterogeneity. In hepatocellular carcinoma models, serial section imaging revealed epidermal growth factor receptor-high subclones preferentially colonizing nutrient-rich zones within 300 μm of artificial vasculature, exhibiting a 2.3-fold proliferation advantage over peripheral populations.[149–151] Spatial transcriptomics further identified elevated Wnt/β-catenin pathway activity in these regions, correlating with immunohistochemical patterns in clinical specimens.[136]

Bioprinted glioblastoma models with concentric architectures simulate temozolomide diffusion gradients, revealing that $CD133^+$ cells located 800 μm from drug release sites demonstrated 4.7-fold higher survival rates, attributable to hypoxia-induced adenosine triphosphate binding cassette subfamily G member 2 upregulation.[146] Intriguingly, macrophage incorporation exacerbated peripheral cell resistance via interleukin-6/Janus kinase/signal transducer and activator of transcription 3 activation, highlighting spatially compartmentalized stroma-tumor interactions in therapeutic evasion.[152]

These models have demonstrated clinical utility in predicting colorectal cancer liver metastasis patterns (82% accuracy), optimizing anti-angiogenic dosing regimens (37% survival extension in murine models, and deconvoluting transforming growth factor-beta/receptor activator of nuclear factor-κB ligand synergy in breast cancer bone niches.[149,153,154] Convergence with spatial omics and smart biomaterials promises to reconstruct tumor evolutionary landscapes at single-cell resolution, heralding a new era in precision oncology research.

4.1.2. Intercellular communication within tumor organoids

Bioprinting allows for the exact positioning of different cell types and biomaterials in a 3D space with the help of a mechanical and computer-assisted system to mimic the *in vivo* spatial architecture of a tissue or tumor and its microenvironment. This facilitates the study of bidirectional signaling between cancer cells and stromal components, such as CAFs, immune cells, and endothelial cells.[105] A key advantage of bioprinting-based preclinical cancer models is the standardization of cell deposition,[155] along with the ability to construct artificial 3D tumors incorporating multiple cell types, structural elements, and ECM. This capability enhances the potential for more accurate personalized medicine strategies.[156] Early research primarily utilized bioprinted cancer cell lines or single-cell suspensions to generate such models.[157] More recently, advancements in dispersing organoids and tumoroids alongside stromal cells have enabled the development of co-culture models that incorporate the TMEs.[158] It also facilitates the construction of vascularized tumor organoids by embedding perfusable channels lined with endothelial cells, thereby simulating nutrient exchange and immune cell trafficking.[39,42,123] Sequential printing of sacrificial inks enables the creation of hierarchical vascular networks that support long-term organoid survival and maturation.[42,159]

The mammary microenvironment has been shown to suppress tumor progression by redirecting cancer cells to adopt a normal mammary epithelial progenitor fate *in vivo*. However, the mechanism(s) by which this alteration occurs have yet to be defined. A 3D bioprinted fibroblast-mediated breast tumor organoid revealed that CAFs enhance ECM remodeling and paracrine communication, promoting tumor stiffness and conferring resistance to radiotherapy. Similarly, researchers evaluated mitochondrial transfer in 3D bioprinted chimeric organoids to test the hypothesis

that mitochondrial transfer from normal mammary epithelial cells to breast cancer cells plays a role in the redirection process. Their results demonstrate that mitochondrial transfer contributes to microenvironmental redirection of cancer cells through alteration of metabolic and molecular functions of the recipient cancer cells, which is the first description of a 3D bioprinter-assisted organoid system for studying mitochondrial transfer. Furthermore, these studies are also the first mechanistic insights into the process of mammary microenvironmental redirection of cancer, providing a framework for new therapeutic strategies to control cancer.[160] Khan et al.[161] introduced a human bone marrow organoid capable of sustaining the proliferation of primary cells derived from individuals with myeloid and lymphoid hematologic malignancies. This model facilitates in-depth investigations into the pathophysiology of blood cancers within their TMEs and offers a valuable *ex vivo* platform for evaluating novel therapeutic agents.[161] Chen et al.[162] generated colorectal cancer microtissues based on patient-specific colonoscopy images by printing photodynamic therapies enclosed by healthy organoids to mimic the tumor's interaction with adjacent normal tissue.[162] The *in vitro* response of these microtissues to standard 5-fluorouracil therapy mirrored patient responses, suggesting the model's potential as a physiologically relevant platform for drug screening. Furthermore, the model enabled the calculation of patient-specific risk for tumor invasion into neighboring tissues by assessing the quantity and proximity of invading tumor cells. This approach offers a real-time quantitative assessment for studying cancer advancement and metastasis.

In a recent study, microtissues comprising patient-derived lung tumoroids were co-cultured with corresponding CAFs and endothelial cells. The process involved printing vessel structures, seeding CAFs, and subsequently printing tumoroids suspended in a hydrogel sourced from porcine lung tissue into the same compartment. Notably, an active fusion between stromal cells and tumoroids occurred, leading to the formation of microvessels that directly engaged with other cell types. Upon administering the drug poziotinib through the vessel structures, it was observed that both endothelial cells and CAFs, along with the CAF-secreted matrix, shielded the lung tumoroids from the treatment. Consequently, this model holds promise for investigating the impact of cell–cell and cell–matrix interactions on the effectiveness of drug delivery to tumor tissues.[163]

In ovarian cancer models, bioprinted microtumors composed of leukemia (HL-60) and stromal cells exhibited dynamic cell–cell interactions, where stromal cells modulated cancer cell proliferation and invasion through cytokine signaling. Such models underscore the role of bioprinting in capturing the dynamic crosstalk within the TME, which drives drug resistance and tumor progression. Additionally, the incorporation of neural cells and lymphatic analogs into bioprinted models has revealed insights into tumor innervation and immune evasion mechanisms.[39,159] These models also capture cytokine-mediated crosstalk, such as CAF-driven ECM remodeling and immunosuppressive signaling, which are pivotal for drug resistance studies.[121]

4.2. High-throughput tumor organoid auto-printing for drug screening

Conventional organoid cultures face challenges in terms of batch-to-batch variability and labor-intensive protocols. Automated bioprinting systems, however, ensure consistent deposition of cells and bioinks, enabling mass production of uniform tumor organoids, which greatly avoids the bias caused by operators' manipulation.[78,159,164] Kim et al.[164] engineered a fully automated workstation that streamlines the entire workflow from tissue dissociation to drug screening, achieving a 20-fold increase in processing efficiency. Capable of handling 200 specimens per run, this system eliminates manual variability while enabling large-scale phenotypic and molecular profiling. Hou et al.[165] engineered a high-throughput screening-compatible approach that standardizes organoid generation in conventional flat-bottom 384- and 1536-well plates.[165] This method integrates magnet-assisted bioprinting technology with cell-repellent surface engineering to ensure precision and scalability. To demonstrate its applicability in automated drug discovery workflows, the researchers conducted a pilot cytotoxicity assessment of approximately 3300 clinically approved compounds. The results underscore the platform's breakthrough to facilitate large-scale drug screening through patient-derived 3D oncology models. By enabling robust analysis of clinically relevant tissues, this innovation represents a critical advancement toward personalized therapeutic development.

For personalized medicine, bioprinted constructs using patient-derived cells have been utilized to predict drug responses. In head and neck squamous cell carcinoma, bioprinted models maintained epithelial phenotypes and exhibited reduced cytotoxicity to radiochemotherapy compared to spheroids, better reflecting clinical resistance patterns.[166,167] Ovarian and colorectal tumor models bioprinted with nanocomposite hydrogels were screened for gemcitabine and oxaliplatin responses, revealing drug-specific resistance mechanisms.[168] These advances highlight the potential of automated bioprinting to generate patient-specific organoids at scale, bridging the gap between *in vitro* assays and clinical outcomes. Tebon et al.[169] introduced an integrated platform combining bioprinted tumor

organoids with label-free, time-resolved imaging using high-speed live cell interferometry and machine learning-driven analytical tools (Figure 6A).[169] Bioprinting generates 3D tumor structures that preserve native histology and transcriptional profiles. Coupled with high-speed live cell interferometry, this system enables non-invasive, parallelized mass quantification of thousands of organoids over time. Machine learning algorithms further enhance segmentation accuracy and phenotypic classification. They also demonstrated the platform's ability to distinguish organoids exhibiting transient or persistent sensitivity versus resistance to targeted therapies. This approach provides a scalable framework for resolving temporal and heterotypic adaptations in tumor populations, offering actionable insights to accelerate personalized therapeutic decision-making. Nonetheless, shortcomings exist in cost constraints, the availability of specific cell types, the time needed for model establishment and growth, and success rates. Parallel innovations in miniaturization have redefined screening economics. Phan et al.[170] pioneered a nanoscale microplate platform (200 nL/well) coupled with artificial intelligence-driven hyperspectral imaging, permitting simultaneous evaluation of 1536 drug combinations per assay.[170] This approach reduces reagent consumption and operational costs to 20% of conventional methods without compromising data resolution. Individual models vary in their representation of important features such as tumor heterogeneity, spatial interactions between tumor and stromal microenvironments, metabolic and nutritional gradients, and immunological responses. Consequently, a strategic integration of diverse models may be necessary to enhance the efficacy of clinical studies by bolstering the foundation of preclinical data.[171]

Long-term organoid modeling enables complex therapeutic screening. However, technical challenges include limited user-friendliness in long-term dynamic cell culture, incompatibility with rapid cell encapsulation in biomimetic hydrogels, and low throughput for compound screening. To address these issues, a micro-solenoid valve-driven bioprinting system was developed by Joshi et al.[171] This system fabricates the alginate-encapsulated Hep3B liver tumor spheroids in a 144-well plate, achieving rapid biomimetic tissue formation for large-scale compound screening.

Bioprinting offers applications beyond TME-mimicking models, including standardized cell dispensing for high-throughput studies. A key limitation, however, is the tendency of bioinks to spread within small wells, compromising the structural integrity required for 3D cell culture.[173] To address this issue, researchers have employed strategies such as mixing patient-derived glioblastoma or sarcoma cells with hyaluronic acid-collagen bioinks, printing them onto gelatin-coated wells, and subsequently replacing the gelatin with culture medium.[174] Alternatively, acoustic bioprinting has been used to deposit small droplets onto hydrophobic substrates, generating bladder cancer-derived tumoroids containing both cancer cells and CAFs.[175] This approach enables the scalable production of uniform tumoroids that recapitulate the TME while remaining compatible with high-throughput drug screening for personalized therapy. While 3D bioprinted models enhance reproducibility in drug testing and facilitate the study of multicellular interactions in a 3D context, they remain static systems. Consequently, they fail to incorporate dynamic mechanical forces (e.g., fluid flow) or chemical gradients, both of which critically influence tumor cell behavior *in vivo*.[176]

5. Beyond organoids: three-dimensional-printed biocompatible accessories

The convergence of 3D-printed biocompatible accessories, like artificial intelligence-driven design, organ-on-chip technologies, and organoid morphology recognition and deconvolution, enhances the functionality and realism of the models, enabling intelligence and automation in the construction of high-fidelity organoid models.[177–179] This section explores the role of functional biocompatible accessories beyond 3D-printed organoid culture, focusing on structural supports, functional interfaces, and integrated systems that augment organoid utility.[180] By leveraging advanced biomaterials, innovative printing techniques, and interdisciplinary engineering, these accessories bridge the gap between *in vitro* organoids and *in vivo* physiological complexity, opening new frontiers in precision medicine, tissue engineering, and regenerative therapy.[181,182]

5.1.icrofluidic devices for perfusable cultures

Microfluidic systems mimic the physiological flow of body fluids, allowing precise control of nutrient delivery, shear stress, and waste removal.[183,184] 3D bioprinting facilitates the fabrication of complex microchannels with integrated sensors or valves, creating organ-on-a-chip platforms that combine organoids with fluidic networks.[89,182,185,186] 3D-printed microfluidics can also create chemical gradients (e.g., oxygen, growth factors) to guide organoid morphogenesis.[187] Researchers have employed printed gradient chambers to induce regional differentiation in hepatic organoids, forming distinct zones of hepatocytes and cholangiocytes, similar to native liver lobules.[188,189] Such spatial control over microenvironments is crucial for modeling organ-level functional zonation.[82,190] Recent advancements in 3D printing technology have enabled the creation of more complex gradient-generating devices,

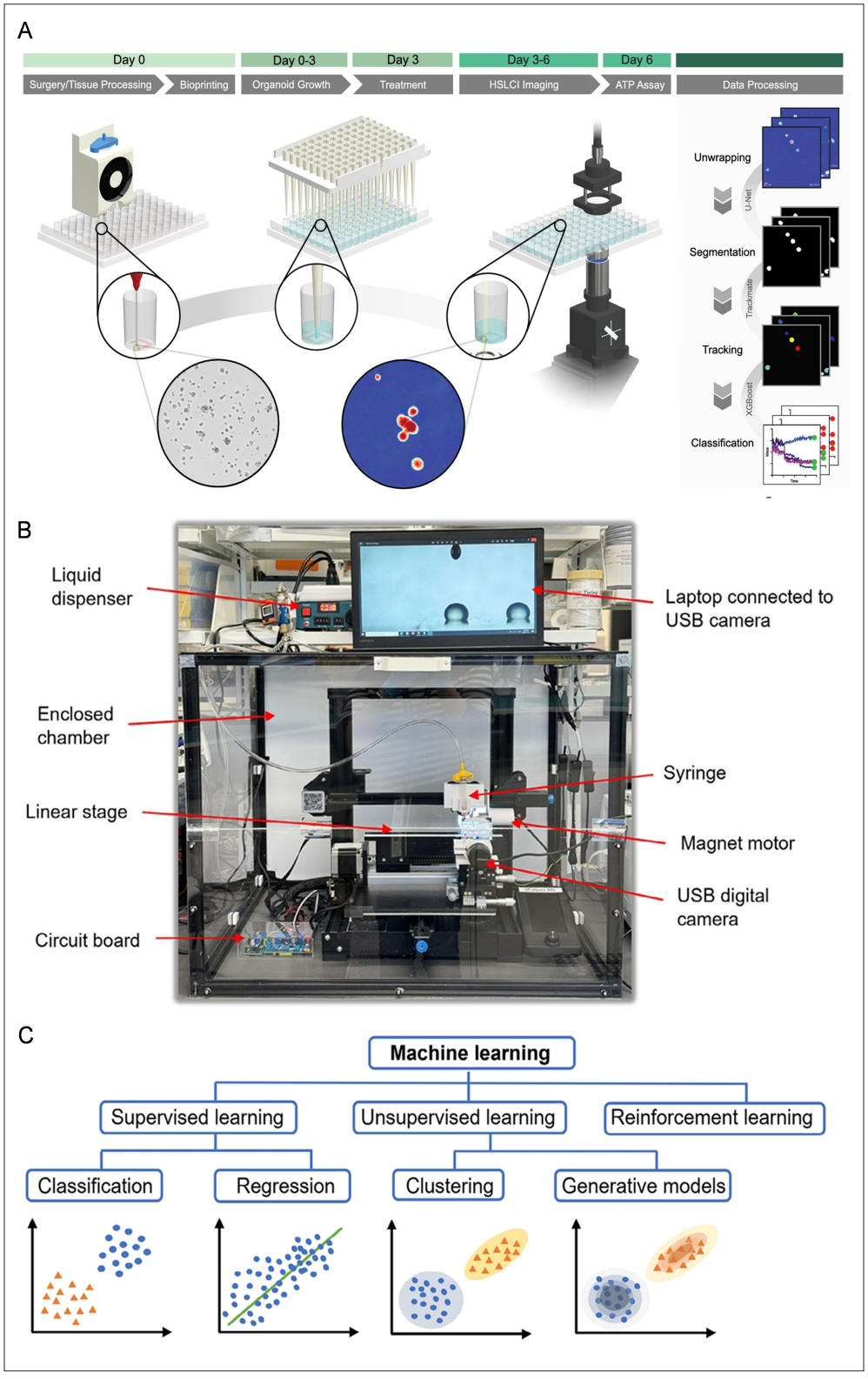

Figure 6. Emerging bioprinting-integrated platforms for high-throughput organoid analysis and fabrication. (A) Extrusion-based bioprinting enables single-organoid tracking with high-speed live cell interferometry (HSLCI). Adapted with permission from Tebon et al.[169] Copyright© Nature 2023. (B) Overview of machine learning setup. (C) Modified and developed cellular droplet three-dimensional bioprinting setup for high-throughput precision. Adapted with permission from Shin et al.[221] Copyright© Wiley 2025.

which can generate multiple gradients simultaneously and with higher precision, further improving the ability to control organoid development.[191–193]

5.2. Sensory accessories for real-time monitoring

Incorporating sensors into 3D printed accessories allows non-invasive monitoring of organoid physiology, including metabolic activity, electrical signals, and mechanical strain.[194]

5.2.1. Biosensors for metabolite detection

Printable conductive materials, like carbon nanotubes and graphene oxide, can be integrated into scaffolds to create electrochemical sensors.[195] For instance, a glucose-sensitive sensor printed within a pancreatic islet organoid scaffold continuously monitored insulin secretion in response to glucose challenges, providing real-time data for diabetes research.[196,197] Similarly, lactate sensors in printed brain organoid cultures correlated metabolic activity with neuronal network maturation, offering insights into neurodevelopmental disorders.[196,198] These biosensors have the potential to revolutionize the field of organoid research by providing real-time, non-invasive monitoring of organoid function, which can help to better understand the underlying mechanisms of disease and develop more effective treatments.

5.2.2. Electrophysiological probes for neural organoids

Traditional organoid research has been constrained by the limitation of surface-level signal acquisition, rendering the spatiotemporal dynamics of internal physiological activities inaccessible, which is a critical drawback, particularly in cardiac and neural organoid studies. To address this challenge, Park et al.[199] developed a soft bioelectrode platform based on liquid metal 3D printing.[199] This system enables customizable geometric parameters (height, diameter) to accommodate diverse organoid structures while maintaining mechanical compliance comparable to biological tissues. This compatibility prevents mechanical damage to cardiac organoids during contraction or fluidic movement, enabling stable, long-term monitoring. The electrode array further facilitates simultaneous electrophysiological monitoring of 32 organoids, successfully capturing drug-induced electrophysiological responses. This scalable capability establishes a robust platform for high-throughput drug screening and disease modeling.

Lee et al.[200] extended the potential of liquid metal microelectrodes through high-resolution 3D printing. By precisely embedding electrodes into specific inner layers of retinal organoids, the researchers achieved spatiotemporally controlled electrophysiological recordings of retinal ganglion cell activity. This approach not only validated developmental patterns of inner retinal signaling but also revealed critical insights into early-stage neural organoid modeling of retinal degeneration. The findings underscore the technology's utility in dissecting disease mechanisms through dynamic, cell-type-specific observations. Both studies leverage liquid metal's mechanical adaptability to overcome the limitations of rigid conventional electrodes, yet their designs diverge to address distinct challenges. Park's approach emphasizes scalability and dynamic stability for cardiac electrophysiology, whereas Lee's work prioritizes submillimeter precision for neural circuit interrogation. This complementary framework establishes a modular toolkit for organoid electrophysiology, enabling researchers to tailor electrode configurations to specific experimental demands. Integration with multimodal sensing technologies could further advance applications in organ development studies, disease progression modeling, and personalized medicine, paving the way for unprecedented insights into biological systems at the organoid scale. The elucidation of brain function in neural organoids necessitates precise electrophysiological monitoring of neuronal activity.[201] To this end, 3D-printed microelectrodes, coated with biocompatible polymers, have been engineered to penetrate cerebral organoids, enabling the detection of action potentials and synaptic connectivity.[202] A pioneering study by Acha et al.[202] employed printed multi-electrode arrays (MEAs) to systematically map electrical signals in cortical organoids. Their findings revealed spontaneous network oscillations resembling those observed in fetal brain development, underscoring the utility of these systems in modeling neurodevelopmental dynamics.[203-205] The research introduced shell-like MEA configurations analogous to electroencephalography caps, designed to interface with the surface of neural organoids while enabling 3D spatiotemporal recording. This design not only facilitated non-invasive longitudinal monitoring of neuronal firing but also demonstrated a statistically significant increase in action potential generation following external stimulation. Crucially, the biocompatible architecture preserved organoid viability, thereby supporting prolonged *in vitro* studies of neurodevelopmental processes.

A novel microfabrication technique has further advanced this field by addressing the mechanical constraints of traditional MEAs. By depositing material layers over a sacrificial template and strategically releasing internal stresses, researchers constructed vertically protruding cantilever microelectrodes. These slender beams extend over 200 μm from their base, allowing deep penetration into organoid interiors. This innovation enables the recording of local field potentials from deeply

embedded neurons, previously inaccessible with surface-based systems, thereby offering unprecedented insights into intracellular network dynamics.

Complementary advancements in 3D microfabrication further expanded the versatility of electrophysiological platforms. For instance, curved microfluidic systems and self-folding electrodes have been proposed to optimize spatial compatibility with diverse organoid morphologies. These customizable tools adapt to the unique structural demands of specific neural organoid models, enhancing data accuracy and experimental reproducibility. Such innovations collectively establish a modular framework for electrophysiological analysis, bridging the gap between *in vitro* organoid systems and complex *in vivo* neural activity.

5.3. Actuating accessories for mechanical stimulation

Mechanical stimuli, such as cyclic stretch and compression, are critical determinants of tissue maturation, particularly in the context of muscular and cardiovascular organoids. To replicate the dynamic mechanical microenvironments encountered *in vivo*, researchers have increasingly employed 3D-printed actuators, including pneumatic and hydraulic microsystems, as precise tools for delivering controlled mechanical signals.[205] This approach has been pivotal in advancing the functional maturation of engineered tissues.

In cardiac organoid models, silicone-based 3D-printed actuators have been instrumental in applying cyclic stretching, which facilitates myofibril alignment and enhances contractile performance.[205,206] Furthermore, studies utilizing 3D-printed piston-driven systems demonstrated that mechanical stimulation can significantly improve the electrophysiological properties of cardiac tissues, rendering them more physiologically relevant for disease modeling, such as arrhythmia studies.[207,208] Recent advancements have expanded this paradigm by incorporating additional mechanical modalities, such as shear stress and torsion, to further refine cardiac organoid maturation, thereby elevating their functional complexity and utility in both research and translational applications.[209,210]

Beyond cardiovascular systems, 3D printing has enabled the development of piezoelectric scaffolds capable of generating ultrasonic vibrations to simulate physiological mechanical loading. Such scaffolds have been shown to promote osteoblast differentiation and mineralization by mimicking *in vivo* mechanical cues, with studies reporting a 40% increase in calcium deposition in bone organoids compared to static culture conditions.[121] The customizable nature of 3D-printed piezoelectric structures further allows tailoring their mechanical properties to specific bone organoid models, thereby optimizing stimulation efficacy and enhancing the structural quality of engineered bone tissues.[211]

5.4. Multicomponent bio-assembly for complex organoid models

5.4.1. Heterotypic co-culture platforms

3D bioprinting enables the precise co-deposition of multiple cell types and biomaterial components, creating heterotypic co-culture systems that replicate complex tissue–tissue interfaces and physiological interactions.[212]

A compelling application is the integration of brain organoids with endothelial cells and astrocytes within perfusable scaffolds, which generates a functional blood–brain barrier model.[213] These platforms exhibit robust tight junction formation and selective permeability, offering a physiologically accurate platform to study neurotoxicity, drug permeability, and blood–brain barrier dysfunction.[214,215] Recent advances have refined these systems by incorporating species-specific cell lines, bioactive ECM components, and dynamic perfusion protocols to better mimic *in vivo* microenvironments, thereby enhancing model fidelity.[216,217]

Similarly, cancer organoids co-cultured with stromal cells or immune cells within 3D-printed matrices recapitulate critical features of TMEs. For instance, colorectal cancer organoids embedded with immune cells in printed matrices enabled the evaluation of immunotherapy efficacy in a context that mirrors clinical tumor-immune interactions.[213] Such systems hold transformative potential for cancer research, offering insights into tumor progression, metastasis, and therapeutic resistance.

Despite these advancements, challenges remain. Heterotypic co-cultures require meticulous regulation of cell–cell interactions, as uncontrolled cross-talk may lead to signal interference or cross-contamination over time. Additionally, maintaining physiological relevance across diverse cell populations demands precise spatiotemporal control of growth factors, mechanical cues, and metabolic gradients, which is a complex interplay that necessitates further optimization.

5.4.2. Miniature bioreactors for scalable culture

The integration of 3D-printed scaffolds with microfluidic bioreactors has enabled high-throughput organoid culture systems capable of parallel production, monitoring, and analysis.[218] These platforms, often equipped with automated sampling and imaging capabilities, are indispensable for accelerating drug discovery and toxicity testing.[201,219]

A notable example is the 3D-printed polycarbonate perfusion bioreactor, which supports the simultaneous culture of hundreds of hepatic organoids under controlled perfusion. By maintaining consistent metabolic activity for up to 4 weeks, these systems address a critical limitation of traditional static cultures and advance their utility in drug metabolism studies.[220] Recent design improvements prioritize uniform nutrient delivery, efficient waste removal, and minimized shear stress, thereby enhancing organoid viability and experimental reproducibility.[175]

To standardize output, another 3D bioprinting platform presents a promising alternative. Shin et al.[221] addressed the limitations of optimization of critical process variables (bioink viscosity, nozzle size, printing duration, pressure, and cell density) by leveraging machine learning to streamline parameter optimization and enable real-time prediction of cellular droplet dimensions.[221] This high-throughput bioprinting system was engineered to generate over 50 cellular droplets per cycle, facilitating the rapid compilation of datasets essential for robust algorithmic training. Five machine learning models were evaluated for performance, with the multilayer perceptron exhibiting superior predictive accuracy and the decision tree achieving the shortest computational latency. To enhance practical utility, these optimized algorithms were embedded into an intuitive interface designed for seamless integration into experimental workflows, which bridges bioprinting automation with data-driven parameter refinement, holding significant potential to advance scalable organoid manufacturing (Figure 6B & C). By harmonizing precision and efficiency, this framework is poised to synergize with diverse biomanufacturing technologies, accelerating applications in drug development, disease modeling, and regenerative medicine.

Complementary to perfusion systems, inkjet bioprinting enables the precise deposition of organoids onto pre-patterned substrates, forming high-density arrays ideal for large-scale screening. A 96-well plate format with printed ECM microdots, for instance, facilitates uniform culture of intestinal organoids and accelerates high-throughput toxicity testing of anticancer agents.[222,223] Such array-based systems significantly streamline drug discovery workflows, reducing time and resource demands while improving data consistency.

Despite these strides, scaling organoid cultures requires balancing system complexity with cost-effectiveness. Future innovations in bioreactor design must prioritize scalability, automation, low-cost accessibility, computer numerical control-driven platform, and integration with artificial intelligence-driven analytics to fully unlock the potential of organoid-based platforms in translational research.[96]

5.5. Challenges and future directions

Despite advancements in printing vascular networks, seamless anatomical and functional integration between engineered vessels and organoid-derived microvasculature remains elusive. Overcoming this hurdle requires innovations in two key areas. First, the co-printing of endothelial cells with angiogenic factors to promote vasculogenesis, and second, the development of advanced imaging or sensor-based tools to evaluate vascular functionality and optimize tissue–tissue interfaces. Meanwhile, short-term biocompatibility does not guarantee safety over extended periods, as degradation byproducts may trigger inflammatory responses or compromise organoid viability. Future efforts must prioritize the development of fully biodegradable materials that mimic the dynamic turnover of native ECM while exerting immunomodulatory effects. Concurrently, systematic investigations into the long-term biological impacts of material degradation are essential to refine strategies for mitigating adverse outcomes.

Current 3D-printed systems excel at providing structural frameworks but often fail to induce functional maturation, such as the formation of innervated muscle or vascularized glomeruli. To bridge this gap, researchers must integrate multifaceted stimuli into engineered environments, including mechanical forces, electrical signaling, and spatiotemporal biochemical gradients. Furthermore, elucidating the molecular and cellular mechanisms governing maturation will inform the design of targeted interventions.

Innovations in artificial intelligence present a transformative opportunity for clinical translation. Artificial intelligence-driven platforms can streamline organoid design through rapid screening, enable high-resolution analysis of multiscale imaging and multi-omics datasets, and facilitate precise preclinical drug testing and disease modeling.[224] Achieving clinical relevance also demands rigorous standardization. Scalable production protocols must ensure precision and reproducibility, while standardized sterilization, cell seeding, and functional validation procedures are indispensable for safe patient applications.

6. Conclusion

Advances in bioprinting have profoundly advanced our comprehension of organoid and tumoroid development, regeneration, pathophysiological mechanisms, drug sensitivity assessment, and clinical translation.[225]

Innovations in culture optimization and the discovery of novel ECM-mimetic scaffold materials have partially mitigated longstanding challenges related to poor standardization and suboptimal cell yield.[226] However, persistent technical barriers impede progress, particularly in balancing geometric precision with the preservation of cellular viability and functional integrity. Current systems often struggle to achieve high-fidelity without compromising the metabolic and physiological activity of encapsulated cells.

To unlock the full potential of 3D bioprinted organoids, future research must prioritize three interrelated avenues: (i) the engineering of advanced bioinks with tunable mechanical, biochemical, and degradation properties to better emulate native tissues, (ii) the refinement of printing methodologies to enhance spatial resolution while minimizing mechanical stress on delicate cellular components, and (iii) the synergistic integration of organoid systems with complementary biofabrication technologies (e.g., microfluidics, organ-on-a-chip platforms) to construct physiologically relevant, multi-tissue models. Such advancements will not only address existing technical limitations but also expand the scope of organoid applications in precision medicine, disease modeling, and high-throughput drug screening.

Acknowledgment

The author team would like to extend their sincere gratitude to the research teams whose works have been cited in this review. Special thanks are given to those who generously granted permission for the reuse of their data. Their valuable contributions have laid a solid foundation for the advancement of 3D-printed organoid research and have provided important insights that shaped the perspectives discussed in this manuscript.

Funding

This work was supported by the National Key Research and Development Program of China (Grant No. 2022YFC2504200) and the National Natural Science Foundation of China (Grant Nos. 82373434 and 82002878).

Conflict of interest

The authors declare no conflict of interest.

Author contributions

Conceptualization: All authors
Funding acquisition: Zhigang Cai, Shang Xie
Resources: Zhigang Cai, Shang Xie, Xiaofeng Shan
Supervision: Zhigang Cai, Shang Xie, Xiaofeng Shan
Validation: Zhigang Cai, Shang Xie, Xiaofeng Shan
Writing–original draft: Lingzi Liao
Writing–review & editing: Shang Xie, Zhigang Cai, Qiushi Feng

Ethics approval and consent to participate

Not applicable.

Consent for publication

Not applicable.

Availability of data

Not applicable.

References

1. Zhao Z, Chen X, Dowbaj AM, et al. Organoids. *Nat Rev Methods Primers*. 2022;2(1):94. doi: 10.1038/s43586-022-00174-y
2. Geng Y, Chen Z, Luo T, et al. Innovative construction and application of bile duct organoids: unraveling the complexity of bile duct diseases and potential therapeutic strategies. *Cancer Lett*. 2025;618:217619. doi: 10.1016/j.canlet.2025.217619
3. Hermans F, Hasevoets S, Vankelecom H, Bronckaers A, Lambrichts I. From pluripotent stem cells to organoids and bioprinting: recent advances in dental epithelium and ameloblast models to study tooth biology and regeneration. *Stem Cell Rev Rep*. 2024;20(5):1184-1199. doi: 10.1007/s12015-024-10702-w
4. Mallya D, Gadre MA, Varadharajan S, Vasanthan KS. 3D bioprinting for the construction of drug testing models-development strategies and regulatory concerns. *Front Bioeng Biotechnol*. 2025;13:1457872. doi: 10.3389/fbioe.2025.1457872
5. Nejati B, Shahhosseini R, Hajiabbasi M, et al. Cancer-on-chip: a breakthrough organ-on-a-chip technology in cancer cell modeling. *Med Biol Eng Comput*. 2025;63(2):321-337. doi: 10.1007/s11517-024-03199-5
6. Hu Y, Zhu T, Cui H, Cui H. Integrating 3D bioprinting and organoids to better recapitulate the complexity of cellular microenvironments for tissue engineering. *Adv Healthc Mater*. 2025;14(3):e2403762. doi: 10.1002/adhm.202403762
7. Huang MS, Christakopoulos F, Roth JG, Heilshorn SC. Organoid bioprinting: from cells to functional tissues. Review. *Nat Rev Bioeng*. 2025;3(2):126-142. doi: 10.1038/s44222-024-00268-0
8. Ju M, Jin Z, Yu X, et al. Gastric cancer models developed via GelMA 3D bioprinting accurately mimic cancer hallmarks,

tumor microenvironment features, and drug responses. *Small*. 2025;21(8):e2409321.
doi: 10.1002/smll.202409321

9. Ding Z, Huang J, Ren Y, et al. 3D bioprinted advanced cartilage organoids with engineered magnetic nanoparticles polarized-BMSCs/alginate/gelatin for cartilage tissue regeneration. Article. *Nano Res*. 2025;18(2)94907084.
doi: 10.26599/nr.2025.94907084

10. Shyu J-F, Chu T-H, Lo Y-C, et al. Fabrication of 3D bioprinting vascularized bone organoid under compressive stimulation for study of osteogenesis and angiogenesis. Meeting Abstract. *J Bone Miner Res*. 2023;38:304-304.

11. Abaci A, Camci-Unal G, Guvendiren M. Three-dimensional bioprinting for medical applications. Article. *MRS Bulletin*. 2023;48(6):624-631.
doi: 10.1557/s43577-023-00546-z

12. Shen N, Li Z, Yang P, et al. Designing methacrylic anhydride-based hydrogels for 3D bioprinting. *IJB*. 2024;11(1):84-138.
doi: 10.36922/ijb.4650

13. Chen Z, Zhang H, Huang J, et al. DNA-encoded dynamic hydrogels for 3D bioprinted cartilage organoids. *Mater Today Bio*. 2025;31:101509.
doi: 10.1016/j.mtbio.2025.101509

14. Shen C, Wang J, Li G, et al. Boosting cartilage repair with silk fibroin-DNA hydrogel-based cartilage organoid precursor. Article. *Bioact Mater*. 2024;35:429-444.
doi: 10.1016/j.bioactmat.2024.02.016

15. Ali EAM, Smaida R, Meyer M, et al. iPSCs chondrogenic differentiation for personalized regenerative medicine: a literature review. *Stem Cell Res Ther*. 2024;15(1):185.
doi: 10.1186/s13287-024-03794-1

16. Lawlor KT, Vanslambrouck JM, Higgins JW, et al. Cellular extrusion bioprinting improves kidney organoid reproducibility and conformation. *Nat Mater*. 2021;20(2):260-271.
doi: 10.1038/s41563-020-00853-9

17. Long B, Mengmeng L, Jiacan S. A perspective on light-based bioprinting of DNA hydrogels for advanced bone regeneration: implication for bone organoids. *Int J Bioprint*. 2023;9(2):688.
doi: 10.18063/ijb.688

18. Wang Z, Wang X, Huang Y, et al. $Ca_v3.3$-mediated endochondral ossification in a three-dimensional bioprinted GelMA hydrogel. Article. *Bio-Des Manuf*. 2024;7(6):983-999.
doi: 10.1007/s42242-024-00287-1

19. Wang J. Engineering large-scale self-mineralizing bone organoids with bone matrix-inspired hydroxyapatite hybrid bioinks. *Adv Mater (Weinheim)*. 2024;36(30):e2309875.
doi: 10.1002/adma.202309875

20. Ren X, Wang J, Wu Y, et al. One-pot synthesis of hydroxyapatite hybrid bioinks for digital light processing 3D printing in bone regeneration. *J Mater Sci Technol*. 2024;188:84-97.
doi: 10.1016/j.jmst.2024.01.001

21. Wang J, Zhou D, Li R, et al. Protocol for engineering bone organoids from mesenchymal stem cells. *Bioact Mater*. 2025;45:388-400.
doi: 10.1016/j.bioactmat.2024.11.017

22. Li H, Chen H, Du C, et al. Effect of hydroxyapatite nanowires on formation and bioactivity of osteoblastic cell spheroid. *ACS Biomater Sci Eng*. 2024;10(12):7413-7428.
doi: 10.1021/acsbiomaterials.4c01159

23. Fang Y, Ji M, Wu B, et al. Engineering highly vascularized bone tissues by 3d bioprinting of granular prevascularized spheroids. *ACS Appl Mater Interfaces*. 2023;15(37):43492-43502.
doi: 10.1021/acsami.3c08550

24. Loukelis K, Koutsomarkos N, Mikos AG, Chatzinikolaidou M. Advances in 3D bioprinting for regenerative medicine applications. *Regen Biomater*. 2024;11:rbae033.
doi: 10.1093/rb/rbae033

25. Bernal PN, Bouwmeester M, Madrid-Wolff J, et al. Volumetric bioprinting of organoids and optically tuned hydrogels to build liver-like metabolic biofactories. *Adv Mater (Deerfield Beach, Fla)*. 2022;34(15):e2110054.
doi: 10.1002/adma.202110054

26. Luo Y, Xu R, Hu Z, et al. Gel-based suspension medium used in 3D bioprinting for constructing tissue/organ analogs. *Gels*. 2024;10(10):644.
doi: 10.3390/gels10100644

27. De Leeuw A, Graf R, Zhang J, et al. Increased cell density increases mineral formation rates and stiffness in 3D bioprinted patient-derived bone organoids using dynamic loading. Meeting Abstract. *Tissue Eng Part A*. 2023;29(11-12):582-583.

28. Wang J, Chen X, Li R, et al. Standardization and consensus in the development and application of bone organoids. *Theranostics*. 2025;15(2):682-706.
doi: 10.7150/thno.105840

29. Park S, Cho SW. Bioengineering toolkits for potentiating organoid therapeutics. *Adv Drug Deliv Rev*. 2024;208:115238.
doi: 10.1016/j.addr.2024.115238

30. Frenz-Wiessner S, Fairley SD, Buser M, et al. Generation of complex bone marrow organoids from human induced pluripotent stem cells. Article. *Nat Methods*. 2024;21(5).
doi: 10.1038/s41592-024-02172-2

31. De Leeuw A, Schadli GN, Steffi C, et al. A novel 3D-bioprinted patient-specific biomimetic bone organoid to model osteogenesis imperfecta. Meeting Abstract. *Tissue Eng Part A*. 2023;29(13-14):582-583.

32. Abbott A. Cell culture: biology's new dimension. *Nature*. 2003;424(6951):870-872.
doi: 10.1038/424870a

33. Li J, Han S, Yu F, Li T, Liao B, Liu F. Mapping the landscape of PSC-CM research through bibliometric analysis. *Front Cardiovasc Med*. 2024;11:1435874. doi: 10.3389/fcvm.2024.1435874

34. Wang Y, Hou Y, Hao T, et al. Model construction and clinical therapeutic potential of engineered cardiac organoids for cardiovascular diseases. *Biomater Transl*. 2024;5(4):337-354. doi: 10.12336/biomatertransl.2024.04.002

35. Nwokoye PN, Abilez OJ. Blood vessels in a dish: the evolution, challenges, and potential of vascularized tissues and organoids. *Front Cardiovasc Med*. 2024;11:1336910. doi: 10.3389/fcvm.2024.1336910

36. Khoury RE, Nagiah N, Mudloff JA, Thakur V, Chattopadhyay M, Joddar B. 3D bioprinted spheroidal droplets for engineering the heterocellular coupling between cardiomyocytes and cardiac fibroblasts. *Cyborg Bionic Syst*. 2021;2021:9864212. doi: 10.34133/2021/9864212

37. Mohr E, Thum T, Bär C. Accelerating cardiovascular research: recent advances in translational 2D and 3D heart models. *Eur J Heart Fail*. Oct 2022;24(10):1778-1791. doi: 10.1002/ejhf.2631

38. Zhang W, Chen Y, Li M, et al. A PDA-functionalized 3d lung scaffold bioplatform to construct complicated breast tumor microenvironment for anticancer drug screening and immunotherapy. *Adv Sci (Weinh)*. 2023;10(26):e2302855. doi: 10.1002/advs.202302855

39. Li S, Li J, Xu J, et al. Removal-free and multicellular suspension bath-based 3D bioprinting. *Adv Mater (Deerfield Beach, Fla)*. 2024;36(48):e2406891. doi: 10.1002/adma.202406891

40. Hoang P, Sun S, Tarris BA, Ma Z. Controlling morphology and functions of cardiac organoids by two-dimensional geometrical templates. *Cells Tissues Organs*. 2023;212(1):64-73. doi: 10.1159/000521787

41. Noël ES. Cardiac construction—recent advances in morphological and transcriptional modeling of early heart development. *Curr Top Dev Biol*. 2024;156:121-156. doi: 10.1016/bs.ctdb.2024.02.005

42. Fang Y, Guo Y, Wu B, et al. Expanding embedded 3D bioprinting capability for engineering complex organs with freeform vascular networks. *Adv Mater (Deerfield Beach, Fla)*. 2023;35(22):e2205082. doi: 10.1002/adma.202205082

43. Cui H, Liu C, Esworthy T, et al. 4D physiologically adaptable cardiac patch: A 4-month in vivo study for the treatment of myocardial infarction. *Sci Adv*. 2020;6(26):eabb5067. doi: 10.1126/sciadv.abb5067

44. Zhang Z, Wu C, Dai C, et al. A multi-axis robot-based bioprinting system supporting natural cell function preservation and cardiac tissue fabrication. *Bioact Mater*. 2022;18:138-150. doi: 10.1016/j.bioactmat.2022.02.009

45. Fareez UNM, Naqvi SAA, Mahmud M, Temirel M. Computational fluid dynamics (CFD) analysis of bioprinting. *Adv Healthc Mater*. 2024;13(20):e2400643. doi: 10.1002/adhm.202400643

46. Abolhassani S, Fattahi R, Safshekan F, Saremi J, Hasanzadeh E. Advances in 4D bioprinting: the next frontier in regenerative medicine and tissue engineering applications. *Adv Healthc Mater*. 2025;14(4):e2403065. doi: 10.1002/adhm.202403065

47. Wu J, Fu J. Toward developing human organs via embryo models and chimeras. *Cell*. 2024;187(13):3194-3219. doi: 10.1016/j.cell.2024.05.027

48. Wu Y, Qin M, Yang X. Organ bioprinting: progress, challenges and outlook. *J Mater Chem B*. 2023;11(43):10263-10287. doi: 10.1039/d3tb01630g

49. Roza Vaez G, Ileana LC, Matthew CM, Vikramaditya GY. Brain organoids: a new, transformative investigational tool for neuroscience research. *Adv Biosyst*. 2018;3(1):174. doi: 10.1002/adbi.201800174

50. Renjitha G, Rakhi P. Bioengineering of brain organoids: advancements and challenges. *Tissue Eng*. 2022:399-414. doi: 10.1016/b978-0-12-824064-9.00002-2

51. Madeline AL, Magdalena R, Carol-Anne M, et al. Cerebral organoids model human brain development and microcephaly. *Nature*. 2013;501(7467):373-379. doi: 10.1038/nature12517

52. Jeong E, Choi S, Cho SW. Recent advances in brain organoid technology for human brain research. *ACS Appl Mater Interfaces*. 2023;15(1):200-219. doi: 10.1021/acsami.2c17467

53. Cadena MA, Sing A, Taylor K, et al. A 3D bioprinted cortical organoid platform for modeling human brain development. *Adv Healthc Mater*. 2024;13(27):e2401603. doi: 10.1002/adhm.202401603

54. Jihoon K, Sujin H, Sunghun C, Yoojin C, Noo Li J. Revealing the clinical potential of high-resolution organoids. *Adv Drug Deliv Rev*. 2024;207:115202. doi: 10.1016/j.addr.2024.115202

55. Natan Roberto de B, Canran W, Surjendu M, et al. Engineered organoids for biomedical applications. *Adv Drug Deliv Rev*. 2023;203:115142. doi: 10.1016/j.addr.2023.115142

56. Zhe L, Weizi G, Fukang L, et al. Vat photopolymerization based digital light processing 3D printing hydrogels in biomedical fields: key parameters and perspective. *Addit Manuf*. 2024;94:104443. doi: 10.1016/j.addma.2024.104443

57. Jennifer Sally S, Anuradha R, Venkatachalam Deepa P. Development of midbrain dopaminergic neurons and the advantage of using hiPSCs as a model system to study Parkinson's disease. *Neuroscience*. 2024;546:1-19. doi: 10.1016/j.neuroscience.2024.03.025

58. Yan Y, Li X, Gao Y, et al. 3D bioprinting of human neural tissues with functional connectivity. *Cell Stem Cell*. 2024;31(2):260-274.e7. doi: 10.1016/j.stem.2023.12.009

59. Layrolle P, Payoux P, Chavanas S. Message in a scaffold: natural biomaterials for three-dimensional (3D) bioprinting of human brain organoids. *Biomolecules*. 2022;13(1):25. doi: 10.3390/biom13010025

60. Gabriel E, Albanna W, Pasquini G, et al. Human brain organoids assemble functionally integrated bilateral optic vesicles. *Cell Stem Cell*. 2021;28(10):1740-1757.e8. doi: 10.1016/j.stem.2021.07.010

61. Jing G, Jiahui K, Minghui L, Xiao L, Jun Y, Haiwei X. Applications of neural organoids in neurodevelopment and regenerative medicine. *Biomed Eng*. 2022. doi: 10.5772/intechopen.104044

62. Tariku Sinshaw T, Frehiwot Bayelign T, Xijin H, et al. A review of advances in 3D and 4D bioprinting: toward mass individualization paradigm. *J Intell Manuf*. 2024. doi: 10.1007/s10845-024-02529-6

63. Wang X, Yang X, Liu Z, et al. 3D bioprinting of an in vitro hepatoma microenvironment model: establishment, evaluation, and anticancer drug testing. *Acta Biomater*. 2024;185:173-189. doi: 10.1016/j.actbio.2024.07.019

64. Zhuang X, Deng G, Wu X, et al. Recent advances of three-dimensional bioprinting technology in hepato-pancreato-biliary cancer models. *Front Oncol*. 2023;13:1143600. doi: 10.3389/fonc.2023.1143600

65. Kim MH, Singh YP, Celik N, et al. High-throughput bioprinting of spheroids for scalable tissue fabrication. *Nat Commun*. 2024;15(1):10083. doi: 10.1038/s41467-024-54504-7

66. Lekkala VKR, Shrestha S, Al Qaryoute A, et al. Enhanced maturity and functionality of vascular human liver organoids through 3D bioprinting and pillar plate culture. *ACS Biomater Sci Eng*. 2025;11(1):506-517. doi: 10.1021/acsbiomaterials.4c01658

67. Kang SY, Kimura M, Shrestha S, et al. A pillar and perfusion plate platform for robust human organoid culture and analysis. *Adv Healthc Mater*. 2024;13(21):e2302502. doi: 10.1002/adhm.202302502

68. Shrestha S, Lekkala VKR, Acharya P, Kang SY, Vanga MG, Lee MY. Reproducible generation of human liver organoids (HLOs) on a pillar plate platform via microarray 3D bioprinting. *Lab Chip*. 2024;24(10):2747-2761. doi: 10.1039/d4lc00149d

69. Gao Z, Liu X, Zhao H, et al. Synthesis of easily-processable collagen bio-inks using ionic liquid for 3D bioprinted liver tissue models with branched vascular networks. *Sci China Chem*. 2023;66(5):1489-1499. doi: 10.1007/s11426-022-1472-6

70. Yan J, Ye Z, Lu Y, et al. 3D bioprinting lobule-like hepatorganoids with induced vascularization for orthotopic implantation. *Mater Today Bio*. 2025;31:101515. doi: 10.1016/j.mtbio.2025.101515

71. Brumberg VA, Bikmulina PY, Pozdnyakov AA, et al. Scaling liver bioprinting: a guide for usage of the hepatic extracellular matrix as a bioink. Review. *Int J Bioprint*. 2025;11(1):57-83. doi: 10.36922/ijb.4343

72. Zhang Y, Li L, Dong L, et al. Hydrogel-based strategies for liver tissue engineering. *Chem Bio Eng*. 2024;1(11):887-915. doi: 10.1021/cbe.4c00079

73. Cross-Najafi AA, Farag K, Chen AM, et al. The long road to develop custom-built livers: current status of 3D liver bioprinting. *Transplantation*. 2024;108(2):357-368. doi: 10.1097/tp.0000000000004668

74. Li W, Liu Z, Tang F, et al. Application of 3D bioprinting in liver diseases. *Micromachines (Basel)*. 2023;14(8):1648. doi: 10.3390/mi14081648

75. Willemse J, van der Laan LJW, de Jonge J, Verstegen MMA. Design by nature: emerging applications of native liver extracellular matrix for cholangiocyte organoid-based regenerative medicine. *Bioengineering (Basel)*. 2022;9(3):110. doi: 10.3390/bioengineering9030110

76. Shi W, Zhang Z, Wang X. The prospect of hepatic decellularized extracellular matrix as a bioink for liver 3D bioprinting. *Biomolecules*. 2024;14(8):1019. doi: 10.3390/biom14081019

77. Kim Y, Kang M, Mamo MG, Adisasmita M, Huch M, Choi D. Liver organoids: current advances and future applications for hepatology. *Clin Mol Hepatol*. 2025;31(Suppl):S327-S348. doi: 10.3350/cmh.2024.1040

78. Li G, He J, Shi J, et al. Bioprinting functional hepatocyte organoids derived from human chemically induced pluripotent stem cells to treat liver failure. *Gut*. 2025; 74(7):1150-1164. doi: 10.1136/gutjnl-2024-333885

79. Sun H, Sun L, Ke X, et al. Prediction of clinical precision chemotherapy by patient-derived 3D bioprinting models of colorectal cancer and its liver metastases. *Adv Sci (Weinh)*. 2024;11(2):e2304460. doi: 10.1002/advs.202304460

80. Chen F, Wei X, Chen K, Wang L, Xu M. Massive fabrication of functional hepatic cancer spheroids by micropatterned GelMA hydrogel chip for drug screening. *Colloids Surf B Biointerfaces*. 2024;244:114171. doi: 10.1016/j.colsurfb.2024.114171

81. Yeo M, Sarkar A, Singh YP, Derman ID, Datta P, Ozbolat IT. Synergistic coupling between 3D bioprinting and vascularization strategies. *Biofabrication*. 2023;16(1):e2302506. doi: 10.1088/1758-5090/ad0b3f

82. Reza HA, Santangelo C, Iwasawa K, et al. Multi-zonal liver organoids from human pluripotent stem cells. *Nature*. 2025; 641(8065):1258-1267.
doi: 10.1038/s41586-025-08850-1

83. Falandt M, Bernal PN, Longoni A, et al. Hybrid supramolecular-covalent bioresin promotes cell migration and self-assembly in light-based volumetric bioprinted constructs. preprint. *bioRxiv*. 2025.
doi: 10.1101/2025.01.06.631505

84. Skylar-Scott MA, Huang JY, Lu A, et al. Orthogonally induced differentiation of stem cells for the programmatic patterning of vascularized organoids and bioprinted tissues. *Nature Biomed Eng*. 2022;6(4):449-462.
doi: 10.1038/s41551-022-00856-8

85. Urkasemsin G, Rungarunlert S, Ferreira JN. Bioprinting strategies for secretory epithelial organoids. *Methods Mol Biol*. 2020;2140:243-249.
doi: 10.1007/978-1-0716-0520-2_16

86. Klangprapan J, Souza GR, Ferreira JN. Bioprinting salivary gland models and their regenerative applications. *BDJ Open*. 2024;10(1):39.
doi: 10.1038/s41405-024-00219-2

87. Liu N, Huang S, Yao B, Xie J, Wu X, Fu X. 3D bioprinting matrices with controlled pore structure and release function guide in vitro self-organization of sweat gland. *Sci Rep*. 2016;6:34410.
doi: 10.1038/srep34410

88. Dai R, Chen W, Chen Y, et al. 3D bioprinting platform development for high-throughput cancer organoid models construction and drug evaluation. *Biofabrication*. 2024;16(3):34410.
doi: 10.1088/1758-5090/ad51a6

89. Shiwarski DJ, Hudson AR, Tashman JW, et al. 3D bioprinting of collagen-based microfluidics for engineering fully-biologic tissue systems. *bioRxiv*. 2024.
doi: 10.1101/2024.01.26.577422

90. Maciel BR, Grimm A, Oelschlaeger C, Schepers U, Willenbacher N. Targeted micro-heterogeneity in bioinks allows for 3D printing of complex constructs with improved resolution and cell viability. *Biofabrication*. 2023;15(4):042004.
doi: 10.1088/1758-5090/acee22

91. Markstedt K, Mantas A, Tournier I, Martínez Ávila H, Hägg D, Gatenholm P. 3D bioprinting human chondrocytes with nanocellulose-alginate bioink for cartilage tissue engineering applications. *Biomacromolecules*. 2015;16(5):1489-96.
doi: 10.1021/acs.biomac.5b00188

92. Maharjan S, Ma C, Singh B, et al. Advanced 3D imaging and organoid bioprinting for biomedical research and therapeutic applications. *Adv Drug Deliv Rev*. 2024;208:115237.
doi: 10.1016/j.addr.2024.115237

93. Gugulothu SB, Chatterjee K. Visible light-based 4D-bioprinted tissue scaffold. *ACS Macro Lett*. 2023;12(4):494-502.
doi: 10.1021/acsmacrolett.3c00036

94. Wang D, Guo Y, Zhu J, et al. Hyaluronic acid methacrylate/pancreatic extracellular matrix as a potential 3D printing bioink for constructing islet organoids. *Acta Biomater*. 2023;165:86-101.
doi: 10.1016/j.actbio.2022.06.036

95. Kim M, Cho S, Hwang DG, et al. Bioprinting of bespoke islet-specific niches to promote maturation of stem cell-derived islets. *Nat Commun*. 2025;16(1):1430.
doi: 10.1038/s41467-025-56665-5

96. Reid JA, Mollica PA, Bruno RD, Sachs PC. Consistent and reproducible cultures of large-scale 3D mammary epithelial structures using an accessible bioprinting platform. *Breast Cancer Res*. 2018;20(1):122.
doi: 10.1186/s13058-018-1045-4

97. Shi W, Mirza S, Kuss M, et al. Embedded bioprinting of breast tumor cells and organoids using low-concentration collagen-based bioinks. *Adv Healthc Mater*. 2023;12(26):e2300905.
doi: 10.1002/adhm.202300905

98. Zhang Y, Li G, Wang J, Zhou F, Ren X, Su J. Small joint organoids 3D bioprinting: construction strategy and application. *Small*. 2024;20(8):e2302506.
doi: 10.1002/smll.202302506

99. Bertassoni LE. Bioprinting of complex multicellular organs with advanced functionality-recent progress and challenges ahead. *Adv Mater (Deerfield Beach, Fla)*. 2022;34(3):e2101321.
doi: 10.1002/adma.202101321

100. Freedman BS, Brooks CR, Lam AQ, et al. Modelling kidney disease with CRISPR-mutant kidney organoids derived from human pluripotent epiblast spheroids. *Nat Commun*. 2015;6:8715.
doi: 10.1038/ncomms9715

101. Votanopoulos KI, Forsythe S, Sivakumar H, et al. Model of patient-specific immune-enhanced organoids for immunotherapy screening: feasibility study. *Ann Surg Oncol*. 2020;27(6):1956-1967.
doi: 10.1245/s10434-019-08143-8

102. Childs CJ, Poling HM, Chen K, et al. Coordinated differentiation of human intestinal organoids with functional enteric neurons and vasculature. *Cell Stem Cell*. 2025;32(4):640-651.e9.
doi: 10.1016/j.stem.2025.02.007

103. Park HS, Park JH, Oh M-K, Yu K-R. Advancements in 3D bioprinting for precision medicine: enhancing patient-derived organoids and extracellular vesicle applications in inflammatory diseases. Article. *Int J Bioprint*. 2024;10(5)4054.
doi: 10.36922/ijb.4054

104. Datta P, Dey M, Ataie Z, Unutmaz D, Ozbolat IT. 3D bioprinting for reconstituting the cancer microenvironment. *NPJ Precis Oncol*. 2020;4:18.
doi: 10.1038/s41698-020-0121-2

105. Augustine R, Kalva SN, Ahmad R, et al. 3D bioprinted cancer models: revolutionizing personalized cancer therapy. *Transl Oncol*. 2021;14(4):101015.
doi: 10.1016/j.tranon.2021.101015

106. Qazi TH, Blatchley MR, Davidson MD, et al. Programming hydrogels to probe spatiotemporal cell biology. *Cell Stem Cell*. 2022;29(5):678-691.
doi: 10.1016/j.stem.2022.03.013

107. Gopalakrishnan S, Bakke I, Hansen MD, et al. Comprehensive protocols for culturing and molecular biological analysis of IBD patient-derived colon epithelial organoids. *Front Immunol*. 2023;14:1097383.
doi: 10.3389/fimmu.2023.1097383

108. Caire R, Audoux E, Courbon G, et al. YAP/TAZ: key players for rheumatoid arthritis severity by driving fibroblast like synoviocytes phenotype and fibro-inflammatory response. *Front Immunol*. 2021;12:791907.
doi: 10.3389/fimmu.2021.791907

109. Günther C, Winner B, Neurath MF, Stappenbeck TS. Organoids in gastrointestinal diseases: from experimental models to clinical translation. *Gut*. 2022;71(9): 1892-1908.
doi: 10.1136/gutjnl-2021-326560

110. Sachs N, Tsukamoto Y, Kujala P, Peters PJ, Clevers H. Intestinal epithelial organoids fuse to form self-organizing tubes in floating collagen gels. *Development*. 2017;144(6):1107-1112.
doi: 10.1242/dev.143933

111. Niklinska-Schirtz BJ, Venkateswaran S, Anbazhagan M, et al. Ileal derived organoids from Crohn's disease patients show unique transcriptomic and secretomic signatures. *Cell Mol Gastroenterol Hepatol*. 2021;12(4):1267-1280.
doi: 10.1016/j.jcmgh.2021.06.018

112. Taebnia N, Zhang R, Kromann EB, Dolatshahi-Pirouz A, Andresen TL, Larsen NB. Dual-material 3D-printed intestinal model devices with integrated villi-like scaffolds. *ACS Appl Mater Interfaces*. 2021;13(49): 8434-58446.
doi: 10.1021/acsami.1c22185

113. Brassard JA, Nikolaev M, Hübscher T, Hofer M, Lutolf MP. Recapitulating macro-scale tissue self-organization through organoid bioprinting. *Nat Mater*. 2021;20(1):22-29.
doi: 10.1038/s41563-020-00803-5

114. Carvalho MR, Yan L-P, Li B, et al. Gastrointestinal organs and organoids-on-a-chip: advances and translation into the clinics. Review. *Biofabrication*. 2023;15(4):042004.
doi: 10.1088/1758-5090/acf8fb

115. Xiaoshuai L, Qiushi W, Rui W. Advantages of CRISPR-Cas9 combined organoid model in the study of congenital nervous system malformations. *Front Bioeng Biotechnol*. 2022;10:932936.
doi: 10.3389/fbioe.2022.932936

116. Gopal S, Rodrigues AL, Dordick JS. Exploiting CRISPR Cas9 in three-dimensional stem cell cultures to model disease. *Front Bioeng Biotechnol*. 2020;8:692.
doi: 10.3389/fbioe.2020.00692

117. Schene IF, Joore IP, Oka R, et al. Prime editing for functional repair in patient-derived disease models. *Nat Commun*. 2020;11(1):5352.
doi: 10.1038/s41467-020-19136-7

118. Inak G, Rybak-Wolf A, Lisowski P, et al. Defective metabolic programming impairs early neuronal morphogenesis in neural cultures and an organoid model of Leigh syndrome. *Nat Commun*. 2021;12(1):1929.
doi: 10.1038/s41467-021-22117-z

119. Zhang W, Ma L, Yang M, et al. Cerebral organoid and mouse models reveal a RAB39b-PI3K-mTOR pathway-dependent dysregulation of cortical development leading to macrocephaly/autism phenotypes. *Genes Dev*. 2020;34(7-8):580-597.
doi: 10.1101/gad.332494.119

120. An HL, Kuo HC, Tang TK. Modeling human primary microcephaly with hiPSC-derived brain organoids carrying CPAP-E1235V disease-associated mutant protein. *Front Cell Dev Biol*. 2022;10:830432.
doi: 10.3389/fcell.2022.830432

121. Cidonio G, Glinka M, Dawson JI, Oreffo ROC. The cell in the ink: Improving biofabrication by printing stem cells for skeletal regenerative medicine. *Biomater*. 2019;209:10-24.
https://doi.org/10.1016/j.biomaterials.2019.04.009

122. Ahn CB, Lee J-H, Kim JH, et al. Development of a 3D subcutaneous construct containing insulin-producing beta cells using bioprinting. *Bio-Des Manuf*. 2022;5(2): 265-276.
doi: 10.1007/s42242-021-00178-9

123. Enrico A, Voulgaris D, Ostmans R, et al. 3D microvascularized tissue models by laser-based cavitation molding of collagen. *Adv Mater (Deerfield Beach, Fla)*. 2022;34(11):e2109823.
doi: 10.1002/adma.202109823

124. Bai L, Zhou D, Li G, Liu J, Chen X, Su J. Engineering bone/cartilage organoids: strategy, progress, and application. *Bone Res*. 2024;12(1):66.
doi: 10.1038/s41413-024-00376-y

125. O'Connor C, Brady E, Zheng Y, Moore E, Stevens KR. Engineering the multiscale complexity of vascular networks. *Nat Rev Mater*. 2022;7(9):702-716.
doi: 10.1038/s41578-022-00447-8

126. Michael S, Sorg H, Peck CT, et al. Tissue engineered skin substitutes created by laser-assisted bioprinting form skin-like structures in the dorsal skin fold chamber in mice. *PLoS One*. 2013;8(3):e57741.
doi: 10.1371/journal.pone.0057741

127. Rioux G, Simard M, Morin S, Lorthois I, Guérin SL, Pouliot R. Development of a 3D psoriatic skin model optimized

for infiltration of IL-17A producing T cells: focus on the crosstalk between T cells and psoriatic keratinocytes. *Acta Biomater*. 2021;136:210-222.
doi: 10.1016/j.actbio.2021.09.018

128. Shin JU, Abaci HE, Herron L, et al. Recapitulating T cell infiltration in 3D psoriatic skin models for patient-specific drug testing. *Sci Rep*. 2020;10(1):4123.
doi: 10.1038/s41598-020-60275-0

129. Lorthois I, Simard M, Morin S, Pouliot R. Infiltration of T cells into a three-dimensional psoriatic skin model mimics pathological key features. *Int J Mol Sci*. 2019;20(7):1670.
doi: 10.3390/ijms20071670

130. Gong L, Li J, Zhang J, et al. An interleukin-4-loaded bi-layer 3D printed scaffold promotes osteochondral regeneration. *Acta Biomater*. 2020;117:246-260.
doi: 10.1016/j.actbio.2020.09.039

131. Derman ID, Rivera T, Garriga Cerda L, et al. Advancements in 3D skin bioprinting: processes, bioinks, applications and sensor integration. *Int J Extrem Manuf*. 2025;7(1):012009.
doi: 10.1088/2631-7990/ad878c

132. Zhou Z, Pang Y, Ji J, et al. Harnessing 3D in vitro systems to model immune responses to solid tumours: a step towards improving and creating personalized immunotherapies. *Nat Rev Immunol*. 2024;24(1):18-32.
doi: 10.1038/s41577-023-00896-4

133. Zhao K-y, Du Y-x, Cao H-m, Su L-y, Su X-l, Li X. The biological macromolecules constructed Matrigel for cultured organoids in biomedical and tissue engineering. Article. *Colloids Surf B Biointerfaces*. 2025;247:114435.
doi: 10.1016/j.colsurfb.2024.114435

134. Di Piazza E, Pandolfi E, Cacciotti I, et al. Bioprinting technology in skin, heart, pancreas and cartilage tissues: progress and challenges in clinical practice. *Int J Environ Res Public Health*. 2021;18(20):10806.
doi: 10.3390/ijerph182010806

135. Wang Y, Li H, Zhang J, Chen M, Pan Y, Lou X. 3D bioprinting inner ear organ of corti organoids induce hair cell regeneration. *J Biomed Mater Res A*. 2025;113(3):e37892.
doi: 10.1002/jbm.a.37892

136. Shukla P, Yeleswarapu S, Heinrich MA, Prakash J, Pati F. Mimicking tumor microenvironment by 3D bioprinting: 3D cancer modeling. *Biofabrication*. 2022;14(3):6d11.
doi: 10.1088/1758-5090/ac6d11

137. Lee Y, Min J, Kim S, Park W, Ko J, Jeon NL. Recapitulating the cancer-immunity cycle on a chip. *Adv Healthc Mater*. 2025;14(1):e2401927.
doi: 10.1002/adhm.202401927

138. Fan H, Demirci U, Chen P. Emerging organoid models: leaping forward in cancer research. *J Hematol Oncol*. 2019;12(1):142.
doi: 10.1186/s13045-019-0832-4

139. Mohamed E-T, Syed Arman R, Rasha B, et al. Unraveling the tumor microenvironment: insights into cancer metastasis and therapeutic strategies. *Cancer Lett*. 2024;591:216894.
doi: 10.1016/j.canlet.2024.216894

140. Wu X, Jin Z, Li B, et al. Deciphering of intra-tumoural heterogeneity and the interplay between metastasis-associated meta-program and myofibroblasts in gastric cancer. *Clin Transl Med*. 2025;15(5):e70319.
doi: 10.1002/ctm2.70319

141. Julia AL, Lance LM, Rakesh KJ. Compressive stresses in cancer: characterization and implications for tumour progression and treatment. *Nat Rev Cancer*. 2024;24(11):768-791.
doi: 10.1038/s41568-024-00745-z

142. Francisco B, Joana C, Maria M, João JS, Carla V. 3D bioprinting models for glioblastoma: from scaffold design to therapeutic application. *Adv Mater*. 2025;37(18):e2501994.
doi: 10.1002/adma.202501994

143. Yan L, Haijun C, Haitao C. Precision spatial control of tumor-stroma interactions in cancer models via 3D bioprinting for advanced research and therapy. *Adv Funct Mater*. 2025;2503391.
doi: 10.1002/adfm.202503391

144. Rong J, Xia L, Qian Z, et al. Anti-tumor immune potentiation targets-engineered nanobiotechnologies: design principles and applications. *Prog Mater Sci*. 2024;142:101230.
doi: 10.1016/j.pmatsci.2023.101230

145. Pengcheng Z, Xuanlong D, Weilu J, Kun F, Yewei Z. Engineered extracellular vesicles for targeted reprogramming of cancer-associated fibroblasts to potentiate therapy of pancreatic cancer. *Signal Transduct Target Ther*. 2024;9(1):1.
doi: 10.1038/s41392-024-01872-7

146. Hermida MA, Kumar JD, Schwarz D, et al. Three dimensional in vitro models of cancer: bioprinting multilineage glioblastoma models. *Adv Biol Regul*. 2020;75:100658.
doi: 10.1016/j.jbior.2019.100658

147. Sun Q, Tan SH, Chen Q, et al. Microfluidic formation of coculture tumor spheroids with stromal cells as a novel 3D tumor model for drug testing. *ACS Biomater Sci Eng*. 2018;4(12):4425-4433.
doi: 10.1021/acsbiomaterials.8b00904

148. Godier C, Baka Z, Lamy L, et al. A 3D bio-printed-based model for pancreatic ductal adenocarcinoma. *Diseases*. 2024;12(9):206.
doi: 10.3390/diseases12090206

149. Meng F, Meyer CM, Joung D, Vallera DA, McAlpine MC, Panoskaltsis-Mortari A. 3D bioprinted in vitro metastatic models via reconstruction of tumor microenvironments. *Adv Mater (Deerfield Beach, Fla)*. 2019;31(10):e1806899.
doi: 10.1002/adma.201806899

150. Drost J, Clevers H. Organoids in cancer research. *Nat Rev Cancer*. 2018;18(7):407-418.
doi: 10.1038/s41568-018-0007-6

151. Li Y, Liu J, Xu S, Wang J. 3D bioprinting: an important tool for tumor microenvironment research. *Int J Nanomed*. 2023;18:8039-8057. doi: 10.2147/ijn.S435845

152. Heinrich MA, Bansal R, Lammers T, Zhang YS, Michel Schiffelers R, Prakash J. 3D-bioprinted mini-brain: a glioblastoma model to study cellular interactions and therapeutics. *Adv Mater (Deerfield Beach, Fla)*. 2019;31(14):e1806590. doi: 10.1002/adma.201806590

153. Zhou X, Zhu W, Nowicki M, et al. 3D bioprinting a cell-laden bone matrix for breast cancer metastasis study. *ACS Appl Mater Interfaces*. 2016;8(44):30017-30026. doi: 10.1021/acsami.6b10673

154. Hughes AM, Kolb AD, Shupp AB, Shine KM, Bussard KM. Printing the pathway forward in bone metastatic cancer research: applications of 3D engineered models and bioprinted scaffolds to recapitulate the bone-tumor niche. *Cancers (Basel)*. 2021;13(3):507. doi: 10.3390/cancers13030507

155. Mazzocchi A, Soker S, Skardal A. 3D bioprinting for high-throughput screening: drug screening, disease modeling, and precision medicine applications. *Appl Phys Rev*. 2019;6(1):011302. doi: 10.1063/1.5056188

156. Kim J, Jang J, Cho D-W. Recapitulating the cancer microenvironment using bioprinting technology for precision medicine. *Micromachines*. 2021;12(9):1122. doi: 10.3390/mi12091122

157. Langer EM, Allen-Petersen BL, King SM, et al. Modeling tumor phenotypes in vitro with three-dimensional bioprinting. *Cell Rep*. 2019;26(3):608-623.e6. doi: 10.1016/j.celrep.2018.12.090

158. Calandrini C, Drost J. Normal and tumor-derived organoids as a drug screening platform for tumor-specific drug vulnerabilities. *STAR Protoc*. 2022;3(1):101079. doi: 10.1016/j.xpro.2021.101079

159. Wu P, Asada H, Hakamada M, Mabuchi M. Bioengineering of high cell density tissues with hierarchical vascular networks for ex vivo whole organs. *Adv Mater (Deerfield Beach, Fla)*. 2023;35(9):e2209149. doi: 10.1002/adma.202209149

160. Bjerring JS, Khodour Y, Peterson EA, Sachs PC, Bruno RD. Intercellular mitochondrial transfer contributes to microenvironmental redirection of cancer cell fate. *FEBS J*. 2025;292(9):2306-2322. doi: 10.1111/febs.70002

161. Khan AO, Rodriguez-Romera A, Reyat JS, et al. Human bone marrow organoids for disease modeling, discovery, and validation of therapeutic targets in hematologic malignancies. Article. *Cancer Discov*. 2023;13(2):364-385. doi: 10.1158/2159-8290.Cd-22-0199

162. Chen H, Wu Z, Gong Z, et al. Acoustic bioprinting of patient-derived organoids for predicting cancer therapy responses. *Adv Healthc Mater*. 2022;11(13):2102784. doi: 10.1002/adhm.202102784

163. Choi Y-m, Lee H, Ann M, Song M, Rheey J, Jang J. 3D bioprinted vascularized lung cancer organoid models with underlying disease capable of more precise drug evaluation. *Biofabrication*. 2023;15(3):034104. doi: 10.1088/1758-5090/acd95f

164. Jungeun K, Hoe Suk K, Ga Yeon K, et al. Abstract P5-02-02: development of automated 3d high-throughput drug screening platform for patient-derived breast cancer organoids. *Cancer Res*. 2022;82:2. doi: 10.1158/1538-7445.sabcs21-p5-02-02

165. Hou S, Tiriac H, Sridharan BP, et al. Advanced development of primary pancreatic organoid tumor models for high-throughput phenotypic drug screening. *SLAS Discov*. 2018;23(6):574-584. doi: 10.1177/2472555218766842

166. Arutyunyan I, Jumaniyazova E, Makarov A, Fatkhudinov T. In vitro models of head and neck cancer: from primitive to most advanced. *J Pers Med*. 2023;13(11):1575. doi: 10.3390/jpm13111575

167. Azhakesan A, Kern J, Mishra A, et al. 3D bioprinted head and neck squamous cell carcinoma (HNSCC) model using tunicate derived nanocellulose (NC) bioink. *Adv Healthc Mater*. 2025;14(7):e2403114. doi: 10.1002/adhm.202403114

168. Baka Z, Godier C, Lamy L, et al. A coculture based, 3D bioprinted ovarian tumor model combining cancer cells and cancer associated fibroblasts. *Macromol Biosci*. 2023;23(3):e2200434. doi: 10.1002/mabi.202200434

169. Tebon PJ, Wang B, Markowitz AL, et al. Drug screening at single-organoid resolution via bioprinting and interferometry. *Nat Commun*. 2023;14(1):3168. doi: 10.1038/s41467-023-38832-8

170. Nhan P, Jenny JH, Bobby T, et al. A simple high-throughput approach identifies actionable drug sensitivities in patient-derived tumor organoids. *Commun Biol*. 2019;2(1):1. doi: 10.1038/s42003-019-0305-x

171. Krendl FJ, Primavesi F, Oberhuber R, et al. The importance of preclinical models for cholangiocarcinoma drug discovery. *Expert Opin Drug Discov*. 2025;20(2):205-216. doi: 10.1080/17460441.2025.2457637

172. Joshi P, Nascimento HSD, Kang SY, et al. Dynamic culture of bioprinted liver tumor spheroids in a pillar/perfusion plate for predictive screening of anticancer drugs. *Biotechnol Bioeng*. 2025;122(4):995-1009. doi: 10.1002/bit.28924

173. Kalla J, Pfneissl J, Mair T, Tran L, Egger G. A systematic review on the culture methods and applications of 3D

tumoroids for cancer research and personalized medicine. *Cell Oncol*. 2025;48(1):1-26.
doi: 10.1007/s13402-024-00960-8

174. Maloney E, Clark C, Sivakumar H, et al. Immersion bioprinting of tumor organoids in multi-well plates for increasing chemotherapy screening throughput. *Micromachines*. 2020;11(2):208.
doi: 10.3390/mi11020208

175. Gong Z, Mao Y, Huang L, et al. Acoustic printing of patient-derived organoids that preserve tumor microenvironment for personalized drug screening. *Adv Mater Technol*. 2023;8(11):2201942.
doi: 10.1002/admt.202201942

176. Nieto D, Jiménez G, Moroni L, López-Ruiz E, Gálvez-Martín P, Marchal JA. Biofabrication approaches and regulatory framework of metastatic tumor-on-a-chip models for precision oncology. *Med Res Rev*. 2022;42(5):1978-2001.
doi: 10.1002/med.21914

177. Wang F, Song P, Wang J, et al. Organoid bioinks: construction and application. *Biofabrication*. 2024;16(3):3467c.
doi: 10.1088/1758-5090/ad467c

178. Wu Z, Liu R, Shao N, Zhao Y. Developing 3D bioprinting for organs-on-chips. *Lab Chip*. 2025;25(5):1081-1096.
doi: 10.1039/d4lc00769g

179. O'Connor CE, Zhang F, Neufeld A, et al. Bioprinted platform for parallelized screening of engineered microtissues in vivo. *Cell Stem Cell*. 2025;1;32(5):838-853.e6.
doi: 10.1016/j.stem.2025.03.002

180. Capeling MM, Czerwinski M, Huang S, et al. Nonadhesive alginate hydrogels support growth of pluripotent stem cell-derived intestinal organoids. *Stem Cell Rep*. 2019;12(2):381-394.
doi: 10.1016/j.stemcr.2018.12.001

181. Baptista LS, Porrini C, Kronemberger GS, Kelly DJ, Perrault CM. 3D organ-on-a-chip: the convergence of microphysiological systems and organoids. *Front Cell Dev Biol*. 2022;10:1043117.
doi: 10.3389/fcell.2022.1043117

182. Bengtsson A, Andersson R, Rahm J, Ganganna K, Andersson B, Ansari D. Organoid technology for personalized pancreatic cancer therapy. *Cell Oncol (Dordr)*. 2021;44(2):251-260.
doi: 10.1007/s13402-021-00585-1

183. Mahdavi R, Hashemi-Najafabadi S, Ghiass MA, et al. Design, fabrication, and characterization of a user-friendly microfluidic device for studying liver zonation-on-chip (ZoC). *Biomed Microdevices*. 2025;27(1):8.
doi: 10.1007/s10544-025-00738-1

184. Myszczyszyn A, Muench A, Lehmann V, et al. A hollow fiber membrane-based liver organoid-on-a-chip model for examining drug metabolism and transport. *Biofabrication*. 2025;17(2):206.
doi: 10.1088/1758-5090/adc3ce

185. Zheng F, Xiao Y, Liu H, Fan Y, Dao M. Patient-specific organoid and organ-on-a-chip: 3D cell-culture meets 3D printing and numerical simulation. *Adv Biol (Weinh)*. 2021;5(6):e2000024.
doi: 10.1002/adbi.202000024

186. Park B, Park J, Han S, et al. Advances in organoid-on-a-chip for recapitulation of human physiological events. *Mater Today*. 2025;84:75-94.
doi: 10.1016/j.mattod.2025.02.002

187. Tonon F, Giobbe GG, Zambon A, et al. In vitro metabolic zonation through oxygen gradient on a chip. *Sci Rep*. 2019;9(1):13557.
doi: 10.1038/s41598-019-49412-6

188. McCarty WJ, Usta OB, Yarmush ML. A microfabricated platform for generating physiologically-relevant hepatocyte zonation. *Sci Rep*. 2016;6(1):26868.
doi: 10.1038/srep26868

189. Mitani S, Takayama K, Nagamoto Y, et al. Human ESC/iPSC-derived hepatocyte-like cells achieve zone-specific hepatic properties by modulation of WNT signaling. *Mol Ther*. 2017;25(6):1420-1433.
doi: 10.1016/j.ymthe.2017.04.006

190. Wang Q, Liu J, Yin W, et al. Microscale tissue engineering of liver lobule models: advancements and applications. *Front Bioeng Biotechnol*. 2023;11:1303053.
doi: 10.3389/fbioe.2023.1303053

191. Saw TB, Doostmohammadi A, Nier V, et al. Topological defects in epithelia govern cell death and extrusion. *Nature*. 2017;544(7649):212-216.
doi: 10.1038/nature21718

192. Gupta K, Ng IC, Balachander GM, et al. Bile canaliculi contract autonomously by releasing calcium into hepatocytes via mechanosensitive calcium channel. *Biomaterials*. 2020;259:120283.
doi: 10.1016/j.biomaterials.2020.120283

193. Warmflash A, Sorre B, Etoc F, Siggia ED, Brivanlou AH. A method to recapitulate early embryonic spatial patterning in human embryonic stem cells. *Nat Methods*. 2014;11(8):847-54.
doi: 10.1038/nmeth.3016

194. Kang R, Park S, Shin S, Bak G, Park JC. Electrophysiological insights with brain organoid models: a brief review. *BMB Rep*. 2024;57(7):311-317.
doi: 10.5483/BMBRep.2024-0077

195. Zhou J, Vijayavenkataraman S. 3D-printable conductive materials for tissue engineering and biomedical applications. *Bioprinting*. 2021;24:e00166.
doi: 10.1016/j.bprint.2021.e00166

196. Liu P. *3D da yin wei liu kong xin pian xi bao fen xi ping tai de gou jian ji qi ying yong [Construction and Application of a 3D-Printed Microfluidic Chip-Based Cell Analysis Platform]* [dissertation]. Shandong Normal University; 2023. Accessed May 20, 2025

https://d.wanfangdata.com.cn/thesis/vChhUaGVzaXNOZXdTMjAyNDA5MjAxNTE3MjUSCUQwMzAyNDMyOBoIeXRhZmhk ZXM%3D.Accessed XXX.

197. Mai S, Inkielewicz-Stepniak I. Graphene oxide nanoparticles and organoids: a prospective advanced model for pancreatic cancer research. *Int J Mol Sci*. 2024;25(2):1066. doi: 10.3390/ijms25021066

198. Salmon I, Grebenyuk S, Abdel Fattah AR, et al. Engineering neurovascular organoids with 3D printed microfluidic chips. *Lab Chip*. 2022;22(8):1615-1629. doi: 10.1039/d1lc00535a

199. Park YG, Kim S, Min S, et al. Soft 3D bioelectrodes for intraorganoid signal monitoring in cardiac models. *Nano Lett*. 2025;25(16):6481-6490. doi: 10.1021/acs.nanolett.5c00069

200. Lee S, Chung WG, Jeong H, et al. Electrophysiological analysis of retinal organoid development using 3D microelectrodes of liquid metals. *Adv Mater (Deerfield Beach, Fla)*. 2024;36(35):e2404428. doi: 10.1002/adma.202404428

201. Dong K, Liu WC, Su Y, et al. Scalable electrophysiology of millimeter-scale animals with electrode devices. *BME Front*. 2023;4:0034. doi: 10.34133/bmef.0034

202. Acha C, George D, Diaz LC, et al. Neuromodulation in neural organoids with shell MEAs. *bioRxiv*. 2025. doi: 10.1101/2025.02.18.637712

203. Saleh MS, Ritchie SM, Nicholas MA, et al. CMU array: a 3D nanoprinted, fully customizable high-density microelectrode array platform. *Sci Adv*. 2022;8(40):eabj4853. doi: 10.1126/sciadv.abj4853

204. Patel D, Shetty S, Acha C, et al. Microinstrumentation for brain organoids. *Adv Healthc Mater*. 2024;13(21):e2302456. doi: 10.1002/adhm.202302456

205. Li TL, Liu Y, Forro C, et al. Stretchable mesh microelectronics for the biointegration and stimulation of human neural organoids. *Biomaterials*. 2022;290:121825. doi: 10.1016/j.biomaterials.2022.121825

206. Mao M, Han K, Gao J, et al. Engineering highly aligned and densely populated cardiac muscle bundles via fibrin remodeling in 3D-printed anisotropic microfibrous lattices. *Adv Mater (Deerfield Beach, Fla)*. 2025;37(9):e2419380. doi: 10.1002/adma.202419380

207. Zilinskaite N, Shukla RP, Baradoke A. Use of 3D printing techniques to fabricate implantable microelectrodes for electrochemical detection of biomarkers in the early diagnosis of cardiovascular and neurodegenerative diseases. *ACS Meas Sci Au*. 2023;3(5):315-336. doi: 10.1021/acsmeasuresciau.3c00028

208. Kalmykov A, Huang C, Bliley J, et al. Organ-on-e-chip: three-dimensional self-rolled biosensor array for electrical interrogations of human electrogenic spheroids. *Sci Adv*. 2019;5(8):eaax0729. doi: 10.1126/sciadv.aax0729

209. Spedicati M, Tivano F, Zoso A, et al. 3D bioartificial stretchable scaffolds mimicking the mechanical hallmarks of human cardiac fibrotic tissue. *Int J Bioprint*. 2024;10(3):2247. doi: 10.36922/ijb.2247

210. Vashistha R, Kumar P, Dangi AK, Sharma N, Chhabra D, Shukla P. Quest for cardiovascular interventions: precise modeling and 3D printing of heart valves. *J Biol Eng*. 2019;13:12. doi: 10.1186/s13036-018-0132-5

211. Chen A, Su J, Li Y, et al. 3D/4D printed bio-piezoelectric smart scaffolds for next-generation bone tissue engineering. *Int J Extreme Manuf*. 2023;5(3):8. doi: 10.1088/2631-7990/acd88f

212. Simonneau C, Duschmalé M, Gavrilov A, et al. Investigating receptor-mediated antibody transcytosis using blood-brain barrier organoid arrays. *Fluids Barriers CNS*. 2021;18(1):43. doi: 10.1186/s12987-021-00276-x

213. Shen C, Zhang ZJ, Li XX, et al. Intersection of nanomaterials and organoids technology in biomedicine. *Front Immunol*. 2023;14:1172262. doi: 10.3389/fimmu.2023.1172262

214. Paone LS, Benmassaoud MM, Curran A, Vega SL, Galie PA. A 3D-printed blood-brain barrier model with tunable topology and cell-matrix interactions. *Biofabrication*. 2023;16(1):260. doi: 10.1088/1758-5090/ad0260

215. Marino A, Tricinci O, Battaglini M, et al. A 3D real-scale, biomimetic, and biohybrid model of the blood-brain barrier fabricated through two-photon lithography. *Small*. 2018;14(6):2959. doi: 10.1002/smll.201702959

216. Carton F, Malatesta M. In vitro models of biological barriers for nanomedical research. *Int J Mol Sci*. 2022;23(16):8910. doi: 10.3390/ijms23168910

217. Sharma A, Fernandes DC, Reis RL, et al. Cutting-edge advances in modeling the blood-brain barrier and tools for its reversible permeabilization for enhanced drug delivery into the brain. *Cell Biosci*. 2023;13(1):137. doi: 10.1186/s13578-023-01079-3

218. Reina-Mahecha A, Beers MJ, van der Veen HC, Zuhorn IS, van Kooten TG, Sharma PK. A review of the role of bioreactors for iPSCs-based tissue-engineered articular cartilage. *Tissue Eng Regen Med*. 2023;20(7):1041-1052. doi: 10.1007/s13770-023-00573-6

219. Xiu Z, Yang Q, Xie F, Han F, He W, Liao W. Revolutionizing digestive system tumor organoids research: exploring

the potential of tumor organoids. *J Tissue Eng*. 2024;15:20417314241255470.
doi: 10.1177/20417314241255470

220. Labour MN, Le Guilcher C, Aid-Launais R, et al. Development of 3D hepatic constructs within polysaccharide-based scaffolds with tunable properties. *Int J Mol Sci*. 2020;21(10):3644.
doi: 10.3390/ijms21103644

221. Shin J, Kang R, Hyun K, et al. Machine learning-enhanced optimization for high-throughput precision in cellular droplet bioprinting. Adv Sci (Weinh). 2025:12(20):e2412831.
doi: 10.1002/advs.202412831

222. Hwang HH, You S, Ma X, et al. High throughput direct 3D bioprinting in multiwell plates. *Biofabrication*. 2021;13(2):2200434.
doi: 10.1088/1758-5090/ab89ca

223. Hu W, Cao M, Liao L, et al. An automated digital microfluidic system based on inkjet printing. *Micromachines (Basel)*. 2024;15(11):2247.
doi: 10.3390/mi15111285

224. Bai L, Wu Y, Li G, Zhang W, Zhang H, Su J. AI-enabled organoids: Construction, analysis, and application. *Bioact Mater*. 2024;31:525-548.
doi: 10.1016/j.bioactmat.2023.09.005

225. Ear PH, Marinoni I, Dayton T, et al. NET models meeting 2024 white paper: the current state of neuroendocrine tumour research models and our future aspirations. *Endocr Oncol*. 2024;4(1):e240055.
doi: 10.1530/eo-24-0055

226. Ma W, Lu H, Xiao Y, Wu C. Advancing organoid development with 3D bioprinting. *OR*. 2025;1(1):40004.
doi: 10.36922/or025040004

ACCSCIENCE PUBLISHING

International Journal of Bioprinting

REVIEW ARTICLE

Three-dimensional bioprinting in human-relevant toxicology: Advanced organ models and translational strategies

Yinpeng Le[1,2], Tanqing Long[2,3], Qi Wang[2], Mengcheng Tang[1], Mingyue Pan[2,4], Qingru Song[2,5], Wenrui Ma[5], Yuxin Su[2], Yutian Feng[2], Ni An[5], Wenzhen Yin[5], Xiangdong Kong[1]*, Yunfang Wang[2,5,6]*, and Juan Liu[2,6]*

[1]Zhejiang-Mauritius Joint Research Center for Biomaterials and Tissue Engineering, School of Materials Science and Engineering, Zhejiang Sci-Tech University, Hangzhou, Zhejiang, China

[2]Hepato-Pancreato-Biliary Center, Beijing Tsinghua Changgung Hospital, School of Clinical Medicine, Tsinghua Medicine, Tsinghua University, Beijing, China

[3]Department of Pharmacology, School of Pharmacy, Tongji Medical College, Huazhong University of Science and Technology, Wuhan, Hubei, China

[4]State Key Laboratory of Natural Medicines and Jiangsu Key Laboratory of Drug Discovery for Metabolic Diseases, Center of Advanced Pharmaceuticals and Biomaterials, China Pharmaceutical University, Nanjing, Jiangsu, China

[5]Clinical Translational Science Center, Beijing Tsinghua Changgung Hospital, Tsinghua Medicine, Tsinghua University, Beijing, China

[6]Ministry of Education Key Laboratory of Digital Intelligence Hepatology, School of Clinical Medicine, Tsinghua Medicine, Tsinghua University, Beijing, China

***Corresponding authors:**
Juan Liu
(lja02720@btch.edu.cn)

Yunfang Wang
(wangyf008@mail.tsinghua.edu.cn)

Xiangdong Kong
(kongxd@zstu.edu.cn)

Citation: Le Y, Long T, Wang Qi, *et al.* Three-dimensional bioprinting for human-relevant toxicology: Advanced organ models and translational strategies. *Int J Bioprint*. 2025;11(4):99-132. doi: 10.36922/IJB025210209

Received: May 21, 2025
Revised: June 25, 2025
Accepted: July 3, 2025
Published online: July 3, 2025

Copyright: © 2025 Author(s). This is an Open Access article distributed under the terms of the Creative Commons Attribution License, permitting distribution, and reproduction in any medium, provided the original work is properly cited.

Publisher's Note: AccScience Publishing remains neutral with regard to jurisdictional claims in published maps and institutional affiliations.

Abstract

Traditional toxicological testing, which relies on animal models and two-dimensional cell cultures, encounters challenges in accurately predicting human-specific responses due to interspecies variability and the inherent limitations of simplified *in vitro* systems. Three-dimensional (3D) bioprinting has emerged as a transformative approach, facilitating the fabrication of physiologically relevant tissue constructs with precise spatial control over cellular and extracellular matrix components. This review critically examines recent advancements in 3D-bioprinted organ models, such as the liver, kidney, and lung, for toxicological assessments, including their applications in drug safety evaluation, environmental pollutant screening, and nanomaterial risk assessment. We further analyze persistent technical barriers concerning resolution limitations, material biocompatibility, and the simulation of multi-organ interactions. Finally, we propose integrative strategies that combine organ-on-a-chip platforms, artificial intelligence-driven design, and standardized validation protocols, aiming to accelerate the translational potential of bioprinted models in regulatory toxicology.

Keywords: Functional simulation; Organ models; Three-dimensional bioprinting; Toxicology testing

1. Introduction

Toxicity arises from adverse biological events triggered by exposure to biological, physical, or chemical agents and manifests as reversible or irreversible dysfunctions, ranging from transient cellular perturbations to severe organ failure and mortality.[1] These outcomes are governed by the interplay between the absorption, distribution, metabolism, and excretion (ADME) properties of toxicants, as well as their interactions with cellular macromolecules.[2] Toxicology, as the scientific discipline dedicated to evaluating toxicity mechanisms, severity, and frequency, has evolved into a cornerstone of modern pharmacology and chemical safety assessment.[3] However, the escalating demand for toxicity testing, fueled by the annual introduction of over 2000 new chemicals across pharmaceuticals, cosmetics, and industrial sectors, has revealed critical limitations in conventional approaches.[4]

Historically, animal testing served as the gold standard for toxicological evaluations.[5] Although these models provide preliminary safety data, interspecies physiological disparities, such as divergent ADME profiles, metabolic pathways, and lifespans, severely undermine the translatability of animal-derived results to humans.[4] For instance, between 38% and 51% of drug-induced liver injuries remain undetected during preclinical animal trials, culminating in costly late-stage clinical failures or post-market withdrawals.[6] Beyond ethical concerns, animal models are characterized by low throughput, prolonged testing cycles, and high operational costs, prompting an urgent need for human-relevant alternatives.[7]

The "Replacement, Reduction, Refinement" (3R) principles have catalyzed a paradigm shift toward *in vitro* systems.[8–10] The global *in vitro* toxicology testing market, valued at USD 10.1 billion in 2022, is projected to reach USD 17.1 billion by 2028, indicating a compound annual growth rate of 9.5%.[11] Early *in vitro* models, including two-dimensional (2D) monocultures and static three-dimensional (3D) constructs, partially address ethical and throughput challenges; however, they fail to replicate the dynamic cell–cell and cell–extracellular matrix (ECM) interactions and tissue-level complexity of human organs.[12,13] For example, 2D-cultured hepatocytes rapidly dedifferentiate, losing cytochrome P450 activity within hours,[14,15] whereas conventional 3D spheroids often develop hypoxic cores due to inadequate nutrient diffusion. Organ-on-a-chip platforms, which integrate microfluidics and mechanical cues, represent a significant leap forward but encounter scalability issues and limited standardization.[7]

Three-dimensional bioprinting has emerged as a transformative technology to overcome these bottlenecks.[16] By enabling layer-by-layer deposition of living cells, biomaterials, and bioactive factors with micrometer-scale precision, bioprinting constructs physiologically relevant tissue architectures, such as vascularized liver lobules, polarized renal tubules, and alveolar-capillary barriers, that mirror native organ functionality.[17–20] Advanced bioinks, including gelatin methacryloyl (GelMA) and decellularized ECM (dECM)-based hydrogels, provide tunable mechanical properties and biochemical niches that maintain cell viability and phenotypic stability.[21] Integrated microfluidic channels ensure sustained oxygenation and nutrient supply, thereby resolving necrosis issues in thick tissues. Notably, bioprinted models exhibit enhanced predictive accuracy for organ-specific toxicities, as demonstrated by their ability to distinguish structural analogs such as trovafloxacin (hepatotoxic) and levofloxacin (non-toxic), a feat unattainable with traditional models.[22]

This review critically evaluates how 3D bioprinting addresses the limitations of existing *in vitro* toxicology models. We first delineate the research trends and the technological evolution from animal testing to organ-on-a-chip systems, highlighting ongoing challenges in physiological fidelity and scalability, as illustrated in Figure 1. Next, we analyze advancements in bioprinting modalities, such as extrusion, laser-assisted, and stereolithography, as well as bioink design and functional tissue fabrication. A central focus is placed on organ-specific applications, such as liver, kidney, and lung toxicity assessments, where bioprinted models outperform conventional approaches in replicating human pathophysiology. We also address unresolved controversies, including the lack of standardized validation protocols and regulatory acceptance barriers. By synthesizing interdisciplinary innovations in materials science, microfluidics, and artificial intelligence, this work aims to outline a roadmap for translating bioprinted platforms into mainstream toxicological practice.

2. A historical perspective on toxicological paradigms

2.1. The foundational era of toxicology

The nascent form of toxicology arose from rudimentary observations of natural phenomena and early experimental inquiries. In the 16th century, Paracelsus introduced the pivotal principle that "the dose makes the poison," thereby establishing the dose–response relationship as the cornerstone of toxicological science and laying the groundwork for subsequent research in the field.[23] By the late 18th century, British physician Percivall Pott's investigation into scrotal cancer among chimney sweeps

revealed the carcinogenic mechanisms of polycyclic aromatic hydrocarbons, marking the advent of modern toxicological studies.[24] In the early 19th century, French scientist Mathieu Orfila systematically validated the effects of toxins through animal experimentation, whereas Magendie and Claude Bernard explored neurotoxic mechanisms.[25–28] These pioneering studies laid the foundation for the experimental methodologies that underpin modern toxicology.

2.2. The era of animal model dominance

The application of animal models in toxicological research has undergone a significant evolution, evolving from preliminary investigations to routine applications. In 1927, J.W. Trevan, drawing upon Paracelsus's foundational principles, introduced the concept of the median lethal dose (LD_{50}). By employing statistical methodologies, Trevan defined LD_{50} as a universal benchmark for evaluating acute toxicity, laying the groundwork for future advancements in toxicity testing.[29,30] This innovation marked a pivotal shift from qualitative to quantitative toxicological analysis, providing a scientific basis for subsequent evaluations. By the mid-20th century, animal experimentation was established as the cornerstone of toxicological investigations.[31] The LD_{50} test was extensively utilized for categorizing the acute toxicity profiles of industrial compounds and pharmaceutical agents, serving as a vital tool for assessing chemical toxicity.[32,33]

Through animal experiments, researchers obtained foundational knowledge regarding the ADME of drugs, as well as their potential toxicities and adverse effects.[34] During this era, animal testing not only played a critical role in drug development but also supported the toxicity assessment of environmental pollutants. However, growing ethical concerns surrounding the extensive use of animal testing, particularly the ethical dilemmas associated with animal suffering, began to emerge. In 1959, the introduction of the 3R principle initiated a paradigm shift in ethical considerations for animal testing.[31] This principle advocated for minimizing animal usage through alternative methods and refining experimental procedures to alleviate animal suffering, steering toxicological research toward exploring efficient *in vitro* models and alternative approaches to reduce reliance on animal testing.[10]

Despite these ethical considerations, animal models remained integral to toxicological studies for decades.[35] They enabled researchers to simulate complex biological processes and evaluate the toxic effects of substances *in vivo*, providing indispensable support for drug development and environmental safety assessments.[36] Nevertheless, advancements in science and technology have spurred the emergence of *in vitro* models and computational simulations, offering additional options and potential avenues for reducing animal testing. Future research should continue to explore the application potential of these novel methods to facilitate sustainable progress in toxicological research.

2.3. Disruption in *in vitro* models: From cell cultures to organ simulation

Over an extended period, toxicological research principally depended on whole-animal experimentation and human observational studies. However, challenges in accurately replicating complex exposure scenarios, coupled with interspecies and individual variability between humans and various animal models, have impeded a holistic understanding of the toxicological effects of exogenous substances, complicating the research processes. Recent advancements in tissue engineering and molecular biology have facilitated the development of highly refined *in vitro* models that emulate human tissue functionality. These include widely utilized 2D and 3D cell culture systems, organoids, and microfluidic chips. Such innovations are progressively diminishing dependence on conventional animal-based approaches in toxicological research.

2.3.1. Two-dimensional monolayer culture

Two-dimensional cell cultures represent a classical *in vitro* model extensively employed in toxicological investigations. Originating from primary cell lines, cancer-derived cell lines, and stem cells, these systems have become indispensable tools in biological research since Harrison's groundbreaking achievement in animal cell culture in 1901.[37] The discovery of HeLa cells in 1951 initiated the extensive utilization of cancer cell lines as readily accessible experimental platforms.[38] Subsequent milestones included the successful isolation and establishment of mouse and human embryonic stem cell lines in 1981 and 1998, respectively.[39,40] Beyond cellular models, Bruce Ames' development of the bacterial reverse mutation assay in 1975, incorporating a liver microsomal metabolic activation system, enabled efficient high-throughput screening for carcinogenic substances, thereby reducing dependence on mammalian experimental systems.[41,42] In 2007, Zeiger[42] achieved a groundbreaking milestone by reprogramming human somatic cells to generate the first induced pluripotent stem cell (iPSC) lines.

Today, widely adopted 2D cell systems encompass human colorectal adenocarcinoma (Caco-2), Madin–Darby canine kidney (MDCK), human alveolar basal epithelial (A549), and bronchial epithelial (BEAS-2B) cell lines, which serve diverse applications in assessing the toxicity of chemicals, pharmaceuticals, and environmental pollutants. For instance, Caco-2 cells are extensively utilized to investigate intestinal absorption and drug

transport mechanisms,[43] MDCK cells are employed to study epithelial permeability in the intestine and kidneys,[43,44] A549 cells are used to evaluate the toxicity of inhaled substances and nanoparticles (NPs), while BEAS-2B cells remain instrumental in examining the respiratory toxicity of chemical agents.[45] The advantages of 2D cell cultures, including their high-throughput capability and cost-effectiveness, render them ideal for large-scale screening and initial toxicity assessments.[46] However, their limitations, such as alterations in cell morphology and functionality, insufficient barrier properties, and limited metabolic capacity, remain significant challenges that warrant careful consideration.[46,47] Advances such as gene editing, co-culture techniques, and optimized culture conditions have provided partial solutions to these inherent limitations. For example, MDCK cells' permeability and metabolic capabilities have been improved via gene transfection techniques that incorporate transport proteins and metabolic enzymes.[44] Similarly, Deguchi *et al.*[48] leveraged human iPSCs with genome editing to generate cytochrome P450 3A4-knockout iPSCs, which were subsequently differentiated into hepatocyte-like cells and intestinal epithelial-like cells. These models have yielded critical insights into cytochrome P450 3A4-mediated hepatic toxicity in early-stage drug development.

2.3.2. Three-dimensional static models

In conventional 2D cell cultures, cells exhibit adhesion patterns, spatial orientation, morphology, and polarity that substantially differ from their physiological states observed *in vivo*.[47] By contrast, 3D culture systems allow cells to adopt spatially organized arrangements, enabling the dynamic regulation of essential physiological processes across temporal and spatial dimensions, thereby facilitating the reconstitution of organ or tissue functionality.[49] Beyond serving as mere structural scaffolds, 3D culture systems are required to maintain the viability of cells, tissues, and organs by emulating physiological microenvironments, including soluble factor signaling, electrical signal transmission, and extracellular matrix-mediated mechanotransduction.[47,49] Increasingly, research highlights the ability of 3D cell models to reproduce *in vivo*-like cell morphology, thereby underscoring their applicability in toxicological investigations.

Early 3D culture approaches involved incorporating cells derived from animal tissues or immortalized human cell lines into hydrogel matrices.[50] For instance, Astashkina *et al.*[50] encapsulated mouse proximal tubular epithelial cells in hydrogel matrices, generating 3D cell models to evaluate endpoints such as cytochrome P450 activity, metabolite production, and kidney injury molecule-1 biomarker expression. Comparisons with 2D-cultured LLC-PK1 and HEK293 cells revealed that 3D proximal tubular epithelial cell models demonstrated biomarker profiles that more closely resembled *in vivo* observations. However, the study also noted a twofold decline in cell viability within 2 weeks, emphasizing a prevalent limitation associated with static 3D culture methodologies.

2.3.3. Organoids and organ-on-a-chip models

The rapid advancements in materials science and biology have driven the development of organoids and organ-on-a-chip technologies—two pioneering 3D culture systems that offer physiologically relevant models for toxicological research.[51] Organoids are self-organizing, 3D cellular structures originating from pluripotent, embryonic, or adult stem cells. These structures recapitulate the functional, structural, and biological complexity of specific organs, offering physiologically robust *in vitro* platforms for toxicological investigations. Since Sato *et al.*[52] successfully established the first intestinal organoid in 2009, organoid technology has evolved to include diverse organ systems, such as the stomach,[53] lung,[54] brain,[55] liver,[56] heart,[57] and kidneys.[58] In toxicological research, organoids offer unique advantages.[59] For example, airway organoids exposed to microplastic fibers can simulate real-world exposure conditions and developmental processes, highlighting phenomena like organoid encapsulation of microplastics, which are not observable in conventional 2D cell models.[60] This capability enables organoids to provide more accurate and sensitive insights into the impacts of harmful environmental factors on human health, serving as dependable platforms for toxicological evaluations.[7]

Organ-on-a-chip technology, based on microfluidic systems, represents a sophisticated platform for mimicking human organ functionality and drug response mechanisms *in vitro*. By precisely controlling fluid shear stress, mechanical strain, and co-culture conditions, these systems reconstruct organ-specific physiological microenvironments. Notably, organ-on-a-chip devices can simulate the functions of individual organs or integrate multiple chips to construct "body-on-a-chip" systems, facilitating explorations of inter-organ communication and pharmacokinetic dynamics. In toxicological evaluations, this technology holds substantial potential. For instance, lung-on-a-chip models can reproduce the complex and integrated organ-level responses of the lungs to bacteria and inflammatory cytokines introduced into the alveolar space. Meanwhile, the lung model reveals that cyclic mechanical strain exacerbates the toxicity and inflammatory response of the lungs to silica NPs.[61] Additionally, multi-organ chip systems provide a comprehensive framework for assessing

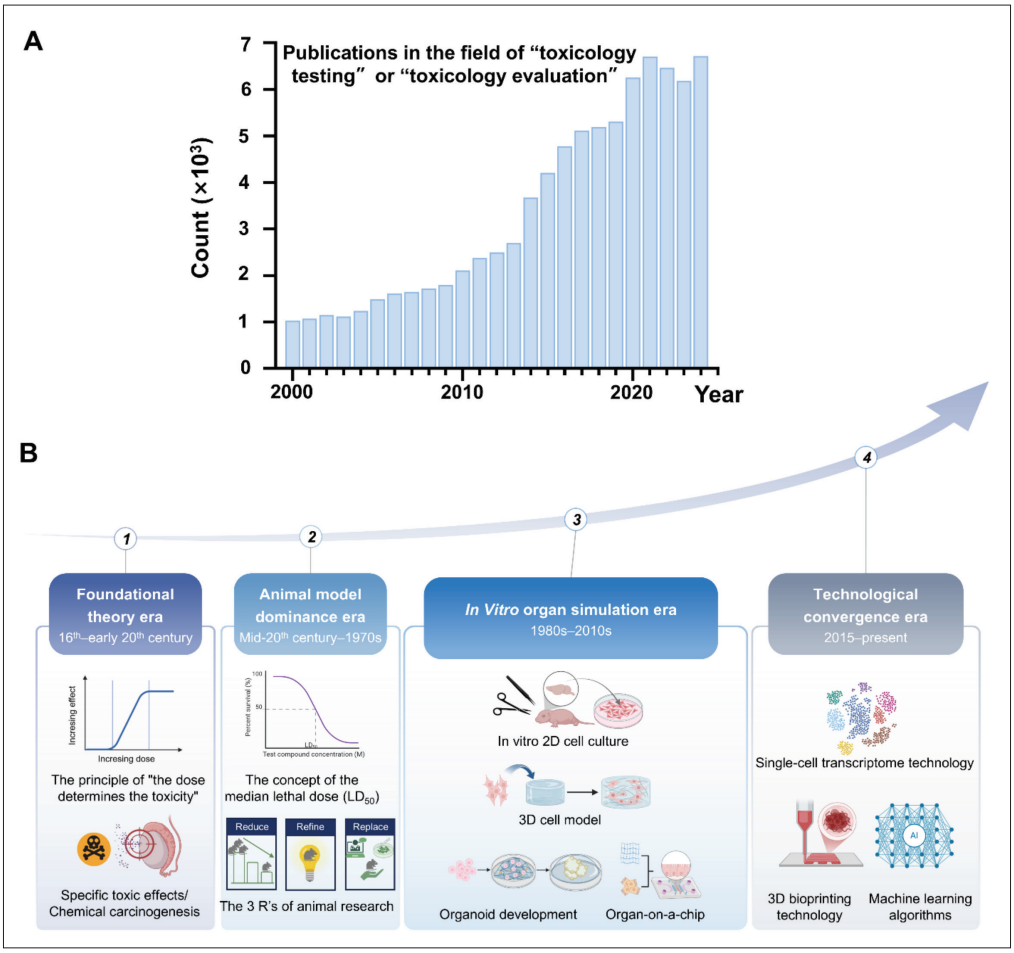

Figure 1. Technological evolution and research trends. (A) The exponential growth of PubMed-listed publications on "toxicology testing" and "toxicology evaluation" since 2000, reflecting the field's rapid transition toward engineered models. (B) Key milestones across four epochs: (i) foundational theory era (16th–early 20th century): dominated by observational studies and median lethal dose (LD_{50}) standardization, (ii) animal model dominance era (mid-20th century–1970s): emergence of cellular assays and early 3R-driven innovations, (iii) *in vitro* organ simulation era (1980s–2010s): rise of organoids and microphysiological systems, and (iv) technological convergence era (2015–present): integration of bioprinting, artificial intelligence-driven design, and multi-omics validation. Created with Biorender [û, NP. (2025). https://BioRender.com/mu9mwhw. Abbreviation: 3Rs, replacement, reduction, and refinement.

drug metabolism, distribution, and toxicity, improving the reliability and precision of toxicological predictions.[62]

2.4. The era of technological convergence: The emergence of precision and systems toxicology

Contemporary toxicological research is characterized by the convergence of multiple advanced technologies, prompting a paradigm shift from organ-specific evaluations to comprehensive system-level biological analyses. 3D bioprinting techniques, employing extrusion-based processes and sacrificial materials such as Pluronic F127, have facilitated the development of vascular networks, extending the viability of liver models to over 30 days while maintaining fluctuations in drug-metabolizing enzyme activity within 15%.[63–65] Photocuring technologies, with a resolution of 5 μm, have successfully replicated the spatial alignment of myocardial fibers, offering improved spatial precision for evaluating cardiac toxicity.[66,67] Single-cell transcriptomics has revealed the diverse responses of pulmonary epithelial cell subpopulations to NP exposure, such as the upregulation of inflammation-specific factors in basal cells.[68] Meanwhile, machine learning algorithms have integrated high-throughput *in vitro* data—including reactive oxygen species (ROS) generation and cell cycle arrest—to forecast organ-level toxicity *in vivo*.[69,70]

In 2022, the United States Food and Drug Administration released the "Strategic Roadmap for Alternative Methods," integrating organ-on-a-chip data as part of the evaluation framework for investigational new drug applications. Despite these advancements, challenges

such as establishing robust validation standards—such as achieving inter-laboratory reproducibility with error margins below 20%—and enhancing the functional maturity of vascular networks persist as areas requiring further attention.[71,72] This phase of technological evolution signifies a critical transition in toxicology, shifting from empirical threshold-based evaluations to system-wide perturbation analyses. Such developments establish a robust foundation for precision medicine and individualized toxicity forecasting.[73]

3. Three-dimensional bioprinting: Foundations and platforms for *in vitro* toxicological models

3.1. Modalities of bioprinting technology: Principles and parameter comparisons

The core of 3D bioprinting technology lies in the precise spatial arrangement of cells and biomaterials, where the selection of printing modalities critically impacts the physiological fidelity and functional sophistication of the generated models. Based on their operational principles, 3D bioprinting strategies are classified into extrusion-based bioprinting, photocuring-based bioprinting, inkjet bioprinting, laser-assisted bioprinting, and other emerging bioprinting modalities.

Extrusion-based bioprinting uses mechanical or pneumatic pressure to deposit high-viscosity bioinks through micro-nozzles. Thermoplastics via fused deposition modeling (FDM) or cell-compatible hydrogels via cold extrusion, as shown in Figure 2A and B, while photocuring approaches such as laser scanning stereolithography and digital light processing achieve subcellular resolution—by layerwise ultraviolet or visible-light crosslinking of methacrylated polymers, as shown in Figure 2C and D. Inkjet bioprinting utilizes thermal bubble or piezoelectric mechanisms to partition low-viscosity bioinks into microdroplets. This modality is categorized into drop-on-demand and continuous inkjet methodologies, as shown in Figure 2F and G. Laser-assisted methods like laser-induced forward transfer and absorption film-assisted laser printing transfer cell-laden bioinks with single-cell (~10 μm) precision while preserving viability,[74,75] as shown in Figure 2E. Emerging techniques—including suspended bioprinting in support baths for ultra-soft constructs, as shown in Figure 2H, and selective laser sintering of biocompatible powders for

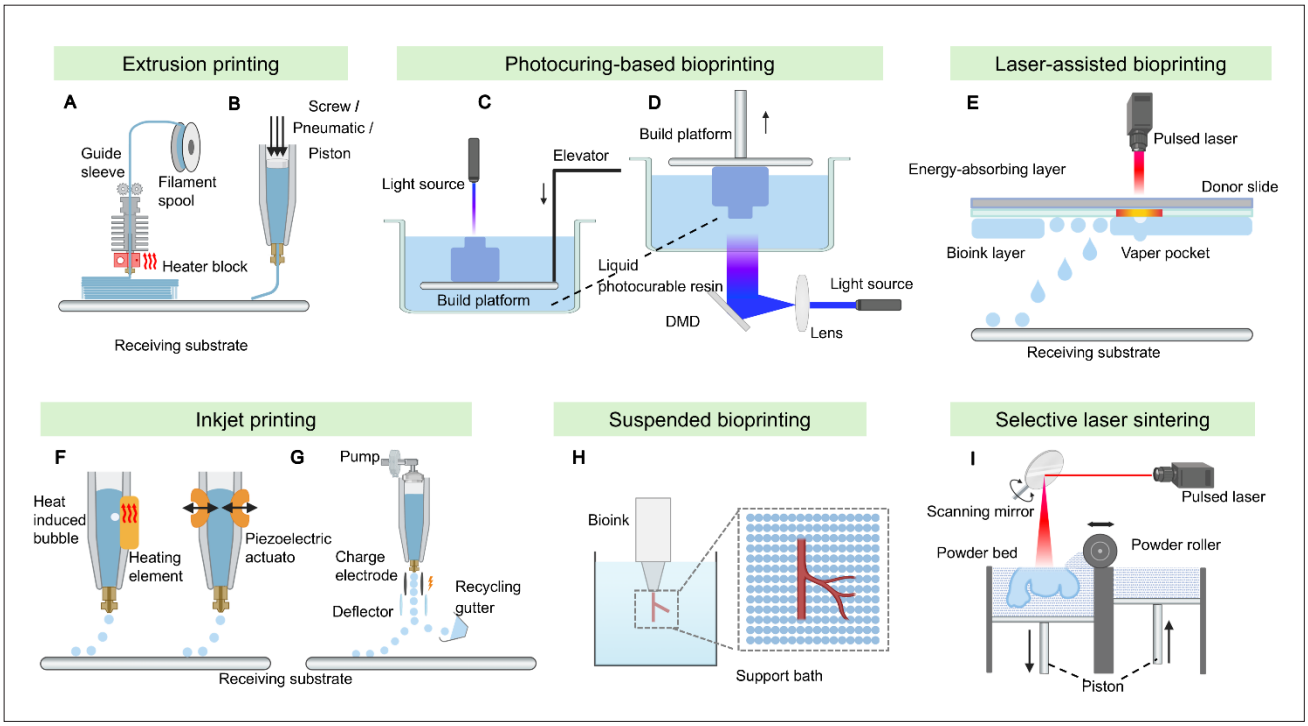

Figure 2. Common three-dimensional printing technologies in the biomedical field. (A) Fused deposition modeling. (B) Cold extrusion. (C) Laser scanning stereolithography. (D) Digital light processing. (E) Laser-assisted bioprinting. (F) Drop-on-demand inkjet bioprinting. (G) Continuous inkjet. (H) Suspended bioprinting. (I) Selective laser sintering. Created with Biorender [û, NP. (2025). https://BioRender.com/9qrb2ez.

robust, porous scaffolds, as shown in Figure 2I—further expand the design space.

The selection of 3D bioprinting modalities requires meticulous evaluation of factors including cell viability, structural complexity, and industrial scalability. Table 1 summarizes critical parameters for each modality, highlighting their proficiency in constructing multi-scale toxicological models, spanning from micro-level precision to macro-level biomimicry.

3.2. Design of bioinks: natural and synthetic materials

In the realm of bioprinting technology, the choice of bioink—the printing material—is crucial for the successful construction of target structures. Commonly used bioinks primarily consist of natural and synthetic polymers, each possessing distinct advantages and limitations. Synthetic materials excel in mechanical properties, rendering them suitable for fabricating structures where lower biological affinity is acceptable. Conversely, natural materials offer superior biocompatibility and bioactivity but often exhibit weaker mechanical performance, making them well-suited for mimicking native tissues. Therefore, the development and selection of appropriate bioinks are crucial for achieving the ultimate goals of bioprinting.[94]

3.2.1. Natural materials

Natural bioinks derive from biodegradable polymers that hydrolyze or undergo enzymatic degradation *in vivo*, yielding biocompatible byproducts. They are broadly classified as animal-derived or non-animal-derived materials.[95] Among animal-derived polymers, collagen and its thermo-responsive derivative gelatin excel at recapitulating native ECM architecture. However, gelatin's slow, temperature-dependent gelation compromises printing fidelity; methacrylation overcomes this by enabling rapid, tunable ultraviolet-mediated crosslinking and adjustable stiffness.[96] Composite formulations—such as gelatin–alginate blends—have demonstrated enhanced mechanical integrity and cell compatibility for soft-tissue constructs.[97] Non-animal polysaccharides like alginate and hyaluronic acid offer mild ionic or photo-crosslinking, customizable mechanics, and minimal immunogenicity. Alginate rapidly gels in divalent-cation baths (e.g., Ca^{2+}), supporting modular constructs and even laser-induced bioprinting with high cell viability.[98] Silk-based inks—from fibroin or recombinant spider silk—provide superior tensile strength and biocompatibility,[99] though natural spider silk's scalability is limited.[100,101] Recombinant variants and silk-like polypeptides now enable tunable hydrogels and porous scaffolds for diverse tissue engineering applications.[99] dECM bioinks preserve organ-specific biochemical cues (collagens, glycosaminoglycans, laminin) that direct cell phenotype and function.[102,103] For instance, cardiac and cartilage dECM enhance cardiomyocyte maturation and upregulate *SOX9*/*COL2A1* expression, respectively.[103] Yet, complex decellularization, variable gelation kinetics, and insufficient native mechanics often necessitate chemical crosslinkers or synthetic blends to balance printability with physiological performance.[102] In summary, natural materials are highly valued in bioprinting for their excellent biocompatibility and bioactivity. However, their mechanical limitations often require reinforcement through composite formulations. By carefully selecting and modifying natural materials, their potential applications in bioprinting can be substantially expanded.

3.2.2. Synthetic materials

Synthetic polymers have precise control over mechanical properties, degradation rates, and batch-to-batch consistency, making them staples in bioprinting. Polyethylene glycol hydrogels are Food and Drug Administration-approved, highly hydrophilic, and resistant to protein fouling. Low-molecular-weight

Table 1. Overview of common bioprinting techniques

Method	Resolution (μm)	Viscosity (mPa·s)	Cell viability	Build speed	Applications
Extrusion-based bioprinting	100	$30–6 \times 10^7$	50–90%	Slow	Construction of tissue-engineered scaffolds and soft tissue models[76–79]
Stereolithography	50	No limitation	85–95%	Fast	Suitable for fabricating high-precision tissue-engineered scaffolds[77,80–82]
Digital light processing	10	Low	85–95%	Fast	Preparation of drug delivery systems and tissue models[81,83–86]
Inkjet bioprinting	50	3–30	80–90%	Fast	Construction of tissue-engineered scaffolds and drug-screening models[84,87,88]
Laser-assisted bioprinting	10	1–300	~90%	Medium	High-precision cell patterning and tissue-engineered scaffold construction[75,77,89–91]
Selective laser sintering	50	Not applicable	Not applicable	Medium	Fabrication of hard tissue models[83,92,93]

polyethylene glycol (<50 kDa) is metabolizable, and its thermal properties permit customizable stiffness and melting behavior.[99,104–106] Polyvinyl alcohol hydrogels, formed via non-toxic freeze–thaw cycles, deliver excellent transparency, biocompatibility, and enhanced mechanical strength without chemical crosslinkers.[99,107] Poly(lactic-co-glycolic acid)—a lactic/glycolic acid copolymer—degrades into endogenous metabolites, but its hydrophobicity and poor cell adhesion often require surface treatments to improve cell–matrix interactions.[108,109] Polycaprolactone offers robust mechanical strength and biodegradability, making it ideal for load-bearing or vascular scaffolds; functionalization and composite strategies further fine-tune its properties for specific tissue targets.[110–112] Thermo-responsive polymers such as poly(N-isopropylacrylamide) and Pluronic enable temperature-controlled gelation. Poly(N-isopropylacrylamide) transitions at ~37°C but lacks innate biodegradability and adhesion, while Pluronic serves as a sacrificial support due to its reversible gelation, though it demands acrylation or blending to sustain cell viability over time.[113,114] Emerging candidates like polyvinylpyrrolidone have shown promise as bioinks at 0–3% w/v, enhancing printability and uniform cell distribution in preliminary studies.[115] In summary, synthetic materials are highly valued in bioprinting for their superior mechanical properties and tunable degradation rates. However, their limited biocompatibility and cell adhesion necessitate optimization via surface modifications or composite strategies. By carefully selecting and modifying synthetic materials, their potential applications in bioprinting can be substantially expanded.

Natural and synthetic materials both possess unique advantages and limitations. In practical applications, a combination of both is often employed to develop superior composite bioinks that fulfill the diverse requirements of tissue engineering and regenerative medicine. Schematic diagrams of common natural materials in 3D printing and molecular structure diagrams of synthetic materials are shown in Figure 3.

3.3. Construction and integrated applications of *in vitro* models using three-dimensional bioprinting

Three-dimensional bioprinting technology, with its exceptional spatial precision, has shown significant promise in advancing *in vitro* toxicological research by providing innovative methodologies for constructing multi-layered

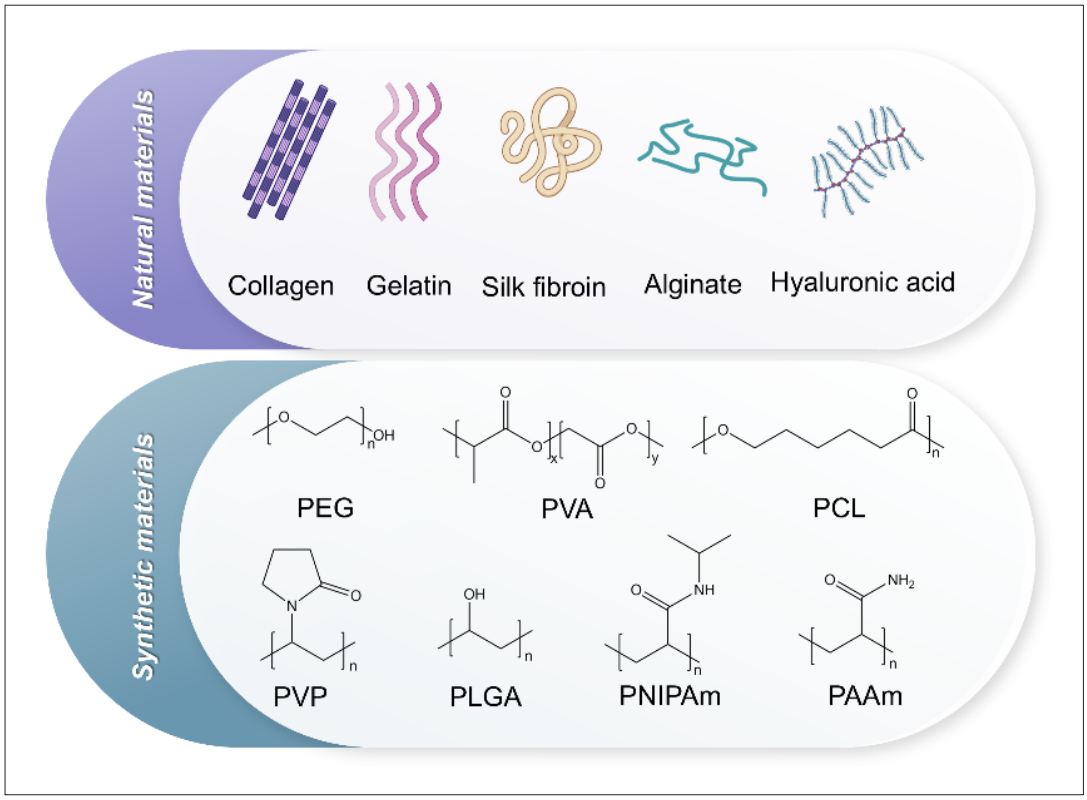

Figure 3. Schematic diagram of natural and synthetic materials commonly used in three-dimensional printing. Partially created with Biorender [û, NP. (2025). https://BioRender.com/3ko1ayt. Abbreviations: PAAm, propylacrylamide; PCL, polycaprolactone; PEG, polyethylene glycol; PLGA, poly(lactic-co-glycolic acid); PNIPAm, poly(N-isopropylacrylamide); PVA, polyvinyl alcohol; PVP, polyvinylpyrrolidone.

models.[116,117] Based on the target of the printing process, the applications of 3D bioprinting are broadly classified into the following two primary approaches: direct printing and indirect printing. Direct printing primarily focuses on the fabrication of tissue and organ models, facilitating the precise replication of human anatomical structures. These models act as indispensable tools for surgical planning, medical education, and regenerative medicine studies. By closely mimicking native tissue architecture, direct printing offers a reliable framework for investigating physiological processes and devising therapeutic interventions.[118] Indirect printing focuses on the development of complex systems, including organ-on-a-chip platforms and sensor-integrated devices. Organ-on-a-chip technology combines microfluidics and biosensors to simulate the physiological functions of human organs, providing a versatile framework for drug screening and disease modeling.[119] These chips allow high-throughput experimentation and predictive assessments, revolutionizing toxicological research.[120] Sensor-integrated platforms leverage embedded electronic components to facilitate real-time observation and analysis of biological processes.[121] These systems provide efficient and accurate tools for biomedical and toxicological research, thereby enhancing the accuracy of experimental processes and the reliability of data. Table 2 summarizes representative applications of 3D bioprinting technologies in tissue modeling, organ-on-a-chip fabrication, and biosensor development, highlighting their adaptability and transformative effects across various disciplines.

3.3.1. Biomimetic construction of tissue-specific models

The construction of tissue-specific models requires the precise replication of critical elements of native tissues, such as ECM composition and mechanical properties.[136] By integrating 3D bioprinting technology with biomaterial processing techniques in tissue engineering, 3D bioprinting enables the rapid fabrication of tissue structures with precise spatial arrangements, thus facilitating the development of physiologically relevant disease models.[137] These models enable detailed analyses of inflammatory responses and immune cell interactions, while offering distinct advantages for studying diseases such as inflammatory bowel disease, Crohn's disease, and colitis. They provide an essential platform for evaluating novel anti-inflammatory therapies.

Almutary *et al.*[138] used 3D bioprinting to create a colitis model integrating Caco-2 and HT-29 cells. Compared to 2D cultures, the 3D model better mimicked intestinal structure and enhanced barrier function. It also verified nanocarrier-based drugs' effectiveness in maintaining intestinal barrier integrity, showing 3D bioprinting's advantages in disease-model construction and drug development. Moreover, Kim *et al.*[139] presented a 3D cell-printing-based skin model for type 2 diabetes patients. Utilizing a hybrid printing platform combining drop-on-demand and extrusion modules, they fabricated a multilayered skin construct that reproduces hallmark diabetic features—insulin resistance, adipocyte hypertrophy, chronic inflammation, and microvascular dysfunction. This innovative *in vitro* model offers a powerful tool for investigating diabetes-related skin pathophysiology and testing topical therapeutics.

Beyond applications in inflammatory disorders, 3D bioprinting has been leveraged to engineer tumor models with remarkable fidelity. By precisely reproducing the complex architecture and cellular heterogeneity of neoplastic tissue, these platforms enable the study of tumor growth, invasion, and metastatic dissemination under physiologically relevant conditions. For instance, Vázquez-Aristizabal *et al.*[140] developed a dECM-based, 3D-printed melanoma model that faithfully mimics the cutaneous microenvironment and malignant phenotype. Their strategy involved formulating a biocompatible "bioink" comprising epidermal, basement membrane, and dermal components, then employing confocal microscopy and surface-enhanced Raman scattering mapping to monitor cell behavior. This system successfully emulated melanoma cell invasion, providing a novel *in vitro* platform for elucidating metastatic mechanisms, as shown in Figure 4A.

The application of 3D bioprinting in toxicological testing also demonstrates substantial potential. Unlike conventional 2D cell cultures, 3D bioprinting offers a novel method for toxicity assessment by simulating more realistic tissue structures, allowing for precise analyses of long-term effects and bioaccumulation of toxic substances. This technology not only facilitates the construction of intricate 3D structures, such as vascularized tissues and neural tissues, but also achieves a degree of precision and complexity unattainable through traditional tissue engineering approaches, as shown in Figure 7.

Additionally, 3D bioprinting is characterized by its high resolution and rapid manufacturing capabilities, allowing for the rapid production of biological tissues or organs while maintaining high cell viability. Another notable feature of 3D bioprinting is its extensive selection of bioink materials, which can be optimized and tailored to fulfill the specific requirements of various tissue types, further expanding its applications in tissue engineering. In cardiovascular tissue engineering, microchannel-based 3D bioprinting has been employed to fabricate novel cardiac patches that promote cell alignment, thereby minimizing the cell requirements for cardiac regeneration

Table 2. Applications of common three-dimensional printing techniques in tissue modeling, organ-on-a-chip fabrication, and biosensor production

Method	Target	Materials	Cell types	Applications
EBB	Three-dimensional scaffolds for bone tissue engineering	Hyaluronic acid; chitosan	MG63	Bone defect repair and bone tissue regeneration research[122]
	In vitro air-blood barrier model	Matrigel	A549; EA.hy926	*In vitro* models for lung disease research and drug testing[17]
	Printable POC biosensors	Organoxilane polymer, AuNR, protein A, IgG	—	Manufacturing stable biosensors for early disease diagnosis[79]
	Human skin tissue	Collagen	HaCaT; HFF-1	*In vitro* models for skin grafts and wound healing research[123]
Inkjet	Multi-cell heterogeneous tissue constructs	SA; collagen	hAFSCs; dSMCs; bECs	Constructing complex tissue models with multiple cell types for tissue engineering research[124]
	Liver-on-a-chip	SA	HepG2; U251	Drug metabolism and diffusion experiments to imitate *in vivo* situations[79]
	Hybrid nasal cartilage with electronic olfaction	GelMA; PEGDMA	Chondrocytes; ADSCs; HUVECs	Electronic olfaction[125]
SLA	Cell loading model	PEGDA; GelMA	NIH 3T3	Cell patterning in tissue engineering and bioengineering[126]
	Vascularized bonemimetic hydrogel	Gelatin; GelMA	HUVEC; C3H10T1/2	Bone tissue engineering, promoting osteogenesis and angiogenesis[127]
	Hydrogel scaffolds	PAA	—	Develop an ultrasensitive fiber-optic pH sensor[128]
	Engineered biofilms with bacteria	PEGDa bioresins	*Escherichia coli*; *Caulobacter crescentus*	Uranium element detection[82]
LAB	Microneedles	PMMA	—	Transdermal delivery of chemotherapeutic drugs via microneedles[129]
	Skin-on-a-chip	Collagen	NIH3T3; HaCaT	Constructing skin-like organs with functions[91]
DLP	Human iPSC-derived hepatic model	GelMA; GMHA	hiPSC-HPCs; HUVECs;vADSCs	Drug screening and disease modeling[86]
	Liver lobule microtissue biosensor	HAMA hydrogel, MWCNTs	HepG2	Aflatoxin B1 detection[130]
	Lung-on-a-chip	Resin (BV-007)	Calu-3	Respiratory toxicological testing and pulmonary drug delivery studies[131]
	Patterned cell-laden heart and liver tissue constructs	GelMA; HdECM	hiPSC-CMs; hiPSC-Heps	Serve as potential physiologically-relevant living human tissue platforms[132]
SLS	Three-dimensional nanocomposite scaffolds for bone tissue engineering	Ca-P/PHBV; CHAp/PLLA	SaOS-2	Bone tissue engineering, constructing biomimetic bone scaffolds[93]
	Cell density sensor	Metallic powder; polyamide; PVC	—	Monitoring cell density[133]
Suspended bioprinting	Multiple-layered vascular models	VdECM; Pluronic F127	HUVECs; HCASMCs	*In vitro* modeling of the initiation of arterial disorders[134]
	Full-size model of the heart	Gelatin microparticles; SA	—	Surgical simulation and training[135]

Abbreviations: ADSCs, adipose-derived stem cells; AuNR, gold nanorods; bECs, bovine aortic endothelial cells; Ca-P/PHBV, calcium phosphate/poly(hydroxybutyrate-co-hydroxyvalerate); CHAp/PLLA, carbonated hydroxyapatite/poly(L-lactic acid); DLP, digital light processing; dSMCs, canine smooth muscle cells; *E. coli*, *Escherichia coli*; EBB, extrusion-based bioprinting; GelMA, gelatin methacrylate; GMHA, glycidyl methacrylate hyaluronic acid; hAFSCs, human amniotic fluid-derived stem cells; HAMA, methylacylated hyaluronic acid; HCASMCs, human coronary artery smooth muscle cells; HdECM, heart decellularized extracellular matrix; hiPSC-Heps, human induced pluripotent stem cell-derived hepatocytes; hiPSC-CMs, human induced pluripotent stem cell-derived cardiomyocytes; hiPSC-HPCs, human induced pluripotent stem cell-derived hepatic progenitor cells; HUVECs, human umbilical vein endothelial cells; IgG, immunoglobulin G; LAB, laser-assisted bioprinting; MWCNTs, multi-walled carbon nanotubes; PAA, poly(acrylic acid); PEGDA, polyethylene glycol diacrylate; PEGDMA, polyethylene glycol dimethacrylate; PMMA, polymethylmethacrylate; PVC, polyvinyl chloride; SA, sodium alginate; SLA, stereolithography; SLS, selective laser sintering; VdECM, vascular decellularized extracellular matrix.

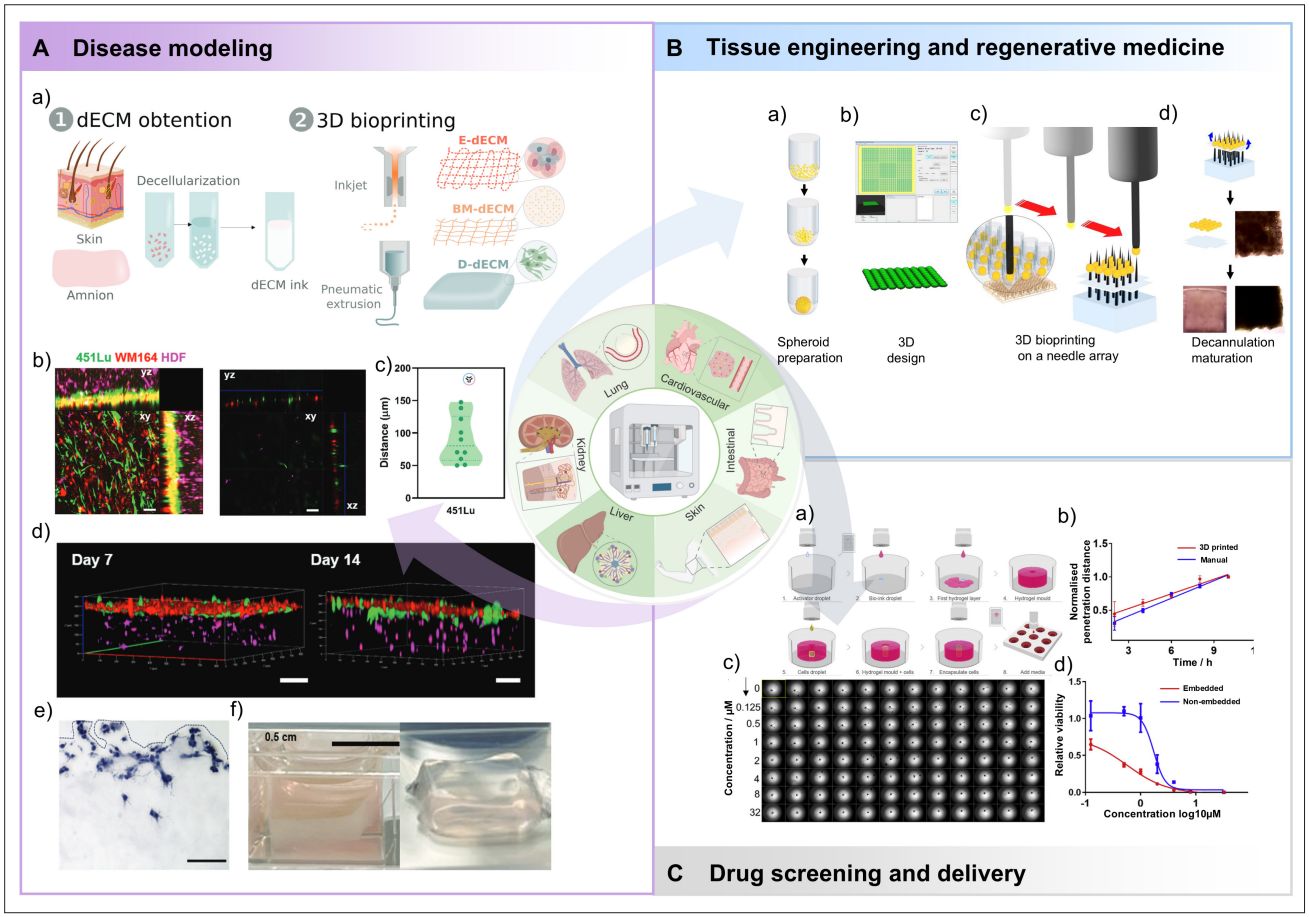

Figure 4. Biomimetic construction of tissue-specific models. (A) Three-dimensional (3D)-printed melanoma invasion model. (a) Workflow for biomaterial formulation and 3D printing of the layered melanoma–dermis construct. (b) Orthogonal maximum-intensity projection showing 451Lu melanoma cells (green) invading the human dermal fibroblast (HDF)-laden dermis (magenta) after 14 days (left), and single-plane detail of a protrusive metastatic cell (right). Scale bar: 100 µm. (c) Measured invasion distances of 451Lu cells into the dermal decellularized extracellular matrix (dECM). (d) 3D reconstructions of the bioprinted model at Days 7 and 14. Scale bars: 150 µm. (e) Hematoxylin and eosin staining of melanoma cells penetrating the dermal matrix. Scale bar: 100 µm. (f) Macroscopic appearance of the layered model at Days 14 and 21 in culture. Scale bar: 0.5 cm. Adapted with permission from Vázquez-Aristizabal *et al.*[140] (B) Schematic of a biomaterial-free 3D bioprinting approach for cardiac tissues. (a) Cardiospheres are formed by aggregating cells in ultra-low attachment 96-well plates. (b) A desired 3D architecture is designed using computer-assisted design software. (c) Cardiospheres are picked up individually using vacuum suction and positioned on a microneedle array by the 3D bioprinter. (d) After fusion, the tissue is removed and cultured further to allow self-healing of needle-induced voids. Adapted with permission from Ong *et al.*[143] (C) Drug penetration and viability in bioprinted spheroids. (a) Diagram of the bioprinting workflow for embedding spheroids in hydrogel. (b) Doxorubicin penetration depth over 10 h in bioprinted *versus* manually formed spheroids (n = 2, three spheroids per group). (c) Operetta image of a full 96-well plate containing bioprinted spheroids prior to treatment. (d) Dose–response curves for embedded and non-embedded spheroids after eight doxorubicin concentrations (n = 2, six spheroids per condition). Adapted with permission from Utama *et al.*[147] Partially created with Biorender [ù, NP (2025). https://BioRender.com/qvrla5y.

and fibrosis prevention.[141] This technology has also been used to produce hydrogel patches for treating myocardial infarction patients.[142] Furthermore, multicellular spheroids have been printed onto needle arrays to form tubular cardiac tissues to evaluate therapeutic efficacy, contractile force, and beating rhythms,[143] as shown in Figure 4B. Scaffold-free bioprinting techniques have also garnered attention for their capacity to fabricate cardiac scaffolds without the use of biomaterials.[144,145]

In pharmaceuticals, the applications of 3D bioprinting are primarily centered on drug screening and delivery systems. By fabricating structures that mimic the spatial and chemical attributes of native tissues, 3D bioprinting supports drug screening and facilitates the development of both simple and complex drug delivery systems. As early as 2003, Mironov *et al.*[146] proposed that perfused and vascularized human tissue or organ structures fabricated through 3D bioprinting could serve as efficient systems for drug screening. Since then, researchers have explored the use of 3D bioprinting to construct biomimetic 3D *in vitro* models that replicate native tissues or organs, allowing for more precise drug screening.

Three-dimensional bioprinting also holds great promise for the development of high-throughput, precision drug-screening assays. Utama *et al.*[147] engineered a bioprinting platform capable of fine-tuning cell number, spheroid diameter, and hydrogel "cup" geometry to mass-produce embedded multicellular spheroids, as shown in Figure 4C. Impressively, this method maintained over 98% cell viability while yielding spheroids whose proliferation, apoptotic profiles, and stem-cell marker expression closely matched those of manually assembled controls. Notably, the model exhibited a size-dependent drug response: larger spheroids, owing to diffusion gradients, displayed significantly elevated half-maximal inhibitory concentration values, and variations in cup dimensions directly influenced pharmacodynamic readouts. These findings offer new insights into modeling solid-tumor chemoresistance with high fidelity. Concurrently, Matsusaki *et al.*[148] utilized inkjet bioprinting to fabricate layered 3D liver-tissue microarrays featuring endothelial-hepatocyte heterotypic architecture; their automated workflow provides a scalable paradigm for preclinical toxicology screening. Although current 3D constructs remain imperfect in replicating native tissue diffusion dynamics, vascularization, and chemical gradient formation, ongoing optimization of physicochemical parameters and microenvironmental design is poised to surmount these limitations and yield more clinically relevant *in vitro* drug-screening platforms.[83]

To enhance the simulation of *in vivo* physiological environments, researchers have employed microfluidic networks to maintain and connect microtissues and organ units, thereby enabling the development of "organ-on-a-chip" devices. By incorporating microfluidic perfusion channels, these chips can recreate vascular systems, dynamic cellular culture environments incorporating mechanical and chemical stimuli, and nutrient and oxygen exchange under controlled concentration gradients. The specific features and applications of organ-on-a-chip technology will be discussed in the following section.

3.3.2. Functional integration of organ-on-a-chip technology

The application of 3D bioprinting in advanced organ-on-a-chip devices serves as a potent tool for improving the biological relevance of disease models and drug testing platforms. Recent advancements in organ-on-a-chip research, including the integration of bioprinting technologies, have effectively addressed numerous limitations inherent to traditional microfluidic chip fabrication. Conventional methods, such as lamination and molding, are labor-intensive, expensive, and ill-suited for fabricating intricate 3D structures.[149,150] Additionally, cell seeding in microchannels typically relies on manual operations or syringe pumps, which are cumbersome, inefficient, and reliant on intricate fluidic connections. Furthermore, most biomimetic organ chips fail to replicate the 3D growth environments of native tissues or support the construction of heterogeneous tissue structures, impeding accurate simulation of dynamic blood flow and heterogeneous cellular distributions at the microscale level in organ systems.[151]

The rapid development of 3D bioprinting, leveraging versatile bioink materials, diverse printing techniques, and flexible 3D design capabilities, has proven to be a transformative solution to overcome these challenges.[16] This technology enables the fabrication of intricate 3D structures and the seamless integration of biomimetic structural and functional units, offering a more streamlined method for fabricating complex tissue and organ models.[16] To date, 3D bioprinting has found successful application in the fabrication and functional modeling of organ-on-a-chip systems for various organs, including the heart, liver, kidney, tumor tissues, and nervous system.[19,152–154]

In the context of organ-on-a-chip fabrication, 3D bioprinting commonly employs the following two methodological approaches: the two-step method and the one-step method. The former entails the separate fabrication of microfluidic chips, followed by the printing of biological tissues or micro-organoids onto the pre-assembled chips.[155,156] While this approach utilizes 3D bioprinting for certain processes, it is labor-intensive and exhibits limited reproducibility. Conversely, the one-step method integrates the entire fabrication process, simultaneously printing both biomimetic structural units and biological functional units, providing a more integrated and efficient solution.[157] Widely utilized bioprinting techniques for organ-on-a-chip systems encompass inkjet printing, extrusion-based printing, and photocuring-based printing.

In the realm of organ-on-chip engineering, 3D printing technologies have demonstrated exceptional versatility and manufacturability, enabling the precise reconstruction of complex biological interfaces. In the context of renal physiology and functional assessment, Lin *et al.*[158] optimized ECM composition and fugitive-ink formulations to co-print vascularized proximal tubules within a highly permeable hydrogel matrix, establishing a closed-loop perfusion circuit. This platform not only facilitated functional co-culture of proximal-tubule epithelial and endothelial cells but also quantified active albumin/glucose reabsorption and recapitulated high-glucose-induced endothelial injury, thereby offering a high-fidelity system for renal physiology studies and nephrotoxicity assessment. For liver function modeling and drug testing applications, Fritschen *et al.*[159] developed an innovative, high-throughput 3D bioprinting platform that integrates drop-on-demand bioprinting

with robotic handling, as shown in Figure 5A. This system employs a sealed, 3D-printed microfluidic chip featuring a central tissue chamber flanked by arterio-venous mimic channels, laying the groundwork for microvascular network self-assembly. By utilizing agarose and fibrinogen bioinks, they successfully constructed a multicellular, vascularized hepatocellular carcinoma model. The platform's automation dramatically enhances both efficiency and reproducibility, and in a HepG2 model, it demonstrated stable microvascular network formation,

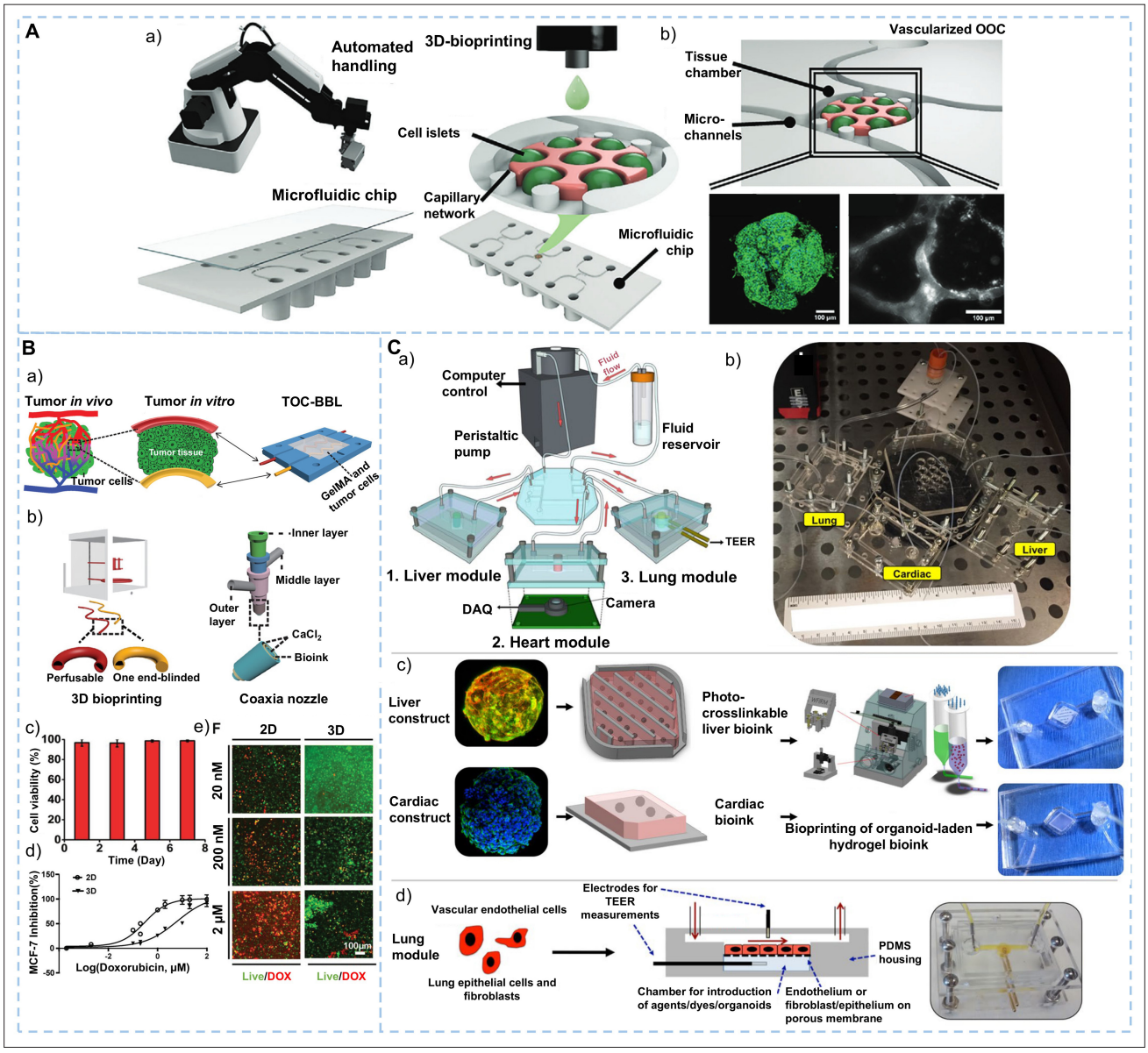

Figure 5. Applications of three-dimensional (3D) printing in organ-on-a-chip design. (A) Schematic of the automated fabrication workflow for vascularized organs-on-chips (OOCs). (a) A robotic platform precisely loads and unloads custom microfluidic chips during the pre- and post-processing stages of 3D bioprinting. (b) Within the chip's tissue chamber, printed HepG2 cells proliferate into spheroidal aggregates as a perfusable microvascular network self-assembles over the culture period. Adapted with permission from Fritschen *et al.*[159] (B) Tumor-on-a-chip with bioprinted blood-lymphatic pair (TOC-BBL). (a) Schematic of TOC-BBL featuring adjacent bioprinted blood and lymphatic vessels. (b) Overview of the custom 3D-printing setup and fabrication workflow for TOC-BBL. (c) Viability quantification of cells within the TOC-BBL platform. (d) Doxorubicin (DOX) dose-response curves for MCF-7 cells in two-dimensional culture *versus* 3D TOC-BBL. (e) Fluorescence micrographs showing MCF-7 viability under increasing DOX concentrations ($p < 0.01$). Scale bar: 100 μm. Adapted with permission from Cao *et al.*[162] Copyright © 2019 Wiley-VCH. (C) Integration of multiple tissues in a modular organ-on-a-chip platform. (a & b) Diagrams and images of the plug-and-play system enabling parallel culture of three tissue types via interconnected microreactors. (c) Liver and cardiac modules are generated by printing spheroids within custom bioinks. (d) Lung models are developed by layering cells over porous membranes, with transendothelial electrical resistance (TEER) sensors integrated for barrier integrity monitoring. Adapted with permission from Skardal *et al.*[165]

robust cell proliferation, and sustained albumin secretion, underscoring its promise for scalable drug screening and toxicity assays.

Cardiovascular disease modeling represents another pivotal application of 3D-printed organ chips. Zhang *et al.*[160] employed microfabrication-enabled 3D printing of GelMA to create a thrombus-on-a-chip, integrating fibroblasts and endothelialized microchannels to simulate thrombosis and fibrotic progression under dynamic flow. Abudupataer *et al.*[161] developed a photocurable bioprinted vascular model containing smooth muscle and endothelial cells, establishing a dynamically perfused vessel construct for vascular disease research. Tumor microenvironment models have likewise advanced beyond single-vessel systems. Cao *et al.*[162] used multi-material bioprinting to generate a tumor-on-a-chip with bioprinted blood-lymphatic pair chip incorporating both perfusable blood vessels and blind-ended lymphatics, modulating GelMA matrix permeability to recapitulate differential drug diffusion kinetics across blood and lymphatic compartments, as shown in Figure 5B. Xie *et al.*[163] further demonstrated electrohydrodynamic jetting to array tumor-cell-GelMA droplets, creating a chip that balances high viability with compatibility for high-throughput screening. Additionally, Johnson *et al.*[164] printed polycaprolactone microchannels via extrusion to fabricate a neural connectivity platform, highlighting 3D printing's customizability in neuro-organ-on-chip design. Collectively, these advances validate the unique strengths of 3D bioprinting for multi-tissue integration and dynamic microenvironment construction, and—through precise control of bioink rheology, spatial resolution, and mechanical properties—significantly enhance the simulation of key pharmacodynamic parameters such as drug penetration and metabolic response. Looking ahead, the fusion of multi-modal bio-fabrication techniques with enhanced vascular network maturation promises to overcome current challenges in long-term culture stability and tissue complexity.

To simulate interactions among multiple organs and better reflect human physiological and pathological processes, Skardal *et al.*[165] constructed a three-organ chip system comprising lung, liver, and heart tissues using 3D extrusion bioprinting, as shown in Figure 5C. By integrating organ-specific bioinks and customized fluidic devices, this system highlighted the utility of multi-organ combinations in evaluating drug efficacy and side effects. The exploration of novel bioprinting techniques continues to address the diverse demands of organ-on-a-chip technology. Elezoglou *et al.*[166] employed laser-induced forward transfer to deposit lung cancer cells onto organ chips, facilitating the study of cancer cell migration, with high-speed camera systems incorporated for real-time observation of bioink ejection mechanisms. Bowser *et al.*[167] used magnetic bioprinting to fabricate central nervous system chips, employing magnetic NPs to create spinal cord spheroids precisely positioned within hydrogel structures. Combined with digital projection lithography, this method enhances structural uniformity and facilitates long-distance 3D neural projections.

These studies highlight the extensive application potential of 3D bioprinting in organ-on-a-chip technology, ranging from single-tissue models to multi-organ systems. 3D bioprinting offers powerful tools for disease research, drug development, and personalized medicine, surpassing the limitations of traditional fabrication methods and fostering innovation in the field.

3.3.3. Customized development of biosensors

The relationship between 3D bioprinting and sensor platforms is characterized by both intricacy and versatility. By enabling the creation of sensors with complex geometries, controlled microstructures, and tailored material combinations, 3D bioprinting facilitates the development of devices that more accurately replicate the characteristics of biological tissues.[168] This capability supports miniaturization, customization, and enhanced flexibility of sensors, thus enhancing their performance and broadening their scope of applications.[168] Widely utilized 3D printing techniques in this field include fused deposition modeling, inkjet printing, direct extrusion, and stereolithography, each facilitating the rapid and cost-efficient production of advanced biomedical sensors.

Regarding inkjet printing, Cagnani *et al.*[169] developed a roll-to-roll inkjet-printed biosensor by precisely depositing tyrosinase-based bioink onto screen-printed carbon electrodes via a slot-die coating process. This biosensor achieved successful dopamine detection with an enzyme activity retention rate exceeding 98%, offering a viable pathway for the scalable, low-cost production of disposable diagnostic devices. Notably, Wang *et al.*[170] introduced an electric-field-driven microscale 3D printing technique capable of finely shaping polydimethylsiloxane doped with multiwalled carbon nanotubes composite microchannels, as shown in Figure 6A. The resulting flexible sensor demonstrated 84% optical transparency and a strain gauge factor as high as 1500. With its exceptional performance in monitoring human motion, this sensor exhibits clear advantages in wearable healthcare applications, enabling comprehensive detection from millimeter-scale joint movement to micron-scale facial expressions.

In the domain of laser fabrication, Wu *et al.*[171] developed a laser direct-write graphene ammonia sensor featuring a

3D porous architecture and an integrated heater design. This innovation reduced response and recovery times to 214 and 222 s, respectively, and achieved a sensitivity of 0.087% 1/ppm. Its dual-mode heating mechanism enhanced gas desorption efficiency, laying the groundwork for the development of wearable respiratory monitoring devices, as shown in Figure 6B. Expanding the frontier of laser technology, Hecht *et al.*[172] employed bubble-assisted laser-induced forward transfer to achieve submicron-scale patterning of polyimide-based bioinks on nitrocellulose substrates, as shown in Figure 6C. This approach enabled the fabrication of a multichannel C-reactive protein detection system while maintaining material integrity under high-energy laser exposure, thus offering a robust manufacturing route for point-of-care diagnostic devices.

Photopolymerization-based 3D printing, known for its high-resolution microstructural fabrication, has opened new avenues in biosensing applications. Cao *et al.*[173] employed stereolithography to construct a paper-based microfluidic screen-printed electrode integrated with reduced graphene oxide-tetraethylene pentamine/Prussian blue composite materials, achieving a glucose detection limit of 25 μM, which is comparable to commercial glucose meters. This integrated approach, which combines microfluidic channels with electrochemical sensing units, significantly enhances detection efficiency and supports personalized diabetes management. Simultaneously, extrusion-based 3D printing has achieved key breakthroughs in multifunctional sensor integration due to its superior material compatibility. Marzo *et al.*[174]

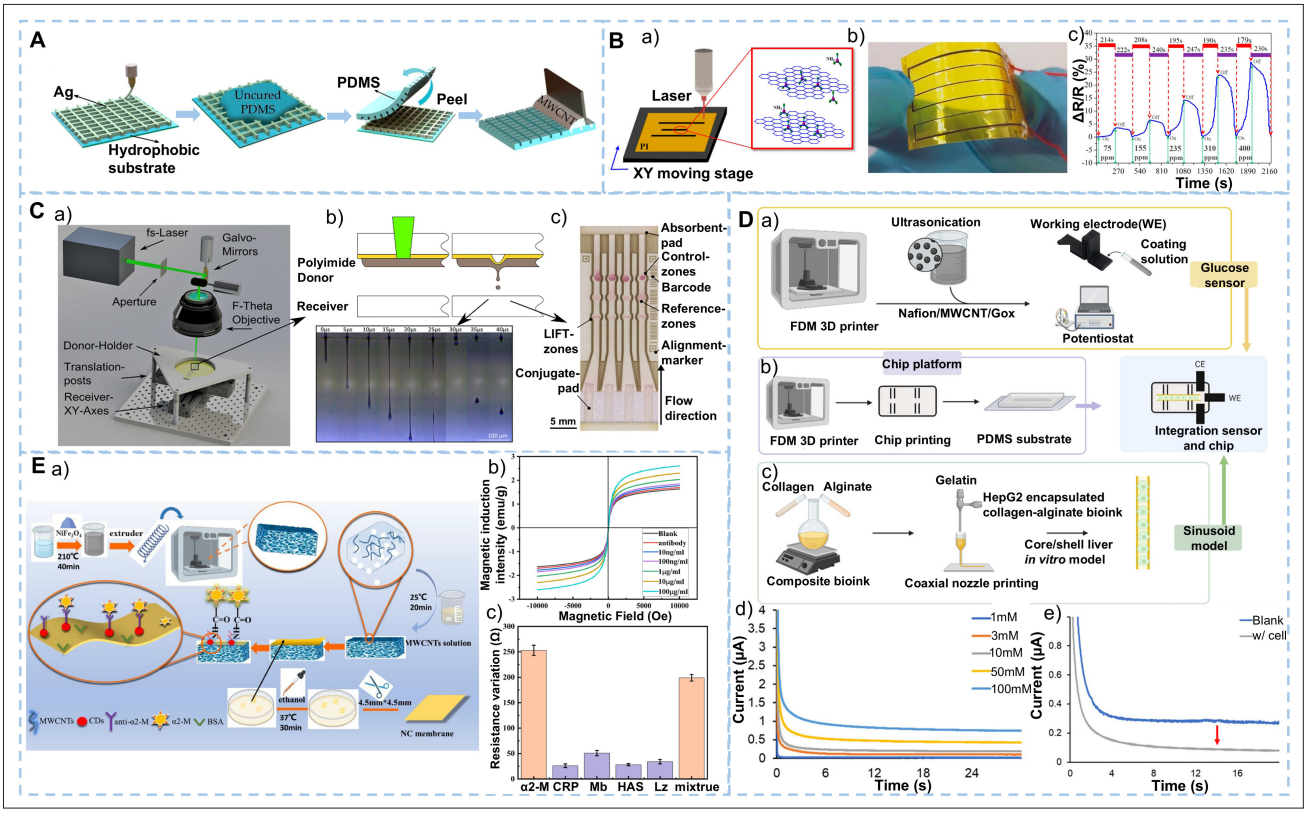

Figure 6. Applications of three-dimensional (3D) printing in biosensor construction. (A) Fabrication of a flexible strain sensor. Process schematic of a flexible strain sensor with embedded multiwalled carbon nanotubes composite microchannel (MWCNT) network. Adapted with permission from Wang *et al.*[170] (B) Laser direct writing for flexible ammonia gas sensor. (a) Schematic of the laser direct writing process. (b) Photograph of a flexible zigzag sensor pattern fabricated via laser writing. (c) Real-time response/recovery curves to ammonia concentrations from 75 to 400 ppm. Adapted with permission from Wu *et al.*[171] (C) Blister-actuated laser-induced forward transfer printing for multifunctional paper biosensors. (a) Overview of the printing setup with typewriter-like receiver movement. (b) Key parameters and stroboscopic imaging of droplet formation at 2.5 μJ. Scale bar: 100 μm. (c) Prototype of a multichannel lateral flow test fabricated entirely by laser printing. Adapted with permission from Hecht *et al.*[172] (D) 3D-printed glucose sensor and cell-culture assay. (a) Fabrication of carbon black (CB)-polylactic acid (PLA) working electrode and surface coating protocol. (b) Assembly of the PLA chip platform onto glass using polydimethylsiloxane (PDMS). (c) Bioprinted sinusoid-mimetic hydrogel (alginate-collagen). Scale bar: 4.5 mm. (d) Chronoamperometric response of the CB-PLA electrode to glucose (1–100 mM). (e) Glucose measurement in 3D-cultured cells on Day 2. Adapted with permission from Lee *et al.*[175] Copyright © 2023 Wiley-VCH. (E) Electrochemical biosensor for α2-macroglobulin. (a) Schematic of sensor fabrication and anti-α2-macroglobulin modification and detection. (b) Magnetization hysteresis loops for α2-macroglobulin at 10 ng/mL–100 μg/mL. (c) Specificity assay against potential interferents. Adapted with permission from Guo *et al.*[176]

developed an enzymatic graphene-polylactic acid (PLA) electrode by embedding horseradish peroxidase directly into the printed structure, enabling hydrogen peroxide detection down to 11.1 μM. Similarly, Lee *et al.*[175] utilized FDM technology to fabricate a carbon black-PLA three-electrode system, incorporating multiwalled carbon nanotube surface modifications to extend the glucose detection range to 1–100 mM (R^2 = 0.9813). This sensor was seamlessly integrated with a liver-on-chip platform, providing a real-time solution for drug toxicity assessment, as shown in Figure 6D. Guo *et al.*[176] further advanced the field by fabricating nickel ferrite/PLA grid substrates via FDM printing and coupling them with carbon quantum dot-based fluorescent probes to construct a magnetoelastic biosensor, as shown in Figure 6E. This device achieved ultrasensitive detection of α2-macroglobulin at 0.506 ng/mL. The dual-mode magnetic-optical signal conversion mechanism offers an innovative tool for early diagnosis of diabetic nephropathy.

In summary, 3D printing technologies demonstrate substantial potential for advancing the development of biosensors and diagnostic devices. From low-cost, rapidly manufactured bioreactors to highly sensitive biosensors, these innovations can be effectively integrated with printed tissue models and organ-on-a-chip systems to enable real-time monitoring, dynamic regulation, and high-throughput analysis of cellular and tissue functions. The convergence of these technologies augments the biomimicry and applicability of organ-on-a-chip systems while unlocking new opportunities for drug development, disease modeling, and personalized medicine.

4. Applications in organ-specific toxicology

Toxicological testing systems comprise four fundamental domains as follows: drug safety assessment, food contaminant screening, environmental toxicity analysis, and evaluation of the biological effects of nanomaterials. Technological advancements in these areas hold strategic importance for public health safety and sustainable development. In drug development, preclinical models' predictive power is limited, causing around 30% of drug candidates to fail due to uncontrollable toxicity or adverse effects, and resulting in huge annual global economic losses.[177] 2D cell models, lacking the tissue-specific microenvironment—such as the ECM topology and multicellular interaction networks—are inadequate for accurately simulating the dynamic interplay between drug metabolism and toxicity.[47] Consequently, critical toxic phenotypes, including hepatotoxicity and QT interval prolongation, show high false negative rates.[178] Environmental toxicology encounters even more significant challenges. According to the United Nations Environment Programme, over 100,000 new synthetic chemicals are introduced into the ecological cycle annually, yet a mere 0.1% are subject to comprehensive toxicity evaluation.[179] Existing *in vitro* detection technologies are limited by their inability to simulate essential aspects of the air–liquid interface and reconstruct chronic exposure effects.[180] This inability to accurately predict the bioaccumulation and transgenerational toxicity of substances such as particulate matter and persistent organic pollutants presents substantial challenges for ecological risk assessment. In the realm of food safety, foodborne pathogenic toxins (e.g., aflatoxin B1), illegal additives, and microplastic contamination collectively lead to direct global economic losses annually.[181,182] Traditional detection methods, which rely on animal testing coupled with high-performance liquid chromatography, are characterized by low throughput, high costs, and ethical concerns. Nanotoxicology research introduces even greater scientific complexities.[183] They exhibit unique properties, such as surface plasmon resonance and quantum size effects, capable of inducing non-dose-dependent toxicities (e.g., mitochondrial autophagy dysfunction).[184] However, conventional *in vitro* models fail to replicate key features such as tissue penetration and the dynamic interactions between NPs and biological barriers, thereby limiting their effectiveness in accurately predicting nanotoxicological outcomes.[185,186]

Three-dimensional bioprinting technology provides a revolutionary solution to these challenges by enabling the construction of biomimetic structures across multiple scales (resolution of 1–200 μm), regulating dynamic perfusion (shear stress of 0.1–20 dyn/cm^2), and reconstructing heterogeneous microenvironments (co-localization of 3+ cell types).[187,188] This technology has significantly advanced toxicological research across key target organs, including the liver (metabolic toxicity), kidney (excretory toxicity), lungs (inhalation toxicity), cardiovascular system (functional toxicity), intestines (absorption toxicity), and skin (contact toxicity), as shown in Figure 7 and Table 3. This section systematically explores the application of 3D bioprinting in toxicology, highlighting its technical breakthroughs from structural biomimicry to functional integration. Furthermore, clinical relevance validation data are provided to support the scientific rationale for substituting traditional methods with 3D bioprinting approaches. By bridging the gap between *in vitro* models and *in vivo* physiology, 3D bioprinting holds the potential to redefine toxicological testing systems, creating pathways for more accurate, efficient, and ethically sound methodologies.

4.1. Liver toxicology

The liver, as the central organ for xenobiotic metabolism, accounts for over 90% of phase I and II detoxification

Table 3. Application of three-dimensional printing technology in extracorporeal toxicity testing for different organs

Target organ	Printing method	Printing object	Materials	Cell types	Applications
Liver	Continuous deposition microextrusion	3D primary liver tissues	NovoGel1 2.0	**PHH**; **HSCs;** HUVECs	Antibiotic drug toxicity testing[194]
	Direct-write	Liver-on-a-chip platform	GelMA	HepG2; C3A	Drug toxicity assessment of APAP[153]
	Extrusion bioprinting	Hepatic model	SA; Gelatin	hiPSC-Heps	Drug-induced hepatotoxicity evaluation of APAP[195]
	Extrusion bioprinting	Liver lobule microarchitecture	ECM-derived microparticles; BA silk fibroin; gelatin; β-D galactose	HLCs; HUVECs; HHSCs	Hepatotoxicity/non-hepatotoxicity drug toxicity testing[196]
	DLP	Liver lobule microtissue biosensor	HAMA; multi-walled carbon nanotubes	HepG2	The detection of AFB1[130]
	Microextrusion	Xeno-free 3D-bioprinted liver model	Matrigel; SA; human collagen	HuH-7	Toxicity testing of OA[197]
	Electro-assisted bioprinting	Disse space organoids	SA; NC Laminin 511	hPSC-HE; hiPSC-EPCs; LX-2	Toxic mechanisms of MPs and TBBPA in liver tissues[189]
	Magnetic levitation and bioprinting	Mini liver models	Magnetic nanoparticles	Fao	Assessment of the toxicity of nanodiamond[198]
Kidney	Coaxial nozzle extrusion bioprinting	Vas-POAC	Pluronic F127; SA; KdECM	RPTEC; Ges	Evaluation of the cisplatin-induced nephrotoxicity capacity[199]
	Extrusion bioprinting	3D convoluted renal proximal tubules	Fibrinogen; gelatin; Pluronic F127; two-part silicone elastomer	PTECs	Cyclosporine A toxicity testing[19]
Lung	Inkjet bioprinting	3D alveolar barrier	Collagen	HULEC-5a; MRC5; NCI-H1703; NCI-H441	Evaluate the physiological impact of ne dust particles[190]
	Inkjet bioprinting	Lung cancer-on-chip	Nusil medical grade silicone elastomer	NCI-H1437	Physiological monitoring and toxicity assessment of DOX/ docetaxel[200]
	SLA	*In vitro* exposure system	Resin	HBECs	Assessing the effects of cannabis inhalation on the lungs[201]
	Extrusion bioprinting	Organoid-based scaffolds	SA; Matrigel; porcine gelatin	Calu-3	Long-term nanoparticle toxicology investigation[202]
Cardiovascular	Coaxial nozzle extrusion bioprinting	Endothelialized myocardium and heart-on-a-chip	SA; GelMA	HUVECs; hiPSC-CMs	Cardiovascular toxicity evaluation[203]
	Microextrusion bioprinting	Tissue-sensor platform	CB; PCL; soft rubber; PDMS; HdECM	hiPSC-CMs; hCFs	Monitoring of drug-induced cardiotoxicity[191]
	μCOP	Cardiac micro-tissue	GelMA; HAGM	hiPSC-CMs; hCFs	Test the impact of CuO NPs on 3D cardiac micro-tissues[204]
Intestinal	SLA	Intestinal microvillus cell sensor	FCONp; MWCNT-CDH; GelMA	RBL-2H3	The detection of wheat allergen gliadin[205]
	Microextrusion bioprinting	Intestinal barrier models	Collagen	Caco-2; HT-29; HDFn	Studying the permeability and toxicity of ibuprofen[206]
Skin	Extrusion-bioprinting	3D thickness skin tissue model constructs	Novogel 2.0; Fibrinogen	NKTC; NDF; NHEK	Screen topical-use compounds for irritation potential[193]

Abbreviations: 3D, three-dimensional; AFB1, Aflatoxin B1; APAP, acetaminophen; CB, carbon black; CuO, copper oxide; DLP, digital light processing; Fao, rat hepatoma cells; FCONp, flower-like copper oxide nanoparticles; GelMA, gelatin methacrylate; GEs, primary human glomerular endothelial cells; HAGM, hyaluronic acid glycidyl methacrylate; HAMA, methylacylated hyaluronic acid; HBECs, primary human bronchial epithelial cells; HCFs, human cardiac fibroblasts; HDFn, human dermal fibroblasts; HdECM, heart decellularized extracellular matrix; HHSCs, human hepatic stellate cells; hiPSC, human induced pluripotent stem cells; hiPSC-EPCs, endothelial progenitor cells; hiPSC-Heps, human induced pluripotent stem cell-derived hepatocytes; hiPSC-CMs, human induced pluripotent stem cell-derived cardiomyocytes; HLCs, hepatocyte-like cells; HSCs, hepatic stellates; HULEC-5a, lung microvascular endothelial cells; HUVECs, human umbilical vein endothelial cells; KdECM, kidney decellularized extracellular matrix; MPs, microplastics; MWCNT-CDH, multiwalled carbon nanotubes; NDF, neonatal human dermal fibroblast; NHEK, normal human epidermal keratinocytes; NKTC, human primary neonatal keratinocytes; OA, Okadaic acid; PCL, polycaprolactone; PDMS, polydimethylsiloxane; PHH, primary human hepatocytes; Pluronic® F127, polyethylene-polypropylene-polyethylene; PTECs, proximal tubule epithelial cells; RBL-2H3, rat basophilic leukemia cells; RPTEC, primary human renal proximal tubule epithelial cells; SA, sodium alginate; SLA, stereolithography apparatus; TBBPA, Tetrabromobisphenol A; Vas-POAC, vascularized proximal tubule-on-a-chip; μCOP, micro-continuous optical printing.

reactions. The biological complexity of its toxicity assessment models plays a pivotal role in determining the validity of toxicological predictions. Traditional 2D hepatic models are hindered by the absence of ECM-mediated polarity signals and interactions with non-parenchymal cells such as stellate and Kupffer cells, resulting in a dramatic reduction in cytochrome P450 enzyme activity—up to 80% within 72 h—severely limiting their utility in chronic toxicity studies.

In drug toxicity testing, particularly with antibiotics like trovafloxacin and its non-toxic analog levofloxacin, traditional methods have frequently failed to accurately evaluate hepatotoxicity, leading to severe consequences. Nguyen *et al.*[194] addressed this issue using 3D-printed human liver tissue models, which not only distinguished the toxicological profiles of these drugs but also maintained drug-induced cytochrome P450 enzyme activity over prolonged durations. Another study demonstrated that 3D-printed HepaRG and human stellate cell liver organoids exhibited substantially higher albumin expression compared to 2D cultures, markedly improving the sensitivity and accuracy of toxicological evaluations, thus offering a novel approach to upgrading toxicity assessment models, particularly for long-term testing.[207]

For instance, Bhise *et al.*[153] developed a 3D-bioprinted liver chip platform that preserved hepatic function for a 30-day culture period and demonstrated toxicity responses comparable to animal models and other *in vitro* systems, innovatively integrating 3D bioprinting with microfluidic bioreactors for drug toxicity assessment. He *et al.*[195] constructed a 3D-bioprinted liver tissue model derived from human induced pluripotent stem cells (hiPSCs), which exhibited exceptional performance in cell growth, liver-specific functions, and drug-induced hepatotoxic responses. This model showed excellent drug responsiveness and high cytochrome P450 1A2 expression in acetaminophen-induced hepatotoxicity tests, providing a new tool for personalized drug screening and toxicological research.

Moreover, 3D-bioprinted liver models that simulate native hepatic lobule microstructures are more sensitive and relevant in predicting drug-induced liver injuries when incorporating non-parenchymal cells, compared to hepatocyte-only models.[196] This provides pharmaceutical companies with a cost-effective and efficient platform for hepatotoxicity screening. In studies on drugs like aspirin, dexamethasone, trovafloxacin mesylate, and troglitazone, 3D-bioprinted liver models demonstrated robust intercellular communication and hepatic metabolic functions, effectively predicting hepatotoxicity and offering substantial support for toxicological screening in drug development.

In the realm of food safety testing, Wang *et al.*[130] developed a 3D-bioprinted "hepatic lobule" microtissue biosensor for aflatoxin B1 detection, combining 3D bioprinting with electrochemical sensing strategies to enhance biomimicry and accuracy, paving the way for novel approaches in mycotoxin detection. For marine biotoxin okadaic acid, researchers created an animal-free 3D-bioprinted liver model that successfully evaluated its hepatotoxicity, highlighting the efficacy of 3D bioprinting in toxicological testing and its substantial implications for long-term stability, functionality, and relevance.[197]

In environmental pollutant testing, Yao *et al.*[189] employed 3D printing to generate hiPSC-derived liver organoids (DOs) from healthy donors and alcoholic liver disease patients to assess the combined toxicity of microplastics and tetrabromobisphenol A (TBBPA), as shown in Figure 7B. Using electro-assisted inkjet printing, the study investigated the accumulation of polystyrene microplastics in DOs and the effects of TBBPA. Results indicated limited impact on DOs from healthy donors at low microplastic and TBBPA doses, whereas alcoholic liver disease patient-derived DOs exhibited heightened sensitivity, as evidenced by marked alterations in gene expression and liver function. This suggests that 3D-printed hiPSC-derived DOs represent a powerful tool for assessing the hepatic impact of environmental toxins, particularly for patients with specific genetic backgrounds.

In materials toxicology, Khanal *et al.*[198] employed scaffold-free bioprinting to fabricate a "mini-liver" model, which, combined with label-free nanoscale technology, assessed the toxicity of nanodiamonds. This model proved to be more sensitive than 2D models by detecting cytotoxicity within 48 h, providing a novel high-resolution approach to nanosafety evaluation.

4.2. Kidney toxicology

Nephrotoxicity continues to be a significant challenge in drug development and chemical safety evaluation, particularly as the renal proximal tubule serves as the primary target for drug-induced nephrotoxicity, which affects over 20% of the global adult population. However, current preclinical approaches, including 2D cell cultures and animal models, are hindered by their short-term functional maintenance *in vitro* or significant interspecies differences, limiting their ability to accurately predict clinical drug responses. The advent of 3D-bioprinted kidney models, which precisely replicate the structure of renal tubules and nephron units, has significantly enhanced the precision of toxicity predictions.

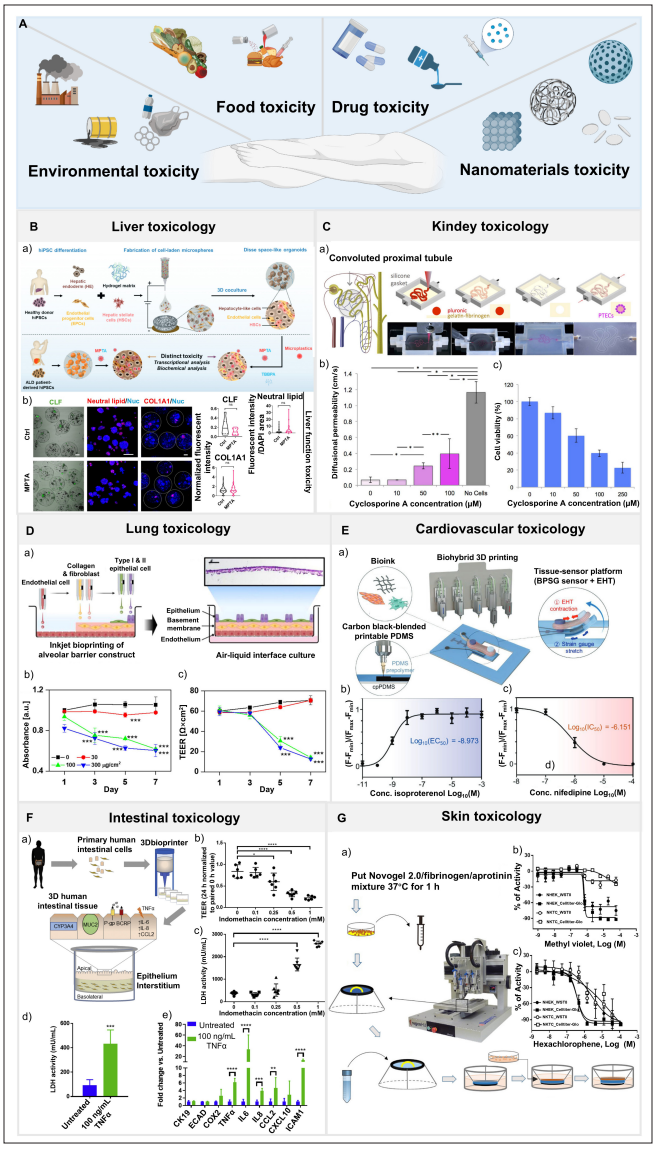

Figure 7. Applications of three-dimensional (3D) printing in organ-specific toxicology. (A) Multidimensional atlas of toxicity sources. Created with Biorender [û, NP. (2025). https://BioRender.com/5bdwv4e. (B) Differential toxicity in human induced pluripotent stem cell (hiPSC)-derived liver organoids from healthy and patient donors upon co-exposure to microplastics and tetrabromobisphenol (TBBPA). (a) Overlay of cholyl-lysyl-fluorescein (CLF) *in situ* staining (green) with bright field images. (b) Maximum projections of neutral lipid staining (red), collagen type 1 alpha chain 1 (COL1A1) immunostaining (yellow green), and 4',6-diamidino-2-phenylindole (DAPI) (blue) within microsphere-encapsulated N_Dos. Scale bar: 100 µm. Quantification of CLF uptake, lipid accumulation, and COL1A1 expression is shown below; statistical significance was assessed by Student's *t*-test ("ns" = not significant). Adapted with permission from Liang *et al.*[189] (C) 3D convoluted renal proximal tubule-on-a-chip. (a) Nephron schematic highlighting the proximal tubule and fabrication workflow using fugitive ink printed within a gelatin–fibrin extracellular matrix (ECM). (b) Diffusional permeability after cyclosporine A treatment (*$p < 0.003$, **$p < 0.02$); (c) Cell viability in a 2D dish control following cyclosporine A exposure (all comparisons $p < 0.005$). Adapted with permission from Homan *et al.*[19] (D) Toxicity assessment of dust particles in a 3D inkjet-printed alveolar barrier model: (a) Experimental workflow schematic; (b) CCK-8 proliferation assay normalized to Day 1 control (data = 1); (c) TEER measurements indicating barrier integrity after dust exposure. Adapted with permission from Kang *et al.*[190] Copyright © 2022 Wiley Periodicals LLC. (E) Tissue-sensor platform with carbon-black-blended PDMS (cpPDMS): (a) Schematic of platform fabrication; (b) Real-time contraction dose-response of engineered heart tissue (EHT) exposed to isoproterenol; (c) Real-time contraction dose-response of EHT exposed to nifedipine. Adapted with permission from Yong *et al.*[191] (F) 3D intestinal tissue model for functional and toxicity testing: (a) Workflow for tissue assembly, functional validation, and toxicity assays; (b) TEER reduction following 24 h incubation with increasing indomethacin doses; (c) LDH release correlating with indomethacin concentration; (d) Morphological changes and LDH increase after TNF-α treatment ($n = 5–6$, ***$p < 0.001$ by *t*-test); (e) Upregulation of inflammatory markers (TNF-α, IL-6, IL-8, CCL2, ICAM) in response to TNF-α ($n = 3$; **$p < 0.01$, ***$p < 0.001$, ****$p < 0.0001$ by two-way ANOVA). Data are mean ± SD. Adapted with permission from Madden *et al.*[192] (G) Full-thickness skin (FTS) model: (a) Bioprinting schematic; (b, c) Cytotoxicity evaluation of methyl violet and hexachlorophene. Adapted with permission from Wei *et al.*[193]

For instance, Homan *et al.*[19] employed an advanced 3D bioprinting technique to fabricate *in vitro* 3D human proximal tubule models, as shown in Figure 7C. These models are fully embedded within an ECM and integrated into perfusable organ-on-a-chip systems, achieving stability for up to 2 months under *in vitro* conditions. By combining 3D cell culture with organ-on-a-chip technology, the researchers created programmable, coiled proximal tubules featuring open lumens surrounded by proximal tubule epithelial cells exposed to physiological shear stress within the chip. Compared to traditional 2D cell cultures, these models exhibited considerable improvements in both morphological and functional attributes, including enhanced epithelial morphology and functional properties.

When tested with the nephrotoxic drug cyclosporin A, the 3D-bioprinted proximal tubule model successfully replicated the microarchitecture and functional characteristics of native renal tissues. The model demonstrated robust intercellular communication and renal metabolic activity, offering a robust platform for precise nephrotoxicity prediction. In comparison to 2D counterparts, the 3D model displayed higher sensitivity and correlation in drug toxicity assessments, facilitating detailed evaluation of drug-induced renal damage. This platform provides pharmaceutical companies with a cost-efficient and dependable nephrotoxicity screening platform, thereby accelerating drug development.

In addition to proximal tubule models, researchers have developed vascularized proximal tubule-on-a-chip systems (Vas-POAC), which outperform earlier single-cell proximal tubule models in replicating physiological conditions.[199] These perfusable Vas-POAC systems facilitate the growth and proliferation of proximal tubule cells alongside adjacent endothelial cells across diverse conditions. After 7 days of *in vitro* culture, Vas-POAC demonstrated mature marker expression of proximal tubule and endothelial cells in both epithelial and luminal endothelial compartments. This encompassed polarized expression of sodium-glucose cotransporter-2 and the de novo synthesis of ECM proteins. Compared to POAC systems that lack vascular components, Vas-POAC exhibited significantly enhanced functional attributes. Furthermore, in cisplatin-induced nephrotoxicity evaluations, Vas-POAC exhibited greater drug tolerance compared to POAC, highlighting its superiority in replicating physiological responses to nephrotoxic agents. These vascularized models enable the screening of drug doses responsible for proximal tubule damage and unlock new opportunities for identifying compounds that disrupt renal tubule formation.

4.3. Lung toxicology

The lungs, as the primary site for gas exchange and exposure to inhaled substances, occupy a pivotal role in toxicological studies. Airborne particulate matter entering the respiratory system through the airways can trigger severe pulmonary diseases, thereby rendering its impact analysis a focal point of research. However, traditional 2D models are significantly limited in their ability to replicate the complex physiological processes of the human body and fail to accurately simulate the effects of particulate matter on alveoli. To address these limitations, Kang *et al.*[190] employed the MicroFab Jetlab II on-demand inkjet bioprinting system to precisely deposit endothelial cells, collagen, fibroblasts, and alveolar epithelial cells onto a porous substrate at high resolution, thereby recreating the 3D, tri-layer architecture of the human alveolar barrier, as shown in Figure 7D. In this multilayer model, exposure to varying concentrations and durations of dust particles led to marked disruption of barrier integrity, induction of apoptosis, elevated secretion of pro-inflammatory cytokines, activation of key signaling pathways and transcription factors, and degradation of the ECM, culminating in increased permeability. Moreover, dust exposure altered the expression of surfactant protein genes, indicating potential impairment of alveolar surfactant function. This high-precision *in vitro* platform faithfully recapitulates *in vivo* pulmonary physiology and offers a powerful tool for particulate matter toxicology studies, accelerating the translation of findings into effective therapeutic strategies. In the field of drug toxicology, Khalid *et al.*[200] created an integrated biosensor-based lung cancer chip platform designed for real-time physiological monitoring and toxicity assessment. Constructed using 3D printing technology, the platform incorporated transparent indium tin oxide electrodes, allowing for visual monitoring via a digitally printed microscope. Optical pH sensors and transendothelial electrical resistance impedance sensors were utilized to continuously monitor the pH of the culture medium and the electrophysiological properties of cells. As a proof of concept, NCI-H1437 lung cancer cells were cultured on a glass-based microfluidic chip, with biosensor data collected in real time. The study evaluated the toxicity of two anticancer drugs, doxorubicin and docetaxel, revealing a marked increase in cell mortality with increasing drug concentrations. Doxorubicin exhibited higher toxicity compared to docetaxel, as confirmed through cell index assessments. Half-maximal inhibitory concentration values calculated via linear regression models were 6.791 μM for doxorubicin and 0.137 nM for docetaxel. Results from live/dead cell assays were consistent with transendothelial electrical resistance impedance evaluations, further validating the dose-dependent increase in cell death.

In the domain of food safety, Chandiramoha *et al.*[201] utilized 3D printing technology to create an *in vitro* exposure system (IVES) to simulate the physiological effects of cannabis inhalation on the lungs. The system was designed to load epithelial cells and expose them to cannabis smoke to mimic pulmonary responses to inhaled substances. The team fabricated a lung-like four-chamber IVES using 3D printing, featuring two inlets, four outlets, and four chamber lids, effectively simulating the "inhalation" process and distributing smoke to four cell-filled chambers before expelling it. During experiments, research-grade cannabis was ignited, with smoke introduced into the IVES via a three-way valve and syringe. Following simulated inhalation, the researchers assessed epithelial cell viability and immune function, finding a marked impairment of cellular immunity. Results revealed that cannabis use could induce symptoms such as coughing, wheezing, and chest tightness. By comparing cytokine levels in the IVES with those extracted from individuals with smoking-related disorders, the study underscored the heightened susceptibility of recreational cannabis users to throat inflammation and other respiratory issues. These findings hold particular relevance in the context of cannabis legalization for medical use. The study also emphasized the potential of 3D printing technology in toxicological research, including aerosol analysis, pathogen impact evaluations, and immune system studies.

In material toxicology, Gerbolés *et al.*[202] investigated the application of 3D bioprinting in fabricating organoid-based scaffolds for long-term NP toxicity studies. This approach aimed to better simulate lung cell exposure to NPs, providing a more accurate model compared to traditional 2D cell cultures. Using a customized 3D bioprinter, the researchers fabricated viscous hydrogels containing cells, composed of alginate, gelatin, and Matrigel, optimized to support cell viability and structural integrity. Immortalized lung cell lines were cultured within the bioprinted scaffolds over extended periods to examine interactions with NPs, including 40 nm fluorescent latex particles and 11–14 nm silver NPs. Results revealed enhanced cell proliferation within the 3D scaffolds, with cell numbers increasing from 5×10^5 to 1.27×10^6 over 14 days, indicating an optimal environment for cellular growth. Lipid peroxidation levels decreased by 91%, indicating reduced oxidative stress, a common response to NP exposure. Additionally, the 3D environment demonstrated minimal cell death over 21 days, underscoring the protective nature of the bioprinted scaffolds. NP diffusion within the 3D scaffolds was another critical observation, with fluorescent NPs permeating the scaffold, effectively replicating *in vivo* conditions. Compared to 2D cultures, cells exposed to silver NPs in the 3D model displayed significantly higher survival rates, highlighting the model's superior replication of *in vivo* NP exposure responses. The study highlighted the numerous advantages of 3D bioprinting in nanotoxicology research, including the creation of physiologically relevant models, enhanced NP diffusion and cellular interactions, and more realistic toxicity assessments. These findings suggest that 3D bioprinting could become a pivotal tool in future nanotoxicology and nanomedicine research, providing a reliable and ethical alternative to traditional methods while adhering to the 3R principles in toxicological studies.

4.4. Cardiovascular toxicology

The heart, as a key target organ for the toxicity of exogenous chemicals, is crucial in drug toxicology research. Zhang *et al.*[203] developed an innovative approach utilizing 3D bioprinting technology to construct endothelialized myocardial and heart-on-a-chip models. Using composite bioinks, the researchers created microfibrillar hydrogel scaffolds via 3D bioprinting and directly incorporated endothelial cells into these scaffolds. Over time, the endothelial cells migrated to the periphery of the microfibers, establishing a continuous endothelial layer. Subsequently, cardiomyocytes were seeded onto these 3D endothelial beds, resulting in organized myocardial tissues that exhibited spontaneous and synchronous contraction. These organoids were embedded into specially designed microfluidic perfusion bioreactors, thereby completing the endothelialized myocardial platform for cardiovascular toxicity evaluation. Using doxorubicin—a common anticancer drug—as a test case, the endothelialized myocardial tissue chip model was evaluated for its cardiovascular toxic response to the drug. Results showed that upon exposure to 10 and 100 mM doxorubicin, cardiomyocyte contraction rates decreased to 70.5% and 1.62%, respectively. Constructs exposed to 10 and 100 mM doxorubicin exhibited reductions in von Willebrand factor levels secreted by endothelial cells to 76.0% and 35.3%, respectively. These findings demonstrate that the endothelialized myocardial tissue chip model effectively simulates the dose-dependent toxic effects of doxorubicin on cardiomyocytes and endothelial cells, providing potential applications for personalized drug screening and mitigating drug-induced cardiovascular toxicity.

Concurrently, Yong *et al.*[191] created a biohybrid 3D printing method to fabricate a tissue-sensor platform, as shown in Figure 7E. This platform consists of an engineered heart tissue (EHT) integrated with dual-column-grafted strain gauge sensors, facilitating wireless, real-time, and continuous monitoring of drug-induced cardiotoxicity. Through a one-step printing process, researchers produced integrated 3D EHT and strain gauge sensors utilizing five distinct inks. By printing two

columns onto the strain gauge to serve as grafts, they increased the contraction force of the EHT and directed its self-assembly along the strain gauge. Additionally, the researchers incorporated a wireless multi-channel electronic system to continuously monitor the contraction force of the EHT, enabling the observation of both acute and chronic drug effects on the myocardium. The study demonstrated that the developed tissue-sensor platform could serve as a test model for drug-induced cardiotoxicity, validating its potential through the observation of acute and chronic effects of drugs such as isoproterenol, nicardipine, and doxorubicin. This platform provides real-time monitoring of myocardial contraction force and rhythm, providing more accurate data on drug effects compared to traditional 2D cardiac models.

In the realm of material toxicology, Miller *et al.*[204] employed advanced 3D bioprinting technology to fabricate iPSC-derived cardiac microtissues for evaluating the toxicity of copper oxide (CuO) NPs. 3D bioprinting was used to construct cardiac microtissues with structural and functional properties that closely resemble human cardiac tissue. These bioprinted tissues included iPSC-derived cardiomyocytes and human cardiac fibroblasts, thus creating a complex tissue environment. CuO NPs were coated with bovine serum albumin to mimic *in vivo* protein adsorption, thereby stabilizing the NPs and enhancing the reliability of experimental outcomes. The study found that exposure to CuO NPs led to significant cytotoxicity in the bioprinted cardiac tissues, as viability assays indicated a median lethal dose of 7.176 μg/mL and complete cell death at 100 μg/mL. Tissue contraction force was notably reduced at 10 μg/mL, underscoring the impact of CuO NPs on cardiac function. Gene expression analysis further elucidated the mechanisms of CuO NP toxicity, revealing a dose-dependent increase in markers of mitochondrial biogenesis and significant upregulation of caspase 3 and caspase 8, suggesting that apoptosis in cardiac tissues is primarily mediated through the extrinsic death receptor pathway. Compared to traditional models, 3D-bioprinted cardiac tissues offer significant advantages, such as an enhanced replication accuracy of cell-cell and cell-matrix interactions, thereby offering authentic assessments of cellular behavior and responses. Additionally, the integration of force measurement capabilities enables direct evaluation of changes in tissue contraction force, which is crucial for understanding the impact of toxins on cardiac health. These findings indicate that 3D bioprinting technology offers a powerful and precise tool for cardiac toxicology research, aiding in the elucidation of toxicity mechanisms and the development of safer materials.

4.5. Intestinal toxicology

As the primary site for drug absorption and metabolism, the small intestine is critical in toxicological testing, facilitating the evaluation of substance absorption efficiency and potential gastrointestinal toxicity.[208] The development of 3D-printed intestinal models, which accurately mimic the crypt-villus architecture, has markedly improved the physiological relevance of these models. For instance, Madden *et al.*[192] presented a 3D primary human intestinal tissue model constructed using Organovo's 3D NovoGen bioprinting system, as shown in Figure 7F. The model utilizes bioprinting technology to create a bilayered structure composed of primary human intestinal epithelial cells and intestinal myofibroblasts, effectively recapitulating key features of native intestinal tissue, including epithelial polarization, tight junctions, and specialized cell types. The engineered 3D intestinal tissue exhibits functional expression of cytochrome P450 enzymes (e.g., cytochrome P450 3A4, cytochrome P450 2C9), with demonstrated metabolic activity and inducibility. It also possesses physiologically relevant barrier properties, enabling discrimination between compounds with high and low permeability, and exhibits functional expression of key drug transporters such as P-glycoprotein and breast cancer resistance protein. In toxicity assessments, the model responds to nonsteroidal anti-inflammatory drug-induced (e.g., indomethacin) and tumor necrosis factor alpha-induced barrier disruption and cytotoxicity, supporting its utility for predicting drug safety and efficacy, rendering it particularly suitable for ADME/toxicological studies.

In another study, researchers utilized advanced biomanufacturing techniques to create three distinct intestinal barrier models: (i) a manually constructed model comprising Caco-2 and HT-29 cells on a collagen bed, (ii) a manually constructed model featuring Caco-2/HT-29 layers on an human dermal fibroblast collagen layer, and (iii) a 3D-bioprinted model incorporating both cell layers.[206] These models were rigorously tested to evaluate their capacity to simulate functional intestinal membranes. Results indicated that while all models successfully replicated the structure and function of the intestinal barrier, the 3D-bioprinted intestinal model exhibited superior epithelial barrier integrity, tight junction formation, microvilli development, and mucus production. Notably, in ibuprofen exposure experiments, the 3D-bioprinted model yielded more predictive responses, highlighting its potential as a reliable *in vitro* tool for drug toxicity testing.

In the field of food safety testing, the innovative application of mimicking "intestinal microvilli" has

demonstrated significant potential. Jiang *et al.*[205] created a biomimetic electrochemical cell sensor utilizing 3D bioprinting for the specific and highly sensitive detection of wheat gluten. The study innovatively synthesized self-assembled flower-like CuO NPs and hydrazide-functionalized multi-walled carbon nanotubes, enhancing sensor performance. Using GelMA hydrogel as the matrix, the researchers combined flower-like CuO NPs with hydrazide-functionalized multi-walled carbon nanotubes to form a conductive bio-composite hydrogel (bioink). Employing stereolithography 3D bioprinting technology, they accurately printed clustered microvilli structures of the small intestine onto screen-printed electrodes and immobilized rat basophilic leukemia cells within the gel framework.

Experimental results revealed that the bioprinted cell sensor could sensitively detect wheat gluten at a cell concentration of 1×10^6 cells/mL with a fixation time of 10 min, exhibiting a linear detection range of 0.1–0.8 ng/mL and a detection limit of 0.036 ng/mL. This 3D-bioprinted electrochemical cell sensor exhibited excellent stability and reproducibility, providing a simple yet novel approach for food safety testing. It shows promise for widespread application in food safety detection and evaluation.

4.6. Skin toxicology

As the primary barrier against external substances, the skin is essential in toxicological testing for identifying potential irritants or allergens. Manually engineered *in vitro* skin models are used to predict skin irritation, corrosion, or sensitization; however, these models face reproducibility issues and inconsistent tissue structure compared to natural tissue.[209] With the development of 3D printing technology, various bioprinting methods have emerged for skin structure reconstruction. Laser-assisted bioprinting is utilized to develop *in vitro* skin tissue.[210] Initially, layers of fibroblast/ECM bioink are printed, followed by layers of keratinocyte/ECM bioink. The resulting skin tissue can be integrated into rodent skin to facilitate wound healing. Another method combines inkjet and extrusion techniques to create full-thickness skin tissue with alternating layers of epidermal and dermal cell lines and ECM.[123] This tissue resembles human skin in terms of cell nucleus distribution and epidermal density. Exposure to 1% Triton X-100 reduces cell viability, while 5% sodium dodecyl sulfate results in complete loss of viability. Recently, a full-thickness model created via the extrusion-based method showed a native like skin structure.[211] Dermis was first fabricated by extruding bioink containing gelatin, alginate, fibrinogen, and fibroblasts, then cross-linked and cultured for 12 days. Subsequently, an epidermal keratinocyte layer was added. By Day 26 of culture, the dermis produced collagen, with evidence of dermal–epidermal junction and epidermal stratification.

Moreover, Wei *et al.*[193] conducted a systematic evaluation of various skin cell models to assess the irritant potential of topically applied compounds, as shown in Figure 7G. Initially, 2D monolayer models of primary neonatal and immortalized human keratinocytes underwent cytotoxicity testing. Then, 46 cytotoxic compounds were tested on 3D tissue models (reconstructed human epidermis and full-thickness skin) for skin irritation potential. Irritant potential was assessed by measuring tissue viability, transendothelial electrical resistance, and levels of cytokines interleukin (IL)-1α and IL-18. Results showed high-concentration irritants reduced tissue viability and transendothelial electrical resistance while increasing IL-1α secretion. At low concentrations, compounds mainly increased IL-18 secretion without affecting other parameters, suggesting potential sensitization. This study first integrated 2D cell models with 3D-bioprinted skin models for large-scale compound screening. Innovatively, it introduced markers like IL-1α and IL-18 secretion levels into the assessment. A high-throughput screening-compatible platform was developed to rapidly and efficiently evaluate the skin irritation potential of environmental chemicals, providing new tools for toxicology and enhancing the efficiency and accuracy of compound screening and chemical safety assessment.

4.7. Other organs toxicology

The application of 3D printing in toxicological research across various organs has also shown significant promise. For gastric toxicity modeling, Hsu *et al.*[212] employed digital light processing technology with flexible photocurable resin to fabricate a physiologically relevant 3D stomach model, inspired by porcine and human gastric structures, featuring realistic rugae. This model demonstrated mechanical properties and hydrophilicity comparable to native stomach tissue. Functionally, it recreated the gastric microenvironment more accurately than 2D systems: *Helicobacter pylori* exhibited enhanced antibiotic resistance due to rugae protection, while the activity of gastric cancer cells (MKN-45) was modulated by the model's flexibility and topography, providing a superior platform for drug screening and toxicity assessment. In the nervous system, Johnson *et al.*[164] developed a biomimetic 3D neural system chip using micro-extrusion bioprinting. The chip's customized microchannels and chambers enabled spatial organization of neural cells (e.g., hippocampal neurons and Schwann cells) and alignment of axonal networks. Using this platform, pseudorabies virus transmission was investigated, revealing Schwann cells' role in axon-to-cell spread and their intrinsic resistance to infection, offering a

novel tool for studying neurotropic viruses and evaluating neurotoxic compounds. Furthermore, 3D-bioprinted brain tumor models, such as glioblastoma, have been utilized to assess neurotoxicity and drug resistance (e.g., to temozolomide) by precisely replicating the tumor microenvironment.[213] In pancreatic research, Kiemen *et al.*[214] integrated serial tissue sectioning with deep learning to construct a 3D model encompassing normal ducts, pancreatic intraepithelial neoplasia, and ductal adenocarcinoma. This approach offers new insights into pancreatic cancer progression and a robust platform for evaluating drug-induced pancreatic toxicity. Collectively, these advances significantly contribute to the development of organ-specific *in vitro t*oxicology models for the stomach, nervous system, and pancreas.

5. Future perspectives and challenges

Three-dimensional bioprinting technology holds significant promise for toxicology research, yet its advancement is impeded by intricate interdisciplinary challenges. From a technical perspective, the trade-off between printing precision and throughput restricts the capacity to accurately replicate complex organ microstructures. Although photopolymerization techniques can achieve high precision, their low throughput characteristics are insufficient to address the requirements of high-throughput screening. Conversely, extrusion-based printing can significantly increase throughput, but challenges such as reduced cell viability and the inability to replicate submicron-scale physiological structures with precision persist. Additionally, the limitations of current material systems restrict the scope of the technology's application. Commercially available bioinks often lack the mechanical adaptability to match the dynamic stiffness variations of natural organs, resulting in structural collapse or functional deterioration during long-term culture, ultimately undermining model stability and reliability.

Biologically, existing models are inadequate for integrating multicellular interaction networks and systemic toxicity responses. While capable of incorporating multiple cell types, they demonstrate notable shortcomings in simulating immune microenvironments and neuroendocrine regulation. Cross-organ toxicity studies face even greater technical hurdles. For instance, in liver-gut co-culture systems, deviations in hemodynamic parameter simulations lead to drug metabolism rates that frequently deviate substantially from clinical data. Furthermore, the absence of standardized systems compounds the challenges associated with technological translation, necessitating improvements in the cross-platform comparability of key parameters to facilitate widespread application of research findings.

Future technological breakthroughs must adhere to a progressive trajectory from structural biomimicry to system integration. Innovations in multiphoton polymerization and microfluidic technologies present opportunities to address the printing bottlenecks of submicron-scale vasculature and neural networks, and to engineer smart, responsive bioinks capable of dynamically simulating tissue remodeling. The construction of multi-organ chips must incorporate physiological pharmacokinetic models and enhance cross-tissue material transfer efficiency via hydrodynamic simulations. Standardization efforts should focus on establishing batch consistency certification for bioinks and functional verification protocols, thereby promoting regulatory acceptance of printed data as partial substitutes for animal testing, ultimately expediting clinical translation.

In terms of building a translational ecosystem, a collaborative innovation network encompassing "biomanufacturing-computational toxicology-clinical medicine" needs to be established. The development of modular desktop bioprinters will effectively lower equipment barriers, while the commercialization of lyophilized bioinks is expected to significantly improve the accessibility and availability of models. The deep integration of artificial intelligence has the potential to autonomously optimize printing parameters and precisely analyze toxicity mechanisms, ultimately supporting the establishment of individualized toxicity warning systems. This technological evolution pathway is poised to transform toxicology research from empirical threshold judgments to mechanism-driven, precise prediction paradigms, providing revolutionary solutions for global public health safety.

Acknowledgments

The authors thank all the lab members for their critical reading and comments on the manuscript. They also acknowledge the Biorender platform (biorender.com) for figure illustrations.

Funding

This project was partially supported by grants from the following sources: the National Key Research and Development Program of China (No. 2022YFA1103400, 2022YFC2406704), the National Natural Science Foundation of China (No. 32371477, 82090051, 92168207), and the Research & Development Program of Zhejiang Province (No. 2024C03075 and No. 2019C04020).

Conflict of interest

The authors declare that they have no competing interests.

Author contributions

Conceptualization: Juan Liu, Yunfang Wang, Xiangdong Kong
Data curation: Yinpeng Le, Tanqing Long, Mingyue Pan, Qingru Song
Formal analysis: Yinpeng Le, Tanqing Long, Wenrui Ma, Yuxin Su
Supervision: Yunfang Wang, Xiangdong Kong
Visualization: Juan Liu, Yinpeng Le, Mengcheng Tang
Writing–original draft: Juan Liu, Yinpeng Le
Writing–review & editing: Yinpeng Le, Tanqing Long, Qi Wang, Wenrui Ma, Yuxin Su, Juan Liu, YuTian Feng, Ni An, Wenzhen Yin
All authors read and approved the final manuscript.

Ethics approval and consent to participate

Not applicable.

Consent for publication

Not applicable.

Availability of data

Not applicable.

References

1. Guengerich FP. Mechanisms of drug toxicity and relevance to pharmaceutical development. *Drug Metab Pharmacok*. 2011;26(1):3-14. doi: 10.2133/dmpk.dmpk-10-rv-062
2. Tsaioun K. Evidence-based absorption, distribution, metabolism, excretion (ADME) and its interplay with alternative toxicity methods. *ALTEX*. 2016;33:343-358. doi: 10.14573/altex.1610101
3. Pognan F, Beilmann M, Boonen HCM, *et al*. The evolving role of investigative toxicology in the pharmaceutical industry. *Nat Rev Drug Discov*. 2023;22(4):317-335. doi: 10.1038/s41573-022-00633-x
4. Ng WL, Yeong WY. The future of skin toxicology testing – three-dimensional bioprinting meets microfluidics. *IJB*. 2019;5(1):237. doi: 10.18063/ijb.v5i2.1.237
5. Worth AP, Berggren E, Prieto P. Chemicals 2.0 and why we need to bypass the gold standard in regulatory toxicology. *Altern Lab Anim*. 2025;53(1):21-25. doi: 10.1177/02611929241296328
6. Hughes B. Industry concern over EU hepatotoxicity guidance. *Nat Rev Drug Discov*. 2008;7(9):719. doi: 10.1038/nrd2677
7. Hu C, Yang S, Zhang T, *et al*. Organoids and organoids-on-a-chip as the new testing strategies for environmental toxicology-applications & advantages. *Environ Int*. 2024;184:108415. doi: 10.1016/j.envint.2024.108415
8. Bock C, Boutros M, Camp JG, *et al*. The organoid cell atlas. *Nat Biotechnol*. 2021;39(1):13-17. doi: 10.1038/s41587-020-00762-x
9. Park SB, Kim EA, Kim KY, Koh, B. Induction of toxicity in human colon cells and organoids by size- and composition-dependent road dust. *RSC Adv*. 2023;13(5):2833-2840. doi: 10.1039/D2RA07500H
10. Vinken M, Grimm D, Baatout S, *et al*. Taking the 3Rs to a higher level: replacement and reduction of animal testing in life sciences in space research. *Biotechnol Adv*. 2025;81:108574. doi: 10.1016/j.biotechadv.2025.108574
11. Markets and Markets. In Vitro Toxicology Testing Market Growth, Drivers, And Opportunities. MarketsandMarkets; 2023. Accessed May 6, 2025. https://www.marketsandmarkets.com/ Market-Reports/ in-vitro-toxicology- testing-market-209577065.html
12. Saraswathibhatla A, Indana D, Chaudhuri O. Cell–extracellular matrix mechanotransduction in 3D. *Nat Rev Mol Cell Biol*. 2023;24(7):495-516. doi: 10.1038/s41580-023-00583-1
13. Sood D, Tang-Schomer M, Pouli D, *et al*. 3D extracellular matrix microenvironment in bioengineered tissue models of primary pediatric and adult brain tumors. *Nat Commun*. 2019;10(1):4529. doi: 10.1038/s41467-019-12420-1
14. Baker BM, Chen CS. Deconstructing the third dimension: how 3D culture microenvironments alter cellular cues. *J Cell Sci*. 2012;125(Pt 13):3015-3024. doi: 10.1242/jcs.079509
15. Jang KJ, Mehr AP, Hamilton GA, *et al*. Human kidney proximal tubule-on-a-chip for drug transport and nephrotoxicity assessment. *Integr Biol (Camb)*. 2013;5(9):1119-1129. doi: 10.1039/c3ib40049b
16. Zhang B, Gao L, Ma L, Luo Y, Yang H, Cui Z. 3D bioprinting: a novel avenue for manufacturing tissues and organs. *Engineering*. 2019;5(4):777-794. doi: 10.1016/j.eng.2019.03.009
17. Horváth L, Umehara Y, Jud C, Blank F, Petri-Fink A, Rothen-Rutishauser B. Engineering an in vitro air-blood barrier by 3D bioprinting. *Sci Rep*. 2015;5(1):7974. doi: 10.1038/srep07974
18. Burke M, Carter BM, Perriman AW. Bioprinting: uncovering the utility layer-by-layer. *J 3D Print Med*. 2017;1(3):165-179. doi: 10.2217/3dp-2017-0006

19. Homan KA, Kolesky DB, Skylar-Scott MA, *et al*. Bioprinting of 3D convoluted renal proximal tubules on perfusable chips. *Sci Rep*. 2016;6(1):34845. doi: 10.1038/srep34845

20. Kang D, Hong G, An S, *et al*. Bioprinting of multiscaled hepatic lobules within a highly vascularized construct. *Small*. 2020;16(13):e1905505. doi: 10.1002/smll.201905505

21. Choudhury D, Tun HW, Wang T, Naing MW. Organ-derived decellularized extracellular matrix: a game changer for bioink manufacturing? *Trends Biotechnol*. 2018;36(8):787-805. doi: 10.1016/j.tibtech.2018.03.003

22. Kaden T, Graf K, Rennert K, Li R, Mosig AS, Raasch M. Evaluation of drug-induced liver toxicity of trovafloxacin and levofloxacin in a human microphysiological liver model. *Sci Rep*. 2023;13(1):13338. doi: 10.1038/s41598-023-40004-z

23. Michaleas SN, Laios K, Tsoucalas G, Androutsos G. Theophrastus bombastus von hohenheim (paracelsus) (1493-1541): the eminent physician and pioneer of toxicology. *Toxicol Rep*. 2021;8:411-414. doi: 10.1016/j.toxrep.2021.02.012

24. Herr HW. Percivall pott, the environment and cancer. *BJU Int*. 2011;108(4):479-481. doi: 10.1111/j.1464-410X.2011.10487.x

25. Bertomeu-Sánchez JR. Animal experiments, vital forces and courtrooms: Mateu orfila, françois magendie and the study of poisons in nineteenth-century france. *Ann Sci*. 2012;69(1):1-26. doi: 10.1080/00033790.2011.637471

26. Michaleas SN, Veskoukis AS, Samonis G, Pantos C, Androutsos G, Karamanou M. Mathieu joseph bonaventure orfila (1787-1853): the founder of modern toxicology. *Maedica (Bucur)*. 2022;17(2):532-537. doi: 10.26574/maedica.2022.17.2.532

27. Ayala RA. Welcome to the new age. Claude bernard's "introduction to the study of experimental medicine" and the shift of medical thought towards science: 150 years later. *Arch Med Res*. 2017;48(4):393-396. doi: 10.1016/j.arcmed.2017.08.006

28. An H, Sg G. Historical milestones and discoveries that shaped the toxicology sciences. *EXS*. 2009;99:1-35. doi: 10.1007/978-3-7643-8336-7_1

29. DePass LR. Alternative approaches in median lethality (LD_{50}) and acute toxicity testing. *Toxicol Lett*. 1989;49(2-3):159-170. doi: 10.1016/0378-4274(89)90030-1

30. Pillai S, Kobayashi K, Michael M, Mathai T, Sivakumar B, Sadasivan P. John william trevan's concept of median lethal dose (LD50/LC50) – more misused than used. *J Pre Clin Clin Res*. 2021;15(3):137-141. doi: 10.26444/jpccr/139588

31. Franco NH. Animal experiments in biomedical research: a historical perspective. *Animals (Basel)*. 2013;3(1):238-273. doi: 10.3390/ani3010238

32. Erhirhie EO, Ihekwereme CP, Ilodigwe EE. Advances in acute toxicity testing: Strengths, weaknesses and regulatory acceptance. *Interdiscip Toxicol*. 2018;11(1):5-12. doi: 10.2478/intox-2018-0001

33. Seidle T, Robinson S, Holmes T, *et al*. Cross-sector review of drivers and available 3Rs approaches for acute systemic toxicity testing. *Toxicol Sci*. 2010;116(2):382-396. doi: 10.1093/toxsci/kfq143

34. Botham PA. Acute systemic toxicity–prospects for tiered testing strategies. *Toxicol In Vitro*. 2004;18(2):227-230. doi: 10.1016/S0887-2333(03)00143-7

35. Mukherjee P, Roy S, Ghosh D, Nandi SK. Role of animal models in biomedical research: a review. *Lab Anim Res*. 2022;38:18. doi: 10.1186/s42826-022-00128-1

36. Khabib MNH, Sivasanku Y, Lee HB, Kumar S, Kue CS. Alternative animal models in predictive toxicology. *Toxicology*. 2022;465:153053. doi: 10.1016/j.tox.2021.153053

37. Harrison RG, Greenman MJ, Mall FP, Jackson CM. Observations of the living developing nerve fiber. *Anat Rec*. 1907;1(5):116-128. doi: 10.1002/ar.1090010503

38. Jones HW. Record of the first physician to see henrietta lacks at the johns hopkins hospital: history of the beginning of the HeLa cell line. *Am J Obstet Gynecol*. 1997;176(6):s227-s228. doi: 10.1016/S0002-9378(97)70379-X

39. Thomson JA, Itskovitz-Eldor J, Shapiro SS, *et al*. Embryonic stem cell lines derived from human blastocysts. *Science*. 1998;282(5391):1145-1147. doi: 10.1126/science.282.5391.1145

40. Martin G. Isolation of a pluripotent cell line from early mouse embryos cultured in medium conditioned by teratocarcinoma stem cells. *PNAS*. 1981;78(12):7634-7638. doi: 10.1073/pnas.78.12.7634

41. Ames BN, Lee FD, Durston WE. An improved bacterial test system for the detection and classification of mutagens and carcinogens. *PNAS*. 1973;70(3):782-786. doi: 10.1073/pnas.70.3.782

42. Zeiger E. The test that changed the world: The ames test and the regulation of chemicals. *Mutat Res Genet Toxicol Environ Mutagene*. 2019;841:43-48. doi: 10.1016/j.mrgentox.2019.05.007

43. Volpe DA. Drug-permeability and transporter assays in caco-2 and mdck cell lines. *Future Med Chem*. 2011;3(16):2063-2077. doi: 10.4155/fmc.11.149

44. Kwatra D, Budda B, Vadlapudi AD, Vadlapatla RK, Pal D, Mitra AK. Transfected mdck cell line with enhanced expression of Cyp3a4 and P-glycoprotein as a model to study their role in drug transport and metabolism. *Mol Pharm*. 2012;9(7):1877-1886.
doi: 10.1021/mp200487h

45. Garcia-Canton C, Minet E, Anadon A, Meredith C. Metabolic characterization of cell systems used in in vitro toxicology testing: lung cell system BEAS-2B as a working example. *Toxicol In Vitro*. 2013;27(6):1719-1727.
doi: 10.1016/j.tiv.2013.05.001

46. Edmondson R, Broglie JJ, Adcock AF, Yang L. Three-dimensional cell culture systems and their applications in drug discovery and cell-based biosensors. *Assay Drug Dev Technol*. 2014;12(4):207-218.
doi: 10.1089/adt.2014.573

47. Kapałczyńska M, Kolenda T, Przybyła W, *et al*. 2D and 3D cell cultures–a comparison of different types of cancer cell cultures. *Arch Med Sci*. 2018;14(4):910-919.
doi: 10.5114/aoms.2016.63743

48. Deguchi S, Shintani T, Harada K, *et al*. In vitro model for a drug assessment of cytochrome P450 family 3 subfamily a member 4 substrates using human induced pluripotent stem cells and genome editing technology. *Hepatol Commun*. 2021;5(8):1385-1399.
doi: 10.1002/hep4.1729

49. Jensen C, Teng Y. Is it time to start transitioning from 2D to 3D cell culture? *Front Mol Biosci*. 2020;7:33.
doi: 10.3389/fmolb.2020.00033

50. Astashkina AI, Mann BK, Prestwich GD, Grainger DW. Comparing predictive drug nephrotoxicity biomarkers in kidney 3-D primary organoid culture and immortalized cell lines. *Biomaterials*. 2012;33(18):4712-4721.
doi: 10.1016/j.biomaterials.2012.03.001

51. Zhao Z, Chen X, Dowbaj AM, *et al*. Organoids. *Nat Rev Methods Primers*. 2022;2:94.
doi: 10.1038/s43586-022-00174-y

52. Sato T, Vries RG, Snippert HJ, *et al*. Single Lgr5 stem cells build crypt-villus structures in vitro without a mesenchymal niche. *Nature*. 2009;459(7244):262-265.
doi: 10.1038/nature07935

53. Broda TR, McCracken KW, Wells JM. Generation of human antral and fundic gastric organoids from pluripotent stem cells. *Nat Protoc*. 2019;14(1):28-50.
doi: 10.1038/s41596-018-0080-z

54. Miller AJ, Dye BR, Ferrer-Torres D, *et al*. Generation of lung organoids from human pluripotent stem cells in vitro. *Nat Protoc*. 2019;14(2):518-540.
doi: 10.1038/s41596-018-0104-8

55. Lancaster MA, Renner M, Martin CA, *et al*. Cerebral organoids model human brain development and microcephaly. *Nature*. 2013;501(7467):373-379.
doi: 10.1038/nature12517

56. Huch M, Dorrell C, Boj SF, *et al*. In vitro expansion of single Lgr5+ liver stem cells induced by wnt-driven regeneration. *Nature*. 2013;494(7436):247-250.
doi: 10.1038/nature11826

57. Lewis-Israeli YR, Wasserman AH, Gabalski MA, *et al*. Self-assembling human heart organoids for the modeling of cardiac development and congenital heart disease. *Nat Commun*. 2021;12(1):5142.
doi: 10.1038/s41467-021-25329-5

58. Takasato M, Er PX, Chiu HS, *et al*. Erratum: kidney organoids from human iPS cells contain multiple lineages and model human nephrogenesis. *Nature*. 2016;536(7615):238.
doi: 10.1038/nature17982

59. Corrò C, Novellasdemunt L, Li VSW. A brief history of organoids. *Am J Physiol Cell Physiol*. 2020;319(1):C151-C165.
doi: 10.1152/ajpcell.00120.2020

60. Winkler AS, Cherubini A, Rusconi F, *et al*. Human airway organoids and microplastic fibers: a new exposure model for emerging contaminants. *Environ Int*. 2022;163:107200.
doi: 10.1016/j.envint.2022.107200

61. Huh D, Matthews BD, Mammoto A, Montoya-Zavala M, Hsin HY, Ingber DE. Reconstituting organ-level lung functions on a chip. *Science*. 2010;328(5986):1662-1668.
doi: 10.1126/science.1188302

62. Oleaga C, Bernabini C, Smith AST, *et al*. Multi-organ toxicity demonstration in a functional human in vitro system composed of four organs. *Sci Rep*. 2016;6(1):20030.
doi: 10.1038/srep20030

63. Liu X, Wang X, Zhang L, *et al*. 3D liver tissue model with branched vascular networks by multimaterial bioprinting. *Adv Healthc Mater*. 2021;10(23):e2101405.
doi: 10.1002/adhm.202101405

64. Xu Y, Hu Y, Liu C, Yao H, Liu B, Mi S. A novel strategy for creating tissue-engineered biomimetic blood vessels using 3D bioprinting technology. *Materials (Basel)*. 2018;11(9):1581.
doi: 10.3390/ma11091581

65. Richards D, Jia J, Yost M, Markwald R, Mei Y. 3D bioprinting for vascularized tissue fabrication. *Ann Biomed Eng*. 2017;45(1):132-147.
doi: 10.1007/s10439-016-1653-z

66. Liu J, Miller K, Ma X, *et al*. Direct 3D bioprinting of cardiac micro-tissues mimicking native myocardium. *Biomaterials*. 2020;256:120204.
doi: 10.1016/j.biomaterials.2020.120204

67. Wang Z, Wang L, Li T, *et al*. 3D bioprinting in cardiac tissue engineering. *Theranostics*. 2021;11(16):7948-7969.
doi: 10.7150/thno.61621

68. Zhou W, Yuan W, Chen Y, *et al*. Single-cell transcriptomics reveals the pulmonary inflammation induced by inhalation of subway fine particles. *J Hazard Mater*. 2024; 463:132896.
doi: 10.1016/j.jhazmat.2023.132896

69. Bai C, Wu L, Li R, Cao Y, He S, Bo X. Machine learning-enabled drug-induced toxicity prediction. *Adv Sci (Weinh)*. 2025;12(16):e2413405.
doi: 10.1002/advs.202413405

70. Guan D, Fan K, Spence I, Matthews S. Combining machine learning models of *in vitro* and *in vivo* bioassays improves rat carcinogenicity prediction. *Regul Toxicol Pharmacol*. 2018;94:8-15.
doi: 10.1016/j.yrtph.2018.01.008

71. Yavvari P, Laporte A, Elomaa L, *et al*. 3D-cultured vascular-like networks enable validation of vascular disruption properties of drugs in vitro. *Front Bioeng Biotechnol*. 2022;10:888492.
doi: 10.3389/fbioe.2022.888492

72. Berglund JD, Galis ZS. Designer blood vessels and therapeutic revascularization. *Br J Pharmacol*. 2003; 140(4):627-636.
doi: 10.1038/sj.bjp.0705457

73. Cook JC, Wu H, Aleo MD, Adkins K. Principles of precision medicine and its application in toxicology. *J Toxicol Sci*. 2018;43(10):565-577.
doi: 10.2131/jts.43.565

74. Guillemot F, Souquet A, Catros S, Guillotin B. Laser-assisted cell printing: principle, physical parameters versus cell fate and perspectives in tissue engineering. *Nanomedicine (Lond)*. 2010;5(3):507-515.
doi: 10.2217/nnm.10.14

75. Guillotin B, Catros S, Guillemot F. Laser assisted bio-printing (LAB) of cells and bio-materials based on laser induced forward transfer (LIFT). In: Schmidt V, Belegratis MR, eds. *Biological and Medical Physics, Biomedical Engineering*. Springer Berlin Heidelberg; 2014:193-209.
doi: 10.1007/978-3-642-41341-4_8

76. Ozbolat IT, Yu Y. Bioprinting toward organ fabrication: challenges and future trends. *IEEE Trans Biomed Eng*. 2013;60(3):691-699.
doi: 10.1109/TBME.2013.2243912

77. Hölzl K, Lin S, Tytgat L, Van Vlierberghe S, Gu L, Ovsianikov A. Bioink properties before, during and after 3D bioprinting. *Biofabrication*. 2016;8(3):032002.
doi: 10.1088/1758-5090/8/3/032002

78. Koch F, Tröndle K, Finkenzeller G, Zengerle R, Zimmermann S, Koltay P. Generic method of printing window adjustment for extrusion-based 3D-bioprinting to maintain high viability of mesenchymal stem cells in an alginate-gelatin hydrogel. *Bioprinting*. 2020;20:e00094.
doi: 10.1016/j.bprint.2020.e00094

79. Yin Z, Guo H, Li Y, Chiu J, Tian L. Ultrastable plasmonic bioink for printable point-of-care biosensors. *ACS Appl Mater Interfaces*. 2020;12(32):35977-35985.
doi: 10.1021/acsami.0c11799

80. Persaud A, Maus A, Strait L, Zhu D. 3D bioprinting with live cells. *Eng Regen*. 2022;3(3):292-309.
doi: 10.1016/j.engreg.2022.07.002

81. Lin H, Zhang D, Alexander PG, *et al*. Application of visible light-based projection stereolithography for live cell-scaffold fabrication with designed architecture. *Biomaterials*. 2013;34(2):331-339.
doi: 10.1016/j.biomaterials.2012.09.048

82. Dubbin K, Dong Z, Park DM, *et al*. Projection microstereolithographic microbial bioprinting for engineered biofilms. *Nano Lett*. 2021;21(3):1352-1359.
doi: 10.1021/acs.nanolett.0c04100

83. Lai J, Wang C, Wang M. 3D printing in biomedical engineering: processes, materials, and applications. *Appl Phy Rev*. 2021;8(2):021322.
doi: 10.1063/5.0024177

84. Murphy SV, Atala A. 3D bioprinting of tissues and organs. *Nat Biotechnol*. 2014;32(8):773-785.
doi: 10.1038/nbt.2958

85. Zhang J, Hu Q, Wang S, Tao J, Gou M. Digital light processing based three-dimensional printing for medical applications. *Int J Bioprint*. 2020;6(1):242.
doi: 10.18063/ijb.v6i1.242

86. Ma X, Qu X, Zhu W, *et al*. Deterministically patterned biomimetic human iPSC-derived hepatic model via rapid 3D bioprinting. *Proc Natl Acad Sci USA*. 2016;113(8): 2206-2211.
doi: 10.1073/pnas.1524510113

87. Saunders RE, Derby B. Inkjet printing biomaterials for tissue engineering: bioprinting. *Int Mater Rev*. 2014;59(8):430-448.
doi: 10.1179/1743280414Y.0000000040

88. Zhang J, Chen F, He Z, Ma Y, Uchiyama K, Lin JM. A novel approach for precisely controlled multiple cell patterning in microfluidic chips by inkjet printing and the detection of drug metabolism and diffusion. *Analyst*. 2016;141(10): 2940-2947.
doi: 10.1039/C6AN00395H

89. Gruene M, Deiwick A, Koch L, *et al*. Laser printing of stem cells for biofabrication of scaffold-free autologous grafts. *Tissue Eng Part C Methods*. 2011;17(1):79-87.
doi: 10.1089/ten.TEC.2010.0359

90. Xu T, Baicu C, Aho M, Zile M, Boland, T. Fabrication and characterization of bio-engineered cardiac pseudo tissues. *Biofabrication*. 2009;1(3):035001.
doi: 10.1088/1758-5082/1/3/035001

91. Koch L, Deiwick A, Schlie S, *et al*. Skin tissue generation by laser cell printing. *Biotechnol Bioeng*. 2012;109(7):1855-1863.
doi: 10.1002/bit.24455

92. Han W, Kong L, Xu M. Advances in selective laser sintering of polymers. *Int J Extrem Manuf*. 2022;4(4):042002. doi: 10.1088/2631-7990/ac9096

93. Duan B, Wang M, Zhou WY, Cheung WL, Li ZY, Lu WW. Three-dimensional nanocomposite scaffolds fabricated via selective laser sintering for bone tissue engineering. *Acta Biomater*. 2010;6(12):4495-4505. doi: 10.1016/j.actbio.2010.06.024

94. Jang J, Yi HG, Cho DW. 3D printed tissue models: present and future. *ACS Biomater Sci Eng*. 2016;2(10):1722-1731. doi: 10.1021/acsbiomaterials.6b00129

95. Jabbari E. Hydrogels for cell delivery. *Gels*. 2018;4(3):58. doi: 10.3390/gels4030058

96. Liu J, Wang Q, Le Y., *et al*. 3D-bioprinting for precision microtissue engineering: advances, applications, and prospects. *Adv Healthc Mater*. 2025;14(10):e2403781. doi: 10.1002/adhm.202403781

97. Zhang T, Yan KC, Ouyang L, Sun W. Mechanical characterization of bioprinted in vitro soft tissue models. *Biofabrication*. 2013;5(4):045010. doi: 10.1088/1758-5082/5/4/045010

98. Gudapati H, Yan J, Huang Y, Chrisey DB. Alginate gelation-induced cell death during laser-assisted cell printing. *Biofabrication*. 2014;6(3):035022. doi: 10.1088/1758-5082/6/3/035022

99. Li J, Wu C, Chu PK, Gelinsky M. 3D printing of hydrogels: rational design strategies and emerging biomedical applications. *Mat Sci Eng R Rep*. 2020;140:100543. doi: 10.1016/j.mser.2020.100543

100. Widhe M, Johansson U, Hillerdahl CO, Hedhammar M. Recombinant spider silk with cell binding motifs for specific adherence of cells. *Biomaterials*. 2013;34(33): 8223-8234. doi: 10.1016/j.biomaterials.2013.07.058

101. Aigner TB, DeSimone E, Scheibel T. Biomedical applications of recombinant silk-based materials. *Adv Mater*. 2018;30(19):e1704636. doi: 10.1002/adma.201704636

102. Brown M, Li J, Moraes C, Tabrizian M, Li-Jessen NYK. Decellularized extracellular matrix: new promising and challenging biomaterials for regenerative medicine. *Biomaterials*. 2022;289:121786. doi: 10.1016/j.biomaterials.2022.121786

103. Kim BS, Das S, Jang J, Cho DW. Decellularized extracellular matrix-based bioinks for engineering tissue- and organ-specific microenvironments. *Chem Rev*. 2020;120(19):10608-10661. doi: 10.1021/acs.chemrev.9b00808

104. D'souza AA, Shegokar R. Polyethylene glycol (PEG): a versatile polymer for pharmaceutical applications. *Expert Opin Drug Deliv*. 2016;13(9):1257-1275. doi: 10.1080/17425247.2016.1182485

105. Veronese FM, Pasut G. PEGylation, successful approach to drug delivery. *Drug Discov Today*. 2005;10(21): 1451-1458. doi: 10.1016/S1359-6446(05)03575-0

106. Yamaoka T, Tabata Y, Ikada Y. Distribution and tissue uptake of poly(ethylene glycol) with different molecular weights after intravenous administration to mice. *J Pharm Sci*. 1994;83(4):601-606. doi: 10.1002/jps.2600830432

107. Schmedlen RH, Masters KS, West JL. Photocrosslinkable polyvinyl alcohol hydrogels that can be modified with cell adhesion peptides for use in tissue engineering. *Biomaterials*. 2002;23(22):4325-4332. doi: 10.1016/S0142-9612(02)00177-1

108. Cheng Y, Deng S, Chen P, Ruan R. Polylactic acid (PLA) synthesis and modifications: a review. *Front Chem China*. 2009;4(3):259-264. doi: 10.1007/s11458-009-0092-x

109. Bee SL, Hamid ZAA, Mariatti M, *et al*. Approaches to improve therapeutic efficacy of biodegradable PLA/PLGA microspheres: a review. *Polym Rev*. 2018;58(3):495-536. doi: 10.1080/15583724.2018.1437547

110. Labet M, Thielemans W. Synthesis of polycaprolactone: a review. *Chem Soc Rev*. 2009;38(12):3484-3504. doi: 10.1039/B820162P

111. Kim J, Park SA, Kim J, Lee J. Fabrication and characterization of bioresorbable drug-coated porous scaffolds for vascular tissue engineering. *Materials*. 2019;12(9):1438. doi: 10.3390/ma12091438

112. Zhang W, Weng T, Li Q, *et al*. Applications of poly(caprolactone)-based nanofibre electrospun scaffolds in tissue engineering and regenerative medicine. *Curr Stem Cell Res Ther*. 2021;16(4):414-442. doi: 10.2174/1574888X15666201014145703

113. Kolesky DB, Truby RL, Gladman AS, Busbee TA, Homan KA, Lewis JA. 3D bioprinting of vascularized, heterogeneous cell-laden tissue constructs. *Adv Mater*. 2014;26(19): 3124-3130. doi: 10.1002/adma.201305506

114. Müller M, Becher J, Schnabelrauch M, Zenobi-Wong M. Nanostructured pluronic hydrogels as bioinks for 3D bioprinting. *Biofabrication*. 2015;7(3):035006. doi: 10.1088/1758-5090/7/3/035006

115. Ng WL, Yeong WY, Naing MW. Polyvinylpyrrolidone-based bio-ink improves cell viability and homogeneity during drop-on-demand printing. *Materials*. 2017; 10(2):190. doi: 10.3390/ma10020190

116. Xiang Y, Miller K, Guan J, Kiratitanaporn W, Tang M, Chen S. 3D bioprinting of complex tissues in vitro: State-

of-the-art and future perspectives. *Arch Toxicol*. 2022;96(3): 691-710.
doi: 10.1007/s00204-021-03212-y

117. Szűcs D, Fekete Z, Guba M, *et al*. Toward better drug development: three-dimensional bioprinting in toxicological research. *Int J Bioprint*. 2023;9(2):663.
doi: 10.18063/ijb.v9i2.663

118. Jain P, Kathuria H, Dubey N. Advances in 3D bioprinting of tissues/organs for regenerative medicine and in-vitro models. *Biomaterials*. 2022;287:121639.
doi: 10.1016/j.biomaterials.2022.121639

119. Wu X, Shi W, Liu X, Gu Z. Recent advances in 3D-printing-based organ-on-a-chip. *EngMedicine*. 2024;1(1):100003.
doi: 10.1016/j.engmed.2024.100003

120. Yoon S, Kilicarslan YD, Jeong U, *et al*. Microfluidics in high-throughput drug screening: Organ-on-a-chip and C. elegans-based innovations. *Biosensors*. 2024;14(1):55.
doi: 10.3390/bios14010055

121. Fuchs S, Johansson S, Tjell AØ, Werr G, Mayr T, Tenje M. In-line analysis of organ-on-chip systems with sensors: integration, fabrication, challenges, and potential. *ACS Biomater Sci Eng*. 2021;7(7):2926-2948.
doi: 10.1021/acsbiomaterials.0c01110

122. Zafeiris K, Brasinika D, Karatza A, *et al*. Additive manufacturing of hydroxyapatite–chitosan–genipin composite scaffolds for bone tissue engineering applications. *Mat Sci Eng C*. 2021;119:111639.
doi: 10.1016/j.msec.2020.111639

123. Lee V, Singh G, Trasatti JP, *et al*. Design and fabrication of human skin by three-dimensional bioprinting. *Tissue Eng Part C Methods*. 2014;20(6):473-484.
doi: 10.1089/ten.tec.2013.0335

124. Xu T, Zhao W, Zhu JM, Albanna MZ, Yoo JJ, Atala A. Complex heterogeneous tissue constructs containing multiple cell types prepared by inkjet printing technology. *Biomaterials*. 2013;34(1):130-139.
doi: 10.1016/j.biomaterials.2012.09.035

125. Jodat YA, Kiaee K, Vela Jarquin D, *et al*. A 3D-printed hybrid nasal cartilage with functional electronic olfaction. *Adv Sci*. 2020;7(5):1901878.
doi: 10.1002/advs.201901878

126. Wang Z, Abdulla R, Parker B, Samanipour R, Ghosh S, Kim K. A simple and high-resolution stereolithography-based 3D bioprinting system using visible light crosslinkable bioinks. *Biofabrication*. 2015;7(4):045009.
doi: 10.1088/1758-5090/7/4/045009

127. Anada T, Pan CC, Stahl AM, *et al*. Vascularized bone-mimetic hydrogel constructs by 3D bioprinting to promote osteogenesis and angiogenesis. *IJMS*. 2019; 20(5):1096.
doi: 10.3390/ijms20051096

128. Yin M, Yao M, Gao S, Zhang AP, Tam H, Wai PA. Rapid 3D patterning of poly(acrylic acid) ionic hydrogel for miniature pH sensors. *Adv Mater*. 2016;28(7):1394-1399.
doi: 10.1002/adma.201504021

129. Kanaki Z, Chandrinou C, Orfanou IM, *et al*. Laser-induced forward transfer printing on microneedles for transdermal delivery of gemcitabine. *IJB*. 2022;8(2):554.
doi: 10.18063/ijb.v8i2.554

130. Wang L, Cao H, Jiang H, Fang Y, Jiang D. A novel 3D bio-printing "liver lobule" microtissue biosensor for the detection of AFB1. *Food Res Int*. 2023;168:112778.
doi: 10.1016/j.foodres.2023.112778

131. Shrestha J, Ghadiri M, Shanmugavel M, *et al*. A rapidly prototyped lung-on-a-chip model using 3D-printed molds. *Organs-on-a-Chip*. 2019;1:100001.
doi: 10.1016/j.ooc.2020.100001

132. Yu C, Ma X, Zhu W, *et al*. Scanningless and continuous 3D bioprinting of human tissues with decellularized extracellular matrix. *Biomaterials*. 2019;194:1-13.
doi: 10.1016/j.biomaterials.2018.12.009

133. Zhang JXJ, Hoshino K. Nanomaterials for molecular sensing. *Molecular Sensors and Nanodevices: Principles, Designs and Applications in Biomedical Engineering*. Academic Press; 2019:413-487 .
doi: 10.1016/b978-0-12-814862-4.00007-7

134. Pan C, Xu J, Gao Q, *et al*. Sequentially suspended 3D bioprinting of multiple-layered vascular models with tunable geometries for in vitro modeling of arterial disorders initiation. *Biofabrication*. 2023;15(4):045017.
doi: 10.1088/1758-5090/aceffa

135. Song KH, Highley CB, Rouff A, Burdick JA. Complex 3D-printed microchannels within cell-degradable hydrogels. *Adv Funct Mater*. 2018;28(31):1801331.
doi: 10.1002/adfm.201801331

136. Tonti OR, Larson H, Lipp SN, *et al*. Tissue-specific parameters for the design of ECM-mimetic biomaterials. *Acta Biomater*. 2021;132:83-102.
doi: 10.1016/j.actbio.2021.04.017

137. Ma X, Liu J, Zhu W., *et al*. 3D bioprinting of functional tissue models for personalized drug screening and in vitro disease modeling. *Adv Drug Deliver Rev*. 2018;132: 235-251.
doi: 10.1016/j.addr.2018.06.011

138. Almutary AG, Alnuqaydan AM, Almatroodi SA, Bakshi HA, Chellappan DK, Tambuwala MM. Development of 3D-bioprinted colitis-mimicking model to assess epithelial barrier function using albumin nano-encapsulated anti-inflammatory drugs. *Biomimetics*. 2023;8(1):41.
doi: 10.3390/biomimetics8010041

139. Kim BS, Ahn M, Cho WW, Gao G, Jang J, Cho DW. Engineering of diseased human skin equivalent using 3D cell printing for representing pathophysiological

hallmarks of type 2 diabetes in vitro. *Biomaterials*. 2021; 272:120776.
doi: 10.1016/j.biomaterials.2021.120776

140. Vázquez-Aristizabal P, Henriksen-Lacey M, García-Astrain C, *et al*. Biofabrication and monitoring of a 3D printed skin model for melanoma. *Adv Healthc Mater*. 2024;13(27):e2401136.
doi: 10.1002/adhm.202401136

141. Tijore A, Irvine SA, Sarig U, Mhaisalkar P, Baisane V, Venkatraman S. Contact guidance for cardiac tissue engineering using 3D bioprinted gelatin patterned hydrogel. *Biofabrication*. 2018;10(2):025003.
doi: 10.1088/1758-5090/aaa15d

142. Melhem MR, Park J, Knapp L, *et al*. 3D printed stem-cell-laden, microchanneled hydrogel patch for the enhanced release of cell-secreting factors and treatment of myocardial infarctions. *ACS Biomater Sci Eng*. 2017;3(9):1980-1987.
doi: 10.1021/acsbiomaterials.6b00176

143. Ong CS, Fukunishi T, Zhang H, *et al*. Biomaterial-free three-dimensional bioprinting of cardiac tissue using human induced pluripotent stem cell derived cardiomyocytes. *Sci Rep*. 2017;7(1):4566.
doi: 10.1038/s41598-017-05018-4

144. Arai K, Murata D, Takao S, Verissiomo AR, Nakayama K. Cryopreservation method for spheroids and fabrication of scaffold-free tubular constructs. *PLoS One*. 2020;15(4):e0230428.
doi: 10.1371/journal.pone.0230428

145. Arai K, Kitsuka T, Nakayama K. Scaffold-based and scaffold-free cardiac constructs for drug testing. *Biofabrication*. 2021;13(4):1-14.
doi: 10.1088/1758-5090/ac1257

146. Mironov V, Boland T, Trusk T, Forgacs G, Markwald RR. Organ printing: computer-aided jet-based 3D tissue engineering. *Trends Biotechnol*. 2003;21(4):157-161.
doi: 10.1016/S0167-7799(03)00033-7

147. Utama RH, Atapattu L, O'Mahony AP, *et al*. A 3D bioprinter specifically designed for the high-throughput production of matrix-embedded multicellular spheroids. *iScience*. 2020;23(10):101621.
doi: 10.1016/j.isci.2020.101621

148. Matsusaki M, Sakaue K, Kadowaki K, Akashi M. Three-dimensional human tissue chips fabricated by rapid and automatic inkjet cell printing. *Adv Healthc Mater*. 2013;2(4):534-539.
doi: 10.1002/adhm.201200299

149. Gale, B.K., Jafek, A.R., Lambert, C.J., *et al*. A review of current methods in microfluidic device fabrication and future commercialization prospects. *Inventions*. 2018; 3(3):60.
doi: 10.3390/inventions3030060

150. Wu J, Gu M. Microfluidic sensing: state of the art fabrication and detection techniques. *J Biomed Opt*. 2011; 16(8):080901.
doi: 10.1117/1.3607430

151. Wu Q, Liu J, Wang X, *et al*. Organ-on-a-chip: Recent breakthroughs and future prospects. *Biomed Eng Online*. 2020;19(1):9.
doi: 10.1186/s12938-020-0752-0

152. Mehrotra S, de Melo BAG, Hirano M, *et al*. Nonmulberry silk based ink for fabricating mechanically robust cardiac patches and endothelialized myocardium-on-a-chip application. *Adv Funct Mater*. 2020;30(12): 1907436.
doi: 10.1002/adfm.201907436

153. Bhise NS, Manoharan V, Massa S, *et al*. A liver-on-a-chip platform with bioprinted hepatic spheroids. *Biofabrication*. 2016;8(1):014101.
doi: 10.1088/1758-5090/8/1/014101

154. Park JY, Ryu H, Lee B, *et al*. Development of a functional airway-on-a-chip by 3D cell printing. *Biofabrication*. 2018;11(1):015002.
doi: 10.1088/1758-5090/aae545

155. Chang R, Emami K, Wu H, Sun W. Biofabrication of a three-dimensional liver micro-organ as an in vitro drug metabolism model. *Biofabrication*. 2010;2(4): 045004.
doi: 10.1088/1758-5082/2/4/045004

156. Chang R, Nam J, Sun W. Direct cell writing of 3D microorgan for in vitro pharmacokinetic model. *Tissue Eng Part C Methods*. 2008;14(2):157-166.
doi: 10.1089/ten.tec.2007.0392

157. Lee H, Cho DW. One-step fabrication of an organ-on-a-chip with spatial heterogeneity using a 3D bioprinting technology. *Lab Chip*. 2016;16(14):2618-2625.
doi: 10.1039/C6LC00450D

158. Lin NYC, Homan KA, Robinson SS, *et al*. Renal reabsorption in 3D vascularized proximal tubule models. *PNAS*. 2019;116(12):5399-5404.
doi: 10.1073/pnas.1815208116

159. Fritschen A, Lindner N, Scholpp S, *et al*. High-scale 3D-bioprinting platform for the automated production of vascularized organs-on-a-chip. *Adv Healthc Mater*. 2024;13(17):2304028.
doi: 10.1002/adhm.202304028

160. Zhang YS, Davoudi F, Walch P, *et al*. Bioprinted thrombosis-on-a-chip. *Lab Chip*. 2016;16(21):4097-4105.
doi: 10.1039/C6LC00380J

161. Abudupataer M, Chen N, Yan S, *et al*. Bioprinting a 3D vascular construct for engineering a vessel-on-a-chip. *Biomed Microdevices*. 2019;22(1):10.
doi: 10.1007/s10544-019-0460-3

162. Cao X, Ashfaq R, Cheng F, *et al*. A tumor-on-a-chip system with bioprinted blood and lymphatic vessel pair. *Adv Funct Mater*. 2019;29(31):1807173. doi: 10.1002/adfm.201807173

163. Xie M, Gao Q, Fu J, Chen Z, He Y. Bioprinting of novel 3D tumor array chip for drug screening. *Bio-des Manuf*. 2020;3(3):175-188. doi: 10.1007/s42242-020-00078-4

164. Johnson BN, Lancaster KZ, Hogue IB, *et al*. 3D printed nervous system on a chip. *Lab Chip*. 2016;16(8):1393-1400. doi: 10.1039/C5LC01270H

165. Skardal A, Murphy SV, Devarasetty M, *et al*. Multi-tissue interactions in an integrated three-tissue organ-on-a-chip platform. *Sci Rep*. 2017;7(1):8837. doi: 10.1038/s41598-017-08879-x

166. Elezoglou E, Chliara M, Chatzipetrou M, *et al*. Laser bioprinting of cells and tumor organoids for organ-on-chip applications. In: *Frontiers in Ultrafast Optics: Biomedical, Scientific, and Industrial Applications XXIII*. Vol PC12411. SPIE; 2023:PC1241107. doi: 10.1117/12.2648068

167. Bowser DA, Moore MJ. Biofabrication of neural microphysiological systems using magnetic spheroid bioprinting. *Biofabrication*. 2019;12(1):015002. doi: 10.1088/1758-5090/ab41b4

168. Han T, Kundu S, Nag A, Xu Y. 3D printed sensors for biomedical applications: a review. *Sensors*. 2019; 19(7):1706. doi: 10.3390/s19071706

169. Cagnani GR, Ibáñez-Redín G, Tirich B, Gonçalves D, Balogh DT, Oliveira ON. Fully-printed electrochemical sensors made with flexible screen-printed electrodes modified by roll-to-roll slot-die coating. *Biosens Bioelectron*. 2020;165:112428. doi: 10.1016/j.bios.2020.112428

170. Wang R, Zhu X, Sun L, *et al*. Cost-effective fabrication of transparent strain sensors via micro-scale 3D printing and imprinting. *Nanomaterials*. 2021;12(1):120. doi: 10.3390/nano12010120

171. Wu D, Peng Q, Wu S, *et al*. A simple graphene NH3 gas sensor via laser direct writing. *Sensors*. 2018; 18(12):4405. doi: 10.3390/s18124405

172. Hecht L, Rager K, Davidonis M, Weber P, Gauglitz G, Dietzel A. Blister-actuated LIFT printing for multiparametric functionalization of paper-like biosensors. *Micromachines*. 2019;10(4):221. doi: 10.3390/mi10040221

173. Cao L, Han GC, Xiao H, Chen Z, Fang C. A novel 3D paper-based microfluidic electrochemical glucose biosensor based on rGO-TEPA/PB sensitive film. *Anal Chim Acta*. 2020;1096:34-43. doi: 10.1016/j.aca.2019.10.049

174. López Marzo AM, Mayorga-Martinez CC, Pumera M. 3D-printed graphene direct electron transfer enzyme biosensors. *Biosens Bioelectron*. 2020;151:111980. doi: 10.1016/j.bios.2019.111980

175. Lee J, Maji S, Lee H. Fabrication and integration of a low-cost 3D printing-based glucose biosensor for bioprinted liver-on-a-chip. *Biotechnol J*. 2023;18(12):e2300154. doi: 10.1002/biot.202300154

176. Guo X, Wang Z, Hou J, *et al*. A novel magnetoelastic biosensor consisting of carbon quantum dots/nitrocellulose membranes and $NiFe_2O_4$/ polylactic acid based on 3D printing for α2-macroglobulin detection. *Chin J Anal Chem*. 2024;52(9):100420. doi: 10.1016/j.cjac.2024.100420

177. Sun D, Gao W, Hu H, Zhou S. Why 90% of clinical drug development fails and how to improve it? *Acta Pharm Sin B*. 2022;12(7):3049-3062. doi: 10.1016/j.apsb.2022.02.002

178. Li X, Zhang R, Zhao B, Lossin C, Cao Z. Cardiotoxicity screening: a review of rapid-throughput in vitro approaches. *Arch Toxicol*. 2016;90(8):1803-1816. doi: 10.1007/s00204-015-1651-1

179. Muir DCG, Getzinger GJ, McBride M, Ferguson PL. How many chemicals in commerce have been analyzed in environmental media? A 50 year bibliometric analysis. *Environ Sci Technol*. 2023;57(25):9119-9129. doi: 10.1021/acs.est.2c09353

180. Godoy P, Hewitt NJ, Albrecht U, *et al*. Recent advances in 2D and 3D in vitro systems using primary hepatocytes, alternative hepatocyte sources and non-parenchymal liver cells and their use in investigating mechanisms of hepatotoxicity, cell signaling and ADME. *Arch Toxicol*. 2013;87(8):1315-1530. doi: 10.1007/s00204-013-1078-5

181. Scharff RL. Economic burden from health losses due to foodborne illness in the united states. *J Food Prot*. 2012;75(1):123-131. doi: 10.4315/0362-028X.JFP-11-058

182. Hussain MA, Dawson CO. Economic impact of food safety outbreaks on food businesses. *Foods*. 2013;2(4):585-589. doi: 10.3390/foods2040585

183. Van Norman GA. Limitations of animal studies for predicting toxicity in clinical trials: is it time to rethink our current approach? *JACC: Basic Transl Sci*. 2019;4(7): 845-854. doi: 10.1016/j.jacbts.2019.10.008

184. Monteiro-Riviere NA. Perspectives of nanotoxicology: introduction. *Wiley Interdiscip Rev Nanomed Nanobiotechnol*. 2022;14(6):e1843. doi: 10.1002/wnan.1843

185. Johnston LJ, Gonzalez-Rojano N, Wilkinson KJ, Xing B. Key challenges for evaluation of the safety of engineered nanomaterials. *NanoImpact*. 2020;18:100219. doi: 10.1016/j.impact.2020.100219

186. Clark KA, White RH, Silbergeld EK. Predictive models for nanotoxicology: current challenges and future opportunities. *Regul Toxicol Pharmacol*. 2011;59(3):361-363. doi: 10.1016/j.yrtph.2011.02.002

187. Yi HG, Kim H, Kwon J, Choi YJ, Jang J, Cho DW. Application of 3D bioprinting in the prevention and the therapy for human diseases. *Sig Transduct Target Ther*. 2021; 6(1):1-17. doi: 10.1038/s41392-021-00566-8

188. Blaeser A, Duarte Campos DF, Puster U, Richtering W, Stevens MM, Fischer H. Controlling shear stress in 3D bioprinting is a key factor to balance printing resolution and stem cell integrity. *Adv Healthc Mater*. 2016;5(3):326-333. doi: 10.1002/adhm.201500677

189. Liang S, Luo Y, Su Y, *et al*. Distinct toxicity of microplastics/ TBBPA co-exposure to bioprinted liver organoids derived from hiPSCs of healthy and patient donors. *IJB*. 2024;10(3):1403. doi: 10.36922/ijb.1403

190. Kang D, Lee H, Jung S. Use of a 3D inkjet-printed model to access dust particle toxicology in the human alveolar barrier. *Biotechnol Bioeng*. 2022;119(12):3668-3677. doi: 10.1002/bit.28220

191. Yong U, Kim D, Kim H, *et al*. Biohybrid 3D printing of a tissue-sensor platform for wireless, real-time, and continuous monitoring of drug-induced cardiotoxicity. *Adv Mater*. 2023;35(11):2208983. doi: 10.1002/adma.202208983

192. Madden LR, Nguyen TV, Garcia-Mojica S, *et al*. Bioprinted 3D primary human intestinal tissues model aspects of native physiology and ADME/Tox Functions. *iScience*. 2018;2:156-167. doi: 10.1016/j.isci.2018.03.015

193. Wei Z, Liu X, Ooka M, *et al*. Two-dimensional cellular and three-dimensional bio-printed skin models to screen topical-use compounds for irritation potential. *Front Bioeng Biotechnol*. 2020;8:109. doi: 10.3389/fbioe.2020.00109

194. Nguyen DG, Funk J, Robbins JB, *et al*. Bioprinted 3D primary liver tissues allow assessment of organ-level response to clinical drug induced toxicity in vitro. *PLoS One*. 2016;11(7):e0158674. doi: 10.1371/journal.pone.0158674

195. He J, Wang J, Pang Y, *et al*. Bioprinting of a hepatic tissue model using humaninduced pluripotent stem cell-derived hepatocytes for drug-induced hepatotoxicity evaluation. *IJB*. 2022;8(3):581. doi: 10.18063/ijb.v8i3.581

196. Janani G, Priya S, Dey S, Mandal BB. Mimicking native liver lobule microarchitecture in vitro with parenchymal and non-parenchymal cells using 3D bioprinting for drug toxicity and drug screening applications. *ACS Appl Mater Interfaces*. 2022;14(8):10167-10186. doi: 10.1021/acsami.2c00312

197. Ali ASM, Berg J, Roehrs V, *et al*. Xeno-free 3D bioprinted liver model for hepatotoxicity assessment. *Int J Mol Sci*. 2024;25(3):1811. doi: 10.3390/ijms25031811

198. Khanal D, Zhang F, Song Y, *et al*. Biological impact of nanodiamond particles – label free, high-resolution methods for nanotoxicity assessment. *Nanotoxicology*. 2019;13(9):1210-1226. doi: 10.1080/17435390.2019.1650970

199. Singh NK, Kim JY, Jang J, Kim YK, Cho DW. 3D cell printing of advanced vascularized proximal tubule-on-a-chip for drug induced nephrotoxicity advancement. *ACS Appl Bio Mater*. 2023;6(9):3750-3758. doi: 10.1021/acsabm.3c00421

200. Khalid MAU, Kim YS, Ali M, Lee BG, Cho YJ, Choi KH. A lung cancer-on-chip platform with integrated biosensors for physiological monitoring and toxicity assessment. *Biochem Engi J*. 2020;155:107469. doi: 10.1016/j.bej.2019.107469

201. Chandiramohan A, Dabaghi M, Aguiar JA, *et al*. Development and validation of an open-source, disposable, 3D-printed *in vitro* environmental exposure system for transwell culture inserts. *ERJ Open Res*. 2021;7(1):00705-02020. doi: 10.1183/23120541.00705-2020

202. Gerbolés AG, Galetti M, Rossi S, *et al*. Three-dimensional bioprinting of organoid-based scaffolds (OBST) for long-term nanoparticle toxicology investigation. *IJMS*. 2023;24(7):6595. doi: 10.3390/ijms24076595

203. Zhang YS, Arneri A, Bersini S, *et al*. Bioprinting 3D microfibrous scaffolds for engineering endothelialized myocardium and heart-on-a-chip. *Biomaterials*. 2016;110:45-59. doi: 10.1016/j.biomaterials.2016.09.003

204. Miller KL, Sit I, Xiang Y, *et al*. Evaluation of CuO nanoparticle toxicity on 3D bioprinted human iPSC-derived cardiac tissues. *Bioprinting*. 2023;32:e00284. doi: 10.1016/j.bprint.2023.e00284

205. Jiang D, Sheng K, Jiang H, Wang L. A biomimetic "intestinal microvillus" cell sensor based on 3D bioprinting for the detection of wheat allergen gliadin. *Bioelectrochemistry*. 2021;142:107919. doi: 10.1016/j.bioelechem.2021.107919

206. Tofani LB, Avelino TM, De Azevedo RJ, *et al*. Biofabricated 3D intestinal models as an alternative to animal based approaches for drug toxicity assays. *Tissue Eng Regen Med*. 2025;22(2):181-194.

doi: 10.1007/s13770-024-00694-6

207. Cuvellier M, Ezan F, Oliveira H, *et al*. 3D culture of HepaRG cells in GelMa and its application to bioprinting of a multicellular hepatic model. *Biomaterials*. 2021;269:120611. doi: 10.1016/j.biomaterials.2020.120611

208. Nguyen DG, Pentoney SL. Bioprinted three dimensional human tissues for toxicology and disease modeling. *Drug Discov Today Technol*. 2017;23:37-44. doi: 10.1016/j.ddtec.2017.03.001

209. Mathes SH, Ruffner H, Graf-Hausner U. The use of skin models in drug development. *Adv Drug Deliv Rev*. 2014;69-70:81-102. doi: 10.1016/j.addr.2013.12.006

210. Michael S, Sorg H, Peck CT, *et al*. Tissue engineered skin substitutes created by laser-assisted bioprinting form skin-like structures in the dorsal skin fold chamber in mice. *PLoS One*. 2013;8(3):e57741. doi: 10.1371/journal.pone.0057741

211. Pourchet LJ, Thepot A, Albouy M, *et al*. Human skin 3D bioprinting using scaffold-free approach. *Adv Healthc Mater*. 2017;6(4):1601101. doi: 10.1002/adhm.201601101

212. Hsu YT, Lee SP, Li CH, Ho MH, Kao CY. Preparation of 3D-printed gastric models with biomimetic mechanical, topographical and fluid dynamic properties. *J Taiwan Inst Chem Eng*. 2024;160:105389. doi: 10.1016/j.jtice.2024.105389

213. Ozbek II, Saybasili H, Ulgen KO. Applications of 3D bioprinting technology to brain cells and brain tumor models: special emphasis to glioblastoma. *ACS Biomater Sci Eng*. 2024;10(5):2616-2635. doi: 10.1021/acsbiomaterials.3c01569

214. Kiemen AL, Forjaz A, Sousa R, *et al*. High-resolution 3D printing of pancreatic ductal microanatomy enabled by serial histology. *Adv Mater Technol*. 2024;9(6):2301837. doi: 10.1002/admt.202301837

ACCSCIENCE PUBLISHING

International Journal of Bioprinting

REVIEW ARTICLE

Advancing sustainability in bioprinting through artificial intelligence

Hongyi Chen[1,2]* and Jie Huang[2]

[1]Department of Computer Science, Faculty of Engineering Sciences, University College London, London, United Kingdom

[2]Department of Mechanical Engineering, Faculty of Engineering Sciences, University College London, London, United Kingdom

Abstract

Sustainable bioprinting is a transformative approach in tissue engineering and regenerative medicine, offering solutions to environmental challenges while advancing functional outcomes. However, achieving true sustainability remains complex, requiring reductions in material waste and energy use, and scalable, resource-efficient fabrication without compromising biological performance. Artificial intelligence (AI) provides a powerful means to meet these demands through data-driven material design, predictive process optimization, and intelligent control systems that improve both efficiency and environmental impact across the bioprinting workflow. This review examines the integration of AI into sustainable bioprinting across four key areas: hydrogel material discovery and development, bioink screening, process parameter optimization, and AI-assisted intelligent printing. AI facilitates the design of eco-friendly hydrogels by predicting molecular interactions and tailoring structural properties. It also improves bioink formulation by optimizing printability, biocompatibility, and mechanical strength, thereby reducing reliance on resource-intensive trial-and-error experimentation. Furthermore, AI algorithms streamline workflows by dynamically adjusting printing parameters to improve fidelity and reduce waste, while advanced AI-assisted systems demonstrate the feasibility of multi-material, contactless bioprinting, aligning with sustainability goals.

Keywords: Artificial intelligence; Biomaterials; Bioprinting; Sustainability

***Corresponding author:**
Hongyi Chen
(hongyi.chen.16@ucl.ac.uk)

Citation: Chen H, Huang J. Advancing sustainability in bioprinting through artificial intelligence. *Int J Bioprint*. 2025;11(4):133-153. doi: 10.36922/IJB025170164

Received: April 24, 2025
Revised: June 16, 2025
Accepted: July 1, 2025
Published online: July 10, 2025

Copyright: © 2025 Author(s). This is an Open Access article distributed under the terms of the Creative Commons Attribution License, permitting distribution, and reproduction in any medium, provided the original work is properly cited.

Publisher's Note: AccScience Publishing remains neutral with regard to jurisdictional claims in published maps and institutional affiliations.

1. Introduction

Bioprinting is an advanced additive manufacturing technique that precisely deposits bioinks, which are composed of cells, biomaterials, and sometimes growth factors, in a layer-by-layer manner to fabricate complex, functional biological structures.[1-3] It is a transformative technology at the intersection of materials science, biology, and engineering.[4] It allows customization of bioink placement and control over architectural features and cell density, significantly enhancing the level of biomimicry of the native cell niche.[5-7] It also enables the fabrication of complex, patient-specific structures tailored for personalized medicine and provides highly relevant, less invasive biological models for comprehensive systemic investigations and evaluations.[8-11] Hydrogels play a pivotal

role as bioink materials due to their high water content, biocompatibility, and ability to mimic the extracellular matrix.

The increasing adoption of bioprinting places sustainability challenges at the forefront of the field. Conventional hydrogel materials, while effective, often rely on finite resources or involve manufacturing processes that generate chemical waste, consume high energy, or raise environmental and ethical concerns. As the demand for bioprinting scales up, particularly in fields such as regenerative medicine, drug screening, and tissue modeling, the need for sustainable, eco-friendly alternatives becomes increasingly urgent.[12,13] In this context, sustainable bioprinting refers to the development and implementation of bioprinting systems, materials, and workflows that minimize environmental impact, optimize resource use, and enhance scalability without compromising biological or functional performance. This includes using hydrogels derived from renewable or recycled sources, such as plant-based polysaccharides, waste-derived biopolymers, or repurposed synthetic polymers, which reduce reliance on petroleum-based feedstocks and promote material circularity. It also involves lowering the carbon footprint of fabrication by optimizing energy consumption during hydrogel synthesis, crosslinking, and printing processes, for instance, through low-temperature curing methods or solvent-free fabrication. Additionally, minimizing material waste during formulation and printing can be achieved through precise control of deposition parameters, reusability of support materials, and predictive modeling that reduces failed prints and redundant experiments. Together, these strategies contribute to a more resource-efficient, environmentally responsible bioprinting workflow aligned with broader sustainability goals in biofabrication and healthcare innovation.

However, implementing these sustainability strategies introduces new challenges. Renewable or recycled hydrogels often exhibit variability in composition and mechanical properties, making it difficult to ensure consistent printability and biological performance. Similarly, optimizing fabrication parameters to reduce energy use or material waste requires fine control over complex, interdependent variables such as viscosity, crosslinking dynamics, nozzle speed, and cell viability. Traditional trial-and-error methods are not only time-consuming and inefficient but also generate additional waste, counteracting sustainability goals. Moreover, the growing diversity of biomaterials, printing techniques, and application-specific design constraints further complicates sustainable bioprinting workflows.

Artificial intelligence (AI) offers a transformative solution to these challenges, providing data-driven insights and predictive capabilities to sustainable bioprinting.[14–16] AI can accelerate the discovery and optimization of hydrogels by predicting their performance based on molecular structure and interactions.[12,13,17] This contributes to the development of hydrogels tailored for specific applications in tissue engineering and drug delivery, and reduces the need for extensive physical testing. Furthermore, AI enables intelligent screening of bioink formulations for printability and functionality, optimizing rheological properties and crosslinking conditions.[14] Beyond material development, AI-assisted algorithms enhance bioprinting processes by optimizing printing parameters, minimizing waste, and improving printing fidelity and performance.[18] Integrating AI into bioprinting enables researchers to address sustainability challenges by accelerating the development process of sustainable biomaterials for bioprinting, minimizing material waste by eliminating unnecessary experimental iterations, and advancing the functionality of this technology.

While previous studies have explored the roles of AI in bioprinting[16,18,19] or discussed general principles of sustainability in biofabrication and AI's potential,[20] a comprehensive synthesis linking these domains remains limited. This review uniquely addresses this gap by proposing a structured, four-pillar framework illustrating how AI directly enhances sustainability in bioprinting: (i) accelerated material discovery (e.g., AlphaFold 3 for biomolecular prediction), (ii) data-driven bioink formulation screening, (iii) dynamic parameter optimization, and (iv) intelligent printing systems. This structure is shown in Figure 1. Furthermore, the review critically discusses implementation challenges and provides a comprehensive roadmap, advancing the current discourse by explicitly integrating AI methodologies with sustainability targets across the entire bioprinting workflow.

2. Bioprinting

2.1. Bioprinting techniques

This review categorizes bioprinting techniques based on their principles for stimuli-responsive deposition of bioinks into four main methods: inkjet bioprinting (using thermal and piezoelectric effects), extrusion-based bioprinting (utilizing air pressure or mechanical forces), laser-assisted bioprinting (using laser for droplet deposition), and stereolithography (using light for solidification), as shown in Figure 2.

Inkjet bioprinters dispense bioink droplets in the picoliter range using either thermal or piezoelectric mechanisms.[22,23] Thermal inkjet printers heat bioink to create pressure pulses that propel droplets, while piezoelectric printers generate acoustic waves to break

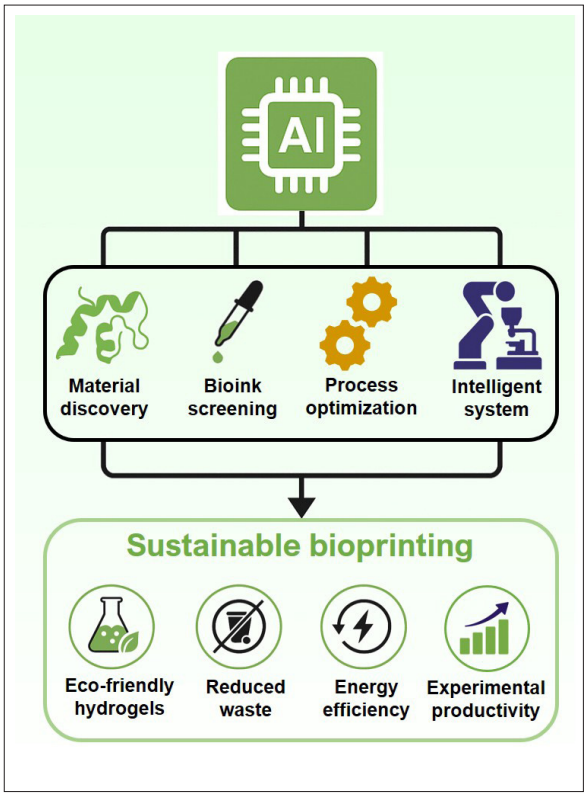

Figure 1. Overview of the structure of this review, which explores how artificial intelligence (AI) supports sustainable bioprinting across four key domains: material discovery, bioink screening, process optimization, and intelligent system integration. These AI-driven strategies contribute to the development of eco-friendly hydrogels, the reduction of material waste, improved energy efficiency, and experimental productivity.

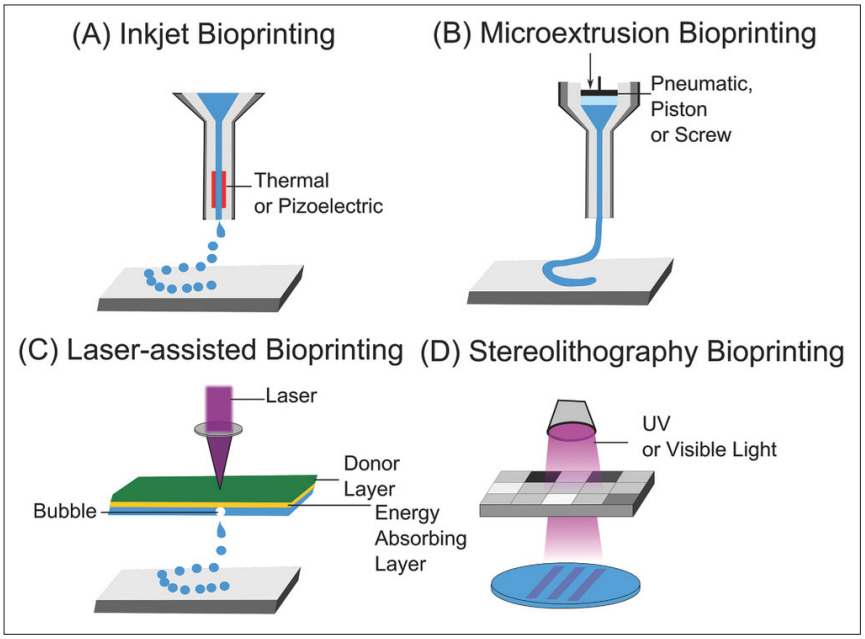

Figure 2. Schematic representation of the four main bioprinting methods. (A) Inkjet bioprinting utilizes piezoelectric or thermal actuators to eject precise, small droplets of bioinks containing hydrogels and cells. (B) Microextrusion bioprinting deposits filaments of viscous bioinks continuously through a nozzle, driven by pneumatic or mechanical (piston or screw-based) force. This technique excels in fabricating constructs with high cell densities and structural integrity. (C) Laser-assisted bioprinting uses a focused laser pulse to vaporize a thin donor layer (typically metallic or energy-absorbing material), generating high-pressure bubbles that propel droplets of bioink onto the substrate. (D) Stereolithography bioprinting employs ultraviolet (UV) or visible light to selectively polymerize photoreactive bioink layer-by-layer, creating a three-dimensional construct. Reprinted from Foyt et al.[21]

bioink into droplets.[23] Inkjet printing is cost-effective and widely available but faces challenges such as cell damage from heat or sound, inconsistent droplet size, and nozzle clogging.[24]

Extrusion-based bioprinters use mechanical or pneumatic systems to deposit continuous bioink filaments with high precision across *x*-, *y*-, and *z*-axes.[25] This method accommodates a wide range of bioink viscosities, supporting structural integrity with higher viscosities or promoting cell viability with lower ones.[26,27] It excels in printing bioinks with varying cell densities and mechanical properties.[28,29]

Laser-assisted bioprinting employs laser-induced forward transfer to deposit bioinks with cell-level precision.[30,31] A laser pulse vaporizes the metal film or bioink layers, creating bubbles that propel droplets onto the substrate. This technique offers exceptional patterning accuracy but is limited by low flow rates, high costs, metallic residues, and small print sizes, restricting its use for larger tissue or organ fabrication.[31]

Stereolithography bioprinting uses photopolymerization to solidify bioink layer-by-layer with ultraviolet (UV) or visible light.[32,33] A light source selectively cures bioink in precise patterns to form complex three-dimensional (3D) structures. As an entire layer is solidified simultaneously with the light projection, this layer-by-layer process can often increase printing speeds.[34] However, its reliance on light-sensitive materials and the potential cytotoxicity of unpolymerized residues may pose challenges.

2.2. Sustainable hydrogels for bioprinting

Hydrogels stand out as bioink materials and are becoming indispensable in bioprinting due to their high-water content, biocompatibility, and ability to mimic the extracellular matrix, supporting cell adhesion, proliferation, and differentiation.[2,35,36] Traditional hydrogels often pose environmental challenges, including resource-intensive production and limited recyclability. Sustainable hydrogels are therefore becoming a focal point in bioprinting due to their potential to address both functional and environmental challenges associated with conventional materials.[37–39] These hydrogels are specifically designed to meet the rigorous demands of bioprinting, such as biocompatibility and biodegradability, while maintaining environmental responsibility. Unlike traditional materials that may rely on finite resources or involve energy-intensive production processes, sustainable hydrogels emphasize minimal environmental impact by utilizing renewable or recycled materials.[40,41] This dual focus on functionality and sustainability makes them an essential component for advancing bioprinting technologies while adhering to eco-friendly principles.

These sustainable hydrogels can be broadly categorized based on their origin and composition, including natural hydrogels, derived from renewable biopolymers, and recycled hydrogels, made from repurposed polymers engineered for reusability.[42,43]

2.2.1. Biopolymers

Biopolymers, which are derived from natural plants, microbes, and other organisms, are more sustainable than synthetic polymers.[44] Hydrogels made from biopolymers are also inherently biocompatible and biodegradable, mimicking the extracellular matrix to promote cell attachment and proliferation. However, their mechanical properties often require enhancement through chemical modifications or blending with other materials to meet the structural demands of bioprinting.

Common biopolymers used for bioprinting include alginate, collagen, and gelatin. Alginate is a natural, water-soluble material primarily derived from brown seaweed and bacteria.[45] It has been used successfully for maintaining a chondrogenic phenotype of chondrocytes and enhancing neocartilage formation.[46,47] Its ionic crosslinking property facilitates printing of stable structures, contributing to its widespread use in bioprinting. Collagen is the main structural protein in the articular cartilage and meniscus extracellular matrix, and can be isolated from numerous biological tissues, retaining key signalling, adhesive, and other biochemical cues.[48] Gelatin is a water-soluble and biodegradable polypeptide produced through collagen hydrolysis. It has been extensively integrated with natural or synthetic hydrogels to enhance the biological properties of hydrogel composites.[47,49,50]

2.2.2. Recycled/upcycled polymers

Recycled or upcycled hydrogels offer another avenue for sustainability.[51] These materials not only reduce environmental waste but also align with circular economy principles by repurposing byproducts into functional biomaterials.[52] These hydrogels prioritize resource efficiency by enabling reuse through chemical or physical modifications, such as phase separation or crosslinking, retaining functionality across bioprinting cycles.[42,51]

Recent advances in hydrogel design have introduced recyclable and upcycled polymers that support sustainable bioprinting by reducing material waste and enabling multiple reuse cycles. Charlet et al.[42] developed recyclable double-network granular hydrogels with a disulfide-based network that allows selective degradation and microgel recovery while preserving printability. Xu et al.[53] created phase-separated supramolecular hydrogels with

enhanced toughness and recyclability under extreme conditions. Ji et al.[54] introduced a salting-out-based method using poly(N-isopropylacrylamide) hydrogels, enabling reversible solidification and dissolution without chemical crosslinkers or post-processing. Collectively, these approaches maintain mechanical performance while promoting circular material use, offering promising pathways for integrating sustainability into future bioprinting workflows.

3. Artificial intelligence for sustainable bioprinting

Despite advances in sustainable hydrogels for bioprinting, challenges remain in balancing printability, biocompatibility, biodegradability, and mechanical strength.[18,55,56] Hydrogels must exhibit optimal rheological properties for smooth deposition while maintaining structural integrity.[57] However, materials often excel in one attribute at the expense of another—for example, natural hydrogels offer high biocompatibility but lack the mechanical robustness needed for complex structures. Beyond material selection, ensuring efficient, reproducible bioprinting is equally complex. Traditional trial-and-error methods lead to resource inefficiencies, waste, and prolonged development cycles. Variability in bioink properties, processing parameters, and post-printing conditions further impacts cell viability, tissue functionality, and print success, undermining sustainability.

AI offers a transformative solution by enhancing material discovery, process optimization, and print quality. Coined by John McCarthy, the term AI refers to the intelligence demonstrated by machines.[58] Early rule-based AI relied on predefined "if-then" rules, facilitating data analysis and automation.[59,60] Classical AI introduced knowledge-based systems that integrated expert reasoning for problem-solving.[61,62] The emergence of machine learning (ML) revolutionized AI, enabling systems to learn from large datasets, recognize complex patterns, and predict material and print outcomes beyond the limitations of predefined rules.[63–66]

By combining the structured, efficient automation of classical AI with the adaptability and predictive capabilities of ML, AI is currently transforming sustainable bioprinting across multiple dimensions.[67–71] In hydrogel design, AI accelerated the discovery of materials that balance functionality, printability, and sustainability by predicting their behavior under diverse conditions and minimizing the resource-intensive nature of traditional development.[17] AI-driven approaches also enhanced material screening processes, ensuring bioinks meet the specific mechanical, biological, and environmental requirements for bioprinting.[14,72,73] Furthermore, AI optimized printing parameters in real-time, improving construct fidelity, reducing waste, and advancing efficiency.[19,74–76] Lastly, AI-assisted intelligent bioprinting technologies enabled powerful bioprinting capabilities with improved sustainability. Together, these innovations demonstrate AI's pivotal role in driving sustainable bioprinting forward, aligning with both ecological and functional demands. AI applications are categorized not only by technical functions but also by their potential impact on sustainability.

3.1. Material discovery and development

AI has revolutionized the incorporation of bioactive molecules into hydrogels, significantly enhancing their functionality for bioprinting applications.[77] Tools like AlphaFold, a deep learning model for protein structure prediction, enable precise identification of molecular interactions, facilitating the integration of bioactive components such as growth factors, peptides, and enzymes into hydrogel matrices for functionalization. AI-driven methods allow the design of hydrogels with tailored properties.

One notable example of AI's potential in modeling molecular interactions is AlphaFold, which has redefined protein structure prediction. AlphaFold, developed in three successive versions (AlphaFold 1, 2, and 3), has revolutionized protein structure prediction. AlphaFold 1 introduced neural networks to predict inter-residue distances, demonstrating significant advancements in protein modeling by leveraging evolutionary data and achieving superior accuracy during the Critical Assessment of Structure Prediction 13.[12] It is used on multiple sequence alignments (MSAs) and gradient descent algorithms to model protein structures, achieving notable success in free modeling domains, particularly for proteins lacking homologous templates. AlphaFold 2 advanced this by incorporating Evoformer blocks to integrate spatial and evolutionary relationships, enabling atomic-level accuracy in 3D structural predictions, as shown in the Critical Assessment of Structure Prediction 14.[13] It achieved near-experimental accuracy for most targets, effectively modeling long-range residue interactions and folding pathways, but remained computationally intensive due to its reliance on MSAs. AlphaFold 3 further enhanced capabilities with a diffusion-based architecture, replacing Evoformer with Pairformer[17] (Figure 3). This eliminates MSA dependency while enabling accurate modeling of protein complexes, including protein–ligand and protein–nucleic acid interactions. Its experimental results demonstrated superior performance in predicting multi-component systems, with applications extending to chemically modified residues and novel biomolecular assemblies.

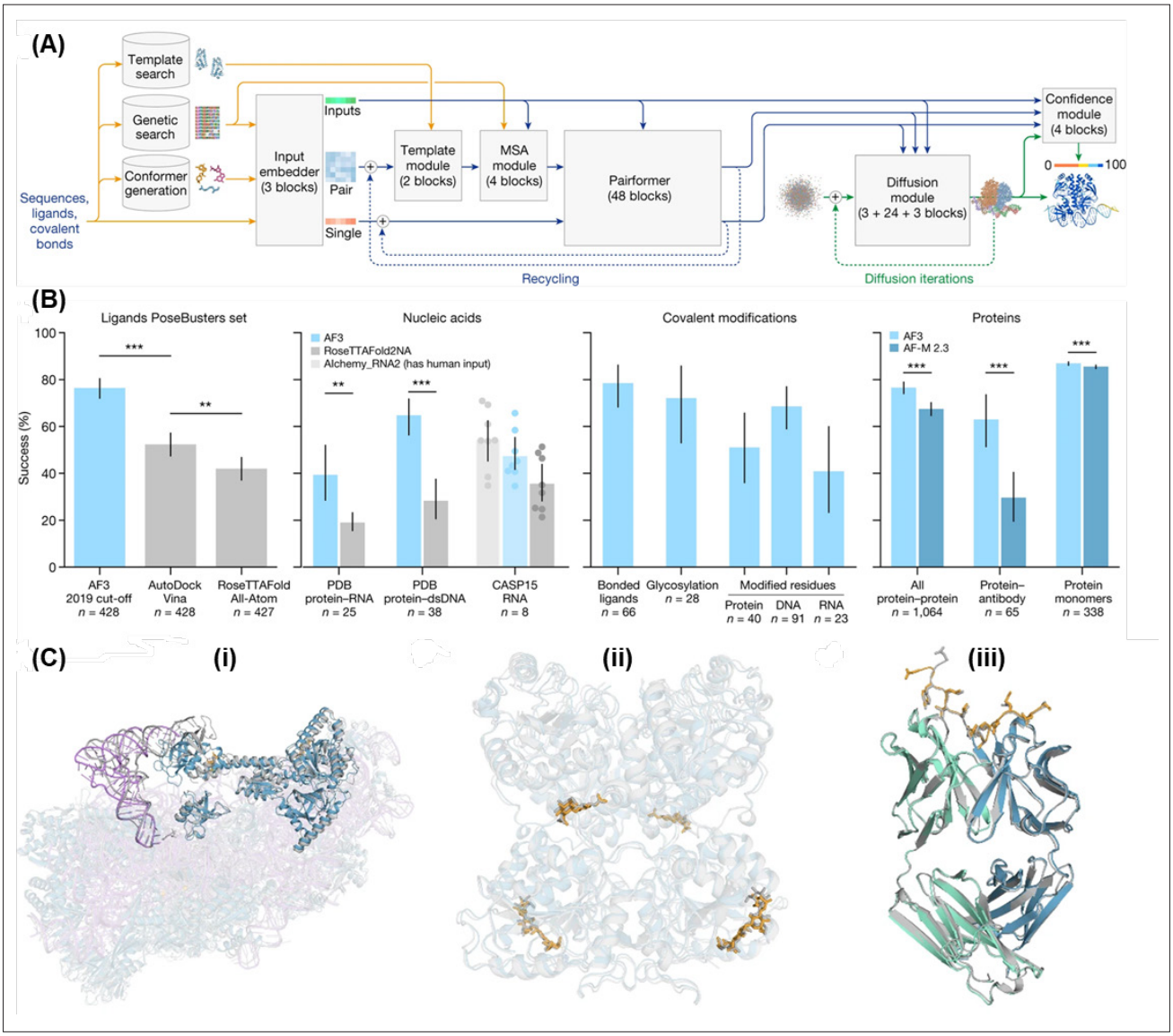

Figure 3. AlphaFold 3 is capable of accurately predicting protein structures, protein–ligand interactions, and multi-component biomolecular complexes using its advanced diffusion-based architecture and Pairformer module. (A) The Pairformer module and diffusion-based architecture of AlphaFold 3 enable precise predictions of biomolecular interactions without reliance on multiple sequence alignments, showcasing its innovative approach to modeling complex biological systems. (B) Success rates in predicting diverse biomolecular complexes, including protein–protein, protein–ligand, and protein–nucleic acid interactions, highlight its capability to identify key functional interactions relevant for material design. (C) Real-world applications of AlphaFold 3 in discovering and modeling biomolecular materials: (i) protein–nucleic acid complexes, (ii) protein–ligand systems, and (iii) ribosomal subunits, demonstrating its potential to guide the development of bioactive hydrogels and other sustainable bioprinting materials. Reprinted from Abramson et al.[17]

Despite AlphaFold's transformative impact on protein modeling, developing comparable AI tools for biomaterial design in bioprinting remains limited by fundamental challenges. One fundamental challenge among these is the absence of large, standardized, and well-annotated open-source datasets that link bioink composition to rheological properties, printability, and biological performance. Unlike protein sequences with defined formats and abundant data, bioinks lack universal representations, and the available datasets are often small, heterogeneous, and inaccessible. This hinders model training, validation, and benchmarking, making it difficult to achieve generalizable or reproducible outcomes. Additionally, the performance of hydrogels often depends not only on molecular configuration but also on mesoscale properties (e.g., porosity, swelling, rheology), which are difficult to encode or predict purely from primary composition. Addressing these limitations requires community-wide efforts in data

sharing, standardization, and the development of open benchmarks to accelerate progress in predictive modeling for bioprinting.

To circumvent these limitations, researchers are turning to other AI strategies, such as multi-objective optimization, that focus on synthesis pathways rather than structural modeling alone. Hardian et al.[78] applied support vector machines and a multi-objective genetic algorithm to optimize the green electrochemical synthesis of zeolitic imidazolate framework-8. Their approach enabled simultaneous prediction and optimization of synthesis parameters to maximize product quality while minimizing environmental impact. The AI-optimized conditions achieved a high yield of 88%, crystallinity of 86%, and 100% purity, while keeping energy consumption at 7 kWh/kg of product, an E-factor of 11 kg waste/kg product, and a carbon footprint of 27 kg carbon dioxide-equivalent/kg product. These results demonstrate the potential of AI to identify synthesis conditions that balance performance with sustainability. Although focused on metal–organic frameworks, the methodology is highly transferable to bioprinting contexts such as bioink and scaffold development, where similar multi-objective trade-offs between material function and environmental impact must be addressed.

These advancements represent a transformative opportunity for sustainable hydrogel and biomaterial discovery in bioprinting. Emerging ML approaches enable predictive modeling at multiple scales, from atomic-level biomolecular interactions to macroscopic material performance, facilitating the rational design of bioinks with optimized mechanical strength, biocompatibility, and biodegradability. Tools like AlphaFold exemplify how deep learning can predict protein–material interactions to guide the development of functional bioactive hydrogels. Complementing this, other AI-driven frameworks have demonstrated the ability to optimize synthesis pathways by balancing material yield with environmental metrics such as energy consumption and carbon footprint. Together, these approaches highlight the broader potential of AI in accelerating sustainable material development for bioprinting. By integrating high-throughput computational modeling with multi-objective optimization, AI reduces reliance on trial-and-error experimentation, conserves resources, and enables the targeted design of novel, eco-friendly bioinks, thus contributing to more efficient and sustainable biofabrication.

3.2. Bioink formulation screening

Once promising hydrogel materials are discovered and selected based on their functional properties tailored to specific applications, the next step is bioink formulation screening to assess their practicality and reliability for bioprinting applications. This requires a detailed analysis of performance indicators, including printability, rheological behavior, crosslinking efficiency, and cellular response under various printing conditions. This stage ensures that hydrogel formulations not only meet theoretical design criteria but also perform effectively during bioprinting. The integration of AI-driven methodologies, such as ML models, enables rapid evaluation and prediction of hydrogel performance, minimizes trial-and-error experimentation, and ensures sustainable, high-quality outcomes in bioprinting applications.[79]

Ink printability is a crucial aspect of 3D printing as it greatly influences the integration and function of printed implants.[2] ML has been used to predict printability from biomaterial formulations to guide the development of inks. Chen et al.[14] used ML learning algorithms to predict printable biomaterial formulations for direct ink writing. The data used in their study consisted of 210 ink formulations with two ink systems: the hydrogel-based system (including both natural and synthetic hydrogels) and the polymer organic solution-based system. The biomaterials include polymers of a range of molecular weights, properties, and functional fillers with different sizes and functions. The inks were 3D-printed using the direct ink writing technique, and their printability was assessed. The ML algorithms (decision tree, random forest, and deep learning) successfully predicted the printability of biomaterial formulations with high accuracy (>88%), as shown in Figure 4A. In addition, a printability map of biomaterial composites was generated using the trained ML algorithms to guide the ink design (Figure 4B). This study has paved the way for using ML in guiding the selection of materials with a range of properties for different types of 3D printing.

AI-driven models can screen potential hydrogel candidates based on their physicochemical and mechanical properties, such as viscosity, shear-thinning behavior, and crosslinking efficiency. Nadernezhad and Groll[80] employed a random forest algorithm to predict the printability of hyaluronic acid-based hydrogel inks based on their rheological properties. They quantitatively assessed the significance of various rheological parameters and identified 13 critical measures that defined the printability of hydrogel formulations. Their trained model statistically predicted that a printable formulation should demonstrate high yield viscosity and minimal plasticity before initiating flow.

Lee et al.[81] presented a ML-based strategy for bioink design, focusing on elastic modulus for shape fidelity and yield stress for extrusion feasibility (Figure 4B). Data

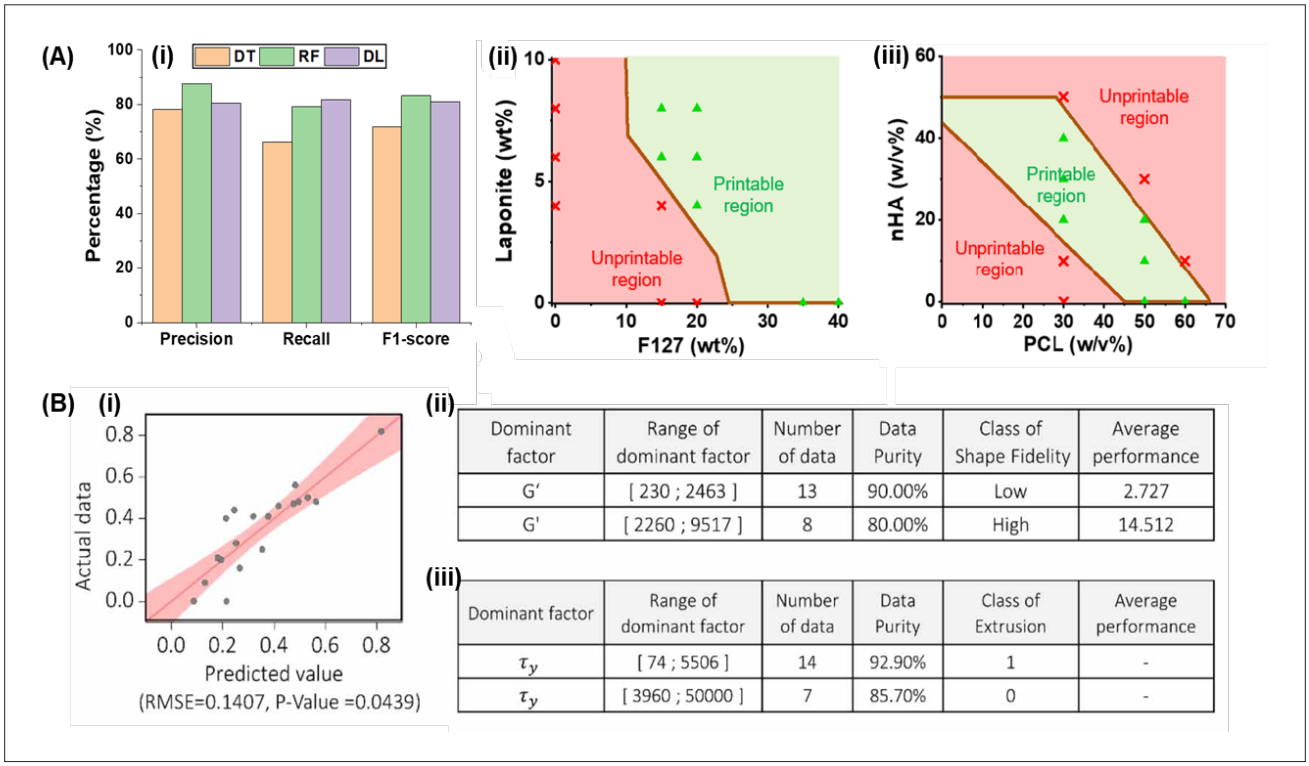

Dominant factor	Range of dominant factor	Number of data	Data Purity	Class of Shape Fidelity	Average performance
G‘	[230 ; 2463]	13	90.00%	Low	2.727
G'	[2260 ; 9517]	8	80.00%	High	14.512

Dominant factor	Range of dominant factor	Number of data	Data Purity	Class of Extrusion	Average performance
τ_y	[74 ; 5506]	14	92.90%	1	-
τ_y	[3960 ; 50000]	7	85.70%	0	-

Figure 4. Machine learning in material screening for bioprinting. (A) Machine learning in predicting the printability of biomaterials for direct ink writing. (i) Prediction performance among decision tree (DT), random forest (RF), and deep learning (DL) models.[14] Reprinted from Chen et al.[14] (B) Machine learning analysis of bioink printability. (i) Correlation between predicted and actual data (root mean squared error [RMSE]: 0.1407, p-value 0.0439) showing model accuracy. (ii) Shape fidelity classification based on elastic modulus. (iii) Extrusion classification based on yield stress. Reprinted with permission from Lee et al.[80] Copyright © 2020, IOP Publishing Ltd.

includes 25 bioink formulations composed of collagen, hyaluronic acid, and fibrin, with input features including component concentrations and output targets such as elastic modulus, yield stress, extrusion feasibility, and shape fidelity. ML analysis correctly classified 84.6% of cases for shape fidelity and 89.5% for extrusion feasibility, demonstrating strong predictive performance. Bioinks with an elastic modulus above 2260 Pa exhibited high shape fidelity, while those with a yield stress above 3960 Pa led to nozzle clogging. Multiple regression analysis (*p*-value: 0.0439) further validated a predictive model for optimizing bioink composition based on collagen, hyaluronic acid, and fibrin concentrations. Future work can focus on expanding the dataset beyond the initial 25 formulations and making it openly available to support more robust model training and improve generalizability across a wider range of bioink materials.

AI-driven bioink formulation screening has the potential to significantly improve the efficiency and accuracy of selecting high-performing bioinks by predicting printability, rheological properties, crosslinking behavior, and cell compatibility. ML models trained on large datasets of hydrogel compositions can rapidly identify optimal formulations, reducing the need for trial-and-error experimentation and minimizing material waste. These advancements ensure that selected bioinks meet the necessary structural and biological requirements, accelerating the development of sustainable and functional materials for bioprinting applications. Current studies often rely on small or focused datasets, such as the 25 formulations in Lee et al.,[81] which may lack model generalizability and reproducibility. While Nadernezhad and Groll[80] and Chen et al.[14] incorporated more datasets (180 and 210 samples, respectively), their scope remains confined to specific material systems. Future efforts should focus on expanding the diversity and scale of training data, incorporating broader input parameters such as crosslinking kinetics and cell viability. Most existing models focus primarily on predicting printability based on rheological or mechanical properties. Thus, future work should broaden predictive targets to include crosslinking behavior, degradation profiles, and biological performance metrics such as cell viability and tissue integration, enabling more holistic and application-specific bioink screening.

3.3. Processing parameters optimization

Besides optimizing bioink formulations, achieving consistent and high-fidelity bioprinted constructs also depends on precise control of printing parameters such as extrusion speed, nozzle pressure, and layer stacking accuracy. Variations in processing conditions can significantly impact construct stability, resolution, and cellular viability.[67,82,83] Traditional approaches to address these challenges involve extensive trial-and-error experiments to fine-tune such parameters and can be time- and resource-consuming. Addressing these complexities through AI-driven optimization offers a transformative approach to enhancing bioprinting efficiency and accuracy.[71,84]

Bone et al.[85] introduced a hierarchical ML (HML) framework for optimizing 3D bioprinting alginate biopolymer (Figure 5A). The dataset included 48 alginate hydrogel prints, with input parameters of ink concentration, flow rate, nozzle speed, and nozzle diameter, and output targets defined as print fidelity metrics (line width and corner radius errors). The HML approach leverages domain knowledge, incorporating integrated system variables (e.g., nozzle speed, flow rate, ink concentration) with middle-layer physical relationships (e.g., effective shear rate, viscosity, proportionality laws) to predict and optimize print fidelity. Experimental validation demonstrated that the HML framework accurately predicts optimal printing parameters, achieving high-fidelity prints with less than 10% dimensional error. The study also highlights the trade-offs in optimizing specific features, such as linewidths and corner radii, emphasizing the need for multi-objective optimization.

Chen et al.[86] demonstrated an AI-driven approach to optimizing 3D bioprinting parameters, enhancing both efficiency and sustainability (Figure 5B). The AI-assisted high-throughput printing–condition–screening system integrates a programmable pneumatic extrusion bioprinter with an AI-powered image-analysis algorithm, systematically optimizing key parameters such as printing pressure, nozzle speed, and printing distance. The model was trained on 280 labeled images of alginate–gelatin hydrogel prints, using deep learning to classify extrusion states and predict optimal print conditions. By automating the screening process, the AI-assisted high-throughput printing–condition–screening system eliminates reliance on extensive trial-and-error experimentation, reducing material waste while ensuring high-quality scaffold fabrication. Experimental results demonstrated that the AI-assisted approach led to a 45% reduction in optimization time, significantly lowering the consumption of bioinks and resources. The optimized hydrogel scaffolds exhibited improved mechanical stability, uniform fiber alignment, and enhanced porosity, factors critical for promoting cell proliferation and tissue regeneration. *In vivo* diabetic wound healing models showed that AI-optimized scaffolds accelerated re-epithelialization, improved collagen deposition, and enhanced vascularization, demonstrating superior therapeutic potential over conventionally printed scaffolds. This AI-assisted workflow minimizes resource consumption, ensures reproducibility, and enhances the scalability of bioprinting.

Fu et al.[87] investigated the effects of printing parameters on the printability of Pluronic F127 hydrogels in extrusion-based 3D bioprinting and introduced an ML-guided optimization framework (Figure 5C). The researchers examined the influence of nozzle temperature, nozzle gauge, path height, and material composition on printability, using the width index as the primary output metric. They trained a support vector machine model on 12 data points selected via uniform design across three key parameters—concentration, nozzle temperature, and path height—and generated a 3D process map that predicted optimal printing regions with over 75% probability of high-fidelity output. While the study demonstrates the potential of ML to reduce trial-and-error and improve parameter selection, the small dataset limits generalizability. Future work should focus on expanding the parameter space and dataset size, incorporating additional variables such as crosslinking conditions and cell viability, and establishing standardized printability metrics to enable broader applicability and model reproducibility across materials and platforms.

Xu et al.[88] developed a predictive framework for assessing cell viability in stereolithography-based 3D-bioprinted gelatin structures, addressing the limitations of physics-based models through an ensemble ML approach combining ridge regression, k-nearest neighbors, random forest, and neural networks. The model was trained and validated on 405 cell viability data points collected from 81 bioprinting conditions, using gelatin methacrylate concentration, UV intensity, UV exposure time, and layer thickness as input features. Results showed that UV exposure time had the greatest impact on cell viability, followed by layer thickness, gelatin methacrylate concentration, and UV intensity.

Zhang et al.[89] developed an integrated framework combining advanced rheological modeling, computational fluid dynamics simulations, and ML to predict as-extruded cell viability in extrusion-based 3D bioprinting. The study used support vector regression to predict Cross power law parameters for alginate inks based on 76 rheological measurements across different concentrations and temperatures, and trained multilayer perceptron regressors

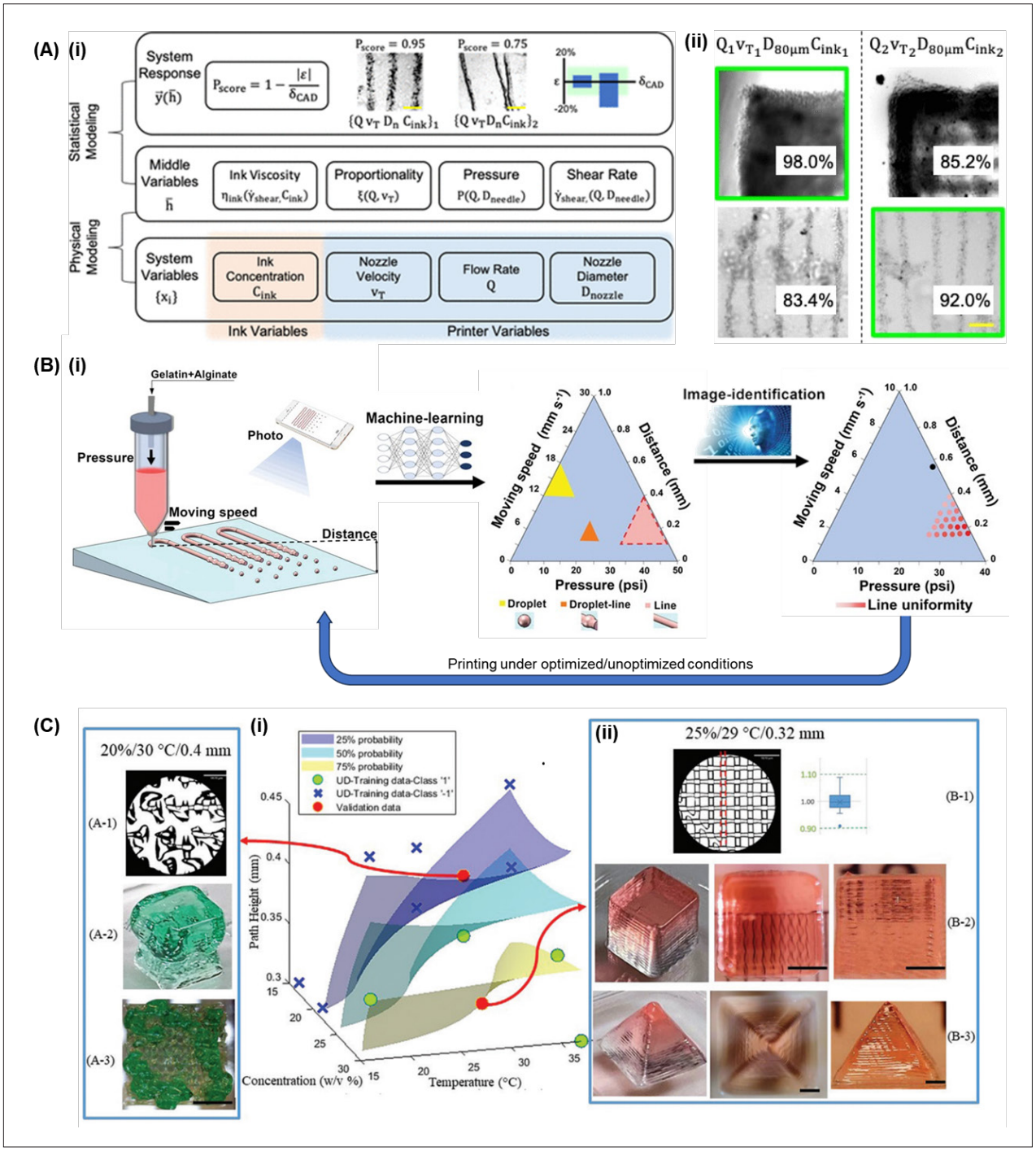

Figure 5. Machine learning in optimizing processing parameters for bioprinting. (A) A hierarchical machine learning model used for optimizing three-dimensional printing parameters. (i) The schematics of the model integrating laboratory-controlled system variables, middle-layer physical relationships, and statistical inference to predict and enhance print fidelity based on dimensional error metrics. (ii) Visualization of trade-offs in optimizing printing parameters for high-fidelity features.[85] Reprinted with permission from Bone et al.[85] Copyright © 2020, American Chemical Society. (B) Artificial intelligence (AI)-assisted high-throughput printing-condition-screening system. Real-time image recognition analyzes printed patterns, classifying them into droplets, droplet lines, or continuous lines. AI-generated phase diagrams guide parameter selection for achieving optimal print fidelity and uniformity, reducing material waste and improving sustainable bioprinting efficiency.[88] Reprinted with permission from Xu et al.[88] Copyright © 2020, Springer Nature. (C) Machine learning-guided parameter optimization in bioprinting. (i) Low-printability validation: Parameters resulted in (A-1) irregular filaments, (A-2) deformed cube, and (A-3) non-uniform grid. (ii) High-printability validation: Optimized parameters produced (B-1) uniform filaments, (B-2) well-formed cube, and (B-3) geometrically accurate pyramid.[87] Scale bar: 1.87 mm for (A-1) and (B-1); 2 mm for (A-3), (B-2), and (B-3). Reprinted from Fu et al.[87]

on 1050 labeled data points collected from simulations and experiments using four cell lines (fibroblast, stem, cancer, and endothelial cells). Input features included wall shear stress (1.0–5.0 kPa) and exposure time (100–700 ms), while the output target was cell viability. Model performance was evaluated using 20-fold cross-validation, yielding high predictive accuracy with R^2 values ranging from 0.866 to 0.964 across cell types.

Rojek et al.[90] presented an AI-driven approach to optimize 3D printing efficiency and reduce material waste by training artificial neural networks on a dataset of 238 input parameters and eight output metrics, including filament usage, cost, and print time, using experimental data from 3D-printed elbow exoskeleton components. The artificial neural network model (multilayer perceptron regressor-142-102-8) achieved strong predictive performance (mean squared error = 0.007; testing quality = 0.9132), allowing a 30-fold reduction in waste and enabling one free print for every 6.67 prints.

Wu and Xu[91] developed a data-driven ensemble learning approach to predict droplet velocity and volume in inkjet-based bioprinting. They conducted a full factorial design with 243 experiments varying polymer concentration, voltage, dwell time, and rise time, training predictive models (random forest, least absolute shrinkage and selection operator, support vector regressor, extreme boosting gradient) on these features using 10-fold cross-validation (R^2 = 0.977–0.978). The ensemble model achieved high predictive accuracy, demonstrating its potential to enhance the precision of droplet-based bioprinting, optimizing process parameters to improve reproducibility and scalability.

AI-driven approaches trained on experimental datasets and computational simulations predict optimal printing conditions, ensuring high-resolution constructs with minimal defects and material waste. They reduce the need for manual adjustments and trial-and-error experimentation, making bioprinting more efficient, scalable, and sustainable. While these developments are promising, current models, such as those by Bone et al.,[85] Fu et al.,[87] and Chen et al.,[86] are often trained on material-specific or relatively small datasets, which may limit their immediate applicability across different bioprinting platforms or bioink types. Some frameworks, like those developed by Zhang et al.[89] and Xu et al.[88] have begun to incorporate cell viability and rheological behavior, reflecting a growing interest in integrating both physical and biological outcomes into predictive models. Others, like Rojek et al.,[90] demonstrate the potential of AI in reducing material waste and energy use, aligning with broader sustainability goals. Looking ahead, expanding the diversity and scale of training datasets, including parameters such as crosslinking kinetics and biological performance, and developing real-time, adaptive control systems could further enhance the robustness and utility of AI in bioprinting.

3.4. Artificial intelligence-assisted intelligent printing

Beyond material development, bioink formulation, and parameter optimization, AI-assisted intelligent printing represents a major step toward adaptive and autonomous bioprinting systems. These systems leverage advanced algorithms, real-time monitoring, and process automation to enhance control, precision, and functionality. Advanced algorithms enable *in situ* bioprinting with acoustic levitation, allowing voxel-by-voxel and contact-free material placement on diverse substrates and expanding the possibilities of bioprinting.[92,93] AI-powered computer vision systems, feedback loops, and predictive modeling have been employed to detect and correct print defects in real time, improving print success rates.[94]

Chen et al.[92] developed an intelligent printing system, AcoustoFab, which combines a phased array of transducers and advanced control algorithms, allowing omnidirectional and multi-material *in situ* bioprinting using acoustic levitation (Figure 6A). AcoustoFab utilizes OpenMPD (multimodal particle-based displays)[95] and the boundary element method[96] algorithms to enable the formation of multiple acoustic traps in proximity to complex sound-scattering surfaces for depositing materials on these complex substrates. The OpenMPD **algorithm** dynamically calculates and updates the positions of multiple acoustic tweezers, allowing control over the levitation and omnidirectional movement of multiple droplets of bioinks in mid-air. The boundary element method algorithm simulates acoustic wave interactions with large, scattering surfaces in real-time, predicting and mitigating potential distortions in the acoustic field. This allows levitating, transporting, and *in situ* depositing of bioinks onto irregular surfaces of diverse orientations, including a human hand. AcoustoFab is capable of printing any soft materials within a wide range of viscosities (1–5,000,000 mPa·s), including biopolymers, composite hydrogels, and bioinks. The embedded cells in the hydrogels also demonstrated high viability post-printing. The contactless nature of AcoustoFab minimizes cross-contamination, mechanical wear, and substrate damage, contributing to reduced material waste and lower failure rates, which is critical in clinical applications. By integrating advanced algorithms with acoustic levitation, AcoustoFab presents a promising approach for intelligent and sustainable biofabrication.[97]

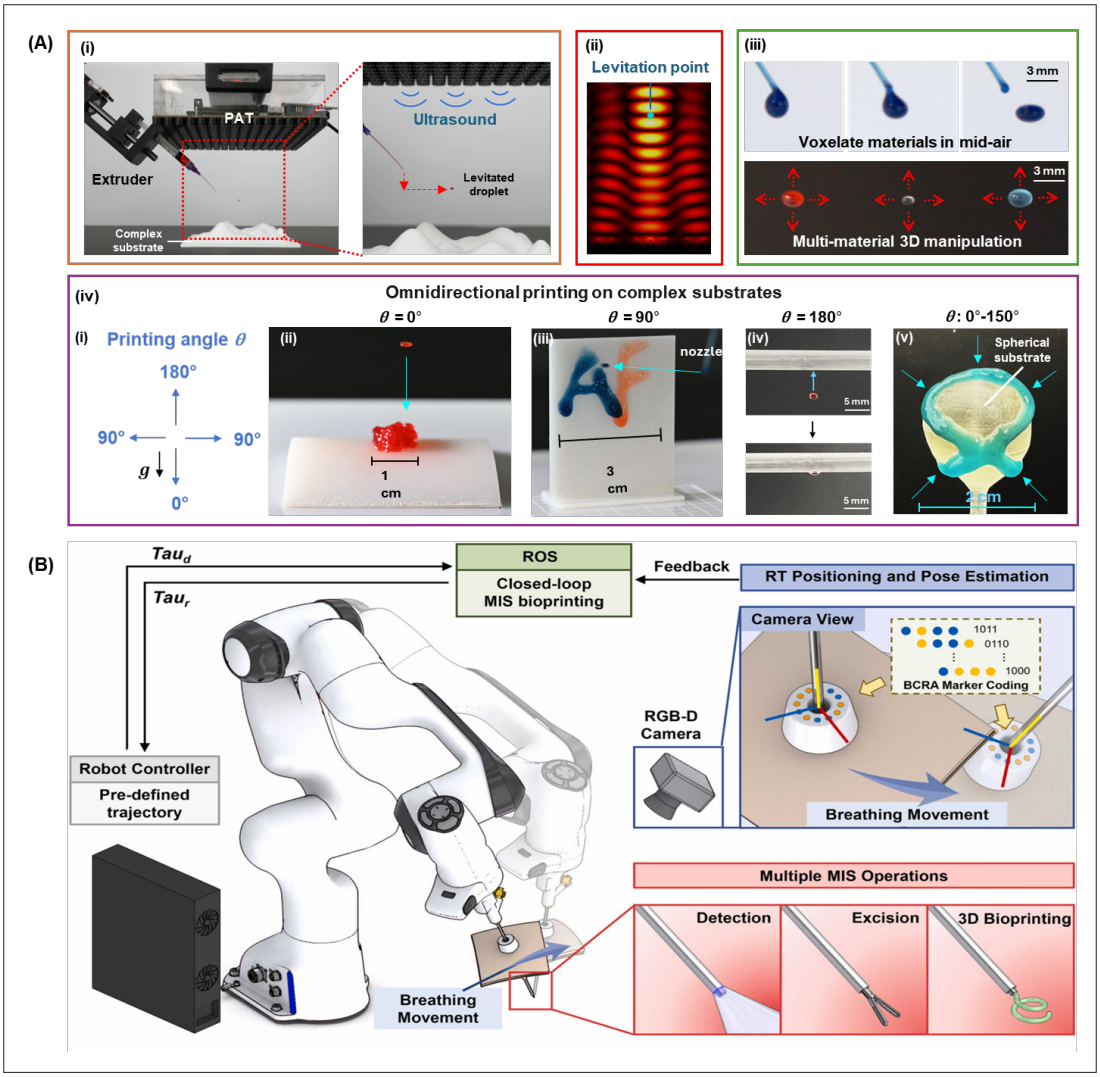

Figure 6. AI-assisted intelligent printing strategies enhance precision, adaptability, and sustainability. (A) Acoustophoretic 3D printing enables omnidirectional, multi-material fabrication. (i) A phased array transducer levitates droplets for precise deposition on complex substrates. (ii) Acoustic field visualization showing the levitation point. (iii) Mid-air voxelation and multi-material manipulation. (iv) Omnidirectional printing at varied angles (0°–180°) on flat (scale bar: 1 cm), vertical (scale bar: 3 cm), inverted (scale bar: 5 mm), and spherical (scale bar: 2 cm) surfaces, demonstrating adaptive and contactless printing.[92] Reprinted from Chen et al.[92] (B) A closed-loop minimally invasive 3D bioprinting system. A seven-axis robotic arm guided by real-time feedback from a RGB-D camera adaptively compensates for dynamic breathing-induced motion. AI-driven path planning minimizes error and material overuse, enhancing printing accuracy, efficiency, and safety in dynamic environments. This supports sustainability by reducing procedural waste and optimizing resource use.[94] Reprinted with permission from Zhao et al.[94] Copyright © 2023, Elsevier. Abbreviations: 3D, three-dimensional; AI: artificial intelligence; BCRA, binary chromatic ring array; MIS, minimally invasive surgery; RGB-D: red green blue-depth; ROS, robot operating system; RT, real-time.

Zhao et al.[94] introduced a closed-loop, AI-assisted bioprinting system that enhances precision, adaptability, and sustainability in minimally invasive surgery (Figure 6B). By integrating robotic-assisted printing, real-time computer vision, and adaptive feedback control, the system dynamically aligned the bioprinting end-effector with moving biological structures, reducing errors and minimizing material waste. A binary chromatic ring array marker enabled automatic trocar tracking, ensuring high accuracy while reducing the need for manual intervention. Additionally, the use of an optimized methacrylate gelatin/poly(ethylene glycol) diacrylates/polyacrylic acid-N-hydroxysuccinimide hydrogel facilitated efficient crosslinking and strong tissue adhesion, promoting targeted biofabrication with minimal excess material usage. The system's millimeter-scale precision, adaptive

alignment at 30 Hz, and low-force application not only improved bioprinting efficiency but also enhanced resource conservation and sustainability by reducing biomaterial waste and optimizing printing parameters in real time. This AI-driven, closed-loop approach exemplifies the potential of intelligent bioprinting systems to advance eco-friendly, high-precision fabrication strategies, contributing to the sustainable evolution of regenerative medicine and biomedical engineering.

Zboinska et al.[98] investigated the robotic 3D printing of cellulose nanofibril-alginate hydrogel membranes for sustainable architectural applications, analyzing the impact of toolpath design and ambient drying on structural integrity, shrinkage, and aesthetics. Results showed that solid deposition with multiple layers led to high shrinkage (~31%) and deformation, while lattice deposition with high porosity reduced shrinkage (~8%) and improved dimensional stability. Asymmetric toolpaths caused non-uniform distortions, and ambient drying significantly affected membrane curvature and flexibility. To enhance scalability and efficiency, classical AI-driven automation can optimize toolpath generation, extrusion control, and drying conditions, ensuring consistent deposition, reducing material waste, and improving sustainability.

AI-assisted intelligent printing marks a significant shift toward adaptive, real-time, and sustainable bioprinting systems. By integrating ML, computer vision, and robotic control, these systems enable precise material deposition on complex or dynamic substrates while minimizing human intervention, error, and material waste. Collectively, these innovations contribute to greater print success rates, reproducibility, and resource efficiency. However, current implementations often remain platform-specific and are tailored to narrow material or geometric constraints, limiting broader applicability. Moving forward, research should focus on developing generalizable AI control frameworks, standardizing performance evaluation metrics, and improving cross-platform interoperability. Additionally, expanding the use of real-time feedback loops, multimodal sensing, and automated decision-making will be key to achieving fully autonomous and clinically scalable intelligent bioprinting systems.

Table 1 presents a comparative overview of recent studies integrating AI or ML with 3D bioprinting, evaluated through the lens of sustainability. Each study is classified by the method used, materials and printing technique employed, and the relevant sustainability contributions. The following sustainability indicators are used:

(i) Sustainable bioink use: Utilization of bioinks derived from renewable, recyclable, or biodegradable sources to reduce environmental impact at the material level.

(ii) Material efficiency: Minimization of material consumption and waste through efficient deposition or improving formulation success rates.

(iii) Process efficiency: Optimization of printing parameters (e.g., speed, temperature, pressure) to reduce errors, enhance energy/resource use during fabrication, or improve throughput.

(iv) Experimental productivity: Application of ML to reduce empirical trial-and-error, accelerate parameter tuning, and improve data yield per experimental cycle.

4. Discussion

4.1. Challenges and potential solutions

The integration of AI into sustainable bioprinting has significantly advanced material development, bioink screening, processing parameter optimization, and intelligent printing. Despite these advancements, challenges remain in realizing the full potential of AI in sustainable bioprinting. Robust AI models require large, diverse, and well-annotated data[99,100]; however, existing datasets frequently suffer from inconsistency in parameter reporting and limited data annotation. This complexity arises from the extensive variability in bioink compositions, bioprinting techniques, and biological systems involved.[74,101] Additionally, standardized metrics to comprehensively measure sustainability in bioprinting are currently lacking. While several general frameworks exist for sustainable manufacturing like the sustainable process index (ecological impact of industrial processes),[102] life cycle assessment (environmental impacts of a product's life cycle),[103,104] and helix of sustainability (industrial raw material use and reuse onto natural processes),[105,106] their direct application to bioprinting remains limited due to the field's unique processes and materials. This absence of universally accepted standards hinders systematic assessment and comparison of sustainable practices, complicating the optimization of sustainability efforts within bioprinting processes.

Another significant challenge is the generalizability of AI models across various materials, bioprinting methods, and evolving conditions.[107,108] AI systems typically perform well within the confines of their training datasets but sometimes struggle when confronted with new, unfamiliar, or dynamically changing scenarios.[109] Factors contributing to this limitation include data scarcity for novel materials, the complexity of accurately modeling intricate multi-material interactions, and the variability in environmental and operational conditions during bioprinting. Addressing these issues will require enhanced AI methodologies, robust validation strategies, and diverse training datasets

Table 1. Summary of artificial intelligence-driven studies in sustainable bioprinting

Study	Artificial intelligence algorithms	Bioink material	Bioprinting process	Sustainability indicators
Chen et al.[14]	Decision tree, random forest, deep learning	Composite hydrogel, polymer	Direct ink writing	Sustainable bioink use; material efficiency; experimental productivity
Lee et al.[81]	Multiple regression	Collagen, hyaluronic acid, fibrin	Extrusion	Process efficiency; experimental productivity
Nadernezhad and Groll[80]	Random forest	Hyaluronic acid-based hydrogel	Extrusion	Sustainable bioink use; process efficiency; experimental productivity
Bone et al.[85]	Hierarchical machine learning	Alginate-based	Extrusion	Sustainable bioink use; process efficiency; experimental productivity
Chen et al.[86]	Image recognition, random forest	Hydrogel scaffold	Extrusion	Material efficiency; process efficiency; experimental productivity
Fu et al.[87]	Support vector machine	Pluronic F127	Extrusion	Process efficiency; experimental productivity
Xu et al.[88]	Ensemble (ridge regression, k-nearest neighbor, random forest, neural network)	Gelatin methacrylate	Stereolithography	Process efficiency; experimental productivity
Zhang et al.[89]	Support vector regressor, multilayer perceptron regressors	Alginate-based	Extrusion	Sustainable bioink use; process efficiency; experimental productivity
Wu and Xu[91]	Random forest, least absolute shrinkage and selection operator, support vector regressor, extreme boosting gradient	Inkjet-compatible polymers	Inkjet	Sustainable bioink use; process efficiency; experimental productivity
Chen et al.[92]	Open multimodal particle-based displays, boundary element method	Soft materials	Direct ink writing	Sustainable bioink use; material efficiency
Zhao et al.[94]	Vision + adaptive feedback	Gelatin-based	Extrusion	Material efficiency; process efficiency
Zboinska et al.[98]	Artificial intelligence-assisted toolpath	Cellulose nanofibril-alginate	Extrusion	Sustainable bioink use; material efficiency

that encompass a broad spectrum of materials, processes, and conditions.[16,18,110,111]

To overcome these challenges, the creation of open-source platforms and collaborative databases is helpful. Such platforms would centralize diverse datasets, reflecting the variety of bioinks, printing parameters, and application-specific conditions, thus enabling more representative and comprehensive AI model training.[112,113] Establishing standardized sustainability metrics such as material efficiency, energy consumption, and waste minimization should also be an integral part of these centralized datasets. Quantifying these aspects would provide clear, measurable insights for sustainable bioprinting, enabling data-driven decisions to optimize AI algorithms, improve resource efficiency, and minimize environmental impact.[114] Collaborative efforts could streamline data collection, eliminate redundancy, and foster a cohesive research community. Furthermore, integrating advanced AI techniques like transfer learning and domain adaptation can enhance AI model generalizability, facilitating adaptability to new materials and dynamic printing environments.[74,115] These initiatives, combined with interdisciplinary collaboration and technological innovation, will help overcome current limitations, paving the way for AI-driven sustainable bioprinting to achieve its full potential.

4.2. Roadmap for artificial intelligence in sustainable bioprinting

In addition to addressing current challenges, a strategic roadmap for future development suggests several directions that could advance sustainability alongside technological progress. In material discovery and development, AI-assisted platforms can leverage hybrid modeling approaches that merge AI-driven predictive models with physics-based simulations to enhance accuracy, reduce experimentation, and minimize resource usage.[77,116,117] Integrating life cycle assessment indicators such as embodied energy, carbon footprint, and toxicity profiles alongside mechanical and biological performance metrics would allow the design of truly

sustainability-aware hydrogel. Open-source datasets that capture both material origin and functional outcomes—such as printability, biocompatibility, and mechanical properties—will be critical in supporting these efforts.

For bioink formulation screening, while predictive models have shown success in assessing printability and rheology, there is a pressing need for AI systems that can generalize across a wider spectrum of bioink chemistries, including those derived from recycled polymers, chemically modified natural materials, and hybrid composites. Future platforms can also integrate a broader array of input features, such as crosslinking kinetics under different conditions, degradation rates over time, and dynamic cell compatibility data, including proliferation, differentiation, and immune responses. These features can be embedded into multi-objective optimization frameworks capable of balancing trade-offs between print fidelity, mechanical integrity, biological performance, and environmental impact.[118]

In processing parameters optimization, future bioprinting equipment should integrate real-time monitoring, feedback control, and adaptive optimization algorithms. This will enable continuous improvement in print quality, significantly reducing material waste and energy consumption during fabrication.[101,119–121] Advanced AI models that incorporate environmental sensors and historical print data could be used to build predictive maintenance systems, flagging deviations before print failure occurs. Furthermore, multimodal sensor fusion (e.g., combining acoustic, visual, and rheological inputs) could enable richer representations of print conditions, allowing for more granular and adaptive parameter control. Reinforcement learning algorithms, in particular, offer great potential for autonomous tuning of parameters in real time by learning optimal action policies based on performance feedback.[122]

Regarding AI-assisted intelligent printing, the development of autonomous bioprinting systems empowered by AI decision-making capabilities should be prioritized. These systems can dynamically adapt to complex and evolving substrates and environmental conditions, improving precision, throughput, and sustainable resource management.[119,120] Advanced systems could combine robotic control, computer vision, and probabilistic planning to enable in situ material placement with high spatial precision, even under uncertain or moving conditions. Real-time reconstruction of the target geometry using multimodal imaging—paired with predictive modeling—could allow these printers to adjust tool paths in real time, minimizing material waste and improving procedural outcomes. A promising approach to achieving this capability is the use of digital twin frameworks, which simulate and update a virtual replica of the bioprinting environment and printed construct in real time based on sensor feedback.[123] Finally, enhancing educational initiatives and workforce training programs that focus on AI, bioprinting technologies, and sustainability principles will be essential to build interdisciplinary expertise and foster widespread adoption of environmentally responsible bioprinting practices.[124,125]

Looking forward, as bioprinting technologies progress toward clinical translation and industrial adoption, integrating sustainability considerations early in the development process is essential. AI's significance in sustainable bioprinting is poised to expand as bioprinting processes become more complex with more intensive data. Continued advancements in computational speed, robustness, and interdisciplinary collaboration will be vital in addressing current limitations and ensuring AI-driven sustainable bioprinting meets both environmental and technological advancement goals in healthcare and biofabrication.

5. Conclusion

The integration of AI in sustainable bioprinting represents a transformative advancement in addressing environmental and functional challenges inherent in conventional bioprinting processes. AI's capabilities in predicting material performance, optimizing bioink formulations, dynamically adjusting printing parameters, and supporting intelligent bioprinting systems substantially reduce reliance on resource-intensive trial-and-error approaches, leading to significant enhancements in sustainability and efficiency. Despite notable progress, significant challenges remain, including dataset standardization, model generalizability, and comprehensive sustainability measurement. Future efforts must prioritize collaborative data-sharing platforms, advanced AI methods, and standardization initiatives. By systematically addressing these challenges, the full potential of AI in sustainable bioprinting can be realized, substantially contributing to ecological responsibility and advancing technological innovations in biofabrication and healthcare applications.

Acknowledgments

None.

Funding

None.

Conflict of interest

The authors declare no conflicts of interest.

Author contributions

Conceptualization: Hongyi Chen
Supervision: Jie Huang
Visualization: Hongyi Chen
Writing–original draft: Hongyi Chen
Writing–review & editing: Hongyi Chen, Jie Huang

Ethics approval and consent to participate

Not applicable.

Consent for publication

Not applicable

Availability of data

Not applicable.

References

1. Murphy SV, De Coppi P, Atala A. Opportunities and challenges of translational 3D bioprinting. *Nat Biomed Eng*. 2020;4(4):370-380. doi: 10.1038/s41551-019-0471-7
2. Mota C, Camarero-Espinosa S, Baker MB, Wieringa P, Moroni L. Bioprinting: from tissue and organ development to in vitro models. *Chem Rev*. 2020;120(19):10547-10607. doi: 10.1021/acs.chemrev.9b00789
3. Kim JJ, Cho D-W. Advanced strategies in 3D bioprinting for vascular tissue engineering and disease modelling using smart bioinks. *Virtual Phys Prototyp*. 2024;19(1):e2395470. doi: 10.1080/17452759.2024.2395470
4. Narayan R, Yoo J, Atala A. 3D bioprinting: physical and chemical processes. *Appl Phys Rev*. 2021;8(3). doi: 10.1063/5.0060283
5. Yilmaz B, Al Rashid A, Mou YA, Evis Z, Koç M. Bioprinting: a review of processes, materials and applications. *Bioprinting*. 2021;23:e00148. doi: 10.1016/j.bprint.2021.e00148
6. Sun X, Ren W, Xie L, et al. Recent advances in 3D bioprinting of tissues and organs for transplantation and drug screening. *Virtual Phys Prototyp*. 2024;19(1):e2384662. doi: 10.1080/17452759.2024.2384662
7. Chua CK, An J, Fan S, et al. A perspective on transformative bioprinting. *IJB*. 2024;11(1):1–29. doi: 10.36922/ijb.3525
8. Jain P, Kathuria H, Dubey N. Advances in 3D bioprinting of tissues/organs for regenerative medicine and in-vitro models. *Biomaterials*. 2022;287:121639. doi: 10.1016/j.biomaterials.2022.121639
9. Faber L, Yau A, Chen Y. Translational biomaterials of four-dimensional bioprinting for tissue regeneration. *Biofabrication*. 2024;16(1):012001. doi: 10.1088/1758-5090/acfdd0
10. Zhang YS, Haghiashtiani G, Hübscher T, et al. 3D extrusion bioprinting. *Nat Rev Methods Primers*. 2021;1(1):75. doi: 10.1038/s43586-021-00073-8
11. Zhou J, See CW, Sreenivasamurthy S, Zhu D. Customized additive manufacturing in bone scaffolds—the gateway to precise bone defect treatment. *Research*. 2023;6:0239. doi: 10.34133/research.0239
12. Senior AW, Evans R, Jumper J, et al. Improved protein structure prediction using potentials from deep learning. *Nature*. 2020;577(7792):706-710. doi: 10.1038/s41586-019-1923-7
13. Jumper J, Evans R, Pritzel A, et al. Highly accurate protein structure prediction with AlphaFold. *Nature*. 2021;596(7873):583-589. doi: 10.1038/s41586-021-03819-2
14. Chen H, Liu Y, Balabani S, Hirayama R, Huang J. Machine learning in predicting printable biomaterial formulations for direct ink writing. *Research*. 2023;6:0197. doi: 10.34133/research.0197
15. Elbadawi M, Li H, Sun S, Alkahtani ME, Basit AW, Gaisford S. Artificial intelligence generates novel 3D printing formulations. *Appl Mater Today*. 2024;36:102061. doi: 10.1016/j.apmt.2024.102061
16. Zhang Z, Zhou X, Fang Y, Xiong Z, Zhang T. AI-driven 3D bioprinting for regenerative medicine: From bench to bedside. *Bioact Mater*. 2025;45:201-230. doi: 10.1016/j.bioactmat.2024.11.021
17. Abramson J, Adler J, Dunger J, et al. Accurate structure prediction of biomolecular interactions with AlphaFold 3. *Nature*. 2024;630(8016):493-500. doi: 10.1038/s41586-024-07487-w
18. Chen H, Zhang B, Huang J. Recent advances and applications of artificial intelligence in 3D bioprinting. *Biophys Rev*. 2024;5(3):031301. doi: 10.1063/5.0190208
19. Thompson A. Employing artificial intelligence to augment 3D bioprinting. *Scilight*. 2024;2024(29):291104. doi: 10.1063/10.0028061
20. Filippi M, Mekkattu M, Katzschmann RK. Sustainable biofabrication: from bioprinting to AI-driven predictive methods. *Trends Biotechnol*. 2025;43(2):290-303. doi: 10.1016/j.tibtech.2024.07.002
21. Foyt DA, Norman MDA, Yu TTL, Gentleman E. Exploiting Advanced Hydrogel Technologies to Address Key Challenges in Regenerative Medicine. *Adv Healthc Mater*. 2018;7(8):1700939.

doi: 10.1002/adhm.201700939

22. Pereira RF, Bártolo PJ. 3D bioprinting of photocrosslinkable hydrogel constructs. *J Appl Polym Sci*. 2015; 132(48).
doi: 10.1002/app.42458

23. Hölzl K, Lin S, Tytgat L, Van Vlierberghe S, Gu L, Ovsianikov A. Bioink properties before, during and after 3D bioprinting. *Biofabrication*. 2016;8(3):032002.
doi: 10.1088/1758-5090/8/3/032002

24. Ng WL, Shkolnikov V. Jetting-based bioprinting: process, dispense physics, and applications. *Bio Des Manuf*. 2024;7(5):771-799.
doi: 10.1007/s42242-024-00285-3

25. Muthusamy S, Kannan S, Lee M, et al. 3D bioprinting and microscale organization of vascularized tissue constructs using collagen-based bioink. *Biotechnol Bioeng*. 2021;118(8):3150-3163.
doi: 10.1002/bit.27838

26. Schwab A, Levato R, D'Este M, Piluso S, Eglin D, Malda J. Printability and shape fidelity of bioinks in 3D bioprinting. *Chem Rev*. 2020;120(19):11028-11055.
doi: 10.1021/acs.chemrev.0c00084

27. Chen H, Stampoultzis T, Papadopoulou A, Balabani S, Huang J. Evaluation of rheological properties and shape fidelity of polycaprolactone/hydroxyapatite inks for 3D printing of osteochondral tissue scaffolds. *Orthop Proc*. 2021;103-B(SUPP_2):96-96.
doi: 10.1302/1358-992X.2021.2.096

28. You S, Xiang Y, Hwang HH, et al. High cell density and high-resolution 3D bioprinting for fabricating vascularized tissues. *Sci Adv*. 2023;9(8):eade7923.
doi: 10.1126/sciadv.ade7923

29. Chen H, Khong J, Huang J. Direct ink writing of polycaprolactone/laponite composite for bone implants: 3D characterization using x-ray micro CT. *Orthop Proc*. 2021;103-B(SUPP_16):74-74.
doi: 10.1302/1358-992X.2021.16.07

30. Guillotin B, Souquet A, Catros S, et al. Laser assisted bioprinting of engineered tissue with high cell density and microscale organization. *Biomaterials*. 2010;31(28):7250-7256.
doi: 10.1016/j.biomaterials.2010.05.055

31. Keriquel V, Oliveira H, Rémy M, et al. In situ printing of mesenchymal stromal cells, by laser-assisted bioprinting, for in vivo bone regeneration applications. *Sci Rep*. 2017;7(1):1778.
doi: 10.1038/s41598-017-01914-x

32. Afridi A, Al Rashid A, Koç M. Recent advances in the development of stereolithography-based additive manufacturing processes: a review of applications and challenges. *Bioprinting*. 2024;43:e00360.
doi: 10.1016/j.bprint.2024.e00360

33. Zuev DM, Nguyen AK, Putlyaev VI, Narayan RJ. 3D printing and bioprinting using multiphoton lithography. *Bioprinting*. 2020;20:e00090.
doi: 10.1016/j.bprint.2020.e00090

34. Mandrycky C, Wang Z, Kim K, Kim D-H. 3D bioprinting for engineering complex tissues. *Biotechnol Adv*. 2016;34(4):422-434.
doi: 10.1016/j.biotechadv.2015.12.011

35. Sun W, Starly B, Daly AC, et al. The bioprinting roadmap. *Biofabrication*. 2020;12(2):022002.
doi: 10.1088/1758-5090/ab5158

36. Fang Y, Guo Y, Wu B, et al. Expanding embedded 3D bioprinting capability for engineering complex organs with freeform vascular networks. *Adv Mater*. 2023;35(22):2205082.
doi: 10.1002/adma.202205082

37. Sheybanikashani S, Zandi N, Hosseini D, Lotfi R, Simchi A. A sustainable and self-healable silk fibroin nanocomposite with antibacterial and drug eluting properties for 3D printed wound dressings. *J Mater Chem B*. 2024; 12(3):784-799.
doi: 10.1039/D3TB02363J

38. Qamruzzaman M, Ahmed F, Mondal MIH. An overview on starch-based sustainable hydrogels: potential applications and aspects. *J Polym Environ*. 2022;30(1):19-50.
doi: 10.1007/s10924-021-02180-9

39. Soman SS, Govindraj M, Hashimi NA, Zhou J, Vijayavenkataraman S. Bioprinting of human neural tissues using a sustainable marine tunicate-derived bioink for translational medicine applications. *IJB*. 2022;8(4):604.
doi: 10.18063/ijb.v8i4.604

40. Arif ZU, Khalid MY, Noroozi R, et al. Additive manufacturing of sustainable biomaterials for biomedical applications. *Asian J Pharm Sci*. 2023;18(3):100812.
doi: 10.1016/j.ajps.2023.100812

41. Whenish R, Ramakrishna S, Jaiswal AK, Manivasagam G. A framework for the sustainability implications of 3D bioprinting through nature-inspired materials and structures. *Bio Des Manuf*. 2022;5(2):412-423.
doi: 10.1007/s42242-021-00168-x

42. Charlet A, Hirsch M, Schreiber S, Amstad E. Recycling of load-bearing 3D printable double network granular hydrogels. *Small*. 2022;18(12):2107128.
doi: 10.1002/smll.202107128

43. Merotto E, Pavan PG, Piccoli M. Three-dimensional bioprinting of naturally derived hydrogels for the production of biomimetic living tissues: benefits and challenges. *Biomedicines*. 2023;11(6):1742.
doi: 10.3390/biomedicines11061742.

44. Guan Q-F, Yang H-B, Han Z-M, Ling Z-C, Yu S-H. An all-natural bioinspired structural material for plastic replacement. *Nat Commun*. 2020;11(1):5401. doi: 10.1038/s41467-020-19174-1

45. Drury JL, Mooney DJ. Hydrogels for tissue engineering: scaffold design variables and applications. *Biomaterials*. 2003;24(24):4337-4351. doi: 10.1016/S0142-9612(03)00340-5

46. Park JY, Choi Y-J, Shim J-H, Park JH, Cho D-W. Development of a 3D cell printed structure as an alternative to autologs cartilage for auricular reconstruction. *J Biomed Mater Res Part B App Biomater*. 2017;105(5):1016-1028. doi: 10.1002/jbm.b.33639

47. Chen H, Gonnella G, Huang J, Di-Silvio L. Fabrication of 3D bioprinted bi-phasic scaffold for bone-cartilage interface regeneration. *Biomimetics*. 2023;8(1):87. doi: 10.3390/biomimetics8010087

48. Critchley S, Kelly D. Bioinks for bioprinting functional meniscus and articular cartilage. *J 3D Print Med*. 2017;1:269-290. doi: 10.2217/3dp-2017-0012

49. Unagolla JM, Jayasuriya AC. Hydrogel-based 3D bioprinting: A comprehensive review on cell-laden hydrogels, bioink formulations, and future perspectives. *Appl Mater Today*. 2020;18:100479. doi: 10.1016/j.apmt.2019.100479

50. Chung JHY, Naficy S, Yue Z, et al. Bio-ink properties and printability for extrusion printing living cells. *Biomater Sci*. 2013;1(7):763-773. doi: 10.1039/C3BM00012E

51. Nordahl SL, Scown CD. Recommendations for life-cycle assessment of recyclable plastics in a circular economy. *Chem Sci*. 2024;15(25):9397-9407. doi: 10.1039/D4SC01340A

52. Oladapo BI, Bowoto OK, Adebiyi VA, Ikumapayi OM. Net zero on 3D printing filament recycling: a sustainable analysis. *Sci Total Environ*. 2023;894:165046. doi: 10.1016/j.scitotenv.2023.165046

53. Xu X, Eatmon YL, Christie KSS, et al. Tough and recyclable phase-separated supramolecular gels via a dehydration–hydration cycle. *JACS Au*. 2023;3(10):2772-2779. doi: 10.1021/jacsau.3c00326

54. Ji D, Liu J, Zhao J, et al. Sustainable 3D printing by reversible salting-out effects with aqueous salt solutions. *Nat Commun*. 2024;15(1):3925. doi: 10.1038/s41467-024-48121-7

55. Sun Y, Yu K, Nie J, et al. Modeling the printability of photocuring and strength adjustable hydrogel bioink during projection-based 3D bioprinting. *Biofabrication*. 2021;13(3):035032. doi: 10.1088/1758-5090/aba413

56. GhavamiNejad A, Ashammakhi N, Wu XY, Khademhosseini A. Crosslinking strategies for 3D bioprinting of polymeric hydrogels. *Small*. 2020;16(35):2002931. doi: 10.1002/smll.202002931

57. Naghieh S, Chen X. Printability–a key issue in extrusion-based bioprinting. *J Pharm Anal*. 2021;11(5):564-579. doi: 10.1016/j.jpha.2021.02.001

58. McCarthy J. The inversion of functions defined by Turing machines. *Automata Studies*. Princeton University Press, Princeton; 1956:177-181.

59. Karthikeyan R, Geetha P, Ramaraj E. Rule based system for better prediction of diabetes. In: *2019 3rd International Conference on Computing and Communications Technologies (ICCCT)*. Chennai, India; 2019: 195-203. doi: 10.1109/ICCCT2.2019.8824842.

60. Liu H, Gegov A, Cocea M. Rule-based systems: a granular computing perspective. *Granul Comput*. 2016;1(4):259-274. doi: 10.1007/s41066-016-0021-6

61. Asemi A, Ko A, Nowkarizi M. Intelligent libraries: a review on expert systems, artificial intelligence, and robot. *Libr Hi Tech*. 2021;39:412-434. doi: 10.1108/LHT-02-2020-0038

62. Wang L, Yan J, Mu L, Huang L. Knowledge discovery from remote sensing images: a review. *WIREs Data Min Knowl Discov*. 2020;10(5):e1371. doi: 10.1002/widm.1371

63. Georgevici AI, Terblanche M. Neural networks and deep learning: a brief introduction. *Intensive Care Med*. 2019;45(5):712-714. doi: 10.1007/s00134-019-05537-w

64. Shane S, Jemin G, Carl B. Scaling distributed artificial intelligence/machine learning for decision dominance in all-domain operations. In: *Proceedings SPIE 12113, Artificial Intelligence and Machine Learning for Multi-domain Operations Applications IV*; 2022:1211306. doi: 10.1117/12.2621199

65. Kumari NMJ, Krishna KKV. Prognosis of diseases using machine learning algorithms: a survey. In: *2018 International Conference on Current Trends Towards Converging Technologies (ICCTCT)*. Coimbatore, India; 2018:1-9. doi: 10.1109/ICCTCT.2018.8550902.

66. Chen Y, Chen H, Harker A, Liu Y, Huang J. A supervised machine learning tool to predict the bactericidal efficiency of nanostructured surface. *J Nanobiotechnol*. 2024;22(1):748. doi: 10.1186/s12951-024-02974-8

67. Bonatti AF, Vozzi G, De Maria C. Enhancing quality control in bioprinting through machine learning. *Biofabrication*. 2024;16(2):022001. doi: 10.1088/1758-5090/ad2189

68. Gan Z, Li H, Wolff SJ, et al. Data-driven microstructure and microhardness design in additive manufacturing using a

self-organizing map. *Engineering*. 2019;5(4):730-735.
doi: 10.1016/j.eng.2019.03.014

69. Ramesh S, Deep A, Tamayol A, Kamaraj A, Mahajan C, Madihally S. Advancing 3D bioprinting through machine learning and artificial intelligence. *Bioprinting*. 2024;38:e00331.
doi: 10.1016/j.bprint.2024.e00331

70. Rathore AS, Nikita S, Thakur G, Mishra S. Artificial intelligence and machine learning applications in biopharmaceutical manufacturing. *Trends Biotechnol*. 2023;41(4):497-510.
doi: 10.1016/j.tibtech.2022.08.007

71. Ng WL, Goh GL, Goh GD, Ten JSJ, Yeong WY. Progress and opportunities for machine learning in materials and processes of additive manufacturing. *Adv Mater*. 2024;36(34):2310006.
doi: 10.1002/adma.202310006

72. Grira S, Mozumder MS, Mourad A-HI, Ramadan M, Khalifeh HA, Alkhedher M. 3D bioprinting of natural materials and their AI-enhanced printability: a review. *Bioprinting*. 2025;46:e00385.
doi: 10.1016/j.bprint.2025.e00385

73. Yu C, Jiang J. A perspective on using machine learning in 3D bioprinting. *IJB*. 2020;6(1):253.
doi: 10.18063/ijb.v6i1.253

74. Sun J, Yao K, An J, Jing L, Huang K, Huang D. Machine learning and 3D bioprinting. *IJB*. 2023;9(4):717.
doi: 10.18063/ijb.717

75. Wu Y, Ding X, Wang Y, Ouyang D. Harnessing the power of machine learning into tissue engineering: current progress and future prospects. *Burns Trauma*. 2024;12.
doi: 10.1093/burnst/tkae053

76. Ma L, Yu S, Xu X, Moses Amadi S, Zhang J, Wang Z. Application of artificial intelligence in 3D printing physical organ models. *Mater Today Bio*. 2023;23:100792.
doi: 10.1016/j.mtbio.2023.100792

77. Li Z, Song P, Li G, et al. AI energized hydrogel design, optimization and application in biomedicine. *Mater Today Bio*. 2024;25:101014.
doi: 10.1016/j.mtbio.2024.101014

78. Hardian R, Liang Z, Zhang X, Szekely G. Artificial intelligence: the silver bullet for sustainable materials development. *Green Chem*. 2020;22(21):7521-7528.
doi: 10.1039/D0GC02956D

79. Greener JG, Kandathil SM, Moffat L, Jones DT. A guide to machine learning for biologists. *Nat Rev Mol Cell Biol*. 2022;23(1):40-55.
doi: 10.1038/s41580-021-00407-0

80. Nadernezhad A, Groll J. Machine learning reveals a general understanding of printability in formulations based on rheology additives. *Adv Sci*. 2022;9(29):2202638.
doi: 10.1002/advs.202202638

81. Lee J, Oh SJ, An SH, Kim W-D, Kim S-H. Machine learning-based design strategy for 3D printable bioink: elastic modulus and yield stress determine printability. *Biofabrication*. 2020;12(3):035018.
doi: 10.1088/1758-5090/ab8707

82. Zhang X, Chang T, Chen H, et al. Optimizing laser parameters and exploring building direction dependence of corrosion behavior in NiTi alloys fabricated by laser powder bed fusion. *J Mater Res Technol*. 2024;33:4023-4032.
doi: 10.1016/j.jmrt.2024.10.105

83. Ng WL, An J, Chua CK. Process, material, and regulatory considerations for 3D printed medical devices and tissue constructs. *Engineering*. 2024;36:146-166.
doi: 10.1016/j.eng.2024.01.028

84. Ng WL, Alvin C, Soon OY, Chua CK. Deep learning for fabrication and maturation of 3D bioprinted tissues and organs. *Virtual Phys Prototyp*. 2020;15(3):340-358.
doi: 10.1080/17452759.2020.1771741

85. Bone JM, Childs CM, Menon A, et al. Hierarchical machine learning for high-fidelity 3D printed biopolymers. *ACS Biomater Sci Eng*. 2020;6(12):7021-7031.
doi: 10.1021/acsbiomaterials.0c00755

86. Chen B, Dong J, Ruelas M, et al. Artificial intelligence-assisted high-throughput screening of printing conditions of hydrogel architectures for accelerated diabetic wound healing. *Adv Funct Mater*. 2022;32(38):2201843.
doi: 10.1002/adfm.202201843

87. Fu Z, Angeline V, Sun W. Evaluation of printing parameters on 3D extrusion printing of pluronic hydrogels and machine learning guided parameter recommendation. *IJB*. 2021;7(4):434.
doi: 10.18063/ijb.v7i4.434

88. Xu H, Liu Q, Casillas J, et al. Prediction of cell viability in dynamic optical projection stereolithography-based bioprinting using machine learning. *J Intell Manuf*. 2022;33(4):995-1005.
doi: 10.1007/s10845-020-01708-5

89. Zhang C, Elvitigala KCML, Mubarok W, Okano Y, Sakai S. Machine learning-based prediction and optimisation framework for as-extruded cell viability in extrusion-based 3D bioprinting. *Virtual Phys Prototyp*. 2024;19(1):e2400330.
doi: 10.1080/17452759.2024.2400330

90. Rojek I, Mikołajewski D, Kopowski J, Kotlarz P, Piechowiak M, Dostatni E. Reducing waste in 3D printing using a neural network based on an own elbow exoskeleton. *Materials*. 2021;14(17):5074.
doi: 10.3390/ma14175074.

91. Wu D, Xu C. Predictive modeling of droplet formation processes in inkjet-based bioprinting. *J Manuf Sci Eng*. 2018;140(10):101007.

doi: 10.1115/1.4040619

92. Chen H, Bansal S, Plasencia DM, et al. Omnidirectional and multi-material in situ 3D printing using acoustic levitation. *Adv Mater Technol*. 2025;10(9):2401792. doi: 10.1002/admt.202401792

93. Wang X, Yang C, Yu Y, Zhao Y. In situ 3D bioprinting living photosynthetic scaffolds for autotrophic wound healing. *Research*. 2022;2022:9794745. doi: 10.34133/2022/9794745

94. Zhao W, Hu C, Lin S, et al. A closed-loop minimally invasive 3D printing strategy with robust trocar identification and adaptive alignment. *Addit Manuf*. 2023;73:103701. doi: 10.1016/j.addma.2023.103701

95. Montano-Murillo R, Hirayama R, Plasencia DM. OpenMPD: a low-level presentation engine for multimodal particle-based displays. *ACM Trans Graph*. 2023;42(2):Article 24. doi: 10.1145/3572896

96. Hirayama R, Christopoulos G, Martinez Plasencia D, Subramanian S. High-speed acoustic holography with arbitrary scattering objects. *Sci Adv*. 2022;8(24):eabn7614. doi: 10.1126/sciadv.abn7614

97. Chen H, Bansal S, Plasencia DM, et al. Omnidirectional and multi-material in situ 3D printing using acoustic levitation (Adv Mater Technol 9/2025). *Adv Mater Technol*. 2025;10(9):2570049. doi: 10.1002/admt.202570049

98. Zboinska MA, Sämfors S, Gatenholm P. Robotically 3D printed architectural membranes from ambient dried cellulose nanofibril-alginate hydrogel. *Mater Des*. 2023;236:112472. doi: 10.1016/j.matdes.2023.112472

99. Arora A, Alderman JE, Palmer J, et al. The value of standards for health datasets in artificial intelligence-based applications. *Nat Med*. 2023;29(11):2929-2938. doi: 10.1038/s41591-023-02608-w

100. Aldoseri A, Al-Khalifa KN, Hamouda AM. Re-thinking data strategy and integration for artificial intelligence: concepts, opportunities, and challenges. *Appl Sci*. 2023;13(12):7082. doi: 10.3390/app13127082

101. Shin J, Lee Y, Li Z, Hu J, Park SS, Kim K. Optimized 3D bioprinting technology based on machine learning: a review of recent trends and advances. *Micromachines*. 2022;13(3):363. doi: 10.3390/mi13030363

102. Narodoslawsky M, Krotscheck C. The sustainable process index (SPI): evaluating processes according to environmental compatibility. *J Hazard Mater*. 1995;41(2):383-397. doi: 10.1016/0304-3894(94)00114-V

103. Kokare S, Oliveira JP, Godina R. Life cycle assessment of additive manufacturing processes: a review. *J Manuf Syst*. 2023;68:536-559. doi: 10.1016/j.jmsy.2023.05.007

104. Finnveden G, Potting J. Life cycle assessment. In: Wexler P, ed. *Encyclopedia of Toxicology (Third Edition)*. Academic Press. Elsevier, Oxford, United Kingdom; 2014:74-77.

105. Luengo-Valderrey M-J, Pando-García J, Periáñez-Cañadillas I, Cervera-Taulet A. Analysis of the impact of the triple helix on sustainable innovation targets in spanish technology companies. *Sustainability*. 2020;12(8):3274. doi: 10.3390/su12083274

106. Hakeem MM, Chin GH, Frendy, Ito H. Regional sustainable development using a Quadruple Helix approach in Japan. *Regl Stud Regl Sci*. 2023;10(1):119-138. doi: 10.1080/21681376.2023.2171313

107. Ektefaie Y, Shen A, Bykova D, Marin MG, Zitnik M, Farhat M. Evaluating generalizability of artificial intelligence models for molecular datasets. *Nat Mach Intell*. 2024;6(12):1512-1524. doi: 10.1038/s42256-024-00931-6

108. Liu S, Chen Y, Wang Z, et al. The cutting-edge progress in bioprinting for biomedicine: principles, applications, and future perspectives. *MedComm*. 2024;5(10):e753. doi: 10.1002/mco2.753

109. Goetz L, Seedat N, Vandersluis R, van der Schaar M. Generalization—a key challenge for responsible AI in patient-facing clinical applications. *NJP Digit Med*. 2024;7(1):126. doi: 10.1038/s41746-024-01127-3

110. Bonatti AF, Vozzi G, Chua CK, Maria CD. A deep learning quality control loop of the extrusion-based bioprinting process. *IJB*. 2022;8(4):620. doi: 10.18063/ijb.v8i4.620

111. Seol Y-J, Kang H-W, Lee SJ, Atala A, Yoo JJ. Bioprinting technology and its applications. *Eur J Cardiothorac Surg*. 2014;46(3):342-348. doi: 10.1093/ejcts/ezu148

112. Mahadik B, Margolis R, McLoughlin S, et al. An open-source bioink database for microextrusion 3D printing. *Biofabrication*. 2023;15(1):015008. doi: 10.1088/1758-5090/ac933a

113. Saalfeld S, Cardona A, Hartenstein V, Tomančák P. CATMAID: collaborative annotation toolkit for massive amounts of image data. *Bioinformatics*. 2009;25(15):1984-1986. doi: 10.1093/bioinformatics/btp266

114. Finny AS. 3D bioprinting in bioremediation: a comprehensive review of principles, applications, and future directions. *Peer J*. 2024;12:e16897. doi: 10.7717/peerj.16897

115. Almadan A, Li W, Al Ibrahim M. Transfer learning with domain adaptation for palynological image segmentation. *Microsc Microanal*. 2023;29(Supplement_1):1898-1899.

doi: 10.1093/micmic/ozad067.980

116. Camacho-Gomez D, Sorzabal-Bellido I, Ortiz-de-Solorzano C, Garcia-Aznar JM, Gomez-Benito MJ. A hybrid physics-based and data-driven framework for cellular biological systems: application to the morphogenesis of organoids. *iScience*. 2023;26(7):107164. doi: 10.1016/j.isci.2023.107164

117. Kwon JS-I. Adding big data into the equation. *Nat Chem Eng*. 2024;1(11):724-724. doi: 10.1038/s44286-024-00142-1

118. Erps T, Foshey M, Luković MK, et al. Accelerated discovery of 3D printing materials using data-driven multiobjective optimization. *Sci Adv*. 2021;7(42):eabf7435. doi: 10.1126/sciadv.abf7435

119. Margarita A, Gugliandolo SG, Santoni S, Moscatelli D, Colosimo BM. A novel solution for real-time in-situ cell distribution monitoring in 3D bioprinting via fluorescence imaging. *Biofabrication*. 2025;17(2):021001. doi: 10.1088/1758-5090/adb891

120. Kaswan KS, Dhatterwal JS, Batra R, Balusamy B, Gangadevi E. 3D bioprinting technology optimization using machine learning. *Comput Intell Bioprint*. 2024:303-321.

121. Chen H, Hardwick J, Gao L, Plasencia DM, Subramanian S, Hirayama R. Acoustics in additive manufacturing: a path toward contactless, scalable, and high-precision manufacturing. *Appl Phys Revi*. 2025;12(3):031305. doi: 10.1063/5.0271688

122. El Bouchefry K, de Souza RS. Chapter 12—learning in big data: introduction to machine learning. In: Škoda P, Adam F, eds. *Knowledge Discovery in Big Data from Astronomy and Earth Observation*. Elsevier, Amsterdam, The Netherlands; 2020:225-249.

123. Jia A, Chee Kai C, Vladimir M. Application of machine learning in 3D bioprinting: focus on development of big data and digital twin. *IJB*. 2021;7(1):342. doi: 10.18063/ijb.v7i1.342.

124. To TT, Al Mahmud A, Ranscombe C. Teaching sustainability using 3D printing in engineering education: an observational study. *Sustainability*. 2023;15(9):7470. doi: 10.3390/su15097470

125. Strielkowski W, Grebennikova V, Lisovskiy A, Rakhimova G, Vasileva T. AI-driven adaptive learning for sustainable educational transformation. *Sustain Dev*. 2024;33(2):1921-1947. doi: 10.1002/sd.3221

ACCSCIENCE PUBLISHING

International Journal of Bioprinting

RESEARCH ARTICLE

Precise tuning of microstructure for surface bacteriostasis using two-photon polymerization 3D printing technology

Fang-Yi Huo[1†], Wentao Zhu[2†], Kan Zhou[3†], Enduo Zhou[1], Lei-Ming Cao[3], Qian Zhu[2], Bo Cai[2*], Lin-Lin Bu[3*], and Hong He[1*]

[1]State Key Laboratory of Oral & Maxillofacial Reconstruction and Regeneration, Key Laboratory of Oral Biomedicine Ministry of Education, Hubei Key Laboratory of Stomatology, Department of Orthodontics, School & Hospital of Stomatology, Wuhan University, Wuhan, Hubei, China

[2]Hubei Key Laboratory of Environmental and Health Effects of Persistent Toxic Substances, School of Environment and Health, Jianghan University, Wuhan, Hubei, China

[3]State Key Laboratory of Oral & Maxillofacial Reconstruction and Regeneration, Key Laboratory of Oral Biomedicine Ministry of Education, Hubei Key Laboratory of Stomatology, Department of Oral & Maxillofacial – Head Neck Oncology, School & Hospital of Stomatology, Wuhan University, Wuhan, Hubei, China

[†]These authors contributed equally to this work.

***Corresponding authors:**
Bo Cai
(bcai@jhun.edu.cn)

Lin-Lin Bu
(lin-lin.bu@whu.edu.cn)

Hong He
(drhehong@whu.edu.cn)

Citation: Huo FY, Zhu W, Zhou K, *et al.* Precise tuning of microstructure for surface bacteriostasis using two-photon polymerization 3D printing technology. *Int J Bioprint.* 2025;11(4):154-164. doi: 10.36922/IJB025150135

Received: April 11, 2025
Revised: May 8, 2025
Accepted: May 19, 2025
Published online: May 19, 2025

Copyright: © 2025 Author(s). This is an Open Access article distributed under the terms of the Creative Commons Attribution License, permitting distribution, and reproduction in any medium, provided the original work is properly cited.

Publisher's Note: AccScience Publishing remains neutral with regard to jurisdictional claims in published maps and institutional affiliations.

Abstract

In nature, many biological surfaces exhibit inherent bacteriostatic property due to the existence of special microstructures. However, the key factors and underlying mechanisms driving this property remain unclear. A significant challenge lies in the lack of proper techniques for precisely fabricating such microstructures as well as finely tuning their morphological parameters. In this study, we adopted a two-photon 3D printing-based approach to fabricate microstructures on specified surfaces with accurate control over their morphology, enabling the investigation of structural bacteriostasis. Through abstracting the subtle morphology on shark skin, we replicated their bacteriostatic microstructures and were able to regulate their morphology at the micron scale. By culturing *Streptococcus mutans* on the surface of these microstructures, we validated their bacteriostatic performance and demonstrated that morphological parameters significantly influenced the efficacy of structural bacteriostasis. Other kinds of microstructures such as micro-holes with bacteriostatic property could also be fabricated and investigated utilizing this two-photon polymerization technology. We believe this strategy offers a powerful tool for researching bacteriostatic mechanisms of various microstructures and will inspire their broad applications in both daily and industrial settings.

Keywords: 3D printing; Antisepsis; Bacteriostatic microstructures; Biomimetics; Two-photon polymerization

1. Introduction

Bacteria have evolutionarily developed robust surface colonization capabilities, allowing them to adhere to a wide range of biological and non-biological surfaces.[1-3] The formation of bacterial biofilms significantly enhances bacterial tolerance to antibiotics,

the host immune system, and other adverse environmental conditions.[4–6] Biofilm-associated infections account for approximately 80% of chronic infections and 50% of nosocomial infections, leading to substantial medical and economic burdens worldwide.[7–9] Anti-bacterial strategies employed across fields such as healthcare, food safety, textiles, and consumer goods comprise physical and chemical approaches. Physical methods, including high temperature/pressure and ultraviolet (UV) radiation, effectively inactivate bacteria but are often limited by material compatibility. Chemical methods, encompassing disinfectants and antibiotics, offer widespread applications but are increasingly challenged by issues like antimicrobial resistance and potential environmental impact.[10–13] Thus, there is an urgent need for innovative approaches to combat bacterial proliferation effectively.

Inspirations for surface bacteriostasis can be derived from nature. Certain biological surfaces, such as cicada wings and lotus leaves, have been shown to possess intrinsic bacteriostatic and anti-wetting properties.[14–16] In the marine environment, biofouling on the surfaces of hard objects has long had a serious impact on shipping, aquaculture, and coastal industries. Its formation originates from biofilms formed by microorganisms and microalgae on the surface of the object in the first place. In order to obtain stable and effective antimicrobial properties, the skin of marine mammals, especially sharks, has been successfully fabricated using bionic replication technology.[17] Interestingly, microstructures imitated from the surfaces of living organisms do exhibit excellent antimicrobial and antifouling properties.[18,19] Additionally, these inherent properties give the material multiple advantages in real-world applications, including extended service life, self-cleaning properties, stability, and avoidance of environmental pollution and safety issues. Therefore, biomimetic antimicrobial materials have become one of the research hotspots in the field of antimicrobial materials that are widely demanded and applied. Gao et al.[20] made membranes with a sea urchin-like texture on the surface by a non-solvent-induced phase separation process and found that such membranes have stronger antimicrobial properties and self-cleaning ability compared to flat membranes. Inspired by the physical antimicrobial form on the surface of insect wings, Li et al.[21] prepared a novel Cu^{2+}-doped nanoarray material on fluorine-doped tin oxide substrate using a one-step hydrothermal method. The surface of this material was uniformly distributed with pyramid-shaped nanoarrays, and the study confirmed that its surface has some physical antibacterial effects against *Staphylococcus aureus* (*S. aureus*) and *Escherichia coli*. The results may be related to the interaction between the morphological effects of the bacteria themselves and the physical structure of the sample surface.

Although various factors affecting the physical inhibitory properties of bionic structures have been reported, such as the type of boundary structure,[22] the type of surface morphology, adherence,[23] and the surface wettability,[24] there is still a large gap in the underlying mechanisms and influencing factors. One of the most notable hindrances lies in the difficulty of precise fabrication and morphology tuning of microstructure with current fabrication methods of chemical synthesis and etching-based techniques.[25–27] Chemical synthesis often requires harsh conditions such as high temperature or high salt environment, while etching-based methods are typically restricted to specific materials such as silicon and glass.[28] More importantly, these fabrication methods face challenges for fine control over individual structural parameters, impeding systematic investigations into the bacteriostatic mechanisms of micro-nano structures.

As an emerging three-dimensional (3D) printing strategy, two-photon polymerization technology enables accurate construction of various 3D topographies on the micron and even submicron scales, providing a powerful tool for research on bacteriostatic micro-nano structures.[29,30] Two-photon polymerization technology was first used for micro- and nano-scale 3D printing in 1965.[31] The near-infrared (NIR) light femtosecond laser acts as a light source to provide sufficient photon flux density to initiate effective polymerization. The resin radical quenching capability and the choice of objective lens determine the resolution of 3D printing, which is now achievable below 100 nm.[32,33] Two-photon polymerization technology can produce nanostructures with very low resolution and arbitrary morphology and has been widely used in cell biology, optical engineering, and medical device development.

In this study, we utilized a strategy based on two-photon polymerization 3D printing technology to precisely regulate the morphological parameters of biomimetic anti-bacterial microstructures, which facilitates our exploration of the key parameters and even the mechanisms behind microstructural bacteriostasis (Figure 1). Specifically, we constructed a shark skin-like bionic microstructure and simplified it to enable us to regulate the morphological parameters of the microstructures. By co-culturing the microstructures with *Streptococcus mutans* (*S. mutans*), we identified their bacteriostatic capacity and confirmed that topographical parameters could significantly affect the bacteriostatic property of the microstructures. Similar results were obtained when we explored the bacteriostatic capacity of other microstructures such as microporous structures. Thus, two-photon polymerization 3D printing

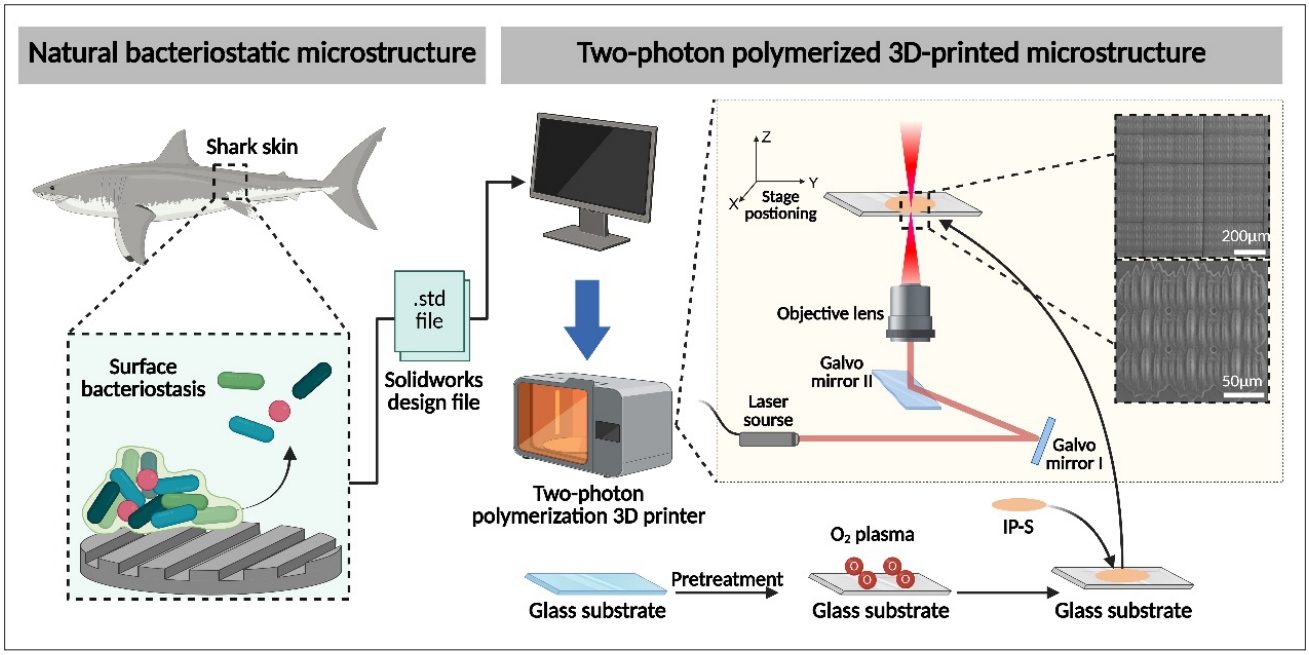

Figure 1. Schematic showing the fabrication of finely tuned bacteriostatic surfaces to inhibit bacterial growth. Bionic microstructures were designed to simulate shark skin using SolidWorks 2019. A photosensitive resin, IP-S, was attached to the substrate surface after pretreatment by oxygen plasma and two-photon polymerization. Finally, the designed bionic bacteriostatic microstructures were accurately constructed on the substrate surface.

technology can be used as a powerful tool to explore the underlying mechanisms and influencing factors of the bacteriostatic capabilities of various microstructures, thereby deepening the understanding of the bacteriostatic mechanisms of micro- and nano-structures and broadening their applications in various aspects of daily life.

2. Materials and methods

2.1. Materials

Photo-sensitive resin (IP-S) and glass substrates were obtained from Nanoscribe, Germany. *S. mutans* was provided by the School & Hospital of Stomatology, Wuhan University, China. Brain-heart infusion (BHI) was obtained from Phygene, China. The reagents of crystal violet and glutaraldehyde were purchased from Sigma-Aldrich, USA. Fluorescent SYTO 9 reagent, phosphate-buffered saline (PBS, 1×, pH = 7.2), and anhydrous ethanol were obtained from Thermo-Fisher Scientific, USA. Agar, propylene glycol monomethyl ether acetone (PGMEA), and isopropanol were purchased from Aladdin, China.

2.2. Design and fabrication of microstructures on glass substrates

The design of the biomimetic microstructures (shark skin denticle simulation and corresponding simplified indented micro-strips) or circular holes microstructure was prepared by SolidWorks 2019 (Dassault Systems – SolidWorks Corporation, USA). Various strips with the same height (3 or 5 μm) and width (2 or 5 μm), yet with different lengths (4, 8, 12, and 16 μm), were arranged in parallel with a 2- or 5-μm-wide gap. Holes with a depth of 3 μm and different diameters (2, 3, and 4 μm) were arranged in parallel, with the spacing between two adjacent holes equal to the hole diameter. The centers of every three adjacent holes formed an equilateral triangle.

For microstructure fabrication, a two-photon laser 3D printer (Photonic Professional GT2, Nanoscribe, Germany) and IP-S were employed. Initially, glass substrates were pre-treated by oxygen plasma (PDC-001, Harrick Plasma, USA) to enhance the affinity between IP-S and the substrates. Subsequently, IP-S was dropped on the glass substrates and placed into the 3D printer for constructing specific microstructures according to design. Finally, PGMEA and isopropanol were employed to develop those microstructures, and PBS was used to wash the substrates to remove excess organic reagents.

2.3. Bacteria cultivation on the surfaces of microstructures

S. mutans was cultured in a BHI solution growth medium and grown at 37°C overnight in static conditions. Substrates with different microstructures were placed into six-well plates and sterilized with ultraviolet (UV) light for 30 min before experiments. Subsequently, *S. mutans* suspension made with BHI broth concentration of 1 × 10^6/mL was inoculated into each well of the six-well

plates to immerse the substrates, which were then left for incubation at 37°C for different periods of time. The substrates were washed gently in PBS three times to remove free bacteria before observation.

2.4. Microscopy and scanning electron microscopy observation

3D-printed microstructures with/without *S. mutans* were observed using a fluorescence microscope equipped with a charge-coupled device (Olympus, Japan). Scanning electron microscopy (SEM; S-3400N, Hitachi, Japan) was employed to further obtain detailed information relating to the microstructures and bacterial proliferation. Substrates with 3D-printed microstructures were sprayed with a thin layer of gold to increase conductivity before SEM imaging. To observe bacteria attached to the microstructures, they were first treated with 2.5% glutaraldehyde solution for 2 h, followed by dehydration using ethanol solutions with different concentrations (30%, 50%, 80%, and 100%, 10 min for each concentration) and complete drying. Then, the microstructures were sprayed with a thin layer of gold for SEM observation.

2.5. Fluorescence staining assays

After incubation with *S. mutans* in BHI solution at 37°C, every substrate with different microstructures was gently washed three times with PBS and then stained by SYTO 9 solution according to the manual from the manufacturer. An inverted fluorescence microscope (NIKON, Japan) was employed to record fluorescent images for bacteria proliferation analysis.

2.6. Statistical analysis

Data were presented as mean ± standard deviation (SD). Unpaired *t*-test or one-way analysis of variance (ANOVA) was used to assess the statistical differences between experimental groups. All the analyses were performed using GraphPad Prism software. A p-value < 0.05 was considered statistically significant.

3. Results

3.1. Two-photon polymerization 3D printing enables construction of biomimetic microstructures and their simplification with bacteriostatic properties

The microstructure of the shark skin surface has been extensively studied for its excellent bacteriostatic properties. Therefore, we first employed the two-photon polymerization-based 3D printing platform (Photonic Professional GT2, Nanoscribe, Germany) to fabricate microstructures inspired by the unique morphology of shark skin.

A drop of IP-S was applied to an oxygen plasma-pretreated glass substrate and processed in the 3D printer to create designed microstructures. As shown in Figure 2a and b, the shark skin denticle simulation was successfully fabricated on the glass substrate. For the feasibility of investigating structural effectiveness, the irregular morphology was abstracted and simplified into a quantifiable, indented micro-strip array with a certain arrangement pattern. The structure that simulates shark skin is characterized by continuous, gentle, longitudinal bulges of varying lengths. The structure of the mimic shark skin is characterized by continuous, gently sloping, and longitudinal rises of varying lengths. We accentuated this feature by simplifying the ridges of the rises into long columns of squares, and the spaces between the ridges were simplified from small slopes to flat surfaces. We then changed the length of the rises from continuously varying to neighboring columns spaced 2 μm apart (ranging from 4 μm increments to 16 μm and then reducing to 4 μm). Finally, this simplified structure featured seven parallel indented micro-strips of varying lengths (4, 8, 12, and 16 μm), with a height of 3 μm, a width of 2 μm, and a spacing of 2 μm, and was fabricated on the glass substrate, as depicted in Figure 2b.

To verify the bacteriostatic efficacy of 3D-printed biomimetic microstructures, *S. mutans*, a representative pathogenic microorganism, was utilized as the model bacterium. The glass substrates, with a 3D-printed flat structure, 3D-printed shark skin denticle simulation, or 3D-printed simplified indented micro-strips, respectively, were co-cultured with *S. mutans* to evaluate bacterial proliferation. In a BHI solution containing 1×10^6 cells/mL, the co-culture of microstructures and *S. mutans* was maintained for 24 h, and bacterial coverage on different surfaces was observed after fluorescent staining and analysis. As shown in Figure 2c, *S. mutans* on the surface with 3D-printed flat structure ("Plane" group) demonstrated vigorous proliferative activity, and their coverage was rapidly expanded. After 8 h of co-cultivation, over half of the surface of the "Plane" group was covered by bacteria. The bacteria continued to proliferate and after 16 h, the "Plane" group was almost entirely covered by bacteria. The rapid proliferation of bacteria serves as a stark reminder, urging us to seek more effective methods of inhibiting their growth.

In contrast, bacterial proliferation on the surface with 3D-printed shark skin denticle simulation ("Simulation" group) was significantly inhibited. After 8 h of co-cultivation, only about 10% of the substrate surface was covered by bacteria, confirming the bacteriostatic properties of the shark skin-inspired microstructure. After 16 and 24 h of co-cultivation, the bacterial coverage in the "Simulation" group gradually increased, but remained substantially lower than in the "Plane" group, at approximately 25% (16 h) and

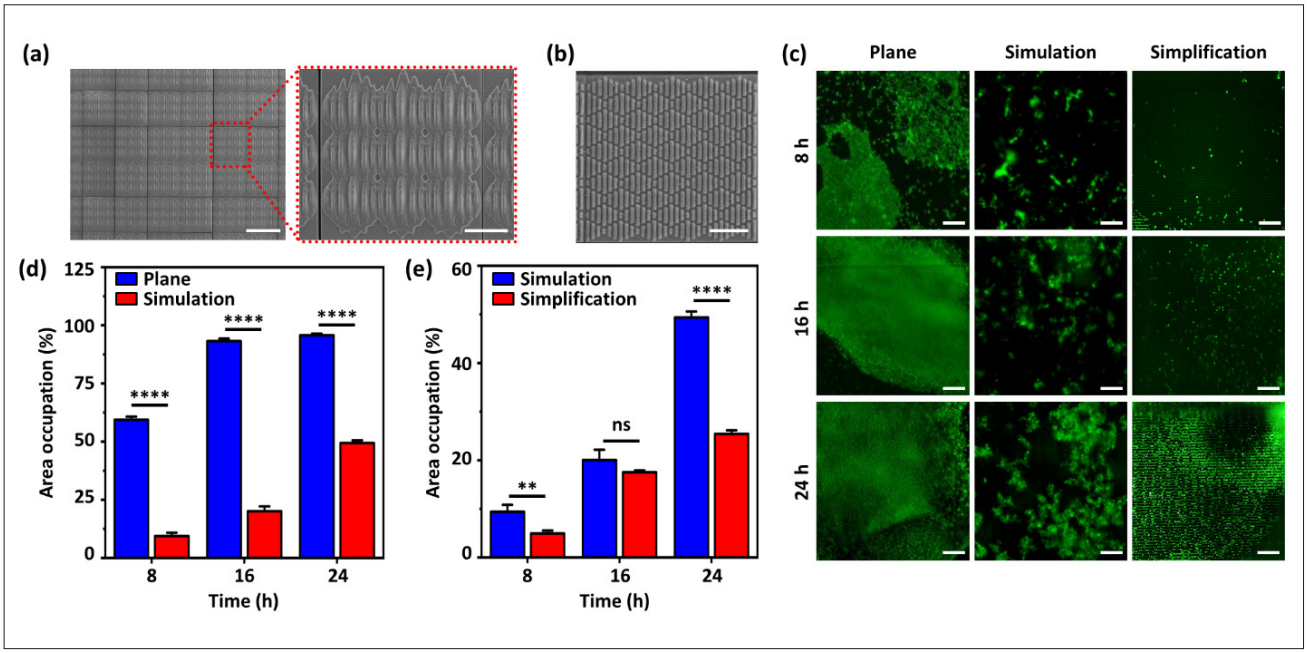

Figure 2. Precisely fabricated shark epidermal structure simulated and simplified microstructure with bacteriostatic ability using two-photon polymerization 3D printing. (a) SEM image of the printed simulated shark skin microstructure. Scale bar: 200 and 50 μm (enlarged). (b) SEM image of the 3D-printed simplified microstructure (the parameters: stripe lengths of 4, 8, and 16 μm; width of 2 μm; height of 3 μm; and distance between stripes of 2 μm). Scale bar: 50 μm. (c) Proliferation of bacteria (green fluorescence-labeled) on flat, shark skin-like microstructures, and simplified microstructures in 24 h. Scale bar: 20 μm. (d) Statistical plot of bacterial proliferation area on the surface with/without printed structures. (e) The simulated and simplified microstructures of shark skin showed significant bacteriostatic effects for at least 24 h. Data are expressed as mean ± SD. n = 3; unpaired t-test; ns, no significance; **p < 0.01; ****p < 0.0001. Abbreviation: SEM, scanning electron microscopy.

50% (24 h), respectively (Figure 2d). The "Simplification" group was obtained by simplifying the microstructure of the sharkskin surface. As shown in Figure 2e, this group exhibited an even lower bacterial coverage after 24 h of co-cultivation compared to the "Simulation" group, indicating that the simplified microstructure possesses superior bacteriostatic properties for at least 24 h. Also, the difference in bacterial proliferation between the "Simplification" and "Simulation" groups implies that the change in microstructural morphology has a significant effect on bacteriostatic properties. Moreover, the simplified structure makes it easier to explore the effect of specific parameter variations on the bacteriostatic properties.

3.2. Influence of different parameters of microstructures on bacterial inhibitory capacity

In order to investigate whether changing the size of the microstructures has an effect on the bacteriostatic effect of the simplified shark skin-like surface microstructures, we utilized two-photon 3D printing to precisely regulate the key parameters of the microstructures, including stripe width (W), height (H), and spacing (S). The standard parameters of the simplified bionic microstructure are as follows: stripe lengths of 4, 8, and 16 μm; W = 2 μm; H = 3 μm; and S = 2 μm (Figure 3a). After 24 h of incubation in BHI solution containing 1 × 10^6/mL *S. mutans*, a limited number of bacteria proliferated on the surface of the simplified 3D-printed bionic microstructures (Figure 3b).

Similarly, we co-cultured *S. mutans* with parameter-adjusted microstructures to specifically evaluate the effect of changing different parameters on the bacterial inhibition performance. On the basis of the standard parameters, we adjusted each of the individual parameters and divided them into three groups: the stripe spacing of "S5" group was adjusted from 2 to 5 μm, the stripe width of "W5" group was adjusted from 2 to 5 μm, and the stripe height of "H5" group was adjusted from 2 to 5 μm. After incubation of different microstructures with *S. mutans* in BHI solution for different periods of time (8, 16, and 24 h), in order to quantitatively analyze the proliferation of *S. mutans*, each substrate of different microstructures was gently washed three times with PBS and then stained with SYTO 9 solution. Fluorescence images were recorded using an inverted fluorescence microscope (Figure 3c). It can be seen that there is a significant difference in the area of the substrate occupied by bacteria proliferating on the surface of the microstructures with different parameters after only 8 h. The area of the substrate occupied by bacteria proliferating on the surface of the microstructures with

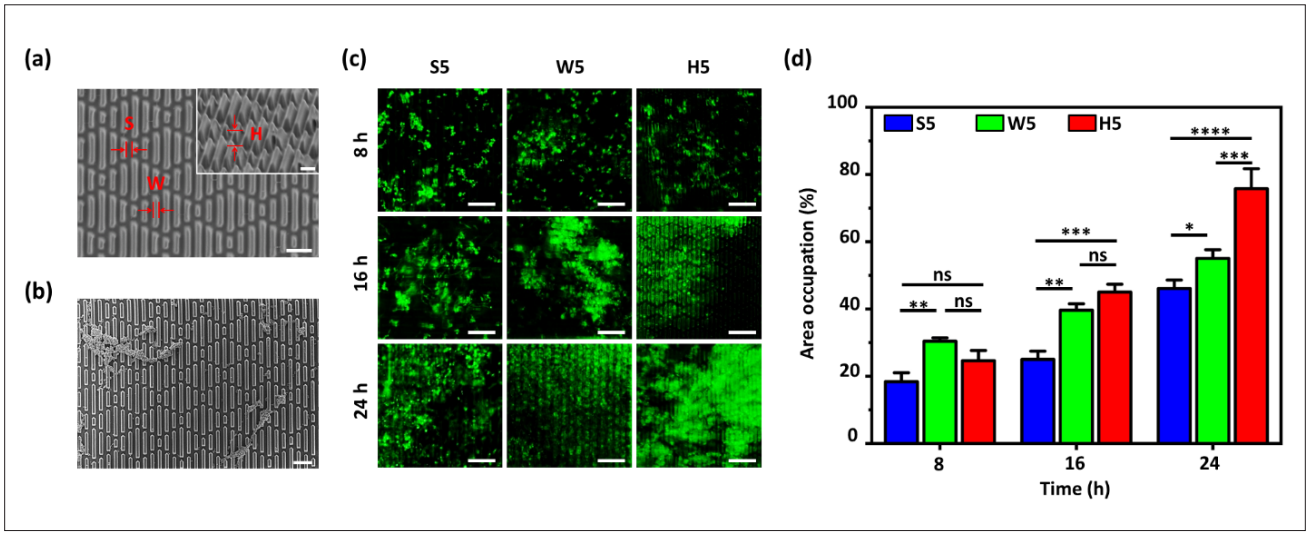

Figure 3. Precise modulation of microstructure morphology using two-photon polymerization 3D printing to investigate the key parameters affecting bacterial inhibition. The standard parameters: stripe lengths of 4, 8, and 16 μm; width (W) of 2 μm; height (H) of 3 μm; and inter-stripe distance (S) of 2 μm. Adjustment of parameters—W: 2–5 μm, H: 2–5 μm, S: 2–5 μm. (a) 3D printing allows precise tuning of microstructural parameters. Scale bar: 10 and 5 μm (inset). (b) SEM image of 3D-printed simplified microstructures with bacterial proliferation on the surface after 24 h. Scale bar: 10 μm. (c) Proliferation of bacteria (green fluorescence-labeled) on printed microstructures with different parameters in 24 h. Scale bar: 30 μm. (d) 24-h proliferation of bacteria on microstructures with different parameters measured in terms of total occupied area on the substrate. Data are expressed as mean ± SD. n = 3; one-way ANOVA; ns, no significance; *p < 0.05; **p < 0.01; ***p < 0.001; ****p < 0.0001. Abbreviation: SEM, scanning electron microscopy.

different parameters was not more than 50% in the "S5" group, but more than 70% in the "H5" group after 24 h. It is hypothesized that the change of a certain parameter of the microstructure has a significant effect on the bacteriostatic function of the microstructure. In addition, the "S5" group was found to maintain the lowest bacterial proliferation at different times compared to the other two groups. It can be hypothesized that there are some specific parameters that can make the physical bacteriostatic capacity of the microstructures the most significant (Figure 3d).

3.3. Bacteriostatic properties of microporous structures alter with structural parameters

In order to explore whether similar structural effects could influence the bacteriostatic capacity, we constructed another microstructure at the micron scale. The surface of this microstructure featured uniformly distributed micropores of the same size, and the diameter of the micropores was used as a parameter adjusted to explore its effect on the bacterial inhibition capacity. To further confirm the effect of parameters on the physical inhibitory capacity, we designed three microporous structures with different pore sizes (pore sizes [*D*] of 2, 3, and 4 μm, respectively) and precisely printed them using two-photon 3D printing technology (Figure 4a). SEM clearly shows bacterial cells proliferated and attached to the 3D-printed microporous structures after 24 h of co-culture with *S. mutans* (Figure 4b). Subsequently, using fluorescent staining and fluorescence microscopy observation records, we compared the substrate area occupied by bacterial proliferation on the surface of microporous structures at different pore sizes. Three groups of microporous substrates with microporous diameters of 2, 3, and 4 μm were recorded as groups "D2," "D3," and "D4." It can be seen that the "D2" group consistently showed the largest bacterial proliferation area at different times, while the bacterial proliferation of the "D3" and "D4" groups was significantly inhibited (Figure 4c and d). In addition, we found a strong link between the magnitude of the parameter and the inhibitory capacity. The "D3" group, which had an area of bacterial proliferation of less than 50%, was significantly better than the other two groups after 24 h. This indicates that the magnitude of this parameter is not a determining factor of antimicrobial performance of the microstructures, as testing needs to be performed to identify the specific value of the parameter that can lead to the most significant antimicrobial performance. Taken together, our findings offer new ideas and methods for the study of antimicrobial mechanisms in microstructures.

4. Discussion

Bacteria have a profound impact on human existence, and their various roles affect our well-being and the environment.[34,35] These microscopic organisms play a crucial role in processes such as food spoilage, material

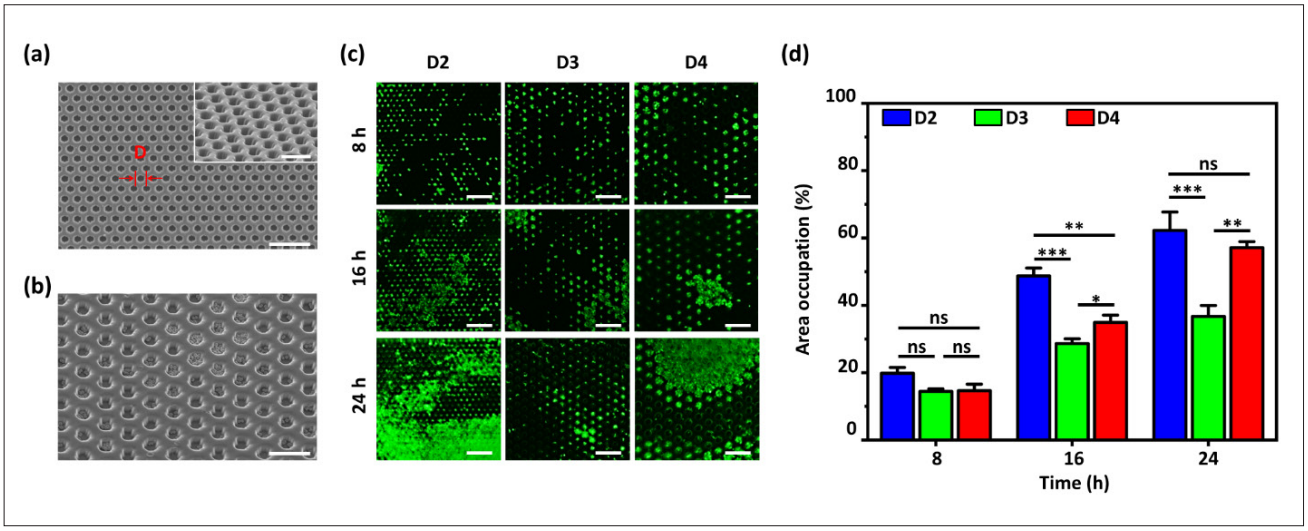

Figure 4. Precise modulation of microstructural morphology using two-photon polymerization 3D printing to study the key parameters affecting the bacterial inhibitory effect. The microstructural parameters: pore diameters (*D*) of 2, 3, and 4 μm. (a) 3D printing can precisely adjust the microstructure parameters. Scale bar: 20 and 10 μm (inset). (b) SEM image of bacterial proliferation on the surface of 3D-printed micropores for 24 h. Scale bar: 10 μm. (c) Proliferation of bacteria (green fluorescence-labeled) on the printed microporous structures with different parameters for 24 h. Scale bar: 30 μm. (d) The total area of the substrate occupied by the proliferating bacteria on the microporous structures with different parameters for 24 h. Data are expressed as mean ± SD. $n = 3$; one-way ANOVA; ns, no significance; *$p < 0.05$; **$p < 0.01$; ***$p < 0.001$. Abbreviation: SEM, scanning electron microscopy.

corrosion, immunity and environmental sustainability, and contributing to a range of diseases.[36–40] Several studies have found that some plant and animal surfaces have inherent antimicrobial capacity, due to the micro- and nano-structures on their surfaces.[41,42] In order to further explore the key factors and mechanisms of microstructure-induced antimicrobial effects, a processing technology that can precisely fabricate specific surface microstructures and accurately control the microstructural parameters is urgently required.

3D printing has emerged as a versatile and favorable platform for manufacturing a wide range of products with elaborate structures.[43,44] Two-photon polymerization 3D printing has been demonstrated to have many advantages in the precise printing of microstructures on a variety of surfaces as well as in the regulation of microstructural morphology, such as mild printing conditions, applicability to a wide range of material surfaces, and precise control of morphology parameters. The strategy of replicating bionic inhibitory microstructures on the surface of objects based on two-photon polymerization 3D printing shows great promise for application.[32,45]

It is now generally accepted that the mechanism of microstructure inhibition is primarily the stretching of the membrane region suspended between the nanocolumns as the bacterial cell encounters the surface of the column. Once the membrane is stretched enough, it will lead to rupture and eventually cell death.[46–48] It is certain that chemical inhibition is not involved in this inhibitory process. Bandara et al.[49] suggested that membrane damage to bacteria is achieved through strong adhesion between the nanopillar and the bacterial extracellular polysaccharide substance (EPS) layer. However, Linklater et al.[50] found that EPS did not play a role in the mechanical bactericidal action on the surface of the nanopillar by labeling the companion bean globulin using a label-tracking method. They also obtained black silicon surfaces with different morphologies and heights of microstructures by plasma etching silicon wafers[51] and found that the different surfaces of microstructures exhibited similar killing efficiencies against both *Pseudomonas aeruginosa* and *S. aureus* cells. However, limited by the etching technique, they could not precisely regulate other parameters of the nanopillars such as length, width, and spacing. This problem can be easily resolved by the two-photon polymerization 3D printing technique. Our study highlights the potential of two-photon polymerization 3D printing technology as an advanced fabrication technique for developing bacteriostatic micro-nano structures. By enabling precise control over microstructural parameters, two-photon polymerization 3D printing provides a powerful tool for systematically investigating the bacteriostatic mechanisms of bioinspired surfaces.

In this study, we simplified the microstructure that simulates shark skin. The simplified microstructure has the following advantages: first, the simplified structure inherits

the core features of the shark skin structure; second, the simplified structure is very regular, with three parameters that can be finely adjusted, including the width, height, and spacing of the rectangular columns, which facilitates the subsequent exploration of the mechanism; third, the simplified structure is relatively simple and intuitive, which is conducive to the generalization, extension, and improvement of the model as a research model; finally, the simplified structure is convenient for fabrication, reducing the cost and time of fabrication. Notably, the simplified microstructures had significant bacterial inhibitory property compared to the simulated structures. Our subsequent studies confirmed the parametric sensitivity of the inhibitory capacity of simplified microstructures. Previous studies, such as the one described above, have found that microstructures can achieve bacterial inhibition by disrupting the cell membranes of bacteria through stretching or cutting.[52] However, this phenomenon was not detected in our experiments using SEM images. In addition, the size change of the micron-scale structures had a negligible effect on the hydrophobicity of the microstructures.[52] The parametric sensitivity of the bacterial inhibitory ability is likely attributed to the following two factors: (i) the spatial restriction effect of the microstructure on the bacteria, and (ii) the effect of microstructure-bacteria contact mode on bacterial proliferation. This also explains the significantly enhanced inhibitory ability of the simplified microstructures, because they are far less smooth and continuous than the simulated ones, and the spatial restriction ability of the spaces between the rectangular columns is stronger than those of the simulated ones. Subsequently, we switched to a microporous structure and adopted an incremental diameter parameter design. The microporous structure is a model of a single parameter controlling the role of spatial restriction compared to the simplified structure of shark skin. From the results, the inhibitory ability of the microporous structure shows similar parametric sensitivity, and the effect of the parameter is dual. Therefore, we recommend enhancing the bacterial inhibitory capacity of both models by adjusting bacteria's spatial restriction and mode of contact with the microstructures.

The findings suggest that certain specialized microstructures exhibit a bacteriostatic effect, which becomes significant only when specific geometric parameters are met. One major limitation of the present study is that the fully delineated mechanism of bacterial inhibition remains uncovered, however, capitalizing on the advantages of two-photon polymerization 3D printing, such as high accuracy, efficiency, simplicity, and low cost, future studies can attempt on large-scale exploration of the mechanism, while expanding the parameter range and strain types. Moreover, the characteristics of microstructures such as morphology, parameters, and the corresponding bacterial inhibitory effect are easy to quantify. The data gathered can then be used to construct independent databases, as well as simulation models equipped with the excellent data processing capability of artificial intelligence, which provides a powerful tool for the screening of microstructures in terms of their morphology, parameters, and mechanism delineation. Taken together, the current research not only deepens our understanding of bacteriostatic mechanisms in micro-nanostructures but also paves the way for the development of next-generation bacteriostatic surfaces with applications in biomedical devices, implants, and healthcare/industrial products.[53–55]

5. Conclusion

In this paper, we demonstrate that parameter and morphology variations affect the physical inhibition of microstructures formed on the surface of an object using two-photon polymerization 3D printing technology. First, the simplified shark skin structures were able to inhibit the proliferation of more than 90% of *S. mutans* within 8 h and retained the same inhibitory effect at more than 70% after 24 h. Second, the height of the nanopillar had the greatest effect on the inhibitory ability of the microstructure against *S. mutans* compared to the spacing and width. This effect was also observed in other microstructures. In conclusion, we propose a novel strategy for exploring the mechanism of bacterial inhibition, i.e., to utilize the high-resolution and precise morphology control capability of two-photon 3D printing technology to precisely control the morphology of microstructures, so as to understand the underlying mechanism of bacterial inhibitory ability and the key influencing factors. This strategy is expected to fill the gap in the mechanism of physical bacterial inhibition, thereby improving the bacterial inhibitory effect and accelerating the application of this technology in industry, medicine, and daily life.

Acknowledgments

None.

Funding

This study was supported by Postdoctoral Science Foundation of China (2018M630883 and 2019T120688), Hubei Province Chinese Medicine Research Project (ZY2023Q015), Natural Science Foundation of Hubei Province (2023AFB665), Central Universities (Wuhan University) Clinical Medicine + X (2042024YXB017), the Medical Young Talents Program of Hubei Province, and Wuhan Young Medical Talents Training Project to L.-L. Bu,

Natural Science Foundation of China (61904057), Natural Science Foundation of Hubei Province (2018CFB124), and Research Programs of Science and Technology, Department of Education of Hubei Province (B2023256) to B. Cai, and International Orthodontics Foundation Young Research Grants Award (IOF2024Y11) to F.-Y. Huo.

Conflict of interest

The authors declare they have no competing interests.

Author contributions

Conceptualization: Fang-Yi Huo, Wentao Zhu, Kan Zhou, Enduo Zhou, Lei-Ming Cao, Qian Zhu, Hong He
Funding acquisition: Hong He
Investigation: Fang-Yi Huo, Wentao Zhu, Kan Zhou
Methodology: Fang-Yi Huo, Wentao Zhu, Kan Zhou, Enduo Zhou, Lei-Ming Cao, Qian Zhu
Project administration: Bo Cai, Lin-Lin Bu, Hong He
Supervision: Bo Cai, Lin-Lin Bu, Hong He
Visualization: Fang-Yi Huo
Writing–original draft: Fang-Yi Huo, Wentao Zhu, Kan Zhou, Enduo Zhou, Lei-Ming Cao, Qian Zhu
Writing–review & editing: All authors
All authors have reviewed and approved the final version of this manuscript for publication.

Ethics approval and consent to participate

Not applicable.

Consent for publication

Not applicable.

Availability of data

Data are available from the corresponding author upon reasonable request.

References

1. Otto M. Physical stress and bacterial colonization. *FEMS Microbiol Rev*. 2014;38(6):1250-1270. doi: 10.1111/1574-6976.12088
2. Byrd AL, Belkaid Y, Segre JA. The human skin microbiome. *Nat Rev Microbiol*. 2018;16(3):143-155. doi: 10.1038/nrmicro.2017.157
3. Muhammad MH, Idris AL, Fan X, et al. Beyond risk: bacterial biofilms and their regulating approaches. *Front Microbiol*. 2020;11:928. doi: 10.3389/fmicb.2020.00928
4. Nobbs AH, Lamont RJ, Jenkinson HF. Streptococcus adherence and colonization. *Microbiol Mol Biol Rev*. 2009;73(3):407-450. doi: 10.1128/mmbr.00014-09
5. Akcalı A, Lang NP. Dental calculus: the calcified biofilm and its role in disease development. *Periodontol 2000*. 2018;76(1):109-115. doi: 10.1111/prd.12151
6. Karygianni L, Ren Z, Koo H, Thurnheer T. Biofilm matrixome: extracellular components in structured microbial communities. *Trends Microbiol*. 2020;28(8):668-681. doi: 10.1016/j.tim.2020.03.016
7. Arciola CR, Campoccia D, Montanaro L. Implant infections: adhesion, biofilm formation and immune evasion. *Nat Rev Microbiol*. 2018;16(7):397-409. doi: 10.1038/s41579-018-0019-y
8. Sharma D, Misba L, Khan AU. Antibiotics versus biofilm: an emerging battleground in microbial communities. *Antimicrob Resist Infect Control*. 2019;8:76. doi: 10.1186/s13756-019-0533-3
9. Roy R, Tiwari M, Donelli G, Tiwari V. Strategies for combating bacterial biofilms: a focus on anti-biofilm agents and their mechanisms of action. *Virulence*. 2018; 9(1):522-554. doi: 10.1080/21505594.2017.1313372
10. Wu H, Moser C, Wang HZ, Høiby N, Song ZJ. Strategies for combating bacterial biofilm infections. *Int J Oral Sci*. 2015;7(1):1-7. doi: 10.1038/ijos.2014.65
11. Nwabuife JC, Omolo CA, Govender T. Nano delivery systems to the rescue of ciprofloxacin against resistant bacteria "E. coli; P. aeruginosa; Saureus; and MRSA" and their infections. *J Control Release*. 2022;349:338-353. doi: 10.1016/j.jconrel.2022.07.003
12. Fu X, Rehman U, Wei L, et al. Silver-dendrimer nanocomposite as emerging therapeutics in anti-bacteria and beyond. *Drug Resist Updat*. 2023;68:100935. doi: 10.1016/j.drup.2023.100935
13. Kalghatgi S, Spina CS, Costello JC, et al. Bactericidal antibiotics induce mitochondrial dysfunction and oxidative damage in Mammalian cells. *Sci Transl Med*. 2013;5(192):192ra85. doi: 10.1126/scitranslmed.3006055
14. Jaggessar A, Shahali H, Mathew A, Yarlagadda P. Bio-mimicking nano and micro-structured surface fabrication for antibacterial properties in medical implants. *J Nanobiotechnology*. 2017;15(1):64. doi: 10.1186/s12951-017-0306-1
15. Shahali H, Hasan J, Cheng HH, Ramarishna S, Yarlagadda PK. A systematic approach towards biomimicry of nanopatterned cicada wings on titanium using electron beam lithography. *Nanotechnology*. 2021;32(6):065301. doi: 10.1088/1361-6528/abbeaa
16. Xu M, Wang X, Wang B, et al. Carbonized lotus leaf/ZnO/Au for enhanced synergistic mechanical and photocatalytic

bactericidal activity under visible light irradiation. *Colloids Surf B Biointerfaces*. 2022;215:112468.
doi: 10.1016/j.colsurfb.2022.112468

17. Satheesh S, Ba-akdah MA, Al-Sofyani AA. Natural antifouling compound production by microbes associated with marine macroorganisms — a review. *Electron J Biotechnol*. 2016;21:26-35.
doi: 10.1016/j.ejbt.2016.02.002

18. Ge X, Ren C, Ding Y, et al. Micro/nano-structured TiO(2) surface with dual-functional antibacterial effects for biomedical applications. *Bioact Mater*. 2019;4:346-357.
doi: 10.1016/j.bioactmat.2019.10.006

19. Wang S, Deng Y, Yang L, Shi X, Yang W, Chen ZG. Enhanced antibacterial property and osteo-differentiation activity on plasma treated porous polyetheretherketone with hierarchical micro/nano-topography. *J Biomater Sci Polym Ed*. 2018;29(5):520-542.
doi: 10.1080/09205063.2018.1425181

20. Gao A, Yan Y, Li T, Liu F. Biomimetic urchin-like surface based on poly (lactic acid) membrane for robust anti-wetting and anti-bacteria properties. *Mater Lett*. 2019;237:240-244.
doi: 10.1016/j.matlet.2018.11.063

21. Li Y-N, Zhao Y, Liu J-J. Precisely engineered bionic Cu-doped titanium dioxide nanoarrays/fluorine-doped tin oxide with excellent antibacterial and antifouling properties. *Tungsten*. 2024;6(3):522-528.
doi: 10.1007/s42864-023-00255-9

22. Zhang Y, Zhao W, Chen Z, et al. Influence of biomimetic boundary structure on the antifouling performances of siloxane modified resin coatings. *Colloids Surf A: Physicochem Eng Aspects*. 2017;528:57-64.
doi: 10.1016/j.colsurfa.2017.05.044

23. Liu M, Wang S, Wei Z, Song Y, Jiang L. Bioinspired design of a superoleophobic and low adhesive water/solid interface. *Adv Mater*. 2009;21(6):665-669.
doi: 10.1002/adma.200801782

24. Cormican CM, Bektaş S, Martin-Martinez FJ, Alexander S. Emerging trends in bioinspired superhydrophobic and superoleophobic sustainable surfaces. *Adv Mater*. 2025;37(12):2415961.
doi: 10.1002/adma.202415961

25. Xu Y, Luan X, He P, et al. Fabrication and functional regulation of biomimetic interfaces and their antifouling and antibacterial applications: a review. *Small*. 2024; 20(21):e2308091.
doi: 10.1002/smll.202308091

26. Shao Z, Shen R, Gui Z, et al. Ethyl cellulose/gelatin/β-cyclodextrin/curcumin nanofibrous membrane with antibacterial and formaldehyde adsorbable capabilities for lightweight and high-performance air filtration. *Int J Biol Macromol*. 2024;254(Pt 2):127862.
doi: 10.1016/j.ijbiomac.2023.127862

27. Wu W, Han C, Liang R, et al. Fabrication and performance of graphene flexible pressure sensor with micro/nano structure. *Sensors (Basel)*. 2021;21(21):7022.
doi: 10.3390/s21217022

28. Gao Y, Ding Q, Li W, Gu R, Zhang P, Zhang L. Role and mechanism of a micro-/nano-structured porous zirconia surface in regulating the biological behavior of bone marrow mesenchymal stem cells. *ACS Appl Mater Interfaces*. 2023;15(11):14019-14032.
doi: 10.1021/acsami.2c22736

29. Chen Y, Wang C, Zhang Z, et al. 3D-printed piezocatalytic hydrogels for effective antibacterial treatment of infected wounds. *Int J Biol Macromol*. 2024;268(Pt 2):131637.
doi: 10.1016/j.ijbiomac.2024.131637

30. Jing X, Fu H, Yu B, Sun M, Wang L. Two-photon polymerization for 3D biomedical scaffolds: Overview and updates. *Front Bioeng Biotechnol*. 2022;10:994355.
doi: 10.3389/fbioe.2022.994355

31. Pao YH, Rentzepis PM. Laser-induced production of free radicals in organic compounds. *Appl Phys Lett*. 1965;6(5):93-95.
doi: 10.1063/1.1754182

32. Zhou X, Liu X, Gu Z. Photoresist development for 3D printing of conductive microstructures via two-photon polymerization. *Adv Mater*. 2024;36(48):2409326.
doi: 10.1002/adma.202409326

33. O'Halloran S, Pandit A, Heise A, Kellett A. Two-photon polymerization: fundamentals, materials, and chemical modification strategies. *Adv Sci (Weinh)*. 2023;10(7):e2204072.
doi: 10.1002/advs.202204072

34. Sanders ME, Akkermans LM, Haller D, et al. Safety assessment of probiotics for human use. *Gut Microbes*. 2010;1(3):164-185.
doi: 10.4161/gmic.1.3.12127

35. Chowdhury MAH, Ashrafudoulla M, Mevo SIU, Mizan MFR, Park SH, Ha SD. Current and future interventions for improving poultry health and poultry food safety and security: a comprehensive review. *Compr Rev Food Sci Food Saf*. 2023;22(3):1555-1596.
doi: 10.1111/1541-4337.13121

36. Chitrakar B, Zhang M, Adhikari B. Dehydrated foods: are they microbiologically safe? *Crit Rev Food Sci Nutr*. 2019;59(17):2734-2745.
doi: 10.1080/10408398.2018.1466265

37. Xu D, Gu T, Lovley DR. Microbially mediated metal corrosion. *Nat Rev Microbiol*. 2023;21(11):705-718.
doi: 10.1038/s41579-023-00920-3

38. Battaglia TW, Mimpen IL, Traets JJH, et al. A pan-cancer analysis of the microbiome in metastatic cancer. *Cell*. 2024;187(9):2324-2335.e19.
doi: 10.1016/j.cell.2024.03.021

39. Yong J, Chew KW, Khoo KS, Show PL, Chang JS. Prospects and development of algal-bacterial biotechnology in environmental management and protection. *Biotechnol Adv*. 2021;47:107684. doi: 10.1016/j.biotechadv.2020.107684

40. Roager HM, Licht TR. Microbial tryptophan catabolites in health and disease. *Nat Commun*. 2018;9(1):3294. doi: 10.1038/s41467-018-05470-4

41. Skoulas E, Manousaki A, Fotakis C, Stratakis E. Biomimetic surface structuring using cylindrical vector femtosecond laser beams. *Sci Rep*. 2017;7:45114. doi: 10.1038/srep45114

42. Li Y, Zhang LY, Zhang C, Zhang ZR, Liu L. Bioinspired antifouling Fe-based amorphous coating via killing-resisting dual surface modifications. *Sci Rep*. 2022;12(1):819. doi: 10.1038/s41598-021-04746-y

43. Zhu W, Ma X, Gou M, Mei D, Zhang K, Chen S. 3D printing of functional biomaterials for tissue engineering. *Curr Opin Biotechnol*. 2016;40:103-112. doi: 10.1016/j.copbio.2016.03.014

44. Su R, Chen J, Zhang X, et al. 3D-printed micro/nano-scaled mechanical metamaterials: fundamentals, technologies, progress, applications, and challenges. *Small*. 2023;19(29):e2206391. doi: 10.1002/smll.202206391

45. Zhang Y, Su Y, Zhao Y, Wang Z, Wang C. Two-photon 3D printing in metal-organic framework single crystals. *Small*. 2022;18(18):e2200514. doi: 10.1002/smll.202200514

46. Ivanova EP, Hasan J, Webb HK, et al. Bactericidal activity of black silicon. *Nat Commun*. 2013;4:2838. doi: 10.1038/ncomms3838

47. Ivanova EP, Hasan J, Webb HK, et al. Natural bactericidal surfaces: mechanical rupture of *Pseudomonas aeruginosa* cells by Cicada wings. *Small*. 2012;8(16):2489-2494. doi: 10.1002/smll.201200528

48. Linklater DP, Nguyen HKD, Bhadra CM, Juodkazis S, Ivanova EP. Influence of nanoscale topology on bactericidal efficiency of black silicon surfaces. *Nanotechnology*. 2017;28(24):245301. doi: 10.1088/1361-6528/aa700e

49. Bandara CD, Singh S, Afara IO, et al. Bactericidal effects of natural nanotopography of dragonfly wing on Escherichia coli. *ACS Appl Mater Interfaces*. 2017;9(8):6746-6760. doi: 10.1021/acsami.6b13666

50. Linklater DP, Juodkazis S, Rubanov S, Ivanova EP. Comment on "Bactericidal Effects of Natural Nanotopography of Dragonfly Wing on Escherichia coli". *ACS Appl Mater Interfaces*. 2017;9(35):29387-29393. doi: 10.1021/acsami.7b05707

51. Wang X, Bhadra CM, Yen Dang TH, et al. A bactericidal microfluidic device constructed using nano-textured black silicon. *RSC Adv*. 2016;6(31):26300. doi: 10.1039/C6RA03864F

52. Zhu WT, Huo FY, Cao LM, et al. Two-photon polymerization 3D printing of biomimetic microstructures for functionalizing surfaces to inhibit bacterial growth. *Chem Eng J*. 2025;511:161907. doi: 10.1016/j.cej.2025.161907

53. Li B, Tan H, Anastasova S, Power M, Seichepine F, Yang GZ. A bio-inspired 3D micro-structure for graphene-based bacteria sensing. *Biosens Bioelectron*. 2019;123:77-84. doi: 10.1016/j.bios.2018.09.087

54. Akbari E, Buntat Z, Afroozeh A, Zeinalinezhad A, Nikoukar A. Escherichia coli bacteria detection by using graphene-based biosensor. *IET Nanobiotechnol*. 2015;9(5):273-279. doi: 10.1049/iet-nbt.2015.0010

55. Krishnamurthi VR, Harris N, Rogers A, Zou M, Wang Y. Interactions of E. coli with cylindrical micro-pillars of different geometric modifications. *Colloids Surf B Biointerfaces*. 2022;209(Pt 2):112190. doi: 10.1016/j.colsurfb.2021.112190

ACCSCIENCE PUBLISHING

International Journal of Bioprinting

RESEARCH ARTICLE

Innovative design and compression performance of selective laser melting-printed tantalum artificial vertebral bodies

Yutao Zhang[1], Wurikaixi Aiyiti[2*], Jintao Li[1,2], Yong Huang[1,3], and Xiaohong Dong[1]

[1]Xinjiang Coal Mine Electromechanical Engineering Technology Research Center, School of Electromechanical Engineering, Xinjiang Institute of Engineering, Urumqi, Xinjiang, China

[2] Xinjiang Additive Remanufacturing Technology Key Laboratory, School of Mechanical Engineering, Xinjiang University, Urumqi, Xinjiang, China

[3]Key Laboratory of Intelligent Manufacturing Technology for Building Steel Structures of Xinjiang Production and Construction Corps, Urumqi, Xinjiang, China

Abstract

Tantalum (Ta) holds considerable potential for clinical applications in artificial vertebral bodies (AVBs) owing to its excellent biocompatibility. A novel Ta AVB structure was engineered by combining thin-walled structure topology optimization with lattice structure filling design methods. Three types of Ta AVBs—designated as AVB-1, AVB-2, and AVB-3—were fabricated using selective laser melting. The influence of sidewall curvature on the mechanical properties and deformation behavior of AVBs was investigated through compression tests and finite element analysis. The elastic modulus and yield strength of the Ta lattice structures ranged from 1.75 to 3.21 GPa and 31 to 65 MPa, respectively. Incorporating topologically thin walls enhanced the elastic modulus and yield strength by factors of 2.26–3.77 and 3–3.62, respectively. A decrease in sidewall curvature was associated with an increase in both elastic modulus and yield strength of the AVBs. Specifically, as the sidewall curvature decreased from 0.027 to 0 mm^{-1}, the elastic modulus and yield strength increased by factors of 2.76 and 2.19, respectively. The yield strengths of the AVBs were comparable to those of human cortical bone. Among the three designs, AVB-2 exhibited the highest yield-strength-to-elastic-modulus ratio (0.029), compared to AVB-1 and AVB-3 (0.024 and 0.019, respectively), suggesting that the optimal sidewall curvature is 0.014 mm^{-1}. AVB-2 effectively mitigated the stress shielding effect while maximizing the load-bearing capacity, indicating its significant potential for clinical applications.

Keywords: Tantalum; Selective laser melting; Artificial vertebral body; Lattice structure; Topology optimization

***Corresponding author:**
Wurikaixi Aiyiti
(wurikaixi@xju.edu.cn)

Citation: Zhang Y, Aiyiti W, Li J, Huang Y, Dong X. Innovative design and compression performance of selective laser melting-printed tantalum artificial vertebral bodies. *Int J Bioprint*. 2025;11(4):165-188. doi: 10.36922/IJB025150133

Received: April 11, 2025
Revised: May 5, 2025
Accepted: May 16, 2025
Published Online: May 16, 2025

Copyright: © 2025 Author(s). This is an Open Access article distributed under the terms of the Creative Commons Attribution License, permitting distribution, and reproduction in any medium, provided the original work is properly cited.

Publisher's Note: AccScience Publishing remains neutral with regard to jurisdictional claims in published maps and institutional affiliations.

1. Introduction

Total *en bloc* spondylectomy is an effective treatment for spinal tumors and tuberculosis. This procedure involves the complete removal of the diseased vertebral body and the

restoration of the spinal stability through the implantation of an artificial vertebral body (AVB).[1] The AVB should possess adequate load-bearing capacity and good osseointegration, with an elastic modulus that closely matches that of human bone to avoid stress shielding.[2] Research aimed at enhancing the performance of AVBs has focused on innovations in materials and optimized structural designs.[3–7]

Current studies have shown that titanium (Ti) and its alloys,[8] polyetheretherketone (PEEK),[9,10] and hydroxyapatite (HA)[11] are potential materials for use in AVBs. Although PEEK has an elastic modulus close to that of human bone, it suffers from limited load-bearing capacity and poor bioactivity, factors that have become bottlenecks in its application.[10] In contrast, HA exhibits excellent biocompatibility, but its low fracture toughness limits its use in this field.[12] To address the limitations associated with the performance of single materials, researchers have attempted to develop composites based on polymers or HA.[13–15]

Owing to their excellent mechanical stability and bioactivity, Ti and its alloys are widely used in bone implants such as hip and knee replacements, dental implants, spinal implants, and cranial defect repairs.[8,16] Compared to PEEK and HA, Ti alloys exhibit superior load-bearing capacities, making them more suitable for applications in load-bearing parts of the human body.[17,18] As a result, Ti alloys have become mainstream materials for the clinical application of AVBs. Furthermore, traditional Ti alloy cages (Ti cages) have been widely adopted for the clinical treatment of spinal diseases.[19–21]

Tantalum (Ta), a transition metal, demonstrates notable physical properties, including a high density (16.68 g/cm^3) and a high melting point (2996 °C). In addition to its reliable mechanical properties, Ta demonstrates superior bioactivity, corrosion resistance, and fracture toughness compared with Ti alloys,[22–24] thereby significantly enhancing the osseointegration of bone implants. Tantalum pentoxide (Ta_2O_5) films, which form readily on the surface of Ta metal, offer excellent corrosion resistance and osteoinductive function.[25] Therefore, Ta has great potential for applications in AVBs.[26] Unfortunately, the elastic moduli of solid Ta (186 GPa) and Ti (110 GPa) considerably exceed that of human bone (0.022–21 GPa),[27] leading to stress shielding of the vertebrae and poor integration of the AVB with the surrounding bone tissue.[28] By utilizing topology optimization and lattice design, the elastic modulus of the Ta AVB can be substantially decreased, enabling better matching with that of human bone.[29]

The lattice structure was fabricated by a periodic arrangement of multiple identical unit cells. Thanks to their superior specific strength and specific stiffness relative to solid materials, lattice structures have garnered significant attention for applications in lightweight design, energy absorption, and biomedicine.[30,31] Moreover, the interconnected open pores within the lattice structure facilitate the ingrowth of cells and blood vessels, thereby significantly improving the osseointegration of bone implants.[32–36] Therefore, incorporating lattice structures into the Ta AVB substantially reduces its elastic modulus and improves its biocompatibility. Chen et al.[37] designed a Ta density-gradient lattice structure. The elastic moduli of these lattice structures ranged from 0.22 to 0.89 GPa, which is similar to that of human cancellous bone. Song and colleagues[38] proposed gyroid porous Ta structures with radially graded porosity. Compression tests showed that the porous Ta structures had a minimum elastic modulus of 0.6 GPa. Ni et al.[39] compared the fatigue performance of a triple periodic minimal surface (TPMS) and rhombic dodecahedron Ta lattice structures. The TPMS structure exhibited higher fatigue resistance than the rhombic dodecahedron and has the potential for use in load-bearing bone implants.

Topology optimization design identifies the optimal force transfer paths and structural morphology by adjusting the distribution of materials within the design domain. This approach reduces material usage while improving the structural mechanical properties.[40] When applied to the structural optimization of bone implants, this design methodology enables regulation of overall stiffness,[41] achieving an optimal balance between maximizing load-carrying capacity and minimizing stress shielding by tailoring the mechanical properties of the implant.[42,43] Kök and colleagues[42] applied topology optimization to the internal structure of dental implants and reported a 30% reduction in stress shielding compared to standard implants. Peng et al.[44] implemented topology optimization in the fixation system of a mandibular implant, resulting in improved mechanical stability. In their work on interbody fusion cages, Smit and colleagues[45] incorporated the structural response of adjacent bone into the topology optimization process, significantly reducing the risk of cage subsidence.

Owing to significant advancements in metal additive manufacturing processes, the preparation of customized bone implants featuring complex structures has become feasible. Selective laser melting (SLM), a representative metal additive manufacturing technology, is characterized by high resolution and high energy input, enabled by precise laser control. This capability makes SLM particularly suitable for producing fine and complex structures, such as lattices and topological configurations, even with high-melting-point materials like Ta.[46,47] Wang

et al.[48] fabricated trabecular Ta specimens using laser powder bed fusion (LPBF) and investigated the effects of annealing temperature and oxygen content on their mechanical properties. Qin and colleagues[49] performed hot isostatic pressing to LPBF-printed TPMS porous Ta, significantly improving its compressive strength without compromising plasticity. Functional gradient Ta lattice structures developed by Chen et al.[37] using LPBF exhibited excellent manufacturability, with a porosity deviation of less than 5.13%.

Extensive research has been conducted on the optimal design of spinal implant structures. However, there remains a notable lack of studies focused on optimizing the overall architecture of AVBs to minimize stress shielding while maximizing load-bearing capacity. Moreover, investigations into the mechanical properties of SLM-fabricated Ta AVBs are limited, especially in comparison with polymer- and Ti alloy-based spinal implants.

In this study, novel Ta AVBs were developed by integrating topology optimization and lattice structure design methods and fabricated using SLM. The influence of sidewall curvature on the mechanical properties and deformation behavior of these AVBs was investigated through compression tests and finite element analysis. The objective was to optimize AVB's overall structure to effectively reduce the stress shielding effect, enhance load-bearing functionality, and align its mechanical properties with those of the human cortical bone. This study aimed to develop a novel Ta AVB with the potential to enhance osseointegration and mitigate the risk of bone resorption in cervical fusion segments and degenerative diseases in the adjacent segments. The logical flow of the introduction section of the article is shown in Figure 1.

2. Materials and methods

2.1. Design method

The Ta AVB was designed to imitate human vertebrae and is composed of a thin-walled and lattice structure, as shown in Figure 2. The height of the AVB was set at 24 mm, and the end face was designed to be elliptical, with a long diameter of 16 mm and a short diameter of 12.6 mm. The thin-walled structure functioned similarly to the cortical bone of the human vertebrae and was used to

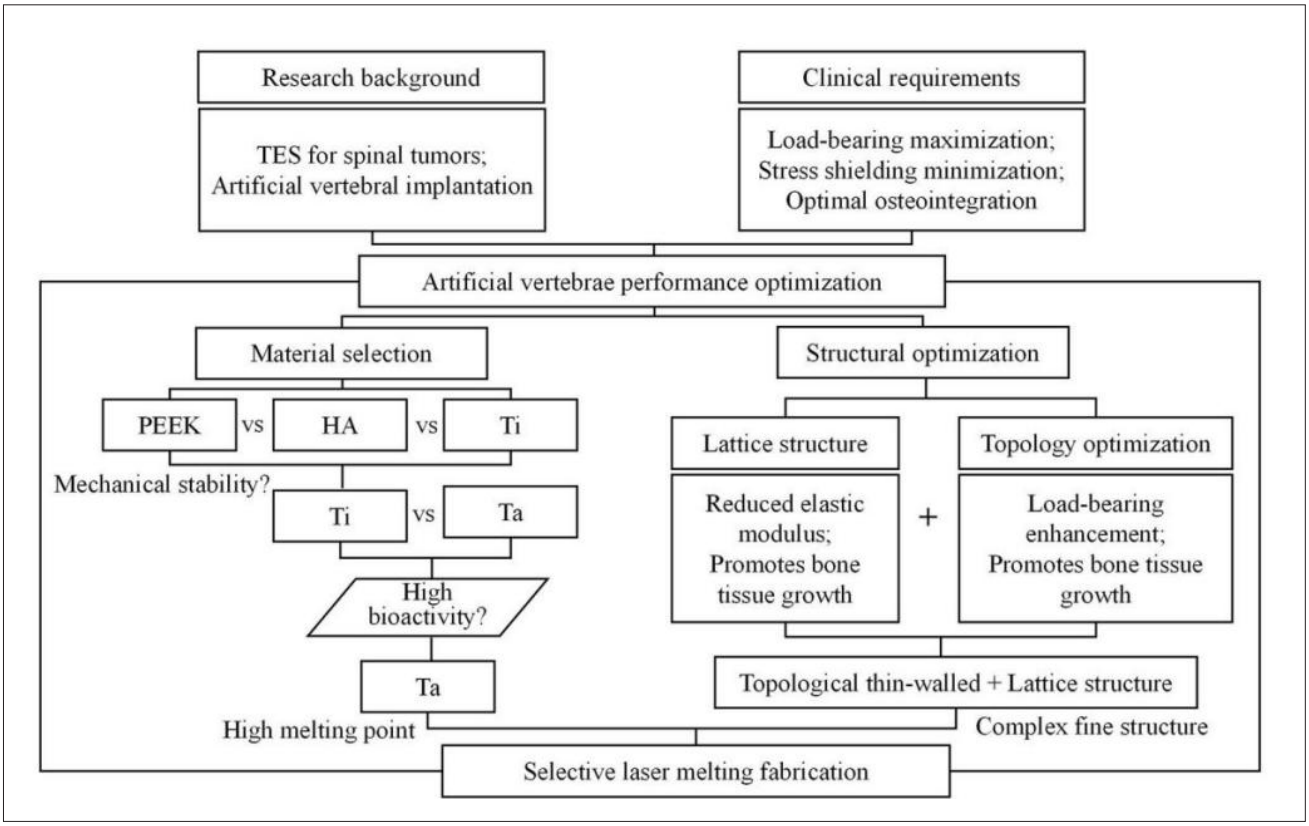

Figure 1. Logical flow of **Introduction** section. Abbreviations: HA: Hydroxyapatite; PEEK: Polyetheretherketone; Ta: Tantalum; TES: Total *en bloc* spondylectomy; Ti: Titanium.

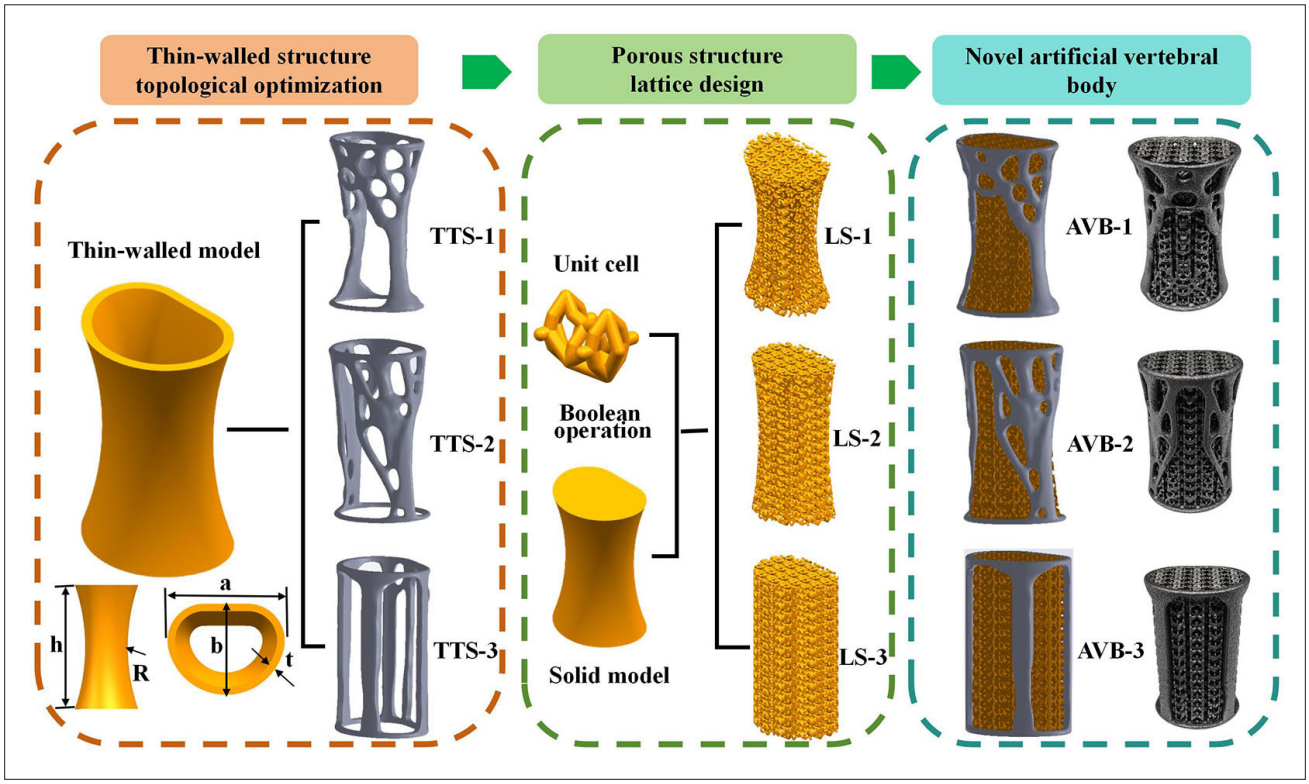

Figure 2. Schematic representation of thin-walled structure topology optimization, lattice structure filling, and artificial vertebral body model design. Abbreviations: a: Long diameter; AVB: Artificial vertebral body; b: Short diameter; h: Height; LS: Lattice structure; R: Radius of curvature; t: Thickness; TTS: Topological thin-walled structure.

enhance load-bearing capacity. Thin walls were designed with pores to provide channels for cell migration, blood vessel growth, and bone tissue formation. To maximize the load-bearing performance of thin walls with pores, a topology optimization design of the thin-walled structure was carried out in this study.

Common methods used for topology optimization of continuum structures include homogenization, variable density, evolutionary structural optimization, level set, and independent continuous mapping (ICM) methods. The variable density method considers continuum structures to consist of elements with variable densities. The element densities vary in the range [0, 1], which transforms the material distribution into a [0, 1] integer programming. An element density of zero indicates that the material at that location can be discarded, while a density of one indicates that the material should be retained. Intermediate densities are brought closer to zero or one by introducing a penalty factor. The relationship between the element density and elastic modulus is defined as follows:

$$E_i = E_{min} + f(\rho_i) \times (E_0 - E_{min}) \quad \text{(I)}$$

where E_i is the elastic modulus of the i-th element, E_{min} is the minimum elastic modulus, $f(\rho_i)$ is the penalty function, and E_0 is the elastic modulus of the initial design domain.

A solid isotropic material with penalization (SIMP) model was used to optimize the load transfer path and material distribution in the thin-walled structures. The penalty function for the SIMP interpolation model is expressed as:

$$f(\rho_i) = \rho_i^P \quad \text{(II)}$$

where ρ_i is the density of the i-th element and P is the penalty factor.

The optimization aims to minimize structural compliance under specific boundary conditions and volume constraints. The mathematical model for topology optimization is as follows[50]:

$$\begin{cases} Find\ \rho = (\rho_1, \rho_2, ..., \rho_n); \\ minC(\rho) = \frac{1}{2}U^T KU = \frac{1}{2}\sum_{i=1}^{n} u_i^T k_0 (\rho_i)^p E_s u_i; \\ s.t.\ \frac{V_\rho}{V_0} \le f; \\ 0 < \rho_{min} < \rho_i \le 1 \end{cases} \quad \text{(III)}$$

where ρ is the density of the element, C is compliance, U is the global displacement vector, K is the global stiffness matrix, n is the number of elements, u_i is the element displacement vector, k_0 is the element stiffness matrix for unit Young's modulus, E_s is the stiffness of the material, p is the penalization factor, V_ρ and V_0 are the material volume and the design domain volume, respectively, f is the prescribed volume fraction, and ρ_{min} is the minimum element density.

Altair OptiStruct™ software (Altair Engineering Inc., USA) was used for the topology optimization design of the thin-walled model. The mesh type was tetrahedral, and the mesh size was set to 0.5 mm. The material properties of Ta were assigned to the mesh elements, with an elastic modulus of 186 GPa, a Poisson's ratio of 0.35, and a density of 16.6 g/cm^3. The boundary conditions were defined such that the bottom surface of the thin-walled model was fully constrained and a pressure of 2 MPa was applied to the top surface. The topology optimization parameters were set to a minimum size of 0.5 and a maximum size of 1. The prescribed volume fraction, penalization factor, and minimum element density were set to 0.3, 3, and 0.01, respectively.

The key design parameters affecting the mechanical properties of thin-walled structures are wall thickness and sidewall curvature. While it is evident that increasing wall thickness enhances load-bearing capacity, sidewall curvature has more complex effects on the mechanical properties of both the thin-walled structure and its internal lattice. Furthermore, an excessively thick outer wall can hinder the inward growth of bone tissue and reduce the fusion rate of the AVBs. This study focused on evaluating the effect of sidewall curvature on the mechanical properties of AVBs with a wall thickness of 1 mm. As shown in Figure 2, three topological thin-walled structures, named TTS-1, TTS-2, and TTS-3, were designed with sidewall curvatures of 0.027, 0.014, and 0 mm^{-1}, respectively.

The interior of the topological thin-walled structure imitated the cancellous bone and was designed as an interconnected porous architecture to enhance osseointegration and promote nutrient transport. The lattice structure was constructed through a periodic arrangement of identical unit cells. A strut is the basic component of a strut-based unit cell and plays a crucial role in determining its mechanical properties. The elastic moduli of unit cells with straight struts can be obtained using the Euler–Bernoulli and Timoshenko beam theories.[51] Based on the Euler–Bernoulli beam theory, the strut displacement along the z-axis under compression is given by:

$$\delta_z = \frac{Fl^3 cos^2\theta}{12E_s I} + \frac{Flsin^2\theta}{E_s A} \quad \text{(IV)}$$

where F is the force on the strut, θ is the angle between the strut and the horizontal axis, A is the cross-sectional area of the strut, and I is the moment of inertia, defined as $I = \pi d^4/64$.

In addition to the strut deformation caused by axial loads and bending moments, the Timoshenko beam theory also considers the strut shear deformation. The strut displacement along the z-axis can be calculated as follows:

$$\delta_z = \frac{Fl^3 cos^2\theta}{12E_s I} + \frac{Flsin^2\theta}{E_s A} + \frac{Flcos^2\theta}{\kappa A G_s} \quad \text{(V)}$$

where κ is the shear coefficient factor, and G_s is the shear modulus of the parent material.

The displacement of the unit cell ($\delta_{UC,Z}$) can be obtained by accumulating strut displacements. Therefore, the strain in the unit cell can be expressed as follows:

$$\varepsilon_{UC,Z} = \frac{\delta_{UC,Z}}{h} \quad \text{(VI)}$$

where h is the height of the unit cell.

According to Hooke's law, the elastic modulus of a unit cell can be calculated as follows:

$$E_{UC,Z} = \frac{\sigma_{UC,Z}}{\varepsilon_{UC,Z}} \quad \text{(VII)}$$

where $\sigma_{UC,Z}$ is the stress of the unit cell along the z-axis.

According to the elastic–plastic cellular solid model proposed by Gibson and Ashby,[52] the plastic collapse stress of the lattice structure under compression can be calculated as:

$$\frac{\sigma_{pl}^{*}}{\sigma_{ys}} = \left(\frac{d}{l}\right)^{2} \quad \frac{1}{2cos^{2}\theta} \tag{VIII}$$

where σ_{ys} is the yield strength of the parent material.

Overall, the design parameters of the struts, such as the ratio of strut diameter to length (d/l), the inclination angle of the strut (θ), and the number of struts (s), have significant effects on the elastic modulus and yield strength of the lattice structures. In our previous study, compared to the conventional body-centered cubic lattice structure, the imitation saddle surface (ISS) featured more slightly angled inclined struts, a greater number of struts and nodes, and a higher strut diameter-to-length ratio. According to our previous results,[53] the ISS lattice structure exhibited a higher yield-stress-to-elastic-modulus ratio than the body-centered cubic lattice, effectively reducing the risk of stress shielding. Therefore, the ISS lattice structure was selected to fill the interior of the AVB.

Three lattice structures, named LS-1, LS-2, and LS-3, were generated through Boolean operations. Their sidewall curvatures were 0.027, 0.014, and 0 mm^{-1}, respectively. AVBs with the same corresponding sidewall curvatures named AVB-1, AVB-2, and AVB-3 were obtained by assembling topological thin-walled structures with lattice structures, as shown in Figure 2. Due to the small overall size of the AVB, a large sidewall curvature resulted in too few unit cells in the central region. Therefore, the maximum sidewall curvature was set at 0.027 mm^{-1} to ensure the stability of the lattice structure during compression.

Previous studies have indicated that bone implants with porosities between 0.6 and 0.8 are favorable for cell and bone tissue growth.[32,33,54] The porosity of the lattice structures (LS-1, LS-2, and LS-3) and the AVBs (AVB-1, AVB-2, and AVB-3) were designed to be 74% and 70%, respectively. The design and actual parameters of the Ta AVB and lattice structure specimens are presented in Table 1.

2.2. Specimen fabrication

Spherical pure Ta powder was used to fabricate the lattice structure and AVB specimens. As shown in Figure 3, the powder particle size distribution was D10 = 20.19 μm, D50 = 33.13 μm, and D90 = 52.37 μm. The chemical composition of the powder is listed in Table 2.

An SLM metal three-dimensional 3D printer (DiMetal-100 Pro; LASERADD, China) was employed to fabricate the Ta lattice structure and AVB specimens. The SLM printing parameters are provided in Table 3. Due to the small strut diameter (0.34 mm) and wall thickness (1 mm), the layer thickness was set to 0.03 mm to ensure high molding precision. The optimal process parameters of 350 W laser power, 650 mm/s scanning speed, and 0.08 mm hatch distance significantly improved the stability and fluidity of the Ta molten pool, reduced the number of defects, and resulted in Ta specimens with densities greater than 99.9%. An interlayer rotation angle of 67° was used to reduce anisotropy. The specimens were fabricated in a closed chamber under high-purity argon gas (99.9999%) to prevent oxidation. Post-processing included sandblasting and ultrasonic cleaning to remove residual powder particles from the printed Ta AVB specimens.

2.3. Morphological characterization

The dry weighing method was adopted to measure the porosity of the specimens, as follows:

$$p = 1 - \frac{m_d}{\rho_t V_a} \tag{IX}$$

where m_d is the mass of the specimen, ρ_t is the theoretical density of Ta, and V_a is the volume of the specimen.

The surface morphology and feature size of the specimens were measured using an ultra-depth microscope (VHX-6000; KEYENCE, Japan). As shown in Table 1, the porosities of the AVB-1, AVB-2, and AVB-3 specimens

Table 1. Design and actual values of selective laser melting-tantalum AVB and LS

Specimens	Porosity (%)		Thin-walled thickness (mm)		Lattice structure diameter (mm)	
	Design	Actual	Design	Actual	Design	Actual
AVB-1	70	71	1	0.98	0.34	0.35
AVB-2	70	69	1	1.02	0.34	0.36
AVB-3	70	69	1	1.04	0.34	0.35
LS-1	74	75	/	/	0.34	0.34
LS-2	74	75	/	/	0.34	0.35
LS-3	74	74	/	/	0.34	0.35

Abbreviations: LS: Lattice structure; AVB: Artificial vertebral body.

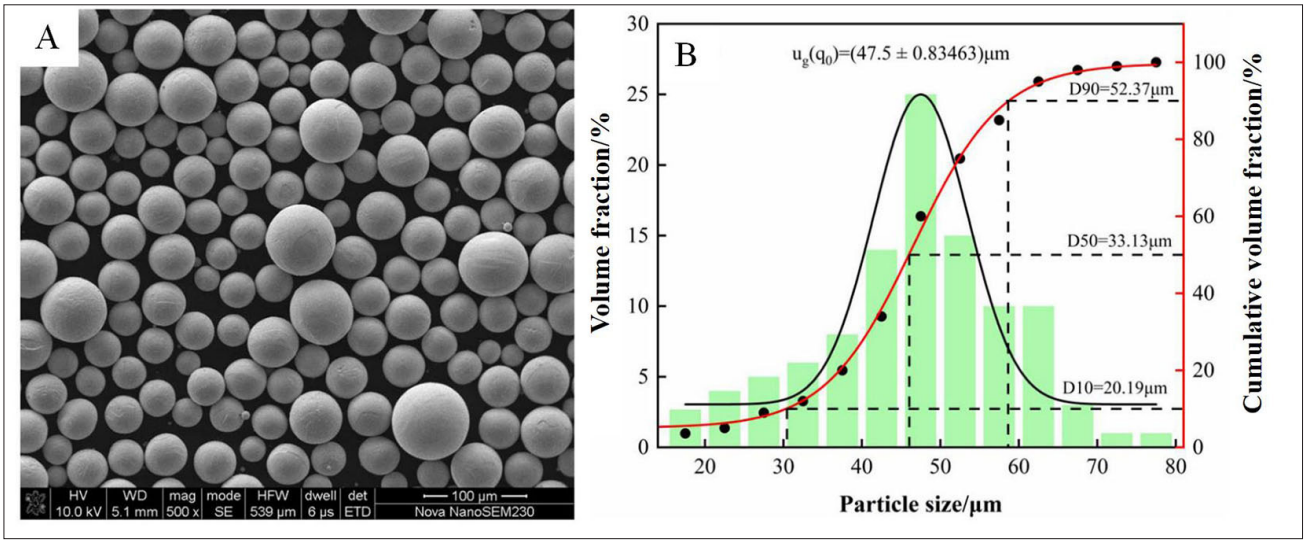

Figure 3. Microstructure (A) and particle size distribution (B) of spherical pure tantalum powder particles used in selective laser melting. Magnification = 500×; scale bar = 100 μm.

Table 2. Chemical composition of the tantalum powder

Elements (wt%)	O	N	C	H	Nb	Mo
	0.021	0.0018	0.0009	0.001	0.001	0.010
	Ti	**Si**	**Fe**	**Ni**	**W**	**Ta**
	0.0013	0.0018	0.0018	0.001	0.009	99.95

Abbreviations: C: Carbon; Fe: Ferrum; H: Hydrogen; Mo: Molybdenum; N: Nitrogen; Nb: Niobium; Ni: Nickel; O: Oxygen; Si: Silicon; Ta: Tantalum; Ti: Titanium; W: Tungsten.

Table 3. Selective laser melting printing parameters

Parameters	Value
Scanning speed	650 mm/s
Laser power	350 W
Layer thickness	0.03 mm
Hatch distance	0.08 mm
Rotation between layers	67°

were within the range of 69%–71%, which was close to the design value of 70%. The porosities of specimens LS-1, LS-2, and LS-3 ranged from 74% to 75%, which was similar to the design value of 74%. The deviations in the actual values of the wall thickness and strut diameter from the design values were less than 10%.

The microscopic morphologies of the AVB specimens are illustrated in Figure 4. The surface and cross-section of the specimens were free of cracks, pores, and unfused defects. A small number of incompletely melted Ta powder particles adhered to the surface of the specimens, which caused a slight deviation in the printing and design dimensions.

2.4. Compression testing

A mechanical universal testing machine (E44 304, MTS, USA) was used to conduct the compressive tests on the specimens. The compression direction was parallel to the specimen building orientation. The loading rate was set to 1 mm/min according to ISO 13314: 2011. A video camera was used to record the deformation of the specimens during compression. The test was terminated when the compression process reached the densification stage. Stress (σ^*) and strain (ε) can be calculated as follows:

$$\begin{cases} \sigma^* = \dfrac{F}{A_0} \\ \varepsilon = \dfrac{\delta}{H} \end{cases} \quad \text{(X)}$$

where F is the loading force, A_0 is the area of the specimen's end face, and H is the height of the specimen. The elastic modulus (E^*) of the specimen was obtained

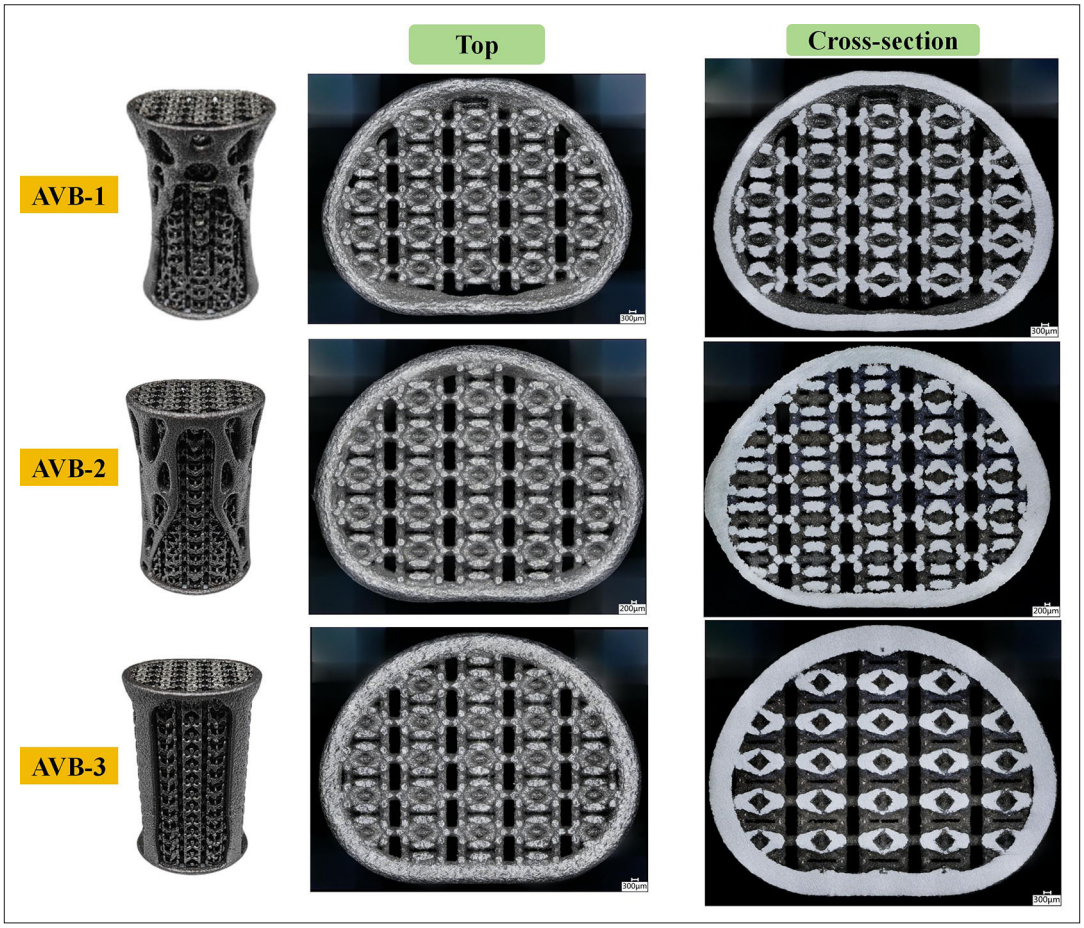

Figure 4. Surface and cross-sectional micromorphologies of tantalum AVBs prepared using selective laser melting. Magnification = 200×; scale bar = 300 μm. Abbreviation: AVB: Artificial vertebral body.

by calculating the slope of the linear elastic phase in the stress–strain curve. The compressive 0.2% offset stress was defined as the yield strength (σ^*_y).

2.5. Finite element analysis

Altair SimSolid (Altair Engineering Inc., USA) was used to simulate the compression of the specimens. SimSolid is a meshless structural analysis software that significantly improves the efficiency of the analysis. The SimSolid computational engine is based on breakthrough extensions of the theory of external approximations, which is an extension of the finite element method. SimSolid can perform the same analyses as other commonly used finite element analysis tools.[55] Previous studies have demonstrated the feasibility and accuracy of SimSolid for analyzing the mechanical properties of bone implants.[56,57]

The finite element model consisted of an upper compression plate, the AVB, and a lower compression plate. The AVB model was placed at the center of the upper and lower plates, as shown in Figure 5. The material properties of Ta were assigned to the AVB model, with an elastic modulus of 186 GPa, Poisson's ratio of 0.35, and a density of 16.6 g/cm^3. The contact conditions between the AVB and plates were set as bonded. The boundary condition specified that the bottom surface of the lower plate was fully constrained, and a displacement along the negative direction of the *z*-axis was applied to the top surface of the upper plate. The sides of the AVB were assigned free boundary conditions. The solution settings and structural analysis were configured to accommodate both stress and material nonlinearity, respectively.

3. Results

3.1. Mechanical properties

The stress–strain curves of typical porous structures, Ta lattice structures, and AVBs under compression are shown in Figure 6. The stress–strain curve can be divided into three phases: linear elastic, plastic deformation, and densification. In the linear elastic phase, stress increases linearly with strain, and the specimen deforms elastically.

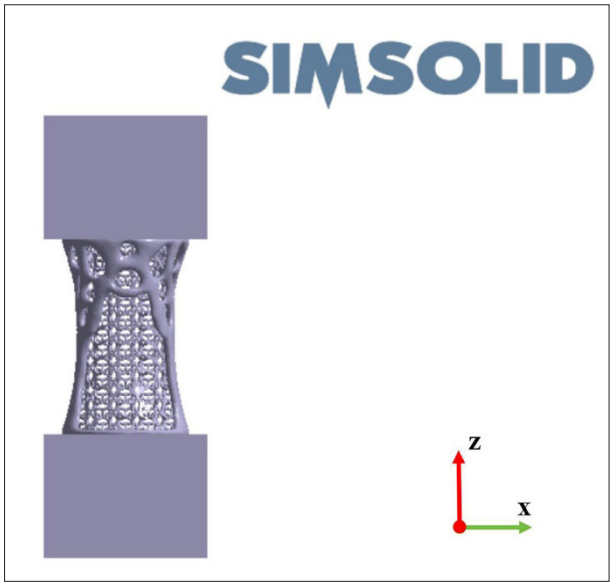

Figure 5. Finite element modeling of the compression process of a tantalum artificial vertebral body.

Upon reaching the yield strength, the specimen enters the plastic deformation phase.

As shown in Figure 6B, during the plastic deformation phase, the stress–strain curves of LS-1, LS-2, and LS-3 are generally smooth, with stress drops observed in regions ①, ②, and ③. In Figure 6C, the stress–strain curve for AVB-1 is smooth, while AVB-2 displays stress oscillations in regions ① and ②. AVB-3 shows a significant decrease in stress after yielding (region ③), but no further stress oscillations occurred during subsequent compression.

The yield strength determines the load-bearing capacity of the AVB, and the elastic modulus dictates its stress-shielding effect from the surrounding bone tissue. Therefore, a higher yield-strength-to-elastic-modulus ratio of the AVB indicates better load-bearing performance while reducing the stress shielding effect. The yield-strength-to-elastic-modulus ratio is calculated as follows:

$$\gamma = \frac{\text{Yield strength}}{\text{Elastic modulus}} = \frac{\sigma_y^* \left(\text{MPa}\right)}{E^* \left(\text{MPa}\right)} \quad \text{(XI)}$$

The elastic modulus, yield strength, and yield-strength-to-elastic-modulus ratio for the Ta lattice structure are shown in Figure 7. The elastic moduli of the LS-1, LS-2, and LS-3 were 1.75, 2.39, and 3.21 GPa, respectively, with yield strengths of 31, 51, and 65 MPa. Despite similar porosities, their elastic moduli and yield strengths varied significantly. This indicates that sidewall curvature has a significant effect on the mechanical properties of the lattice structure. The elastic modulus and yield strength of the lattice structure increased as the sidewall curvature decreased. The yield-strength-to-elastic-modulus ratios for LS-2 and LS-3 (0.021 and 0.02, respectively) were higher than those of LS-1 (0.018).

The elastic modulus, yield strength, and yield-strength-to-elastic-modulus ratios of the Ta AVBs are shown in Figure 8. The elastic moduli of AVB-1, AVB-2, and AVB-3 were 4.38, 5.32, and 12.1 GPa, respectively, with yield strengths of 107, 153, and 235 MPa, respectively. Compared to LS-1, LS-2, and LS-3, AVB-1, AVB-2, and AVB-3 exhibited substantially higher elastic moduli and yield strengths. This indicates that the topological thin-walled structure can significantly improve the load-bearing capacity of the lattice structure. Similar to the lattice structures, reducing the sidewall curvature of AVBs could enhance their load-bearing capacity. AVB-2 had the highest yield-strength-to-elastic-modulus ratio (0.029), which was significantly higher than that of AVB-1 and AVB-3 (0.024 and 0.019, respectively). Zhang et al.[58] successfully fabricated a Ti6Al4V AVB featuring a dual-graded lattice structure using SLM. The dual-grade porous AVB exhibited an elastic modulus of 2631.1 MPa and a yield strength of 53.13 MPa. Notably, the yield-strength-to-elastic-modulus ratio of 0.020 for this artificial vertebra closely resembles that of AVB-3. In contrast, the solid PEEK artificial vertebrae, developed by Wang and colleagues[59] using fused deposition modeling, achieved a yield strength of 94 MPa. Furthermore, the yield strengths of the diamond-lattice PEEK and PEEK/carbon-fiber cages with 48% porosity, as designed by Zhang et al.,[60] were 162 and 118 MPa, respectively, approximating the

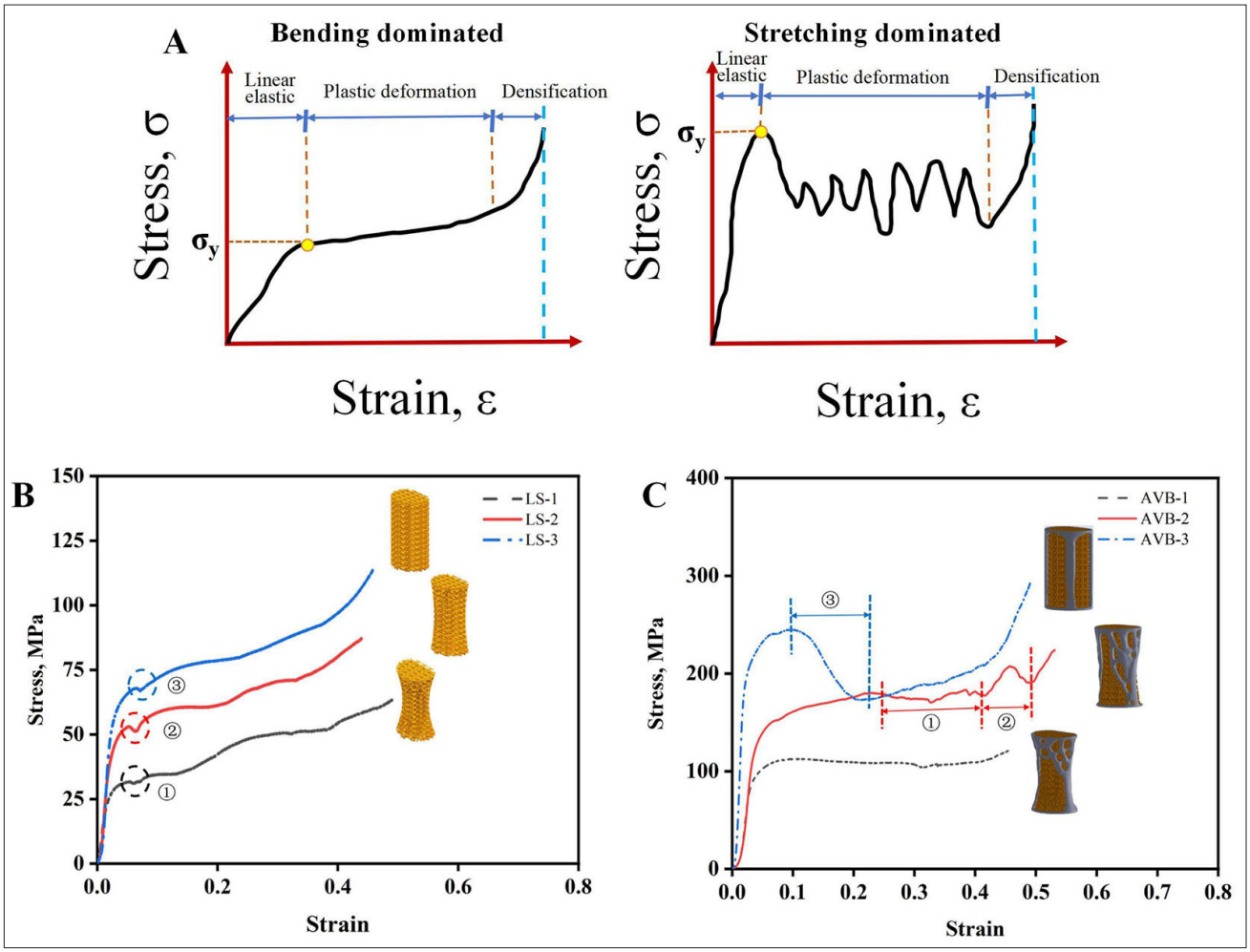

Figure 6. Stress–strain response curves of selective laser melting-printed tantalum lattice structure and artificial vertebral body specimens during compression: (A) elastic–plastic porous structure model, (B) tantalum lattice structures, and (C) tantalum artificial vertebral bodies. Abbreviations: LS: Lattice structure; AVB: Artificial vertebral body.

yield strength of human cortical bone. The Ti6Al4V multi-segment AVB, fabricated by Kang and colleagues,[3] demonstrated a maximum compressive load capacity of 72.72 kN, significantly surpassing that of AVB-1, AVB-2, and AVB-3. This enhanced performance is attributed to its thin-wall thickness of 1.5 mm, which is considerably greater than the 0.5–1.0 mm thickness employed in this study.

3.2. Deformation and failure behavior

The deformation behaviors of LS-1, LS-2, and LS-3 under different strains during the compression tests are shown in Figures 9–11. The Ta lattice structures (LS-1, LS-2, and LS-3) were composed of periodically arranged ISS unit cells. An inclined strut is an essential component of the ISS unit cell. Under external loading, the inclined struts underwent bending deformation caused by bending moments and formed plastic hinges near the nodes, leading the lattice structure to collapse. The unit cells in the middle of the LS-1 and LS-2 specimens deformed first, and their orientations were not inclined. LS-3 maintained a uniform deformation in the XOZ plane, and an X-shaped shear band appeared in the YOZ plane. The unit cells within the shear band deformed first, and the orientations of the peripheral unit cells in the specimen were inclined. Specimens LS-1, LS-2, and LS-3 exhibited varying degrees of expansion during compression, with LS-3 exhibiting the most pronounced expansion.

The deformation behaviors of the AVB-1, AVB-2, and AVB-3 with different strains are shown in Figures 12–14. The deformation behaviors of the Ta AVBs were determined by the deformation of the topological thin-walled and lattice structures, as well as the interaction between them.

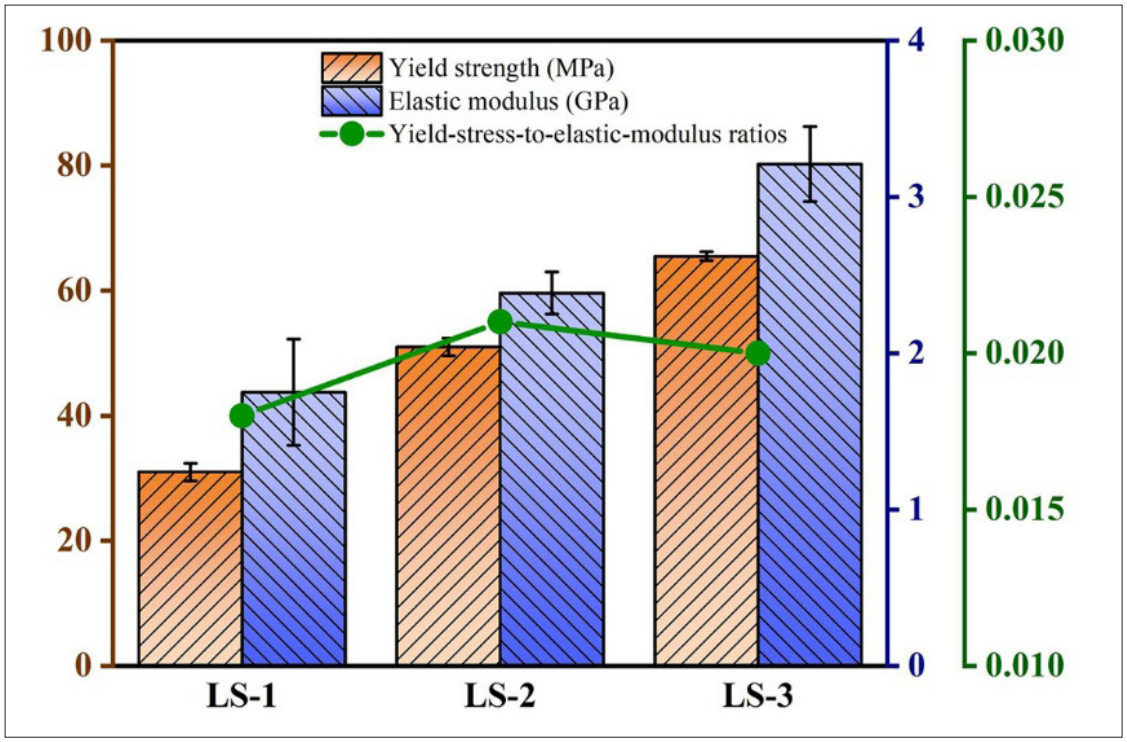

Figure 7. Yield strength, elastic modulus, and yield-stress-to-elastic-modulus ratios of selective laser melting-printed LSs during compression. Abbreviation: LS: Lattice structure.

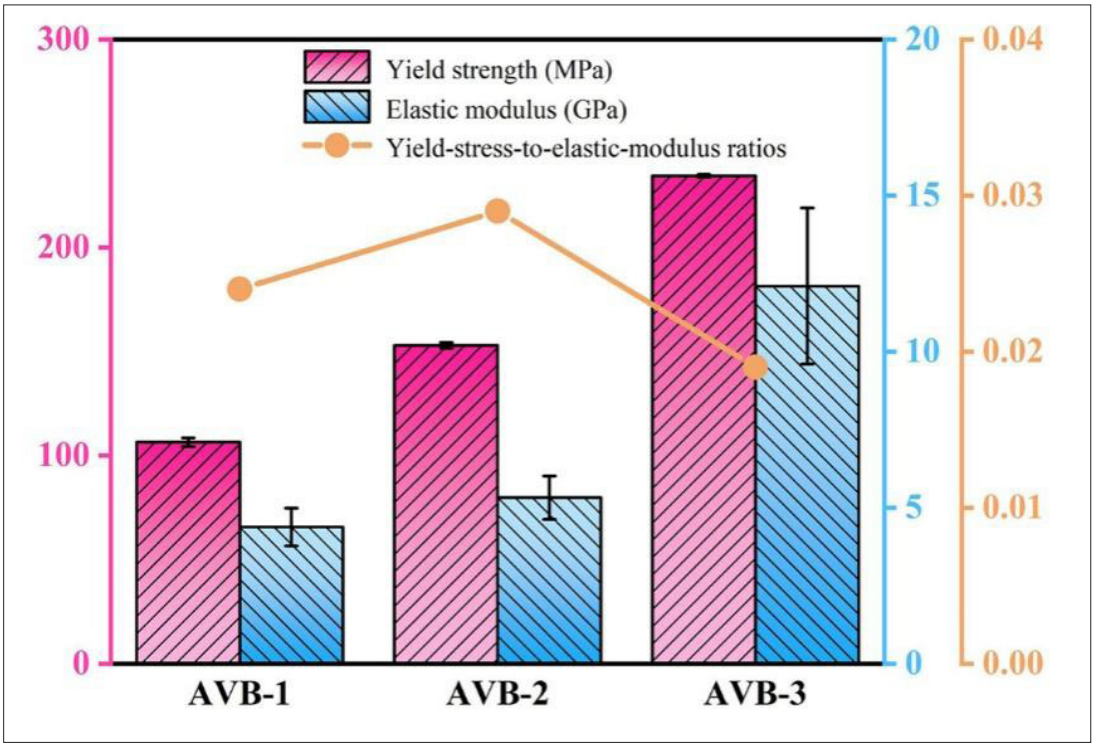

Figure 8. Yield strength, elastic modulus, and yield-stress-to-elastic-modulus ratios of selective laser melting-printed tantalum AVBs during compression. Abbreviation: AVB: Artificial vertebral body.

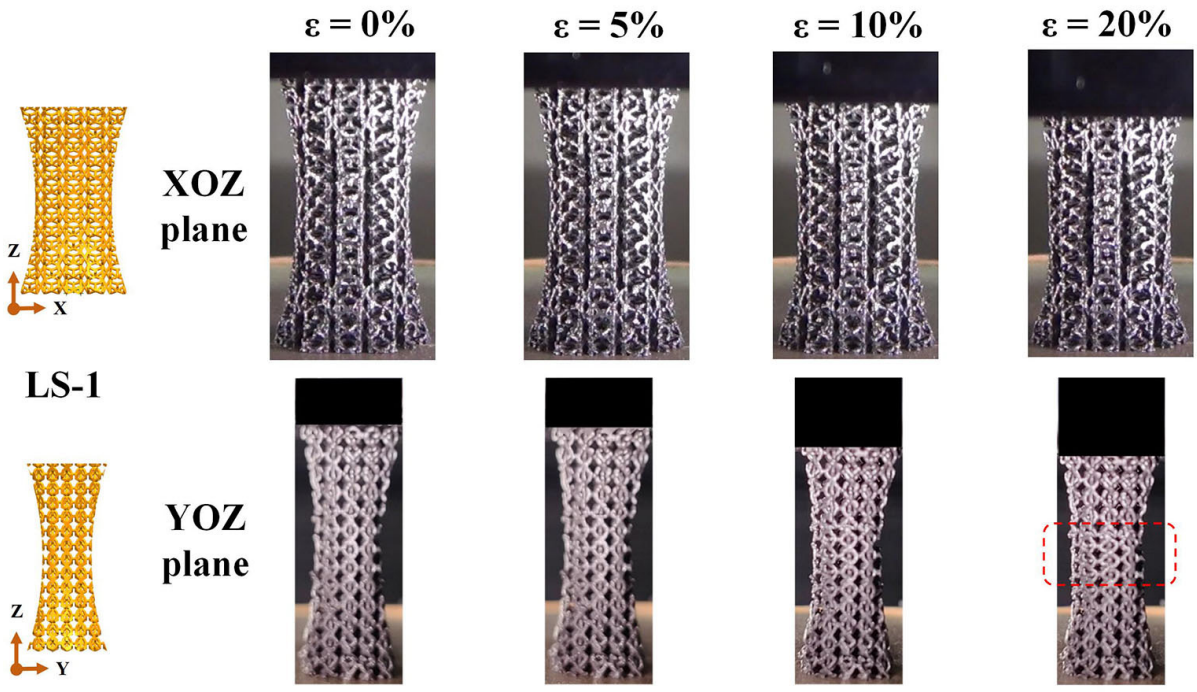

Figure 9. Deformation behavior and failure characteristics of the tantalum LS-1 in the XOZ and YOZ observation planes at 0%, 5%, 10%, and 20% strains. Abbreviation: LS: Lattice structure.

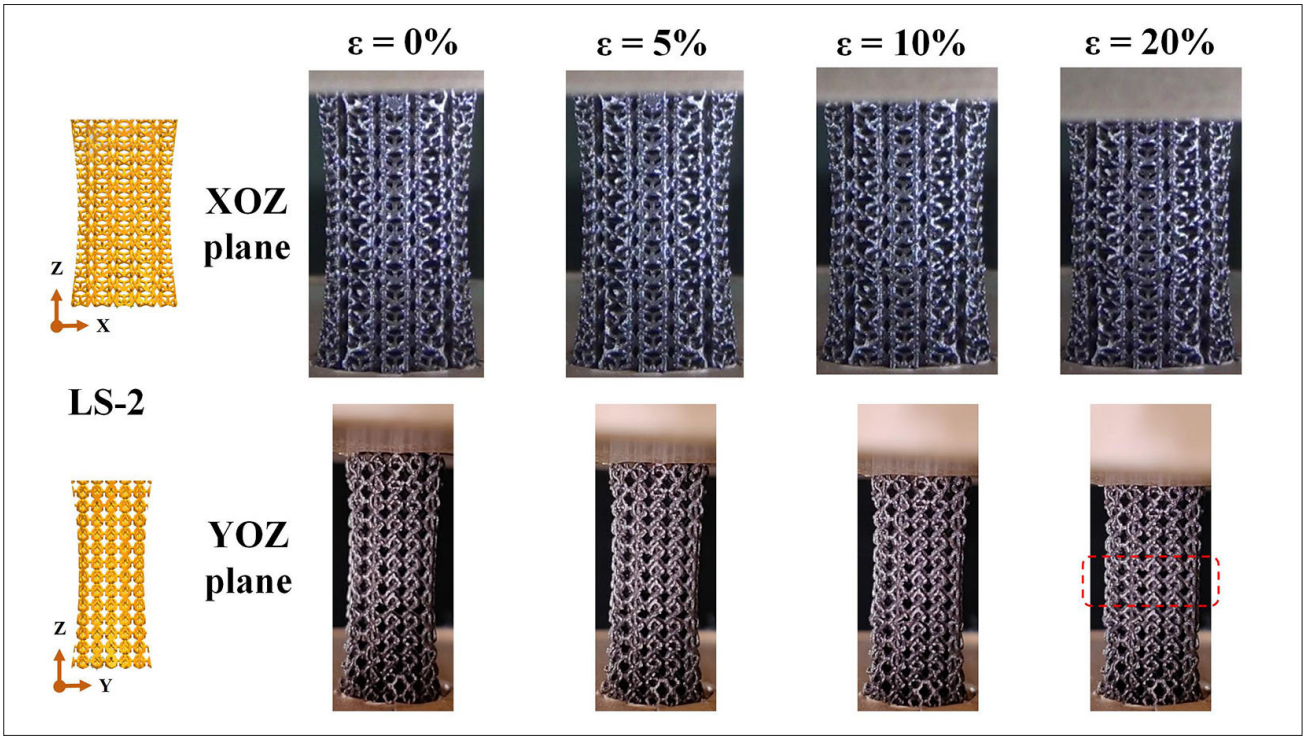

Figure 10. Deformation behavior and failure characteristics of the tantalum LS-2 in the XOZ and YOZ observation planes at 0%, 5%, 10%, and 20% strains. Abbreviation: LS: Lattice structure.

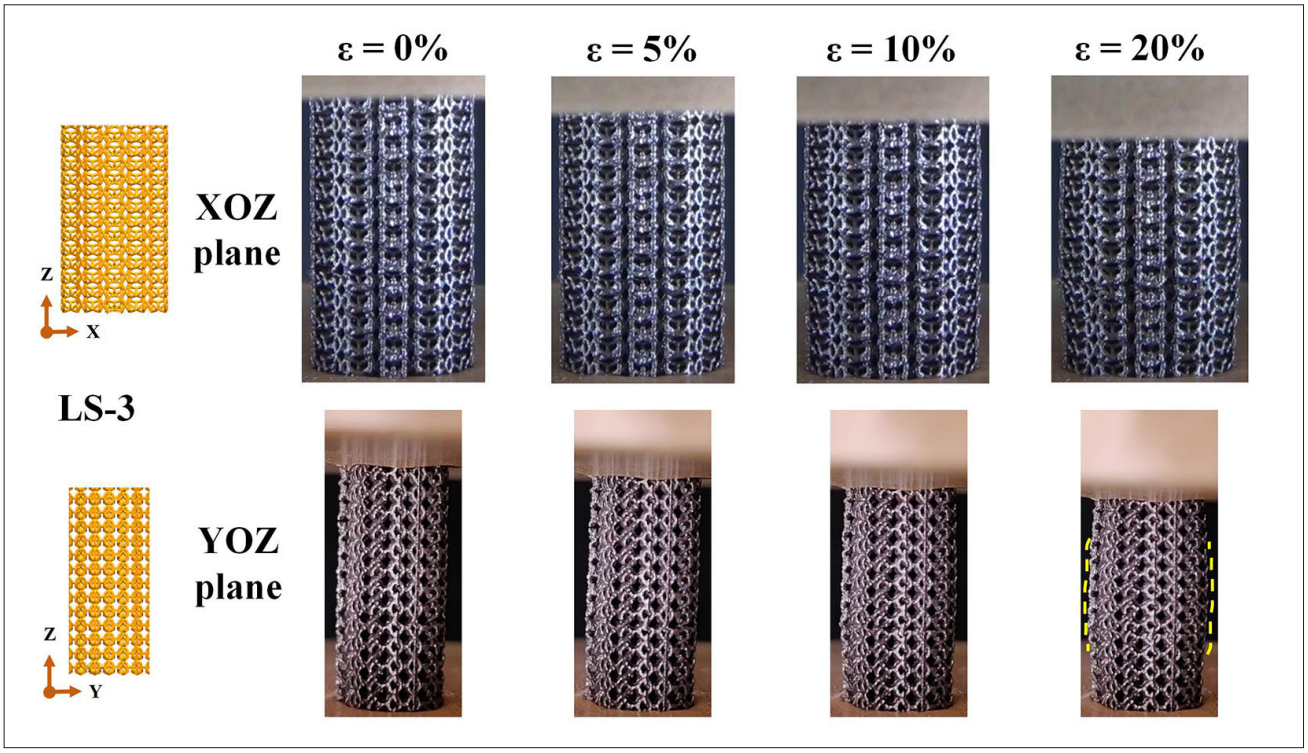

Figure 11. Deformation behavior and failure characteristics of the tantalum LS-3 in the XOZ and YOZ observation planes at 0%, 5%, 10%, and 20% strains. Abbreviation: LS: Lattice structure.

As shown in Figure 12, the topological thin-wall of AVB-1 exhibited "S"- and "C"-shaped bending deformations in the XOZ and YOZ planes, respectively. Similarly, AVB-2 underwent "C"-shaped bending deformation in both the XOZ and YOZ planes (Figure 13). In areas ① and ② of Figure 14, the topological thin wall of AVB-3 buckled in the XOZ and YOZ planes, unlike AVB-1 and AVB-2.

The finite-element simulation results of the compression process for the lattice structures and AVB specimens are shown in Figures 15 and 16, respectively. The deformation modes of the lattice structures and AVBs predicted by finite element simulation were consistent with the experimental outcomes. As shown in Figure 15, LS-1 exhibited instability due to larger sidewall curvature and fewer unit cells in the middle, compared to LS-2 and LS-3. The von Mises stress was concentrated in the middle of LS-1 and LS-2, while no significant stress concentration was observed in LS-3. Figure 16 shows that the main struts of the topologically thin walls in AVB-1 and AVB-2 underwent bending deformation, whereas those in AVB-3 underwent buckling deformation, in agreement with the test results. Significant stress concentrations were revealed in the regions with the most severe deformations of the topologically thin wall and lattice structure. In the YOZ plane, the topologically thin walls and lattice structures of AVB-1, AVB-2, and AVB-3 deformed in the same direction. This indicates that the interaction forces between the topological thin-walled and lattice structures have a significant effect on the mechanical properties and deformation behavior of the AVB.

4. Discussion

The main factors determining the stress–strain response of the Ta lattice structure and AVB are material properties, structure type, and deformation mode. The stress–strain curves of LS-1, LS-2, and LS-3 were smooth in the plastic deformation stage without obvious stress oscillations due to the toughness of Ta and the bending-dominated nature of ISS.[53] During compression of the lattice structures, individual incomplete unit cell positions tended to fill in adjacent voids, resulting in stress reduction in regions ①, ②, and ③ of the stress–strain curves for LS-1, LS-2, and LS-3 (Figure 6B).

TTS-1 and TTS-2 had sidewall curvatures of 0.027 and 0.014 mm^{-1}, respectively, and underwent bending deformation during compression. Meanwhile, LS-1 and LS-2 were bending-dominant lattice structures. Therefore, AVB-1 and AVB-2 belong to the bending-dominated type of porous structure, and their stress–strain curves were

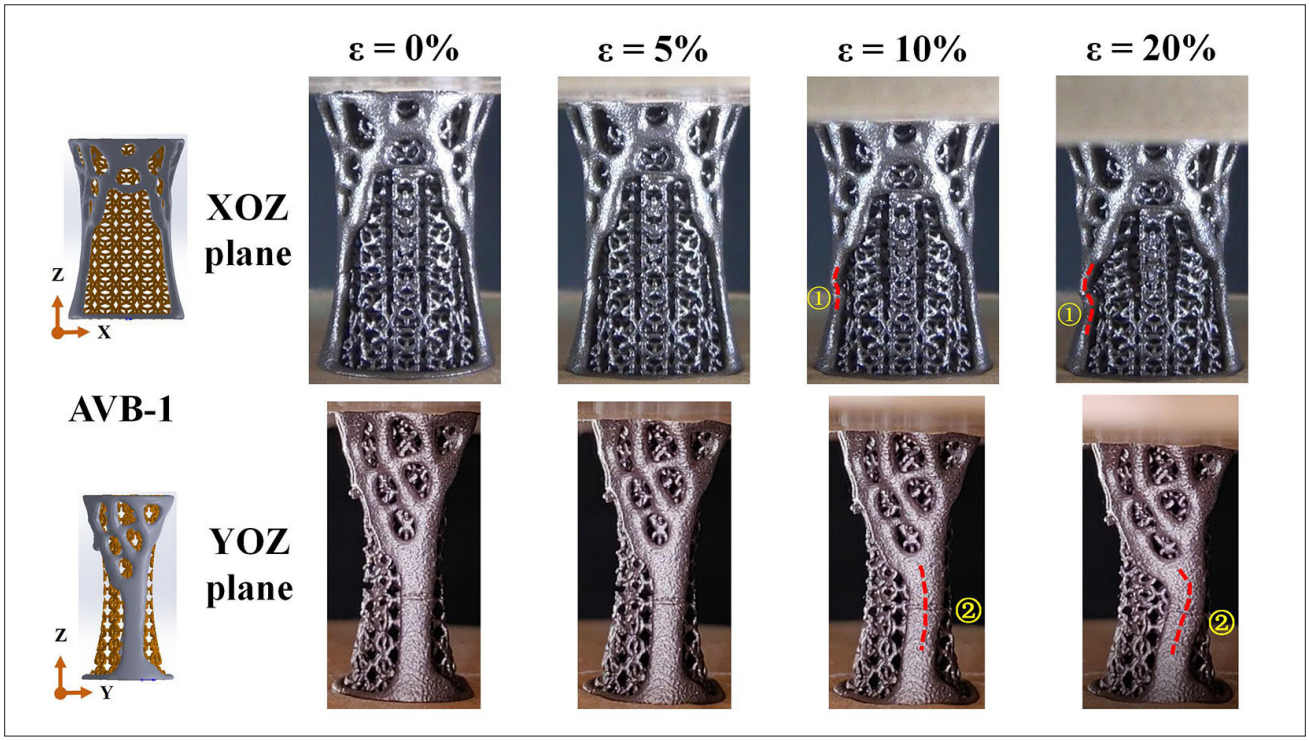

Figure 12. Deformation behavior and failure characteristics of the tantalum AVB-1 in the XOZ and YOZ observation planes at 0%, 5%, 10%, and 20% strains. Abbreviation: AVB: Artificial vertebral body.

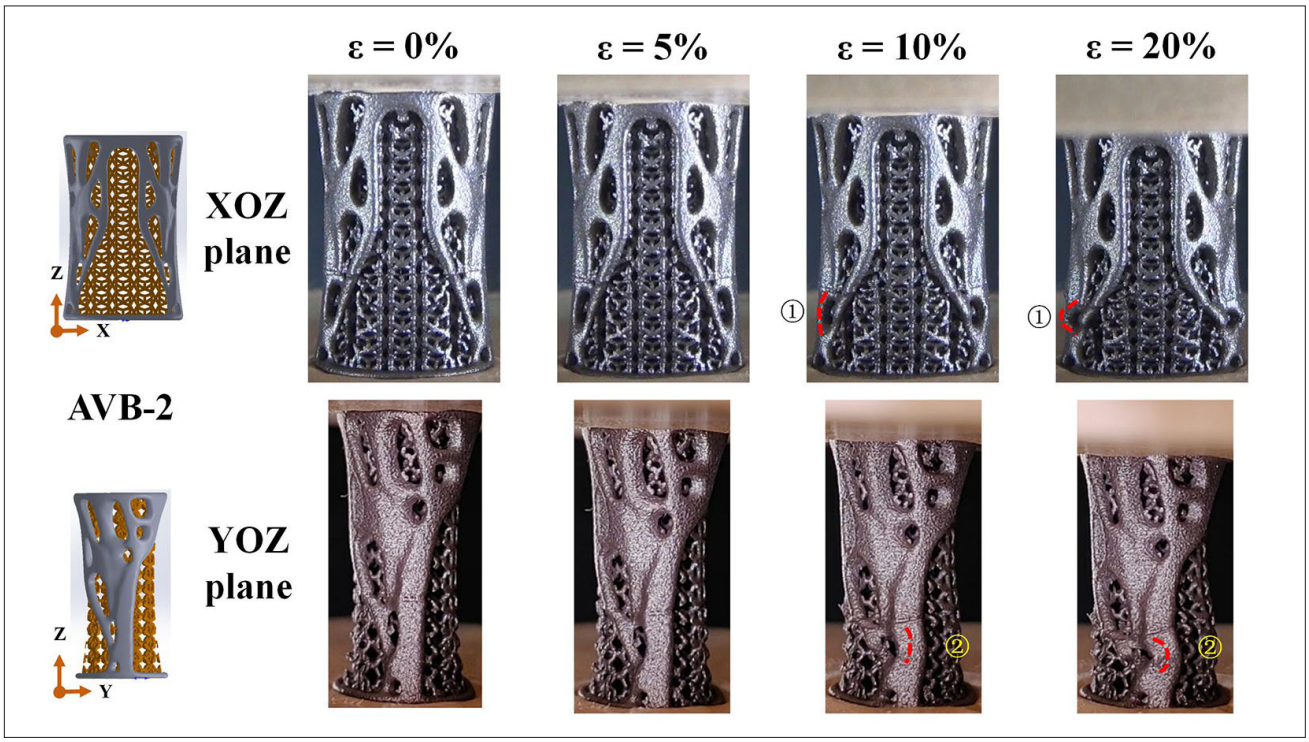

Figure 13. Deformation behavior and failure characteristics of the tantalum AVB-2 in the XOZ and YOZ observation planes at 0%, 5%, 10%, and 20% strains. Abbreviation: AVB: Artificial vertebral body.

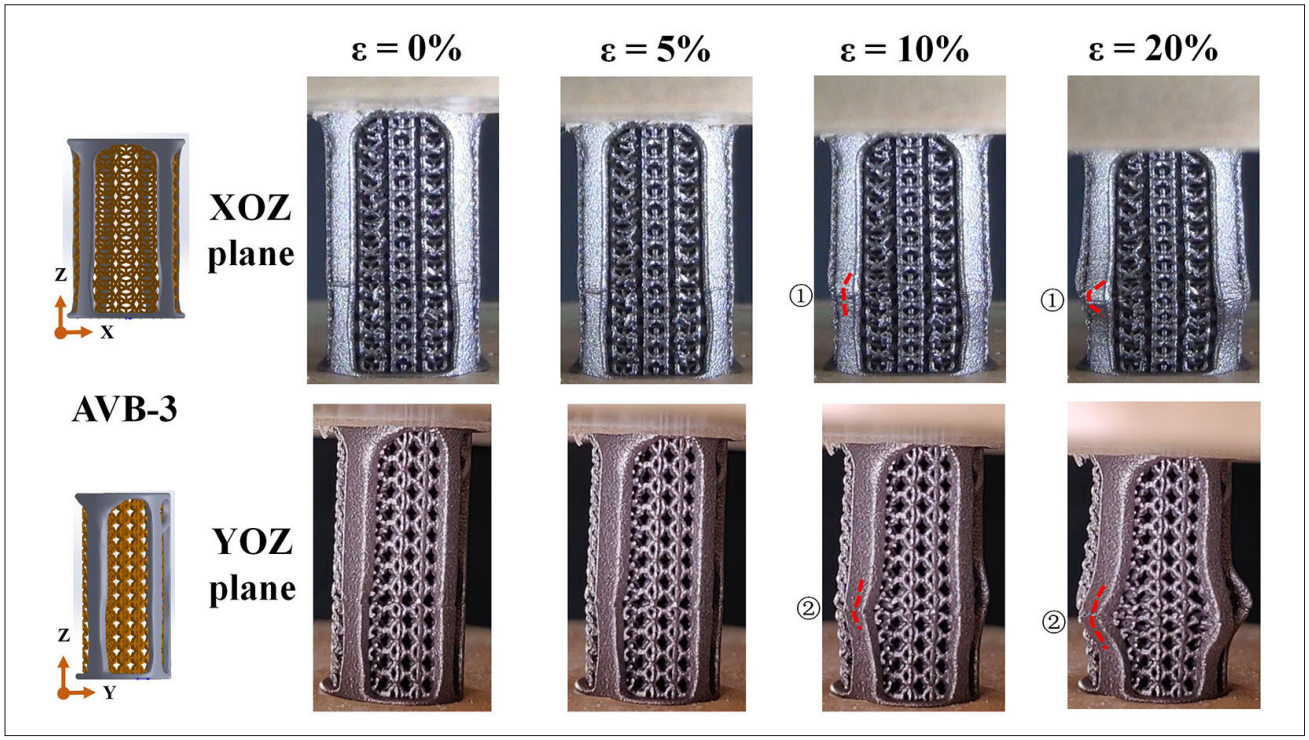

Figure 14. Deformation behavior and failure characteristics of the tantalum AVB-3 in the XOZ and YOZ observation planes at 0%, 5%, 10%, and 20% strains. Abbreviation: AVB: Artificial vertebral body.

smooth overall in the plastic deformation stage without stress oscillation, as shown in Figure 6C. Regions ① and ② in the stress–strain curve of AVB-2 correspond to the plastic deformation of the topologically thin wall. The stress reduction in region ① was attributed to the topological thin wall peeling off from the internal lattice structure. As the strain increased, the topologically thin wall fractured at the location with the greatest degree of bending, causing a stress reduction in region ②.

The topological thin-walled structure of AVB-3 consisted of vertical struts, which were stretching-dominated. The lattice structure consisted of ISS unit cells, which were bending-dominated. Therefore, the stress–strain curve of AVB-3 combines the characteristics of stretching-dominated and bending-dominated porous structures. The buckling deformation of the topologically thin wall, its separation from the lattice structure, and subsequent fracture significantly reduced the stress during the plastic deformation phase (region ③). After the fracture of the topologically thin wall of AVB-3, the bending-dominated lattice structures became the main load-bearing components. As a result, the subsequent compression process yielded smooth curves without stress oscillations until the sample was densified, as exhibited in Figure 6C.

When the unit cells fill the limited space and form lattice structures with varying sidewall curvatures, maintaining the same porosity for LS-1, LS-2, and LS-3 requires sacrificing the integrity of some unit cells. Consequently, these compromised unit cells cannot fully exhibit their load-bearing capabilities. Reducing the sidewall curvatures of the solid model results in an increase in the filling space, thereby enhancing the number of unit cells within the lattice structure. The number of intact unit cells in LS-1, LS-2, and LS-3 was 117, 195, and 247, respectively. Therefore, as depicted in Figure 7, LS-3 exhibited the highest yield strength and elastic modulus.

The sidewall struts of TTS-1 and TTS-2 were bending-dominant. As the sidewall curvature increased, the angle between the struts and the horizontal decreased, leading to a reduction in both strength and elastic modulus. When the sidewall curvature was zero, the thin wall of TTS-3 consisted of vertical struts with stretching-dominated mechanical properties, which significantly enhanced the load-bearing capacity of the AVB. However, the sidewall curvature had a different effect on the forces between the lattice and topological thin-walled structures.

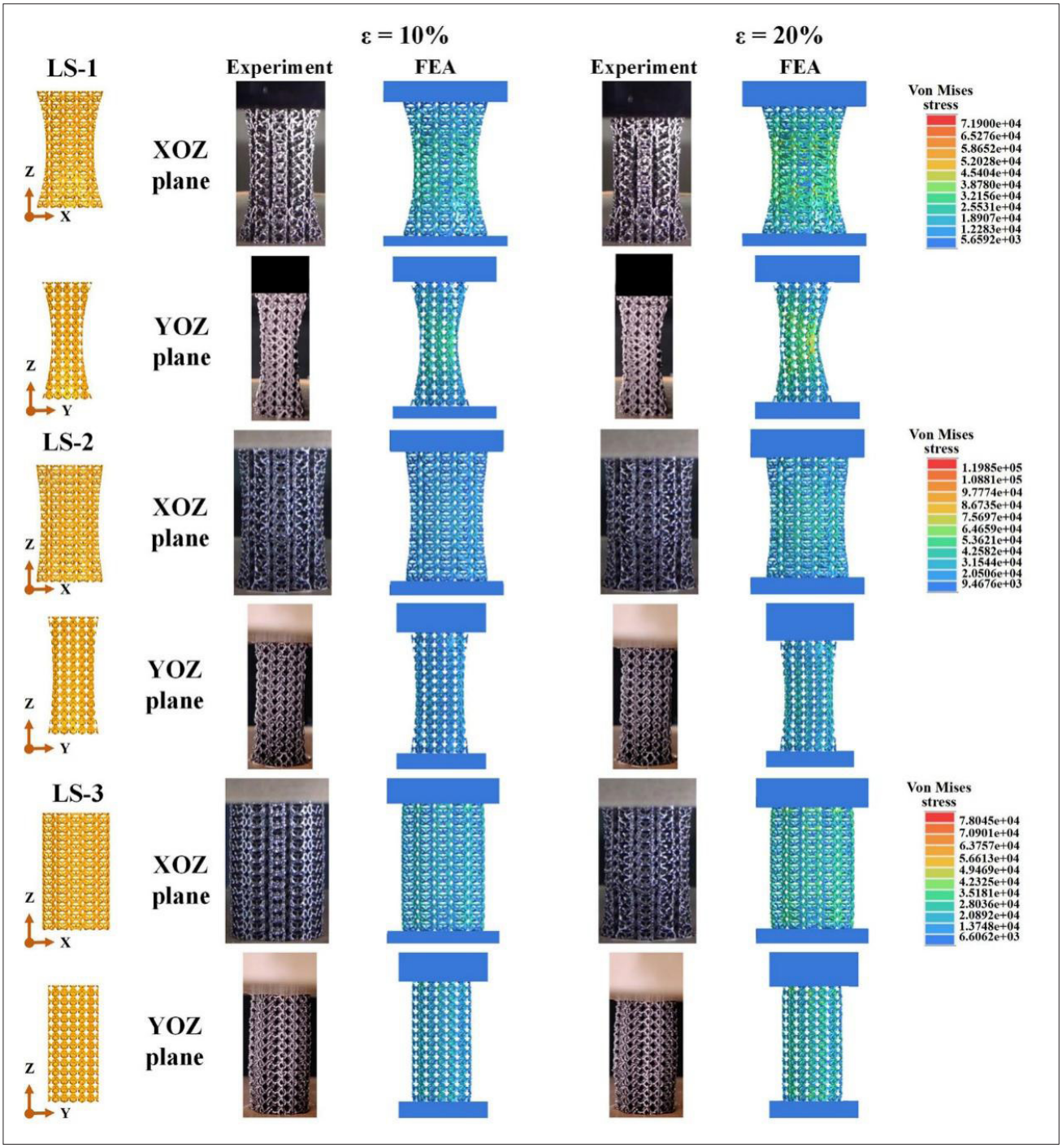

Figure 15. Comparison of experimental and FEA results for tantalum LSs at 10% and 20% strain in the XOZ and YOZ observation planes. Abbreviations: LS: Lattice structure; FEA: Finite element analysis.

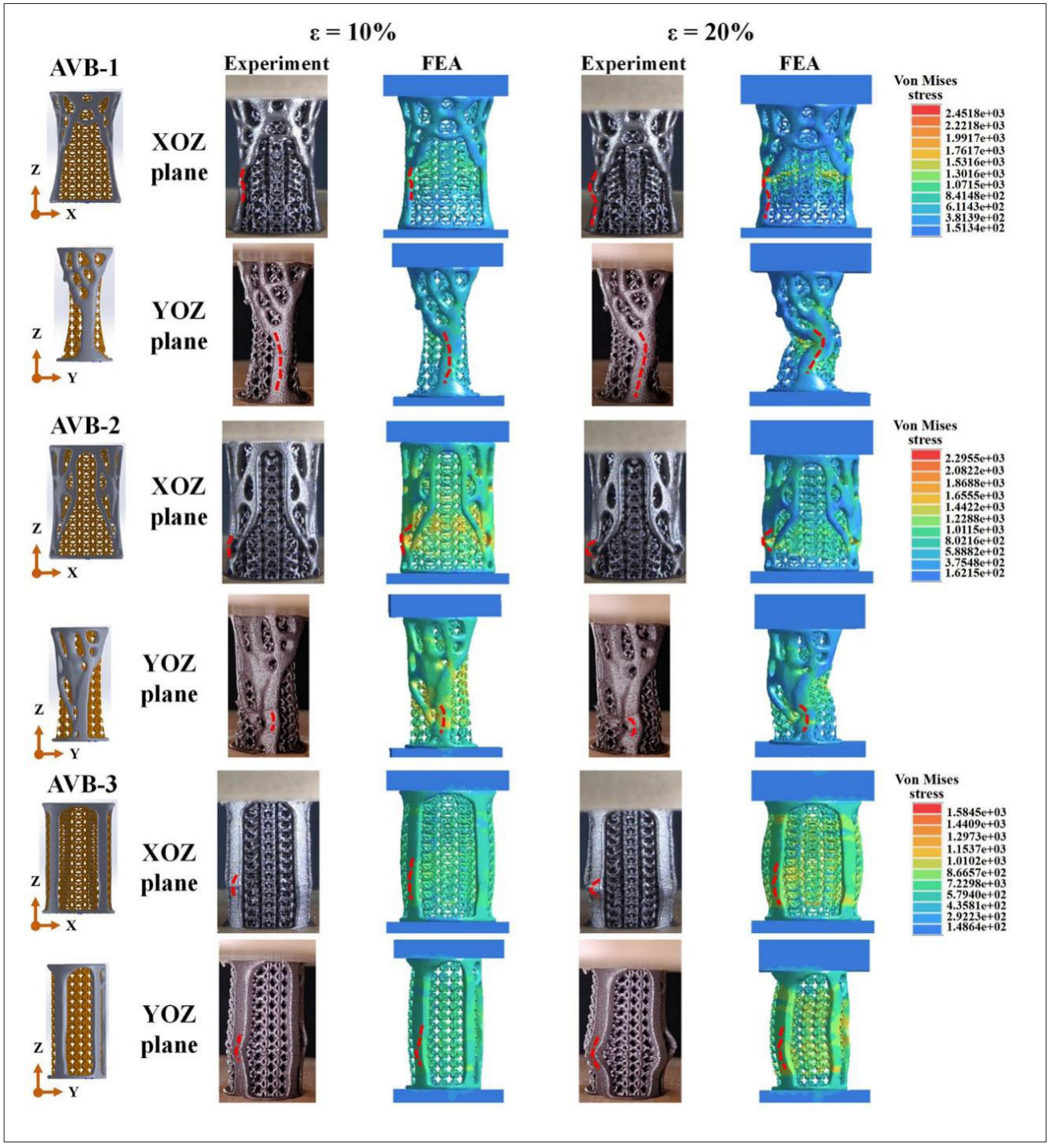

Figure 16. Comparison of experimental and FEA results for tantalum AVBs at 10% and 20% strain in the XOZ and YOZ observation planes. Abbreviations: AVB: Artificial vertebral body; FEA: Finite element analysis.

The absence of horizontal orientation constraints caused the lattice structure to expand outward during compression. The force and deformation characteristics of topological thin-walled and artificial vertebral samples during compression are displayed in Figure 17. The topological thin-walled structures of AVB-1 and AVB-2 featured specific sidewall curvatures, which led to the formation of plastic hinges at the center of the sidewall under compression. The inward bending of the topological thin-walled structure created an interaction force with the outwardly expanding lattice structure, as shown in Figure 17. In other words, the topological thin-walled structure restricted the inclination of the peripheral unit cells of the lattice structure, imposing horizontal constraints on the internal lattice and inhibiting its outward expansion. The interaction force between the topological thin-walled and lattice structures in AVB-1 and AVB-2 enhanced both the elastic modulus and the yield strength of the AVB. An increase in sidewall curvature led to a higher interaction force, thereby enhancing the load-bearing capacity of the AVB.

The topologically thin wall of AVB-3 consisted of vertical struts with zero sidewall curvature. As depicted in Figure 17, the outward expansion of the lattice structures provided a source of perturbation for vertical strut buckling during compression. This accelerated the buckling deformation of the vertical struts, thereby reducing the load-bearing capacity of the AVB. Therefore, sidewall curvature had different effects on the elastic modulus and yield strength of the AVB. The focus of this study was to regulate sidewall curvature to develop an AVB exhibiting optimal mechanical properties.

After implantation, the AVB was osseointegrated with the upper and lower cervical vertebral segments, thereby performing a load-bearing function and restoring intervertebral height. An AVB requires adequate yield strength, and its elastic modulus should closely match that of human bone. This reduces the risk of stress shielding and promotes osseointegration. The elastic modulus and yield strength of human cortical bone range from 7.7 to 21.8 GPa and 103 to 222 MPa, respectively.[27] The yield strengths of AVB-1, AVB-2, and AVB-3 were within the range of human cortical bone yield strength. This demonstrated that the load-bearing capacities of AVB-1, AVB-2, and AVB-3 met the requirements for the replacement of diseased vertebrae. As exhibited in Figure 8, compared to AVB-1 and AVB-3, AVB-2 exhibited the highest yield-strength-to-elastic-modulus ratio. This design effectively reduced the stress shielding effect while maximizing the load-bearing function.

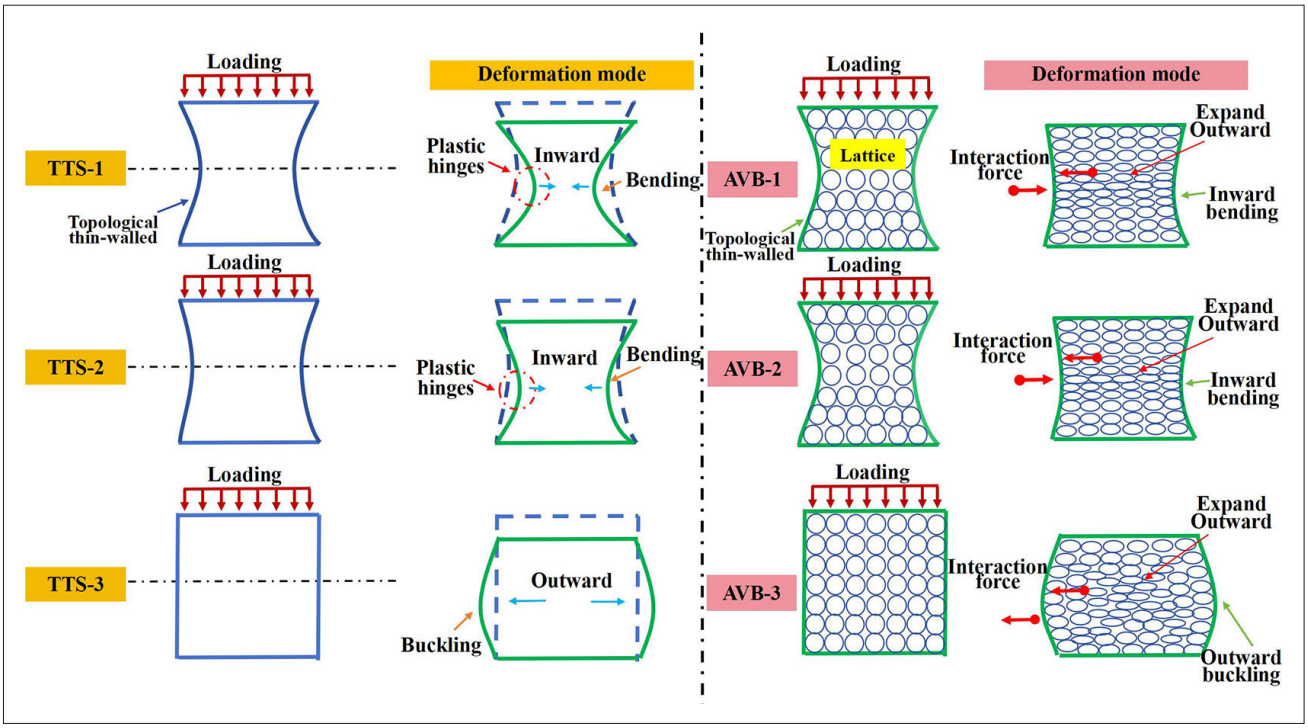

Figure 17. Schematic representation of the force and deformation characteristics of TTSs and AVBs. Abbreviations: AVB: Artificial vertebral body; TTS: Topologically thin-walled structure.

The topological thin-walled TTS-3 consisted of vertical struts that significantly enhanced the elastic modulus and yield strength of AVB-3. However, owing to TTS-3's insufficient constraint on the expansion deformation of the lattice structure during compression, the vertical struts buckled, and the thin-walled structure exhibited premature yielding (Figure 17). This resulted in the lowest yield-strength-to-elastic-modulus ratio of AVB-3. Because the sidewall curvature of the topologically thin wall in AVB-1 was larger than that in AVB-2, the interaction force between the topologically thin wall and the lattice structure in AVB-1 was greater than that in AVB-2. This interaction force exerted a more pronounced enhancement on the elastic modulus than on the yield strength. Therefore, as shown in Figure 8, the yield-strength-to-elastic-modulus ratios of AVB-2 were higher than those of AVB-1. AVB-2, with a sidewall curvature of 0.014 mm^{-1}, has potential for clinical application because it can meet the daily load-bearing requirements of the human cervical spine while reducing the risk of stress shielding.

Ti mesh is widely used in the clinical treatment of spinal tumors owing to its simple structure. Although Ti mesh is effective for spinal reconstruction, it is poorly adapted to vertebral bone in terms of size, shape, and mechanical properties, which seriously affects the therapeutic effect. Surgeons need to cut the Ti mesh size on-site according to the patient's intervertebral height during the surgery, resulting in an increase in surgical time and difficulty. The shape of the end face of the Ti mesh cannot match the curvature of the end plate, leading to stress concentration at the contact surface between the Ti mesh and the end plate, thereby increasing the risk of subsidence. Moreover, the Ti mesh has an insufficient load-bearing capacity, and most of the load is carried by the fixation system, which produces stress shielding of the contacted vertebrae, resulting in bone resorption and stress collapse. According to clinical reports, there are still a large number of cases of poor osseointegration, inadequate immediate and long-term stability, and short *in vivo* survival cycles after Ti mesh implantation.[21,61,62]

In this study, the Ta artificial vertebra was custom-designed based on the shape and anatomical dimensions of the vertebrae of a specific patient. The height of the AVB remained the same as the intervertebral height, avoiding on-site adjustment and reducing the difficulty of surgery. The upper and lower end faces of the customized artificial vertebrae can be accurately fitted to the endplate, thereby reducing stress concentration at the contact interface and lowering the risk of subsidence. Meanwhile, AVB-2 exhibited the highest yield-strength-to-elastic-modulus ratio, which could prevent excessive load transfer along the fixation system and reduce the stress shielding effect. Therefore, AVB-2 has a lower risk of subsidence than conventional Ti mesh in clinical applications.

The deformation behavior of AVBs was closely related to their mechanical properties. The sidewall curvatures of the LS-1 and LS-2 specimens were 0.027 and 0.014 mm^{-1}, respectively, resulting in a reduced number of intact unit cells in the central region compared with the upper and lower sections of the specimens. This explains why the unit cells in the middle of specimens LS-1 and LS-2 deformed first during compression, as depicted in Figures 9 and 10. The reason for the appearance of the shear band in the YOZ plane of the LS-3 specimen (Figure 11) was that the maximum shear stress formed at an angle of 45° to the axial compression direction. The unit cells in this shear band deformed first. The asymmetry of the ISS unit cell prevented the formation of a shear band in the XOZ plane of the LS-3 specimen.

In the Ta AVB specimen, the material density distribution of the topologically thin wall significantly influenced its deformation behavior. During the load transfer process, the area with the highest material density in the topological thin wall exhibited the highest load-carrying capacity and lowest deformation tendency. In contrast, areas with lower material density showed diminished load-carrying capacity and a tendency to yield prematurely. As shown in Figures 12 and 13, along the *z*-axis direction of the specimens, the material densities in regions ① and ② of the topologically thin walls in AVB-1 and AVB-2 varied. The material density in the upper part of these regions was greater than that in the lower part. Consequently, plastic hinges formed first in these regions, resulting in bending deformation.

The topologically thin walls of the AVB-3 specimen experienced failure as a result of plastic deformation in regions ① and ②, as displayed in Figure 14. The topologically thin wall of AVB-3 comprised vertical struts and exhibited no variation in material density in regions ① and ②. Under compressive loading, the internal lattice expanded outward, acting as a perturbation source for vertical strut buckling and accelerating the instability of the topologically thin wall (Figure 17).

As exhibited in Figure 16, the finite element results indicated that the stress concentrations were localized in areas with alternating material densities within the topologically thin walls of AVB-1 and AVB-2 (regions ① and ②). AVB-3 displayed pronounced stress concentrations at locations where the vertical struts buckled. This stress accumulation initially caused the structure in these areas to deform.

5. Conclusion

Novel AVB models were designed through topology optimization, and Ta AVBs were successfully manufactured using the SLM process. The effects of sidewall curvature on the mechanical properties and deformation mechanisms of the Ta AVB were investigated using compression tests and finite element analysis. The conclusions are as follows.

The elastic modulus and yield strength of the Ta lattice structures ranged from 1.75 to 3.21 GPa and 31 to 65 MPa, respectively. With the addition of topologically thin walls, the elastic modulus and yield strength were enhanced by factors of 2.26–3.77 and 3–3.62, respectively. Topological thin-walled structures can significantly increase the load-bearing capacity of the lattice structures.

As the sidewall curvature decreased, the elastic modulus and yield strength of the AVB increased. When the sidewall curvature decreased from 0.027 to 0 mm^{-1}, the elastic modulus and yield strength of the Ta AVB increased by factors of 2.76 and 2.19, respectively.

The yield strengths of the Ta AVBs (ranging from 107 to 235 MPa) were similar to those of the human cortical bone (103–222 MPa). AVB-2 exhibited the highest yield-strength-to-elastic-modulus ratio (0.029) compared to that of AVB-1 and AVB-3 (0.024 and 0.019, respectively). This indicated that the optimal sidewall curvature of the topological thin wall is 0.014 mm^{-1}. At this sidewall curvature, the Ta AVB effectively reduced the stress shielding effect while maximizing the load-bearing function. Therefore, AVB-2 not only fully exerted its load-bearing function but also has the potential to promote osseointegration and reduce the risk of bone absorption in cervical fusion segments and degenerative diseases in adjacent segments.

The deformation modes of the Ta AVB during compression determined its stress–strain response. The deformation modes of AVB-1 and AVB-2 involved the bending deformation of the topologically thin walls and lattice structures. In AVB-3, the compressive expansion effect of the lattice acted as a perturbation source for topological thin-wall buckling, accelerating its collapse.

Finite element analysis is an effective method for predicting and evaluating the biomechanical properties of bone implants in clinical applications. Previous studies have demonstrated the feasibility and accuracy of using the finite element method to evaluate the biomechanical properties of bone implants in human load-bearing sites, such as the hip joints,[63] pelvis,[64] intervertebral discs,[65] knee joints,[66] and lumbar vertebrae.[67] The strain and stress distribution on the AVB significantly affect the contacted vertebrae and adjacent intervertebral discs, articular cartilage, and vertebral bodies. Therefore, finite element analysis of the biomechanics of the Ta AVB in the human spine will be the focus of future research. Furthermore, research on the fatigue performance of Ta AVBs under long-term dynamic loading in the human spine is an important future investigation. The biological properties of Ta artificial vertebra will be verified by *in vivo* and *in vitro* tests in future studies.

Acknowledgments

None.

Funding

This work was supported by the Natural Science Foundation of Xinjiang Uygur Autonomous Region, China under grant number 2023D01A86, the Scientific and Technological Research Projects in Key Areas of Xinjiang Production and Construction Corps, China under grant number 2024ABO49, and the Key Research and Development Program of Xinjiang Uygur Autonomous Region, China under grant number 2023B01016.

Conflict of interest

The authors declare that they have no competing interests.

Author contributions

Conceptualization: Yutao Zhang
Data curation: Jintao Li
Investigation: Yutao Zhang, Jintao Li, Yong Huang, Xiaohong Dong
Methodology: Wurikaixi Aiyiti
Supervision: Wurikaixi Aiyiti
Validation: Yutao Zhang
Writing–original draft: Yutao Zhang, Wurikaixi Aiyiti
Writing–review & editing: Wurikaixi Aiyiti

Ethics approval and consent to participate

Not applicable.

Consent for publication

Not applicable.

Availability of data

The data supporting the findings of this study are available from the corresponding author upon reasonable request.

References

1. Shimizu T, Kato S, Yokogawa N, et al. Total en bloc spondylectomy for primary tumors of the thoracic

and lumbar spine: a review article. *Semin Spine Surg.* 2024;36(4):101137.
doi: 10.1016/j.semss.2024.101137

2. Kandziora F, Schnake KJ, Klostermann CK, Haas NP. Vertebral body replacement in spine surgery. *Unfallchirurg.* 2004;107(5):354-371.
doi: 10.1007/s00113-004-0777-z

3. Kang J, Dong E, Li X, et al. Topological design and biomechanical evaluation for 3D printed multi-segment artificial vertebral implants. *Mater. Sci. Eng. C-Mater. Biol. Appl.* 2021;127:112250.
doi: 10.1016/j.msec.2021.112250

4. Zhang YW, Deng L, Zhang XX, et al. Three-dimensional printing-assisted cervical anterior bilateral pedicle screw fixation of artificial vertebral body for cervical tuberculosis. *World Neurosurg.* 2019;127:25-30.
doi: 10.1016/j.wneu.2019.03.238

5. Perez Roman RJ, Boddu JV, Bashti M, et al. The use of carbon fiber-reinforced instrumentation in patients with spinal oncologic tumors: a systematic review of literature and future directions. *World Neurosurg.* 2023;173:13-22.
doi: 10.1016/j.wneu.2023.01.090

6. Chen G, Yin M, Liu W, et al. A novel height-adjustable nano-hydroxyapatite/polyamide-66 vertebral body for reconstruction of thoracolumbar structural stability after spinal tumor resection. *World Neurosurg.* 2019;122:e206-e214.
doi: 10.1016/j.wneu.2018.09.213

7. Kong F, Nie Z, Liu Z, Hou S, Ji J. Developments of nano-TiO_2 incorporated hydroxyapatite/PEEK composite strut for cervical reconstruction and interbody fusion after corpectomy with anterior plate fixation. *J Photochem Photobiol B-Biol.* 2018;187:120-125.
doi: 10.1016/j.jphotobiol.2018.07.016

8. Abd-Elaziem W, Darwish MA, Hamada A, Daoush WM. Titanium-based alloys and composites for orthopedic implants applications: a comprehensive review. *Mater. Des.* 2024;241:112850.
doi: 10.1016/j.matdes.2024.112850

9. Kurtz SM, Devine JN. PEEK biomaterials in trauma, orthopedic, and spinal implants. *Biomaterials.* 2007;28(32):4845-4869.
doi: 10.1016/j.biomaterials.2007.07.013

10. Ma H, Suonan A, Zhou J, et al. PEEK (Polyether-ether-ketone) and its composite materials in orthopedic implantation. *Arab J Chem.* 2021;14(3):102977.
doi: 10.1016/j.arabjc.2020.102977

11. Liu C, Xu M, Wang Y, et al. Exploring the potential of hydroxyapatite-based materials in biomedicine: a comprehensive review. *Mater Sci Eng R-Rep.* 2024;161:100870.
doi: 10.1016/j.mser.2024.100870

12. Minagar S, Berndt CC, Wang J, Ivanova E, Wen C. A review of the application of anodization for the fabrication of nanotubes on metal implant surfaces. *Acta Biomater.* 2012;8(8):2875-2888.
doi: 10.1016/j.actbio.2012.04.005

13. Jiang H. F, Aihemaiti P, Aiyiti W, Kasimu A. Study of the compression behaviours of 3D-printed PEEK/CFR-PEEK sandwich composite structures. *Virtual Phys Prototyp.* 2022;17(2):138-155.
doi: 10.1080/17452759.2021.2014636

14. Zheng J, Zhao H, Ouyang Z, et al. Additively-manufactured PEEK/HA porous scaffolds with excellent osteogenesis for bone tissue repairing. *Compos Pt B-Eng.* 2022;232:109508.
doi: 10.1016/j.compositesb.2021.109508

15. Li S, Li G, Hu J, et al. Porous polyetheretherketone-hydroxyapatite composite: a candidate material for orthopedic implant. *Compos Commun.* 2021;28:100908.
doi: 10.1016/j.coco.2021.100908

16. Aufa AN, Hassan MZ, Ismail Z. Recent advances in Ti-6Al-4V additively manufactured by selective laser melting for biomedical implants: prospect development. *J Alloy Compd.* 2022;896:163072.
doi: 10.1016/j.jallcom.2021.163072

17. Depboylu FN, Yasa E, Poyraz O, Minguella-Canela J, Korkusuz F, Lopez MAD. Titanium based bone implants production using laser powder bed fusion technology. *J Mater Res Technol.* 2022;17:1408-1426.
doi: 10.1016/j.jmrt.2022.01.087

18. Mirkhalaf M, Men Y, Wang R, No Y, Zreiqat H. Personalized 3D printed bone scaffolds: a review. *Acta Biomater.* 2023;156:110-124
doi: 10.1016/j.actbio.2022.04.014

19. Wu Y, Feng P, Kong Q, et al. Treatment of lumbosacral tuberculosis with significant vertebral body loss using single-stage posterior surgical management with a structural autograft combined with a titanium mesh cage. *World Neurosurg.* 2021;148:e10-e16.
doi: 10.1016/j.wneu.2020.11.104

20. Zhang HQ, Li M, Wang YX, et al. Minimum 5-year follow-up outcomes for comparison between titanium mesh cage and allogeneic bone graft to reconstruct anterior column through posterior approach for the surgical treatment of thoracolumbar spinal tuberculosis with kyphosis. *World Neurosurg.* 2019;127:e407-e415.
doi: 10.1016/j.wneu.2019.03.139

21. Jang J. W, Lee J. K, Lee J. H, Hur H, Kim T. W, Kim S. H. Effect of posterior subsidence on cervical alignment after anterior cervical corpectomy and reconstruction using titanium mesh cages in degenerative cervical disease. *J Clin Neurosci.* 2014;21(10):1779-1785.
doi: 10.1016/j.jocn.2014.02.016

22. Bencharit S, Byrd WC, Altarawneh S, et al. Development and applications of porous tantalum trabecular metal-

enhanced titanium dental implants. *Clin Implant Dent Relat Res.* 2014;16(6):817-826.
doi: 10.1111/cid.12059

23. Piglionico S, Bousquet J, Fatima N, Renaud M, Collart-Dutilleul PY, Bousquet P. Porous tantalum vs. titanium implants: enhanced mineralized matrix formation after stem cells proliferation and differentiation. *J Clin Med.* 2020;9(11):3657.
doi: 10.3390/jcm9113657

24. Li X, Wang L, Yu XM, et al. Tantalum coating on porous Ti6Al4V scaffold using chemical vapor deposition and preliminary biological evaluation. *Mater Sci Eng C-Mater Biol Appl.* 2013;33(5):2987-2994.
doi: 10.1016/j.msec.2013.03.027

25. Wang X, Ning B, Pei X. Tantalum and its derivatives in orthopedic and dental implants: osteogenesis and antibacterial properties. *Colloid Surf B-Biointerfaces.* 2021;208:112055.
doi: 10.1016/j.colsurfb.2021.112055

26. Wang X, Liu W, Jiang C, et al. Research progress on the osteogenic properties of tantalum in the field of medical implant materials. *J Mater Res Technol*. 2024;30:1706-1715.
doi: 10.1016/j.jmrt.2024.03.200

27. Ataee A, Li Y, Brandt M, Wen C. Ultrahigh-strength titanium gyroid scaffolds manufactured by selective laser melting (SLM) for bone implant applications. *Acta Mater.* 2018;158:354-368.
doi: 10.1016/j.actamat.2018.08.005

28. Zhang Y, Yang J, Wan W, et al. Evaluation of biological performance of 3D printed trabecular porous tantalum spine fusion cage in large animal models. *J Orthop Transl.* 2025;50:185-195.
doi: 10.1016/j.jot.2024.10.010

29. Wang X, Xu S, Zhou S, et al. Topological design and additive manufacturing of porous metals for bone scaffolds and orthopaedic implants: a review. *Biomaterials*. 2016;83:127-141.
doi: 10.1016/j.biomaterials.2016.01.012

30. Chen LY, Liang SX, Liu YJ, Zhang LC. Additive manufacturing of metallic lattice structures: unconstrained design, accurate fabrication, fascinated performances, and challenges. *Mater Sci Eng R-Rep.* 2021;146:100648.
doi: 10.1016/j.mser.2021.100648

31. Benedetti M, du Plessis A, Ritchie RO, Dallago M, Razavi SMJ, Berto F. Architected cellular materials: a review on their mechanical properties towards fatigue-tolerant design and fabrication. *Mater Sci Eng R-Rep*. 2021;144:100606.
doi: 10.1016/j.mser.2021.100606

32. Wang Z, Zhang M, Liu Z, et al. Biomimetic design strategy of complex porous structure based on 3D printing Ti-6Al-4V scaffolds for enhanced osseointegration. *Mater Des.* 2022;218:110721.
doi: 10.1016/j.matdes.2022.110721

33. Zhang BQ, Pei X, Zhou CC, et al. The biomimetic design and 3D printing of customized mechanical properties porous Ti6Al4V scaffold for load-bearing bone reconstruction. *Mater Des.* 2018;152:30-39.
doi: 10.1016/j.matdes.2018.04.065

34. Lu HZ, Ma HW, Luo X, et al. Microstructure, shape memory properties, and invitro biocompatibility of porous NiTi scaffolds fabricated via selective laser melting. *J Mater Res Technol.* 2021;15:6797-6812.
doi: 10.1016/j.jmrt.2021.11.112

35. Deng FY, Liu LL, Li Z, Liu JC. 3D printed Ti6Al4V bone scaffolds with different pore structure effects on bone ingrowth. *J Biol Eng.* 2021;15(1):4.
doi: 10.1186/s13036-021-00255-8

36. Guo Z, Wang C, Du C, Sui J, Liu J. Effects of topological structure on antibacterial behavior and biocompatibility of implant. *Procedia CIRP*. 2020;89:126-131.
doi: 10.1016/j.procir.2019.12.003

37. Chen J, Song C, Deng Z, et al. Functional gradient design of additive manufactured gyroid tantalum porous structures: manufacturing, mechanical behaviors and permeability. *J Manuf Process.* 2024;125:202-216.
doi: 10.1016/j.jmapro.2024.07.054

38. Song C, Chen J, Lei H, et al. Radial gradient design enabling additively manufactured low-modulus gyroid tantalum structures. *Int J Mech Sci.* 2024;262:108710.
doi: 10.1016/j.ijmecsci.2023.108710

39. Ni X, Sun Q, Wang J, et al. Development and characterization of minimal surface tantalum scaffold with high strength and superior fatigue resistance. *J Mater Res Technol.* 2025;36:1226-1239.
doi: 10.1016/j.jmrt.2025.03.108

40. Liu J, Zou Z, Li Z, et al. A clustering-based multiscale topology optimization framework for efficient design of porous composite structures. *Comput Methods Appl Mech Eng.* 2025;439:117881.
doi: 10.1016/j.cma.2025.117881

41. Noman AA, Shaari MS, Mehboob H, Azman AH. Recent advancements in additively manufactured hip implant design using topology optimization technique. *Results Eng.* 2025;25:103932.
doi: 10.1016/j.rineng.2025.103932

42. Kök HI, Kick M, Akbas O, et al. Reduction of stress-shielding and fatigue-resistant dental implant design through topology optimization and TPMS lattices. *J Mech Behav Biomed Mater.* 2025;165:106923.
doi: 10.1016/j.jmbbm.2025.106923

43. Xiong W, Ding X, Zhang H, et al. Topology optimization of embracing fixator considering bone remodeling to mitigate stress shielding effect. *Med Eng Phys.* 2024;125:104122.
doi: 10.1016/j.medengphy.2024.104122

44. Peng W, Cheng K, Liu Y, et al. Biomechanical and mechanostat analysis of a titanium layered porous implant for mandibular reconstruction: the effect of the topology optimization design. *Mater Sci Eng C-Mater Biol Appl.* 2021;124:112056.
doi: 10.1016/j.msec.2021.112056

45. Smit T, Aage N, Haschtmann D, Ferguson SJ, Helgason B. Anatomically and mechanically conforming patient-specific spinal fusion cages designed by full-scale topology optimization. *J Mech Behav Biomed Mater.* 2024; 159:106695.
doi: 10.1016/j.jmbbm.2024.106695

46. Gao H, Jin X, Yang J, et al. Porous structure and compressive failure mechanism of additively manufactured cubic-lattice tantalum scaffolds. *Mater Today Adv.* 2021;12:100183.
doi: 10.1016/j.mtadv.2021.100183

47. du Plessis A, Razavi SMJ, Benedetti M, et al. Properties and applications of additively manufactured metallic cellular materials: a review. *Prog Mater Sci.* 2022;125:100918.
doi: 10.1016/j.pmatsci.2021.100918

48. Wang J, Ni X, Sun Q, et al. Additively manufactured trabecular porous tantalum: effects of annealing temperature and oxygen content on mechanical properties. *J Mater Res Technol*. 2025;35:4055-4070.
doi: 10.1016/j.jmrt.2025.02.030

49. Qin F, Chen L, Zhou G, Shi Q, Liu B, Liu X. Improved compressive strength of laser powder bed fused porous tantalum by hot isostatic pressing. *Addit Manuf.* 2025;102:104729.
doi: 10.1016/j.addma.2025.104729

50. Liu L, Yi B, Wang T, Li Z, Zhang J, Yoon GH. Investigation on numerical analysis and mechanics experiments for topology optimization of functionally graded lattice structure. *Addit Manuf.* 2021;47:102275.
doi: 10.1016/j.addma.2021.102275

51. Ahmadi SM, Campoli G, Yavari SA, et al. Mechanical behavior of regular open-cell porous biomaterials made of diamond lattice unit cells. *J Mech Behav Biomed Mater.* 2014;34:106-115.
doi: 10.1016/j.jmbbm.2014.02.003

52. Gibson LJ, Ashby MF, eds. *Cellular Solids: Structure and Properties*. Cambridge: Cambridge University Press; 1999.

53. Zhang YT, Aiyiti W, Du S, Jia R, Jiang HF. Design and mechanical behaviours of a novel tantalum lattice structure fabricated by SLM. *Virtual Phys Prototyp.* 2023;18(1):e2192702.
doi: 10.1080/17452759.2023.2192702

54. Ataee A, Li Y, Fraser D, Song G, Wen C. Anisotropic Ti-6Al-4V gyroid scaffolds manufactured by electron beam melting (EBM) for bone implant applications. *Mater Des.* 2018;137:345-354.
doi: 10.1016/j.matdes.2017.10.040

55. Regassa Hunde B, Debebe Woldeyohannes A. Future prospects of computer-aided design (CAD) – a review from the perspective of artificial intelligence (AI), extended reality, and 3D printing. *Results Eng*. 2022;14:100478.
doi: 10.1016/j.rineng.2022.100478

56. Benady A, Meyer SJ, Golden E, Dadia S, Katarivas Levy G. Patient-specific Ti-6Al-4V lattice implants for critical-sized load-bearing bone defects reconstruction. *Mater Des.* 2023;226:111605.
doi: 10.1016/j.matdes.2023.111605

57. Moscol-Albañil I, Solórzano-Requejo W, Rodriguez C, Ojeda C, Díaz Lantada A. Innovative AI-driven design of patient-specific short femoral stems in primary hip arthroplasty. *Mater Des.* 2024;240:112868.
doi: 10.1016/j.matdes.2024.112868

58. Zhang T, Liu F, Chen J, et al. Dual-graded lattice with mechanical bionics to enhance fatigue performance. *Int J Mech Sci.* 2024;279:109474.
doi: 10.1016/j.ijmecsci.2024.109474

59. Wang B, Liu M, Ke W, Hua W, Zeng X, Yang C. Finite element analysis of additive manufactured porous peek artificial vertebral bodies in lumbar total en bloc spondylectomy. *Spine J*. 2025;25(5):1042-1049.
doi: 10.1016/j.spinee.2024.10.026

60. Zhang H, Guo Z, Zhang Z, Wu G, Sang L. Biomimetic design and fabrication of PEEK and PEEK/CF cage with minimal surface structures by fused filament fabrication. *J Mater Res Technol.* 2023;26:5001-5015.
doi: 10.1016/j.jmrt.2023.08.236

61. Hu B, Wang L, Song Y, et al. A comparison of long-term outcomes of nanohydroxyapatite/polyamide-66 cage and titanium mesh cage in anterior cervical corpectomy and fusion: a clinical follow-up study of least 8 years. *Clin Neurol Neurosurg.* 2019;176:25-29.
doi: 10.1016/j.clineuro.2018.11.015

62. Chen Y, Chen D, Guo Y, et al. Subsidence of titanium mesh cage: a study based on 300 cases. *Clin Spine Surg.* 2008;21(7):489-492.
doi: 10.1097/BSD.0b013e318158de22

63. Lostado Lorza R, Somovilla Gomez F, Corral Bobadilla M, et al. Comparative analysis of healthy and cam-type femoroacetabular impingement (FAI) human hip joints using the finite element method. *Appl Sci-Basel.* 2021;11(23).
doi: 10.3390/app112311101

64. McCartney W, MacDonald B, Ober CA, Lostado-Lorza R, Gómez FS. Pelvic modelling and the comparison between plate position for double pelvic osteotomy using artificial cancellous bone and finite element analysis. *BMC Vet Res.* 2018;14(1):100.
doi: 10.1186/s12917-018-1416-1

65. Gómez FS, Lorza RL, Bobadilla MC, García RE. Improving the process of adjusting the parameters of finite element

models of healthy human intervertebral discs by the multi-response surface method. *Materials*. 2017;10(10). doi: 10.3390/ma10101116

66. Íñiguez-Macedo S, Somovilla-Gómez F, Lostado-Lorza R, Corral-Bobadilla M, Martínez-Calvo MÁ, Sanz-Adán F. The process of designing a rotating platform artificial knee prosthesis with posterior stabilizers by finite element analysis. *Int J Interact Des Manuf.* 2018;12(3):853-864. doi: 10.1007/s12008-017-0428-6

67. Somovilla-Gómez F, Lostado-Lorza R, Corral-Bobadilla M, Escribano-García R. Improvement in determining the risk of damage to the human lumbar functional spinal unit considering age, height, weight and sex using a combination of FEM and RSM. *Biomech Model Mechanobiol.* 2020;19(1):351-387. doi: 10.1007/s10237-019-01215-4

ACCSCIENCE PUBLISHING

International Journal of Bioprinting

RESEARCH ARTICLE

Construction of gelatin–alginate scaffolds containing chondrocytes using 3D bioprinting technology for the study of *in vitro* cartilage senescence

Hanxiao Qin[1†], Fanqing Xu[1†], Jianfeng Li[2*], and Yi Ding[1*]

[1]Department of Spine Surgery, Ganzhou People's Hospital, Ganzhou, Jiangxi, China

[2]Innovation Platform of Regeneration and Repair of Spinal Cord and Nerve Injury, Department of Orthopedics Surgery, The Seventh Affiliated Hospital, Sun Yat-sen University, Shenzhen, Guangdong, China

Abstract

Osteoarthritis (OA) is an age-related degenerative joint disease characterized by progressive cartilage deterioration. Chondrocyte senescence is recognized as a key contributor to the onset and progression of OA. Establishing reliable cartilage senescence models is, therefore, essential for elucidating the underlying mechanisms and developing preventive strategies for OA. 3D-bioprinted models offer significant advantages in precisely controlling tissue architecture, enabling spatial delivery of bioactive molecules, and supporting dynamic cell culture. In this study, we employed 3D bioprinting technology to construct cartilage models and subsequently established cartilage senescence models using hydrogen peroxide (H_2O_2). Firstly, gelatin–sodium alginate hydrogel scaffolds provided favorable mechanical strength and porosity, creating a supportive microenvironment for chondrocyte proliferation. Secondly, these scaffolds exhibited excellent biocompatibility and effectively promoted extracellular matrix synthesis and secretion. By comparing H_2O_2-induced 2D chondrocyte senescence models with 3D-bioprinted cartilage senescence models, our results demonstrated that the 3D models more closely mimicked the molecular characteristics of naturally aged human cartilage. Therefore, the 3D-bioprinted cartilage senescence models represent a promising experimental platform for investigating the pathogenesis and prevention of age-related OA.

Keywords: 2D chondrocyte senescence; 3D bioprinting; 3D cartilage senescence; Articular cartilage-laden scaffolds; Bioactive bioink

1. Introduction

Articular cartilage is a specialized connective tissue that lacks vascular, neural, and lymphatic systems. It possesses unique biomechanical properties, including toughness and viscoelasticity, which are essential for its roles in load-bearing and providing lubrication during joint movement.[1,2] However, defects in articular cartilage—caused by traumatic injury, chronic inflammation, or aging—can lead to serious clinical manifestations, such as joint pain, impaired mobility, and irreversible joint dysfunction.[3]

†These authors contributed equally to this work.

***Corresponding authors:**
Yi Ding
(dingyi@mail.gzsrmyy.com)

Jianfeng Li
(lijf68@mail3.sysu.edu.cn)

Citation: Qin H, Xu F, Li J, Ding Y. Construction of gelatin–alginate scaffolds containing chondrocytes using 3D bioprinting technology for the study of *in vitro* cartilage senescence. *Int J Bioprint*. 2025;11(4):189-208. doi: 10.36922/IJB025150136

Received: April 11, 2025
1st revised: May 12, 2025
2nd revised: May 22, 2025
Accepted: May 27, 2025
Published online: May 30, 2025

Copyright: © 2025 Author(s). This is an Open Access article distributed under the terms of the Creative Commons Attribution License, permitting distribution, and reproduction in any medium, provided the original work is properly cited.

Publisher's Note: AccScience Publishing remains neutral with regard to jurisdictional claims in published maps and institutional affiliations

If left untreated, these lesions often progress to degenerative conditions such as osteoarthritis (OA). The World Health Organization (WHO) estimates that the global population affected by OA will approach 1 billion by 2030, placing a significant burden on healthcare systems and household economies worldwide.[4] Cellular senescence within OA-affected joints has been identified as a key contributor to disease pathogenesis.[5,6] Increasing evidence demonstrates that senescence-associated changes occur in several joint components, including cartilage, synovium, and meniscus.[7,8] Nevertheless, there remains a lack of suitable models to investigate the relationship between cartilage and OA progression. Developing cartilage aging models is, therefore, essential for studying the pathogenesis and advancement of OA.

In recent decades, research has focused on elucidating the mechanisms of chondrocyte senescence, identifying therapeutic agents, and optimizing treatment strategies using various experimental models-including animal models, 2D cell cultures, and advanced 3D systems.[9,10] Current animal models used to study chondrocyte senescence typically rely on natural aging or surgical interventions in combination with gene knockouts targeting anti-senescence pathways.[11] For example, histological analysis of 18-month-old guinea pigs has revealed moderate to severe chondrocyte senescence, characterized by significant reductions in proteoglycan and collagen content, closely mimicking human cartilage degeneration.[12] Additionally, in *Del1* heterozygous (*Del1*+/−) mice, histological assessments from 3 to 22 months of age displayed accelerated knee cartilage degeneration due to impaired type II collagen gene expression.[13] However, despite their relevance, animal models present several limitations, including long experimental durations and high costs, which restrict their use in large-scale OA research.[14]

In contrast, 2D models offer simplicity, convenience, and high experimental control, and have been widely adopted across various research areas.[15] For instance, hydrogen peroxide (H_2O_2) treatment has been reported to induce oxidative and inflammatory stress in rat chondrocytes, promoting cellular senescence.[16] Nevertheless, 2D systems fall short in recapitulating the biomechanical cues, as well as the complex cell–cell and cell–matrix interactions present in native cartilage tissue.[17] To address these limitations, 3D culture technologies have been developed to more accurately mimic *in vivo* conditions. These models retain the advantages of 2D systems while offering a microenvironment that better preserves cellular phenotype and behavior. 3D culture models can be broadly categorized into scaffold-free 3D cell cultures, scaffold-based systems, explant models, bioreactors, organoids, organ-on-a-chip platforms, and 3D-bioprinted constructs.[18]

Scaffold-free 3D culture systems simulate *in vivo* cell growth conditions without external matrices or supports.[19] Co-culturing articular chondrocytes (ACs) with mesenchymal stem cells and chitosan/hyaluronic acid nanoparticles has been reported to promote chondrogenic differentiation.[20] However, these models are limited by high cultivation costs, short cell viability, and increased susceptibility to apoptosis. Scaffold-based 3D models, developed to overcome the limitations of scaffold-free systems provide a more physiologically relevant tissue-like environment. These models support more native-like 3D cellular behaviors. Embedding chondrogenic factors into hydrogel matrices for cell encapsulation has been demonstrated to enhance cartilage formation.[21] Although several issues remain, such as high cost, limited scalability, slow proliferation, and challenges in standardization, continued refinement is needed to improve model reliability.

Explant models involve the *in vitro* culture of tissue samples excised from live organisms under sterile conditions.[22] For example, treating cartilage explants with interleukin-1β can induce chondrocyte senescence.[23] However, limitations include technical complexity, inability to fully mimic the *in vivo* microenvironment, and species-specific differences, all of which must be addressed through technological and methodological advances. Bioreactors provide dynamic culture conditions under tightly controlled parameters and have been used to separate cartilage and bone units independently. While promising, their application is hindered by high maintenance costs, operational complexity, and membrane contamination risks.[24]

Organoids, which are 3D structures derived from adult or pluripotent stem cells, have gained attention for their ability to mimic real organ architecture and function. They offer advantages over traditional 2D cultures and patient-derived explants in terms of structural fidelity and genetic similarity.[25] For instance, human periosteum-derived cells have been demonstrated to self-assemble *in vitro* and form bone organoids capable of autonomous regeneration upon transplantation into mice.[26] Despite rapid progress, organoids still only partially reproduce native organ functions and are often limited in longevity and physiological complexity.[27,28]

Organ-on-a-chip systems combine microfluidics and 3D printing technologies to replicate the microarchitecture of organs on a chip.[29] A human-induced pluripotent stem cells-derived osteochondral chip has been used to simulate

OA-related pathology and effectively model bone–cartilage interactions under both healthy and diseased conditions.[30] However, this technology faces challenges in terms of reproducibility, organ maturity, and the integration of key elements, such as vasculature, innervation, and immune cells. Further technical development is essential for expanding its utility in disease modeling and drug screening.[31,32]

3D bioprinting represents a cutting-edge platform that enables the fabrication of living tissues using bioinks composed of cells, growth factors, and biocompatible materials.[33] Compared to other 3D models, bioprinting offers superior spatial precision, structural fidelity, and mechanical tunability, making it especially attractive for regenerative medicine and disease modeling. In cartilage tissue engineering, the scaffold material must possess excellent biocompatibility, mechanical integrity, and support for cellular activity.[34,35] Gelatin (Gel) and sodium alginate (Alg) are widely used in 3D bioprinting due to their favorable biological properties and printability. Recent studies have successfully encapsulated chondrocytes in Gel–Alg hydrogels using bioprinting, maintaining high cell viability and regional gene expression.[36–39] Another study developed Gel–Alg-based bioinks crosslinked with calcium chloride to fabricate scaffolds with robust mechanical properties and biocompatibility. These scaffolds supported long-term chondrocyte survival and functionality *in vitro* and demonstrated effective cartilage repair *in vivo*.[39]

In this study, we established a novel cartilage senescence model using Gel–Alg hydrogels at three different concentration ratios. ACs were encapsulated in 3D-bioprinted constructs, followed by H_2O_2-induced senescence. The innovation lies in the integration of biofabricated cartilage with precisely engineered structural and biochemical cues, coupled with oxidative stress-induced aging. This two-stage modeling strategy, which mimics age-related cartilage degeneration, has not been reported in current OA models (Figure 1). The resulting platform provides a physiologically relevant microenvironment that supports AC viability, maintains region-specific phenotypic markers, and reproduces senescence-associated changes under oxidative stress. This 3D-bioprinted cartilage senescent model offers a promising experimental system for investigating OA pathogenesis and developing targeted therapeutic interventions.

2. Materials and methods

2.1. Preparation of bioinks

Three different Gel–Alg bioink formulations were prepared for the 3D bioprinting of hydrogel scaffolds: 7% Gel + 3% Alg (7 Gel–3 Alg), 8% Gel + 2% Alg (8 Gel–2 Alg), and 9% Gel + 1% Alg (9 Gel–1 Alg). Briefly, accurately weighed amounts of 7% Gel (3.5 g) and 3% Alg (1.5 g) (Biosharp, China) were UV-sterilized (254 nm) for 3 h. The sterilized powders were then aseptically transferred into a 50 mL centrifuge tube containing 10 mL of culture medium. The tube was sealed with parafilm to maintain sterility. The mixture was homogenized by continuous agitation at 150 rpm in a 60°C incubator shaker for 3 h to ensure complete dissolution.[40] The resulting bioinks were loaded into 3D bioprinting cartridges using sterile 3 mL Pasteur pipettes and centrifuged at 800 rpm for 3 min to remove air bubbles. The prepared bio-inks were stored at 4°C and remained stable for up to 7 days.

2.2. Viscosity and printability of bioinks

To assess the viscoelastic properties of Gel–Alg bioinks with three different concentration ratios, a rotational rheometer (Thermo Fisher, United States of America [USA]) was employed. Briefly, the bioinks were thoroughly mixed to eliminate air bubbles and then loaded between the parallel plates of the rheometer, with the initial gap set at 1 mm. Shear rates ranging from 0.1 to 1000 s^{-1} were applied, and measurements were conducted at a constant temperature of 25°C. The viscosity (η) versus shear rate curve was recorded to evaluate the shear-thinning behavior of the bioinks.

2.3. Fabrication of 3D-bioprinted scaffolds

Hydrogel scaffolds were fabricated using 3D bioprinting technology. Briefly, a stereolithography file of the scaffold model was designed using Autodesk Fusion 360 CAD software (Figure 2A) and imported into a 3D bioprinter (Regenovo, China) for fabrication. Gel and Alg were selected as the scaffold materials. A nozzle with an inner diameter of 0.34 mm was used, and scaffolds were printed layer-by-layer with an alternating 0–90° stacking pattern to ensure high structural precision. Immediately after printing, the scaffolds were crosslinked in 3% sterile $CaCl_2$ solution (Sigma, USA) for 5 min,[41] rinsed with sterile phosphate-buffered saline (PBS), and prepared for subsequent experiments.

2.4. Surface morphology analysis

The microstructure and surface morphology of the 3D-bioprinted Gel–Alg hydrogel scaffolds were examined using field emission scanning electron microscopy (SEM) (Jeol, Japan). Briefly, the scaffolds were freeze-dried under a vacuum for 24 h to preserve their structural integrity. The dried samples were then fractured to obtain cross-sectional views for microscopic analysis. To improve electron conductivity, the surfaces were treated with a gold jet machine (Jeol, Japan). Imaging was performed at an acceleration voltage of 10 kV.

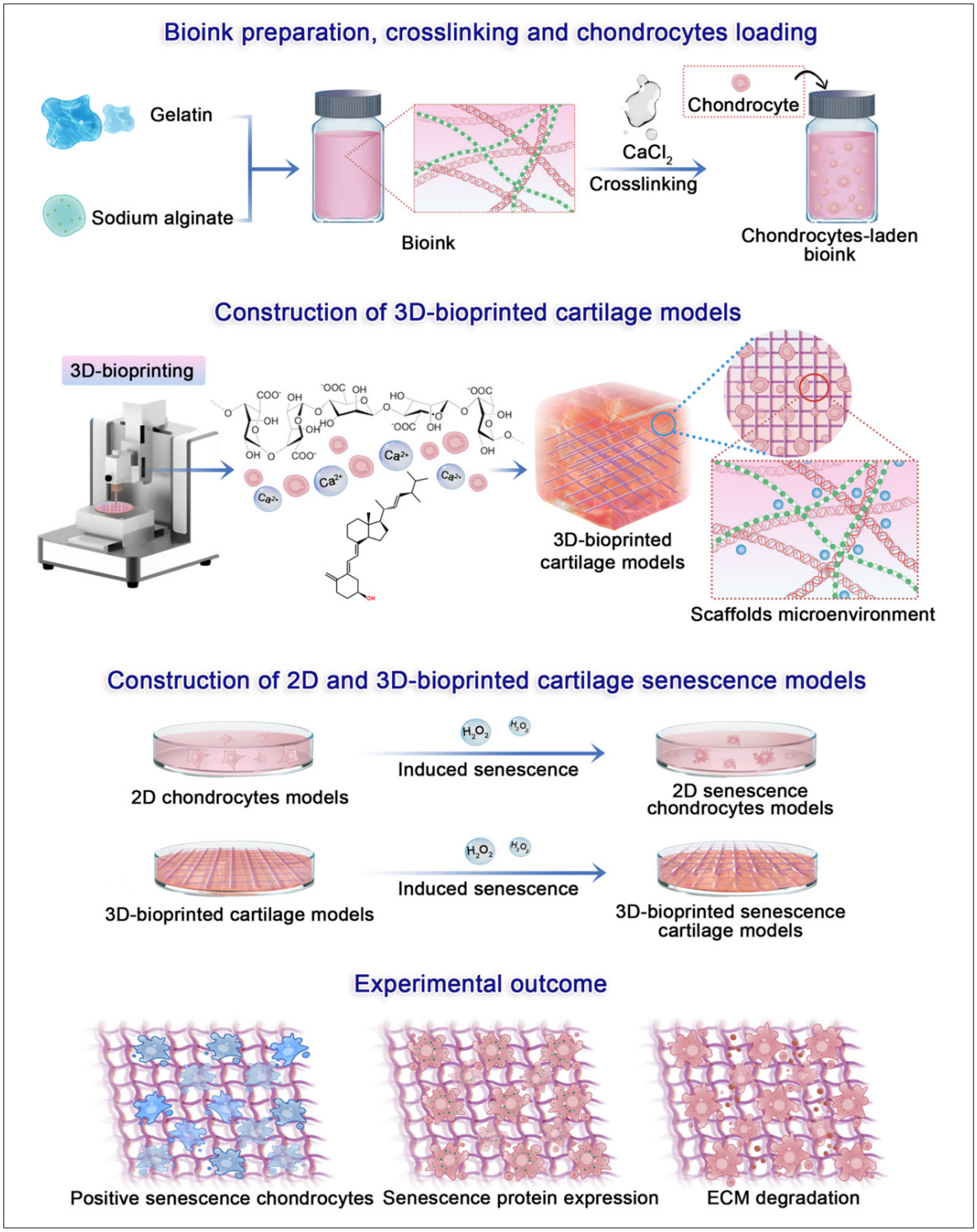

Figure 1. Schematic demonstration of 3D-bioprinted cartilage models that can be externally induced using H_2O_2 to build cartilage senescence models and the construction of 2D chondrocyte senescence models. Abbreviation: ECM, extracellular matrix.

2.5. Mechanical strength analysis

To evaluate the mechanical properties of the 3D-bioprinted Gel–Alg hydrogel scaffolds, a universal testing machine (Instron, USA) was used. Briefly, the scaffolds were fabricated into 3D-bioprinted rectangular columns with dimensions of 8 × 8 × 8 mm and subjected to uniaxial compression at a rate of 1 mm/min until 50% strain was reached. The compressive Young's modulus was calculated from the linear region of the initial 10% of the stress–strain curve, while toughness was determined by measuring the area under the curve. All measurements were performed in triplicate.

2.6. Water absorption and degradation behavior

The swelling and water absorption properties of the 3D-bioprinted hydrogel scaffolds were evaluated using the conventional weighing method. Briefly, the scaffolds were freeze-dried to obtain their initial dry weight (W0) and then immersed in 2 mL of PBS. The wet samples were maintained in a 37°C incubator. At specific time intervals (100, 200, 300, 400, and 500 min), the scaffolds were removed, and excess water was blotted with filter paper. The wet weight (Wt) of each scaffold was recorded. The percentage of swelling rate and water content was calculated using **Equation I**:

$$\text{Water content}\ (\%) = \frac{(\text{Wt} - \text{W0})}{\text{W0}} \times 100\% \qquad \text{(I)}$$

where W0 is the initial dry weight, and Wt is the wet weight of each sample at a different time point. Each sample was independently run in triplicate.

The *in vitro* degradation behavior of the 3D-bioprinted hydrogel scaffolds was evaluated using a gravimetric analysis method. Briefly, the scaffolds were freeze-dried, and their initial dry weight (W0) was recorded. The scaffolds were immersed in PBS (pH 7.4) containing type II collagenase (COL2) and maintained in a shaker at 37°C with a shaking speed of 40 rpm. At specific time points (0, 2, 4, 6, 8, and 10 h), the samples were removed, dried, and weighed again (Wt). Each experiment was performed in triplicate to ensure the reliability of the results. The degradation rate of the scaffolds was calculated using **Equation II**:

$$\text{Degradation rate}\ (\%) = \frac{(\text{W0} - \text{Wt})}{\text{W0}} \times 100\% \qquad \text{(II)}$$

where W0 is the initial weight, and Wt is the measured weight at each time period. Each sample was independently run in triplicate.

2.7. Porosity test

The porosity of the 3D-bioprinted Gel–Alg hydrogel scaffolds was measured using the ethanol displacement method. Briefly, the scaffolds were freeze-dried to remove internal moisture. The dried scaffolds were accurately weighed (W0). Subsequently, the dimensions of the freeze-dried scaffolds were measured using a vernier caliper to calculate their theoretical volume (V0). The dried scaffolds were then placed in a test tube pre-filled with ethanol, ensuring complete immersion of the scaffolds. The tube was sealed and placed under a vacuum for 2 h to allow ethanol to fully infiltrate the pores of the scaffolds.[42] The process was monitored continuously until no bubbles were observed, indicating complete displacement. After removal, the scaffolds were gently blotted with filter paper to remove excess ethanol and immediately weighed (W1). The experiment was repeated three times independently to ensure data reliability. The porosity of the scaffolds was calculated using **Equation III**:

$$\text{Porosity}(\%) = \frac{(\text{W1} - \text{W0})}{\rho\,\text{V0}} \times 100\% \qquad \text{(III)}$$

where W0 is the initial weight, W1 is the measured weight at each time period, ρ is the density of ethanol, and V0 is the scaffold volume.

2.8. Isolation and amplification of articular chondrocytes

All four-week-old male Sprague-Dawley (SD) rats were provided by the Department of Laboratory Animals of the Zhejiang Province Experimental Animal Center. The study strictly adhered to the guidelines of the Institutional Animal Care and Use Committee of Hangzhou Institute of Medicine Chinese Academy of Sciences and was in accordance with the principles of the Declaration of Helsinki for the care and use of animals. After anesthesia, four-week-old male SD rats were euthanized, and the carcasses were disinfected by immersion in 75% ethanol for 20 min. The skin was removed, and the lumbar spine was isolated, discarding the tail and ankles while preserving the hip and knee joints. The joints were then rinsed with 75% ethanol. Under aseptic conditions, the joint capsule was opened, and the surrounding muscle tissue was carefully removed. The meniscus was excised to expose the articular cartilage. Cartilage from the knee joint and femoral head was harvested and rinsed with PBS. The tissue was transferred into a trypsin–EDTA solution (Sigma, USA) and digested on a shaker at 37°C and 85 rpm for 30 min. Following digestion, the samples were washed with PBS and transferred to a centrifuge tube containing 0.2% COL2 (Sigma, USA) for further digestion at 37°C for 4 h under

agitation.[43] When visible cartilage fragments were reduced, an equal volume of Dulbecco's Modified Eagle Medium (DMEM) (Gibco, USA), supplemented with 10% fetal bovine serum (FBS) (Bio Channel, China), was added to terminate the enzymatic reaction. The mixture was centrifuged at 1200 rpm for 10 min, the supernatant was discarded, and the cell pellet was collected. The cells were seeded in DMEM containing 10% FBS and 1% penicillin–streptomycin (Gibco, China). AC growth was monitored under a microscope, and the culture medium was replaced every 2–3 days. When the primary ACs reached 80–90% confluence, they were used for subsequent staining identification and 3D bioprinting of cartilage models.

2.9. Identification of articular chondrocytes

2.9.1. Safranin O staining

The ACs were rinsed three times with PBS to remove the residual culture medium. Subsequently, 4% paraformaldehyde (PFA) was added, and the cells were fixed at room temperature for 20 min. After fixation, the samples were washed three times with PBS for 5 min each to remove the fixative. The fixed samples were then immersed in Safranin O staining solution (Suzhou Haixing Biosciences, China) and incubated at room temperature for 10 min. Following staining, the samples were thoroughly rinsed with distilled water to remove excess dye. Dehydration was performed using a graded ethanol series (70, 90, and 100%) for 2 min each. Finally, the stained samples were observed under an optical microscope.

2.9.2. Alcian Blue staining

The ACs were rinsed three times with PBS to remove the residual culture medium. Subsequently, 4% PFA was added, and the cells were fixed at room temperature for 20 min. The fixed samples were then immersed in Alcian Blue staining solution (Suzhou Haixing Biosciences, China) and incubated at room temperature for 30 min. Following staining, the samples were thoroughly rinsed with distilled water to remove excess dye. Dehydration was performed using a graded ethanol series (70, 90, and 100%) for 2 min each. Finally, the stained samples were observed under an optical microscope.

2.9.3. Toluidine Blue staining

The ACs were rinsed three times with PBS to remove the residual culture medium. Subsequently, the cells were fixed with 4% PFA at room temperature for 20 min. A 0.1% Toluidine Blue staining solution (pH 2.5–3.0) (Suzhou Haixing Biosciences, China) was added to cover the samples, followed by incubation at room temperature for 10–15 min. The samples were then quickly immersed in a 0.1% acetic acid solution for 5–10 s for differentiation and rinsed three times with distilled water for 1 min each. Dehydration was performed using a graded ethanol series (70, 90, and 100%) for 2 min each. Finally, the stained samples were observed under an optical microscope.

2.10. Construction of 3D-bioprinted cartilage models

The primary ACs of SD rats were selected as seed cells, and three different concentration ratios of Gel–Alg natural polymer hydrogels were used as scaffolds to construct cartilage models using 3D bioprinting technology. Based on preliminary research, the optimal Gel–Alg ratios were determined to be 7:3, 8:2, and 9:1. The bioinks were thoroughly mixed on a shaker at 60°C. For each formulation, 500 μL of bioink was transferred to a printing cartridge, and 50 μL of ACs suspension was immediately added to the cartridge and mixed with the hydrogel. Printing was performed on a 4°C 3D printer platform, with the filament diameter set to 200 μm, the number of layers set to four, and the printing spacing set to 0.22 mm. Printing parameters, including extrusion pressure (0.25, 0.3, 0.35, and 0.4 Mpa), printing speed (5, 8, 10, and 12 mm/s), and printing nozzle temperature (16, 18, and 20°C), were dynamically adjusted during the process to optimize the printing outcome. After printing, the cartilage models were crosslinked in a sterile 3% $CaCl_2$ solution for 3 min and rinsed with sterile PBS to remove residual crosslinking agents. The cartilage model was then transferred to DMEM culture and placed in a cell culture chamber at 37 °C and 5% CO_2 to support cartilage tissue growth.

2.11. Live/dead cell assay

The potential damage to AC viability during the 3D bioprinting process was assessed using live/dead staining assay. After printing, the constructs were cultured in 10% FBS DMEM for 1 day. Prior to the experiment, the culture medium was removed, and the constructs were rinsed with sterile PBS. The constructs were then incubated for 15 min in an assay buffer solution containing 4 μM calcein AM and 4.5 μM propidium iodide (Biosharp, China). After staining, the constructs were rinsed again with sterile PBS. A fluorescent microscope (Nikon, Japan) was used for observation at a wavelength of 490 ± 10 nm. Cell viability was quantified using ImageJ software (Media Cybernetics, USA).

2.12. Cell counting kit-8 assay

The proliferation activity of ACs within the hydrogel scaffolds was evaluated using the cell counting kit-8 (CCK-8) assay. After printing, the constructs were cultured in 10% FBS DMEM for 1 day. On days 1, 4, and 7, the medium was replaced with fresh medium containing 10% CCK-8 (Shenzhen JHHS Biotech, China) and incubated at

37 °C for 2 h. Subsequently, the absorbance at 450 nm was measured using a microplate reader (Tecan, Switzerland). Ten samples from each group were included for statistical analysis.

2.13. Extracellular matrix secretion assay

The secretion of extracellular matrix (ECM) (proteoglycans and glycosaminoglycans [GAGs]) by ACs in 3D-bioprinted cartilage models was detected using Safranin O and Toluidine Blue staining (Suzhou Haixing Biosciences, China) to evaluate the formation and function of cartilage tissue. After printing, the constructs were cultured in 10% FBS DMEM for 5 days. Prior to the experiment, the 3D-bioprinted cartilage models were rinsed with sterile PBS to remove residual culture medium. Subsequently, the samples were fixed with 4% PFA at room temperature for 1 h and washed with sterile PBS to remove the fixative. The fixed samples were then immersed in Safranin O and Toluidine Blue staining solutions, respectively, and incubated at room temperature for 40 min. After staining, the samples were thoroughly rinsed with distilled water to remove excess dye. Dehydration was performed using a graded ethanol series (70, 90, and 100%). Finally, the stained samples were observed under an optical microscope (Olympus, Japan).

2.14. Construction of 2D articular chondrocyte senescence models

The effects of oxidative stress on 2D AC models and 2D AC senescence models were established using H_2O_2 induction. A 3% H_2O_2 stock solution (Biosharp, China) was diluted with a serum-free medium by volume to prepare H_2O_2 solutions at concentrations of 0 (control group), 100, 300, 500, and 700 μM. These were used for constructing the 2D AC senescence models. The optimal H_2O_2 concentration for constructing the senescence model was determined through β-galactosidase staining (Biosharp, China), and this concentration was subsequently used for constructing the 3D-bioprinted cartilage senescence models. Briefly, the 3% H_2O_2 stock solution was sequentially diluted to the control group, 100, 300, 500, and 700 μM using a gradient dilution method. Subsequently, the 2D AC models were rinsed with sterile PBS to remove the residual culture medium on the surface. Finally, the 2D AC models were cultured with different concentrations of H_2O_2 for 2, 6, and 12 h to determine the optimal concentration and time for inducing the senescence model. After the induction of the senescence model was completed, the H_2O_2 diluent was removed, and the models were rinsed with sterile PBS for subsequent detection.

2.15. β-galactosidase staining analysis

The β-galactosidase staining was used to determine the optimal H_2O_2 concentration and induction time for constructing the 2D AC senescence model, and the optimal conditions were applied to construct the 3D-bioprinted cartilage senescence model. Briefly, the H_2O_2 diluent was removed, and the samples were rinsed with PBS. Then, 1 mL of β-galactosidase staining fixative (Beijing LABLEAD Inc, China) was added, and the cells were fixed at room temperature for at least 15 min. Subsequently, the fixative was removed, and the samples were rinsed with PBS. Next, 2 mL of working staining solution containing X-Gal substrate was added, and the samples were incubated overnight at 37°C. Finally, β-galactosidase activity was observed using a fluorescence microscope, and quantitative analysis was performed using ImageJ software.

2.16. Construction of 3D-bioprinted cartilage senescence models

We constructed the 3D-bioprinted cartilage senescence models using the optimal H_2O_2 concentration and induction time (determined previously in **Section 2.15**). Briefly, the complete medium was removed, and the samples were rinsed with sterile PBS. Subsequently, 500 μM H_2O_2 diluent was added, and the samples were cultured for 2 h. Finally, the H_2O_2 diluent was removed, and the samples were rinsed with PBS for subsequent detection.

2.17. Cell viability analysis of senescence models

The cell viability of 2D AC senescence models and 3D-bioprinted cartilage senescence models was evaluated using the CCK-8 assay to compare the proliferation of cells in both models under senescence conditions. Briefly, the 2D AC senescence models and 3D-bioprinted cartilage senescence models were transferred into 24-well plates and cultured in a complete medium. After 24 h of culture, the complete medium was removed, and the samples were rinsed with sterile PBS. The medium was then replaced with fresh medium containing 10% CCK-8 (Biosharp, China) and incubated at 37°C for 2 h. Subsequently, the absorbance at 450 nm was measured using a microplate reader (Tecan, Switzerland). Ten samples from each group were included for statistical analysis.

2.18. Western blot analysis

The differences in senescence-related protein expression between 2D AC senescence models and 3D-bioprinted cartilage senescence models were explored using Western blot. Briefly, total protein was extracted from the 2D AC senescence models and 3D-bioprinted cartilage senescence models using radioimmunoprecipitation lysis buffer (Thermo Fisher, China) supplemented with 1% protease inhibitor and phosphatase inhibitor (Thermo Fisher, China). The protein concentration was determined using the bicinchoninic acid assay (Thermo Fisher, China). Equal amounts of protein were electrophoresed by sodium dodecyl sulfate–polyacrylamide gel electrophoresis and

transferred to polyvinylidene fluoride (PVDF) blotting membranes (Millipore, USA). The membranes were incubated with Fast Blocking Buffer (Epizyme, China) at room temperature for 15 min and then incubated overnight at 4°C with primary antibodies against p16 (1:600) (Biosharp, China), p21 (1:800) (Biosharp, China), and β-actin (1:1000) (Hangzhou UpingBio Technology, China). The membranes were washed with DAPI (4',6-Diamidino-2-phenylindole) TBST (Tris-buffered saline with Tween 20) (Thermo Fisher, China) and incubated with horseradish peroxidase-coupled secondary antibodies (1:2000) (Jackson, USA) at room temperature for 1 h. After washing the PVDF membranes again, the bands were visualized using an enhanced chemiluminescence solution (Biosharp, China) and a Gel Analysis System (Cytiva, USA).

2.19. Immunofluorescence

The expression differences in 2D AC senescence models and 3D-bioprinted cartilage senescence models were observed using immunofluorescence staining to evaluate the molecular characteristics of both models under senescence conditions. Briefly, the 2D AC senescence models and 3D-bioprinted cartilage senescence models were rinsed three times with PBS to remove the residual culture medium. Subsequently, 4% PFA was added, and the samples were fixed at room temperature for 20 min. After fixation, the samples were washed three times with PBS for 5 min each to remove the fixative. Then, 0.1% Triton X-100 (Biosharp, China) was added, and the samples were permeabilized at room temperature for 10 min to enhance antibody penetration. The samples were rinsed three times with PBS for 5 min each. Next, a 5% bovine serum albumin solution (Thermo Fisher, China) was added, and the samples were blocked at room temperature for 30 min to reduce non-specific binding. After blocking, the samples were rinsed once with PBS to remove the blocking solution. Diluted primary antibodies p16 (1:300) (Biosharp, China), p21 (1:300) (Biosharp, China), and COL2 (1:300) (Thermo Fisher, China) were added, and the samples were incubated overnight at 4°C. The samples were then washed three times with PBS for 5 min each to remove unbound primary antibodies. Fluorescently labeled secondary antibodies Alexa Fluor 488 (1:500) (Thermo Fisher, China) and Alexa Fluor 594 (1:500) (Thermo Fisher, China) were added, and the samples were incubated at room temperature in the dark for 1 h. After incubation, the samples were washed three times with PBS for 5 min each to remove unbound secondary antibodies. DAPI solution (1:1000) (Thermo Fisher, China) was added, and the samples were incubated at room temperature in the dark for 5 min to stain the nuclei. The samples were rinsed three times with PBS for 5 min each. Finally, the samples were observed under a fluorescence microscope, and the fluorescence signals of p16, p21, and COL2 were detected using different excitation wavelengths (488 and 594 nm). Images were captured and quantitatively analyzed using ImageJ analysis software.

2.20. Statistical analysis

All data were processed and analyzed using OriginPro 2022 (OriginLab Corporation, USA). Statistical significance was determined using one-way or two-way analysis of variance, followed by Tukey's post-hoc test for multiple comparisons. All the experiments were performed in triplicate, and the results were presented as the mean ± standard deviation. The statistical significance was set as: ns, no significant; $^{*}p < 0.05$; $^{**}p < 0.01$; $^{***}p < 0.001$; and $^{****}p < 0.0001$.

3. Results and discussion

3.1. 3D bioprinting and characterization of gelatin and sodium alginate hydrogel scaffolds

Three different concentration ratios of Gel–Alg were prepared (Figure 2B). The bioink should exhibit high viscoelasticity under high shear stress to increase printability. Optimal viscoelastic properties ensure stable bioink extrusion through 3D bioprinting nozzles while maintaining structural integrity.[44,45] Alg is a naturally occurring block copolymer composed of polymer chains of β-D-mannuronic acid (M) and α-L-guluronic acid (G). It is an ideal biomaterial for bioprinting hydrogels, as its printability can be readily tuned by adjusting the polymer density and crosslinking with $CaCl_2$.[46–48] Alg alone lacks mammalian cell adhesion ligands, but incorporating Gel can promote cell adhesion and differentiation, as well as adjust the viscosity of the hydrogel.[49] Thus, this study chose the Gel–Alg bioink with optimal viscoelastic properties and printability. At a shear rate of 200 s^{-1}, the viscosity of the 7 Gel–3 Alg bioink was measured at 5.30 ± 0.73 Pa·s, whereas the viscosities of 8 Gel–2 Alg and 9 Gel–1 Alg bioinks were 2.27 ± 0.30 Pa·s and 1.95 ± 0.36 Pa·s, respectively (Figure 2D). These findings indicate that 7 Gel–3 Alg exhibited optimal shear-thinning behavior, making it highly suitable for extrusion-based 3D bioprinting. In the low strain range (0.01–10%), G' and G" were relatively constant. However, 7 Gel–3 Alg demonstrated G' of 7830 ± 8.54 Pa and G" of 948 ± 0.41 Pa, higher than those of 8 Gel–2 Alg (G' = 2113 ± 0.61 Pa; G" = 216 ± 0.21 Pa) and 9 Gel–1 Alg (G' = 1542 ± 0.89 Pa; G" = 66 ± 0.86 Pa) (Figure 2E), indicating superior linear viscoelastic properties of 7 Gel–3 Alg.

Employing a layer-by-layer 0–90° alternating stacking strategy, precise Gel–Alg hydrogel scaffolds were fabricated. After 3D bioprinting, the scaffolds underwent $CaCl_2$ crosslinking to enhance mechanical properties.[50–52]

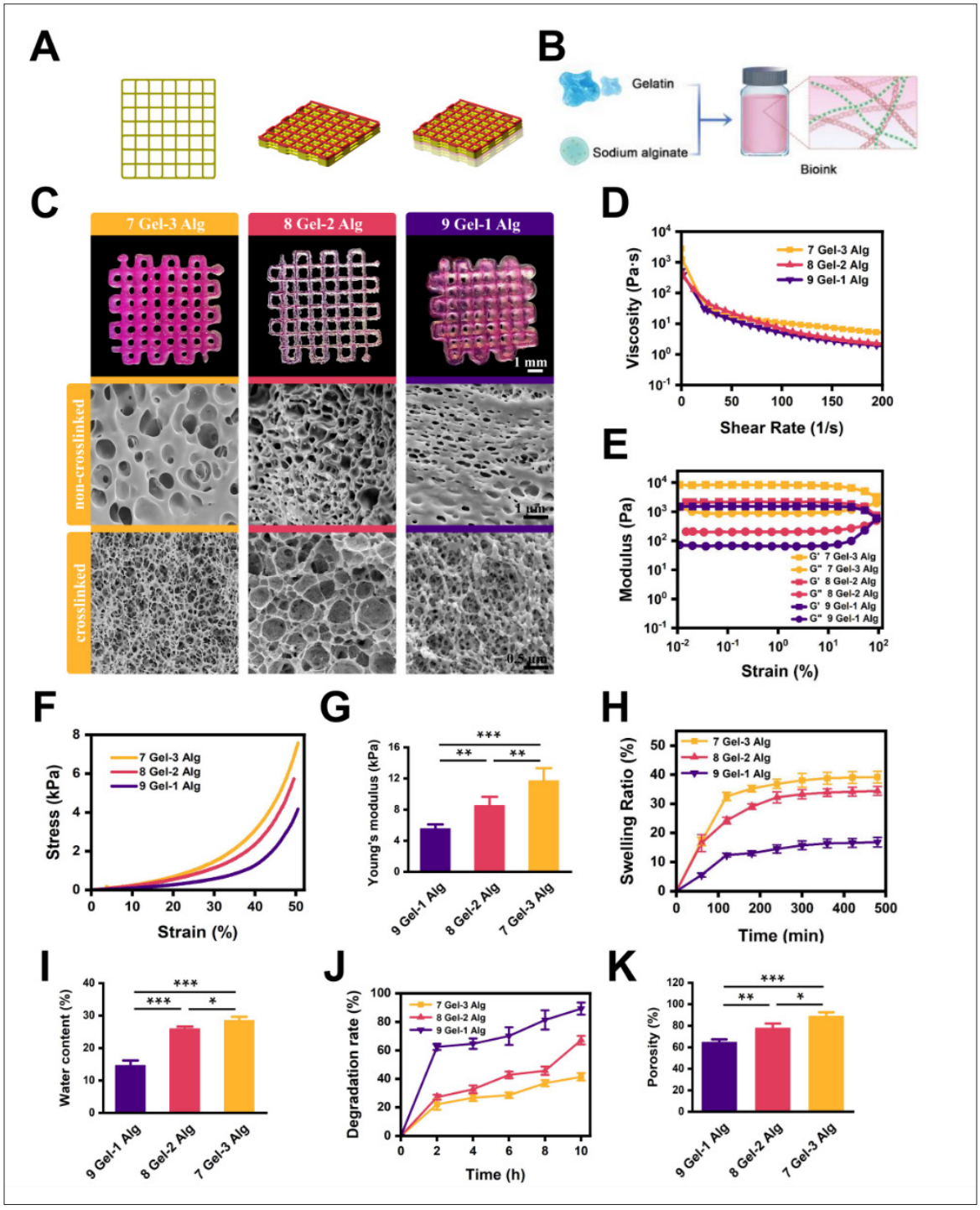

Figure 2. Construction and characterization of a 3D-bioprinted hydrogel scaffold. (A) Single-layer and multi-layer models of 3D-bioprinted hydrogel scaffolds. (B) Schematic illustration of natural bioink preparation. (C) Structural profiles of the printed Gel–Alg hydrogel scaffolds; SEM images of non-crosslinked and crosslinked Gel–Alg hydrogel scaffolds. (D and E) The viscosity (D) and modulus (E) of the natural bioink. (F) Stress–strain curves of the Gel–Alg hydrogel scaffolds. (G) Statistical Young's modulus of the Gel–Alg scaffolds. (H and I) Swelling performance (H) and water content (I) of the Gel–Alg hydrogel scaffolds. (J) *In vitro* degradation performance of the scaffolds. (K) Porosity of the Gel–Alg hydrogel scaffolds. All statistical data are represented as mean ± standard deviation ($n = 3$; $^{*}p < 0.05$, $^{**}p < 0.01$, $^{***}p < 0.001$). Scale bar: 1 mm (C). Abbreviations: ACs, articular chondrocytes; Alg, alginate; GAGs, glycosaminoglycans; Gel, gelatin; SEM, scanning electron microscopy; sGAGs, sulfated glycosaminoglycans.

However, printing smaller models with a diameter of less than 10 mm was challenging due to the limitations of extruded 3D printing technology.[53] Although laser-assisted bioprinting has higher precision and can be used to construct Gel–Alg hydrogel scaffolds, it is challenging to maintain their bioactivity. This study prioritized physical crosslinking for improved biocompatibility, avoiding cytotoxicity associated with UV-initiated chemical crosslinking.[54] To eliminate potential mineral deposits from residual calcium ions on the scaffold surface, constructs were rinsed with sterile PBS. Figure 2C displays the structural profiles of Gel–Alg hydrogel scaffolds at three different concentration ratios. Furthermore, SEM images reveal microstructures of the scaffolds in both crosslinked and non-crosslinked states. Figure 2C also indicates that the 3D-bioprinted Gel–Alg scaffolds maintained a stable multi-layered grid structure with tightly stacked layers and an interconnected porous network suitable for AC growth. The pore sizes of the 7 Gel–3 Alg, 8 Gel–2 Alg, and 9 Gel–1 Alg scaffolds are 5.47 ± 0.87 μm, 2.29 ± 0.048 μm, and 1.18 ± 0.061 μm, respectively. High-magnification observations revealed dense pore walls formed by Alg crosslinking intertwined with Gel-derived microfiber structures, providing rough surfaces that enhance cell adhesion and increase specific surface area. The uniformity of printed fiber diameters and seamless interlayer fusion suggest that structural integrity was maintained through optimized printing parameters.

The mechanical strength was evaluated to confirm the stability of the polymer network following physical crosslinking, and the stress–strain curves were plotted (Figure 2F). Based on previous research, a higher concentration of Gel–Alg hydrogels ionic-crosslinked with $CaCl_2$ significantly enhanced the mechanical strength of the scaffolds.[55] Therefore, according to Figure 2G, Young's modulus of the 7 Gel–3 Alg scaffold is 11.7 ± 1.66 kPa, significantly higher than the values for 8 Gel–2 Alg and 9 Gel–1 Alg (8.52 ± 6.67 kPa and 5.56 ± 2.23 kPa, respectively). This suggests superior stiffness under load, crucial for maintaining structural integrity and performance in physiological conditions.

The swelling behavior was assessed to evaluate the hydrophilicity of the Gel–Alg scaffolds, which is crucial for maintaining a hydrated microenvironment conducive to nutrient diffusion, cellular viability, and growth.[56] All scaffolds demonstrated rapid water absorption in the first 120 min, followed by a deceleration in absorption from 120 to 240 min, with equilibrium swelling achieved after 240 min. The equilibrium swelling ratios of 8 Gel–2 Alg and 9 Gel–1 Alg were 34.4 ± 1.48% and 16.8 ± 1.48%, significantly lower than that of 7 Gel–3 Alg (39.2 ± 3.22%). This difference is attributed to the denser structure of 7 Gel–3 Alg, as supported by SEM analysis (Figure 2H).

To further determine the water content of Gel–Alg hydrogel scaffolds at swelling equilibrium in deionized water, gravimetric analysis was conducted. The results revealed similar equilibrium water contents of 7 Gel–3 Alg and 8 Gel–2Alg scaffolds at approximately 30%, reflecting similar hydrophilic properties (Figure 2I). This hydrophilicity is likely due to hydrophilic groups (–NH2, –COOH, and –OH) within the molecular chains of Gel and Alg components.[57] Water absorption and swelling are critical for retaining structural integrity and cellular microenvironments. Thus, achieving adequate swelling capacity is essential for optimal scaffold performance.

The degradation behavior was evaluated in the COL2 solution to assess scaffold stability. Following 2 h of incubation, 8 Gel–2 Alg and 9 Gel–1 Alg scaffolds exhibited significant mass loss, with degradation rates of 67.2 ± 2.90% and 89.2 ± 4.76% after 10 h, respectively. This observation suggests that increased Gel content accelerates degradation. In contrast, the 7 Gel–3 Alg scaffold exhibited a degradation rate of 41.4 ± 2.86% after 10 h, indicating that Alg enhances degradation resistance proportionally with its concentration in the composite (Figure 2J).

The porosity of the scaffolds was further evaluated, and the porosity of the 7 Gel–3 Alg, 8 Gel–2 Alg, and 9 Gel–1 Alg scaffolds was 88.9 ± 3.67%, 77.91 ± 4.66%, and 64.63 ± 2.48%, respectively. SEM comparisons attributed the superior porosity of 7 Gel–3 Alg to its structured pore network with multi-scale pore distribution, fostering efficient nutrient and fluid transport to create an optimal environment for cellular adhesion and proliferation (Figure 2K).

3.2. *In vitro* biocompatibility and cartilage extracellular matrix secretion by gelatin and sodium alginate hydrogel scaffolds

ACs isolated from the knee joints of four-week-old male SD rats were cultured for integration with 3D-bioprinted Gel–Alg hydrogel scaffolds (Figure 3A). After isolation and expansion, primary ACs were stained with Safranin O, Alcian Blue (pH 1.0), and Toluidine Blue to confirm ECM synthesis capacity. Studies have demonstrated that the Gel component provides a scaffold that mimics the ECM of ACs, while the Alg component imparts mechanical properties similar to those of cartilage. Gel–Alg promotes the secretion of AC ECM, manifesting as increased cell viability, higher levels of collagen II and proteoglycan expression, and elevated GAG content.[58,59] Safranin O

staining indicated a proteoglycan-rich matrix, while Alcian Blue (under acidic conditions) identified sulfated glycosaminoglycans (sGAGs) through distinct cyanophilic interactions. Toluidine Blue confirmed the presence of anionic GAGs via γ-metachromatic purple coloration (Figure 3B). The morphological assessment revealed cells adopting rounded or polygonal shapes with pericellular lacunae formation, establishing a baseline for evaluating 3D hydrogel scaffolds in cartilage ECM homeostasis.

In vitro biocompatibility and cellular viability were validated through CCK-8 and live/dead assays. Prior studies

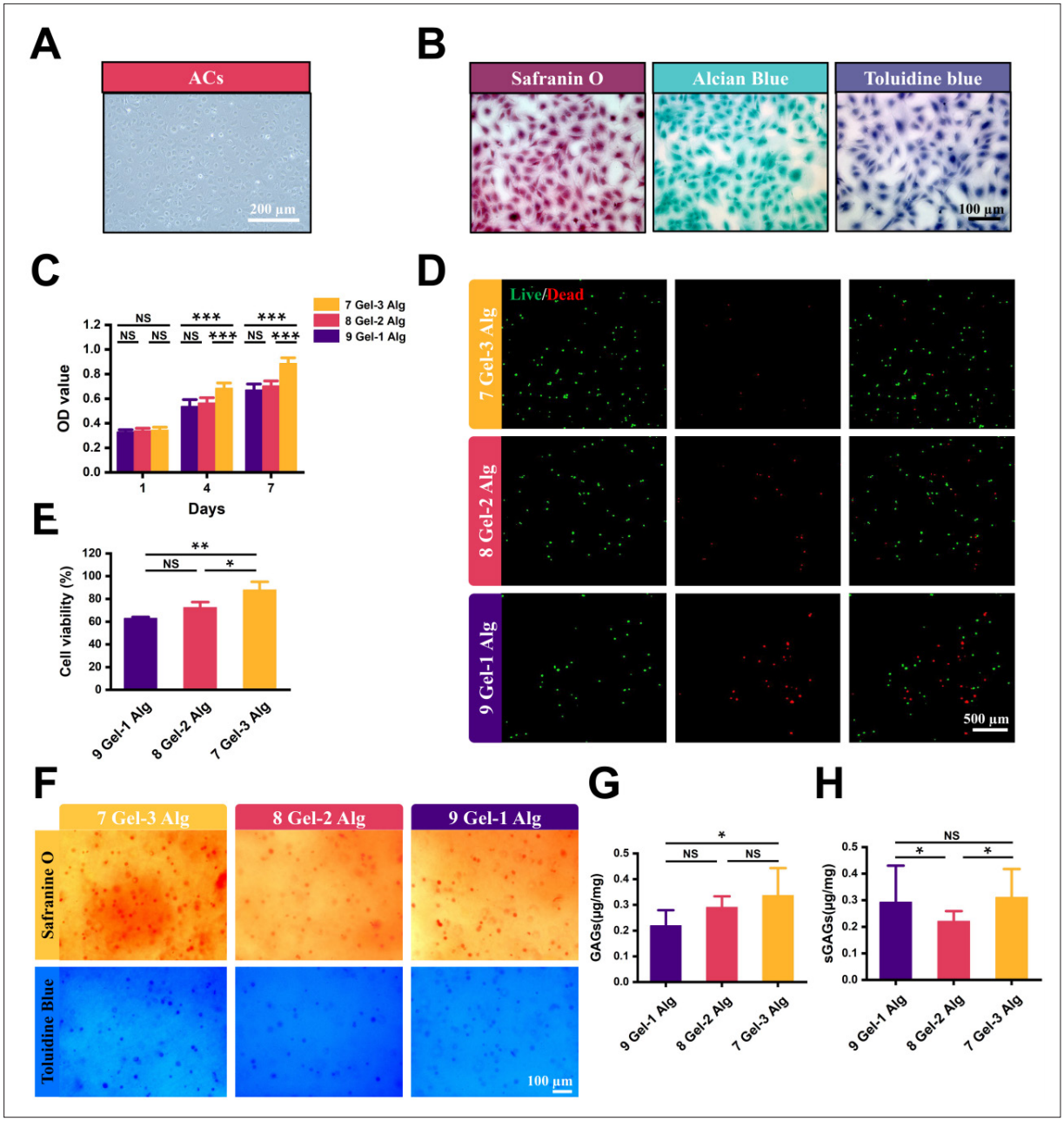

Figure 3. The 3D-bioprinted Gel–Alg hydrogel scaffolds support the survival, proliferation, and extracellular matrix secretion of the embedded cells. (A and B) The morphology (A) and staining (Safranin O, Alcian Blue, and Toluidine Blue) (B) of primary ACs. (C) Quantitative analysis of the AC proliferation rate *in vitro* 2D culture. (D) Cell viability determined by live/dead staining. (E) Quantification analysis of AC viability. (F) Safranin O and Toluidine Blue staining of 3D-bioprinted cartilage model. (G and H) Quantification analysis of GAGs (G) and sGAGs (H). All statistical data are represented as mean ± standard deviation ($n = 5$; $^{*}p < 0.05$, $^{**}p < 0.01$, $^{***}p < 0.001$). Scale bars: 100, 200, and 500 μm. Abbreviations: ACs, articular chondrocytes; Alg, alginate; GAGs, glycosaminoglycans; Gel, gelatin; NS, non-significant; OD, optical density; sGAGs, sulfated glycosaminoglycans.

indicate that decreased cell viability primarily results from high shear stress at the nozzle tip during printing.[60–62] In this study, 7 Gel–3 Alg hydrogel scaffolds exhibited the highest absorbance values compared to 8 Gel–2 Alg and 9 Gel–1 Alg (Figure 3C). These findings confirm that 3D-bioprinted 7 Gel–3 Alg scaffolds significantly enhance cellular viability and proliferation. Live/dead assays on AC-laden scaffolds after 1 day displayed cell viabilities of 87.9 ± 7.60%, 72.4 ± 5.03%, and 62.9 ± 0.83% for 7 Gel–3 Alg, 8 Gel–2 Alg, and 9 Gel–1 Alg, respectively (Figure 3D and E). After 7 days, AC-laden Gel–Alg hydrogel scaffolds stained with Safranin O and Toluidine Blue revealed the spatial distribution of negatively charged GAGs, proteoglycans, and sGAGs, enabling quantitative evaluation of tissue maturation (Figure 3F). The quantitative analysis results indicate that the 7 Gel–3 Alg scaffolds had higher GAG and sGAG contents compared to the 8 Gel–2 Alg and 9 Gel–1 Alg scaffolds (Figure 3G and H).

3.3. Development and functional characterization of a 2D chondrocytes senescence model

Approximately 3 × 10^6 ACs were exposed to H_2O_2 at concentrations of 0 (control), 100, 300, 500, and 700 μM for 2, 6, and 12 h to simulate oxidative stress-induced senescence and assessed via SA-β-galactosidase activity assays (Figure 4A). Previous studies have reported that during the process of ACs senescence, SA-β-gal activity was observed, involving senescence-associated markers (p16 and p21).[63,64] At 2 h, the SA-β-galactosidase-stained senescent cell rates were 4.67 ± 1.52%, 21.0 ± 3.61%, 58.0 ± 10.15%, 85.0 ± 3.61%, and 57.33 ± 6.11% in the control, 100, 300, 500, and 700 μM H_2O_2 groups, respectively (Figure 4B and C). Compared to the control group, the 500 μM H_2O_2 group achieved peak senescence ($p < 0.001$), while extensive apoptosis was observed at 700 μM. At 6 h, the SA-β-galactosidase-positive cell rates were 6.33 ± 1.53%, 35.33 ± 8.33%, 75.0 ± 3.00%, 50.33 ±

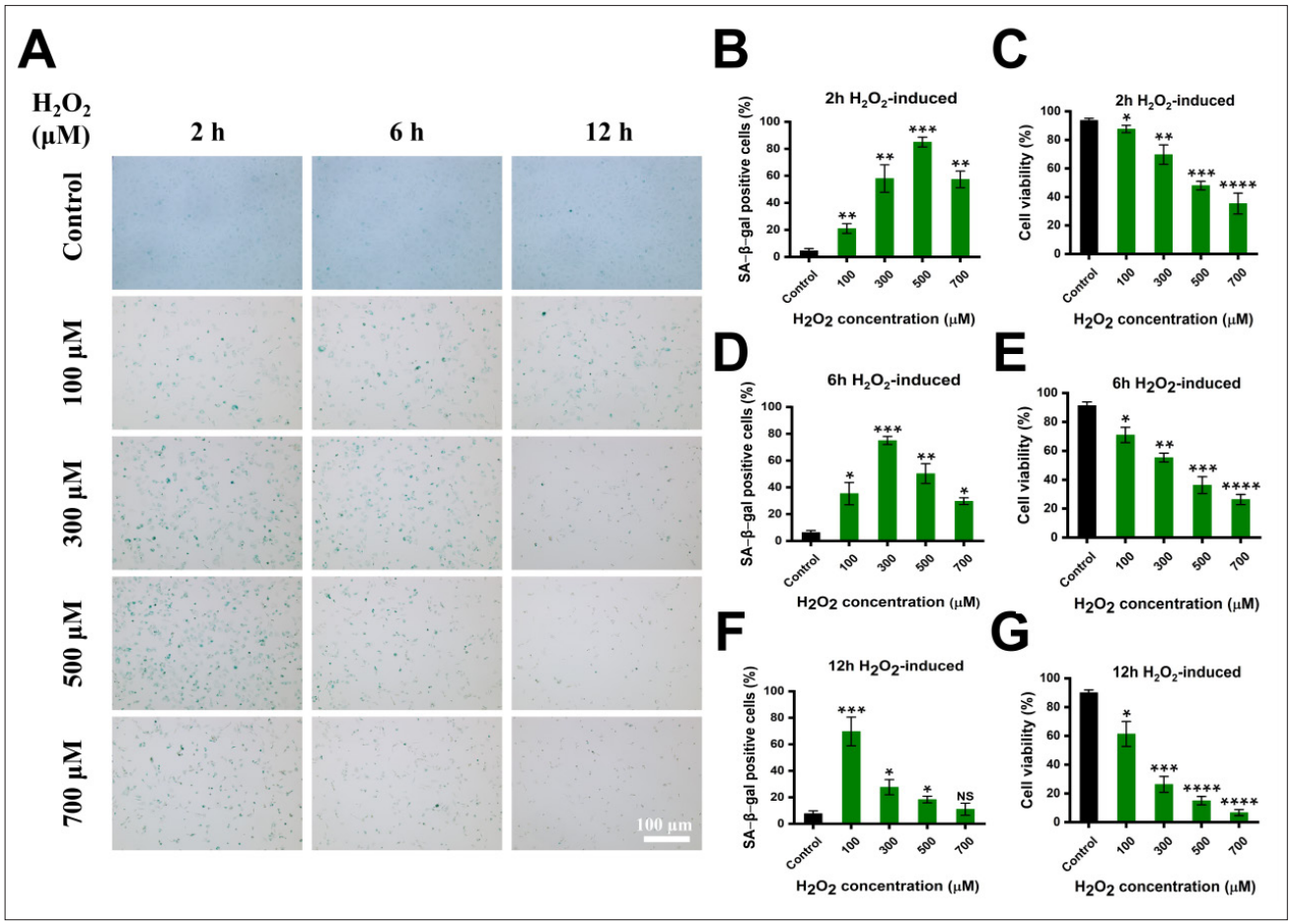

Figure 4. Construction of 2D AC senescence models. (A) β-Galactosidase staining of 2D ACs. (B–G) Quantitative analysis of the rate of AC senescence (B, D, and F) and viability (C, E, and F) following H_2O_2 induction at 2 (B and C), 6 (D and E), and 12 h (F and G). All statistical data are represented as mean ± standard deviation ($n = 3$; *$p < 0.05$, **$p < 0.01$, ***$p < 0.001$). Scale bar: 100 μm (A). Abbreviations: AC, articular chondrocyte.

7.37%, and 29.67 ± 2.52%, respectively (Figure 4D and E). Compared to the control group, the 300 μM H_2O_2 group exhibited significant senescence ($p < 0.001$), with apoptosis observed at higher concentrations. At 12 h, the SA-β-galactosidase-positive cell rates were 7.67 ± 2.08%, 69.67 ± 10.79%, 27.67 ± 5.69%, 18.33 ± 2.52%, and 11.0 ± 4.58%, respectively (Figure 4F and G). Compared to the control group, the 100 μM H_2O_2 group reached peak senescence ($p < 0.001$), while apoptosis was evident at higher concentrations.

These findings suggest that high-concentration oxidative stress overwhelms cellular regulatory mechanisms, causing macromolecular lesions and ultimately disrupting redox homeostasis.[65–67] The optimal conditions for inducing AC senescence were identified as a 2-h exposure to 500 μM H_2O_2, resulting in 85.0 ± 3.61% SA-β-gal-positive cells without significant apoptosis ($p < 0.001$ vs. control); and the 500 μM H_2O_2 concentration was applied to induce senescence in 3D-bioprinted cartilage models. Prolonged exposure (6 and 12 h) induced significant apoptosis (50.33–29.67% viable cells), making these conditions unsuitable for further studies.

The expression levels of senescence-associated proteins p21 and p16 were assessed through Western blot analysis and immunofluorescence, followed by semi-quantitative analysis using ImageJ software. The senescence phenotype is not limited to cell cycle arrest; senescent cells are metabolically active and exhibit changes in protein expression and secretion, leading to Senescence-Associated Secretory Phenotype development.[68] Results indicated significant H_2O_2-induced effects on AC senescence. As illustrated in Figure 5A, Western blot and semi-quantitative analysis revealed dose-dependent upregulation of p21 and p16 in the 500 μM group versus controls (Figure 5B and C). These results were further validated by immunofluorescence staining, and semi-quantitative analysis revealed markedly elevated expression levels of senescence-associated proteins p21 and p16 in the 500 μM H_2O_2 group compared to the control, with enhanced green fluorescence intensity indicating robust protein accumulation (Figure 5D–G). Collectively, H_2O_2 treatment significantly promotes p21 and p16 expression in a concentration-dependent manner, accelerating AC senescence.

3.4. Construction and functional characterization of a 3D-bioprinted cartilage senescence model

The protocol for inducing AC senescence was optimized to 500 μM H_2O_2 for 2 h, as previously validated. After inducing senescence in the 3D-bioprinted cartilage model enriched with approximately 3 × 10^6 ACs, sterile PBS was used to rinse away residual H_2O_2. The 3D bioprinting technology enabled the construction of aging models that more accurately simulate the intracellular environment, increase cell interaction with biogenic ECM, and improve the stability and accuracy of senescence phenotype.[69] This study assessed p21 and p16 expression levels through Western blot and immunofluorescence staining, with semi-quantitative evaluation using ImageJ software. As displayed in Figure 6A, Western blot and semi-quantitative analysis revealed dose-dependent upregulation of p21 and p16 in the 500 μM group versus controls (Figure 6B and C). These results were further validated by immunofluorescence staining, and semi-quantitative analysis revealed markedly elevated expression levels of senescence-associated proteins p21 and p16 in the 500 μM H_2O_2 group compared to the control, with enhanced green fluorescence intensity indicating substantial protein accumulation (Figure 6D–G). These results suggest that H_2O_2 accelerates senescence in cartilage models through oxidative stress responses.

To further evaluate alterations in COL2 content within the 3D-bioprinted cartilage models of the control and 500 μM groups, semi-quantitative analysis was performed using immunofluorescence techniques. As illustrated in Figure 7A and B, immunofluorescence staining and semi-quantitative evaluation demonstrated a statistically significant reduction in COL2 expression in the 500 μM group compared to the control, indicative of oxidative stress-induced degradation of the cartilage matrix. Collectively, the semi-quantitative assessment of COL2 highlights the dual impact of oxidative stress on both cellular senescence and ECM disruption in the 3D-bioprinted cartilage model, thereby advancing our mechanistic understanding of pathological cartilage aging processes.

4. Conclusion

In this study, three different concentration ratios of Gel–Alg natural polymer hydrogels (7 Gel–3 Alg, 8 Gel–2 Alg, and 9 Gel–1 Alg) were used as tissue engineering scaffolds. Primary ACs served as seed cells and were combined with 3D bioprinting technology to construct cartilage models. Among the tested concentrations, the optimal hydrogel concentration ratio was identified as 7 Gel–3 Alg. Compared to the 8 Gel–2 Alg and 9 Gel–1 Alg hydrogel scaffolds, the 7 Gel–3 Alg hydrogel scaffold exhibited excellent biocompatibility, mechanical properties, and biological functions, such as promoting ECM secretion. Furthermore, 2D AC senescence models and 3D-bioprinted cartilage

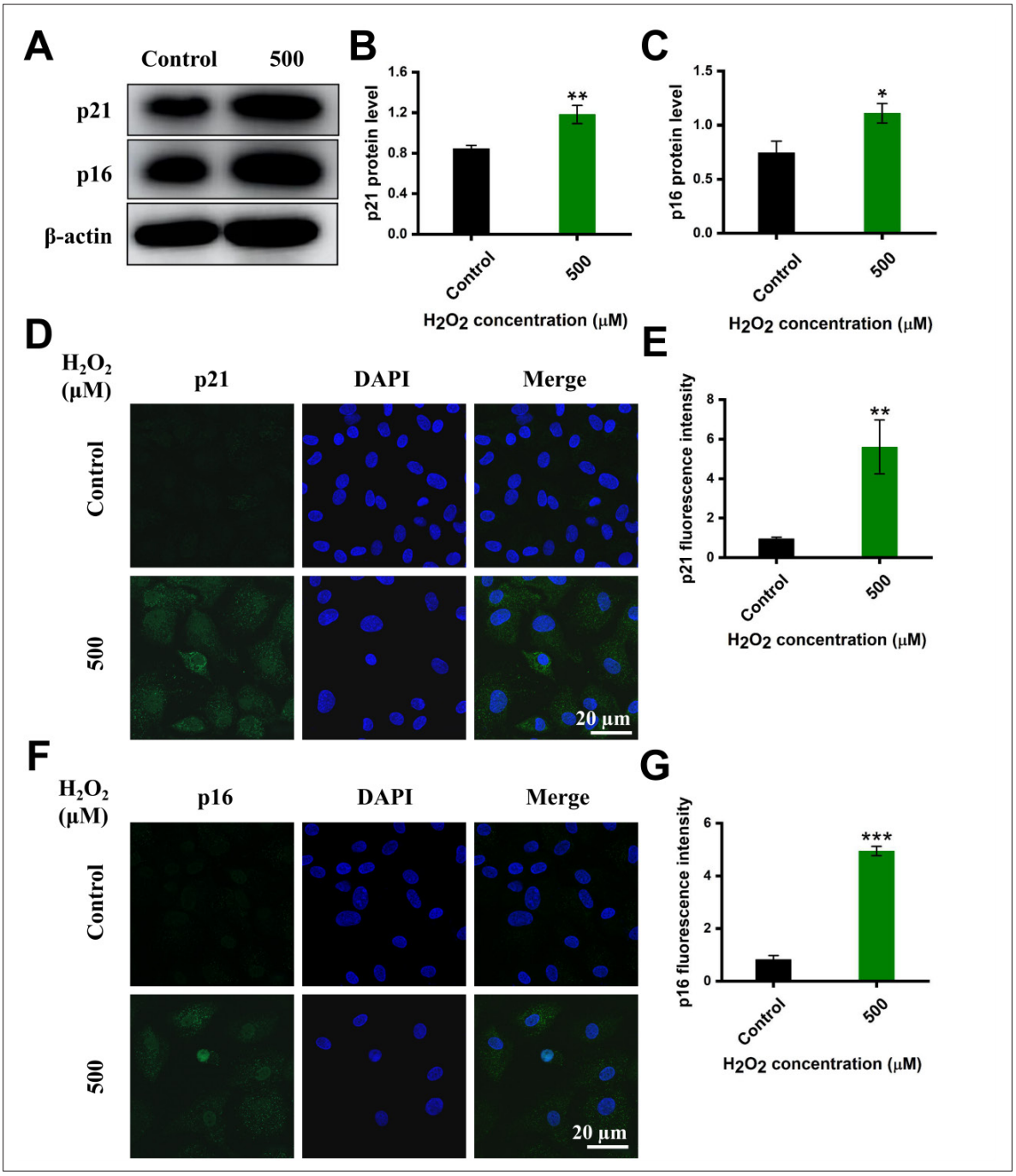

Figure 5. H_2O_2 promotes the expression of senescence-associated proteins p21 and p16 in a 2D AC senescence model. (A) Western blot analysis of p21 and p16 in the 2D AC senescence model. (B and C) Summary of quantitative data of p21 (B) and p16 (C) in the 2D AC senescence model. (D and E) Immunofluorescence staining analysis (D) and summary of quantitative data (E) of p21 in the 2D AC senescence model. (F and G) Immunofluorescence staining analysis (F) and summary of quantitative data (G) of p16 in the 2D AC senescence model. All statistical data are represented as mean ± standard deviation ($n = 3$; $^*p < 0.05$, $^{**}p < 0.01$, $^{***}p < 0.001$). Scale bars: 20 μm (D and F). Abbreviation: AC, articular chondrocyte.

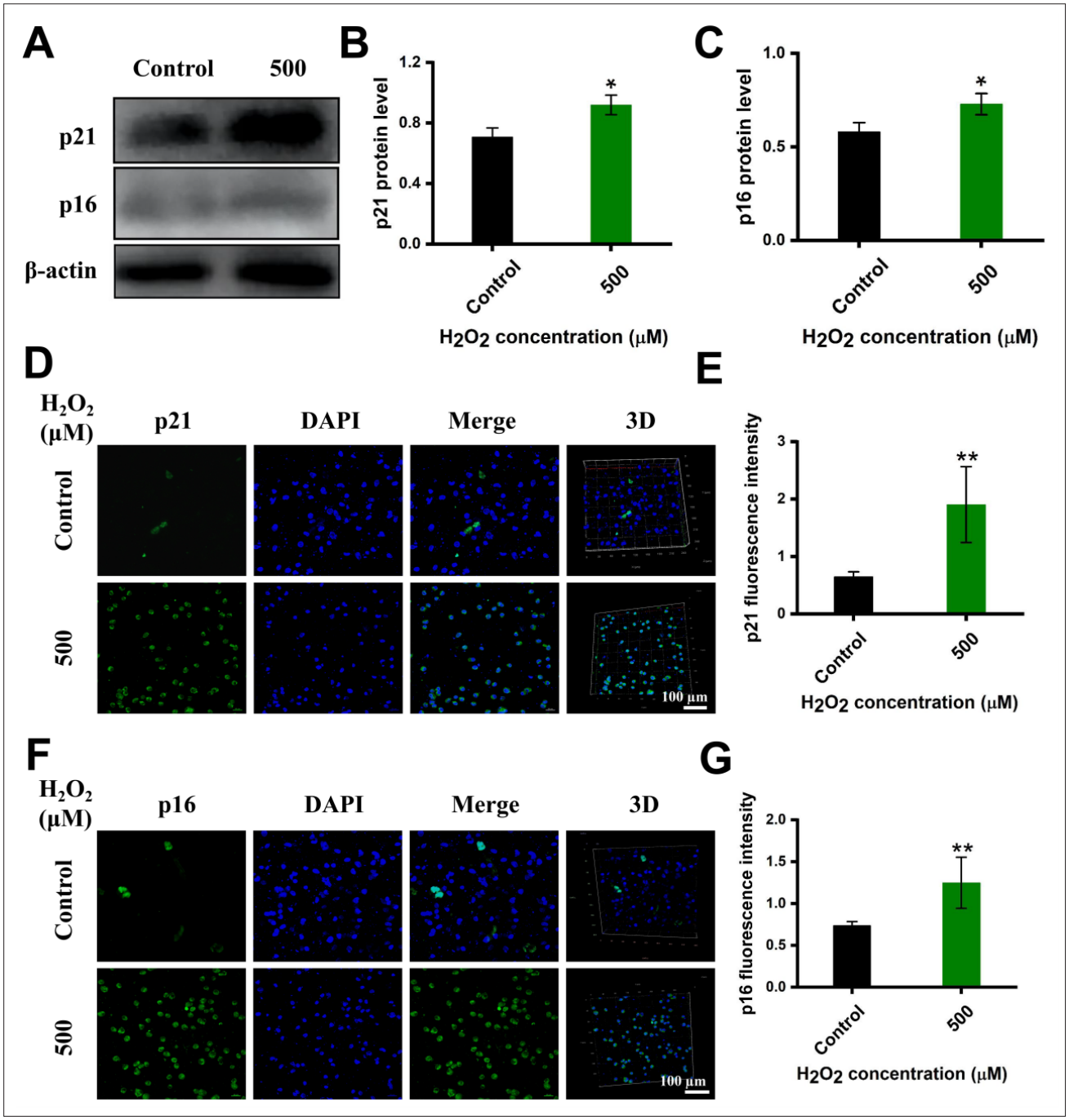

Figure 6. H_2O_2 promotes the expression of senescence-associated proteins p21 and p16 in a 3D-bioprinted cartilage senescence model. (A) Western blot analysis of p21 and p16 in the 3D-bioprinted cartilage senescence models. (B and C) Summary of quantitative data of p21 (B) and p16 (C) in the 3D-bioprinted cartilage senescence models. (D and E) Immunofluorescence staining analysis (D) and summary of quantitative data (E) of p21 in the 3D-bioprinted cartilage senescence models. (F and G) Immunofluorescence staining analysis (F) and summary of quantitative data (G) of p16 in the 3D-bioprinted cartilage senescence models. All statistical data are represented as mean ± standard deviation ($n = 3$; $^*p < 0.05$, $^{**}p < 0.01$). Scale bars: 100 μm (D and F).

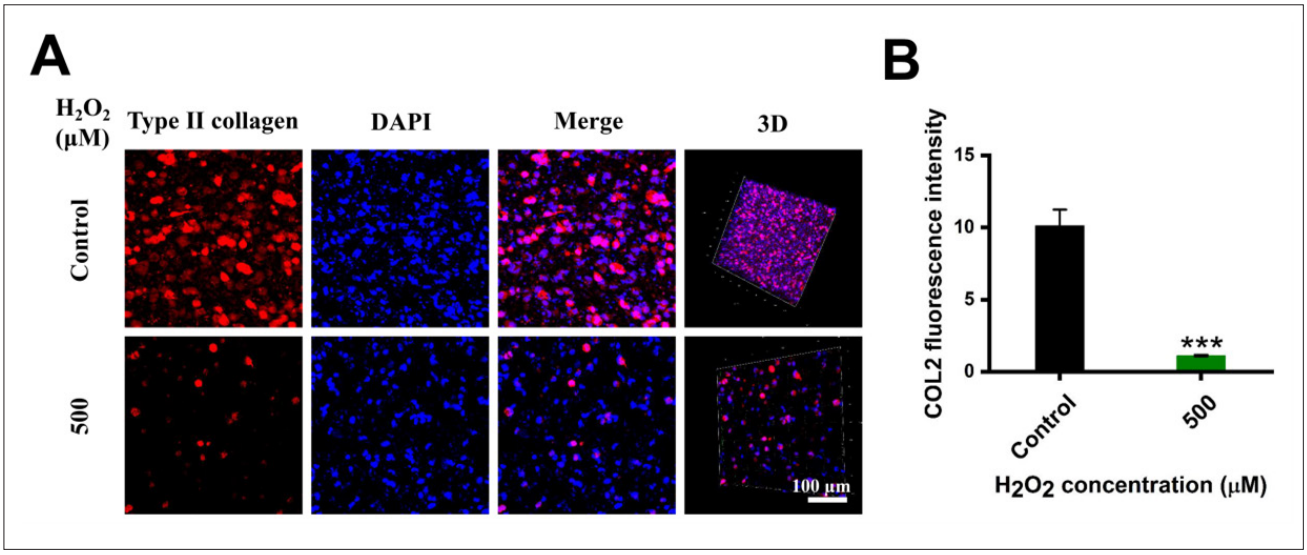

Figure 7. H_2O_2 reduces the expression of type II collagen in the 3D-bioprinted cartilage senescence model. Immunofluorescence staining analysis (A) and summary of quantitative data (B) for type II collagen in the 3D-bioprinted cartilage senescence models. All statistical data are represented as mean ± standard deviation ($n = 3$; ***$p < 0.001$). Scale bar: 100 μm.

senescence models were developed, and the optimal H_2O_2 concentration and induction time for constructing the senescence models were determined to be 500 μM and 2 h, respectively. Compared to the 2D AC senescence models, the 3D-bioprinted cartilage senescence models more closely resembled the natural aging state of human cartilage in terms of aging-related molecular expression. However, this study used SD rat ACs instead of humans and lacked comprehensive characterization of aging-related markers, including inflammatory factors and senescence-related proteins. These limitations reduce the translational relevance of the model for elucidating the mechanisms underlying OA development in humans. Future work should focus on developing more human-compatible *in vitro* OA models. Overall, the 3D-bioprinted cartilage senescence model may provide a valuable new experimental platform for research on the prevention and treatment of aging-related OA and the mechanisms underlying its development and progression.[70–72]

Acknowledgments

The authors are grateful to the Core Technology Platform of the Hangzhou Institute of Medicine Chinese Academy of Sciences for providing the essential resources for this study.

Funding

This study was supported by the Shenzhen Science and Technology Innovation Committee (JCYJ20230807110259002 and JCYJ20240813150201003) and the Ganzhou Municipal Science and Technology Project (2022-YB1396).

Conflict of interest

The authors declare no conflicts of interest.

Author contributions

Conceptualization: Hanxiao Qin
Formal analysis: Hanxiao Qin, Fanqing Xu
Investigation: Hanxiao Qin, Fanqing Xu
Methodology: All authors
Writing–original draft: Hanxiao Qin
Writing–review & editing: All authors
All the authors have read and approved the final manuscript.

Ethics approval and consent to participate

The animal experiments were conducted in accordance with the "Regulations on the Management of Experimental Animals" and were approved by the Experimental Animal Ethics Committee of Hangzhou Institute of Medicine Chinese Academy of Sciences (approval no. 2023R0025).

Consent for publication

Not applicable.

Availability of data

Data is available from the corresponding author upon reasonable request.

References

1. Li Y, Li L, Wang M, et al. O-alg-THAM/gel hydrogels functionalized with engineered microspheres based on mesenchymal stem cell secretion recruit endogenous stem cells for cartilage repair. *Bioact Mater*. 2023;28(5):255-272. doi: 10.1016/j.bioactmat.2023.05.003.
2. Guo X, Xi L, Yu M, et al. Regeneration of articular cartilage defects: therapeutic strategies and perspectives. *Tissue Eng Rev*. 2023;14(3):20417314231164765. doi: 10.1177/20417314231164765.
3. Liu Z, Lu T, Ma L, et al. DNA demethylation of promoter region orchestrates SPI-1-induced ADAMTS-5 expression in articular cartilage of osteoarthritis mice. *J Cell Physiol*. 2024;239(2):e31170. doi: 10.1002/jcp.31170.
4. Bank NC, Sanghvi P, Hecht CJ, et al. The epidemiology of posttraumatic osteoarthritis of the knee in the United States: an analysis of 948,853 patients from 2000 to 2022. *J Am Acad Orthop Surg*. 2024;32(7):313-320. doi: 10.5435/JAAOS-D-23-00662.
5. Zhang XX, He SH, Liang X, et al. Aging, cell senescence, the pathogenesis and targeted therapies of osteoarthritis. *Front Pharmacol*. 2021;12:728100. doi: 10.3389/fphar.2021.728100.
6. Loeser RF. Aging processes and the development of osteoarthritis. *Curr Opin Rheumatol*. 2013;25(1):108-113. doi: 10.1097/BOR.0b013e32835a9428.
7. June RK, Liu-Bryan R, Long F, et al. Emerging role of metabolic signaling in synovial joint remodeling and osteoarthritis. *J Orthop Res*. 2016;34(12):2048-2058. doi: 10.1002/jor.23420.
8. Ray A, Ray BK. An inflammation-responsive transcription factor in the pathophysiology of osteoarthritis. *Biorheology*. 2008;45(3-4):399-409.
9. Yang Y, Zhao X, Wang S, et al. Ultra-durable cell-free bioactive hydrogel with fast shape memory and on-demand drug release for cartilage regeneration. *Nat Commun*. 2023;14(1):7771. doi: 10.1038/s41467-023-43334-8.
10. Hu Y, Lyu C, Teng L, et al. Glycopolypeptide hydrogels with adjustable enzyme-triggered degradation: a novel proteoglycans analogue to repair articular-cartilage defects. *Mater Today Bio*. 2023;20(5):100659. doi: 10.1016/j.mtbio.2023.100659.
11. Zeng Q, Gong Y, Zhu N, et al. Lipids and lipid metabolism in cellular senescence: emerging targets for age-related diseases. *Ageing Res Rev*. 2024;97(6):102294. doi: 10.1016/j.arr.2024.102294.
12. Jimenez PA, Glasson SS, Trubetskoy OV, et al. Spontaneous osteoarthritis in Dunkin Hartley guinea pigs: histologic, radiologic, and biochemical changes. *Lab Anim Sci*. 1997;47(6):598-601.
13. Säämänen AK, Salminen HJ, Dean PB, et al. Osteoarthritis-like lesions in transgenic mice harboring a small deletion mutation in type II collagen gene. *Osteoarthritis Cartilage*. 2000;8(4):248-257. doi: 10.1053/joca.2000.0298.
14. Murakami T, Ishida T, Tanaka S, et al. Inflammation and subsequent nociceptor sensitization in the bone marrow are involved in an animal model of osteoarthritis pain. *Life Sci*. 2023;324(7):121736. doi: 10.1016/j.lfs.2023.121736.
15. Seo JE, Le Y, Revollo J, et al. Evaluating the mutagenicity of N-nitrosodimethylamine in 2D and 3D HepaRG cell cultures using error-corrected next generation sequencing. *Arch Toxicol*. 2024;98(6):1919-1935. doi: 10.1007/s00204-024-03731-4.
16. Yagi M, Endo K, Komori K, et al. Comparison of the effects of oxidative and inflammatory stresses on rat chondrocyte senescence. *Sci Rep*. 2023;13(1):7697. doi: 10.1038/s41598-023-34825-1.
17. Shboul SA, DeLuca VA, Dweiri YA, et al. Can 3D bioprinting solve the mystery of senescence in cancer therapy? *Ageing Res Rev*. 2022;81(11):101732. doi: 10.1016/j.arr.2022.101732.
18. Żuchowska A, Baranowska P, Flont M, et al. Review: 3D cell models for organ-on-a-chip applications. *Anal Chim Acta*. 2024;1301(5):342413. doi: 10.1016/j.aca.2024.342413.
19. Ziadlou R, Barbero A, Martin I, et al. Anti-inflammatory and chondroprotective effects of vanillic acid and epimedin C in human osteoarthritic chondrocytes. *Biomolecules*. 2020;10(6):932. doi: 10.3390/biom10060932.
20. Huang S, Song X, Li T, et al. Pellet coculture of osteoarthritic chondrocytes and infrapatellar fat pad-derived mesenchymal stem cells with chitosan/hyaluronic acid nanoparticles promotes chondrogenic differentiation. *Stem Cell Res Ther*. 2017;8(1):264. doi: 10.1186/s13287-017-0719-7.
21. Stüdle C, Vallmajó-Martín Q, Haumer A, et al. Spatially confined induction of endochondral ossification by functionalized hydrogels for ectopic engineering of osteochondral tissues. *Biomaterials*. 2018;171(7):219-229. doi: 10.1016/j.biomaterials.2018.04.025.
22. Castro-Viñuelas R, Viudes-Sarrión N, Rojo-García AV, et al. Mechanical loading rescues mechanoresponsiveness in a human osteoarthritis explant model despite Wnt activation. *Osteoarthritis Cartilage*. 2025;33(6):692-702. doi: 10.1016/j.joca.2024.02.945.
23. Byron CR, Trahan RA. Comparison of the effects of interleukin-1 on equine articular cartilage explants and

cocultures of osteochondral and synovial explants. *Front Vet Sci*. 2017;4(9):152.
doi: 10.3389/fvets.2017.00152.

24. Lin H, Lozito TP, Alexander PG, et al. Stem cell-based microphysiological osteochondral system to model tissue response to interleukin-1beta. *Mol Pharm*. 2014;11(7):2203-2212.
doi: 10.1021/mp500136b.

25. Dönges L, Damle A, Mainardi A, et al. Engineered human osteoarthritic cartilage organoids. *Biomaterials*. 2024;308(7):122549.
doi: 10.1016/j.biomaterials.2024.122549.

26. Hall GN, Mendes LF, Gklava C, et al. Developmentally engineered callus organoid bioassemblies exhibit predictive in vivo long bone healing. *Adv Sci (Weinh)*. 2020;7(2):1902295.
doi: 10.1002/advs.201902295.

27. SunY, You Y, Wu Q, et al. Genetically inspired organoids prevent joint degeneration and alleviate chondrocyte senescence via Col11a1-HIF1alpha-mediated glycolysis-OXPHOS metabolism shift. *Clin Transl Med*. 2024;14(2):e1574.
doi: 10.1002/ctm2.1574.

28. Shen C, Wang J, Li G, et al. Boosting cartilage repair with silk fibroin-DNA hydrogel-based cartilage organoid precursor. *Bioact Mater*. 2024;35(2):429-444.
doi: 10.1016/j.bioactmat.2024.02.016.

29. Thompson CL, Hopkins T, Bevan C, et al. Human vascularised synovium-on-a-chip: a mechanically stimulated, microfluidic model to investigate synovial inflammation and monocyte recruitment. *Biomed Mater*. 2023;18(6):065013.
doi: 10.1088/1748-605X/acf976.

30. Lin Z, Li Z, Li EN, et al. Osteochondral tissue chip derived from iPSCs: modeling OA pathologies and testing drugs. *Front Bioeng Biotechnol*. 2019;7(12):411.
doi: 10.3389/fbioe.2019.00411.

31. Ong LJY, Fan X, Sun AR, et al. Controlling microenvironments with organs-on-chips for osteoarthritis modelling. *Cells*. 2023;12(4):579.
doi: 10.3390/cells12040579.

32. Rothbauer M, Reihs EI, Fischer A, et al. A progress report and roadmap for microphysiological systems and organ-on-a-chip technologies to be more predictive models in human (knee) osteoarthritis. *Front Bioeng Biotechnol*. 2022;10(6):886360.
doi: 10.3389/fbioe.2022.886360.

33. Nu Aye KT, Ferreira JN, Chaweewannakorn C, et al. Advances in the application of iron oxide nanoparticles (IONs and SPIONs) in three-dimensional cell culture systems. *SLAS Technol*. 2024;29(3):100132.
doi: 10.1016/j.slast.2024.100132.

34. Wu KY, Tabari A, Mazerolle E, et al. Towards precision ophthalmology: the role of 3D printing and bioprinting in oculoplastic surgery, retinal, corneal, and glaucoma treatment. *Biomimetics (Basel)*. 2024;9(3):145.
doi: 10.3390/biomimetics9030145.

35. Jiu J, Liu H, Li D, et al. 3D bioprinting approaches for spinal cord injury repair. *Biofabrication*. 2024;16(3):032003.
doi: 10.1088/1758-5090.

36. Das S, Valoor R, Ratnayake P, et al. Bioprinting complex cartilaginous structures with clinically compliant biomaterials. *Adv Funct Mater*. 2015;25(48):7406-7417.
doi: 10.1021/acsabm.3c01194.

37. Schuurman W, Levett PA, Pot MW, et al. Gelatin–methacrylamide hydrogels as potential biomaterials for fabrication of tissue-engineered cartilage constructs. *Macromol Biosci*. 2013; 13(5):551-561.
doi: 10.1002/mabi.201200471.

38. Ávila HM, Schwarz S, Rotter N, et al. 3D bioprinting of human chondrocyte-laden nanocellulose hydrogels for patient-specific auricular cartilage regeneration. *Bioprinting*. 2016;1–2:22-35.
doi: 10.1016/j.bprint.2016.08.003.

39. Markstedt K, Mantas A, Tournier I, et al. 3D Bioprinting human chondrocytes with nanocellulose–alginate bioink for cartilage tissue engineering applications. *Biomacromolecules*. 2015;16(5):1489-1496.
doi: 10.1021/acs.biomac.5b00188.

40. Rastogi P, Kandasubramanian B Review of alginate-based hydrogel bioprinting for application in tissue engineering. *Biofabrication*. 2019;11(4):042001.
doi: 10.1088/1758-5090/ab331e.

41. Zhang X, Liu K, Qin M, et al. Abundant tannic acid modified gelatin/sodium alginate biocomposite hydrogels with high toughness, antifreezing, antioxidant and antibacterial properties. *Carbohydr Polym*. 2023;309(6):120702.
doi: 10.1016/j.carbpol.2023.120702.

42. Lai Y, Cao H, Wang X, et al. Porous composite scaffold incorporating osteogenic phytomolecule icariin for promoting skeletal regeneration in challenging osteonecrotic bone in rabbits. *Biomaterials*. 2018;153(1):1-13.
doi: 10.1016/j.biomaterials.2017.10.025.

43. Liu Z, Fang R, Meng Q The method of type II collagenase digestion can quickly obtain a large number of highly purified rat articular cartilage cells. *J Clin Rehabil Tissue Eng Res*. 2011;15(10):9323-9326.
doi: 10.3969/j.issn.1673-8225.2011.50.004.

44. Chen W, Xu Y, Li Y, et al. 3D printing electrospinning fiber-reinforced decellularized extracellular matrix for cartilage regeneration. *Chem Eng J*. 2020;15(2):122986.
doi: 10.1016/j.cej.2019.122986.

45. Wu Y, (William) Lin ZY, Wenger AC, et al. 3D bioprinting of liver-mimetic construct with alginate/cellulose nanocrystal hybrid bioink. *Bioprinting*. 2018;9(3):1-6. doi: 10.1016/j.bprint.2017.12.001.

46. Chung JHY, Naficy S, Yue Z, et al. Bio-ink properties and printability for extrusion printing living cells. *Biomater Sci*. 2013;1(7):763-773. doi: 10.1039/c3bm00012e.

47. Duan B, Hockaday LA, Kang KH, et al. 3D bioprinting of heterogeneous aortic valve conduits with alginate/gelatin hydrogels. *Biomed Mater Res*. 2013;101(5):1255-1264. doi: 10.1002/jbm.a.34420.

48. Ferris CJ, Gilmore KJ, Beirne S, et al. Bio-ink for on-demand printing of living cells. *Biomater Sci*. 2013;1(2):224-230. doi: 10.1039/c2bm00114d.

49. Skardal A, Atala A. Biomaterials for integration with 3-D bioprinting. *Ann Biomed Eng*. 2015;43(3):730-746. doi: 10.1007/s10439-014-1207-1.

50. Hu W, Wang Z, Xiao Y, et al. Advances in crosslinking strategies of biomedical hydrogels. *Biomater Sci*. 2019;7(3):843-855. doi: 10.1039/c8bm01246f.

51. Shanto PC, Al Fahad Md A, Jung HI, et al. Multi-functional dual-layer nanofibrous membrane for prevention of postoperative pancreatic leakage. *Biomaterials*. 2024;307(6):122508. doi: 10.1016/j.biomaterials.2024.122508.

52. Mohamadhoseini M, Mohamadnia Z. Alginate-based self-healing hydrogels assembled by dual cross-linking strategy: fabrication and evaluation of mechanical properties. *Int J Biol Macromol*. 2021;191(11):139-151. doi: 10.1016/j.ijbiomac.2021.09.062.

53. Miri AK, Khalilpour A, Cecen B, et al. Multiscale bioprinting of vascularized models. *Biomaterials*. 2019;198(4):204-216. doi: 10.1016/j.biomaterials.2018.08.006.

54. Bhaladhare S, Bhattacharjee S. Chemical, physical, and biological stimuli responsive nanogels for biomedical applications (mechanisms, concepts, and advancements): a review. *Int J Biol Macromol*. 2023;226(1):535-553. doi: 10.1016/j.ijbiomac.2022.12.076.

55. Giuseppe MD, Law N, Webb B, et al. Mechanical behaviour of alginate-gelatin hydrogels for 3D bioprinting. *J Mech Behav Biomed Mater*. 2018;79(3):150-157. doi: 10.1016/j.jmbbm.2017.12.018.

56. Caliari SR, Burdick JA. A practical guide to hydrogels for cell culture. *Nat Methods*. 2016;13(5):405-414. doi: 10.1038/nmeth.3839.

57. Mahmoudi C, Douma NT, Mahmoudi H, et al. Developing and characterizing a biocompatible hydrogel obtained by cross-linking gelatin with oxidized sodium alginate for potential biomedical applications. *Polymers (Basel)*. 2024;16(22):3143. doi: 10.3390/polym16223143.

58. Schwarz S, Kuth S, Distler T, et al. 3D printing and characterization of human nasoseptal chondrocytes laden dual crosslinked oxidized alginate-gelatin hydrogels for cartilage repair approaches. *Mater Sci Eng*. 2020;116(11):111189. doi: 10.1016/j.msec.2020.111189.

59. Zhao P, Deng C, Xu H, et al. Fabrication of photo-crosslinked chitosan gelatin scaffold in sodium alginate hydrogel for chondrocyte culture. *Bio Med Mater Eng*. 2014;24(1):633-641. doi: 10.3233/bme-130851.

60. Xu HQ, Liu JC, Zhang ZY, et al. A review on cell damage, viability, and functionality during 3D bioprinting. *Mil Med Res*. 2022;9(1):70. doi: 10.1186/s40779-022-00429-5.

61. Shi P, Laude A, Yeong WY. Investigation of cell viability and morphology in 3D bio-printed alginate constructs with tunable stiffness. *J Biomed Mater Res*. 2017;105(4):1009-1018. doi: 10.1002/jbm.a.35971.

62. Soltan N, Ning L, Mohabatpour F, et al. Printability and cell viability in bioprinting alginate dialdehydegelatin scaffolds. *ACS Biomater Sci Eng*. 2019;5(6):2976-2987. doi: 10.1021/acsbiomaterials.9b00167.

63. Coryell PR, Diekman BO, Loeser RF. Mechanisms and therapeutic implications of cellular senescence in osteoarthritis. *Nat Rev Rheumatol*. 2021;17(1):47-57. doi: 10.1038/s41584-020-00533-7.

64. Lou C, Deng A, Zheng H, et al. Pinitol suppresses TNF-α-induced chondrocyte senescence. *Cytokine*. 2020;130:155047. doi: 10.1016/j.cyto.2020.155047.

65. Arra M, Swarnkar G, Ke K, et al. Generation in chondrocytes is a potential therapeutic target for osteoarthritis. *Nat Commun.* 2020;11(1):3427. doi: 10.1038/s41467-020-17242-0.

66. Ma MW, Wang J, Zhang Q, et al. NADPH oxidase in brain injury and neurodegenerative disorders. *Mol Neurodegener.* 2017;12(1):7. doi: 10.1186/s13024-017-0150-7.

67. Liang H, Luo R, Li G, et al. The proteolysis of ECM in intervertebral disc degeneration. *Int J Mol Sci*. 2022;23(3):1715. doi: 10.3390/ijms23031715.

68. Coppé JP, Desprez PY, Krtolica A, et al. The senescence-associated secretory phenotype: the dark side of tumor suppression. *Annu Rev Pathol*. 2010;5:99-118. doi: 10.1146/annurev-pathol-121808-102144.

69. Sun Y, Wu Q, Dai K, et al. Generating 3D-cultured organoids for preclinical modeling and treatment of degenerative joint disease. *Signal Transduct Target Ther*. 2021;6(1):380. doi: 10.1038/s41392-021-00675-4.

70. Gao F, Xu Z, Liang Q, et al. Osteochondral regeneration with 3D-printed biodegradable high-strength supramolecular polymer reinforced-gelatin hydrogel scaffolds. *Adv Sci*. 2019;6(15):1900867.
doi: 10.1002/advs.201900867.

71. Gao F, Xu Z, Liang Q, et al. Direct 3D printing of high strength biohybrid gradient hydrogel scaffolds for efficient repair of osteochondral defect. *Adv Funct Mater*. 2018;28(13): 1706644.
doi: 10.1002/adfm.201706644.

72. Chen D, Wu JY, Kennedy KM, et al. Tissue engineered autologous cartilage-bone grafts for temporomandibular joint regeneration. *Sci Transl Med*. 2020;12(565):eabb6683.
doi: 10.1126/scitranslmed.abb6683.

ACCSCIENCE PUBLISHING

International Journal of Bioprinting

RESEARCH ARTICLE

Painting bio: A vector-based method for precise G-code generation across scales in biofabrication

Zan Lamberger[1], Camilla Mussoni[1], Nathaly Chicaiza Cabezas[1], Florian Heck[1], Sarah Zwingelberg[2], Sven Heilig[1], Taufiq Ahmad[1], Jürgen Groll[1], and Gregor Lang[1]*

[1]Department for Functional Materials in Medicine and Dentistry, University Hospital of Würzburg, Würzburg, Germany

[2]Laboratory for Experimental Ophthalmology I, Department of Ophthalmology, University Hospital Düsseldorf, Düsseldorf, Germany

Abstract

This study introduces a standardized approach to generating and assembling G-code for biofabrication, ensuring compatibility and convergence across diverse machines and scales. By using vector-based drawing software, such as Adobe Illustrator, shapes are designed as paths and converted into modular G-code blocks (subroutines). This vector-based approach allows for the straightforward design of complex structures, such as organic shapes, by simply drawing them to scale, avoiding the need for labor-intensive construction. These blocks are assembled into a final script with a modified version of Notepad++ that enhances code segmentation and provides real-time visualization. Unlike many commercial slicers, this method offers precise control over the print path—a critical advantage in biofabrication, where anisotropic structures are essential for directed cell growth and orientation-specific mechanical properties needed in biomimetic tissue design. The method's versatility is demonstrated across techniques from micro-scale applications, such as melt electrowriting, to macro-scale approaches like bioprinting, freeform printing, and in-gel printing. This process streamlines code generation, allowing both simple and complex shapes to be efficiently produced. Although paths are drawn in 2D, stacking layers enables 3D constructs. The method's standardized, relative G-code format—compatible with most devices—supports easy transfer across machines with clearly marked, machine-specific segments, creating a unified and adaptable codebase for a range of fabrication scales and techniques.

Keywords: Bioprinting; Freeform; Fused deposition modeling; G-code; Melt electrowriting

***Corresponding author:**
Gregor Lang
(gregor.lang@uni-wuerzburg.de)

Citation: Lamberger Z, Mussoni C, Cabezas NC, *et al.* Painting bio: A vector-based method for precise G-code generation across scales in biofabrication. *Int J Bioprint.* 2025;11(4):209-224. doi: 10.36922/ijb.6239

Received: November 18, 2024
Revised: December 11, 2024
Accepted: December 12, 2024
Published Online: December 12, 2024

Copyright: © 2024 Author(s). This is an Open Access article distributed under the terms of the Creative Commons Attribution License, permitting distribution, and reproduction in any medium, provided the original work is properly cited.

Publisher's Note: AccScience Publishing remains neutral with regard to jurisdictional claims in published maps and institutional affiliations.

1. Introduction

Biofabrication plays a crucial role in the development of *in vitro* test systems, tissue models, and organs by utilizing machines to automate the production processes. These machines, which include a wide range of computer numerical control (CNC)-based devices,[1] are central to biofabrication, enabling applications from 2D processes such as laser cutting to complex 3D techniques like melt electrowriting (MEW),[2] fused filament

fabrication (FFF),[3,4] and bioprinting.[5,6] Despite their versatility, these machines require carefully choreographed movements, necessitating the creation of corresponding movement codes. The standard input for these machines is G-code, which combines machine-specific commands with movement instructions for the axis motors. These movements are typically input as coordinates, either absolute or relative, meaning that the system must generate or deduce the trajectory that the machine should follow.[4] For simple movements, such as bioprinting evaluation patterns[7–9] or basic MEW grids,[10] it is possible to manually write coordinates. However, this approach becomes cumbersome, prone to errors, and time-consuming, particularly when scaling or adjusting complex shapes. In these cases, parametric coding is often used, where mathematical functions allow for quick adjustments such as scaling, rotating, or adding grids by modifying a few parameters.[11] However, while parametric methods are effective for certain geometries, they face challenges with programming complex shapes, non-repetitive elements, and high precision. Furthermore, these methods often require significant mathematical competence and may not be compatible with all machines, making them less flexible. Some programs, such as Full Control G-code,[12] allow for the generation of code for specific shapes but are still limited in their ability to handle irregular or highly complex designs.

Some academic groups have developed G-code generators for bioprinting and MEW based on algorithmic shapes of a geometrical unit repetition/in sequence[13–15]; however, these tools lack in freedom of designing un-patterned and irregular shapes, or shapes that were not considered by the developers. On the other end of the spectrum are 3D shapes, for which slicers are commonly used, such as those employed in fused deposition modeling (FDM) 3D printing. The slicer converts a 3D mesh into a sequence of horizontal paths that the machine follows to fabricate the object, optimizing the trajectory based on the slicer's established parameters for efficient production.[9,16] While these slicers are useful for regular FDM 3D printing, they are limited by their design parameters and cannot be easily adapted for other biofabrication techniques where more control is required. For example, while there may be parallels between FDM and 3D extrusion bioprinting, the paths and deposition patterns for plastic FDM-printed objects are vastly different from those required for bioprinted tissues, especially considering factors like cell orientation and material properties, limiting the use of FDM slicers for bioprinting applications. While some bioprinters also have their own integrated slicing software that is better adapted to bioprinting,[17] the programs still falter when attempting to produce complex printing geometries, unusual infill patterns, irregular printing sequences, etc., which were not conceived/predicted by the developers. Despite the ability to precisely tune the printing parameters by adding breaks, printhead swaps or modifying extrusion/pressure on certain parts of the print are often not granted. This leaves the users without any reasonable alternatives for achieving/fine-tuning their desired print.

Alongside the challenge of generating G-code, there is a lack of standardized approaches compatible with the diverse machines used in biofabrication.[14,17–19] For example, while both bioprinters and MEW devices are three-axis CNC machines, their G-code generation methods differ significantly. This means that operators must relearn how to generate codes for each device, complicating the transfer of designs and hindering the convergence of different fabrication techniques into a unified system. Converging these methods is essential for biofabrication, as tissues are hierarchical structures that require precise control at multiple scales.[20–22] Achieving this integration allows for the accurate fabrication of complex tissues, from micro-scale cellular patterns to macro-scale tissue layers.

Additionally, using absolute coordinates makes transferring designs or adjusting starting positions challenging, as each coordinate needs recalculating or re-slicing the object entirely. This highlights the need for more adaptable, standardized approaches to streamline the transfer of designs across different biofabrication techniques.

We present a versatile and intuitive method for generating G-codes by drawing paths in vector-based programs, such as Adobe Illustrator. These paths are converted into relative G-code blocks and assembled into the final script using the text editor Notepad++, where machine-specific commands and necessary instructions are added. This approach provides full control over shapes, enabling the quick generation of both simple and complex geometries, while allowing easy adjustments and parameter changes. It is user-friendly, making it accessible to less experienced users without deep programming knowledge, and streamlines the process, reducing time on development, and troubleshooting. Although paths are drawn in 2D, stacking layers or modifying designs allows for 3D constructs, facilitating complex structures.

Herein, we demonstrated the new method's advantages and precision in various biofabrication techniques, including MEW, FDM, freeform printing, and bioprinting. This approach ensures flexibility and control, enabling the creation of intricate geometries and precise patterns tailored to each technique. It also promotes convergence in biofabrication by facilitating code transfer across different

machines, as the format—comprising alternating relative G-code blocks and machine-specific segments—is widely interpretable. Using vector graphics simplifies the creation of complex organic structures, which would otherwise require intricate calculations, making the method scalable from micro-scale applications like MEW to macro-scale bioprinting, offering a unified, standardized approach across biofabrication methods

2. Materials and methods

2.1. Materials

If not stated otherwise, all chemicals were supplied by Carl Roth GmbH + Co. KG Karlsruhe, Germany in analytical grade.

2.2. Path drawing and exporting

The paths were drawn using Adobe Illustrator. Most lines and strokes consist of paths and can be segmented accordingly using the cut path or merge path functions when selecting the anchor points. The arrowheads were added to the path endpoints and the path directions inverted if the arrowhead was not at the endpoint. Each of the paths was separately exported as a .dxf file by selecting it and going to the export option and saving as .dxf.

2.3. Path conversion to relative G-code

The exported paths were converted to relative G-code using the provided code converter program "Easy DXF stack generator" (EDSTAG) (description in the Supplementary File) through a drag-and-drop approach, thereby converting the .dxf files to a .txt document containing the code. Using the "Check dependencies" button in the EDSTAG interface, the necessary components Notepad++ and EDSTAG can be checked and automatically updated/downloaded for the following workflow.

2.4. Code assembly

The relative G-code segments (subroutines) were copy-pasted into Notepad++ modified with a custom coding language (download available in the Supplementary File), which allows ;{ and ;} signs to define segments of the code as collapsable units. The G-code segments were hence arranged accordingly and commented with these; the machine commands and other relevant G commands were also added here. With the use of the NCnetic plugin (https://ncnetic.com) for Notepad++, the codes could be visualized as print paths as a further point of quality control.

2.5. Addition of extrusion and gradual Z-increase

The desired extrusion and Z-increases per code segment were added by defining these at the start of the subroutine in Notepad++ by commenting these with ;EBSTART:*extrusion factor* (mm^3/mm) and at the end ;EBSTOP. The Z-increase per segment was defined with ;ZBSTART:*total height increase* (mm/block) and ended with ;ZBSTOP. The .txt/.gcode file was then dragged into the provided conversion program, and the E and Z added/calculated for the segments.

2.6. Production of grid polycaprolactone MEW scaffolds

Polycaprolactone (PCL) box scaffolds were produced using MEW. The printing was conducted at a room temperature of 20 °C with 40% humidity, a PCL (Purac PC12, Corbion, Amsterdam, the Netherlands) melt temperature of 95 °C, a pressure of 1 bar, and a print bed movement rate of 1000 mm/min onto a grounded steel build plate covered by a thin water-soluble poly (vinyl alcohol) (PVA; 30–70 kDa, Merck KGaA, Darmstadt, Germany) coating a 2.5 kV voltage difference applied over the 30 G needle (Nordson EFD, Ebensfeld, Germany), at a printing distance of 1.4 mm. Before application, the PVA was dissolved using 70% ethanol. The scaffolds were removed, washed in 70% ethanol, and dried.

2.7. MEW of complex shapes

Complex geometry PCL scaffolds were produced and printed at a room temperature of 20 °C with 40% humidity, a PCL (Purac PC12, Corbion, Amsterdam, the Netherlands) melt temperature of 95 °C, a pressure of 1 bar, and a print bed movement rate of 50–70 mm/s onto a grounded steel build plate, with 3.5 kV voltage difference applied over the 22 G needle (Nordson EFD, Ebensfeld, Germany), at a printing distance of 2.2 mm. The wolf pattern was produced using similar parameters, except that a 25 G needle (Nordson EFD, Ebensfeld, Germany), a pressure of 2 bar, and a speed of 120 mm/s were used, with pauses added between segments where needed.

2.8. FDM printing onto scaffolds

The scaffolds were laser-cut based on the red-drawn pattern (Rayjet, Trotec, Plymouth, MA, USA). The speed and intensity of the laser were varied to achieve a complete separation of the remaining scaffold. The scaffolds were then reinforced as previously described,[23] with polylactic acid (PLA; Form Futura, Amsterdam, the Netherlands), using a 0.4 mm nozzle, a layer height of 0.28 mm, and a nozzle temperature of 180°C. The fine scaffolds were printed using a 0.1 mm nozzle and PCL (Facilan Ortho, 3D4makers, Haarlem, The Netherlands) filament at a nozzle temperature of 130°C.

2.9. Freeform printing

Freeform printing was conducted at a room temperature of 20°C with 40% humidity, using a poly-2-propyloxazoline (n = 100 units, synthesized as described previously[24]) at a melt temperature of 210°C in a syringe, a pressure of 1 bar

using nitrogen, and a print bed movement rate of 30 mm/s using a 20 G steel needle.

2.10. 2D and 3D extrusion bioprinting

Pluronic F-127 (KGaA, Darmstadt, Germany) at a concentration of 30% w/v in water was printed using an Inkredible+ bioprinter (Cellink Bioprinting AB, Gothenburg, Sweden) equipped with a 25 G conical nozzle (Nordson EFD, OH, USA). The different colors were achieved by adding food dye. For the print with the fibers, PCL fibers with a size of 15 × 300 µm, produced as described previously,[25,26] were added to the pluronic at a 2% w/v ratio.

2.11. Embedded bioprinting

Printing was conducted into a cubical container filled with the support bath consisting of 1% w/v xanthan gum (Cosphaderm X34, Cosphatec GmbH, Hamburg, Germany). The ink used was 1% w/v xanthan gum, stained with different colorings. Printing was conducted using a BioX (Cellink Bioprinting AB, Gothenburg, Sweden) equipped with a 20 G 45-mm long syringe nozzle (Nordson EFD, OH, USA).

2.13. Scanning electron microscopy

The samples were analyzed using a scanning electron microscopy (SEM) device (Crossbeam CB 340 SEM, Carl Zeiss).

3. Results and discussion

3.1. General principle and code processing

The drawing-coding method involves defining the paths that the machine should follow. These paths can be drawn as a continuous line or as several connected segments, with the direction and sequence of points specified. The paths are then exported and converted into relative movement codes in G-code. In this case, we used Adobe Illustrator, but other vector drawing software that can export separate paths such as .dxf files may also be used. The entire workflow is straightforward, as illustrated in Figure 1A, starting with drawing the paths as lines in Illustrator. Illustrator is preferred because manipulating the lines and paths is convenient; anchor points can be added to split or combine paths, as shown in Figure 1B. The direction of the paths can be indicated by adding arrowheads, and the thickness of the lines can be adjusted to simulate the width of the deposited fiber or strut, making the visualization of the print more realistic. Additionally, many researchers are already familiar with or have experience using this software for creating manuscript illustrations.

The paths are exported as .dxf files and then converted into relative G-code blocks using the self-developed code converter "Easy DXF stack generator" (EDSTAG). These files can be quickly converted via drag-and-drop or by opening them from within the program, as shown in Figure 1C. The EDSTAG simplifies the .dxf to relative G-code conversion, exporting only the necessary relative G-code that most devices can interpret, without any extraneous commands beyond the coordinates. The software utilizes the free tool dxf2gcode for the file conversion, automating the process and filtering out unnecessary code for our specific workflow. While the user does not need to interact with dxf2gcode directly, it can remain open for troubleshooting purposes. The direction of the paths is shown in the EDSTAG using arrows, and the direction can be reversed if needed by selecting the "Invert direction" option in the program.

These blocks of code can then be copied into Notepad++ and assembled. Notepad++ is modified with a custom coding language, provided by the authors in the Supplementary File, to simplify G-code writing, as demonstrated in Figure 1D. This modification allows users to define collapsible code segments using demarcations like ;{ and ;} to mark the start and end of each segment, respectively. These markers also function as comments, so the machine ignores these lines. This feature improves the readability of the code, as subroutines can be neatly organized, segmented, and collapsed. Additionally, collapsible segments within other segments can also be defined.

Each relative G-code block defining a path can be treated as a subroutine. Using relative code makes it easier to control movement, repetition, multiplication, and other actions, while also facilitating the combination of different path segments and subroutines. Between subroutines, additional commands—such as absolute starting coordinates, breaks, speed changes, and pressure adjustments—can be inserted as needed. In most cases, the G91 command must be added before the segments to instruct the machine to interpret the code as relative, rather than the default G90 for absolute coordinates. Similarly, continuous paths can be split into several segments to allow for the insertion of additional commands between them. Since the subroutines are all exported as G-code with G1 movement codes, they can be interpreted by most CNC machine-based devices. The device-specific commands can be added later, before or after the subroutines, to assemble the final functional code.

Additionally, by using the NCnetic plugin, the code can be visualized in real time, as shown in Figure 1E. After assembling the code, it can be exported as is, or, if necessary, extrusion and Z-increase modifiers can be added to specific code segments by designating them in Notepad++. This is similar to the previously mentioned

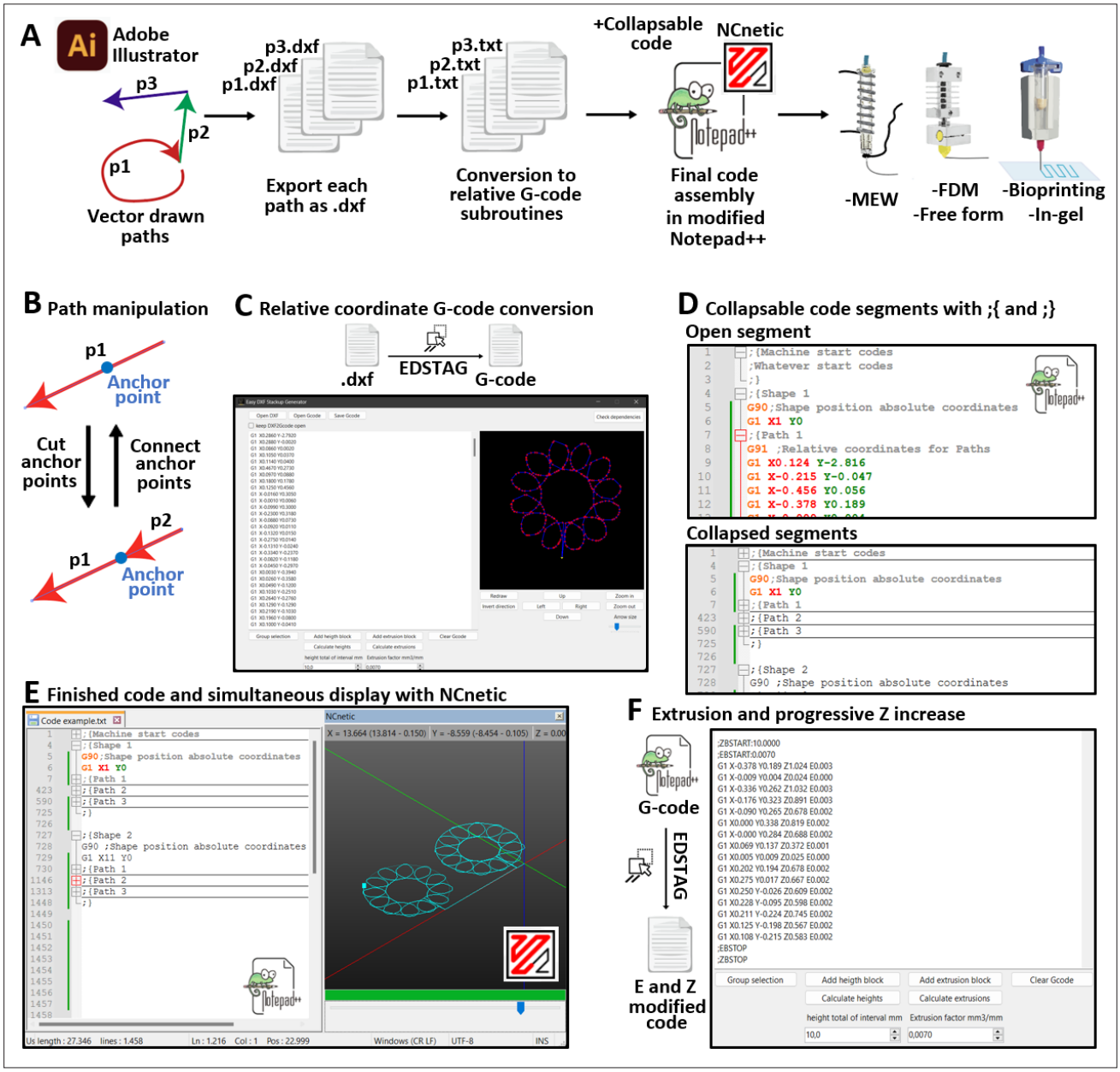

Figure 1. Working principle of the drawing to G-code conversion and the assembly thereof. (A) Schematic figure of the steps involved in the conversion process. (B) A simple depiction showing how paths in Adobe Illustrator can be manipulated by using anchor points and cutting/connecting them to generate more separate paths to export. (C) Schematic depiction showing the conversion of .dxf files of the paths into relative G-code by drag-and-drop approach into the provided converter "Easy DXF stack generator" (EDSTAG), as shown as shown in the respective screenshot. (D) Example of composed relative G-code and other code features in Notepad++, segmented into collapsable sections using the defined markers at the start and end of the segment. (E) Example of a short, finished code in Notepad++, with collapsed sections, using the display function of NCnetic to visualize the print paths. (F) Schematic displaying the addition of E and increasing *Z* height per segment using the designated text prompt before and after the segment and then dragging the modified .txt file into the EDSTAG again to calculate these or add these directly in EDSTAG. Abbreviations: FDM, fused deposition modeling; MEW, melt electrowriting.

demarcations for collapsible code segments but is defined using ;EBSTART:extrusion factor (where the extrusion factor, which is the amount of extrusion per mm, must be calculated by the user as it varies between machines) and ends with ;EBSTOP. This means that the segment and amount of extrusion therein can be defined/adapted this way. Similarly, when wanting to add segments where the *Z* gradually increases per segment, such as for diagonally ascending lines or spirals, the *Z*-increase per segment is defined with ;ZBSTART:total height increase in mm and ends with ;ZBSTOP. Both of these commands can alternatively be added by using the "Add extrusion block" or "Add height block" functions in the EDSTAG, whereby the extrusion factor and *Z* height can be input directly in the designated fields in the program. In both cases, either by importing the code with the designated Z- and E-block commands, or doing it locally in EDSTAG, the EDSTAG can then automatically calculate the extrusion (*E*) and *Z* height values for these blocks based on the extrusion factor or height of the interval, by clicking the "Calculate extrusions" and "Calculate heights" buttons, as illustrated in Figure 1F.

This method of generating codes is intuitive, and because it is based on relative G-code blocks, it is easy to adapt the code for use on different devices, as also demonstrated by the variety of different machines used herein shown in Figure S1, Supporting Information. This flexibility is particularly beneficial for machines that interpret non-G1 commands differently or cannot process anything beyond simple movement codes. The drawing and subroutine approach significantly simplifies the horizontal transfer of codes between various biofabrication devices, compared to complex programmed and parametric codes. Moreover, it enhances the convergence capabilities of different fabrication methods and machines.

3.2. Application and practical examples for use in MEW

3.2.1. Melt-electrowritten grids

In biofabrication, many substrates are composed of melt-electrowritten meshes with various geometries, such as boxes, triangles, and other variations of these shapes.[10,27] For simpler cases, it is common to manually write the coordinates or create parametric, adaptable designs. However, the drawing approach presented in this paper can also be conveniently applied to these tasks. A single layer of the repetitive grid structure can be drawn, with the paths connected into a continuous pattern, defined as a subroutine, and repeated for each layer as needed. Commands such as pressure or speed changes can also be integrated between separate layers or within sections of a layer, as demonstrated in Figures 2A and S2, Supporting Information. It is helpful for each layer to start and end at the same point to ensure consistent alignment. Additionally, different layer structures can be intermixed to create more complex scaffold shapes. The method's advantages become more apparent when dealing with more complex grid structures that are challenging to write manually, such as intersections at 45° that should meet at the center of a box, as shown in Figure 2B. One key benefit is that the geometries are visible before printing, allowing for a clearer preview of the result. The repetition of layers and the combination of different patterns can be visualized beforehand, facilitating the generation of more intricate shapes, such as hexagon-like patterns with a single box layer crossing through them, as shown in Figure 2C. Furthermore, the shapes can be easily scaled or transformed in the vector drawing software, making it simple to adjust the design as needed.

3.2.2. Complex melt-electrowritten shapes

The major advantages of the drawing method become especially evident when working with more complex shapes. MEW is not only capable of producing fine grids but also larger, more intricate scaffolds using thicker fibers—tasks that are otherwise difficult to program manually. Combining this with a vector drawing program offers additional benefits, such as the ability to draw the code over an image to scale, as demonstrated with a cornea membrane reinforcement printed, as shown in Figure 3A. Furthermore, the software allows for easy adaptation and transformation of the drawn shape into different configurations, such as changing a round structure into a square, as shown in Figure 3B.

The drawing method is particularly advantageous for creating non-repetitive shapes or those with paths that are difficult to conceptualize and therefore hard to code using conventional methods. For instance, the spiral pattern with loops in Figure 3C exemplifies a complex design that would be challenging to program through other means. Additionally, hand-drawn patterns can be seamlessly converted into code using this approach, as demonstrated with the rose design in Figure 3D. This type of pattern would be impossible to generate using parametric or function-based programming and can only be created by tracing or transferring individual points.

Another versatile feature of the method is its ability to convert text into an outline and connect the paths accordingly to form a printable design, as shown in Figure 3E. More complicated shapes, like the wolf design in Figure 3F, can be broken down into multiple paths, with distinct pauses or varying speed settings for each path, offering more control over the parameters and improving print quality. The method also benefits from Illustrator's

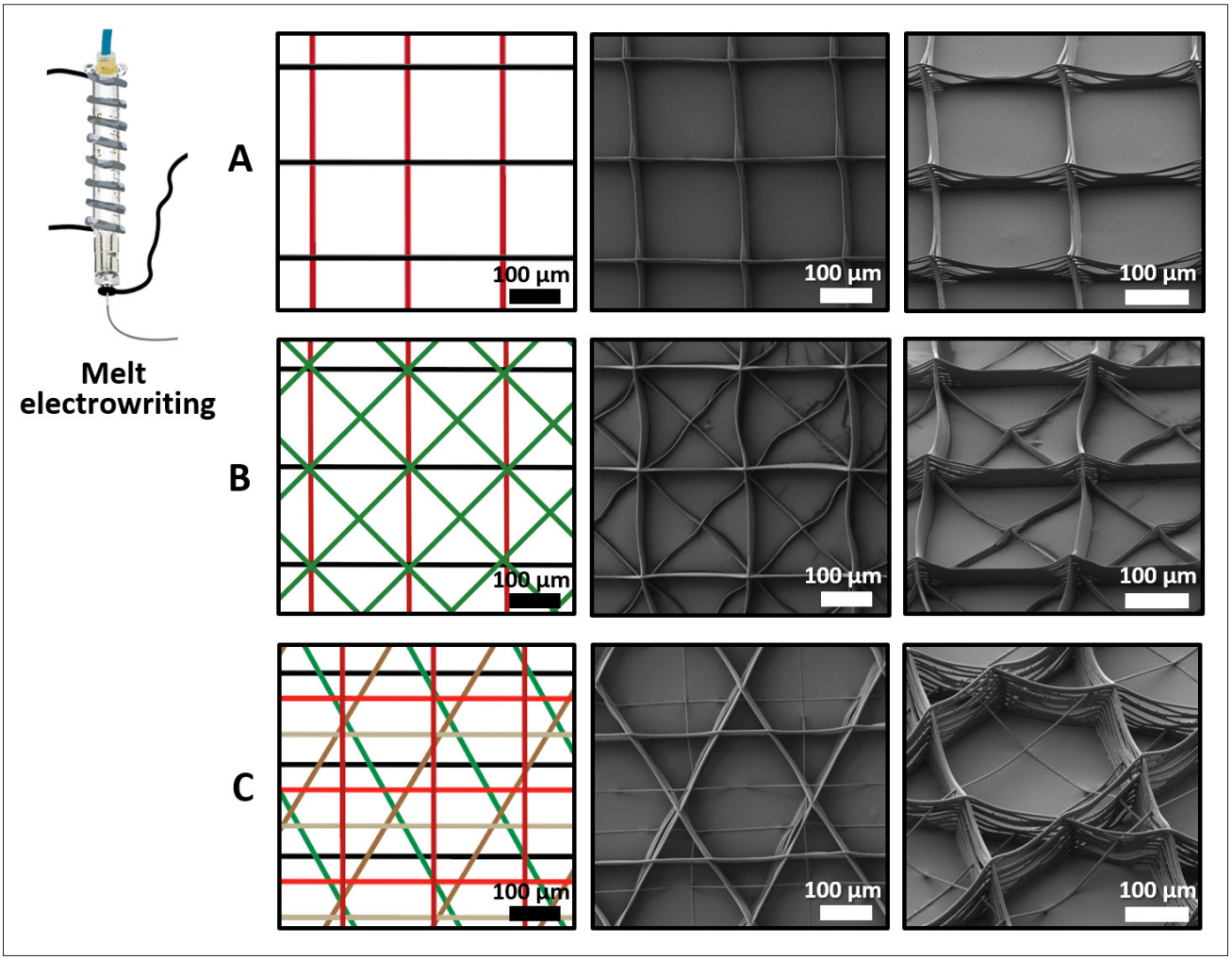

Figure 2. Basic grid-shaped melt-electrowritten scaffolds. Illustrations of the scaffold lattices in the vector drawing program on the left and their printed equivalents from a top and side view in the middle and right, respectively. (A) An example of a simple box-shaped scaffold. (B) A box-shaped scaffold with fibers crossing over in the middle of the box in the lower layers. (C) A hexagon-like scaffold with an intersecting hanging fiber layer.

built-in functions, such as Image Trace, which can convert images into vector graphics. These vector images consist of paths that can be combined or simplified, enabling quicker generation of the desired print shape. This was demonstrated with the conversion and printing of the institute's logo in Figure 3G and H.

3.3. Applications of FDM 3D printing in laboratory

Fused deposition modeling (FDM) 3D printing is a widely used technique that relies on CNC-based programming. Although FDM slicing programs can print most objects, they have limitations in terms of adaptability. In certain scientific or production applications, the slicing algorithm may not produce an ideal path or printing sequence. For example, when reinforcing electrospun or MEW substrates with FDM, the slicer generates a sequence of prints that may not be compatible with the specific requirements of the application.[23] If the code is generated by the slicer, the sequence in which the rings are printed is determined by the program's algorithm, which may not be compatible with our application, as exemplarily shown in Figure S3A, Supporting Information. Moreover, the printhead may travel over areas that should not be exposed to heat, as the slicer cannot anticipate where subsequent prints will be, and there is no better pathfinding option available. Using the drawing-to-G-code method, these problems can be resolved by manually drawing the rings and the paths in between them, thus defining the proper printing sequence, as demonstrated in Figure 4A. This method also facilitates the combination of multiple technologies. For example, if the substrate is laser-cut before FDM printing, the reinforcements can follow the same geometry, and the

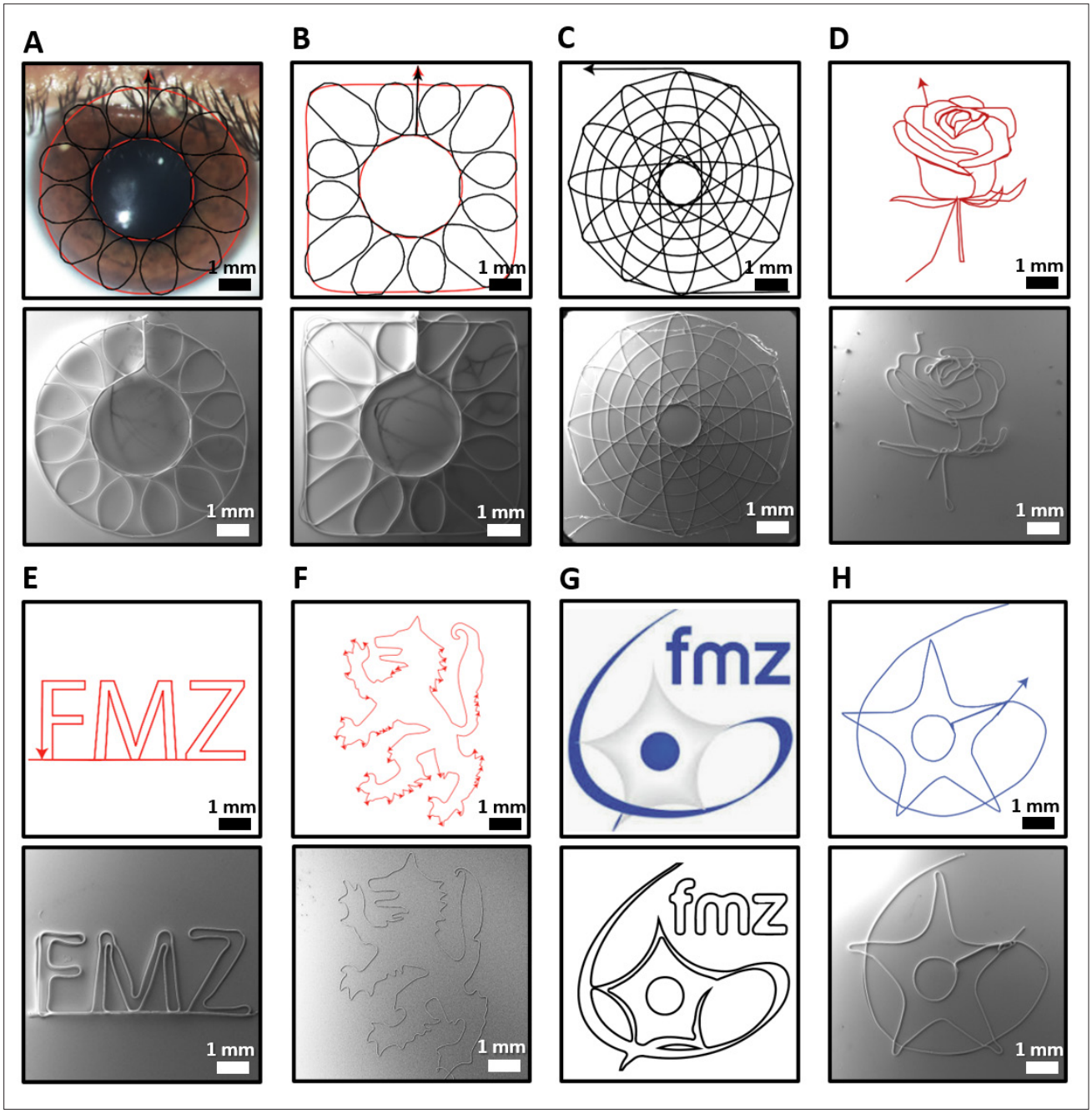

Figure 3. Utilization of the drawing method for melt-electrowriting complexer shapes. The drawn paths are shown above the printed equivalents. (A) A cornea-shaped scaffold. (B) The cornea-shaped scaffold transformed to a square instead of round shape. (C) A complex continuous spiral pattern. (D) A rose made by hand drawing the path in the illustration program, which was then printed as such. (E) Text connected to make an uninterrupted shape and the printed example. (F) A wolf emblem outline consisting of several paths for adding pauses in between. (G) The institute's logo and its conversion to an outline made of paths. (H) Shows a simplified version of the institute's logo, which has been converted into a printable vector. The result of MEW is depicted in the SEM is shown below. Abbreviations: MEW, melt electrowriting; SEM, scanning electron microscopy.

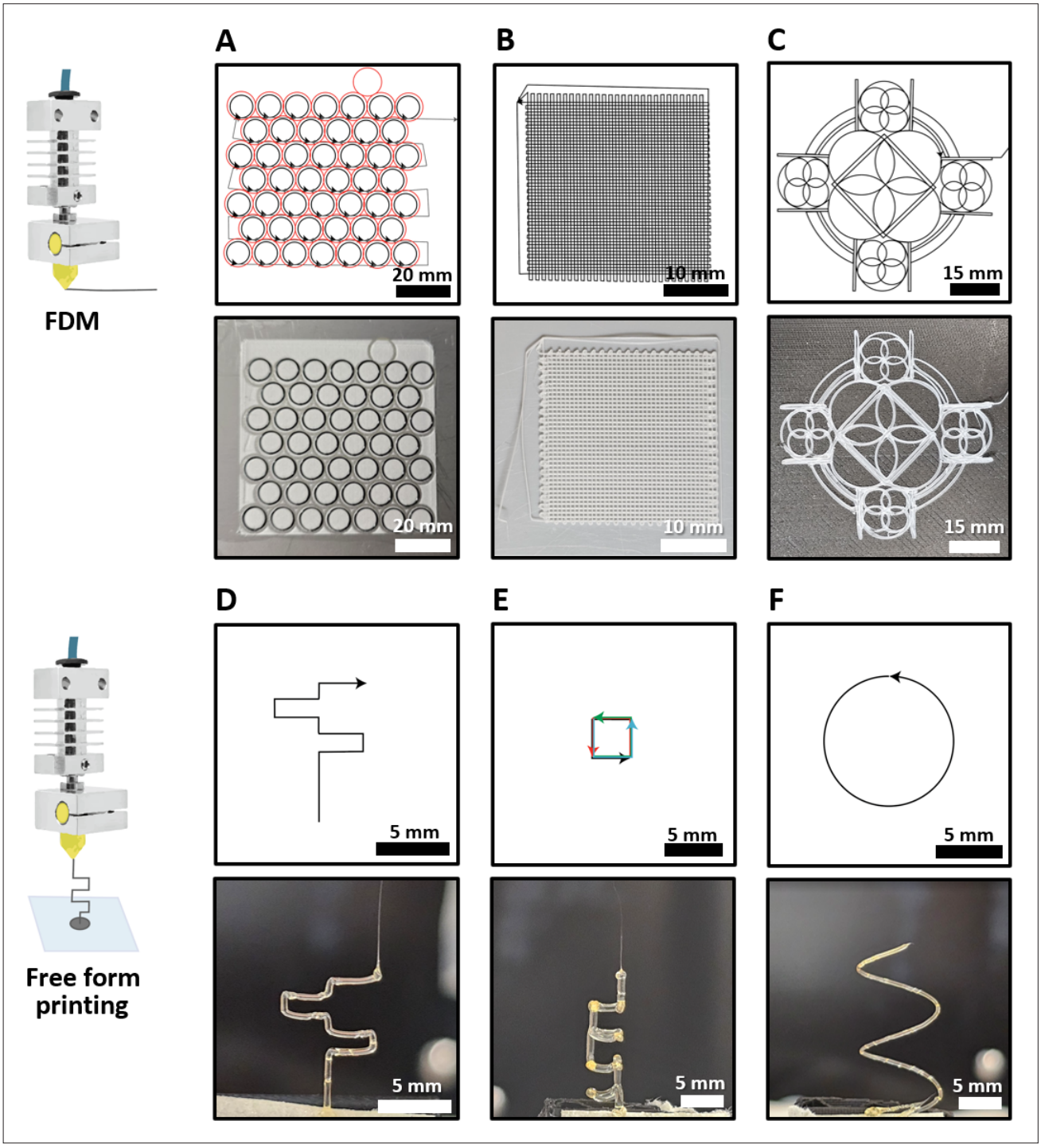

Figure 4. Application in fused deposition modeling (FDM) and freeform printing. (A) The pattern for a laser cutter in red as well as the black path for FDM-printing reinforcement rings after laser cutting, with only the circular parts of the black pattern being extruded; the printed result is shown beneath the illustrative picture. (B) A continuously printed grid pattern and pore size of 200 μm, as well as (C) a complex continuous pattern with a fiber diameter of 0.1 mm. Various freeform-printed shapes are generated by (D) exchanging the *Y*- for *Z* axis commands or (E) adding *Z* steps between different planes of the drawing or (F) through a gradual increase in *Z* along the whole shape.

pattern for both the laser cutting and the FDM process can be the same illustration. This approach eliminates the need for separate design phases in different programs.

Another scenario where regular FDM slicers struggle is when processing objects such as grid structures or lattices with small strut diameters, which are best printed as a continuous pattern. In contrast, traditional slicers require the printhead to jump between segments and start extrusion multiple times per layer, leading to poor bed adhesion, reduced print quality, stringing, and weaker scaffold strength, as shown on the sliced version of a grid in Figure S3B, Supporting Information. Using the drawing method, these codes can easily be generated, not only for simple grid structures, as shown in Figure 4B, but also for more complex shapes, as demonstrated in Figure 4C.

The ability to surpass the limitations of conventional slicers is also crucial for freeform printing techniques, such as the one demonstrated with polyoxazolines,[28] where pathfinding and complex 3D structures are too difficult for traditional layer-by-layer FDM slicers to process, resulting in incorrect prints. In this case, we used the method to print structures initially drawn in the *X*–*Y* plane, with the *Y*-coordinate replaced by *Z*, to create a 3D structure in the *X*–*Z* plane, as shown in Figure 4D. This principle can also be applied to scaffold segments, enabling the printing of lattices that are flexible in the *X*, *Y*, and *Z* directions, as demonstrated in Figure 4E. Similarly, a progressive increase in *Z* height can be added to code segments, provided the desired height range and the start and end of each segment are defined, typically for the entire subroutine or path section. This approach allows for the programming and printing of shapes like spirals and arches, as shown in Figure 4F.

3.4. G-code conversion used for extrusion-based bioprinting

One aspect of extrusion-based additive manufacturing is the processing of liquid materials such as silicon, elastomers, or hydrogels such as bioinks, which are applied in the field of bioprinting.[29,30]

3.4.1. 2D bioprinting shapes

In the field of biofabrication using biomaterial inks or bioinks, different aqueous-based scaffolds are produced with the aim of inhabiting them with cells.[31,32] These range from simple 2.5D shapes meant to primarily assess printability of the ink or cell survival,[8,33] to more complex grids or actual organ or tissue-shaped structures intended as drug testing alternatives or tissue replacements. Simple structures consisting of one layer or only a few layers can be drawn in Adobe Illustrator and assembled as shown in the previous sections. Some desired printing patterns can be drawn as only one continuous path and printed as such. For example, a simple meandering pattern in Figure 5A, such as the one used for assaying ink/printing properties, or even complicated shapes such as the outline of a heart in Figure 5B, can be produced. Splitting the illustration into several paths also enables toggling of the extrusion in between these, turning it off and on again when desired, as shown in Figure 5C. The toggling of the extrusion depends on the machine that is used but can usually be done by either adding/removing the E command to each G1 where it should extrude, or adding the pressure on/off commands, which are often machine-specified with a pressure quantity. Shapes can also be stacked into several layer constructs or used conveniently for multimaterial printing approaches with more than one extruder as in Figure 5D and a detailed rundown shown in Figure S4, Supporting Information. Therefore, for instance, having the ability to use different colors for each path/printhead makes the whole process and patterns more comprehensive and intuitive. The swapping of the printhead can then just be added in the code before the corresponding paths are followed and *vice versa* for swapping back to the original printhead. For maintaining the correct positioning, the simplest way is to have the start point of each printhead kept the same and then drawing a path to the point at which the extrusion should start. Another alternative is to accommodate for the difference in printhead position and just continue with the second printhead at the position the previous one left of.

The ability to draw the paths freely also allows for the creation of custom infill patterns, which can mimic the alignment of collagen fibers or muscle fibers in tissues, such as in the example of the heart shown in Figure 5E. By controlling the start and stop of extrusion, adjusting printhead movements, and customizing the infill and other paths, complex prints can be generated quickly—prints that would otherwise be very time-consuming to create. An example of this is the institute logo with infill and dual-material extrusion shown in Figure 5F. In general, the method allows for the effortless tracing and printing of even complex shapes. With full control over the printing paths, tissue alignment in the direction of printing can be optimized, such as by incorporating fibers as guiding structures for cells.[33,34] as demonstratively shown with fibers aligned in Figure 5G.

3.4.2. 3D bioprinting

3D bioprinting enables the generation of several-layer constructs, with the working principle remaining the same as previously described. An increase in the *Z* direction is added between each layer. The advantage over conventional slicers in these applications lies in the full control over

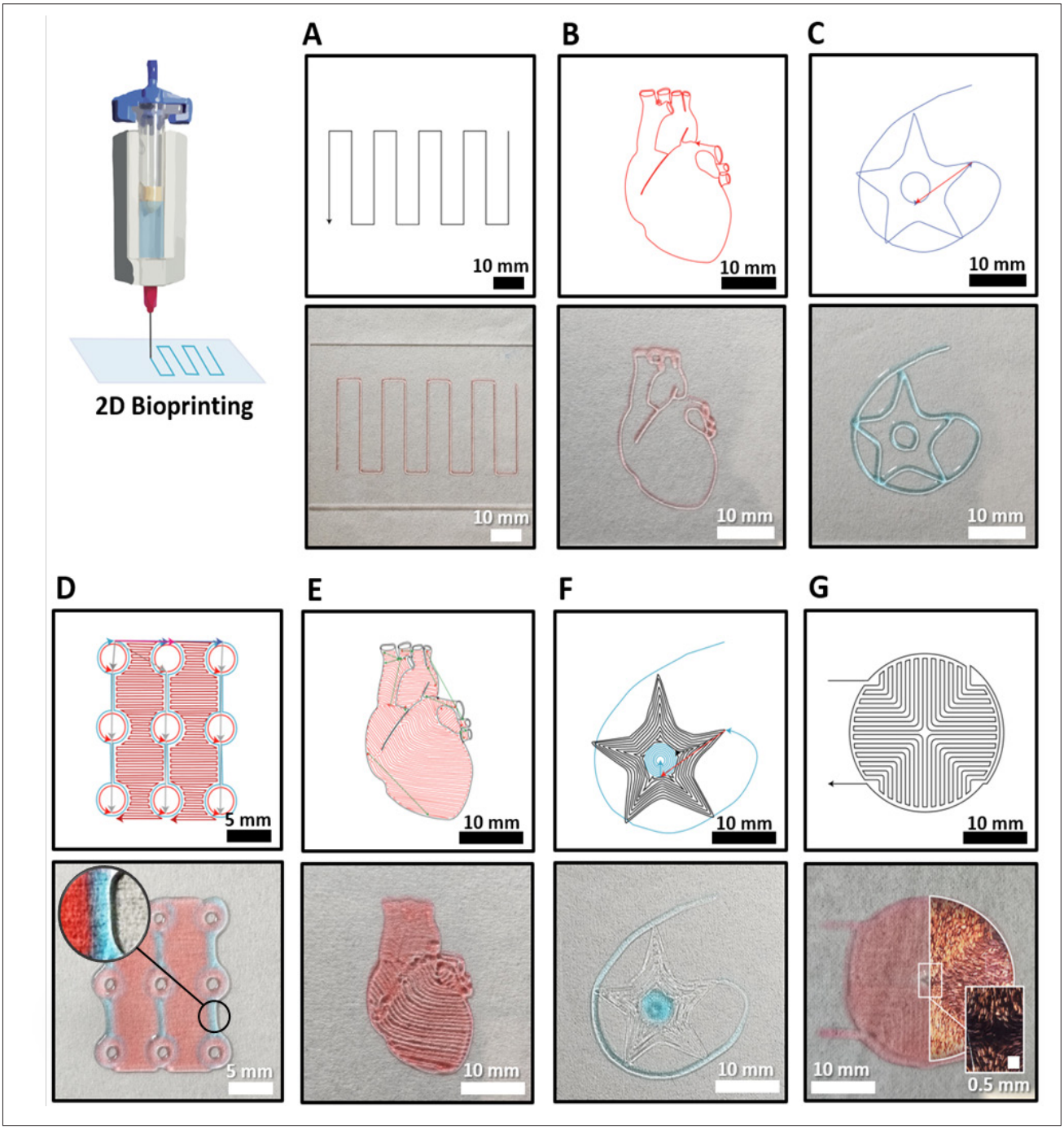

Figure 5. Vector drawing for 2D bioprinting applications. (A) A simple meandering pattern. (B) The outline of a heart drawn and printed. (C) The outline of the department logo. The drawn blue part is extruded while the red line is the unextruded print path. (D) A pattern printed with two different materials. The colors of the paths correspond to the different materials used, with additional travel paths drawn from the origin for each of the sections. The magnified inset shows the interface of the two materials with increased contrast, offering a clearer view of the transition. (E) A 2D heart shape with the red infill mimicking different tissue directions and connecting paths between the sections drawn in green. (F) The institute logo with a drawn infill pattern, printed with two materials, with the unextruded connecting path drawn in red. (G) A concentrically arranged pattern with an additional 15 × 300 µm polycaprolactone (PCL) fibers aligned during printing.

infill direction and shape, as well as the sequence and path direction.

To illustrate this code-generation approach, several exemplary bioprinted structures were created on glass slides. For example, when generating structures that require a specific shift in orientation in the direction of the layer infill lines—such as those mimicking collagen or cell alignment in tissues like the cornea or heart—this method proves beneficial.[35,36] As demonstrated in Figure 6A, a

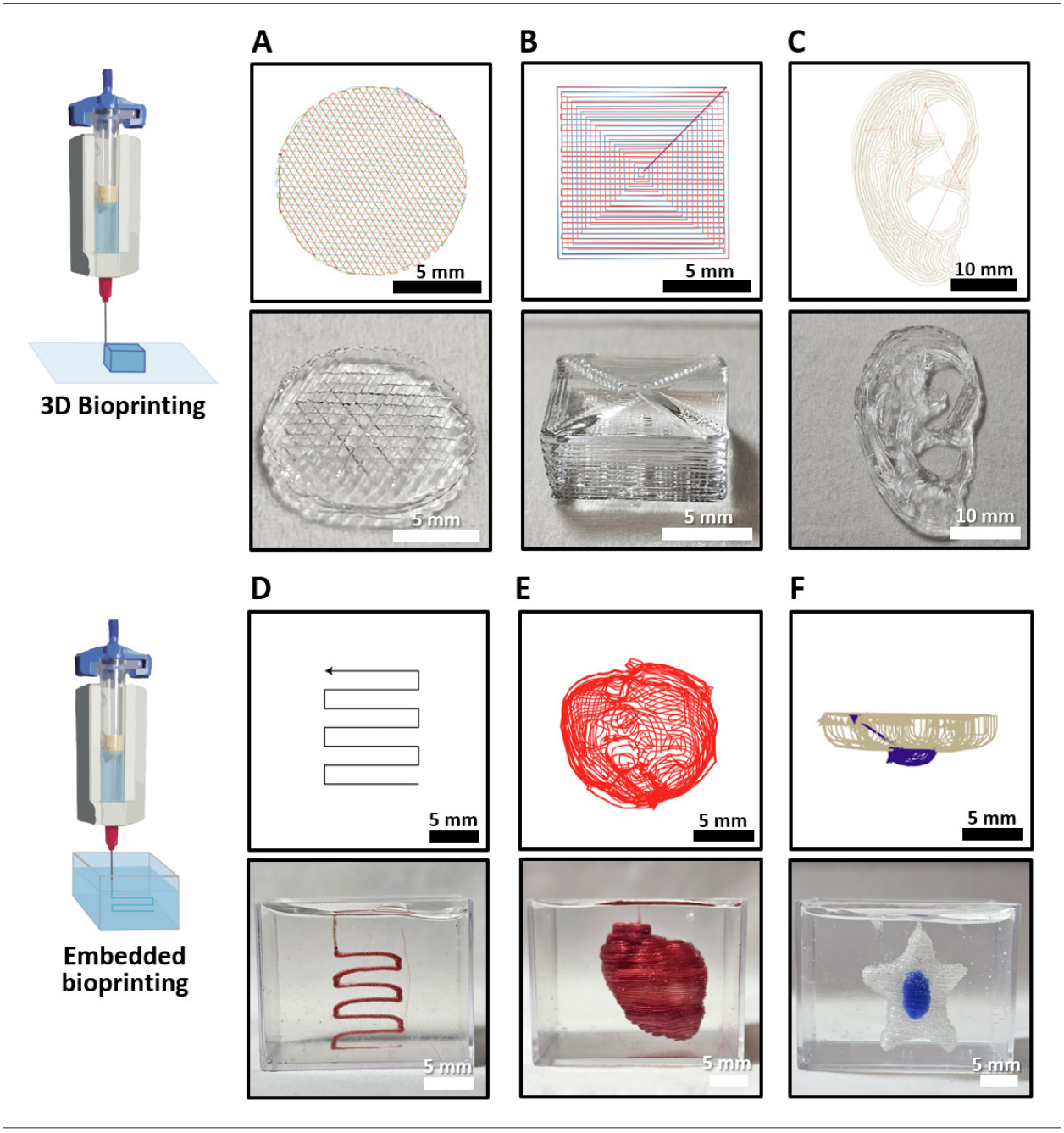

Figure 6. Use of the path drawing method for generating 3D bioprinting codes. (A) A three-layer circular print with the printing path shifted by 45° for each layer. (B) A cubical print with the spiraling blue top/bottom pattern and the red solid infill pattern. (C) An ear printed in several interconnected layers, with unextruded connecting paths drawn in red. Embedded bioprinting of a (D) meander in the *Z* direction by swapping the *Y* for *Z* coordinates, and (E) a 3D heart printed layer by layer, with each layer drawn separately. (F) The 3D cell from the institute's logo (as shown in Figure 3G) printed with two different materials.

circular pattern was printed with the infill direction shifted by 45° for each layer.

Additionally, to showcase the advantage of free infill control, a cube was printed with the infill orientation consistently at a 90° angle to the edge, as shown in Figure 6B. This would be challenging to achieve using a conventional FDM slicer. More complex shapes, such as an ear in Figure 6C, can also be generated. The key advantage is the ability to freely determine the paths and transitions between layers, reducing unnecessary extrusion stops, and improving overall pathfinding. For easier conversion of a 3D object into a layer-by-layer approach, an FDM slicer can be used to generate each sliced layer, which then serves as a backbone for drawing the desired print paths.

3.4.3. Embedded bioprinting

Embedded bioprinting was employed to print more intricate shapes without the need for supports. The flexibility in the *Z* direction was demonstrated through the creation of a meandering pattern, as shown in Figure 6D. Additionally, a layer-by-layer 3D heart structure was successfully printed using this coding approach, as depicted in Figure 6E. The method also facilitates precise multimaterial printing, making the creation of multimaterial objects relatively straightforward, such as the 3D institute logo printed in two colors, as shown in Figure 6F. Furthermore, by using 3D design software like Blender, more complex shapes and paths that are not feasible to create with a traditional layer-by-layer approach can be designed. These 3D paths can then be integrated with the Adobe Illustrator-generated paths when compiling the G-code, effectively merging the two approaches and providing a unified, flexible visualization of the final design.

5. Conclusion

Automation in biofabrication is crucial for improving reproducibility and yield in the production of biologically relevant substrates.[1] A key element of this automation is the ability to efficiently control and program the machines involved. Since many biofabrication devices operate with three degrees of freedom or Cartesian architecture,[37,38] G-code is typically used for machine control. However, generating G-code can be cumbersome, especially for those without expertise in parametric programming or manual coordinate input.

To address this, we developed a straightforward, user-friendly G-code generation method that is adaptable to most biofabrication machines. By leveraging vector-based illustration programs like Adobe Illustrator, users can draw and segment paths into linear subroutines, which are then exported as relative G-code blocks. These blocks are easily sequenced to create the desired machine instructions. This method makes the creation of new patterns and codes intuitive, allowing for easy manipulation and visualization of shapes directly within the drawing software. It also enables rapid prototyping and quick adaptations of designs, making it especially useful for those less experienced in writing G-code or working with parametric programming.

The real advantage of this method becomes apparent when working with complex geometries or non-repetitive structures. The combination of intuitive path drawing and real-time visualization provides a level of flexibility and ease of use that parametric programming cannot offer. Additionally, because most of the generated code consists of relative G1 movements, it is easy to adapt the code for use on different machines, even those with varying software or G-code flavors. This enhances the horizontal transfer of code between different devices, making the method versatile for a wide range of applications.

Furthermore, the vector-based approach significantly streamlines the integration of multiple fabrication methods. When combining different processes, such as laser cutting and FDM, alignment and scaling can be a challenge if generated by separate software. However, by using the drawing method, paths for different processes can be drawn in the same file, ensuring that they are scaled and fit together seamlessly. This facilitates the integration of multiple machines and technologies into a cohesive automated workflow, improving both the speed and reliability of biofabrication processes. It eliminates the need to adapt proprietary slicers for FDM to bioprinting needs, allowing users to rapidly generate print codes and maintain full control over the printing paths. The method supports the production of complex 3D objects with precise spatiotemporal control over the printing sequence, material deposition, and infill patterns. This capability is crucial for biofabrication, especially in aligning cells with the print path direction, as when using fibrous filler materials.[26] Such fibrous particles can align as they flow through the nozzle, forming anisotropic internal structures that impart biomimetic, direction-dependent properties. It also allows for the fabrication of complex, geometrically irregular organic structures, which is critical for replicating the intricate geometry of biological tissues. These features ensure the production of functional, mechanically appropriate structures for biomedical applications.

Thus, this drawing-based G-code generation method offers an efficient, intuitive solution for biofabrication, making complex shapes and multimaterial printing more accessible while providing robust flexibility for adapting to different machines and fabrication techniques.

Acknowledgments

The authors would also like to thank Dr. Philipp Stahlhut for SEM imaging. They acknowledge Christi_ko for fixing bugs relevant for this project and of course dwrobel, jp1357, neveruml, rli, treki, andyz, innerbushman, poofjunior, propcoder, sanzamoyski, and seb_kuzminsky for developing dxf2gcode.

Funding

This work was supported by the German Research Foundation (DFG, Deutsche Forschungsgemeinschaft) under project number 326998133, as part of the Collaborative Research Center/Transregio 225 (SFB/TRR 225) "Biofabrication." The participating subprojects include A07 (PIs: Gregor Lang, Natascha Schäfer, and Dirk Schubert), C06 (PIs: Taufiq Ahmad and Janina Müller-Deile), B04 (PIs: Jürgen Groll and Süleyman Ergün), and B02 (PIs: Jürgen Groll and Iwona Cicha). Additional support was provided by the DFG Priority Programme SPP 2416, CodeChi, project number 525934737 (PIs: Sarah Zwingelberg and Gregor Lang). They also thank the Graduate School of Life Sciences (GSLS) at the University of Würzburg for supporting their Ph.D. students.

Conflict of interest

The authors declare they have no competing interests.

Author contributions

Conceptualization: Zan Lamberger, Gregor Lang
Funding acquisition: Gregor Lang
Investigation: Zan Lamberger
Methodology: Zan Lamberger, Camilla Mussoni, Nathaly Chicaiza Cabezas, Florian Heck, Sven Heilig
Project administration: Gregor Lang, Sarah Zwingelberg
Resources: Gregor Lang, Jürgen Groll
Writing–original draft: Zan Lamberger
Writing–review & editing: Zan Lamberger, Camilla Mussoni, Gregor Lang, Taufiq Ahmad, Sarah Zwingelberg, Jürgen Groll

Ethics approval and consent to participate

Not applicable.

Consent for publication

Not applicable.

Availability of data

Data are available from the corresponding author upon reasonable request.

References

1. Groll J, Boland T, Blunk T, et al. Biofabrication: reappraising the definition of an evolving field. *Biofabrication*. 2016;8(1):13001.
doi: 10.1088/1758-5090/8/1/013001

2. Eichholz KF, Gonçalves I, Barceló X, Federici AS, Hoey DA, Kelly DJ. How to design, develop and build a fully-integrated melt electrowriting 3D printer. *Addit Manuf*. 2022;58:102998.
doi: 10.1016/j.addma.2022.102998

3. Tofail SA, Koumoulos EP, Bandyopadhyay A, Bose S, O'Donoghue L, Charitidis C. Additive manufacturing: scientific and technological challenges, market uptake and opportunities. *Mater Today*. 2018;21(1):22-37.
doi: 10.1016/j.mattod.2017.07.001

4. Brown AC, Beer D de. Development of a stereolithography (STL) slicing and G-code generation algorithm for an entry level 3-D printer. In: AFRICON, 2013. IEEE; 2013:1-5.
doi: 10.1109/AFRCON.2013.6757836

5. Tashman JW, Shiwarski DJ, Feinberg AW. Development of a high-performance open-source 3D bioprinter. *Sci Rep*. 2022;12(1):22652.
doi: 10.1038/s41598-022-26809-4

6. Correia Carreira S, Begum R, Perriman AW. 3D bioprinting: the emergence of programmable biodesign. *Adv Healthc Mater*. 2020;9(15):e1900554.
doi: 10.1002/adhm.201900554

7. Gillispie G, Prim P, Copus J, et al. Assessment methodologies for extrusion-based bioink printability. *Biofabrication*. 2020;12(2):22003.
doi: 10.1088/1758-5090/ab6f0d

8. Lamberger Z, Schubert DW, Buechner M, et al. Advanced optical assessment and modeling of extrusion bioprinting. *Sci Rep*. 2024;14(1):13972.
doi: 10.1038/s41598-024-64039-y

9. Fortunato GM, Nicoletta M, Batoni E, Vozzi G, Maria C de. A fully automatic non-planar slicing algorithm for the additive manufacturing of complex geometries. *Addit Manuf*. 2023;69:103541.
doi: 10.1016/j.addma.2023.103541

10. Devlin BL, Allenby MC, Ren J, et al. Materials design innovations in optimizing cellular behavior on melt electrowritten (MEW) scaffolds. *Adv Funct Mater*. 2024;34(18):2313092.
doi: 10.1002/adfm.202313092

11. Lin Y-J, Lee TS. An adaptive tool path generation algorithm for precision surface machining. *Computer-Aided Design*. 1999;31(4):237-247.
doi: 10.1016/S0010-4485(99)00024-X

12. Gleadall A. FullControl GCode Designer: Open-source software for unconstrained design in additive manufacturing. *Addit Manuf*. 2021;46:102109. doi: 10.1016/j.addma.2021.102109

13. Chansoria P, Rütsche D, Wang A, et al. Synergizing algorithmic design, photoclick chemistry and multi-material volumetric printing for accelerating complex shape engineering. *Adv Sci (Weinh)*. 2023;10(26):e2300912. doi: 10.1002/advs.202300912

14. Devlin BL, Kuba S, Hall PC, et al. A melt Electrowriting Toolbox for automated g-code generation and toolpath correction of flat and tubular constructs. *Adv Mater Technol*. 2024;9(22):2400419. doi: 10.1002/admt.202400419

15. Vernon MJ, Lu J, Padman B, et al. Engineering heart valve interfaces using melt electrowriting: biomimetic design strategies from multi-modal imaging. *Adv Healthc Mater*. 2022;11(24):e2201028. doi: 10.1002/adhm.202201028

16. Bhandari S. A graph-based algorithm for slicing unstructured mesh files. *Addit Manuf Lett*. 2022;3:100056. doi: 10.1016/j.addlet.2022.100056

17. Pakhomova C, Popov D, Maltsev E, Akhatov I, Pasko A. Software for bioprinting. *IJB*. 2020;6(3):279. doi: 10.18063/ijb.v6i3.279

18. Dávila JL, Manzini BM, Da Lopes Fonsêca JH, et al. A parameterized g-code compiler for scaffolds 3D bioprinting. *Bioprinting*. 2022;27:e00222. doi: 10.1016/j.bprint.2022.e00222

19. Ueng S-K, Huang H-K, Huang H-C. A G-code generator for volumetric models. *Appl Sci*. 2019;9(18):3868. doi: 10.3390/app9183868

20. Castilho M, Ruijter M de, Beirne S, et al. Multitechnology biofabrication: a new approach for the manufacturing of functional tissue structures? *Trends Biotechnol*. 2020;38(12):1316-1328. doi: 10.1016/j.tibtech.2020.04.014

21. Ruijter M de, Ribeiro A, Dokter I, Castilho M, Malda J. Simultaneous micropatterning of fibrous meshes and bioinks for the fabrication of living tissue constructs. *Adv Healthc Mater*. 2019;8(7):e1800418. doi: 10.1002/adhm.201800418

22. Koch F, Thaden O, Tröndle K, Zengerle R, Zimmermann S, Koltay P. Open-source hybrid 3D-bioprinter for simultaneous printing of thermoplastics and hydrogels. *HardwareX*. 2021;10:e00230. doi: 10.1016/j.ohx.2021.e00230

23. Lamberger Z, Mussoni C, Murenu N, et al. Streamlining the highly reproducible fabrication of fibrous biomedical specimens towards standardization and high throughput. *Adv Healthc Mater*. 2024;Early View:e2402527. doi: 2024. 10.1002/adhm.202402527

24. Bloksma MM, Weber C, Perevyazko IY, et al. Poly(2-cyclopropyl-2-oxazoline): from rate acceleration by cyclopropyl to thermoresponsive properties. *Macromolecules*. 2011;44(11):4057-4064. doi: 10.1021/ma200514n

25. Murenu N, Kasteleiner M, Lamberger Z, et al. Impact of polymorphic microfibers for establishment of neuronal model. *Nano Select*. 2024;Early View:e202400122. doi: 10.1002/nano.202400122

26. Lamberger Z, Priebe V, Matthias R, Lang G. A versatile method to produce monomodal nano- to micro-fiber fragments as fillers for biofabrication. *Small Methods*. 2024;Early View:2401060. doi: 10.1002/smtd.202401060

27. Türker E, Andrade Mier MS, Faber J, et al. Breast tumor cell survival and morphology in a brain-like extracellular matrix depends on matrix composition and mechanical properties. *Adv Biol (Weinh)*. 2024;8(9):e2400184. doi: 10.1002/adbi.202400184

28. Mair V, Paulus I, Groll J, Ryma M. Freeform printing of thermoresponsive poly(2-cyclopropyl-oxazoline) as cytocompatible and on-demand dissolving template of hollow channel networks in cell-laden hydrogels. *Biofabrication*. 2022;14(2):2207270. doi: 10.1088/1758-5090/ac57a7

29. Herzberger J, Sirrine JM, Williams CB, Long TE. Polymer design for 3D printing elastomers: recent advances in structure, properties, and printing. *Prog Polymer Sci*. 2019;97:101144. doi: 10.1016/j.progpolymsci.2019.101144

30. Decante G, Costa JB, Silva-Correia J, Collins MN, Reis RL, Oliveira JM. Engineering bioinks for 3D bioprinting. *Biofabrication*. 2021;13(3):032001. doi: 10.1088/1758-5090/abec2c

31. Levato R, Jungst T, Scheuring RG, Blunk T, Groll J, Malda J. From shape to function: the next step in bioprinting. *Adv Mater*. 2020;32(12):e1906423. doi: 10.1002/adma.201906423

32. Bettendorf E, Schmid R, E. Horch R, et al. Bioprinted keratinocyte and stem cell laden constructs for skin tissue engineering. *IJB*. 2024;10(6):3925. doi: 10.36922/ijb.3925

33. Schaefer N, Andrade Mier MS, Sonnleitner D, et al. Rheological and biological impact of printable PCL-fibers as reinforcing fillers in cell-laden spider-silk bio-inks. *Small Methods*. 2023;7(10): e2201717. doi: 10.1002/smtd.202201717

34. Choi S, Lee KY, Kim SL, et al. Fibre-infused gel scaffolds guide cardiomyocyte alignment in 3D-printed ventricles. *Nat Mater*. 2023;22(8):1039-1046. doi: 10.1038/s41563-023-01611-3

35. Kim H, Jang J, Park J, et al. Shear-induced alignment of collagen fibrils using 3D cell printing for corneal stroma tissue engineering. *Biofabrication*. 2019;11(3):35017. doi: 10.1088/1758-5090/ab1a8b

36. Eghbali M, Weber KT. Collagen and the myocardium: fibrillar structure, biosynthesis and degradation in relation to hypertrophy and its regression. *Mol Cell Biochem*. 1990;96(1):1-14. doi: 10.1007/BF00228448

37. Reizabal A, Kangur T, Saiz PG, et al. MEWron: an open-source melt electrowriting platform. *Addit Manuf*. 2023;71:103604. doi: 10.1016/j.addma.2023.103604

38. Zhang YS, Haghiashtiani G, Hübscher T, et al. 3D extrusion bioprinting. *Nat Rev Methods Primers*. 2021;1(1):75. doi: 10.1038/s43586-021-00073-8

ACCSCIENCE PUBLISHING

International Journal of Bioprinting

RESEARCH ARTICLE

High-resolution 3D printing of collagen I-based scaffolds via Schiff-base interaction for enhanced osteogenic differentiation

Kaixuan Li[1,2†], Hanxiao Huang[1,2,3†], Peng Ge[1,2], and Cailiang Shen[1,2*]

[1]Department of Orthopedics, The First Affiliated Hospital of Anhui Medical University, Hefei, Anhui, China

[2]Laboratory of Spinal and Spinal Cord Injury Regeneration and Repair, Department of Spine Surgery, The First Affiliated Hospital of Anhui Medical University, Hefei, Anhui, China

[3]Department of Stomatology, The First Affiliated Hospital of Anhui Medical University, Hefei, Anhui, China

Abstract

Collagen I is a key extracellular matrix (ECM) component in bone tissue and one of the most important biomaterials for bone tissue engineering applications. However, printing high-resolution mesh scaffold from collagen I remains challenging due to its relatively weak ink shape fidelity. While previous efforts have attempted to improve printability by increasing ink viscosity, such approaches often compromise ink flowability and yield only modest improvements in printing resolution. To solve this issue, we blended oxidized cellulose with collagen I to form a Schiff-base interaction. The resulting hydrogel exhibited lower viscosity but a more apparent linear rheological characteristic, as demonstrated by our large amplitude oscillation sweep results. This enhanced rheological profile enabled the fabrication of scaffolds with a printing resolution approaching 150 μm—one of the highest reported for collagen I-based scaffolds. Scaffolds with this scale of rod diameter and pore size greatly enhanced the proliferation and osteogenic differentiation of mesenchymal stem cells. Correspondingly, the expression of key osteogenic markers, including N-cadherin, HIF-1α, and β-catenin, was upregulated. These findings broaden our understanding of scaffold design and processing optimization of collagen I-based scaffolds and may advance their application in bone tissue engineering.

Keywords: 3D printing; Collagen I; Osteogenic differentiation; Printing resolution

†These authors contributed equally to this work.

***Corresponding author:**
Cailiang Shen
(shencailiang@ahmu.edu.cn)

Citation: Li K, Huang H, Ge P, Shen C. High-resolution 3D printing of collagen I-based scaffolds via Schiff-base interaction for enhanced osteogenic differentiation. *Int J Bioprint*. 2025;11(4):225-241. doi: 10.36922/IJB025140116

Received: April 1, 2025
1st revised: May 23, 2025
2nd revised: May 28, 2025
Accepted: May 29, 2025
Published online: June 3, 2025

Copyright: © 2025 Author(s). This is an Open Access article distributed under the terms of the Creative Commons Attribution License, permitting distribution, and reproduction in any medium, provided the original work is properly cited.

Publisher's Note: AccScience Publishing remains neutral with regard to jurisdictional claims in published maps and institutional affiliations.

1. Introduction

Collagen I is a key extracellular matrix (ECM) compound in bone tissue and has been considered one of the most ideal biomaterials for bone tissue engineering.[1,2] It is highly biocompatible and contains surface Arg-Gly-Asp (RGD) groups that bind to specific cell receptors, promoting cell adhesion.[3,4] Therefore, it is superior to general thermoplastic biopolymers and ceramics for a broad field of tissue engineering applications. Also, collagen I has been shown to promote osteogenic differentiation of stem cells more effectively than many other natural biopolymers like gelatin.[5] For these reasons,

some studies have blended it with other biopolymers or ceramics to produce bone tissue scaffolds.[6–9] However, printing a high-resolution scaffold composed of collagen I is challenging, presumably due to its weak gelation strength, especially in comparison to gelatin.[10,11] While gelatin macromolecules undergo a unique transition from random flexible coils to rigid triple helix structures under cooling, this process does not occur in collagen I.[12] Instead, its viscosity increases only through greater chain entanglement at lower temperatures.[13] As a result, the shape fidelity of collagen I-based hydrogels is relatively weak, yielding generally poor printing resolution. High scaffold resolution is crucial to provide a large surface area for cell adhesion, absorption of nutrition and growth factors, and biochemical reactions necessary for ECM synthesis,[14,15] as well as to generate a high number of rod junctions to facilitate cell migration according to the Random Walk Model.[16] Therefore, it is important to achieve high resolution with collagen I-based scaffolds so that both structural and compositional characteristics can be optimized simultaneously.

To achieve this goal, recent studies have utilized cryogenic printing to facilitate ink solidification. In this process, the hydrogel ink is printed onto a readily-cooled 2D plate or into a 3D well.[6,17–20] To further improve the printing performance, some studies attempted to use lower temperatures or added rigid nanoscale fillers to maximize viscosity.[21–23] Although these approaches improve the shape fidelity and printing resolution to some extent, achieving a resolution finer than 200 μm remains difficult.[6,17–20] Also, increasing ink viscosity inevitably reduces flowability, complicating extrusion and reducing the continuity and uniformity of the printed structures.[24,25]

Given the low strength of the hydrogel formed by collagen I macromolecular entanglement, a promising solution is to introduce external bonding for stabilization. Among the commonly applied chemical modifications for hydrogel rheology, Schiff-base interactions are frequently used. This reversible bonding can be weakened by shear stress during extrusion and reformed afterward. So, Shiff-base hydrogels exhibit shear-thinning behavior, maintaining both flowability and shape fidelity.[26] Some recent studies have applied Shiff-base interactions to gelatin-based hydrogels, resulting in increased ink rigidity and mechanical properties.[27–30] Following this principle, we introduced Schiff-base interactions into a collagen I-based hydrogel to study its effects on rheological properties, printing performances, and its ability to promote mesenchymal stem cell (MSC) proliferation and osteogenic differentiation—assessing its potential prospects in bone tissue engineering.

In this study, we overcame the hurdle of printing high-resolution natural hydrogel-based mesh scaffolds by blending oxidized cellulose and collagen I to form a hydrogel ink with Schiff-base interactions and printing it under cryogenic conditions. The resulting scaffolds featured pore and rod sizes as small as 150 μm. We investigated how these dimensions influenced MSC proliferation and osteogenic differentiation, and discussed the possible underlying mechanisms. This study not only advances the understanding of optimal scaffold dimensions for osteogenic differentiation but also achieves simultaneous optimization of scaffold composition and structure. We believe this work contributes significantly to scaffold design and optimization for bone tissue engineering applications.

2. Materials and methods

2.1. Materials

Collagen I, alginate (β-D-mannuronicacid/-L-guluronicacid ratio (M/G) = 1:1), gelatin (gel strength ~200 Bloom, biotech grade), sodium peroxide, genipin, and anhydrous calcium chloride ($CaCl_2$) were all supplied by Macklin (China). Hydroxymethyl cellulose was provided by Sigma Aldrich (USA).

2.2. Oxidation of cellulose and preparation of hydrogel inks

Hydroxymethyl cellulose was dissolved in deionized water in a 4% w/v concentration (4 g in every 100 mL of water) in a 100 mL flask. The solution was heated at 37°C for 1 h and stirred constantly with a magnetic bar. Then, 0.2 w/v sodium peroxide was added to the solution in a dark environment, and the solution was stirred at 40°C for 1 h. The resulting solution was denoted as "oxidized cellulose solution". A schematic of the reactions is shown in Figures 1 and 2. Then, 8% w/v collagen I and 8% w/v gelatin was added to the oxidized cellulose solution by stirring at 37°C for 1 h. Lastly, 25% w/v alginate was added to each solution and stirred at 37°C for 1 h. For the collagen I-based hydrogel inks, the ink containing non-oxidized cellulose was denoted as "ink A," while the ink containing cellulose oxidized by sodium peroxide was denoted as "ink B". In the meantime, a crosslinking solution was prepared by dissolving 2% w/v genipin and 20% w/v $CaCl_2$ in deionized water. Fourier transform infrared spectroscopy (FTIR) characterization was performed on hydrogels containing ink A or B using a Bruker FTIR instrument (Germany).

2.3. 3D printing and post-treatment handling

3D printing was conducted with an extrusion-based 3D printer (Regenovo, China). The printer was equipped with a 3D cryogenic well, and the extrusion force was driven by compressed air. Tapered plastic needles were used for

printing (inner diameter: 200 μm; outer diameter: 220 μm). The temperature of the 3D cryogenic well was set to −1°C for printing both collagen I and gelatin-based inks, and a total of seven layers were printed with each ink. Three samples were printed using ink B and with rod distances (distance between the centerline of adjacent rods) of 300, 450, and 600 μm, and were denoted as "sample 1," "sample 2," and "sample 3", respectively. Another scaffold was printed with gelatin-based ink and a rod distance of 600 μm, denoted as "sample 4". The layer height and extrusion pressure were both set to 0.14 mm. The printing pressure was set to 0.18 MPa for printing collagen I-based ink and 0.25 MPa for printing gelatin-based ink. Upon the completion of printing, the crosslinking solution was added dropwise to the scaffolds until fully immersed. The scaffolds were then removed and stored in a refrigerator at −20°C.

2.4. Morphological study

All printed scaffolds were freeze-dried and loaded into the chamber of a scanning electron microscope (SEM; Zeiss, Germany) and vacuumed again. SEM observation was conducted under a secondary electron (SE) mode with an accelerating voltage of 3kV. ImageJ software (1.8.0, National Institute of Health, USA) was used to analyze the average rod diameter and pore size of all scaffolds.

2.5. Rheology

Rheological studies were conducted with an Anton Paar MCR 302e rheometer (Anton Paar, Austria), equipped with a 25 mm parallel plate and an isothermal chamber. Inks A and B were tested to evaluate the effect of Schiff-base formation on improving ink shape fidelity. Steady-shear flow test was performed from 0.1 to 100 s^{-1} at −1°C for each ink. An oscillation temperature sweep test was conducted from 37 to −5°C at a constant frequency of 1 rad/s and a strain of 0.5%. Lastly, a large amplitude oscillation sweep (LAOS) test was conducted at a constant frequency of 1 rad/s across a strain range of 0.1–1000%.

2.6. Thermal study

Differential scanning calorimetry (DSC) test was conducted on hydrogel ink A and B using a HITACHI DSC 200 instrument (HITACHI, Japan) under a nitrogen environment. A cooling process from 30 to −10°C was applied at a rate of 1°C/min.

2.7. Mechanical study

Tensile tests were conducted on scaffold samples 1–4 using a universal test machine (UTM 4103, Shenzhen SUNS Technology Stock Co., Ltd., China). A loading rate of 1 mm/min was applied, and each group of scaffolds was tested in triplicate.

2.8. Cell culture and characterizations

2.8.1. Cell seeding

MSCs were extracted from 2-week-old Sprague Dawley mice. Before seeding cells, all scaffolds (samples 1–4) were immersed in 75% ethanol for 10 min, washed once with phosphate-buffered saline solution (Beyotime, China), exposed to UV radiation for 30 min, and immersed in an (α-MEM) Minimum Essential Medium (Vivacell, China) containing 10% fetal bovine serum (Gibco, Australia), penicillin (10 kU/mL) and 10 mg/mL streptomycin solution (10 mg/mL, Beyotime, China) for 24 h. This modified medium was denoted as "complete medium". MSCs (passage 2) were seeded onto the scaffolds at a density of 10^6 cells/mL. Cell culture was conducted in an incubator (Thermo Fisher Scientific, USA) at 37°C with 5% CO_2. After 24 h, once cell adhesion was observed, the complete medium was replaced with an osteogenic induction medium containing an additional 50 μM ascorbic acid, 10 mM β-glycerol phosphate, and 100 nM dexamethasone (all from Sigma Aldrich, USA).

2.8.2. Cell counting kit-8 test

On days 1, 3, and 5 of culture, a cell counting kit (CCK)-8 test was conducted to assess cell proliferation. The α-MEM medium containing 10% CCK-8 cell counting agent (Beyotime, China) was added and incubated for 1 h. A total of 100 μL of cell supernatant was used to measure the Optical Density (OD) value at a wavelength of 450 nm using a spectrophotometer (Multiskan GO, Thermofisher Scientific, USA).

2.8.3. Cell morphology staining

MSCs were seeded onto scaffolds placed in a 24-well plate. Actin-Tracker Red (Beyotime, China) and 4'6-diamidino-2-phenylindole (DAPI; Beyotime, China) were used for immunofluorescence staining to visualize the cytoskeleton and nuclei, respectively. An upright fluorescence microscope (DM6 B, Leica, Germany) was used for observation. The excitation/emission wavelengths were 496/516 nm for Actin-Tracker Red and 480/340 nm for DAPI, respectively.

2.8.4. Western blot

On days 7 and 21 of cell culture, protein was extracted from MSCs. Cells were lysed in Radio Immunoprecipitation Assay (RIPA) buffer (Beyotime, China), and total protein concentration was determined using the Bradford assay (Sangon Biotech, China). Protein of equal amounts was separated on a 12% Sodium Dodecyl Sulfate Polyacrylamide (SDS-PAGE) Gel Electrophoresis gel and transferred onto a 0.22 μm-pore size polyvinylidene difluoride membrane (Sigma-Aldrich, USA) under a constant current of 252 mA. The membranes were then blocked with 5% skim milk

and incubated overnight at 4°C with primary antibodies targeting N-cadherin (NCAD), alkaline phosphatase (ALP), osteocalcin (OCN), hypoxia-inducible factor 1α (HIF-1α), β-catenin, and GADPH. After being washed three times with Tris-buffered saline with Tween-20 (Beyotime, China), the membranes were incubated at room temperature with horseradish peroxidase-conjugated secondary antibodies for 1.5 h. Lastly, an enhanced chemiluminescence detection kit (Beyotime, China) was used to visualize the immunoreactive bands.

2.9. Statistical analyses

Each experiment was performed independently in a minimum of three replicates. Statistical analyses were conducted using either Student's *t*-test or one-way analysis of variance, as appropriate, to evaluate differences between treatment groups. All analyses were performed using GraphPad Prism 7 (GraphPad Software, Inc., USA). The *p*-value less than 0.05 was considered statistically significant.

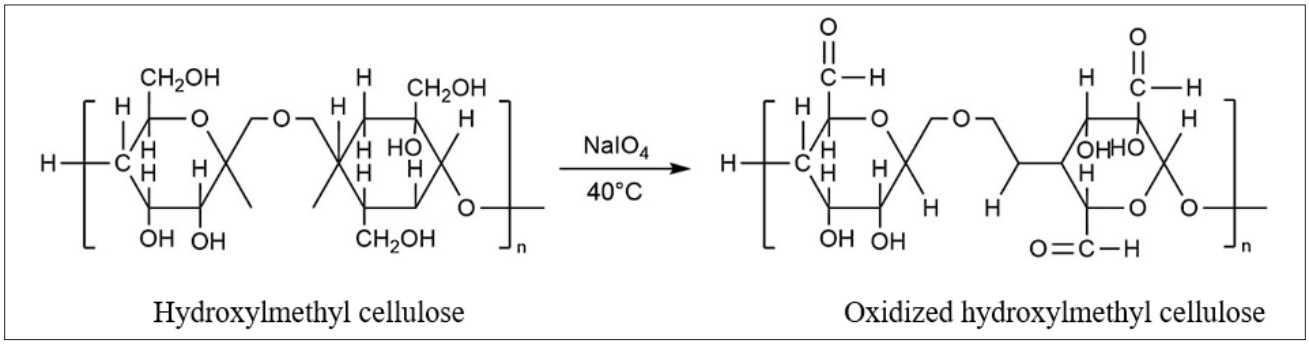

Figure 1. A schematic of cellulose oxidization. Abbreviation: $NaIO_4$, sodium periodate.

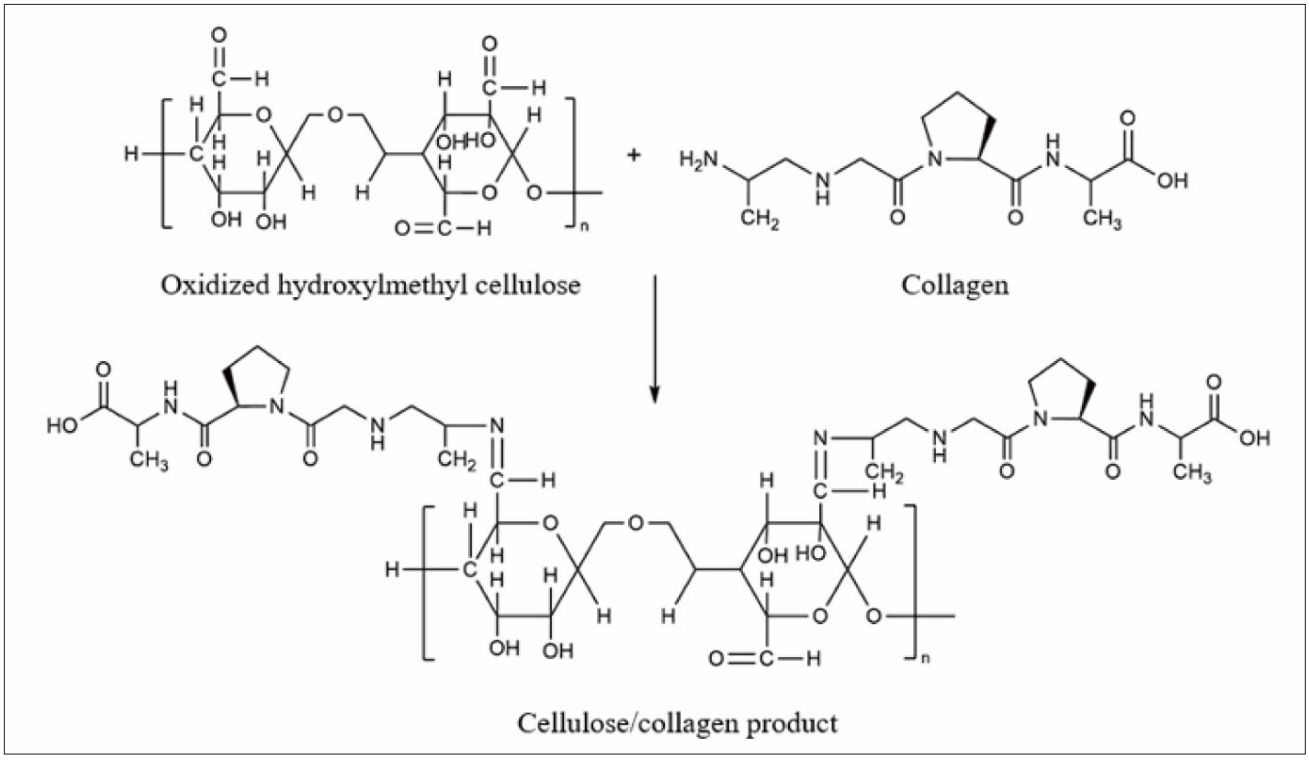

Figure 2. A schematic of Schiff-base interaction formation between collagen and hydroxylmethyl cellulose

3. Results

3.1. FTIR analysis

Following the oxidation of cellulose by sodium peroxide, the hydroxyl groups (–OH) were converted to aldehyde groups. In the FTIR spectra, ink A showed a characteristic –OH peak at 1075 cm^{-1},[31] which was markedly reduced in ink B, indicating successful oxidation. In addition, the characteristic amide peak of collagen I at 1542 cm^{-1} was prominent in ink A but nearly absent in ink B (Figure 3), suggesting its consumption via Schiff-base reactions.[32]

3.2. Rheological study

At the printing temperature of –1 °C, ink A exhibited higher viscosity than ink B. This was consistent with its lower tan δ value and steeper stress–strain curve slope, indicating greater stiffness (Figures 4 and 5). Both inks demonstrated shear-thinning behavior, as viscosity decreased monotonically with increasing shear rate (Figure 4B). LAOS analysis revealed more flattened Lissajous curves for ink B compared to ink A, indicating more linear viscoelastic behavior (Figure 6A). Additionally, ink B showed A higher strain-hardening ratio (Figure 6B), suggesting better structural recovery and printability. The greater linear rheological characteristic of ink B may contribute to its improved shape fidelity during printing.

3.3. Morphological study

Cryogenic 3D printing (Figure 7) was attempted using ink A and B. An optimum combination of pressure and speed parameters was evaluated for each ink until rod breakage occurred. Printing with ink A was more challenging due to its weaker gelation strength, which limited resolution improvements at higher printing speeds and led to frequent rod breakage (Figure 7B). In contrast, ink B enabled smoother printing, likely due to Schiff-base-induced structural reinforcement (Figure 7C). As a result, samples 1–3 scaffolds were printed using ink B, while sample 4 was printed using a gelatin-based hydrogel ink.

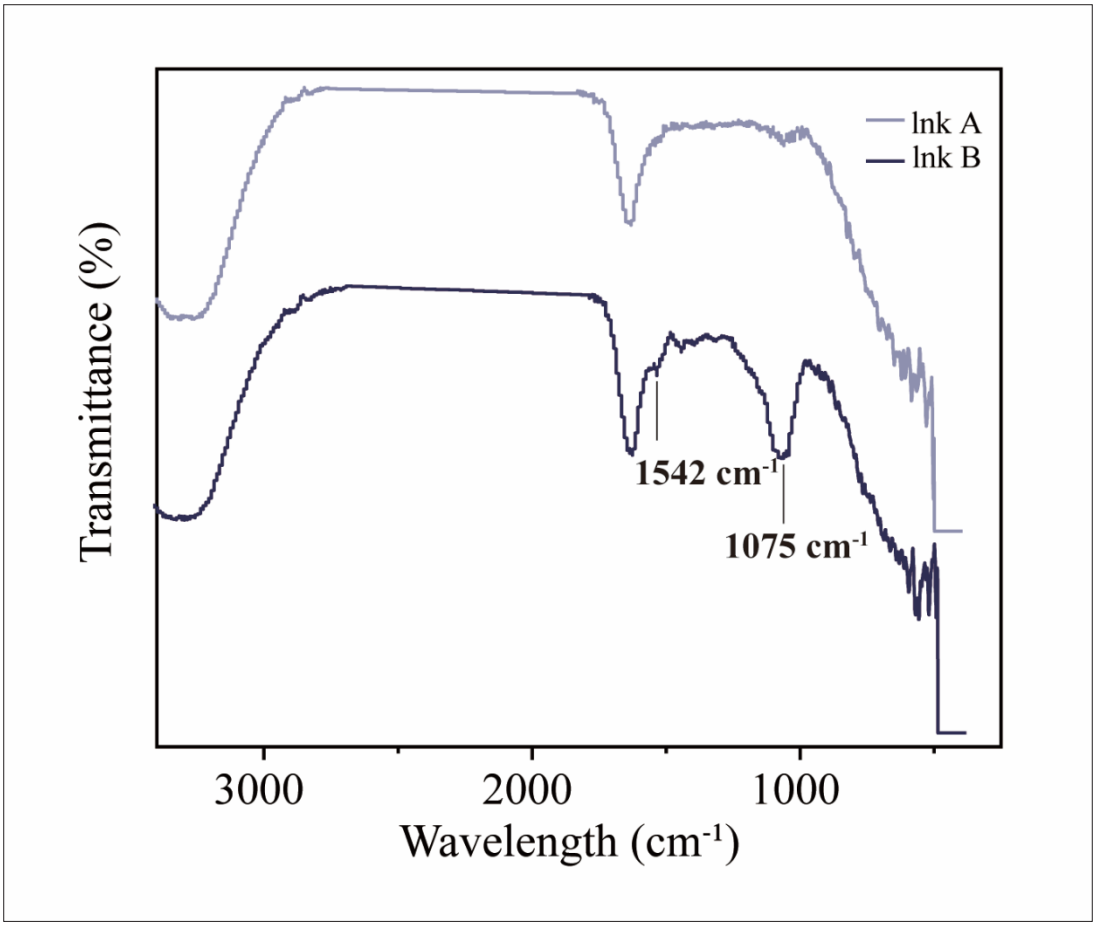

Figure 3. FTIR spectra for ink A (cellulose/collagen I/alginate hydrogel) and B (oxidized cellulose/collagen I/alginate hydrogel). Abbreviation: FTIR: Fourier transform infrared spectroscopy.

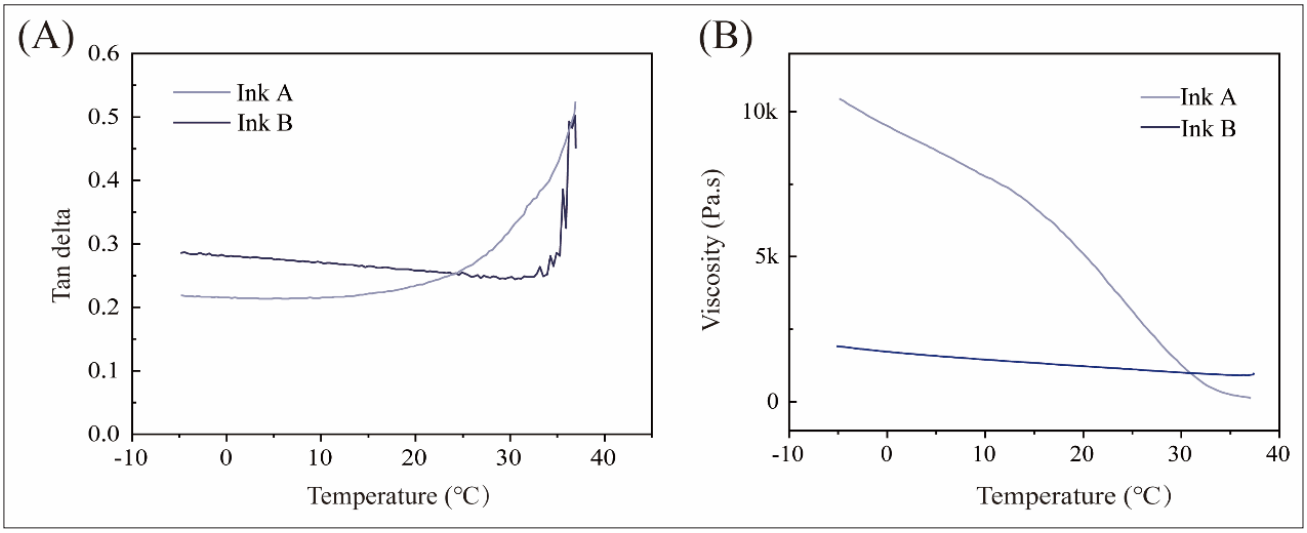

Figure 4. Oscillatory temperature sweep test results for hydrogel inks. Tan δ versus temperature curve (A) and dynamic viscosity versus temperature (B) for ink A (cellulose/collagen I/alginate hydrogel) and B (oxidized cellulose/collagen I/alginate hydrogel).

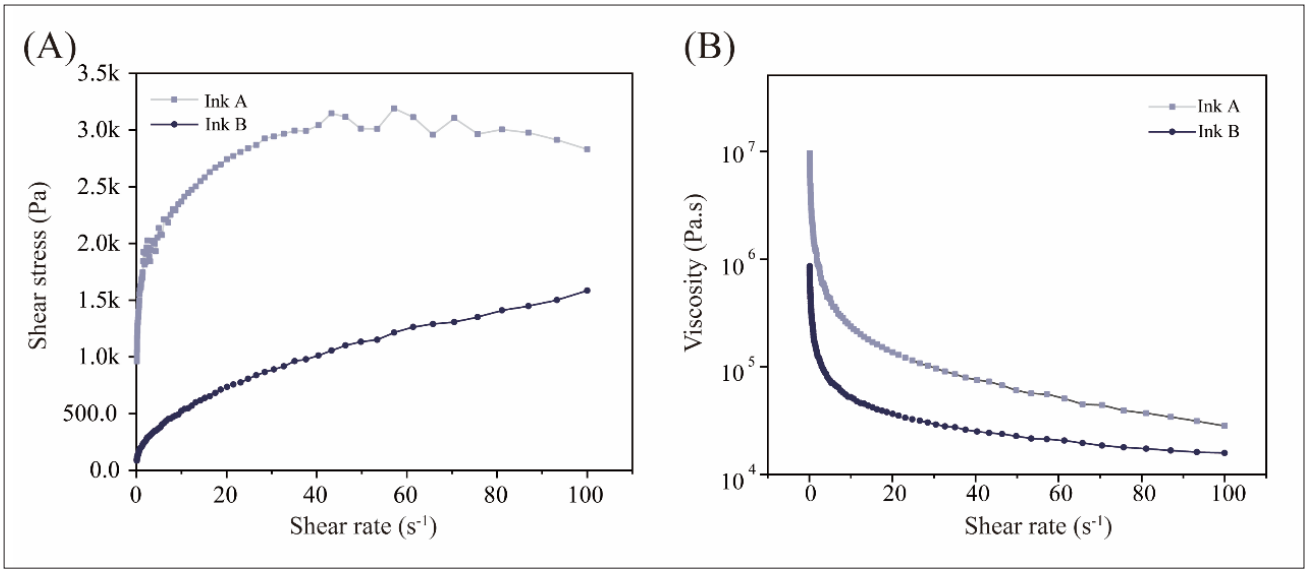

Figure 5. Steady shear flow test results for hydrogel inks. Shear stress versus shear rate curve (A) and viscosity versus shear rate curve (B) for ink A (cellulose/collagen I/alginate hydrogel) and B (oxidized cellulose/collagen I/alginate hydrogel).

The microstructures of samples 1–4 were examined using SEM (Figure 8), and the average rod diameter and pore size were recorded (Table 1). The printing resolution approached 150 μm, representing one of the highest printing resolutions reported for collagen I-based scaffolds to date.[33]

To evaluate the dimensional stability during cell culture, microscale images of the scaffolds were also captured post-swelling (Figure 9). As shown in Table 1, only minor increases in rod diameter were observed, whereas the pore size exhibited slightly greater expansion. Overall, the swelling extent across samples 1–4 was significantly lower than typically reported values, which often exceed 100–200% dimensional increase.[34,35] This stability is likely attributable to the Schiff-base interactions between oxidized cellulose and collagen I.

3.4. Thermal study

The DSC curves for ink A and B are shown in Figure 10. Neither formulation exhibited an apparent phase transition process in the cooling process. Therefore, the printability

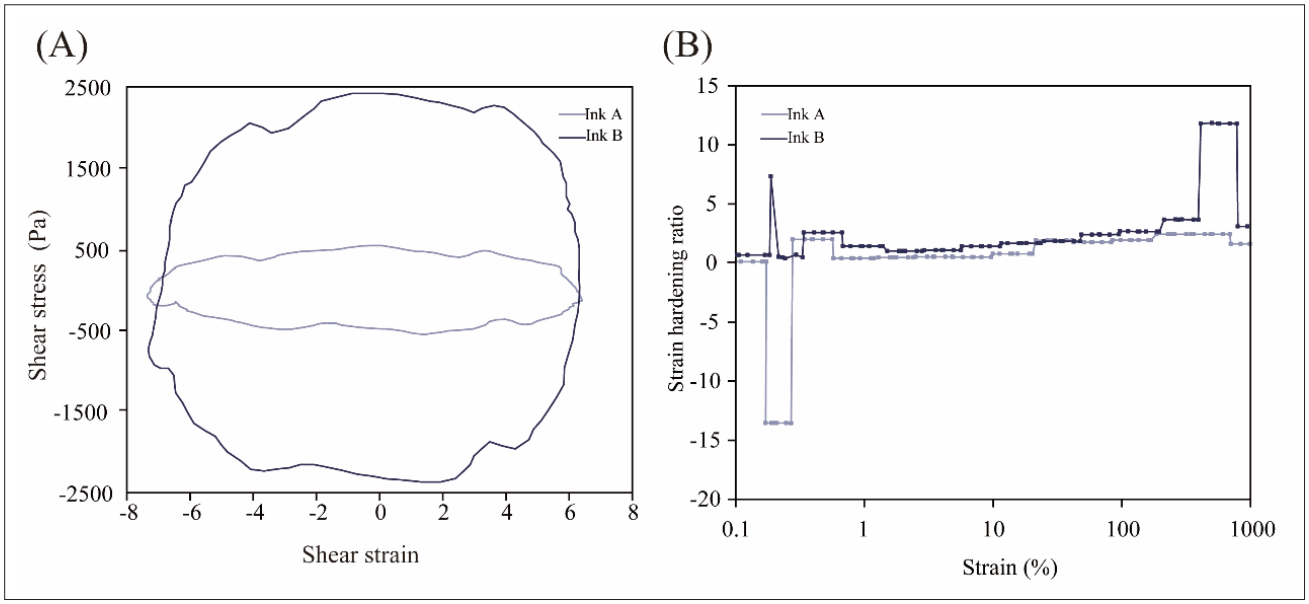

Figure 6. LAOS test results for hydrogel inks. Lissajous curve (A) and strain-hardening curve (B) for ink A (cellulose/collagen I/alginate hydrogel) and B (oxidized cellulose/collagen I/alginate hydrogel). Abbreviation: LAOS: Large amplitude oscillation sweep.

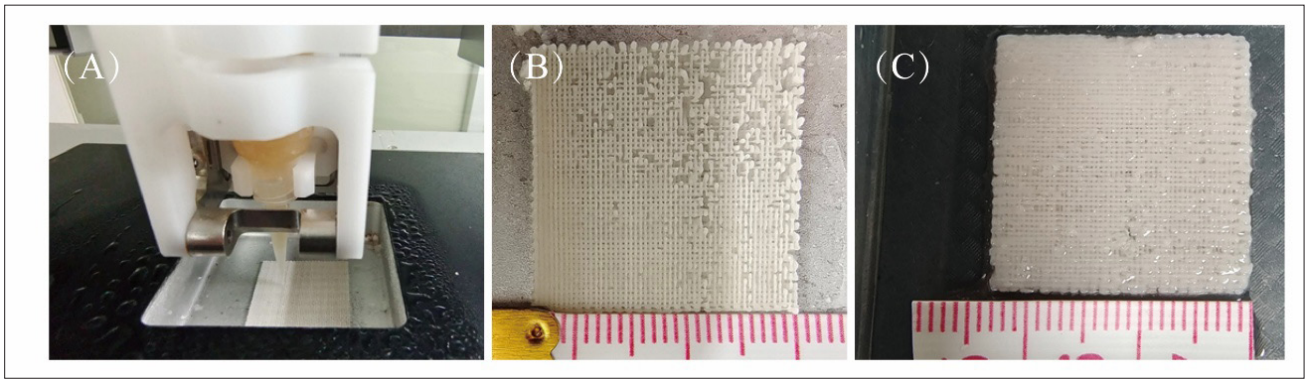

Figure 7. Macroscale images of hydrogel scaffolds. (A) Cryogenic 3D printing setup. (B) 3D-printed scaffold using ink A (cellulose/collagen I/alginate hydrogel). (C) 3D-printed scaffold using ink B (oxidized cellulose/collagen I/alginate hydrogel). The edge length of each scaffold square is 24 mm.

Table 1. Average rod diameter and pore size of scaffold samples before and after swelling

Sample	Before swelling		After swelling	
	Rod diameter (μm)	Pore size (μm)	Rod diameter (μm)	Pore size (μm)
1	158±13	65±13	174±21	140±19
2	173±27	144±42	149±26	192±36
3	184±24	222±16	259±33	350±29
4	237±22	233±17	228±22	324±24

Note: Data are presented as mean ± standard deviations (n = 3).

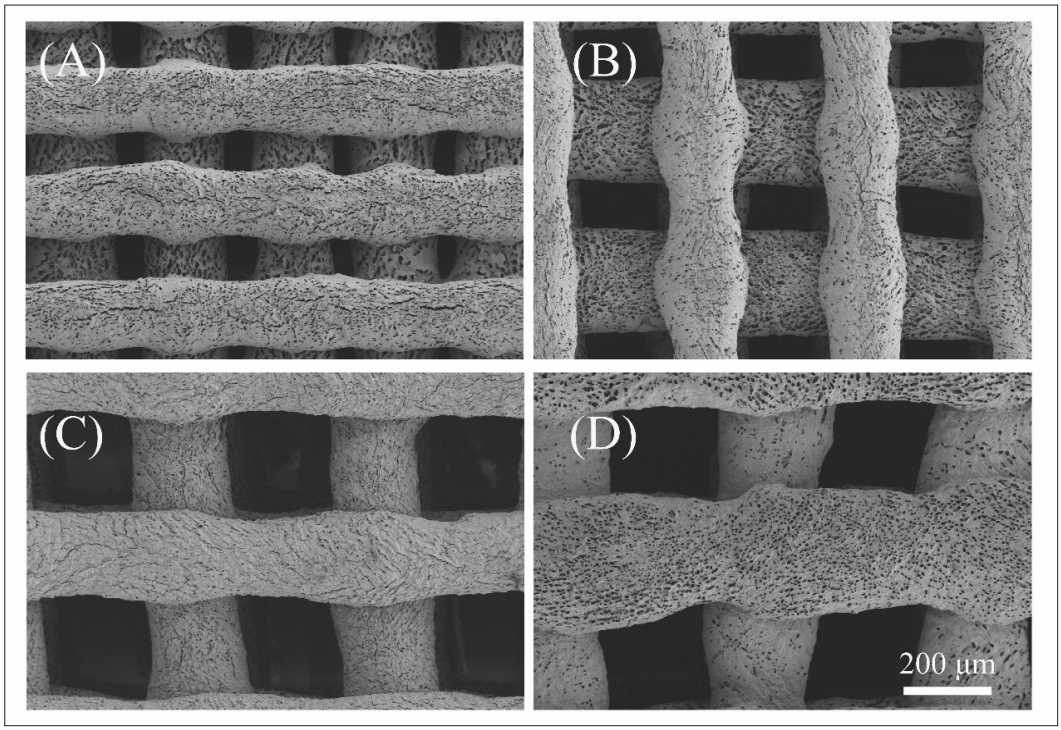

Figure 8. Microscale SEM images of crosslinked scaffolds. (A) Sample 1; (B) Sample 2; (C) Sample 3; (D) Sample 4. The scale bar shown is applicable to all panels. Abbreviation: SEM: Scanning electron microscopy.

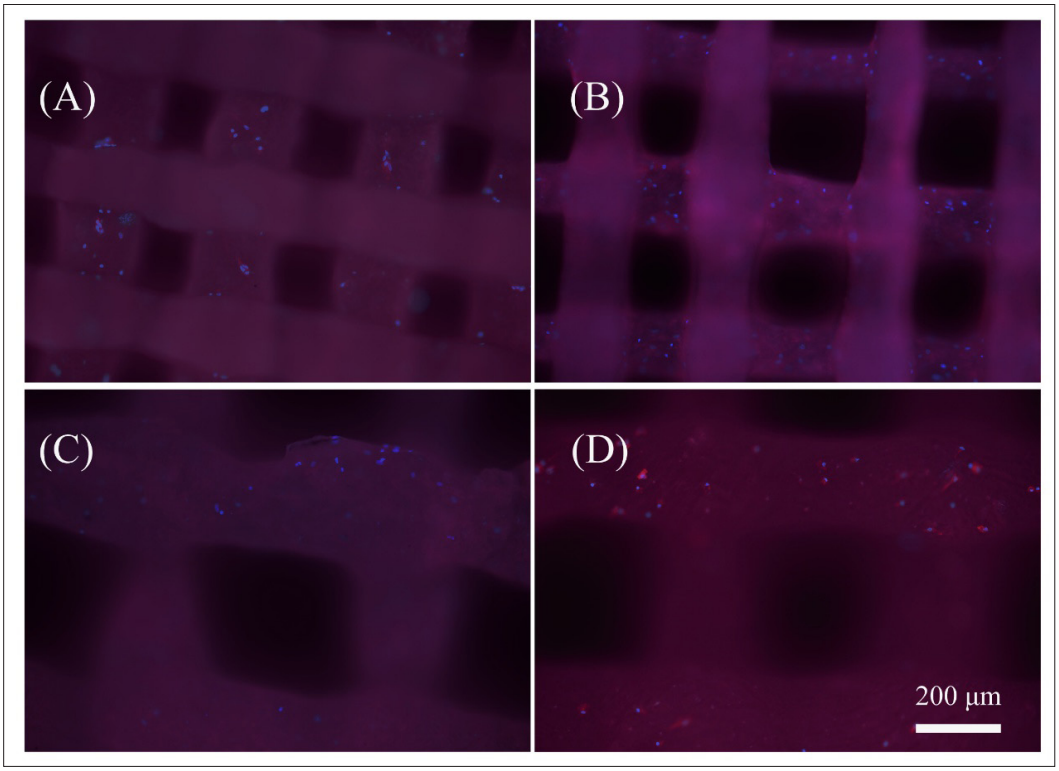

Figure 9. Microscale images of scaffolds seeded with MSCs and stained with DAPI and actin. (A) Sample 1; (B) Sample 2; (C) Sample 3; (D) Sample 4. The scale bar shown is applicable to all panels. Abbreviations: DAPI: 4'6-diamidino-2-phenylindole; MSCs: Mesenchymal stem cells.

and structural integrity of the scaffolds relied primarily on the intrinsic rheological properties of the hydrogel inks, including viscosity, viscoelasticity, and linear rheology. As discussed in **Section 3.2.**, ink B demonstrated enhanced linear rheological characteristics of ink B—presumably due to Schiff-base interaction—which contributed to its superior shape fidelity.

3.4. Mechanical study

Tensile testing was conducted on scaffolds from samples 1–4, and the average elastic moduli were calculated from the linear regions of the stress–strain curves (Figure 11). The moduli were 11.41 ± 0.18 MPa (sample 1), 7.02 ± 1.35 MPa (sample 2), 6.99 ± 0.49 MPa (sample 3), and 4.75 ± 1.84 MPa (sample 4). The highest modulus in sample 1 can be attributed to its smallest rod diameter and pore size, which increased the number of crosslinking junctions and improved resistance to deformation under tensile stress.

3.5. Cell study

On day 5, the OD value of sample 1 was lower than both samples 2 and 3 (Figure 12), which was presumably caused by its lower porosity. According to the western blot (WB) results, the expression of OCN and ALP was the highest in sample 2, indicating the highest level of osteogenic differentiation of MSCs. The NCAD and HIF-1α expressions were also elevated in sample 2, reflecting a higher level of cell condensation and a more hypoxic condition. Lastly, the expression of β-catenin, an osteogenic-related marker, was also most upregulated in sample 2 (Figure 13).

4. Discussion

4.1. Ink rheological properties, printing quality, and post-treatments

Typically, the viscosity and rigidity of hydrogel inks, as measured through steady shear flow and oscillatory rheological tests, are used to evaluate shape fidelity during printing.[24] These are often conducted at a constant strain within the linear elastic region of the ink (0.5–1%).[36] When the hydrogel ink was printed at a relatively low speed, the induced strain remained within this linear range, making such tests appropriate for measuring shape fidelity. However, higher printing resolution often requires significantly higher speed, which can generate large strains—sometimes exceeding 100%.[14] Under such large

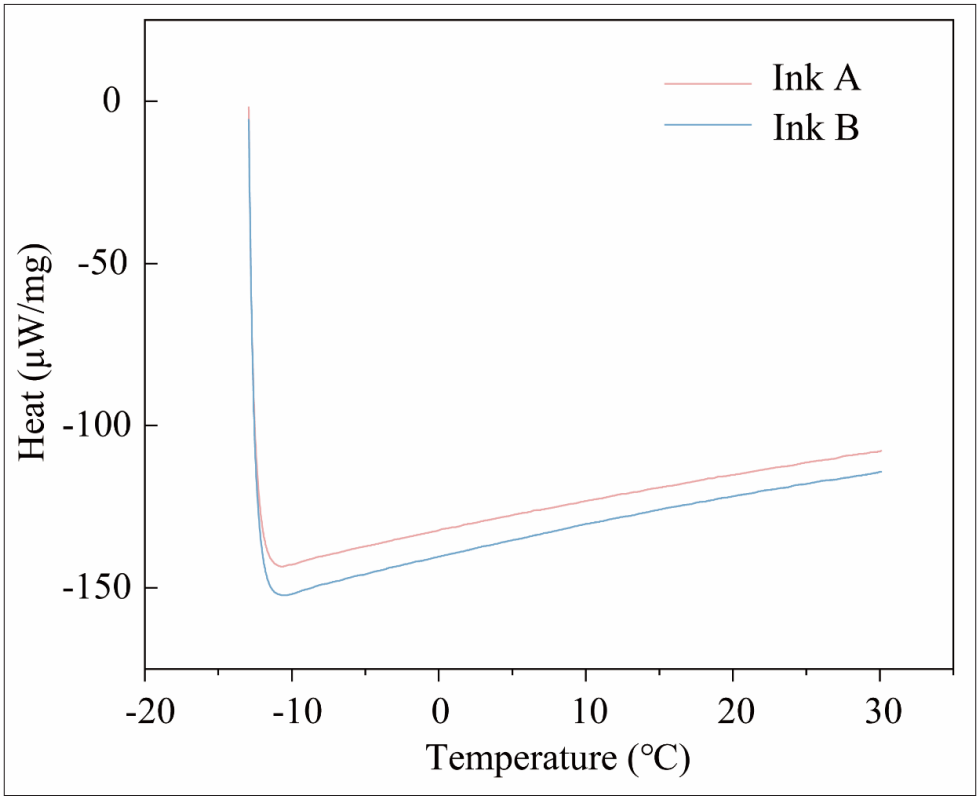

Figure 10. DSC heat flow curve for ink A (cellulose/collagen I/alginate hydrogel) and B (oxidized cellulose/collagen I/alginate hydrogel). Abbreviation: DSC: Differential scanning calorimetry.

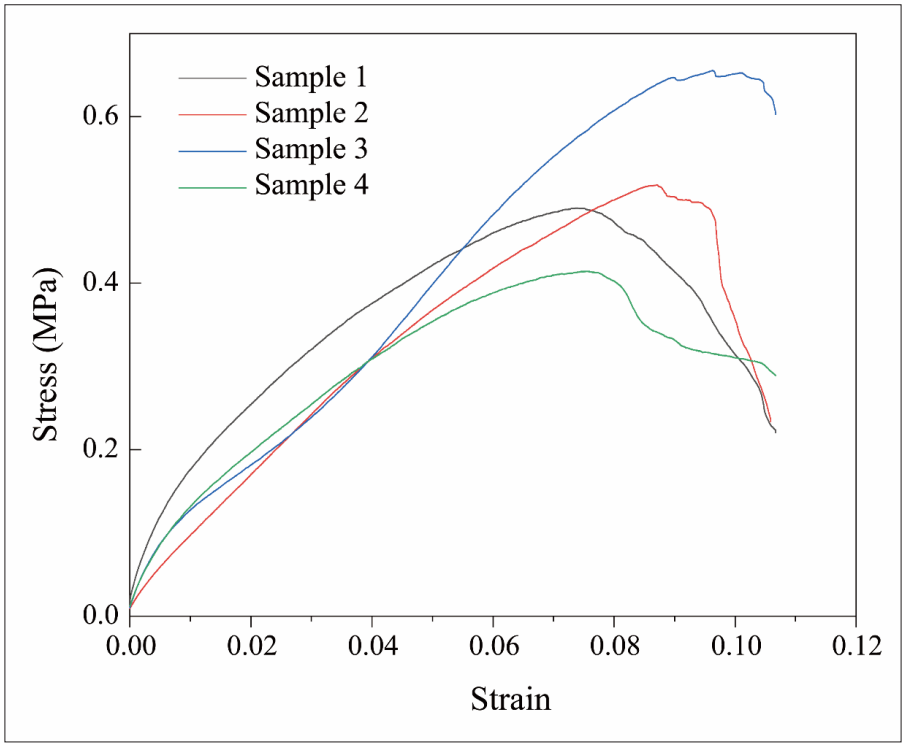

Figure 11. Stress–strain curves of the four scaffold samples

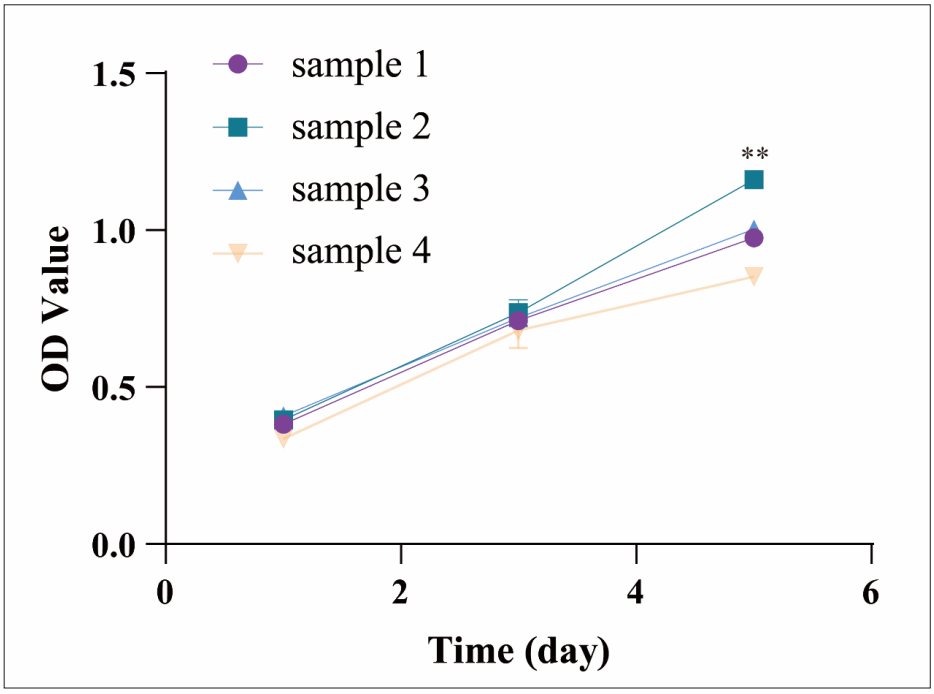

Figure 12. CCK-8 results for the scaffold samples on days 1–5. Data are presented as mean ($n = 3$); ** $p < 0.01$ (compared to control group). Abbreviations: CCK: cell counting kit; DSC: Differential scanning calorimetry.

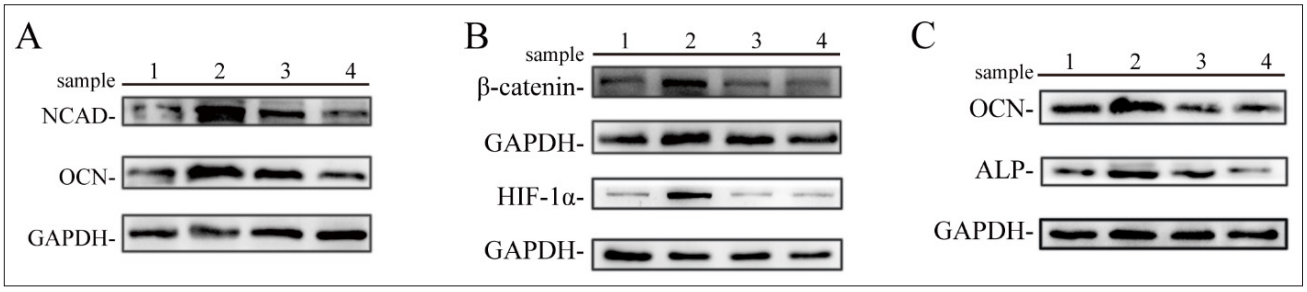

Figure 13. WB images for the four scaffold samples. (A) Expression of NCAD and OCN on day 7. (B) Expression of HIF-1α and β-catenin on day 7. (C) Expression of OCN and ALP on day 21. Abbreviations: ALP, alkaline phosphatase; HIF-1α, hypoxia inducible factor-1α; NCAD, N-cadherin; OCN, osteocalcin; WB, western blot.

strain conditions, LAOS testing provides a more accurate reflection of the ink's rheological behaviors.

Our results showed that although ink A demonstrated higher viscosity and stiffness under low-strain conditions (0.5%), it exhibited weaker linear rheological characteristics across the wider strain range (1–1000%). Linear rheology refers to the regime where stress is directly proportional to strain, resembling the behavior of an ideal Hookean spring.[37] In contrast, inks with strong non-linear behavior resemble viscous fluids and are less able to maintain internal stress under deformation.[38,39] Therefore, inks with stronger linear rheological behavior, such as ink B, are better suited for maintaining structural integrity during high-speed printing. This was further supported by the higher strain-hardening ratio observed in ink B.

The formation of the Schiff-base interaction may disturb the entanglement of collagen I macromolecules and reduce viscosity. Under a larger strain, however, the bonding strength of the Schiff base could be stronger than that of the collagen entanglement. Presumably, due to this reason, ink B with this Schiff-base interaction exhibited a stronger linear rheological characteristic and improved shape fidelity.

In this study, we utilized a moderate cryogenic printing condition at −1, which was unlikely to cause the denaturation of collagen I. According to previous studies, the collagen-to-gelatin transition must involve a heating process,[1,40,41] which was opposite to the temperature condition in cryogenic printing. There are also studies utilizing freeze-drying (at −20°C or lower) to produce collagen-based foam scaffolds, followed by cell and animal studies, indicating that the bioactivity of collagen composition was maintained.[42–45]

For the crosslinking reaction, genipin was used in this study. The reaction involves the bonding of its aldehyde group to the amine group of collagen and gelatin. In other words, the reaction only changes the terminal chemical groups of collagen and gelatin molecules, rather than changing their molecular structure or conformation.[46,47] Therefore, the use of genipin was unlikely to induce denaturation of collagen I. Genipin, a naturally derived crosslinker obtained from the plant *Gardenia jasminoides* Ellis, has been used in traditional Chinese medicine for a long time.[48,49] It has been utilized as a biocompatible and cell-friendly crosslinker to replace synthetic crosslinkers with toxicity, such as formaldehyde and glutaraldehyde.[50] Therefore, it has been used as a routine and standardized crosslinker in drug delivery and post-treatment of biopolymer 3D printing in many studies.[6,51–59] Based on the CCK-8 test results in our study, MSCs proliferated over time, which confirmed that genipin was non-toxic to cells.

4.2. Effects of scaffold structure on cell proliferation

In this study, MSC proliferation was highest in sample 2 from day 1 to day 5. It had a smaller pore size than samples 3 and 4, which likely provided a larger surface area for cell attachment and improved the seeding efficiency and density of MSCs. Though sample 1 had the smallest pore size among all, its pores were even smaller than the rod diameter, rendering a low overall porosity. This limited porosity may have hindered the diffusion of solvents carrying water, nutrition, and metabolic waste, potentially affecting cell proliferation.[60]

In short, our results were inconsistent with some existing studies regarding the effect of pore size on cell proliferation. For example, Sun et al.[61] found that polycaprolactone scaffolds with a medium pore size (350 μm) promoted the proliferation of MSCs more than those with smaller (150 μm) and larger (750 μm) pores. Diao et al.[62] found that tricalcium phosphate scaffolds with a pore size of 300 μm promoted MSC proliferation more than those with 100 and 500 μm-size pores. In contrast, in our study, the pore size at 144 μm exhibited the highest level of cell proliferation. We believe this difference was attributable to the type of scaffold biomaterials. Compared to rigid thermoplastic biopolymers and bioceramics, the

hydrogel scaffolds used in this study were viscoelastic and hydrophilic, and therefore, more favorable for cell adhesion and migration.[63–65] Additionally, the collagen I composition had the surface RGD groups that guided and promoted cell adhesion, and it was also superior in nutrient adsorption during cell culture. Presumably due to these reasons, the use of the collagen I-based hydrogel could "switch" the optimum pore size to a smaller dimension.

In recent years, gelatin has been routinely used as a key component for producing hydrogel scaffolds, as it is a naturally derived protein with a surface RGD group like collagen.[14,26,29,66–70] Though gelatin-based scaffolds have shown significantly improved outcomes in cell adhesion and proliferation compared to metal and thermoplastic biopolymers,[14,71] they remain inferior to scaffolds containing collagen I for bone tissue engineering. Compared to gelatin, collagen I is a native component of bone and has been shown to have a greater osteogenic-promoting effect.[5,72,73] Therefore, we achieved a high printing resolution with a hydrogel ink containing 8% w/v collagen I, which improved the biochemical and structural properties of the scaffolds and could synergistically promote osteogenic differentiation of MSCs. Therefore, our work steps further than recent studies utilizing gelatin-based scaffolds.

4.3. Possible mechanism related to the effect of scaffold structure on osteogenic differentiation

To our best knowledge, studies on the effects of structure on osteogenic differentiation are generally lacking in mesh scaffolds. In the few studies applying scaffolds with relatively big pore sizes (300–700 μm), the level of osteogenic differentiation increased monotonically in smaller pores within this range.[74] However, it is still necessary to produce scaffolds with much higher resolution to further explore their potential to promote osteogenic differentiation and investigate the possible underlying mechanisms.

In this study, the level of osteogenic differentiation was higher in sample 3 than in sample 4, indicating the advantage of using collagen I over gelatin. Among the collagen I-based scaffolds, sample 2 led to the highest level of osteogenic differentiation compared to samples 3 and 4. According to our WB test results, the expression of NCAD was the highest in sample 2, indicating the highest level of cell condensation and cell–cell communication, which could promote osteogenic differentiation, as reported in existing studies.[75–77] Additionally, the expression of NCAD was also the highest in sample 2 and maybe another contributor to promoting osteogenic differentiation.[78] Since MSC proliferation was highest in sample 2, it presumably led to a higher cell density, which promoted cell condensation and the formation of a hypoxic condition. These factors may have contributed to the upregulated expression of NCAD and HIF-1α. In addition, the expression of β-catenin was also highest in sample 2, and the upregulation of this factor has been shown to promote osteogenic differentiation in multiple studies.[79] We believe these findings could deepen our understanding of how scaffold dimensions and structures influence osteogenic differentiation and shed light on the possible mechanisms involved.

4.4. Broader impact of our study in bone tissue engineering

We believe the findings of this study offer several important contributions to the field of bone tissue engineering. First, our results provide insight into resolving the long-standing trade-off between cell proliferation and osteogenic differentiation in scaffold design.[62,68,74,80] Conventionally, smaller pores (100–150 μm) are known to promote osteogenic differentiation, but they often hinder cell proliferation. In bone tissue engineering, both factors are important: while higher proliferation increases the total production of ECM components, differentiation determines the proportion of bone-specific ECM components.[81,82] More importantly, our results indicated that higher cell proliferation may actually promote osteogenic differentiation by upregulating the expression of NCAD and HIF-1α. This highlights the importance of addressing both proliferation and differentiation in tandem rather than in isolation. In this study, such a trade-off was successfully solved in sample 2, which exhibited the highest levels of both proliferation and osteogenic differentiation, indicating that an optimal pore size can support both processes simultaneously.

Second, our work addresses a key challenge in scaffold development: the difficulty of optimizing both the compositional and structural properties for bone regeneration. Although collagen I is widely regarded as one of the most favorable biomaterials for bone tissue engineering,[83] previous studies have either failed to fabricate high-resolution collagen I-based mesh scaffolds or have achieved high-resolution scaffolds using alternative materials such as bioplastics, metals, or ceramics.[6,84,85] In our study, we addressed the printability limitations of collagen I-based hydrogels by introducing a Schiff-base interaction, which enhanced ink rheology and enabled the successful printing of high-resolution scaffolds. This allowed us to simultaneously optimize both composition and structure, enhancing the scaffold's performance in supporting bone regeneration.

Lastly, much of the recent progress in bone tissue engineering has focused on biochemical enhancements, such as incorporating novel growth factors to stimulate osteogenesis.[86–89] In contrast, studies focusing on structural

optimization have been relatively limited, presumably due to material processing constraints and insufficient scaffold resolution to promote osteogenic differentiation.[14] While growth factors can be effective, their use often introduces added cost, complexity in formulation and release control, and potential safety concerns, all of which pose challenges for clinical translation.[90] Our results demonstrate that by achieving a high printing resolution with a collagen I-based scaffold, it is possible to promote both cell proliferation and osteogenic differentiation without relying on external biochemical agents. This presents a more straightforward and potentially more clinically translatable approach. We believe this study will inspire further exploration into the role of scaffold's structural characteristics in promoting bone tissue regeneration.

5. Conclusion

In this study, we successfully addressed the limited printability of collagen I-based hydrogels by incorporating a Shiff-base interaction, enabling the fabrication of high-resolution scaffolds with rod diameters and pore sizes below 200 μm. This improved printing resolution was primarily attributed to an enhanced linear rheological characteristic of the hydrogel ink, rather than an increase in viscosity. We also identified an optimal combination of pore size and rod diameter that simultaneously promoted MSC proliferation and osteogenic differentiation. Mechanistic insights revealed that these effects were associated with the upregulation of NCAD, HIF-1α, and β-catenin expression. To conclude, we successfully designed and fabricated scaffolds with both optimized compositional and structural characteristics to support the proliferation and osteogenic differentiation of MSCs. We believe this study broadens our understanding of scaffold design and optimization, offering valuable insights for future applications in bone tissue engineering.

Acknowledgments

The authors would like to thank the Center for Scientific Research of Anhui Medical University for their valuable assistance in the experiments.

Funding

This work was supported by the National Natural Science Foundation of China (82272551), Hefei Comprehensive National Science Center Institute of Health and Medicine (JKS2023001), and the University Natural Science Research Project of Anhui Province (2022AH051152).

Conflict of interest

The authors declare no competing interests.

Author contributions

Conceptualization: Hanxiao Huang
Funding acquisition: Cailiang Shen
Investigation: Kaixuan Li, Hanxiao Huang, Peng Ge
Methodology: Kaixuan Li, Hanxiao Huang
Formal analysis: Kaixuan Li
Writing–original draft: Kaixuan Li, Hanxiao Huang
Writing–review & editing: Kaixuan Li, Cailiang Shen

Ethics approval and consent to participate

All animal work involved in this study was approved by Experimental Animal Ethics Committee of Anhui Medical University (Approval no.: LLSC20250455).

Consent for publication

Not applicable.

Availability of data

Data is available from the corresponding author upon reasonable request.

References

1. Dille MJ, Haug IJ, Draget KI. Chapter 34—gelatin and collagen. In: Phillips GO, Williams PA, eds. *Handbook of Hydrocolloids*. 3rd ed. Duxford, United Kingdom: Woodhead Publishing; 2021:1073-1097.

2. Marques CF, Diogo GS, Pina S, Oliveira JM, Silva TH, Reis RL. Collagen-based bioinks for hard tissue engineering applications: a comprehensive review. *J Mater Sci Mater Med*. 2019;30(3):32
doi: 10.1007/s10856-019-6234-x.

3. Hersel U, Dahmen C, Kessler H. RGD modified polymers: biomaterials for stimulated cell adhesion and beyond. *Biomaterials*. 2003;24(24):4385-4415.
doi: 10.1016/S0142-9612(03)00343-0

4. Ruoslahti E, Pierschbacher MD. New perspectives in cell adhesion: RGD and integrins. *Science*. 1987;238(4826):491-497
doi: 10.1126/science.2821619.

5. Kim NR, Lee DH, Chung P-H, Yang H-C. Distinct differentiation properties of human dental pulp cells on collagen, gelatin, and chitosan scaffolds. *Oral Surg Oral Med Oral Pathol Oral Radiol Endod*. 2009;108(5):e94-e100.
doi: 10.1016/j.tripleo.2009.07.031.

6. Suo H, Zhang J, Xu M, Wang L. Low-temperature 3D printing of collagen and chitosan composite for tissue engineering. *Mater Sci Eng C*. 2021;123(12): 111963.

doi: 10.1016/j.msec.2021.111963.

7. Bacakova L, Novotna K, Hadraba D, Musilkova J, Slepicka P, Beran M. Influence of biomimetically mineralized collagen scaffolds on bone cell proliferation and immune activation. *Polymers*. 2022;14(3):602. doi: 10.3390/polym14030602

8. Dewey MJ, Johnson EM, Slater ST, Milner DJ, Wheeler MB, Harley BA, Mineralized collagen scaffolds fabricated with amniotic membrane matrix increase osteogenesis under inflammatory conditions. *Regen Biomater*. 2020;7(3):247-258. doi: 10.1093/rb/rbaa005

9. Eviana Putri NR, Wang X, Chen Y, Li X, Kawazoe N, Chen G. Preparation of PLGA-collagen hybrid scaffolds with controlled pore structures for cartilage tissue engineering. *Prog Nat Sci Mater Int*. 2020;30(5):642-650. doi: 10.1016/j.pnsc.2020.07.003.

10. Gómez-Guillén MC, Giménez B, López-Caballero ME, Montero MP. Functional and bioactive properties of collagen and gelatin from alternative sources: a review. *Food Hydrocoll*. 2011;25(8):1813-1827. doi: 10.1016/j.foodhyd.2011.02.007.

11. Gurumurthy B, Janorkar AV. Improvements in mechanical properties of collagen-based scaffolds for tissue engineering. *Curr Opin Biomed Eng*. 2021;17:100253. doi: 10.1016/j.cobme.2020.100253.

12. Kokol V, Pottathara YB, Mihelčič M, Perše LS. Rheological properties of gelatine hydrogels affected by flow- and horizontally-induced cooling rates during 3D cryo-printing. *Colloids Surf A Physicochem Eng Asp*. 2021;616(3):126356. doi: 10.1016/j.colsurfa.2021.126356.

13. Gautieri A, Vesentini S, Redaelli A, Buehler MJ. Viscoelastic properties of model segments of collagen molecules. *Matrix Biol*. 2012;31(2):141-149. doi: 10.1016/j.matbio.2011.11.005.

14. Huang H, Li K, Hou J, Shen C. A study of the temperature-dependent stress yielding behavior of a gelatin-based hydrogel ink and its effects on the enhancement of the 3D printing resolution. *Polym Test*. 2024;137(3):108501. doi: 10.1016/j.polymertesting.2024.108501.

15. Sobral JM, Caridade SG, Sousa RA, Mano JF, Reis RL. Three-dimensional plotted scaffolds with controlled pore size gradients: effect of scaffold geometry on mechanical performance and cell seeding efficiency. *Acta Biomater*. 2011;7(3):1009-1018. doi: 10.1016/j.actbio.2010.11.003.

16. Harley BAC, Kim HD, Zaman MH, Yannas IV, Lauffenburger DA, Gibson LJ. Microarchitecture of three-dimensional scaffolds influences cell migration behavior via junction interactions. *Biophys J*. 2008;95(8):4013-4024. doi: 10.1529/biophysj.107.122598.

17. Lee H, Yang GH, Kim M, Lee J, Huh J, Kim G. Fabrication of micro/nanoporous collagen/dECM/silk-fibroin biocomposite scaffolds using a low temperature 3D printing process for bone tissue regeneration. *Mater Sci Eng C*. 2018;84:140-147. doi: 10.1016/j.msec.2017.11.013

18. Yang L, Jin S, Shi L, et al. Cryogenically 3D printed biomimetic scaffolds containing decellularized small intestinal submucosa and Sr2+/Fe3+ co-substituted hydroxyapatite for bone tissue engineering. *Chem Eng J*. 2022;431(4):133459. doi: 10.1016/j.cej.2021.133459

19. Jiang S, Yu Z, Zhang L, et al. Effects of different aperture-sized type I collagen/silk fibroin scaffolds on the proliferation and differentiation of human dental pulp cells. *Regen Biomater*. 2021;8(4):rbab028. doi: 10.1093/rb/rbab028.

20. Kim G, Ahn S, Yoon H, Kim Y, Chun W. A cryogenic direct-plotting system for fabrication of 3D collagen scaffolds for tissue engineering. *J Mater Chem*. 2009;19(46):8817-8823. doi: 10.1039/B914187A.

21. Dutta SD, Hexiu J, Patel DK, Ganguly K, Lim KT. 3D-printed bioactive and biodegradable hydrogel scaffolds of alginate/gelatin/cellulose nanocrystals for tissue engineering. *Int J Biol Macromol*. 2021;167:644-658. doi: 10.1016/j.ijbiomac.2020.12.011.

22. Liu D, Dong X, Han B, Huang H, Qi M. Cellulose nanocrystal/collagen hydrogels reinforced by anisotropic structure: shear viscoelasticity and related strengthening mechanism. *Comp Commun*. 2020;21:100374. doi: 10.1016/j.coco.2020.100374.

23. Zhang W, Shi K, Yang J, et al. 3D printing of recombinant collagen/chitosan methacrylate/nanoclay hydrogels loaded with Kartogenin nanoparticles for cartilage regeneration. *Regen Biomater*. 2024;11:rbae097. doi: 10.1093/rb/rbae097.

24. Townsend JM, Beck EC, Gehrke SH, Berkland CJ, Detamore MS. Flow behavior prior to crosslinking: the need for precursor rheology for placement of hydrogels in medical applications and for 3D bioprinting. *Prog Polym Sci*. 2019;91(43):126-140. doi: 10.1016/j.progpolymsci.2019.01.003.

25. Huang H, Dean D. 3-D printed porous cellulose acetate tissue scaffolds for additive manufacturing. *Addit Manuf*. 2020;31:100927. doi: 10.1016/j.addma.2019.100927

26. Wang Y, Yang S, Cai H, et al. A dual-crosslinking electroactive hydrogel based on gelatin methacrylate and dibenzaldehyde-terminated telechelic polyethylene glycol for 3D bio-printing. *Sci Rep*. 2024;14(1):4118. doi: 10.1038/s41598-024-54853-9.

27. Heid S, Becker K, Byun J, et al. Bioprinting with bioactive alginate dialdehyde-gelatin (ADA-GEL) composite bioinks: time-dependent in-situ crosslinking via addition of calcium-

silicate particles tunes in vitro stability of 3D bioprinted constructs. *Bioprinting*. 2022;26:e00200. doi: 10.1016/j.bprint.2022.e00200.

28. Jiang Y, Zhou J, Yang Z, et al. Dialdehyde cellulose nanocrystal/gelatin hydrogel optimized for 3D printing applications. *J Mater Sci*. 2018;53(16):11883-11900. doi: 10.1007/s10853-018-2407-0.
29. Aghajanzadeh MS, Imani R, Nazarpak MH. In situ forming aldehyde-modified xanthan/gelatin hydrogel for tissue engineering applications: synthesis, characterization, and optimization. *J Mater Sci*. 2023;58(35):14187-14206. doi: 10.1007/s10853-023-08878-6.
30. Cheng Q-P, Hsu S-h. A self-healing hydrogel and injectable cryogel of gelatin methacryloyl-polyurethane double network for 3D printing. *Acta Biomater*. 2023; 164(3):124-138. doi: 10.1016/j.actbio.2023.04.023.
31. Tohamy H-AS, Taha G, Sultan M. Dialdehyde cellulose/ gelatin hydrogel as a packaging material for manganese oxides adsorbents for wastewater remediation: characterization and performance evaluation. *Int J Biol. Macromol*. 2023;248:125931. doi: 10.1016/j.ijbiomac.2023.125931.
32. Lu Y, Zhao M, Peng Y, et al. A physicochemical double-cross-linked gelatin hydrogel with enhanced antibacterial and anti-inflammatory capabilities for improving wound healing. *J Nanobiotechnol*. 2022;20(1):426. doi: 10.1186/s12951-022-01634-z.
33. Kim MH, Lee YW, Jung W-K, Oh J, Nam SY. Enhanced rheological behaviors of alginate hydrogels with carrageenan for extrusion-based bioprinting. *J Mech Behav Biomed Mater*. 2019;98:187-194. doi: 10.1016/j.jmbbm.2019.06.014.
34. Basu P, Saha N, Saha P. Swelling and rheological study of calcium phosphate filled bacterial cellulose-based hydrogel scaffold. *J Appl Polym Sci*. 2020;137(14):48522. doi: 10.1002/app.48522
35. Li Q, Xu S, Feng Q, et al. 3D printed silk-gelatin hydrogel scaffold with different porous structure and cell seeding strategy for cartilage regeneration. *Bioact Mater*. 2021;6(10):3396-3410. doi: 10.1016/j.bioactmat.2021.03.013.
36. Huang H, Ayariga J, Ning H, Nyairo E, Dean D. Freeze-printing of pectin/alginate scaffolds with high resolution, overhang structures and interconnected porous network. *Addit Manuf*. 2021;4:102120. doi: 10.1016/j.addma.2021.102120.
37. Townsend AK, Wilson HJ. Small- and large-amplitude oscillatory rheometry with bead–spring dumbbells in Stokesian dynamics to mimic viscoelasticity. *J Non-Newton Fluid Mech*. 2018;261(1):136-152. doi: 10.1016/j.jnnfm.2018.08.010.
38. Hyun K, Wilhelm M, Klein CO, et al. A review of nonlinear oscillatory shear tests: analysis and application of large amplitude oscillatory shear (LAOS). *Prog Polym Sci*. 2011;36(12):1697-1753. doi: 10.1016/j.progpolymsci.2011.02.002.
39. Wang Y, Selomulya C. Food rheology applications of large amplitude oscillation shear (LAOS). *Trends Food Sci Technol*. 2022;127(4):221-244. doi: 10.1016/j.tifs.2022.05.018.
40. Liu D, Nikoo M, Boran G, Zhou P, Regenstein JM. Collagen and gelatin. *Annu Rev Food Sci Technol*. 2015;6:527-557. doi: 10.1146/annurev-food-031414-111800.
41. Komsa-Penkova R, Koynova R, Kostov G, Tenchov B. Discrete reduction of type I collagen thermal stability upon oxidation. *Biophys Chem*. 2000;83(3):185-195. doi: 10.1016/S0301-4622(99)00135-0.
42. Offeddu GS, Ashworth JC, Cameron RE, Oyen ML. Structural determinants of hydration, mechanics and fluid flow in freeze-dried collagen scaffolds. *Acta Biomater*. 2016;41:193-203. doi: 10.1016/j.actbio.2016.05.024.
43. Varley MC, Neelakantan S, Clyne TW, Dean J, Brooks RA, Markaki AE. Cell structure, stiffness and permeability of freeze-dried collagen scaffolds in dry and hydrated states. *Acta Biomater*. 2016;33:166-175. doi: 10.1016/j.actbio.2016.01.041.
44. O'Brien FJ, Harley BA, Yannas IV, Gibson L. Influence of freezing rate on pore structure in freeze-dried collagen-GAG scaffolds. *Biomaterials*. 2004;25(6):1077-1086. doi: 10.1016/S0142-9612(03)00630-6.
45. Sionkowska A, Kozłowska J. Properties and modification of porous 3-D collagen/hydroxyapatite composites. *Int J Biol Macromol*. 2013;52(1):250-259. doi: 10.1016/j.ijbiomac.2012.10.002.
46. Solorio L, Zwolinski C, Lund AW, Farrell MJ, Stegemann JP. Gelatin microspheres crosslinked with genipin for local delivery of growth factors. *J Tissue Eng Regen Med*. 2010;4(7):514-523. doi: 10.1002/term.267.
47. Nickerson MT, Patel J, Heyd DV, Rousseau D, Paulson AT. Kinetic and mechanistic considerations in the gelation of genipin-crosslinked gelatin. *Int J Biol Macromol*. 2006;39(4):298-302. doi: 10.1016/j.ijbiomac.2006.04.010.
48. Manickam B, Nair R, Elumalai M. 'Genipin' – the natural water soluble cross-linking agent and its importance in the modified drug delivery systems: an overview. *Curr Drug Deliv*. 2014;11(1):139. doi: 10.2174/15672018113106660059.
49. Adamiak K, Sionkowska A. Current methods of collagen cross-linking: review. *Int J Biol Macromol*. 2020;161(8):550-560.

doi: 10.1016/j.ijbiomac.2020.06.075.

50. Gao L, Gan H, Meng Z, et al. Effects of genipin cross-linking of chitosan hydrogels on cellular adhesion and viability. *Colloids Surf B Biointerfaces*. 2014;117:398–405. doi: 10.1016/j.colsurfb.2014.03.002.

51. Oustadi F, Imani R, Haghbin Nazarpak M, Sharifi AM. Genipin-crosslinked gelatin hydrogel incorporated with PLLA-nanocylinders as a bone scaffold: synthesis, characterization, and mechanical properties evaluation. *Polym Adv Technol*. 2020;31(8):1783-1792. doi: 10.1002/pat.4905.

52. Zafeiris K, Brasinika D, Karatza A, et al. Additive manufacturing of hydroxyapatite–chitosan–genipin composite scaffolds for bone tissue engineering applications. *Mater Sci Eng C*. 2021;119:111639. doi: 10.1016/j.msec.2020.111639.

53. Kim YB, Lee H, Kim GH. Strategy to achieve highly porous/biocompatible macroscale cell blocks, using a collagen/genipin-bioink and an optimal 3D printing process. *ACS Appl Mater Interfaces*. 2016;8(47):32230-32240. doi: 10.1021/acsami.6b11669.

54. Hafezi F, Scoutaris N, Douroumis D, Boateng J. 3D printed chitosan dressing crosslinked with genipin for potential healing of chronic wounds. *Int J Pharm*. 2019;560:406-415. doi: 10.1016/j.ijpharm.2019.02.020.

55. Yu Y, Xu S, Li S, Pan H. Genipin-cross-linked hydrogels based on biomaterials for drug delivery: a review. *Biomater Sci*. 2021;9(5):1583-1597. doi: 10.1039/D0BM01403F.

56. Shao Y, Gan N, Gao B, He B. Sustainable 3D-printed β-galactosidase immobilization coupled with continuous-flow reactor for efficient lactose-free milk production. *Chem Eng J*. 2024;481:148557. doi: 10.1016/j.cej.2024.148557.

57. Liu F, Li W, Liu H, et al. Preparation of 3D printed chitosan/polyvinyl alcohol double network hydrogel scaffolds. *Macromol Biosci*. 2021;21(4):2000398. doi: 10.1002/mabi.202000398.

58. Erben A, Hörning M, Hartmann B, et al. Precision 3D-printed cell scaffolds mimicking native tissue composition and mechanics. *Adv Healthc Mater*. 2020;9(24):2000918. doi: 10.1002/adhm.202000918.

59. Saito-Diaz K, Dietrich P, Saini T, et al. Genipin rescues developmental and degenerative defects in familial dysautonomia models and accelerates axon regeneration. *Sci Transl Med*. 2024;16(774):eadq2418. doi: 10.1126/scitranslmed.adq2418.

60. Luo C, Wang C, Wu X, et al. Influence of porous tantalum scaffold pore size on osteogenesis and osteointegration: a comprehensive study based on 3D-printing technology. *Mater Sci Eng C*. 2021;129(5):112382. doi: 10.1016/j.msec.2021.112382.

61. Sun Y, Wu Q, Zhang Y, Dai K, Wei Y. 3D-bioprinted gradient-structured scaffold generates anisotropic cartilage with vascularization by pore-size-dependent activation of HIF1α/FAK signaling axis. *Nanomed Nanotechnol Biol Med*. 2021;37(5):102426. doi: 10.1016/j.nano.2021.102426.

62. Diao J, OuYang J, Deng T, et al. 3D-plotted beta-tricalcium phosphate scaffolds with smaller pore sizes improve in vivo bone regeneration and biomechanical properties in a critical-sized calvarial defect rat model. *Adv Healthc Mater*. 2018;7(17):1800441. doi: 10.1002/adhm.201800441.

63. Bauer A, Gu L, Kwee B, et al. Hydrogel substrate stress-relaxation regulates the spreading and proliferation of mouse myoblasts. *Acta Biomater*. 2017;62(7):82-90. doi: 10.1016/j.actbio.2017.08.041.

64. Ma Y, Han T, Yang Q, et al. Viscoelastic cell microenvironment: hydrogel-based strategy for recapitulating dynamic ECM mechanics. *Adv Funct Mater*. 2021;31(24):2100848. doi: 10.1002/adfm.202100848.

65. Chaudhuri O, Cooper-White J, Janmey PA, Mooney DJ, Shenoy VB, Effects of extracellular matrix viscoelasticity on cellular behaviour. *Nature*. 2020;584(7822):535-546. doi: 10.1038/s41586-020-2612-2.

66. Serag E, Eltawila AM, Salem EM, El-Maghraby A, Abd El-Aziz AM. Development of an innovative cylindrical carbon nanofiber/gelatin-polycaprolactone hydrogel scaffold for enhanced bone regeneration. *Int J Biol Macromol*. 2025;306(8):141250. doi: 10.1016/j.ijbiomac.2025.141250.

67. Kalogeropoulou M, Díaz-Payno PJ, Mirzaali MJ, van Osch GJVM, Fratila-Apachitei LE, Zadpoor AA. 4D printed shape-shifting biomaterials for tissue engineering and regenerative medicine applications. *Biofabrication*. 2024;16(2):022002. doi: 10.1088/1758-5090/ad1e6f.

68. Kim H, Yang GH, Choi C, Cho Y, Kim G. Gelatin/PVA scaffolds fabricated using a 3D-printing process employed with a low-temperature plate for hard tissue regeneration: fabrication and characterizations. *Int J Biol Macromol*. 2018;120:119-127. doi: 10.1016/j.ijbiomac.2018.07.159.

69. Wu S-C, Chang W-H, Dong G-C, Chen K-Y, Chen Y-S, Yao C-H. Cell adhesion and proliferation enhancement by gelatin nanofiber scaffolds. *J Bioact Compat Polym*. 2011;26(6):565-577. doi: 10.1177/0883911511423563.

70. Wang J, Dongyang Z, Guangchao W, et al. Enhanced bone regeneration with bioprinted GelMA/Bentonite scaffolds inspired by bone matrix. *Virtual Phys Prototyp*. 2024;19(1):e2345765.

doi: 10.1080/17452759.2024.2345765.

71. Salehi Abar E, Vandghanooni S, Torab A, Jaymand M, Eskandani M. A comprehensive review on nanocomposite biomaterials based on gelatin for bone tissue engineering. *Int J Biol Macromol.* 2024;254(1):127556. doi: 10.1016/j.ijbiomac.2023.127556.

72. Xu L, Anderson AL, Lu Q, Wang J. Role of fibrillar structure of collagenous carrier in bone sialoprotein-mediated matrix mineralization and osteoblast differentiation. *Biomaterials*. 2007;28(4):750-761. doi: 10.1016/j.biomaterials.2006.09.022.

73. Shi H, Li Y, Xu K, Yin J. Advantages of photo-curable collagen-based cell-laden bioinks compared to methacrylated gelatin (GelMA) in digital light processing (DLP) and extrusion bioprinting. *Mater Today Bio*. 2023;23(5):100799. doi: 10.1016/j.mtbio.2023.100799.

74. Di Luca A, Ostrowska B, Lorenzo-Moldero I, et al. Gradients in pore size enhance the osteogenic differentiation of human mesenchymal stromal cells in three-dimensional scaffolds. *Sci Rep*. 2016;6(1):22898. doi: 10.1038/srep22898.

75. Xu L, Meng F, Ni M, Lee Y, Li G. N-cadherin regulates osteogenesis and migration of bone marrow-derived mesenchymal stem cells. Mol Biol Rep. 2013;40(3):2533-2539. doi: 10.1007/s11033-012-2334-0.

76. Zhu M, Lin S, Sun Y, Feng Q, Li G, Bian L. Hydrogels functionalized with N-cadherin mimetic peptide enhance osteogenesis of hMSCs by emulating the osteogenic niche. *Biomaterials*. 2016;77:44-52. doi: 10.1016/j.biomaterials.2015.10.072.

77. Guntur AR, Rosen CJ, Naski MC. N-cadherin adherens junctions mediate osteogenesis through PI3K signaling. *Bone*. 2012;50(1):54-62. doi: 10.1016/j.bone.2011.09.036.

78. Burzi IS, Parchi PD, Barachini S, et al. Hypoxia promotes the stemness of mesangiogenic progenitor cells and prevents osteogenic but not angiogenic differentiation. *Stem Cell Rev Rep*. 2024;20(7):1830-1842. doi: 10.1007/s12015-024-10749-9.

79. Hu L, Chen W, Qian A, Li Y-P. Wnt/β-catenin signaling components and mechanisms in bone formation, homeostasis, and disease. *Bone Res.* 2024;12(1):39. doi: 10.1038/s41413-024-00342-8.

80. Swanson WB, Omi M, Zhang Z, et al. Macropore design of tissue engineering scaffolds regulates mesenchymal stem cell differentiation fate. *Biomaterials*. 2021;272(1):120769. doi: 10.1016/j.biomaterials.2021.120769.

81. Koons GL, Diba M, Mikos AG. Materials design for bone-tissue engineering. *Nat Rev Mater*. 2020;5(8):584-603. doi: 10.1038/s41578-020-0204-2

82. James AW. Review of signaling pathways governing MSC osteogenic and adipogenic differentiation. *Scientifica* 2013;2013(1):684736. doi: 10.1155/2013/684736.

83. Vijayalekha A, Anandasadagopan SK, Pandurangan AK. An overview of collagen-based composite scaffold for bone tissue engineering. *Appl Biochem Biotechnol.* 2023;195(7):4617-4636. doi: 10.1007/s12010-023-04318-y.

84. Li Y, Liu Y, Li R, et al. Collagen-based biomaterials for bone tissue engineering. *Mater Des.* 2021;210(7):110049. doi: 10.1016/j.matdes.2021.110049.

85. Mu X, Agostinacchio F, Xiang N, et al. Recent advances in 3D printing with protein-based inks. *Prog Polym Sci*. 2021;115:101375. doi: 10.1016/j.progpolymsci.2021.101375.

86. Ho-Shui-Ling A, Bolander J, Rustom LE, Johnson AW, Luyten FP, Picart C. Bone regeneration strategies: engineered scaffolds, bioactive molecules and stem cells current stage and future perspectives. *Biomaterials*. 2018;180:143-162. doi: 10.1016/j.biomaterials.2018.07.017.

87. Zhao H-y, Wu J, Zhu J-j, et al. Research advances in tissue engineering materials for sustained release of growth factors. *BioMed Res Int.* 2015;2015(6):808202. doi: 10.1155/2015/808202

88. De Witte T-M, Fratila-Apachitei LE, Zadpoor AA, Peppas NA. Bone tissue engineering via growth factor delivery: from scaffolds to complex matrices. *Regen Biomater*. 2018;5(4):197-211. doi: 10.1093/rb/rby013

89. Shrivats AR, McDermott MC, Hollinger JO. Bone tissue engineering: state of the union. *Drug Discov Today*, 2014;19(6):781-786. doi: 10.1016/j.drudis.2014.04.010.

90. Oryan A, Alidadi S, Moshiri A, Bigham-Sadegh A. Bone morphogenetic proteins: a powerful osteoinductive compound with non-negligible side effects and limitations. *BioFactors*. 2014;40(5):459-481. doi: 10.1002/biof.1177.

ACCSCIENCE PUBLISHING

International Journal of Bioprinting

RESEARCH ARTICLE

Rapid 3D reconstruction in fetal ultrasound imaging using artificial intelligence and medical 3D printing

Wenjuan Zhang[1†], Jiahe Liang[2,3,4†], Linbin Lai[1†], Zewen Zhang[1], Yitong Guo[2†], Na Hou[2†], Zekai Zhang[2], Zhuojun Mao[2], Tiesheng Cao[2], Yu Li[5], Lijun Yuan[2*], and Airong Qian[1*]

[1]Xi'an Key Laboratory of Special Medicine and Health Engineering, School of Life Sciences, Northwestern Polytechnical University, Xi'an, Shaanxi, China

[2]Department of Ultrasound Diagnosis, Tangdu Hospital, Fourth Military Medical University, Xi'an, Shaanxi, China

[3]State Key Laboratory for Manufacturing Systems Engineering, Xi'an Jiaotong University, Xi'an, Shaanxi, China

[4]NMPA Key Laboratory for Research and Evaluation of Additive Manufacturing Medical Devices, Xi'an Jiaotong University, Xi'an, Shaanxi, China

[5]Xi'an Key Laboratory of Stem Cell and Regenerative Medicine, Institute of Medical Research, Northwestern Polytechnical University, Xi'an, Shaanxi, China

[†]These authors contributed equally to this work.

***Corresponding authors:**
Lijun Yuan
(yuanlj@fmmu.edu.cn)

Airong Qian
(qianair@nwpu.edu.cn)

Citation: Zhang W, Liang J, Lai L, *et al*. Rapid 3D reconstruction in fetal ultrasound imaging using artificial intelligence and medical 3D printing. *Int J Bioprint*. 2025;11(4):242-255. doi: 10.36922/IJB025200192

Received: May 12, 2025
Revised: May 30, 2025
Accepted: June 1, 2025
Published online: June 1, 2025

Copyright: © 2025 Author(s). This is an Open Access article distributed under the terms of the Creative Commons Attribution License, permitting distribution, and reproduction in any medium, provided the original work is properly cited.

Publisher's Note: AccScience Publishing remains neutral with regard to jurisdictional claims in published maps and institutional affiliations.

(This article belongs to the *Special Issue: 3D-Printed Biomedical Devices*)

Abstract

Congenital heart disease (CHD) has been one of the most serious problems in newborns. For fetal heart health care, 3D modeling and printing technology have been adopted in the diagnosis of CHD during antenatal care. However, the development of 3D printing techniques and their clinical applications have been hindered by the manual processing of ultrasound (US) volume data in clinical practice. To overcome this problem, we present an interactive semi-automatic method based on deep learning that uses manual processing results from expert sonographers for training. The accuracy, interpretability, and variability of the performances were evaluated on the validation set. The results demonstrated that compared with a physician with less than 3 years of experience, a better Faster- region-based convolutional neural network-based threshold was achieved using our proposed fetal heart reconstruction technique (FRT), with enhanced performance based on the outflow tract view and three-vessel view. No significant difference was found among the clinical parameters, in proportion, measured from the model rebuilt using FRT and US volume data. Furthermore, the reconstruction time of the fetal heart blood pool model was reduced from approximately 5 h to 5 min. Our results indicate that deep learning has the ability to process US data accurately, representing an important step towards the reconstruction of the fetal heart digital model, which is critical for advancing clinical diagnosis and treatment of CHD during pregnancy.

***Keywords*:** 3D printing technology; Congenital heart disease; Deep learning; Reconstruction of ultrasound imaging data

1. Introduction

Congenital heart disease (CHD) is the most common cause of infant mortality, affecting 2.4 to 13.7 per 1000 newborns.[1] Obstetric ultrasound (US) has been the gold standard imaging method for the detection and diagnosis of fetal malformations during the antenatal period. Initially, the International Society of Ultrasound in Obstetrics and Gynecology (ISUOG) emphasized the use of four-chamber view (FCV) in fetal cardiac examinations. Subsequent guidelines introduced the outflow tract view (OTV) and three-vessel view (TVV) to visualize the overall cardiac structure for a comprehensive assessment.[2] Recent advancements in 3D US techniques have significantly enhanced the visualization of spatial structures of the fetal heart.[3] However, 3D structures cannot be comprehended thoroughly based on 2D images, which usually leads to low-efficiency treatment strategy planning for the fetus.[4]

In medical imaging, deep learning approaches have gained prominence in recent years.[5] Mofrad et al.[6] utilized deep learning to augment and assist clinicians in the automated diagnosis of adult heart diseases. Nonetheless, constructing accurate fetal heart models from US data remains challenging due to the small heart size. To address this, we employed deep learning for precise fetal heart modeling, aiding in diagnosis and prenatal screening. Moreover, 3D printing technology offers opportunities to create tangible fetal heart models, benefiting various facets of fetal healthcare such as surgeon training, personalized pre-surgical planning, and doctor–patient communication.[7–10] In this study, we employed PolyJet multi-material 3D printing due to its high resolution (~200 μm), excellent surface finish, and ability to reproduce small and complex anatomical structures such as fetal heart chambers and vessels. Compared with fused deposition modeling (FDM) or stereolithography (SLA), PolyJet offers greater accuracy and material flexibility, making it particularly well-suited for fabricating detailed fetal cardiac models for clinical and educational applications. In parallel, the integration of machine learning into additive manufacturing processes has garnered increasing attention. Zhang et al.[11] provided a comprehensive review of how neural networks and reinforcement learning are being utilized to optimize printing parameters, material formulations, and fabrication efficiency. Similarly, Li et al.[12] highlighted the role of big data and digital twin frameworks in enabling adaptive and intelligent control of 3D printing workflows. While these efforts are primarily focused on manufacturing engineering, our work addresses the upstream phase—employing deep learning to enhance the fidelity of anatomical models derived from US data, which ultimately contributes to higher-quality medical 3D printing outputs. However, the time and resources required for image segmentation pose significant limitations to the clinical application of 3D printing techniques. To address the limitations of both manual processing and existing deep learning models, we propose a semi-automatic segmentation pipeline that introduces two key innovations. Firstly, a region-limited Faster Region-based Convolutional Neural Network (R-CNN)-based position detector is applied to isolate fetal heart structures from noisy US backgrounds, reducing false positives caused by rib shadowing and organ overlap. Secondly, instead of relying solely on fully automated thresholding, the system integrates expert-in-the-loop adjustments, allowing sonographers to interactively fine-tune segmentation based on grayscale analysis. This hybrid strategy offers improved interpretability, flexibility, and clinical usability—filling a critical gap between automated artificial intelligence (AI) tools and practical medical workflow.

In this study, we introduced the fetal heart reconstruction technique (FRT) for the semi-automatic segmentation and post-processing of fetal echocardiography (Figure 1). Initially, we converted US volume scans into sequential 2D images and performed detailed frame-by-frame segmentation of the fetal heart using FCV, OTV, and TVV to train and test the R-CNN. The R-CNN then identified the fetal heart's position within the echocardiogram data and generated a segmentation mask. The FRT was subsequently employed to perform segmentation of the US images, generating results for reconstructing a basic digital model of the fetal heart. Ultimately, these digital fetal heart models were 3D printed. This method offers a semi-automated approach to rapidly reconstruct fetal heart models from US data, presenting a new diagnostic strategy for clinical fetal heart analysis.

2. Methods

2.1. Study participants

The study was approved by the Ethics Committee of the Second Affiliated Hospital of Air Force Medical University (approval no. TDLL-202402-01). All pregnant women in this study were informed of the safety and limitations of US and signed an informed consent form prior to examination. We retrospectively studied the echocardiographic volume datasets obtained by 4D US with Spatiotemporal Image Correlation from 100 normal fetuses as compulsory supervised learning cases. All of the fetuses were singletons and were selected from prenatal screening tests in the Department of Ultrasound Diagnosis at Tangdu Hospital (China) from January 2019 to May 2021.

2.2. Data acquisition

The scanning operation was strictly performed in accordance with the practice guidelines updated by the

ISUOG. All pregnant women were told to relax and lie in the supine position. Echocardiographic volume data were obtained by a Voluson E10 US system (GE Healthcare, USA [Campanella, #25]) equipped with an eM6C electric matrix transducer (2–7 MHz) to ensure that the fetus was in the supine position and its cardiac apex facing towards the front (11, 12, or 1 o'clock directions). Once data collection was initiated, the pregnant woman was told to avoid making any movement and hold her breath in order to minimize stitching artifacts. Meanwhile, principal sections, including the abdominal transverse section, the standard FCV, the left ventricular outflow tract section, the right ventricular outflow tract section, and the three-vessel section and its derivative sections, were examined strictly in accordance using the three-segment analysis method to ensure the proper condition of fetal hearts. Finally, the end-systolic phase with valves completely closed was precisely selected using M-mode; the data set was saved and output in Cartesian volume format for editing and 3D modeling.

2.3. Preprocessing of volume data into 2D images

A standard full scanned data includes 50–100 volume data, consisting of each time phase of the fetal heart. In this study, one end-diastolic volume data contained the spatial structure of the fetal heart extracted from each individual and can be decomposed into 50–70 2D images—depending on the size of the heart—spaced 0.02 cm apart from each other. All images were saved in JPEG format. According to the suggestions of ISUOG, images were divided into FCV, OTV, and TVV. To generate the label that can be trained by Deep Neural Network (DNN), the graphical image annotation tool "LabelImg" was used by professional sonographers to annotate data. A standard data stream is made up of a JPEG 2D image as data and an annotation (in XML format) as the label. The complete dataset contained 5255 data streams from 110 unique individuals. Images were randomly split into 3297, 1097, and 403 images as the training, validation, and test sets, respectively. Each image and annotation was manually rechecked by two sonographers who did not participate in the annotation of original data to confirm the reliability of the data set. The summary statistics of data are presented in Table 1.

2.4. Model development and training for fetal heart position detection

As displayed in Figure 1, FRT is an interactive method of medical image segmentation, combining both position detection and interactive binary threshold segmentation. Position detection was performed using the Faster-R-CNN architecture, which contains a feature extractor, region proposal networks (RPNs), region of interest (ROI) pooling, and a classifier.[13] A convolutional neural network (CNN) was used to extract the potential feature in the detection field during image classification, as it can accurately identify human-identifiable phenotypes and characteristics that are not recognized by human experts.[14–18] The Visual Geometry Group (VGG) CNN architecture—without complete connection and classification layers—is retrained by backpropagation and was used as the feature extractor.[19] Each image was resized to 300 × 300 pixels to ensure compatibility with the dimensions of the VGG network architecture before processing in the feature extractor. Region proposals are the output of RPN, which consists of classification and regression layers. The classification layer has a score that represents the ROI or the background, while the regression layer has four coordinates that indicate the position of the fetal heart. ROI pooling, characterized by the non-fixed size of feature maps, is used to collect region proposals generated by RPNs and feature maps, creating a vector with a similar shape to the feature map. In the classifier, bounding box regression and classification layers were used to generate a more accurate target detection box and proposal class.

For detecting the position of the fetal heart, the parameters were initialized randomly and trained using the same learning rate of 0.001, momentum of 0.9, and batch size of 16 to minimize the function loss for each object proposal. The model was trained using the training set and tested using the test set. The data were split such that the same US image was not in both training and test sets. Both training and test were performed in Python using Google's TensorFlow deep learning framework.[20] The training was terminated if the internal validation loss did not decrease for 10 epochs (early stopping criteria), and

Table 1. Summary statistics of the training, test, and validation sets

View	Training	Test	Validation	Total
FCV	1462	627	224	2313
OTV	1096	470	164	1730
TVV	739	317	156	1212
Total	3297	1097	403	5255

Note: The values in the table refer to the number of annotated 2D ultrasound images. Abbreviations: FCV: Four-chamber view; OTV: Outflow tract view; TVV: Three-vessel view.

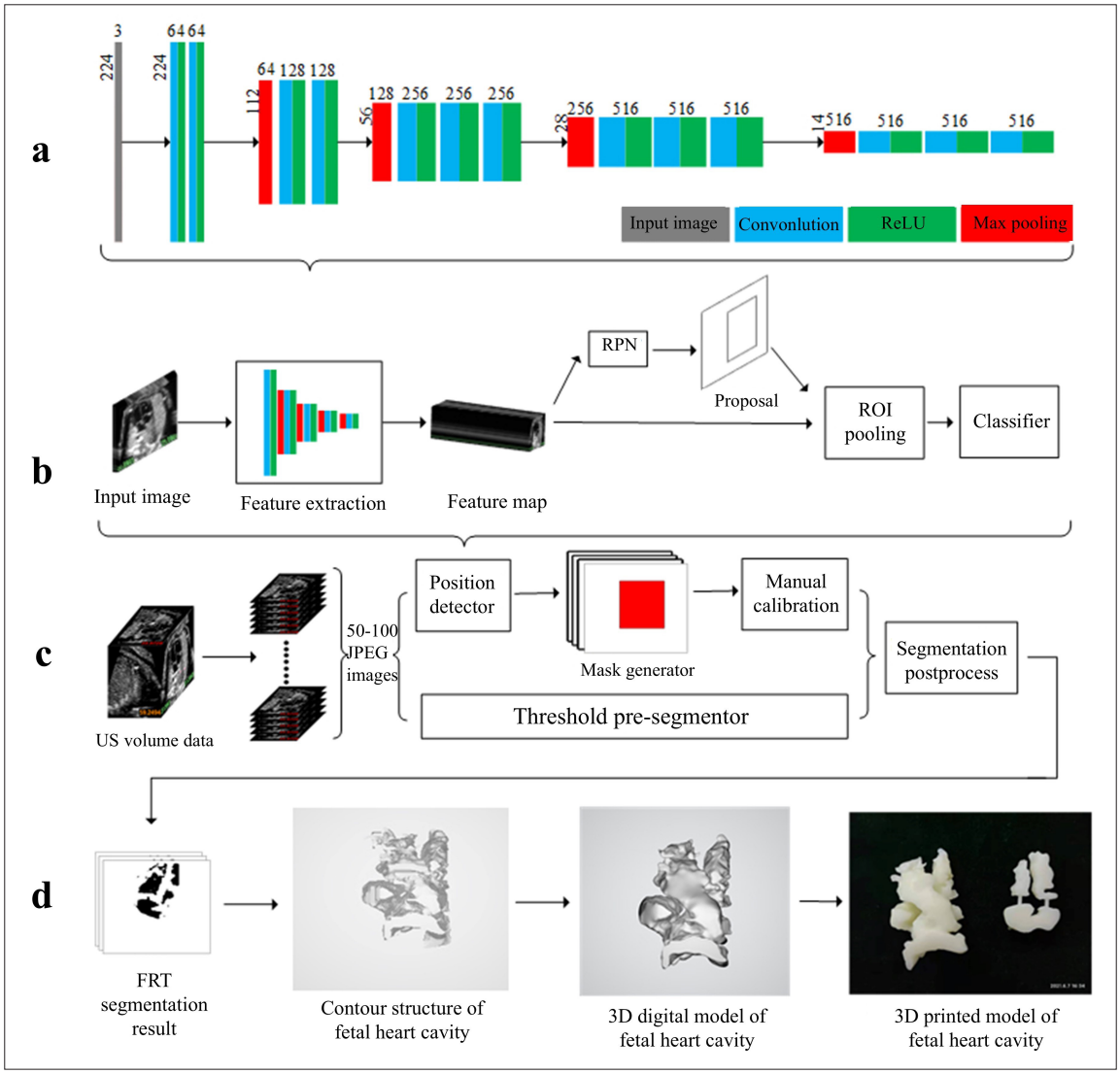

Figure 1. Workflow of reconstructing a 3D fetal heart cavity digital model using FRT. (A) Feature extraction: the number by the left of each layer represents the width and height, while the number on the top of each layer represents the depth; different colors represent different operations on the layer. (B) Position detection: feature maps generated by feature extraction were shared between the RPN and ROI pooling layer; proposals and feature maps collected by ROI pooling were sent to the classifier for classification and bounding box regression. (C) Framework of FRT: US volume data were divided into 2D images for segmentation; FRT used position detection to generate masks for the restriction segment area; manual calibration was performed to solve errors in the restriction area, and the masks were then multiplied with the binary results; finally, FRT segmentation results were obtained by post-processing. (D) Different stages of reconstructing the 3D-printed model of the fetal heart cavity (from the left to right): contour structures of the initial model, digital model after processing, and the 3D-printed model. Abbreviations: FRT: Fetal heart reconstruction technique; RPN: Region proposal networks; ROI: Region of interest; US: Ultrasound.

the maximum number of epochs was set to 10,000. All training was performed on a Linux operating system with one available P100 GPU and 16 GB RAM.

2.5. Reconstruction of fetal heart

Mimics software (Research Edition 21.0, Materialise NV, Belgium) is widely used in medical 3D printing and performs well in the analysis and segmentation of mineralized tissues, such as bones and teeth, in computed tomography and magnetic resonance imaging images. However, the threshold segmentation method provided by Mimics software is incapable of accurately distinguishing the region of the blood pool due to the influence of rib-shading occlusion and celiac region. For this reason, FRT uses AI to narrow down the area to be segmented as much as possible. Moreover, the segmentation results from FRT can be imported into Mimics software to rebuild the 3D model. A fetal heart position detector was used to identify

the segmented area that contains the entire structure of the heart, further generating the position mask. The mask is a matrix whose shape and position directly correspond to those of the image. To ensure that all subsequent operations are within the scope of the mask, all elements of the mask within the segmented area were labeled 1, while other elements were labeled 0. The restricted area was obtained by multiplying the mask with the original image; the grayscale distribution of the original image and the restricted area was calculated and plotted as curves. Sonographers could select an appropriate threshold to segment the restricted area by relying on the curves. By repeating the operation for each image decomposed from the echocardiographic volume data, the segmentation of scan data was obtained. Finally, the smoothing algorithm and seed fill algorithm were employed during the post-processing of segmentation.[21]

The fetal heart is a continuous solid body. Therefore, if the interval between adjacent layers of the image scanned by ultrasonic instrument (d) is small, it can be assumed that the images and their segmentations are similar between layers, or at least not significantly different. An end-diastolic volume data consists of coronal, axial, and sagittal raw sectioned images. Axial raw sectioned images were generated at 0.2 cm intervals and were sent to FRT for segmentation. Surface reconstruction of the entire structures of the fetal heart was simultaneously achieved by stacking the outlines of the segmentation results layer by layer. (x, y, z) is the coordinate of a point on the model, and $model\ (x, y, z)$ indicates whether the point is part of the model; 1 denotes "yes" and 0 denotes "no." The concept of similarity, $dst_i\ (x, y)$ indicates whether the point is part of the model on the 2D segmentation result of layer i from FRT. Therefore, the mathematical representation of the model is:

$$model\ (x, y, z) = dst_i\ (x, y) \tag{I}$$

where, in normal circumstances, $z = i$.

Removal of free structure and surface smoothing was performed in Mimics software during model post-processing to obtain a smoother and more intuitive digital model. Thereafter, the 3D model was printed with an SLA 3D printer (J750, Stratasys, USA) using photosensitive material.

2.6. 3D printing process

The 3D digital fetal heart models were fabricated into physical models using a Stratasys J750 PolyJet 3D printer (Stratasys, USA). This multi-material inkjet technology was selected for its capability to achieve high-resolution prints with smooth surface finishes, which are essential for accurately reproducing the intricate anatomical details of the fetal heart, such as chambers and vessels.

A key characteristic of the Stratasys J750 system is that fundamental print parameters, unlike those in many FDM or SLA systems, are largely controlled internally and are not user-adjustable. Instead, print characteristics are primarily determined by the selection and combination of photopolymer materials. For this study, a blend of flexible, rubber-like material and rigid resin was chosen. This material combination resulted in models with a Shore D hardness of approximately 60, providing a balance of structural stability and pliability. The models were printed at a high-quality setting, achieving a layer resolution of 200 μm. These properties enhance the models' utility for clinical visualization, education, and diagnostic communication.

2.7. Evaluation

To evaluate the performance of the segmentation task, the labels from the test set were used as the standard to calculate the positive prediction rate, recalling rate, mean intersection over union (mIOU), and Dice similarity coefficient (DSC). According to the standard label (sl) from experienced sonographers and segmentation result (sr), the pixel can be divided into four categories: true positive (TP; sl: 1, sr: 1), false positive (FP; sl: 0, sr: 1), true negative (TN; sl: 0, sr: 0), and false negative (FN; sl: 1, sl: 0). For the segmentation result of a single ultrasonic image, the values of TP, FP, TN, and FN are the total number of pixels of the corresponding category, respectively. Therefore, the positive prediction rate (P) and recalling rate (R) are defined as:

$$P = \frac{TP}{TP + FP} \tag{II}$$

$$R = \frac{TP}{TP + FN} \tag{III}$$

According to the prediction rate and recalling rate, the mIOU and DSC can be defined as:

$$mIOU = \frac{TP}{TP + FN + FP} \tag{IV}$$

$$DSC = \frac{2 \times TP}{\left(TP + FN\right) + \left(TP + FP\right)} \tag{V}$$

Since the assessment of performance on 2D images alone is insufficient to verify the accuracy of spatial structures of the 3D digital model, digital models rebuilt by different methods (e.g., manual reconstruction by doctors of varying experience and deep learning-based methods) were printed into physical models. The long diameter of the left ventricle (LDLV), long diameter of the right ventricle (LDRV), long diameter of the left atrium (LDLA), the transverse diameter of the left atrium (TDLA), long diameter of the right atrium (LDRA), and transverse diameter of right atrium (TDRA) were measured based on the physical model using a vernier caliper (Figure 6F). In addition, the same measurements were performed by sonographers of varying experience (junior doctor: <3 years of experience; middle doctor: 3–6 years of experience; senior doctor: >6 years of experience) on US volume data using the Voluson E10 US system. Notably, amplifying fine structures is an advantage of the 3D-printed model. Direct comparison of specific values is not scientific, as the length of each part changes with the magnification. Thus, with LDLV as the benchmark, the rest of the metrics were converted into ratios relative to LDLV. Finally, a one-way analysis of variance (ANOVA) was performed for comparisons among clinical evaluation values in proportion.

The performance of the segmentation task was evaluated using Python data analysis and manipulation tools, such as Numpy, Pandas, and Matplotlib. For evaluation of the performance of the 3D structure, one-way ANOVA was performed for comparisons among multiple groups using GraphPad PRISM 5.0. For all experiments, significance was defined as: $^{*}p < 0.05$, $^{**}p < 0.01$, and $^{***}p < 0.001$. No statistical method was used to predetermine the sample size.

3. Results

3.1. Segmentation performance

For reconstructing the 3D digital model of the fetal heart, identifying the blood pool in fetal hearts was the most important step in the process. Accuracy, interpretability, and variability were all important indicators for reconstruction. To investigate the accuracy of FRT, the mIOU/DSC of segmentations from three different views—using the thresholding method in Mimics software—were 0.242/0.381 for FCV, 0.165/0.278 for OTV, and 0.121/0.214 for TVV, respectively. Using the FRT method, there was a significant improvement in the performance from different views (FCV: 0.701/0.823; OTV: 0.681/0.809; TVV: 0.602/0.746). Furthermore, smoothing and removal of free small objects also enhanced performance based on FCV and OTV (FCV: 0.714/0.832; OTV: 0.687/0.813) after calibration. In summary, FRT performance is better based on OTV and TVV and worse based on FCV relative to segmentation conducted by junior doctors. Details of the evaluation indicators of the segmentation results using different methods are displayed in Table 2.

3.2. Interpretability of results

To further investigate the interpretability of the significant improvements achieved by the position detector, we hypothesized that it reduces the influences of noise, shadow, and other factors in US images by limiting the area of image processing. The grayscale distribution maps of the segmentation area indicated that there was a significant decrease in the number of pixels in the grayscale range of 20–40 (Figures 2 and 3).

Combined with the original images, these reduced pixels were mainly distributed in the shadow and noise of the non-target region. The recall rate of FRT significantly improved, and the positive prediction rate

Table 2. Segmentation performance of different methods

Method	FCV		OTV		TVV	
	IOU	DSC	IOU	DSC	IOU	DSC
Threshold	0.242	0.381	0.165	0.278	0.121	0.214
U-Net	0.712	0.830	0.593	0.740	0.431	0.591
Junior doctor	0.798	0.887	0.658	0.789	0.530	0.684
FRT-Default	0.701	0.823	0.681	0.809	0.602	0.746
FRT-IA	0.714	0.832	0.687	0.813	0.599	0.744

Note: IOU and DSC were used to evaluate the segmentation performance across different methods (rows); "FRT-Default" refers to segmentation by FRT using default parameters without manual interaction; "FRT-IA" refers to segmentation by FRT with manual interaction. Abbreviations: DSC: Dice similarity coefficient; FCV: Four-chamber view; FRT: Fetal heart reconstruction technique; IOU: Intersection over union; OTV: Outflow tract view; TVV: Three-vessel view.

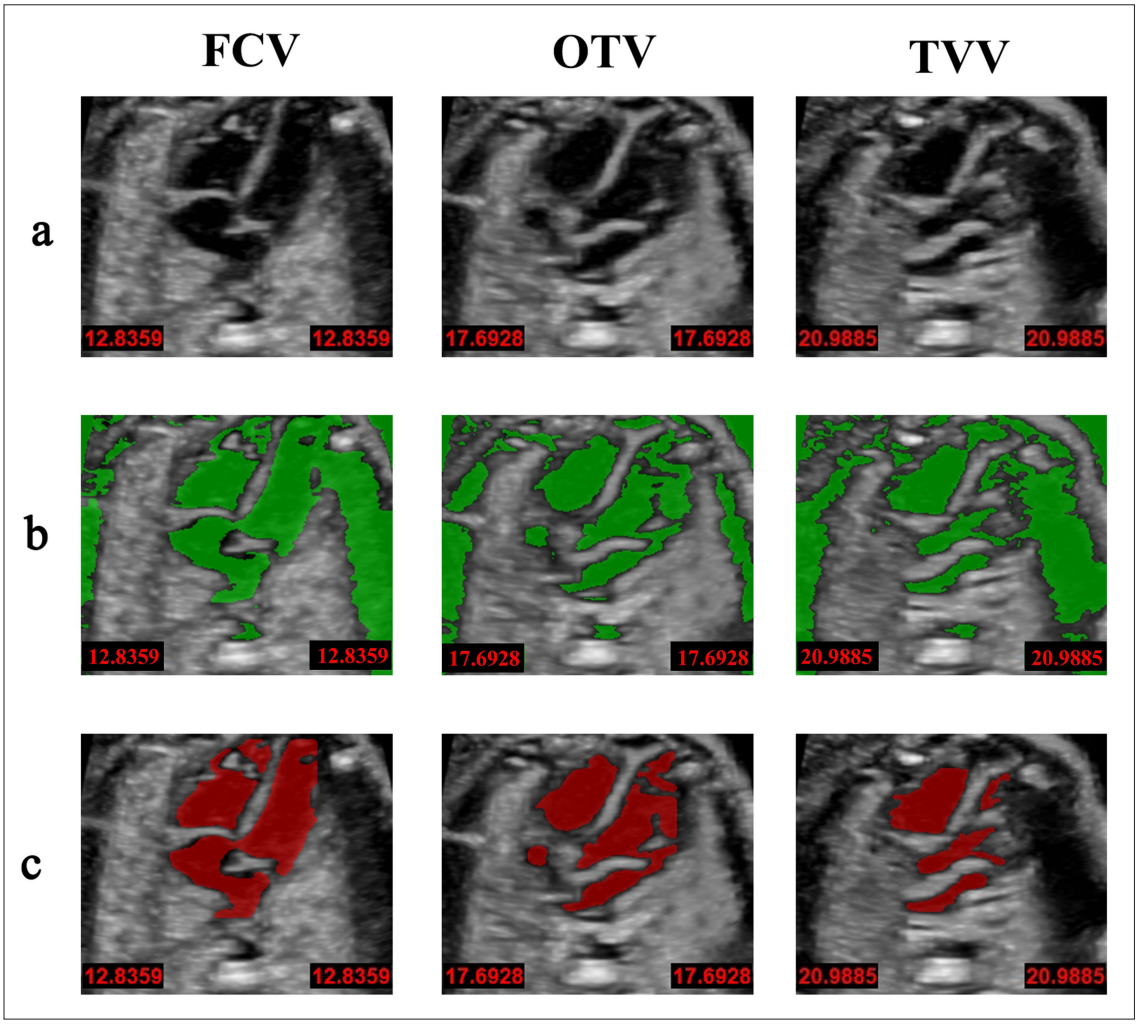

Figure 2. Examples of the segmentation results by threshold and FRT from different views (FCV, OTV, and TVV): (A) original images; (B) threshold segmentation results, and (C) FRT segmentation result. Abbreviations: FCV: Four-chamber view; FRT: Fetal heart reconstruction technique; OTV: Outflow tract view; TVV: Three-vessel view.

slightly decreased, validating our hypothesis to an extent. Although deep learning has achieved remarkable progress over the past decade, the robustness and interpretability of automated medical image segmentation have not been sufficiently addressed. To overcome the limitation, FRT used interactive image segmentation through manual correction by expert sonographers. As displayed in Table 2, the IOU and DSC of FRT from different views had advantages over that of U-Net, which is an automated method designed for fast and precise segmentation of biomedical images. These findings demonstrated that FRT had greater segmentation performance compared to U-Net.

3.3. Comparison with variation

Reconstruction of the 3D digital model relies on the segmentation results of each layer. The reliability of the 3D digital model was affected by the segmentation performance across all layers within the US volume data, making the variability of segmentation performance crucial for 3D model reconstruction. A box plot was plotted, and the standard deviations (STDs) were calculated to investigate the variability of segmentation results using different methods on the validation set (Figure 4). Compared with other methods, the variance IOU/DSC of OTV (FRT-Default: median: 0.692/0.818, STD: 0.055/0.038; FRT-IA: median: 0.693/0.819, STD: 0.069/0.051) and TVV (FRT-Default: median: 0.609/0.757, STD: 0.096/0.087; FRT-IA: median: 0.613/0.760, STD: 0.101/0.091) segmented by FRT were smaller. However, on FCV, junior doctors achieved better performance than that of FRT (median: 0.8104/0.8953, STD: 0.040/0.025). In addition, compared to FRT and junior doctors, U-Net demonstrated no

significant advantage across the three views (FCV: median: 0.6721/0.804, STD: 0.076/0.055; OTV: median: 0.654/0.791, STD: 0.142/0.138; TVV: median: 0.547/0.707, STD: 0.158/0.165). These results indicated that FRT had achieved a non-inferior performance compared with junior doctors, consistent with the results in Table 2.

3.4. Analysis of spatial structures of 3D models

All cases in the validation set were successfully rebuilt and printed using FRT to assess the accuracy of the 3D digital model and 3D-printed physical model (Figure 5). Our findings indicate that the physical model can intuitively display the spatial structures and morphologic characteristics of the blood pool in the fetal heart. Likewise, the 3D-printed physical models were well-matched with digital models, and the FRT model achieved the best accuracy among these models based on the structure of the whole heart, as well as the OTV and FCV of the fetal heart. To further investigate the accuracy

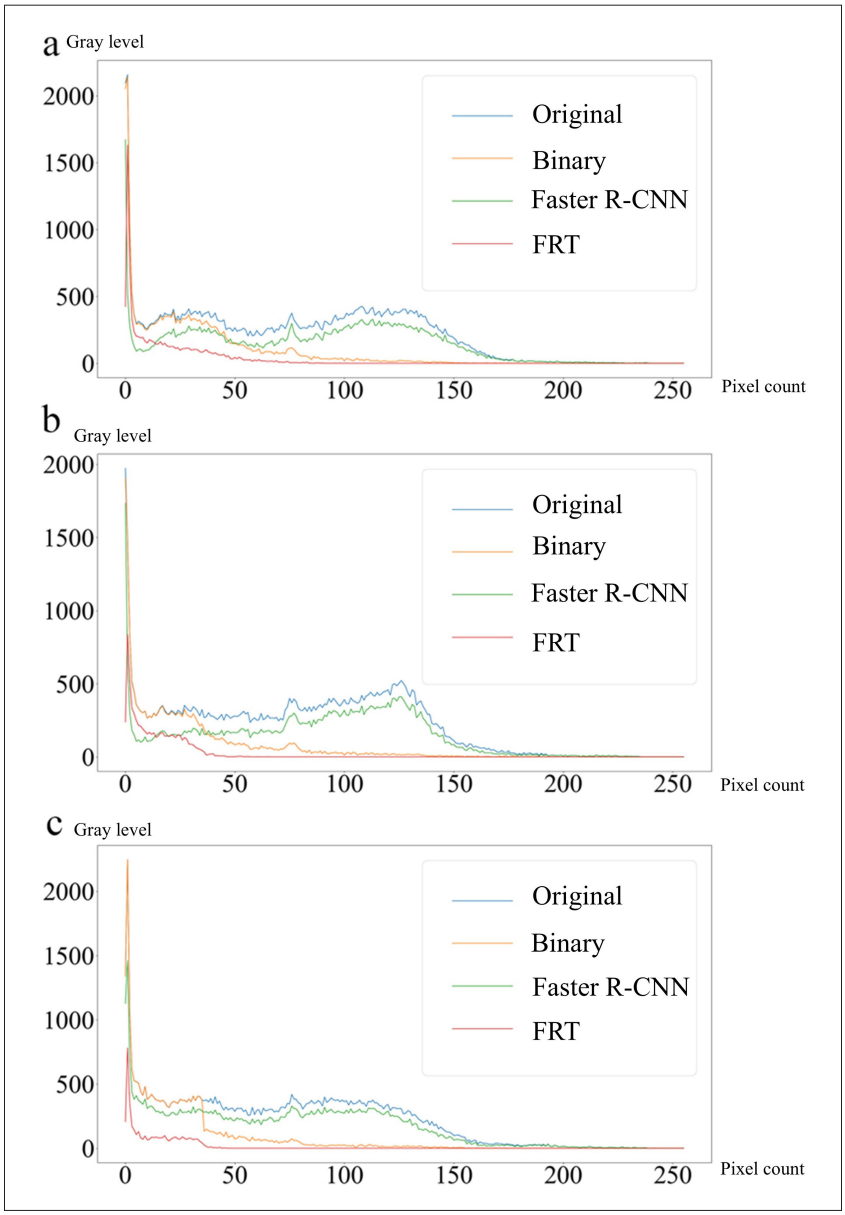

Figure 3. Grayscale distribution curves at different views: (A) FCV, (B) OTV, and (C) TVV. The blue curve represents the original image; the green curve represents the Faster-R-CNN position detector; the orange curve represents the binary threshold; and the red curve represents FRT. FRT utilized position detection to reduce the influence of noise, shadow, and other factors in US images by limiting the range of image processing. Abbreviations: FCV: Four-chamber view; FRT: Fetal heart reconstruction technique; OTV: Outflow tract view; R-CNN: Region-based convolutional neural network; TVV: Three-vessel view; US: Ultrasound.

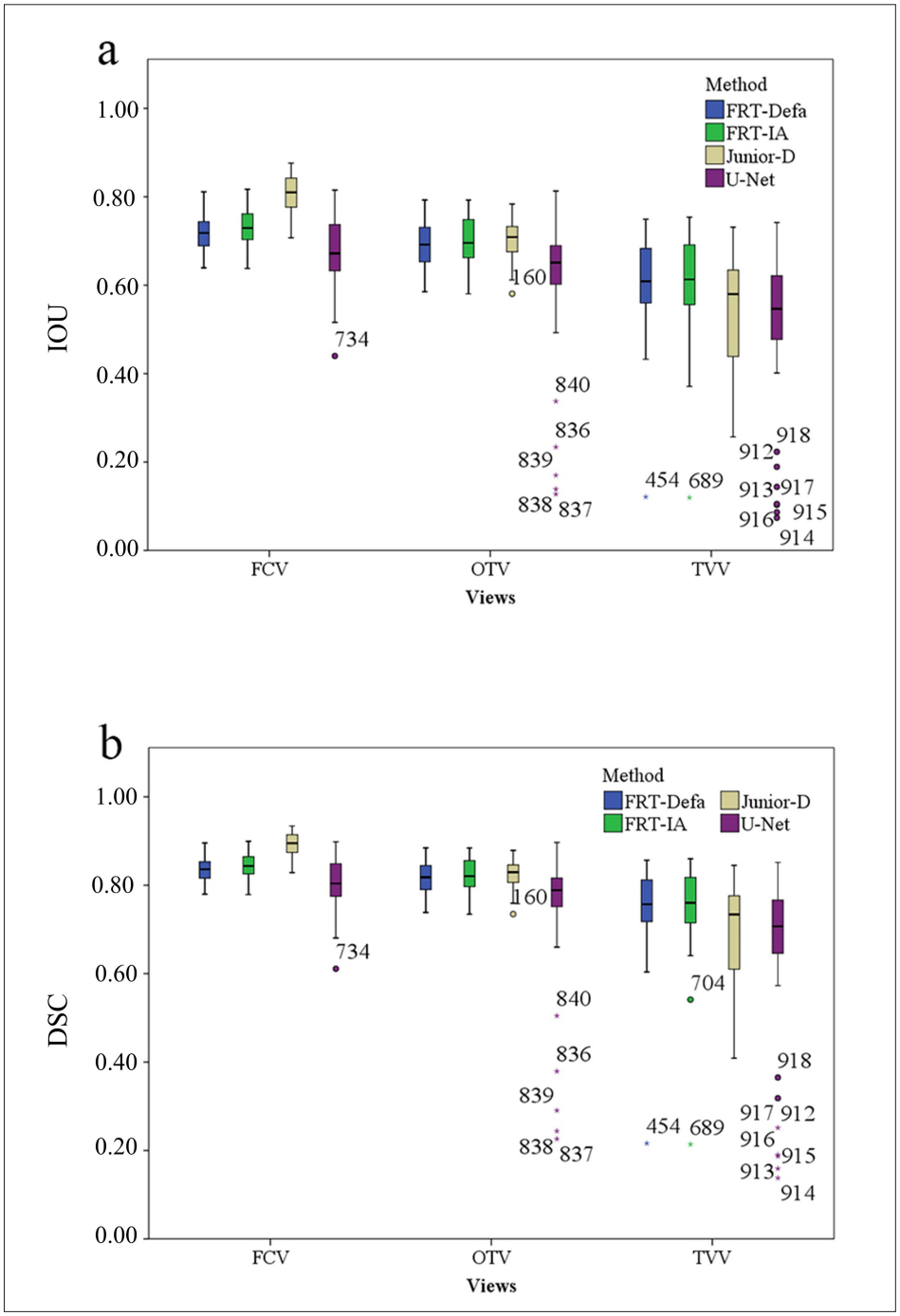

Figure 4. Variability of segmentation results using different methods. (a) Box plot of IOU variance using different methods. (b) Box plot of DSC variance using different methods. Box plots display the median as a thick line, the 25th and 75th percentiles as upper and lower bounds of the box, and individual points for data values that lie more than 1.5× the interquartile range from the median. Abbreviations: DSC: Dice similarity coefficient; FCV: Four-chamber view; IOU: Intersection over union; OTV: Outflow tract view; TVV: Three-vessel view.

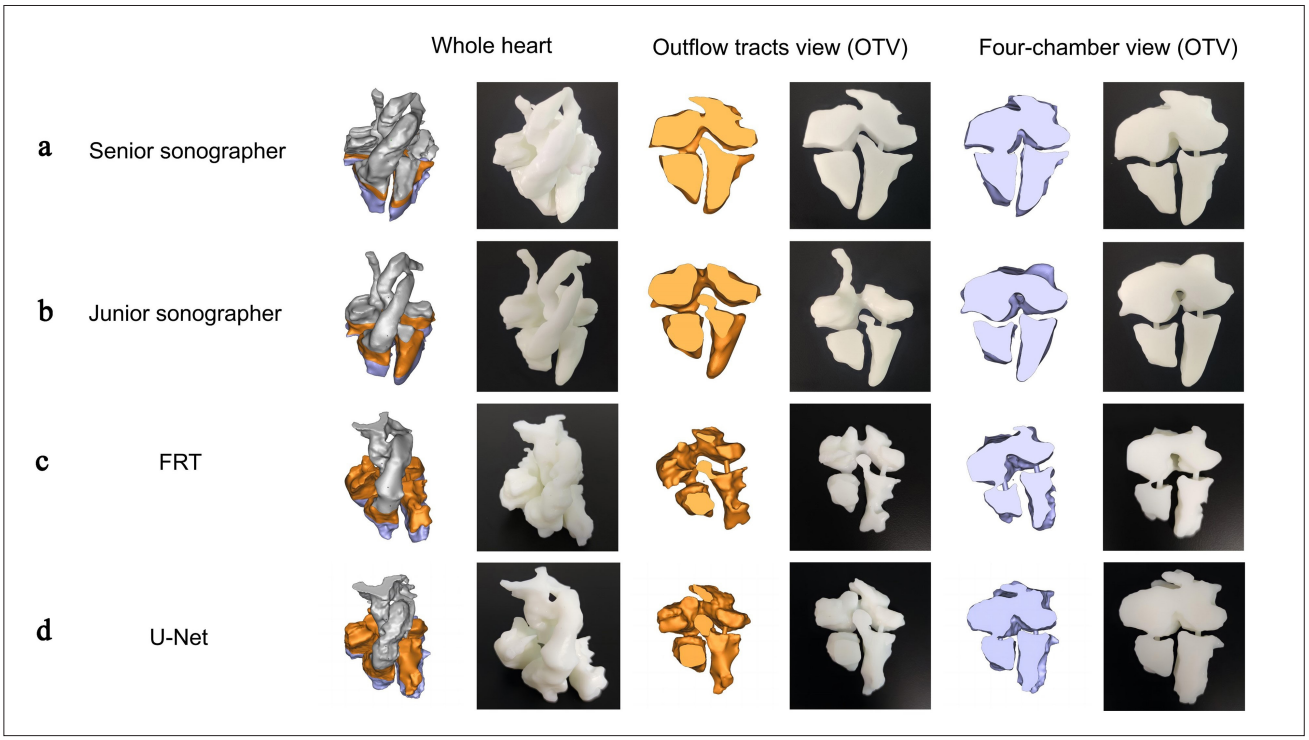

Figure 5. Examples of the 3D digital model and 3D-printed physical model of the blood pool in the fetal heart reconstructed by different methods based on the whole heart structure, OTV, and FCV: (A) manually reconstructed by a senior sonographer, (B) manually reconstructed by a junior sonographer, (C) reconstructed using FRT, and (D) reconstructed using U-Net. Abbreviations: FRT: Fetal heart reconstruction technique; OTV: Outflow tract view; FCV: Four-chamber view.

of clinical evaluation values, digital models were measured using Measure 3D Distance in Mimics software, while physical models were measured with a vernier caliper. At present, the same metrics were measured using a Voluson E10 US system with conventional 2D echocardiography to analyze the consistency among US volume data, the digital model, and the physical model. We found that there was no significant difference, in proportion, in the clinical evaluation values (LDLV, LDRV, LDLA, TDLA, LDRA, and TDRA) of US volume data measured by physicians and those measured using 3D models (Figure 6).

4. Discussion

The FRT is an advanced deep learning algorithm developed in the USA, designed to achieve cutting-edge reconstruction of fetal heart blood pool models. This groundbreaking technology combines deep learning detectors with traditional computer vision techniques to accurately segment ultrasonic images, ensuring the utmost structural precision in the resulting digital model. FRT represents a pioneering method for reconstructing fetal heart models through deep learning technology, surpassing the efficiency of human sonographers in model rebuilding. With just a single GPU, FRT enables the completion of ultrasonic image segmentation tasks for each patient within a mere minute following parameter specification. This is a remarkable improvement over the efficiency of human experts, which can take significantly longer. Consequently, FRT overcomes two major limitations in fetal heart remodeling: the time-consuming and labor-intensive nature of the process. Furthermore, FRT holds the potential to greatly benefit clinicians and patients through its applications in medical 3D printing technology.

At present, US is widely used for prenatal examinations across the world due to its relative safety, cost-effectiveness, non-invasive nature, real-time display, operator comfort, and experience.[22] However, US images have their unique limitations, including lower imaging quality, high dependence on operator or diagnostician experience, and significant variations between observers and systems used by the same observer.[23] In this context, there is a pressing need for a more objective, accurate, visual, intelligent, and integrated method for US analysis in prenatal healthcare. Deep learning has demonstrated remarkable success in medical image analysis, providing automatic tools and state-of-the-art performance.[15,17,18,24–27] Furthermore, the

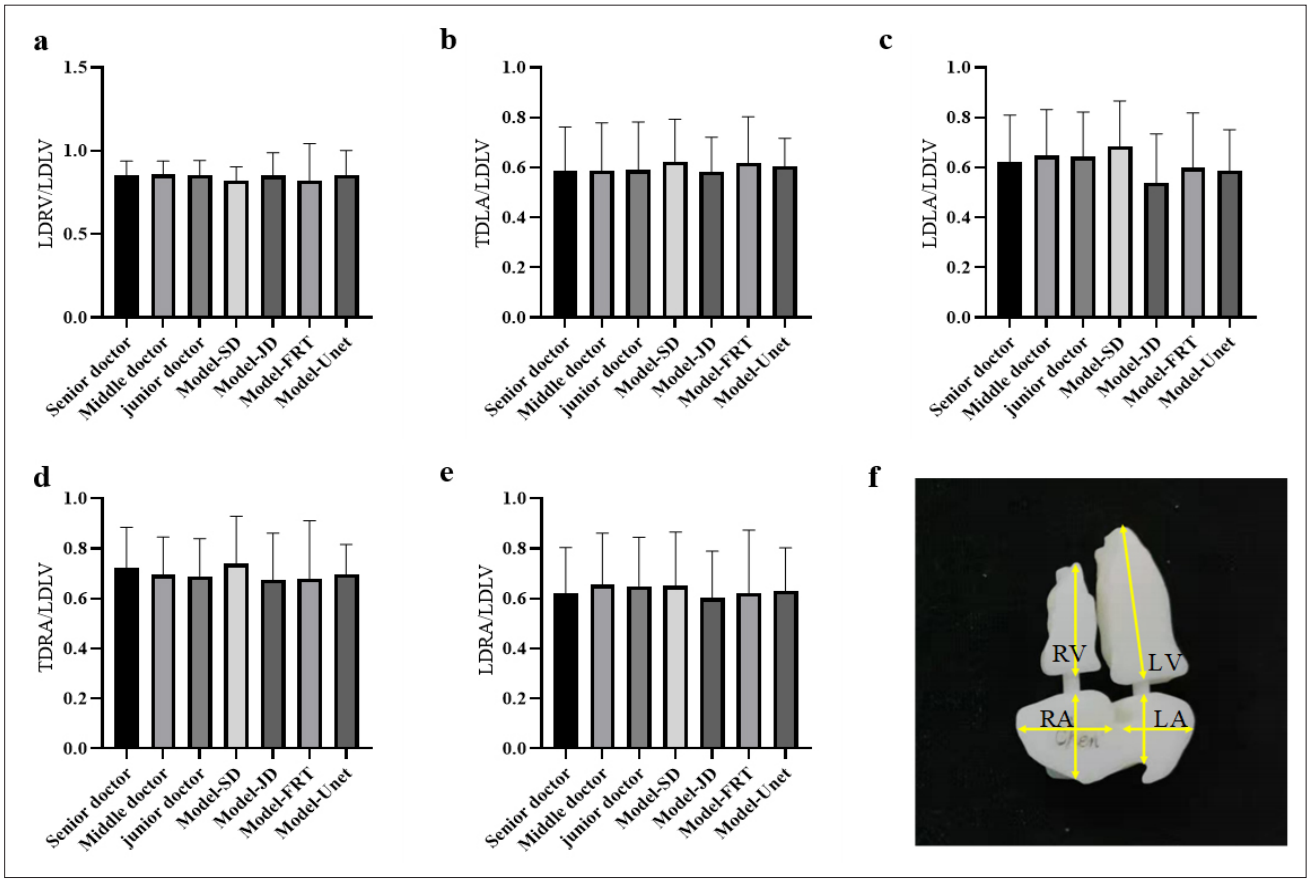

Figure 6. Variance analysis and significance test of clinical evaluation parameters (n = 3). (A) Histogram of the ratio of LDRV to LDLV. (B) Histogram of the ratio of TDLA to LDLV. (C) Histogram of the ratio of LDLA to LDLV. (D) Histogram of the ratio of TDRA to LDLV. (E) Histogram of the ratio of LDRA to LDLV. (F) Diagram of LDLV, LDRV, LDLA, TDLA, LDRA, and TDRA. Four parts are marked in the figure: the horizontal lines of the corresponding parts indicate the transverse diameters, while the vertical line indicates the long diameter. Abbreviations: LDLV: Long diameter of left ventricle; LDRV: Long diameter of right ventricle; TDLA: Transverse diameter of left atrium; LDLA: Long diameter of left atrium; TDRA: Transverse diameter of right atrium; LDRA: Long diameter of right atrium.

availability of digital models and 3D printing has opened the door to visualized prenatal examinations, offering benefits such as personalized preoperative planning, surgical simulations, enhanced medical education, and improved doctor–patient communication. Despite these advantages, 4D US scanning systems, viewable only on 2D screens, are more commonly preferred by hospitals due to the laborious and time-consuming nature of traditional manual remodeling methods.[28] FRT, however, can effectively address these limitations by semi-automating image processing tasks, thereby facilitating fast reconstruction of fetal heart models that combine seamlessly with 3D printing technology. This enables a quicker, more visualized, and intelligent approach to prenatal cardiac examination. Comparing FRT to end-to-end methods, our interactive semi-automatic algorithm offers greater flexibility and interpretability to sonographers. It allows for the adjustment of relevant parameters to enhance segmentation accuracy, granting healthcare professionals more control over the process. Moreover, the application of deep learning in this context is not merely a computational convenience, but a necessary enabler of clinical progress. The fetal heart is exceptionally small, with indistinct boundaries and low image contrast, making manual segmentation challenging and prone to variability. Traditional image processing tools are often insufficient to achieve reliable anatomical reconstruction under these conditions. FRT's integration of AI-driven detection and interactive thresholding directly addresses these challenges, demonstrating that AI can be purposefully designed to overcome domain-specific limitations, not just automate existing workflows. While the proposed FRT framework does not directly optimize 3D printing parameters, such as print path, material composition, or

support structures, its impact on the quality of printed fetal heart models is significant. By producing anatomically accurate and clean digital reconstructions with minimal noise and well-defined boundaries, FRT substantially reduces the need for manual mesh correction and improves the fidelity of 3D-printed outputs. In this aspect, the deep learning pipeline acts as an upstream quality enhancer for additive manufacturing. Therefore, future studies may explore extending AI involvement to the printing process itself—such as adaptive slicing strategies or automated printability evaluation—to further improve the efficiency and accuracy of model production.

In terms of practical workflow efficiency, FRT significantly outperforms traditional manual methods. Manual reconstruction of a fetal heart digital model typically requires clinicians to segment US volume data layer by layer from 2D slices—a labor-intensive and time-consuming process. With FRT, most segmentation tasks are automated, while clinicians can interactively calibrate the output using threshold adjustments. This semi-automatic pipeline reduces the reconstruction time for a single digital heart cavity model from approximately 5 h to just 5 min. Even without human interaction, the process can be completed in 2 min, albeit with slightly reduced accuracy. These findings demonstrate the considerable clinical value of FRT, particularly in reducing workload and enabling timely decision-making in prenatal care.

Nonetheless, FRT does have some limitations. Firstly, the size and quality of the dataset have a direct impact on the accuracy of the deep learning model. The dataset used in FRT comprises 4852 data streams from 100 unique individuals, which could potentially limit the model's performance. To address this challenge, interactive segmentation that incorporates user knowledge is integrated, resulting in a more robust segmentation performance. Secondly, while FRT significantly reduces the time required for digital model reconstruction, it is not yet capable of achieving real-time analysis of fetal heart functions. Several limitations contribute to this challenge: (i) obtaining a more robust performance through the interactive method is time-consuming; (ii) the low quality of US images and the high variation between different operators make it difficult to extract useful features, limiting the performance of end-to-end DNNs; and (iii) the limited training data available represents a bottleneck for the application of deep learning methods in prenatal US image analysis. In summary, the results of our research represent a crucial advancement in the reconstruction of digital fetal heart models using US volume data and deep learning technology. FRT significantly reduces the time and labor costs associated with reliable model construction, paving the way for the future development of real-time analysis systems based on 3D digital models, as opposed to the current 2D anatomical section-based approach. Future research efforts will focus on achieving real-time analysis of 3D fetal hearts, further enhancing the field of prenatal healthcare.

5. Conclusion

In this study, a fetal heart 3D digital model was constructed using FRT based on US volume data. The model may be used to enhance the clinical diagnosis and treatment of CHD during pregnancy. Our results indicate that deep learning has the ability to process US data accurately, representing an important step towards reconstructing fetal heart digital model and advancing clinical diagnosis and treatment of CHD during pregnancy.

Acknowledgments

None.

Funding

This work was supported by the Key Research and Development Project of Shaanxi Province (2021LLRH-08).

Conflict of interest

The authors declare that they have no competing financial interests or personal relationships that could have appeared to influence the work reported in this paper.

Author contributions

Conceptualization: Lijun Yuan, Airong Qian
Data Curation: Zekai Zhang, Zhuojun Mao
Investigation: Wenjuan Zhang, Linbin Lai
Methodology: Jiahe Liang, Zewen Zhang
Resources: Yitong Guo, Na Hou
Supervision: Tiesheng Cao, Yu Li, Lijun Yuan, Airong Qian
Writing–original draft: Wenjuan Zhang, Linbin Lai
Writing–review & editing: Tiesheng Cao, Yu Li

Ethics approval and consent to participate

This study involved human subjects and was conducted in accordance with the ethical principles outlined in the Declaration of Helsinki. The research protocol titled "Three-dimensional Fast Reconstruction in Fetal Ultrasound Imaging Using Artificial Intelligence Techniques and Three-dimensional (3D) Bioprinting" was reviewed and approved by the Institutional Review Board (IRB) of Tangdu Hospital, Air Force Medical University (approval no.: TDLL-202402-01; date: January 5, 2024).

Consent for publication

Prior to participation, all subjects provided written informed consent. The study adhered to strict confidentiality and data protection measures to ensure the privacy of participants. No additional ethical concerns or conflicts of interest were identified during the research.

Availability of data

The clinical imaging data used in this study are restricted by ethical data protection permissions and are not available for distribution.

References

1. Benjamin EJ, Muntner P, Alonso A, et al. Heart disease and stroke statistics-2019 update: a report from the American Heart Association. *Circulation*. 2019;139(10):e56-e528. doi: 10.1161/cir.0000000000000659
2. International Society of Ultrasound in Obstetrics and Gynecology, Carvalho JS, Allan LD, et al. ISUOG practice guidelines (updated): sonographic screening examination of the fetal heart. *Ultrasound Obstet Gynecol*. 2013;41(3):348-59. doi: 10.1002/uog.12403
3. Jantarasaengaram S, Vairojanavong K. Eleven fetal echocardiographic planes using 4-dimensional ultrasound with spatio-temporal image correlation (STIC): a logical approach to fetal heart volume analysis. *Cardiovasc Ultrasound*. 2010;8:41. doi: 10.1186/1476-7120-8-41
4. Huang J, Shi H, Chen Q, et al. Three-dimensional printed model fabrication and effectiveness evaluation in fetuses with congenital heart disease or with a normal heart. *J Ultrasound Med*. 2021;40(1):15-28. doi: 10.1002/jum.15366
5. Fu Y, Lei Y, Wang T, Curran WJ, Liu T, Yang X. Deep learning in medical image registration: a review. *Phys Med Biol*. 2020;65(20):20tr01. doi: 10.1088/1361-6560/ab843e
6. Madani A, Ong JR, Tibrewal A, Mofrad MRK. Deep echocardiography: data-efficient supervised and semi-supervised deep learning towards automated diagnosis of cardiac disease. *NPJ Digit Med*. 2018;1:59. doi: 10.1038/s41746-018-0065-x
7. Ackland DC, Robinson D, Redhead M, Lee PVS, Moskaljuk A, Dimitroulis G. A personalized 3D-printed prosthetic joint replacement for the human temporomandibular joint: from implant design to implantation. *J Mech Behav Biomed Mater*. 2017;69:404-411. doi: 10.1016/j.jmbbm.2017.01.048
8. Diment LE, Thompson MS, Bergmann JHM. Clinical efficacy and effectiveness of 3D printing: a systematic review. *BMJ Open*. 2017;7(12):e016891. doi: 10.1136/bmjopen-2017-016891
9. Hosny A, Dilley JD, Kelil T, et al. Pre-procedural fit-testing of TAVR valves using parametric modeling and 3D printing. *J Cardiovasc Comput Tomogr*. 2019;13(1):21-30. doi: 10.1016/j.jcct.2018.09.007
10. Costello JP, Olivieri LJ, Su L, et al. Incorporating three-dimensional printing into a simulation-based congenital heart disease and critical care training curriculum for resident physicians. *Congenit Heart Dis*. 2015;10(2):185-90. doi: 10.1111/chd.12238
11. Ng WL, Goh GL, Goh GD, Ten JSJ, Yeong WY. Progress and opportunities for machine learning in materials and processes of additive manufacturing. *Adv Mater*. 2024;36(34):e2310006. doi: 10.1002/adma.202310006
12. Jin L, Zhai X, Wang K, et al. Big data, machine learning, and digital twin assisted additive manufacturing: a review. *Mater Des*. 2024;244:113086. doi: 10.1016/j.matdes.2024.113086
13. Ren S, He K, Girshick R, Sun J. Faster R-CNN: towards real-time object detection with region proposal networks. *IEEE Trans Pattern Anal Mach Intell*. 2017;39(6):1137-1149. doi: 10.1109/TPAMI.2016.2577031
14. Bell S, Zitnick CL, Bala K, Girshick R. Inside-outside net: detecting objects in context with skip pooling and recurrent neural networks. *Proc CVPR IEEE*. 2016:2874-2883. doi: 10.1109/Cvpr.2016.314
15. Ardila D, Kiraly AP, Bharadwaj S, et al. End-to-end lung cancer screening with three-dimensional deep learning on low-dose chest computed tomography. *Nat Med*. 2019;25(6):954-961. doi: 10.1038/s41591-019-0447-x
16. Poplin R, Varadarajan AV, Blumer K, et al. Prediction of cardiovascular risk factors from retinal fundus photographs via deep learning. *Nat Biomed Eng*. 2018;2(3):158-164. doi: 10.1038/s41551-018-0195-0
17. Esteva A, Kuprel B, Novoa RA, et al. Dermatologist-level classification of skin cancer with deep neural networks. *Nature*. 2017;542(7639):115-118. doi: 10.1038/nature21056
18. Coudray N, Ocampo PS, Sakellaropoulos T, et al. Classification and mutation prediction from non-small cell lung cancer histopathology images using deep learning. *Nat Med*. 2018;24(10):1559-1567. doi: 10.1038/s41591-018-0177-5
19. Simonyan K, Zisserman A. Very deep convolutional networks for large-scale image recognition. *arXiv*. 2015. doi: 10.48550/arXiv.1409.1556
20. Abadi M, Agarwal A, Barham P, et al. TensorFlow: large-scale machine learning on heterogeneous distributed systems. *arXiv*. 2016. doi: 10.48550/arXiv.1603.04467

21. Bradski G, Kaehler A. *Learning OpenCV: Computer Vision with the OpenCV Library*. Cambridge: O'Reilly; 2008. doi: 10.1109/MRA.2009.933612

22. Bishop KC, Kuller JA, Boyd BK, Rhee EH, Miller S, Barker P. Ultrasound examination of the fetal heart. *Obstet Gynecol Surv*. 2017;72(1):54-61. doi: 10.1097/OGX.0000000000000394

23. Liu S, Wang Y, Yang X, et al. Deep learning in medical ultrasound analysis: a review. *Engineering*. 2019;5(2):261-275. doi: 10.1016/j.eng.2018.11.020

24. Ouyang D, He B, Ghorbani A, et al. Video-based AI for beat-to-beat assessment of cardiac function. *Nature*. 2020;580(7802):252-256. doi: 10.1038/s41586-020-2145-8

25. Campanella G, Hanna MG, Geneslaw L, et al. Clinical-grade computational pathology using weakly supervised deep learning on whole slide images. *Nat Med*. 2019;25(8):1301-1309. doi: 10.1038/s41591-019-0508-1

26. Litjens G, Kooi T, Bejnordi BE, et al. A survey on deep learning in medical image analysis. *Med Image Anal*. 2017;42:60-88. doi: 10.1016/j.media.2017.07.005

27. Luijten B, Cohen R, de Bruijn FJ, et al. Adaptive ultrasound beamforming using deep learning. *IEEE Trans Med Imaging*. 2020;39(12):3967-3978. doi: 10.1109/TMI.2020.3008537

28. Liaw CY, Guvendiren M. Current and emerging applications of 3D printing in medicine. *Biofabrication*. 2017; 9(2):024102. doi: 10.1088/1758-5090/aa7279

ACCSCIENCE PUBLISHING

International Journal of Bioprinting

RESEARCH ARTICLE

Neural cell responses to spinal implant biomaterials in a 3D-bioprinted cell culture model

David J. Wen[1†], Javad Tavakoli[1,2†*], and Joanne L. Tipper[1,2*]

[1]School of Biomedical Engineering, Faculty of Engineering and Information Technology, University of Technology Sydney, Sydney, Australia

[2]School of Engineering, STEM College, RMIT University, Melbourne, Australia

(This article belongs to the *Special Issue*: *Bioprinting of Nanomaterials for Biomedical Applications*)

Abstract

Spinal implants are vital for treating spinal disorders, yet wear particle-induced complications threaten their long-term success. Despite this, the direct effects of implant-derived particles on neural cells remain largely unexplored, especially given the limitations of conventional 2D culture models to capture such complex interactions. The current study introduces a novel *in vitro* platform consisting of a 3D-bioprinted gelatin methacryloyl (GelMA) hydrogel embedded with neural cells (C6 astrocyte-like and NG108-15 neurons) and spinal implant biomaterial particles, designed to model the spinal cord microenvironment with enhanced physiological relevance. As the first of its kind, this cell-particle-laden system supports the evaluation of neural cell responses to spinal biomaterial particles, including polymers, PEEK-OPTIMA™ and polyethylene Ceridust® 3615, zirconia-toughened alumina (ZTA) ceramic, and CoCrMo metal alloy. The bioprinted platform demonstrated excellent compatibility with various neural cell types and particle compositions, enabling a wide range of biological assays. Cell viability within the 3D model was comparable to traditional 2D cultures, affirming its ability to sustain cell survival while offering improved biomimicry. Biological assays assessing cell viability, reactive oxygen species (ROS) production, and DNA damage provided critical insights into material-specific and time-dependent cellular responses. While no significant cytotoxic effects were observed in short-term cultures, distinct variations in ROS production, and viability emerged based on biomaterial type and exposure duration. Overall, this versatile 3D-bioprinted system presents a robust, scalable tool for mechanistic and toxicological studies of spinal implant wear particles under physiologically relevant conditions.

Keywords: 3D model; Biomaterial particles; Bioprinting; C6 Astrocyte-like cells; Cell viability; Nevural cells; NG108-15 cells; Reactive oxygen species

†These authors contributed equally to this work.

***Corresponding authors:**
Javad Tavakoli
(javad.tavakoli@rmit.edu.au)

Joanne L. Tipper
(joanne.tipper@rmit.edu.au)

Citation: Wen DJ, Tavakoli J, Tipper JL. Neural cell responses to spinal implant biomaterials in a 3D-bioprinted cell culture model. *Int J Bioprint*. 2025;11(4):256-277. doi: 10.36922/IJB025180174

Received: April 29, 2025
Revised: June 4, 2025
Accepted: June 10, 2025
Published online: June 10, 2025

Copyright: © 2025 Author(s). This is an Open Access article distributed under the terms of the Creative Commons Attribution License, permitting distribution, and reproduction in any medium, provided the original work is properly cited.

Publisher's Note: AccScience Publishing remains neutral with regard to jurisdictional claims in published maps and institutional affiliations.

1. Introduction

In the absence of effective tissue engineering strategies to regenerate damaged intervertebral discs, spinal implants remain essential in the treatment of both degenerative and traumatic spinal conditions.[1] These implants are crucial in restoring

stability and functionality to affected regions, offering relief and improving the quality of life for patients.[2,3] Despite their effectiveness, the materials used in spinal implants, including metals, polymers, and ceramics, can generate wear particles over time.[4,5] These particles, particularly in combinations such as metal-on-polymer in total disc replacements, may pose potential risks to surrounding tissues.[6,7] On the other hand, the long-term success of spinal implants is frequently compromised by the generation of wear particles, which can trigger adverse biological responses.[8]

Several studies have analyzed clinical data and examined periprosthetic tissues, revealing a range of detrimental effects associated with spinal implant wear particles.[9–11] These effects include inflammation, hypersensitivity, neurological symptoms, pain, pseudotumor formation, and osteolysis.[12–15] Such responses underscore the importance of understanding the biological impact of wear particles and their potential to disrupt the healing process, as well as overall implant functionality and longevity.[16] Histological analysis of spinal periprosthetic tissues obtained during revision surgery revealed a marked increase in the inflammatory cytokines like tumor necrosis factor-alpha (TNF-α) and interleukin (IL)-6 in regions of inflammation.[17–19] This finding strongly associates stainless steel wear particles with the initiation and continuation of chronic inflammatory responses, highlighting their potential role in long-term complications following spinal implant procedures.[20,21] Both stainless steel and titanium wear debris from spinal instrumentation have been shown to initiate a macrophage-driven inflammatory cascade, resulting in increased local production of TNF-α.[22–24] This cytokine, in turn, drives osteoclastogenesis and promotes apoptosis in nearby cells, contributing to bone resorption and tissue degradation.[21,25]

While clinical studies following revision surgery have highlighted the biological effects of spinal wear particles on periprosthetic tissues, their direct impact on the spinal cord remains largely unexplored. However, recent *in vitro* research has demonstrated that exposure of porcine dural cells and organ cultures to cobalt–chromium–molybdenum (CoCrMo) nanoparticles significantly upregulates the pro-inflammatory chemokine IL-8.[26–28] This increased IL-8 expression compromises endothelial cell integrity, disrupting the blood-spinal cord barrier, and potentially increasing its permeability.[29] These changes could have serious implications for neuroinflammation and the vulnerability of spinal tissues. Furthermore, CoCrMo particle exposure induces substantial structural alterations in the dura mater, including elevated expression of matrix metalloproteinases (MMP-1, MMP-3, MMP-9, and MMP-13), as well as tissue inhibitor of metalloproteinase-1 (TIMP-1).[30] These findings suggest that CoCrMo particles promote tissue remodeling and the loosening of collagen fibers, which could facilitate the penetration of nanoparticles into the dura mater and possibly the spinal cord.[7] Evidence also showed that *in vivo* epidurally introduced particles can penetrate both the dural barrier and the blood-spinal cord barrier, potentially allowing migration into deeper neural structures. Additionally, the rapid circulation of cerebrospinal fluid from the subarachnoid space into the spinal canal—especially through perivascular pathways—may further enhance nanoparticle transport and infiltration into spinal tissues, raising concerns about their potential neurotoxic effects.[31,32] Motivated by these findings, an *in vitro* study using CoCr and stainless-steel wear particles demonstrated that CoCr particles significantly reduced glial cell viability and induced DNA damage in both astrocytes and microglial cells.[26] Notably, CoCr particles also caused a dose-dependent increase in glial fibrillary acidic protein (GFAP) expression, indicating astrocyte activation. In contrast, while stainless steel wear particles induced DNA damage in both glial and astrocyte cells, their impact on glial cell viability was minimal, with only the ions released from stainless steel causing a significant decline in glial cell viability.

To the best of our knowledge, only a limited number of studies have investigated the biological impacts of metallic wear particles and the potential neurotoxic effects of wear debris from different material types remain largely unexplored. To address this gap, the current study employs a 3D-bioprinted neural cell culture model based on gelatin methacryloyl (GelMA) hydrogels to evaluate the biological effects of ceramic, polymer, and metal wear particles. This advanced *in vitro* model more accurately mimics the cellular and extracellular matrix interactions observed *in vivo*, providing a more physiologically relevant test system than traditional 2D cell cultures. As such, it allows for a controlled investigation into cell viability, oxidative stress responses, and potential DNA damage induced by wear particles from varying material compositions.

Understanding the impact of wear particles on neural cells is crucial for advancing spinal implant design, optimizing biomaterial selection, and minimizing the neurotoxic risks associated with implant degradation. The insights gained from this study could play a pivotal role in developing neuroprotective strategies for spinal surgery, while also contributing to the improvement of long-term implant biocompatibility. By addressing these factors, the findings could help enhance patient outcomes and extend the functional lifespan of spinal implants.

2. Materials and methods

2.1. Cell culture preparation

2.1.1. Neural cell lines and cell culture media

C6 astrocyte-like (rat glioma) and NG108-15 (derived from mouse neuroblastoma fused with rat glioma) cell lines were obtained from the American Tissue Culture Collection (ATCC) and the European Collection of Cell Culture (ECACC), respectively. The cell culture medium for C6 astrocyte-like cells consisted of Ham's F-12 nutrient mix (Sigma-Aldrich, Germany) supplemented with 10% (v/v) fetal bovine serum (FBS) (Bovogen, Australia). For NG108-15 cells, the cryopreservation medium comprised Dulbecco's Modified Eagle's Medium (DMEM; Gibco, USA) supplemented with 20% (v/v) FBS and 10% (v/v) dimethyl sulfoxide (DMSO; Sigma-Aldrich). For cell culture, the cryopreservation medium was further supplemented with 100 U/mL penicillin (Gibco) and 100 μg/mL streptomycin (Gibco).

2.1.2. Cell culture

Cell passaging was performed when cultures reached approximately 70–80% confluence. Before passaging, a complete cell culture medium and trypsin (Gibco) were pre-warmed to 37°C in a water bath (Thermoline Scientific, Australia). The existing medium in the culture flask was aspirated, and the cells were washed with Dulbecco's Phosphate Buffered Saline solution (PBS; Sigma-Aldrich). Subsequently, 0.25% (v/v) trypsin-EDTA (Gibco) was added (1 mL for a T25 flask and 3 mL for a T75 flask), and the flasks were incubated at 37°C with 5% CO_2 for 3 min. An equal volume of complete medium was then added to neutralize the trypsin. The cell suspension was transferred to a 15 mL centrifuge tube and centrifuged (Thermoline Scientific) at 300 × *g* for 5 min. Following centrifugation, the supernatant was aspirated and the cells were then transferred into new culture flasks containing fresh medium and maintained at 37°C with 5% CO_2 (Heracell™ VIOS 160i, Thermo Fisher Scientific, USA). Cell culture was conducted both in isolation and co-culture conditions. When required, cell counting was performed using a hemocytometer and the trypan blue (Sigma-Aldrich) exclusion assay.

2.2. Particles

2.2.1. Particle types

This study utilized a variety of particulate materials, encompassing polymers, metals, and ceramics. The polymer particles included polyetheretherketone (PEEK-OPTIMA™; from Invibio Biomaterial Solutions, UK) and polyethylene (Ceridust® 3615; from Hoechst, Germany). The ceramic particles were composed of zirconia-toughened alumina (ZTA; Inframat Advanced Materials, USA), while the metallic particles were made from a cobalt–chromium–molybdenum (CoCrMo) alloy (American Elements, USA). These materials were selected to represent common biomaterials used in spinal implants, providing a comprehensive analysis of the biological impact of wear debris from diverse material types.

2.2.2. Particle preparation and separation

Sequential filtration was performed to separate particles by size using 25 mm polycarbonate membrane filters (8, 0.8, and 0.1 μm pore sizes; Whatman). Membrane filters were sterilized by washing with 70% (v/v) ethanol, rinsing with deionized water, air-drying at room temperature, and exposing them to ultraviolet (UV) light for 30 min. A 100 mg particle sample was suspended in 20 mL of distilled water in a 50 mL centrifuge tube and then sonicated (Unisonics Australia) for 40 min to ensure uniform dispersion (5 g/L concentration). Immediately after sonication, the suspension was filtered through the membranes. The filters were carefully transferred to sterile Petri dishes using tweezers and dried in an oven (Skope, New Zealand) at 50°C for at least 30 min. The size-separated particles were then subjected to scanning electron microscopy (SEM; Zeiss; EVO LS 15) characterization and cell culture experiments.

2.2.3. Scanning electron microscopy imaging

Dried filters were directly coated with a 3 nm layer of gold/palladium or carbon using a sputter coater before SEM imaging. PEEK-OPTIMA™, Ceridust® 3615, and ZTA samples were coated with gold/palladium, while CoCrMo samples were coated with carbon. Imaging was performed at 5 kV or 10 kV with a working distance of 4.9–21 mm. Four magnifications (100×, 400×, 700×, and 1500×) were used, with at least three images captured per magnification for each filter and material.

2.2.4. Particle characterization

The SEM images were analyzed using ImageJ open-source software (Open-source image processing software developed by the National Institutes of Health [NIH] in the USA) to measure particle size, area distribution, and morphology. Measurements included particle area, perimeter, length (Feret's diameter along the major axis), and width (Feret's diameter along the minor axis). Particles were categorized into size ranges: <0.1, 0.1–0.8, 1.0–8, and >8 μm. Additionally, the particle count per image area (N/A) and the average particle area within each size range (P/N) were calculated. A minimum of 100 particles per material were manually measured by outlining each particle. To minimize human error, overlapping or agglomerated particles were excluded from the analysis.

2.3. Development of 3D model using bioprinting

2.3.1. Preparation of GelMA hydrogel

GelMA (CELLINK, Sweden) hydrogel solution was prepared using the CELLINK GelMA Kit, which included GelMA powder and the photoinitiator lithium phenyl-2,4,6-trimethylbenzoylphosphinate (LAP; CELLINK). LAP was dissolved in PBS and mixed at 60°C for 20 min to achieve a 0.25% (w/v) solution, which was then filter-sterilized (0.22 μm) in a class II biosafety cabinet (Thermoline Scientific). The sterilized LAP/PBS solution was subsequently added to GelMA powder and mixed at 50°C for 20 min to obtain a 5% (w/v) GelMA solution. The 5% (w/v) GelMA concentration was selected based on our previous findings, which identified this formulation as optimal for supporting the viability of neuronal and astrocyte-like cells over a 7-day culture period under standard conditions.[33]

2.3.2. Preparation of cell-laden GelMA hydrogel

Neural cells (C6 astrocyte-like and NG108-15) were cultured separately at 37°C with 5% (v/v) CO_2 until reaching 80% confluence (as explained in **Section 2.1**). The culture medium was then removed, and trypsin was added for 3 min to detach the cells. An equal volume of culture medium was used to neutralize the trypsin, and the cell suspension was transferred to a 15 mL Falcon tube for centrifugation at 300 × *g* for 5 min. The supernatant was carefully aspirated, and the resulting cell pellet was resuspended in fresh culture medium (as explained in **Section 2.1**) to achieve a final concentration of 1×10^4 cells/mL. Subsequently, 100 μL of this cell suspension was added to 1 mL of GelMA hydrogel solution. The mixture was thoroughly homogenized by gentle aspiration in a 15 mL centrifuge tube to ensure uniform cell distribution within the cell-laden GelMA hydrogel.

2.3.3. Preparation of cell-laden GelMA hydrogel embedded with particles

Particle stock solutions were first prepared in cell culture media at a concentration of 1 mg/mL. Added to 100 μL of cell suspension (1×10^4 cells/mL) were 1.3 μL of PEEK-OPTIMA™, 1 μL of Ceridust® 3615, 2.5 μL of ZTA, and 4.2 μL of CoCrMo (Table 1) to achieve the desired specific particle volumes (μm³/cell). PEEK-OPTIMA™ and Ceridust® 3615 3D model particles were incorporated at a concentration of 100 μm³ per cell, whereas ZTA and CoCrMo model particles were introduced at 50 μm³ per cell. Additionally, CoCrMo model particles were prepared at two additional concentrations—0.5 and 5 μm³ per cell—to assess dose-dependent effects. The final cell/particle suspensions were mixed with 1 mL of GelMA hydrogel. These dosing strategies were informed by previous 2D *in vitro* studies in the existing literature.[26,34,35]

2.3.4. Bioprinting of 3D droplet hydrogels

The resulting GelMA hydrogel solutions were then loaded into a 3 mL cartridge for 3D bioprinting. After securely attaching the nozzle to the cartridge, the assembly was placed into the temperature-controlled print head of the bioprinter (CELLINK BIO X6). The bioprinting parameters, including extrusion pressure, printing speed, and temperature, were subsequently optimized to fabricate simple droplet hydrogels within the well plates. Finally, the printed hydrogels were photocrosslinked by exposure to UV light at 365 nm with an intensity of 19.42 mW/cm² for 120 s. The bioprinted cell-laden GelMA droplets (with or without model particles) were cultured, as explained in **Section 2.1**.

2.4. Three-dimensional biological assessments

2.4.1. Three-dimensional cell viability assay

GelMA hydrogel droplets were bioprinted into 48-well plates and cultured at 37°C and 5% (v/v) CO_2 for 5 days. A luminescent ATP detection assay kit (CellTiter-Glo 3D Cell Viability Assay Kit; Promega, USA), consisting of two fluorescent dyes, namely a green fluorescent calcein AM dye (for live cells; Invitrogen, USA) and an ethidium homodimer-1 dye (for dead cells; Invitrogen), was used to evaluate cell viability on Days 1, 3, and 5. In addition, the DNA of cells was stained with a blue-fluorescent Hoechst 33342 dye (Life Technologies, USA). Briefly, 50 μL of lysis buffer was added to each well to facilitate cell membrane

Table 1. Particle mass to prepare suspensions with desired concentrations

Particle	Volume (μm³)	Density (g/cm³)	Mass (μg per cell)	Cell number (per droplet)	Particle mass (μg per droplet)
PEEK-OPTIMA™	100	1.3	1.3×10^{-4}	1×10^4	1.3
Ceridust® 3615	100	1	1×10^{-4}	1×10^4	1
ZTA	50	5	2.5×10^{-4}	1×10^4	2.5
CoCrMo	50	8.4	4.2×10^{-4}	1×10^4	4.2

Abbreviations: CoCrMo, cobalt–chromium–molybdenum; PEEK, polyetheretherketone; ZTA, zirconia-toughened alumina.

disruption and ATP stabilization. The plate was then shaken for 5 min at 50 × *g*. Following cell lysis, 50 µL of luminescent substrate solution was added to each well. The plate was shaken again under the same conditions for an additional 5 min to ensure proper mixing and reaction initiation. Subsequently, the plate was incubated in the dark at room temperature for 10 min to allow the luminescent signal to stabilize. Luminescence, which is directly proportional to the intracellular ATP content and hence viable cell number, was then measured using a microplate reader (Varioskan LUX, Thermo Scientific). For qualitative analysis, GelMA droplet hydrogels were imaged immediately using a confocal EVOS M5000 microscope at 10× magnification with green fluorescent protein (GFP; emission: 525/50 nm), red fluorescent protein (RFP; emission: 593/40 nm), and 4',6-diamidino-2-phenylindole (DAPI; emission: 447/60 nm) emission filters for calcein AM, ethidium homodimer-1, and Hoechst 33342 stains, respectively. Three replicates of GelMA droplets were bioprinted for each particle type and a total of three images were taken for each droplet. In addition, a negative control of cell only and a positive control of 5% (v/v) DMSO was utilized, and a particle-only control was also used to ensure that particles did not interfere with the luminescent readings for this assay.

2.4.2. Reactive oxygen species detection assay

The DCFDA - Cellular ROS Assay Kit (Abcam, UK) was used to measure the production of reactive oxygen species (ROS) by cells in different particle model bioprinted droplets. The cell culture media was aspirated from each well, and bioprinted droplets were washed with ROS assay buffer. The cells were stained with 100 µL diluted DCFDA (2′,7′-dichlorofluorescin diacetate; a cell-permeant reagent) solution and incubated at 37°C and 5% (v/v) CO_2 for 45 min. The positive control was established by using 100 µL of 200 µM hydrogen peroxide, followed by a 2-h incubation (96 well plate). Subsequently, fluorescence was measured with a plate reader at excitation and emission of 485 and 535 nm, respectively.

2.4.3. DNA damage

To evaluate the impact of model wear particles on DNA integrity in C6 astrocyte-like cells, γ-H2AX foci formation—a marker of DNA double-strand breaks—was assessed at multiple time points (1, 2, and 4 h post-exposure). For immunofluorescent detection, bioprinted droplets were first washed with PBS and permeabilized with 100 µL of 0.5% Triton X-100 solution for 3 min at room temperature. The droplets were then washed twice with PBS, followed by the addition of 50 µL of primary antibody solution targeting γ-H2AX (Abcam). Samples were incubated at 37°C in a humidified atmosphere with 5% CO_2 for approximately 45 min. After incubation, the droplets were washed again with PBS, and 50 µL of a fluorescently labeled secondary antibody was added, followed by a 25-min incubation under the same conditions. After a final PBS wash, mounting medium containing Hoechst dye was applied to stain cell nuclei. The droplets were then imaged using a fluorescence microscope to quantify γ-H2AX foci formation.

2.5. Biological assessments in 2D

To assess cell viability in 2D culture, a luminescent ATP assay kit (Abcam) was used. Briefly, before conducting the luminescent ATP detection assay, cells were seeded into 96-well plates. Fifty microliter of lysis buffer was added to each well to facilitate cell membrane disruption and ATP stabilization. The plate was then shaken for 5 min at 50 × *g*. Following cell lysis, 50 µL of luminescent substrate solution was added to each well. The plate was shaken again under the same conditions for an additional 5 min to ensure proper mixing and reaction initiation. Subsequently, the plate was incubated in the dark at room temperature for 10 min to allow the luminescent signal to stabilize. Luminescence, which is directly proportional to the intracellular ATP content and hence viable cell number, was then measured using a microplate reader (Days 1, 3, and 7). Fluorescence microscopy (DP80 and Nikon ECLIPSE Ti2, Japan) was utilized for imaging fluorescently stained cells for qualitative analysis of cell viability. An inverted microscope (Olympus CKX53, Japan) was used for bright-field microscopy.

2.6. Statistical analysis

Statistical analysis was performed using the SPSS software, v22.0 (IBM Corp., Armonk, NY, USA). Two-way analysis of variance (ANOVA) was utilized to assess cell viability and ROS levels between 3D model particles. Fixed factors included cell culture time points and biomaterial types, analyzed with statistical significance of 0.05. Post-hoc multiple comparisons were conducted using a Bonferroni adjustment. All experiments included at least three biological replicates. In addition, statistical significance was analyzed within 3D model particles using one-way ANOVA tests. For proportional or percentage data that does not follow a binomial distribution, an arcsine transformation was used to help normalize the distribution of data.

3. Results

3.1. Particle characterization

This study utilized particles from various materials, including PEEK-OPTIMA™, Ceridust® 3615, ZTA, and CoCrMo alloy. Particle characterization involved size distribution analysis and morphological assessment

(Figure 1). Sequential filtration using polycarbonate membrane filters (8, 0.8, and 0.1 µm pore sizes) categorized particles into >8, 0.8–8, and 0.1–0.8 µm size ranges. SEM analysis revealed that PEEK-OPTIMA™ particles exhibited a granular or irregular morphology across all size ranges (Figure 1), with a mean diameter of 7.6 ± 3.9 µm and a size range of 0.54–83.2 µm. While 95% of particles were <8 µm, 43% were in the submicron range. Larger particles (>8 µm) accounted for ~50% of the total particle area (Figure 2a). Ceridust® 3615 particles displayed a granular and polygonal morphology (Figure 1), with a mean diameter of 6.4 ± 2.7 µm and a size range of 0.49–22.1 µm. Approximately, 92.3% of particles were <8 µm, with a notable proportion (1%) in the 0.1–0.8 µm range (Figure 2b).

Similarly, ZTA particles exhibited granular and polygonal morphology (Figure 1), with a mean diameter of 3.7 ± 3.5 µm and a size range of 0.45–20.3 µm. Most particles (99%) were <8 µm, with 73% in the 0.8–8.0 µm range. Additionally, 99.5% of the total particle area was within this range (Figure 2c). In contrast, CoCrMo particles were primarily globular, with some polygonal shapes (Figure 1). Their mean diameter was 5.9 ± 1.2 µm, within a size range of 2.1–11.6 µm. Most particles (88%) were <8 µm, with 88.5% falling in the 0.8–8.0 µm range. However, while 11.5% of particles were >8 µm, they contributed to 56.2% of the total particle area (Figure 2b).

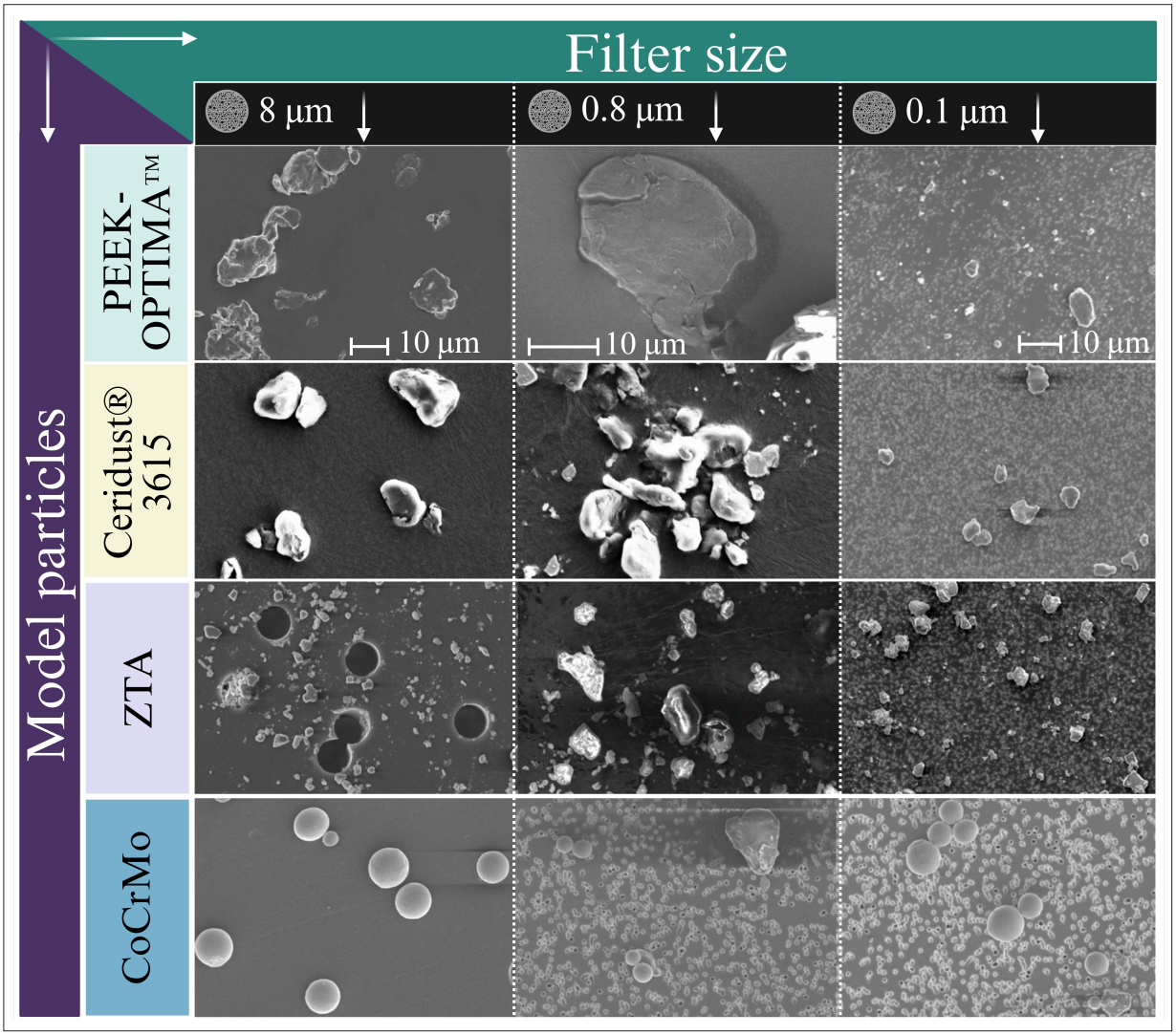

Figure 1. SEM images of model particles, including aggregates and microsized particles, collected using 8, 0.8, and 0.1 µm filters. A consistent scale bar of 10 µm was applied across all SEM images (each filter size) for uniform comparison. Abbreviations: CoCrMo: Cobalt–chromium–molybdenum; PEEK: Polyetheretherketone; SEM: Scanning electron microscopy; ZTA: Zirconia-toughened alumina.

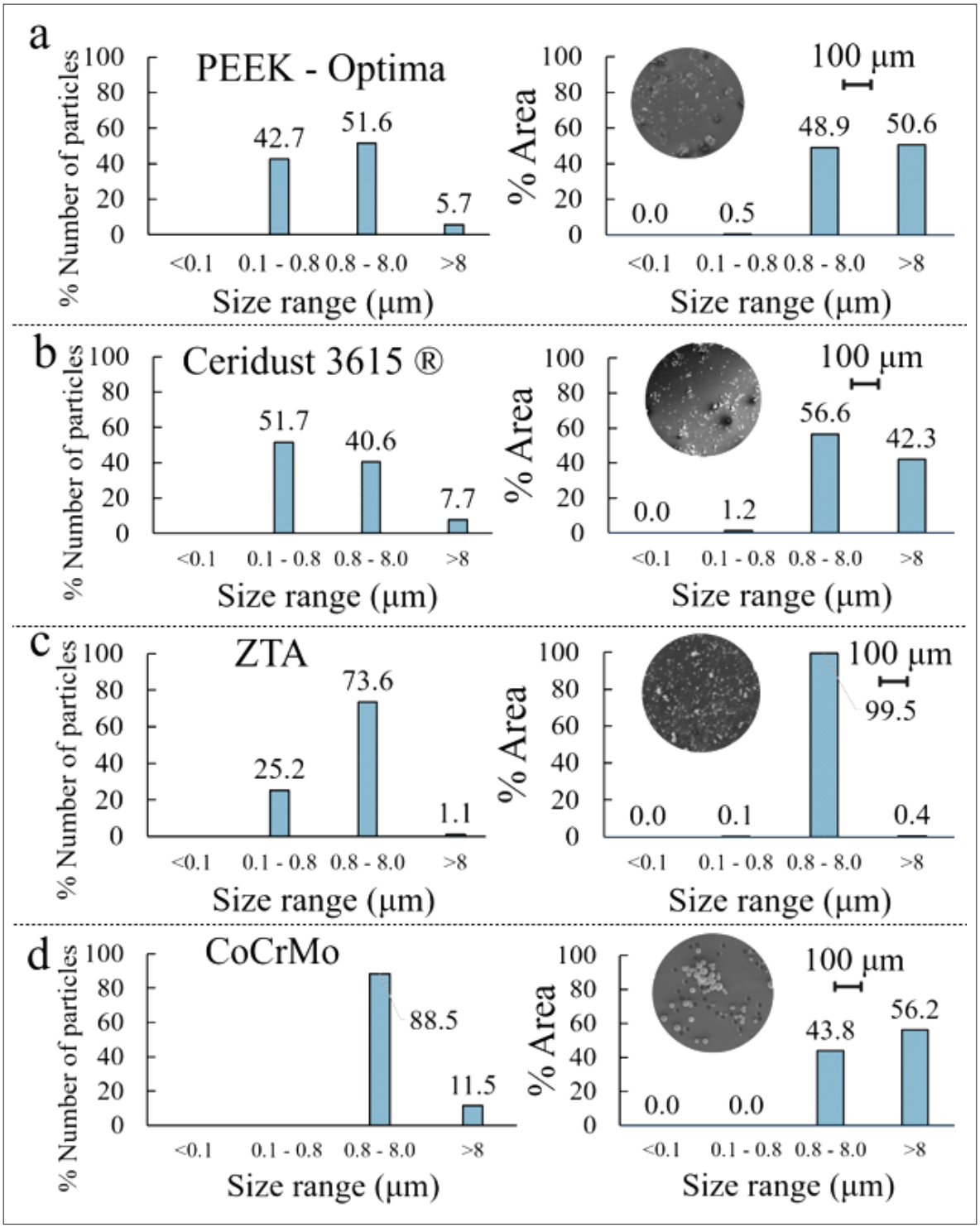

Figure 2. The percentage frequency and area distribution of various model particles determined from the SEM images, as a function of particle size: (a) PEEK-OPTIMA™, (b) Ceridust® 3615, (c) ZTA, and (d) CoCrMo. Abbreviations: CoCrMo: Cobalt–chromium–molybdenum; PEEK: Polyetheretherketone; SEM: Scanning electron microscopy; ZTA: Zirconia-toughened alumina.

3.2. Optimization of 3D bioprinting process and cell viability

In this study, extrusion pressure was the primary variable parameter, while bed temperature, print head temperature, and print speed were maintained at constant values of 10°C, 24°C, and 11 mm/s, respectively. Our findings indicate that an extrusion pressure of 6 kPa facilitated the generation of consistent GelMA droplets with satisfactory structural integrity (Figure 3a and b). Furthermore, the effect of four distinct nozzle gauge sizes—20G, 22G, 25G, and 27G—was evaluated for the droplet printing of GelMA hydrogels mixed with particles. The print speed and extrusion pressure were fixed at 11 mm/s and 6 kPa, respectively. Nozzles with gauge sizes of 20G (0.58 mm inner diameter) and 22G (0.41 mm inner diameter) successfully extruded the GelMA hydrogel–particle mixture. Conversely, nozzles with gauge sizes of 25G (0.25 mm inner diameter) and 27G (0.20 mm inner diameter) failed to achieve consistent extrusion of the bioink–particle mixture. Based on these observations, the 22G nozzle was selected for the fabrication of 3D model particle constructs, both with and without the incorporation of neural cells (Figure 3c).

To assess the biocompatibility and proliferation potential of neural cells within the 3D-bioprinted environment, cell viability was evaluated at Days 1, 3, and 7 within 5% (w/v) GelMA hydrogels and compared to 2D cell culture models as a control (Figure 3d and e). Both C6 Astrocyte-like and NG108-15 cells were seeded at an initial concentration of 1×10^4 cells/mL across both 2D and 3D models (Figure 3f). A progressive increase in cell viability was observed from Day 1 to Day 7 in both environments. Notably, the proliferation rates of cells within the GelMA hydrogels were comparable to those in the 2D control (Figure 3d and e). Qualitative analysis further confirmed enhanced proliferation over the 7 days of cell culture. By Day 7, NG108-15 cells exhibited neurite outgrowth, indicating that the bioprinted 3D droplets supported the growth of these cells. The incidence of cell death remained minimal throughout the 7-day culture period, as evidenced by the sparse presence of red dots from propidium iodine staining.

3.3. Biological assessments

3.3.1. Cell viability

The viability of C6 astrocyte-like and NG108-15 cells was assessed over a 5-day culture period in both experimental groups (cells embedded with model particles in 3D-bioprinted hydrogels) and control groups (cells embedded without particles) (Figure 4). Luminescence readings, indicative of cellular metabolic activity, showed a continuous increase in viability for C6 astrocyte-like cells across the 5 days (Figure 4a). A comparable trend was observed for NG108-15 cells; however, a slight decline in viability was noted on Day 5 compared to Day 3, suggesting a potential sensitivity to prolonged culture conditions or particle exposure (Figure 4b).

Our statistical analysis, conducted using separate one-way ANOVA tests, indicated that the viability of C6 astrocyte-like cells showed no significant differences between the control group (cells-only embedded in 3D-bioprinted hydrogels) and our embedded model particles in 3D-bioprinted hydrogels: CrCoMo (p = 0.65), ZTA (p = 0.34), PEEK-OPTIMA™ (p = 0.058), and Ceridust® 3615 (p = 0.94). Comparable results were observed for NG108-15 cells. Our statistical analysis revealed no significant differences in NG108-15 cell viability between the control group (cells-only in 3D-printed hydrogels) and cell exposed to model particles in 3D-bioprinted hydrogels: CrCoMo (p = 0.32), ZTA (p = 0.83), PEEK-OPTIMA™ (p = 0.64), and Ceridust® 3615 (p = 0.56). Additionally, there were no significant variations in the viability of C6 astrocyte-like and NG108-15 cells across different particle volumes (0.5, 5, and 50 μm³ per cell) within the CrCoMo model particle (p < 0.46). However, for both cell types, a significant revduction in viability (p < 0.05) was observed in the positive control (cells exposed to DMSO) at each time point when compared to the cell-only negative control.

We performed a two-way ANOVA statistical analysis to assess the impact of culture time, biomaterial type, and their interaction on the viability of C6 astrocyte-like cells. The assessment was based on estimated marginal mean luminescent values (±95% confidence interval [CI]) obtained from an ATP assay, which served as an indicator of cell viability (Figure 5). These values were measured for C6 astrocyte-like cells exposed to different model particles or at different dose concentrations over time (Table 2).

Our statistical analysis demonstrated a significant interaction between culture time and biomaterial type (p < 0.001, Figure 5a). Additionally, both culture time and biomaterial type had a significant impact on the viability of C6 astrocyte-like cells (p < 0.001, Figure 5b and c). The post hoc analysis further revealed significant differences in cell viability across the culture time points (Days 1, 3, and 5), with a progressive increase from Day 1 to Day 3, which continued through Day 5 (Figure 5b).

We observed no significant difference in cell viability (p < 0.9) for CoCrMo model particles across varying volumes (0.5, 5, and 50 μm³ per cell, Tables 1 and 2). However, the overall cell viability was significantly higher for CoCrMo (50 μm³ per cell) compared to PEEK-OPTIMA™, Ceridust® 3615, and ZTA model particles (p < 0.001). No significant differences in cell viability were found between PEEK-OPTIMA™ and Ceridust® (p = 0.6) or between

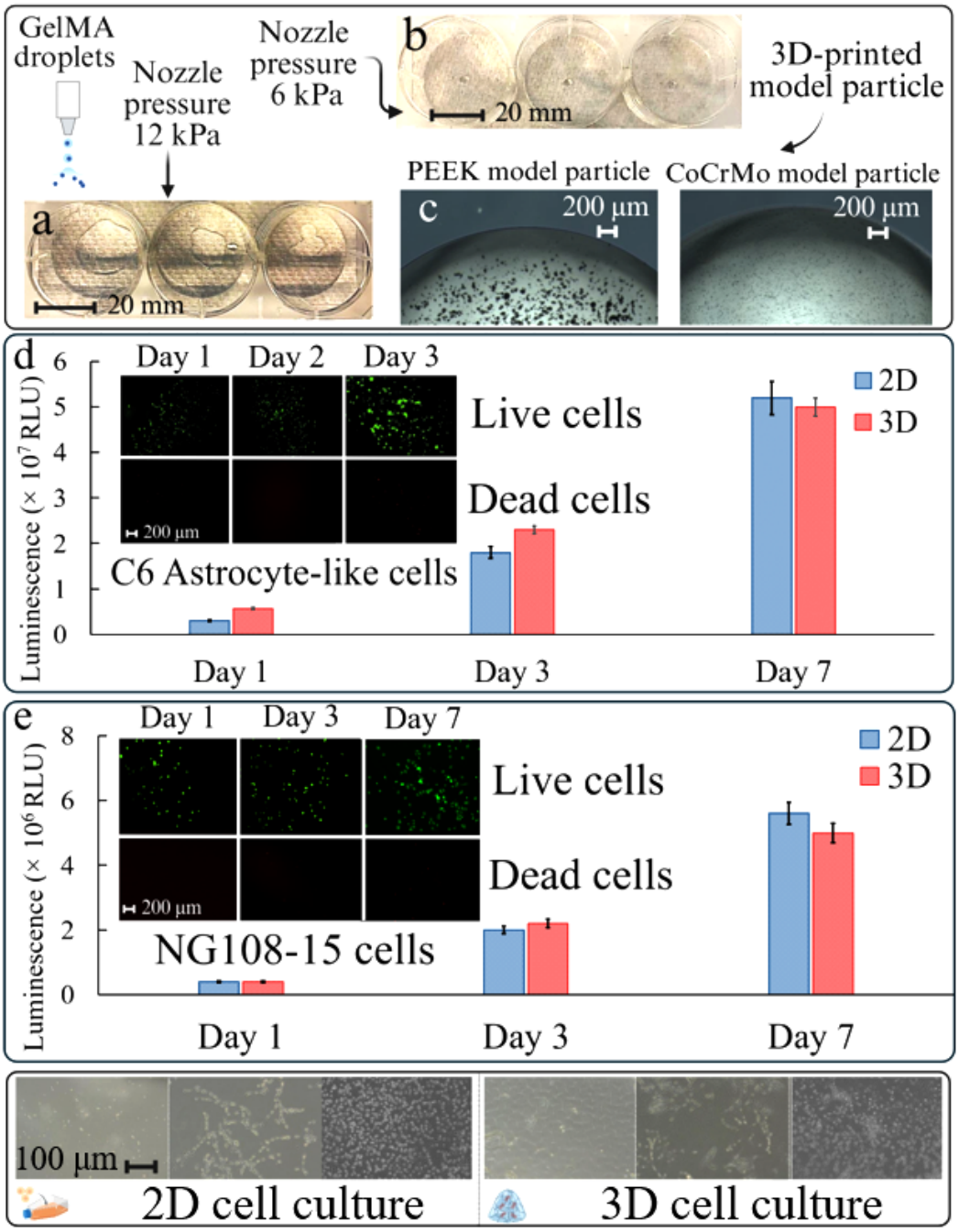

Figure 3. Photographic images of 3D-bioprinted droplet GelMA hydrogels with 5% (w/v) concentration using a BIO X6 bioprinter at 12 kPa (a) and 6 kPa (b). (c) Microscopic images of bioprinted 5% (w/v) GelMA hydrogel droplets, embedded with PEEK-OPTIMA™ (100 µm³ per cell, left) and CoCrMo (50 µm³ per cell, right) particles. The printing parameters of nozzle temperature, extrusion pressure, and speed were 24°C, 6 kPa, and 11 mm/s, respectively. Qualitative and quantitative analyses of cell viability in 3D models for C6 astrocyte-like (d) and NG108-15 cells (e) compared to 2D cell culture models (control), including fluorescence microscopy images of cells in 3D-bioprinted GelMA (5% w/v). (f) Bright-field microscope images of C6 astrocyte-like cells in 2D cell culture (top) compared to C6 astrocyte-like cells in 3D GelMA hydrogels (bottom) at Days 1, 3, and 7 (cell density for 2D and 3D cell culture models = 1×10^4 cells/mL). Abbreviations: CoCrMo: Cobalt–chromium–molybdenum; GelMA: Gelatin methacryloyl; PEEK: Polyetheretherketone; SEM: Scanning electron microscopy; ZTA: Zirconia-toughened alumina.

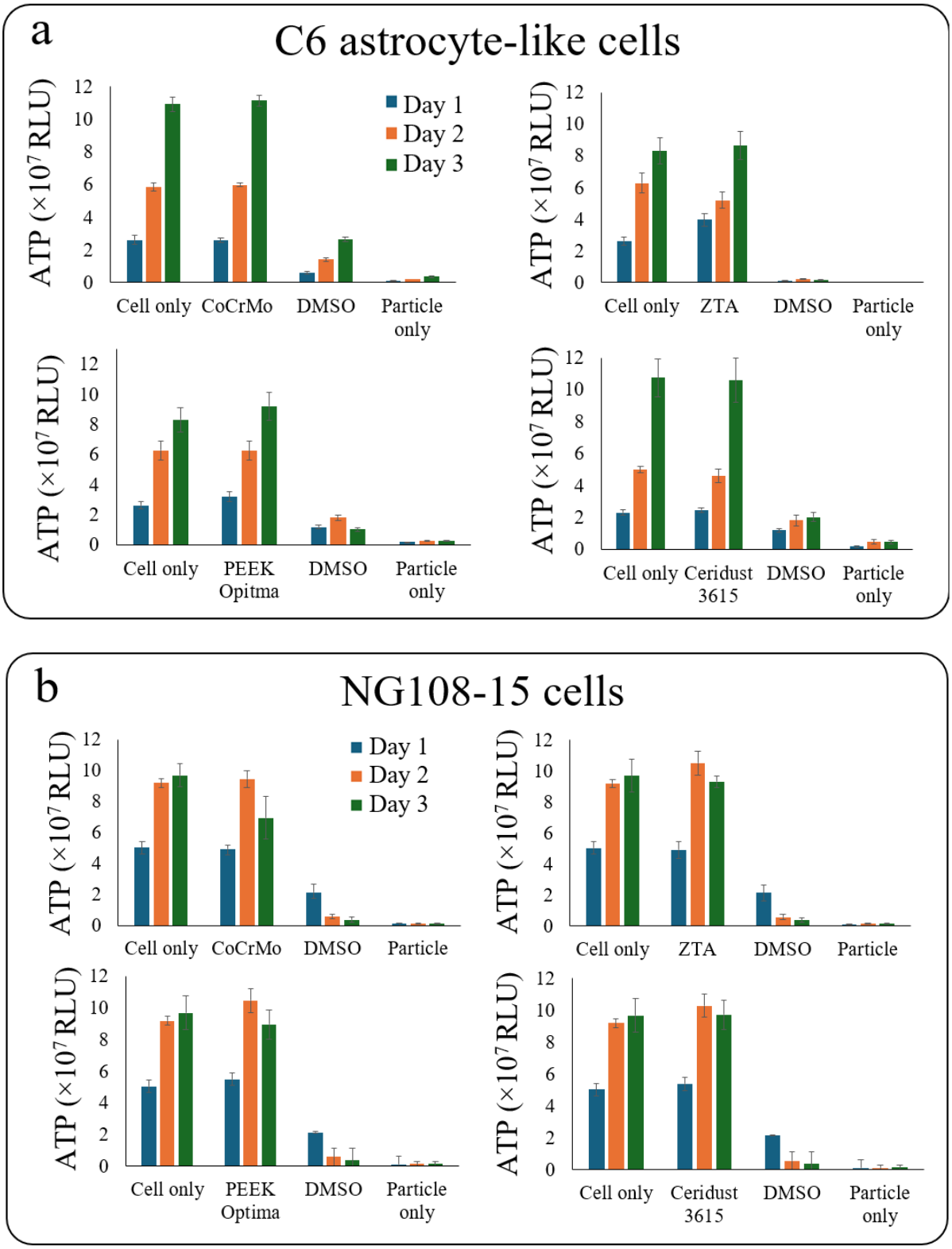

Figure 4. Cell viability comparison between the control sample (cell-only in 3D-bioprinted hydrogel) and CoCrMo, ZTA, PEEK-OPTIMA™, and Ceridust® 3615 model particles for C6 astrocyte-like (a) and NG108-15 cells (b). Abbreviations: CoCrMo: Cobalt–chromium–molybdenum; DMSO: Dimethyl sulfoxide; PEEK: Polyetheretherketone; ZTA: Zirconia-toughened alumina.

Table 2. Viability assessment of C6 astrocyte-like cells for various 3D model particles

Model particles	Culture time		
	Day 1	Day 3	Day 5
CoCrMo (0.5 μm³ per cell)	2.2 ± 0.09	6.0 ± 0.13	11.0 ± 0.24
CoCrMo (5 μm³ per cell)	2.7 ± 0.12	6.3 ± 0.21	11.0 ± 0.2
CoCrMo (50 μm³ per cell)	2.6 ± 0.17	6.0 ± 0.15	11.1 ± 0.66
PEEK-OPTIMA™	0.42 ± 0.06	0.72 ± 0.06	1.1 ± 0.09
Ceridust® 3615	0.25 ± 0.02	0.46 ± 0.04	1.0 ± 0.14
ZTA	0.39 ± 0.03	0.52 ± 0.02	0.52 ± 0.02

Notes: Data expressed as mean (±95% CI) luminescent values (×10⁶ RLU), determined by means of ATP assay.

Abbreviations: CoCrMo: Cobalt–chromium–molybdenum; PEEK: Polyetheretherketone; ZTA: Zirconia-toughened alumina.

Ceridust® 3615 and ZTA (p = 0.9). Notably, our post hoc analysis revealed a significant difference in cell viability between PEEK-OPTIMA™ and ZTA model particles (p = 0.021), where the cell viability was significantly lower after exposure to ZTA particles compared to PEEK-OPTIMA™ particles (Figure 5c).

Using the same approach, we also assessed the viability of NG108-15 cells. Our statistical analysis revealed a marginally significant interaction between culture time and biomaterial type (p < 0.051, Figure 5d). Both culture time and biomaterial type significantly influenced the viability of neuronal NG108-15 cells (p < 0.01; Figure 5e and f). Additionally, the post hoc analysis indicated that cell viability was significantly lower for CoCrMo compared to PEEK-OPTIMA™ (p = 0.007), Ceridust® 3615 (p = 0.002), and ZTA (p = 0.005) 3D model particles. No significant differences in the viability of NG108-15 cells were found between PEEK-OPTIMA™, Ceridust® 3615, and ZTA model particles (p < 0.71). Furthermore, the viability of NG108-15 cells varied significantly across culture time points (p < 0.001), with a progressive increase from Day 1 (5.2 ± 0.19) to Day 3 (10.1 ± 0.18), followed by a significant decrease on Day 5 (8.7 ± 0.18) (Figure 5e).

The proliferation of C6 astrocyte-like and NG108-15 cells across all 3D model particles was qualitatively evaluated (Figure 6) and compared to the negative control (C6 astrocyte-like cell-only 3D-bioprinted hydrogel). Qualitative assessment of cell viability, visualized using

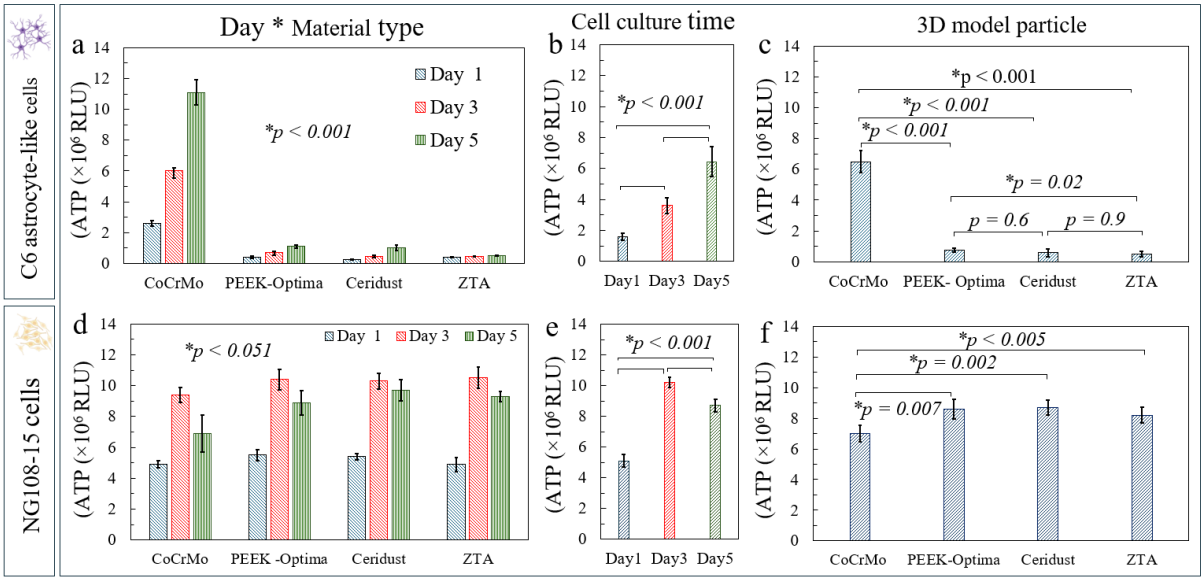

Figure 5. Estimated marginal means of cell viability, determined by means of ATP assay. (a, d) Interaction effects between culture duration and biomaterial type; (b, e) main effect of culture time; and (c, f) 3D model particles (material types) effects on the viability of C6 astrocyte-like cells (top) and NG108-15 cells (bottom). PEEK-OPTIMA™ and Ceridust® 3615 3D model particles were incorporated at a concentration of 100 μm³ per cell, whereas ZTA and CoCrMo model particles were introduced at 50 μm³ per cell. Abbreviations: CoCrMo: Cobalt–chromium–molybdenum; PEEK: Polyetheretherketone; ZTA: Zirconia-toughened alumina.

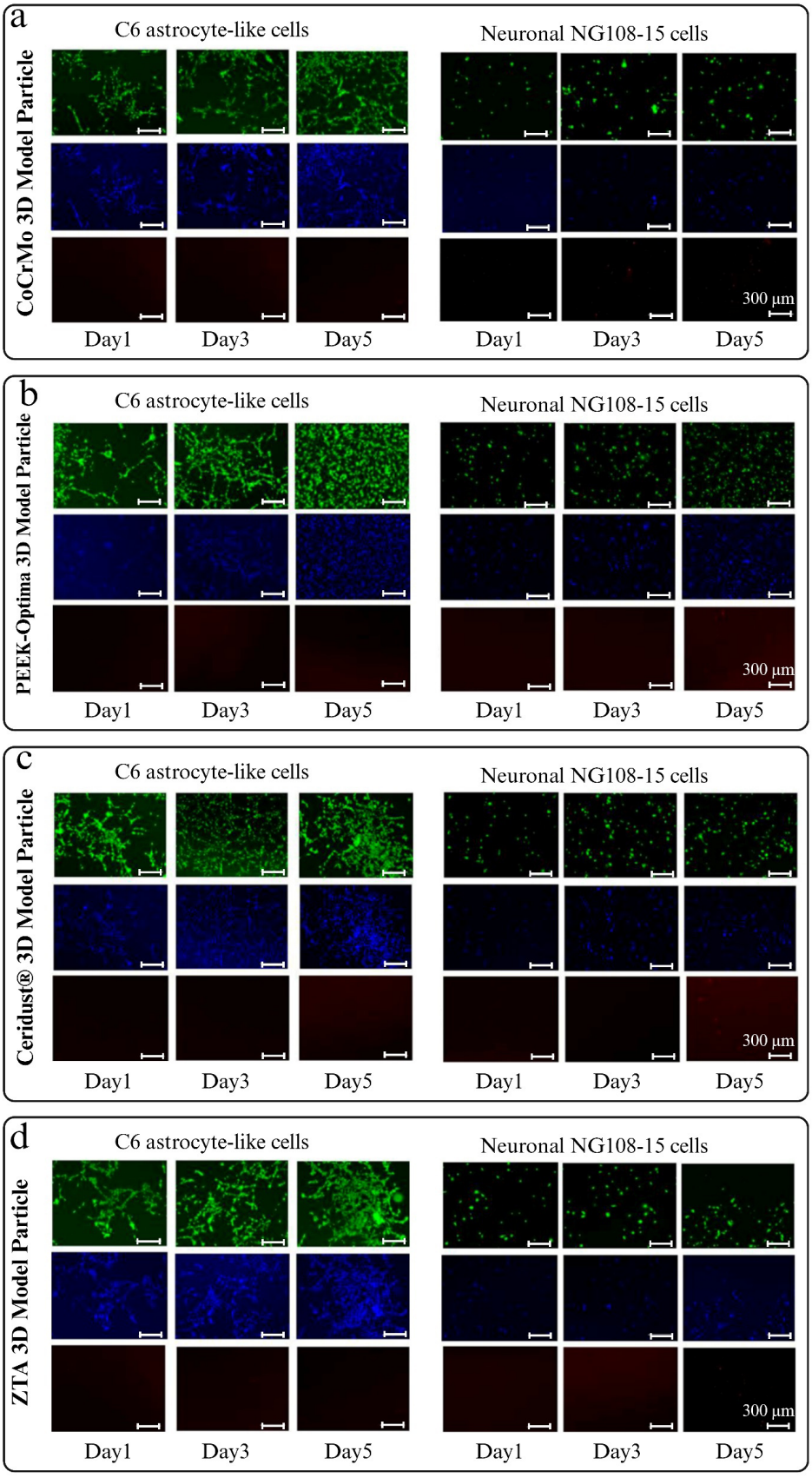
a
C6 astrocyte-like cells
Neuronal NG108-15 cells
CoCrMo 3D Model Particle
300 μm
Day1
Day3
Day5
Day1
Day3
Day5
b
C6 astrocyte-like cells
Neuronal NG108-15 cells
PEEK-Optima 3D Model Particle
300 μm
Day1
Day3
Day5
Day1
Day3
Day5
c
C6 astrocyte-like cells
Neuronal NG108-15 cells
Ceridust® 3D Model Particle
300 μm
Day1
Day3
Day5
Day1
Day3
Day5
d
C6 astrocyte-like cells
Neuronal NG108-15 cells
ZTA 3D Model Particle
300 μm
Day1
Day3
Day5
Day1
Day3
Day5

Figure 6. Qualitative analysis of the effect of CoCrMo (a), PEEK-OPTIMA™ (b), Ceridust® 3615 (c), and ZTA (d) model particles embedded in 3D-bioprinted GelMA on the viability of C6 astrocyte-like and NG108-15 cells (Days 1, 3, and 5). Live cells were stained with green-fluorescent calcein AM, cell nuclei with blue-fluorescent Hoechst, and dead cells with red-fluorescent propidium iodide. All scale bars = 300 μm. Abbreviations: CoCrMo: Cobalt–chromium– molybdenum; GelMA: Gelatin methacryloyl; PEEK: Polyetheretherketone; ZTA: Zirconia-toughened alumina.

live/dead fluorescence staining, supported the quantitative results. Live C6 astrocyte-like and NG108-15 cells were identified by green fluorescence (calcein AM), nuclei by blue fluorescence (Hoechst), and dead cells by red fluorescence (propidium iodide). Representative images from Days 1, 3, and 5 revealed cell viability patterns consistent with the luminescence-based measurements, confirming the material-dependent and time-dependent effects of CoCrMo, PEEK-OPTIMA™, Ceridust® 3615, and ZTA 3D model particles on both cell types.

3.3.2. Oxidative stress

The production of ROS by both C6 astrocyte-like and NG108-15 cells was assessed across all 3D model particles. Oxidative stress was measured on Days 3 and 5 using a DCFDA probe, where ROS production was directly proportional to the intensity of the green fluorescence. The estimated marginal mean (±95% CI) of fluorescent intensity, reflecting ROS production in C6 astrocyte-like and NG108-15 cells exposed to various model particles, is presented in Figure 7.

Statistical analysis revealed a significant interaction between culture duration and biomaterial type on ROS production in C6 astrocyte-like cells ($p = 0.003$; Figure 7a). Both the main effect of culture time ($p < 0.01$; Figure 7b) and the type of biomaterial used in the 3D model particles ($p = 0.032$; Figure 7c) were also statistically significant. Post hoc comparisons indicated that ROS production was markedly higher in cells exposed to CoCrMo particles compared to those exposed to PEEK-OPTIMA™ ($p = 0.007$), Ceridust® 3615 ($p = 0.025$), and ZTA ($p = 0.028$). No significant differences in ROS levels were observed among the PEEK-OPTIMA™, Ceridust® 3615, and ZTA groups ($p = 0.946$), suggesting a relatively comparable oxidative stress response among these materials.

Statistical analysis of ROS production by NG108-15 cells on Days 3 and 5 showed no significant interaction between culture duration and material type ($p = 0.34$; Figure 7d). Similarly, the main effect of culture time on ROS levels was not statistically significant ($p = 0.24$; Figure 7e). However, the type of biomaterial used in the 3D model particles had a significant overall effect on ROS production ($p = 0.04$; Figure 7f). Post hoc comparisons revealed that NG108-15 cells exposed to PEEK-OPTIMA™ particles produced significantly lower ROS compared to those exposed to CoCrMo ($p = 0.018$), Ceridust® 3615

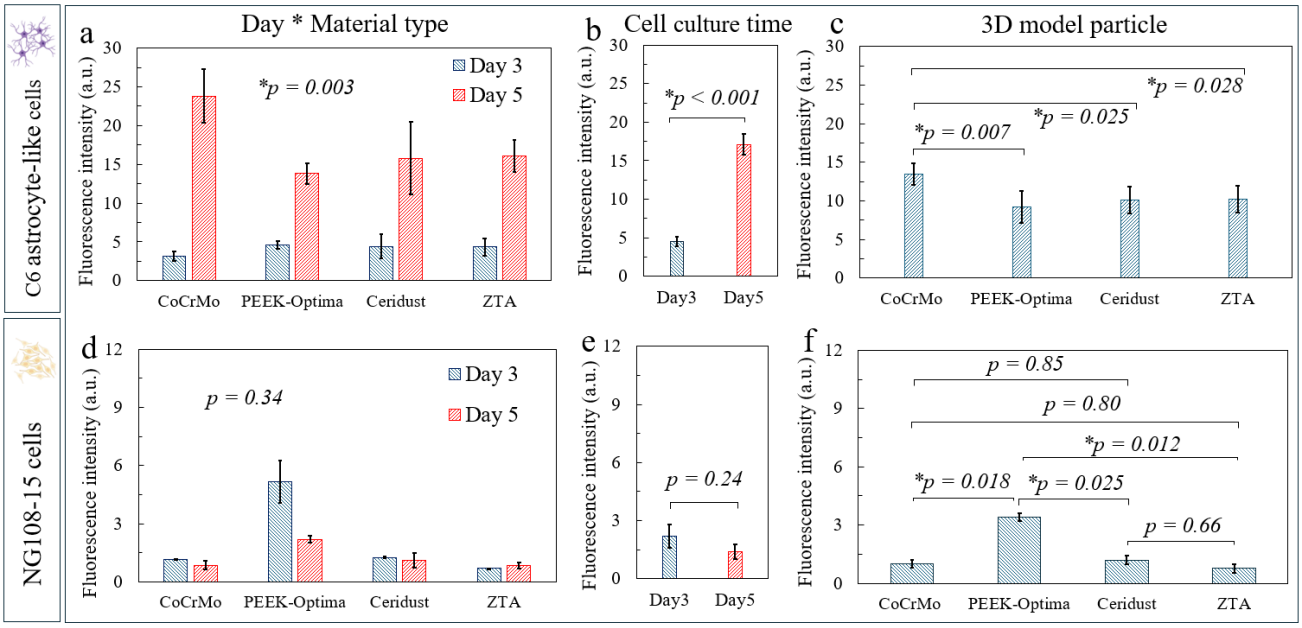

Figure 7. Reactive oxygen species (ROS) production by different cell types. (a, d) Effects of interaction between cell culture time and biomaterial type; (b, e) effects of culture time; and (c, f) effects of 3D model particles on the ROS production in C6 astrocyte-like (top) and NG108-15 cells (bottom). Abbreviations: CoCrMo: Cobalt–chromium–molybdenum; PEEK: Polyetheretherketone; ZTA: Zirconia-toughened alumina.

($p = 0.025$), and ZTA ($p = 0.012$). No significant differences in ROS levels were observed between CoCrMo and Ceridust® ($p = 0.85$), CoCrMo and ZTA ($p = 0.80$), or between Ceridust® 3615 and ZTA ($p = 0.66$). These findings suggest a relatively higher oxidative stress response in cells exposed to materials other than PEEK-OPTIMA™.

Quantitative analyses of C6 astrocyte-like cells showed that the positive control (cells with hydrogen peroxide) exhibited elevated ROS levels, as evidenced by the increased fluorescence intensity, compared to the cell-only negative control (Figure A1 in Appendix). The average fluorescence intensity of the positive control on Day 5 was significantly higher (approximately 70 times; $p < 0.05$) than that produced by all of the model particles (average fluorescence intensity < 22 ± 3.9 a.u.). Notably, all model particles did not induce significant ROS production compared to the cell-only negative control (average fluorescence intensity = 23.5 ± 5.4 a.u.). Similar results were observed for NG108-15 cells, where the positive control demonstrated higher ROS production (average fluorescence intensity = 37.1 ± 2.6 a.u.) than the cell-only negative control (average fluorescence intensity = 7.7 ± 5.8 a.u.) and any of the model particles (average fluorescence intensity < 2.1 ± 0.2 a.u.; $p < 0.05$) (**Figure S1, Supporting Information**). However, no significant increase in ROS production was detected in NG108-15 cells exposed to any of the model particles compared to the cell-only negative control.

The production of ROS by both C6 astrocyte-like and NG108-15 cells, embedded in 3D-bioprinted model particles, was qualitatively assessed using the DCFDA probe on Day 3. Production of ROS was proportional to the intensity of the green fluorescence (Figure 8a and b).

3.3.3. DNA integrity analysis

The DNA integrity of C6 astrocyte-like cells exposed to various model particles was assessed using a DNA damage assay that quantifies γ-H2AX foci as a marker of DNA strand breaks. DNA damage was evaluated at the 1-h mark, as genotoxic materials can induce immediate DNA strand breaks. Our findings revealed no detectable DNA damage in C6 astrocyte-like cells, as evidenced by the absence of γ-H2AX foci (Figure 8b).

4. Discussion

The primary objective of this study was to develop an advanced 3D spinal cord cellular model using bioprinting technology. While 3D bioprinting has been widely used in different biomedical studies,[36–38] this is the first study to engineer a 3D-bioprinted model that integrates neural cells with spinal implant wear particles and relevant biomaterials, establishing an advanced *in vitro* platform for evaluating the biological impact of wear debris. This novel approach offers a more physiologically relevant alternative to traditional 2D culture systems, enabling improved simulation of the *in vivo* microenvironment and more accurate assessment of cellular responses to biomaterial-associated particles.

We selected commercially available model particles derived from PEEK-OPTIMA™, Ceridust® 3615, ZTA ceramic, and CoCrMo alloy to represent a broad spectrum of biomaterials commonly used in spinal implant applications. This selection ensured comprehensive coverage of polymeric, ceramic, and metallic materials relevant to current clinical practice. Prior to embedding into neural cell-laden bioprinted GelMA hydrogels, the particles were thoroughly characterized for their size and morphology.

The SEM analysis of PEEK-OPTIMA™ model particles revealed irregular, granular morphologies. The particle size distribution showed a mode size between 0.1 and 0.8 μm, with an average diameter of 7.58 ± 3.97 μm. Notably, 95% of the particles were smaller than 8 μm. These results are consistent with those of Du et al.,[39] who reported that 99% of commercially available PEEK particles were under 5 μm, although their mean particle size was smaller (1.05 μm) compared to our findings. Furthermore, Hallab et al.[40] reported that PEEK-OPTIMA™ particles exhibited granular to flake-like morphologies, with 95% of the particles falling within the 1–10 μm size range, findings that are consistent with our current observations. The SEM analysis of Ceridust® 3615 particles revealed a predominantly granular morphology with noticeable agglomeration, aligning with observations reported by Liu et al.[35] In our study, the average particle size was 8.75 ± 2.35 μm following filtration through an 8 μm filter, and 5.27 ± 3.80 μm after passing through a 0.8 μm filter. These values are comparable to those reported by Green et al.,[41] who investigated murine peritoneal macrophage responses to polyethylene particles using Ceridust® 3615. Their work involved sequential filtration through 10, 1, 0.4, and 0.1 μm filters, resulting in particle sizes of 7.2 ± 3.15, 4.3 ± 1.89, 0.49 ± 0.11, and 0.21 ± 0.069 μm, respectively. ZTA particles in our study exhibited both granular and polygonal morphologies, with a size range of 0.1–0.8 μm and an average size of 3.69 ± 3.48 μm. These findings are consistent with those of Asif,[34] who also reported agglomerated structures of ZTA particles. In comparison, Germain et al.[42] investigated alumina powder and reported a smaller mean particle size of 0.5 ± 0.2 μm. The observed size discrepancy may be attributed to differences in particle generation and filtration techniques, as Germain et al. used a pin-on-plate wear simulator and employed finer filter membranes during particle separation.[42] The CoCrMo

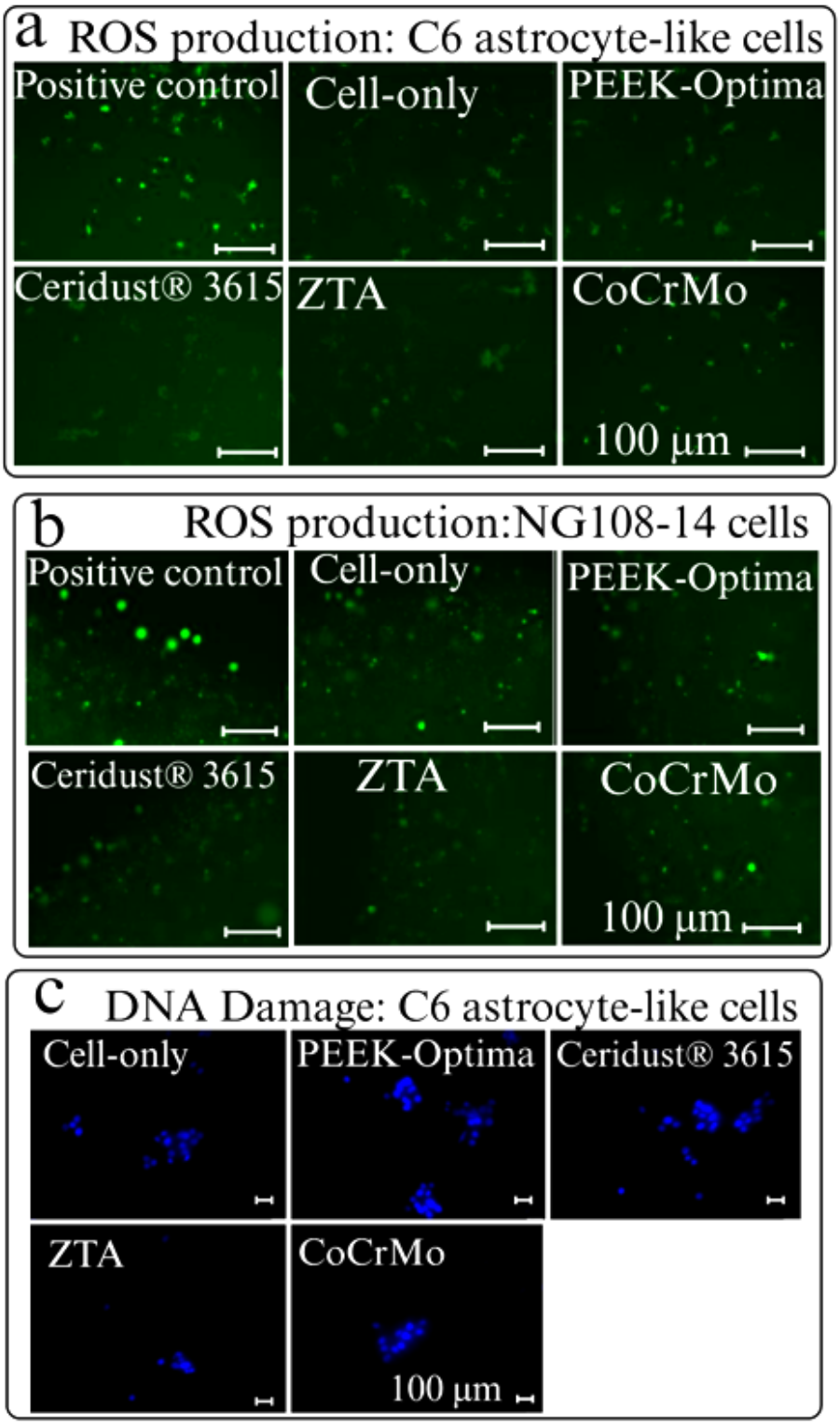

Figure 8. Fluorescence microscopy images showing ROS production in C6 astrocyte-like cells (a) and NG108-15 cells (b) embedded in 3D model particles after 3 days of culture. Oxidative stress was assessed using the DCFDA probe, which detects ROS activity. The intensity of green fluorescence correlates with ROS production. (c) DNA damage analysis via γ-H2AX immunofluorescence for C6 astrocyte-like cells exposed to different 3D model particles. Scale bars = 100 µm. Abbreviations: CoCrMo: Cobalt–chromium–molybdenum; PEEK: Polyetheretherketone; ROS: Reactive oxygen species; ZTA: Zirconia-toughened alumina.

particles predominantly exhibited a globular shape, with a mean size of 5.86 ± 1.20 μm, aligning with findings from Germain et al., who reported a mean size of 9.87 ± 5.67 μm for commercially available CoCr particles. However, when comparing these to clinically relevant CoCr particles generated via a pin-on-plate wear simulator, Germain et al.[42] and Lee et al.[26] observed aggregates and granular shapes, with some polygonal shards. Their reported mode size ranges for CoCr particles were 10–20 and 30–39 nm, respectively, while the mode size range in our study was 0.8–8 μm. This significant discrepancy in particle size may help explain the differences in biological responses observed in the current study.

In this study, bioprinting was used to create a 3D model incorporating neural cells and biomaterial particles for the first time. This platform offers significant advantages over traditional hydrogel casting methods, such as enhanced spatial precision for cellular placement and the ability to better replicate the *in vivo*-like organization of tissues.[43,44] By combining 5% (w/v) GelMA hydrogels and neural cells in bioprinted hydrogels, we established a promising 3D cell culture model for investigating neural cell responses to wear particles. The successful printing of model particles integrated with hydrogels and cells using extrusion-based bioprinting techniques demonstrated the potential of this approach. Printing parameters were adapted from previous studies, such as Rad et al.,[33] who successfully used GelMA hydrogels and neural cells in 3D-bioprinted constructs for spinal cord injury models. The temperature-sensitive properties of GelMA were key, as it undergoes reversible gelation with temperature change. Rad et al.[33] found that higher concentrations of GelMA (15% w/v) were needed at temperatures ≥32°C, while lower concentrations (2.5% w/v) were more effective at ≤22°C. Additionally, the current study confirmed that extrusion pressure was crucial for maintaining the structural integrity of GelMA constructs—too much pressure caused overflow, while insufficient pressure hindered extrusion. The nozzle size also played a critical role in successful extrusion, especially when printing hydrogels containing particles of metals, polymers, and ceramics. Smaller nozzles (25G, 0.25 mm; and 27G, 0.20 mm) were more likely to clog, whereas larger nozzles (20G, 0.58 mm; and 22G, 0.41 mm) enabled consistent, successful extrusion of cell-laden hydrogels with particles. Our results showed comparable growth and proliferation of cells in both 2D- and 3D-bioprinted cultures over 7 days. These findings were consistent with Rad et al.,[33] who reported similar results using 5% (w/v) GelMA hydrogel for the same cell lines.

In this study, C6 astrocyte-like and NG108-15 cells were exposed to model particles, with PEEK-OPTIMA™ and Ceridust® 3615 particles administered at a concentration of 100 μm³ per cell, and ZTA and CoCrMo particles at 50 μm³ per cell. In all model particle groups, 95% of the particles ranged from 0.1 to 8 μm in size. We assessed cell viability, ROS production, and DNA damage over 7 days to capture both immediate and cumulative cellular responses to model particles. Initial testing of CoCrMo particles at concentrations of 0.5, 5, and 50 μm³ per cell showed no significant differences in biological responses, prompting the selection of 50 μm³ per cell for further testing. No significant changes in cell viability or ROS production were observed between the cell-only controls and model particle groups for both cell types, likely due to the short culture duration. However, the study revealed significant variations in cell viability and ROS production, which were influenced by culture time, biomaterial type, and the interactions between particles and cells.

The literature on neural cell responses to different model particles, particularly in studies comparing the biological impact of various particles using 3D *in vitro* models, remains limited. One notable study by Hallab et al.[40] investigated macrophage reactivity to PEEK-OPTIMA™ particles versus ultra-high-molecular-weight polyethylene (UHMWPE) particles, using differentiated human macrophages and primary human monocytes. They found that PEEK-OPTIMA™ particles (0.7 and 2.4 μm) did not significantly affect cell viability after 24 or 48 h.[40] This finding is especially relevant, as our study is the first to examine neural cell responses to PEEK-OPTIMA™ particles *in vitro*. Hallab et al.[40] also reported that PEEK-OPTIMA™ particles induced significant increases in proinflammatory cytokine levels compared to the control, though their inflammatory response was less pronounced than that of UHMWPE particles. Although our current study did not focus on inflammation, future research should investigate the impact of PEEK-OPTIMA™ particles on cytokine production in neural cells. Additionally, Hallab et al.[45] conducted an *in vivo* study using a rabbit model to explore the effects of PEEK-OPTIMA™ particles via epidural and intradiscal injections, which resulted in neurological damage. This highlights the critical need to understand the biological effects of PEEK-OPTIMA™ particles on neural cells and tissues.[30,45,46] In line with these findings, our study observed no major negative impact on cell viability, with similar results between the cell-only and 3D model particle groups. However, a noteworthy observation was the significantly higher production of ROS by NG108-15 cells exposed to PEEK-OPTIMA™ particles. This increase in ROS production warrants further investigation into the potential long-term effects of PEEK-OPTIMA™ particles in spinal environments. Understanding how PEEK-OPTIMA™ interacts with neural tissues is essential for evaluating its safety and clinical outcomes. Such knowledge

is critical for guiding clinicians and patients in the use of PEEK-OPTIMA™ in spinal implants, as the interactions with neural cells may influence the implants' long-term success and health implications.

Previous studies have explored the biological responses to Ceridust® 3615 particles using *in vitro* gel encapsulation techniques. Green et al.[41] encapsulated Ceridust® 3615 particles in 1% (w/v) agarose gel, then centrifuged the mixture to create a monolayer of particles. Murine peritoneal macrophages were seeded on top, and after 24 h, no significant impact on cell viability was observed at a 100 μm³ per cell concentration compared to the cell-only control. This technique was later adapted by Liu et al.,[35] who used a 0.4% (w/v) agarose gel without centrifugation, enhancing the gel's porosity and dispersing the particles more widely. They also replaced murine macrophages with human peripheral blood mononuclear cells and found similar results, with no significant effect on cell viability after 24 h. Further supporting these findings, Yarrow-Wright's study[47] confirmed that the Ceridust® 3615 particles did not adversely affect the viability of either human peripheral blood mononuclear cells or murine peritoneal macrophages in agarose and collagen gels. However, no studies have yet investigated the response of neural cells to Ceridust® 3615 particles *in vitro*. This gap highlights the need for further research into how Ceridust® 3615 interacts with neural cells, especially within 3D *in vitro* models. The current study used GelMA hydrogels to culture C6 astrocyte-like and NG108-15 cells, following the method of Rad et al.,[33] who demonstrated cell viability over 7 days. The particle size of Ceridust® 3615 (>99%) aligned with that reported by Green et al.[41] Consistent with prior findings, no significant reduction in cell viability, ROS production, or DNA damage was observed in either cell type exposed to Ceridust® 3615 particles. The lack of adverse effects may be due to the particle size, as larger particles are less likely to be internalized by cells.[41] Future studies should investigate the impact of clinically relevant particle sizes on neural cell responses. Additionally, studies by Hallab et al.[40] and Liu et al.[35] found no significant release of osteolytic cytokines from cells exposed to Ceridust® 3615. Future research should explore its impact on neural cell inflammatory responses, offering further insights for clinical applications.

The biological impact of BIOLOX Delta ZTA wear particles has been investigated in studies involving fibroblasts and peripheral blood mononuclear cells, with Asif[34] reporting minimal biological effects and suggesting potential improvements in long-term clinical performance. Although ZTA is used in spinal cages, concerns about the brittleness of ZTA under certain loading conditions continue to limit its use in spinal implants, as fractures can occur under excessive mechanical forces.[48] In the current study, neural cells were exposed to ZTA model particles at a dosage of 50 μm³, and cell viability was assessed over 5 days. No significant changes in cell viability were observed in either C6 astrocyte-like or NG108-15 cells, compared to the cell-only negative control. Interestingly, significantly lower ROS production was observed in the 3D ZTA model compared to other particle types. Although previous research has not explored neural cell responses to ZTA particles, similar studies on other cell types, such as L929 fibroblasts, have reported comparable findings. Germain et al.[42] observed no significant reduction in cell viability when fibroblasts were exposed to commercially available ceramic powders but noted cytotoxic effects when U937 human macrophages were exposed to clinically relevant ceramic wear particles at a dose of 50 μm³ per cell. The lack of cytotoxicity observed in our study with neural cells aligns with the findings in fibroblasts. Additionally, Asif[34] reported no adverse effects on L929 cell viability when exposed to BIOLOX Delta ceramic particles at a similar dosage. Furthermore, ZTA particles in our study did not induce ROS production or DNA damage in either C6 astrocyte-like or NG108-15 cells, reinforcing the conclusion that ZTA particles are biologically inert in neural cell cultures. These results are consistent with those of Asif,[34] who found no significant oxidative stress or DNA damage in peripheral blood mononuclear cells exposed to ceramic particles. However, their study also revealed that clinically relevant ceramic wear particles at the same dosage did induce DNA damage, highlighting differences in biological effects between model particles and clinically relevant materials. Future studies should focus on using clinically relevant ceramic wear particles at the same dosage (50 μm³ per cell) to determine if the cytotoxic effects observed in fibroblasts extend to neural cells. This approach will provide a clearer understanding of the potential biological risks associated with ceramic-based spinal implants in a clinically relevant context.

Prior research by Lee et al. utilized Type I rat tail collagen gel to examine the responses of primary astrocytes and microglia to CoCrMo wear particles at doses ranging from 0.5 to 50 μm³ per cell over 5 days.[26] Their findings revealed a significant reduction in astrocyte viability at the highest dose (50 μm³) after 2 and 5 days. However, the use of collagen hydrogels introduced limitations, such as poor structural integrity and batch-to-batch variability, which could affect the results. In contrast, the current study demonstrated that C6 astrocyte-like cells maintained viability across all CoCrMo particle doses (0.5–50 μm³ per cell) over the same exposure period. A notable reduction in NG108-15 cell viability was observed only at the highest dose (50 μm³) after 5 days, compared to the cell-only

negative control. These findings suggest that the 3D model used in this study offers improved stability and reliability, allowing for a more accurate evaluation of neural cell responses to CoCrMo particles. The distinct responses of C6 astrocyte-like and NG108-15 cells to CoCrMo particles likely stem from their differing sensitivities to foreign materials. Astrocytes, known for their structural support and role in tissue repair within the central nervous system, exhibit greater resilience to such exposure. In contrast, the more sensitive NG108-15 cells are less equipped to tolerate foreign materials. These findings highlight the need for further research to understand the cellular mechanisms behind these responses, which is essential for improving the safety and effectiveness of spinal implants and minimizing neural tissue damage. No significant oxidative stress or DNA damage was detected in C6 astrocyte-like or NG108-15 cells following 24 h of exposure to model CoCrMo particles. This contrasts with findings by Lee et al.,[26] who reported significant DNA damage in primary astrocytes under similar conditions. The discrepancy may stem from differences in cell models, particle characteristics, or experimental conditions, underscoring the need for further research to clarify the varying cellular responses to CoCrMo particles. The discrepancies between this study and Lee et al.'s investigation can be attributed to key differences in the experimental models, particularly the type and size of CoCrMo particles used.

In the current study, we developed a novel 3D-bioprinted spinal cord model integrating neural cells with spinal implant wear particles and biomaterials, establishing the first *in vitro* platform of its kind to assess the biological effects of wear debris. While the 3D constructs in this study were deposited in droplet format, the use of a bioprinter was essential for ensuring precise and reproducible placement, volumetric consistency, and homogeneous distribution of cells and particles across replicates. Unlike manual pipetting, the bioprinter allowed for controlled deposition of defined volumes and bioink compositions, which is critical when evaluating cellular responses to different biomaterial particles. Additionally, bioprinting supports future scalability and integration into more complex architectures, which aligns with our longer-term aim of developing advanced neural tissue models. Compared to traditional casting, bioprinting offers superior control over the distribution and organization of cells and particles within hydrogels.[49] In casting, sedimentation and uneven mixing often lead to heterogeneous distribution, whereas bioprinting ensures uniform dispersion by precisely depositing cell-particle-laden hydrogels. Bioprinting also applies minimal and consistent mechanical stress on cells during fabrication, reducing unintended shear forces common in casting or manual handling.[50] Additionally, gelation can be finely controlled in bioprinting through synchronized light exposure or temperature regulation, leading to reproducible and structurally stable constructs. This controlled environment results in higher fidelity in model architecture and better mimics the native tissue microenvironment. Despite the valuable insights gained, one of the limitations of the current study was the use of commercially available model particles, not clinically representative wear-simulated particles, particularly in terms of size, morphology, and chemical composition. As these particles differ from those typically generated in clinical settings, future studies should aim to replicate these experiments with clinically relevant particles to better understand neural cell responses *in vitro* within the same 3D-bioprinted GelMA hydrogel model. Moreover, examining the cumulative or synergistic effects of multiple biomaterial wear particles, such as those from metals, ceramics, and polymers, could provide deeper insights into the overall impact on neural tissue, particularly in the context of multi-material spinal implants. Expanding the scope in these areas will enhance the clinical relevance of the findings and support the development of safer, more effective biomaterials for spinal and neural tissue applications. While no significant difference in cell viability was observed between the 2D and 3D cultures, this is a positive outcome, as cell viability often decreases in 3D systems due to limited nutrient diffusion. The ability of our 3D-bioprinted model to maintain comparable viability suggests good biocompatibility and supports its use for further physiological studies. Future work will focus on evaluating neural-specific functions and comparing cell behavior in this model to native tissue to further validate its physiological relevance. Another limitation of this study was the use of cell lines (C6 and NG108-15), which do not fully represent the functionality and cellular heterogeneity of the spinal cord, particularly due to the absence of microglia. These cell lines were chosen to establish a robust and reproducible 3D-bioprinted model and to assess the feasibility of incorporating spinal implant biomaterial-derived particles in the 3D-bioprinted system. Future work should focus on incorporating primary or induced pluripotent stem cell (iPSC)-derived neural cells, including microglia, to enhance the physiological relevance of the model.

5. Conclusion

This study established a 3D-bioprinted spinal cord cellular model that integrates neural cells with spinal implant wear particles. It represents the first *in vitro* platform designed to investigate the biological effects of wear debris in a physiologically relevant context. By incorporating model particles with diverse morphologies (ranging from irregular to spherical), sourced from different biomaterials, and

administering them in a 3D-bioprinted GelMA hydrogel, we enabled precise and reproducible evaluation of particle–cell interactions. Short-term exposure did not significantly impact cell viability or ROS production across the tested conditions. However, our results revealed significant variations in cell viability and ROS production, which were influenced by culture time, biomaterial type, and the interactions between particles and cells. In particular, CoCrMo particles had a greater impact on cell viability compared to the other biomaterials tested. These findings underscore the potential of this bioprinted platform as a powerful tool for future long-term mechanistic studies and preclinical assessments of spinal implant biocompatibility.

Acknowledgments

None.

Funding

None.

Conflict of interest

The authors declare they have no competing interests

Author contributions

Conceptualization: Joanne L. Tipper
Formal analysis: Joanne L. Tipper, David J. Wen, Javad Tavakoli
Investigation: David J. Wen
Methodology: Joanne L. Tipper, David J. Wen, Javad Tavakoli
Writing–original draft: Javad Tavakoli, David J. Wen
Writing–review & editing: Joanne L. Tipper, Javad Tavakoli

Ethics approval and consent to participate

Not applicable.

Consent for publication

Not applicable.

Availability of data

Data is available from the corresponding author upon reasonable request.

References

1. Tavakoli J, Diwan AD, Tipper JL. Advanced strategies for the regeneration of lumbar disc annulus fibrosus. *Int J Mol Sci*. 2020;21(14):4889.
doi: 10.3390/ijms21144889

2. Wen DJ, Tavakoli J, Tipper JL. Lumbar total disc replacements for degenerative disc disease: a systematic review of outcomes with a minimum of 5 years follow-up. *Global Spine J*. 2024;14(6):1827-1837.
doi: 10.1177/21925682241228756

3. Zeegers W, Bohnen L, Laaper M, Verhaegen M. Artificial disc replacement with the modular type SB Charite III: 2-year results in 50 prospectively studied patients. *Eur Spine J*. 1999;8:210-217.
doi: 10.1007/s005860050160

4. Vicars R, Hyde PJ, Brown TD, et al. The effect of anterior–posterior shear load on the wear of ProDisc-L TDR. *Eur Spine J*. 2010;19(8):1356-1362.
doi: 10.1007/s00586-010-1396-8

5. Vicars R, Prokopovich P, Brown TD, et al. The effect of anterior-posterior shear on the wear of CHARITÉ total disc replacement. *Spine (Phila Pa 1976)*. 2012;37(9):E528-E534.
doi: 10.1097/BRS.0b013e31823cbd6e

6. Hallab NJ. A review of the biologic effects of spine implant debris: fact from fiction. *SAS J*. 2009;3(4):143-160.
doi: 10.1016/j.esas.2009.11.005

7. Chang B-S, Brown PR, Sieber A, Valdevit A, Tateno K, Kostuik JP. Evaluation of the biological response of wear debris. *Spine J*. 2004;4(6):S239-S244.
doi: 10.1016/j.spinee.2004.07.014

8. Ganko R, Madhavan A, Hamouda W, et al. Spinal implant wear particles: generation, characterization, biological impacts, and future considerations. *iScience*. 2025;28(4):112193.
doi: 10.1016/j.isci.2025.112193

9. Punt IM, Austen S, Cleutjens JP, et al. Are periprosthetic tissue reactions observed after revision of total disc replacement comparable to the reactions observed after total hip or knee revision surgery? *Spine (Phila Pa 1976)*. 2012;37(2):150-159.
doi: 10.1097/brs.0b013e3182154c22

10. San-Juan R, Paredes I, Ramírez-Nava E, et al. Reduction of instrumentation-related spine surgical site infections after optimization of surgical techniques. a single center retrospective analysis. *Global Spine J*. 2024;14(2):438-446.
doi: 10.1177/21925682221109557

11. Xu R, Ebraheim NA, Nadaud MC, Phillips ER. Local tissue of the lumbar spine response to titanium plate-screw system. *Spine (Phila Pa 1976)*. 1996;21(7):871-873.
doi: 10.1097/00007632-199604010-00020

12. Lin T-h, Tamaki Y, Pajarinen J, et al. Chronic inflammation in biomaterial-induced periprosthetic osteolysis: NF-κB as a therapeutic target. *Acta Biomater*. 2014;10(1):1-10.
doi: 10.1016/j.actbio.2013.09.034

13. Zairi F, Remacle JM, Allaoui M, Assaker R. Delayed hypersensitivity reaction caused by metal-on-metal total disc replacement: case report. *J Neurosurg Spine*. 2013;19(3):389-391.
doi: 10.3171/2013.6.spine121010

14. Zeh A, Planert M, Siegert G, Lattke P, Held A, Hein W. Release of cobalt and chromium ions into the serum following implantation of the metal-on-metal Maverick-type artificial lumbar disc (Medtronic Sofamor Danek). *Spine (Phila Pa 1976)*. 2007;32(3):348-352. doi: 10.1097/01.brs.0000253599.89694.c0

15. AlZeedi M, Al Rawahi S, Muwanis M, Alraiyes TM, Al Farii H, Jarzem P. Pseudotumor after total disc replacement in the lumbar spine: a case report and review of the literature. *N Am Spine Soc J*. 2022;9:100107. doi: 10.1016/j.xnsj.2022.100107

16. Tavakoli J, Hu Q, Tipper JL, Tang Y. Aggregation-induced emission biomarkers for early detection of orthopaedic implant failure. *Aggregate*. 2024;5(6):e645. doi: 10.1002/agt2.645

17. Austen S, Punt IM, Cleutjens JP, et al. Clinical, radiological, histological and retrieval findings of Activ-L and Mobidisc total disc replacements: a study of two patients. *Eur Spine J*. 2012;21:513-520. doi: 10.1007/s00586-011-2141-7

18. Yang G, Gu M, Chen W, et al. SPHK-2 promotes the particle-induced inflammation of RAW264.7 by maintaining consistent expression of TNF-α and IL-6. *Inflammation*. 2018;41(4):1498-1507. doi: 10.1007/s10753-018-0795-6

19. Yoshitake F, Itoh S, Narita H, Ishihara K, Ebisu S. Interleukin-6 directly inhibits osteoclast differentiation by suppressing receptor activator of NF-kappaB signaling pathways. *J Biol Chem*. 2008;283(17):11535-11540. doi: 10.1074/jbc.m607999200

20. Ayers R, Miller M, Schowinsky J, Burger E, Patel V, Kleck C. Three cases of metallosis associated with spine instrumentation. *J Mater Sci Mater Med*. 2017;29(1):3. doi: 10.1007/s10856-017-6011-7

21. Punt IM, Cleutjens JPM, de Bruin T, et al. Periprosthetic tissue reactions observed at revision of total intervertebral disc arthroplasty. *Biomaterials*. 2009;30(11):2079-2084. doi: 10.1016/j.biomaterials.2008.12.071

22. Cunningham BW, Orbegoso CM, Dmitriev AE, et al. The effect of spinal instrumentation particulate wear debris: an in vivo rabbit model and applied clinical study of retrieved instrumentation cases. *Spine J*. 2003;3(1):19-32. doi: 10.1016/S1529-9430(02)00443-6

23. Lin T-h, Yao Z, Sato T, et al. Suppression of wear-particle-induced pro-inflammatory cytokine and chemokine production in macrophages via NF-κB decoy oligodeoxynucleotide: a preliminary report. *Acta Biomater*. 2014;10(8):3747-3755. doi: 10.1016/j.actbio.2014.04.034

24. Luo G, Li Z, Wang Y, et al. Resveratrol protects against titanium particle-induced aseptic loosening through reduction of oxidative stress and inactivation of NF-κB. *Inflammation*. 2016;39(2):775-785. doi: 10.1007/s10753-016-0306-6

25. Hallab NJ, Cunningham BW, Jacobs JJ. Spinal implant debris-induced osteolysis. *Spine (Phila Pa 1976)*. 2003;28(20S):S125-S138. doi: 10.1097/00007632-200310151-00006

26. Lee H, Phillips JB, Hall RM, Tipper JL. Neural cell responses to wear debris from metal-on-metal total disc replacements. *Eur Spine J*. 2020;29(11):2701-2712. doi: 10.1007/s00586-019-06177-w

27. Papageorgiou I, Marsh R, Tipper JL, Hall RM, Fisher J, Ingham E. Interaction of micron and nano-sized particles with cells of the dura mater. *J Biomed Mater Res B Appl Biomater*. 2014;102(7):1496-1505. doi: 10.1002/jbm.b.33129

28. Behl B, Papageorgiou I, Brown C, et al. Biological effects of cobalt-chromium nanoparticles and ions on dural fibroblasts and dural epithelial cells. *Biomaterials*. 2013;34(14):3547-3558. doi: 10.1016/j.biomaterials.2013.01.023

29. Papageorgiou I, Abberton T, Fuller M, Tipper JL, Fisher J, Ingham E. Biological effects of clinically relevant cocr nanoparticles in the dura mater: an organ culture study. *Nanomaterials*. 2014;4(2):485-504. doi: 10.3390/nano4020485

30. Cunningham BW, Hallab NJ, Hu N, McAfee PC. Epidural application of spinal instrumentation particulate wear debris: a comprehensive evaluation of neurotoxicity using an in vivo animal model. *J Neurosurg Spine*. 2013;19(3):336-350. doi: 10.3171/2013.5.spine13166

31. Stoodley MA, Jones NR, Brown CJ. Evidence for rapid fluid flow from the subarachnoid space into the spinal cord central canal in the rat. *Brain Res*. 1996;707(2):155-164. doi: 10.1016/0006-8993(95)01228-1

32. Stoodley MA, Brown SA, Brown CJ, Jones NR. Arterial pulsation-dependent perivascular cerebrospinal fluid flow into the central canal in the sheep spinal cord. *J Neurosurg*. 1997;86(4):686-693. doi: 10.3171/jns.1997.86.4.0686

33. Rad MA, Mahmodi H, Filipe EC, Cox TR, Kabakova I, Tipper JL. Micromechanical characterisation of 3D bioprinted neural cell models using Brillouin microspectroscopy. *Bioprinting*. 2022;25:e00179. doi: 10.1016/j.bprint.2021.e00179

34. Asif IM. *Characterisation and Biological Impact of Wear Particles from Composite Ceramic Hip Replacements*. University of Leeds; 2018. https://etheses.whiterose.ac.uk/id/oai_id/oai:etheses.whiterose.ac.uk:20563

35. Liu A, Richards L, Bladen CL, Ingham E, Fisher J, Tipper JL. The biological response to nanometre-sized polymer particles. *Acta Biomater*. 2015;23:38-51. doi: 10.1016/j.actbio.2015.05.016

36. Kim A, Mo K, Choe S, Shin M, Yoon H. Comprehensive insight into 3D bioprinting technology for brain tumor modelling. *IJB*. 2024;10(6):4166.
doi: 10.36922/ijb.4166

37. Tang H, Zhao E, Lai Y, et al. 3D bioprinting techniques and hydrogels for osteochondral integration regeneration. *IJB*. 2024;10(6):4472.
doi: 10.36922/ijb.4472

38. Hou Y-C, Cui X, Qin Z, et al. Three-dimensional bioprinting of artificial blood vessel: process, bioinks, and challenges. *IJB*. 2023;9(4):740.
doi: 10.18063/ijb.740

39. Du Z, Zhu Z, Wang Y. The degree of peri-implant osteolysis induced by PEEK, CoCrMo, and HXLPE wear particles: a study based on a porous Ti6Al4V implant in a rabbit model. *J Orthop Surg Res*. 2018;13(1):23.
doi: 10.1186/s13018-018-0736-y

40. Hallab NJ, McAllister K, Brady M, Jarman-Smith M. Macrophage reactivity to different polymers demonstrates particle size- and material-specific reactivity: PEEK-OPTIMA® particles versus UHMWPE particles in the submicron, micron, and 10 micron size ranges. *J Biomed Mater Res B Appl Biomater*. 2012;100B(2):480-492.
doi: 10.1002/jbm.b.31974

41. Green TR, Fisher J, Stone M, Wroblewski BM, Ingham E. Polyethylene particles of a 'critical size' are necessary for the induction of cytokines by macrophages in vitro. *Biomaterials*. 1998;19(24):2297-2302.
doi: 10.1016/s0142-9612(98)00140-9

42. Germain M, Hatton A, Williams S, et al. Comparison of the cytotoxicity of clinically relevant cobalt–chromium and alumina ceramic wear particles in vitro. *Biomaterials*. 2003;24(3):469-479.
doi: 10.1016/s0142-9612(02)00360-5

43. Bishop ES, Mostafa S, Pakvasa M, et al. 3-D bioprinting technologies in tissue engineering and regenerative medicine: Current and future trends. *Genes Dis*. 2017;4(4):185-195.
doi: 10.1016/j.gendis.2017.10.002

44. Yu J, Park SA, Kim WD, et al. Current advances in 3D bioprinting technology and its applications for tissue engineering. *Polymers*. 2020;12(12):2958.
doi: 10.3390/polym12122958

45. Hallab NJ, Bao Q-B, Brown T. Assessment of epidural versus intradiscal biocompatibility of PEEK implant debris: an in vivo rabbit model. *Eur Spine J*. 2013;22:2740-2751.
doi: 10.1007/s00586-013-2904-4

46. Stratton-Powell AA, Pasko KM, Brockett CL, Tipper JL. The biologic response to polyetheretherketone (PEEK) wear particles in total joint replacement: a systematic review. *Clin Orthop Relat Res*. 2016;474(11):2394-2404.
doi: 10.1007/s11999-016-4976-z

47. Yarrow-Wright LE. *Development of a Novel 3D In Vitro Model to Measure Cellular Response to Antioxidant Doped Highly Cross-Linked Ultra High Molecular Weight Polyethylene Wear Debris*. University of Leeds; 2018.
https://etheses.whiterose.ac.uk/id/oai_id/oai:etheses.whiterose.ac.uk:24128

48. Kölle L, Ignasiak D, Ferguson SJ, Helgason B. Ceramics in total disc replacements: a scoping review. *Clin Biomech*. 2022;100:105796.
doi: 10.1016/j.clinbiomech.2022.105796

49. Jaksa L, Aryeetey OJ, Hatamikia S, et al. 3D-printed multi-material liver model with simultaneous mechanical and radiological tissue-mimicking features for improved realism. *IJB*. 2023;9(4):721.
doi: 10.18063/ijb.721

50. Yuk JC, Nam KH, Park SH. Additive-manufactured synthetic bone model with biomimicking tunable mechanical properties for evaluation of medical implants. *IJB*. 2024;10(1):1067.
doi: 10.36922/ijb.1067

Appendix

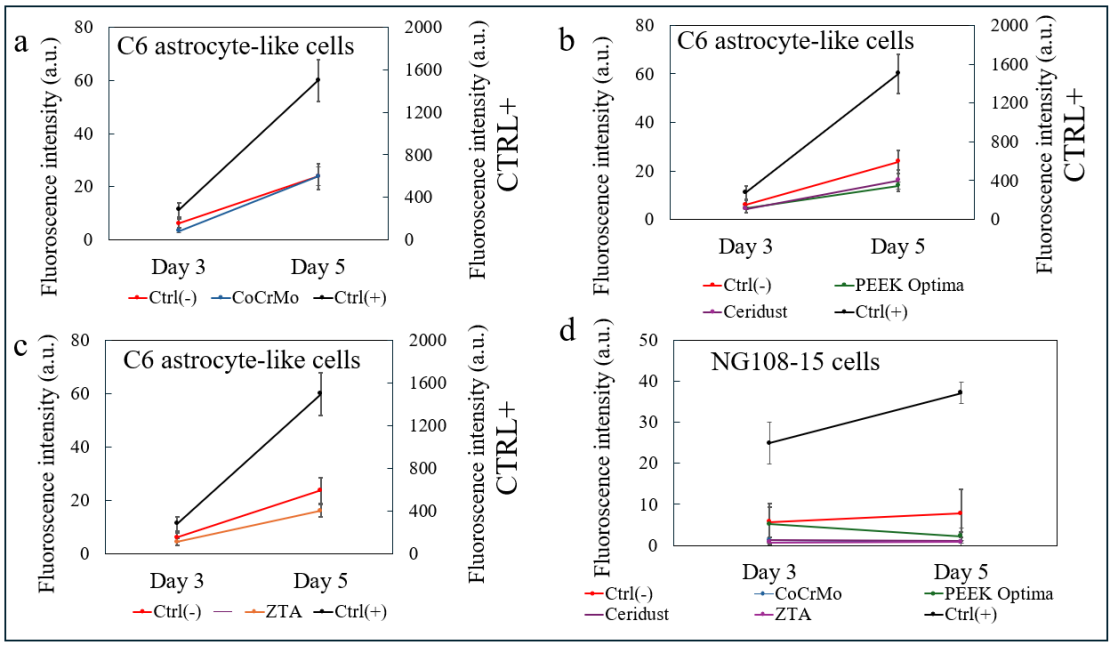

Figure A1. Comparison of ROS production by C6 astrocyte-like cells between controls (negative: cell-only; and positive: cell-H_2O_2) and 3D model particles: (a) CoCrMo, (b) PEEK-OPTIMA™ and Ceridust®, and (c) ZTA. (d) Comparison of ROS production by NG108-15 cells between controls (negative: cell-only; and positive: cell-H_2O_2) and all 3D model particles. Abbreviations: CoCrMo: Cobalt–chromium–molybdenum; PEEK: Polyetheretherketone; ROS: Reactive oxygen species; ZTA: Zirconia-toughened alumina.

ACCSCIENCE PUBLISHING

International Journal of Bioprinting

RESEARCH ARTICLE

Dual-strategy modification for three-dimensional-printed silk methacryloyl hydrogels: Nanofiber reinforcement and poly(ethylene oxide)-induced porosity

Bingxue Xv†, Xin An†, Ning Zhou, Wenxin Meng, Yvmeng Luo, and Guomin Wu*

College & Hospital of Stomatology, Anhui Medical University, Key Lab. of Oral Diseases Research of Anhui Province, Hefei 230032, China.

Abstract

Hydrogels have emerged as promising scaffolds for cartilage tissue engineering due to their structural mimicry of native articular cartilage extracellular matrix. However, conventional hydrogels typically exhibit only nanoscale porosity and poor mechanical properties, which limit nutrient delivery, metabolic waste exchange, and structural fidelity. To address these challenges, we developed an innovative cell-laden porous silk methacryloyl (SilMA) hydrogel system with biomechanical reinforcement using three-dimensional (3D) bioprinting. The porous architecture was created through a water-in-water emulsification strategy employing poly(ethylene oxide) (PEO) as a sacrificial template. This pore-forming process resulted in a remarkable structural modulation, achieving an increase of over 100% in average pore diameter and a 75% enhancement in overall porosity compared to hydrogels without PEO. However, this structural modification compromised the compressive modulus by approximately 50%. Therefore, homogenized electrospun silk fibroin nanofibers (NFs) were incorporated into the bio-ink to improve the mechanical properties and optimize surface topography. The introduction of NFs (1–2 wt%) not only recovered the compressive strength and modulus (close to SilMA hydrogels) but also improved the 3D printability of PEO/SilMA hydrogels. Additionally, the hydrogel demonstrated excellent biocompatibility and markedly upregulated expression of chondrogenic-related genes, including *COL2A1*, *ACAN*, and *SOX9*. Furthermore, the subcutaneous implantation experiments in non-obese diabetic/severe combined immunodeficiency mice further confirmed the potential of PEO/NF/SilMA hydrogels in promoting cartilage formation. Therefore, this study proposes a promising dual-strategy approach for cartilage tissue engineering, integrating NFs reinforcement and PEO-induced porosity.

Keywords: Cartilage regeneration; Electrospun nanofiber; Poly(ethylene oxide); Silk methacryloyl; Three-dimensional bioprinting.

†These authors contributed equally to this work.

***Corresponding author:**
Guomin Wu
(wuguomin@ahmu.edu.cn)

Citation: Xv B, An X, Zhou N, Meng W, Luo Y, Wu G. Dual-strategy modification for three-dimensional-printed silk methacryloyl hydrogels: Nanofiber reinforcement and poly(ethylene oxide)-induced porosity. *Int J Bioprint*. 2025;11(4):278-296. doi: 10.36922/IJB025140118

Received: April 1, 2025
1st revised: May 10, 2025
Accepted: May 19, 2025
Published Online: May 19, 2025

Copyright: © 2025 Author(s). This is an Open Access article distributed under the terms of the Creative Commons Attribution License, permitting distribution, and reproduction in any medium, provided the original work is properly cited.

Publisher's Note: AccScience Publishing remains neutral with regard to jurisdictional claims in published maps and institutional affiliations.

1. Introduction

Articular cartilage injuries caused by aging, obesity, occupational injury, and trauma often develop into osteoarthritis, a leading cause of disability worldwide. While approximately 300 million people were affected in 2019, this number surged to 3.53 billion by 2021.[1] Articular cartilage is a highly hydrated connective tissue devoid of nerves, blood vessels, and lymphatic vessels, consisting primarily of chondrocytes and dense extracellular matrix (ECM).[2] These histological structural characteristics limit its self-repair capacity, placing a substantial burden on the global healthcare system and economy. In response, advancements in tissue engineering and regenerative medicine have led to the development of various scaffolds designed to support cartilage repair.[3–5]

Hydrogels are three-dimensional (3D) hydrophilic polymer networks capable of water absorption. They mimic the biphasic structure of cartilage, offering a suitable environment for cell growth and matrix formation.[6] Compared to conventional two-dimensional cultures (2D), 3D cell cultivation within hydrogels more accurately replicates *in vivo* conditions, enhancing matrix production. Nevertheless, uneven cell distribution within these gels can hinder uniform matrix formation.[7] 3D bioprinting emerges as a refined technique, precisely controlling biomaterial deposition and cellular placement, and fabricating intricate and biomimetic scaffolds.[8] It can also produce large channels (typically hundreds of micrometers) within the scaffolds. However, the intrinsic pore structure of most hydrogel scaffold materials is often limited to the submicron or nanometer scale, which impedes the acquisition of nutrients and the exchange of metabolic waste in hydrogels, potentially compromising long-term cell viability and tissue functionality.[9]

Porous hydrogels exhibit advantages over their non-porous counterparts in supporting 3D cell culture. However, traditional methods of porosity introduction,[10,11] such as particle leaching, gas foaming, and freeze-drying, involve cytotoxic agents, rendering them unsuitable for live cell encapsulation or integration with 3D printing.[12] The Pluronic micellar template method offers a gentle, all-aqueous approach to hydrogel pore formation, but struggles to create macropores due to micelle size constraints.[13] Consequently, developing a biocompatible, porous bio-ink that supports cell encapsulation remains a formidable challenge. Alternative strategies, like phase separation in emulsions, are hindered by surfactant-induced cytotoxicity, restricting their use in 3D bioprinting.[14,15] The water-in-water system circumvents this issue by segregating two hydrophilic polymer solutions beyond a critical concentration, forming two immiscible aqueous phases without surfactants. The higher volume fraction is used as the continuous phase, and the smaller volume fraction is used as the dispersed phase (water-in-water emulsion).[16] Combining ultraviolet (UV)-curable gelatin precursors with poly(ethylene oxide) (PEO) solutions has yielded porous hydrogels compatible with 3D printing.[17] However, gelatin's inherent mechanical weakness might be exacerbated by internal porosity, limiting its utility in osteochondral engineering. Thus, enhancing hydrogel mechanical stability while retaining porosity is crucial.[18]

Silk fibroin (SF), a natural polymer known for its robust mechanical properties, biocompatibility, degradability, aqueous processability, and functionalizable chemical groups, presents a promising matrix for biomedical scaffolds.[5,19] Silk methacryloyl (SilMA) and methacrylated SF serve as an advanced bio-ink for 3D printing, outperforming methacrylated gelatin in simulating tissues like the heart, blood vessels, trachea, and cartilage. Kim et al.[20] detailed the synthesis of SilMA and its characterization in 3D-printed hydrogel applications for tissue engineering. It was found that a 30% SilMA hydrogel was suitable for cartilage tissue engineering, fulfilling mechanical and biological requirements. Although the high concentration of SilMA enhanced mechanical properties and clinical operability, it also significantly reduced the pore size of the hydrogel (well below 100 μm), which diverges from the ideal pore size for cartilage scaffolds (150–250 μm).[21] This reduction in porosity hinders efficient gas–liquid exchange, adversely affecting the cells loaded in the hydrogel scaffold material through 3D bioprinting. A recent study has explored the fabrication of porous gelatin methacryloyl hydrogels by incorporating PEO. However, this approach also compromised the mechanical properties of the hydrogel.[22]

Recent advances in nanotechnology have integrated nanomaterials into hydrogels to enhance their mechanical properties, broadening their tissue engineering applications. Electrospun NFs are widely used as tissue regeneration scaffolds due to their structure and size resembling collagen fibers in the ECM, as well as their high specific surface area.[23,24] However, the inherent 2D architecture of electrospun membranes substantially limits cellular infiltration into the scaffold interior, compromising their effectiveness in 3D tissue regeneration. This structural limitation has driven recent investigations into developing 3D nanofibrous scaffolds with enhanced cellular interactivity. In our previous study, we developed an innovative 3D SF aerogel by incorporating short electrospun SF NFs into an SF hydrogel matrix, followed by freeze-drying. The resulting nanofibrous aerogel exhibited significantly improved mechanical properties compared to conventional hydrogels. More importantly,

the incorporated nanofibrous architectures substantially enhanced the proliferation and osteogenic differentiation of bone marrow-derived mesenchymal stem cells, suggesting great potential for bone tissue engineering applications.[25]

Therefore, in this study, we developed a 3D printable, NF-reinforced porous SilMA hydrogel designed for cartilage regeneration. PEO was used as a template to increase internal pore structure, and short electrospun SF NFs were incorporated to enhance its mechanical and biological properties. A notable advantage of the water-in-water emulsion system is its inherently low and unstable interfacial tension. The addition of short NFs is expected to improve emulsion stability by reducing the interfacial free energy.[26] Our approach includes characterization of the hydrogel's physicochemical properties, *in vitro* evaluation of biocompatibility and bioactivity, and *in vivo* assessment of chondrogenic ability through subcutaneous implantation in non-obese diabetic/severe combined immunodeficiency mice.

2. Materials and methods

2.1. Materials

Silkworm cocoons were obtained from the Jiangnan Mulberry Silkworm Base (China). Lithium phenyl (2,4,6-trimethylbenzoyl) phosphate (LAP), lithium bromide (LiBr), and hexafluoroisopropanol were obtained from the Shanghai Aladdin Biochemical Technology Co., Ltd. (China), rhodamine-B, PEO, 424 mM glycidyl methacrylate (GMA), and dimethylmethylene blue from Sigma–Aldrich Corporation (United States), Hoechst 33258 and type II collagenase from MedChemExpress LLC (United States), and dialysis bags from Biomedical Instruments Inc (China). Phosphate buffered saline (PBS) was purchased from Thermo Fisher Scientific Inc. (United States), F-12 medium and fetal bovine serum from Gibco (United States), and Live/dead cell staining kit from Shanghai Beyotime Bio-Tech Co., Ltd. (China).

2.2. Extraction of silk fibroin and preparation of nanofibrous film

The silkworm cocoons were first degummed.[27] Then, 10 g of the degummed cocoons were dissolved in a 9.3 mol/L LiBr aqueous solution at 60°C with constant stirring at 300 rpm for 4 h. The resulting solution was dialyzed using a 12–14 kDa dialysis membrane for 4 days to obtain SF. The SF was then dissolved in hexafluoroisopropanol to prepare a 7% (w/w) solution, which was stirred overnight. The solution was then loaded into a 10 mL syringe with an 8-gauge metal needle and connected to electrospinning equipment with the following parameters: a high voltage of 16 kV, a solution flow rate of 15 μL/min, and a distance of 15 cm between the needle and the collector plate. After electrospinning, the NF membrane was placed in a fume hood overnight, followed by cross-linking with absolute ethanol for 15 min and drying at room temperature.[28] The electrospun NFs were subsequently weighed and homogenized in deionized water to obtain a suspension of short NFs, which was stored at 4°C for further use.

2.3. Synthesis of silk methacryloyl

Briefly, degummed silk was dissolved in LiBr and reacted at 60°C for an hour under constant stirring at 300 rpm. GMA (424 mM) was then added to the solution, and the mixture was stirred for an additional 3 h for the functionalization reaction between SF and GMA. The reaction mixture was transferred to a dialysis membrane (molecular weight cut-off: 12,000–14,000) and dialyzed against deionized water for 4 days. Finally, the dialyzed solution was freeze-dried to obtain SilMA for future use.[20]

2.4. Preparation of silk methacryloyl hydrogels with poly(ethylene oxide)-induced porosity and nanofiber reinforcement

The prepared silk NF membrane samples were homogenized to form short NF suspensions. SilMA powder, LAP powder (Aladdin, China), and the NF suspensions were thoroughly mixed and dissolved in the culture medium to prepare a final solution with concentrations of 30% w/v for SilMA, 0.25% w/v for LAP, and 1 and 2% w/v for NFs. This composite solution was used as the non-porous hydrogel precursor solution. PEO (molecular weight = 300,000) powder was dissolved separately in the culture medium to prepare a 1.6% w/v solution. The hydrogel precursor and PEO solutions were then mixed at a volume ratio of 2:1 to form a two-phase aqueous emulsion, which served as the porous hydrogel precursor solution. The porous hydrogel was prepared using UV light-induced cross-linking, followed by PEO precipitation through immersion. Regarding 3D bioprinting, the hydrogel structures were fabricated using a digital light processing (DLP) 3D bioprinter (ZJ-BP01, Zhongjian 3D Technology Co., China) equipped with a 405 nm UV light source (intensity: 20 mW/cm^2). The printer was integrated with a temperature-controlled vat (maintained at 4°C) to prevent premature gelation of the photopolymerizable hydrogel precursor. The detailed 3D printing parameters are shown in Table 1.

2.5. Characterization

2.5.1. Proton nuclear magnetic resonance and Fourier transform infrared spectroscopy

SF and SilMA were weighed and dissolved in 0.5 mL of deuterated dimethyl sulfoxide. The resulting solutions were transferred to a nuclear magnetic resonance (NMR) tube to determine proton NMR (1H-NMR). For Fourier Transform infrared spectroscopy (FTIR), SF, SilMA,

Table 1. Three-dimensional printing parameters

Project	Parameter
Digital model	
Low-temperature cylinder	Cell-laden poly(ethylene oxide)/ nanofiber/silk methacryloyl bio-ink
Print parameter	
Printing model	Lattice shape
Cube dimension	6.6 × 7.8 × 3.0 mm
Pattern filing	Cross-mesh
Strand spacing	0.6 mm
Layer height	0.6 μm
Number of layers	4
Temperature	25.0°C
Print parameter	
Layer thickness	0.02 mm
Base layer count	5
Base exposure time	30 s
Exposure time	8 s
Transition layer count	0
Transition type	Linear
Transition layer delay	0 s
Base lifting delay (before)	2 s
Base lifting delay (after)	0.5 s
Base retract delay	2 s
Lifting delay (before)	2 s
Cross-linking	Blue light (405 nm, 20 mW/cm^2)
Print platform	
Resolution	X:1920 pixels and Y: 1080 pixels

SilMA hydrogels, and soaked PEO/SilMA hydrogels were lyophilized and ground into powder. Each sample was mixed with a small amount of finely ground LiBr and exposed to infrared light for FTIR detection.

2.5.2 Morphology and porosity

A scanning electron microscope (SEM) (Model: GeminiSEM 300, ZEISS, Germany) was used to observe the internal structure of each group of hydrogels and the distribution of NFs (15 kV accelerating voltage). The SEM images were statistically analyzed using ImageJ software (version 1.51j8) for pore size and porosity of each group of hydrogel structures with and without microporous structures (n = 3). The pore size structures and PEO emulsion droplets in the hydrogels were directly observed using optical microscopy (DM6 B, Leica, Germany). The hydrogels were labeled with rhodamine-B, followed by hematoxylin and eosin (HE) staining. The microporous structures of the hydrogels were then observed with an orthostatic microscope (DM6 B, Leica, Germany).

2.5.2. Swelling properties

Hydrogel samples (diameter = 10 mm, height = 3 mm) were prepared, and their initial weights were recorded as M0. Each group of hydrogel samples was transferred into a 12-well plate, and 3 mL of PBS solution was added to each well. The plate was placed in a constant-temperature incubator at 37°C. The samples were removed at the predetermined time points (1, 3, 6, 9, 12, and 24 h), and excess surface moisture was quickly absorbed using highly absorbent filter paper. The samples were photographed, and the observations were recorded. The samples were weighed again, and the weights were recorded as M1. The swelling ratio of the hydrogel was calculated using the following formula in **Equation I**:

$$(M1-M0) / M0 \times 100\% \quad (I)$$

2.5.3. Mechanical test

The mechanical properties of each group of hydrogels were measured using a universal material compression machine (RIGOL, China). Cylindrical samples (diameter = 10 mm, height = 6 mm), prepared using silicon molds, and 3D-printed grid-like samples (described in **Section 2.4**) were subjected to uniaxial compression testing at a rate of 5 mm/min. Stress–strain curves/elastic modulus were obtained (n = 3). The compressive modulus was calculated as the slope of the linear elastic region within the 20–40% strain interval of the stress–strain curve. To evaluate the fatigue resistance of the 3D-printed scaffolds, cyclic compressive loading-unloading tests were conducted under 50% strain for 500 consecutive cycles at a rate of 5 mm/min, without intermittent recovery periods.

2.5.4. Rheological measurements

The light-curing properties of the gel precursors were evaluated through rheological analysis. Dynamic rheological experiments were conducted using a rotational rheometer (Anton Paar, Austria) equipped with a 25 mm measuring rotor to assess the rheological properties of the PEO/NF/SilMA composite hydrogels at 25°C. The gel point test was performed in time–scan oscillation mode under 10% strain, 1 Hz frequency, and a 0.5 mm gap, with UV illumination for 100 s. The gel point was determined as the intersection of the curves where the storage modulus (G′) surpassed the loss modulus (G″). For the amplitude scan, the G′ and G″ were measured by maintaining a constant frequency at 10 rad/s and varying strain values from 0.01 to 1%. For the frequency scan, G′ and G″ were measured

by keeping the shear strain constant at 1% and varying the frequency range from 0.158 to 25.1 rad/s.

2.6. Isolation and cultivation of rat articulator chondrocytes

The cartilage from the knee joints of 24-h old male Sprague Dawley rats (n = 4) (Laboratory Animal Center of Anhui Medical University (Hefei, Anhui Province, China) was extracted under sterile conditions. The cartilage slices were washed with PBS and then digested with 0.25% trypsin (BioFroxx, Germany) for 30 min, followed by three additional PBS washes. Subsequently, the slices were digested with 0.3% type II collagenase (MCE, United States) at 37°C for 4 h. The digested solution was filtered through a 70 μm cell strainer (BioSharp, China) to remove collagen impurities and then centrifuged at 1000 rpm for 5 min to collect articulator chondrocytes (ACs). The cells were cultured and expanded in Dulbecco's Modified Eagle Medium/F-12 complete medium at 37°C, 95% humidity, and 5% carbon dioxide. ACs from passages 2–3 were used for experiments. For the cell-laden 3D printing, the ACs were mixed into the bio-ink before printing. The cell-loaded hydrogels were immersed in a culture medium immediately following the 3D printing process.

2.7 *In vitro* cytocompatibility and cartilage formation

2.7.1. Live/dead cell staining

Hydrogels loaded with ACs (1×10^6 cells/mL) were prepared and incubated for 1 and 7 days to evaluate cell viability. Cell viability was assessed using a live/dead staining kit (Beyotime, China). The staining solution was prepared by diluting the dyes to a final concentration of 2.5 μM calcein acetoxymethyl ester and 1.25 μM propidium iodide. The AC-laden hydrogels were immersed in 400 μL of the diluted staining solution and incubated at 37°C for 30 min in the dark. The growth of ACs within the hydrogels was observed using a confocal microscope (ZEISS, Germany).

2.7.2. Quantification of DNA and glycosaminoglycan

For the quantitative measurement of DNA and glycosaminoglycan (GAG) content in hydrogels, AC-laden hydrogel samples were incubated for 7 and 14 days in Eppendorf tubes containing 1 mL of PBS, followed by homogenization using a homogenizer. Then, 2 μL of proteinase K solution (Ron, China) was added to the homogenized solution, and the mixture was incubated in a water bath at 56°C for 6 h. After centrifugation, the supernatant was collected. DNA content was determined using Hoechst 33258 dye (MCE, United States). The fluorescence intensity of each sample was measured using a microplate reader (PerkinElmer, United States) at an excitation wavelength of 360 nm and an emission wavelength of 460 nm. GAG content in the supernatant was quantified using the dimethylmethylene blue colorimetric method (n = 3).

2.7.3. Histological analyses

To assess the viability and distribution of ACs within the hydrogel during *in vitro* culture, hydrogel samples containing cells were cultured for 21 days. The samples were then fixed with 4% paraformaldehyde, embedded in paraffin, and sectioned at 5 μm. Sections were stained with HE, Safranin O, and Alcian Blue to evaluate the survival of ACs after 21 days of culture.

2.7.4. Real-time quantitative polymerase chain reaction

The expression levels of MKI67, collagen II (*COL2A1*), aggrecan (*ACAN*), and SRY-box transcription factor 9 (*SOX9*) genes in ACs were evaluated using real-time quantitative polymerase chain reaction (RT-qPCR) across different hydrogel groups. Total RNA was isolated from the cells using Trizol reagent, followed by reverse transcription to synthesize complementary DNA. RT-qPCR was conducted using TB Green Premix Ex Taq™ II FAST qPCR kit (Takara Bio, United States). Data was analyzed using the $2^{-\Delta\Delta CT}$ method to determine means and standard deviations. The primer sequences utilized in this study are detailed in Table S1. This experiment was repeated thrice, with each group having three replicate wells per repetition.

2.8. Formation of *in vivo* cartilage

2.8.1. Subcutaneous implantation of articulator chondrocyte-laden hydrogels in non-obese diabetic/severe combined immunodeficiency mice

Animal experiments were approved by the Animal Welfare Ethics Committee of the Anhui Provincial Center for Disease Control and Prevention (No.: 2024024). Porous and non-porous hydrogel precursors were prepared as described previously. ACs were mixed into the prepared hydrogel precursors at a concentration of 1×10^8 cells/mL, serving as the bio-ink. The bioprinting parameters are detailed in Table 1. During the bioprinting process, the photocrosslinkable bio-ink was cured under continuous UV light irradiation. After bioprinting, the cell-laden constructs were cultured in a complete medium for 7 days and then transplanted into both sides of the back of male non-obese diabetic/severe combined immunodeficiency mice (n = 4) to observe *in vivo* cartilage formation.

2.8.2. Histological and immunohistochemical staining

The specimens were collected and subjected to histological and immunohistochemical analyses. Briefly, the samples were fixed with 4% paraformaldehyde, embedded in

paraffin, and sectioned at 5 μm. The sections were stained with HE, Safranin O, and Alcian Blue, and immunohistochemically stained for collagen II (Col-II) and collagen I (Col-I). The positive area and average optical density values of Col-II and Col-I were statistically analyzed through Image J software (version 1.51j8).

2.9. Statistical analysis

All data were expressed as mean ± standard deviation. The data were analyzed using one-way analysis of variance with GraphPad Prism version 9.5.1, and $p < 0.05$ was considered statistically significant.

3. Results and discussion

3.1. Preparation of silk methacryloyl hydrogels and electrospun silk fibroin nanofibers

Figure 1A displays the ^{1}H-NMR spectra of the prepared SF and SilMA. Notably, the presence of vinyl methacrylate signals at δ = 6.2–6.0 parts per million (ppm) and δ = 5.8–5.6 ppm in the spectrum of SilMA, along with the methyl group signal at δ = 1.8 ppm and a gradual decrease in the lysine methylene signal at δ = 2.9 ppm, suggests that the lysine residues in SF underwent chemical modification. Additionally, a detectable signal at δ = 3.2–3.6 ppm was observed, which is attributed to hydrogen in the adjacent carbon–nitrogen bond. In the FTIR spectrum of SF, the characteristic β-sheet amide I, amide II, and amide III bands were identified. For SilMA, in addition to these β-sheet features, a weak absorption band at 1297 cm^{-1} was observed, corresponding to the CHOH group stretching from the alcohol group in GMA following the epoxy ring opening. Furthermore, a change at 1118 cm^{-1} was also detected, corresponding to methylene rocking vibrations of the vinyl methacrylate group in GMA (Figure 1B).[20] Collectively, FTIR and ^{1}H-NMR spectra demonstrated the successful extraction and methacrylation of SF. As demonstrated in Figure S1A, the SilMA solution containing LAP transitioned from a liquid to an immobile gel state under UV irradiation. Additionally, SEM images (Figure S1B) revealed that the electrospun SF NFs exhibited uniform, smooth morphology, and nanoscale diameters, confirming successful SF NF fabrication.

3.2. Preparation of nanofiber-enhanced porous silk methacryloyl hydrogels

The water-in-water emulsion principle, describing the phase separation that occurs when two hydrophilic polymer solutions are mixed under specific conditions, was applied in this study to create pores in the hydrogel. This phenomenon requires polymer concentrations to exceed a critical threshold (1.6% w/v for PEO was chosen based on previous studies), disrupting thermodynamic equilibrium and forming immiscible aqueous phases.[29] As shown in Figure 1C, both SilMA and PEO/SilMA groups exhibited acceptable 3D printing performances. The PEO/SilMA combination yielded translucent matte-white hydrogels, while NFs-incorporated groups exhibited opaque white coloration with significantly enhanced printability, consistent with previous findings.[30–32] While nanomaterials enhanced hydrogel formability and mechanical strength in 3D bioprinting, it was noticeable that excessive nanomaterial concentrations might compromise mechanical reinforcement. The sample with 3% NFs could not be formed during the 3D printing in this study. Regarding the concentration of PEO, initial trials using a 1:1 volumetric ratio of 2%NF/SilMA and PEO emulsion produced unprintable hydrogels (Figure S2). Therefore, a revised 2:1 mixing ratio was selected. To evaluate potential PEO residue in hydrogels after immersion-induced precipitation, SilMA and PEO/SilMA hydrogels soaked for 2 days were lyophilized and analyzed using FTIR spectroscopy (Figure 1B). The near-identical FTIR spectra of both hydrogel groups confirmed complete PEO removal after the 2-day immersion. This outcome establishes a biocompatible foundation for cell-laden hydrogel fabrication using PEO-based assembly.

3.3. Characterization of nanofiber-enhanced porous silk methacryloyl hydrogels

3.3.1. Morphology and porosity

Figure 2A schematically illustrates the internal structures of SilMA, PEO/SilMA, and PEO/NF/SilMA hydrogels. Optical microscopy revealed PEO emulsion droplets within the matrix to characterize the NF-enhanced porous hydrogels. Due to the reduced light transmittance in hydrogels after NF incorporation, SilMA, and PEO/SilMA hydrogels were selected for structural observation. As shown in Figure 2B, the SilMA group contained small droplets formed through self-cross-linking, while the PEO/SilMA group exhibited significantly larger near-spherical PEO emulsion droplets, confirming the pore-forming effect of PEO phase separation. The hydrogel microstructure was characterized using SEM, rhodamine B staining, and HE staining (Figure 2C). SEM images revealed a well-defined porous architecture in the PEO-incorporated groups, while only cross-linking-induced micropores were observed in non-porous counterparts. Although NFs were detectable as nanofillers, their incorporation did not compromise the microporous structure of SilMA hydrogels. In NF-containing groups, NFs were primarily localized within the hydrogel matrix and on pore walls, resulting in an increased surface roughness compared to NF-free samples. Notably, the 1%NF/SilMA and 2%NF/SilMA groups exhibited limited NF dispersion areas with visible aggregation and surface pits. With the introduction

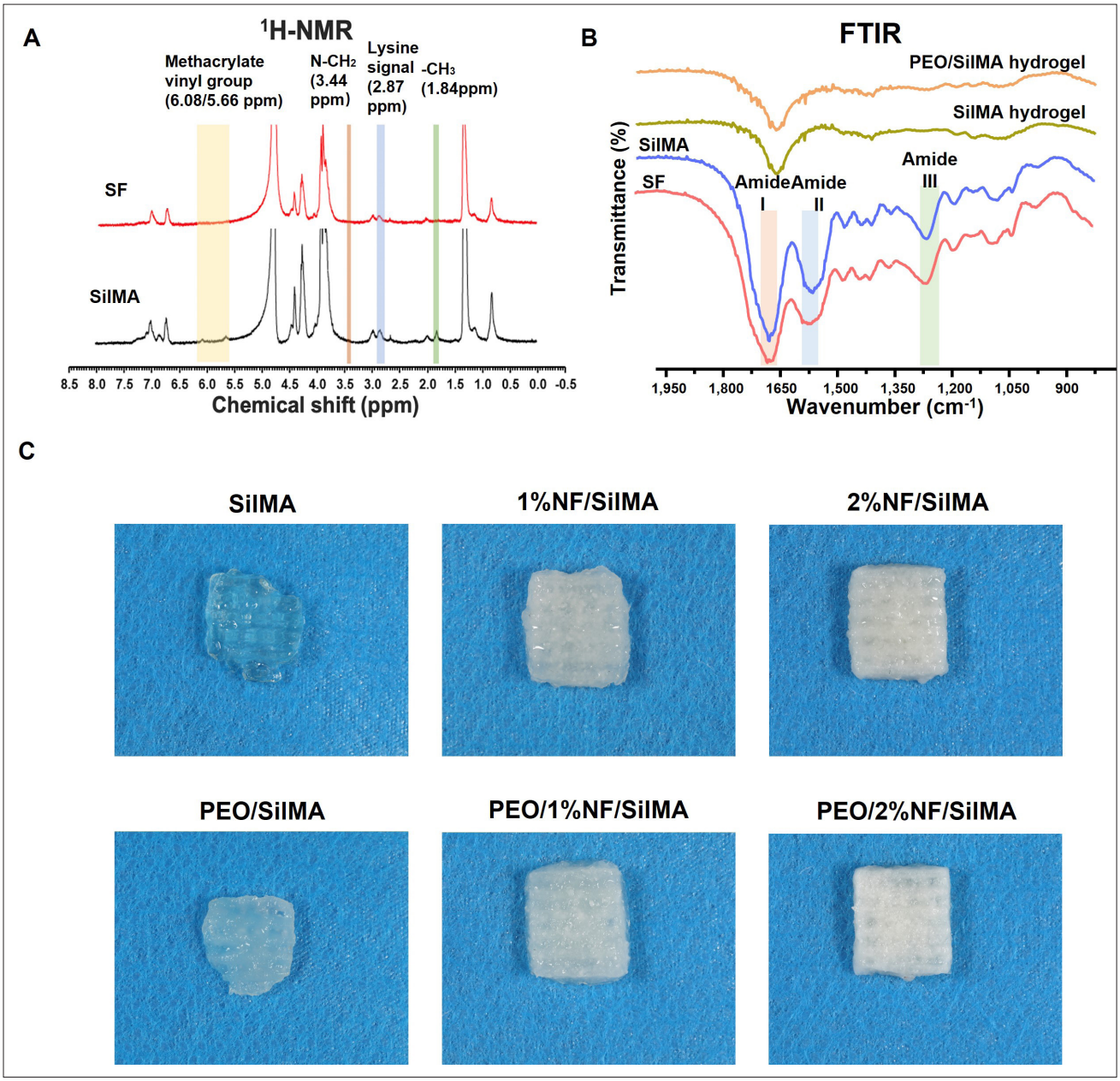

Figure 1. Preparation and characterization of SilMA-based hydrogels with NF-enhanced mechanics and PEO-induced porosity. (A) The 1H-NMR spectra of SF and SilMA. (B) FTIR spectra of SF, SilMA, freeze-dried SilMA hydrogels, and PEO/SilMA hydrogels after 2-day immersion in deionized water. (C) Photographs of three-dimensional-printed hydrogel scaffolds of SilMA, 1%NF/SilMA, 2%NF/SilMA, PEO/SilMA, PEO/1%NF/SilMA, and PEO/2%NF/SilMA. Abbreviations: 1H-NMR, proton nuclear magnetic resonance; FTIR, Fourier transform infrared spectroscopy; NF, nanofibers; PEO, poly(ethylene oxide); SEM, scanning electron microscopy; SF, silk fibroin; SilMA, silk methacryloyl.

of PEO, PEO/1%NF/SilMA and PEO/2%NF/SilMA groups showed improved NFs distribution uniformity compared to 1%NF/SilMA and 2%NF/SilMA groups. The PEO/1%NF/SilMA group achieved optimal NF dispersion within the hydrogel matrix and along pore walls, whereas minor NF aggregation persisted in the PEO/2%NF/SilMA group. This phenomenon might be due to the higher NF concentration per interfacial area exceeding optimal dispersion capacity,[33] whereas the 1% formulation maintains favorable spatial distribution under equivalent geometric constraints. Rhodamine B staining was achieved by conjugating the dye with the SilMA cross-linking network, enabling red fluorescence emission from the hydrogel matrix while the pores appeared dark. The

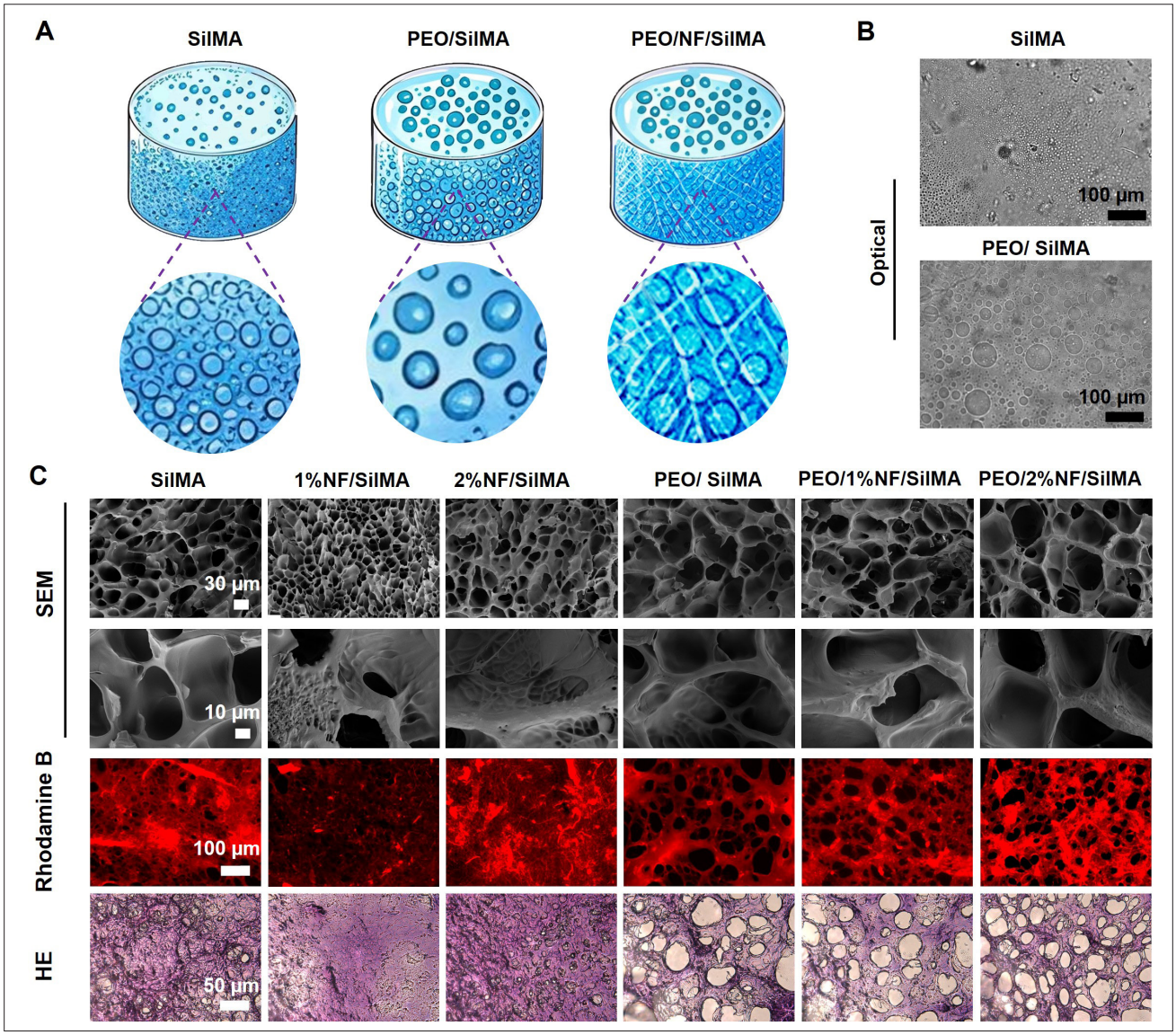

Figure 2. Morphology and porosity. (A) The schematic diagram illustrates the internal porosity of SilMA, PEO/SilMA, and PEO/NF/SilMA hydrogels. (B) Optical microscope images of SilMA and PEO/SilMA hydrogels. Scale bar: 100 μm; magnification: 10×. (C) SEM image, rhodamine-B staining (the hydrogel network coupled with rhodamine shows red fluorescence, and the pore structure shows a dark area), and HE staining images of the six groups of hydrogels. Scale bars: 10, 30, 50, and 100 μm; magnification: 1000×, 300×, 200×, 100×. Abbreviations: HE, hematoxylin and eosin; NF, nanofibers; PEO, poly(ethylene oxide); SEM, scanning electron microscopy; SilMA, silk methacryloyl.

results revealed significantly increased pore quantity and size in porous groups. NFs were observed as filamentous structures within the hydrogel matrix. HE staining further confirmed PEO-derived pores.

Quantitative analysis of pore size distribution and porosity was performed using ImageJ software on SEM images of six hydrogel groups (Figure 3A–F). The histograms demonstrated more centralized pore distributions in PEO/1%NF/SilMA and PEO/2%NF/SilMA compared to PEO/SilMA. This phenomenon suggests that incorporating short NFs may enhance emulsion droplet stability by reducing interfacial free energy at the phase boundaries.[34] SilMA had an average pore diameter of 20.07 ± 4.67 μm, consistent with previous literature,[20] while 1%NF/SilMA and 2%NF/SilMA groups exhibited average pore diameters of 17.25 ± 3.59 μm and 16.25 ± 3.59 μm, respectively. Incorporating NFs reduced the pore size of SilMA hydrogels, though no significant difference was observed between 1%NF/SilMA and

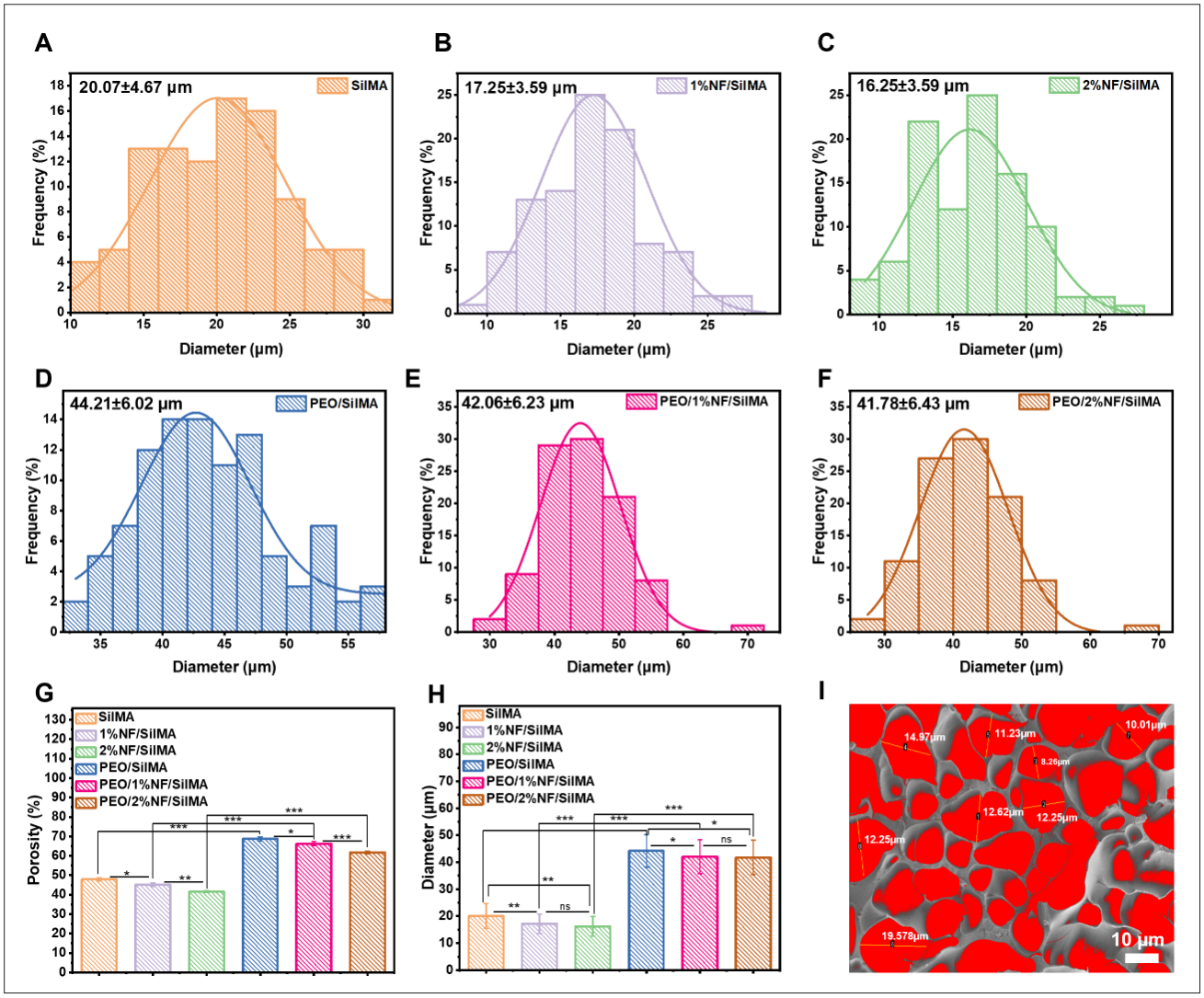

Figure 3. Quantitative analysis of pore distribution and pore size. (A–F) Pore diameter distribution in each group of samples, statistical analysis of 100 pores randomly selected from each group. (G) Average aperture statistics. (H) Porosity statistics. (I) Statistical method of pore diameter and pore area. Scale bar: 100 μm; magnification: 1000×. *Note*: Statistical significance at $*p < 0.05$, $**p < 0.01$, $***p < 0.001$. Abbreviations: NF, nanofibers; ns, non-significant; PEO, poly(ethylene oxide); SilMA, silk methacryloyl.

2%NF/SilMA. For PEO-incorporated groups, the average pore diameters increased to 44.2 ± 6.02 μm, 42.06 ± 6.23 μm, and 41.78 ± 6.23 μm for PEO/SilMA, PEO/1%NF/SilMA, and PEO/2%NF/SilMA, respectively, representing an approximate two-fold enlargement compared to non-porous counterparts. The statistical analysis of pore size and porosity of different groups of hydrogels is displayed in Figure 3G and H. It can be seen that incorporating PEO not only significantly increased the pore size in the samples but also enhanced their porosity (by approximately 50%). Previous articles have reported that a scaffold porosity of around 70% is required for sufficient cell infiltration and regeneration.[35,36] The porosity ranges between 60 and 70% in the groups with pores induced by PEO. This implies that PEO was highly necessary for the pore formation of 3D-printed SilMA hydrogel in this study. The increase in pore size and porosity of the hydrogel will facilitate the exchange of nutrients and oxygen for chondrocytes within the gel.[37,38]

However, the most suitable scaffold pore size for cartilage regeneration is approximately 150–250 μm.[21,39,40] Herein, 3D printing technology was adopted to create a microporous structure in the hydrogel, resulting in a dual-level structure that combines macropores and micropores. This structure is advantageous for promoting

cell proliferation, chondrogenesis, and angiogenesis. As shown in Figure S3, the spacing between the two strands of the PEO/SilMA group scaffold (612.6 ± 32.8 μm) closely matched the strand spacing and layer height set for 3D printing (600 μm). However, with the addition of NFs, the distance between the strands decreased. When 2% NF was added, the spacing between the strands was reduced to approximately 400 μm (378.9 ± 89.2 μm). This phenomenon may be due to: (i) the relatively large length of the NFs, causing the fibers located at the edges of the strands to be fixed at the mesh edges after the hydrogel was photocured, or (ii) the introduction of NFs led to a decrease in the fluidity of the printing bio-ink, reducing the printing accuracy. Although this large pore size did not reach the size recommended in the literature (about 200 μm),[41] a previous study has reported that scaffolds with a pore size of 400 μm could promote proteoglycan production and chondrogenic marker gene expression more effectively than those with smaller pore sizes of 200 and 100 μm.[42] While smaller macropores could be achieved by setting a smaller strand spacing or layer height to 400 μm before 3D printing, the possible unevenness or aggregation of NFs during preparation could reduce printing reproducibility. Therefore, a strand spacing of 600 μm was chosen for 3D printing in this study.

3.3.2. Swelling and mechanical properties

The swelling behavior of hydrogels was systematically evaluated to assess their hydrophilicity and structural stability—two critical determinants for nutrient diffusion and long-term functionality in cartilage regeneration. Macroscopic observation (Figure S4) revealed significant volumetric expansion in PEO-modified groups, with pore architectures maintained throughout the 24-h PBS immersion, contrasting with the non-porous controls. Quantitative swelling kinetics (Figure 4A) demonstrated a biphasic absorption pattern: rapid initial swelling (0–12 h, >80% equilibrium absorption) followed by gradual stabilization. Notably, PEO/SilMA and PEO/1%NF/SilMA groups exhibited prolonged swelling phases, achieving equilibrium swelling ratios of 170.1 ± 7.50% and 162.7 ± 2.76% at 24 h, respectively. This delayed equilibration might be attributed to the hierarchical pore structure (relative macroporosity from PEO leaching combined with inherent SilMA microporosity), which creates capillary-driven fluid transport pathways distinct from conventional homogeneous networks. Compared to a previous study that reported the swelling rate of only 6% for nanosilicate-reinforced SF hydrogel, measured using the same method,[43] the NF/SilMA/PEO hydrogels in this study had outstanding swelling behavior.

The regenerative capacity of the scaffold also fundamentally depends on its mechanical properties. These properties must be robust enough to withstand articulation and handling during implantation. Additionally, they should not be overly strong to the extent that they cause stress shielding of mechanosensitive cells.[44] In this study, to investigate the differences in the mechanical properties between grid-like hydrogels with macroporous structures fabricated via 3D printing and those without macropores, we also prepared cylindrical samples using molds and subjected them to compression testing. Figure 4B and C shows the compression test results of the cylindrical samples, while Figure 4D and E displays the mechanical properties of the 3D-printed grid-like samples. In general, the compressive strength of cylindrical samples was slightly higher than that of the corresponding 3D-printed samples. The compressive strength of the cylindrical SilMA hydrogels reached 1235.8 ± 172.1 kPa, while the strength of the grid-like samples was only 930.2 ± 85.6 kPa. Although the latter is slightly lower, this value was also close to the compressive strength of 3D-printed 30% SilMA hydrogel reported in previous studies.[20] Regarding the compressive modulus, the grid-like samples in each group exhibited better performance compared to the cylindrical samples. It is speculated that the cylindrical samples could transfer and disperse stress better, reducing local stress concentration and resulting in higher compressive strength. In the grid structure, stress tends to concentrate at the nodes, leading to earlier material failure. The reason for the larger compressive modulus of the grid structure could be attributed to the better force dispersion by the truss structure, causing less deformation of the scaffold. Notably, using PEO in the preparation of SilMA hydrogel significantly reduced its compressive strength and modulus. However, the addition of NFs could reverse this negative influence. The PEO/2%NF/SilMA group possessed similar mechanical properties to the SilMA group for both cylinder shape and grid-like structure. Specifically, the compressive modulus of the 3D-printed PEO/2%NF/SilMA (815.0 ± 73.1 kPa) had reached that of native cartilage (around 0.81 ± 0.56 MPa),[45] indicating the promising potential for cartilage repair applications. In addition, the strength of the hydrogel is not invariably augmented with an increase in the concentration of NFs. The 2%NF/SilMA exhibited obvious mechanical deterioration compared to SilMA and 1%NF/SilMA. This aligns with previous reports suggesting that excessive nanomaterial concentrations may compromise mechanical reinforcement.[32,33] This could also be explained by the percolation theory predictions—excessive NF loading induces aggregation, creating stress concentration points rather than continuous reinforcing networks. However, the 3D-printed PEO/2%NF/SilMA groups showed better mechanical properties than the

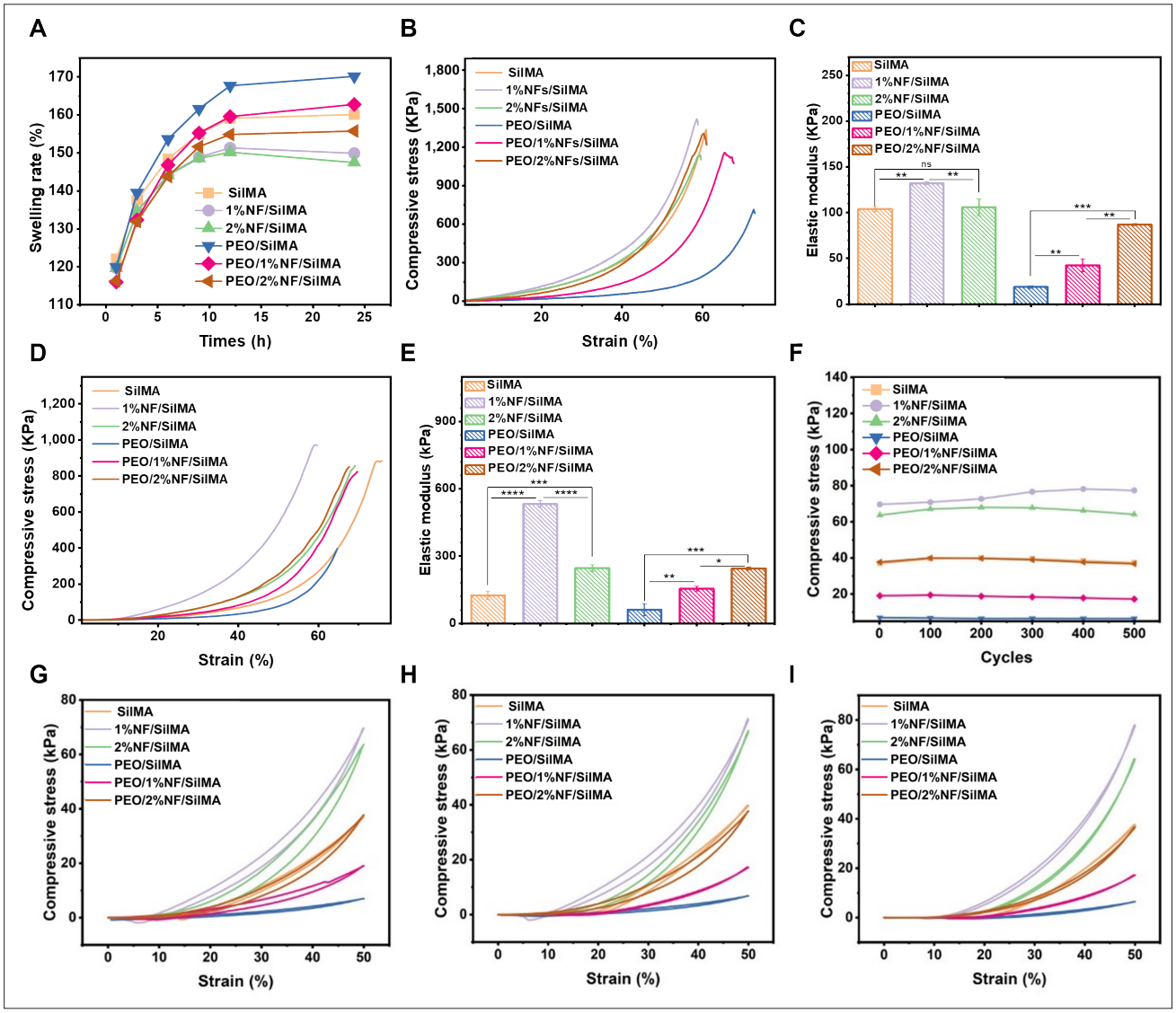

Figure 4. Swelling performance and mechanical properties. (A) Swelling kinetic profiles at different time points (1, 3, 6, 9, 12, and 24-h). (B and C) Stress–strain diagram and compression modulus of different cylindrical groups. (D and E) Stress–strain diagram and compression modulus of different three-dimensional-printed groups. (F) Compressive strength of each 3D-printed group at different cycles during the cyclic compressive loading testing. Stress–strain curves of each group at the (G) 1st, (H) 100th, and (I) 500th cycle, respectively. *Note*: Statistical significance at $^{*}p < 0.05$, $^{**}p < 0.01$, $^{***}p < 0.001$. Abbreviations: NF, nanofibers; PEO, poly(ethylene oxide); SilMA, silk methacryloyl .

3D-printed PEO/1%NF/SilMA groups. This result might be due to the reduction of uneven fiber aggregation caused by a relatively high concentration of NFs during the PEO-induced pore formation process.

As previous studies have shown, NFs, as gel fillers, could effectively enhance their fatigue resistance properties,[24] which is also crucial for cartilage scaffold materials that are subjected to stress. The results of cyclic compressive loading-unloading tests performed on 3D-printed grid-like samples (Figure 4F–I) demonstrated the positive effect of the introduction of NFs to the prepared hydrogels. The compressive strength of the hydrogels in each group did not significantly decrease after 500 compression cycles (Figure 4F), and they showed the same trend between groups (Figure 4D). In addition, by comparing the cyclic compression curves of the 1st, 100th, and 500th compression (Figure 4G–I), it can be observed that the area of the hysteresis loop of the hydrogel scaffolds in each group became smaller and more stable after repeated cyclic compressions. Figure S5 specifically shows the stress–strain curves of each group within 500 cycles of compression,

which further suggests that as the number of compressions increased, the structures, such as the polymer chains and cross-linking networks inside the hydrogel scaffolds, gradually became stable with reduced energy dissipation. It indicates that the material had a certain degree of self-adaptability and stability. When subjected to repeated loads, it was able to ensure that the mechanical properties were maintained and energy consumption was reduced, making it suitable for cartilage repair scenarios that involve bearing dynamic loads.

3.3.3. Rheological performance

The viscoelastic properties of hydrogels were rigorously characterized through oscillatory rheometry, providing critical insights into their structural integrity under dynamic loading. Strain sweep tests (Figure 5A–F) revealed that the storage modulus (G′) exceeded the loss modulus (G″) within the strain range of 0.01–1%, indicating solid-like behavior. The G′ and G″ curves of 1%NF/SilMA, PEO/1%NF/SilMA, and PEO/2%NF/SilMA remained parallel in this range, suggesting enhanced structural stability due to NF incorporation. However, the 2%NF/SilMA group exhibited a declining trend near 1% strain, indicating partial structural disruption. Frequency sweep tests (Figure 5G–K) showed minimal stress changes at low frequencies and significant changes at high frequencies. The increase in G′ for 1%NF/SilMA, PEO/1%NF/SilMA, and PEO/2%NF/SilMA groups confirmed improved hardness and stability with NFs. Conversely, the decrease in G′ for the 2%NF/SilMA indicated mechanical degradation. The rise in G″ in NF-containing groups suggested weak interfacial bonding between NFs and the hydrogel matrix, as well as suboptimal cross-linking, consistent with mechanical performance results.[20]

The UV-curable hydrogel underwent a rapid formation of its structural network within seconds under UV light, which was effectively monitored and characterized using rheological methods. A transition from G" > G' to G' > G" was observed, indicating a shift from viscosity-dominated to elasticity-dominated behavior in the hydrogel (Figures 5K and S6). The gelation times for different groups were summarized based on the crossover points in the local plots (Figure 5L). Notably, the gelation times of 1%NF/SilMA and 2%NF/SilMA groups showed no significant difference compared to the SilMA group, which suggested that the 30% SilMA hydrogel inherently possesses a densely crosslinked network, and the addition of NFs does not accelerate the gelation process. Jin et al.[46] have reported that excessive incorporation of nanomaterials may disrupt the curing system of hydrogels.[33,46] In the case of PEO/SilMA hydrogels, the extended gelation time is likely due to the dispersed cross-linking network caused by the presence of PEO emulsion.

3.4. *In vitro* study of cytocompatibility and cartilage tissue engineering

3.4.1. Live/dead cell staining

Compared to conventional 2D cell culture systems, 3D culture better replicates physiological microenvironments. Scaffold materials must simultaneously support long-term cell survival and actively promote cartilage regeneration.[47,48] We evaluated AC performance in hydrogels through viability and proliferation assays. Cell-laden hydrogels were cultured for 1 and 7 days, with viability assessed via live/dead staining. On Day 1, all groups showed sparse viable ACs (green fluorescence) with minimal dead cells (red fluorescence) (Figure 6A). Prolonged culture revealed significant cell population growth, confirming hydrogel biocompatibility for extended cultivation. The hydrogels with pores formed by PEO demonstrated higher AC density than the regular controls, indicating that PEO incorporation significantly enhanced proliferation, aligning with established literature.

3.4.2. DNA content and glycosaminoglycan deposition

The proliferation of ACs within the hydrogel scaffolds was further quantified through DNA quantification after 7- and 14-day cultures (Figure 6B). While all groups showed time-dependent increases, PEO-modified hydrogels consistently exhibited higher DNA content than their non-porous counterparts at both time points. These findings confirm that hydrogels with larger pore size and porosity produced by PEO create superior 3D microenvironments for AC proliferation.[22] GAG deposition serves as a key indicator of chondrocyte functionality.[49] Therefore, GAG secretion of AC in hydrogels was further measured (Figure 6C). Given that initial cell seeding density influences GAG quantification, we normalized GAG values to DNA content to eliminate inter-sample variability (Figure 6D). On Day 7, it can be seen that incorporating PEO enhanced cell proliferation and GAG production but adding NFs had no noticeable effect. This trend, induced by PEO modification, was intensified with prolonged culture on Day 14. At that time, the introduction of NFs also exhibited a significant positive effect on GAG deposition, especially for the 1% concentration. The enhanced performance of porous hydrogels might be attributed to PEO-induced porosity, which facilitates oxygen and nutrient transport.[50] Additionally, the exceptional GAG deposition observed in the PEO/1%NF/SilMA group could be attributed to the homogeneous distribution of NFs and larger pores within the hydrogel matrix, which modulated ACs' behavior at the microscale.

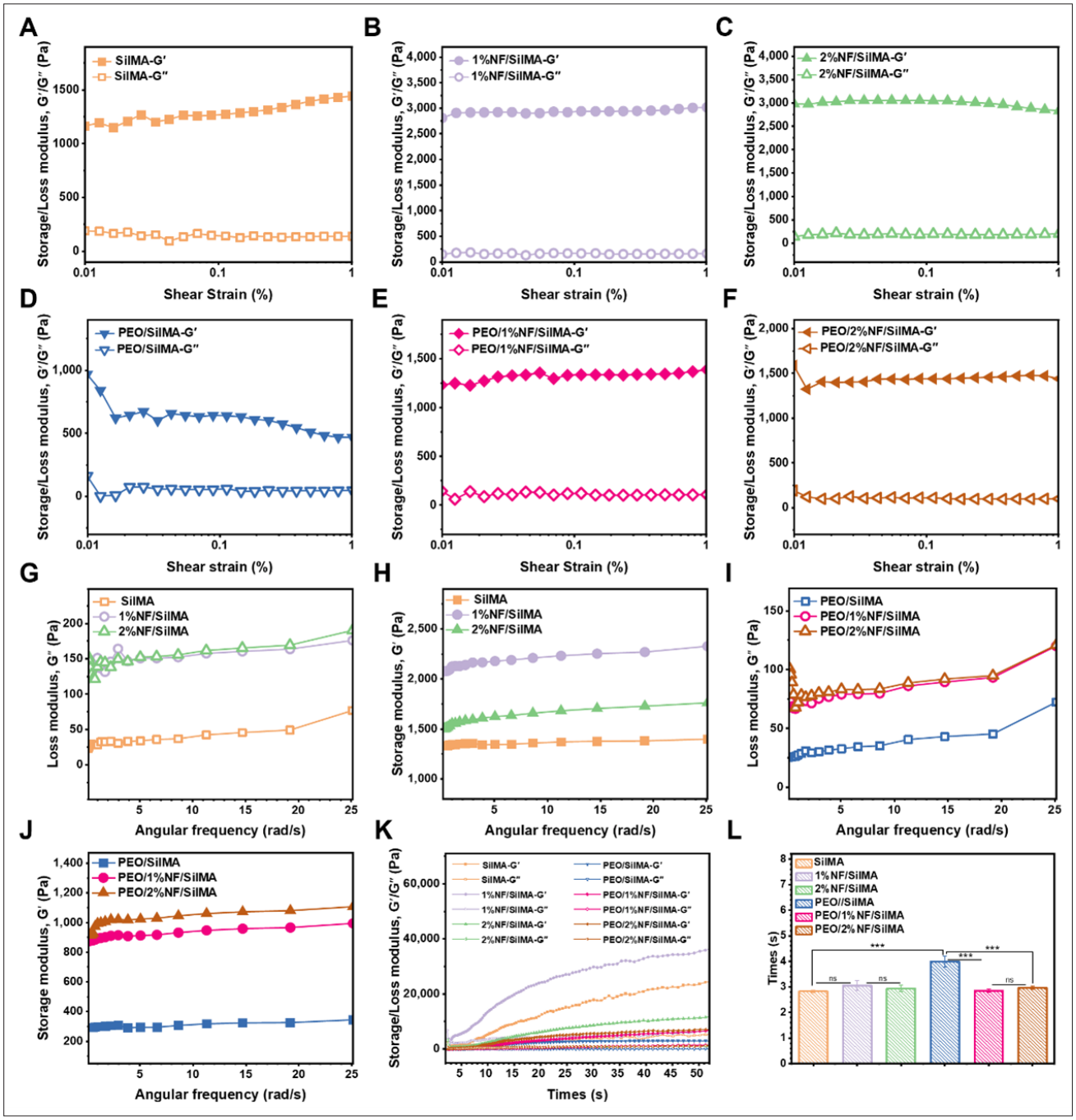

Figure 5. Rheological analysis of hydrogels. (A–F) The loss modulus (G") and storage mode (G') of each group of hydrogels depend on the change of amplitude scanning. (G–J) The G" and storage mode G' of each group depend on the change of frequency scanning. (K) UV time oscillation scan to observe the G" and storage mode G'. (L) The gel time point of each group of hydrogels according to the UV time oscillation scan. *Note*: Statistical significance at $^{*}p < 0.05$, $^{**}p < 0.01$, $^{***}p < 0.001$. Abbreviations: NF, nanofibers; ns, non-significant; PEO, poly(ethylene oxide); SilMA, silk methacryloyl; UV, ultraviolet.

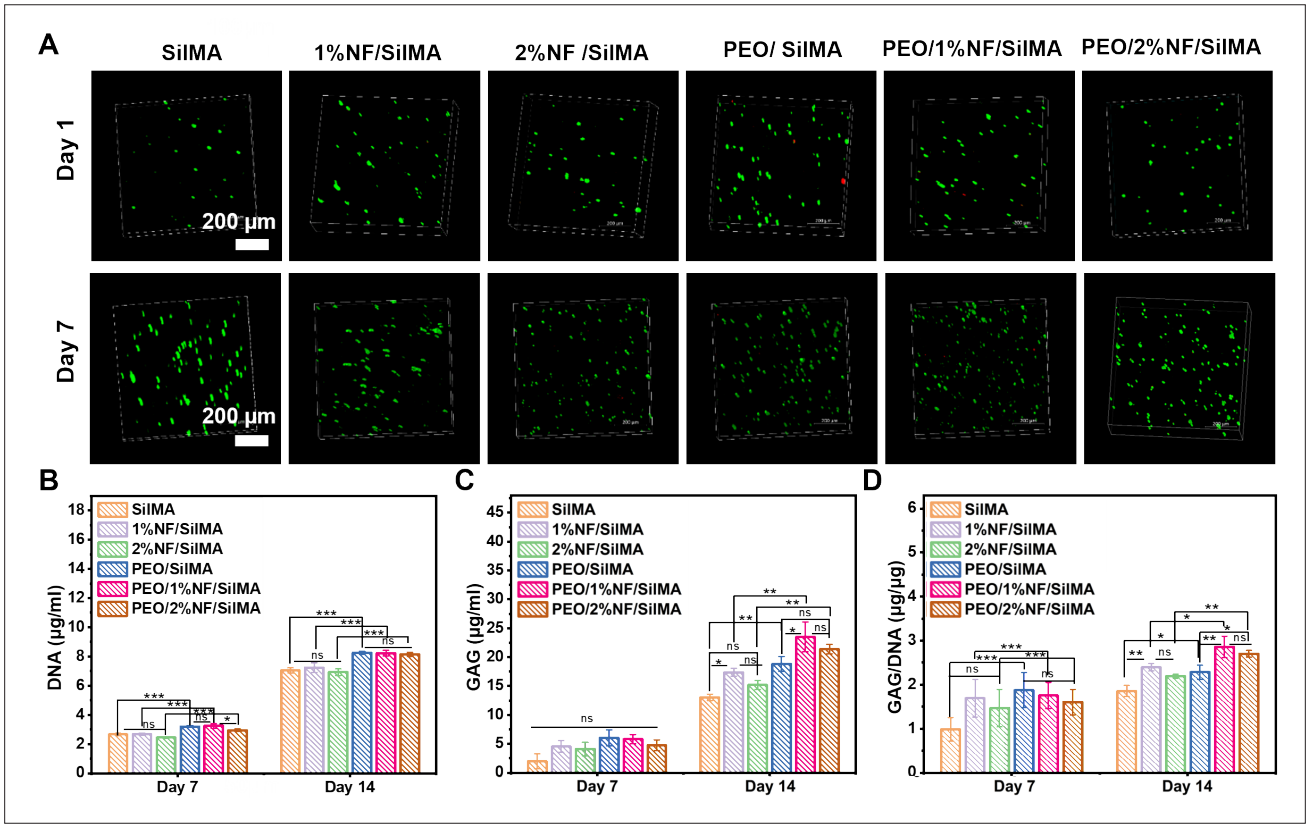

Figure 6. Cytocompatibility of the prepared hydrogel scaffolds. (A) Live/dead cell staining (green fluorescence indicates viable cells, and red fluorescence denotes dead cells). Scale bar: 200 μm; magnification: 100×. (B) DNA content. (C) GAG content. (D) GAG/DNA ratio. *Note*: Statistical significance at $^{*}p < 0.05$, $^{**}p < 0.01$, $^{***}p < 0.001$. Abbreviations: GAG, glycosaminoglycan; NF, nanofibers; ns, non-significant; PEO, poly(ethylene oxide); SilMA, silk methacryloyl.

3.4.3. Histological analysis and real-time quantitative polymerase chain rechain

Hydrogels cultured for 21 days were subjected to HE, Safranin O, and Alcian Blue staining for biocompatibility assessment. As shown in Figure 7A, ACs were distributed evenly in the hydrogels of each group and displayed relatively round morphology (HE). Safranin O (with its typical red color) and Alcian Blue densely stained the pericellular region and interterritorial matrix region, indicating a proteoglycan-rich matrix. By comparing the different groups, it was found that the number of cells in the groups modified by PEO was significantly higher. Moreover, more deposition of GAG was found in the ECM of NF-reinforced groups, especially for the PEO/1%NF/SilMA group. The results were consistent with DNA and GAG content quantification.

The RT-qPCR analysis revealed distinct gene expression profiles (Figure 7B). At Day 1, 1%NF/SilMA and 2%NF/SilMA showed comparable MKI67 (proliferation marker) levels to SilMA controls, while PEO/1%NF/SilMA and PEO/2%NF/SilMA displayed upregulated MKI67 gene expression. Compared to the groups without PEO addition, PEO-modified groups exhibited higher expression of the MKI67 gene. These results are in accordance with the live/dead staining and DNA quantification results. By Day 7, the expression of chondrogenesis-related genes was detected. The gene expression of *COL2A1*, *ACAN*, and *SOX9* decreased in non-porous NF-reinforced groups but increased significantly in PEO-modified groups. This could be due to high cell proliferation at Day 7, leading to a further decrease in the porosity and pore size of the scaffold structure. This reduction may have given rise to relatively limited nutrient transport and gas exchange within the hydrogel scaffolds, causing a decrease in the expression of chondrogenesis-related genes. However, the numerous pores induced by PEO improved this situation. The PEO/1%NF/SilMA group demonstrated the highest chondrogenic gene expression, consistent with high GAG production. SEM imaging (Figure 2C) revealed that the PEO/1%NF/SilMA hydrogels exhibited NF-attached pore walls with moderate surface roughness,

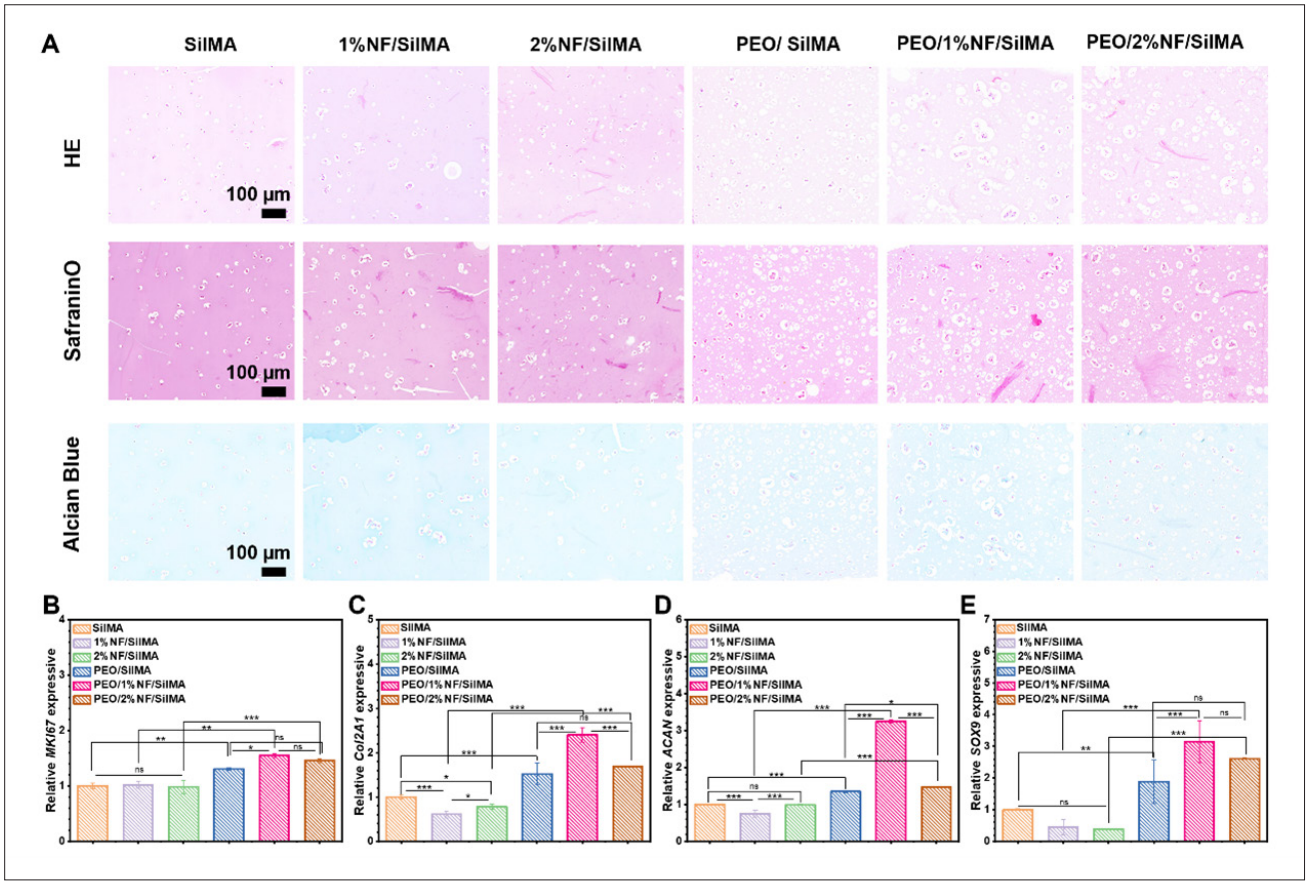

Figure 7. *In vitro* chondrogenesis effect. (A) The growth of internal cells and extracellular matrix deposition was observed by histological staining (HE, Safranin O, and Alcian Blue staining). Scale bar: 100 μm; magnification: 200×. Relative gene expression of (B) MKI67, (C) *COL2A1*, (D) *ACAN*, and (E) *SOX9* of articulator chondrocytes loaded in the prepared hydrogels. *Note*: Statistical significance at $^{*}p < 0.05$, $^{**}p < 0.01$, $^{***}p < 0.001$. Abbreviations: HE, hematoxylin and eosin; NF, nanofibers; ns, non-significant; PEO, poly(ethylene oxide); SilMA, silk methacryloyl.

which could enhance intercellular signaling and ECM secretion. In contrast, PEO/2%NF/SilMA showed irregular pits on partial pore walls due to NF aggregation, potentially impeding cell-cell communication. Previous studies demonstrated that optimized microtopographical features (e.g., wavy surfaces) significantly improved cell retention and matrix synthesis compared to flat/grooved surfaces.[51] The NF-reinforced porous groups demonstrated significantly upregulated gene expression.

3.5. Effect of *in vivo* cartilage formation

To investigate the *in vivo* cartilage formation effect of the prepared hydrogels, 3D-printed AC-laden hydrogels were implanted subcutaneously into non-obese diabetic/severe combined immunodeficiency mice, and the representative images of histological and histochemical staining are displayed in Figure 8. Compared to *in vitro* cultures, the result showed a more noticeable trend among the groups. HE staining revealed sparsely distributed cells in the SilMA, 1%NF/SilMA, and 2%NF/SilMA groups, whereas PEO-modified groups exhibited significantly increased porosity with AC clusters localized within the pores. There were large lacunae around the cells, embedded in the basophilic ECM (HE). Notably, the cartilage tissue regeneration performance of the SilMA, 1%NF/SilMA, and 2%NF/SilMA groups was similar to their *in vitro* culture result, possibly due to the limited porosity and smaller pore size. However, PEO-modified groups had visible cartilage formation in contrast with *in vitro* culture. The PEO/1%NF/SilMA group had the highest number of cells and cartilage-like structures, followed by the PEO/2%NF/SilMA and PEO/SilMA groups. Safranin O and Alcian Blue staining demonstrated positive ECM production in PEO-modified hydrogels. Col-II and Col-I immunohistochemical results correspond to the HE, Safranin O, and Alcian Blue findings. The PEO/1%NF/SilMA group exhibited increased Col-II deposition with concurrent higher Col-I accumulation than the PEO/2%NF/SilMA group.

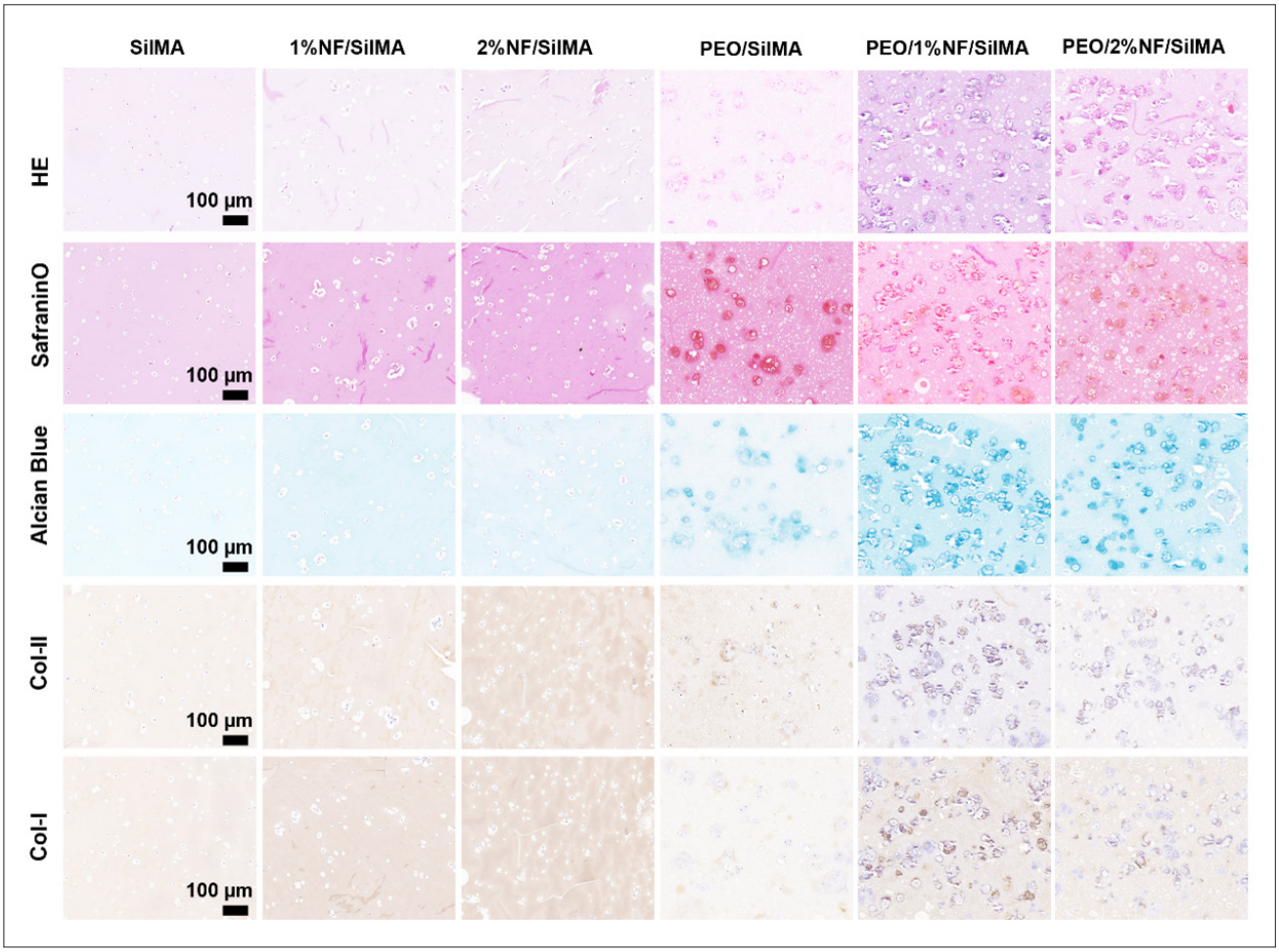

Figure 8. *In vivo* cartilage formation effect. Histological staining (HE, Safranin O, and Alcian Blue) and immunohistochemical staining images for Col-II and Col-I of each group. Scale bar: 100 μm; magnification: 200×. Abbreviations: Col I, collagen I; Col II, collagen II; HE, hematoxylin and eosin; NF, nanofibers; PEO, poly(ethylene oxide); SilMA, silk methacryloy.

As shown in Figure S7, the groups with PEO-induced porosity exhibited significantly higher Col-II and Col-I immunopositivity and average optical density compared to non-porous controls, especially for the PEO/1%NF/SilMA group. These observations coincided with the quantitative GAG measurements and chondrogenic gene expression analysis. However, due to the limitations of the animal model, these results were still unable to demonstrate which group had a better effect on cartilage formation under the weight-bearing environment. In addition, it is worth noting that the materials prepared in this study mainly contain only one type of bioactive substance, SF. This simplified composition offers a simpler system for future mechanistic studies.

4. Conclusion

This study successfully developed a dual-strategy approach for modifying 3D-printed SilMA hydrogels, combining PEO-induced porosity and NF reinforcement to enhance their cartilage tissue regeneration performance. The innovative water-in-water emulsification strategy created a porous architecture that significantly increased the average pore diameter (by over 100%) and overall porosity (75%), albeit with a significant reduction in mechanical properties. The incorporation of homogenized NFs effectively compensated for this mechanical deficit without substantially compromising porosity, while concurrently improving the 3D printability of SilMA/PEO hydrogels. Results demonstrated that the 3D printed grid-like PEO/2%NF/SilMA group had compressive strength and elastic modulus comparable to pure SilMA hydrogels but with enhanced biological functionality. Remarkably, the PEO/NF/SilMA hydrogels exhibited improved biocompatibility and marked upregulation of chondrogenic genes (*COL2A1*, *ACAN*, and *SOX9*), particularly in the PEO/1%NF/SilMA group. *In vivo* subcutaneous

implantation experiments also demonstrated the potential of SilMA/NF/PEO hydrogels in promoting cartilage tissue formation. Collectively, this novel dual-strategy approach provides a promising solution for reconciling the conflicting demands of porosity enhancement and mechanical reinforcement in cartilage tissue engineering scaffolds, achieving optimized structural and functional properties with significant potential for clinical translation.

Acknowledgments

The authors thank the Center for Scientific Research of Anhui Medical University for their valuable help in our experiment.

Funding

This research was funded by the National Natural Science Foundation of China (No. 82201034), and partially funded by Hefei Municipal Natural Science Foundation (No. 202348), Anhui Medical University Enhancement Program for Basic and Clinical Collaborative Research (No. 2022xkjT017), Anhui Provincial Institute of Translational Medicine Research Fund Project (No. 2021zhyx-C69), Anhui Medical University Graduate Research and Practice Innovation Program (No. YJS20230160).

Conflicts of interest

The authors declare they have no competing interests.

Author contributions

Conceptualization: Bingxue Xv, Xin An, Guomin Wu
Formal analysis: Bingxue Xv, Wenxin Meng, Ning Zhou
Investigation: Bingxue X,v Xin An,cYvmeng Luo
Methodology: Bingxue Xv, Guomin Wu
Writing – original draft: Bingxue Xv, Xin An
Writing – review & editing: Guomin Wu, Wenxin Meng, Ning Zhou, Yvmeng Luo

Ethics approval and consent to participate

Animal experiments were approved by the Animal Welfare Ethics Committee of the Anhui Provincial Center for Disease Control and Prevention (No.: 2024024).

Consent for publication

Not applicable.

Availability of data

All data generated or analyzed during this study are included in this published article and its supplementary information files.

References

1. Ferrari AJ, Santomauro DF, Aali A, Abate YH, Abbafati C, Murray CJL. Global incidence, prevalence, years lived with disability (YLDs), disability-adjusted life-years (DALYs), and healthy life expectancy (HALE) for 371 diseases and injuries in 204 countries and territories and 811 subnational locations, 1990–2021: a systematic analysis for the Global Burden of Disease Study 2021. *Lancet*. 2024;403(10440):2133-2161.
doi: 10.1016/s0140-6736(24)00757-8

2. Bayir E, Sahinler M, Celtikoglu MM, Sendemir A. Bioreactors in tissue engineering: mimicking the microenvironment. *Biomaterials for Organ and Tissue Regeneration*. Cambridge, UK: Elsevier. 2020:709-752.
doi: 10.1016/B978-0-08-102906-0.00018-0

3. Li Y, Li L, Li Y, Feng L, Wang B, Li G. Enhancing cartilage repair with optimized supramolecular hydrogel-based scaffold and pulsed electromagnetic field. *Bioact. Mater*. 2023;22:312-324.
doi: 10.1016/j.bioactmat.2022.10.010

4. Zhang Y, Liu X, Zeng L, Zhang J, Zuo J, Chen X. Polymer fiber scaffolds for bone and cartilage tissue engineering. *Adv Funct Mater*. 2019;29(36):1903279.
doi: 10.1002/adfm.201903279

5. Kundu, B., Rajkhowa, R., Kundu, S.C., Wang, X. Silk fibroin biomaterials for tissue regenerations. *Adv Drug Deliv Rev*. 2013;65(4):457-470.
doi: 10.1016/j.addr.2012.09.043

6. Huang K, Zhang Q-Y, Tan J, Nie R, Feng Z-Y, Xie H-Q. Accelerated cartilage regeneration through immunomodulation and enhanced chondrogenesis by an extracellular matrix hydrogel encapsulating kartogenin. *Chem Eng Jl*. 2024;497:154993.
doi: 10.1016/j.cej.2024.154993

7. Faber L, Yau A, Chen Y. Translational biomaterials of four-dimensional bioprinting for tissue regeneration. *Biofabrication*. 2023;16(1):012001.
doi: 10.1088/1758-5090/acfdd0

8. Zhang YS, Oklu R, Dokmeci MR, Khademhosseini A. Three-dimensional bioprinting strategies for tissue engineering. *Cold Spring Harb Perspect Med*. 2018;8(2):a025718.
doi: 10.1101/cshperspect.a025718

9. Li Q, Xu S, Feng Q, Dai Q, Yao L, Cao X. 3D printed silk-gelatin hydrogel scaffold with different porous structure and cell seeding strategy for cartilage regeneration. *Bioact. Mater*. 2021;6(10):3396-3410.
doi: 10.1016/j.bioactmat.2021.03.013

10. Khademhosseini A, Langer R. Microengineered hydrogels for tissue engineering. *Biomaterials*. 2007;28(34):5087-5092.
doi: 10.1016/j.biomaterials.2007.07.021

11. Gao C, Dai W, Wang X, Zhang L, Wang Y, Cai Q. Magnesium gradient-based hierarchical scaffold for dual-lineage

regeneration of osteochondral defect. *Adv Funct Mater*. 2023;33(43):2304829 .
doi: 10.1002/adfm.202304829

12. Annabi N, Nichol JW, Zhong X, et al. Controlling the porosity and microarchitecture of hydrogels for tissue engineering. *Tissue Eng Part B Rev*. 2010;16(4):371-383.
doi: 10.1089/ten.TEB.2009.0639

13. Santos MI, da Silva LCE, Bomediano MP, Catori DM, Gonçalves MC, de Oliveira MG. 3D printed nitric oxide-releasing poly(acrylic acid)/F127/cellulose nanocrystal hydrogels. *Soft Matter*. 2021;17(26):6352-6361.
doi: 10.1039/d1sm00163a

14. Shahbazi M, Jäger H, Huc-Mathis D, et al. Depletion flocculation of high internal phase pickering emulsion inks: a colloidal engineering approach to develop 3D printed porous scaffolds with tunable bioactive delivery. *ACS Appl Mater Interfaces*. 2024;16(33):43430-43450.
doi: 10.1021/acsami.4c11035

15. Li K, Shi Z, Meng Z. Study on the foam properties of peanut oil body (POB)-based oil-in-water-in-oil (O/W/O) foamed emulsion gel: the key role played by the interface between the water phase and the outer oil phase. *Food Chem*. 2025;464:141663.
doi: 10.1016/j.foodchem.2024.141663

16. Frith WJ. Mixed biopolymer aqueous solutions-phase behaviour and rheology. *Adv Colloid Interface Sci*. 2010;161(1-2):48-60.
doi: 10.1016/j.cis.2009.08.001

17. Ying GL, Jiang N, Maharjan S, Yin YX, Chai RR, Zhang YS. Aqueous two-phase emulsion bioink-enabled 3D bioprinting of porous hydrogels. *Adv Mater*. 2018;30(50):1805460.
doi: 10.1002/adma.201805460

18. Wang L-S, Du C, Toh WS, Wan ACA, Gao SJ, Kurisawa M. Modulation of chondrocyte functions and stiffness-dependent cartilage repair using an injectable enzymatically crosslinked hydrogel with tunable mechanical properties. *Biomaterials*. 2014;35(7):2207-2217.
doi: 10.1016/j.biomaterials.2013.11.070

19. Zhou Y, Liang K, Zhao S, Zhan C, Li J, Xiao P. Photopolymerized maleilated chitosan/methacrylated silk fibroin micro/nanocomposite hydrogels as potential scaffolds for cartilage tissue engineering. *Int J Biol Macromol*. 2018;108:383-390.
doi: 10.1016/j.ijbiomac.2017.12.032

20. Kim SH, Yeon YK, Lee JM, Chao JR, Lee Y, Park CH. Precisely printable and biocompatible silk fibroin bioink for digital light processing 3D printing. *Nat Commun*. 2018;9(1):1620.
doi: 10.1038/s41467-018-03759-y

21. Zhang Q, Lu H, Kawazoe N, Chen G. Pore size effect of collagen scaffolds on cartilage regeneration. *Acta Biomater*. 2014;10(5):2005-2013.
doi: 10.1016/j.actbio.2013.12.042

22. Ying G, Jiang N, Parra-Cantu C, Tang G, Zhang J, Zhang YS. Bioprinted injectable hierarchically porous gelatin methacryloyl hydrogel constructs with shape-memory properties. *Adv Funct Mater*. 2020;30(46):2003740.
doi: 10.1002/adfm.202003740

23. Wang C, Su Y, Xie J. Advances in electrospun nanofibers: versatile materials and diverse biomedical applications. *Acc Mater Res*. 2024;5(8):987-999.
doi: 10.1021/accountsmr.4c00145

24. Huang T, Zeng Y, Li C, Zhou Z, Xu J, Wang K. Application and development of electrospun nanofiber scaffolds for bone tissue engineering. *ACS Biomater Sci Eng*. 2024;10(7):4114-4144.
doi: 10.1021/acsbiomaterials.4c00028

25. Long M, Wu G, Tao F, Ma S, Dong X, Deng H. Nanofibrous textured silk aerogel with 3D channel arrays and adjustable mechanical properties for bone tissue regeneration. *Int J Biol Macromol*. 2024;278(Pt 2):134372.
doi: 10.1016/j.ijbiomac.2024.134372

26. Song Y, Shimanovich U, Michaels TCT, et al. Fabrication of fibrillosomes from droplets stabilized by protein nanofibrils at all-aqueous interfaces. *Nat Commun*. 2016;7(1):12934.
doi: 10.1038/ncomms12934

27. Rockwood DN, Preda RC, Yücel T, Wang X, Lovett ML, Kaplan DL. Materials fabrication from *Bombyx mori* silk fibroin. *Nat Protoc*. 2011;6(10):1612-1631.
doi: 10.1038/nprot.2011.379

28. Ma X, Wu G, Dai F, et al. Chitosan/polydopamine layer by layer self-assembled silk fibroin nanofibers for biomedical applications. *Carbohydr Polym*. 2021;251:117058.
doi: 10.1016/j.carbpol.2020.117058

29. Nicolai T, Murray B. Particle stabilized water in water emulsions. *Food Hydrocoll*. 2017;68:157-163.
doi: 10.1016/j.foodhyd.2016.08.036

30. Sawyer Mt, Eixenberger J, Nielson O, Manzi J, Francis C, Estrada D. Correlative imaging of three-dimensional cell culture on opaque bioscaffolds for tissue engineering applications. *ACS Appl Biomater*. 2023;6(9):3717-3725.
doi: 10.1021/acsabm.3c00408

31. Yoon J, Han H, Jan J. Nanomaterials-incorporated hydrogels for 3D bioprinting technology. *Nano Converg*. 2023;10(1):52.
doi: 10.1186/s40580-023-00402-5

32. Chang A, Babhadiashar N, Barrett-Catton E, Asuri P. Role of nanoparticle-polymer interactions on the development of double-network hydrogel nanocomposites with high mechanical strength. *Polymers*. 2020;12(2):470.
doi: 10.3390/polym12020470

33. Cheng Y, Cheng G, Xie C, Yin C, Dong X, Li Z. Biomimetic silk fibroin hydrogels strengthened by silica nanoparticles distributed nanofibers facilitate bone repair. *Adv Healthc Mater*. 2021;10(9):2001646.
doi: 10.1002/adhm.202001646

34. Lee J, Sultan M, Kim S, et al. Artificial auricular cartilage using silk fibroin and polyvinyl alcohol hydrogel. *Int J Mol Sci*. 2017;18(8):1707.
doi: 10.3390/ijms18081707

35. Karageorgiou V, Kaplan D. Porosity of 3D biomaterial scaffolds and osteogenesis. *Biomaterials*. 2005;26(27):5474-5491.
doi: 10.1016/j.biomaterials.2005.02.002

36. Lutzweiler G, Ndreu Halili A, Engin Vrana N. The overview of porous, bioactive scaffolds as instructive biomaterials for tissue regeneration and their clinical translation. *Pharmaceutics*. 2020;12(7):602.
doi: 10.3390/pharmaceutics12070602

37. Navaei A, Saini H, Christenson W, Sullivan RT, Ros R, Nikkhah M. Gold nanorod-incorporated gelatin-based conductive hydrogels for engineering cardiac tissue constructs. *Acta Biomater*. 2016;41:133-146.
doi: 10.1016/j.actbio.2016.05.027

38. Chen S, Lei T, Zhang Y, Wu H, He S, Liu Y. Nanofiber induced silk fibroin nanofiber/silk fibroin (SFNF/SF) fibrous scaffolds for 3D cell culture. *Fibers Polym*. 2023;24(2):433-444.
doi: 10.1007/s12221-023-00113-y

39. Wang C-C, Yan K-C, Lin K-H, Liu H-C, Lin F-H. A highly organized three-dimensional alginate scaffold for cartilage tissue engineering prepared by microfluidic technology. *Biomaterials*. 2011;32(29):7118-7126.
doi: 10.1016/j.biomaterials.2011.06.018

40. Jia L, Zhang Y, Yao L, Zhang P, Ci Z, Zhou G. Regeneration of human-ear-shaped cartilage with acellular cartilage matrix-based biomimetic scaffolds. *Appl Mater Today*. 2020;20:100639.
doi: 10.1016/j.apmt.2020.100639

41. O'Brien FJ, Harley BA, Yannas IV, Gibson LJ. The effect of pore size on cell adhesion in collagen-GAG scaffolds. *Biomaterials*. 2005;26(4):433-441.
doi: 10.1016/j.biomaterials.2004.02.052

42. Im GI, Ko JY, Lee JH. Chondrogenesis of adipose stem cells in a porous polymer scaffold: influence of the pore size. *Cell Transplant*. 2012;21(11):2397-2405.
doi: 10.3727/096368912X638865

43. Sheng R, Chen J, Wang H, Luo Y, Liu J, Zhang W. Nanosilicate-reinforced silk fibroin hydrogel for endogenous regeneration of both cartilage and subchondral bone. *Adv Healthc Mater*. 2022;11(17):e2200602.
doi: 10.1002/adhm.202200602

44. Braxton T, Lim K, Alcala-Orozco C, et al. Mechanical and physical characterization of a biphasic 3D printed silk-infilled scaffold for osteochondral tissue engineering. *ACS Biomater Sci Eng*. 2024;10(12):7606-7618.
doi: 10.1021/acsbiomaterials.4c01865

45. Li H, Li J, Yu S, Wu C, Zhan W. The mechanical properties of tibiofemoral and patellofemoral articular cartilage in compression depend on anatomical regions. *Sci Rep*. 2021;11(1):6128.
doi: 10.1038/s41598-021-85716-2

46. Jin R, Xu B, Guo D, et al. Advanced chemical modification technology of inorganic oxide nanoparticles in epoxy resin and mechanical properties of epoxy resin nanocomposites: a review. *Nano Mater Sci*. 2024;18(8);1707.
doi: 10.3390/ijms18081707

47. Shao C, Li Y, Chi J, Ye F, Zhao Y. Hierarchically inverse opal porous scaffolds from droplet microfluidics for biomimetic 3D cell co-culture. *Engineering*. 2021;7(12):1778-1785.
doi: 10.1016/j.eng.2020.06.031

48. Luo B, Wang S, Song X, Chen S, Qi Q, You Z. An encapsulation-free and hierarchical porous triboelectric scaffold with dynamic hydrophilicity for efficient cartilage regeneration. *Adv Mater*. 2024;36(27):2401009.
doi: 10.1002/adma.202401009

49. Chen Y, Mehmood K, Chang Y-F, Tang Z, Li Y, Zhang H. The molecular mechanisms of glycosaminoglycan biosynthesis regulating chondrogenesis and endochondral ossification. *Life Sci*. 2023;335:122243.
doi: 10.1016/j.lfs.2023.122243

50. Jia L, Hua Y, Zeng J, Liu W, Wang D, Jiang H. Bioprinting and regeneration of auricular cartilage using a bioactive bioink based on microporous photocrosslinkable acellular cartilage matrix. *Bioact Mater*. 2022;16:66-81.
doi: 10.1016/j.bioactmat.2022.02.032

51. Bettahalli NMS, Arkesteijn ITM, Wessling M, Poot AA, Stamatialis D. Corrugated round fibers to improve cell adhesion and proliferation in tissue engineering scaffolds. *Acta Biomater*. 2013;9(6):6928-6935.
doi: 10.1016/j.actbio.2013.02.029

ACCSCIENCE PUBLISHING

International Journal of Bioprinting

RESEARCH ARTICLE

Three-dimensional bioprinted silk fibroin–hydroxypropyl cellulose scaffold loaded with tendon stem/progenitor cells for the prevention of heterotopic ossification following Achilles tendon injury

Xianzong Ning[1,2], Rui Du[1], Minghao Zhang[1], Yutao Yang[1], Fei Yu[1], Xiaoming Xu[2], Baoyuan Meng[2], and Kai Yan[1]*

[1]Division of Sports Medicine and Adult Reconstructive Surgery, Department of Orthopedic Surgery, Nanjing Drum Tower Hospital, Affiliated Hospital of Medical School, Nanjing University, Nanjing, Jiangsu, China

[2]Division of Sports Medicine and Joint Surgery, Department of Orthopedic Surgery, Nanjing Pukou People's Hospital, Liangjiang Hospital, Southeast University, Nanjing, Jiangsu, China

Abstract

Achilles tendon injury is a common musculoskeletal disorder, particularly prevalent among athletes and middle-aged/elderly populations. Heterotopic ossification (HO) following Achilles tendon injury is a frequent complication that significantly compromises patients' quality of life and athletic performance. Conventional conservative treatments and surgical interventions for HO often yield suboptimal outcomes, failing to restore native tendon functionality. Tissue engineering strategies integrating biomaterials and cells offer promising solutions for tendon regeneration and functional recovery. Three-dimensional bioprinting presents unique advantages in fabricating tissue-engineered scaffolds through precise control of architectural geometry and internal microstructure. In this study, we developed a novel silk fibroin (SF)–hydroxypropyl cellulose (HPC)–tendon stem/progenitor cell (TSPC) bioink with exceptional cytocompatibility and rheological properties. This bioink demonstrated superior printability for fabricating porous Achilles tendon scaffolds with high mechanical strength (elastic modulus: 85 MPa), controlled biodegradability, and optimal porosity (91%). *In vitro* experiments revealed that SF– HPC–TSPCs scaffolds promoted TSPC survival, migration, proliferation, and tenogenic differentiation within the scaffold microenvironment. *In vivo* assessments demonstrated that the scaffolds exhibited excellent biocompatibility, elicited no systemic inflammatory or immune responses, and effectively prevented HO in rat models of Achilles tendon injury. This study establishes a groundbreaking approach for addressing post-traumatic HO in tendon regeneration.

Keywords: Achilles tendon injury; Heterotopic ossification; Silk fibroin; Three-dimensional bioprinting; Tissue-engineered scaffold

***Corresponding author:**
Kai Yan (yank1214@163.com)

Citation: Ning X, Du R, Zhang M, *et al.* Three-dimensional bioprinted silk fibroin–hydroxypropyl cellulose scaffold loaded with tendon stem/progenitor cells for the prevention of heterotopic ossification following Achilles tendon injury. *Int J Bioprint.* 2025;11(4):297-314. doi: 10.36922/IJB025210203

Received: May 19, 2025
Revised: June 3, 2025
Accepted: June 17, 2025
Published online: June 17, 2025

Copyright: © 2025 Author(s). This is an Open Access article distributed under the terms of the Creative Commons Attribution License, permitting distribution, and reproduction in any medium, provided the original work is properly cited.

Publisher's Note: AccScience Publishing remains neutral with regard to jurisdictional claims in published maps and institutional affiliations.

1. Introduction

Achilles tendon injury commonly manifests as tendinopathy, particularly in athletes and middle-aged/elderly populations. The high incidence of this injury is primarily associated with intensive physical activity, overuse, and age-related degenerative changes.[1] Post-injury clinical manifestations typically include pain, swelling, and restricted mobility, significantly impairing patients' quality of life and athletic performance.[2]

Heterotopic ossification (HO) following Achilles tendon injury refers to the pathological formation of ectopic bone within tendon tissues or adjacent soft tissues and is a frequent complication. Research indicates that HO in tendons often occurs after severe trauma or surgical intervention. For instance, HO incidence rates reach 54% following distal biceps tendon repair,[3] and 52.1% of patients develop HO after severe radial head fractures.[4] Furthermore, the prevalence of HO in the Achilles tendon increases with age—potentially due to upregulated bone morphogenetic protein (BMP) expression in tendon stem/progenitor cells (TSPCs).[5] The pathological progression of HO involves endochondral ossification, encompassing three distinct phases: the inflammatory stage, chondrogenesis, and terminal osteogenesis.[6] Although the precise mechanisms remain incompletely elucidated, HO development is closely linked to inflammatory responses, aberrant activation of osteogenic signaling pathways, and alterations in mechanical stress.[7–10] Emerging evidence suggests that the inflammatory cascade and hypoxic microenvironment during the acute phase of tendon injury may potentiate HO initiation.[11] Crucially, the BMP signaling pathway has been identified as a pivotal regulator of ectopic bone formation.[12] Age-dependent upregulation of BMP expression in injured tendons enhances the osteogenic differentiation capacity of TSPCs, thereby accelerating HO pathogenesis.[5] Furthermore, alterations in mechanical loading—whether excessive or insufficient—have been implicated as HO triggers, as demonstrated by load-dependent osteogenic induction in a preclinical model.[10]

Currently, there is no unified standard for treating HO following Achilles tendon injury. Common clinical approaches include conservative and surgical therapies. Conservative treatments primarily involve pharmacological interventions, such as non-steroidal anti-inflammatory drugs to reduce inflammation and inhibit HO progression, as well as physical therapy to promote healing by improving local blood circulation and enhancing tendon flexibility. However, these approaches show limited efficacy, especially in advanced ossification stages.[13] Surgical treatments focus on removing HO bone tissue and reconstructing tendon architecture. While effective in restoring tendon function, surgical procedures carry risks of post-operative complications such as infection and reinjury.[14,15] Traditional therapeutic strategies often prove inadequate for restoring the original biomechanical function of the Achilles tendon.[16]

Recent advancements in tissue engineering have opened new avenues for tendon repair. By combining scaffolds, cells, and growth factors, tissue engineering facilitates tendon regeneration and functional recovery. The selection of biomaterials is pivotal in designing tissue-engineered scaffolds. An ideal scaffold must exhibit excellent biocompatibility and mechanical properties to support cell adhesion and proliferation while maintaining sufficient mechanical strength to endure physiological loads.[17] Additionally, the scaffold's microstructure should closely resemble native tissue architecture to direct cell alignment and tissue regeneration.[18]

Three-dimensional (3D) bioprinting demonstrates significant advantages in the fabrication of tissue-engineered scaffolds.[19,20] First, this technology allows precise control over scaffold geometry and internal microstructure, enabling the design of personalized and complex architectures.[20] Second, 3D bioprinting enables the simultaneous deposition of cells and biomaterials, creating cell-laden scaffolds with biological activity, which is critical for promoting tissue regeneration.[21] Additionally, the mechanical properties and biological functions of scaffolds can be optimized by modulating printing parameters such as nozzle pressure and layer thickness.[22,23] Bioink formulation is central to 3D bioprinting, primarily composed of biomaterials and seed cells. The selection of biomaterials remains an active research area, with current options broadly classified into synthetic polymers and natural biomaterials. Natural biomaterials have attracted extensive scientific interest due to their superior biocompatibility and low cytotoxicity.[24,25] Xu et al.[26] constructed a poly(lactide-co-glycolide) (PLGA)/type I collage biphasic scaffold using 3D bioprinting technology, which effectively promoted tendon repair and inhibited HO, achieving an 86% reduction in heterotopic bone volume. However, fragments released during collagen degradation can act as potent initiators, activating inflammatory mechanisms that may interfere with the tissue repair process.[27] Moreover, the acidic degradation products of PLGA may alter the local pH, thereby inducing inflammatory responses and compromising biocompatibility.[28]

Silk fibroin (SF), a natural biomaterial, has attracted considerable interest due to its exceptional biocompatibility and tunable biodegradability.[29–31] In its native state, SF predominantly adopts a random coil conformation.[32] However, chemical modifications in hydroxyl-rich

environments can induce structural reorganization into ordered β-sheet configurations.[33] This conformational transition not only enhances SF's mechanical properties but also expands its biomedical applicability.[34] Hydroxypropyl cellulose (HPC), another biomaterial characterized by an abundance of hydroxyl groups, has been widely employed to optimize SF performance. The incorporation of HPC facilitates SF's structural transition from random coils to β-sheets, thereby improving mechanical robustness and structural stability.[35] Notably, HPC-mediated molecular interactions induce the formation of dual-network hydrogels through this conformational shift, resulting in superior mechanical strength and elasticity.[36] These SF–HPC composite hydrogels demonstrate significant potential for biomedical applications, particularly in leveraging their synergistic biocompatibility and controlled degradation profiles.

TSPCs, first identified in 2007,[37] are multi-potent cells capable of differentiating into tenocytes, chondrocytes, and osteoblasts, playing a pivotal role in tendon repair.[38] TSPCs address this challenge by undergoing tenogenic differentiation to promote collagen synthesis and extracellular matrix deposition, thereby facilitating functional tissue regeneration.[39] Furthermore, TSPCs enhance tendon healing through immunomodulatory effects, stimulation of tenocyte proliferation, and acceleration of collagen remodeling.[40] In tissue engineering, TSPCs are frequently integrated with biomaterial scaffolds to orchestrate neo-tendon formation. The combination of TSPCs with biocompatible scaffolds provides a biomimetic microenvironment that supports cell adhesion, migration, proliferation, and lineage-specific differentiation. For instance, decellularized tendon scaffolds functionalized with collagen have demonstrated efficacy in promoting TSPC proliferation and tenogenic commitment, ultimately enhancing the functional regeneration of damaged tendons.[40] This synergistic approach exhibits substantial potential for advancing tendon tissue engineering applications.

In summary, this study pioneers the development of a novel SF–HPC–TSPC bioink, formulated with SF as the matrix, HPC as a reinforcing agent, and TSPCs as the cellular component. We first characterized the rheological properties of this bioink and subsequently employed it for 3D bioprinting of tissue-engineered Achilles tendon scaffolds. The printed scaffolds were rigorously evaluated for mechanical properties, degradation behavior, and porous microstructure. *In vitro* investigations systematically assessed the scaffold's ability to regulate TSPC survival, migration, proliferation, and tenogenic differentiation. Furthermore, *in vivo* studies validated the scaffold's efficacy in preventing HO following Achilles tendon injury while concurrently evaluating systemic inflammatory and immune responses.

2. Materials and methods

2.1. Formulation of bioink

A total of 1.0 g SF, 1.0 g HPC, and TSPCs at a density of 5×10^6 cells/mL were added to 10 mL phosphate-buffered saline (PBS). The mixture was gently homogenized using a magnetic stir bar at 100 rpm for 10 min to avoid cellular damage. To identify the optimal bioink composition, cross-combinations of SF (0.5 g, 1.0 g, 1.5 g) and HPC (1.5 g, 1.0 g, 0.5 g) were systematically tested. The 1:1 SF–HPC ratio (1.0 g SF + 1.0 g HPC) demonstrated superior rheological properties and was selected for subsequent experiments. For the SF control bioink, 2.0 g SF and TSPCs (5×10^6 cells/mL) were dissolved in 10 mL PBS under identical mixing conditions. During the experimental process, we observed that the viscosity of the SF–HPC bioink was proportional to the concentration of HPC. However, when bioink with an SF–HPC ratio of 1.5:0.5 was used for 3D printing, the viscosity was too low to prevent scaffold collapse. Conversely, bioink with an SF–HPC ratio of 0.5:1.5 tended to cause nozzle clogging during 3D printing. Therefore, a 1:1 SF–HPC ratio was determined to be the optimal formulation. TSPCs (No. CP-R165) used in the experiments were purchased from Procell Life Science & Technology Co., Ltd (China). Experiments were conducted using cells at passages 2–3, as this stage is considered optimal for maintaining cellular functionality.

2.2. Rheological characterization of bioink

The rheological properties of the bioinks were analyzed using a modular advanced rheometer system (Thermo, USA). Dynamic viscosity was measured under shear rate sweeps from 0.1 to 100 s^{-1} at 37°C. Frequency-dependent storage modulus (G') and loss modulus (G") were determined through dynamic frequency sweep tests conducted over 30 min at 37°C.

2.3. Three-dimensional bioprinting of tissue-engineered Achilles tendon scaffolds

The SF–HPC–TSPCs bioink formulated in **Section 2.1** was employed to fabricate tissue-engineered Achilles tendon scaffolds using a multi-nozzle 3D bioprinter (Discovery, Switzerland). A computer-aided design model of the scaffold structure was first created, followed by loading the bioink into the pressure-assisted nozzle cartridge of the bioprinter. Printing parameters were set to a nozzle pressure of 0.25 mPa and a deposition speed of 1.0 mm/s. Scaffolds with final dimensions of 2 × 3 × 15 mm (width × height × length) were bioprinted onto sterile petri dishes under controlled environmental conditions (25°C; 60% relative humidity).

2.4. Mechanical testing of tissue-engineered Achilles tendon scaffolds

Scaffolds were centrally positioned on a testing fixture and subjected to uniaxial tensile loading at a constant rate of 1.0 mm/min using a universal mechanical testing machine (Instron, USA). Pressure was applied until scaffold rupture occurred, with mechanical parameters (stress, strain) automatically recorded. Elastic modulus was calculated from the linear elastic region of the stress-strain curves. Additionally, cyclic tensile testing was performed on both SF and SF–HPC scaffolds. Data visualization and analysis were performed using GraphPad Prism 9.0 (GraphPad, USA) and Origin Pro 2023 software (Origin Lab, USA).

2.5. Degradation assessment of scaffolds

For *in vitro* degradation, scaffolds were incubated in PBS containing 0.1 U/mL proteinase XIV or enzyme-free PBS at 37°C. Specimens were retrieved on days 0, 2, 4, 8, and 16, followed by gravimetric analysis to calculate degradation rates. For *in vivo* degradation, scaffolds were subcutaneously implanted into nude mice (BALB/c-nu; male' 6 weeks old; obtained from Weitong Lihua Limited Company (China); n = 24) under sodium pentobarbital anesthesia (50 mg/kg, intramuscular). Animals were sacrificed at predetermined intervals (0, 2, 4, 8, and 16 days) for scaffold retrieval and degradation rate calculation using the same gravimetric protocol.

2.6. Scanning electron microscopy analysis of scaffold microarchitecture

Scaffolds were imaged using a scanning electron microscope (SEM; Hitachi, Japan). Prior to imaging, scaffolds were pre-cooled at −20°C for 4 h, transferred to −80°C for 15 min, and lyophilized in a pre-chilled freeze dryer for 12 h. Specimens were sectioned, mounted on SEM stubs, and sputter-coated with 10 nm gold/palladium (Quorum, UK) to enhance conductivity. Microstructural images were acquired at an accelerating voltage of 5 kV. Porosity and pore size distribution were quantified from SEM images using ImageJ (NIH, USA).

2.7. Live/dead cell staining

TSPC-seeded scaffolds were cultured for 72 h in Dulbecco's modified eagle medium/nutrient mixture F12 medium supplemented with 10% fetal bovine serum. Cells were stained using a viability/cytotoxicity kit (Thermo, USA) containing 4 μM calcein-acetoxymethyl (live cells; green) and 2 μM ethidium homodimer-1 (EthD-1; dead cells; red) for 30 min at 37°C. Fluorescent images were captured with a confocal microscope (Leica, Germany) at 488 nm/530 nm (calcein) and 552 nm/617 nm (EthD-1) excitation/emission. Cell viability was calculated as (live cells/total cells) × 100 using ImageJ with the Cell Counter plugin.

2.8. Transwell migration assay

To evaluate the migratory capacity of TSPCs in SF and SF–HPC scaffolds, a Transwell migration assay was conducted. SF and SF–HPC scaffolds containing 1×10^5 cells were placed in the upper chamber of Transwell inserts (Corning, USA) with serum-free medium. The lower chamber was filled with 500 μL complete medium containing 10% fetal bovine serum. After 36 h incubation, scaffolds were removed, and non-migrated cells on the upper membrane surface were carefully wiped off. Migrated cells on the lower membrane were fixed with 4% paraformaldehyde and stained with 0.5% crystal violet. Three random fields per insert were imaged under an inverted microscope (Nikon, Japan), and migrated cells were quantified using ImageJ with the Cell Counter plugin.

2.9. Scratch wound healing assay

TSPCs were harvested from SF and SF–HPC scaffolds and seeded into six-well plates until 80–90% confluency. A uniform scratch wound was created using a sterile 200 μL pipette tip. Wound closure was monitored at 0, 12, 24, and 36 h under phase-contrast microscopy (Leica, Germany). Wound width was measured at three predefined positions per well using ImageJ.

2.10. Cell Counting Kit-8 proliferation assay

TSPCs (1×10^3 cells/well), harvested from scaffolds, were seeded into 96-well plates (Corning, US) in triplicate. Cell proliferation was assessed at 12, 24, and 72 h using a Cell Counting Kit-8 (CCK-8; Dojindo, Japan). After 4 h of incubation with CCK-8 reagent at 37°C, absorbance at 450 nm was measured using a microplate reader (Thermo, USA).

2.11. Quantitative reverse transcription polymerase chain reaction

TSPC-laden scaffolds were cultured for 2 and 4 weeks. Total RNA was extracted using TRIzol reagent (Thermo, USA) following scaffold homogenization. After centrifugation (10,000 rpm; 10 min; 4°C), RNA was reverse-transcribed into cDNA using the SuperScript IV First-Strand Synthesis System (Thermo, USA). Quantitative reverse transcription polymerase chain reaction (PCR) was performed on a QuantStudio 5 System (Thermo, USA) using PowerUp SYBR Green Master Mix. Gene expression of tenogenic (scleraxis [*Scx*]), chondrogenic (SRY-box transcription factor 9 [*Sox9*]), and osteogenic (bone morphogenetic protein 2 [*Bmp2*]) markers was normalized to glyceraldehyde 3-phosphate dehydrogenase.

2.12. Achilles tendon transection repair and scaffold implantation in rats

Male Sprague–Dawley rats (**aged 4–6 weeks;** obtained from Weitong Lihua Limited Company (China); n = 36)

were anesthetized with 3% sodium pentobarbital (0.8 mL/kg; intravenous). The skin and subcutaneous tissue of the hind paw heel were incised layer by layer to expose the Achilles tendon, which was then transected at its midportion using a scalpel. In the control group, the severed tendons were repaired directly with 4-0 absorbable sutures using a modified Kessler technique. The subcutaneous tissue and skin were subsequently closed in layers with 3-0 absorbable sutures. In the scaffold group, appropriately sized scaffolds were sutured to the tendon stumps with 4-0 absorbable sutures prior to the layered closure of subcutaneous tissue and skin with 3-0 absorbable sutures. This animal experiment was approved by the Ethics Committee of Drum Tower Hospital, School of Medicine, Nanjing University (No. 2021AE01031).

2.13. Micro-computed tomography imaging for heterotopic ossification quantification

Micro-computed tomography (CT) scanning (Skyscan, Belgium) was performed on control, SF, and SF–HPC groups at 2, 4, and 8 weeks post-Achilles tendon transection to quantify HO volume. Scan parameters included a 65 kV source voltage, 300 μA current, and 18 μm isotropic voxel size. Raw data were reconstructed using Mimics Research 20.0 (Materialise, Belgium), and HO volumes were segmented and calculated in Magics 25.0 (Materialise, Belgium) using a fixed Hounsfield unit threshold (800–3000).

2.14. Histological analysis

Tendon specimens harvested at 8 weeks were fixed in 4% paraformaldehyde for 72 h, decalcified in 15% EDTA with daily solution renewal, and paraffin-embedded. Sections (5 μm thick) were stained as follows: hematoxylin and eosin (H&E) for general tissue morphology; Safranin O for proteoglycan/cartilage matrix visualization; and BMP-2 immunohistochemistry (IHC) using an anti-BMP-2 primary antibody (ab214821; Abcam, UK) and 3,3'-diaminobenzidine chromogen.

2.15. Hematological profiling

Systemic inflammatory and immune responses were assessed via complete blood count analysis (Sysmex, Japan) at days 3, 7, and 14 post-implantation. Key parameters included: leukocyte count (white blood cell [WBC]; $\times 10^9$/L), erythrocyte count (red blood cell; $\times 10^{12}$/L), neutrophil count ($\times 10^9$/L), neutrophil percentage, lymphocyte count ($\times 10^9$/L), lymphocyte percentage, monocyte count ($\times 10^9$/L), monocyte percentage, interleukin-6 concentration (IL-6), and tumor necrosis factor-α concentration (TNF-α).

2.16. Statistical analysis

All data are expressed as mean ± standard deviation. Intergroup comparisons were analyzed using a one-way analysis of variance with Tukey's post-hoc test (for ≥3 groups) or unpaired Student's *t*-test (for two groups) using GraphPad Prism 9.0. Significance thresholds were defined as: $^*p < 0.05$, $^{**}p < 0.01$, $^{***}p < 0.001$, $^{****}p < 0.0001$.

3. Results and discussion

3.1. Rheological properties of bioinks

To evaluate the rheological properties of SF and SF–HPC bioinks, steady-state shear tests and dynamic oscillatory tests were performed. The shear rate–viscosity curve (Figure 1A) demonstrated that the viscosities of both SF

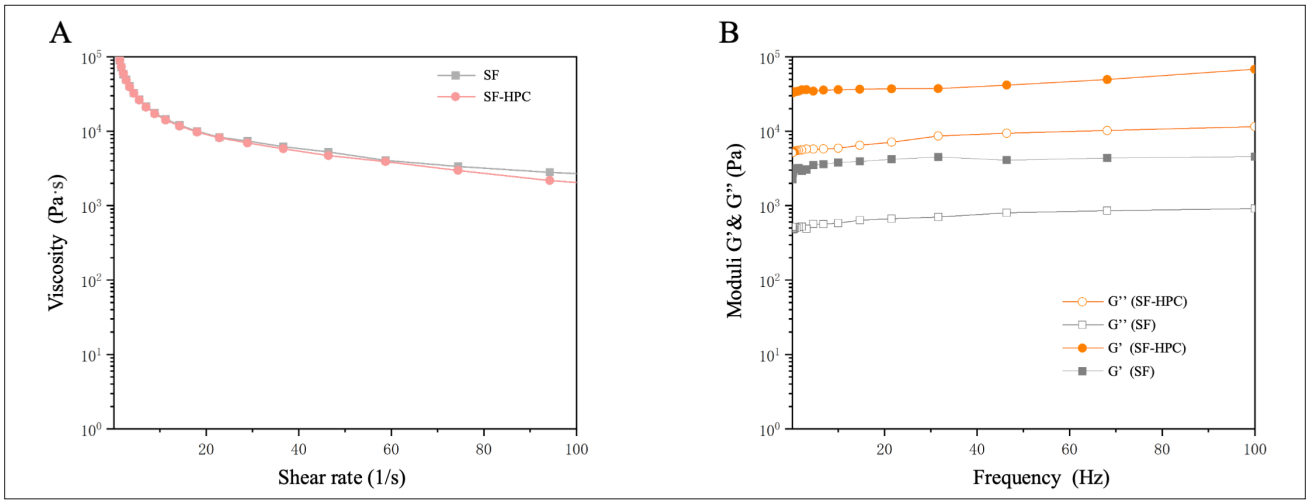

Figure 1. Rheological characterization of SF and SF–HPC bioinks. (A) Shear rate-dependent viscosity curves. (B) Frequency-dependent storage modulus (G') and loss modulus (G"). Abbreviations: HPC, hydroxypropyl cellulose; SF, silk fibroin.

and SF–HPC bioinks gradually decreased with increasing shear rate, indicating favorable shear-thinning behavior. Shear-thinning capability is one of the core requirements for extrusion-based 3D bioprinting.[41] At the high shear rate near the printer nozzle, viscosity decreased significantly, enabling the bioinks to pass through the micro-nozzle with low resistance, thereby preventing nozzle clogging due to high viscosity. Upon exiting the nozzle, the shear rate abruptly dropped, and viscosity rapidly recovered, enhancing scaffold shape stability and preventing structural collapse or deformation. Equally important, when using cell-laden bioinks for 3D printing, shear-thinning properties enable smooth extrusion under lower printing pressure, reducing cell membranes or extracellular matrix damage caused by high shear stress and improving cell viability.[42] Following extrusion, rapid viscosity recovery immobilizes cells, preventing gravity or flow-induced migration during the molding stage and ensuring uniform cell distribution within the printed structure.

The frequency–modulus curve (Figure 1B) showed that the G' and G" of both SF and SF–HPC bioinks remained relatively stable with increasing frequency. Notably, the G' of both bioinks exceeded their respective G", indicating that both formulations exhibited stable gel-like behavior. Furthermore, the G' of SF–HPC bioinks was higher than that of SF bioinks, suggesting that the incorporation of HPC into SF enhanced cross-linking and promoted a more stable network within the bioink. In conclusion, excellent rheological properties are crucial for successful extrusion-based 3D bioprinting, as they directly affect the bioinks' extrusion controllability, structural fidelity, cell viability, and ultimately the functionality of engineered tissues.[43]

3.2. Three-dimensional bioprinting of tissue-engineered Achilles tendon scaffolds and bending tests

Extrusion-based 3D bioprinting was employed to fabricate tissue-engineered Achilles tendon scaffolds with dimensions of 2 mm × 3 mm × 15 mm (Figure 2A–C). During the printing process, the bioink extruded smoothly from the nozzle without clogging. The printed scaffolds maintained structural integrity with no observable deformation or collapse, demonstrating excellent printing fidelity. Bending tests revealed that the scaffolds could be bent to 180° without fracture and fully recovered to their original shape after unloading (Figure 2D1–D3). SF–HPC scaffolds showed no fracture during bending, indicating superior toughness and ductility. Complete shape recovery after bending further confirmed their appropriate elastic modulus. Previous studies have demonstrated that scaffold toughness, ductility, and elastic modulus are critical factors for tendon injury repair.[44] Specifically, the Achilles tendon undergoes significant tension during physical activities

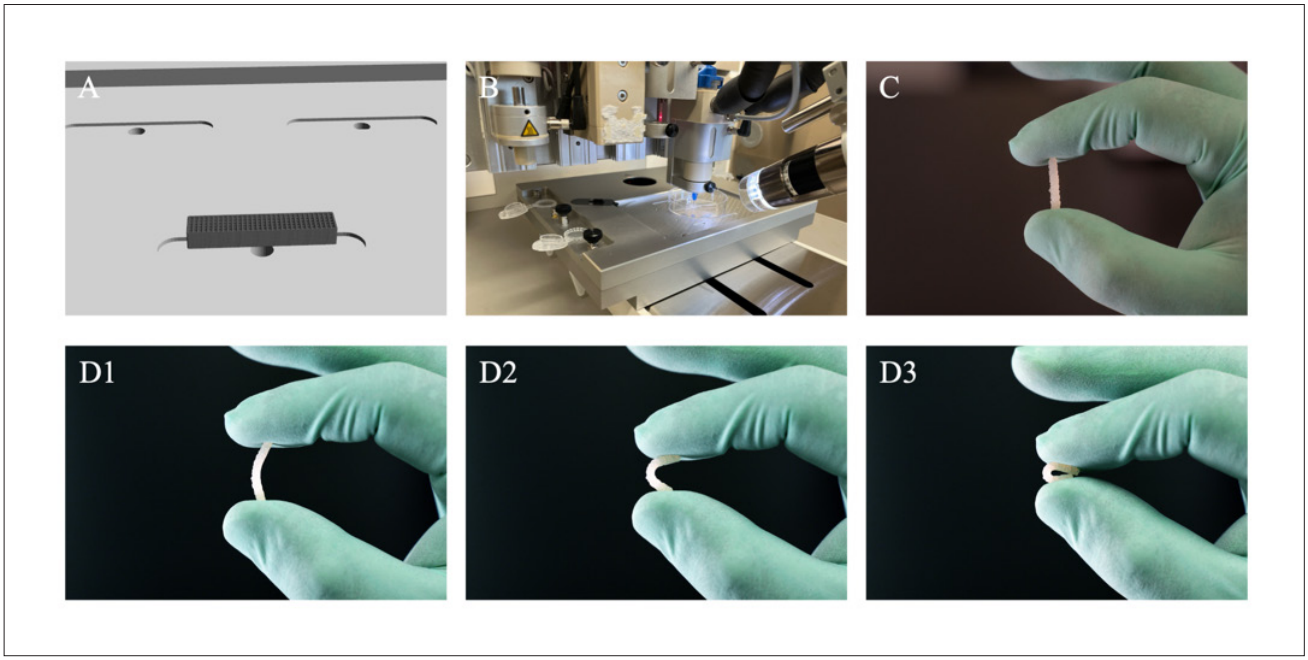

Figure 2. Fabrication and bending test of 3D bioprinted tissue-engineered Achilles tendon scaffolds. (A) Digital design model prior to bioprinting. (B) 3D bioprinting process. (C) Macroscopic view of the printed scaffold. (D1–D3) Sequential bending test demonstrating elastic recovery (180° bending angle) and preserved structural integrity (no fractures observed). Abbreviation: 3D, three-dimensional.

and must deform to accommodate mechanical loads. Our findings suggest that the SF–HPC scaffolds possess optimal toughness, ductility, and elastic modulus to withstand the tensile forces required for functional Achilles tendon repair.

3.3. Elastic modulus and degradation properties of tissue-engineered Achilles tendon scaffolds

In the design of tissue-engineered Achilles tendon scaffolds, elastic modulus is a critical determinant of scaffold functionality and biocompatibility.[45] The scaffold's elastic modulus must closely match that of the native Achilles tendon to avoid stress-shielding effects.[46,47] An excessively high elastic modulus may cause the scaffold to bear the majority of mechanical loads, thereby reducing mechanical stimulation to surrounding native tissue and impairing regeneration. Conversely, an insufficient elastic modulus could compromise structural support, leading to deformation or fracture and a failure to transmit mechanical signals effectively. In this study, the elastic modulus of SF–HPC scaffolds was measured at 85 MPa, significantly higher than that of pure SF scaffolds (55 MPa) (Figure 3A and B). Notably, the elastic modulus of SF–HPC scaffolds approached values comparable to native Achilles tendon tissue. Additionally, cyclic tensile testing was performed on both SF and SF–HPC scaffolds. The results demonstrated that, compared to SF scaffolds, SF–HPC scaffolds maintained a well-preserved elastic modulus after multiple cycles of tensile loading, indicating favorable resistance to stress fatigue (Figure 3C and D).

Tissue-engineered scaffolds are typically biodegradable and gradually absorbed during neo-tissue formation.[48] The degradation rate must be synchronized with the development of mechanical properties in the regenerating tissue to ensure a stable mechanical environment throughout the healing process.[49] Degradation tests demonstrated that both SF and SF–HPC scaffolds underwent degradation in PBS solution, protease XIV solution, and *in vivo* conditions (Figure 3E–G). Notably, SF–HPC scaffolds exhibited more stable degradation rates that closely matched the remodeling kinetics of tendon tissue.

This study identified the elastic modulus of the 3D-bioprinted tissue-engineered tendon scaffold as the primary contributor to enhanced tendon repair. The scaffolds' modulus was engineered to match the biomechanical properties of the injured tendon, thereby providing sufficient mechanical support during healing while preventing secondary damage from excessive

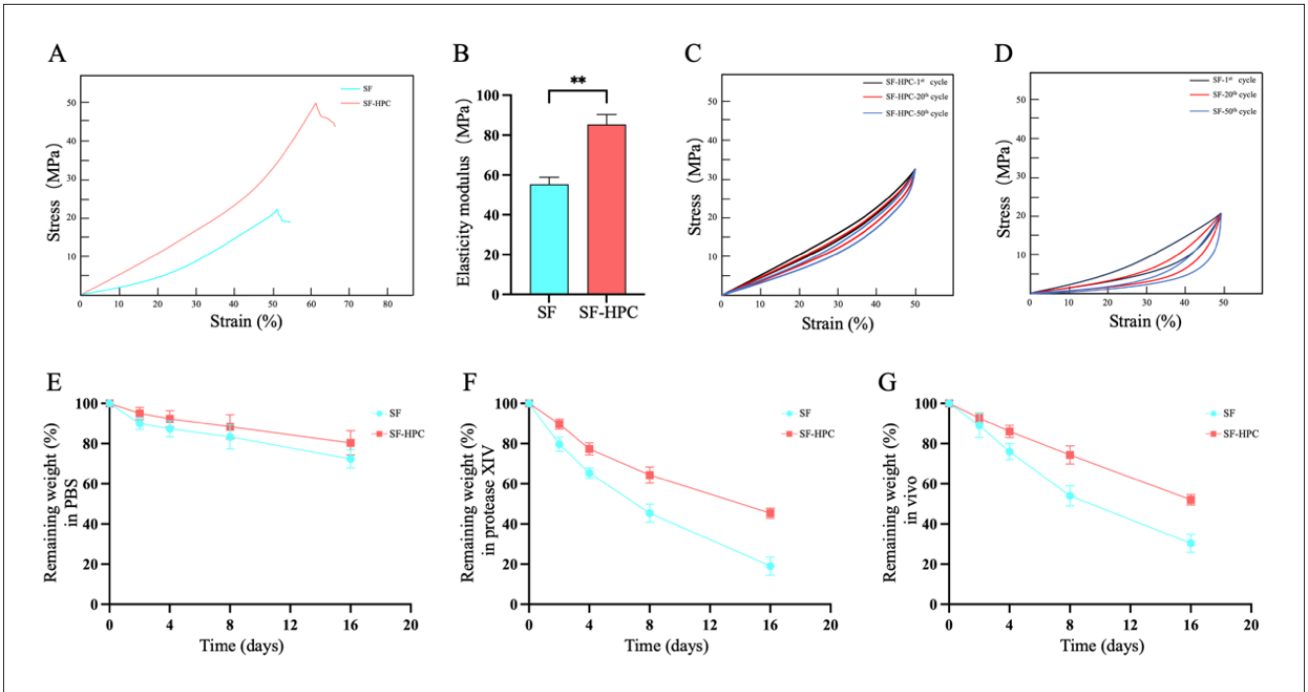

Figure 3. Mechanical and degradation properties of SF and SF–HPC tissue-engineered Achilles tendon scaffolds. (A) Stress–strain curves. (B) Elastic modulus. (C) Cyclic tensile testing of SF–HPC scaffolds. (D) Cyclic tensile testing of SF scaffolds. (E) *In vitro* degradation in PBS. (F) Enzymatic degradation in protease XIV solution. (G) *In vivo* degradation profile. $n = 3$; $^{**}p < 0.01$. Abbreviations: HPC, hydroxypropyl cellulose; SF, silk fibroin; PBs, phosphate-buffered saline.

stress concentration. Furthermore, as supported by prior research, an optimal elastic modulus maintains physiological tendon function and significantly enhances the proliferation of tendon-derived cells on the scaffolds, ultimately facilitating superior tendon regeneration.[50]

3.4. Pore structure analysis of tissue-engineered Achilles tendon scaffolds

To analyze the pore structure of tissue-engineered Achilles tendon scaffolds, SEM was performed on both SF and SF–HPC scaffolds. The SEM results revealed that SF–HPC scaffolds exhibited a more uniform pore distribution compared to SF scaffolds (Figure 4A1, A2, B1, and B2). The pore size of SF–HPC scaffolds predominantly ranged between 50–150 μm, whereas SF scaffolds showed pore sizes primarily distributed within 0–50 μm (Figure 4D). Furthermore, SF–HPC scaffolds demonstrated a porosity of 91%, significantly higher than the 78% porosity observed in SF scaffolds (Figure 4C). The porous architecture, porosity, and pore size of tissue-engineered scaffolds are critical determinants of their biofunctionality, as these parameters directly regulate cell migration, proliferation, differentiation, and nutrient transport.[51] The interconnected porous structure provides a 3D growth space for cells, facilitating adhesion, proliferation, and migration.[52] High porosity enhances cell infiltration and nutrient diffusion, thereby promoting cellular activities within the scaffold.[53]

3.5. Cell viability, migration, proliferation, and differentiation in tissue-engineered Achilles tendon scaffolds

To evaluate cell viability within the scaffolds, a live/dead cell staining assay was performed on SF and SF–HPC scaffolds. The results demonstrated that SF–HPC scaffolds exhibited 92% cell viability, significantly higher than the 85% viability observed in SF scaffolds (Figure 5A–C). The superior viability in SF–HPC scaffolds indicates the non-cytotoxic nature of the scaffold material and the absence of cellular damage from degradation products. Furthermore, the interconnected porous architecture facilitated nutrient exchange, which contributed to enhanced cellular survival.[54]

To assess cell migration capacity within the scaffolds, Transwell assays and scratch wound assays were conducted. The Transwell assay showed that the SF–HPC group exhibited an average of 115 migrated cells per microscopic field, significantly higher than the 85 cells observed in the SF group (Figure 5D–F). Scratch assay results revealed a gradual narrowing of the scratch gap over time in both

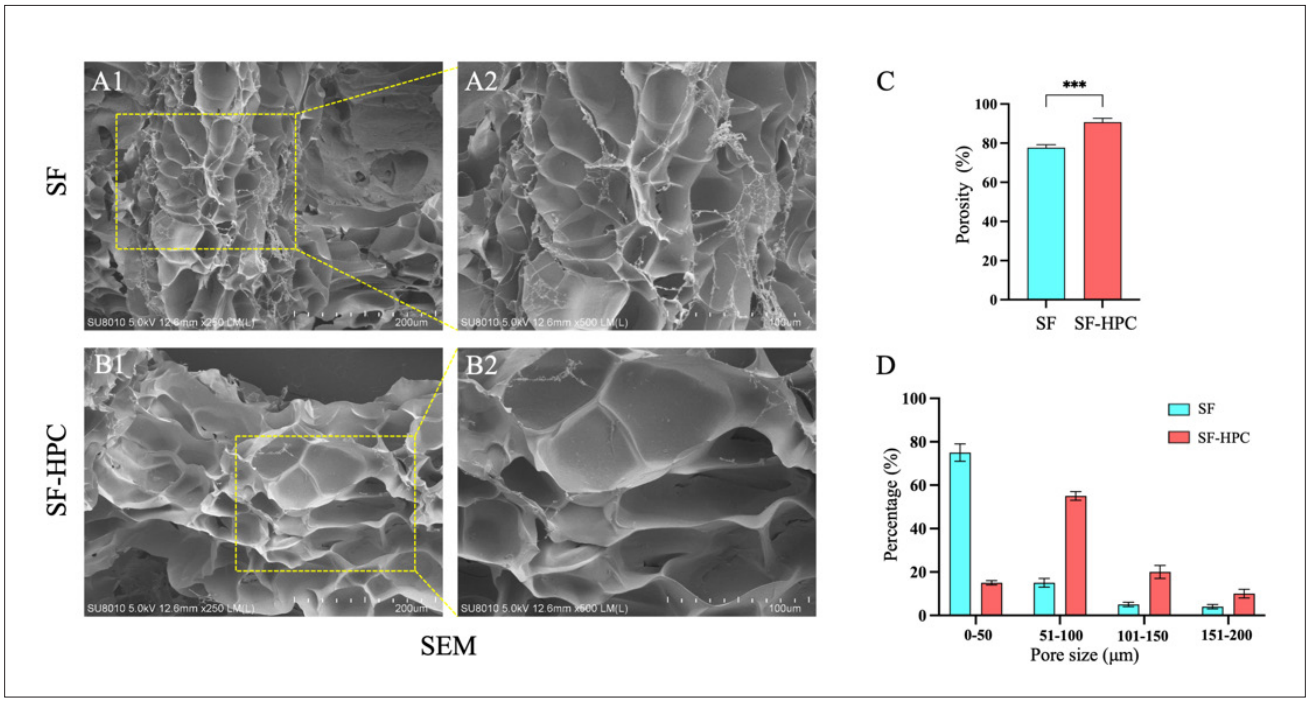

Figure 4. SEM characterization, porosity, and pore size distribution of SF and SF–HPC tissue-engineered Achilles tendon scaffolds. (A1, A2) Representative SEM images of SF scaffolds. (B1, B2) Representative SEM images of SF–HPC scaffolds. Scale bars: (A1, B1) 200 μm, (A2, B2) 100 μm; magnification: (A1, B1) 250×, (A2, B2) 500×. (C) Porosity comparison between SF and SF–HPC scaffolds. (D) Pore size distribution of SF and SF–HPC scaffolds. $n = 3$; ***$p < 0.001$. Abbreviations: HPC, hydroxypropyl cellulose; SF, silk fibroin; SEM, scanning electron microscopy.

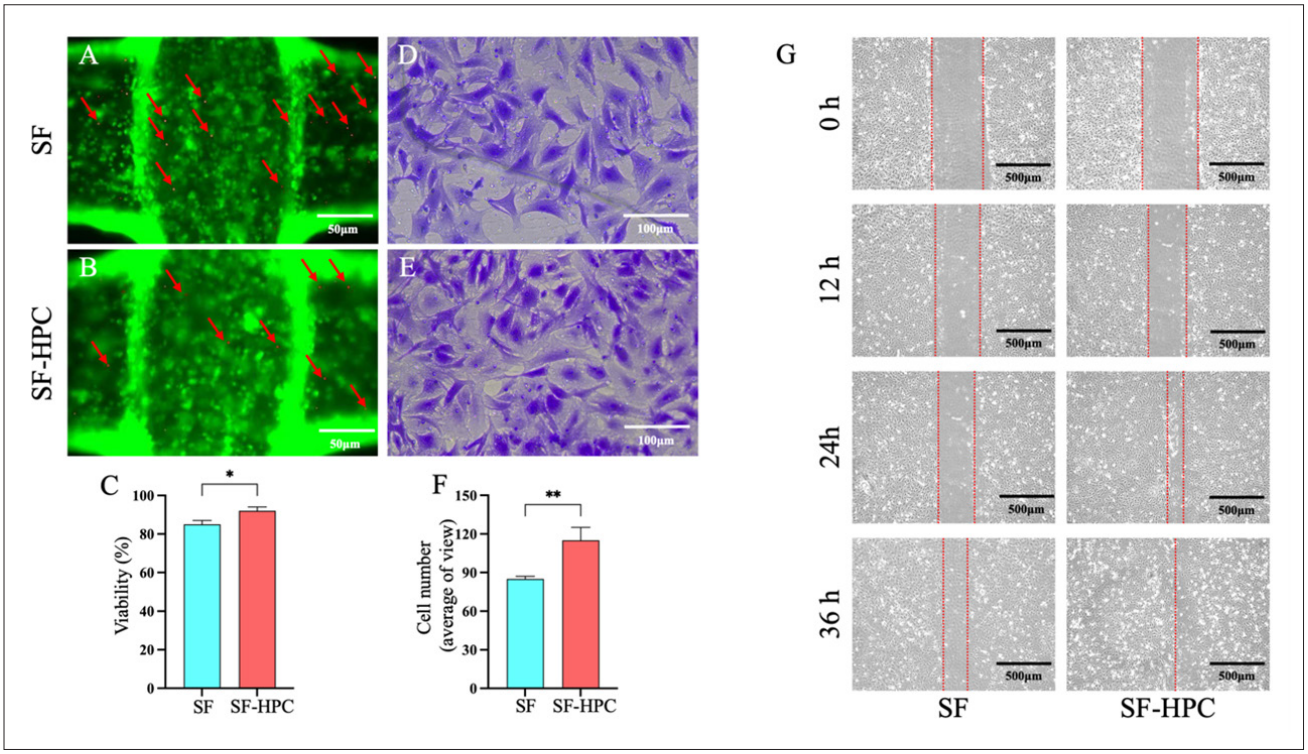

Figure 5. Cell viability and migration capacity in SF and SF–HPC tissue-engineered Achilles tendon scaffolds. (A, B) representative live/dead staining images of cells in SF and SF–HPC scaffolds after 72 h of culture. (C) Quantitative analysis of cell viability at 72 h. (D, E) Representative images of Transwell migration assay after 36 h. (F) Quantification of migrated cells per field in Transwell assays after 36 h. (G) Scratch assay images showing cell migration at 0, 12, 24, and 36 h. Scale bars: (A) 50 μm, (B) 50 μm, (D) 100 μm, (E) 100 μm, (G) 500 μm; magnifications: (A) 200×, (B) 200×, (D) 500×, (E) 500×, (G) 100×. $n = 3$; $^{*}p < 0.05$, $^{**}p < 0.01$. Abbreviations: HPC, hydroxypropyl cellulose; SF, silk fibroin.

groups (Figure 5G). The SF–HPC group demonstrated a narrower scratch gap and stronger cell migration capability compared to the SF group. Cell migration within scaffolds is critical for scaffold–host tissue integration.[55] Migratory cells infiltrate the defect site and fill the interface between the scaffold and host tissue, thereby promoting seamless integration.

To evaluate cell proliferation within the scaffolds, a CCK-8 assay was performed. The results showed gradual cell proliferation in both SF and SF–HPC scaffolds over time. At 12, 24, and 72 h, the SF–HPC group exhibited significantly higher proliferative activity compared to the SF group (Figure 6A). Cell proliferation is a pivotal factor in determining scaffold functionality and regenerative efficiency.[56] Proliferatively active TSPCs rapidly colonize the scaffold surface, migrate to the defect site, and secrete extracellular matrix components such as collagen, thereby forming a structural framework for neo-tendon tissue and accelerating Achilles tendon repair.

To assess the tenogenic differentiation capacity of TSPCs within the scaffolds, SF and SF–HPC scaffolds seeded with TSPCs were cultured *in vitro* and analyzed by PCR at weeks 2 and 4. The results demonstrated that the expression of the tenogenic marker *Scx* in the SF–HPC group was significantly higher than in the SF group at both time points. Conversely, the expression levels of chondrogenic (*Sox9*) and osteogenic (*Bmp2*) markers were significantly lower in the SF–HPC group compared to the SF group (Figure 6B–D). These findings indicate that SF–HPC scaffolds preferentially promote tenogenic differentiation of TSPCs.

The tenogenic differentiation capacity of TSPCs is a central driver of functional tissue regeneration. Tenogenically differentiated TSPCs mature into tenocytes, which directly synthesize and assemble type I collagen fibers—the critical structural component responsible for the mechanical strength of Achilles tendons.[57] Tenocyte activity governs collagen fiber alignment, density, and crosslinking, thereby determining the structural integrity of regenerated tendon tissue.[58]

In the pathological progression of HO following Achilles tendon injury, SOX-9 and BMP2 are key molecular drivers of aberrant bone formation.[59] SOX-9, a master transcriptional regulator of chondrogenesis,

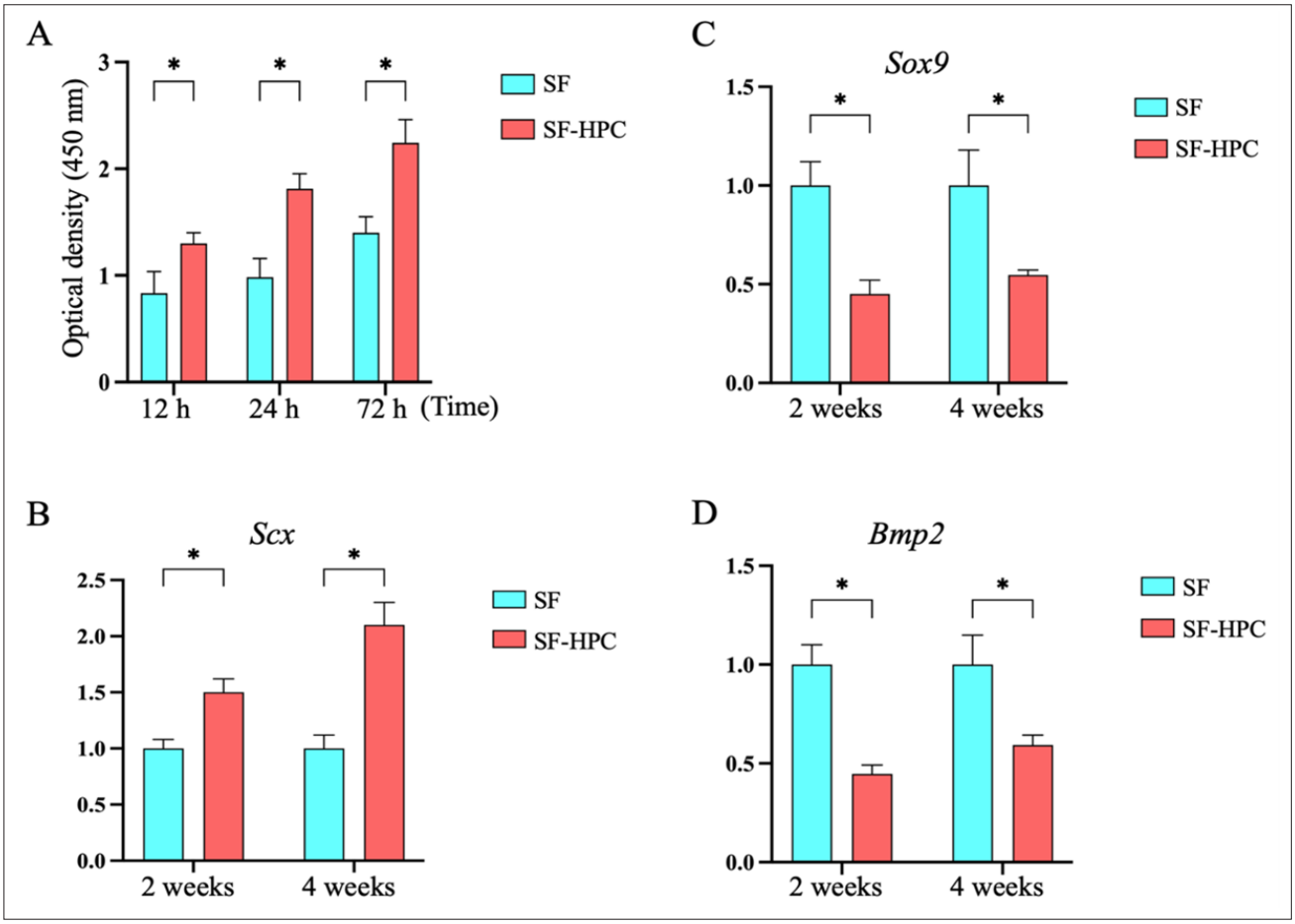

Figure 6. Proliferation and differentiation capacities of TSPCs in SF and SF–HPC tissue-engineered Achilles tendon scaffolds. (A) Proliferation analysis of TSPCs using the Cell Counting Kit-8 assay. (B–D) Quantitative polymerase chain reaction analysis of lineage-specific gene expression (*Scx*: tenogenic marker; *Sox9*: chondrogenic marker; *Bmp2*; osteogenic marker). $n = 3$; $^*p < 0.05$. Abbreviations: *Bmp2*, bone morphogenetic protein 2; HPC, hydroxypropyl cellulose; *Scx*, scleraxis; SF, silk fibroin; *Sox9*, SRY-box transcription factor; TSPCs, tendon stem/progenitor cells.

controls the expression of type II collagen and aggrecan. Downregulation of *Sox9* suppresses chondrogenic differentiation of TSPCs, eliminating the cartilage template required for endochondral ossification and thereby preventing HO initiation at its source. BMP2 activates osteogenic gene programs via the Smad1/5/8 signaling pathway, driving stem cell differentiation into osteoblasts and subsequent bone matrix deposition.[60] Reduced *Bmp2* expression directly disrupts this cascade, effectively minimizing HO and preventing tendon calcification or joint mobility impairment.

Within tissue-engineered Achilles tendon scaffolds, cellular viability, migration, proliferation, and differentiation collectively form a dynamic synergistic network that drives functional tissue regeneration.[61] Cell viability is the prerequisite for all subsequent cellular activities—high viability ensures the safety and biocompatibility of biomaterials while providing viable cellular resources for migration and proliferation. Cell migration orchestrates the directional distribution of cells toward the defect site, facilitating scaffold–host tissue interfacial integration and simultaneously creating pathways for vascularization and innervation. Cell proliferation replenishes cellular populations to fully cover the injury area, preventing delayed repair. The terminal differentiation of TSPCs into tenocytes marks the culmination of tendon regeneration, wherein tenocytes restore tendon mechanical properties through the secretion of aligned collagen fibers.

3.6. *In vivo* study on tissue-engineered Achilles tendon scaffolds for the prevention of post-traumatic heterotopic ossification

To evaluate the efficacy of tissue-engineered Achilles tendon scaffolds in preventing HO following tendon injury, an *in vivo* rat study was conducted. Achilles tendon injury

models were established via mid-tendon transection in rats (Figure 7E). Following transection, rats in the control group received no intervention beyond layered closure of fascia and skin. Rats implanted with SF scaffolds at the injury site were designated as the SF group, while those receiving SF–HPC scaffolds comprised the SF–HPC group. At 2, 4, and 8 weeks post-operatively, micro-CT scans were performed on all groups to quantify HO volume at the injury site. At 8 weeks, the skin and subcutaneous fascia overlying the Achilles tendon were surgically exposed for gross morphological evaluation. Tendon specimens were subsequently harvested for histological analyses, including H&E staining, Safranin O staining, and IHC staining.

Micro-CT results revealed no significant HO tissue at the Achilles tendon site in any group at 2 weeks post-operatively (Figure 7A1–C1). By 4 weeks, HO tissue volumes of approximately 2.1 mm^3, 1.7 mm^3, and 0.2 mm^3 were observed in the control, SF, and SF–HPC groups, respectively. The SF–HPC group exhibited a significantly smaller HO volume compared to both the control and SF groups (Figure 7A2–C2, D). At 8 weeks post-operatively, HO volumes increased to approximately 4.6 mm^3 in the control group and 2.4 mm^3 in the SF group, whereas the SF–HPC group maintained minimal HO (0.5 mm^3). The SF–HPC group consistently demonstrated significantly reduced HO volume compared to the other two groups at this time point (Figure 7A3–C3, D).

Gross examination and histological staining of rat Achilles tendons at 8 weeks post-operatively revealed that, in the control group, evident HO tissue was present at both the proximal and distal insertion sites of the tendon, accompanied by inflammatory hyperplasia and scar tissue formation (Figure 7A4). The SF group exhibited minimal HO tissue at the insertion sites, with sporadic scar tissue and irregular tendon morphology (Figure 7B4). In contrast, the SF–HPC group displayed no grossly visible HO tissue,

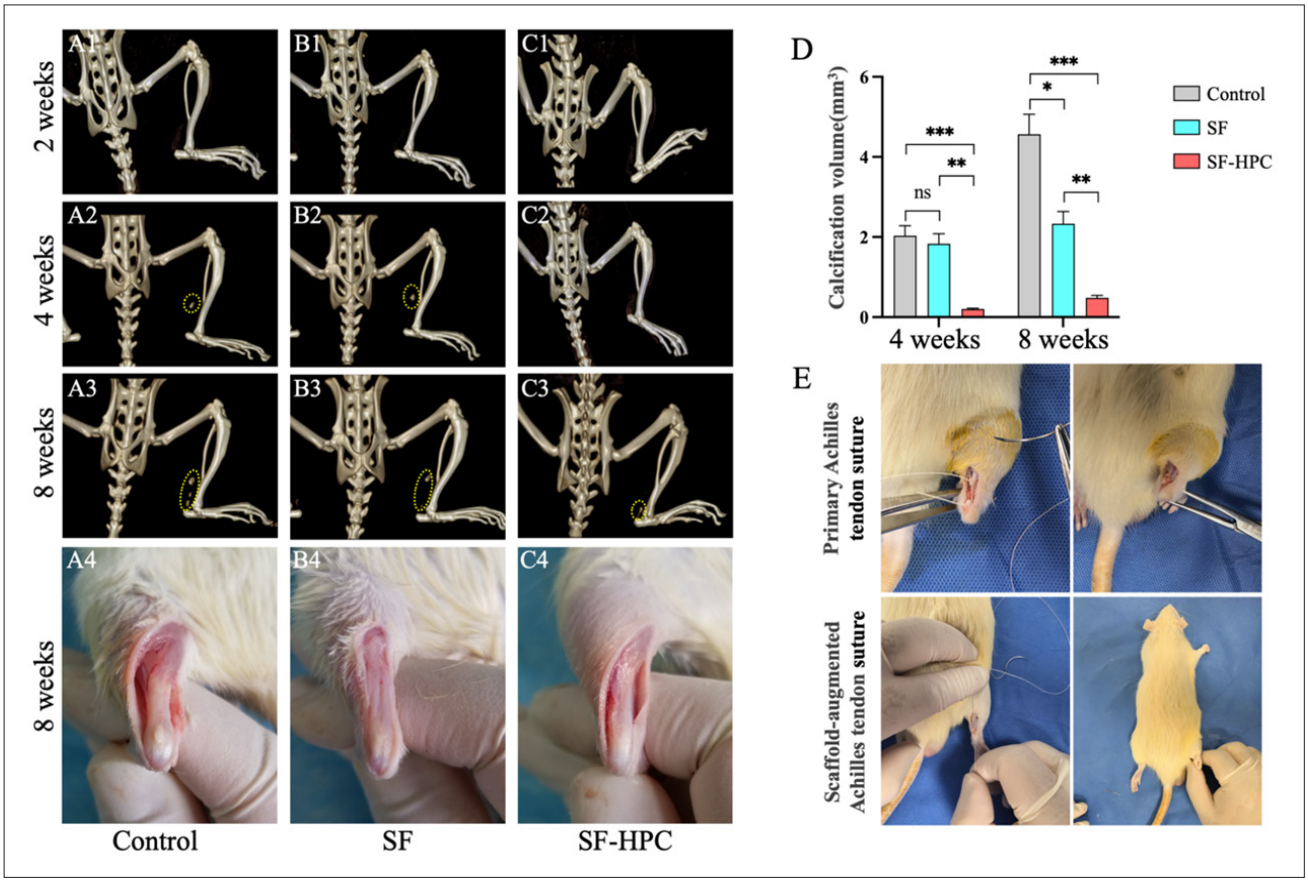

Figure 7. Evaluation of heterotopic ossification in rat models. (A1–A4) Micro-computed tomography reconstruction images of hindlimbs at 2, 4, and 8 weeks post-tenotomy, and gross morphology of regenerated tendons at 8 weeks in the control group. (B1–B4) Corresponding images for the SF group. (C1–C4) Corresponding images for the SF–HPC group. (D) Quantification of calcified tissue volume in Achilles tendons at 4 and 8 weeks post-operation. (E) Representative intraoperative photographs of primary suture versus scaffold-augmented suture in rat Achilles tendon. $n = 3$; $^*p < 0.05$, $^{**}p < 0.01$, $^{***}p < 0.001$. *Note*: Yellow dashed circles indicate regions of heterotopic ossification. Abbreviations: HPC, hydroxypropyl cellulose; SF, silk fibroin.

no significant inflammatory hyperplasia or scar tissue, and preserved tendon morphology (Figure 7C4).

Histological evaluation via H&E staining demonstrated extensive ossified tissue within the Achilles tendons of the control group, moderate ossification in the SF group, and minimal ossification in the SF–HPC group (Figure 8A1, B1, and C1). Safranin O staining corroborated these findings, showing similar spatial patterns of pathological matrix distribution (Figure 8A2, B2, and C2). IHC staining revealed widespread BMP-2-positive regions in the control group, localized BMP2 expression in the SF group, and only sporadic BMP2 signals in the SF–HPC group (Figure 8A3, B3, and C3). Quantitative IHC analysis confirmed a significantly reduced BMP-2-positive area in the SF–HPC group compared to both control and SF groups (Figure 8D).

In assessing the *in vivo* efficacy of tissue-engineered scaffolds for preventing post-traumatic HO, micro-CT, H&E staining, Safranin O staining, and IHC staining served as complementary and indispensable analytical modalities. Together, these techniques provided multi-dimensional insights into tissue quantification (micro-CT), histoarchitecture (HE), matrix composition (Safranin O), and molecular signaling (IHC), establishing a robust framework for evaluating therapeutic outcomes.[62–65]

3.7. Evaluation of systemic inflammatory and immune responses following implantation of tissue-engineered Achilles tendon scaffolds

To assess systemic inflammatory and immune responses after scaffold implantation, venous blood was collected from rats at 3, 7, and 14 days post-operatively following Achilles tendon transection. The measured parameters included WBC count, red blood cell count, neutrophil count, neutrophil percentage, lymphocyte count, lymphocyte percentage, monocyte count, and monocyte percentage.

The WBC count results demonstrated a gradual decrease over time across all groups. Notably, the control group exhibited a significant acute inflammatory response at post-operative day 3, while the SF–HPC group showed lower WBC counts compared to both the Control and SF groups (Figure 9A). These findings indicate that scaffold implantation did not induce marked systemic inflammatory reactions.

Red blood cell counts increased progressively in all groups. However, the control group displayed a significant

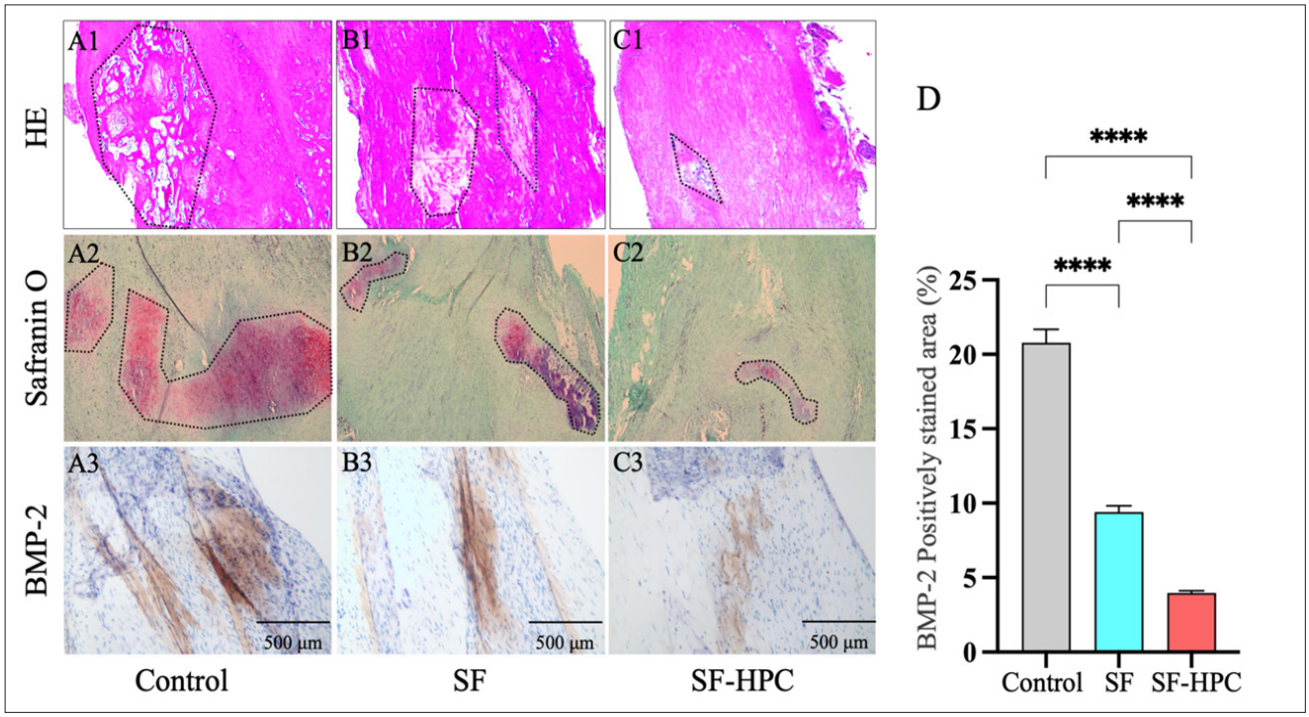

Figure 8. Histopathological and molecular characterization of regenerated Achilles tendons at eight weeks post-tenotomy. (A1, B1, C1) Representative hematoxylin and eosin (HE) staining of tendon tissues in control, SF, and SF–HPC groups. (A2, B2, C2) Safranin O staining for proteoglycan deposition. (A3, B3, C3) Immunohistochemical staining of BMP-2 expression. Scale bar: 500 μm; magnification: 100×. (D) Quantification of BMP-2 positively stained areas in immunohistochemical analysis. $n = 3$; ****$p < 0.0001$. *Note*: Black dashed boxes demarcate calcified regions. Abbreviations: BMP-2, bone morphogenetic protein 2; HPC, hydroxypropyl cellulose; SF, silk fibroin.

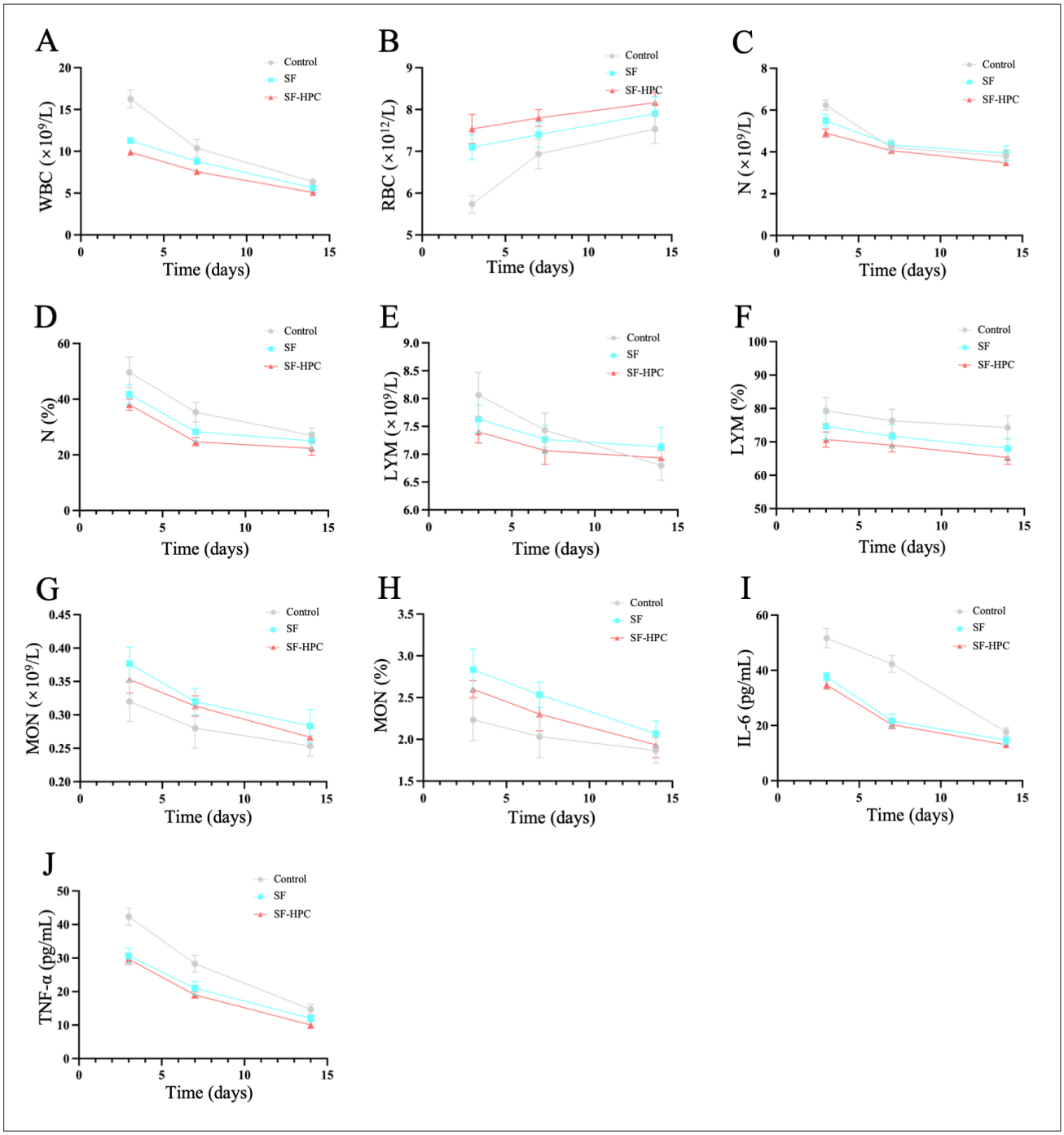

Figure 9. Systemic inflammatory profiles in rat models after Achilles tenotomy. (A) WBC count. (B) RBC count. (C) Neutrophil (N) count. (D) Neutrophil (N) percentage. (E) LYM count. (F) LYM percentage. (G) MON count. (H) MON percentage. (I) IL-6 concentration. (J) TNF-α concentration. $n = 3$; $^{*}p < 0.05$, $^{**}p < 0.01$, $^{***}p < 0.001$. Abbreviations: HPC, hydroxypropyl cellulose; SF, silk fibroin; LYM, lymphocyte; RBC, red blood cell; WBC, white blood cell; MON, monocyte; IL-6, interleukin-6; TNF-α, tumor necrosis factor-α.

reduction in red blood cell count at post-operative day 3, suggesting substantial hemorrhage and erythrocyte loss during the early post-operative phase (Figure 9B).

Neutrophil counts and percentages gradually returned to baseline levels in all groups. The control group showed abnormally elevated neutrophil counts and percentages at day 3, exceeding normal physiological ranges, whereas the SF and SF–HPC groups maintained neutrophil parameters within normal limits (Figure 9C and D). These results further confirm the absence of acute inflammatory responses following scaffold implantation.

Lymphocyte counts and percentages normalized progressively across all groups, with no significant intergroup differences observed (Figure 9E and F). This pattern indicates that tendon transection surgery alone did not elicit chronic inflammatory responses, regardless of the intervention.

Similarly, monocyte counts and percentages returned to baseline levels across all groups over the observation period (Figure 9G and H). Collectively, these hematological profiles demonstrate that neither scaffold implantation nor surgical injury provoked detectable immune dysregulation.

Additionally, serum levels of pro-inflammatory cytokines (IL-6 and TNF-α) were quantified at post-operative days 3, 7, and 14. IL-6 levels in the control group significantly surged at post-operative day 3, exceeding those in both the SF and SF–HPC groups ($p < 0.05$). By post-operative day 14, IL-6 levels in the control group returned to baseline. In contrast, no statistically significant difference was observed between the SF and SF–HPC groups, both of which exhibited a gradual decline in IL-6 concentrations, returning to near-baseline levels by post-operative day 7 and fully normalizing by post-operative day 14 (Figure 9I). A similar trend was observed for TNF-α (Figure 9J). Collectively, these findings indicate that neither SF nor SF–HPC scaffolds induced sustained elevation of inflammatory cytokines post-implantation, with cytokine levels largely restored within 1–2 weeks.

SF intrinsically possesses immunomodulatory properties. As demonstrated in previous research, SF-based materials attenuate pro-inflammatory cytokine secretion (e.g., TNF-α, IL-6) through suppression of inflammatory pathways such as nuclear factor kappa-light-chain-enhancer of activated B cell signaling.[66] This reduction in pro-inflammatory cytokines directly impairs neutrophil and monocyte recruitment, thereby decreasing WBC infiltration into inflammatory sites—a phenomenon reflected by diminished peripheral blood WBC counts.[67]

In the prevention of post-traumatic HO by tissue-engineered Achilles tendon scaffolds, attenuated inflammatory and immune responses play a critical role in regulating key pathological mechanisms.[13] Pro-inflammatory cytokines upregulate BMP-2 and Wnt signaling pathways, driving stem cell differentiation toward osteoblasts.[68] Suppression of inflammatory responses directly inhibits these pathways, thereby reducing ectopic bone matrix deposition.

Neutrophil-derived reactive oxygen species and matrix metalloproteinases (MMPs) disrupt the local microenvironment, promoting calcium salt deposition. A hypoimmune response inhibits immune cell-mediated aberrant repair processes.[69,70] A low-inflammatory microenvironment downregulates BMP-2/Smad1/5 signaling while upregulating tenogenic markers such as *Scx*, directing stem cell differentiation toward tenocytes rather than osteoblasts. Concurrently, reduced MMP activity preserves type I collagen integrity by minimizing its degradation, maintaining ordered collagen fiber alignment, and enhancing mechanical stability.[70–72]

In summary, reduced inflammatory and immune responses play a crucial role in preventing HO of the Achilles tendon by suppressing osteogenic signaling, optimizing stem cell differentiation, and blocking aberrant repair processes.

Collectively, the SF–HPC scaffold demonstrates exceptional mechanical properties, tunable degradation kinetics, and favorable biocompatibility, enabling effective tendon repair while preventing HO. Compared to collagen scaffolds, SF-based scaffolds provide superior degradation resistance and mechanical strength. Although collagen offers excellent biocompatibility, its low mechanical integrity and rapid degradation may lead to premature loss of structural support post-implantation. In contrast, appropriately cross-linked SF scaffolds maintain biocompatibility while enhancing mechanical robustness and controlling degradation rates, thereby providing sustained tissue support.[73] A distinct advantage over PLGA scaffolds lies in SF's ability to better facilitate cell adhesion and proliferation,[74] a finding corroborated by our experimental results.

4. Conclusion

This study successfully formulated an SF–HPC–TSPC bioink, utilizing SF as the base material, HPC as a reinforcing agent, and TSPCs as seed cells. The developed bioink exhibited excellent cytocompatibility and favorable rheological properties. It enabled 3D bioprinting of porous tissue-engineered Achilles tendon scaffolds with high mechanical strength and controlled

biodegradability, achieving an elastic modulus of 85 MPa and a porosity of 91%. *In vitro* studies demonstrated that SF–HPC scaffolds significantly enhanced TSPCs viability, migration, proliferation, and tenogenic differentiation. *In vivo* evaluations confirmed the scaffolds' superior biocompatibility, as they elicited no detectable systemic inflammatory or immune responses. Importantly, the SF–HPC scaffolds effectively prevented HO in our rat Achilles tendon injury model.

Acknowledgments

None.

Funding

This work was supported by the National Major Research Plan of the National Natural Science Foundation of China (NSFC) (92368201), the National Key Research and Development Project (2021YFA1201404), the Major Project of NSFC (81991514), and the Jiangsu Province Medical Innovation Center of Orthopedic Surgery (CXZX202214).

Conflict of interest

The authors declare that they have no competing interests.

Author contributions

Conceptualization: Kai Yan, Xianzong Ning
Formal analysis: Minghao Zhang, Yutao Yang
Funding acquisition: Xianzong Ning, Kai Yan
Investigation: Xianzong Ning, Kai Yan, Rui Du
Methodology: Kai Yan, Rui Du
Visualization: Kai Yan, Xiaoming Xu, Baoyuan Meng
Writing–original draft: Kai Yan, Rui Du
Writing–review & editing: Kai Yan, Fei Yu

Ethics approval and consent to participate

All animal experiments in this study were conducted in accordance with standard procedures and approved by the Ethics Committee of Nanjing Drum Tower Hospital Affiliated with Nanjing University Medical School (Approval No.: 2021AE01031).

Consent for publication

Not applicable.

Availability of data

The data supporting the findings of this study are available on request from the corresponding author upon reasonable request.

References

1. Traweger A, Scott A, Kjaer M, et al. Achilles tendinopathy. *Nat Rev Dis Primers*. 2025;11(1):20.
doi: 10.1038/s41572-025-00602-9

2. Fischer S. Acute rupture of the Achilles tendon: diagnostics, treatment and aftercare. *Unfallchirurgie (Heidelb)*. 2024;127(8):597-606.
doi: 10.1007/s00113-024-01454-w

3. Geuskens W, Caekebeke P, VAN Riet R. Prevalence and clinical implications of heterotopic ossification after distal biceps tendon repair. *Acta Orthop Belg*. 2023;89(4):695-700.
doi: 10.52628/89.4.12447

4. Fischer CS, Porsche J, Leyder D, Schüll D, Histing T, Ziegler P. Heterotopic ossification following severe radial head fractures: clinical outcome and associated factors. *Jt Dis Relat Surg*. 2025;36(1):47-55.
doi: 10.52312/jdrs.2025.1992

5. Dai G, Li Y, Liu J, et al. Higher BMP Expression in tendon stem/progenitor cells contributes to the increased heterotopic ossification in achilles tendon with aging. *Front Cell Dev Biol*. 2020;8:570605.
doi: 10.3389/fcell.2020.570605

6. Yu T, Zhang J, Zhu W, et al. Chondrogenesis mediates progression of ankylosing spondylitis through heterotopic ossification. *Bone Res*. 2021;9(1):19.
doi: 10.1038/s41413-021-00140-6

7. Wang Z, Yi X, Liu Y, Liu Q, Li Z, Yu A. Differential expression profiles and functional prediction of circRNA in mice with traumatic heterotopic ossification. *Front Immunol*. 2022;13:1090529.
doi: 10.3389/fimmu.2022.1090529

8. Xu L, Xu K, Wu Z, et al. Pioglitazone attenuates advanced glycation end products-induced apoptosis and calcification by modulating autophagy in tendon-derived stem cells. *J Cell Mol Med*. 2020;24(3):2240-2251.
doi: 10.1111/jcmm.14901

9. Tachibana N, Chijimatsu R, Okada H, et al. RSPO2 defines a distinct undifferentiated progenitor in the tendon/ligament and suppresses ectopic ossification. *Sci Adv*. 2022;8(33):eabn2138.
doi: 10.1126/sciadv.abn2138

10. Wang T, Chen P, Chen L, et al. Reduction of mechanical loading in tendons induces heterotopic ossification and activation of the β-catenin signaling pathway. *J Orthop Transl*. 2021;29:42-50.
doi: 10.1016/j.jot.2021.03.004

11. Pierantoni M, Hammerman M, Silva Barreto I, et al. Spatiotemporal and microstructural characterization of heterotopic ossification in healing rat Achilles tendons. *FASEB J*. 2023;37(6).
doi: 10.1096/fj.202201018RRR

12. Yamaguchi H, Li M, Kitami M, Swaminathan S, Mishina Y, Komatsu Y. Enhanced BMP signaling in Cathepsin K-positive tendon progenitors induces heterotopic ossification. *Biochem Biophys Res Commun*. 2023;688:149147. doi: 10.1016/j.bbrc.2023.149147

13. Magnusson SP, Agergaard AS, Couppé C, et al. Heterotopic ossification after an achilles tendon rupture cannot be prevented by early functional rehabilitation: a cohort study. *Clin Orthop Relat Res*. 2020;478(5):1101-1108. doi: 10.1097/corr.0000000000001085

14. Agarwal S, Loder S, Levi B. Heterotopic ossification following upper extremity injury. *Hand Clin*. 2017;33(2): 363-373. doi: 10.1016/j.hcl.2016.12.013

15. Delgado Caceres M, Angerpointner K, Galler M, et al. Tenomodulin knockout mice exhibit worse late healing outcomes with augmented trauma-induced heterotopic ossification of Achilles tendon. *Cell Death Dis*. 2021;12(11):1049. doi: 10.1038/s41419-021-04298-z

16. Walden G, Liao X, Donell S, Raxworthy MJ, Riley GP, Saeed A. A clinical, biological, and biomaterials perspective into tendon injuries and regeneration. *Tissue Eng Part B Rev*. 2017;23(1):44-58. doi: 10.1089/ten.TEB.2016.0181

17. No YJ, Castilho M, Ramaswamy Y, Zreiqat H. Role of biomaterials and controlled architecture on tendon/ligament repair and regeneration. *Adv Mater*. 2020;32(18):e1904511. doi: 10.1002/adma.201904511

18. Sensini A, Cristofolini L. Biofabrication of electrospun scaffolds for the regeneration of tendons and ligaments. *Materials (Basel)*. 2018;11(10):1963. doi: 10.3390/ma11101963

19. Yan K, Zhang X, Liu Y, et al. 3D-bioprinted silk fibroin-hydroxypropyl cellulose methacrylate porous scaffold with optimized performance for repairing articular cartilage defects. *Mater Des*. 2023;225:111531. doi: 10.1016/j.matdes.2022.111531

20. Zhang X, Liu Y, Zuo Q, et al. 3D bioprinting of biomimetic bilayered scaffold consisting of decellularized extracellular matrix and silk fibroin for osteochondral repair. *Int J Bioprint*. 2021;7(4):401. doi: 10.18063/ijb.v7i4.401

21. Park W, Gao G, Cho DW. Tissue-specific decellularized extracellular matrix bioinks for musculoskeletal tissue regeneration and modeling using 3d bioprinting technology. *Int J Mol Sci*. 2021;22(15):7837. doi: 10.3390/ijms22157837

22. Jiu J, Liu H, Li D, et al. 3D bioprinting approaches for spinal cord injury repair. *Biofabrication*. 2024;16(3). doi: 10.1088/1758-5090/ad3a13

23. Zhang Y, Sun Y, Luo J, et al. Hydrogel-based materials for mandibular reconstruction. *MSAM*. 2025;4(2). doi: 10.36922/msam025070006

24. Li H, Zeng S, Zhou L. Biocompatible nanogels with tunable size and tailorable properties: a simple synthesis by self-assembly and disulfide crosslinking of amphiphilic hyperbranched peach gum polysaccharide. *Int J Biol Macromol*. 2025;309(Pt 4):143083. doi: 10.1016/j.ijbiomac.2025.143083

25. Zhang DKY, Brockman JM, Adu-Berchie K, et al. Subcutaneous biodegradable scaffolds for restimulating the antitumour activity of pre-administered CAR-T cells. *Nat Biomed Eng*. 2025;9(2):268-278. doi: 10.1038/s41551-024-01216-4

26. Xu Y, Huang J, Mai Y, et al. CBD-conjugated BMP-inhibiting exosomes on collagen scaffold dual-target Achilles tendon repair: synergistic regeneration and heterotopic ossification prevention. *Mater Today Bio*. 2025;32:101790. doi: 10.1016/j.mtbio.2025.101790

27. Avenoso A, Bruschetta G, D'Ascola A, et al. Hyaluronan fragments produced during tissue injury: A signal amplifying the inflammatory response. *Arch Biochem Biophys*. 2019;663:228-238. doi: 10.1016/j.abb.2019.01.015

28. Kim JK, Go EJ, Ko KW, et al. PLGA microspheres containing hydrophobically modified magnesium hydroxide particles for acid neutralization-mediated anti-inflammation. *Tissue Eng Regen Med*. 2021;18(4):613-622. doi: 10.1007/s13770-021-00338-z

29. Wang Y, Feng X, Chen X. Autonomous bioelectronic devices based on silk fibroin. *Adv Mater*. 2025;37(22):e2500073. doi: 10.1002/adma.202500073

30. Shen C, Zhou Z, Li R, et al. Silk fibroin-based hydrogels for cartilage organoids in osteoarthritis treatment. *Theranostics*. 2025;15(2):560-584. doi: 10.7150/thno.103491

31. Wang F, Lei H, Tian C, et al. An efficient biosynthetic system for developing functional silk fibroin-based biomaterials. *Adv Mater*. 2025;37(7):e2414878. doi: 10.1002/adma.202414878

32. Cai G, Zhao W, Zhu T, Oliveira AL, Yao X, Zhang Y. Effects of protein conformational transition accompanied with crosslinking density cues in silk fibroin hydrogels on the proliferation and chondrogenesis of encapsulated stem cells. *Regen Biomater*. 2025;12:rbaf019. doi: 10.1093/rb/rbaf019

33. Ben X, Lu X, Zhao G, Wei Z, Yang J, Kan Y. Internal secondary structural conformational states of silk fibroin studied by raman spectroscopy with band deconvolution analysis. *Biomacromolecules*. 2025;26(3):1992-2002. doi: 10.1021/acs.biomac.4c01827

34. Ji X, Li Y, Wang J, et al. Silk protein gene engineering and its applications: recent advances in biomedicine driven by molecular biotechnology. *Drug Des Devel Ther*. 2025;19:599-626.
doi: 10.2147/dddt.S504783

35. Yin J, Fang Y, Xu L, Ahmed A. High-throughput fabrication of silk fibroin/hydroxypropyl methylcellulose (SF/HPMC) nanofibrous scaffolds for skin tissue engineering. *Int J Biol Macromol*. 2021;183:1210-1221.
doi: 10.1016/j.ijbiomac.2021.05.026

36. Su D, Yao M, Liu J, Zhong Y, Chen X, Shao Z. Enhancing mechanical properties of silk fibroin hydrogel through restricting the growth of β-sheet domains. *ACS Appl Mater Interfaces*. 2017;9(20):17489-17498.
doi: 10.1021/acsami.7b04623

37. Bi Y, Ehirchiou D, Kilts TM, et al. Identification of tendon stem/progenitor cells and the role of the extracellular matrix in their niche. *Nat Med*. 2007;13(10):1219-1227.
doi: 10.1038/nm1630

38. He W, Jiang C, Zhou P, Hu X, Gu X, Zhang S. Role of tendon-derived stem cells in tendon and ligament repair: focus on tissue engineer. *Front Bioeng Biotechnol*. 2024;12:1357696.
doi: 10.3389/fbioe.2024.1357696

39. Chen J, Jiang C, Yin L, et al. A review of the role of tendon stem cells in tendon-bone regeneration. *Med Sci Monit*. 2023;29:e940805.
doi: 10.12659/msm.940805

40. Lu J, Chen H, Lyu K, et al. The functions and mechanisms of tendon stem/progenitor cells in tendon healing. *Stem Cells Int*. 2023;2023:1258024.
doi: 10.1155/2023/1258024

41. Jahani A, Nourbakhsh MS, Ebrahimzadeh MH, Mohammadi M, Yari D, Moradi A. Biomolecules-loading of 3D-printed alginate-based scaffolds for cartilage tissue engineering applications: a review on current status and future prospective. *Arch Bone Jt Surg*. 2024;12(2):92-101.
doi: 10.22038/abjs.2023.73275.3396

42. Li M, Shi T, Yao D, Yue X, Wang H, Liu K. High-cytocompatible semi-IPN bio-ink with wide molecular weight distribution for extrusion 3D bioprinting. *Sci Rep*. 2022;12(1):6349.
doi: 10.1038/s41598-022-10338-1

43. Delkash Y, Gouin M, Rimbeault T, et al. Bioprinting and in vitro characterization of an eggwhite-based cell-laden patch for endothelialized tissue engineering applications. *J Funct Biomater*. 2021;12(3):45.
doi: 10.3390/jfb12030045

44. Kolluru PV, Lipner J, Liu W, et al. Strong and tough mineralized PLGA nanofibers for tendon-to-bone scaffolds. *Acta Biomater*. 2013;9(12):9442-9450.
doi: 10.1016/j.actbio.2013.07.042

45. Jacob S, Reshmy R, Antony S, et al. Nanocellulose in tissue engineering and bioremediation: mechanism of action. *Bioengineered*. 2022;13(5):12823-12833.
doi: 10.1080/21655979.2022.2074739

46. Veronesi F, Giavaresi G, Bellini D, Casagranda V, Pressato D, Fini M. Evaluation of a new collagen-based medical device (ElastiCo®) for the treatment of acute Achilles tendon injury and prevention of peritendinous adhesions: An in vitro biocompatibility and in vivo investigation. *J Tissue Eng Regen Med*. 2020;14(8):1113-1125.
doi: 10.1002/term.3085

47. Webb WR, Dale TP, Lomas AJ, et al. The application of poly(3-hydroxybutyrate-co-3-hydroxyhexanoate) scaffolds for tendon repair in the rat model. *Biomaterials*. 2013;34(28):6683-6694.
doi: 10.1016/j.biomaterials.2013.05.041

48. Kim SH, Park JH, Kwon JS, et al. NIR fluorescence for monitoring in vivo scaffold degradation along with stem cell tracking in bone tissue engineering. *Biomaterials*. 2020;258:120267.
doi: 10.1016/j.biomaterials.2020.120267

49. Salehi S, Koeck K, Scheibel T. Spider silk for tissue engineering applications. *Molecules*. 2020;25(3):737.
doi: 10.3390/molecules25030737

50. Xie Y, Zhang F, Akkus O, King MW. A collagen/PLA hybrid scaffold supports tendon-derived cell growth for tendon repair and regeneration. *J Biomed Mater Res B Appl Biomater*. 2022;110(12):2624-2635.
doi: 10.1002/jbm.b.35116

51. Shirosaki Y, Tsukatani Y, Okamoto K, Hayakawa S, Osaka A. Preparation and drug release profile of chitosan-siloxane hybrid capsules coated with hydroxyapatite. *Pharmaceutics*. 2022;14(5):1111.
doi: 10.3390/pharmaceutics14051111

52. Fei Y, Ma Y, Zhang H, Li H, Feng G, Fang J. Nanotechnology for research and treatment of the intestine. *J Nanobiotechnol*. 2022;20(1):430.
doi: 10.1186/s12951-022-01517-3

53. Sadeghzadeh H, Mehdipour A, Dianat-Moghadam H, et al. PCL/Col I-based magnetic nanocomposite scaffold provides an osteoinductive environment for ADSCs in osteogenic cues-free media conditions. *Stem Cell Res Ther*. 2022;13(1):143.
doi: 10.1186/s13287-022-02816-0

54. Zheng A, Wang X, Xin X, et al. Promoting lacunar bone regeneration with an injectable hydrogel adaptive to the microenvironment. *Bioact Mater*. 2023;21:403-421.
doi: 10.1016/j.bioactmat.2022.08.031

55. Eggermont LJ, Rogers ZJ, Colombani T, Memic A, Bencherif SA. Injectable cryogels for biomedical applications. *Trends Biotechnol*. 2020;38(4):418-431.
doi: 10.1016/j.tibtech.2019.09.008

56. Yao X, Yang Y, Zhou Z. Non-mulberry silk fiber-based composite scaffolds containing millichannels for auricular cartilage regeneration. *ACS Omega*. 2022;7(17):15064-15073. doi: 10.1021/acsomega.2c00846

57. Wang Y, Jin S, Luo D, et al. Functional regeneration and repair of tendons using biomimetic scaffolds loaded with recombinant periostin. *Nat Commun*. 2021;12(1):1293. doi: 10.1038/s41467-021-21545-1

58. Markel DC, Dietz P, Provenzano G, Bou-Akl T, Ren WP. Attachment and growth of fibroblasts and tenocytes within a porous titanium scaffold: a bioreactor approach. *Arthroplast Today*. 2022;14:231-236.e1. doi: 10.1016/j.artd.2021.12.003

59. Lin L, Shen Q, Xue T, Yu C. Heterotopic ossification induced by Achilles tenotomy via endochondral bone formation: expression of bone and cartilage related genes. *Bone*. 2010;46(2):425-431. doi: 10.1016/j.bone.2009.08.057

60. Cai Z, Wu B, Ye G, et al. Enhanced osteogenic differentiation of human bone marrow mesenchymal stem cells in ossification of the posterior longitudinal ligament through activation of the BMP2-Smad1/5/8 pathway. *Stem Cells Dev*. 2020;29(24):1567-1576. doi: 10.1089/scd.2020.0117

61. Zhang H, Liu MF, Liu RC, Shen WL, Yin Z, Chen X. Physical microenvironment-based inducible scaffold for stem cell differentiation and tendon regeneration. *Tissue Eng Part B Rev*. 2018;24(6):443-453. doi: 10.1089/ten.TEB.2018.0018

62. Brownley RC, Agarwal S, Loder S, et al. Characterization of heterotopic ossification using radiographic imaging: evidence for a paradigm shift. *PLoS One*. 2015;10(11):e0141432. doi: 10.1371/journal.pone.0141432

63. Foley KL, Hebela N, Keenan MA, Pignolo RJ. Histopathology of periarticular non-hereditary heterotopic ossification. *Bone*. 2018;109:65-70. doi: 10.1016/j.bone.2017.12.006

64. Ng J, Wei Y, Zhou B, et al. Ectopic implantation of juvenile osteochondral tissues recapitulates endochondral ossification. *J Tissue Eng Regen Med*. 2018;12(2):468-478. doi: 10.1002/term.2500

65. Fujihara R, Chiba Y, Nakagawa T, et al. Histomorphometry of ectopic mineralization using undecalcified frozen bone sections. *Microsc Res Tech*. 2018;81(11):1318-1324. doi: 10.1002/jemt.23140

66. Yuan J, Sun W, Zhang Z, et al. 5-Fluorouracil/curcumin loaded silk fibroin hydrogel for the adjuvant therapy in colorectal cancer. *Biomater Adv*. 2025;168:214108. doi: 10.1016/j.bioadv.2024.214108

67. Yeo D, Hwang SJ, Song YS, Lee HJ. Humulene inhibits acute gastric mucosal injury by enhancing mucosal integrity. *Antioxidants (Basel)*. 2021;10(5):761. doi: 10.3390/antiox10050761

68. Jian J, Sun L, Cheng X, Hu X, Liang J, Chen Y. Calycosin-7-O-β-d-glucopyranoside stimulates osteoblast differentiation through regulating the BMP/WNT signaling pathways. *Acta Pharm Sin B*. 2015;5(5):454-460. doi: 10.1016/j.apsb.2015.06.005

69. Winterbourn CC, Kettle AJ, Hampton MB. Reactive oxygen species and neutrophil function. *Annu Rev Biochem*. 2016;85:765-792. doi: 10.1146/annurev-biochem-060815-014442

70. Hong SY, Jiang HC, Xu WC, Zeng HS, Wang SG, Qin BL. Bioinformatics analysis reveals the potential role of matrix metalloproteinases in immunity and urolithiasis. *Front Immunol*. 2023;14:1158379. doi: 10.3389/fimmu.2023.1158379

71. Lu P, Chen Z, Wu M, et al. Type I collagen extracellular matrix facilitates nerve regeneration via the construction of a favourable microenvironment. *Burns Trauma*. 2024;12:tkae049. doi: 10.1093/burnst/tkae049

72. Gong SQ, Tang L, Liu Z, et al. NDGA enhances the physicochemical and anti-biodegradation performance of dentin collagen. *Oral Dis*. 2023;29(8):3525-3539. doi: 10.1111/odi.14453

73. Georgopoulou A, Papadogiannis F, Batsali A, et al. Chitosan/gelatin scaffolds support bone regeneration. *J Mater Sci Mater Med*. 2018;29(5):59. doi: 10.1007/s10856-018-6064-2

74. Chachlioutaki K, Karavasili C, Adamoudi E, et al. Silk sericin/PLGA electrospun scaffolds with anti-inflammatory drug-eluting properties for periodontal tissue engineering. *Biomater Adv*. 2022;133:112723. doi: 10.1016/j.msec.2022.112723

ACCSCIENCE PUBLISHING

International Journal of Bioprinting

RESEARCH ARTICLE

Optimizing nozzle design in extrusion-based 3D bioprinting to minimize mechanical stress and enhance cell viability

Lorenzo Lombardi[1], Annachiara Scalzone[2,3]*, Chiara Ausilio[1], Piergiorgio Gentile[2,4]*, and Daniele Tammaro[1]

[1]Department of Chemical, Materials and Production Engineering, Polytechnic School and Basic Sciences, University of Naples Federico II, Naples, Campania, Italy

[2]School of Engineering, Faculty of Science, Agriculture and Engineering, Newcastle University, Newcastle upon Tyne, Tyne and Wear, United Kingdom

[3]Center for Advanced Biomaterials for Health Care, Italian Institute of Technology, Naples, Campania, Italy

[4]Center for Biomaterials and Tissue Engineering, Polytechnic University of Valencia, Valencia, Valencia, Spain

Abstract

Extrusion-based three-dimensional bioprinting is a widely used technique for fabricating cell-laden constructs in tissue engineering and regenerative medicine. However, the mechanical stresses experienced by cells during the printing process can negatively affect their viability. This study examines the influence of nozzle geometry—specifically contraction angle and outlet diameter—on stress distribution and its effects on cell survival. Through a combination of experimental analysis and theoretical modeling, the impacts of nozzle design on the balance between shear and extensional stresses during bioprinting are explored. The findings highlight the importance of optimizing nozzle parameters to minimize mechanical damage and enhance post-printing cell viability. The proposed model provides a framework for guiding nozzle design, offering insights into the development of customized bioprinting strategies that enhance construct fidelity and biological functionality. These results contribute to advancing bioprinting techniques for applications in tissue engineering and regenerative medicine.

Keywords: Customized nozzles; Extensional stress; Extrusion bioprinting

***Corresponding authors:**
Annachiara Scalzone (annachiara.scalzone@iit.it)

Piergiorgio Gentile (pgentil@upvnet.upv.es)

Citation: Lombardi L, Scalzone A, Ausilio C, Gentile P, Tammaro D. Optimizing nozzle design in extrusion-based 3D bioprinting to minimize mechanical stress and enhance cell viability. *Int J Bioprint*. 2025;11(4):315-327. doi: 10.36922/IJB025190182

Received: May 5, 2025
Revised: June 4, 2025
Accepted: June 16, 2025
Published online: June 16, 2025

Copyright: © 2025 Author(s). This is an Open Access article distributed under the terms of the Creative Commons Attribution License, permitting distribution and reproduction in any medium, provided the original work is properly cited.

Publisher's Note: AccScience Publishing remains neutral with regard to jurisdictional claims in published maps and institutional affiliations.

1. Introduction

Three-dimensional (3D) printing, also known as additive manufacturing or rapid prototyping, has been introduced since the late 1980s and provides a new paradigm for engineering design and manufacturing. This technique involves creating objects bottom-up by depositing material in a layer-by-layer pattern pre-designed in digital files, and, as a result, complex structures can be easily fabricated.[1] Over the past decades, additive manufacturing has been widely exploited in tissue engineering, giving rise to a specialized branch known as bioprinting, which integrates 3D printing

technology with cell biology and biomaterial science. This technology has revolutionized regenerative medicine by enabling the fabrication of complex, patient-specific tissues and organoids through the precise deposition of living cells, bioactive molecules, and extracellular matrix components.[2,3] The bioprinting technique is driven by the critical need to address significant challenges in regenerative medicine, particularly organ transplantation and tissue engineering.[4] Therefore, this approach not only offers a potential alternative to alleviate the organ shortage crisis[5] but also advances fields such as personalized medicine,[6] *in vitro* disease modeling, and high-throughput drug screening, offering sophisticated models that can better mimic human tissue architecture and function compared to conventional 2D cultures.[7]

Cell manipulation and deposition are fundamental to tissue engineering, prompting the development of various advanced methodologies to overcome associated challenges.[8] Human tissues exhibit a wide range of cellular densities, reflecting their diverse structures and functions. For example, native human tissues typically have a cell density of 1–3 billion cells per milliliter. This high cell density is essential for maintaining the complex architecture and functionality of various tissues.[9]

Several bioprinting techniques have been developed to process high-density cell-based bioinks. These include inkjet-based, laser-assisted, and extrusion-based bioprinting. Inkjet-based bioprinting, which relies on precise droplet deposition, is advantageous for its high resolution and ability to print multiple cell types simultaneously. However, it is limited by low cell density and potential nozzle clogging. Meanwhile, laser-assisted bioprinting offers superior resolution and cell viability by using laser pulses to transfer bioink onto a substrate; however, it requires complex setups and expensive materials. Among these, extrusion-based bioprinting remains the most scalable and adaptable method for fabricating large-scale tissue constructs with high cell density and structural integrity.[10]

Extrusion-based bioprinting operates by dispensing bioink—typically composed of living cells embedded in hydrogels—through a nozzle under applied pressure to create 3D constructs.[11] Common biomaterials used in this method include hydrogel-based inks, such as gelatin methacryloyl (GelMA), which is widely used due to its biocompatibility, tunable physicochemical properties, and ability to form stable hydrogels upon photo-cross-linking.[12] However, this technique requires highly viscous bioinks, which expose cells to significant mechanical stresses, particularly shear stress and extensional stress, that critically impact cell viability and post-printing function.[13,14] These mechanical forces can disrupt cell membranes, causing damage that adversely affects cell viability and, consequently, the functionality of the printed structures. Indeed, these stresses ultimately reduce cell viability to as low as 45%, depending on bioink viscosity, cell concentration, and nozzle diameter. During the printing process, shear stress primarily affects cells at the narrow tip of the needle.[15] In contrast, extensional stress occurs as cells pass through the constriction in the nozzle, where the channel narrows from the larger diameter of the syringe to the smaller diameter of the needle.[16]

Recent studies suggest that the extensional stress experienced by cells during the bioprinting process plays a significant role in cell membrane rupture, affecting their post-printing viability.[17,18] It is well-established that extensional flow is more effective than simple shear flow in deforming and disrupting droplets, bubbles, or vesicles.[19] Compared to shear stress, extensional stress is more likely to cause severe cell damage.[20,21] Despite this, most existing models of cell damage during bioprinting primarily focus on shear stress and do not adequately address the effects of extensional stress.[22] To fill this gap, Ning et al.[16] explored how both shear and extensional stresses generated during extrusion-based bioprinting contribute to cell damage. However, the role of nozzle design in influencing cell damage remains unexamined. Nozzle geometry, particularly contraction angle and final diameter, has the potential to modulate the relative contribution of shear and extensional stresses, thereby impacting cell viability.

This study hypothesizes that optimized nozzle design, specifically focusing on the contraction angle and final diameter, significantly enhances cell viability by reducing extensional stress during bioprinting. This work aims to investigate the feasibility of producing in-house nozzles that improve cell viability during the extrusion-based bioprinting process. Starting from the identification of a gap in bioprinting, represented by the lack of specific nozzles for different processes, tests were conducted to demonstrate the feasibility of performing a bioprinting process with custom-designed nozzles. Through a combination of simple analytical relationships and a computational cell damage model, a practical tool for optimizing nozzle design to minimize cell damage during the bioprinting process was proposed.

2. Materials and methods

2.1. Nozzle design and manufacturing

The 3D-printed nozzles for the bioprinter were produced using a stereolithography 3D printer (Anycubic Photon Mono X 6Ks, Anycubic, China) based on a digitally

designed model (Figure 1A). The fabricated nozzles are shown in Figure 1B, where their transparent structure enables visual inspection of their geometric accuracy.

Additionally, Figure 1B presents a longitudinally sectioned nozzle, providing a clear view of the internal channel and revealing any potential deviations from the intended geometry. To assess shape fidelity, the nozzle's internal structure was scanned using a confocal microscope (Leica DCM3D, Leica, Germany). The resulting 3D surface measurements are presented in Figure 1C and D, showing a tilted view and a top–down view, respectively. These scans offered accurate spatial data on the internal channel, facilitating the evaluation of manufacturing accuracy and identifying any deformations introduced during the 3D printing process.

A comparison of Figure 1A, B, and D demonstrates that the stereolithography-based 3D printing process achieved high shape fidelity. All nozzles included a converging section defined by a contraction angle (θ) and were further characterized by their inlet diameter (d_1), outlet diameter (d_2), and land length (LL). The values of these parameters for the nozzles fabricated and tested in this study are summarized in Table 1.

2.2. Cell culture

Human telomerase reverse transcriptase immortalized bone marrow stromal cell line Y201 was kindly supplied by Professor Paul Genever (University of York) at passage 84. The Y201 cells were cultured in Dulbecco's modified Eagle medium (DMEM, 1×) supplemented with 10% v/v fetal bovine serum (Sigma-Aldrich, USA) and 1% v/v

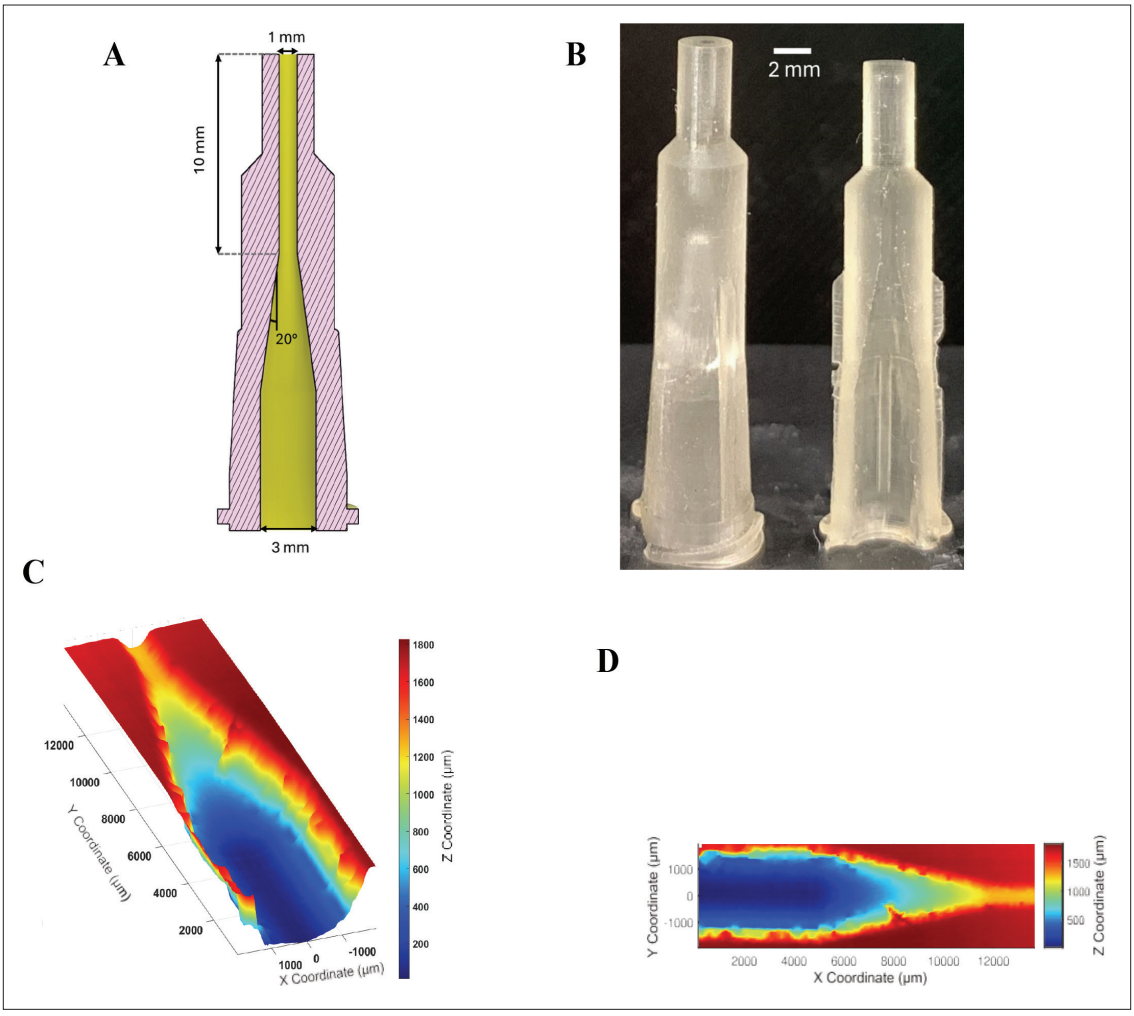

Figure 1. Designed nozzle analysis. (A) A cross-sectional image of the nozzle 3D model. (B) A 3D-printed nozzle model with a d_1 of 3 mm, d_2 of 1 mm, LL of 10 mm, and θ of 20°. (C & D) Confocal microscopy images of the nozzle interior reveal the internal surface topology and roughness, with the color scale representing height variations.

Table 1. Geometrical parameters for different nozzle configurations

d_1 (mm)	d_2 (mm)	LL (mm)	θ (°)
3	0.50	5	40, 80, 90
3	0.50	10	40, 80
3	0.75	5	40, 80, 90
3	0.75	10	40, 80, 90
3	1.00	5	40, 80, 90
3	1.00	10	40, 80

penicillin–streptomycin. The cells were maintained in a 5% CO_2, humidified incubator at 37°C. The Y201 cell line was selected for its reproducibility, robust growth, and common use in tissue engineering applications, including mechanobiology. Although the precise elastic modulus of Y201 cells has not been experimentally measured to date, an estimated value of 1000 Pa was used based on literature data for immortalized mesenchymal stromal cells under similar conditions. Before encapsulation in GelMA, the cells were detached by removing the culture medium and washing with 10 mL of phosphate-buffered saline (PBS). 3 mL of trypsin were added to facilitate detachment. Following incubation, 8 mL of fresh culture medium was added to neutralize the trypsin, and 10 mL of the cell suspension was transferred to a Falcon tube for centrifugation at 1200 rpm for 5 min. After centrifugation, the supernatant was discarded, and the cell pellet was resuspended in 10 mL of DMEM. Once counted, the cell suspension was divided into two separate flasks, and the volume was adjusted to 25 mL using culture medium to maintain appropriate cell density before GelMA encapsulation.

2.3. Gelatin methacrylate hydrogel synthesis

Type A gelatin derived from porcine skin (Sigma-Aldrich, USA) was dissolved in Dulbecco's PBS (DPBS, Gibco, USA) at 50°C to prepare a 10 wt.% uniform solution. Methacrylic anhydride (Sigma-Aldrich, USA) was added at a rate of 2 mL/min under continuous stirring to a final volume of 20 mL. The reaction was performed at 50°C for 3 h, ensuring thorough methacrylation of the gelatin. The resulting solution was then diluted 5× with additional warm DPBS (40°C) to reduce viscosity and facilitate purification. To remove unreacted methacrylic anhydride and by-products, the GelMA solution was dialyzed against deionized water using a 12–14 kDa cutoff dialysis tube for 3 d at 50°C. The purified GelMA was then frozen at −80°C, lyophilized, and stored at −80°C until further use. For cross-linking, a water-soluble photoinitiator, lithium phenyl(2,4,6-trimethylbenzoyl) phosphinate (Tokyo Chemical Industry, Japan), was used at a concentration of 5mg/mL. The GelMA constructs were exposed to ultraviolet light (405 nm, 10 mW/cm^2) for 15 s to initiate cross-linking.

2.4. Bioprinting procedure

Bioprinting was conducted using the Dr. INVIVO 4D2 bioprinter (Rokit Healthcare, Korea). Prior to printing, the syringe and bed temperatures were set to 25°C and 15°C, respectively, to maintain the bioink in a viscous state inside the syringe while ensuring optimal gelation on the printing bed (Table 2). A 9 cm-diameter Petri dish was placed on the bed surface, and the extruding syringe (BD Plastipak 10 mL Hypodermic Syringe, Becton Dickinson and Co., USA) was securely mounted in the extrusion unit. The bioprinter was then calibrated using its semi-automatic calibration system, following the on-screen instructions. The printing velocity was set to 5 mm/s, and with a 14 mm diameter syringe, this resulted in a flow rate (Q) of 7.7×10^{-7} m^3/s. The entire printing process was performed under sterile conditions. The bioprinter's chamber and bed were thoroughly disinfected with 70% isopropanol, and disposable 9 × 9 cm Petri dishes were used as printing substrates. To evaluate nozzle performance, multiple nozzles were tested by bioprinting a single drop. Following extrusion, each drop underwent photocuring at 405 nm, 10 mW/cm^2 for 15 s to initiate cross-linking (Figure 2).

2.5. Evaluation of cell viability and morphology

Cell viability was assessed using a Live/Dead kit (L3224, Thermo Fisher Scientific, UK), which combines Calcein-AM and ethidium bromide to provide two-color discrimination between live (green) and dead (red) cells. Samples were washed twice with DPBS before incubation with the staining solutions: 4 μM ethidium homodimer-1 and 10 μM calcein diluted in DPBS. Samples were incubated for 30 min at 37°C prior to fluorescence imaging using the EVOS M5000 Imaging System (Thermo Fisher Scientific, USA). Multiple images were obtained for each sample, and z-stacks were captured in three distinct regions of the samples. Z-projections were analyzed with Image-J software (NIH, USA). Each experimental trial was conducted in three replicates.

Table 2. Bioprinting parameters used in this study

Parameter	Value
Bed temperature	15 °C
Dispenser temperature	25 °C
Extrusion time	2 s
Printing velocity	5 mm/s
Extrusion height	0.5 mm

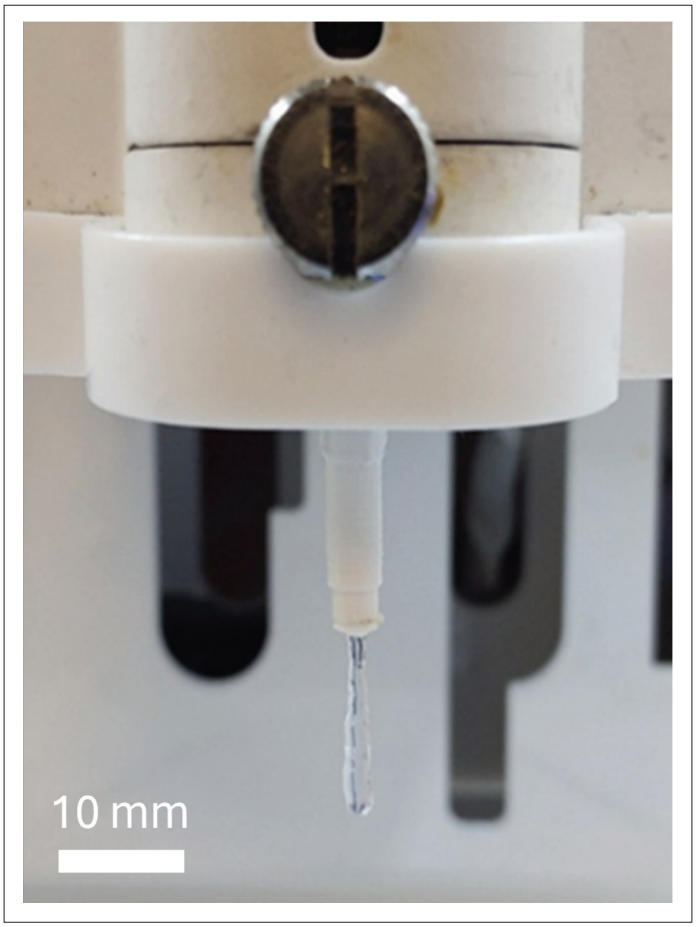

Figure 2. Close-up view of the 3D-printed bioprinter nozzle in operation, dispensing a bioink filament. The transparent nature of the nozzle allows for visual inspection of fluid extrusion.

3. Results and discussion

Extrusion-based bioprinting subjects cells to mechanical stresses, primarily shear stress along the nozzle walls and extensional stress in the contraction zone (Figure 3). While shear stress predominantly impacts cells at the narrow tip of the nozzle, extensional stress is more critical in causing cell damage as the bioink passes through the nozzle's contraction section. Recent studies highlight that extensional stress is often more detrimental than shear stress, as it induces membrane deformation, disrupts the cytoskeleton, and reduces cell viability.[16,22]

To investigate these effects, Y201 cell-loaded GelMA bioink was extruded through different nozzles, and cell viability was assessed 30 min post-printing. Live/dead staining and quantitative viability analysis revealed a consistent correlation between nozzle design and cell viability, highlighting the detrimental effect of larger contraction angles (Figure 4). Live cell counts indicated a higher concentration of viable cells (green) with a smaller nozzle contraction angle, whereas a greater number of dead cells (red) were observed with a larger contraction angle. This suggests that a larger contraction angle induces higher extensional stress, leading to increased cell damage. The elevated stress intensity at greater contraction angles aligns with theoretical models, which predict that wider contraction zones amplify extensional stress, particularly in highly viscous bioinks.[15] This intensified stress potentially contributed to localized membrane rupture and increased cellular damage.

To better interpret the findings and assess the significance of each stress contribution to cellular deformation and damage, a previously described approach was adopted.[16] According to the model, the fraction of dead cells resulting from shear stress at the needle tip is expressed as:

$$D_s = \frac{2\int_0^{\frac{d_2}{2}} r\left(1-e^{-a_1\sigma_s t_s}\right)dr}{d_2^2} \quad \text{(I)}$$

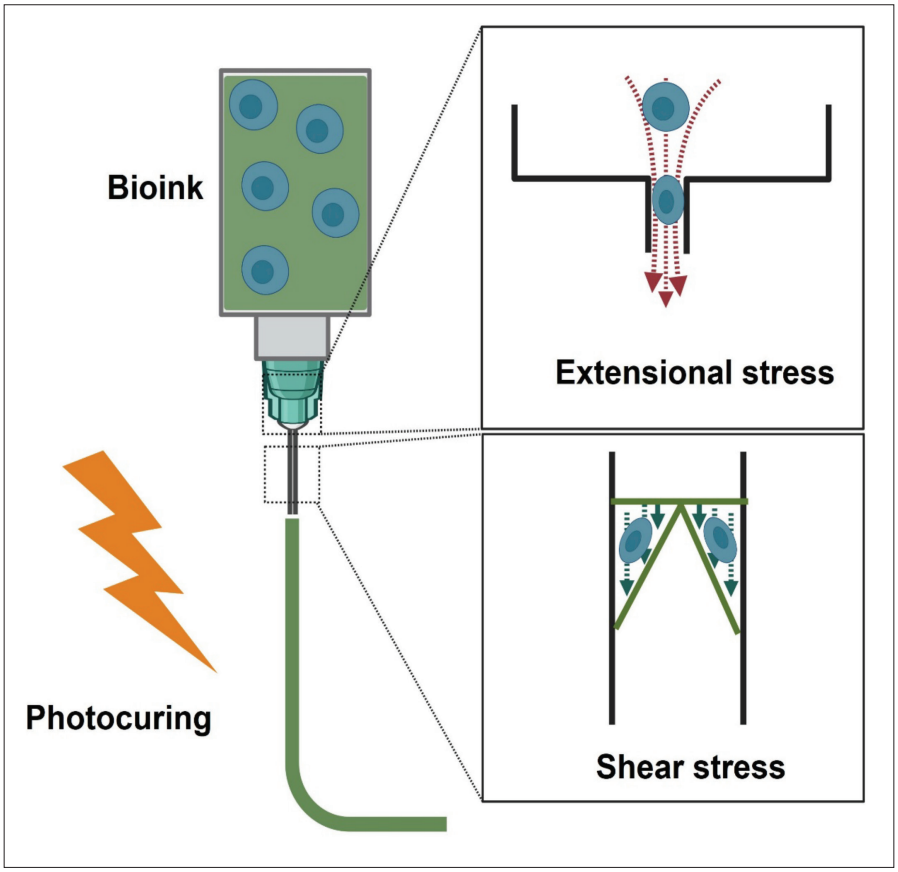

Figure 3. Schematic representation of the extrusion-based bioprinting process with 365 nm photocuring. During extrusion, the bioink undergoes extensional and shear stresses, affecting cellular behavior.

where σ_s is $\frac{\Delta P r}{2}$, representing the shear stress in the capillary after the converging section at a radial position $0 \leq r \leq d_2/2$. Here, L is the capillary length, and ΔP is the pressure drop in the capillary, which can be estimated using Poiseuille's law. The residence time of the cells in the capillary (t_s) is V_c/Q, where V_c is the volume of the cylindrical capillary, and Q is the volumetric flow rate.

In contrast, the damage to cells in the converging section is due to both extensional and shear stresses. The total pressure drop in the converging section can be expressed as:

$$P_c = P_{c,s} + P_{c,e} \quad \text{(II)}$$

where $P_{c,s}$ and $P_{c,e}$ are the pressure drops associated with shear and extensional flows, respectively.[23] According to Cogswell relations,[24] these components are given by:

$$P_s = \frac{2C\dot{\gamma}_c^n}{3n\tan\theta}\left[1-\left(\frac{d_2}{d_1}\right)^{3n}\right] \quad \text{(III)}$$

$$P_e = \eta\tan\theta\dot{\gamma}_c\left[1-\left(\frac{d_2}{d_1}\right)^{3}\right] \quad \text{(IV)}$$

where $\dot{\gamma}_c$ is calculated by $4Q/\pi(d_2/2)^3$, which is the shear rate, and C and n are the consistency index and power-law exponent of the fluid, respectively. A constant viscosity (η) of 0.15 Pa·s, was adopted for this analysis based on literature values obtained under matching GelMA concentration and temperature conditions.[25] The flow was approximated as Newtonian, with a flow behavior index (n) of 1. This assumption is supported by literature data indicating only weak shear-thinning behavior for GelMA under similar conditions; specifically, fitting of published rheological data yields a flow behavior index of approximately 0.92, validating the use of the Newtonian approximation in

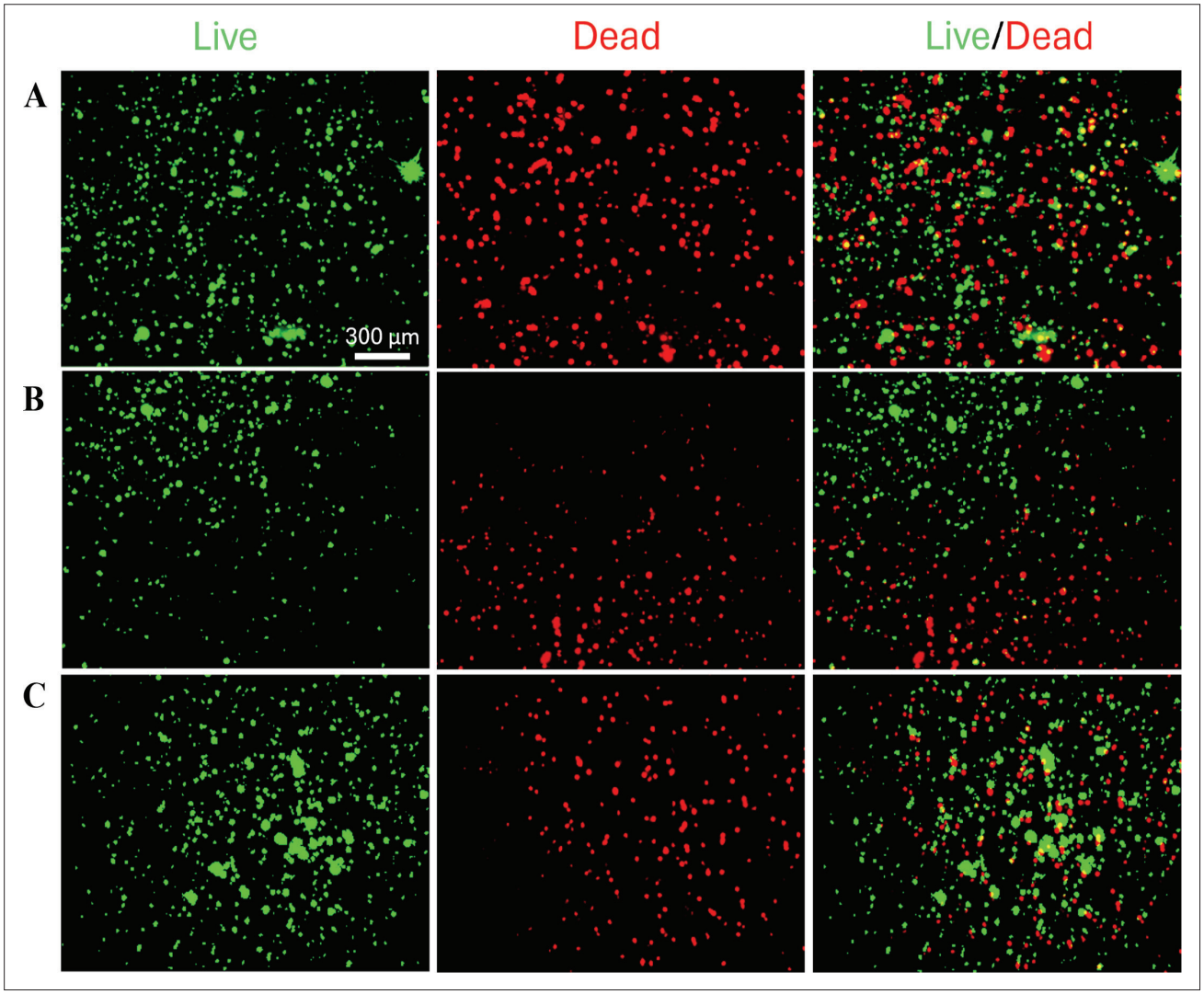

Figure 4. Cell viability assessment using Live/Dead staining 30 min after bioprinting. The images display live cells (green) and dead cells (red) following bioprinting with three different nozzle configurations: (A) d_1 = 3 mm, d_2 = 1 mm, LL = 5 mm, θ = 90°; (B) d_1 = 3 mm, d_2 = 1 mm, LL = 5 mm, θ = 80°; (C) d_1 = 3 mm, d_2 = 1 mm, LL = 5 mm, θ = 40°. Scale bar: 300 μm, magnification: 5×.

the current model. The average extensional stress in the converging section is given by[24]:

$$\sigma_e = (3/8)(n+1)P_c \quad \text{(V)}$$

Using this, the fraction of damaged cells due to extensional stress in the converging section can be expressed as[16]:

$$D_e = 1 - e^{-a_2\sigma_e} \quad \text{(VI)}$$

In **Equations I and VI**, the parameters a_1 and a_2 were obtained by fitting the model to experimental data. The overall fraction of damaged cells in the nozzle is expressed as[16]:

$$D_t = D_e + (1 - D_e)D_s \quad \text{(VII)}$$

Figure 5 demonstrates the fraction of dead cells (D_t) as a function of θ in the nozzle of a 3D bioprinter. Each plot corresponds to a unique combination of d_1, d_2, and LL. The experimental results reveal a clear dependence of D_t on θ, with D_t increasing with θ, and a minimal cell death was observed when θ was 40°. This trend is consistent

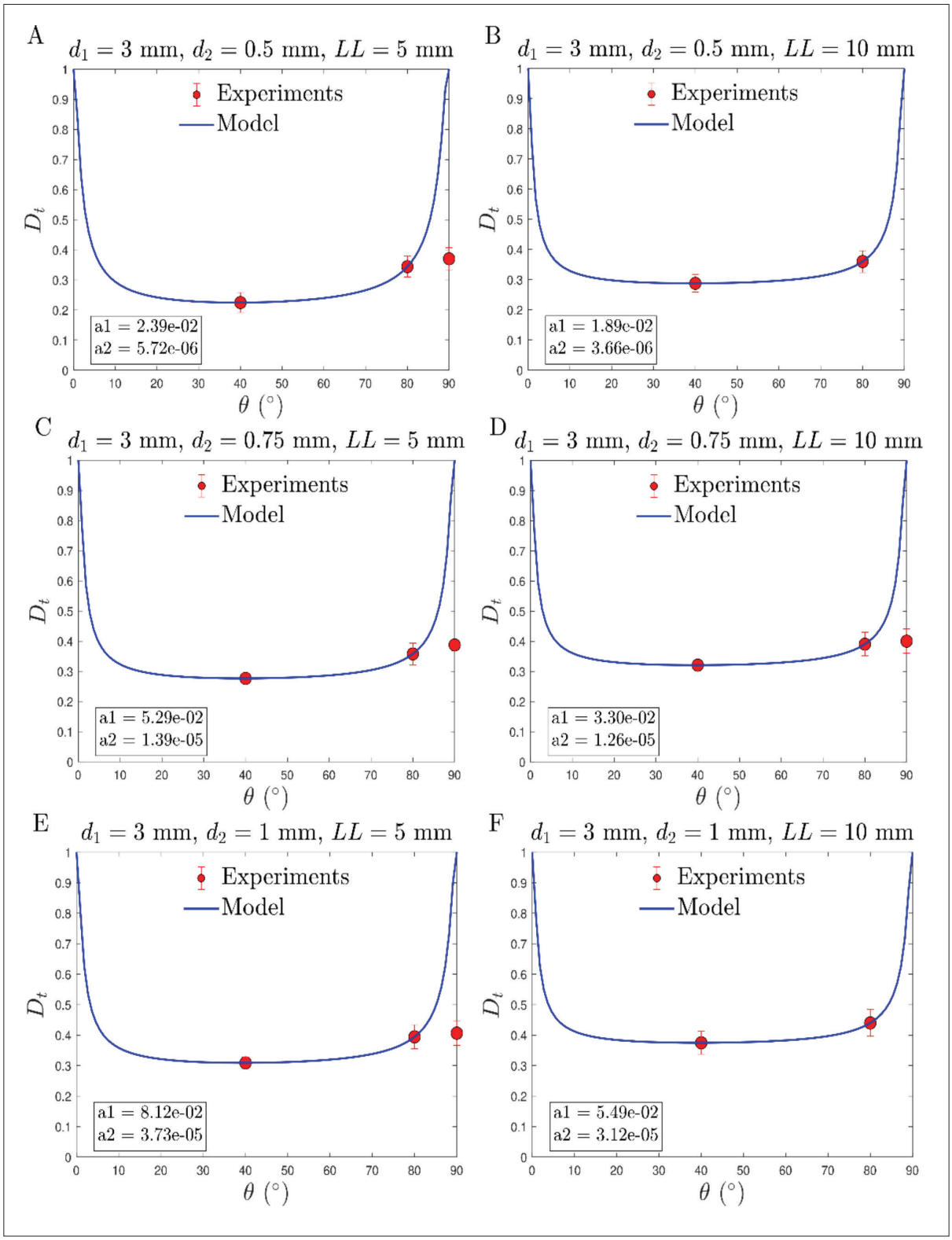

Figure 5. Comparison between experimental data and model predictions for the fraction of damaged cells (D_t) as a function of the converging section angle (θ). Each subplot corresponds to different nozzle geometries with a fixed inlet diameter ($d_1 = 3$ mm): (A) $d_2 = 0.5$ mm, $LL = 5$ mm; (B) $d_2 = 0.5$ mm, $LL = 10$ mm; (C) $d_2 = 0.75$ mm, $LL = 5$ mm; (D) $d_2 = 0.75$ mm, $LL = 10$ mm; (E) $d_2 = 1.0$ mm, $LL = 5$ mm; (F) $d_2 = 1.0$ mm, $LL = 10$ mm.

across all geometric configurations. The effects of d_2 and LL were also apparent in the plots. Increasing d_2 (from 0.5 to 1 mm) generally led to a higher D_t. Similarly, increasing LL (from 5 to 10 mm) enhanced D_t, particularly at larger angles, potentially due to prolonged exposure to stress in the longer capillary.

When comparing subplots Figure 5A and B, the effect of increasing LL from 5 to 10 mm at a fixed d_2 of 0.5 mm becomes evident, with cell damage increasing significantly at higher θ. Similarly, comparing Figure 5A and C at a fixed LL of 5 mm and increasing d_2 from 0.5 to 0.75 mm, a moderate increase in cell damage was observed, highlighting the interplay between d_2 and θ. This comparative trend remains consistent across other geometries.

The model (**Equation VII**) predicted a non-monotonic relationship between D_t and θ. Across all geometric configurations, minimal cell death was predicted at intermediate angles ($\theta \approx 30$–$60°$), whereas extreme angles ($\theta \to 0°$ and $\theta \to 90°$) resulted in significantly higher D_t. This behavior is attributed to the combined effects of shear and extensional stress. At small angles, cells were subjected to prolonged shear and extensional stress within the converging section. As $\theta \to 0°$, the length and volume of the converging section diverge, leading to a sharp increase in cell death. Conversely, at large angles, the abrupt contraction induced significant extensional stress, which damaged the cells. The analytical model predicted a diverging D_t as $\theta \to 90°$.

Deviations between the experimental data and the model were observed when θ is 90°, potentially due to unaccounted factors in the analytical model, such as the intrinsic resistance of cells to deformation. These discrepancies highlight the complexity of the underlying mechanisms and suggest potential areas for improvement in the model.

The observed increase in cell death with increasing LL can be intuitively explained by the combined effects of increased shear stress and prolonged stress duration, as a longer LL provides more time for cells to experience flow-induced stresses. However, the decrease in D_t observed at smaller capillary diameters may appear counterintuitive (Figure 6). One would expect that, as the capillary diameter decreases, the shear stress increases significantly, resulting in higher cell damage. This observation suggests that the duration of exposure to shear stress may play a more critical role than the magnitude of the shear stress in determining D_t.

To assess the relative importance of shear stress, extensional stress, and t_s, it is convenient to introduce three non-dimensional parameters that incorporate the fluid properties and geometrical parameters varied in this study. From a physical perspective, when considering cells as elastic particles, the elastic capillary number, Ca_e, emerges as a key parameter in characterizing their behavior under

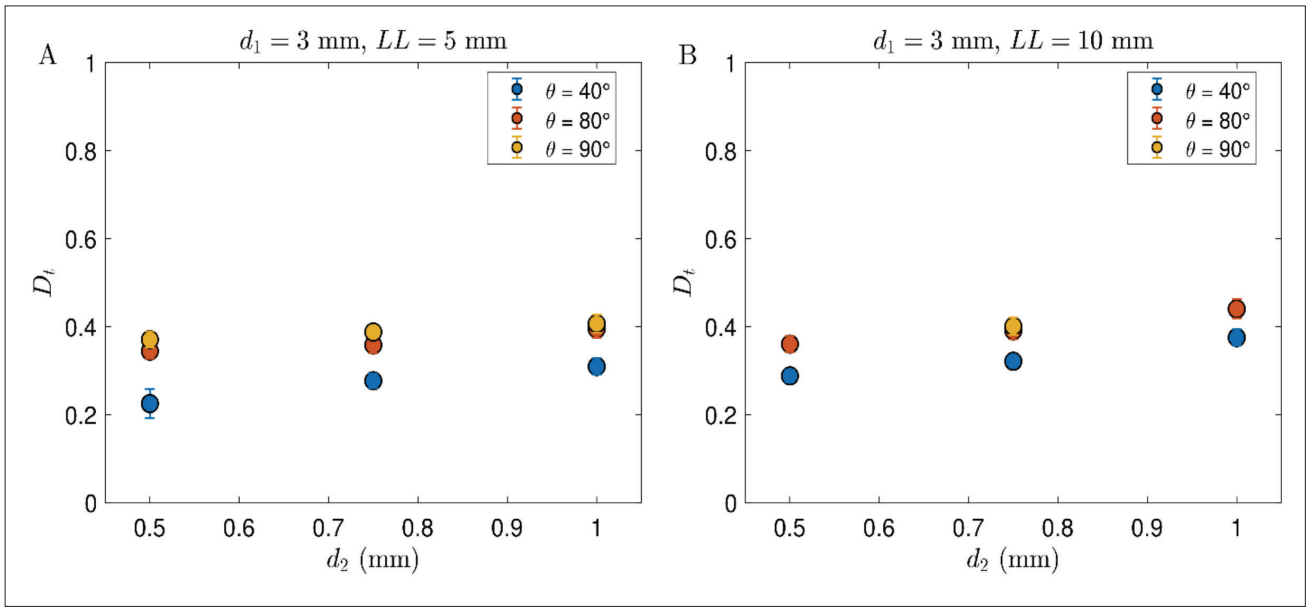

Figure 6. Fraction of damaged cells (D_t) as a function of the outlet diameter (d_2) for different converging section angles (θ). (A) LL = 5 mm. (B) LL = 10 mm.

flow conditions.[26] This dimensionless number quantifies the relative importance of fluid viscous stresses compared to the elastic stresses of the particle. The expression for Ca_e depends on the type of flow. For example, in extensional flow, it is defined as:

$$Ca_e = \eta \dot{\epsilon} / G \quad \text{(VIII)}$$

where G is the elastic modulus of the cell, and $\dot{\epsilon}$ is the elongation rate.

Literature values, supported by compression tests on immortalized human mesenchymal stem cells at similar temperatures,[27,28] indicate an elastic modulus of approximately 1000 Pa for Y201 cells, which was used in this analysis. While this value is an approximation due to the lack of specific mechanical characterization of Y201 cells in the literature, it provides a reasonable estimate for calculating dimensionless capillary numbers. In the case of shear flow, the Ca_e becomes:

$$Ca_s = \eta \dot{\gamma} / G \quad \text{(IX)}$$

where $\dot{\gamma}$ is the shear rate.

In the present study, both types of flow—extensional and shear flows—are encountered. Additionally, a non-dimensional residence time, τ_s, can be defined as:

$$\tau_s = t_s / t_c \quad \text{(X)}$$

where t_s is the actual residence time in the capillary and t_c is calculated by η/G, representing the characteristic timescale of the system.

The fraction of damaged cells can be effectively visualized as a function of the non-dimensional parameters described earlier, as shown in Figure 7A. Data corresponding to a 90° contraction angle was excluded from the analysis because, in this scenario, $Ca_e \to \infty$. In this plot, the color gradient represents the τ_s, and the planes were generated by

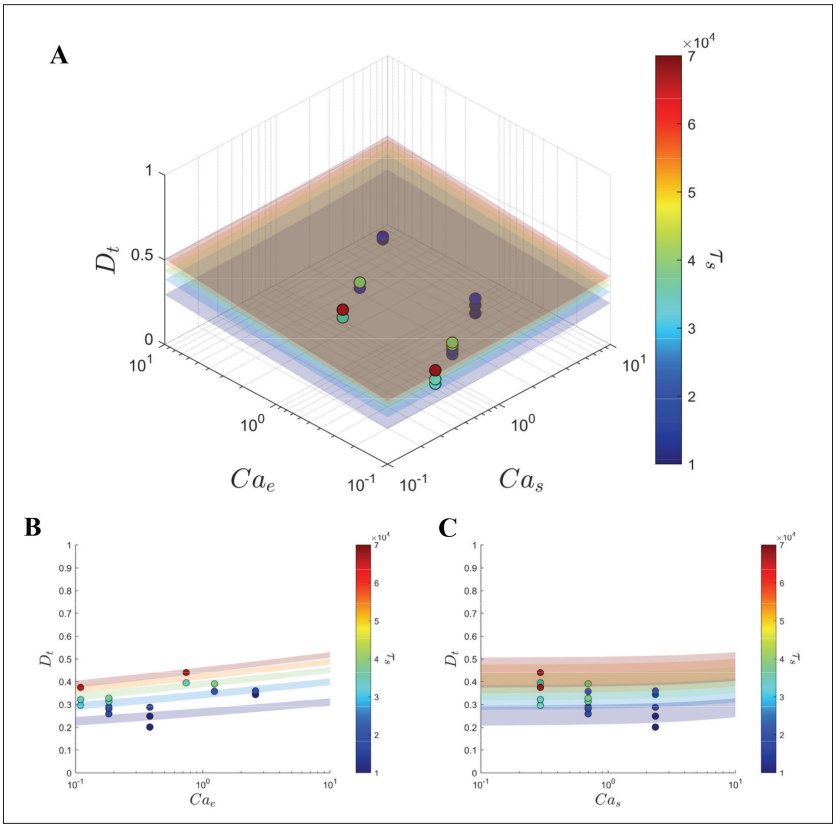

Figure 7. Fraction of damaged cells (D_t) as a function of the elastic capillary numbers in extensional (Ca_e) and shear (Ca_s) flows, with non-dimensional residence time (τ_s) represented by the color scale. (A) A 3D surface plot illustrating the relationship between D_t, Ca_s, and Ca_e, with experimental data points color-coded according to τ_s. (B) A 2D projection of D_t vs. Ca_e, showing how cell damage increases with extensional flow effects. (C) A 2D projection of D_t vs. Ca_s, highlighting the influence of shear flow on cell damage. The colored planes represent fits to experimental data using **Equations XI** and **XII**. The obtained fitting parameters are: $a = 0.0100$, $b = 0.0100$, $c = 0.7000$, $d = 0.0892$, and $e = 0.3629$.

fitting a modified expression for cell damage under shear and extensional stresses. These expressions consider an exponential dependence on Ca_e, Ca_s, and τ_s:

$$D_s = 1 - e^{-aCa_s^b \tau_s^c} \quad \text{(XI)}$$

$$D_e = 1 - e^{-dCa_e^e} \quad \text{(XII)}$$

where a, b, c, d, and e are fitting parameters determined by fitting **Equations XI and XII** to all experimental data.

As illustrated in Figure 7B, an increase in Ca_e resulted in a higher D_t for a given τ_s. This is consistent with the understanding that higher values of Ca_e correspond to greater cell deformation in extensional flows, leading to increased cell damage. The color gradient representing τ_s further highlights that lower residence times are associated with reduced fractions of damaged cells.

In Figure 7A, the effect of increasing τ_s is apparent, with transitions between nearly parallel planes in the parameter space of Ca_e, Ca_s, and τ_s. Conversely, the impact of shear stress was significantly less pronounced, as shown in Figure 7C. The data reveal a weak dependence of D_t on Ca_s for a given τ_s. However, an increase in τ_s still leads to a notable increase in cell damage. This weak correlation between D_t and Ca_s can explain the observed behavior of D_t with varying d_2, as seen in Figure 5. A reduction in d_2 increases Ca_s and, consequently, the shear stress. However, this increase in shear stress is relatively ineffective in deforming and damaging cells, as shown in Figure 7C. Simultaneously, a decrease in d_2 reduces the residence time in the capillary, thereby limiting the exposure of cells to shear stress and ultimately reducing cell damage.

The non-linear dependence of cell deformability on Ca_e, Ca_s, and τ_s is highly influenced by the specific response of cells to these flow conditions, making accurate modeling challenging. The introduction of fitting parameters helps address this complexity. Notably, the greater effectiveness of extensional flows in deforming particles compared to shear flows has been previously highlighted by Grace,[19] also emphasizing the importance of exposure time to shear conditions in determining particle deformation.

4. Conclusion

This study comprehensively examines the influence of nozzle design on cell viability in extrusion-based 3D bioprinting. Through experimental observations and theoretical modeling, it is demonstrated that nozzle geometry—particularly θ and d_2—plays a critical role in modulating mechanical stresses that affect cells. Optimizing these parameters can minimize extensional stress, thereby improving post-printing viability.

The findings indicate that extensional stress, rather than shear stress, is a primary cause of cell damage, particularly in the contraction region of the nozzle. Based on the results, it is recommended that nozzle designs with intermediate θ (30–60°) be used to balance extensional and shear stresses, thus optimizing cell viability. Furthermore, reducing capillary length and d_2 can decrease exposure time to mechanical stress, thereby improving cell survival. These parameters should be prioritized when designing nozzles for sensitive or high-density cell bioinks.

The proposed model helps to understand the relationship between nozzle geometry and stress-induced cellular damage, offering another perspective that can guide future nozzle designs to improve bioprinting results. From an application standpoint, engineering customized nozzles with optimized geometries holds great promise for enhancing bioprinting outcomes, ultimately advancing regenerative medicine and tissue engineering. The findings from this study provide critical insights that can inform the design of next-generation bioprinters capable of producing high-fidelity, cell-rich constructs with enhanced biological functionality.

In conclusion, this study highlights the crucial role of nozzle design in bioprinting. By systematically refining nozzle geometry, it can reduce mechanical stress, enhance cell viability, and improve the overall quality of bioprinted tissues, bringing bioprinting closer to clinical applications in regenerative medicine. With the rise of innovative bioprinting techniques—such as printing within a self-healing support bath that can be subsequently washed away to enable the fabrication of complex structures—it would be highly beneficial to develop long needles capable of penetrating deeply into the support material. Long needles—whose extended capillary length could increase cell exposure to mechanical stress—are increasingly necessary for support-bath-based printing strategies. The current findings on the role of needle length offer a valuable starting point for optimizing such designs.

Acknowledgments

None.

Funding

None.

Conflict of interest

The authors declare they have no competing interests.

Author contributions

Conceptualization: Annachiara Scalzone, Piergiorgio Gentile, Daniele Tammaro
Formal analysis: Lorenzo Lombardi
Investigation: Lorenzo Lombardi, Annachiara Scalzone, Chiara Ausilio
Methodology: All authors
Writing–original draft: Lorenzo Lombardi, Annachiara Scalzone, Chiara Ausilio
Writing–review & editing: Piergiorgio Gentile, Daniele Tammaro

Ethics approval and consent to participate

Not applicable.

Consent for publication

Not applicable.

Availability of data

Data are available upon request via lorenzo.lombardi@unina.it and annachiara.scalzone@iit.it.

References

1. Jim´enez M, Romero L, Dom´ınguez IA, Espinosa MdM, Dom´ınguez M. Additive manufacturing technologies: an overview about 3D printing methods and future prospects. *Complexity.* 2019;2019:9656938. doi: 10.1155/2019/9656938
2. Gu BK, Choi DJ, Park SJ, Kim MS, Kang CM, Kim CH. 3-Dimensional bioprinting for tissue engineering applications. *Biomater Res.* 2016;20(1):1–8. doi: 10.1186/s40824-016-0058-2
3. Jose RR, Rodriguez MJ, Dixon TA, Omenetto F, Kaplan DL. Evolution of bioinks and additive manufacturing technologies for 3D bio-printing. *ACS Biomater Sci Eng.* 2016;2(10):1662–1678. doi: 10.1021/acsbiomaterials.6b00088
4. Bertassoni LE, Bertassoni LE. Bioprinting of complex multicellular organs with advanced functionality—recent progress and challenges ahead. *Adv Mater.* 2022; 34(3):2101321. doi: 10.1002/ADMA.202101321
5. Parihar A, Pandita V, Kumar A, et al. 3D printing: advancement in biogenerative engineering to combat shortage of organs and bioapplicable materials. *Regen Eng Transl Med.* 2021;8:173–199. doi: 10.1007/S40883-021-00219-W
6. Lam EHY, Yu F, Zhu S, Wang Z. 3D bioprinting for next-generation personalized medicine. *Int J Mol Sci.* 2023;24(7):6357. doi: 10.3390/IJMS24076357
7. Mazzocchi A, Soker S, Skardal A. 3D bioprinting for high-throughput screening: drug screening, disease modeling, and precision medicine applications. *Appl Phys Rev.* 2019;6:1–12. doi: 10.1063/1.5056188
8. Chen A, Wang W, Mao Z, et al. Multimaterial 3D and 4D bioprinting of heterogenous constructs for tissue engineering. *Adv Mater.* 2024;36(34):2307686. doi: 10.1002/adma.202307686
9. You S, Xiang Y, Hwang HH, et al. High cell density and high-resolution 3D bioprinting for fabricating vascularized tissues. *Sci Adv.* 2023;9(8):eade7923. doi: 10.1126/sciadv.ade7923
10. Scalzone A, Tonda-Turo C, Ferreira AM, Gentile P. 3D-printed soft hydrogels for cell encapsulation. In: Azevedo HS, Mano JF, Borges J, eds. *Soft Matter for Biomedical Applications.* Royal Society of Chemistry. London, UK; 2021:594–625. doi: 10.1039/9781839161124-00594. Soft Matter Series.
11. Levato R, Jungst T, Scheuring RG, Blunk T, Groll J, Malda J. From shape to function: the next step in bioprinting. *Adv Mater.* 2020;32(12):1906423. doi: 10.1002/adma.201906423
12. Ying G, Jiang N, Yu C, Zhang YS. Three-dimensional bioprinting of gelatin methacryloyl (GelMA). *Bio Des Manuf.* 2018;1:215–224. doi: 10.1007/S42242-018-0028-8
13. Pedde RD, Mirani B, Navaei A, et al. Emerging biofabrication strategies for engineering complex tissue constructs. *Adv Mater.* 2017;29(19):1606061. doi: 10.1002/adma.201606061
14. Tian X, Li M, Chen X. Bio-rapid-prototyping of tissue engineering scaffolds and the process-induced cell damage. *J Biomim Biomater Tissue Eng.* 2013;17:1–23. doi: 10.4028/www.scientific.net/JBBTE.17.1
15. Lucas L, Aravind A, Emma P, Christophe M, Edwin-Joffrey C. Rheology, simulation and data analysis toward bioprinting cell viability awareness. *Bioprinting.* 2021;21:e00119. doi: 10.1016/J.BPRINT.2020.E00119
16. Ning L, Betancourt N, Schreyer DJ, Chen X. Characterization of cell damage and proliferative ability during and after bioprinting. *ACS Biomater Sci Eng.* 2018;4(11):3906–3918. doi: 10.1021/acsbiomaterials.8b00714
17. Bae YB, Jang HK, Shin TH, et al. Microfluidic assessment of mechanical cell damage by extensional stress. *Lab Chip.* 2016;16(1):96–103. doi: 10.1039/C5LC01006C
18. Ning L, Chen X. A brief review of extrusion-based tissue scaffold bio-printing. *Biotechnol J.* 2017;12(8):1600671. doi: 10.1002/BIOT.201600671

19. Grace HP. Dispersion phenomena in high viscosity immiscible fluid systems and application of static mixers as dispersion devices in such systems. *Chem Eng Commun.* 1982;14(3-6):225–277.
doi: 10.1080/00986448208911047

20. Aguado BA, Mulyasasmita W, Su J, Lampe KJ, Heilshorn SC. Improving viability of stem cells during syringe needle flow through the design of hydrogel cell carriers *Tissue Eng Part A.* 2012;18(7-8):806–815.
doi: 10.1089/TEN.TEA.2011.0391

21. Down LA, Papavassiliou DV, O'Rear EA. Significance of extensional stresses to red blood cell lysis in a shearing flow. *Ann Biomed Eng.* 2011;39:1632–1642.
doi: 10.1007/S10439-011-0262-0

22. Boularaoui S, Al Hussein G, Khan KA, Christoforou N, Stefanini C. An overview of extrusion-based bioprinting with a focus on induced shear stress and its effect on cell viability. *Bioprinting.* 2020;20:e00093.
doi: 10.1016/J.BPRINT.2020.E00093

23. Cogswell FN. Measuring the extensional rheology of polymer melts. *Trans Soc Rheol.* 1972;16(3):383–403.
doi: 10.1122/1.549257

24. Cogswell FN. Converging flow of polymer melts in extrusion dies. *Polym Eng Sci.* 1972;12(1):64–73.
doi: 10.1002/PEN.760120111

25. Alam K, Iqbal M, Hasan A, Al-Maskari N. Rheological characterization of biological hydrogels in aqueous state. *J Appl Biotechnol Rep.* 2020;7(3):171–175.
doi: 10.30491/JABR.2020.109994

26. Villone MM, Maffettone PL. Dynamics, rheology, and applications of elastic deformable particle suspensions: a review. *Rheol Acta.* 2019;58:109–130.
doi: 10.1007/S00397-019-01134-2

27. Tan SCW, Pan WX, Ma G, Cai N, Leong KW, Liao K. Viscoelastic behaviour of human mesenchymal stem cells. *BMC Cell Biol.* 2008;9(9):40.
doi: 10.1186/1471-2121-9-40

28. Nikolaev NI, Mu¨ller T, Williams DJ, Liu Y. Changes in the stiffness of human mesenchymal stem cells with the progress of cell death as measured by atomic force microscopy. *J Biomech.* 2014;47(3):625–630.
doi: 10.1016/j.jbiomech.2013.12.004

ACCSCIENCE PUBLISHING

International Journal of Bioprinting

RESEARCH ARTICLE

Three-dimensional bioprinting of gelatin methacryloyl hydrogel with a tri-layered vascularized architecture for full-thickness skin regeneration

Yichen Luo[1], Dan Li[2], Cai Lin[3], Xue Zhou[1], Jien Ma[4]*, and Bin Zhang[1]*

[1]State Key Laboratory of Fluid Power & Mechatronic Systems, School of Mechanical Engineering, Zhejiang University, Hangzhou, Zhejiang, China

[2]Department of Electro-Hydraulic Technology and Equipment Research Center, Binhai Industrial Technology Research Institute of Zhejiang University, Tianjin, China

[3]Department of Burn, The First Affiliated Hospital of Wenzhou Medical University, Wenzhou, Zhejiang, China

[4]Department of Electrical Engineering, College of Electrical Engineering, Zhejiang University, Hangzhou, Zhejiang, China

(This article belongs to the *Special Issue: Advances in 3D Bioprinting*)

Abstract

The skin is the largest organ of the human body and is the primary barrier against external stressors. However, in cases of severe skin damage or pathological conditions, the body's natural physiological repair mechanisms are often insufficient to support effective skin tissue repair and regeneration. Bioprinting, a form of three-dimensional (3D) printing technology, utilizes various biomaterials and cells to construct complex 3D structures, offering the potential to overcome the limitations of conventional tissue-engineered skin and to develop functional skin substitutes. In this study, we developed a 3D bioprinter with excellent printing performance to fabricate vascularized skin substitutes. Through methacrylic anhydride-mediated modification of gelatin, we synthesized gelatin methacryloyl (GelMA) with varying degrees of substitution. The resulting GelMA hydrogel exhibited excellent mechanical properties, swelling ratio, porosity, and rheological properties. To create a hydrogel-multicellular composite bio-ink, we adjusted the concentration of the GelMA solution and co-cultured human immortalized epidermal cells, human foreskin fibroblasts, and human umbilical vein endothelial cells to optimize biological function. Importantly, by fine-tuning the printing parameters, the 3D extrusion-printed lines successfully fused into a continuous membrane, enhancing interlayer bonding and mechanical integrity. This process enabled the construction of a vascularized skin substitute with distinct reticular and papillary layers. In addition, the 3D-printed vascularized skin was implanted into skin defect models established in *BALB/c* nude mice and New Zealand rabbits to investigate its regenerative capabilities. These findings hold significant implications for the utilization of 3D-printed vascularized skin for improving skin injury repair, thereby advancing the field of skin tissue engineering.

Keywords: Three-dimensional bioprinting; Gelatin methacryloyl; Skin injury; Vascularized skin

***Corresponding authors:**
Bin Zhang
(zbzju@zju.edu.cn)

Jien Ma
(majien@zju.edu.cn)

Citation: Luo Y, Li D, Lin C, Zhou X, Ma J, Zhang B. Three-dimensional bioprinting of gelatin methacryloyl hydrogel with a tri-layered vascularized architecture for full-thickness skin regeneration. *Int J Bioprint*. 2025;11(4):328-349. doi: 10.36922/IJB025090069

Received: February 26, 2025
1st revised: March 24, 2025
2nd revised: April 14, 2025
Accepted: April 15, 2025
Published online: April 16, 2025

Copyright: © 2025 Author(s). This is an Open Access article distributed under the terms of the Creative Commons Attribution License, permitting distribution, and reproduction in any medium, provided the original work is properly cited.

Publisher's Note: AccScience Publishing remains neutral with regard to jurisdictional claims in published maps and institutional affiliations.

1. Introduction

The skin is the largest organ of the human body, comprising the epidermis, dermis, and subcutaneous tissue arranged in distinct layers. It serves as a critical protective barrier. However, conditions such as burns, trauma, ulcers, and cancer can cause varying degrees of skin damage. For large-area skin defects, skin grafting is often required. The most common clinical grafting techniques are split-thickness and full-thickness skin grafts. Since these methods use autologous skin, they carry minimal risk of immune rejection and generally result in favorable recovery outcomes. However, their application is limited by the availability of donor sites. Therefore, developing a straightforward method to fabricate skin substitutes remains highly desirable.

Three-dimensional (3D) bioprinting enables the precise spatial organization of biomaterials and cells to create functional skin substitutes. This technology deposits bio-inks layer-by-layer to recreate native tissue microenvironments. Currently, 3D bioprinting skin substitute methods include inkjet printing, laser printing, photopolymerization printing, and extrusion printing. Inkjet printing, the earliest technology applied in bioprinting, was used by Lee *et al.*[1] from Konkuk University to construct dermal and epidermal skin substitutes by printing cell-containing collagen/fibrinogen. Michael *et al.*[2] fabricated a bilayer skin substitute using laser technology, employing a tissue-engineered skin scaffold as a base, on which they printed layers of dermal fibroblasts and keratinocytes and applied it to treat skin defects in mice. However, skin substitutes constructed using inkjet printing often suffer from poor mechanical strength, while the metal absorption substrate used in laser printing may release metal particles under high-energy laser exposure, potentially contaminating the cells. Photopolymerization printing materials must possess photosensitive properties, which limits their application in constructing skin substitutes. Extrusion printing, which uses air pressure or screw extrusion to push bio-ink through a nozzle, deposits it on the platform according to the preset path to form the printed structure.[3–6] Compared to other printing methods, it is highly suitable for constructing complex biological tissues and organs with multiple cells and materials. It is widely applied in research on printing skin substitutes.

Bio-ink selection is critical for skin bioprinting, requiring optimal printability, biocompatibility, and certain mechanical properties.[7–9] Both natural and synthetic biopolymers have been explored for 3D-printed skin constructs. Common natural biopolymers include gelatin, collagen, hyaluronic acid, cellulose, alginate, chitosan, and decellularized extracellular matrix derived from animal tissues. Synthetic biopolymers include polyethylene glycol,[10] polyethylene glycol,[11] polylactic acid,[12] polycaprolactone,[13] and poly(lactic-co-glycolic acid).[14] Gelatin methacrylate (GelMA) is a modified gelatin-based hydrogel renowned for its superior photocrosslinking properties. The hydrogel contains matrix metalloproteinases and arginine-glycine-aspartic acid sequences, facilitating cell migration, adhesion, proliferation, and differentiation. GelMA boasts a range of advantageous properties, including excellent thermosensitivity, outstanding photocrosslinking capability, non-toxicity, and good biocompatibility. Zhao *et al.*[15] reconstructed a multilayer epidermis, which benefited from the sufficient hardness of high-concentration GelMA (20% w/v). According to the research of Xu *et al.*,[16] low-concentration GelMA with large pores, although having weak material stiffness, is beneficial to the growth and proliferation of fibroblasts. This concentration-dependent behavior enables precise layering of skin substitutes.

Currently, research on skin substitutes focuses on constructing skin models with appendage structures, including blood vessels,[17,18] nerves,[19,20] and hair follicles,[21-23] to enhance graft survival and enable more physiologically relevant drug testing. Various bioprinting strategies have been explored to create such complex structures. For instance, Motter *et al.*[24] developed a bilayered skin substitute using collagen-based bio-inks containing human follicle dermal papilla cells, fibroblasts, and keratinocytes, which formed follicular structures during culture. Researchers from Tsinghua University utilized GelMA[25] and Matrigel[26] as matrix hydrogels to encapsulate epidermal stem cells and skin precursor-derived cells obtained from mice. The newly formed skin at the site of skin defects in mice exhibited the formation of vascular and follicular appendages, among other structures. Dai *et al.*[27] from the National Taiwan University utilized a composite hydrogel mixed with polyurea and gelatin as the dermal ink, loaded with human fibroblasts and endothelial progenitor cells, and used keratinocytes as the epidermal ink to construct a pre-vascularized bilayer skin substitute. This was then implanted into a nude mouse defect model to validate its repair and angiogenesis effects. Ma *et al.*[28] employed a composite hydrogel scaffold made of strontium silicate, cold-set gelatin, sodium alginate (SA), and methylcellulose, on which vascular endothelial cells and fibroblasts were deposited to form a pre-vascularized skin (VS) scaffold. *In vivo* experiments demonstrated that this skin substitute actively promoted vascular formation. Barros *et al.*[29] used a mixture of GelMA and SA hydrogels to encapsulate vascular endothelial cells, and GelMA hydrogel to encapsulate fibroblasts, constructing the pre-vascularized and dermal layers layer-by-layer. On the surface of the dermal layer, a multi-layered keratinocyte layer was rapidly formed by

repeatedly dropping a low-concentration gelatin solution containing keratinocytes, ultimately resulting in a pre-vascularized multi-layered skin substitute. Despite these advances, significant challenges remain. Many studies primarily assess endothelial cell viability without fully characterizing *in vitro* microvascular network formation or functionality. Effective vascularization is critical for nutrient delivery, oxygenation, and tissue integration, yet current methods often fail to recapitulate the hierarchical vascular networks found in native skin.

Therefore, this study aimed to construct a multi-layered skin substitute with a vascularized structure. First, we modified gelatin with methacrylic anhydride to obtain GelMA hydrogels with different degrees of functionalization. We then characterized the physicochemical properties, printability, and biocompatibility of the GelMA. By adjusting the concentration of GelMA solutions and optimizing the culture parameters for epidermal cells, dermal cells, and vascular endothelial cells, we prepared a hydrogel-based, cell-compatible composite ink for VS. Using 3D extrusion printing technology, we constructed a stable *in vitro* dermal VS substitute. Additionally, the 3D-printed VS was implanted into skin defect models to further investigate its reparative effects on damaged tissue. We believe this study provides a promising skin substitute for clinical applications and offers valuable insights for future research.

2. Methods

2.1. Three-dimensional bioprinting equipment

We independently developed a 3D bioprinting device. The device comprises a temperature control module, a motion module, a material supply module, and a control module. The constructed 3D bioprinting device is shown in Figure 1,

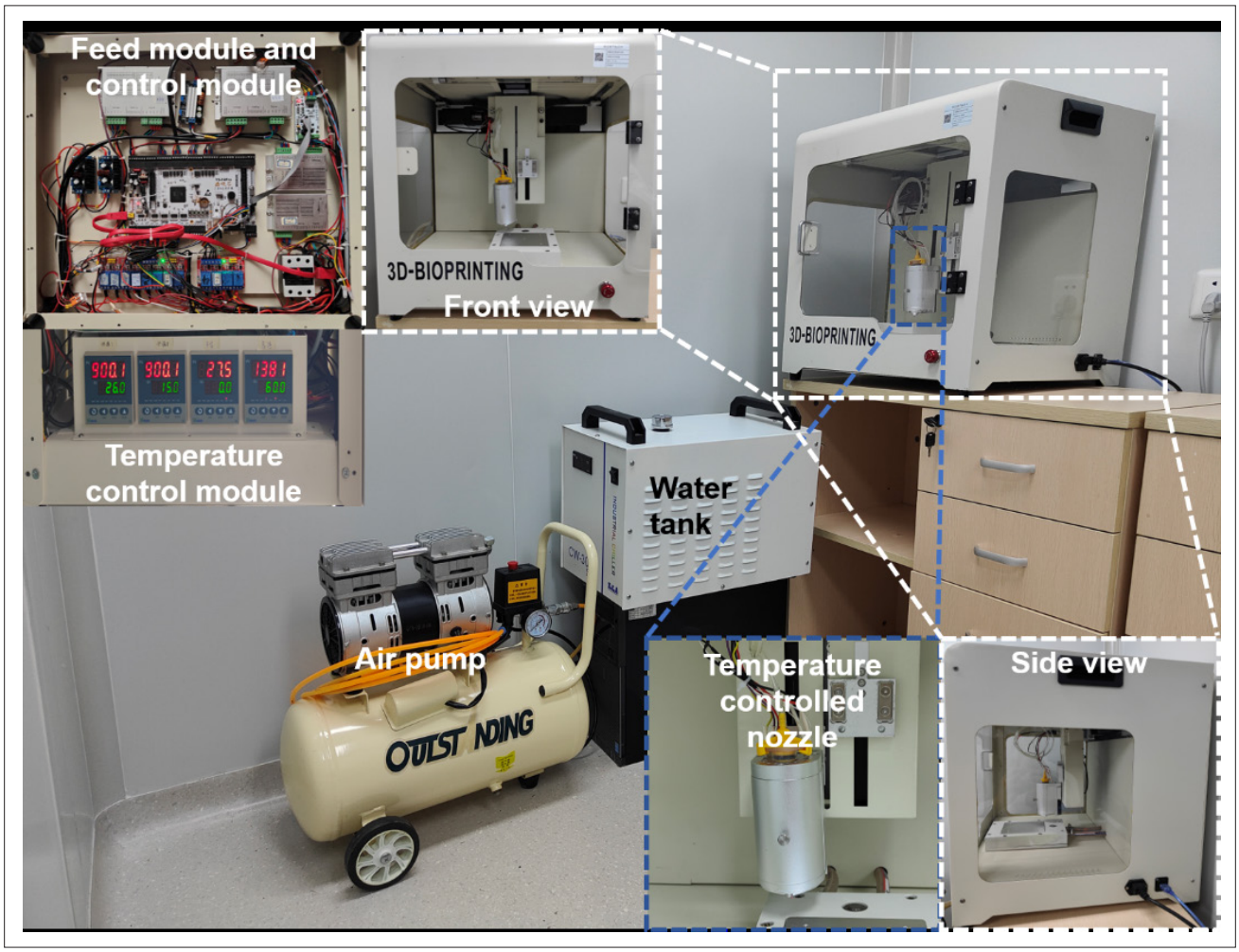

Figure 1. Overall assembly diagram of the printing equipment system.

in which the constant temperature controller of the feeding and control module and the temperature control module are distributed inside the chassis. The overall size of the printing device is 450 mm × 450 mm × 500 mm, and it can be used as a desktop-level printer. The software-controlled host computer system is programmed with LabVIEW software, and the lower computer is developed with an STM32F407 single-chip microcomputer (LabVIEW 2020, STM32F407 single-chip microcomputer 5.0+).

2.2. Print device test

Vasovascular skin substitute printing involves multi-ink printing. The repetitive positioning accuracy of the printing nozzle has a great influence on the final forming quality.[30,31] This equipment was designed with a reset sensor button in the *z*-axis direction, which was used to locate the knife each time the nozzle was replaced. This paper defines the repetitive positioning accuracy of nozzle replacement as D (**Equation I**). The *x*-axis deviation is ΔX, the *y*-axis deviation is ΔY, and n is the number of random tests.

$$D = \frac{\sum_{i=1}^{n}\sqrt{\Delta X^2+\Delta Y^2}\times 100\%}{n} \quad \text{(I)}$$

The SA/gelatin composite hydrogel was printed in the shape of a five-pointed star and an ear using a single-nozzle printing method, and the parameters selected are shown in Table 1. Multi-ink simulation printing of a 10% (w/v) GelMA hydrogel mixed with different ink colors was used to print a multi-layer skin.

2.3. Synthesis of gelatin methacrylate

In this study, GelMA was synthesized using an improved process. Briefly, 10 g of type A gelatin (Sigma, Germany) was dissolved in 100 mL of 0.25 M sodium bicarbonate (Macklin, China) buffer solution with a pH of 8.5. Methacrylic anhydride (Sigma, Germany) was added, and the mixture was stirred at 50°C for 2 h. After that, it was centrifuged at 4000 rpm for 10 min to remove the precipitate, and the clear supernatant extract was retained. Then, 200 mL of warm sodium bicarbonate solution was added to adjust the pH to 7.4, and the mixture was stirred at 40°C for 0.5 h. The solution after the reaction was put into a dialysis bag with a molecular weight cutoff of 12–14 kDa and dialyzed in pure water at 40°C for 1 week. The solution was filtered through a 0.22 μm filter membrane and freeze-dried for 3 days, resulting in white porous foamy GelMA, which was stored at –80°C. The synthesized GelMA was verified using proton nuclear magnetic resonance (JEOL, Japan), and the formula is presented in **Equation (II)**.

$$DoF = \left(1-\frac{lysine\ methylene\ pronton\ of\ GelMA}{lysine\ methylene\ pronton\ of\ Gelatin}\right)\times 100\% \quad \text{(II)}$$

2.4. Characterization of gelatin methacrylate

The GelMA was dissolved in phosphate buffer saline (PBS) containing 0.5% (w/v) lithium phenyl-2,4,6-trimethylbenzoylphosphinate and filtered using a 0.22-μm filter membrane. Finally, GelMA at concentrations of 5% (w/v), 10% (w/v), 15% (w/v), and 20% (w/v) was obtained as the bio-ink, and their mechanical modulus, swelling ratios, porosity, and rheological properties were measured, respectively.

The GelMA mechanical modulus was tested using a dynamic thermomechanical analyzer (DMATAQ800, TA Instruments, United States), employing uniaxial tensile and compression methods. In the tensile test, the sample was made into a dumbbell shape with a thickness of 4 mm, and the cross-sectional area of the middle section of the dumbbell was 16 mm^2. A pre-stress of 0.01 N was applied, and the dumbbell sample was clamped at a strain rate of 0.1 N/min from 0.01 to 10 N until the sample was crushed. In the compression test, the sample was shaped cylindrically with a diameter of 12 mm and a thickness of 2 mm, and the GelMA cylinder was compressed at a strain rate of 10 N/min in the range of 0.01–18 N until the sample was crushed. The swelling sample resulted in a cylindrical hydrogel with a diameter of 12 mm and a thickness of 2 mm. After the sample was prepared, it was immediately weighed as W_0 and then transferred to a 12-well plate of PBS and stored in a 37°C and 5% carbon dioxide incubator for 24 h. After taking it out, the surface water was absorbed using dust-free paper, and the wet weight W_d was measured. The formula is as follows in **Equation (III)**.

$$SR = \frac{W_d - W_0}{W_0}\times 100\% \quad \text{(III)}$$

The GelMA samples were freeze-dried and split into two halves to expose the cross-section, followed by coating

Table 1. Model printing parameters

Structure	Needle model	Extrusion pressure	Print speed	Print temperature	Print layers
Five-pointed star model	30 G	0.7 bar	2 mm/s	27°C	10
Human ear model	30 G	0.9 bar	4 mm/s	27°C	81

with gold-palladium. The morphology of samples was observed using scanning electron microscopy (SU-8010, Hitachi, Japan), with a working distance of 9 mm and an accelerating voltage of 15 kV, and analyzed using ImageJ (**ImageJ2 2.14.0**). The rheological properties of GelMA hydrogel samples were measured using an MCR302 rotational rheometer (Anton Paar, Austria). At a fixed frequency of 1 Hz, the storage modulus (G') and loss modulus (G'') were measured as the temperature decreased from 40 to 4°C at a rate of 5°C/min. To assess the effect of temperature on viscosity, measurements were taken at a constant shear rate of 50/s within the same temperature range. At 25°C, the relationship between the shear rate and viscosity was observed within the 0–500/s range.

2.5. Cell culture

Human umbilical vein endothelial cells (HUVECs), human foreskin fibroblasts (HFF), and human immortalized epidermal cells (HaCaT) (SUNNCELL, China) were cultured in Dulbecco's modified Eagle Medium/Nutrient Mixture F-12 supplemented with 15% fetal bovine serum and 1% penicillin/streptomycin at 37°C and 5% carbon dioxide. HUVECs and HFF were routinely passaged onto a tissue culture flask and were discarded after 8 and 12 passages, respectively, to ensure the representation of key characteristics. Culture media was changed every 2 days, and cells were sub-cultured upon reaching 80–90% confluency.

2.6. Printability and biocompatibility

According to the gel point test results of the GelMA hydrogel, printing tests were carried out for GelMA with concentrations of 5%, 10%, 15%, and 20% (w/v) within the temperature ranges of 13–17, 15–19, 17–21, and 20–24°C, respectively. The printing speed was 6 mm/s, the pressure was 0.1–1.2 bar, the needle type was 30 G, and a two-layer grid structure was printed. A smaller needle diameter typically improves printing resolution but may compromise cell viability due to higher shear stress. Therefore, we selected a 30 G needle to balance resolution and cell viability.

For cell-loaded printing, 10% (w/v) GelMA loaded with HFF cells (1×10^6/mL) were used to print the grid and film structures. During printing, the nozzle temperature was controlled at 18°C, and the low-temperature platform temperature was controlled at 8°C; the needle type selected was 30 G. After printing, the samples were irradiated with 405 nm blue light for 60 s, followed by the addition of culture medium and incubation. Both samples were dyed with LIVE/DEAD® Viability/Cytotoxicity Kit (Thermo Fisher, United States) within an hour after printing and on the 7th day after printing.

2.7. Cell viability and proliferation assays

The HFF cells (1.0×10^6 cells/mL) were added to 5%, 10%, 15%, and 20% concentrations of GelMA. Cell viability was measured by red or green fluorescent dye uptake with LIVE/DEAD® Viability/Cytotoxicity Kit. The samples were cultured in a humidified 5% carbon dioxide incubator at 37°C for 1, 3, and 7 days. The fluorescence images of the cell-laden structures were collected using confocal laser scanning microscopy (ZEISS LSM780, Oberkochen, Germany). Cell proliferation was determined using cell counting kit-8 assays (Medchemexpress, United States). The cells encapsulated in the GelMA were cultured in a humidified 5% carbon dioxide incubator at 37°C for 1, 2, 3, 4, 5, 6, and 7 days. The samples were incubated at 37°C for 2 h, and cell viability was quantified by measuring the ultraviolet absorbance of the solution at 450 nm using a microplate reader (RT-6100, Rayto, China).

2.8. F-actin fluorescent labeling

For the fluorescent staining of F-actin, the samples were washed twice in PBS and then fixed with 4% paraformaldehyde for 10 min at room temperature. After a 3× 10-min rinse with PBS, the samples were permeabilized with 5% Triton-X 100 for 3 min, washed thrice for 10 min in PBS, and stained with TRITC phalloidin for 30 min at 37°C in the dark. It was then washed thrice for 5 min in PBS. The samples were then counterstained with 100 nM 4′,6-diamidino-2-phenylindole (DAPI; Slarbio, China) for 15 min at room temperature in the dark and then washed twice for 5 min in PBS. The images of the samples were observed using confocal laser scanning microscopy (**Leica, Germany**) and analyzed using ImageJ software.

2.9. Western blot

Western blot was performed using a previously described method.[32] The HFF cells (1×10^6 cells/mL) encapsulated in the GelMA were cultured at 37°C and 5% carbon dioxide for 7 days. The samples were lysed in radioimmunoprecipitation assay buffer (Solarbio, China) with phenylmethanesulfonyl fluoride (Servicebio, China) on ice, followed by centrifugation for 5 min (12,000 rpm, 4°C). The protein was quantified using the bicinchoninic acid protein assay kit (HK Bio, China). The supernatants (10 μg protein) were subjected to SDS-PAGE (Servicebio, China) electrophoresis and transferred onto polyvinylidene difluoride membranes (Servicebio, China). The non-specific sites were blocked with 5% fat-free milk in tris-buffered saline with Tween-20 buffer (Servicebio, China) on a shaker at room temperature for 2 h. The membranes were then incubated with primary antibodies for collagen I (1:1000) and GAPDH (1:1000) (Servicebio, China) overnight at 4°C. Subsequently, the membranes were incubated with goat anti-Rabbit immunoglobulin

G, horseradish peroxidase secondary antibody (1:5000) (Abcam, United States) at room temperature for 2 h. Signal detection was performed using an enhanced chemiluminescence detection kit (Servicebio, China), and images were captured using the ChemiDoc XRS+ system (Bio-Rad, United States). Band intensities were quantified using ImageJ software.

2.10. Hematoxylin and eosin and Masson staining, immunohistology, and image analysis

The samples were fixed in 4% paraformaldehyde for 48 h and washed thrice for 5 min in PBS, followed by processing according to standard methods of paraffin wax embedding, dewaxing, and tissue sectioning. The samples were cut into 5-μm-thick sections using a microtome (RM2016, Leica, China) for hematoxylin and eosin (H&E) and Masson (BHBT, China) staining. The sections were immersed in xylene (I-20 min, II-20 min, and III-15 min) and sequentially immersed in ethanol solutions (100% twice, 85%, and 75%) for 5 min. Then, the sections were immersed in a hematoxylin solution for 5 min, washed with tap water for a minute, and dipped in 1% acid alcohol for 10 s. They were further immersed in a bluing solution for 5 min and then in an eosin Y solution for 2 min. After washing with tap water for a minute, the sections were sequentially immersed in a series of ethanol solutions (75%, 85%, 95%, and 100% twice) for 5 min in each solution for dehydration. After two immersions in xylene for 5 min each, the specimens were sealed with Neutral Balsam. Masson staining was performed following the instructions in the manual. Samples were visualized using an optical microscope (DMiLLED, Leica, China).

The sections (5 μm thick) were treated for epitope recovery and then incubated in 10% goat serum in PBS to block non-specific staining for immunohistological analysis. Skin sections were stained with rabbit antihuman (Abcam, United States) diluted in a 1:100 ratio in a 1× PBS solution containing 1% bovine serum albumin at 4 °C overnight, followed by washing and labeling with Alexa Fluor 488 goat anti-rabbit antibody (1:500; Abcam, United States) for an hour at room temperature. The sections were then counterstained with DAPI. The images of the samples were observed using confocal laser scanning microscopy. HUVECs suspension (1×10^6 cells/mL) was mixed with 3% GelMA hydrogels and cultured for 1, 7, and 14 days at 37 °C and 5% carbon dioxide, followed by staining with platelet endothelial cell adhesion molecule-1 (PECAM-1/CD31) immunofluorescence and F-actin fluorescence as described above.

2.11. Cell migration

To assess HUVEC migration in response to GelMA concentration gradients, a test model was constructed using 3–3% and 3–5% GelMA hydrogel pairings in the left–right regions of a 6-well plate. In each well, the left-hand region was filled with 3% (w/v) GelMA hydrogel containing HUVECs at a concentration of 1×10^6 cells/mL, while the right-hand region was filled with blank GelMA hydrogels at either 3% (w/v) or 5% (w/v), depending on the test condition. The culture medium was uniformly added over the hydrogels, and the plate was placed in an incubator. The migration behavior of HUVECs during the subsequent cultivation process was observed under the microscope.

2.12. Single concentration line fusion into the film plane printing

The GelMA with a concentration of 20% (w/v) was printed into samples with groove textures and smooth planar films by extrusion. After photocuring, HaCaT cell suspension was added to the surface and cultured in a 37°C 5% carbon dioxide incubator. Cell adhesion on the sample surface was recorded on the first and fifth days. The samples on the fifth day were used for cytoskeleton and nuclear staining.

2.13. Multi-concentration print layer fusion

The 20% (w/v) GelMA and 5% (w/v) GelMA bio-inks were prepared for layer printing, which was divided into full crosslinked printing (FCP) and partial crosslinked printing (PCP). For FCP, the bottom layer of 20% (w/v) GelMA ink was photocured for 100 s to achieve a higher degree of crosslinking. In contrast, for PCP, the bottom layer of 20% (w/v) GelMA ink was photocured for 10 s to limit crosslinking, while the upper layer of 5% (w/v) GelMA ink was photocrosslinked for 100 s. Frozen sections of the samples were made, and the cross sections were observed under a microscope. Meanwhile, the samples were soaked in the medium for 96 h, and after being taken out, a tensile test was performed using the method described previously.

2.14. Printing of vascularized skin substitutes

The 3% (w/v) GelMA bio-ink containing HUVECs (1×10^6 cells/mL) and blank 5% GelMA bio-ink were prepared. The extrusion method was used to construct circular dermal substitutes with microvascular network structures in the areas of the letters U, J, and ZJU. After 14 days, F-actin staining was performed as described previously. Bio-inks containing HFF cells (1×10^6 cells/mL) in 5% (w/v) GelMA and blank 20% (w/v) GelMA were prepared. The dermal layer and epidermal base were constructed using a layer-by-layer printing approach. After 14 days of culture in a Transwell, H&E and Masson staining were performed as described. Then, a 5% (w/v) GelMA layer containing HFF cells as the reticular layer, a 3% (w/v) GelMA layer containing HUVECs as the papillary layer, and a blank 20% (w/v) GelMA layer as the epidermal basal layer were sequentially built from the bottom up. HaCaT cells (1×10^7

cells/mL) were seeded onto the epidermal base to construct the skin substitute structure, and fluorescence staining was performed after 14 days of culture.

2.15. *BALB/c* nude mice and rabbit full-thickness excisional wound creation and transplantation

All animal procedures were performed according to the protocols approved by the Zhejiang University Health Sciences Animal Care and Use Committee. All experiments were performed following Animal Care and Use Committee guidelines and regulations. All mice were male *BALB/c* nude (n = 12; 4), aged 6 weeks and weighing between 16 and 20 g, were divided into three groups: untreated (control), blank GelMA (BG), and VS. A dimension of 2 × 1 cm^2 ($L \times W$) full-thickness skin was removed from the dorsal midline surface of mice, and a printed hydrogel was implanted into the wound. A Band-Aid was applied to cover the wounds. Then, the wounds were wrapped with sterile gauze and surgical tape to prevent bandage damage and photographed at 0, 1, 2, and 3 weeks, respectively. The mice were euthanized after 3 weeks for analysis. The New Zealand rabbits (n = 12; 3), aged 4 months and weighing between 2 and 3 kg, were divided into four groups: untreated (control), GelMA (blank), epidermis skin (E), and endothelial keratinocyte skin (EK). A dimension of 3 × 3 cm^2 ($L \times W$) full-thickness skin was removed from the dorsal of rabbits, and the wound was treated as described above. The wounds were photographed at 0, 1, 2, 3, and 4 weeks, respectively, and the rabbits were euthanized after 4 weeks for analyses.

2.16. Statistical analysis

All data analyses were performed using the Statistical Package for Social Sciences version 17.0. Statistical significance was analyzed using a one-way analysis of variance, with the Bonferroni method applied for multiple comparison corrections to adjust the p-values of individual tests. A p-value of ≤0.05 was considered statistically significant and marked with an asterisk (*). As the level of significance increased, the number of asterisks correspondingly increased. All data are presented as mean ± standard deviation.

3. Results and discussion

3.1. Replacing the sprinkler head: Positioning accuracy adjustment and print testing

The repeated positioning was randomly tested 10 times. After replacing the inner tube, the repeated positioning accuracy of the printhead in the XY plane was 104.93 μm. Since the printing structure is a single-layer membrane plane, the displacement deviation in the XY plane has a relatively small impact. This accuracy can meet the requirements of constructing a multi-layer skin structure by planar printing (Figure 2A). With excellent formability, the SA/gelatin composite hydrogel[33] was used for the extrusion printing of a five-pointed star model and a human ear model (Figure 2B). The printing system offers stable output and can construct complex, large-volume hydrogel tissues, meeting the requirements for skin substitute printing. The height of the printed multi-layer model can reach over 4 mm (Figure 2C), meeting the thickness requirement of 1–4 mm for human skin.[34] The multi-layer structure of the model is visible, which meets the construction requirements of the multi-layer skin substitutes in this study.

3.2. Characterization of gelatin methacryloyl

The proton nuclear magnetic resonance spectroscopy spectra (Figure 3A) showed the degree of modification of methacryloyl groups to gelatin molecules. The appearance of peaks at δ = 5.4 and 5.7 ppm (the protons of the methacrylate vinyl group of methacryloyl) and the disappearance of peak at δ = 3.0 ppm (the protons of the methylene of lysine signal) indicated that methacryloyl was successfully grafted on the gelatin. Using the peak area normalization method, the degree of functionalization of GelMA samples was improved from 30% to 90%.

The results of tensile and compression tests are shown in Figure 3B and C. The data interval in the strain range of 2–10% was selected to calculate the elastic modulus. It was observed that the mechanical properties of the tensile modulus and the compression modulus of GelMA hydrogels with different concentrations become stronger as the concentration increases. This characteristic provides a theoretical basis for studying the functional performance of skin cells in GelMA with varying concentrations.

Hydrogel swelling is a phenomenon where the hydrogel absorbs water and increases in volume. The swelling is caused by the balance between osmotic pressure and elastic force. The osmotic pressure results from the difference in solute concentration inside and outside the hydrogel. This difference drives water molecules to penetrate from the low-concentration region to the high-concentration region, thus causing the hydrogel to expand. The elastic force comes from the cross-linking points between polymer chains and entropy elasticity, which work together to resist excessive expansion. Figure 3D shows that the swelling ratio of GelMA hydrogels is negatively correlated with the concentration, and there are significant differences among groups. This can directly reflect the pore structure of the hydrogel. Generally, the pore structure is also larger for hydrogel components with a larger swelling ratio.

Scanning electron microscopy (Figure 3E) reveals significant differences in pore structure sizes among groups. Wang *et al.*[35] demonstrated that larger pores facilitate more

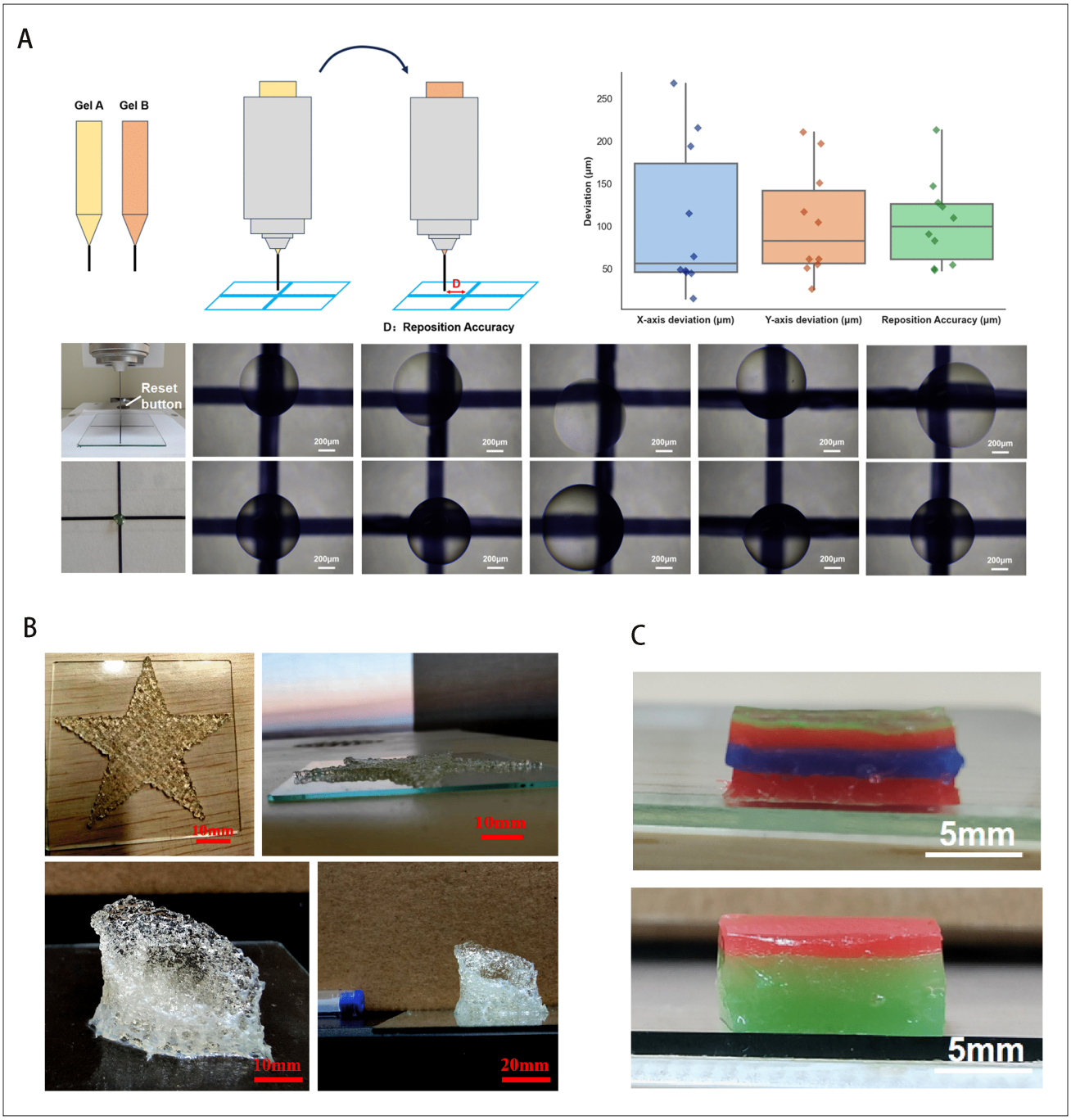

Figure 2. Printing device testing. (A) Principle of the printhead repeatability positioning test, repeatability positioning test values, and representative microscopy images of the repeatability positioning test. Scale bar: 200 μm. (B) Sodium alginate/gelatin printed five-pointed star and human ear models. Scale bar: 10 and 20 mm. (C) Multi-layered structure printing tests of 10% (w/v) gelatin methacryloyl with different dyes. Scale bar: 5 mm.

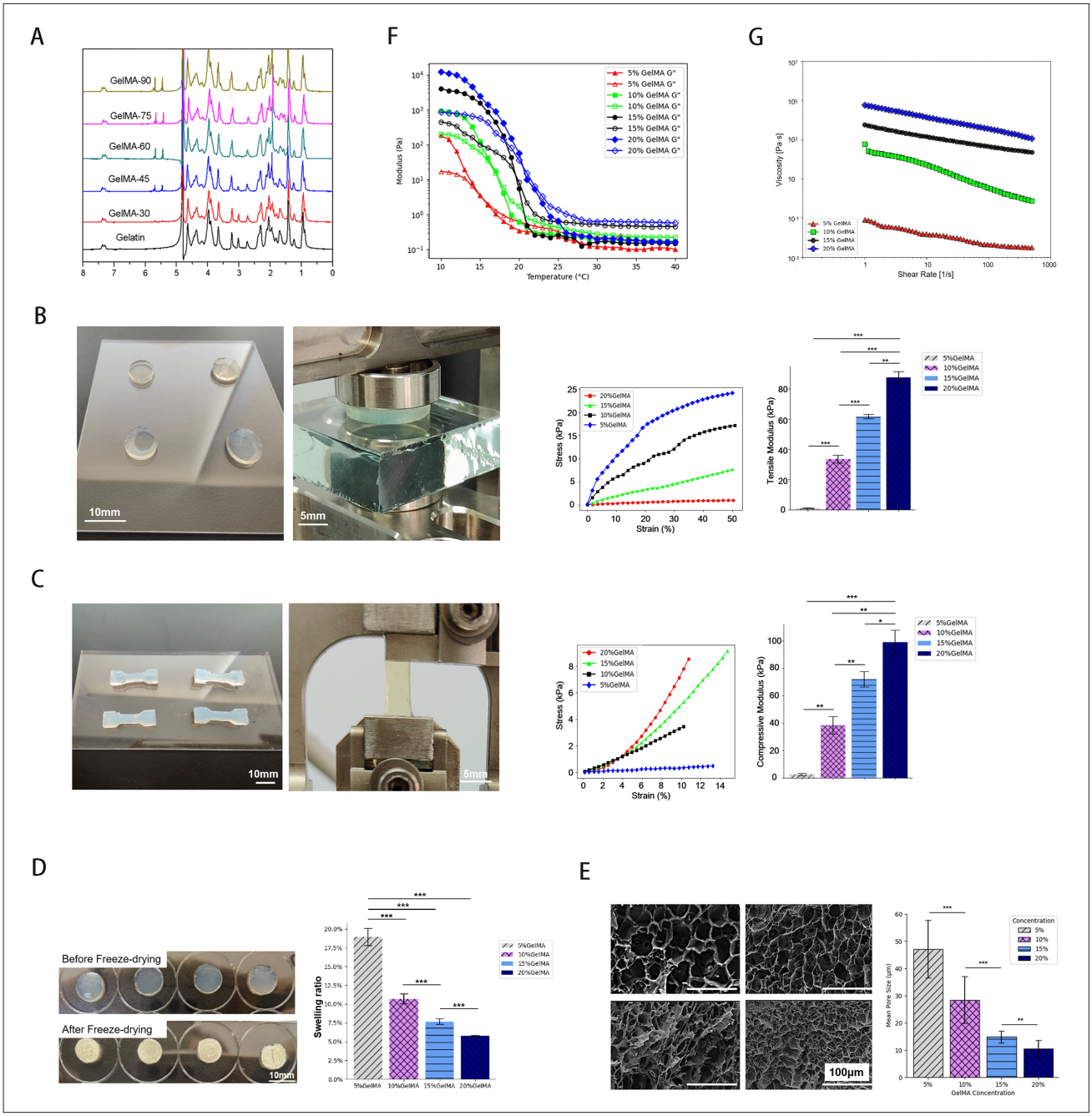

Figure 3. Characterization of gelatin methacryloyl (GelMA). (A) Quantification of the degree of functionalization of GelMA using proton nuclear magnetic resonance spectroscopy. (B) Compression testing of samples, experimental procedures, and quantification of compression modulus. Scale bars: 5 and 10 mm. (C) Tensile testing of samples, experimental procedures, and quantification of tensile modulus. Scale bars: 5 and 10 mm. (D) Samples of GelMA before and after freeze-drying, and quantification of swelling ratio. Scale bar: 10 mm. (E) Scanning electron microscopy images of GelMA: representative electron micrographs and quantification of GelMA porosity. Scale bar: 100 μm, magnification 500×. (F) Determination of gelation point in GelMA hydrogels. (G) Rheological characterization of GelMA. Data were analyzed via a one-way analysis of variance and are shown as mean ± standard deviation (*$p < 0.05$, **$p < 0.01$, ***$p < 0.001$, $n = 3$). For a better overview, only the significant differences are indicated.

efficient transport of nutrients and oxygen while providing sufficient space for cell attachment and extension, enabling them to perform their biological functions. Human fibroblasts and vascular endothelial cells are relatively large, necessitating the selection of hydrogels with larger pores, i.e., lower-concentration GelMA hydrogels, as carriers for printing.

The rheological properties of hydrogels directly influence the material flow and molding quality during the printing process. Rheology refers to the property of hydrogels to deform and recover under external force. Figure 3F indicates that for GelMA of all concentrations, both G' and G'' decrease as the temperature rises, but the decrease rate of G' is greater. The intersection point of G' and G" represents the gel point. When the temperature is lower than the gel-point temperature, $G' > G''$ for the hydrogel shows a solid state; conversely, above the gel point, where $G'' > G'$, it shows a liquid state. Figure 3G shows the "shear-thinning" phenomenon of GelMA hydrogels, where the viscosity decreases as the shear rate increases. This may be because when subjected to a large shear force, the entanglement points of the polymer chains inside the hydrogel are opened, and the structure undergoes directional stretching, resulting in a decrease in viscosity. Kim *et al.*[36] and Won-woo *et al.*[37] have demonstrated the shear-thinning behavior of porous hydrogels.

3.3. Printability and biocompatibility

The printing test results are shown in Figure 4A. All GelMA hydrogels of different concentrations have a printable interval and can form a stable and regular two-layer hydrogel grid structure. When the concentration of GelMA hydrogel increases, its suitable printing pressure and temperature will also increase. For a single concentration of GelMA, if the printing pressure or temperature is too low, over-gelling and irregular extrusion will occur. Conversely, under-gelling and excessive softening extrusion will occur if the printing pressure or temperature is too high.

Cell viability staining (Figure 4B) shows that HFF cells' survival rates for both mesh and membrane structures on Day 0 and Day 7 are greater than 90%, and the cell viability increased with prolonged culture time. This indicates that GelMA is a hydrogel bio-ink with excellent biocompatibility, allowing cells to maintain good vitality. Song *et al.*[38] demonstrated that bio-inks made from GelMA exhibit cell morphology on the first day of cell seeding on the GelMA bio-ink, with cell confluence exceeding 90% by the seventh day.

3.4. Skin cells adapted to composite ink

The HFF cell line is derived from human neonatal foreskin tissue. It has the normal functions of human fibroblasts, such as secreting extracellular matrix and growth factors, and is often used to study the role of fibroblasts in tissue repair and regeneration. HFF cells have a high survival rate at 5%, 10%, 15%, and 20% (w/v) GelMA (Figure 5A and C). On the first day, HFF cells in the 5% (w/v) GelMA group had slightly extended. By the seventh day, almost all cells in the 5% (w/v) GelMA group had extended and multiplied exponentially. In the 10% (w/v) GelMA group, only some cell extension and a small amount of proliferation were observed, while cells in other groups remained spherical. When HFF cells in the 5% (w/v) GelMA group were cultured until the tenth day, the cells extended into long, spindle-shaped structures, and the extension length exceeded 200 μm (Figure 5B). Type I collagen is a fibrous collagen that maintains tissue elasticity in the human dermis and is mainly secreted by fibroblasts. Fibrinogen, as a natural biomaterial with excellent biocompatibility, is a key material for manufacturing skin substitutes in traditional tissue engineering.[39] According to the numerical analysis of the gray value, the content of type I collagen in the 5% (w/v) GelMA group is significantly higher than that in the high-concentration groups but slightly lower than that in the fibrinogen group (Figure 5D). Therefore, among GelMA groups with different concentrations, 5% (w/v) GelMA is more suitable for the functional performance of human skin fibroblasts.

The human skin epidermis mainly comprises keratinocytes, melanocytes, and Langerhans cells. Keratinocytes are derived from the ectoderm and account for over 90% of human epidermal cells. Scholars have conducted extensive research on the culture methods of keratinocytes. Research shows that keratinocytes must be cultured under air–liquid interface conditions to differentiate into a multi-layer epidermal structure *in vitro*.[40-42] Keratinocytes can attach and proliferate on the surfaces of 5%, 10%, 15%, and 20% (w/v) GelMA solidified through manual dropping (Figure 5E). On Day 2, HaCaT cells in the 20% (w/v) group grew in a sheet-like manner. By Day 5, HaCaT cells in the 20% (w/v) group formed a film and covered the hydrogel surface, which was significantly better than the other three groups. Moreover, higher concentration results in better attachment and proliferation of HaCaT cells throughout the growth and reproduction cycle. By Day 10, there was an obvious basal-epidermal layer interface in the 20% (w/v) GelMA group and the collagen group, with clear epidermal structures, and the thicknesses were 53.63 ± 11.27 and 52.26 ± 26.33 μm, respectively. By Day 28, a relatively thick epidermal layer structure could be seen in both groups of samples, with thicknesses of 130.61 ± 8.84 and 119.29 ± 18.87 μm, respectively, both approaching the 200 μm thickness of the human epidermis. However, the printed GelMA group

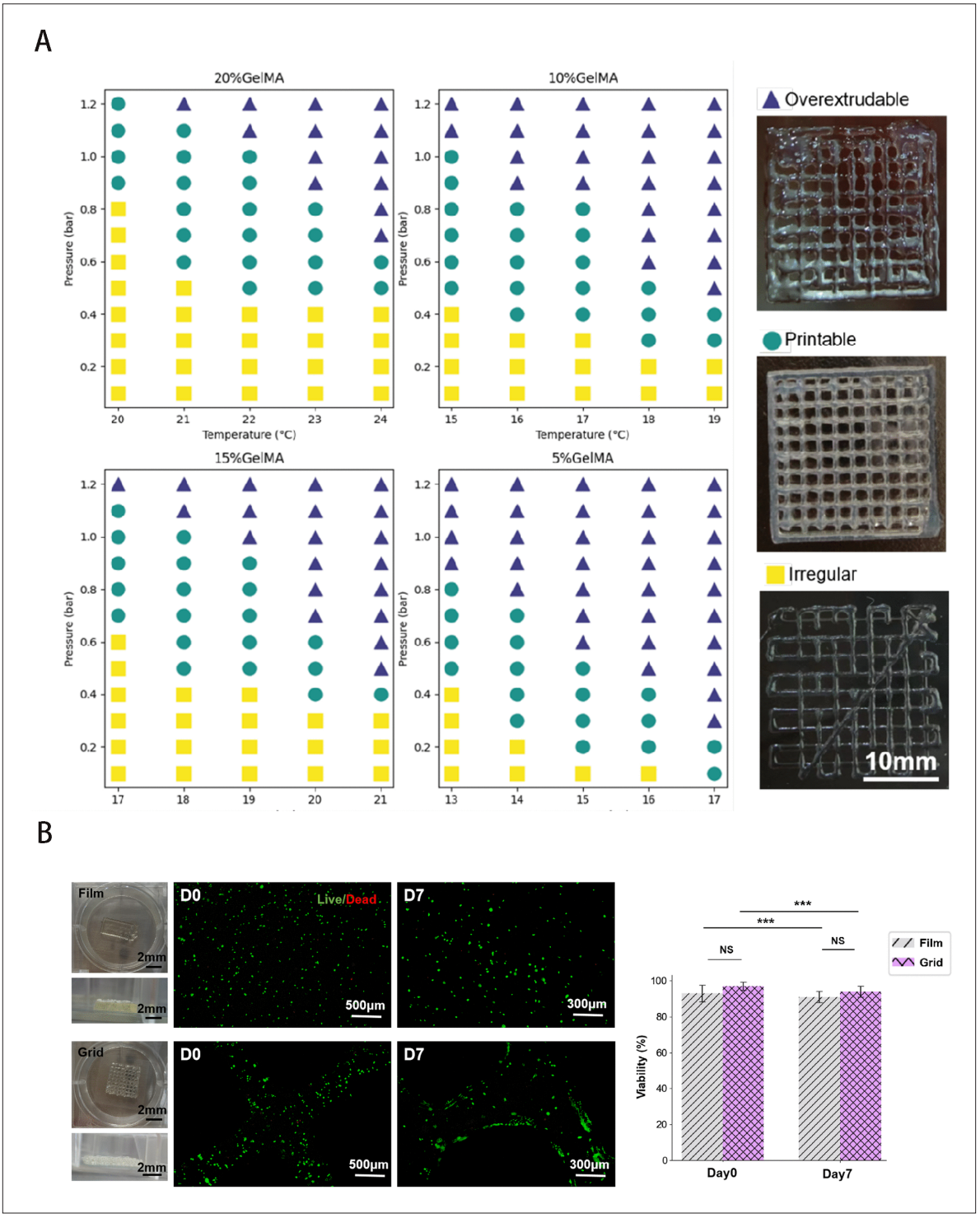

Figure 4. Printability and biocompatibility of gelatin methacryloyl (GelMA). (A) Printing tests of GelMA at different concentrations under varying temperatures and pressures. Overextrudable: GelMA is overly softened during extrusion, and the extruded material cannot maintain its original linear structure after exiting the nozzle, resulting in softening, collapse, and formation of lines with uneven widths. Printable: GelMA is smoothly extruded, forming continuous and stable linear structures. Irregular: GelMA is irregularly extruded, with intermittent or discontinuous extrusion from the nozzle, leading to broken lines and discontinuous structures. Scale bar: 10 mm. (B) Human foreskin fibroblast cells-laden printing examples of 10% (w/v) GelMA in membrane/grid forms, with live/dead staining microscopy images at Day 0 and Day 7, and quantification of cell viability using ImageJ. Data were analyzed via a one-way analysis of variance and are shown as mean ± standard deviation (*$p < 0.05$, **$p < 0.01$, ***$p < 0.001$, $n = 3$). Scale bars: 2 mm, 300 μm, and 500 μm; magnification: 100× and 40×.

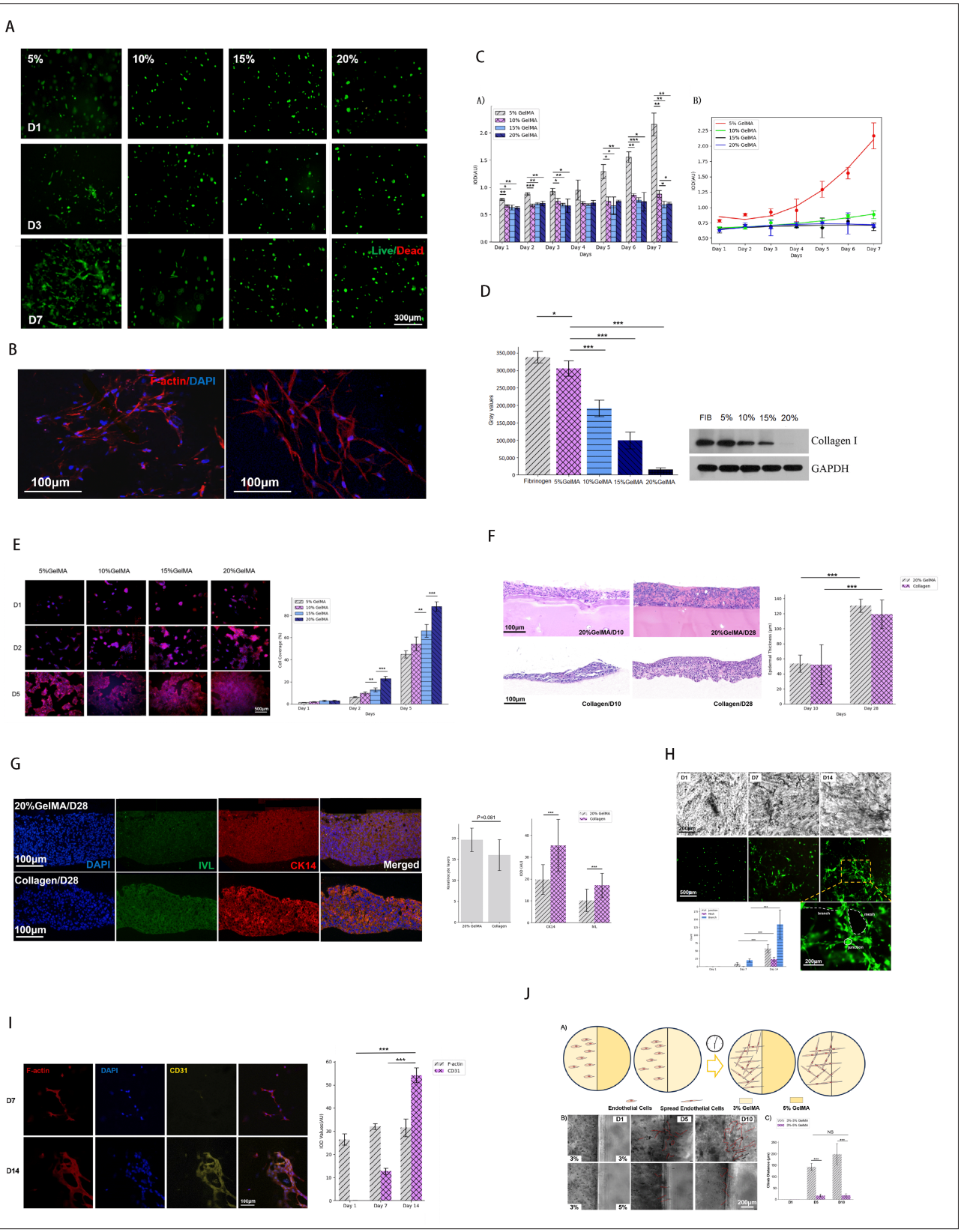
A
5%
10%
15%
20%
D1
D3
D7
Live/Dead
300μm
B
F-actin/DAPI
100μm
100μm
C
A)
5% GelMA
10% GelMA
15% GelMA
20% GelMA
IOD/AU
Day 1
Day 2
Day 3
Day 4
Day 5
Day 6
Day 7
Days
B)
IOD/AU
D
Gray values
Fibrinogen
5%GelMA
10%GelMA
15%GelMA
20%GelMA
FIB 5% 10% 15% 20%
Collagen I
GAPDH
E
5%GelMA
10%GelMA
15%GelMA
20%GelMA
D1
D2
D5
500μm
Cell Coverage (%)
F
100μm
20%GelMA/D10
20%GelMA/D28
Collagen/D10
Collagen/D28
Epidermal Thickness (μm)
Day 10
Day 28
20% GelMA
Collagen
G
20%GelMA/D28
100μm
DAPI
IVL
CK14
Merged
Collagen/D28
100μm
P=0.081
Keratinocyte layers
20% GelMA
Collagen
IOD /AU
CK14
IVL
H
D1
D7
D14
200μm
500μm
200μm
I
F-actin
DAPI
CD31
D7
D14
100μm
IOD Values/AU
Day 1
Day 7
Day 14
J
A)
Endothelial Cells
Spread Endothelial Cells
3% GelMA
6% GelMA
B)
D1
D5
D10
3%
3%
3%
5%
200μm
C)
NS

Figure 5. Skin cell-compatible composite ink. (A) Live/dead staining to assess the viability and stretching of human foreskin fibroblast (HFF) cells in 5%, 10%, 15%, and 20% (w/v) gelatin methacryloyl (GelMA). Scale bar: 300 μm; magnification: 50×. (B) F-actin/4′,6-diamidino-2-phenylindole (DAPI) staining of HFF cells cultured in 5% (w/v) GelMA for 10 days. Scale bar: 100 μm. (C) Cell counting kit-8 (CCK-8) assay to measure the proliferation of HFF cells in 5%, 10%, 15%, and 20% (w/v) GelMA from Day 1 to Day 7. (D) Western blot analysis of collagen I protein expression in HFF cells cultured in 5%, 10%, 15%, and 20% (w/v) GelMA, quantifying collagen I expression using ImageJ. (E) Proliferation of human immortalized epidermal cells (HaCaT) cells on the surface of 5%, 10%, 15%, and 20% (w/v) GelMA, with quantification of HaCaT cells surface coverage using ImageJ. Scale bar: 500 μm. (F) Hematoxylin and eosin staining of HaCaT cells cultured on 20% (w/v) GelMA and collagen surfaces for 10 and 28 days, with quantification of epidermal thickness using ImageJ. Scale bar: 100 μm; magnification: 50×. (G) Immunofluorescence staining of Involucrin (IVL) and Cytokeratin 14 (CK14) in HaCaT cells cultured on 20% (w/v) GelMA and collagen surfaces for 10 and 28 days, with quantification of keratinocyte layer number and IVL/CK14 expression using ImageJ. Scale bar: 100 μm. (H) Fluorescence microscopy images of human umbilical vein endothelial cells (HUVECs) spreading in 3% (w/v) GelMA at D1, D7, and D14, with quantification of junction, mesh, and branch formation using ImageJ. Scale bars: 200, 500 μm; magnification: 50×. (I) Immunofluorescence staining of platelet endothelial cell adhesion molecule-1 (PECAM-1/CD31) and F-actin in HUVECs cultured in 3% (w/v) GelMA at Day 7 and Day 14, quantifying CD31 and F-actin expression using ImageJ. Scale bar: 100 μm. (J) Schematic diagram of the HUVECs migration experiment from 3% (w/v) GelMA to 3% (w/v) GelMA or 5% (w/v) GelMA, with microscopy images of cell migration at D7 and D14, and quantification of migration distance using ImageJ. Scale bar: 200 μm; magnification: 50×. The red dashed lines mark areas where partial cell extension and interconnected microvascular structures are observed. Data were analyzed via a one-way analysis of variance and are shown as mean ± standard deviation ($^{*}p < 0.05$, $^{**}p < 0.01$, $^{***}p < 0.001$, $n = 3$). For a better overview, only the significant differences are indicated. Abbreviations: ALI, air–liquid interface; FIB, fibrinogen; GAPDH, glyceraldehyde-3-phosphate dehydrogenase; IOD, integrated optical density

displayed a more uniform and flat epidermal structure (Figure 5F). Involucrin (IVL) is a highly reactive soluble transamidase substrate protein present in keratinocytes of the epidermis and other stratified squamous epithelia, synthesized in the spinous layer. It is highly expressed in the granular layer and serves as a marker of the terminal differentiation of keratinocytes. Cytokeratin 14 (CK14) is a member of the intermediate fiber albumen type I keratin family that pairs with type II keratin CK5 to form the basic keratin of stratified squamous epithelial keratinocytes, including the epidermis and non-keratinized stratified squamous epithelial mucosa. It is highly expressed in the undifferentiated basal cell layer, containing stem cells, and down-regulated in differentiated basal cell layers. The GelMA and collagen groups had a cell structure of more than 10 layers, with no obvious difference between them, similar to the structure of the human skin epidermis. CK14 and IVL were significantly expressed in the GelMA and fibrinogen groups (Figure 5G). The observed pattern of CK14 and IVL co-expression in the same region may be attributed to the unique microenvironment of *in vitro* culture, where the differentiation process of keratinocytes might not fully replicate the *in vivo* scenario, leading to overlapping expression of markers that are typically spatially separated. The 20% (w/v) GelMA is more conducive to the growth and proliferation of HaCaT cells on its surface, and the keratinocytes on its surface have a high degree of functional expression. Therefore, 20% (w/v) GelMA loaded with HaCaT cells was selected as the bio-ink for constructing the epidermal base layer.

The human vascular system is a complex and precise network that spreads throughout the body and is responsible for transporting oxygen and nutrients to all body parts while removing waste and carbon dioxide through blood circulation. In the subcutaneous tissue, there are arterioles and venules. The arterioles and venules, formed by their branching, pass through the dermis and form a rich microvascular network in the upper layer of the dermis (papillary layer), which supplies oxygen and nutrients to the epidermis.[43,44] The construction of the microvascular network in the upper layer of the dermis is of great significance for the construction of the skin epidermal barrier function. As shown in Figure S1, Supporting Information, HUVECs were cultured in 3% (w/v), 5% (w/v), and 7% (w/v) GelMA hydrogels, respectively, and observed under a microscope every 3 days for imaging. In the 3% (w/v) GelMA hydrogel group, HUVECs began to extend and elongate by Day 3, and extensive microvascular formation was observed by Day 9. In the 5% (w/v) GelMA hydrogel group, slight cell elongation was noted by Day 9, while no significant changes were observed in the 7% (w/v) GelMA hydrogel group. In conclusion, the 3% (w/v) GelMA hydrogel is more suitable for HUVEC culture. When the 3% (w/v) GelMA bio-ink containing HUVEC-green fluorescent protein (1×10^6 /mL) was cultured for 7 days after solidification, the vascular endothelial cells began to spread and intersect to form some connection points, showing a tube-forming phenomenon. On the 14th day, the tube-forming effect of vascular endothelial cells was apparent, producing many branches, connection points, and grid structures (Figure 5H). PECAM-1/CD31 is a transmembrane glycoprotein belonging to the immunoglobulin superfamily. It is a major marker of vascular endothelial cells. It is often used to identify the structure of vascular endothelial cells, and its expression level can reflect the functionality of vascular endothelial cells.[45] During the incubation of 3% (w/v) GelMA bio-ink containing HUVEC-green fluorescent protein (1×10^6 /mL) from 7 to 14 days, the expression of CD31 in vascular endothelial cells increased

(Figure 5I), indicating that when vascular endothelial cells form tubes, the intercellular signal transduction and other interaction mechanisms may occur more intensively, and the cell functional activities are more frequent.

In the 3% (w/v) GelMA samples, HUVECs exhibited spreading by Day 5. Cell migration into the blank hydrogel was observed in the 3–3% (w/v) test samples, with a migration distance of 197.12 ± 47.51 μm by Day 10, nearly equivalent to the length of a single HUVEC. In contrast, no migration was observed in the 3–5% (w/v) test samples, with no significant change in migration distance between Days 5 and 10 (Figure 5J). This may be because the small pore structures within the higher-concentration hydrogel restrict the inward growth of HUVECs. This property supports the controlled construction of microvascular network distribution regions, enabling the formation of a papillary layer with a microvascular network and a reticular layer without one. A VS substitute with distinct layered characteristics can be constructed based on this.

3.5. Single-concentration line fusion for planar film printing and multi-concentration layer fusion

Numerous studies have confirmed that the morphology and mechanical properties of hydrogel substrates have

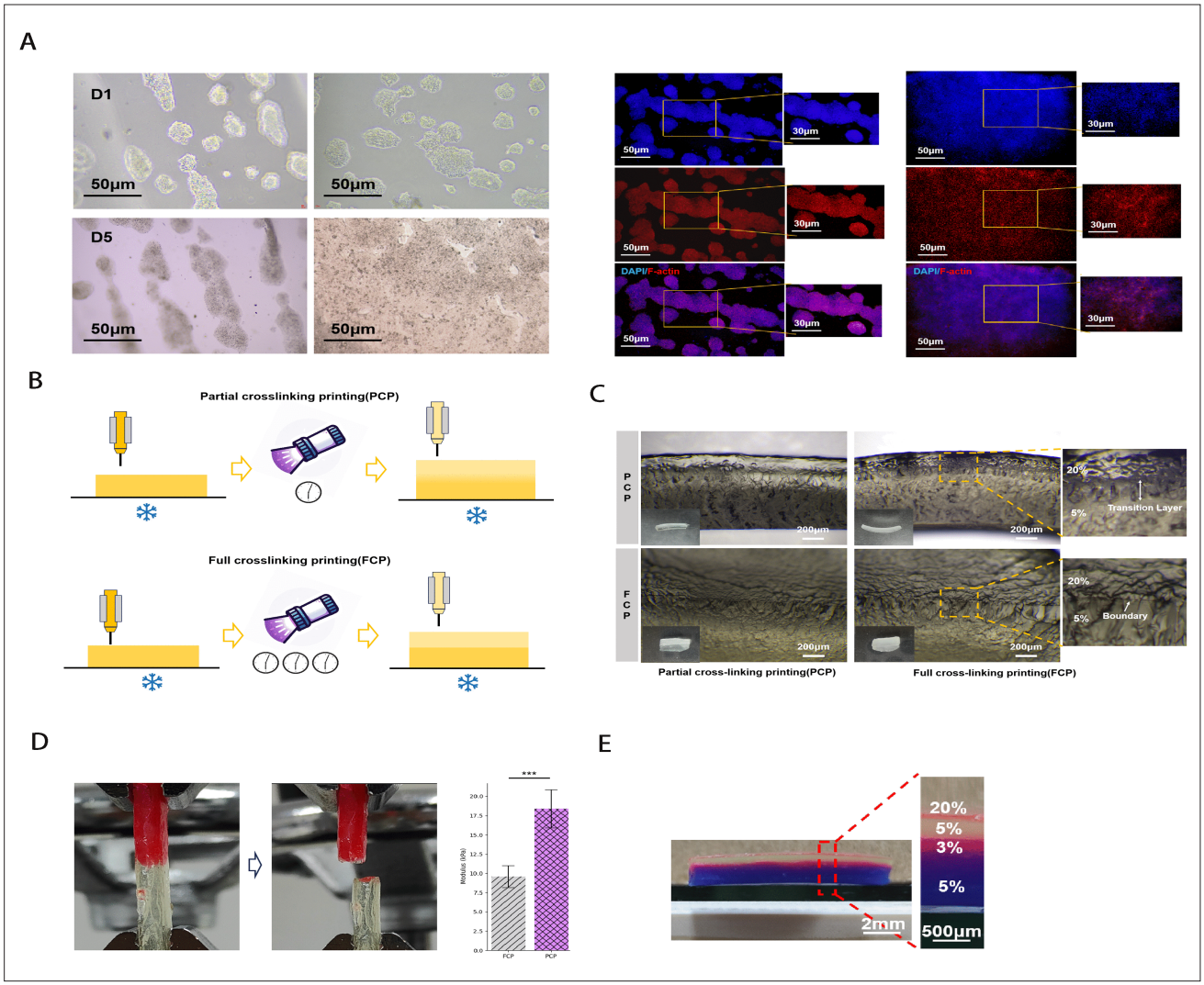

Figure 6. Single-concentration line fusion and multi-concentration layer fusion of gelatin methacryloyl. (A) Exemplary microscope images of human immortalized epidermal cells on grooved and flat substrates at Day 1 and Day 5, with F-actin and 4′,6-diamidino-2-phenylindole staining (DAPI) at Day 5. Scale bars: 50 and 30 μm; magnification: 40× and 100×. (B) Schematic diagram of the partial concentration printing (PCP) and full concentration printing (FCP) layer fusion printing processes. (C) Exemplary microscope images of the interface in PCP and FCP layer fusion printing. Scale bar: 200 μm; magnification: 40×. (D) Tensile testing of the layered fusion printed structures, showing significant differences in tensile modulus between PCP and FCP; statistical significance at ***$p < 0.005$. (E) Multi-layered skin structure model printed using the FCP layer fusion method. Scale bars: 2 mm and 500 μm.

a significant impact on the growth characteristics of cells, such as cell-oriented growth and the degree of differentiation and maturation.[46-48] HaCaT cell suspension was dropped onto the surface of 20% (w/v) GelMA samples with groove textures and smooth planar film, respectively. On Day 1, HaCaT cells on the grooved samples exhibited a clear tendency to grow along the grooves, while cells on the smooth planar membranes appeared scattered and clustered. By Day 5, HaCaT cells on the grooved samples continued to grow along the grooves without forming a continuous layer. In contrast, cells on the smooth planar membranes had largely converged into a continuous layer (Figure 6A).

The multi-concentration layer fusion process is shown in Figure 6B. The cross-sectional images show that the bilayer structure printed using the PCP method exhibited a transitional layer, whereas the structure printed using the FCP method showed a distinct boundary between layers (Figure 6C). To quantify the interlayer bonding strength, the samples were cultured *in vitro* for 96 h to simulate the skin substitute. Tensile testing results (Figure 6D) revealed that the fracture strength at the bonding interface of FCP was 9.6 ± 1.4 kPa, while that of PCP was 18.4 ± 2.5 kPa. The PCP method effectively enhanced the bonding strength between different layers, increasing it by 91.67% compared with the FCP method. The reason may be that the upper-layer ink in the PCP printing method can form an intertwined structure with the lower-layer ink, thus improving the inter-layer bonding strength. Based on the PCP process, a four-layer skin model was printed by mixing pigments into inks of different concentrations (Figure 6E). The thickness of each layer can be controlled to vary, with the thick layer exceeding 1 mm and the thin layer less than

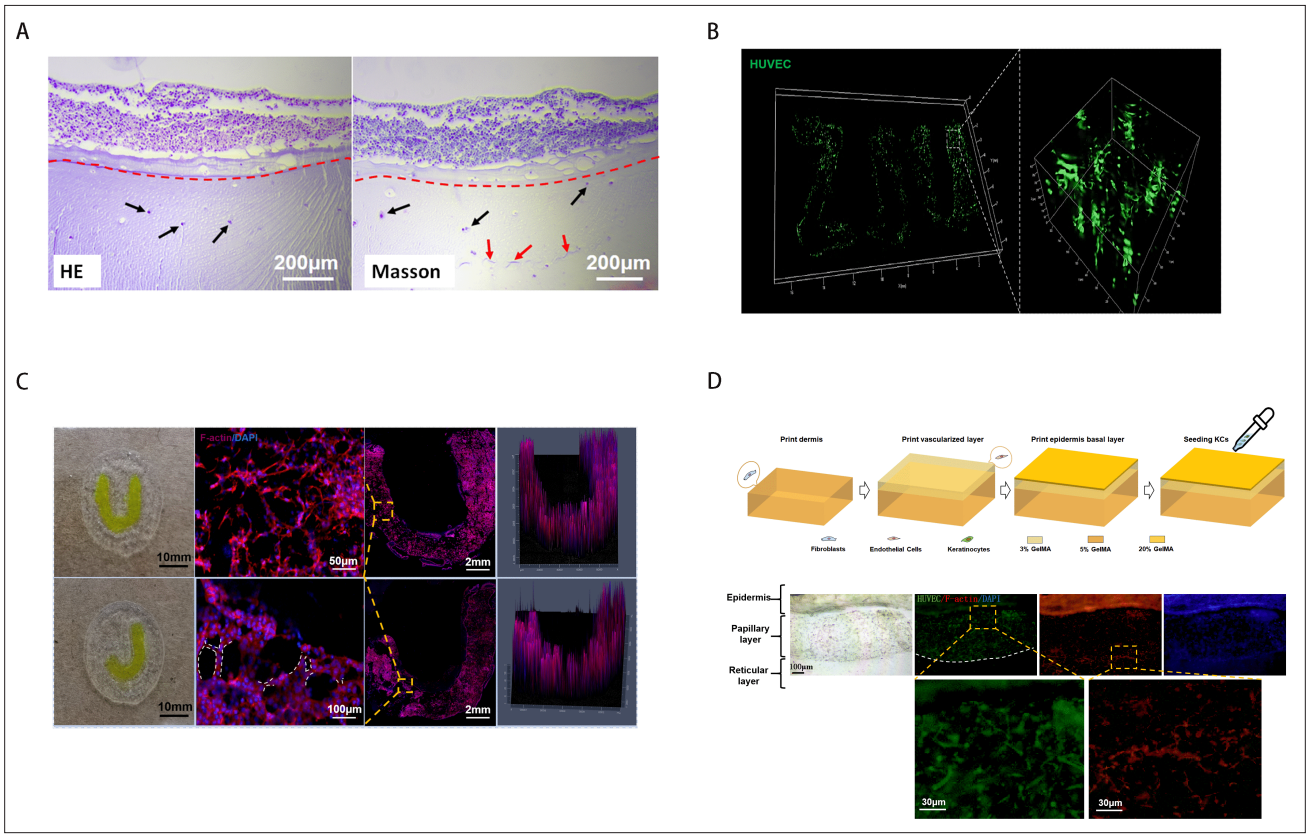

Figure 7. Printed vascularized skin substitutes. (A) Hematoxylin and eosin (HE) and Masson staining of the bilayered skin. The red dashed line indicates the dermo-epidermal junction, black arrows point to fibroblast nuclei in the dermis, and red arrows indicate collagen fibers. Scale bar: 200 μm, magnification: 40×. (B) Laser confocal microscopy images of vascularization in a defined ZJU region within human umbilical vein endothelial cells (HUVECs)-laden gelatin methacryloyl (GelMA). (C) Exemplary confocal microscopy images of self-assembled microvascular networks forming "U" and "J" shapes. The "U" and "J" shapes were printed using 3% (w/v) GelMA containing HUVECs, while the surrounding area was printed using blank 5% GelMA. Scale bars: 10 mm, 2 mm, 50 μm, and 100 μm; magnification: 100×. (D) Schematic diagram of the construction of vascularized dermal skin. Vascularized dermal models were constructed and subjected to immunofluorescence staining: green fluorescent protein for HUVECs, F-actin for HaCaT cells and human foreskin fibroblast (HFF) cells, and DAPI for nuclei of HUVECs, HaCaT cells, and HFF cells. The white dashed line indicates the boundary between the papillary and reticular layers. Scale bar: 30 and 100 μm.

60 μm. The layers exhibited clear morphology and stable printing structure.

3.6. Printing of vascularized dermal skin substitutes

The vascularized dermal skin substitute comprises the epidermis, papillary, and reticular layers. Initially, a bilayer skin substitute of the dermis and epidermis was constructed (Figure 7A), followed by a dermal substitute with a controllable microvascular network distribution (Figure 7B and C). These were then integrated to create a vascularized dermal skin substitute with a dermal-epidermal interface and a microvascular network in the papillary layer (Figure 7D). After 14 days of culture in a Transwell, the bilayer skin substitute exhibited distinct dermal and epidermal layers. The red dashed line in the figure shows the interface between the 20% and 5% (w/v) GelMA layers of the dermal and epidermal layers, respectively. The black arrow in the figure points to the nucleus of fibroblasts in the dermis, and the red arrow points to the collagen fibers stained by Masson, indicating that fibroblasts in this structure have exerted biological functions and synthesized and secreted collagen (Figure 7A). Trujillo *et al.*[49] demonstrated that encapsulating microcarriers seeded with HUVECs into a vascular endothelial growth factor (VEGF)-containing hydrogel resulted in extensive vascular sprouting similar to that observed in Matrigel. In contrast, our study utilized pure GelMA hydrogel without the addition of VEGF and successfully constructed a disc-

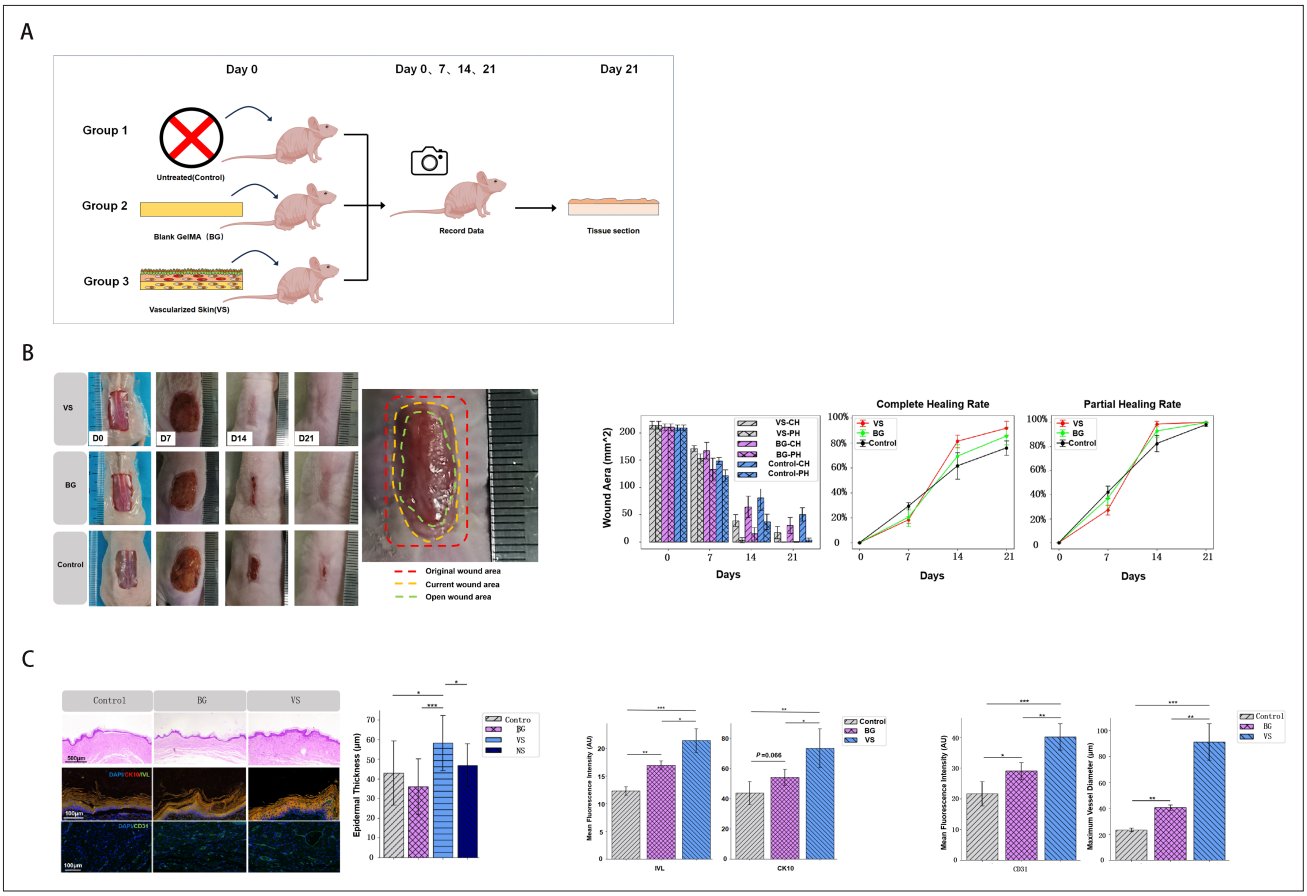

Figure 8. Repair of dorsal skin defects in *BALB/c* nude mice. (A) Flowchart of the dorsal skin defect repair experiment in *BALB/c* nude mice. (B) Photographs of dorsal skin defect healing in *BALB/c* nude mice at Day 0, Day 7, Day 14, and Day 21. By Day 21, the partial healing rates in all three groups were close to 100%, with no significant differences. However, there were significant differences in the complete healing rates of the epidermis among the three groups. The vascularized skin (VS) group showed a significantly higher complete healing rate (91.78 ± 5.42%) compared to the blank gelatin methacryloyl (BG) group (85.51 ± 6.96%) and the control group (75.99 ± 5.81%). (C) Hematoxylin and eosin (HE) and immunohistochemical staining of the healed dorsal skin defects in *BALB/c* nude mice. HE indicated significant differences in epidermal thickness between the VS and other groups. The expression of involucrin (IVL) and cytokeratin 10 (CK10) proteins in the newly formed epidermis of the dorsal skin showed significant differences between the VS group and the control and BG groups. Additionally, platelet endothelial cell adhesion molecule-1 (PECAM-1/CD31) expression and the maximum vascular diameter in the newly formed skin significantly differed between the VS group and the control and BG groups. Data were analyzed via a one-way analysis of variance and are shown as mean ± standard deviation (*$p < 0.05$, **$p < 0.01$, and ***$p < 0.001$, $n = 3$). For a better overview, only the significant differences are indicated. Scale bars: 100 μm and 500 μm; magnification: 100× and 40×. Abbreviations: CH, complete healing; PH, partial healing.

shaped dermal substitute featuring microvascular network structures in the shapes of "U," "J," and "ZJU" letter patterns (Figure 7B and C). After 14 days of culture, the tube-forming phenomenon was evident within the letter structures, with distinct interconnected branches and grid structures. The microvascular network was well-formed and confined to the areas of lower-concentration ink, without migrating to regions of higher-concentration ink. The structures marked by the white dotted line represent the tube-forming branches, indicating that the lumen diameter of the self-assembled microvessels is between 5 and 20 μm. From the fluorescence staining of the structure of the constructed skin substitute (Figure 7D), it can be seen that each layer is stratified. The cells in the reticular, papillary, and epidermal layers are orderly distributed according to the layer structure. Among them, the HFF cells in the reticular layer and the HUVECs in the papillary layer are spread and elongated.

3.7. Validation of printed vascularized skin substitutes in mice

BALB/c nude mice are an immunodeficient experimental animal model that shows no rejection reaction to many foreign tissues and cells.[50] Moreover, *BALB/c* nude mice have completely hairless skin, making them a suitable experimental animal for skin-healing evaluation.[51] The skin injury repair experiment process in *BALB/c* nude mice is illustrated in Figure 8A. The healing progress of the dorsal wounds was regularly photographed and recorded, and ImageJ was used to quantitatively measure the wound areas of complete and partial healing. At 21 days, the partial healing rates for all three groups were close to 100%, with the VS group at 100 ± 0%, the BG group at 99.75 ± 0.51%, and the control group at 98.08 ± 1.46%. However, there were significant differences in the degree of complete epidermal healing. The VS group had a significantly higher complete healing rate (91.78 ± 5.42%) compared to the BG group (85.51 ± 6.96%) and the control group (75.99 ± 5.81%) (Figure 8B). This phenomenon may be because the VS substitute contains fibroblasts and vascular cells, which can secrete cell growth factors to attract autologous cells to migrate to the wound, thus accelerating the healing process. Additionally, the upper epidermal structure can enhance the recruitment of autologous epidermal cells, effectively promoting epidermal regeneration. Wei *et al.*[52] developed miR-17-5p-engineered small extracellular vesicles (sEVs17-OE) and encapsulated them in GelMA hydrogel for treating diabetic wounds. Gel-sEVs17-OE effectively accelerated wound healing by promoting angiogenesis and collagen deposition. Cytokeratin 10 (CK10), a type I keratin and intermediate filament protein, is involved in the keratinization process of the skin, helping to maintain skin integrity and barrier function. Its expression level reflects the degree of keratinocyte differentiation. By Day 21, all three groups exhibited "ridge" structures in the epidermis, but there were differences in thickness. The epidermal thickness in the VS group was significantly greater than that in the other two groups, and the expression of IVL and CK10 in the VS group was higher than that in the other two groups, indicating that the epidermal reconstruction in the VS group was superior. This might be due to the VS group's faster healing speed and earlier entry into the epidermal-reconstruction stage. In addition, the vascularized dermal skin substitute contains an epidermal layer. The epidermal cells of the layer perform biological functions such as extracellular matrix secretion in the early healing stage, resulting in a better-matured healed epidermal layer. The CD31 fluorescence intensity and maximum vascular aperture in the VS group were higher than those in the other two groups. This may be because the cells in the vascularized dermal skin substitute continuously secrete cytokines and extracellular matrix during the healing process, accelerating the onset of biological functions and promoting the vascularization process of the newly-formed skin (Figure 8C). Zhang *et al.*[53] investigated using GelMA-HAMA-fibrin as a scaffold material, with human keratinocytes, fibroblasts, and umbilical vein endothelial cells as seed cells. They conducted a full-thickness skin wound healing experiment in a nude mouse model, and the results demonstrated that the printed organoid hydrogel significantly accelerated wound closure rates and improved epithelial regeneration in the nude mice.

3.8. Validation of printed vascularized skin substitutes in rabbits

Previous studies have shown that GelMA hydrogel positively affects the repair of full-thickness skin defects in rabbits.[54-56] The process of skin injury repair in New Zealand rabbits is illustrated in Figure 9A. The healing progress of the wounds was regularly photographed and recorded, and ImageJ was used to quantitatively measure the wound healing rate (Figure 9B). By Day 28, all groups except the untreated group had completely healed. By Day 21, the EK group had fully healed, while the untreated group (control), GelMA (Blank) group, and E group had healing rates of 96.43 ± 0.71%, 98.16 ± 0.46%, and 99.48 ± 0.38%, respectively. The VS and bilayer skin groups showed significantly higher healing rates than the other groups, indicating faster healing speeds. On Day 28, H & E staining was performed on the newly formed skin tissue and the host's native skin tissue (Figure 9C). The EK group showed significantly superior results compared to the other groups. The epidermal layer had developed a "ridge"-like structure and papillae, which were tightly integrated with the dermal layer. Additionally, melanocyte-like cells were observed in the basal layer. The E group also exhibited a "ridge"-like

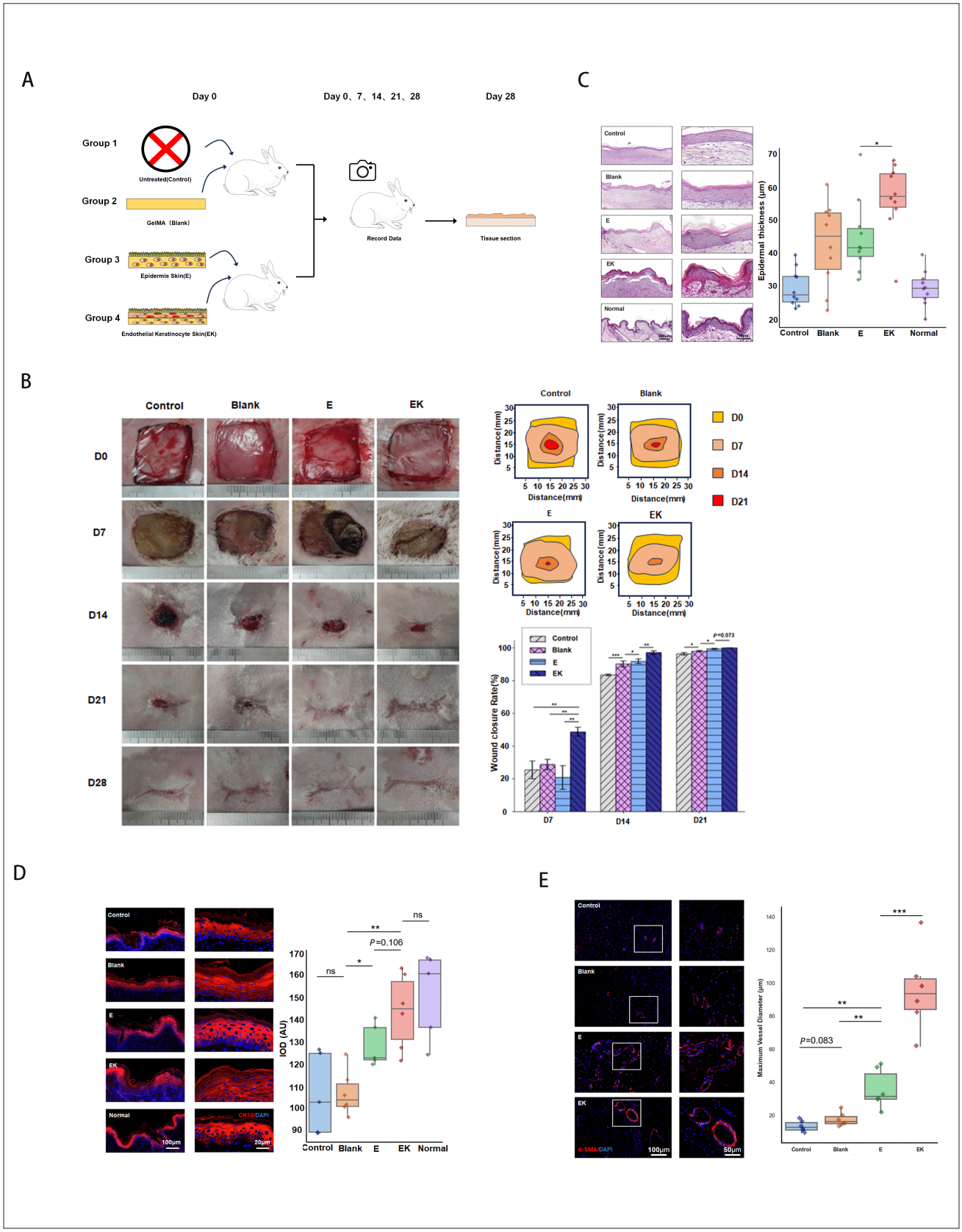
A
Day 0
Day 0、7、14、21、28
Day 28
Group 1
Untreated(Control)
Group 2
GelMA（Blank）
Group 3
Epidermis Skin(E)
Group 4
Endothelial Keratinocyte Skin(EK)
Record Data
Tissue section
C
Control
Blank
E
EK
Normal
Epidermal thickness (μm)
B
Control
Blank
E
EK
D0
D7
D14
D21
D28
Distance(mm)
Wound closure Rate(%)
P=0.073
D
CK10/DAPI
100μm
20μm
IOD (AU)
P=0.106
ns
E
α-SMA/DAPI
50μm
Maximum Vessel Diameter (μm)
P=0.083

Figure 9. Repair of dorsal skin defects in New Zealand rabbits. (A) Flowchart of the dorsal skin defect repair experiment in New Zealand rabbits. (B) Photographs of dorsal skin defect healing in New Zealand rabbits at Day 0, Day 7, Day 14, Day 21, and Day 28. By Day 28, all groups except the control group had completely healed. At Day 21, the endothelial keratinocyte skin (EK) group had already achieved complete healing, showing significant differences compared to the control group (96.43 ± 0.71%), blank group (98.16 ± 0.46%), and epidermis skin (E) group (99.48 ± 0.38%). (C) Hematoxylin and eosin staining revealed that the EK and E groups had developed a "ridge-like" structure in the epidermis. However, the dermo-epidermal junction in the E group was less defined compared to the EK group. The epidermal thickness in the EK group (56.59 ± 10.68 μm) was significantly greater than that in the E group (45.65 ± 13.81 μm). Scale bars: 50 and 200 μm; magnification: 200× and 40×. (D) Cytokeratin 10 (CK10) protein expression in the newly formed epidermis of New Zealand rabbits. The EK group showed significantly higher CK10 expression than the control and blank groups, but no significant difference was observed compared to the E group. Scale bars: 20 and 100 μm. (E) Alpha-smooth muscle actin protein expression in small blood vessels and measurement of the maximum vascular diameter in the newly formed skin of New Zealand rabbits. The EK group exhibited the largest vascular diameter (95.36 ± 24.87 μm), which was significantly different compared to the control group (13.53 ± 3.32 μm), blank group (17.69 ± 4.13 μm), and E group (35.83 ± 11.70 μm). Scale bars: 50 and 100 μm. Data were analyzed via a one-way analysis of variance and are shown as mean ± standard deviation (*$p < 0.05$, **$p < 0.01$, and ***$p < 0.001$, $n = 3$). Abbreviation: IOD, integrated optical density.

structure, but its integration with the dermal layer was less robust than that of the EK group. Tissue sections were subjected to CK10 staining (Figure 9D). The expression levels of CK10 in the EK and E groups were significantly higher than those in the other experimental groups. Specifically, the EK group (143.84 ± 8.55) showed a slightly higher expression level than the E group (128.30 ± 4.83). This indicates a higher degree of epidermal differentiation in these two groups, possibly due to the presence of epidermal cells. In contrast, the EK group has a more mature epidermal structure due to its accelerated early repair and longer epidermal generation time than the double-layer skin group. Moreover, it had more vascular cells/structures for oxygen supply for epidermal cell generation, resulting in a more mature epidermal structure. Alpha-smooth muscle actin (α-SMA) is mainly expressed in smooth muscle cells of the middle layer of blood vessels. In this experiment, α-SMA was selected as a marker for vascular characterization (Figure 9E), labeling newly formed small blood vessels in the subcutaneous tissue. The maximum vascular diameters for each group were as follows: control group (13.53 ± 3.32 μm), Blank group (17.69 ± 4.13 μm), E group (35.83 ± 11.70 μm), and EK group (95.36 ± 24.87 μm). It can be seen that the EK group, which contained vascular endothelial cells, had a much stronger ability for blood vessel regeneration than the other three groups. The double-layer skin group also had a higher blood vessel regeneration ability than the first two experimental samples because its repair speed was faster than the other two groups, and it contained fibroblasts, which could secrete VEGF and other factors that promote vascular cell formation. In summary, the 28-day experiment on back skin defects of New Zealand rabbits fully demonstrated that both the double-layer and VS substitutes were effective in repairing skin defects. Compared with the former, the latter showed improvements in promoting rapid wound healing, epidermal differentiation and shaping, and blood vessel neogenesis. Future studies must incorporate positive control groups (e.g., commercial collagen-based skin substitutes or autografts) and extend the experimental duration to provide more comprehensive insights.

4. Conclusion

This study successfully developed a method for constructing a 3D bioprinted VS substitute. By proposing a single-component hydrogel-cell-compatible composite ink, a GelMA hydrogel-cell-compatible ink targeting fibroblasts, keratinocytes, and vascular endothelial cells was formulated. Based on this, a gradient vascularization dermal skin substitute containing a reticular layer, a papillary layer, and an epidermal layer was gradually constructed. The 3D-printed VS was implanted into *BALB/c* nude mice and New Zealand rabbit skin defect models, validating the effectiveness of the VS substitute in promoting skin healing and angiogenesis. The VS substitute constructed by 3D bioprinting provides a promising strategy for treating skin injuries.

Acknowledgments

The authors thank Zhejiang University for providing the experimental equipment.

Funding

This work was supported by the National Key Research and Development Program of China (Grant No. 2018YFA0703000) and the Key Science and Technology Program of Zhejiang Province (Grant No. 2023C03170 and 2023C03071).

Conflict of interest

The authors declare no conflict of interest.

Author contributions

Conceptualization: Yichen Luo, Bin Zhang, Jien Ma
Data curation: Yichen Luo, Dan Li, Bin Zhang
Figure and visualization: Yichen Luo, Dan Li
Formal analysis: Yichen Luo

Investigation and resources: Yichen Luo,
Methodology and software: Yichen Luo, Cai Lin, Xue Zhou
Project administration and funding acquisition: Bin Zhang
Supervision: Bin Zhang, Jien Ma
Validation: Yichen Luo, Dan Li, Cai Lin, Xue Zhou
Writing – original draft: Yichen Luo, Dan Li
Writing – review & editing: Yichen Luo, Bin Zhang
All authors have read and agreed to the published version of the manuscript.

Ethics approval and consent to participate

The Institutional Animal Care and Use Committee of Zhejiang University approved the design of this study (Approval number: 31324 and 31325).

Consent for publication

Not applicable.

Availability of data

The data that support the findings of this study are available on request from the corresponding author. Additional method descriptions can be found in the supplementary method**.**

References

1. Lee SG, Lee S, Bae HK, et al. Evaluation of the therapeutic efficacy of human skin equivalents manufactured through droplet-based bioprinting/nebulization technology. *Mol cell Toxicol*. 2024;20(1):129-138.
doi: 10.1007/s13273-023-00330-9

2. Michael S, Sorg H, Peck CT, et al. Tissue engineered skin substitutes created by laser-assisted bioprinting form skin-like structures in the dorsal skin fold chamber in mice. *PLoS ONE*. 2013;8(3):e57741.
doi: 10.1371/journal.pone.0057741

3. Kafrashian Z, Brück S, Rogin P, et al. Segmented, side-emitting hydrogel optical fibers for multimaterial extrusion printing. *Adv Mater*. 2025;37(4): e2309166.
doi: 10.1002/adma.202309166

4. Lin Z, Qiu X, Cai Z, et al. High internal phase emulsions gel ink for direct-ink-writing 3D printing of liquid metal. *Nat Commun*. 2024;15(1):4806.
doi: 10.1038/s41467-024-48906-w

5. Zhang C, Hua W, Mitchell K, Jin Y. Multiscale embedded printing of engineered human tissue and organ equivalents. *Proc Natl Acad Sci USA*. 2024;121(9): e2313464121.
doi: 10.1073/pnas.2313464121

6. Sobreiro-Almeida R, Santos SC, Decarli MC, et al. Leveraging blood components for 3D printing applications through programmable ink engineering approaches. *Adv Sci*. 2024;11(47):2406569.
doi: 10.1002/advs.202406569

7. Dong T, Hu J, Dong Y, et al. Advanced biomedical and electronic dual-function skin patch created through microfluidic-regulated 3D bioprinting. *Bioact Mater*. 2024;40: 261-274.
doi: 10.1016/j.bioactmat.2024.06.015

8. Bebiano LB, Presa R, Vieira F, Lourenco BN, Pereira RF. Bioinspired and photo-clickable thiol-ene bioinks for the extrusion bioprinting of mechanically tunable 3D skin models. *Biomimetics (Basel)*. 2024;9(4):228.
doi: 10.3390/biomimetics9040228

9. Gu Z, Fu J, Lin H, He Y. Development of 3D bioprinting: from printing methods to biomedical applications. *Asian J Pharm Sci*. 2020;15(5): 529-557.
doi: 10.1016/j.ajps.2019.11.003

10. Selvam SP, Ayyappan S, Jamir SI, Sellappan LK, Manoharan S. Recent advancements of hydroxyapatite and polyethylene glycol (PEG) composites for tissue engineering applications–a comprehensive review. *Eur Polym J*. 2024;215: 113226.
doi: 10.1016/j.eurpolymj.2024.113226

11. Taite LJ, Rowland ML, Ruffino KA, Smith BRE, Lawrence MB, West J L. Bioactive hydrogel substrates: probing leukocyte receptor–ligand interactions in parallel plate flow chamber studies. *Ann Biomed Eng*. 2006;34: 1705-1711.
doi: 10.1007/s10439-006-9173-x

12. Coudane J, Nottelet B, Mouton J, Garric X, Berghe HVD. Poly (ε-caprolactone)-based graft copolymers: synthesis methods and applications in the biomedical field: a review. *Molecules*. 2022;27(21):7339.
doi: 10.3390/molecules27217339

13. Milosevic M, Stojanovic DB, Simic V, et al. Preparation and modeling of three-layered PCL/PLGA/PCL fibrous scaffolds for prolonged drug release. *Sci Rep*. 2020;10(1):11126.
doi: 10.1038/s41598-020-68117-9

14. Chen Y, Li J, Lu J, Ding M, Chen Y. Synthesis and properties of Poly (vinyl alcohol) hydrogels with high strength and toughness. *Polym Test*. 2022;108:107516.
doi: 10.1016/j.polymertesting.2022.107516

15. Zhao X, Lang Q, Yildirimer L, et al. Photocrosslinkable gelatin hydrogel for epidermal tissue engineering. *Adv Health Mater*. 2016;5(1):108-118.
doi: 10.1002/adhm.201500005

16. Xu W, Molino BZ, Cheng F, et al. On low-concentration inks formulated by nanocellulose assisted with gelatin methacrylate (GelMA) for 3D printing toward wound healing application. *ACS Appl Mater Interfaces*. 2019;11(9):8838-8848.
doi: 10.1021/acsami.8b21268

17. Mazio C, Casale C, Imparato G, et al. Pre-vascularized dermis model for fast and functional anastomosis with host vasculature. *Biomaterials*. 2019;192:159-170. doi: 10.1016/j.biomaterials.2018.11.018

18. Xu H, Liu Z, Wei Y, et al. Complexation-induced resolution enhancement pleiotropic small diameter vascular constructs with superior antibacterial and angiogenesis properties. *Adv Healthc Mater*. 2023;12(29):2301809. doi: 10.1002/adhm.202301809

19. Wan H, Cao Y, Lo LW, Zhao J, Sepúlveda N, Wang C. Flexible carbon nanotube synaptic transistor for neurological electronic skin applications. *ACS Nano*. 2020;14(8):10402-10412. doi: 10.1021/acsnano.0c04259

20. Vidal SEL, Tamamoto KA, Nguyen H, Abbott RD, Cairns DM, Kaplan DL. 3D biomaterial matrix to support long term, full thickness, immuno-competent human skin equivalents with nervous system components. *Biomaterials*. 2019;198:194-203. doi: 10.1016/j.biomaterials.2018.04.044

21. Xiong M, Yang X, Shi Z, et al. Programmable artificial skins accomplish antiscar healing with multiple appendage regeneration. *Adv Mater*. 2024;36(50): 2407322. doi: 10.1002/adma.202407322

22. Xia Y, Yan S, Wei H, et al. Multifunctional porous bilayer artificial skin for enhanced wound healing. *ACS Appl Mater Interfaces*. 2024;16(27):34578-34590. doi: 10.1021/acsami.4c05074

23. Ma J, Qin C, Wu J, et al. 3D multicellular micropatterning biomaterials for hair regeneration and vascularization. *Mater Horiz*. 2023;10(9):3773-3784. doi: 10.1039/d3mh00528c

24. Motter Catarino C, Cigaran Schuck D, Dechiario L, Karande P. Incorporation of hair follicles in 3D bioprinted models of human skin. *Sci Adv*. 2023;9(41):eadg0297. doi: 10.1126/sciadv.adg0297

25. Chen H, Ma X, Gao T, et al. Robot-assisted in situ bioprinting of gelatin methacrylate hydrogels with stem cells induces hair follicle-inclusive skin regeneration. *Biomed Pharmacother*. 2023;158:114140. doi: 10.1016/j.biopha.2022.114140

26. Zhao W, Chen H, Zhang Y, et al. Adaptive multi-degree-of-freedom in situ bioprinting robot for hair-follicle-inclusive skin repair: a preliminary study conducted in mice. *Bioeng Transl Med*. 2022;7(3):e10303. doi: 10.1002/btm2.10303

27. Dai LG, Dai NT, Chen TY, Kang LY, Hsu SH. A bioprinted vascularized skin substitute with fibroblasts, keratinocytes, and endothelial progenitor cells for skin wound healing. *Bioprinting*. 2022;28:e00237. doi: 10.1016/j.bprint.2022.e00237

28. Ma J, Qin C, Wu J, et al. 3D printing of strontium silicate microcylinder-containing multicellular biomaterial inks for vascularized skin regeneration. *Adv Healthc Mater*. 2021;10(16):2100523. doi: 10.1002/adhm.202100523

29. Barros NR, Kim HJ, Gouidie MJ, et al. Biofabrication of endothelial cell, dermal fibroblast, and multilayered keratinocyte layers for skin tissue engineering. *Biofabrication*. 2021;13(3):035030. doi: 10.1088/1758-5090/aba503

30. Xiang P, Yan L, Ge L, He X, Du N, Liu X. Development of a radial-flux machine with multi-shaped magnet rotor and non-ferromagnetic yoke for low torque ripple and rotor mass. *IEEE Trans Ind Appl*. 61;2025:2897-2910. doi: 10.1109/TIA.2025.3532558

31. Xiang P, Yan L, Guo Y, He X, Gerada C, Chen IM. A concentrated-flux-type pm machine with irregular magnets and iron poles. *IEEE/ASME Trans Mech*. 2023;29(1): 691-702. doi: 10.1109/TMECH.2023.3293505

32. Guo J, Gu H, Yin S, et al. Hepatocyte-derived Igκ promotes HCC progression by stabilizing electron transfer flavoprotein subunit α to facilitate fatty acid β-oxidation. *J Exp Clin Cancer Res*. 2024;43(1):280. doi: 10.1186/s13046-024-03203-8

33. Liu C, Qin W, Wang Y, et al. 3D printed gelatin/sodium alginate hydrogel scaffolds doped with nano-attapulgite for bone tissue repair. *Int J Nanomed*. 2021;16:8417-8432. doi: 10.2147/IJN.S339500

34. Pierce MC, Strasswimmer J, Hyle Park B, Cense B, De Boer JF. Birefringence measurements in human skin using polarization-sensitive optical coherence tomography. *J Biomed Opt*. 2004;9(2):287-291. doi: 10.1117/1.1645797

35. Wang Y, Liu Y, Chen S, et al. Enhancing bone regeneration through 3D printed biphasic calcium phosphate scaffolds featuring graded pore sizes. *Bioact Mater*. 2024;46:21–36. doi: 10.1016/j.bioactmat.2024.11.024

36. Kim BS, Yang WK, Jeong SK, et al. 3D cell printing of in vitro stabilized skin model and in vivo pre-vascularized skin patch using tissue-specific extracellular matrix bioink: a step towards advanced skin tissue engineering. *Biomaterials*. 2018;168:38-53. doi: 10.1016/j.biomaterials.2018.03.040

37. Won-woo C, Minjun A, Byoung SK, Dong-Woo C. Blood-lymphatic integrated system with heterogeneous melanoma spheroids via in-bath three-dimensional bioprinting for modelling of combinational targeted therapy. *Adv Sci*. 2022;9(29):2202093. doi: 10.1002/advs.202202093

38. Song J, Liu T, Liao Z, et al. Digital light processing bioprinting neural systems with porous hydrogel in structure and function for disease models. *Cell Rep Phys Sci*. 2024;5(12):102311. doi: 10.1016/j.xcrp.2024.102311

39. Zandi N, Daniele M, Brown A. Advances in fibrin-based bioprinting for skin tissue regeneration: exploring design, and innovative approaches. *Biomed Mater Devices*. 2025;3:330-348.
doi: 10.1007/s44174-024-00198-w

40. Fauzi MB, Rashidbenam Z, Bin Saim A, Binti Hj Idrus R. Preliminary study of in vitro three-dimensional skin model using an ovine collagen type i sponge seeded with co-culture skin cells: submerged versus air-liquid interface conditions. *Polymers*. 2020;12(12): 2784.
doi: 10.3390/polym12122784

41. Monsuur HN, Boink MA, Weijers EM, et al. Methods to study differences in cell mobility during skin wound healing in vitro. *J Biomech*. 2016;49(8):1381-1387.
doi: 10.1016/j.jbiomech.2016.01.040

42. Petry L, Kippenberger S, Meissner M, et al. Directing adipose-derived stem cells into keratinocyte-like cells: impact of medium composition and culture condition. *J Eur Acad Dermatol Venereol*. 2018;32(11):2010-2019.
doi: 10.1111/jdv.15010

43. Colin E, Plyer A, Golzio M, Meyer N, Faver G, Orlik X. Imaging of the skin microvascularization using spatially depolarized dynamic speckle. *J Biomed Opt*. 2022;27(4):046003.
doi: 10.1117/1.Jbo.27.4.046003

44. Hu X, Wang L, Deng J, et al. Dietary nitrate accelerates the healing of infected skin wounds in mice by increasing microvascular density. *Biochem Biophys Res Commun*. 2023;686:149176.
doi: 10.1016/j.bbrc.2023.149176

45. Fu T, Sullivan DP, Gonzalez AM, et al. Mechanotransduction via endothelial adhesion molecule CD31 initiates transmigration and reveals a role for VEGFR2 in diapedesis. *Immunity*. 2023;56(10):2311-2324.e6.
doi: 10.1016/j.immuni.2023.08.001

46. Park H, Collignon AM, Lepry WC, et al. Acellular dense collagen-S53P4 bioactive glass hybrid gel scaffolds form more bone than stem cell delivered constructs. *Mater Sci Eng C Mater Biol Appl*. 2021;120:111743.
doi: 10.1016/j.msec.2020.111743

47. Trappmann B, Gautrot JE, Connelly JT, et al. Extracellular-matrix tethering regulates stem-cell fate. *Nat Mater*. 2012;11(7): 642-649.
doi: 10.1038/nmat3339

48. Singh A, Dalal N, Tayalia P. An interplay of matrix stiffness, dimensionality and adhesivity on cellular behavior. *Biomed Mater*. 2023;18(2): 025010.
doi: 10.1088/1748-605X/acb7c0

49. Trujillo S, Gonzalez-Garcia C, Rico P, et al. Engineered 3D hydrogels with full-length fibronectin that sequester and present growth factors. *Biomaterials*. 2020; 252:120104.
doi: 10.1016/j.biomaterials.2020.120104

50. Ito M, Hiramatsu H, Kobayashi K, et al. NOD/SCID/γ c null mouse: an excellent recipient mouse model for engraftment of human cells. *Blood*. 2002;100(9):3175-3182.
doi: 10.1182/blood-2001-12-0207

51. Albanna M, Binder KW, Murphy SV, et al. In situ bioprinting of autologous skin cells accelerates wound healing of extensive excisional full-thickness wounds. *Sci Rep*. 2019;9(1):1856.
doi: 10.1038/s41598-018-38366-w

52. Wei Q, Su J, Meng S, et al. MiR-17-5p-engineered sEVs encapsulated in GelMA hydrogel facilitated diabetic wound healing by targeting PTEN and p21. *Adv Sci (Weinh)*. 2024;11(13):2307761.
doi: 10.1002/advs.202307761

53. Zhang G, Zhang Z, Cao G, et al. Engineered dermis loaded with confining forces promotes full-thickness wound healing by enhancing vascularisation and epithelialisation. *Acta Biomater*. 2023; 170: 464-478.
doi: 10.1016/j.actbio.2023.08.049

54. Jin T, Fu Z, Zhou L, et al. GelMA loaded with platelet lysate promotes skin regeneration and angiogenesis in pressure ulcers by activating STAT3. *Sci Rep*. 2024; 14(1): 18345.
doi: 10.1038/s41598-024-67304-2

55. Chen L, Ye JL, Gao C, Deng F, Liu W, Zhang Q. Design and fabrication of gelatin-based hydrogel loaded with modified amniotic extracellular matrix for enhanced wound healing. *Heliyon*. 2023;9(10):e20521.
doi: 10.1016/j.heliyon.2023.e20521

56. Hao X, Luo J, Huang Y, et al. Injectable antiswelling and high-strength bioactive hydrogels with a wet adhesion and rapid gelling process to promote sutureless wound closure and scar-free repair of infectious wounds. *ACS Nano*. 2023;17(21): 22015-22034.
doi: 10.1021/acsnano.3c08625

ACCSCIENCE PUBLISHING

International Journal of Bioprinting

RESEARCH ARTICLE

Immunomodulation and bone repair of 3D-printed SrBG/PCL scaffolds with PDA coating

Qiping Huang[1,2†], Xiang Li[1†], Qinghong Fan[1†], Qian Du[1], Guangquan Zhao[1,2], Yuanhao Lv[1,2], Yixiao Wang[1], Weikang Xu[2,3,4*], and Qingde Wa[1*]

[1]Department of Orthopedic Surgery, The Second Affiliated Hospital of Zunyi Medical University, Zunyi, Guizhou, China

[2]Institute of Biological and Medical Engineering, Guangdong Academy of Sciences, Guangdong Chinese Medicine Intelligent Diagnosis and Treatment Engineering Technology Research Center, Guangzhou, Guangdong, China

[3]Guangdong Provincial Key Laboratory of Medical Electronic Instruments and Materials, Guangdong Institute of Medical Instruments, Guangzhou, Guangdong, China

[4]National Engineering Research Center for Healthcare Devices, Guangdong Institute of Medical Instruments, Guangzhou, Guangdong, China

[†]These authors contributed equally to this work.

***Corresponding authors:**
Weikang Xu
(759200816@qq.com)

Qingde Wa
(wqd887zsy@126.com)

Citation: Huang Q, Li X, Fan Q, *et al.* Immunomodulation and bone repair of 3D-printed SrBG/PCL scaffolds with PDA coating. *Int J Bioprint*. 2025;11(4):350-377. doi: 10.36922/IJB025210211

Received: March 4, 2025
Revised: May 21, 2025
Accepted: June 5, 2025
Published online: June 6, 2025

Copyright: © 2025 Author(s). This is an Open Access article distributed under the terms of the Creative Commons Attribution License, permitting distribution, and reproduction in any medium, provided the original work is properly cited.

Publisher's Note: AccScience Publishing remains neutral with regard to jurisdictional claims in published maps and institutional affiliations.

Abstract

3D-printed polycaprolactone (PCL) scaffolds are widely used for bone tissue engineering but suffer from deficiencies, such as difficulty in cell adhesion, lack of osteogenic activity, and poor immunomodulatory capacity. Enhancing the biological responsiveness of PCL scaffolds remains a key focus in bone tissue engineering. In this study, the following three types of scaffolds were prepared: (i) PCL, (ii) strontium (Sr)-doped bioactive glass (SrBG)/PCL, and (iii) polydopamine (PDA)/SrBG/PCL. The scaffolds were assayed *in vitro* for their effect on the expression of osteoinductive differentiation markers (ALP, RUNX2, and COL1), and their influence on macrophage (MP) (CD206, ARG, TNF-α, IL1β, IL-10, and IL-12) behavior was evaluated. Their effect on bone defect repair was assessed *in vivo* using micro-computed tomography (micro-CT), hematoxylin and eosin (HE) staining, Masson staining, and immunofluorescence staining (iNOS, CD163, BMP-2, and VEGF). The results demonstrated that PDA/SrBG/PCL scaffolds significantly promoted the proliferation and osteogenic differentiation of bone marrow mesenchymal stem cells (BMSCs), inhibited the differentiation of MPs to the M1 phenotype, and promoted the differentiation of MPs to the M2 phenotype, resulting in better pro-osteogenic, immunomodulatory, and angiogenic effects *in vivo*. This observation may be associated with the release of Sr^{2+} from SrBG, and surface modification with PDA further enhanced the immunomodulation and bone repair ability of the scaffold. The study demonstrated that the PDA/SrBG/PCL scaffolds exhibit excellent bone repair capabilities and hold strong potential for applications in bone tissue engineering.

***Keywords*:** 3D printing; Bone repair; Immunomodulation; Polycaprolactone; Polydopamine; Strontium-doped bioglass

1. Introduction

Bone defects refer to the destruction of bone tissue caused by trauma, infection, tumors, or other pathological conditions.[1] Tissue engineering is a promising strategy for reconstructing bone defects, and it has received much attention recently. To enhance repair effectiveness, many past studies have explored the composition, degradation properties, and bone-regenerative properties of composite scaffolds.[2–4] Although the mechanical properties and degradation characteristics of scaffolds have significantly improved, bone repair results remain unsatisfactory, limiting their clinical application.[5,6] In addition, scaffold–tissue interactions play a central role in tissue repair.[7] Therefore, elucidating and modulating scaffold–tissue interactions is essential to improve repair outcomes. Recent studies have found that bone filler materials trigger innate and adaptive immune responses after implantation.[8,9] Excessive immune responses may lead to chronic inflammation, fibrosis, and implant failure, increasing the risk of secondary surgery.[10–12] Therefore, reducing inappropriate immune responses triggered during early implant stages is particularly important. Macrophages (MPs) play a key immunoregulatory role in bone defect repair, with M1 (pro-inflammatory) and M2 (anti-inflammatory) MPs regulating bone formation, remodeling, and repair by secreting different cytokines.[13,14]

Biodegradable polymers create favorable conditions for regenerating new bone tissue and defect repair compared to permanent implants.[15] In comparison with inorganic materials, polymer materials have better degradability, higher biocompatibility, and more stable mechanical properties.[16,17] Among various degradable materials, synthetic polyesters have controlled biodegradability *in vivo* and are non-toxic.[18] Synthetic polyester-based materials have better mechanical properties than natural polymers and are more suitable for bone repair.[19] Among them, polycaprolactone (PCL) has good biocompatibility and can be effectively combined with biological tissues.[20,21] However, PCL has low bioactivity, poor cell adhesion, and lacks osteogenic activity.[22,23] In addition, Tang et al.[24] prepared *Panax notoginseng* saponin (PNS)-PCL scaffolds via 3D printing to evaluate their reparative effect on vascular injury in rabbit carotid arteries, and the inflammation scoring results indicated that pure PCL scaffolds exhibited poor anti-inflammatory performance. Therefore, PCL needs to be compounded with other biomaterials to enhance its osteogenic activity and immunomodulatory ability.

Bioactive glass (BG) is an inorganic bioactive material that can form strong bonds with hard and soft tissues, and it is widely used in bone tissue engineering due to its excellent biocompatibility, degradability, and bone-enhancing properties.[25] Research has demonstrated that mesoporous BG (MBG) effectively enhances apatite production rate.[26] Zhao et al.[27] used an MBG composite fibrin hydrogel for maxillofacial bone defect implantation, and MBG enhanced the mechanical strength, bioactivity, and osteogenic properties of the hydrogel. In addition, BG exhibits excellent cytocompatibility and antimicrobial effects as a coating material for metal implants.[28,29] In contrast, recent studies have reported that exosomes generated from MBG-stimulated mesenchymal stem cells (MSCs) are significantly more productive and exhibit enhanced immunomodulatory and bone repair capabilities.[30] In recent years, strontium-doped BG (SrBG) has received attention for its ability to promote osteoblast proliferation, osteogenic differentiation, and angiogenesis.[31] Sr^{2+} inhibits the expression of inflammatory genes and provides a favorable environment for tissue repair.[32] In addition, Sr^{2+} has immunomodulatory effects and is concentration-dependent.[33] Ding et al.[34] found that SrBG was able to mobilize monocytes from the spleen to reach the bone defect site and convert them into M2 MPs to promote bone tissue regeneration. SrBG promotes bone repair by activating the Akt signaling pathway to promote M2 MP polarization and release osteogenesis-related cytokines.[35] Although PCL/SrBG composite scaffolds displayed better bioactivity and osteogenic induction compared to PCL scaffolds, PCL/SrBG scaffolds alone were still insufficient to induce significant osteogenic differentiation.[36,37] Poh et al.[38] cultured PCL and PCL/SrBG scaffolds under non-osteoinductive conditions to evaluate their positive effect on osteoinductive differentiation; the PCL/SrBG scaffolds did not exhibit any significant osteoinductive differentiation ability, which may be related to the concentration of Sr^{2+} released by the scaffolds. Polydopamine (PDA) is an implant surface modification material with good hydrophilicity, biocompatibility, antimicrobial properties, and bone-enhancing properties.[39] More importantly, the PDA coating has a large number of catecholamine groups for scavenging reactive oxygen species (ROS) and anti-inflammatory properties that inhibit M1 MP polarization and activate MP polarization toward the M2 phenotype, thereby promoting the expression of osteogenesis-related cytokines.[40] Jin et al.[41] demonstrated that PDA inhibits pro-inflammatory cytokine expression in MPs by downregulating the TLR-4-MYD88-NF-κB pathway. Moreover, PDA can regulate ROS production and upregulate heme oxygenase 1 (HO-1) expression, thereby influencing MP phenotypic differentiation and suppressing the inflammatory response. In this study, we innovatively and synergistically used PDA and SrBG to modify the surface and interior of PCL scaffolds to enhance the cell adhesion and proliferation of the scaffolds.[42] PDA coating

can better regulate the concentration of Sr^{2+} released from the scaffold, helping to modulate the immune microenvironment and promote bone regeneration.

Briefly, we used PCL scaffolds as the basis for constructing PDA/SrBG/PCL composite scaffolds (Figure 1). These were prepared by loading SrBG, followed by surface modification with PDA. The study systematically evaluated the physical properties, biocompatibility, osteogenic differentiation, and immunomodulation of PCL, SrBG/PCL, and PDA/SrBG/PCL scaffolds to optimize new bone defect repair materials.

2. Materials and methods

2.1. Materials

Ethyl orthosilicate (TEOS), cyclohexane, triethyl phosphate (TEP), calcium nitrate tetrahydrate (CN), strontium nitrate, sodium hydroxide, anhydrous ethanol, and methylene chloride were purchased from Guangzhou Chemical Reagent Factory (China). Dodecyl amine (DDA) was purchased from Shanghai Aladdin Reagents Co. (China). Deionized water was purchased from Merck Millipore (Germany). PCL (molecular weight: 54,000) was purchased from Jinan Dai Gang Biotechnology Co. (China). Vitamin C and sodium β-glycerophosphate were purchased from Shanghai McLean Biochemical Technology Co., Ltd. (China). Dexamethasone was purchased from J&K Scientific (China). Hipure RNA kit, HiFiScript cDNA synthesis kit, and Ultra SYBR mixture (low ROX) were purchased from CWBIO (China). Alkaline phosphatase (ALP) kit, BCA protein assay kit, and RIPA lysate were provided by Bi Yun Tian Biotechnology (China). Dulbecco's modified Eagle's medium (DMEM), fetal serum, penicillin-streptomycin solution, phosphate buffer, trypsin, and CCK-8 kit were provided by ATCC (United States of America [USA]). Rat bone marrow MSCs (BMSCs) and MPs (RAW264.7) were provided by ATCC (USA). PDA was purchased from Tangshan Wei Hao Co.,

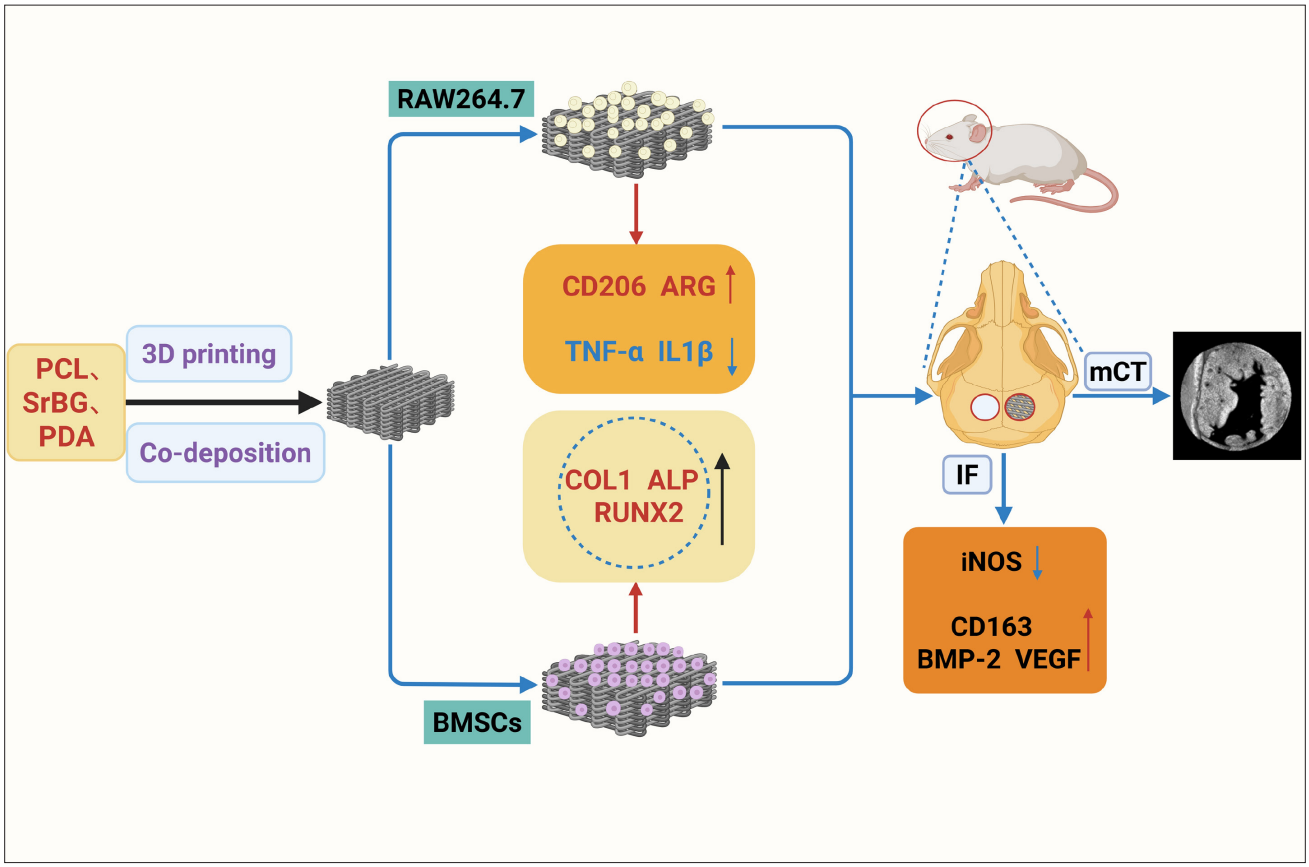

Figure 1. Schematic diagram of the development and systematic assessment of various PCL scaffolds. Abbreviations: ALP, alkaline phosphatase; ARG, arginase; BMP-2, bone morphogenetic protein-2; BMSCs, bone marrow mesenchymal stem cells; CD163, hemoglobin scavenger receptor; CD206, cluster of differentiation 206 (mannose receptor); COL1, Type I collagen; IF, immunofluorescence; IL, interleukin; INOS, inducible nitric oxide synthase; mCT, micro-CT; Runx2, Runt-related transcription factor 2; TNF-a, tumor necrosis factor-α; PCL, polycaprolactone; PDA, polydopamine; SrBG, strontium substituted bioactive glasses; VEGF, vascular endothelial growth factor.

Ltd. (China). Sprague-Dawley (SD) rats were provided by Chongqing Teng Xin Hua Fu Laboratory Animal Sales Co, Ltd. (China) (animal qualification certificate no. SYXK [Qian] 2021-0003).

2.2. Preparation of PCL, SrBG/PCL, and PDA/SrBG/PCL scaffolds

2.2.1. Preparation of SrBG

The molar ratio of the components of SrBG was designed as 60 SiO_2:30 CaO:6 SrO:4 P_2O_5. The specific experimental method for the preparation of micro- and nano-SrBG microspheres using the sol–gel method is described below.

The experimental temperature was maintained at 40°C using a water bath, and 5 g of DDA was fully dissolved in a mixture of deionized water and anhydrous ethanol. After that, 16.5 mL of TEOS and TEP was sequentially added to the solution using a syringe pump at a speed of 0.5 mL/min. CN and strontium nitrate were then added slowly, and the solution was stirred continuously for 3 h. Thereafter, the solution was kept at room temperature for 24 h to obtain a glass sol, which was subsequently washed and centrifuged to obtain a white precipitate. The precipitate was pre-frozen in the refrigerator at –20°C for 2 h and then freeze-dried. Finally, the freeze-dried precipitate was heated in a muffle furnace at 650°C for 3 h to obtain the SrBG, which was dried and stored after ball milling and sieving.

2.2.2. Preparation of SrBG/PCL scaffolds

Approximately 100 mg of SrBG powder was dispersed in 10 mL of dichloromethane solution containing 1 g PCL. After stirring, the solution was poured into glass dishes, and the dichloromethane was fully evaporated to obtain the scaffold raw material SrBG/PCL. The SrBG/PCL was transferred to the 3D printer (EFL-BP-6603, Suzhou Institute of Intelligent Manufacturing, China), and the printing parameters were set as: diameter: 5 mm, number of layers: 5 layers, layer thickness: 0.2 mm, infill density: 75%, barrel temperature: 65°C, and nozzle temperature: 70°C. The SrBG/PCL was heated, melted, and subsequently printed into cylindrical 3D scaffolds (diameter: 5 mm; height: 1 mm), referred to as the SBP group. For comparison, PCL was directly loaded into the 3D printer to fabricate a cylindrical 3D scaffold, designated as group P.

2.2.3. Preparation of PDA/SrBG/PCL scaffolds

The SrBG/PCL scaffolds were then modified using PDA. A Tris–HCl buffer (pH 8.5) was first prepared using 1.21 g Tris-base and 100 mL deionized water, and it was then stored at room temperature until further use. Thereafter, approximately 0.25 g dopamine hydrochloride (2.5 g/L) was added to the Tris–HCl buffer and stirred. The ready-to-use solution was stored in the dark until further use. At room temperature, the 3D-printed SrBG/PCL scaffolds were soaked in the weakly basic dopamine solution and shaken at 30°C on a shaking bed for 6 h. The SrBG/PCL scaffolds were then washed with deionized water to remove unattached polydopamine and dried to obtain the PDA/SrBG/PCL scaffolds (referred to as the PSBP group).

2.3. Scaffold characterization

2.3.1. Morphology of SrBG

The micromorphology of SrBG was characterized using a field emission scanning electron microscope (SEM) (Merlin, Germany); the particle size distribution of SrBG was analyzed using dynamic light scattering (DLS) (Malvern Panalytical, England).

2.3.2. Surface morphology of the scaffolds

The surface morphology and structure of the P, SBP, and PSBP scaffolds were observed using SEM (Merlin, Germany) at an accelerating voltage of 10 kV after gold-spraying the surface of the scaffolds. The average pore area of the scaffold fiber surface was statistically analyzed using ImageJ software.

2.3.3. Hydrophilicity of the scaffolds

The scaffolds were placed on a contact angle tester (c, KRUSS, Germany), and a 2-μL droplet was placed on the surface of the scaffolds. The position of the sample in contact with the droplet was adjusted to align with the baseline of the measurement; photographs were taken to obtain a still image of the droplet, and the magnitude of the contact angle (θ) was calculated using contact angle measurement software DSA25 for each scaffold group.

2.3.4. Porosity of the scaffolds

The mass of the dried scaffold sample (M0), the total mass of the specific gravity bottle containing anhydrous ethanol at room temperature (M1), the total mass of the bottle and sample after sonication for 10 min to remove air bubbles (M2), and the remaining mass after the sample was removed (M3) were measured accordingly. The porosity of the obtained scaffolds was calculated using **Equation (I)**:

$$\text{Porosity} = \frac{M2 - M3 - M0}{M1 - M3} \quad \text{(I)}$$

2.3.5. Ion release profile of the scaffolds

Each scaffold (approximately 20 mg) was immersed in 5 mL phosphate-buffered saline (PBS) and shaken at 37°C and 60 rpm. Samples were collected on days 1 and 3, and the concentration of Sr^{2+} was measured using the

inductively coupled plasma optical emission spectrometer (ICP-OES) (Agilent 5110, Agilent Technologies, America).

2.3.6. Thermodynamic analysis of the scaffolds

The thermal weight loss data of the scaffolds were determined using a thermogravimetric analyzer (NETZSCH, Germany), in which the samples were heated from room temperature to 800°C at a rate of 10°C/min in a nitrogen atmosphere.

2.3.7. Mechanical strength of the scaffolds

The mechanical properties of the scaffolds were analyzed by placing the scaffolds on an INSTRON tester (34 sc-5, Instron, America), drying them, and compressing them at a rate of 1 mm/min.

2.4. *In vitro* experiments

2.4.1. Cell culture and scaffold sterilization

The BMSCs and RAW264.7 cells were cultured in a cell culture incubator (MCO-18AIC, PHC, Japan) at 37°C and 5% CO_2. The basal medium used was high glucose medium (DMEM), supplemented with 10% fetal bovine serum (FBS), 100 μg/mL penicillin, and 100 μg/mL streptomycin. During culture, the medium was changed daily or every 2 days, depending on the cell condition. Cells were passaged upon reaching 70–80% confluency, and only cells from passages 3 to 5 were used. Before the experiment, each group of scaffolds was immersed in a 75% ethanol solution for 2 h; the scaffolds were rinsed three times and stored overnight in PBS inside an ultraviolet (UV) sterilizer (30–800 L, Sheng Zhi Yuan and Science and Education Equipment Co., China).

2.4.2. Cell activity assay

After BMSCs adhered and proliferated on the scaffold surface for 3 days, the morphology and distribution of cells on the scaffold surface were observed by staining the cells on the scaffold surface with a live-dead cell dye. The morphology and distribution of cells on the scaffold surface were observed using an inverted fluorescence microscope (Leica Microsystems, Germany).

2.4.3. Histocompatibility assessment

Rat bone marrow MSCs (BMSCs) were utilized to evaluate the histocompatibility of different cells with the scaffolds. Briefly, sterile scaffold samples were placed in 48-well plates, and the samples were inoculated with 5×10^4 BMSCs. The supernatant was aspirated after 1, 3, and 7 days of incubation, and the rate of cell proliferation on the different scaffolds was assessed using the CCK-8 kit assay, which was performed using an enzyme marker (Tecan Spark, Austria) to measure the absorbance (optical density [OD]) at 450 nm.

2.4.4. ALP staining and activity analysis

The scaffolds and BMSCs of each group were cultured with an osteogenic induction solution. After 7 days of culture, ALP dye was added to stain the samples, and the absorbance (OD) at 405 nm was measured by an enzyme marker. The cellular activity of the composite scaffold group relative to the control group was calculated from the measured OD values. The ALP-stained cells on the scaffold surface were observed using an inverted fluorescence microscope (Leica Microsystems, Germany).

2.4.5. In vitro osteogenic capacity

Approximately 1×10^5 BMSCs were added to 48-well plates containing the scaffold samples. After 24 h of incubation, the supernatant was aspirated and discarded. Complete medium, osteogenic induction medium (100 mL complete medium + 0.39 mg dexamethasone + 1.76 mg vitamin C + 306.11 mg sodium β-glycerophosphate), or MP-conditioned medium was added, respectively; the culture medium was changed regularly. After 7 and 14 days of osteogenic induction, the expression of osteogenic marker genes of ALP (*ALP*), Runt-associated transcription factor 2 (*RUNX2*), and collagen type I (*COL1*) was measured using real-time fluorescence quantitative polymerase chain reaction (qRT-PCR). *GAPDH* was used as the internal reference gene. ALP activity was measured on days 7 and 14 using the ALP kit combined with the BCA method.

2.4.6. MP polarization gene expression levels

RAW264.7 cells were inoculated into the scaffold samples and transferred to 48-well plates at a density of 5×10^4 cells per well. The complete medium was changed every 2–3 days. The medium removed from each set of samples was collected and mixed with osteogenic induction solution at a ratio of 1:5 to prepare MP-conditioned medium for backup. The expression of the M1 MP immune marker genes, including tumor necrosis factor-α (*TNF-α*) and recombinant human interleukin 1β (*IL1β*), and the M2 MP immune marker genes, including CD206 (*CD206*) and arginase (*ARG*), were detected using qRT-PCR on days 1 and 3. *GAPDH* was used as the internal reference gene. As shown in Table 1, the base sequences of each gene are presented.

2.4.7. ELISA assay

The concentrated washing solution (phosphate buffer [PBS] containing Tween-20, with a pH value of 7.2–7.4.) was heated in a water bath to dissolve the crystals completely. The concentrated washing solution was diluted with distilled water at a 1:20 ratio. Substrate solutions A (chromogenic reagent A, hydrogen peroxide) and B (chromogenic reagent B, tetramethylbenzidine) were mixed thoroughly in a 1:1 volume ratio and used within 15 min after mixing. All reagents, including standards,

Table 1. Specific primers for immunoregulatory and osteogenesis-related genes

Gene	Primer sequence (5'–3')	
	Forward	Reverse
TNF-α	GGGTGTTCATCCATTCTC	GGTCACTGTCCCAGCAT
IL1β	TACAGGCTCCGAGATGAACA	AGGCCACAGGTATTTTGTCG
ARG	CATATCTGCCAAAGACATCG	GGTCTCTTCCATCACCTTGC
CD206	ATGGATGTTGATGGCTACTGG	TTCTGACTCTGGACACTTGC
ALP	GGAGATGGTATGGGCGTCTC	GGACCTGAGCGTTGGTGTTA
RUNX2	GCCGGGAATGATGAGAACTA	GGACCGTCCACTGTCACTTT
COL1	CGCTGGCAAGAATGGCGATC	ATGCCTCTGTCACCTTGTTCG
GAPDH	TGAACTAACACAGAGGAGGATCAG	GCTTAGGGCATGAGCTTGAC

quality controls (QCs), and samples, were equilibrated to room temperature before use. Working solutions were prepared as instructed by the kit. The required number of ELISA strips was removed from the aluminum foil pouch, while the remaining strips were resealed in a self-sealing bag and stored at 4°C. Wells were designated for standards, 0 value, blanks, and samples. Each standard received 50 μL of standards at different concentrations, 0 value wells received 50 μL of sample diluent, blank wells were left empty, and sample wells received 50 μL of test samples. Then, 100 μL of horseradish peroxidase (HRP)-labeled detection antibody was added to all standard, 0 value, and sample wells. Plates were sealed and incubated at 37°C for 60 min in a water bath or thermostat. After incubation, the sealing film was removed, the liquid was discarded, and the plate was gently blotted dry with absorbent paper. Each well was then filled with washing solution and allowed to stand for 20 s. The reaction plate was then shaken with washing solution, and the plate was patted dry with absorbent paper; this process was repeated five times. If an automatic plate washer was used, the plate was washed according to the manufacturer's instructions, with a 30-s programmed soak included to improve assay precision. After the final wash, the plate was thoroughly blotted dry on clean, non-abrasive paper. Substrate solutions A and B were mixed in a 1:1 volume ratio, and 100 μL of the mixture was added to each well. The plate was then covered with sealing film and incubated in the dark at 37°C for 15 min in a water bath or thermostat. After incubation, 50 μL of stop solution was added to each well, and the absorbance (OD) of each well was measured at 450 nm using a microplate reader.

2.5. *In vivo* assessment of osteogenic performance of scaffolds

2.5.1. Establishment of rat cranial defect model

In order to test the bone reparative ability of the scaffold material *in vivo*, a model of bilateral bone defects in the skull of SD rats was established. The scaffolds were cylindrical (diameter: 5 mm; height: 1 mm) and were irradiated and sterilized (10 kGy) before implantation.

The animal experimental study was approved by the Animal Ethics Committee of Zunyi Medical University (approval no. ZMU21-2412-019). The animal model was established with 36 SD rats (280–320 g), kept under the same conditions. The rats were randomly distributed into the blank, P, SBP, and PSBP groups, respectively. Bone regeneration was assessed using a bilateral critical-sized cranial defect model (5 mm diameter), with the defect area in the cranial bone measuring approximately 5 mm in diameter and 2 mm in height. Scaffolds from the three groups—P, SBP, and PSBP—were implanted into the defect sites, and the scalp was sutured.

The animal model was developed as described herein. SD rats were weighed and anesthetized. The surgical area of the skull was shaved, the animals were fixed in the prone position, disinfected with 1% iodophor, and covered with sterile sheets. A midline incision approximately 2 cm in length was made along the cranial vault, and the subcutaneous tissue was separated using the handle of a scalpel. The periosteum was neatly incised along the sagittal suture of the skull, and the subperiosteal tissues were carefully peeled off with the handle of the scalpel, fully exposing the parietal, occipital, and part of the frontal bone bilaterally. A 5-mm diameter round full-layer bone defect was created on both sides of the parietal midline of the rat skull using a low-speed hollow ring drill (1400–1500 rpm), taking care to avoid damaging the dura mater. At the start of drilling, gentle manual pressure was applied to initiate cranial penetration, which was reduced near completion to prevent injury to the underlying dura and blood vessels. The drill was then tilted at an angle of 20°–30° in forward, backward, left, and right directions without additional external force, allowing gravity to facilitate intermittent

penetration of the cranial bone. A small number of the cranial connections were retained. After testing the skull with ophthalmic forceps for looseness, the skull was removed along the peripheral circular defect. The defect area was repeatedly rinsed with saline, and the scaffold was implanted into the cranial defect site of rats; no material was placed in the blank group. The wound was closed using a 4-0 absorbable suture, and antibiotics were injected for 3 consecutive days postoperation to prevent infection. The implantation process of the scaffold is presented in Figure 2A–C.

2.5.2. Postoperative observational indicators

Vital signs, activity, diet, urination and defecation, and incision recovery of SD rats were observed after surgery, with particular attention paid to the presence of abdominal distension to prevent the occurrence of intestinal obstruction.

2.5.3. Specimen collection

At 1, 2, and 3 months post-surgery, SD rats were euthanized to obtain liver, kidney, and skull specimens, which were immersed in 4% paraformaldehyde.

2.5.4. Hematoxylin and eosin staining

Rat liver, kidney, and skull specimens with completed decalcification were fixed, embedded, and sectioned. Paraffin sections were deparaffinized in water by sequential immersion in xylene for 20 min (twice), followed by 95% ethanol for 5 min, 80% ethanol for 5 min, and 75% ethanol for 5 min, before washing them with tap water.

Frozen sections were removed from a –20°C freezer and brought to room temperature. The sections were fixed with tissue fixative for 15 min and then rinsed with running water. For pretreatment, the sections were treated with "HD Constant Staining Pretreatment Solution" for 1 min. The sections were then stained with hematoxylin staining solution for 3–5 min, washed with tap water, differentiated with differentiation solution, washed again with tap water, returned to blue using the "Return to Blue Solution," and finally rinsed with running water. Later, the slices were dehydrated in 95% alcohol for 1 min, then stained in an eosin staining solution for 15 s. The sections were sequentially dehydrated in 80% anhydrous ethanol (2 min), 95% ethanol (2 min), and 100% ethanol (2 min), followed by clearing in n-butanol (2 × 2 min) and xylene (2 × 2 min). Sections were then mounted using neutral gum. Under a light microscope, the nuclei appeared blue and the cytoplasm red.

2.5.5. Masson staining

Cranial specimens with completed decalcification were fixed, embedded, and sectioned. Paraffin sections were deparaffinized in water by sequential immersion in xylene for 20 min (twice), followed by 95% ethanol for 5 min, 80% ethanol for 5 min, and 75% ethanol for 5 min, before washing with tap water.

Frozen sections were removed from the –20°C freezer, brought to room temperature, fixed with tissue fixative for 15 min, and rinsed with running water. The sections were immersed in Weigert's iron hematoxylin solution overnight, followed by rinsing under running tap water. Sections were immersed in a 1:1 mixture of Lichun Red Acidic Compound Red solution (a mixed dyeing solution composed of the main dyes Acid Red 112 and Acid Red 87) and 1% phosphomolybdic acid aqueous solution for 1 min, washed with tap water, differentiated for a few seconds in differentiation solution, and finally rinsed with tap water. The slices were stained with aniline blue solution for 6 min and then rinsed in tap water. They were subsequently immersed in 0.2% glacial acetic acid for 1 min. Without

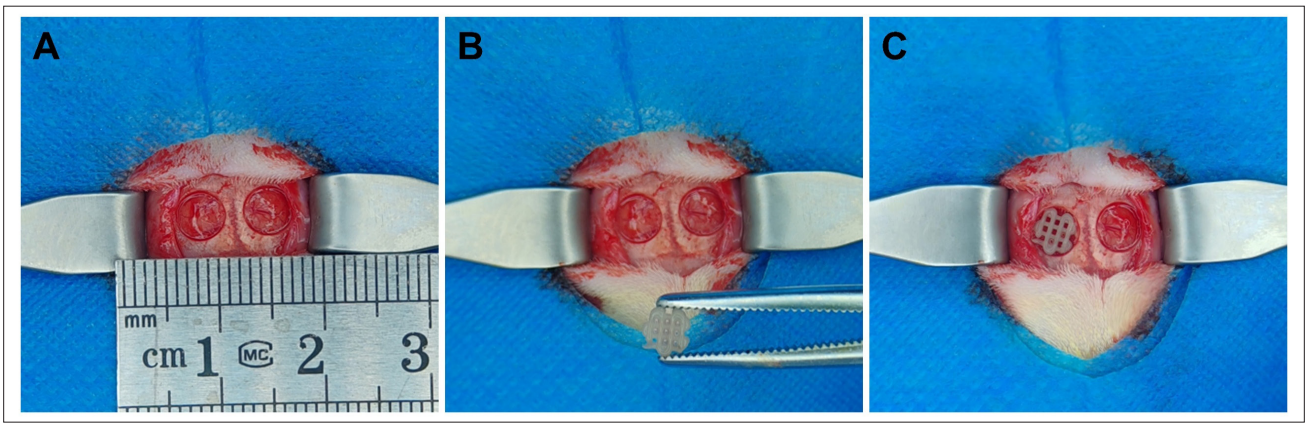

Figure 2. Preparation of the bilateral cranial bone defect model (diameter: 5 mm) and implantation of scaffolds in SD rats. (A) Establishment of bilateral cranial defects in SD rats. (B) Scaffolds implantation process. (C) Scaffolds implantation in the defect area. Abbreviation: SD, Sprague-Dawley.

further washing, the slices were drained and directly stained in 1% hydrochloric acid in alcohol for 2–30 s. After rinsing, the sections were further differentiated with 1% acetic acid and dehydrated in two tanks of anhydrous ethanol (75% and 95%). For sealing, the sections were immersed in a third vat of anhydrous ethanol (99%) for 5 min, xylene for 5 min for transparency, and sealed with neutral gum. Collagen fibers appeared blue, while myofibrils, fibrin, and erythrocytes were stained red under a light microscope.

2.5.6. Micro-computed tomography

Micro-computed tomography (micro-CT) analysis was performed using a ZKKS-MCT-Sharp scanner (Zhong Ke Kai Sheng, China). Cranial specimens from each group at 1-, 2-, and 3-months post-operation were fixed in the scanner along the long axis. Scanning parameters were set as follows: voltage at 70 kV, power at 7 W, four-frame superimposition, an angular gain of 0.72°, and an exposure time of 100 ms. Each sample was rotated 360° to complete the scan. The scanned images were denoised and reconstructed to obtain 3D images. Bone repair and bone growth in the cranial defects of rats were observed; the bone volume fraction of the newborn bone in the cranial defects of rats was calculated using a Bruker high-resolution micro CT (CTAn). Finally, the cranial micro-CT data of rats from different subgroups were statistically analyzed to compare the differences.

2.5.7. Immunofluorescence staining

The SD rats were euthanized at postoperative months 1, 2, and 3, and the cranial tissues were removed and fixed in 4% paraformaldehyde for 48 h. The cranial specimens were then placed in a 10% EDTA demineralization solution for decalcification. To determine the new bone formation, hematoxylin and eosin (HE) staining, Masson staining, and immunofluorescence staining were performed on the sections of each sample. Sections with 5 μm thickness were cut from paraffin-embedded tissues for histological assessment. These sections were immersed in 3% (w/v) H_2O_2 and blocked with 3% (v/v) Bull serum albumin (BSA) solution. After enzymatic antigen repair, the sections were again incubated with the following primary antibodies: BMP-2 (rat, 1:100 dilution; Abcam, USA); VEGF (rat, 1:200 dilution; Abcam, USA); CD163 (rat, 1:100 dilution; Abcam, USA); and iNOS (rat, 1:2000 dilution; Abcam, USA). After rinsing twice with PBS, the samples were incubated with the corresponding horseradish peroxidase-labeled secondary antibodies and then visualized by staining with 4',6-diamidino-2-phenylindole (DAPI). Cell nuclei were stained with hematoxylin.

2.6. Statistical analysis

Data were processed using SPSS 29.0 software (IBM, China). The experimental data were expressed as mean ± standard deviation, and comparisons between groups were statistically analyzed using one-way analysis of variance (ANOVA) and independent samples *t*-tests. Graphs were plotted using GraphPad Prism (GraphPad Software, America) and Origin software (Beijing Tianyan Rongzhi Software Co., Ltd, China). Statistically significant differences are indicated by $^{*}p < 0.05$, $^{**}p < 0.01$, and $^{***}p < 0.001$.

3. Results

3.1. Scaffold preparation and characterization

3.1.1. Characterization of SrBG

The microscopic morphology of SrBG was characterized using SEM. The SrBG prepared consisted of many regular stacks of small particles with well-dispersed glass particles arranged in clusters (Figure 3A). DLS analysis (Figure 3B) revealed that the SrBG particle size distribution was 350–700 nm, with the most prevalent size being 493.9 nm, accounting for about 38% of the total distribution.

3.1.2. Characterization and physicochemical properties of P, SBP, and PSBP scaffolds

The surface morphology of the composite scaffolds (P, SBP, and PSBP) is presented in Figure 4A. Compared to the P scaffolds, the pore size of the SBP scaffolds did not change significantly, and the surface became roughened by the addition of SrBG. The surface of the SBP scaffolds had SrBG particles attached, but the pores on the surface became smaller, and the number of pores decreased. After the addition of PDA to the SBP scaffolds, there was no significant change in the pore size of the scaffolds, but the number of pores was further reduced, mainly because the PDA coating covered the original pores. At higher magnification (× 2000), the surface of PSBP scaffolds was smoother compared to the SBP scaffolds, and SrBG particle attachment was observed on the surface of PSBP scaffolds. The porosity of the P, SBP, and PSBP scaffolds was 68.29 ± 5.62%, 65.00 ± 2.62%, and 60.53 ± 2.87%, respectively (Figure 4C). The porosity of the PSBP scaffold was slightly lower than that of the P and SBP scaffolds, but the difference was not significant, consistent with the results of SEM. The contact angles of the scaffolds in each group were examined by the static contact angle method (Figure 4B1); the contact angles of the P, SBP, and PSBP scaffolds were 99.01 ± 2.62°, 72.04 ± 2.27°, and 0°, respectively (Figure 4B2). Generally, a smaller contact angle would indicate a more hydrophilic material. Overall, the addition of PDA and SrBG significantly improved the hydrophilicity of PCL materials, and the PSBP scaffolds had better hydrophilicity compared to the P and SBP scaffolds. The SBP and PSBP scaffolds were immersed in PBS, and the release of Sr^{2+} was measured on days 1 and 3. The SBP and PSBP scaffolds

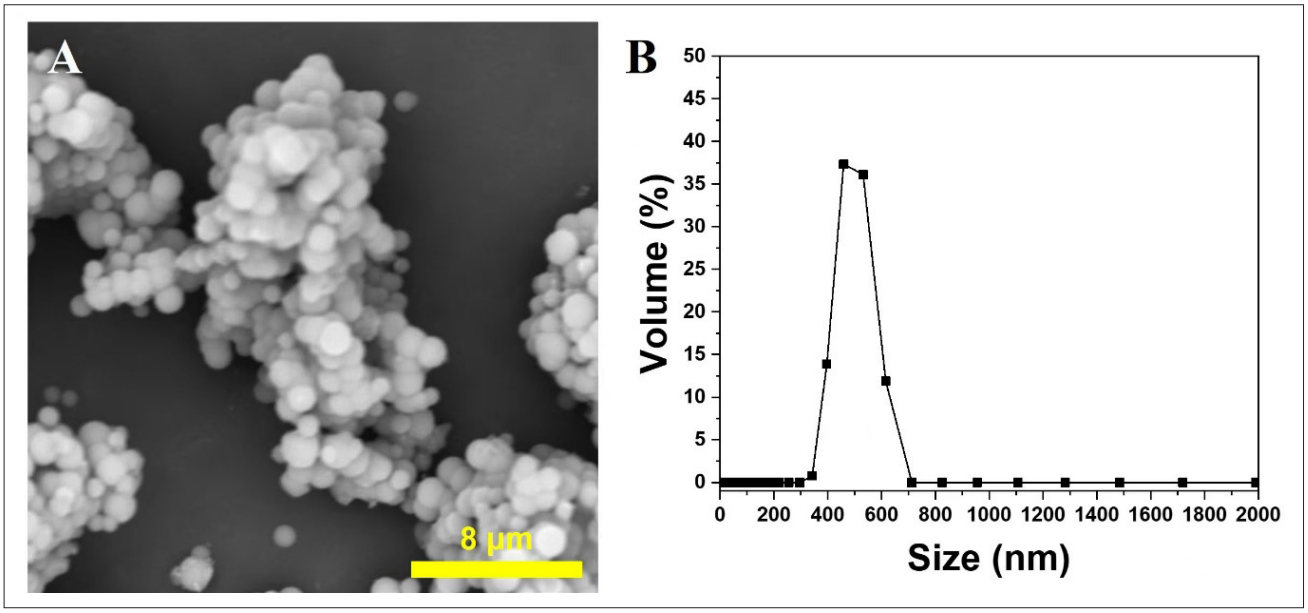

Figure 3. Characterization of SrBG. (A) SEM image of the surface morphology of SrBG. (B) Particle size distribution of SrBG. Scale bar: 8 μm (A). Abbreviations: SEM, scanning electron microscope; SrBG, strontium doped bioglass.

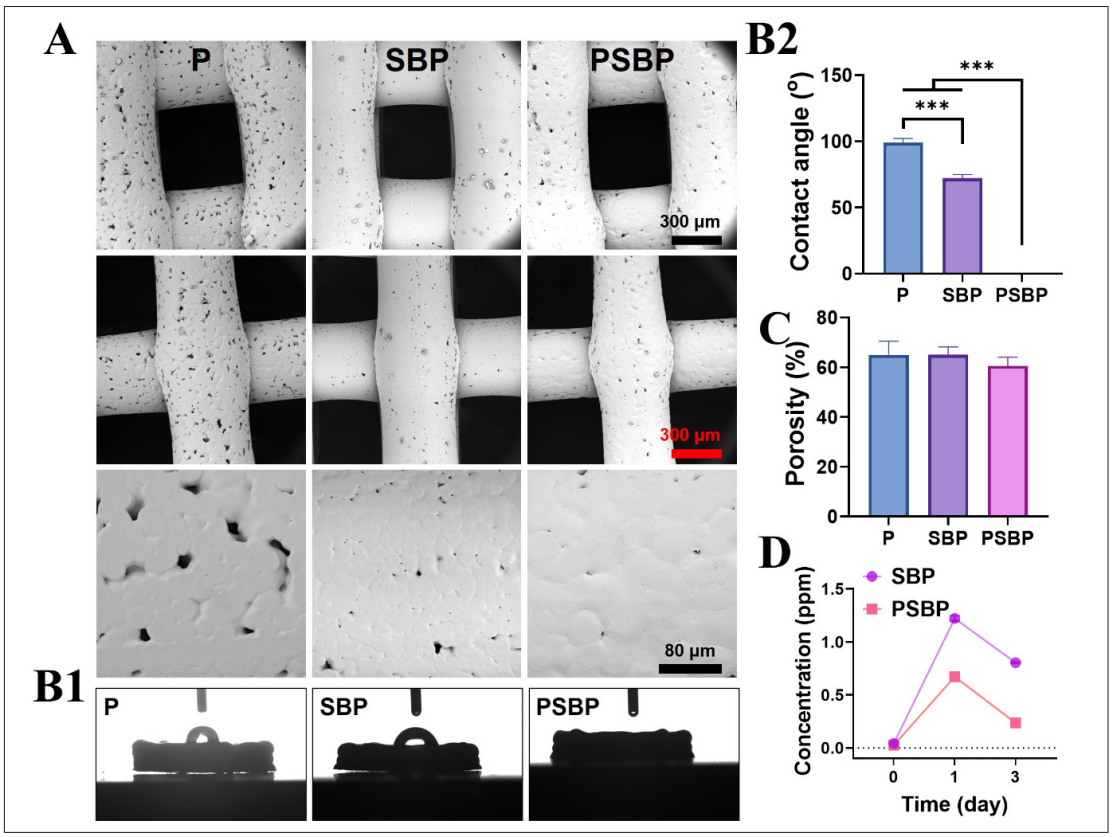

Figure 4. Characterization of each group of stents. (A) SEM images of the P, SBP, and PSBP scaffold surface. (B1 and B2) Contact angle and hydrophilicity analysis of P, SBP, and PSBP scaffolds. Static water contact angle photos of the stents (B1) Static water contact Angle data of the stents (B2) ($n = 3$; ***$p < 0.001$). (C) Porosity analysis of P, SBP, and PSBP scaffolds ($n = 6$). (D) Sr^{2+} release from SBP and PSBP scaffolds. Scale bars: 300 μm (A, top and middle); 80 μm (A, bottom). Abbreviations: P, polycaprolactone (PCL); PSBP, polydopamine (PDA)/strontium (Sr)-doped bioactive glass (SrBG)/polycaprolactone (PCL); SBP, strontium (Sr)-doped bioactive glass (SrBG)/polycaprolactone (PCL); SEM, scanning electron microscope.

continuously released Sr^{2+} over time, but the total Sr^{2+} released from the PSBP scaffolds was lower than that of the SBP scaffolds (Figure 4D).

Thermogravimetric analyses of the P, SBP, and PSBP scaffolds were performed accordingly. The thermogravimetric analysis (TG) curves in Figure 5A revealed that all three groups of scaffolds started to decompose at 250–300°C. The P scaffold displayed weight loss at approximately 300°C, and no further weight loss was observed at approximately 450°C; the SBP and PSBP scaffolds exhibited weight loss at approximately 250°C, and no further weight loss was observed at approximately 350°C. These observations suggest that the SBP and PSBP scaffolds had higher thermal stability than the P scaffolds. Thermogravimetric analysis revealed that the weight loss of the P, SBP, and PSBP scaffolds was 97.73%, 89.35%, and 88.78%, respectively. The residual inorganic content in each scaffold closely matched the theoretical proportions of the incorporated SrBG (0%, 9.09%, and 9.09%, respectively). The mechanical properties of the P, SBP, and PSBP scaffolds were examined by compressive testing experiments. The compressive strengths of the P, SBP, and PSBP scaffolds were 5.47 ± 1.41, 15.96 ± 0.87, and 22.52 ± 3.69 MPa, respectively (Figure 5B1). The compressive modulus of the P, SBP, and PSBP scaffolds was 1166.30 ± 314.05, 3321.26 ± 24.21, and 4878.65 ± 398.81 MPa, respectively (Figure 5B2). With the gradual addition of SrBG and PDA, the compressive strength and compressive modulus of the P, SBP, and PSBP scaffolds gradually increased, and the difference was statistically significant ($p < 0.05$).

3.2. *In vitro* experimental results

3.2.1. Biocompatibility of P, SBP, and PSBP scaffolds

To observe the cellular activity of the scaffolds, the composite P, SBP, and PSBP scaffolds were co-cultured with BMSCs for 3 days and subsequently observed by live-dead cell staining. The fluorescence on the PSBP scaffold was more obvious than that in the P and SBP scaffolds, and the amount of adhered BMSCs was significantly higher in the PSBP scaffold compared to the P and SBP scaffolds; only a small amount of BMSCs were attached to the SBP scaffold, while almost no BMSCs were observed on the P scaffold (Figure 6A). These observations suggest that the PSBP scaffold was the most favorable for cell adhesion and proliferation. To assess the potential cytotoxicity and cell proliferation of the P, SBP, and PSBP scaffolds, a CCK-8 cell proliferation assay was performed. The P, SBP, and PSBP scaffolds were co-cultured with BMSCs for 1, 3, and 7 days. After 1 day of co-culture, no significant difference in cell proliferation was observed between the three scaffold groups; after 3 days of co-culture, cell proliferation in the PSBP scaffold was significantly higher

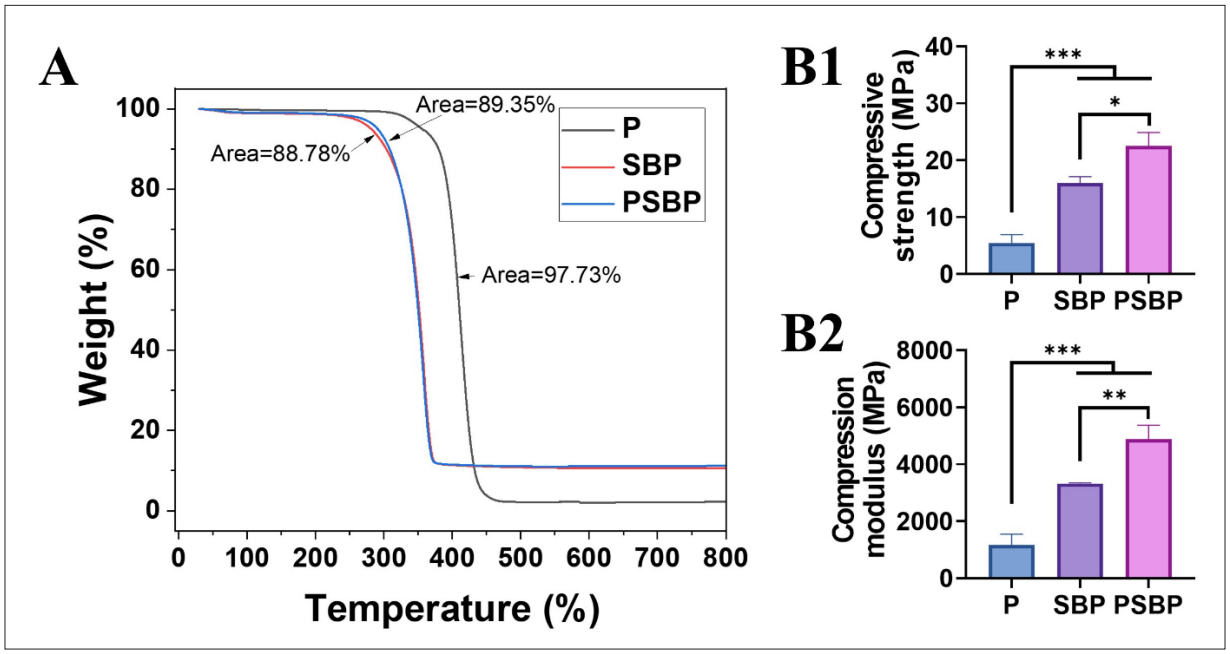

Figure 5. Thermodynamic and compressive performance characterization of the support. (A). Thermogravimetric analysis of the P, SBP, and PSBP scaffolds to evaluate their thermal stability and decomposition behavior. (B1 and B2) The compressive strength (B1) and compression modulus (B2) of the P, SBP, and PSBP scaffolds (n = 3; *p < 0.05, **p < 0.01, ***p < 0.001). Abbreviations: P, polycaprolactone (PCL); PSBP, polydopamine (PDA)/strontium (Sr)-doped bioactive glass (SrBG)/polycaprolactone (PCL); SBP, strontium (Sr)-doped bioactive glass (SrBG)/polycaprolactone (PCL).

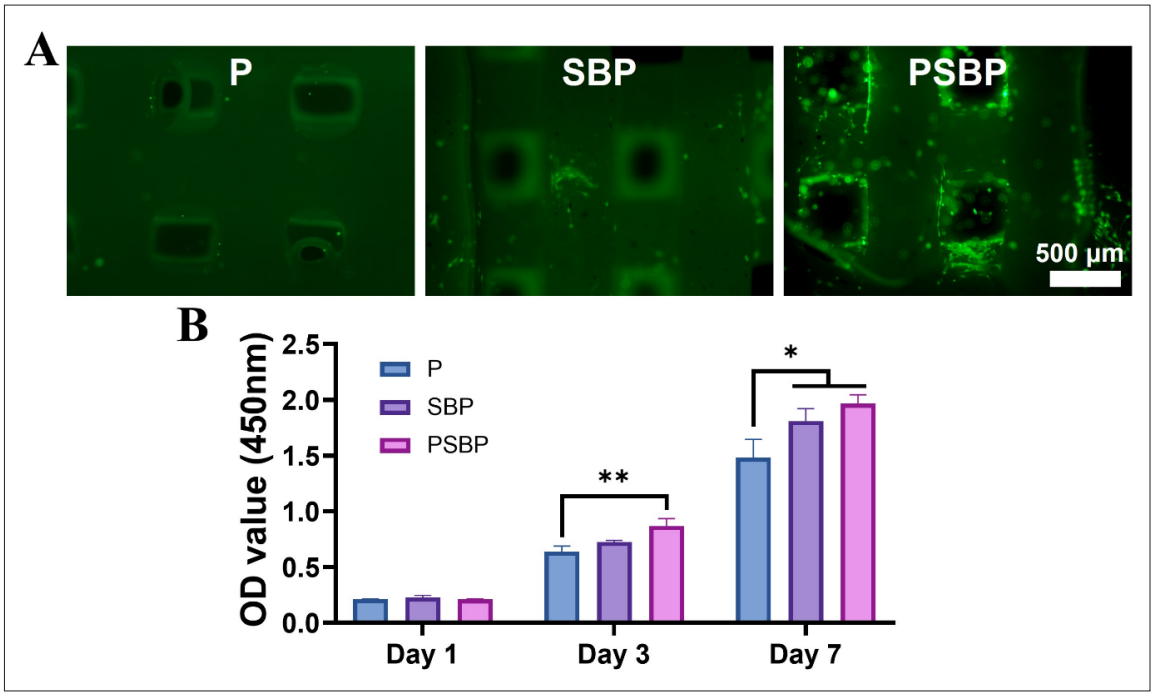

Figure 6. BMSCs viability assay on scaffolds. (A) Live-dead cell staining after 3 days of co-culturing BMSCs within P, SBP, and PSBP scaffolds. (B) Cell proliferation within the P, SBP, and PSBP scaffolds on days 1, 3, and 7 ($n = 3$; $^{*}p < 0.05$, $^{**}p < 0.01$). Scale bar: 500 μm (A). Abbreviations: BMSCs, bone marrow mesenchymal stem cells; OD, optical density; P, polycaprolactone (PCL); PSBP, Polydopamine (PDA)/strontium (Sr)-doped bioactive glass (SrBG)/polycaprolactone (PCL); SBP, strontium (Sr)-doped bioactive glass (SrBG)/polycaprolactone (PCL).

than that in the P scaffold ($p < 0.01$); after 7 days of co-culture, cell proliferation in the PSBP and SBP scaffolds was significantly higher compared to the P scaffold ($p < 0.05$).

3.2.2. Bone-enhancing properties of P, SBP, and PSBP scaffolds

To assess the early osteogenic activity of the scaffolds, the P, SBP, and PSBP scaffolds were co-cultured with BMSCs for 7 days and then subjected to ALP staining. The P scaffold exhibited weaker and lighter ALP staining, indicating a limited effect on promoting osteoblast differentiation. In contrast, the SBP scaffold, which included SrBG, displayed markedly increased and intensified intracellular ALP staining. The PSBP scaffold, incorporating both SrBG and PDA, demonstrated the most pronounced ALP staining, suggesting a synergistic enhancement of osteogenic differentiation (Figure 7A1). The ALP activity in the PSBP scaffold was significantly higher than that in the P and SBP scaffolds ($p \leq 0.001$) (Figure 7A2). To assess the effects of the scaffolds on the osteogenic differentiation of BMSCs, the expression of osteogenesis-related genes (*COL1*, *ALP*, and *RUNX2*) was assessed after co-culturing BMSCs with the scaffolds for 7 and 14 days in MP medium. The expressions of *COL1*, *ALP*, and *RUNX2* were significantly upregulated in the PSBP scaffold compared to the P and SBP scaffolds, suggesting a positive effect on bone differentiation. On day 14, *ALP* expression in the PSBP scaffold was 7.1 and 2.4 times higher than that in the SBP and P scaffolds, respectively; *RUNX2* expression in the PSBP scaffold was 10.3 and 3.2 times higher than that in the SBP and P scaffolds, respectively; and *COL1* expression in the PSBP scaffold was 8.5 and 7.1 times higher than that in the SBP and P scaffolds, respectively (Figure 7B). These observations indicate that the PSBP scaffold had better immunomodulatory ability to promote the osteogenic differentiation of BMSCs compared to the P and SBP scaffolds ($p < 0.05$).

3.2.3. Immunomodulatory capacity of P, SBP, and PSBP scaffolds

To assess the immunomodulatory properties of the scaffolds, the expression of MP polarization-related genes was detected by co-culturing RAW264.7 cells with the P, SBP, and PSBP scaffolds for 1 and 3 days. The expression of M2-MP polarization genes (*CD206* and *ARG*) was significantly upregulated in the PSBP scaffold compared to the P and SBP scaffolds (Figure 8A3 and A4). In contrast, the PSBP scaffold significantly inhibited the expression of M1–MP polarization genes (*TNF-α* and *IL1β*) (Figure 8A1 and A2). On day 3, *ARG* gene expression in the PSBP scaffold was 7.1 and 4.3 times higher than that in the

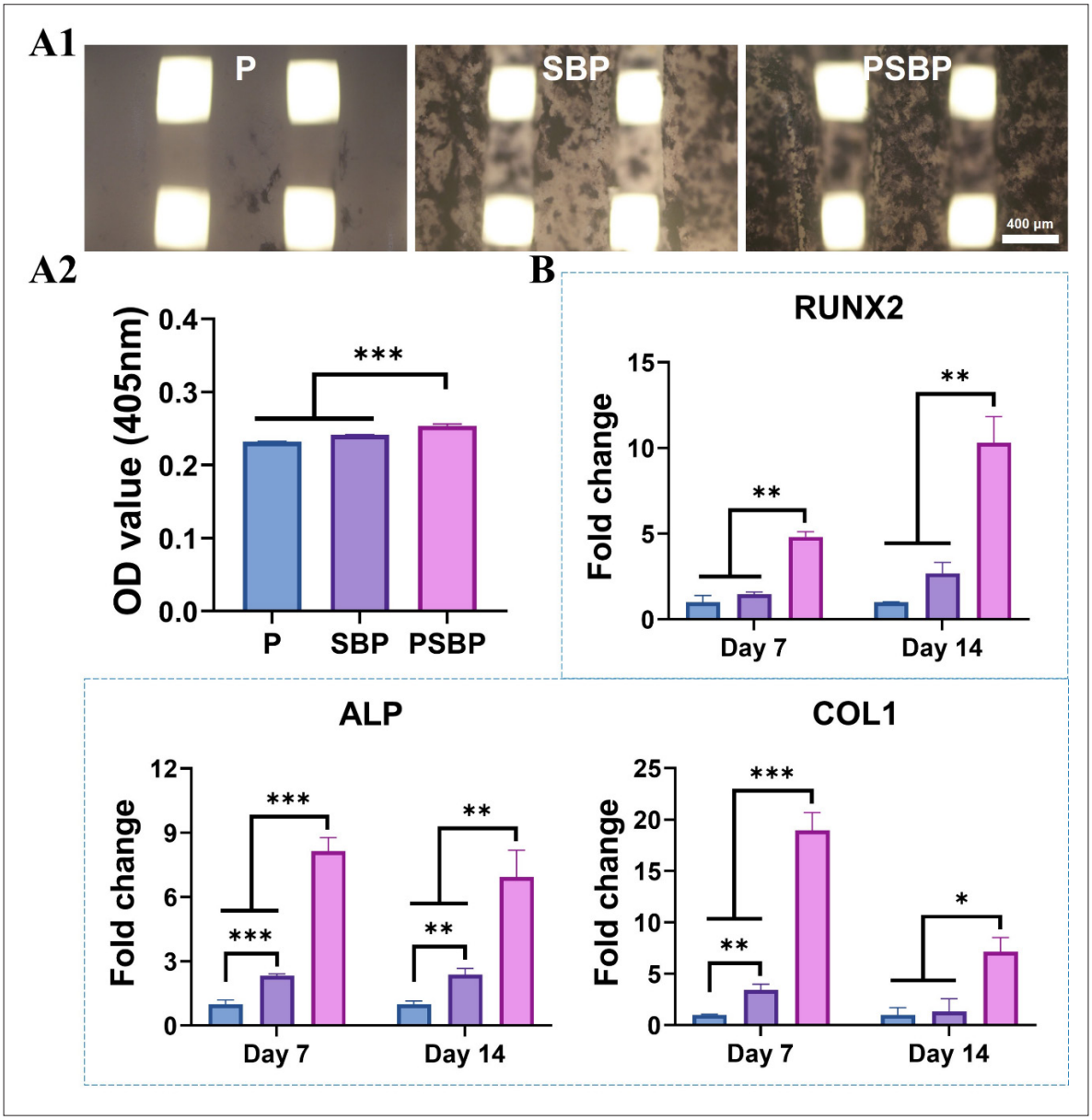

Figure 7. The effect of scaffolds on the osteogenic differentiation performance of BMSCs in vitro. (A1 and A2) ALP staining (A1) and ALP activity analysis (A2) of P, SBP, and PSBP scaffolds co-cultured with BMSCs. (B) Expression of osteogenesis-related genes in the P, SBP, and PSBP scaffolds co-cultured with BMSCs ($n = 3$; *$p < 0.05$, **$p < 0.01$, ***$p < 0.001$). Scale bar: 400 μm (A1). Abbreviations: BMSCs, bone marrow mesenchymal stem cells; OD, optical density; P, polycaprolactone (PCL); PSBP, polydopamine (PDA)/strontium (Sr)-doped bioactive glass (SrBG)/polycaprolactone (PCL); SBP, strontium (Sr)-doped bioactive glass (SrBG)/polycaprolactone (PCL).

SBP and P scaffolds, respectively; *CD206* gene expression in the PSBP scaffold was 6.5 and 1.6 times higher than that in the SBP and P scaffolds, respectively; *TNF-α* gene expression in the P and SBP scaffolds was 2.3 and 2.6 times higher than that in the PSBP scaffold, respectively; and *IL1β* gene expression in the P and SBP scaffolds was 12.3 and 14.2 times higher than that in the PSBP scaffold, respectively. To further verify the immunomodulatory effect of the scaffolds, the levels of pro-inflammatory factor IL-12 and anti-inflammatory factor IL-10 were detected by ELISA assay. Compared to the SBP scaffold, the PSBP scaffold suppressed the expression level of pro-inflammatory factor IL-12 and increased the expression level of anti-inflammatory factor IL-10 ($p < 0.05$) (Figure 8B1 and B2).

3.3. *In vivo* experimental results

3.3.1. Hepatotoxicity and nephrotoxicity of P, SBP, and PSBP scaffolds

To assess the biosafety of the scaffolds, liver and kidney tissues of rats in each scaffold group were sampled at postoperative months 1, 2, and 3, and tissue sections were HE-stained to observe the presence or absence of lesions in these organs. It was observed that specific structures in the rat liver (Figure 9) and kidney (Figure 10)—such as the central vein, the confluent area, hepatocytes, glomeruli, and mesangial cells—in each scaffold group had a clear morphology and boundaries, with no signs of inflammatory cell infiltration. This suggests that the composite scaffolds have good biocompatibility, as they did not have any toxicity effects on the rat liver and kidney.

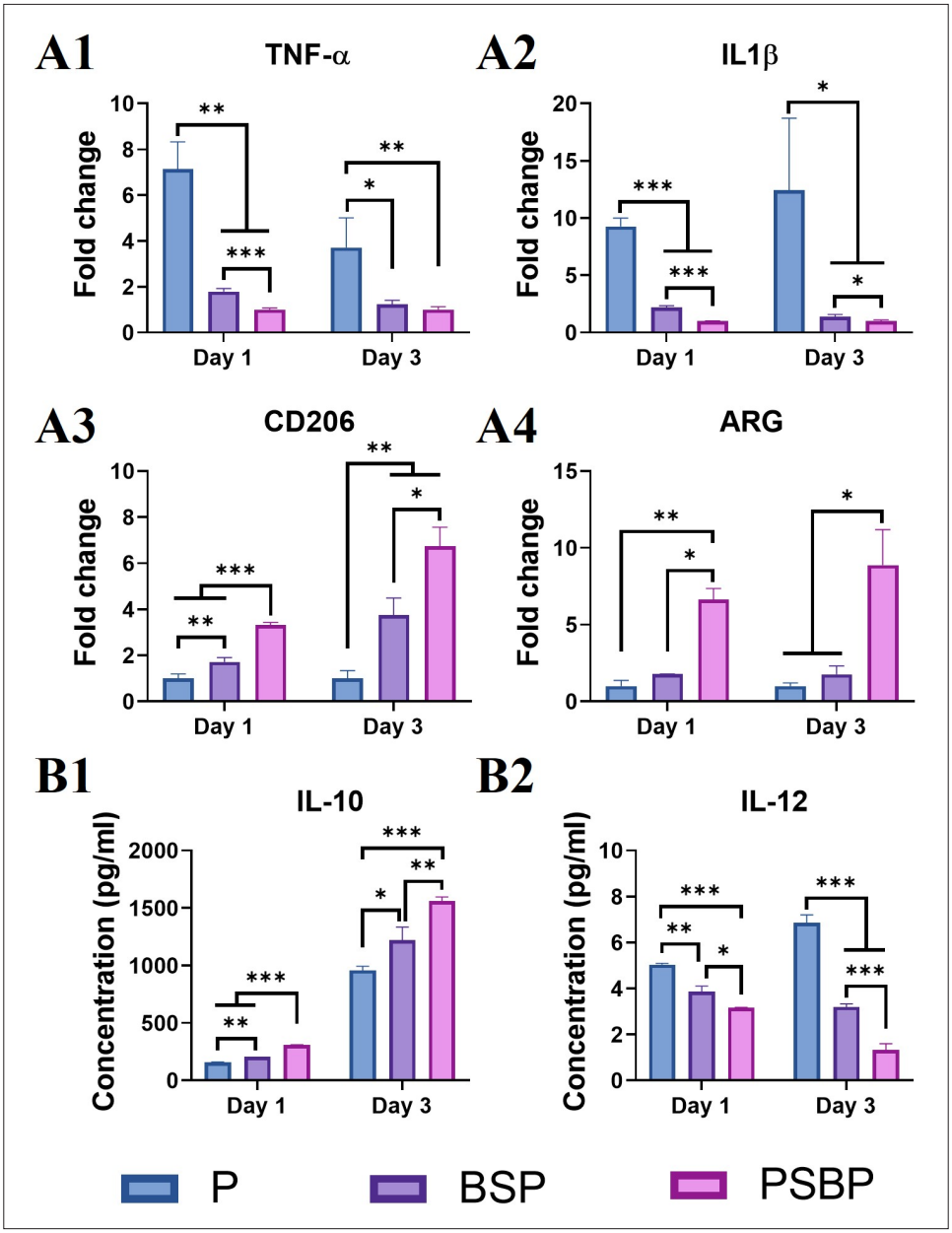

Figure 8. The effect of scaffolds on Macrophage Typing Polarization in vitro. (A1–A4) Expression of macrophage polarization-related genes on P, SBP, and PSBP scaffolds: *TNF-α* (A1), *IL1β* (A2), *CD206* (A3), and *ARG* (A4). (B1 and B2) Expression levels of IL-10 (B2) and IL-12 (B1) in the P, SBP, and PSBP scaffolds. $n = 3$; $^{*}p < 0.05$, $^{**}p < 0.01$, $^{***}p < 0.001$. Abbreviations: P, polycaprolactone (PCL); PSBP, polydopamine (PDA)/strontium (Sr)-doped bioactive glass (SrBG)/polycaprolactone (PCL); SBP, strontium (Sr)-doped bioactive glass (SrBG)/polycaprolactone (PCL).

3.3.2. Micro-CT of rat skull

In order to evaluate the bone repair effect of the three scaffolds *in vivo*, we constructed a bone defect model in SD rats and performed cranial bone sampling at postoperative months 1, 2, and 3; micro-CT scanning was performed to evaluate the repair of the bone defect area. As displayed in Figure 11A, in the blank group, the amount of new bone production in the bone defect area was low at postoperative months 1 and 2, and there was still no significant increase in new bone tissue at postoperative month 3, indicating that the bone repair effect was relatively poor in the absence of scaffolding implantation. Conversely, in the P scaffold, there was a low amount of new bone production at postoperative month 1, and in months 2 and 3, increasing new bone tissue was observed, but large bone defects remained visible, indicating that the bone repair ability of the P scaffold was limited. Compared to the P scaffold, the SBP scaffold—with the addition of SrBG—displayed bone growth along the composite scaffold in the defective area at month 1, gradually increasing over subsequent months until the bone trabeculae covered almost 50% of the defective area at the end of month 3, indicating that the addition of SrBG could promote the repair of bone defects. In contrast, the PSBP scaffold—with the addition of PDA—displayed more bone growth across all time points compared to the P and SBP scaffolds; the defect area was seen to be significantly filled with bone trabeculae at month 1, gradually increasing in subsequent months until almost complete coverage of the bone defect area with bone trabeculae at the end of month 3. The bone volume fraction (Figure 11B) and bone density (Figure 11C) of the bone defect area in each scaffold group

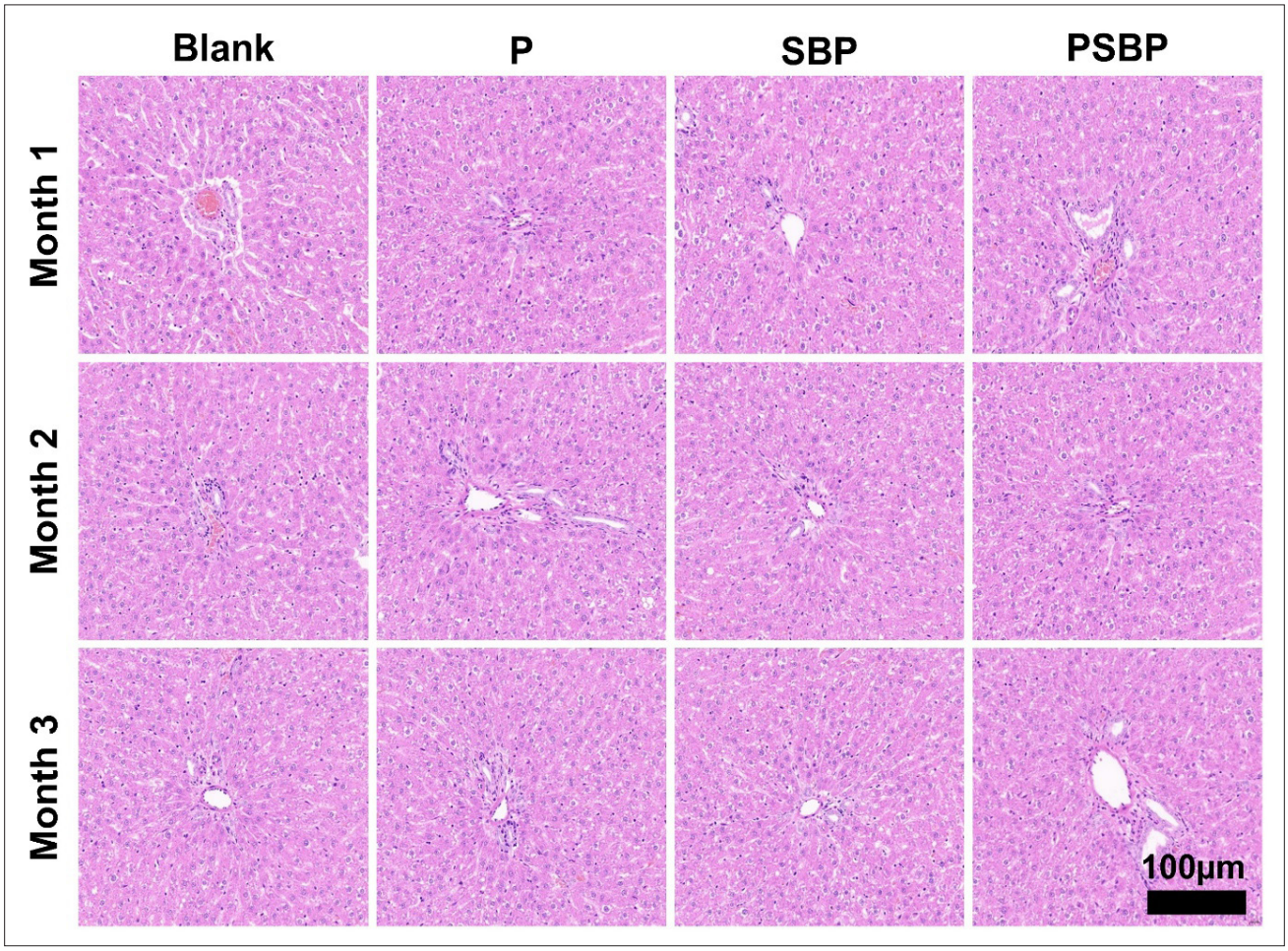

Figure 9. Hematoxylin and eosin (HE) staining of rat liver in each scaffold group. Scale bar: 100 μm. Abbreviations: P, polycaprolactone (PCL); PSBP, polydopamine (PDA)/strontium (Sr)-doped bioactive glass (SrBG)/polycaprolactone (PCL); SBP, strontium (Sr)-doped bioactive glass (SrBG)/polycaprolactone (PCL).

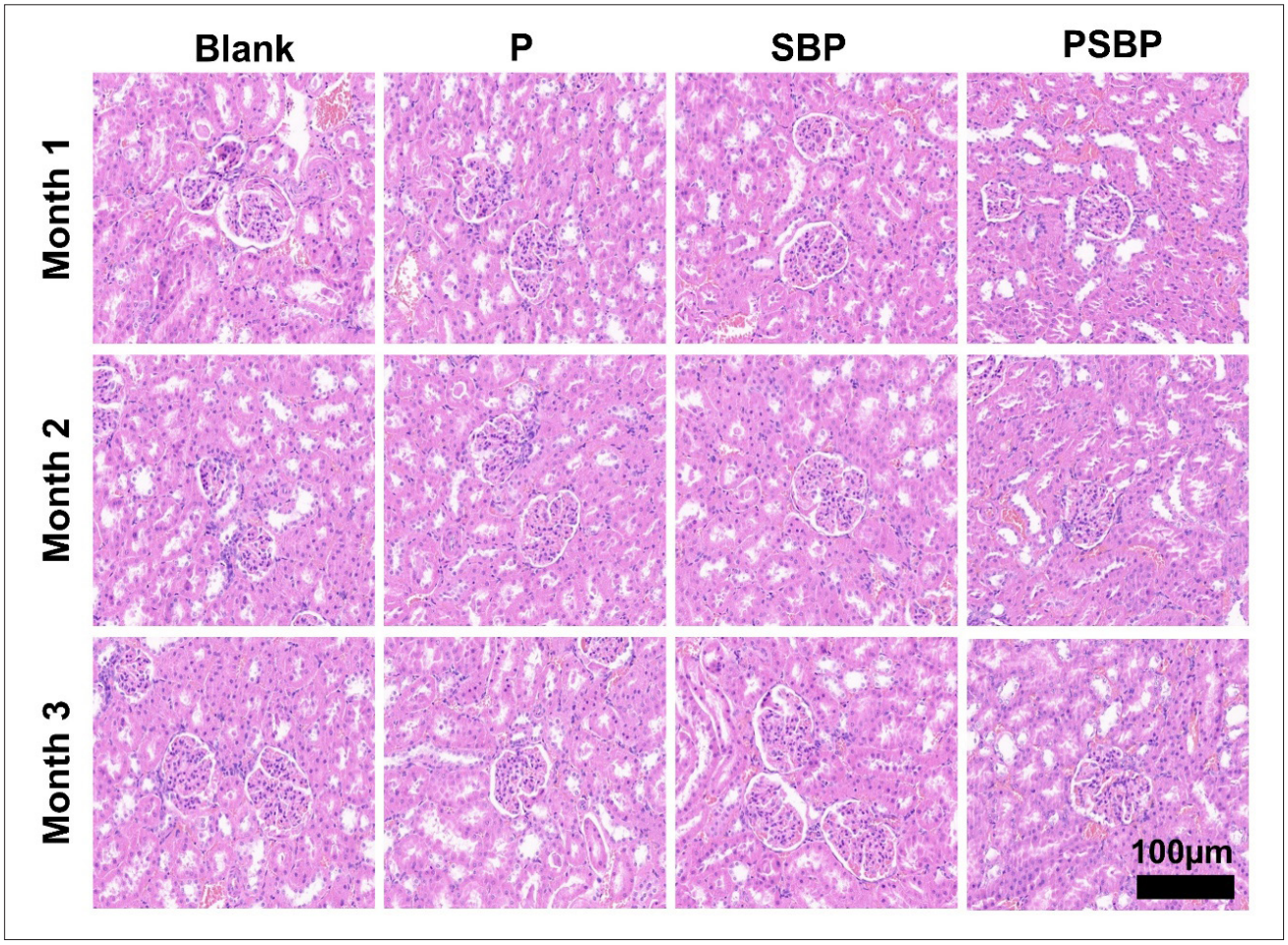

Figure 10. Hematoxylin and eosin (HE) staining of rat kidneys in each scaffold group. Scale bar: 100 μm. Abbreviations: P, polycaprolactone (PCL); PSBP, polydopamine (PDA)/strontium (Sr)-doped bioactive glass (SrBG)/polycaprolactone (PCL); SBP, strontium (Sr)-doped bioactive glass (SrBG)/polycaprolactone (PCL).

were statistically analyzed at postoperative months 1, 2, and 3. The PSBP scaffold displayed the best bone repair effect (among the scaffold types) relative to the blank group ($p < 0.05$). The bone mineral density results were consistent with the bone volume fraction analysis.

3.3.3. HE and Masson staining of rat skull specimens

At 1, 2, and 3 months after surgery, the rats were euthanized; skull specimens were collected and analyzed by HE staining and Masson staining to assess the formation of new bone tissue in the bone defect area. HE staining at postoperative month 1 revealed that the blank group had more fibrous tissue but less new bone tissue in the bone defect area. The P and SBP scaffolds displayed a small amount of new bone in the defect area, while the PSBP scaffold displayed a large amount of new bone formation. At postoperative month 2, the new bone tissue in the PSBP group was progressively darker in color and more widely distributed compared to the other scaffold groups; new bone tissue gradually formed in the pores of the stent, and new bone tissue was observed at the defect interface and inside the material. At postoperative month 3, the new bone tissue in the PSBP group was continuous and more widely distributed, and the area of the new bone was significantly larger than that of the blank, P, and SBP scaffold groups (Figure 12).

The results of Masson staining are displayed in Figure 13. At postoperative month 1, the SBP and PSBP scaffold groups had more light blue collagen tissue and red muscle fiber tissue compared to the blank and P scaffold groups. In subsequent months, the neoplastic bone tissue of each scaffold group further matured, exhibiting dark blue mature collagen, which was most significant in the PSBP scaffold group. These results indicated that PSBP scaffolds could promote bone defect repair.

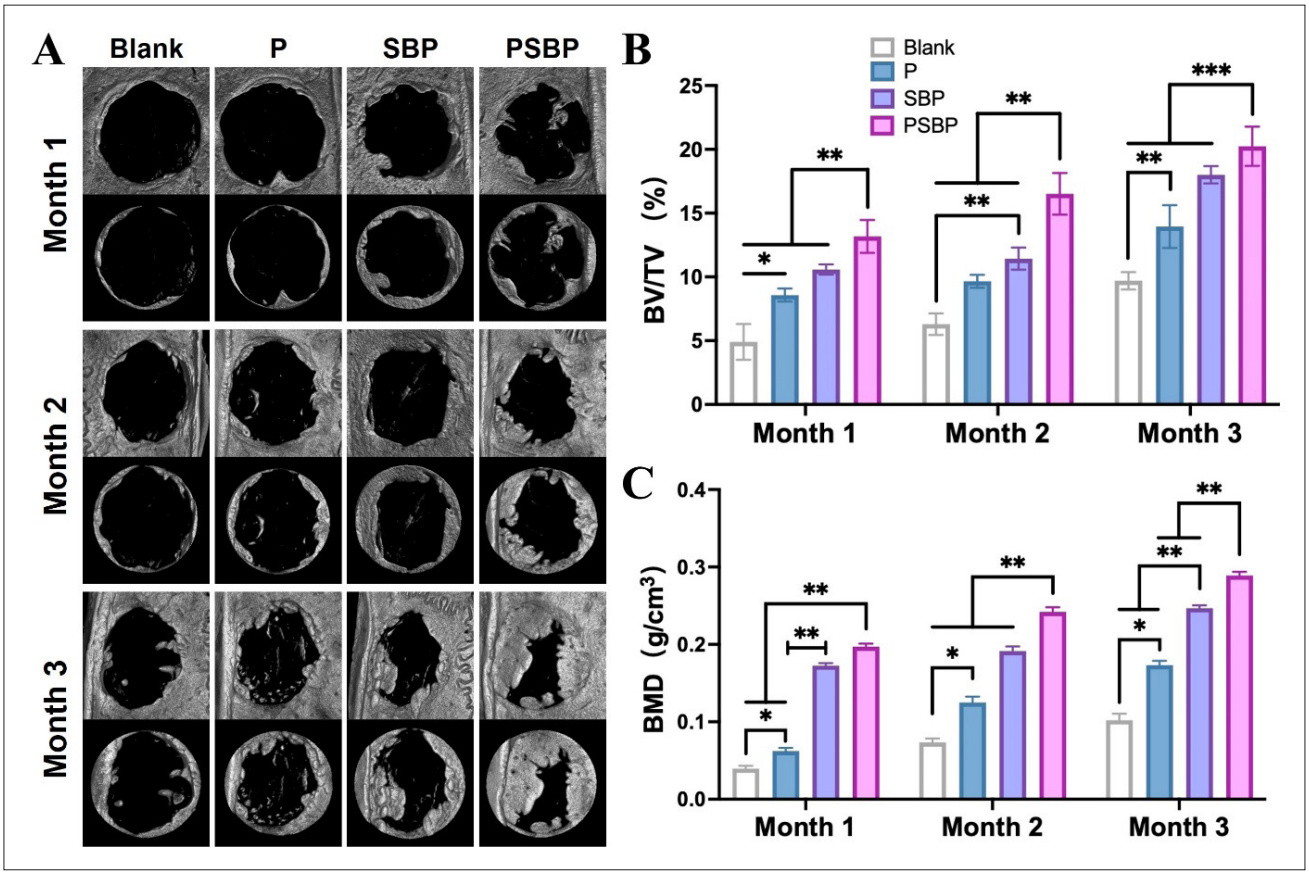

Figure 11. Micro-CT assessment of bone defect repair outcomes. (A) Micro-CT analysis of the cranial bone defect area for each scaffold group. (B and C) Bone volume fraction (BV/TV%) (B) and bone mineral density (BMD) (C) in the bone defect area for each scaffold group ($n = 3$; $^{*}p < 0.05$, $^{**}p < 0.01$, $^{***}p < 0.001$). Abbreviations: Micro-CT, micro computed tomography; P, polycaprolactone (PCL); PSBP, polydopamine (PDA)/strontium (Sr)-doped bioactive glass (SrBG)/polycaprolactone (PCL); SBP, strontium (Sr)-doped bioactive glass (SrBG)/polycaprolactone (PCL).

3.3.4. Immunofluorescence staining of rat skull specimens

To further assess the immunomodulation, pro-angiogenic, and osteogenic differentiation ability of the scaffolds, iNOS (red), CD163 (green), VEGF (red), and BMP-2 (green) were detected by immunofluorescence staining in each scaffold group. The results for immunofluorescence staining are displayed in Figure 14.

In immunomodulation, iNOS and CD163 serve as key markers for MP polarization, representing the M1 and M2 phenotypes, respectively. At postoperative months 1 and 2, the expression of iNOS (red) in new bone tissue in the bone defect area was the highest in the blank group. In contrast, the red fluorescence intensity in the bone defect area progressively decreased across the P, SBP, and PSBP scaffold groups. At postoperative month 3, the PSBP scaffold group had the weakest red fluorescence. Conversely, the expression of CD163 (green) gradually increased over postoperative months 1, 2, and 3, with the PSBP scaffold group emitting the strongest fluorescence at postoperative month 3. These observations suggest that the PSBP scaffolds promoted the expression of M2 MPs and inhibited the expression of M1 MPs, thereby inducing better immunomodulation to facilitate bone defect repair.

In terms of vascularization, at postoperative months 1, 2, and 3, the expression of VEGF (red) in the bone defect area of all groups gradually increased. Among them, the PSBP scaffold group exhibited the strongest fluorescence intensity and the largest expression area, indicating that PSBP scaffolds more effectively promoted vascularization in the bone defect area, thereby facilitating bone defect repair.

In terms of osteogenesis, at postoperative months 1, 2, and 3, the expression of BMP-2 (green) was the lowest in the blank group, but gradually increased in the P, SBP, and PSBP scaffold groups. At postoperative month 3, the PSBP

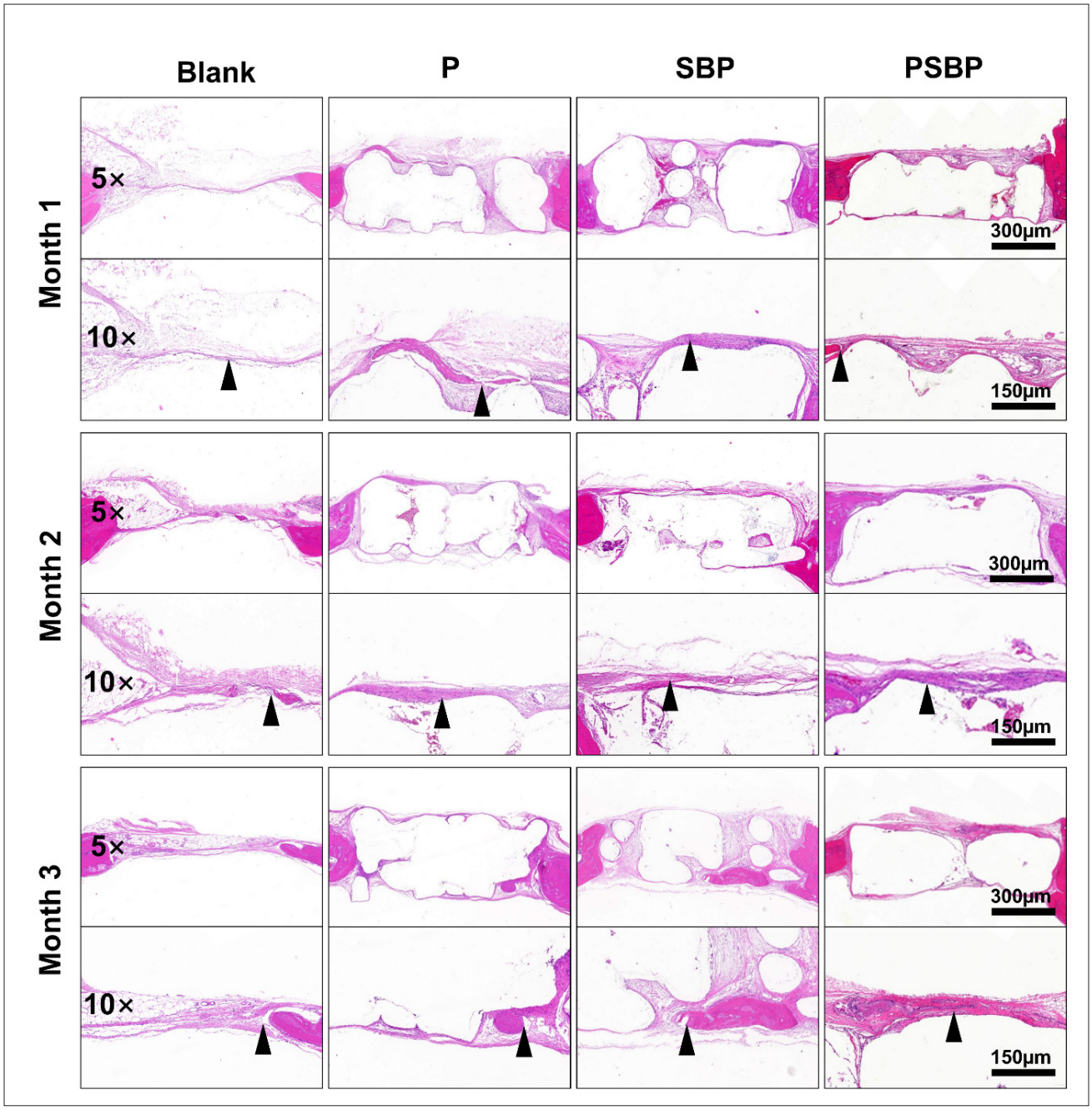

Figure 12. Hematoxylin and eosin (HE) staining of the bone defect area of rats in each scaffold group. Arrows indicate area of new bone. Scale bars: 300 μm (top, 5×), 150 μm (bottom, 10×). Abbreviations: P, polycaprolactone (PCL); PSBP, polydopamine (PDA)/strontium (Sr)-doped bioactive glass (SrBG)/polycaprolactone (PCL); SBP, strontium (Sr)-doped bioactive glass (SrBG)/polycaprolactone (PCL).

scaffold group exhibited the strongest green fluorescence, with a significantly larger positive staining area compared to the other groups, indicating a superior bone repair effect.

4. Discussion

Ideal tissue engineering scaffolds should have good osteoconductivity, biodegradability, plasticity, and a certain degree of mechanical strength to provide a suitable environment for tissue regeneration and cell growth, adhesion, and proliferation.[43] PCL is used as the main material for bone tissue engineering scaffolds due to its high plasticity and biodegradation *in vivo*, providing space for new bone tissue and blood vessels to grow.[44] However, PCL is biologically inert and needs to be compounded

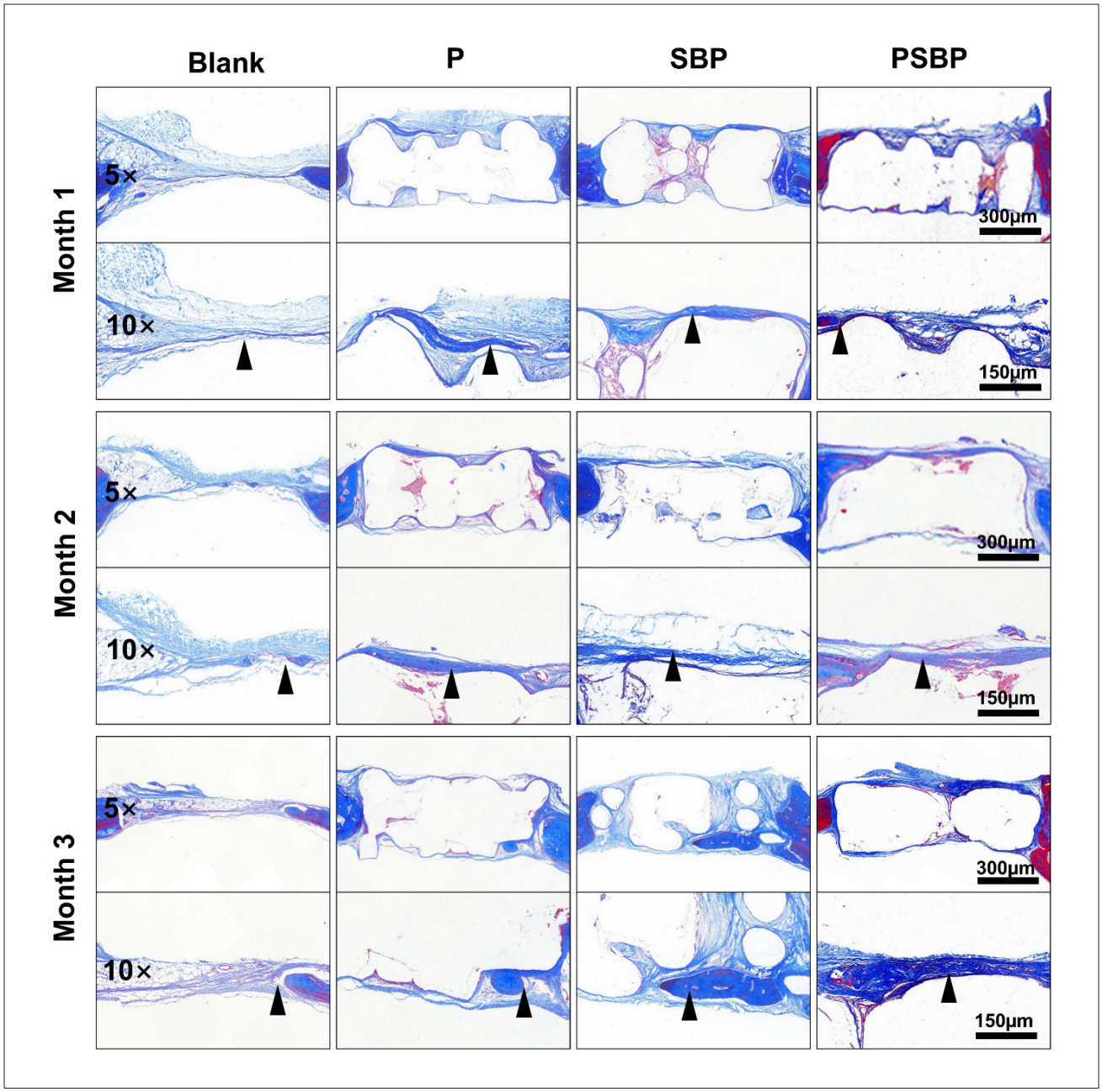

Figure 13. Masson staining of the bone defect area of rats in each scaffold group. Arrows indicate area of new bone. Scale bars: 300 μm (top, 5×), 150 μm (bottom, 10×). Abbreviations: P, polycaprolactone (PCL); PSBP, polydopamine (PDA)/strontium (Sr)-doped bioactive glass (SrBG)/polycaprolactone (PCL); SBP, strontium (Sr)-doped bioactive glass (SrBG)/polycaprolactone (PCL).

with other materials for better bone restoration.[45] SrBG has demonstrated certain advantages as a bone repair material due to its good osteogenic ability and immunomodulatory properties.[46] As displayed in Figure 3, SrBG comprises numerous uniformly arranged small spherical particles with a particle size distribution between 350 and 700 nm. Among them, SrBG particles measuring 493.9 nm account for the largest proportion (approximately 38%) of the total, which favors cell adhesion. In addition, functionalization of the material surface with PDA increases the hydrophilicity and surface adhesion of the material, thus effectively improving its biocompatibility.[39,47] Likewise, 3D printing technology can personalize the geometric shape of the scaffold according to the shape of the bone defect, allowing

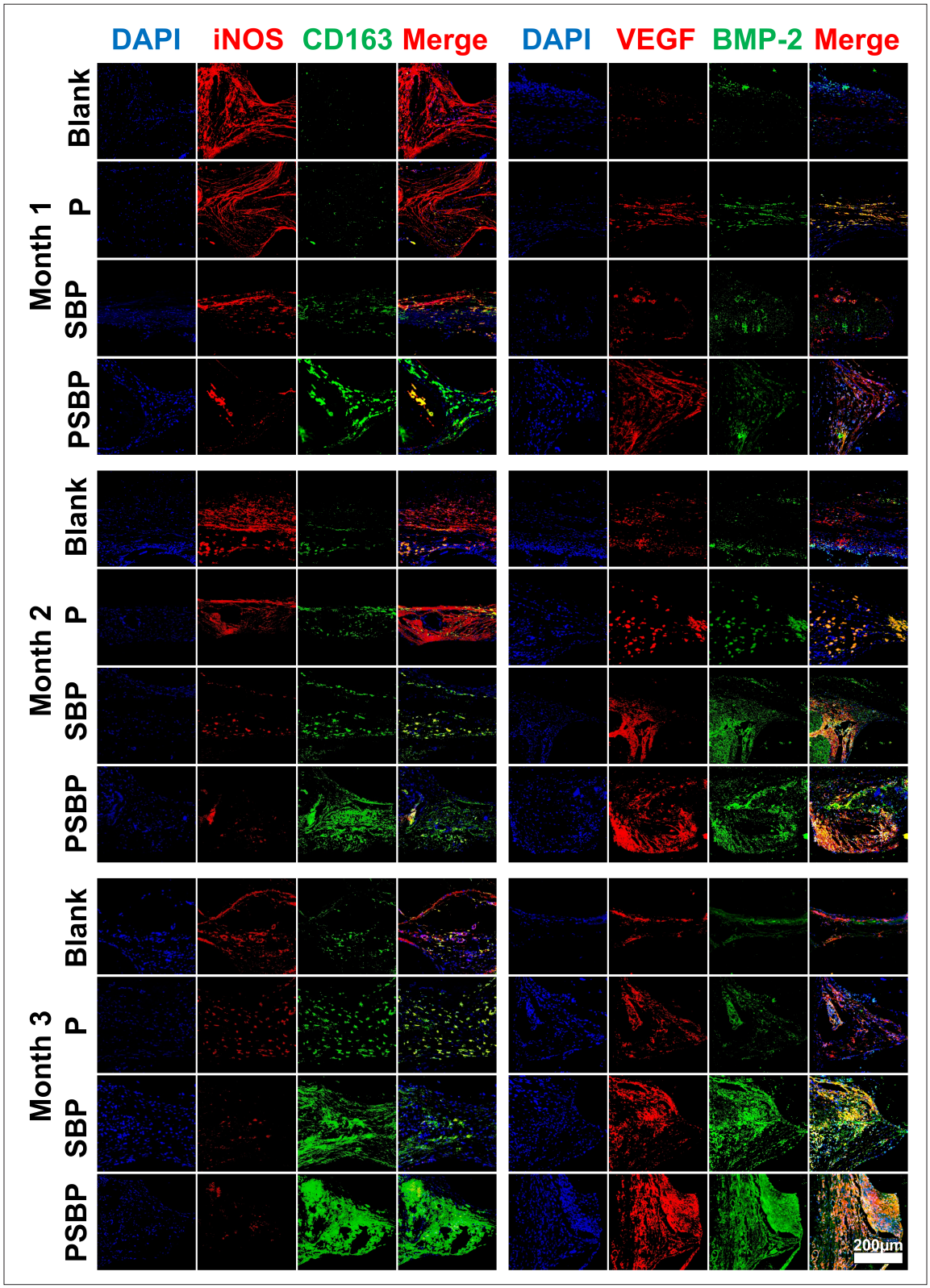

Figure 14. Immunofluorescence staining of iNOS, CD163, VEGF, and BMP-2 in the bone defect area of rats in each scaffold group. Scale bar: 200 μm. Abbreviations: P, polycaprolactone (PCL); PSBP, polydopamine (PDA)/strontium (Sr)-doped bioactive glass (SrBG)/polycaprolactone (PCL); SBP, strontium (Sr)-doped bioactive glass (SrBG)/polycaprolactone (PCL).

for better fit at the bone defect site and more effective bone defect repair.[48–50] In this study, P and SBP scaffolds were prepared by 3D printing, and PSBP scaffolds were obtained by co-deposition of PDA with SBP scaffolds. The physical properties, biocompatibility, and immunomodulatory ability of the scaffolds were evaluated by *in vitro* and *in vivo* experiments, and the effects of the scaffolds toward osteogenic differentiation *in vitro* and bone defect repair *in vivo* were assessed.

The three scaffold groups (P, SBP, and PSBP) were characterized accordingly. Firstly, the surface morphology of the scaffolds was observed by SEM (Figure 4A). There was no significant difference in the pore size among the three scaffold groups. However, after SrBG addition and PDA modification, the PSBP scaffolds had SrBG particles attached to their surface, resulting in smaller and fewer surface pores and a smoother surface. Secondly, good porosity is necessary for the scaffold to fulfill its bone repair function.[51] As displayed in Figure 4C, all three scaffold groups exhibited high porosity, with PSBP scaffolds having a slightly lower porosity than P and SBP scaffolds. This is due to the filling of some pores during PDA modification of the SBP scaffolds.[52] It is further demonstrated by the average aperture of each group of scaffolds as shown in Appendix Figure A1, where the smallest average aperture of the scaffolds was observed in the PSBP group. The high porosity of the scaffolds facilitates cell adhesion, growth, and vascular ingrowth.[50] Nonetheless, the differences between the scaffold groups were not significant, and the slight decrease in porosity had little effect on cell growth and angiogenesis. PDA in the PSBP scaffolds filled the fiber pores, significantly enhancing their compressive properties (Figure 5B1 and B2) and inhibiting Sr^{2+} release (Figure 4D) compared to SBP scaffolds. Moreover, filling the porous structure on the fibers increased the scaffolds' compressive strength and reduced their degradation rate, consistent with the trends observed in a previous study.[53] Studies have demonstrated that PDA functionalization of scaffold surfaces strongly attaches reactive groups—such as catecholamines and amines—to the material surface via covalent bonds, thereby improving hydrophilicity, adhesion, and biocompatibility.[54–56] As displayed in Figure 4B1 and B2**,** the PSBP scaffolds featured better hydrophilicity after the addition of SrBG and PDA, providing more favorable conditions for cell adhesion and proliferation. Zhao et al.[57] reported that SrBG effectively improved the mechanical properties and bone repair capability of calcium aluminate cement. In terms of mechanical properties, the compressive strength and modulus of the PSBP scaffolds were significantly higher than those of the P and SBP scaffolds, likely associated with the addition of SrBG and PDA. This suggests that the PSBP scaffolds possessed strong mechanical properties and could withstand greater mechanical loads. In Figure 5A, the thermogravimetric analysis revealed that the mass of the remaining inorganic particles in each scaffold group was close to the theoretical proportion of the mixed SrBG, and all three scaffolds exhibited good thermal stability.

Biocompatibility of the stent is a prerequisite for its biological functioning.[58] As presented in Figure 6A, the results of the live-dead cell assay indicated that the PSBP scaffold had a higher number of adhered and proliferated BMSCs compared to the other scaffold groups, indicating non-cytotoxicity. Meanwhile, results of the CCK-8 proliferation assay indicated that the PSBP scaffold could promote BMSC proliferation significantly better than the other scaffold groups, which was consistent with the live-dead cell staining results. However, the scaffold degradation products post-implantation and the substances generated by their interaction with the body's microenvironment may be potentially toxic to the host.[59] To evaluate the *in vivo* toxicity of the scaffolds, an SD rat model was established in this study. HE staining analysis of liver and kidney tissues revealed no obvious damage or abnormal reaction, highlighting the good biosafety for all three scaffold groups (Figures 9 and 10).

Ideal bone repair materials must be biocompatible and possess strong osteogenic differentiation capacity.[57] However, PCL is limited by its insufficient osteogenic capacity, high hydrophobicity, and lack of sufficient cell attachment sites.[60,61] To overcome these shortcomings, Hench et al.[62] used the sol–gel method to prepare SiO_2-CaO-P_2O_5 ternary BGs, characterized by numerous microporous structures, a large specific surface area, and a fast rate of surface hydroxyapatite (HA) generation, enabling them to form strong chemical bonds with human bone tissue. In this study, SrBG was compounded in PCL scaffolds, and the scaffolds were modified using PDA to detect osteogenesis-related genes. ALP is a phenotypic marker of early osteogenesis.[63] As displayed in Figure 7A1 and A2**,** the PSBP scaffolds strongly induced osteogenic differentiation, as indicated by ALP activity and staining results. In addition, qRT-PCR revealed that after co-culturing BMSCs with the three scaffold groups under osteogenic induction conditions, the expression of osteogenesis-related genes (*COL1*, *ALP*, and *RUNX2*) was significantly upregulated in the PSBP scaffold group compared to the P and SBP scaffold groups (Figure 7B). This observation was consistent with the ALP activity and staining results.

The immune microenvironment plays a crucial role in bone repair, and MP phenotypic switching is critical for bone defect repair.[64] To regulate the microenvironment's

effect on bone repair, some studies have combined MBG with PCL to prepare MBG/PCL scaffolds that possess better immune-regulating and bone-repair capabilities.[65] Another study prepared SrBG by doping Sr^{2+} into MBG, leading to a significantly enhanced immunomodulatory capacity by promoting M2 MP polarization.[66] The PSBP scaffolds effectively upregulated the expression of M2 MP polarization genes (*CD206* and *ARG*) while suppressing the expression of M1 MP polarization genes (*TNF-α* and *IL1β*) (Figure 8). This may be related to the release of various ions from SrBG, including Sr^{2+}, Si^{4+}, Ca^{2+}, and P^{5+}.[67] These ions enhanced the scaffold's immunomodulatory properties by inhibiting M1 MP polarization and promoting M2 MP polarization.[68,69] Results from the Sr^{2+} release experiments demonstrated that Sr^{2+} from the SBP and PSBP scaffolds was continuously released over time (Figure 4D). The overall Sr^{2+} release concentration in the PSBP scaffold group was lower than that in the SBP scaffold group. ELISA experiments indicated that PSBP scaffolds inhibited the expression of the pro-inflammatory factor IL-12 and increased the expression of the anti-inflammatory factor IL-10 at a greater extent compared to SBP scaffolds (Figure 8B1 and B2), suggesting that the relatively low Sr^{2+} concentration in the PSBP scaffolds facilitates better immune microenvironment coordination to promote osteogenesis. Römer et al.[70] found that adding 3 mM (approximately 263 ppm) of Sr^{2+} to the culture medium significantly inhibited the expression of the pro-inflammatory factor IL-6 in human periodontal cells compared to a control group. Buache et al.[71] reported that 10 μM Sr-doped bidirectional calcium phosphate significantly inhibited the expression of TNF-α and IL-6 in human primary monocytes. Both SrBG extracts (Sr^{2+} concentration: 6.227 ppm and 10 μM [approximately 0.88 ppm]), which are obtained after immersing SrBG in cell culture medium and processed, significantly inhibited the expression of TNF-α, IL1β, and IL-6 and elevated the expression of anti-inflammatory factors IL-1ra, IL-10, and Arg-1. Lower Sr^{2+} concentrations correlated with a lower expression of pro-inflammatory factors and a higher expression of anti-inflammatory factors.[33] This is consistent with the results in the present study, validating that PSBP scaffolds have excellent immunomodulatory capabilities.

Micro-computed tomography (micro-CT) is a non-invasive, high-resolution imaging technique that enables clear visualization of the internal microstructure of bone tissue, especially for detecting new bone tissue in small animals.[60,72] To evaluate the *in vivo* bone repair effects of the three scaffold groups, this study established a bilateral cranial bone defect model in SD rats. SD rats were chosen for their low cost and size, which is suitable for surgical manipulation.[73,74] Micro-CT was used to observe new bone growth in the bone defect area. The bone repair effect was then microscopically evaluated using quantitative indexes, such as bone mineral density and bone volume fraction.[75] The micro-CT 3D-reconstructed images highlighted that the PSBP scaffolds—as bone defect-filling materials—exhibited significant new bone growth (Figure 11A). Likewise, the bone volume fraction and bone density analysis results were consistent with the micro-CT results (Figure 11B and C), further validating that PSBP scaffolds have better bone repair effects compared to the other scaffolds. In addition, HE staining, a commonly used method to observe tissue growth, was performed on rat cranial specimens from all scaffold groups to observe bone tissue structure.[76] The HE staining results revealed that at postoperative months 1, 2, and 3, the PSBP scaffold group had more bone tissue formation than the SBP, P, and blank scaffold groups (Figure 12). Masson staining results also indicated that the PSBP scaffold group exhibited better osteogenesis (Figure 13).

The immunomodulatory capacity of implanted scaffolds is important in promoting osteogenic differentiation and angiogenesis.[77] To further assess the immunomodulation and bone repair effects of each scaffold group, immunofluorescence staining was used to analyze cranial defect repair in rats. Generally, iNOS and CD163 are used as polarization markers for M1 and M2 MPs, respectively.[78,79] It has been reported that PDA reduces the expression of M1 MP markers by scavenging ROS[80,81] and that Sr^{2+} activates the PI3K/AKT/mTOR pathway to promote M2 MP polarization.[66] In this study, the immunofluorescence staining results demonstrated that the PSBP scaffolds significantly upregulated the expression of the M2 MP marker CD163 and downregulated the expression of the M1 MP marker iNOS (Figure 14). This suggests that the PSBP scaffolds promoted MP polarization of M1 MPs to M2 MPs, resulting in more M2 MPs in the immune microenvironment. This polarization attenuated the inflammatory response in the early stage of bone repair and promoted bone defect repair.[82,83] In addition, more M2 MPs contributed to osteogenesis on the scaffold surface, ultimately leading to good osseointegration.[84] Therefore, PSBP scaffolds have good immunomodulatory properties, and PDA, together with Sr^{2+}, promotes MP polarization toward the M2 phenotype. In promoting bone repair, BMP-2, a key osteoinductive growth factor, induces targeted differentiation of undifferentiated BMSCs into osteoblasts and promotes osteoblast differentiation and maturation, thereby accelerating bone defect repair.[85,86] In this study, the PSBP scaffolds expressed higher levels of BMP-2 at the defect site, suggesting a strong osteogenic induction ability. Additionally, vascularization is a key part of the bone repair process and directly affects the repair and remodeling

of bone tissue.[87] VEGF expression is strongly associated with neovascularization,[88] and our immunofluorescence staining results demonstrated that the PSBP scaffolds effectively promoted VEGF expression. This enhancement is attributed to the synergistic pro-angiogenic effects of Sr^{2+} and Si^{4+} released by SrBG.[89] Furthermore, surface modification with PDA further enhanced angiogenesis and maturation of the cell as well as tissue.[90,91]

Overall, the PDA/SrBG/PCL composite scaffolds prepared in this study can better regulate the immune microenvironment, promote blood vessel regeneration, and facilitate bone defect repair. Nonetheless, the study had several limitations, namely the short observation period and the preliminary *in vivo* investigation, thereby warranting further investigation into the mechanism of bone defect repair.

5. Conclusion

In this study, a PDA/SrBG/PCL composite scaffold was fabricated, combining the multifunctional properties of material modification, immunomodulation, and osteogenesis induction. Overall, the PDA/SrBG/PCL scaffolds facilitated bone differentiation *in vitro* and bone repair in an *in vivo* cranial defect model. Therefore, the composite scaffold may potentially overcome the clinical limitations of traditional PCL scaffolds and mark a shift from mere structural replacement to functional reconstruction in bone tissue engineering, offering a valuable reference for the future development of advanced bone repair materials.

Acknowledgments

None.

Funding

This research was supported by the National Natural Science Foundation of China (82160577, 32000964), the Zunyi City Innovation Team Fund (Zunyi Science Talent [2024] No. 4), Guangdong Province Science and Technology Plan Project (2024A1515012265), and the Hainan Academician Innovation Center (Nanfan Medical Materials and Health Technology Innovation Center) (2022GDASZH-2022020402-01).

Conflict of interest

The authors declare no financial and personal relationships with other entities or organizations that can inappropriately influence the present work. They also have no professional or other personal interest of any nature or kind with any product, service, and/or company that could be construed as influencing the position presented in, or the review of, the current manuscript.

Author contributions

Conceptualization: Qiping Huang, Xiang Li, Weikang Xu, Qingde Wa
Data curation: Qiping Huang, Xiang Li, Qinghong Fan, Qian Du, Guangquan Zhao, Yuanhao Lv, Yixiao Wang, Weikang Xu, Qingde Wa
Formal analysis: Qiping Huang, Xiang Li, Qian Du, Guangquan Zhao, Yuanhao Lv, Yixiao Wang
Funding acquisition: Weikang Xu, Qingde Wa
Investigation: Qiping Huang, Xiang Li
Methodology: Qiping Huang, Xiang Li
Project administration: Qiping Huang, Xiang Li, Qian Du, Guangquan Zhao, Yuanhao Lv, Yixiao Wang
Resources: Qiping Huang, Xiang Li
Validation: Weikang Xu, Qingde Wa
Visualization: Weikang Xu, Qingde Wa
Writing – original draft: Qiping Huang, Xiang Li
Writing – review and editing: Weikang Xu, Qingde Wa

Ethics approval and consent to participate

All animal experiments were performed according to the protocol approved by the Institutional Animal Care and Use Committee of Guangdong Quality Supervision and Testing Station for Medical and Health Care Appliances (Approval ID: ZMU21-2412-019).

Consent for publication

Not applicable.

Availability of data

Upon reasonable request, data can be obtained from the corresponding author.

References

1. Chi J, Wang M, Chen J, et al. Topographic orientation of scaffolds for tissue regeneration: recent advances in biomaterial design and applications. *Biomimetics (Basel).* 2022;7(3):131.
doi: 10.3390/biomimetics7030131

2. Yang X, Wang Y, Zhou Y, et al. The application of polycaprolactone in three-dimensional printing scaffolds for bone tissue engineering. *Polymers (Basel).* 2021;13(16):2754.
doi: 10.3390/polym13162754

3. Mancuso E, Shah L, Jindal S, et al. Additively manufactured BaTiO(3) composite scaffolds: a novel strategy for load bearing bone tissue engineering applications. *Mater Sci Eng C Mater Biol Appl.* 2021;126:112192.
doi: 10.1016/j.msec.2021.112192

4. Gómez-Lizárraga KK, Flores-Morales C, Del Prado-Audelo ML, et al. Polycaprolactone- and polycaprolactone/ceramic-

based 3D-bioplotted porous scaffolds for bone regeneration: a comparative study. *Mater Sci Eng C Mater Biol Appl*. 2017;79:326-335.
doi: 10.1016/j.msec.2017.05.003

5. Zhao QM, Sun YY, Wu CS, et al. Enhanced osteogenic activity and antibacterial ability of manganese-titanium dioxide microporous coating on titanium surfaces. *Nanotoxicology*. 2020;14(3):289-309.
doi: 10.1080/17435390.2019.1690065

6. Zurita-Méndez NN, Carbajal-De la Torre G, Flores-Merino MV, Espinosa-Medina MA. Development of bioactive glass-collagen-hyaluronic acid-polycaprolactone scaffolds for tissue engineering applications. *Front Bioeng Biotechnol*. 2022;10:825903.
doi: 10.3389/fbioe.2022.825903

7. Tian B, Wang N, Jiang Q, et al. The immunogenic reaction and bone defect repair function of ε-poly-L-lysine (EPL)-coated nanoscale PCL/HA scaffold in rabbit calvarial bone defect. *J Mater Sci Mater Med*. 2021;32(6):63.
doi: 10.1007/s10856-021-06533-7

8. Blum C, Taskin MB, Shan J, et al. Appreciating the first line of the human innate immune defense: a strategy to model and alleviate the neutrophil elastase-mediated attack toward bioactivated biomaterials. *Small*. 2021;17(13):e2007551.
doi: 10.1002/smll.202007551

9. Moore EM, Maestas DR, Jr., Cherry CC, et al. Biomaterials direct functional B cell response in a material-specific manner. *Sci Adv*. 2021;7(49):eabj5830.
doi: 10.1126/sciadv.abj5830

10. Knecht RS, Bucher CH, Van Linthout S, et al. Mechanobiological principles influence the immune response in regeneration: implications for bone healing. *Front Bioeng Biotechnol*. 2021;9:614508.
doi: 10.3389/fbioe.2021.614508

11. Zhang B, Su Y, Zhou J, et al. Toward a better regeneration through implant-mediated immunomodulation: harnessing the immune responses. *Adv Sci (Weinh)*. 2021;8(16):e2100446.
doi: 10.1002/advs.202100446

12. Ben Letaifa R, Klaylat T, Tarchala M, et al. Osteoimmunology: an overview of the interplay of the immune system and the bone tissue in fracture healing. *Surgeries*. 2024;5(2):402-414.
doi: 10.3390/surgeries5020033

13. Jiang F, Zhao H, Zhang P, et al. Challenges in tendon-bone healing: emphasizing inflammatory modulation mechanisms and treatment. *Front Endocrinol (Lausanne)*. 2024;15:1485876.
doi: 10.3389/fendo.2024.1485876

14. Sadowska JM, Ginebra MP. Inflammation and biomaterials: role of the immune response in bone regeneration by inorganic scaffolds. *J Mater Chem B*. 2020;8(41):9404-9427.
doi: 10.1039/d0tb01379j

15. Wei S, Wang Y, Sun Y, *et al*. Biodegradable silk fibroin scaffold doped with mineralized collagen induces bone regeneration in rat cranial defects. *Int J Biol Macromol*. 2023;235:123861.
doi: 10.1016/j.ijbiomac.2023.123861

16. Kawcher Alam M, Sahadat Hossain M, Anisur Rahman Dayan M, *et al*. Fabrication and characterization of a bioscaffold using hydroxyapatite and unsaturated polyester resin. *ACS Omega*. 2024;9(13):15210-15221.
doi: 10.1021/acsomega.3c09599

17. Ye B, Wu B, Su Y, et al. Recent advances in the application of natural and synthetic polymer-based scaffolds in musculoskeletal regeneration. *Polymers (Basel)*. 2022;14(21):4566.
doi: 10.3390/polym14214566

18. Dong C, Tan G, Zhang G, et al. The function of immunomodulation and biomaterials for scaffold in the process of bone defect repair: a review. *Front Bioeng Biotechnol*. 2023;11:1133995.
doi: 10.3389/fbioe.2023.1133995

19. Handley EL, Callanan A. Effects of electrospun fibers containing ascorbic acid on oxidative stress reduction for cardiac tissue engineering. *J Appl Polym Sci*. 2023;140(32):e54242.
doi: 10.1002/app.54242

20. Homaeigohar S, Boccaccini AR. Nature-derived and synthetic additives to poly(ε-caprolactone) nanofibrous systems for biomedicine; an updated overview. *Front Chem*. 2021;9:809676.
doi: 10.3389/fchem.2021.809676

21. Gniesmer S, Brehm R, Hoffmann A, et al. In vivo analysis of vascularization and biocompatibility of electrospun polycaprolactone fibre mats in the rat femur chamber. *J Tissue Eng Regen Med*. 2019;13(7):1190-1202.
doi: 10.1002/term.2868

22. Han Y, Jia B, Lian M, et al. High-precision, gelatin-based, hybrid, bilayer scaffolds using melt electro-writing to repair cartilage injury. *Bioact Mater*. 2021;6(7):2173-2186.
doi: 10.1016/j.bioactmat.2020.12.018

23. Zhao S, Xie K, Guo Y, et al. Fabrication and biological activity of 3D-printed polycaprolactone/magnesium porous scaffolds for critical size bone defect repair. *ACS Biomater Sci Eng*. 2020;6(9):5120-5131.
doi: 10.1021/acsbiomaterials.9b01911

24. Tang C, Shen Y, Xing Y, et al. 3D-printed stents loaded with *Panax notoginseng* saponin for promoting re-endothelialization and reducing local inflammation in the carotid artery of rabbits. *ACS Biomater Sci Eng*. 2024;10(10):6483-6497.
doi: 10.1021/acsbiomaterials.4c00925

25. Liu J, Du G, Yu H, et al. Synthesis of hierarchically porous bioactive glass and its mineralization activity. *Molecules*. 2023;28(5):2224.
doi: 10.3390/molecules28052224

26. Liang J, Lu X, Zheng X, et al. Modification of titanium orthopedic implants with bioactive glass: a systematic review of in vivo and in vitro studies. *Front Bioeng Biotechnol.* 2023; 11:1269223.
doi: 10.3389/fbioe.2023.1269223

27. Zhao H, Wang X, Jin A, et al. Reducing relapse and accelerating osteogenesis in rapid maxillary expansion using an injectable mesoporous bioactive glass/fibrin glue composite hydrogel. *Bioact Mater*. 2022;18:507-525.
doi: 10.1016/j.bioactmat.2022.03.001

28. Oliver JN, Su Y, Lu X, et al. Bioactive glass coatings on metallic implants for biomedical applications. *Bioact Mater*. 2019;4:261-270.
doi: 10.1016/j.bioactmat.2019.09.002

29. Chakraborty A, Bodhak S, Tah I, et al. Tailored bioactive glass coating: navigating devitrification toward a superior implant performance. *ACS Biomater Sci Eng*. 2024;10(8): 5300-5312.
doi: 10.1021/acsbiomaterials.4c01032

30. Wa Q, Luo Y, Tang Y, et al. Mesoporous bioactive glass-enhanced MSC-derived exosomes promote bone regeneration and immunomodulation in vitro and in vivo. *J Orthop Translat*. 2024;49:264-282.
doi: 10.1016/j.jot.2024.09.009

31. Lin K, Wang X, Zhang N, Shen Y. Strontium (Sr) strengthens the silicon (Si) upon osteoblast proliferation, osteogenic differentiation and angiogenic factor expression. *J Mater Chem B*. 2016;4(21):3632-3638.
doi: 10.1039/c6tb00735j

32. Liu X, Huang H, Zhang J, et al. Recent advance of strontium functionalized in biomaterials for bone regeneration. *Bioengineering (Basel)*. 2023;10(4):414.
doi: 10.3390/bioengineering10040414

33. Zhao F, Lei B, Li X, et al. Promoting in vivo early angiogenesis with sub-micrometer strontium-contained bioactive microspheres through modulating macrophage phenotypes. *Biomaterials*. 2018;178:36-47.
doi: 10.1016/j.biomaterials.2018.06.004

34. Ding J, Zhao J, Wang L, et al. Regulated contribution of local and systemic immunity to new bone regeneration by modulating B/Sr concentration of bioactive borosilicate glass. *Mater Today Bio*. 2023;19:100585.
doi: 10.1016/j.mtbio.2023.100585

35. Li M, Wang M, Wen Y, et al. Signaling pathways in macrophages: molecular mechanisms and therapeutic targets. *MedComm. (2020)*. 2023;4(5):e349.
doi: 10.1002/mco2.349

36. Terzopoulou Z, Baciu D, Gounari E, et al. Composite membranes of poly(ε-caprolactone) with bisphosphonate-loaded bioactive glasses for potential bone tissue engineering applications. *Molecules*. 2019;24(17):3067.
doi: 10.3390/molecules24173067

37. Sheng X, Li C, Wang Z, et al. Advanced applications of strontium-containing biomaterials in bone tissue engineering. *Mater Today Bio*. 2023;20:100636.
doi: 10.1016/j.mtbio.2023.100636

38. Poh PS, Hutmacher DW, Stevens MM, Woodruff MA. Fabrication and in vitro characterization of bioactive glass composite scaffolds for bone regeneration. *Biofabrication*. 2013;5(4):045005.
doi: 10.1088/1758-5082/5/4/045005

39. Ma T, Wang CX, Ge XY, Zhang Y. Applications of polydopamine in implant surface modification. *Macromol Biosci*. 2023;23(10):e2300067.
doi: 10.1002/mabi.202300067

40. Qin D, Zhao Y, Cheng R, et al. Mussel-inspired immunomodulatory and osteoinductive dual-functional hydroxyapatite nanoplatform for promoting bone regeneration. *J Nanobiotechnology*. 2024;22(1):320.
doi: 10.1186/s12951-024-02593-3

41. Jin L, Yuan F, Chen C, et al. Degradation products of polydopamine restrained inflammatory response of LPS-stimulated macrophages through mediation TLR-4-MYD88 dependent signaling pathways by antioxidant. *Inflammation*. 2019;42(2):658-671.
doi: 10.1007/s10753-018-0923-3

42. Park J, Lee SJ, Jung TG, et al. Surface modification of a three-dimensional polycaprolactone scaffold by polydopamine, biomineralization, and BMP-2 immobilization for potential bone tissue applications. *Colloids Surf B Biointerfaces*. 2021;199:111528.
doi: 10.1016/j.colsurfb.2020.111528

43. Ye G, Bao F, Zhang X, et al. Nanomaterial-based scaffolds for bone tissue engineering and regeneration. *Nanomedicine (Lond)*. 2020;15(20):1995-2017.
doi: 10.2217/nnm-2020-0112

44. Bharadwaz A, Jayasuriya AC. Recent trends in the application of widely used natural and synthetic polymer nanocomposites in bone tissue regeneration. *Mater Sci Eng C Mater Biol Appl*. 2020;110:110698.
doi: 10.1016/j.msec.2020.110698

45. Fazeli N, Arefian E, Irani S, et al. 3D-printed PCL scaffolds coated with nanobioceramics enhance osteogenic differentiation of stem cells. *ACS Omega*. 2021;6(51): 35284-35296.
doi: 10.1021/acsomega.1c04015

46. Abd El-Hamid HK, El-Kheshen AA, Abdou AM, Elwan RL. Incorporation of strontium borosilicate bioactive glass in calcium aluminate biocement: physicomechanical, bioactivity and antimicrobial properties. *J Mech Behav Biomed Mater*. 2023;144:105976.
doi: 10.1016/j.jmbbm.2023.105976

47. Zhao Q, Gao S. Poly (butylene succinate)/silicon nitride nanocomposite with optimized physicochemical properties,

biocompatibility, degradability, and osteogenesis for cranial bone repair. *J Funct Biomater.* 2022;13(4):231. doi: 10.3390/jfb13040231

48. Wu Y, Liu J, Kang L, et al. An overview of 3D printed metal implants in orthopedic applications: present and future perspectives. Heliyon. 2023;9(7):e17718. doi: 10.1016/j.heliyon.2023.e17718
49. Zhang L, Yang G, Johnson BN, Jia X. Three-dimensional (3D) printed scaffold and material selection for bone repair. *Acta Biomater.* 2019;84:16-33. doi: 10.1016/j.actbio.2018.11.039
50. Toosi S, Javid-Naderi MJ, Tamayol A, et al. Additively manufactured porous scaffolds by design for treatment of bone defects. *Front Bioeng Biotechnol.* 2023;11:1252636. doi: 10.3389/fbioe.2023.1252636
51. Bouakaz I, Drouet C, Grossin D, et al. Hydroxyapatite 3D-printed scaffolds with gyroid-triply periodic minimal surface porous structure: fabrication and an in vivo pilot study in sheep. *Acta Biomater.* 2023;170:580-595. doi: 10.1016/j.actbio.2023.08.041
52. Du J, Zhou Y, Bao X, et al. Surface polydopamine modification of bone defect repair materials: characteristics and applications. *Front Bioeng Biotechnol.* 2022;10:974533. doi: 10.3389/fbioe.2022.974533
53. Ghalia MA, Alhanish A. Mechanical and biodegradability of porous PCL/PEG copolymer-reinforced cellulose nanofibers for soft tissue engineering applications. *Med Eng Phys.* 2023;120:104055. doi: 10.1016/j.medengphy.2023.104055
54. Xiao L, Li Y, Geng R, et al. Polymer composite microspheres loading (177)Lu radionuclide for interventional radioembolization therapy and real-time SPECT imaging of hepatic cancer. *Biomater Res.* 2023;27(1):110. doi: 10.1186/s40824-023-00455-x
55. Mahnavi A, Shahriari-Khalaji M, Hosseinpour B, et al. Evaluation of cell adhesion and osteoconductivity in bone substitutes modified by polydopamine. *Front Bioeng Biotechnol.* 2022;10:1057699. doi: 10.3389/fbioe.2022.1057699
56. Wang H, Yuan C, Lin K, et al. Modifying a 3D-printed Ti6Al4V implant with polydopamine coating to improve BMSCs growth, osteogenic differentiation, and in situ osseointegration in vivo. *Front Bioeng Biotechnol.* 2021;9:761911. doi: 10.3389/fbioe.2021.761911
57. Zhao ZH, Ma XL, Ma JX, et al. Sustained release of naringin from silk-fibroin-nanohydroxyapatite scaffold for the enhancement of bone regeneration. *Mater Today Bio.* 2022;13:100206. doi: 10.1016/j.mtbio.2022.100206
58. Devi VK A, Ray S, Arora U, et al. Dual drug delivery platforms for bone tissue engineering. *Front Bioeng Biotechnol.* 2022;10:969843. doi: 10.3389/fbioe.2022.969843
59. S S, R G AP, Bajaj G, et al. A review on the recent applications of synthetic biopolymers in 3D printing for biomedical applications. *J Mater Sci Mater Med.* 2023;34(12):62. doi: 10.1007/s10856-023-06765-9
60. Wang S, Gu R, Wang F, et al. 3D-Printed PCL/Zn scaffolds for bone regeneration with a dose-dependent effect on osteogenesis and osteoclastogenesis. *Mater Today Bio.* 2022;13:100202. doi: 10.1016/j.mtbio.2021.100202
61. Murugan S, Parcha SR. Fabrication techniques involved in developing the composite scaffolds PCL/HA nanoparticles for bone tissue engineering applications. *J Mater Sci Mater Med.* 2021;32(8):93. doi: 10.1007/s10856-021-06564-0
62. Labbaf S, Tsigkou O, Müller KH, et al. Spherical bioactive glass particles and their interaction with human mesenchymal stem cells in vitro. *Biomaterials.* 2011;32(4): 1010-1018. doi: 10.1016/j.biomaterials.2010.08.082
63. Ma YX, Jiao K, Wan QQ, et al. Silicified collagen scaffold induces semaphorin 3A secretion by sensory nerves to improve in-situ bone regeneration. *Bioact Mater.* 2022;9: 475-490. doi: 10.1016/j.bioactmat.2021.07.016
64. Qiu P, Li M, Chen K, et al. Periosteal matrix-derived hydrogel promotes bone repair through an early immune regulation coupled with enhanced angio- and osteogenesis. *Biomaterials.* 2020;227:119552. doi: 10.1016/j.biomaterials.2019.119552
65. Zhang Y, Yu W, Ba Z, et al. 3D-printed scaffolds of mesoporous bioglass/gliadin/polycaprolactone ternary composite for enhancement of compressive strength, degradability, cell responses and new bone tissue ingrowth. *Int J Nanomed.* 2018;13:5433-5447. doi: 10.2147/ijn.S164869
66. Qiu H, Xiong H, Zheng J, et al. Sr-incorporated bioactive glass remodels the immunological microenvironment by enhancing the mitochondrial function of macrophage via the PI3K/AKT/mTOR signaling pathway. *ACS Biomater Sci Eng.* 2024;10(6):3923-3934. doi: 10.1021/acsbiomaterials.4c00228
67. Ajita J, Saravanan S, Selvamurugan N. Effect of size of bioactive glass nanoparticles on mesenchymal stem cell proliferation for dental and orthopedic applications. *Mater Sci Eng C Mater Biol Appl.* 2015;53:142-149. doi: 10.1016/j.msec.2015.04.041

68. Feito MJ, Casarrubios L, Oñaderra M, et al. Response of RAW 264.7 and J774A.1 macrophages to particles and nanoparticles of a mesoporous bioactive glass: a comparative study. *Colloids Surf B Biointerfaces*. 2021;208:112110. doi: 10.1016/j.colsurfb.2021.112110

69. Xu H, Zhu Y, Hsiao AW, et al. Bioactive glass-elicited stem cell-derived extracellular vesicles regulate M2 macrophage polarization and angiogenesis to improve tendon regeneration and functional recovery. *Biomaterials*. 2023;294:121998. doi: 10.1016/j.biomaterials.2023.121998

70. Römer P, Desaga B, Proff P, et al. Strontium promotes cell proliferation and suppresses IL-6 expression in human PDL cells. *Ann Anat*. 2012;194(2):208-211. doi: 10.1016/j.aanat.2011.09.008

71. Buache E, Velard F, Bauden E, et al. Effect of strontium-substituted biphasic calcium phosphate on inflammatory mediators production by human monocytes. *Acta Biomater*. 2012;8(8):3113-3119. doi: 10.1016/j.actbio.2012.04.045

72. Palczewska-Komsa MP, Gapiński B, Nowicka A. The influence of new bioactive materials on pulp-dentin complex regeneration in the assessment of cone bone computed tomography (CBCT) and computed micro-tomography (Micro-CT) from a present and future perspective-a systematic review. *J Clin Med*. 2022;11(11):3091. doi: 10.3390/jcm11113091

73. Mohan S, Karunanithi P, Raman Murali M, et al. Potential use of 3D CORAGRAF-loaded PDGF-BB in PLGA microsphere seeded mesenchymal stromal cells in enhancing the repair of calvaria critical-size bone defect in rat model. *Mar Drugs*. 2022;20(9):561. doi: 10.3390/md20090561

74. Lee JB, Seo MS. Mandibular incisors with two canals are associated with the presence of the distolingual root in mandibular first molars: a cone-beam computed tomographic study. BMC Oral Health. 2022;22(1):145. doi: 10.1186/s12903-022-02184-4

75. Song W, Zhao L, Gao Y, et al. Dual growth factor-modified microspheres nesting human-derived umbilical cord mesenchymal stem cells for bone regeneration. *J Biol Eng*. 2023;17(1):43. doi: 10.1186/s13036-023-00360-w

76. Wang C, Wu J, Liu L, et al. Improving osteoinduction and osteogenesis of Ti6Al4V alloy porous scaffold by regulating the pore structure. *Front Chem*. 2023;11:1190630. doi: 10.3389/fchem.2023.1190630

77. Okizaki S, Ito Y, Hosono K, et al. Suppressed recruitment of alternatively activated macrophages reduces TGF-β1 and impairs wound healing in streptozotocin-induced diabetic mice. *Biomed Pharmacother*. 2015;70:317-325. doi: 10.1016/j.biopha.2014.10.020

78. Zhu C, Kros JM, van der Weiden M, et al. Expression site of P2RY12 in residential microglial cells in astrocytomas correlates with M1 and M2 marker expression and tumor grade. *Acta Neuropathol Commun*. 2017;5(1):4. doi: 10.1186/s40478-016-0405-5

79. Lisi L, Ciotti GM, Braun D, et al. Expression of iNOS, CD163 and ARG-1 taken as M1 and M2 markers of microglial polarization in human glioblastoma and the surrounding normal parenchyma. *Neurosci Lett*. 2017;645:106-112. doi: 10.1016/j.neulet.2017.02.076

80. Wu S, Dong R, Xie Y, et al. CO-loaded hemoglobin/EGCG nanoparticles functional coatings for inflammation modulation of vascular implants. *Regen Biomater*. 2025;12:rbae148. doi: 10.1093/rb/rbae148

81. Luo R, Su J, Zhang W, et al. Targeted delivery of NO donor and ROS scavenger for synergistic treatment of rheumatoid arthritis. *Biomed Pharmacother*. 2024;174:116540. doi: 10.1016/j.biopha.2024.116540

82. Chen X, Wang M, Chen F, et al. Correlations between macrophage polarization and osteoinduction of porous calcium phosphate ceramics. *Acta Biomater*. 2020;103:318-332. doi: 10.1016/j.actbio.2019.12.019

83. Alhamdi JR, Peng T, Al-Naggar IM, et al. Controlled M1-to-M2 transition of aged macrophages by calcium phosphate coatings. *Biomaterials*. 2019;196:90-99. doi: 10.1016/j.biomaterials.2018.07.012

84. Ye J, Xie C, Wang C, et al. Promoting musculoskeletal system soft tissue regeneration by biomaterial-mediated modulation of macrophage polarization. *Bioact Mater*. 2021;6(11):4096-4109. doi: 10.1016/j.bioactmat.2021.04.017

85. Gélébart P, Cuenot S, Sinquin C, et al. Microgels based on Infernan, a glycosaminoglycan-mimetic bacterial exopolysaccharide, as BMP-2 delivery systems. *Carbohydr Polym*. 2022;284:119191. doi: 10.1016/j.carbpol.2022.119191

86. Kathami N, Moreno-Vicente C, Martín P, et al. rhBMP-2 induces terminal differentiation of human bone marrow mesenchymal stromal cells only by synergizing with other signals. *Stem Cell Res Ther*. 2024;15(1):124. doi: 10.1186/s13287-024-03735-y

87. Li T, Peng M, Yang Z, et al. 3D-printed IFN-γ-loading calcium silicate-β-tricalcium phosphate scaffold sequentially activates M1 and M2 polarization of macrophages to promote vascularization of tissue engineering bone. *Acta Biomater*. 2018;71:96-107. doi: 10.1016/j.actbio.2018.03.012

88. Liu Y, Li Z, Li W, et al. Discovery of β-sitosterol's effects on molecular changes in rat diabetic wounds and its impact on angiogenesis and macrophages. *Int Immunopharmacol*. 2024;126:111283.

doi: 10.1016/j.intimp.2023.111283

89. Mao L, Xia L, Chang J, et al. The synergistic effects of Sr and Si bioactive ions on osteogenesis, osteoclastogenesis and angiogenesis for osteoporotic bone regeneration. *Acta Biomater*. 2017;61:217-232.
doi: 10.1016/j.actbio.2017.08.015

90. Zhu X, Wu S, Yang K, et al. Polydopamine-modified konjac glucomannan scaffold with sustained release of vascular endothelial growth factor to promote angiogenesis. *Int J Biol Macromol*. 2024;271(Pt 1):132333.
doi: 10.1016/j.ijbiomac.2024.132333

91. Cheng S, Wang D, Ke J, et al. Improved in vitro angiogenic behavior of human umbilical vein endothelial cells with oxidized polydopamine coating. *Colloids Surf B Biointerfaces*. 2020;194:111176.
doi: 10.1016/j.colsurfb.2020.111176

Appendix

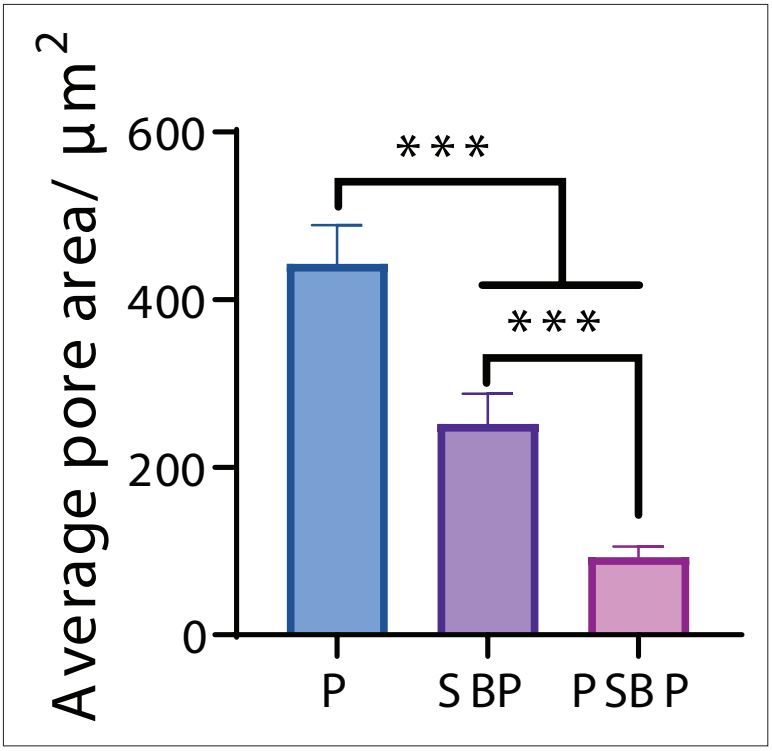

Figure A1. Pore area on the fibers of three groups of scaffolds ($n = 6$; ***$p < 0.001$). Abbreviations: P, polycaprolactone (PCL); PSBP, polydopamine (PDA)/strontium (Sr)-doped bioactive glass (SrBG)/polycaprolactone (PCL); SBP, strontium (Sr)-doped bioactive glass (SrBG)/polycaprolactone (PCL).

ACCSCIENCE PUBLISHING

International Journal of Bioprinting

RESEARCH ARTICLE

Multiscale vascularized tumor-on-a-chip via bioprinting for drug research

Jing Liu[1], Ying Zhao[1], Bihan Ren[1], Dingming Li[1], Tianma He[1], Haizhongshi Zhang[1], Zhenlei Zhang[1], and Haochen Liu[2]*

[1]Department of Biological Engineering, School of Biology, Food and Environment, Hefei University, Hefei, Anhui, China

[2]Department of Cardiovascular Surgery, Xi'an Children's Hospital, Xi'an, Shaanxi, China

Abstract

Current *in vitro* tumor models often fail to recapitulate the hierarchical vascular architecture and dynamic interactions of the tumor microenvironment (TME), limiting their utility in cancer research. In this study, we present a multiscale vascularized tumor model integrating coaxial bioprinting, inkjet printing, and fused deposition modeling (FDM) to address this challenge. Firstly, coaxial bioprinting enabled the fabrication of dual-layered vasculature with an endothelium layer and a smooth muscle layer. Secondly, tumor spheroids with precise size control (±10 μm) were generated via inkjet printing by modulating Methacrylate Gelatin (GelMA) concentration and valve actuation time. An FDM-printed chip was designed to co-culture these components under perfusion, facilitating the self-organization of a microvascular network around tumor spheroids. After 11 days of dynamic culture, the model demonstrated tumor-driven angiogenic sprouting and early metastatic behavior, validated by the upregulation of metastasis-related genes (CD44, MMP2, N-cadherin) in vascularized cohorts. Drug testing with paclitaxel revealed dose-dependent suppression of tumor proliferation and invasion. This platform not only mimics the structural and functional complexity of the TME but also provides a scalable, physiologically relevant tool for investigating tumor–vascular crosstalk and evaluating anti-cancer therapeutics.

Keywords: 3D bioprinting; Coaxial printing; Drug research; Inkjet printing; Tumor-on-a-chip; Vascularized tumor model

***Corresponding author:**
Haochen Liu
(haochen1010@163.com)

Citation: Liu J, Zhao Y, Ren B, *et al.* Multiscale vascularized tumor-on-a-chip via bioprinting for drug research. *Int J Bioprint.* 2025;11(4):378-391. doi: 10.36922/IJB025180180

Received: May 1, 2025
1st revised: June 11, 2025
2nd revised: June 24, 2025
3rd revised: June 26, 2025
Accepted: June 26, 2025
Published online: June 26, 2025

Copyright: © 2025 Author(s). This is an Open Access article distributed under the terms of the Creative Commons Attribution License, permitting distribution and reproduction in any medium, provided the original work is properly cited.

Publisher's Note: AccScience Publishing remains neutral with regard to jurisdictional claims in published maps and institutional affiliations.

1. Introduction

Cancer is currently the second leading cause of death worldwide, following cardiovascular diseases. According to the World Health Organization, nearly 10 million cancer-related deaths were reported globally in 2022, accounting for one-sixth of total mortality, with a rising prevalence in underdeveloped regions.[1] Despite significant advances in cancer research, the molecular mechanisms underlying tumorigenesis and progression remain poorly understood, contributing to the high failure rate and exorbitant costs of anti-cancer drug development.[2] A major challenge lies in the lack of *in vitro* models that accurately replicate the human tumor microenvironment (TME), leading to discrepancies between preclinical drug testing and clinical outcomes.[3] The TME is a highly dynamic ecosystem,

comprising tumor cells, stromal cells, vascular networks, and the extracellular matrix (ECM), where intricate interactions govern tumor progression, drug penetration, and therapeutic response.[4] Thus, the development of *in vitro* tumor models that integrate multiscale vascular networks and recapitulate TME dynamics is essential to overcoming current research bottlenecks.

Traditional 2D cell models, though simple and suitable for high-throughput screening, fail to replicate the 3D cell–cell interactions, metabolic gradients, and drug diffusion barriers of solid tumors.[5,6] Animal models, while capable of mimicking *in vivo* tumor environments, face limitations due to high costs, species-specific discrepancies, and ethical concerns.[7] In contrast, 3D tumor models better approximate the TME by simulating spatial cell arrangements, heterogeneity, and ECM physicochemical properties.[8] At present, tumor spheroid-based models are the primary focus of 3D tumor models. These models, resembling human tumors in morphology, high cell density, and chemical environment, effectively establish physiological metabolic gradients.[9] Furthermore, these models are often integrated with tumor cells and fibroblasts. The latter, by secreting angiogenic factors such as vascular endothelial growth factor (VEGF), plays an essential role in tumor growth, invasion, metastasis, and angiogenesis.[10–12] The fabrication of tumor spheroids primarily relies on traditional techniques, including ultra-low adhesion methods,[13] hanging drop techniques,[14–16] and droplet overlay methods.[17–19] While these approaches are simple to operate, they exhibit significant limitations; for instance, they lack precise control over spheroid diameter.[20–22] Furthermore, most current studies are restricted to monoculture systems of tumor cells, failing to systematically integrate key functional units of the TME, such as perfusable vascular networks and immune cell infiltration.[23–25]

Blood vessels, as pivotal functional units of the TME, not only deliver oxygen and nutrients but also regulate immune cell infiltration and drug delivery.[26] Native vasculature features a complex tri-layered structure (intima, media, adventitia), where endothelial and smooth muscle cells synergistically maintain vascular tone, barrier function, and paracrine signaling.[27–30] Existing *in vitro* vascular models, however, primarily rely on endothelial-lined hollow channels, which neither mimic layered vascular structures nor support long-term perfusion.[31–35] While 3D bioprinting offers new avenues for constructing spatially controlled vascularized models, integrating multiscale vascular networks (from macrovessels to capillaries) with tumor spheroids remains technically challenging.[36] In this study, we present an innovative multiscale vascularized tumor model developed through the integration of coaxial bioprinting, inkjet printing, and fused deposition modeling (FDM). Notably, coaxial bioprinting enabled the fabrication of dual-layered vascular constructs featuring endothelial and smooth muscle layers, a design strategy aimed at mimicking native vascular architecture. Concurrently, inkjet printing achieved high-precision tumor spheroid generation (±10 μm dimensional consistency), effectively addressing the heterogeneity limitations inherent in conventional spheroid formation techniques. The FDM-fabricated perfusion culture chip further advanced the system's functionality by facilitating dynamic tumor–vascular co-culture and enabling real-time microenvironment monitoring. Preliminary mechanistic investigations leveraging this integrated platform revealed insights into paclitaxel-mediated suppression of tumor metastasis. Collectively, this model successfully simulated tumor-associated vascular radial growth, early metastatic events, and drug responses, providing a robust platform for investigating tumor–vascular interactions and evaluating anti-angiogenic therapies.

2. Materials and methods

2.1. Materials

Human fetal lung fibroblast 1 (HFL1; CCL-153), human umbilical vein endothelial cells (HUVECs; CRL-1730), human aortic vascular smooth muscle cells (HA-VSMCs; CRL-1999), and human hepatocellular carcinoma G2 (HepG2; HB-8065) were purchased from the American Type Culture Collection (ATCC, United States of America [USA]). Dulbecco's Modified Eagle Medium (DMEM), 0.25% Trypsin-EDTA, and phosphate-buffered saline (PBS) were obtained from Wuhan Servicebio Technology Co., Ltd. (China). Fetal bovine serum (FBS) was sourced from Lonsa Sience SRL (Uruguay). Penicillin-streptomycin was purchased from Gibco (USA). Anhydrous calcium chloride, propidium iodide (PI), DiO (green cell membrane fluorescent probe), DiI (orange cell membrane fluorescent probe), 4% paraformaldehyde, Triton X-100, gelatin (bloom number: 240~270), and bovine serum albumin (BSA) were obtained from Sangon Biotech Co., Ltd. (China). Lithium phenyl-2,4,6-trimethylbenzoylphosphinate (LAP), fibronectin, methacrylic anhydride, and Calcein-AM were obtained from Shanghai Aladdin Biochemical Technology Co., Ltd. (China). Pluronic F-127, Phalloidin-FITC, alginate, and fibrinogen were purchased from Sigma-Aldrich Corporation (USA). Thrombin was obtained from Yeasen Biotech Co., Ltd. (China). Total RNA extraction commercial kit, reverse transcription kit, and 2× Universal Blue SYBR Green qPCR Master Mix were obtained from Mei5 Biotechnology (China). Gelatin methacryloyl (GelMA) and type I rat tail collagen were synthesized in-house. Anti-CD31 antibody (152 μg/mL) was obtained

from Cell Signaling Technology (USA), and Alexa Fluor 568 donkey anti-rabbit IgG (H+L) (2 mg/mL) was obtained from Thermo Fisher (USA).

2.2. Cell culture

The cells (HFL1, HUVECs, HA-VSMCs, and HepG2) were maintained in high-glucose DMEM medium supplemented with 10% (v/v) FBS and 1% (v/v) penicillin-streptomycin at 37 °C in a humidified incubator (STIK, China) with 5% CO_2. When the cells reached 90% confluence, they were passaged at an appropriate ratio using 0.25% Trypsin-EDTA. The culture medium was refreshed every 2–3 days.

2.3. Preparation of type I collagen

The skin of the rat tail was removed to extract the silver-colored tendons, which were washed thoroughly and blotted dry. After cutting the tendons into small pieces, they were immersed in 0.1% acetic acid for 7 days. The solution was centrifuged at 8000 rpm (6738 × *g*) for 30 min, and the supernatant was collected and freeze-dried. The lyophilized collagen was weighed and dissolved in 0.1% acetic acid supplemented with 1% penicillin-streptomycin to prepare a 10% collagen solution, which was stored at 4°C.

2.4. Preparation of GelMA

Gelatin was dissolved in PBS and heated at 50 °C for 2 h until fully dissolved. The solution was stirred on a magnetic stirrer, and methacrylic anhydride (MA) was added dropwise for a complete reaction. The reaction mixture was centrifuged at 4500 rpm (2132 × *g*) for 10 min, after which the supernatant was dialyzed in distilled water at 37°C for 7 days, and the dialyzed solution was subsequently freeze-dried. Both GelMA and the original gelatin were characterized by 1H-NMR (Figure S1, Supporting Information), demonstrating the successful synthesis of GelMA (30–50% substitution rate).[37] The resulting GelMA was dissolved in sterile complete medium to prepare a 14% solution, which was stored at 4°C.

2.5. Fabrication of bilayered vessels

2.5.1. Bioink preparation

The outer shell bioink consisted of HA-VSMCs embedded in a matrix containing 8 mg/mL rat tail collagen, 1% (w/v) sodium alginate, 0.25% (w/v) LAP, and 3% (w/v) GelMA. The inner sacrificial ink was a thermosensitive composite composed of 3% (w/v) $CaCl_2$ and 4% (w/v) Pluronic F-127. Crosslinking of the outer shell bioink was achieved through ionic gelation by Ca^{2+}, while Pluronic F-127 served as a temporary scaffold to maintain the hollow structure during printing. Notably, rat tail collagen must be neutralized to physiological pH with NaOH under ice-bath conditions, and the mixing of the outer shell bioink should also be performed at 4 °C. The internal sacrificial ink needs to be pre-dissolved at 4 °C in advance. The entire operation process is strictly carried out in compliance with aseptic operation specifications.

2.5.2. Printing and post-processing

Coaxial extrusion-based printing was performed using a 20G/25G nozzle, with flow rates of 2.5 and 3.0 mL/min for the outer and inner inks, respectively. The printed tubular structures were immersed in 2% $CaCl_2$ solution for 2 min to induce ionic crosslinking, rinsed with PBS, and then photocrosslinked under 405 nm light for 30 s. Subsequently, fibronectin (1 mg/mL) was infused into the lumen via a sterile syringe and incubated dynamically at 37 °C for 15 min, with inversion every 5 min. HUVECs suspended in 2 mg/mL collagen (1×10^6 cells/mL) were then loaded into the lumen in two steps, 12 h apart, with rotation to ensure uniform endothelial coverage. All procedures were conducted under sterile conditions.

2.6. Tumor spheroid formation

Tumor spheroids were fabricated via inkjet bioprinting. A bioink was prepared by mixing a cell suspension containing HepG2 (6×10^7 cells/mL) and HFL1 (2×10^7 cells/mL) at a 3:1 ratio of HepG2/HFL1,[4,9] with a base ink containing 10% (w/v) GelMA and 0.5% (w/v) LAP at a 1:1 ratio. Optimized printing parameters (e.g., pressure, valve timing, and viscosity) were applied to generate uniform droplets at 37°C. The printed microspheres were deposited onto low-attachment culture dishes and crosslinked under 405 nm light for 30 s to obtain tumor spheroids with controlled diameters.

2.7. Chip design and fabrication

A custom-designed microfluidic culture chip was fabricated using polylactic acid (PLA) via FDM. The chip featured a central channel (diameter: 2 mm) for embedding the bilayered vascular construct, and four radial culture chambers for establishing a vascularized TME. The PLA chip was bonded to a glass slide using medical-grade adhesive and sealed with a coverslip to form a closed culture system (Figure 1). Regarding the disinfection of the culture system, it is worth noting that all autoclave-tolerant components (silicone tubing, stainless-steel connectors) were sterilized via autoclaving at 121°C for 30 min. For non-autoclavable FDM-printed chips (disposable products), a sequential protocol was implemented as follows: immersion in 75% ethanol for 30 min, thorough rinsing with PBS, and UV treatment for 30 min.

2.8. Construction of the multiscale vascularized tumor model

The bilayered vessel was positioned in the central channel and connected to a perfusion loop using silicone tubing (inner diameter: 1 mm). A pre-chilled matrix, which was

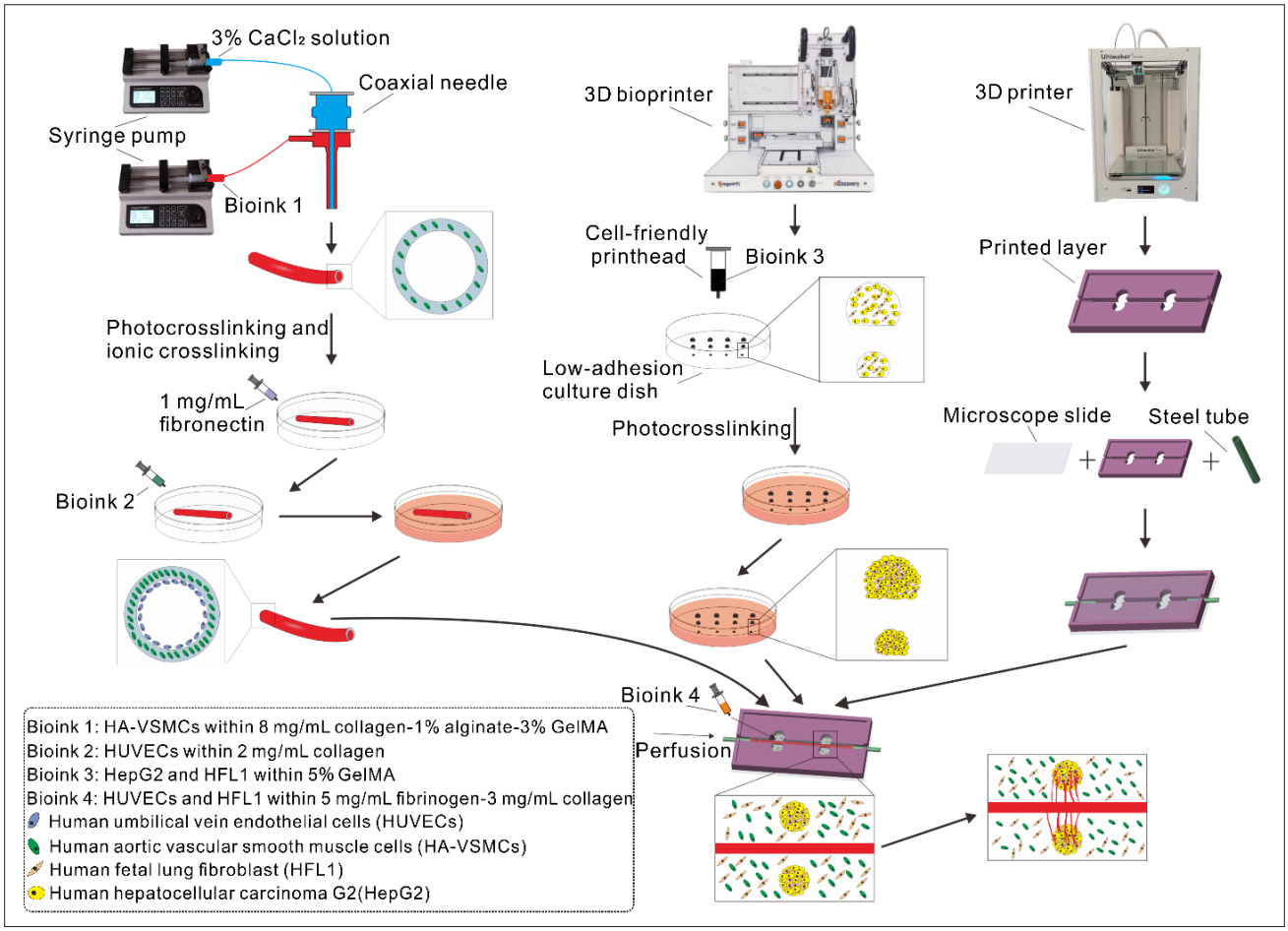

Figure 1. Preparation of an *in vitro* tumor model.

formulated with 10 mg/mL fibrinogen and 6 mg/mL type I collagen, was prepared. This matrix was then mixed in a 1:1 ratio with a solution containing HUVECs (2×10^6 cells/mL), HFL1 (1×10^6 cells/mL), tumor spheroids, and 10 U/mL thrombin. The mixture was injected into the chip chambers and allowed to gel at 37 °C for 15 min. Continuous perfusion culture was initiated using a peristaltic pump (BT100-2J; LongerPump, China) at a flow rate of 50 μL/min to mimic physiological conditions.

2.9. Live/dead cell staining

Cell viability was assessed using Calcein-AM/PI staining. Calcein-AM (5 μM) and PI (10 μg/mL) were added to the culture system and incubated at 37 °C and 5% CO_2 for 30 min. Samples were washed three times with PBS to remove excess dye. Fluorescence images were captured using a high-content imaging system (CQ1; Yokogawa, Japan) with excitation wavelengths of 488 nm (Calcein-AM) and 561 nm (PI). ImageJ was used to quantify fluorescence intensity and calculate the ratio of viable cells.

2.10. Spheroid monitoring

HepG2 and HFL1 were labeled with DiO (green) and DiI (red) fluorescent dyes, respectively, and then used to prepare tumor spheroids as described. The CQ1 imaging system was used to observe and record spheroid morphology on Days 1, 3, and 7.

2.11. Immunofluorescence staining

Samples were fixed with 4% paraformaldehyde for 10–20 min, permeabilized with 0.1% Triton X-100 for 5–10 min at room temperature, and washed with PBS. After blocking with 5% BSA for 30 min, samples were incubated with primary antibodies overnight at 4 °C or for 1–2 h at room temperature. After PBS washes, fluorescently labeled secondary antibodies were applied for 1 h in the dark. The final concentrations of the antibodies were as follows: anti-CD31 antibody at 152 ng/mL, and Alexa Fluor 568 donkey

anti-rabbit IgG at 4 μg/mL. Staining results were imaged using the CQ1 fluorescence microscope to analyze protein expression and localization.

2.12. Cytoskeleton staining

Fixed and permeabilized samples were stained with Phalloidin-FITC (10 μg/mL) in the dark at room temperature for 1 h. After three washes with PBST (0.1% Triton X-100 in PBS, pH 7.4), samples were imaged using the CQ1 system under 488 nm excitation to visualize cytoskeletal structures.

2.13. Quantitative reverse transcription polymerase chain reaction

Gene expression was analyzed by quantitative reverse transcription polymerase chain reaction (qRT-PCR). Total RNA was extracted using a commercial kit following the manufacturer's instructions. RNA concentration and purity were assessed using a microvolume spectrophotometer (LB 915; Colibri, Germany). Complementary DNA (cDNA) was synthesized from RNA using a commercial reverse transcription kit. SYBR Green-based qRT-PCR (Roche, Switzerland) was performed using primers listed in **Table 1**. Gene expression was normalized to glyceraldehyde-3-phosphate dehydrogenase (GAPDH) and analyzed using the $2^{-\Delta\Delta Ct}$ method.

2.14. Statistical analysis

Quantitative data are presented as mean ± standard deviation (SD) for at least three samples per test ($n \geq 3$). Prior to statistical testing, all datasets were assessed for normality using the Shapiro-Wilk test. Only data conforming to a normal distribution were subjected to parametric analysis. The p-values were calculated via a two-tailed Student's t-test for comparisons between two groups or one-way analysis of variance (ANOVA) for multiple group comparisons. Significance levels are indicated as * for $p < 0.05$, ** for $p < 0.01$, *** for $p < 0.001$, and N.S. for no significant difference.

3. Results and discussion

3.1. Fabrication of hollow tubes using a coaxial nozzle

To achieve a balance between the mechanical properties and biocompatibility of the hollow tubes, we systematically investigated the formulation of alginate, collagen, and GelMA in the bioink. As displayed in Figure 2A, under a fixed GelMA concentration of 3% (w/v), stable hollow tube formation was achieved when the alginate concentration ranged from 1% to 1.5% (w/v) and collagen was maintained at 5 mg/mL. However, this formulation exhibited limited biocompatibility and failed to support the formation of a dense endothelial layer. Through further optimization, we found that increasing the collagen concentration to 8 mg/mL while maintaining alginate at 1% (w/v) resulted in a composite bioink (3% GelMA, 1% alginate, and 8 mg/mL collagen) with the best overall performance in terms of printability, structural integrity, and cellular compatibility. Unlike coaxial strategies relying on homogeneous bioinks,[38,39] our approach achieves dual-layered microvessels with physiological mechanical properties and sustained cell viability. To meet the requirements for constructing multiscale vascular networks, we further

Table 1. Primer sequences

Gene	Primer sequence (5'–3')	
	Forward	Reverse
GAPDH	ACAACTTTGGTATCGTGGAAGG	GCCATCACGCCACAGTTTC
CD40	GCTTCTTCTCCAATCAGTCAT	ACCTCCAAGTTCTTATCCTCA
Casp-4	CTACGATGTGGTGGTGAA	TGATGTCTGGTGTTCTGAG
CD44	AGAAGGTGTGGGCAGAAGAA	AAATGCACCATTTCCTGAGA
CD70	TGCTGCTGGTGGTGTTTA	CCTCTGTTGCTGCTTACTGA
CD133	GGCCCAGTACAACACTACCAA	ATTCCGCCTCCTAGCACTGAA
CXCL12	TGCCAGAGCCAACGTCAAG	CAGCCGGGCTACAATCTGAA
CXCR4	TGACGGACAAGTACAGGCTGC	CCAGAAGGGAAGCGTGATGA
Fas	GTTGTTGACCATCCTTGTT	TCACGACTGGAGGTTCTA
MMP2	GTGCTGAAGGACACACTAAAGAAGA	TTGCCATCCTTCTCAAAGTTGTAGG
MMP9	AGACCTGGGCAGATTCCAAAC	CGGCAAGTCTTCCGAGTAGT
N-cadherin	AGCCAACCTTAACTGAGGAGT	GGCAAGTTGATTGGAGGGATG
Tnfrsf11b	AGAGTGAGGCAGGCTATT	TGAGGAGAGGAAGGAAGG

adjusted the inner and outer diameters, as well as the wall thickness, of the hollow tubes by switching coaxial needle sizes (Figure 2B). The mechanical properties of the printed hollow tubes were evaluated using a universal testing machine. As displayed in Figure 2C, the tubes exhibited a tensile strain of approximately 23% and a tensile stress of about 0.54 MPa, closely matching the mechanical characteristics of native small-diameter vessels, such as rat mesenteric arteries.[40–42] To further verify the structural integrity and permeability of the hollow tubes, we perfused a red dye solution through the lumen. As presented in Figure 2D, the dye rapidly filled the entire tube and then diffused uniformly into the surrounding medium, confirming the tube's permeability. Notably, the structural stability of the printed tubes was reinforced through the synergistic crosslinking of GelMA by 405 nm light and alginate by Ca^{2+} ions. To support optimal growth and proliferation of HA-VSMCs and HUVECs, we sought to maximize the proportion of collagen in the bioink. However, when the collagen concentration exceeded 8 mg/mL, the viscosity of the bioink significantly increased, which hindered the stability of the printing process and the formation of consistent hollow structures.

3.2. Fabrication of double-layered blood vessels

To evaluate the biological activity of the smooth muscle and endothelial layers within the double-layered blood vessels, we employed Calcein-AM/PI dual fluorescence staining to independently assess cell viability in each layer (Figure 3). For the smooth muscle layer, HA-VSMCs were cultured from Day 1 to Day 10, and the results (Figure 3A and B) revealed a pronounced time-dependent increase in cell proliferation. Throughout the culture period, cell viability consistently remained above 90%, indicating robust and

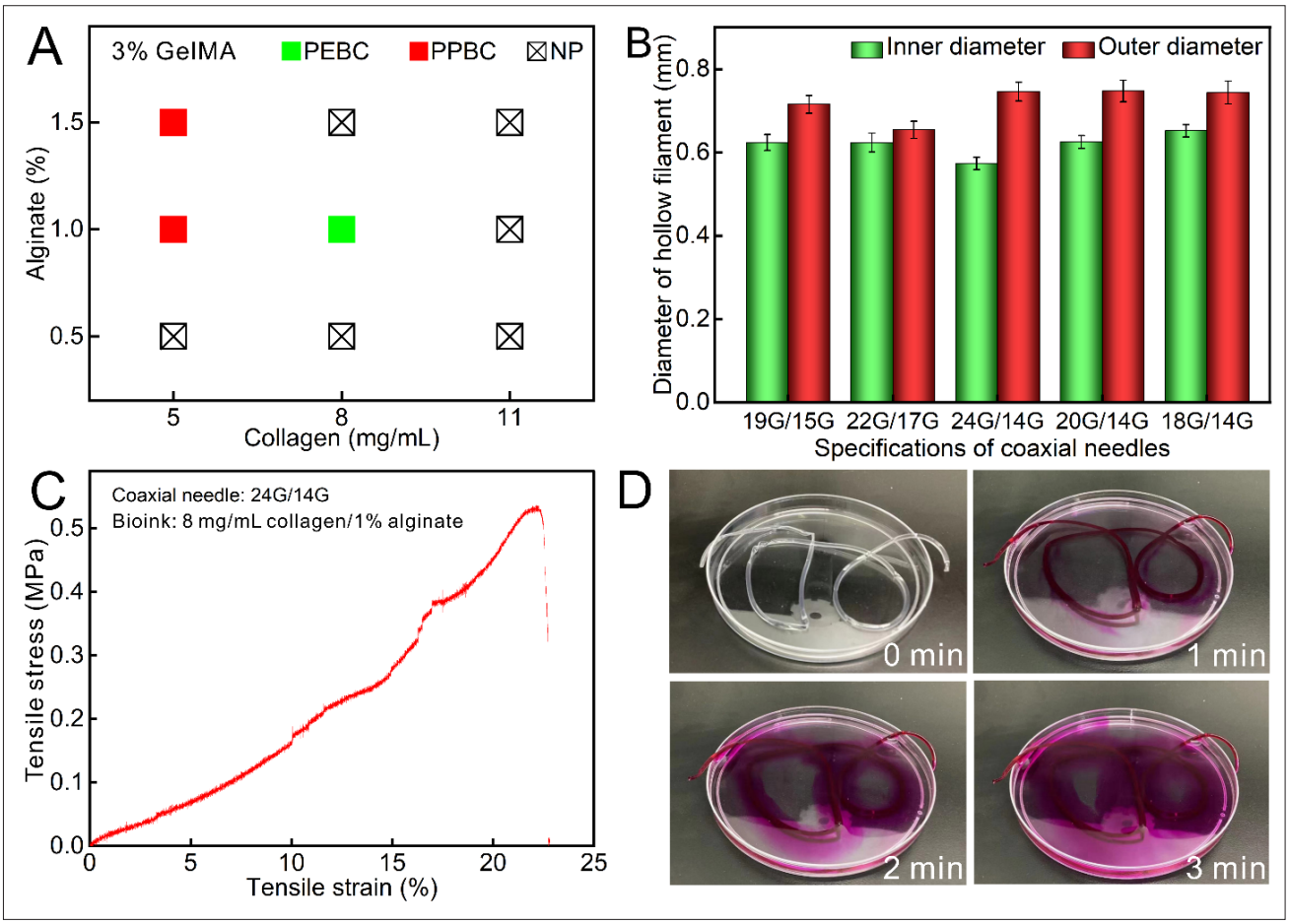

Figure 2. Fabrication and characterization of hollow tubes using coaxial bioprinting. (A) Printability and biocompatibility map of composite bioinks (GelMA, PEBC, PPBC, and NP). (B) Tunable inner and outer diameters of hollow tubes fabricated with different coaxial nozzle configurations. (C) Mechanical properties of hollow tubes. (D) Visualization of tube permeability and diffusivity using perfused red dye. Experiments were independently repeated at least three times ($n \geq 3$). Abbreviations: GelMA, Methacrylate Gelatin; NP, non-printable; PEBC, printable with excellent biocompatibility; PPBC, printable with poor biocompatibility.

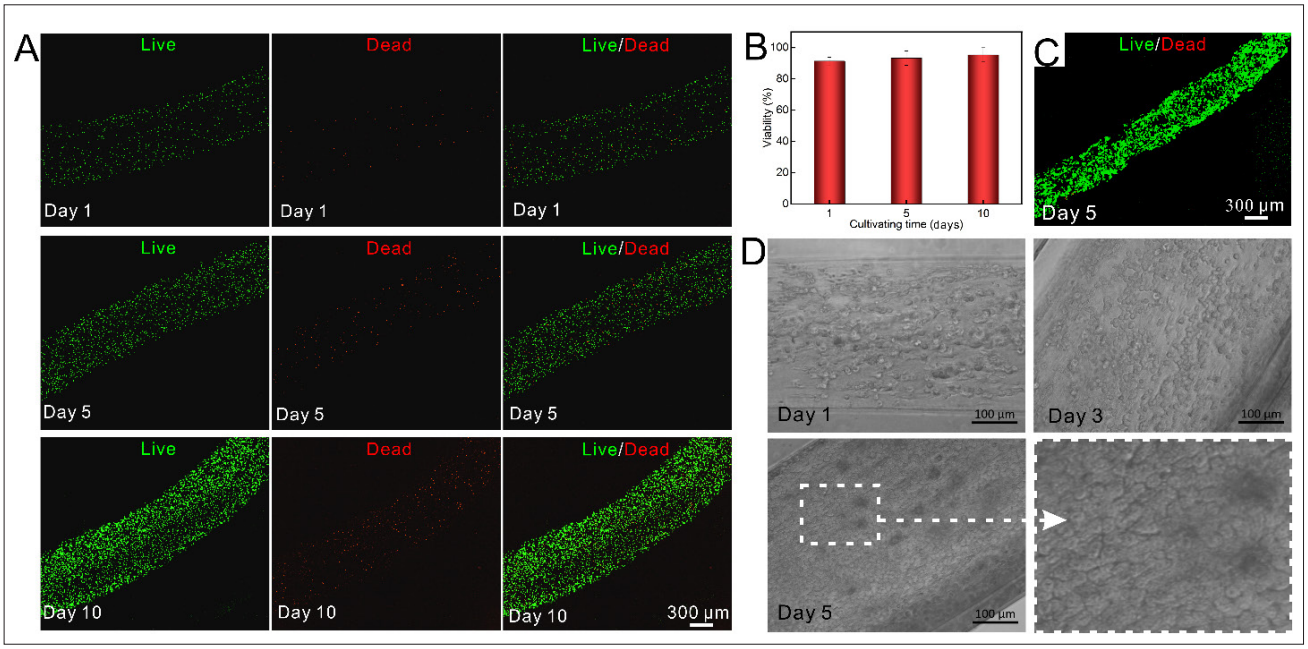

Figure 3. Evaluation of cell viability and morphology in double-layered vascular structures. (A) Temporal evaluation of smooth muscle cell proliferation from Day 1 to Day 10. (B) Quantitative analysis of HA-VSMCs viability embedded in the outer layer of hollow tubes. (C) Live/dead staining of endothelial cells (HUVECs) after 5 days of dynamic perfusion. (D) Formation of a continuous and dense inner monolayer. Experiments were independently repeated at least three times ($n \geq 3$). Scale bars: 300 μm (A and C); 100 μm (D). Abbreviations: HA-VSMCs, human aortic vascular smooth muscle cells; HUVECs, human umbilical vein endothelial cells.

sustained metabolic activity in the smooth muscle layer. For the endothelial layer, HUVECs were subjected to dynamic perfusion for 5 days. As displayed in Figure 3C and D, the cells formed a continuous, densely packed monolayer and maintained high viability (>90%). To enable a more intuitive assessment of morphology and viability, the two cell layers were cultured and stained separately. This strategy demonstrated excellent cell survival and proliferation in both layers. The successful formation of a dense endothelial layer is essential for mimicking the physiological functions of native blood vessels, including molecular exchange, inflammatory response regulation, and barrier protection. These results collectively suggest that the engineered double-layered vessel structure provides a biologically relevant and functional platform, making it highly suitable for downstream drug screening and vascular research applications.[43,44]

3.3. Fabrication and culture of tumor microspheroids

To construct tumor spheroids with precisely controlled dimensions, a high-resolution inkjet bioprinting strategy was innovatively employed in this study (Figure 4A). By tuning the GelMA concentration and the valve opening time of the droplet dispenser, the droplet volume could be precisely regulated. Subsequent crosslinking under 405 nm light enabled the formation of structurally stable tumor spheroids. As displayed in Figure 4B and C, under a fixed GelMA concentration of 5% (w/v), increasing the valve opening time from 200 to 500 μs led to a significant increase in the average spheroid diameter, from 154 to 430 μm. Conversely, when the valve opening time was held constant at 300 μs, increasing the GelMA concentration from 3% to 6% (w/v) raised the solution viscosity, thereby reducing droplet volume and leading to a decrease in spheroid diameter from 293 to 221 μm. This behavior is consistent with a viscosity-dominated droplet breakup mechanism in fluid dynamics,[45,46] suggesting that synergistic optimization of printing parameters enables sub-millimeter-level control over spheroid size. To monitor the formation and evolution of tumor microspheroids over time, HepG2 and HFL1 were pre-labeled with DiO (green) and DiI (red), respectively (Figure 4D). Under low-adhesion culture conditions, dispersed cells gradually self-assembled into multicellular aggregates and eventually matured into compact tumor microspheroids. As displayed in Figure 4E, the spheroids developed with a defined architecture and initial cell density. Initial total cell density was found to play a key role in spheroid formation. When the cell density reached 5×10^7 cells/mL, dense spheroids formed within only 3 days (Figure 4E). Notably, the low-adhesion culture environment effectively prevented cell migration from the aggregates, thereby ensuring structural

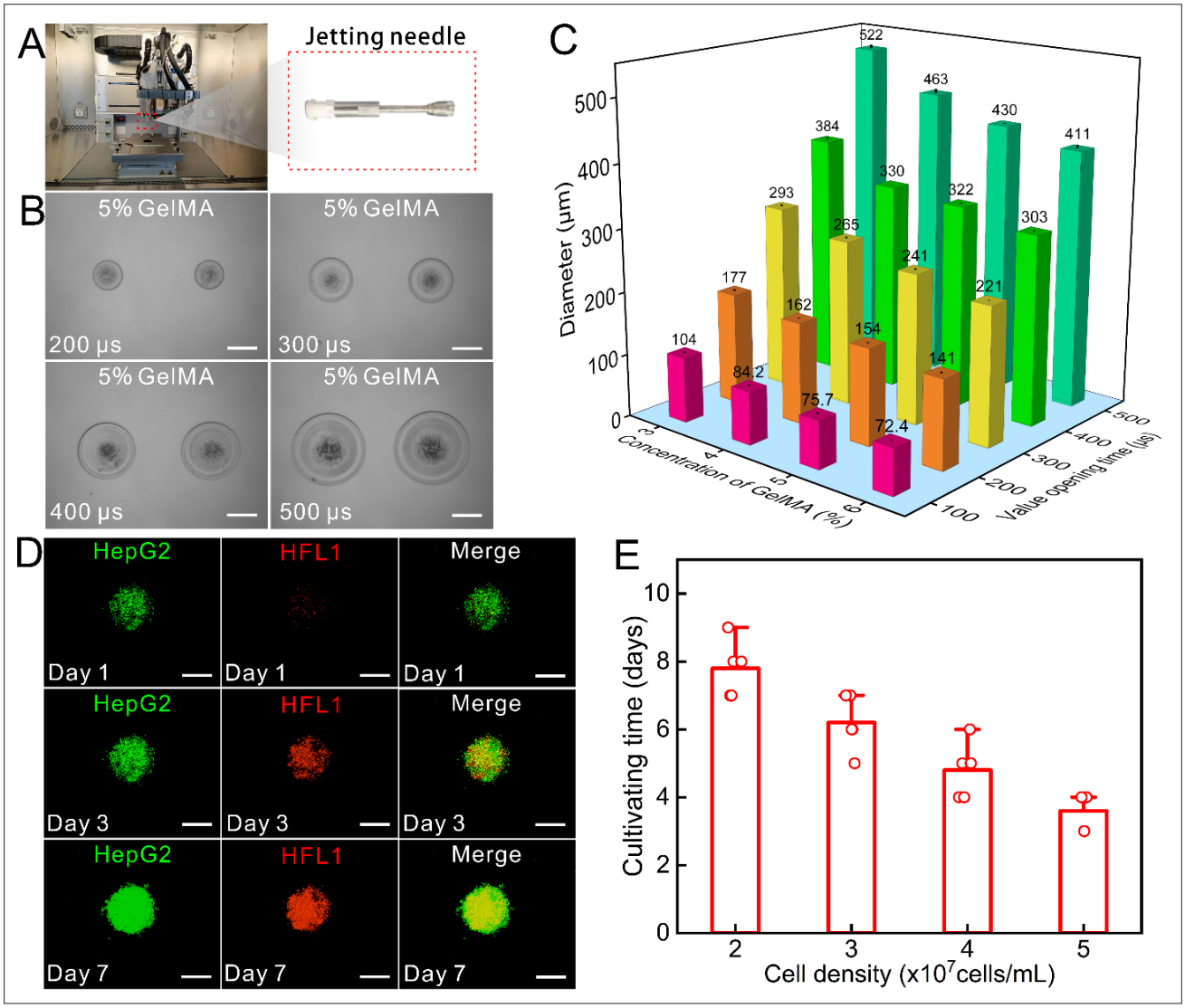

Figure 4. Controlled generation of tumor spheroids via high-precision inkjet bioprinting. (A) Schematic and appearance of the inkjet printing setup; jetting needle (red-dotted box). (B) Size-controlled tumor spheroids printed by varying valve opening times. (C) Statistical chart of initial microspheroid diameters prepared under different printing conditions. (D) Fluorescence images of DiO-labeled HepG2 (green) and DiI-labeled HFL1 (red) aggregating into compact spheroids under low-adhesion conditions. (E) Influence of initial total cell density on spheroid formation dynamics. Experiments were independently repeated at least three times ($n \geq 3$). Scale bars: 200 μm (B and D). Abbreviation: GelMA, Methacrylate Gelatin.

stability and consistent size of the spheroids throughout the subsequent perfusion culture. To further characterize spheroid viability, we performed Calcein-AM/PI staining on tumor spheroids at Days 1, 3, and 7. As presented in Figure S3, Supporting Information, the results demonstrate a progressive formation of a central necrotic core by Day 7—a typical feature of the tumor spheroid architecture that reflects *in vivo* solid tumor physiology.

3.4. Construction and characterization of a multiscale vascularized tumor model

To develop a biomimetic TME model, we first established microvascular networks (prevascular structures formed by HUVECs through self-assembly in a 3D ECM) through the co-culture of HUVECs and HFL1. A matrix composed of 5 mg/mL fibrinogen and 3 mg/mL collagen was used as the extracellular scaffold. Under dynamic perfusion conditions, the co-culture system exhibited robust microvascular formation (Figure 5A). Compared to the HUVEC-only control group, the presence of HFL1 significantly enhanced the elongation and maturation of endothelial cells, likely through VEGF secretion (Figure 5B).[47,48] This observation is consistent with previous studies demonstrating the synergistic role of fibroblasts and endothelial cells in angiogenesis, further supporting the

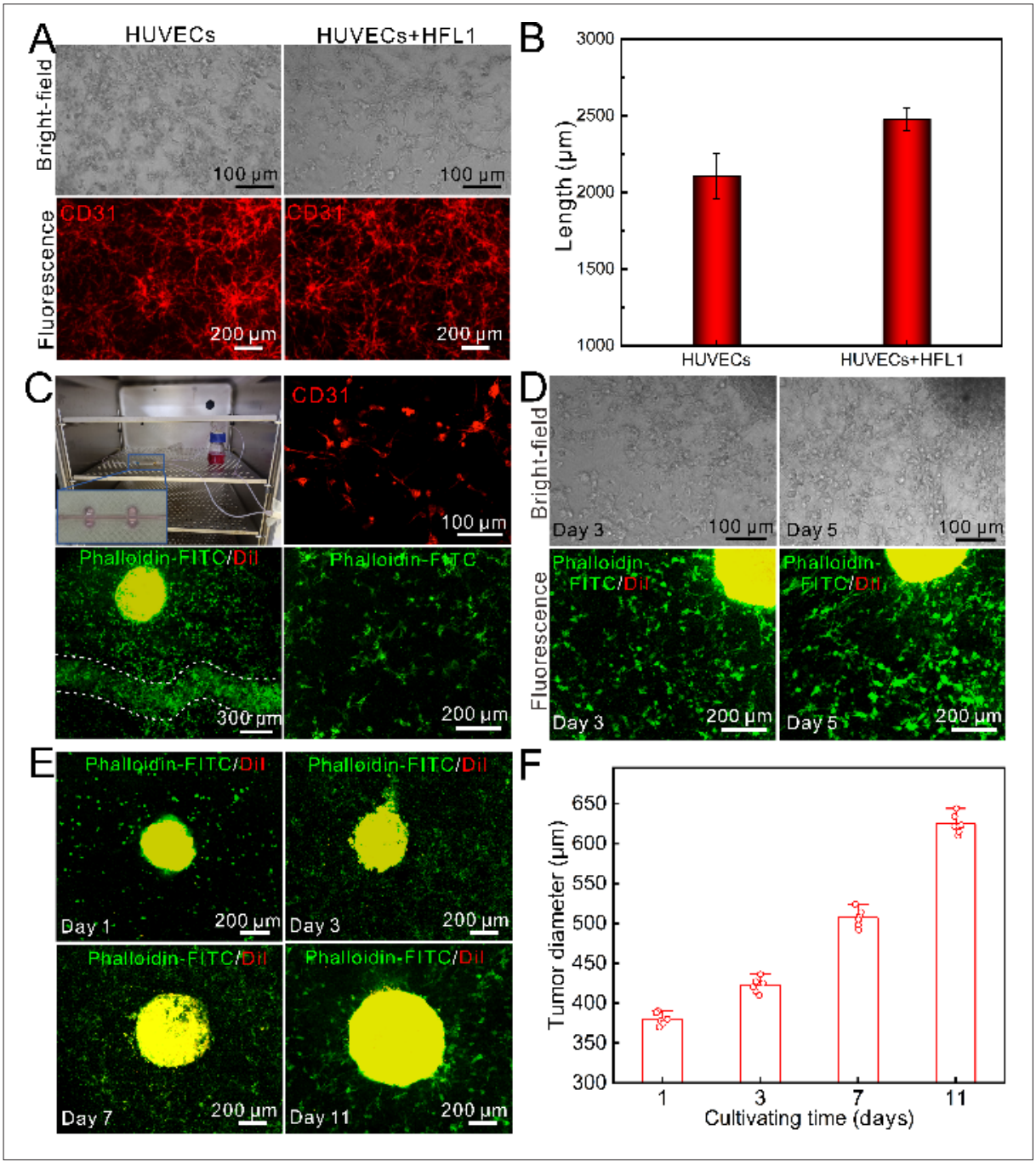

Figure 5. Construction and characterization of the multiscale vascularized tumor model. (A) Comparison of microvascular networks formed with and without HFL1. (B) Quantitative analysis of endothelial elongation in both conditions (i.e., with and without HFL1). (C) Photograph of a multi-level vascularized tumor model cultivation system (C, top-left); fluorescent images of the vascularized tumor region after 7 days of cultivation in the system: CD31 immunofluorescence staining (C, top-right), cellular skeleton staining of the local microvascular network. (D) On Days 3 and 5, bright-field imaging (D, top) and cell skeleton staining (D, bottom) were performed within the perfusion apparatus. (E) Tumor spheroid growth and migration dynamics were tracked under perfusion culture. (F) Quantitative measurement of tumor spheroid size over time. Experiments were independently repeated at least three times ($n \geq 3$). Scale bars: 100 μm (A, top; C, top-right; D, top); 200 μm (A, bottom; C, bottom-right; D, bottom; E); 300 μm (C, bottom-left). Abbreviation: HUVECs, human umbilical vein endothelial cells.

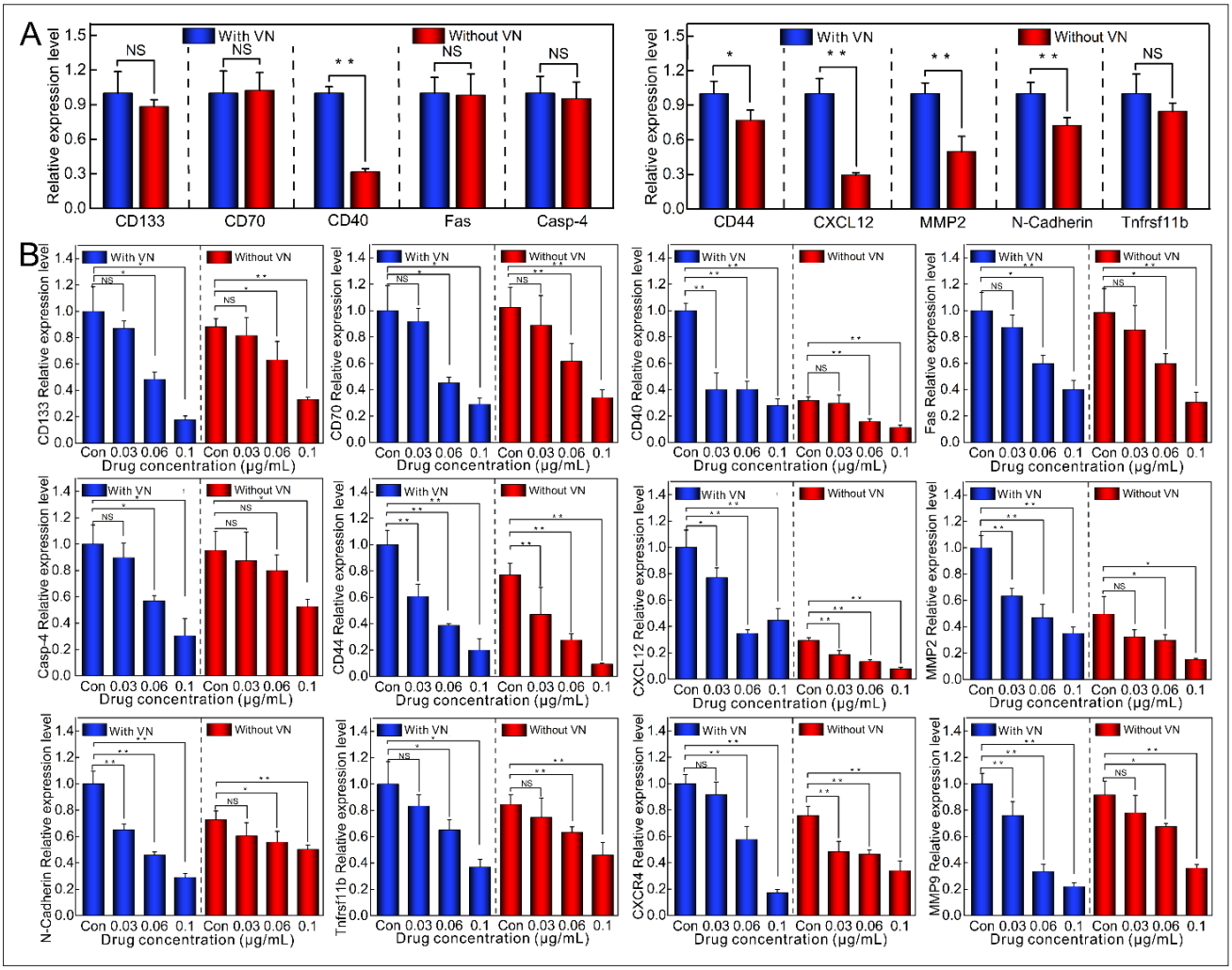

Figure 6. Vascular networks modulate tumor metastasis and drug efficacy in vascularized tumor models. (A) Gene expression levels of markers associated with metastasis and tumor stemness/survival in models with or without vascular networks. (B) Dose-dependent inhibitory effect of paclitaxel on key gene expression, indicating reduced invasiveness and viability in vascularized tumor models. Experiments were independently repeated at least three times ($n \geq 3$). $p < 0.05$, ** for $p < 0.01$, *** for $p < 0.001$, and N.S. for no significant difference. Abbreviations: Con, control; VN, vascular network.

necessity of a co-culture strategy for recapitulating tumor-induced vascularization.[49,50] Building upon the successful generation of microvascular networks, we integrated these with the double-layered vessels and tumor spheroids into a perfusion-compatible chip, resulting in a multiscale vascularized tumor model (Figure 5C). After 3 days of perfusion culture, immunofluorescence staining revealed that CD31-positive endothelial cells and Phalloidin-FITC-stained cytoskeletal structures adopted elongated, physiologically relevant morphologies, indicating active molecular transport capabilities within the microvascular network. By Day 5, radially oriented neovessels emerged around the tumor spheroids (Figure 5D), suggesting that the secretion of growth factors (e.g., VEGF and CXCL12) from the tumor may have induced directional angiogenic sprouting.[51] Furthermore, the tumor spheroids exhibited significant growth under dynamic conditions. The diameter increased from an initial 370 to 620 μm after 11 days of culture (Figure 5E), accompanied by the development of internal metabolic gradients,[52] which may have further stimulated vascular remodeling through hypoxia-induced signaling pathways. Notably, some tumor cells were observed to invade beyond the spheroid boundary in the later stages of culture (Figure 5F), indicating that the model can faithfully recapitulate early tumor invasion behavior, thus offering a visual platform for studying metastatic mechanisms. In addition, during the model design process, we prioritized the use of cell lines that could be co-cultured

under unified culture conditions to ensure stability and consistency. This approach allowed us to establish a robust and reproducible system; however, we acknowledge that it may not fully capture the complexity of the native TME, particularly the diverse phenotypes of tumor-associated fibroblasts. Therefore, this model represents a proof-of-concept framework, which we plan to refine in future studies by incorporating primary cells to enhance physiological relevance. Taken together, these results demonstrate that the multiscale vascularized tumor model not only achieves spatial integration of vascular networks and tumor spheroids but also supports dynamic interactions between the two components. The formation of microvessels is regulated by the synergistic interaction between fibroblasts and endothelial cells, while the tumor spheroids influence vascular morphology through paracrine signaling, forming a bidirectional, biomimetic microenvironment. This model thus serves as a highly representative *in vitro* platform for investigating tumor–vascular crosstalk and evaluating anti-angiogenic therapies.

3.5. Influence of the vascular network on tumor behavior and drug evaluation

To assess the physiological relevance and drug evaluation potential of the multiscale vascularized tumor model, we selected paclitaxel as a model chemotherapeutic agent and investigated the regulatory effects of the vascular network on tumor cell proliferation, metastasis, and drug sensitivity. Quantitative real-time PCR (qRT-PCR) analysis revealed that, in the presence of a vascular network, the expression levels of metastasis-related genes (CD44, CXCL12, MMP2, N-cadherin) and pro-survival genes (CD40) were significantly upregulated compared to those in models lacking vascularization (Figure 6A). The simultaneous upregulation of CD44 and MMP2 suggests that the vascular microenvironment may promote an invasive tumor phenotype by enhancing ECM remodeling.[53] Further dose-dependent experiments with paclitaxel (0.03–0.1 μg/mL) revealed a progressive suppression of these gene expressions (Figure 6B). Specifically, at 0.1 μg/mL paclitaxel, MMP2 and CD44 expression levels decreased to 32% and 28% of the control group, respectively, indicating that the drug effectively inhibited the metastatic potential of tumor cells by disrupting microtubule stability. In addition, Figure S2, Supporting Information demonstrated that the diameter of tumor spheres expanded from ~500 μm on Day 1 to ~750 μm on Day 7, whereas the tumor spheres in the drug-treated group (0.1 μg/mL paclitaxel) exhibited a diameter of only ~650 μm on Day 7, indicating that paclitaxel treatment significantly inhibited the volumetric growth of tumor spheres. These findings confirm that the incorporation of a vascular network within the tumor model significantly modulates tumor cell behavior and enhances the biological relevance of drug response assays. The ability of the model to recapitulate key features of tumor–vascular interactions makes it a powerful tool for evaluating anti-cancer drugs under conditions that more closely mimic *in vivo* tumor physiology.

4. Conclusion

In this study, we successfully developed a multiscale vascularized tumor model by integrating coaxial bioprinting, inkjet printing, and FDM techniques. This model was designed to precisely replicate the dynamic characteristics of the TME, including the mechanical and physiological properties of double-layered vessels, the size controllability of tumor spheroids, and the radial distribution of microvascular networks. Our results demonstrate that the formation of microvessels relies on the synergistic interactions between fibroblasts and endothelial cells, while the tumor spheroids secrete angiogenic factors that induce directional vascular sprouting. This bidirectional crosstalk highlights the model's capability to reproduce critical tumor–vascular interactions. Moreover, drug testing using this platform revealed a concentration-dependent inhibitory effect of paclitaxel on tumor progression, validating the model's potential for preclinical pharmacological screening. Despite these achievements, some limitations remain—including the complexity of fabrication procedures, the lack of immune microenvironment simulation, and challenges in maintaining long-term stability—and the absence of quantitative assessment of endothelial barrier function (e.g., using molecular permeability markers). Future work will aim to enhance the model's biomimicry by incorporating immune components, regulating dynamic oxygen gradients, and incorporating advanced metrics (e.g., fluorescent dextran diffusion or Trans-Epithelial Electrical Resistance [TEER]) to rigorously evaluate physiological transport and endothelial barrier function. Additionally, combining this platform with patient-derived tumor organoids may enable personalized drug sensitivity testing, while single-cell omics technologies could further elucidate the molecular networks underlying tumor-–vascular–immune interactions. Taken together, this study provides a versatile and physiologically relevant *in vitro* platform for the investigation of tumor progression, drug response, and mechanisms of therapy resistance, with broad applications in cancer research and precision medicine.

Acknowledgments

The authors would like to express our gratitude to Tao Ding, Wenqi Wei, and Weihao Teng for their valuable assistance in the preparation of bioink.

Funding

This research was funded by the University Natural Science Research Project of Anhui Province (grant number: 2024AH051533), the Talent Research Foundation of Hefei University (grant number: 21-22RC26), the Natural Science Foundation of Hubei Province (grant number: 2023AFB411), and the Talent Research Foundation of Hefei University (grant number: 20RC40).

Conflict of interest

The authors declare that they have no financial and personal relationships with other people or organizations that can inappropriately influence the study. They also have no professional or other personal interest of any nature or kind in any product, service, and/or company that could be construed as influencing the position presented in, or the review of, the article.

Author contributions

Conceptualization: Jing Liu, Haochen Liu
Formal analysis: Haizhongshi Zhang, Zhenlei Zhang
Investigation: Ying Zhao, Bihan Ren, Jing Liu
Methodology: Dingming Li, Tianma He
Writing–original draft: Jing Liu, Ying Zhao
Writing–review & editing: Haochen Liu

Ethics approval and consent to participate

Not applicable.

Consent for publication

Not applicable.

Availability of data

Data are available from the corresponding author upon reasonable request.

References

1. Lunt N. The global challenge of cancer governance. *World Med Health Pol*. 2023;15(4):672-681.
doi: 10.1002/wmh3.577

2. Sung H, Ferlay J, Siegel RL, et al. Global cancer statistics 2020: GLOBOCAN estimates of incidence and mortality worldwide for 36 cancers in 185 countries. *CA Cancer J Clin*. 2021;71(3):209-249.
doi: 10.3322/caac.21660

3. Sontheimer-Phelps A, Hassell BA, Ingber DE. Modelling cancer in microfluidic human organs-on-chips. *Nat Rev Cancer*. 2019;19(2):65-81.
doi: 10.1038/s41568-018-0104-6

4. Li CP, Li SB, Du K, Li P, Qiu BS, Ding WP. On-chip replication of extremely early-stage tumor behavior. *Acs Appl Mater Inter*. 2021;13(17):19768-19777.
doi: 10.1021/acsami.1c03740

5. Stock K, Estrada MF, Vidic S, et al. Capturing tumor complexity: comparative analysis of 2D and 3D tumor models for drug discovery. *Sci Rep-Uk*. 2016;6:28951.
doi: 10.1038/srep28951

6. Nie J, Gao Q, Fu JZ, He Y. Grafting of 3D bioprinting to in vitro drug screening: a review. *Adv Healthc Mater*. 2020;9(7):e190177310.
doi: 10.1002/adhm.201901773

7. Li JZ, Zhou YJ, Chen WL, et al. A novel 3D in vitro tumor model based on silk fibroin/chitosan scaffolds to mimic the tumor microenvironment. *Acs Appl Mater Inter*. 2018;10(43):36641-36651.
doi: 10.1021/acsami.8b10679

8. Lee G, Kim SJ, Park JK. Fabrication of a self-assembled and vascularized tumor array bioprinting on a microfluidic chip. *Lab Chip*. 2023;23(18):4079-4091.
doi: 10.1039/d3lc00275f

9. Nashimoto Y, Okada R, Hanada S, et al. Vascularized cancer on a chip: the effect of perfusion on growth and drug delivery of tumor spheroid. *Biomaterials*. 2020;229:119547.
doi: 10.1016/j.biomaterials.2019.119547

10. Lee VK, Lanzi AM, Ngo H, Yoo SS, Vincent PA, Dai GH. Generation of multi-scale vascular network system within 3D hydrogel using 3D bio-printing technology. *Cell Mol Bioeng*. 2014;7(3):460-472.
doi: 10.1007/s12195-014-0340-0

11. Eckermann CW, Lehle K, Schmid SA, Wheatley DN, Kunz-Schughart LA. Characterization and modulation of fibroblast/endothelial cell co-cultures for the preformation of three-dimensional tubular networks. *Cell Biol Int*. 2011;35(11):1097-1110.
doi: 10.1042/Cbi20100718

12. Enzerink A, Rantanen V, Vaheri A. Fibroblast nemosis induces angiogenic responses of endothelial cells. *Exp Cell Res*. 2010;316(5):826-835.
doi: 10.1016/j.yexcr.2009.11.012

13. Friedrich J, Ebner R, Kunz-Schughart LA. Experimental anti-tumor therapy in 3-D: spheroids - old hat or new challenge? *Int J Radiat Biol*. 2007;83(11–12):849-871.
doi: 10.1080/09553000701727531

14. Amann A, Zwierzina M, Gamerith G, et al. Development of an Innovative 3D cell culture system to study tumour - stroma interactions in non-small cell lung cancer cells. *Plos One*. 2014;9(3):e92511.
doi: 10.1371/journal.pone.0092511

15. Jing JF, Xiao H, Lin XW, et al. Cutting and Bonding Parafilm® to fast prototyping flexible hanging drop chips for 3d spheroid cultures. *Cell Mol Bioeng*. 2021;14(2):187-199.

doi: 10.1007/s12195-020-00660-x

16. Hurrell T, Ellero AA, Masso ZF, Cromarty AD. Characterization and reproducibility of HepG2 hanging drop spheroids toxicology. *Toxicol in Vitro*. 2018;50:86-94. doi: 10.1016/j.tiv.2018.02.013

17. Meenach SA, Tsoras AN, McGarry RC, Mansour HM, Hilt JZ, Anderson KW. Development of three-dimensional lung multicellular spheroids in air- and liquid-interface culture for the evaluation of anticancer therapeutics. *Int J Oncol*. 2016;48(4):1701-1709. doi: 10.3892/ijo.2016.3376

18. Costa EC, Gaspar VM, Coutinho P, Correia IJ. Optimization of liquid overlay technique to formulate heterogenic 3D co-cultures models. *Biotechnol Bioeng*. 2014;111(8):1672-1685. doi: 10.1002/bit.25210

19. Fennema E, Rivron N, Rouwkema J, van Blitterswijk C, de Boer J. Spheroid culture as a tool for creating 3D complex tissues. *Trends Biotechnol*. 2013;31(2):108-115. doi: 10.1016/j.tibtech.2012.12.003

20. Habanjar O, Diab-Assaf M, Caldefie-Chezet F, Delort L. 3D cell culture systems: tumor application, advantages, and disadvantages. *Int J Mol Sci*. 2021;22(22):12200. doi: 10.3390/ijms222212200

21. Gao W, Wu D, Wang Y, et al. Development of a novel and economical agar-based non-adherent three-dimensional culture method for enrichment of cancer stem-like cells. *Stem Cell Res Ther*. 2018;9(1):243. doi: 10.1186/s13287-018-0987-x

22. Jeong Y, Tin A, Irudayaraj J. Flipped well-plate hanging-drop technique for growing three-dimensional tumors. *Front Bioeng Biotechnol*. 2022;10:898699. doi: 10.3389/fbioe.2022.898699

23. de Barros NR, Gomez A, Ermis M, et al. Gelatin methacryloyl and Laponite bioink for 3D bioprinted organotypic tumor modeling. *Biofabrication*. 2023;15(4):045005. doi: 10.1088/1758-5090/ace0db

24. Wu L, Li H, Liu Y, et al. Research progress of 3D-bioprinted functional pancreas and in vitro tumor models. *Int J Bioprint*. 2024;10(1):1256. doi: 10.36922/ijb.1256

25. Singh S, Ray LA, Shahi Thakuri P, et al. Organotypic breast tumor model elucidates dynamic remodeling of tumor microenvironment. *Biomaterials*. 2020;238:119853. doi: 10.1016/j.biomaterials.2020.119853

26. Zhou X, Nowicki M, Sun H, et al. 3D bioprinting-tunable small-diameter blood vessels with biomimetic biphasic cell layers. *ACS Appl Mater Inter*. 2020;12(41):45904-45915. doi: 10.1021/acsami.0c14871

27. Meng FB, Meyer CM, Joung D, Vallera DA, McAlpine MC, Panoskaltsis-Mortari A. 3D bioprinted in vitro metastatic models via reconstruction of tumor microenvironments. *Adv Mater*. 2019;31(10):1806899. doi: 10.1002/adma.201806899

28. Nie J, Gao Q, Xie CQ, et al. Construction of multi-scale vascular chips and modelling of the interaction between tumours and blood vessels. *Mater Horizons*. 2020;7(1):82-92. doi: 10.1039/c9mh01283d

29. Gao G, Kim H, Kim BS, et al. Tissue-engineering of vascular grafts containing endothelium and smooth-muscle using triple-coaxial cell printing. *Appl Phys Rev*. 2019;6(4):041402. doi: 10.1063/1.5099306

30. Duong V, Dang TT, Hwang CH, Back SH, Koo KI. Coaxial printing of double-layered and free-standing blood vessel analogues without ultraviolet illumination for high-volume vascularised tissue. *Biofabrication*. 2020;12(4): 045033. doi: 10.1088/1758-5090/abafc6

31. Kwak TJ, Lee E. In vitro modeling of solid tumor interactions with perfused blood vessels. *Sci Rep-Uk*. 2020;10(1): 20142. doi: 10.1038/s41598-020-77180-1

32. Ahn J, Kim D, Koo DJ, et al. 3D microengineered vascularized tumor spheroids for drug delivery and efficacy testing. *Acta Biomater*. 2023;165:153-167. doi: 10.1016/j.actbio.2022.10.009

33. Dey M, Kim MH, Dogan M, et al. Chemotherapeutics and CAR-T cell-based immunotherapeutics screening on a 3D bioprinted vascularized breast tumor model. *Adv Funct Mater*. 2022;32(52):2203966. doi: 10.1002/adfm.202203966

34. Ozturk MS, Lee VK, Zou HY, Friedel RH, Intes X, Dai GH. High-resolution tomographic analysis of in vitro 3D glioblastoma tumor model under long-term drug treatment. *Sci Adv*. 2020;6(10):eaay7513. doi: 10.1126/sciadv.aay7513

35. Hwang DG, Choi YM, Jang J. 3D bioprinting-based vascularized tissue models mimicking tissue-specific architecture and pathophysiology for studies. *Front Bioeng Biotech*. 2021;9:685507. doi: 10.3389/fbioe.2021.685507

36. Nashimoto Y, Hayashi T, Kunita I, et al. Integrating perfusable vascular networks with a three-dimensional tissue in a microfluidic device. *Integr Biol-Uk*. 2017;9(6):506-518. doi: 10.1039/c7ib00024c

37. Velez C, Cheng K, Crosby C. Synthesis and Characterization of Gelatin Methacryloyl: Introducing Chemistry Students to the Applications of Hydrogels in Medicine. *J Chem Educ*. 2024;101(3):1171-1179. doi: 10.26434/chemrxiv-2023-qbrh6

38. Millik SC, Dostie AM, Karis DG, et al. 3D printed coaxial nozzles for the extrusion of hydrogel tubes toward modeling vascular endothelium. *Biofabrication*. 2019;11(4):045009. doi: 10.1088/1758-5090/ab2b4d

39. Siminska-Stanny J, Nicolas L, Chafai A, et al. Advanced PEG-tyramine biomaterial ink for precision engineering of perfusable and flexible small-diameter vascular constructs

via coaxial printing. *Bioact Mater*. 2024;36:168-184.
doi: 10.1016/j.bioactmat.2024.02.019

40. Elliott MB, Gerecht S. Three-dimensional culture of small-diameter vascular grafts. *J Mater Chem B*. 2016;4(20):3443-3453.
doi: 10.1039/c6tb00024j

41. Xia Y, Zhou HY, Ou JS, Liu YQ. The potential of a new natural vessel source: decellularized intercostal arteries as sufficiently long small-diameter vascular grafts. *Bioengineering (Basel)*. 2024;11(7): 700.
doi: 10.3390/bioengineering11070700

42. Carrabba M, Fagnano M, Ghorbel MT, et al. Development of a novel hierarchically biofabricated blood vessel mimic decorated with three vascular cell populations for the reconstruction of small-diameter arteries. *Adv Funct Mater*. 2024;34(7):adfm.202300621.
doi: 10.1002/adfm.202300621

43. Haase K, Offeddu GS, Gillrie MR, Kamm RD. Endothelial regulation of drug transport in a 3D vascularized tumor model. *Adv Funct Mater*. 2020;30(48):2002444.
doi: 10.1002/adfm.202002444

44. Marei I, Abu Samaan T, Al-Quradaghi MA, et al. 3D tissue-engineered vascular drug screening platforms: promise and considerations. *Front Cardiovasc Med*. 2022;9:847554.
doi: 10.3389/fcvm.2022.847554

45. Ma DF, Liang D, Zhu CY, et al. The breakup dynamics and mechanism of viscous droplets in Y-shaped microchannels. *Chem Eng Sci*. 2021;231:116300.
doi: 10.1016/j.ces.2020.116300

46. Sur S, Rothstein J. Drop breakup dynamics of dilute polymer solutions: effect of molecular weight, concentration, and viscosity. *J Rheol*. 2018;62(5):1245-1259.
doi: 10.1122/1.5038000

47. Cho WJ, Elbasiony E, Singh A, Mittal SK, Chauhan SK. IL-36 gamma augments ocular angiogenesis by promoting the vascular endothelial growth factor-vascular endothelial growth factor receptor axis. *Am J Pathol*. 2023;193(11):1740-1749.
doi: 10.1016/j.ajpath.2023.01.003

48. Sitohy B, Chang S, Sciuto TE, et al. Early actions of anti-vascular endothelial growth factor/vascular endothelial growth factor receptor drugs on angiogenic blood vessels. *Am J Pathol*. 2017;187(10):2337-2347.
doi: 10.1016/j.ajpath.2017.06.010

49. Truelsen SLB, Mousavi N, Wei HC, et al. The cancer angiogenesis co-culture assay: quantification of the angiogenic potential of tumoroids. *Plos One*. 2021;16(7):e0253258.
doi: 10.1371/journal.pone.0253258

50. Rodoplu D, Matahum JS, Hsu CH. A microfluidic hanging drop-based spheroid co-culture platform for probing tumor angiogenesis. *Lab Chip*. 2022;22(7):1275-1285.
doi: 10.1039/d1lc01177d

51. Chang CW, Seibel AJ, Avendano A, Cortes-Medina MG, Song JW. Distinguishing specific CXCL12 isoforms on their angiogenesis and vascular permeability promoting properties. *Adv Healthc Mater*. 2020;9(4):e1901399.
doi: 10.1002/adhm.201901399

52. Zhou L, Wang L, Song X, Zhang X, Xiao Y. A tetrazine-based ratiometric sensor quantifying ph gradient in tumorspheres through bio-orthogonal labeling. *Anal Chem*. 2025;97(22):11486-11495.
doi: 10.1021/acs.analchem.5c00291

53. Lee S, Park J, Cho S, et al. Hyaluronan network remodeling by ZEB1 and ITIH2 enhances the motility and invasiveness of cancer cells. *J Clin Invest*. 2025;135(11):e180570.
doi: 10.1172/JCI180570

ACCSCIENCE PUBLISHING

International Journal of Bioprinting

RESEARCH ARTICLE

Fabrication of an *in vitro* three-dimensional tumor model using liver-derived decellularized extracellular matrix/gelatin methacrylate bioink for investigating cancer characteristics and drug resistance

Chunyang Zhang[1,2†], Yunze Xu[1,2†], Hongwei Yu[1,2], Xiaochang Lu[1,3], Ying Fang[1,2], Changyong Li[1,3], Weihong Ji[1,3], Shibin Wang[1,2], Aizheng Chen[1,3], and Chaoping Fu[1,2*]

[1]Institute of Biomaterials and Tissue Engineering & Fujian Provincial Key Laboratory of Biochemical Technology, Huaqiao University, Xiamen, Fujian, China

[2]College of Materials Science and Engineering, Huaqiao University, Xiamen, Fujian, China

[3]College of Chemical Engineering, Huaqiao University, Xiamen, Fujian, China

(This article belongs to the *Special Issue*: *Advanced Strategies in 3D Bioprinting for Disease Modelling*)

Abstract

Three-dimensional (3D) printing has emerged as a promising technique for creating *in vitro* tumor models that replicate the tumor microenvironment, with the potential to reduce or replace the use of experimental animals. The incorporation of 3D decellularized extracellular matrix (dECM) hydrogels significantly enhances cellular responsiveness and functionality in drug screening. However, the limited printability of dECM restricts its application in e*x vivo* 3D disease models. To address this limitation, researchers have developed a blended bioink composed of dECM, gelatin methacrylate (GelMA), and gelatin, specifically tailored for direct ink writing-based 3D bioprinting. This formulation exhibits favorable shear-thinning behavior, enhanced viscosity, and thermal-sensitive properties, making it suitable for 3D bioprinting. The combination of dECM with GelMA and gelatin not only improves the printability of the bioink but also enhances the resolution of the printed scaffolds. Furthermore, dECM demonstrated positive effects on human hepatocellular carcinoma (HepG2) cells, promoting proliferation, migration, and cell spheroid formation. A 3D liver cancer model was successfully created *in vitro* by printing HepG2 cells encapsulated in the bioink containing dECM. This model exhibited characteristics akin to *in vivo* solid tumors, including notable cell proliferation, protein secretion, and substantial cell spheroid formation (up to 78.83 ± 9.41 μm on day 8). Additionally, it showed drug resistance, with 46.23% and 31.34% cell viability observed at 100 μg/mL concentrations of doxorubicin and paclitaxel, respectively. These findings underscore the potential of bioprinted 3D tumor models composed of GelMA, gelatin, and dECM as valuable platforms for the evaluation of anticancer drugs.

Keywords: 3D tumor model; Decellularized extracellular matrix; Drug evaluation; Gelatin methacrylate; Printability

†These authors contributed equally to this work.

***Corresponding author:**
Chaoping Fu
(fuchp@hqu.edu.cn)

Citation: Zhang C, Xu Y, Yu H, *et al*. Fabrication of an *in vitro* three-dimensional tumor model using liver-derived decellularized extracellular matrix/gelatin methacrylate bioink for investigating cancer characteristics and drug resistance. *Int J Bioprint*. 2025;11(4):392-408. doi: 10.36922/IJB025160142

Received: April 14, 2025
Revised: May 24, 2025
Accepted: June 9, 2025
Published online: June 10, 2025

Copyright: © 2025 Author(s). This is an Open Access article distributed under the terms of the Creative Commons Attribution License, permitting distribution, and reproduction in any medium, provided the original work is properly cited.

Publisher's Note: AccScience Publishing remains neutral with regard to jurisdictional claims in published maps and institutional affiliations.

1. Introduction

Cancer is a pervasive global public health challenge, significantly impacting human life and well-being. In recent years, effective treatments for cancer include surgical resection,[1,2] radiotherapy,[3,4] and chemotherapy.[5,6] Nevertheless, the 5-year survival rate of patients remains suboptimal. On one hand, current treatments fail to achieve a complete cure. On the other hand, our understanding of the complex mechanisms and characteristics of tumors remains incomplete, hindering the development of effective therapies and drugs.[7,8] Currently, preclinical research on anticancer drugs heavily relies on two-dimensional (2D) cell and animal models. However, the simplicity of 2D cell models and the limitations of animal experiments, such as long timelines, limited reproducibility, and high costs, hinder the development of effective tumor treatments.[9–11] Thus, there is an urgent need for sophisticated models that accurately simulate three-dimensional (3D) solid tumors *in vivo*. Such models hold great promise for facilitating more comprehensive tumor research, improving pharmacological evaluations, and accelerating drug development.

The emergence of 3D cell culture technology has revolutionized the advancement of *in vitro* tumor models. Within a 3D culture system, the establishment of an extracellular matrix (ECM) and the incorporation of diverse signals that mimic the growth characteristics of tumor cells are of utmost importance.[12–15] Through the implementation of 3D culture, tumor models can be meticulously crafted by manipulating the properties of the matrix or scaffold, thereby facilitating the investigation of morphogenesis, angiogenesis, invasion, pharmacology, and other tumor-related attributes.[16,17] Consequently, 3D bioprinting emerges as a promising approach for the construction of standardized 3D tumor models. By harnessing the capabilities of 3D printing technology, bioprinting enables the seamless integration of cells and biological materials, layer by layer, resulting in the generation of tissue-like structures.[18,19]

Natural hydrogels like fibrinogen, cellulose, chitosan, alginate, and hyaluronic acid are extensively used as bioinks in bioprinting for their controllable mechanical properties and excellent biocompatibility.[20–23] Bioprinting significantly enhances the reproducibility and standardization of 3D tumor models, making it ideal for preclinical research.[24,25] 3D-bioprinted tissues help reduce model variability, improve the consistency and reliability of drug screening data, and lower the risk and cost of drug screening.[26–28] However, establishing a tumor model relies on critical cellular, biochemical, and mechanobiological cues. Although both natural and synthetic polymers have been used, they cannot fully replicate the complex ECM *in vivo*, which is a crucial microenvironment for cells.[29] The ECM is a complex and dynamic network that provides essential structural support and significantly influences various cellular functions,[30–33] including proliferation,[34] migration,[35] differentiation,[36,37] and signal transduction.[38,39] Consequently, accurately simulating or reconstructing the ECM *in vitro* is critical for developing tumor models that closely mimic physiological conditions.[40,41]

Decellularization technology offers a promising method to selectively eliminate cellular components from tissues or organs while retaining the essential ECM components, biological functions, and structural integrity. This advanced technique has significantly broadened the use of ECM materials in the biomedical field.[42,43] However, decellularized ECM (dECM)-based bioinks suffer from suboptimal printability due to inadequate mechanical properties, unstable thermo-responsive behavior, and variable rheological properties, which limit their broader application in 3D bioprinting.[44,45]

In this study, we aimed to tackle the challenges posed by the limited printability of dECM-based bioinks while also developing an optimized bioink derived from liver tissue that demonstrates superior 3D printability. Our formulation not only improved printability but also exhibited excellent biocompatibility and favorable interactions with HepG2 cells, a liver cancer cell line. To comprehensively evaluate the physical and biological attributes of our bioink, we conducted a series of assessments encompassing morphology analysis, rheological characterization, degradation evaluation, swelling behavior analysis, 3D printability testing, and cytotoxicity analysis.

2. Materials and methods

2.1. Materials

Gelatin, methacrylic anhydride, sodium dodecyl sulfate, and ciprofloxacin were purchased from Aladdin Reagent Co., Ltd. (China). The porcine liver was procured from Mankouxiang Ecological Farming Cooperative Co., Ltd. (China). Cell Counting Kit (CCK)-8 and Dulbecco's Modified Eagle Medium were obtained from Keygen Biotech Corp., Ltd. (China). The bicinchoninic acid kit was purchased from Shanghai Biyuntian Biotechnology Co., Ltd. (China). The DNA kit was obtained from Cwbio, China; the glycosaminoglycan (GAG) kit from Genmed, China; and the collagen kit from Chondrex, United States of America (USA). Paclitaxel (PTX) and doxorubicin (DOX) were purchased from Solarbio Science and Technology Co., Ltd. (China). Calcein-acetoxymethyl/propidium iodide and acridine orange/ethidium bromide reagent kits were obtained from Solarbio Science and Technology Co., Ltd. (China).

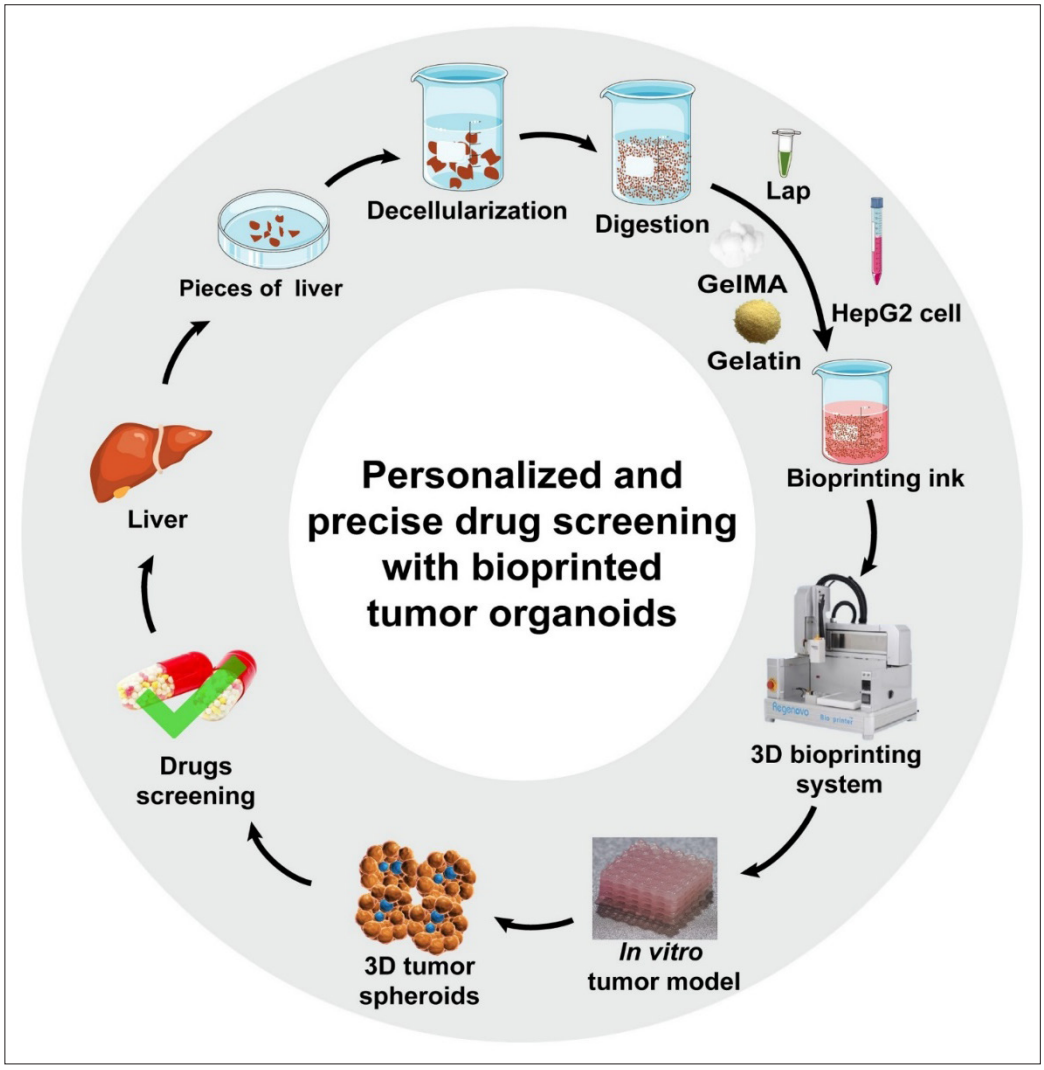

Schematic 1. Schematic diagram of the technological approach for this research. Abbreviations: GelMA, gelatin methacrylate; HepG2, human hepatocellular carcinoma; LAP, lithium phenyl-2,4,6-trimethylbenzoylphosphinate; 3D, three-dimensional.

2.2. Preparation and characterization of gelatin methacrylate and decellularized extracellular matrix

Initially, 10 g of gelatin was dissolved in 100 mL of phosphate-buffered saline (PBS) at 60°C, followed by the slow addition of 3 mL of methacrylic anhydride and stirring at 50°C for 3 h. The reaction was terminated by the addition of 500 mL of PBS. The resulting mixture was dialyzed against deionized water for 3 days (molecular weight: 12–14 kDa). After dialysis, the solution was filtered through a 0.22 μm membrane, and the filtrate was collected, pre-frozen at –80°C, then freeze-dried for 2 days and stored at –20°C in a sealed container. Finally, 20 mg of gelatin methacrylate (GelMA) sample was dissolved in 1 mL of deuterium oxide for proton nuclear magnetic resonance analysis to verify the synthesis. The Fourier-transform infrared (FTIR) spectra of freeze-dried GelMA were obtained using a NICOLET iS50 (Thermo Fisher Scientific, USA) equipped with a diamond attenuated total reflection module, analyzing the functional groups within the wavenumber range of 4000–500 cm^{-1}. Thermogravimetric analysis was conducted to investigate the thermal weight loss behavior of gelatin and GelMA (~10 mg). The analysis was performed under a nitrogen atmosphere, with a gas flow rate of 50 mL/min and a heating rate of 10°C/min, up to a final temperature of 500°C.

The preparation of dECM was carried out by combining chemical detergent and enzymatic treatment. Initially, 500 g wet liver tissue samples were cut into 10 × 10 mm^2 pieces and cleaned with ultrapure water for 30 min. Subsequently, the samples were treated with a 1% sodium dodecyl sulfate

solution for 14 h, followed by treatment with a DNase solution of 100 U/mL for 6 h, and washed with sterile PBS for 3 days, with 5 mg ciprofloxacin added to prevent bacterial contamination. The resulting decellularized liver matrix (DLM) was collected, washed with sterile PBS, freeze-dried, and stored at –20°C overnight. After 72 h of freeze-drying, the DLM was then digested in a solution of hydrochloric acid and pepsin. The digestion process took place at 37°C and 250 rpm for 6 h. The pepsin concentration was maintained at 1 mg/mL, with a hydrochloric acid concentration of 0.1 M and a ratio of 1:10 between the weight of DLM and the amount of pepsin used. After digestion, the pH was adjusted to neutral using a sodium hydroxide solution. The digested mixture was then subjected to dialysis with a 1000 D cutoff membrane for 3 days, with water replenished every 4 h. Finally, the dialyzed dECM was collected and freeze-dried for further use.

Both native liver tissues and DLM were immersed in a 4% paraformaldehyde solution for 24 h to fix the tissues. Following fixation, the tissues were embedded in the paraffin. Paraffined sections were cut into thin slices of 5 μm for deparaffinization and rehydration. Cell component residues were then observed by hematoxylin and eosin staining. In addition, 5-μm-thick sections of native and decellularized liver tissues were stained using the nuclear stain, 4',6-diamidino-2-phenylindole. The staining process was performed at room temperature for 5 min. Collagen I and III were also observed by immunohistochemical staining of tissue collagen.

For DNA, protein, collagen, GAG content, and proteomic analysis of dECM, a Tissue DNA extraction kit (Sigma-Aldrich, USA) was used to determine DNA content, a hydroxyproline assay kit (Aladdin Biotechnology Co., China) was employed to measure collagen content, and a GAG enzyme-linked immunosorbent assay kit (Sinopharm Chemical Reagent Co., China) was used to assess GAG content as an indicator of residual cells in dECM. A microplate reader (Thermo Scientific™ Multiskan™ GO, USA) was used to quantify the DNA, GAG, and collagen content.

2.3. Preparation of three-dimensional printing bioinks and characterization

Five different printing bioinks were prepared with varying compositions and ratios as follows: (i) 10% (w/v) GelMA (GM); (ii) 10% (w/v) GelMA and 5% (w/v) gelatin (GM/G); and (iii–v) GM/G combined with dECM at concentrations of 1%, 3%, and 5% (w/v), labeled as GM/G/d-1, GM/G/d-3, and GM/G/d-5, respectively. The components were dissolved in a PBS solution containing 0.25% (w/v) lithium phenyl-2,4,6-trimethylbenzoylphosphinate.

For morphology characterization, the bioinks with different ratios were cross-linked using ultraviolet (UV) light and subsequently immersed in PBS for 12 h to reach swelling equilibrium. After freeze-drying, the samples were fractured at the midpoint and coated with gold for 60 s using a conductive gel to secure them onto the holder. The fracture surface morphology of the hydrogels was then observed using scanning electron microscopy (SEM). Additionally, the internal pore sizes of the hydrogels were quantitatively analyzed using the Nano Measure software.

For rheological measurements, all tests were conducted using a rotational parallel plate rheometer (MCR 302, Anton Paar, Austria). A volume of 5 mL of each bioink was pipetted onto the bottom plate of the stage, with the gap distance set to 1 mm. Shear rate sweeps were conducted in the range of 0.1–800 s^{-1} at room temperature. Temperature–viscosity measurements were performed from 40 to 15°C. The storage modulus (*G'*) and loss modulus (*G"*) of the bioinks were evaluated by changing the temperature from 40 to 5°C, with a cooling rate of 5°C/min.

2.4. Three-dimensional printing

To bring the bioink to a pre-gel state, it was placed at 4°C for 20 min. Subsequently, the bioink cartridges were loaded into a 3D bioprinter, with the nozzle temperature set to 25°C and the print platform maintained at 4°C. During the printing process, the extrusion pressure was set to 0.25 MPa and the fill spacing was 1.2 mm. A porous scaffold with dimensions of 20 mm × 20 mm × 3 mm (length × width × height) was printed. After extrusion, the printed porous scaffold was exposed to UV light at an intensity of 30 mW/cm^2 for 30 s to induce cross-linking. To evaluate the printability of the bioink and the print resolution of the porous scaffold, the scaffold's surface morphology was analyzed using SEM, and the Pr value[44] was calculated. This value was determined based on the circularity of an enclosed area, as shown in **Equation (I)**:

$$c = 4\Pi A/L\text{^}2 \quad \text{(I)}$$

where c is circularity, L is the perimeter, and A is the area. A perfect circle yields a value of 1. For square shapes, the maximum circularity value is π/4. Therefore, the Pr parameter for square shapes can be calculated using **Equation (II)**:

$$Pr = \Pi / 4C\,L^2 / 16A \quad \text{(II)}$$

To measure the swelling ability of scaffolds, the freeze-dried scaffolds were first weighed and recorded as *Wd*. The scaffolds were then immersed in PBS (pH 7.4) at

room temperature, and their mass wet weight (*Ws*) was measured at 0, 2, 4, 6, and 12 h. The water swelling ratio (*Sr*) was calculated as a percentage using the following formula (**Equation III**):

$$Sr = (Ws - Wd)/Wd \times 100\% \quad \text{(III)}$$

To evaluate the degradation behavior of the composite porous scaffold, it was first subjected to swelling equilibrium, then freeze-dried and accurately weighed. Subsequently, the scaffold was immersed in a culture medium and incubated in a 37°C cell culture incubator. After 3, 6, and 9 days, the scaffold was retrieved, freeze-dried again, and its mass was recorded. The degradation rate of the hydrogel was calculated using the following formula (**Equation IV**):

$$D = (Wc - Wd)/Wc \times 100\% \quad \text{(IV)}$$

Cell cytotoxicity of printed scaffolds was assessed using L929 cells. The cells were cultured in Roswell Park Memorial Institute (RPMI) medium and maintained at 37°C with 100% humidity and 5% carbon dioxide. The cells were passaged every 2 days. The cytotoxicity of the scaffolds was assessed by extract assay. Briefly, using the culture medium as an extraction solvent, the freeze-dried scaffolds were soaked at a ratio of 0.2 g/mL for 24 h. A cell density of 8×10^3 was seeded into each well, and 100 μL of the corresponding scaffold extract was added. Three replicates were set for each group. After 24 and 48 h of culture, CCK-8 was added and viability was a 2-h incubation; the absorbance at 562 nm was measured to calculate cell viability. Similarly, live/dead staining was performed using calcein-acetoxymethyl/propidium iodide staining, where green indicates live cells and red indicates dead cells, to observe cell growth.

2.5. Three-dimensional *in vitro* tumor model construction

Human hepatocellular carcinoma (HepG2) cells were cultured in five types of gels at a density of 6×10^4 cells/mL and were crosslinked for 30 s with a 405 nm UV light. An appropriate medium was added to wash the scaffold, and the liquid culture was then changed. After 1, 2, and 3 days of culture, the absorbance was measured using the CCK-8 method. Simultaneously, the effect of the above hydrogels on HepG2 migration was determined using scratch assays. First, approximately 1×10^6 cells were seeded onto a six-well plate and incubated until they attained 80% confluence. A sterile 200 μL pipette tip was used to scratch the cell monolayer across the center, creating a cross-shaped wound in each well. Then, 500 μL of the hydrogel precursors were added to each scratch well. Images of the cells were captured at 0, 12, and 24 h using an Olympus microscope ($n = 3$). Finally, quantitative analysis was performed using Image J software (National Institutes of Health, Germany).

Liver-derived GelMA/dECM bioinks were utilized to fabricate an *in vitro* 3D liver cancer tumor model. Briefly, HepG2 cells were collected by centrifugation and suspended in the bioinks at a density of 1×10^6 cells/mL. The 3D printing procedure was performed as described previously. Finally, the bioprinted scaffold was transferred to a six-well plate, rinsed with PBS, and incubated in the culture medium.

To assess the cell viability of the tumor model, 3D scaffolds (3D control and 3D-dECM) cultured for 2, 4, 6, and 8 days, along with 2D cultured cells, were removed and washed twice with PBS to remove the culture medium. The cell proliferation was analyzed using CCK-8 for both 2D and 3D cultures. Meanwhile, live/dead staining was used to assess the survival state of cells.

For cell morphology, the sizes of tumor spheroids were monitored during 3D culture, with photographs taken for 2, 4, 6, and 8 days using an optical microscope. The sizes of tumor spheroids were quantified using Image J software (National Institutes of Health, Germany). Cells cultured in 2D were observed using phalloidin staining.

To assess liver function, culture supernatants were collected on day 8, and parameters including alanine aminotransferase (ALT), aspartate aminotransferase (AST), albumin (ALB), and total bile acid (TBA) were analyzed using a multimode microplate reader.

2.6. Chemosensitivity assay

The chemosensitivity of the 3D and 2D culture samples was assessed by treating them with various concentrations of different drugs. After 6 days of cultivation, the samples were treated with PTX and amrubicin hydrochloride. Specifically, PTX was dissolved in 0.1% dimethyl sulfoxide and diluted with the culture medium, while amrubicin hydrochloride was dissolved in ultrapure water and similarly diluted. The drug concentrations used were 10, 20, 30, 50, 100, and 200 μg/mL. Each well was filled with the corresponding drug concentration, and cell viability and survival rate were measured using the CCK-8 assay after 12 and 24 h. Live/dead staining was performed simultaneously to assess cell survival.

2.7. Statistical analysis

At least three independent experiments were performed, unless otherwise stated. One-way analysis of variance and *t*-tests were used to analyze the differences between the

experimental groups. Statistical significance was indicated as follows: * $p < 0.05$, ** $p < 0.01$, *** $p < 0.001$.

3. Results and discussion

3.1. Gelatin methacrylate and liver decellularized extracellular matrix preparation and characterization

In this experiment, chemical and enzymatic treatments were employed for decellularization, as illustrated in Figure 1A. After decellularization, the liver tissue became translucent, indicating the effective removal of cellular components. The resulting dECM was lyophilized into a white powder. To evaluate the efficacy of decellularization, quantitative analysis of DNA and main biological components, histological staining, and morphological analysis were performed. Figure 1B depicts the results of hematoxylin and eosin and 4',6-diamidino-2-phenylindole staining, which clearly demonstrate the absence of cellular components in DLM. SEM images revealed a porous layered fiber structure in the decellularized tissue. Morphological observations of the dECM powder confirmed that the hydrochloric acid and pepsin mixture successfully digested the DLM into particles averaging approximately 700 μm in size (Figure 1C). Figure 1D illustrates the content of biological components, with DNA levels decreasing

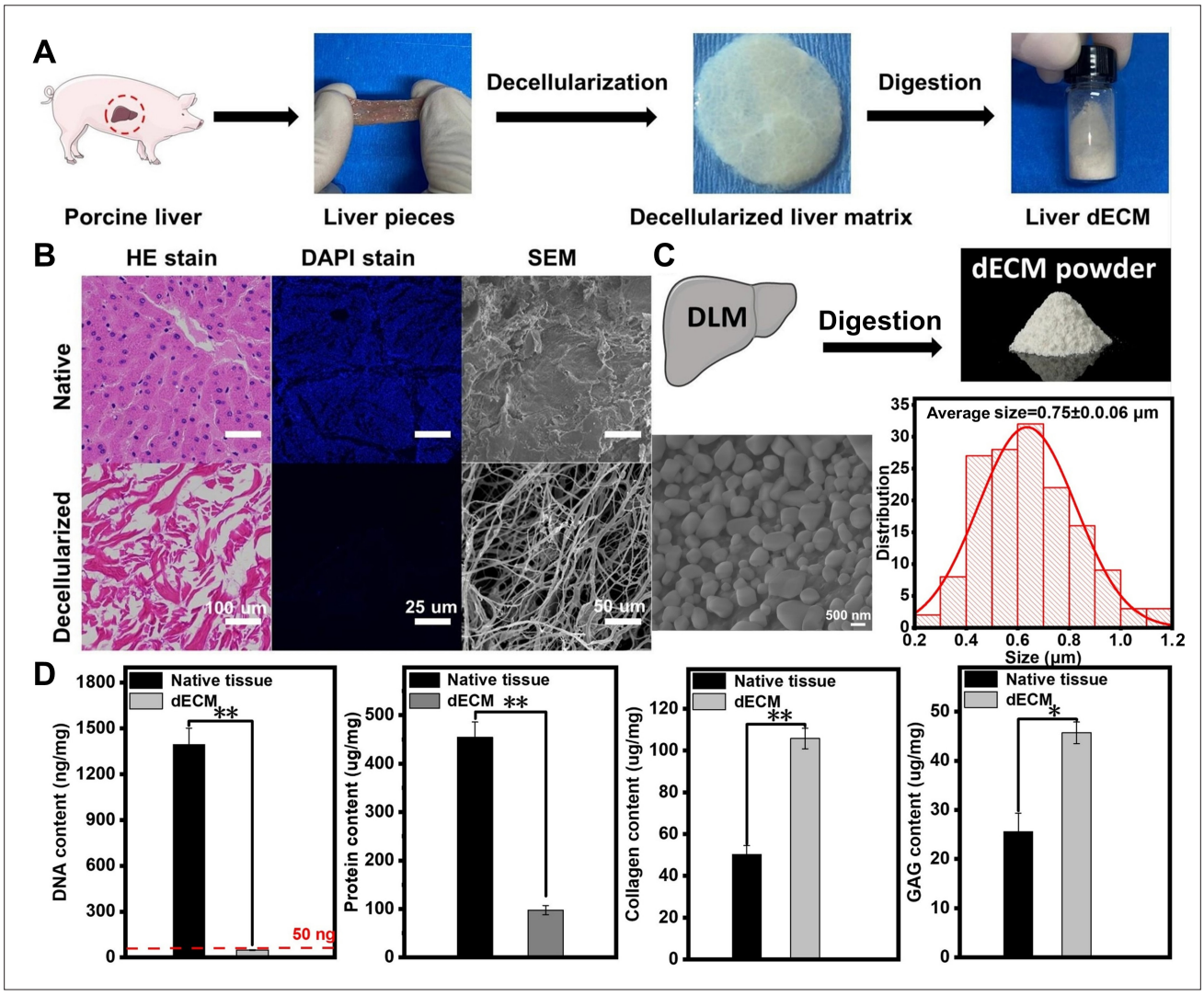

Figure 1. Determination of liver decellularization. (A) The process of decellularized extracellular matrix (dECM) preparation. (B) Hematoxylin and eosin (HE) and 4',6-diamidino-2-phenylindole (DAPI) staining, as well as scanning electron microscopy (SEM) images of the decellularized liver matrix (DLM). Scale bars = 100, 25, and 50 μm, respectively; magnification = 40×, 160×, and 80×, respectively. (C) Morphology of dECM powder. Scale bar = 500 nm; Magnification = 12,000×. (D) Content of biological components ($n = 3$; * $p < 0.05$, ** $p < 0.01$). Abbreviation: GAG, glycosaminoglycan.

to below 50 ng/mg, meeting safety standards for other tissue-derived materials.[46]

The proton nuclear magnetic resonance, FTIR, and the thermogravimetric curves results of gelatin and GelMA are shown in Figure S1, Supporting Information. Protein content significantly decreased after decellularization, while substantial amounts of GAGs and collagen remained, indicating the favorable biological properties of the dECM (collagen I and III staining are shown in Figure S2, Supporting Information). Our previous study reported the proteomic analysis of liver-derived dECM, identifying "catalytic activity" and "cellular process" as the top-ranked molecular function and biological process, respectively.[47] Furthermore, cell viability assays and live/dead staining were performed to assess the impact of decellularization on the cell compatibility of native liver tissue. As shown in Figure S3, Supporting Information, the extract from native liver tissue exhibited significant cytotoxicity, inhibiting cell proliferation, and inducing extensive cell death. In contrast, the DLM group demonstrated normal cell proliferation, nearly matching that of the blank group.

3.2. Hydrogel preparation and characterization

Scanning electron microscopy was applied to inspect the internal morphology of five hydrogels. As shown in Figure 2A, all groups exhibited a macroporous structure (pore size > 50 nm), with average pore sizes of 72.40, 62.74, 43.34, 36.51, and 30.02 μm (Figure 2B). The average pore sizes were 72.40 μm for GM and 62.74 μm for GM/G without dECM. Upon the addition of dECM, the pore size decreased to below 50 μm, with smaller pore sizes corresponding to higher dECM content. These findings suggest that the incorporation of dECM reduces pore size and effectively enhances the compactness of the structure. In addition, dECM particles were visible in the SEM images of dECM-containing groups, appearing as dense and irregular inclusions within the hydrogel network, further confirming their successful integration into the scaffold.

Rheological properties play a crucial role in studying the structure and characteristics of hydrogels, providing valuable guidance for parameter settings in 3D printing. Figure 2C displays the shear viscosity measurements of the printing bioinks at room temperature. It was observed that as the shear rate increased, the viscosity of the bioinks gradually decreased, demonstrating shear-thinning behavior, which is desirable for extrusion-based 3D printing applications.[48] Furthermore, the viscosity increased with rising dECM content, primarily attributed to the higher solid content in the mixture. This viscosity trend also held true for temperature-dependent measurements, as shown in Figure 2D. *G*' and *G*" were utilized to describe the elastic and viscous responses of hydrogels, respectively. As depicted in Figure 2E, as the temperature continuously decreased, the *G*' value initially exceeded the *G*" value, indicating a more dominant elastic behavior. However, a reversal occurred as the temperature approached a certain point. Specifically, the *G*" value of GM/G/d-5 started to increase and eventually surpassed the *G*' value around 24.5°C, indicating a gradual transition from a solid to a liquid state. Among the bioink formulations, GM exhibited the lowest solid–liquid transition temperature, occurring at approximately 15°C. The addition of gelatin increased the solid–liquid transition temperature of the mixture, leading to variations in the transition behavior. The diversity observed among the composite dECM groups could be attributed to differences in dECM content, where a higher proportion of dECM resulted in a higher solid content within the mixture, leading to a more pronounced *G*' value and a delayed transition from solid to liquid state.

3.3. Printing and characterization of gelatin methacrylate/decellularized extracellular matrix bioink three-dimensional scaffold

For the fabrication of printed constructs, the bioinks were extruded from the printer nozzle and stacked to achieve the desired shape. Subsequently, ultraviolet irradiation was applied to induce photo-crosslinking and ensure the curing of the hydrogels (Figure S6). To assess the accuracy of the printed shapes, hydrogels were printed in single-layer grids, featuring square voids between the filaments. The perimeter and area of these void spaces were calculated to determine a printability parameter, Pr. A Pr value of 1 corresponds to a perfect square shape, while values <1 indicate a more circular shape, and values >1 suggest the presence of jagged edges. In our study, all three bioink blends demonstrated Pr values close to 1: GM/G/d-5 = 0.914 ± 0.007, GM/G/d-3 = 0.879 ± 0.04, and GM/G/d-1 = 0.857 ± 0.020, all of which were higher than that of GM/G (0.803 ± 0.022). Notably, pure GelMA could not be successfully printed under these specific printing conditions, highlighting the ideal printability achieved with the developed bioink formulations (Figure 3A). Furthermore, SEM images revealed a more distinct grid structure, indicating superior printability for the GM/G/d-5 bioink compared to other blends, as shown in Figure 3B. To more robustly verify printability beyond simple lattice patterns, complex geometries were also printed using GM/G/d-5, including stylized "HQU" letters, a six-pointed star, and a biomimetic flower-like mesh. As shown in Figure S7, Supporting Information, these shapes maintained sharp edges and fine lattice features, demonstrating the bioink's fidelity under challenging design conditions.

Figure 3C illustrates the swelling properties of the five scaffolds after being immersed in PBS for 12 h. The GM

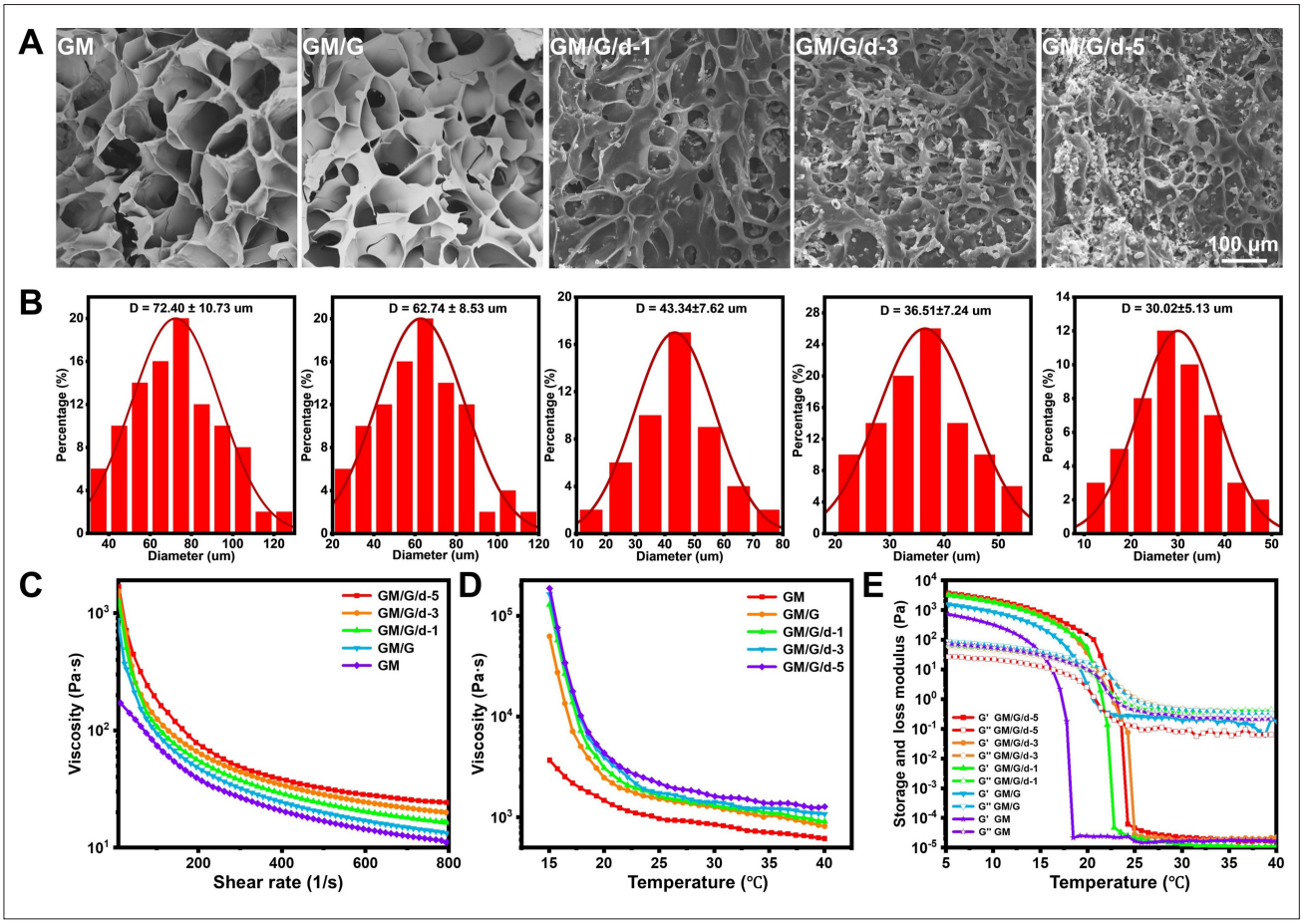

Figure 2. Hydrogel preparation and characterization. (A) Scanning electron microscopy images of five different hydrogels. Scale bar: 100 μm; magnification = 100×. (B) Distribution of macroporous structure diameter of five different hydrogels. (C) Shear rate-dependent viscosity, (D) shear rate-dependent temperature, and (E) viscosity-dependent temperature of different biomaterial ink formulations. Notes: GM: 10% (w/v) gelatin methacrylate (GelMA); GM/G: 10% (w/v) GelMA and 5% (w/v) gelatin; GM/G/d-1, GM/G/d-3, and GM/G/d-5: GM/G combined with decellularized extracellular matrix at concentrations of 1%, 3%, and 5% (w/v), respectively.

scaffold exhibited an Sr of 8.92 within this period, while the GM/G scaffold showed an Sr of 8.05. The scaffolds containing 1%, 3%, and 5% dECM composites exhibited Srs of 7.49, 7.01, and 6.13, respectively. These results indicate that the addition of gelatin and dECM reduced the water absorption capacity due to the higher solid content in the hydrogel, resulting in smaller pore sizes. In contrast, the pure GelMA hydrogel exhibited larger pores, leading to a faster equilibrium rate of swelling and a higher water absorption capacity. Figure 3D presents the *in vitro* degradation properties of the different composite scaffolds. The degradation curves demonstrate that all scaffolds exhibited relatively fast degradation. This could be attributed to the disruption of the physical cross-linking structure of gelatin, as well as the reduced degree of cross-linking caused by the high content of dECM. Over the 9-day experimental observation period, the GM scaffold showed the slowest degradation rate at 14.52 ± 1.03%. In contrast, the GM/G/d-5 group exhibited the fastest degradation rate at 39.74 ± 4.03%. The degradation rates for GM/G, GM/G/d-1, and GM/G/d-3 were measured at 19.9 ± 2.39%, 23.85 ± 2.67%, and 32.14 ± 3.01%, respectively.

Biocompatibility is an essential property of scaffold materials, and L929 cells were applied for scaffold cytotoxicity testing. As shown in Figure 3E, L929 cells grew and proliferated normally in the scaffold extract, in which the cell survival rate was above 90% at both 24- and 48-h intervals. Consistent growth was observed whether cells were cultured in the extract or fresh culture medium, and there was no significant difference between groups. As shown in Figure S4, Supporting Information, the live/dead staining of cells at 48 h where the L929 cell growth density was similar within the field of view, and the group with 5%

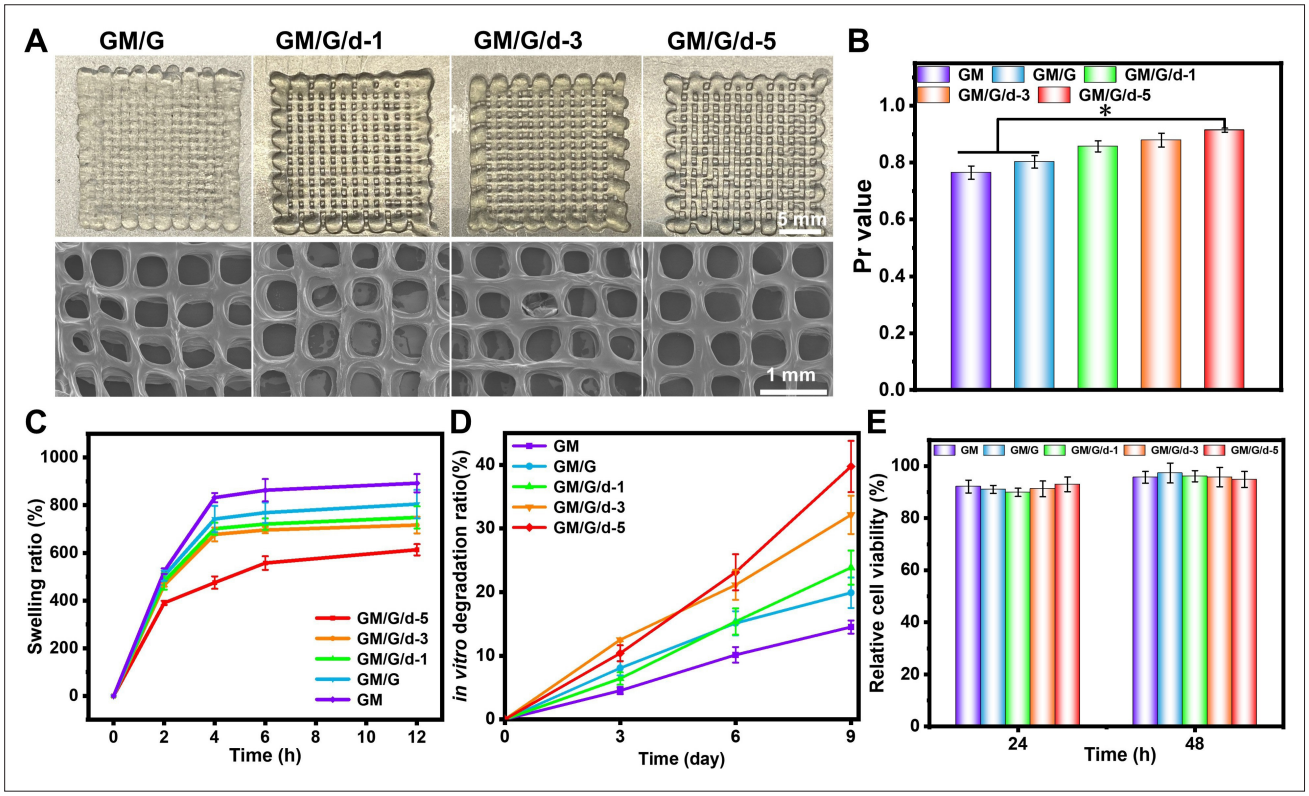

Figure 3. Three-dimensional printing of different scaffolds using five different bioinks and characterizations. (A) Images of scaffolds for each hydrogel. Scale bars: 5 and 1 mm; magnifications = 2.5× and 10×. (B) Printability parameters were calculated as described. Pr = 1 indicates a perfect square. (C) Swelling analysis (n = 3). (D) Degradation analysis (n = 3). (E) Cell viability of five different scaffolds (n = 3). The horizontal lines indicate no significant difference between those groups. * $p < 0.05$. Notes: GM: 10% (w/v) gelatin methacrylate (GelMA); GM/G: 10% (w/v) GelMA and 5% (w/v) gelatin; GM/G/d-1, GM/G/d-3, and GM/G/d-5: GM/G combined with decellularized extracellular matrix at concentrations of 1%, 3%, and 5% (w/v), respectively.

dECM content had relatively more cells. Therefore, the five 3D scaffolds prepared had no apparent cytotoxicity and excellent biocompatibility.

3.4. *In vitro* three-dimensional tumor model construction and assays

Cell migration and growth are fundamental behaviors of tumor cells and tissues.[49] In the CCK-8 assay, hydrogels supplemented with dECM (GM/G/d-1/3/5) demonstrated enhanced cell proliferation compared to the pure GelMA hydrogel, as indicated by higher optical density (OD) values after 3 days (Figure 4A). Additionally, in the scratch wound assay, HepG2 cells cultured with dECM exhibited superior migration capacity compared to those cultured on GM/G and pure GelMA hydrogels (Figure 4B) at 48 h. Figure 4C shows that at 12 h post-scratching, hydrogel solutions containing dECM display enhanced cell migration, with a larger cell migration area than GM and GM/G. By the 48-h mark, the scratch was almost completely healed in the group containing 5% dECM. Considering the overall interaction between each bioink and HepG2 cells, we selected the GM/G/d-5 bioink composition to construct the subsequent 3D *in vitro* tumor model.

3.5. Cell viability and protein expression

To evaluate cell proliferation in the 3D tumor model and 2D culture, CCK-8 and live/dead staining assays were utilized to analyze cell proliferation activity on days 2, 4, 6, and 8. The OD value on day 2 was used as the baseline, and the OD values on days 4, 6, and 8 were normalized accordingly. Fluorescent staining images of live and dead cells under 2D and 3D culture conditions are presented in Figure 5A. Under 2D culture conditions, characterized by rapid cell proliferation, the cells exhibited healthy growth, with only a few dead cells observed. By day 8, the cells had nearly completely covered the surface of the culture plate. Under 3D culture conditions, cells initially grew as individual cells during the first 2 days without aggregation. However, cell spheroids were observed on day 4, and the number and size of cell spheroids significantly increased on days 6 and 8, indicating cell aggregation and growth in a 3D environment with the potential to

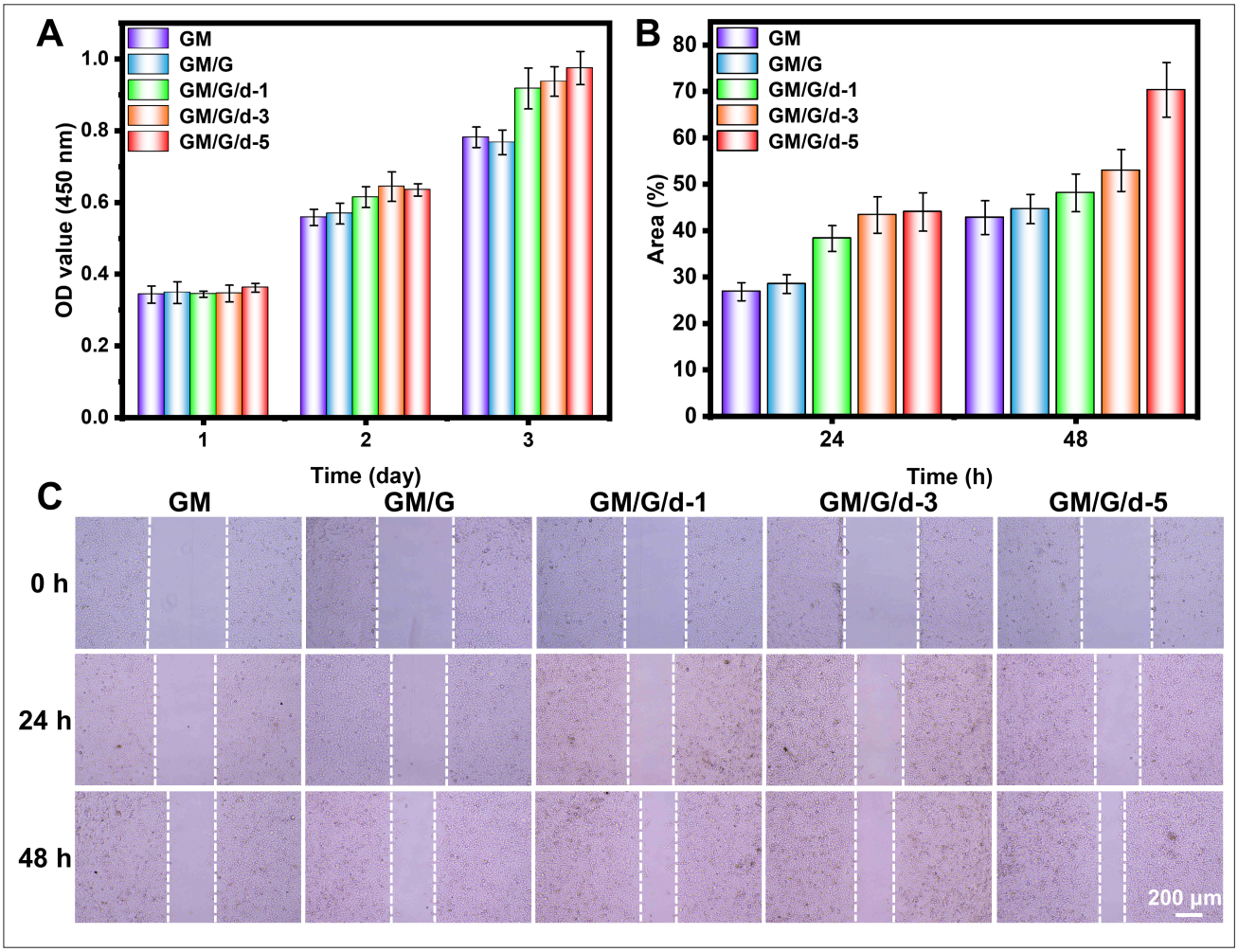

Figure 4. *In vitro* three-dimensional tumor model construction. (A) Cell viability of five different hydrogels encapsulated human hepatocellular carcinoma (HepG2) cells ($n = 3$). (B) Quantification of the migration area ($n = 3$). (C) Cell migration of HepG2 cells in different hydrogel precursor solutions. Scale bar = 200 μm; magnification = 20×. Notes: GM: 10% (w/v) gelatin methacrylate (GelMA); GM/G: 10% (w/v) GelMA and 5% (w/v) gelatin; GM/G/d-1, GM/G/d-3, and GM/G/d-5: GM/G combined with decellularized extracellular matrix at concentrations of 1%, 3%, and 5% (w/v), respectively. Abbreviation: OD, optical density.

develop into microspheres or tissues *in vitro*. As depicted in Figure 5B, under 2D culture conditions, HepG2 cells exhibited proliferation rates of 5.17, 8.77, and 10.17 times on days 4, 6, and 8, respectively, compared to day 2. In contrast, under 3D-dECM culture conditions, HepG2 cells displayed proliferation rates of 5.96, 10.44, and 15.44 times on days 4, 6, and 8, compared to day 2. Under 3D control culture conditions, the corresponding rates were 5.14, 8.99, and 13.78 times. A significant difference in cell proliferation activity was observed on day 4, with a highly significant difference by day 8, indicating enhanced cell proliferation under 3D culture conditions. While cell proliferation in 2D culture was inhibited upon covering the entire surface of the culture plate, the 3D culture provided an additional dimension for cell growth, allowing continuous proliferation. The addition of dECM provided cells with ECM components which could significantly enhance the metabolic activity of cells. Furthermore, the levels of cell protein secretion increased with cultivation time under both 2D and 3D cultures, as demonstrated in Figure 5C. Under 2D culture, protein expression levels were 1.51, 2.37, and 3.58 times higher on days 4, 6, and 8, respectively, compared to day 2. Under 3D culture, protein expression levels were 1.89, 3.34, and 4.75 times higher on days 4, 6, and 8, respectively, compared to day 2. Significant differences in protein secretion levels between 2D and 3D cultures were observed on days 2 and 4, and by day 8, the disparity between the 3D and 2D culture groups became even more pronounced. However, the total protein expression of the 3D control group without dECM was lower than that

of the experimental group, which was consistent with the cell proliferation activity. Together, the data showed that 3D-dECM *in vitro* model had better maintenance of tumor metabolic activity when dECM was supplemented. We propose that the dECM/GelMA bioink-constructed *in vitro* 3D tumor model facilitates cell–ECM interactions and provides adequate space for cellular growth.

3.6. Cellular morphological changes and liver function expression

As depicted in Figure 6A, cells grown under 2D culture conditions exhibited adherent growth to the surface with plump morphology and rapid proliferation. In contrast, under 3D culture conditions, the cells gradually aggregated and formed cell spheres. The addition of 5% dECM during the spheroid formation accelerated cell growth, with numerous aggregates forming on day 4 and larger sphere sizes observed. On day 6 of cultivation, numerous cell spheroids were evident in the 3D-dECM group (marked by red circles), while the 3D control group showed only a few (marked by red arrows). By day 8, both groups exhibited abundant cell spheroids under 3D culture conditions (marked by red circles), with the 3D-dECM group demonstrating greater spheroid size and quantity. By measuring the size of the cell spheroids, it was determined that the average diameters of the 3D control group on days 6 and 8 were 46.64 ± 6.38 and 54.37 ± 9.72 μm, respectively, whereas those of the 3D-dECM group were 67.41 ± 7.3 and 78.83 ± 9.41 μm, respectively (Figure S5, Supporting Information). Under 2D culture conditions, the cells grew as a monolayer without aggregation into cell spheres. Thus, the inclusion of dECM promoted the growth of cell spheres and facilitated the formation of larger cell spheres. These findings align with the results obtained from the co-cultivation of cell materials and scratch experiments discussed in **Section 3.4**, where the presence of 5% dECM demonstrated enhanced interaction with cells, leading to significant improvements in the growth, proliferation, and migration of HepG2 cells.

Liver function markers, such as ALT, AST, ALB, and TBA, were significantly improved in the 3D microenvironment, indicating a positive effect on liver injury and pathological markers of liver cancer cells.[50] The culture supernatants from three groups (2D, 3D control, and 3D-dECM) were analyzed, and the results were normalized to the 2D group to allow comparative evaluation of liver-specific protein expression. Figures 6B–D and S8, Supporting Information illustrate the

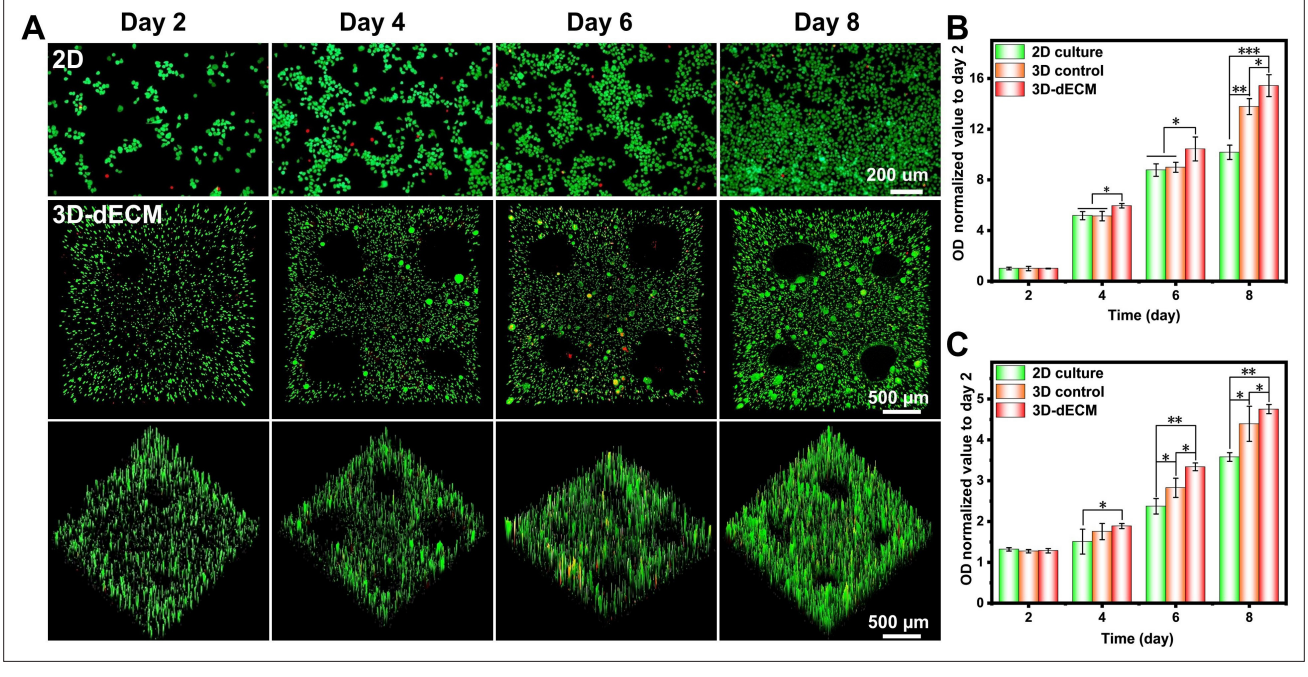

Figure 5. Cell viability and protein expression. (A) Representative live/dead fluorescence images of human hepatocellular carcinoma (HepG2) cells under two-dimensional (2D) and three-dimensional (3D) cultures on days 2, 4, 6, and 8. Scale bars: 200 and 500 μm; magnifications = 20× and 10×. (B) Cell proliferation of HepG2 cells under 2D and 3D culture from day 2 to day 8 ($n = 3$). (C) Total protein of HepG2 cells under 2D and 3D culture from day 2 until day 8 ($n = 3$). The horizontal lines indicate no significant difference between those groups. *$p < 0.05$, **$p < 0.01$, ***$p < 0.001$. Abbreviations: dECM, decellularized extracellular matrix; OD, optical density.

changes in these markers. The expression of pathological markers was higher in the 3D culture group compared to the 2D group. After 8 days of culture, the levels of ALT, AST, and TBA in the 3D-dECM group were 3.26 ± 0.47, 1.73 ± 0.21, and 2.01 ± 0.24 times higher, respectively, compared to the 2D culture conditions. The 3D control group exhibited significantly higher ALB secretion than the 2D group ($p < 0.001$), while the 3D-dECM group showed further enhancement ($p < 0.05$) relative to the 3D control, indicating that the inclusion of liver-derived dECM further promoted hepatic functionality. Moreover, the group treated with added dECM showed higher expression levels of these markers compared to the group without dECM treatment, suggesting that the 3D culture tumor model more closely resembles an *in vivo* solid tumor.

3.7. Chemoresistance

To assess the drug toxicity of PTX and DOX on tumor cells in different culture conditions and drug concentrations, both drugs were introduced to 2D and 3D tumor models, followed by a 24-h incubation period. Figure 7A and B illustrates the distinct effects of drug treatment in 2D and 3D culture environments. In 2D cultures, a substantial

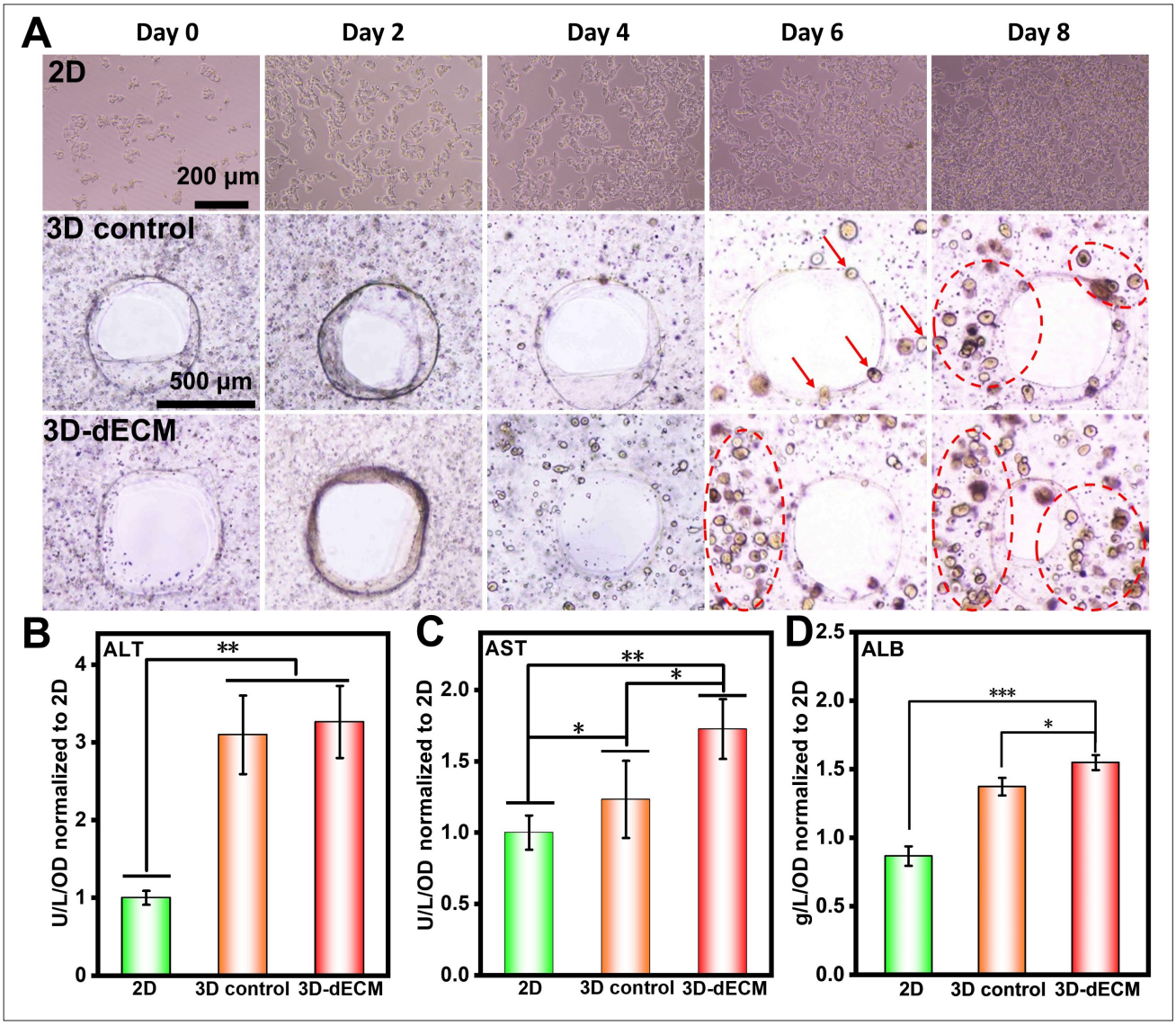

Figure 6. Cellular morphological change and liver function expression. (A) Cell morphology under different culture conditions: two-dimensional (2D) culture, the three-dimensional (3D) control group, and 3D-decellularized extracellular matrix (dECM). Scale bars: 200 and 500 μm; magnifications = 20× and 10×. Liver function indexes: (B) ALT, (C) AST, and (D) ALB ($n = 3$). (The horizontal lines indicate no significant difference between those groups. *$p < 0.05$, **$p < 0.01$). Abbreviations: ALB, albumin; ALT, alanine aminotransferase; AST, aspartate aminotransferase; OD, optical density.

number of cells exhibited red staining, indicating cell death, while only a small fraction remained viable. In contrast, within 3D cultures, limited cell death was observed after 12 h, primarily among cells that had not formed spheroids. By the 24-h mark, most of these non-spheroid cells had succumbed to treatment. However, the spheroids predominantly displayed green staining, with only a few showing red staining. These results highlight the enhanced drug resistance of cell spheroids, which is consistent with findings from previous studies. Cell viability and staining were assessed at 12- and 24-h time points, respectively. As shown in Figure 7C and D, under 2D culture conditions, treatment with DOX resulted in cell survival rates of 36.23% and 18.88% at a drug concentration of 100 μg/mL after 12 and 24 h, respectively. For PTX, the survival rates were 21.04% and 14.04% under the same conditions and time points. In contrast, within the 3D-dECM culture group, the survival rate for cells treated with DOX was 46.23% after 12 h and 31.34% after 24 h, at a drug concentration of 100 μg/mL. Similarly, following treatment with PTX, the survival rate was 41.36% at 12 h and 34.72% at 24 h. These findings suggest that cells exhibited greater drug resistance in 3D culture conditions. This resistance can be attributed to the enhanced survival mechanisms of cell spheroids, which form through cellular aggregation, as well as reduced drug penetration and uptake within the spheroid structure. hrough UV-Vis spectroscopic analysis, it was further revealed that significantly lower doxorubicin uptake was detected in 3D-dECM constructs compared to 2D cultures, indicative of limited drug penetration due to the hydrogel matrix and spheroidal structure (Figure S9). Specifically, it has been reported that 3D culture alone can

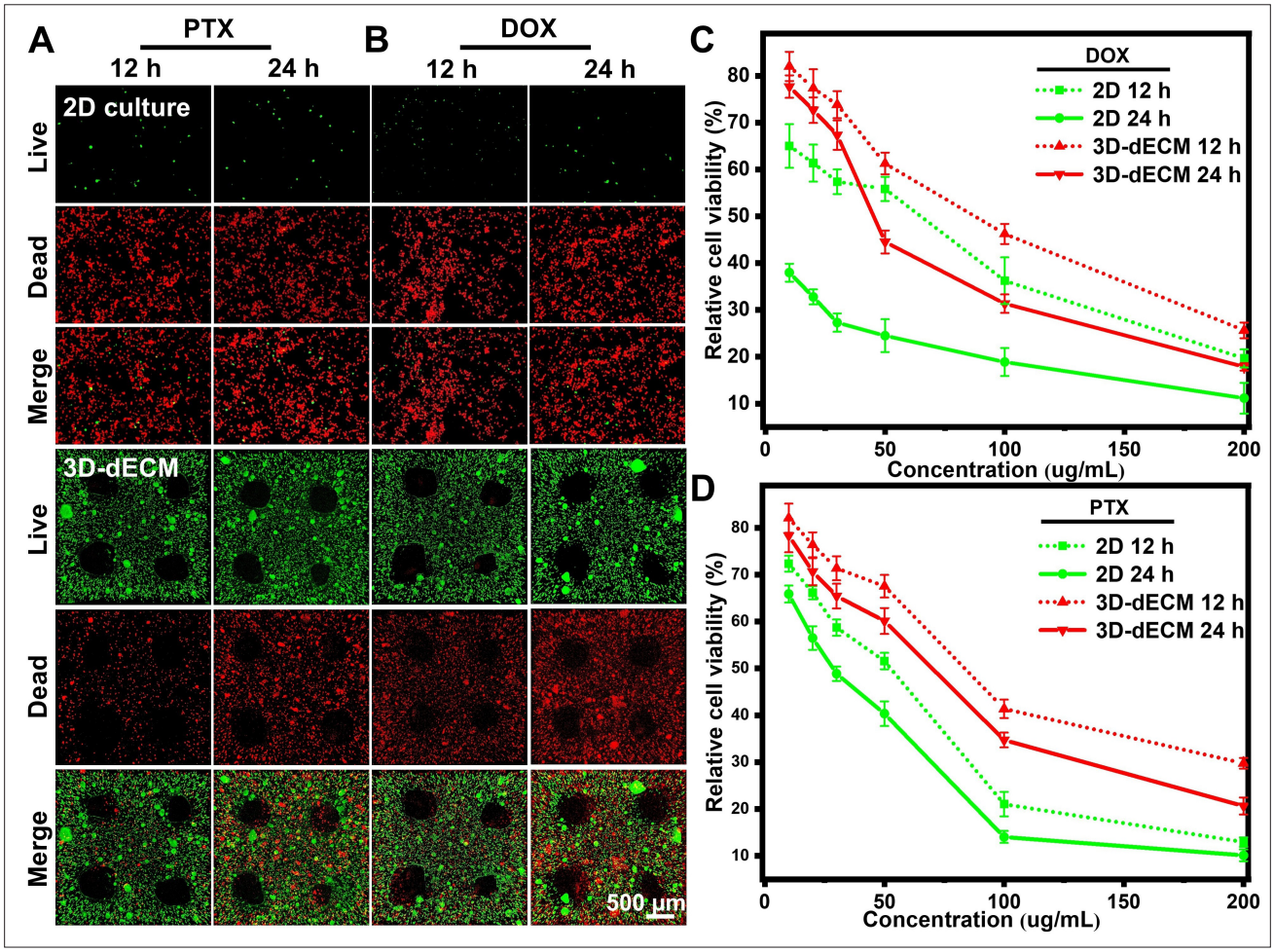

Figure 7. Chemoresistance of human hepatocellular carcinoma (HepG2) cells cultured in three-dimensional (3D)-decellularized extracellular matrix (dECM) constructs compared to two-dimensional (2D) planar culture. Live/dead staining of HepG2 cells in 3D-dECM constructs and 2D culture after (A) PTX and (B) DOX treatment at 12 and 24 h. Scale bar: 500 μm; magnification = 20× and 10×. Relative cell viability after (C) DOX and (D) PTX at 12 and 24 h (n = 3). Abbreviations: DOX, doxorubicin; PTX, paclitaxel.

promote hepatocyte-like phenotypes through improved cell–cell and cell–matrix interactions.[51] Furthermore, the use of maintenance medium[52] and galactosylated substrates that mimic liver-specific glycosylation patterns[53] can further enhance hepatic gene expression, protein secretion, and metabolic functions *in vitro*. These functional enhancements may increase the cellular capacity for drug detoxification, efflux transporter activity, or resistance to apoptosis, thereby contributing to the chemoresistant phenotype observed in 3D tumor models.

4. Conclusion

This study implemented an integrated approach that combines chemical decellularization with enzymatic treatment to optimize the preparation conditions for dECM. Comprehensive assessments of the physicochemical properties and biocompatibility of dECM confirmed its safety and effectiveness. To address the inherent limitations of dECM in printability, composite bioinks consisting of GelMA, gelatin, and dECM were formulated and systematically analyzed. Rheological assessments, structural imaging, and extended shape printing demonstrated that the incorporation of dECM not only enhanced the mechanical integrity and structural fidelity of the bioinks, but also maintained excellent biocompatibility. Furthermore, an *in vitro* 3D liver cancer model was developed using GelMA, gelatin, and dECM, enabling a comprehensive investigation of tumor growth dynamics, metabolic activity, protein secretion, and drug resistance. The findings underscore that 3D printing technology serves as an effective methodology for constructing *in vitro* tumor models, with dECM significantly promoting cell proliferation, migration, and aggregation. Notably, the liver cancer model developed through this innovative approach demonstrated significantly enhanced cell proliferation, protein expression, and drug resistance compared to conventional 2D culture systems. This model not only provides critical insights into tumor biology but also presents a robust platform for the screening of novel targeted therapies, thereby paving the way for advancements in cancer research and treatment.

Acknowledgments

The authors thank the Instrumental Analysis Center of Huaqiao University for their FT-IR, NMR, SEM, and CLSM measurement support.

Funding

This work was supported by the National Natural Science Foundation of China (NSFC, 32271410 and 32071323, and 32301117), the Natural Science Foundation of Fujian Province (No. 2022J01297), the Fundamental Research Funds for the Central Universities (ZQN-1107), and the Science and Technology Projects in Fujian Province (2022FX1 and 2023Y4008).

Conflict of interest

The authors declare that they have no known competing financial interests or personal relationships that could have appeared to influence the work reported in this paper.

Author contributions

Conceptualization: Chunyang Zhang, Chaoping Fu
Formal analysis: Chunyang Zhang, Chaoping Fu
Funding acquisition: Shibin Wang, Aizheng Chen, Chaoping Fu
Investigation: Chunyang Zhang, Yunze Xu, Xiaochang Lu
Methodology: Chunyang Zhang, Yunze Xu, Hongwei Yu
Project administration: Shibin Wang, Aizheng Chen, Chaoping Fu
Supervision: Chaoping Fu
Visualization: Chunyang Zhang, Ying Fang, Hongwei Yu
Writing–original draft: Chunyang Zhang
Writing–review & editing: Changyong Li, Weihong Ji, Chaoping Fu

Ethics approval and consent to participate

Not applicable.

Consent for publication

Not applicable.

Availability of data

Additional data and materials not included in the manuscript or supplementary materials are available from the corresponding authors upon reasonable request.

References

1. De Santibañes M, Pekolj J, Sanchez Claria R, De Santibañes E, Mazza OM. Technical implications for surgical resection in locally advanced pancreatic cancer. *Cancers*. 2023;15(5):1509.
doi: 10.3390/cancers15051509

2. Zaher A, Foromera J, Capanu M, Chou J, Faleck DM. Sa1848 extent of surgical resection for ibd-associated neoplasia and colorectal cancer outcomes. *Gastroenterology*. 2024;166(5):S-549-S-550.
doi: 10.1016/S0016-5085(24)01733-5

3. Yu X, Wang X, Sun L, Yamazaki A, Li X. Tumor microenvironment regulation - enhanced radio - immunotherapy. *Biomater Adv*. 2022;138:212867.
doi: 10.1016/j.bioadv.2022.212867

4. Pan S, Sun Z, Zhao B, et al. Therapeutic application of manganese-based nanosystems in cancer radiotherapy. *Biomaterials*. 2023;302:122321. doi: 10.1016/j.biomaterials.2023.122321

5. Moy B, Rumble RB, Carey LA, for the Chemotherapy and Targeted Therapy for Endocrine-Pretreated or Hormone Receptor–Negative Metastatic Breast Cancer Expert Panel. Chemotherapy and targeted therapy for endocrine-pretreated or hormone receptor–negative metastatic breast cancer: ASCO guideline rapid recommendation update. *JCO*. 2023;41(6):1318-1320. doi: 10.1200/JCO.22.02807

6. Garg V, Kumar L. Metronomic chemotherapy in ovarian cancer. *Cancer Lett*. 2023;579:216469. doi: 10.1016/j.canlet.2023.216469

7. Michalczyk K, Pawlik J, Czekawy I, Kozłowski M, Cymbaluk-Płoska A. Complementary methods in cancer treatment—cure or curse? *IJERPH*. 2021;18(1):356. doi: 10.3390/ijerph18010356

8. Li Y, Xu X. Nanomedicine solutions to intricate physiological-pathological barriers and molecular mechanisms of tumor multidrug resistance. *J Control Release*. 2020;323:483-501. doi: 10.1016/j.jconrel.2020.05.007

9. Mao S, He J, Zhao Y, et al. Bioprinting of patient-derived *in vitro* intrahepatic cholangiocarcinoma tumor model: establishment, evaluation and anti-cancer drug testing. *Biofabrication*. 2020;12(4):045014. doi: 10.1088/1758-5090/aba0c3

10. Xu X, Liu Y, Liu Y, et al. Functional hydrogels for hepatocellular carcinoma: Therapy, imaging, and in vitro model. *J Nanobiotechnol*. 2024;22(1):381. doi: 10.1186/s12951-024-02547-9

11. Li W, Hu X, Yang S, et al. A novel tissue-engineered 3D tumor model for anti-cancer drug discovery. *Biofabrication*. 2018;11(1):015004. doi: 10.1088/1758-5090/aae270

12. Vitale S, Calapà F, Colonna F, et al. Advancements in 3D in vitro models for colorectal cancer. *Adv Sci*. 2024;11(32):2405084. doi: 10.1002/advs.202405084

13. Lv J, Du X, Wang M, Su J, Wei Y, Xu C. Construction of tumor organoids and their application to cancer research and therapy. *Theranostics*. 2024;14(3):1101-1125. doi: 10.7150/thno.91362

14. Van Tienderen GS, Conboy J, Muntz I, et al. Tumor decellularization reveals proteomic and mechanical characteristics of the extracellular matrix of primary liver cancer. *Biomater Adv*. 2023;146:213289. doi: 10.1016/j.bioadv.2023.213289

15. Krujatz F, Dani S, Windisch J, et al. Think outside the box: 3D bioprinting concepts for biotechnological applications – recent developments and future perspectives. *Biotechnol Adv*. 2022;58:107930. doi: 10.1016/j.biotechadv.2022.107930

16. Levato R, Dudaryeva O, Garciamendez-Mijares CE, et al. Light-based vat-polymerization bioprinting. *Nat Rev Methods Primers*. 2023;3(1):47. doi: 10.1038/s43586-023-00231-0

17. Kumar S, Tharayil A, Thomas S. 3D bioprinting of nature-inspired hydrogel inks based on synthetic polymers. *ACS Appl Polym Mater*. 2021;3(8):3685-3701. doi: 10.1021/acsapm.1c00567

18. Yang K, Wang L, Vijayavenkataraman S, Yuan Y, Tan ECK, Kang L. Recent applications of three-dimensional bioprinting in drug discovery and development. *Adv Drug Deliv Rev*. 2024;214:115456. doi: 10.1016/j.addr.2024.115456

19. Bian S, Hu X, Zhu H, et al. 3D bioprinting of artificial skin substitute with improved mechanical property and regulated cell behavior through integrating patterned nanofibrous films. *ACS Nano*. 2024;18(28):18503-18521. doi: 10.1021/acsnano.4c04088

20. Kronemberger GS, Spagnuolo FD, Karam AS, Chattahy K, Storey KJ, Kelly DJ. Rapidly degrading hydrogels to support biofabrication and 3D bioprinting using cartilage microtissues. *ACS Biomater Sci Eng*. 2024;10(10):6441-6450. doi: 10.1021/acsbiomaterials.4c00819

21. Pérez Del Río E, Rey-Vinolas S, Santos F, et al. 3D printing as a strategy to scale-up biohybrid hydrogels for T cell manufacture. *ACS Appl Mater Interfaces*. 2024;16(38):50139-50146. doi: 10.1021/acsami.4c06183

22. Pramanick A, Hayes T, Sergis V, McEvoy E, Pandit A, Daly AC. 4D bioprinting shape-morphing tissues in granular support hydrogels: Sculpting structure and guiding maturation. *Adv Funct Mater*. 2025;35(5):2414559. doi: 10.1002/adfm.202414559

23. Patel ZH, Charania AA, Punjani Z, et al. Evaluating anticancer agents on 3D bioprinted organoid tumors (BOT) to reduce cost and accelerate therapeutic discovery. *JCO*. 2022;40(16_suppl):e13500. doi: 10.1200/JCO.2022.40.16_suppl.e13500

24. Kankala RK, Zhang YS, Kang L, Ambrosio L. Editorial: Polymeric microarchitectures for tissue regeneration and drug screening. *Front Bioeng Biotechnol*. 2023;11:1144991. doi: 10.3389/fbioe.2023.1144991

25. Wang Y, Jeon H. 3D cell cultures toward quantitative high-throughput drug screening. *Trends Pharmacol Sci*. 2022;43(7):569-581. doi: 10.1016/j.tips.2022.03.014

26. González-Callejo P, García-Astrain C, Herrero-Ruiz A, et al. 3D bioprinted tumor-stroma models of triple-negative breast cancer stem cells for preclinical targeted therapy evaluation. *ACS Appl Mater Interfaces*. 2024;16(21):27151-27163. doi: 10.1021/acsami.4c04135

27. Ferreira LP, Gaspar VM, Mano JF. Decellularized extracellular matrix for bioengineering physiomimetic 3D in vitro tumor models. *Trends Biotechnol*. 2020;38(12):1397-1414. doi: 10.1016/j.tibtech.2020.04.006

28. García-Astrain C, Henriksen-Lacey M, Lenzi E, et al. A scaffold-assisted 3D cancer cell model for surface-enhanced Raman scattering-based real-time sensing and imaging. *ACS Nano*. 2024;18(17):11257-11269. doi: 10.1021/acsnano.4c00543

29. Ebrahimighaei R, Tarassova N, Bond SC, et al. Extracellular matrix stiffness controls cardiac fibroblast proliferation via the nuclear factor-Y (NF-Y) transcription factor. *Biochim Biophys Acta Mol Cell Res*. 2024;1871(2):119640. doi: 10.1016/j.bbamcr.2023.119640

30. Fu Y, Zhou Y, Wang K, Li Z, Kong W. Extracellular matrix interactome in modulating vascular homeostasis and remodeling. *Circ Res*. 2024;134(7):931-949. doi: 10.1161/CIRCRESAHA.123.324055

31. Guo WY, Wang WH, Xu PY, Kankala RK. Decellularised extracellular matrix-based injectable hydrogels for tissue engineering applications. *Biomater Transl*. 2024;5(2):114-128. doi: 10.12336/biomatertransl.2024.02.003

32. Naba A. Mechanisms of assembly and remodelling of the extracellular matrix. *Nat Rev Mol Cell Biol*. 2024;25(11):865-885. doi: 10.1038/s41580-024-00767-3

33. Zhou Z, Zhang Y, Zeng Y, et al. Effects of nanomaterials on synthesis and degradation of the extracellular matrix. *ACS Nano*. 2024;18(11):7688-7710. doi: 10.1021/acsnano.3c09954

34. Bhar B, Ranta P, Samudrala PK, Mandal BB. Omentum extracellular matrix-silk fibroin hydroscaffold promotes wound healing through vascularization and tissue remodeling in the diabetic rat model. *ACS Biomater Sci Eng*. 2024;10(2):1090-1105. doi: 10.1021/acsbiomaterials.3c01877

35. Tam NW, Becker A, Mangiarotti A, Cipitria A, Dimova R. Extracellular vesicle mobility in collagen I hydrogels is influenced by matrix-binding integrins. *ACS Nano*. 2024;18(43):29585-29601. doi: 10.1021/acsnano.4c07186

36. Puistola P, Kethiri A, Nurminen A, et al. Cornea-specific human adipose stem cell-derived extracellular matrix for corneal stroma tissue engineering. *ACS Appl Mater Interfaces*. 2024;16(13):15761-15772. doi: 10.1021/acsami.3c17803

37. Na J, Yang Z, Shi Q, et al. Extracellular matrix stiffness as an energy metabolism regulator drives osteogenic differentiation in mesenchymal stem cells. *Bioact Mater*. 2024;35:549-563. doi: 10.1016/j.bioactmat.2024.02.003

38. Tao M, Ao T, Mao X, et al. Sterilization and disinfection methods for decellularized matrix materials: review, consideration and proposal. *Bioact Mater*. 2021;6(9):2927-2945. doi: 10.1016/j.bioactmat.2021.02.010

39. Snyder Y, Jana S. Strategies for development of decellularized heart valve scaffolds for tissue engineering. *Biomaterials*. 2022;288:121675. doi: 10.1016/j.biomaterials.2022.121675

40. Lian L, Xie M, Luo Z, et al. Rapid volumetric bioprinting of decellularized extracellular matrix bioinks. *Adv Mater*. 2024;36(34):2304846. doi: 10.1002/adma.202304846

41. Niu R, Xin Q, Xu E, Yao S, Chen M, Liu D. Nanostarch-stimulated cell adhesion in 3D bioprinted hydrogel scaffolds for cell cultured meat. *ACS Appl Mater Interfaces*. 2024;16(18):23015-23026. doi: 10.1021/acsami.4c03585

42. Bae M, Kim JJ, Kim J, Cho DW. Decellularized extracellular matrix for three- dimensional bioprinted in vitro disease modeling. *Int J Bioprint*. 2024;10(2):1970. doi: 10.36922/ijb.1970

43. Shin M, Galarraga JH, Kwon MY, Lee H, Burdick JA. Gallol-derived ECM-mimetic adhesive bioinks exhibiting temporal shear-thinning and stabilization behavior. *Acta Biomater*. 2019;95:165-175. doi: 10.1016/j.actbio.2018.10.028

44. Ouyang L, Yao R, Zhao Y, Sun W. Effect of bioink properties on printability and cell viability for 3D bioplotting of embryonic stem cells. *Biofabrication*. 2016;8(3):035020. doi: 10.1088/1758-5090/8/3/035020

45. Brumberg VA, Bikmulina PY, Pozdnyakov AA, et al. Scaling liver bioprinting: a guide for usage of the hepatic extracellular matrix as a bioink. *Int J Bioprint*. 2025;11(1):57-83. doi: 10.36922/ijb.4343

46. Ouyang L, Yao R, Zhao Y, Sun W. Effect of bioink properties on printability and cell viability for 3D bioplotting of embryonic stem cells. *Biofabrication*. 2016;8(3):035020. doi: 10.1088/1758-5090/8/3/035020

47. Choudhury D, Tun HW, Wang T, Naing MW. Organ-derived decellularized extracellular matrix: a game changer for bioink manufacturing? *Trends Biotechnol*. 2018;36(8):787-805. doi: 10.1016/j.tibtech.2018.03.003

48. Xu P, Kankala RK, Wang S, Chen A. Decellularized extracellular matrix-based composite scaffolds for tissue engineering and regenerative medicine. *Regen Biomater*. 2023;11:rbad107. doi: 10.1093/rb/rbad107

49. Khati V, Ramachandraiah H, Pati F, Svahn HA, Gaudenzi G, Russom A. 3D bioprinting of multi-material decellularized liver matrix hydrogel at physiological temperatures. *Biosensors*. 2022;12(7):521. doi: 10.3390/bios12070521

50. Myojin Y, Hikita H, Sugiyama M, et al. Hepatic stellate cells in hepatocellular carcinoma promote tumor growth via growth differentiation factor 15 production. *Gastroenterology*. 2021;160(5):1741-1754.e16.
doi: 10.1053/j.gastro.2020.12.015

50. Wang Y, Kankala RK, Zhang J, et al. Modeling endothelialized hepatic tumor microtissues for drug screening. *Adv Sci*. 2020;7(21):2002002.
doi: 10.1002/advs.202002002

52. Baharvand H, Hashemi SM, Kazemi Ashtiani S, Farrokhi A. Differentiation of human embryonic stem cells into hepatocytes in 2D and 3D culture systems in vitro. *Int J Dev Biol*. 2006;50(7):645-652.
doi: 10.1387/ijdb.052072hb

53. Krueger WH, Tanasijevic B, Barber V, et al. Cholesterol-secreting and statin-responsive hepatocytes from human ES and iPS cells to model hepatic involvement in cardiovascular health. *PLoS ONE*. 2013;8(7):e67296.
doi: 10.1371/journal.pone.0067296

54. Gevaert E, Billiet T, Declercq H, Dubruel P, Cornelissen R. Galactose-functionalized gelatin hydrogels improve the functionality of encapsulated Hepg2 cells. *Macromol Biosci*. 2014;14(3):419-427.
doi: 10.1002/mabi.201300320

ACCSCIENCE PUBLISHING

International Journal of Bioprinting

RESEARCH ARTICLE

Investigation of humidity-driven swelling–shrinking behavior of filaments in material extrusion of medical-grade biodegradable hydrogel

Kaicheng Yu[1,2†], Yifeng Yao[1,2†], Qiang Gao[1,2*], Le Xu[1,2], Wei Zhang[3], Min Zhu[4], Peng Zhang[1,2], Swee Leong Sing[5*], and Lihua Lu[1,2*]

[1]School of Mechatronics Engineering, Harbin Institute of Technology, Harbin, Heilongjiang, China

[2]Chongqing Research Institute of HIT, Chongqing, China

[3]Key Laboratory of Data Analytics and Optimization for Smart Industry, Northeastern University, Shenyang, Liaoning, China

[4]School of Electrical Engineering and Automation, Harbin Institute of Technology, Harbin, Heilongjiang, China

[5]Department of Mechanical Engineering, College of Design and Engineering, National University of Singapore, Singapore

(This article belongs to *the Special Issue: Advances in 3D Bioprinting*)

†These authors contributed equally to this work.

***Corresponding authors:**
Qiang Gao (gaoq@hit.edu.cn)

Swee Leong Sing (sweeleong.sing@nus.edu.sg)

Lihua Lu (lihual@hit.edu.cn)

Citation: Yu K, Yao Y, Gao Q, *et al*. Investigation of humidity-driven swelling–shrinking behavior of filaments in material extrusion of medical-grade biodegradable hydrogel. *Int J Bioprint*. 2025;11(4):409-425. doi: 10.36922/IJB025220222

Received: May 27, 2025
Revised: June 18, 2025
Accepted: June 29, 2025
Published online: June 30, 2025

Copyright: © 2025 Author(s). This is an Open Access article distributed under the terms of the Creative Commons Attribution License, permitting distribution, and reproduction in any medium, provided the original work is properly cited.

Publisher's Note: AccScience Publishing remains neutral with regard to jurisdictional claims in published maps and institutional affiliations.

Abstract

Material extrusion using medical-grade biodegradable hydrogel demonstrates significant potential for manufacturing biocompatible scaffolds in regenerative medicine. However, unpredictable geometric variations in the fabricated models, such as swelling or shrinking, impede the development of complex three-dimensional (3D) hydrogel architectures for *in vitro*-functionalized tissues and organs. A primary cause of structural deformation, such as wrinkling or even collapse, is improper humidity control during the 3D printing process. Therefore, there is a need to investigate the swelling–shrinking behavior of hydrogels under varying ambient humidity and to determine optimal humidity levels for the printing process. This study established a thermal–humidity–multiphase flow coupling field simulation model to numerically investigate the humidity-driven swelling–shrinking behavior of hydrogel filaments. The optimal 3D printing humidity levels were determined for hydrogel filaments with diameters of 0.2, 0.3, and 0.4 mm, which were found to be 90, 80, and 60%, respectively. Using these humidity settings, several structures were fabricated, demonstrating moderated moisture loss of 3D architecture. Notably, a human ear model was successfully printed, achieving an effective size of 20 mm (length) × 10 mm (width) × 10 mm (height). Our research can benefit the future development in tissue engineering and regenerative medicine.

Keywords: 3D printing; Coupling field simulation; Humidity control; Medical hydrogel

1. Introduction

Recently, three-dimensional (3D) printing has emerged as a promising technique in tissue engineering and regenerative medicine,[1,2] driving significant advancements in the fabrication of *in vitro*-functionalized tissues and organs.[3,4] Through this additive manufacturing technology, biomimetic 3D architectures with complex geometric structures can be created using a variety of biocompatible materials.[5,6]

Material extrusion,[7,8] material jetting,[9,10] and vat photopolymerization[11,12] are three well-established 3D printing technologies for fabricating human-scale organs and physiologically relevant disease models. Of these, material extrusion has garnered increasing attention due to its cost-effectiveness and ease of operation.[13,14] The 3D printing process is typically actuated by mechanical force or pneumatic pressure, and the materials are extruded from a fine nozzle. Well-arranged filaments are then deposited on a two-axis substrate along a predefined trajectory.[15,16] Subsequently, a 3D biomimetic architecture is constructed through layer-by-layer deposition.

Currently, medical-grade biodegradable hydrogels have become well-acclaimed bio-inks adopted in material extrusion.[17] These hydrogels closely mimic the biochemical and physical properties of the native extracellular matrix, offering advantages for regenerative medical applications,[18] such as excellent biocompatibility, prominent drug-encapsulating capability, and negligible cytotoxicity.[19] This makes hydrogel materials highly promising candidates for developing tissue engineering scaffolds as delivery vehicles for biologically active substances or cells.[20]

However, as hydrogels are water-insoluble 3D polymeric networks that retain large volumes of fluid, they demonstrate pronounced humidity-driven swelling–shrinking behavior.[21] A wealth of biodegradable hydrogels, such as Pluronic F-127 (F-127), poly(ethylene glycol) diacrylate (PEG-DA), and polyvinyl alcohol (PVA), demonstrate uncontrollable swelling–shrinking behavior when the ambient humidity is unstable. This high susceptibility to the ambient humidity variation often leads to unpredictable geometric sizes in 3D bioprinted structures, which may alter their physical properties. Therefore, humidity control has emerged as a significant parameter in hydrogel-based 3D printing. For example, Chang et al.[22] fabricated a multicomponent 3D structure of micro-vessel fragments using F-127 with a material extrusion device and highlighted humidity as a significant parameter in ensuring the precise deposition of hydrogel and maintaining the structural fidelity of printed architectures. Similarly, Lv et al.[23] created a 3D-printed architecture with stomata-like microstructures using PEG-DA hydrogel, where regulated humidity induced geometric variations that enabled the opening and closing functions of rhombus-shaped stomata. Dai et al.[24] prepared a humidity-driven, dynamically colorful display platform via material extrusion of PVA hydrogel. The platform's optical properties could be modulated by the humidity-driven swelling behavior of the hydrogel, enabling a controllable color of the 3D-printed platform. Additionally, Sun et al.[25] developed a 3D-printed, flexible humidity sensor with a composite of carbon nanotubes, polyaniline, and gelatin. In this system, changes in humidity induced deformation of the gelatin hydrogel, resulting in detectable variation in the electrical resistance of the composite material.

Although there is a broad consensus that humidity plays a crucial role in 3D-printed hydrogel architectures, identifying optimal humidity conditions for hydrogel 3D printing remains challenging. During the extrusion process, continuous hydrogel filaments are deposited onto a plate and remain exposed to ambient air until the 3D structure is fabricated. As water constitutes the majority of hydrogel volume, any variation in moisture content directly impacts the geometry of the 3D-printed filaments.[26]

When 3D printing occurs under inappropriate ambient humidity, the concentration of water in the ambient air is remarkably lower than that within the hydrogel filaments. This disparity causes moisture to evaporate from the surface of filaments, as water diffuses outward and transforms into vapor. The resulting moisture loss leads to filament shrinkage. In contrast, if the ambient humidity is excessively high, moisture from the ambient air may diffuse back into the hydrogel, increasing its water content and causing filament swelling.[27] Such humidity-driven geometric variations often cause deviations from the predefined 3D-printed filaments. These cumulative errors during layer-by-layer deposition can lead to wrinkling or even collapse of the fabricated architecture, ultimately rendering it unsuitable for medical applications.

These challenges hinder the reliable fabrication of biomimetic hydrogel architectures, thereby making the manufacture of functional human-scale tissue or organs impractical.[28] To address these problems, efforts have been made in recent research. For example, Search et al.[29] developed a humidity-controlled chamber capable of maintaining constant humidity levels from 25 to 80%, enabling more stable hydrogel 3D printing conditions. Matamoros et al.[30] prepared an atmospheric chamber to accommodate a self-designed 3D printing device, in which humidity was precisely controlled to maintain the geometry of the 3D-printed architectures. Likewise, Yu et al.[31] proposed a humidity-controlled enclosure for regulating ambient humidity distribution during

hydrogel 3D printing, maintaining levels above 70% to prevent the shrinkage and collapse of the 3D-printed hydrogel structures.

Although prior studies have attempted to regulate ambient humidity during hydrogel 3D printing, most efforts—including the work by Yu et al.[31]—have primarily focused on the external environmental control of the printing space. Specifically, they proposed a humidity-controlled atmospheric enclosure and developed a fluid–thermal–humidity coupled finite element method (FEM) model to simulate the spatial distribution of humidity within the printing chamber. This strategy successfully improved macro-scale environmental stability and reduced the likelihood of structure collapse caused by low humidity. However, their approach only addresses the ambient airfield and does not account for the behavior of individual hydrogel filaments under humidity fluctuations at the material level. In particular, the internal diffusion of water within hydrogel filaments, the associated volumetric deformation, and the interface-driven geometric evolution remain unmodeled. Consequently, their framework is incapable of predicting localized distortion, interlayer error accumulation, or structure failure due to filament-scale swelling and shrinkage.

However, the omission of humidity-driven swelling–shrinking behavior of 3D-printed hydrogel filaments in prior studies has critically limited the advancement of hydrogel-based 3D printing and hindered progress toward reliable biomanufacturing. During the hydrogel printing process, local humidity exerts a significant impact on the geometric variation of fabricated hydrogel models. To preserve the shape of 3D-printed hydrogel constructs, the ambient humidity must be precisely regulated to an optimal level.

Existing research generally focuses on the invention of novel humidity-controlled devices[29–31] to precisely regulate the ambient humidity of 3D-printed structures. However, these studies typically rely on the trial-and-error method to identify optimal humidity levels, a method that is time-consuming, lacks reliability, and suffers from poor repeatability. Such limitations fall short of meeting the requirements for manufacturing biomimetic 3D architectures.

The 3D printing of biomimetic scaffolds aims to produce a range of complex 3D architectures that accurately replicate the natural structure of human tissues and organs.[32] Given the tremendous difference in the sizes of various tissues and organs, hydrogel filaments of varying diameters are often required during the printing process. For example, 3D architectures with larger volumes usually consist of thicker filaments to provide a better load-bearing property,[33] while thinner filaments are generally adopted for smaller constructs to achieve a higher resolution.[34] In such complex circumstances, identifying an optimal humidity level for hydrogel 3D printing becomes increasingly challenging. Therefore, there is an urgent need to investigate the humidity-driven swelling–shrinking behavior of 3D-printed hydrogel filaments.

In this study, the influence of ambient humidity during the 3D printing process on the swelling–shrinking behavior of 3D-printed hydrogel filaments was investigated through numerical simulations and experimental validation. A two-phase flow simulation model, coupled with heat transfer and water vapor transport, was developed based on FEM. The geometric variation of hydrogel filaments with various diameters under varying humidity conditions was estimated, and the optimal humidity levels for hydrogel 3D printing were identified. Subsequently, a series of 3D printing trials was conducted using hydrogel materials with and without the optimal ambient humidity. The results demonstrated that the shrinkage of filaments and the collapse of fabricated 3D architectures were effectively prevented by maintaining the humidity at an optimal level.

2. Materials and methods

This study proposed a 2D thermal–humidity–multiphase flow coupling field simulation model for humidity-driven swelling–shrinking behavior of hydrogel filaments.

In the 3D printing of hydrogel structures, well-arranged filaments were smoothly deposited. The local humidity within the printing space plays a significant role in influencing the geometric variation of these hydrogel filaments. To accurately regulate the humidity field within the printing space, a novel configuration of an extrusion-based 3D printer (SIA bioprinter PRO, Shenyang Institute of Automation, China) was employed, as demonstrated in Figure 1. The feasibility and reliability of this setup were validated in previous research.[31] The 3D printing device comprises a temperature-controlled horizontal plate and a humidity-controlled atmospheric enclosure. During the printing process, the print head operates within this enclosure, allowing the humidity in the printing space to be precisely maintained at a constant value.

2.1. Finite element method modeling for the printed filament

To estimate the humidity-driven swelling–shrinking behavior of printed filaments, a two-phase flow simulation model coupled with heat transfer and water vapor transport was developed using COMSOL Multiphysics 6.2 (COMSOL, USA). Mechanical components not directly interacting with the printed filament, such as the

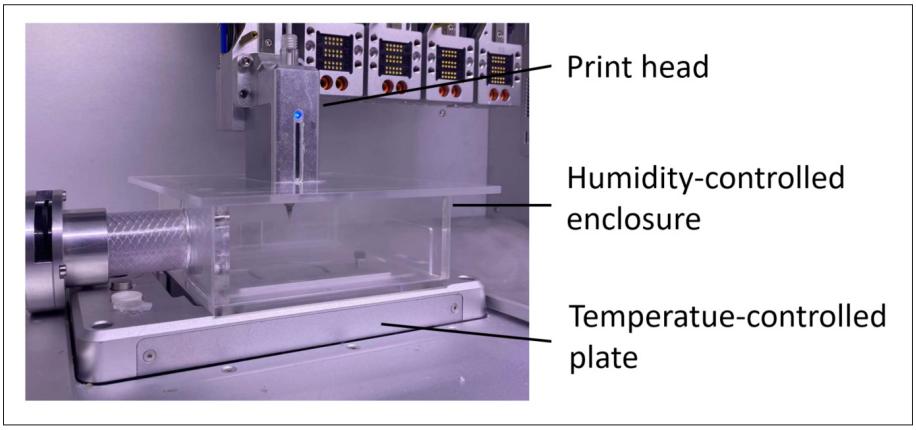

Figure 1. A high-precision 3D printing device with controllable humidity in the printing space.

humidity-controlled enclosure and the 3D print head, were excluded from the analysis. During the material extrusion process, continuous filaments with uniform diameters were extruded from a circular nozzle. Due to gravitational effects, a compressive deformation occurred at the bottom of each filament upon deposition on the horizontal plate, resulting in a cross-sectional profile that was approximately semi-circular in shape.

To better visualize the physical configuration of the printing system, a 3D schematic model of the setup was constructed and rendered to produce the schematic shown in Figure 2. This schematic illustrates the dimensional simplification process from the full 3D printing environment to the 2D FEM model and visualizes the boundary conditions and computational mesh used for simulation. To analyze the geometric variation of the deposited filament, the developed FEM model was based on a semi-circular filament cross-section with variable diameter (d). To ensure the accuracy of the calculation, the ambient air domain near the filament was also incorporated, as it forms an essential part of the entire printing space. Since the filament cross-section and the ambient air domain showed a mirror symmetry, only half of the geometry was modeled in 2D, with a symmetry boundary condition applied to improve modeling efficiency. Geometrical features, such as shallow grooves and chamfers, were omitted to further improve the calculation efficiency. The final computational mesh, auto-generated by COMSOL, comprised 14,090 domain elements.

To estimate the swelling–shrinking behavior of hydrogel filaments, a moving mesh was employed in the FEM model to represent both the computational mesh of the printed filament and the ambient air domain within a two-phase flow framework. Given that the majority of the hydrogel's volume consisted of liquid, the printed filament was modeled as the first liquid phase. The adjacent ambient air domain, composed of moist air, was defined as the other liquid phase. The interface between the hydrogel filament and the ambient air was treated as a fluid–fluid boundary, while the outer boundary of the air domain was regarded as an outlet boundary.

The printing platform used in this study was equipped with a high-precision temperature control system (±1°C), enabling stable thermal conditions at the filament–substrate interface. Consequently, the top surface of the plate was considered a cold source. The material parameters of the hydrogel (e.g., diffusion coefficient, viscosity, and thermal conductivity), although known to be temperature-dependent, were treated as constant values corresponding to room temperature, based on steady-state data from the literature. For the filament material, a well-acclaimed medical hydrogel material, F-127, was adopted in the FEM model. The simulation parameters are summarized in Table 1. To investigate the swelling–shrinking behavior of filaments under varying humidity conditions, a series

Table 1. Selected simulation parameters

Component	Material	Thermal conductivity (W/m/K)	Dynamic viscosity (Pa·s)	Thermal capacity (J/kg/K)	Density (kg/m^3)
Ambient air	Air	0.0267	17.90×10^{-6}	1005	1.225
Printed filament	F-127	0.250	1.00×10^{-1}	4200	1095
Plate	Polymethyl methacrylate	0.192	–	1465	1180

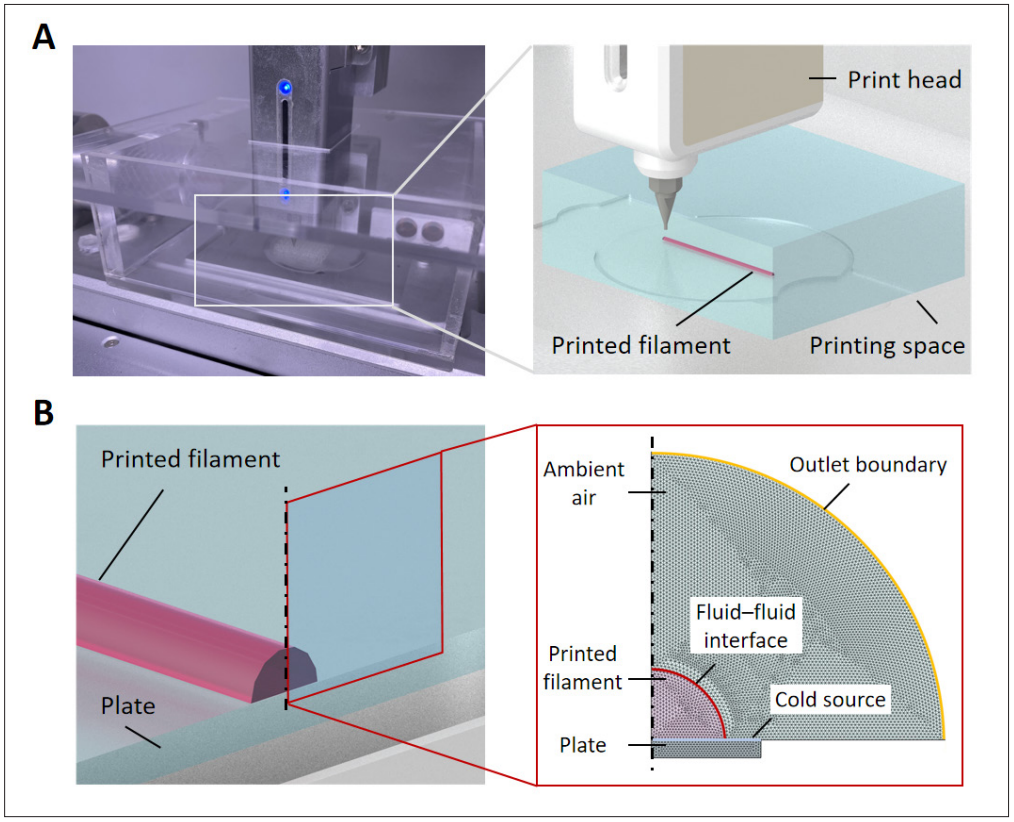

Figure 2. Finite element method modeling for investigating the humidity-driven swelling–shrinking behavior of hydrogel filaments. (A) Schematic diagram showing the extrusion process of a hydrogel filament. (B) Simplified model and computational mesh of the printed filament.

of analyses were conducted across various diameters and relative humidity (RH) values.

2.2. The boundary conditions of the finite element method modeling

2.2.1. Two-phase flow modeling of the printed filament

To simulate the swelling–shrinking behavior of hydrogel filaments under varying ambient RH conditions, the two-phase flow method was employed in the FEM model. A phase field method is suitable for modeling two immiscible fluids with stable interfaces. It enables a sharp transition between the two fluid phases, resulting in a high-resolution representation of the fluid–fluid interface. The dynamics of two-phase flow is governed by a widely adopted Cahn–Hilliard theory[35]:

$$\frac{\partial \phi}{\partial t} + u \cdot \nabla \phi = \nabla \cdot \frac{\gamma \lambda}{\omega^2} \nabla \Psi \quad \text{(I)}$$

$$\Psi = -\nabla \cdot \omega^2 \nabla \phi + (\phi^2 - 1)\phi \quad \text{(II)}$$

where ϕ is the dimensionless phase field variable, which takes a value of 1 or −1 to distinguish one fluid phase from another; $\boldsymbol{u}$ is the velocity vector; γ is the mobility rate, which determines the time scale of the Cahn–Hilliard diffusion; λ and ω are the mixing energy density and the interface thickness parameter, respectively, which are both highly related to the materials; and Ψ is the phase field auxiliary variable. These parameters were calculated in the COMSOL software without artificial settings.

2.2.2. Flow condition of the ambient air

To conduct further analysis based on the two-phase flow model, the flow conditions within the ambient air were also considered. During the evaporation process of the printed filament, water contained within the hydrogel filament diffuses into the ambient air and transitions into vapor. Conversely, water vapor from the ambient air is absorbed into the hydrogel during the swelling process. This transfer of water vapor results in a slight flow of moist air within the ambient air domain. The Reynolds number (R_e) was employed to determine this type of flow condition[36]:

$$R_e = \frac{\rho u L}{\mu} \quad \text{(III)}$$

where ρ is the density of moist air;u is the flow speed; μ is the dynamic viscosity of the fluid; and L is the characteristic length, which can be estimated according to the proposed FEM model:

$$L = \frac{D_1 + D_2}{2} \quad \text{(IV)}$$

where D_1 and D_2 are the diameters of the printed filament and the ambient air domain, respectively. Given the low speed of the moist airflow, the value of R_e was estimated to be lower than 2300. It implies that the flow condition of the ambient air should be defined as laminar flow in the FEM model. Furthermore, as the density of fluid exhibits little fluctuation with pressure in the model, the laminar flow in the ambient air domain was regarded as incompressible.

2.2.3. Cold source of the plate

According to the configuration presented in Figure 1, hydrogel filaments are deposited onto a temperature-controlled plate during the 3D printing of hydrogel architectures. Hence, the top surface of the plate, represented as a cold source in Figure 2, was defined as a temperature boundary. Specifically, the initial temperatures of the plate, the ambient air, and the printed filament were all set to room temperature in the FEM model.

2.2.4. Water vapor transport at the fluid–fluid interface

When hydrogel filaments are exposed to ambient air with inappropriate RH levels, moisture exchange between the hydrogel filaments and the surrounding environment often results in swelling or shrinking of the filaments. To account for water vapor transport across the fluid–fluid interface, the transport of diluted species model was utilized in the FEM simulation. To achieve the calculation of the diffusion and the convection process of water vapor, a widely adopted mass conservation equation, which is associated with Fick's laws of diffusion,[37] was employed:

$$\frac{\partial c}{\partial t} + \nabla \cdot \mathbf{J} + \mathbf{u} \cdot \nabla c = 0 \quad \text{(V)}$$

$$\mathbf{J} = -D' \nabla c \quad \text{(VI)}$$

where c is the concentration of water vapor; D' denotes the diffusion coefficient; and **J** is the diffusive flux vector, which measures the amount of substance that flows through a unit area during a unit time interval.

According to the mass conservation equation (**Equation V**), directly using RH as an input parameter in the calculation is impractical. Hence, to analyze geometric variations under a variety of RH conditions, the relationship between the vapor concentration and RH must be clarified[38]:

$$RH = \frac{c_v}{c_{sat}} \quad \text{(VII)}$$

where the c_v and c_{sat} are the concentration and saturation concentration of water vapor, respectively. When defining RH in the FEM model, a conversion from RH to c_v must be implemented in advance. By inputting the calculated c_v and corresponding c_{sat} into the simulation, the geometric variation of printed filaments under various ambient RH conditions can be calculated. In the model, the c_v was set to the same value for both the ambient air and the outlet boundary.

2.3. Preparation of hydrogel filaments for experimental validation

To validate the reliability of the calculation results, printing trials were conducted using hydrogel filaments. F-127, selected for these trials, is a well-acclaimed medical hydrogel material in regenerative medicine due to its excellent biodegradation properties and outstanding biocompatibility.

In this study, a 30% (w/v) F-127 solution was prepared for the 3D printing experiments. Specifically, the mixture of 1.5 g F-127 powder (P2443-1KG, Sigma-Aldrich, USA) and 5 mL phosphate-buffered saline (Thermo Fisher Scientific Inc., USA) was prepared and stored at 4°C for 24 h. Before each 3D printing, the prepared 30% (w/v) F-127 solution was transferred into syringes and centrifuged for 10 min at 4°C to remove air bubbles within the hydrogel material. Hydrogel filaments with diameters of 0.2, 0.3, and 0.4 mm were then extruded using a self-designed high-precision 3D printing device. A humidity-controlled enclosure was used to maintain a constant ambient RH for hydrogel filaments during and after the deposition process. To evaluate the geometric variation of the printed filaments under the RH of 50, 60, 70, 80, and 90%, an electronic digital microscope (Inskam-316, Aomekie, China) was employed to capture micrographs of the filament cross-sections. Representative geometric variations of hydrogel

filaments with various diameters under the RH of 50% are demonstrated in Figure 3.

2.4. Preparation of 3D-printed ear model

The widely adopted F-127 hydrogel was employed for the 3D printing trials. Before the experiment, the 30% (w/v) F-127 solution was prepared and stained with red ink to facilitate the microscopic observation of the printed structures. Three digital models of human ears with identical shapes but various sizes were designed, with a height ratio of 2:3:4. For the smallest ear model, F-127 was extruded through a 0.2 mm nozzle under ambient RH levels of 90 and 80%. For the medium-sized ear model, a 0.3 mm nozzle was adopted, and the ambient RH was controlled at 80 and 70%. Lastly, for the largest ear model, F-127 material was printed employing a 0.4 mm nozzle under the ambient RH of 60 and 50%. To evaluate the print quality of each 3D architecture, photographs of the overall view were taken using an electronic digital microscope (Inskam-316, Aomekie, USA), while top-view micrographs were taken using an optical microscope (PH50-3A43L-A1600X, Phenix, China).

2.5. Statistical analysis

All experimental results were obtained from at least three independent replicates. For each group, data are presented as mean ± standard deviation. Statistical significance was evaluated using one-way analysis of variance (ANOVA) followed by Tukey's Honestly Significant Difference test for post-hoc comparisons. A p-value < 0.05 was considered statistically significant.

3. Results and discussion

3.1. Analysis of the calculation results

The numerical investigation of the humidity-driven swelling–shrinking behavior was conducted based on three types of printed filaments with diameters of 0.2, 0.3, and 0.4 mm. For the evaporation process of each hydrogel filament, the initial RH was set to 50, 60, 70, 80, and 90%. To mimic the actual working conditions of the extrusion process, the cold source and room temperature were set to 25°C.

Figure 4 illustrates the transient-state RH distribution in the ambient air of the 0.2 mm filaments. The continuous movement of the fluid–fluid interface reflects the geometric variation of each hydrogel filament during the evaporation process. As presented in the figure, high-humidity moist air is gathered near the printed filament. Due to the water vapor diffusion from the hydrogel material, the humidity field in the ambient air domain demonstrates a

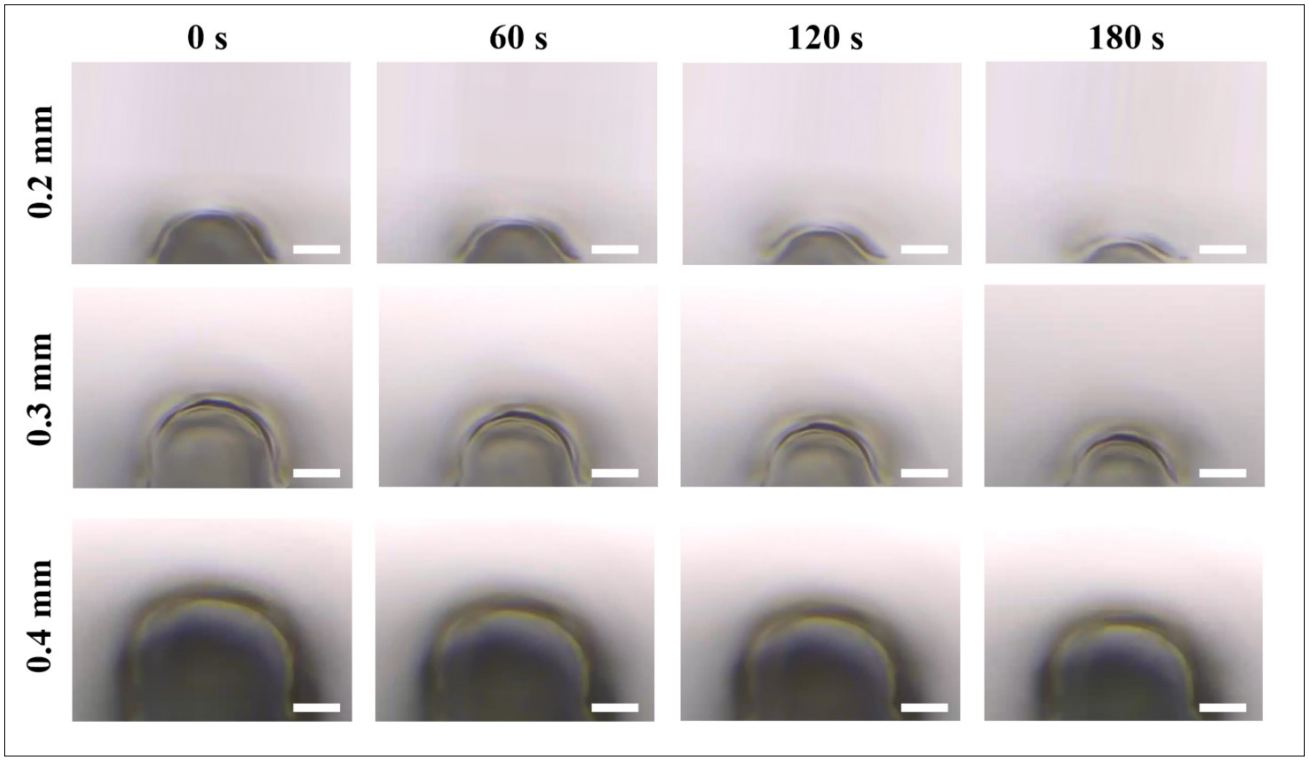

Figure 3. Micrographs of deposited hydrogel filaments with various diameters under a relative humidity of 50%. Scale bar: 0.1 mm; Magnification: 64×.

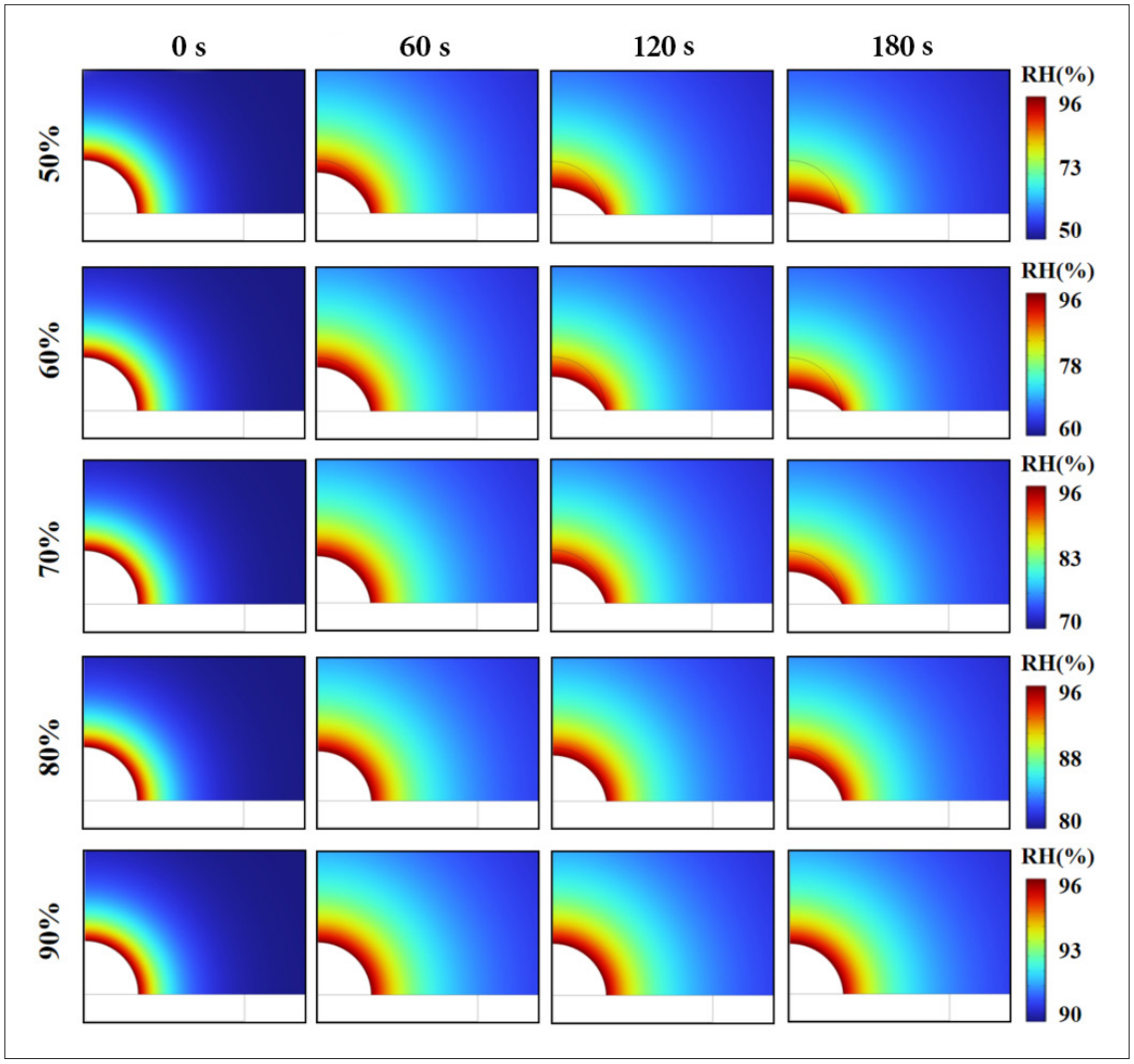

Figure 4. Humidity distribution in the ambient air with a filament diameter of 0.2 mm, illustrating the geometric variation of the printed filament under various relative humidity (RH) conditions.

moisture gradient in the radial direction. When the RH is defined to a low value, such as 50%, the rate of moisture loss is significantly increased, leading to the most severe geometric shrinkage of the printed filament.

The process from deposition to the complete collapse of the entire hydrogel structure lasts for approximately 180 s. Given that 3D printing of large-scale architectures is typically time-consuming, such a rapid geometric decrease is unacceptable during the fabrication process. As the ambient RH increases, the concentration of water in the ambient air approaches that within the hydrogel filament. This leads to insufficient moisture transfer and vapor diffusion, moderating the geometric shrinkage of the just-printed hydrogel filaments. Figure 5 and 6 demonstrate the geometric variations of the 0.3 and 0.4 mm filaments, respectively.

With increasing filament diameter, the geometric shrinkage of the hydrogel filaments is alleviated. Among the three types of hydrogel filaments with various diameters, the 0.4 mm filament exhibits the largest initial volume and contains the greatest amount of water. This implies a higher moisture retention capacity during the evaporation process. Therefore, compared with the 0.2 and 0.3 mm filaments, the 0.4 mm filament demonstrates superior shape stability when exposed to moist air at the same RH.

As the RH increases, both the 0.3 and 0.4 mm filaments ultimately demonstrate swelling behavior. When the

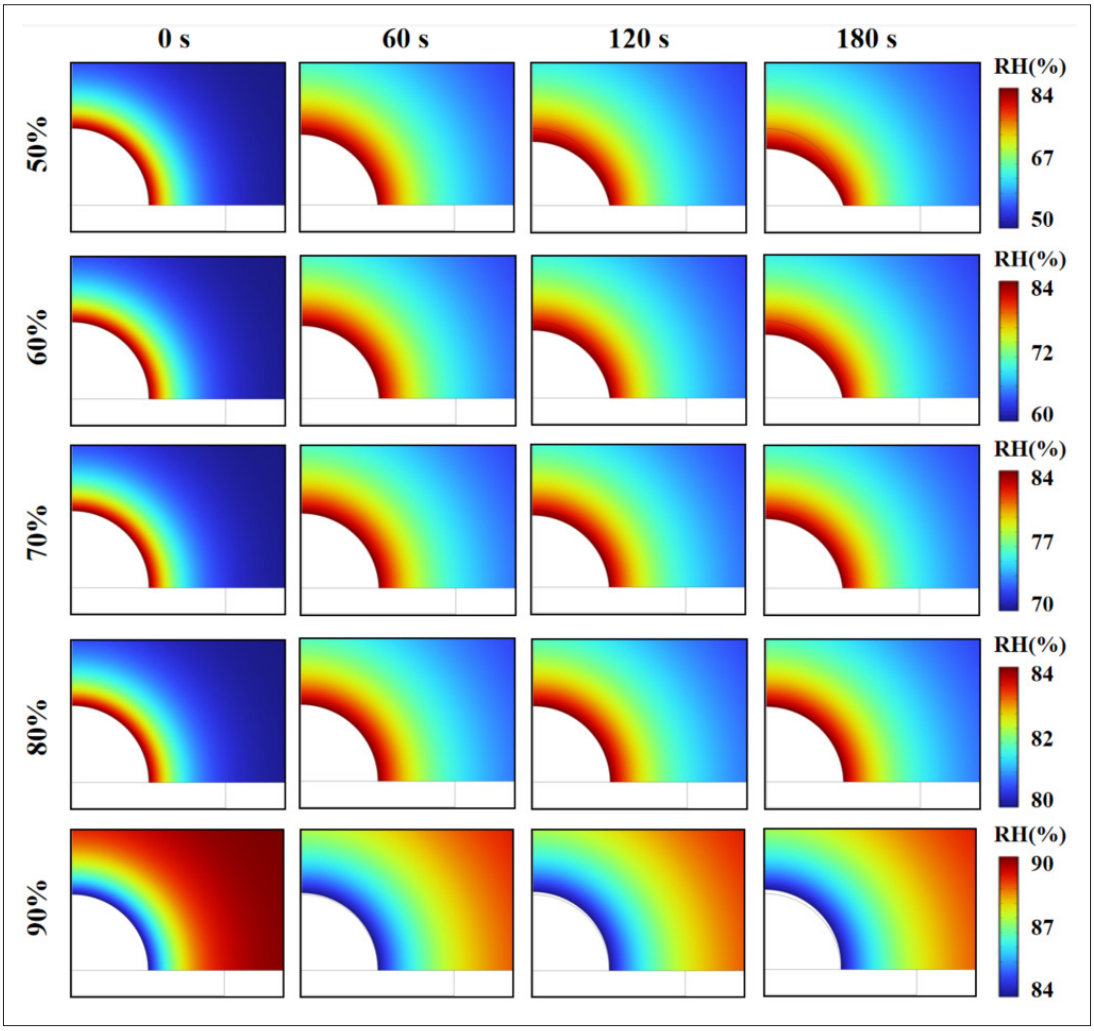

Figure 5. Humidity distribution in the ambient air with a filament diameter of 0.3 mm, illustrating the geometric variation of the printed filament under various relative humidity (RH) conditions.

concentration of water vapor in the ambient air exceeds that within the hydrogel, moisture absorption occurs at the fluid–fluid interface, leading to geometric swelling of the printed filaments.[39]

The swelling–shrinking behavior of printed filaments was quantitatively compared and investigated (Figure 7). As demonstrated in Figure 7A, the original and deformed shapes of the filament are outlined separately using dashed lines. During the humidity-driven geometric transforming process, the height of each printed filament was measured and symbolized as "H2," while the height of the original shape of the filament was symbolized as "H1," which corresponded to the radius of the original filament. To quantitatively evaluate the extent of geometric shrinkage, the ratio of H2 to H1 was calculated for each printed filament.

As demonstrated in Figure 7B, five geometric variation curves are obtained for the 0.2 mm filament. All curves display a clear linear reduction over time, with the most pronounced shrinkage observed at an RH of 50%. Likewise, the geometric variation curves of the 0.3 mm filament, as presented in Figure 7C, show similar trends when the RH is not more than 80%. However, the geometric variation curve exhibits an increasing trend at an RH of 90%. In Figure 7D, linear increases in the curves of 0.4 mm filaments occur when the RH is not lower than 70%, with the most prominent swelling occurring at 90% RH.

Generally, significant geometric variations of extruded filaments are not permitted in the manufacturing of 3D biomimetic architectures.[40] To meet the strict requirements of medical applications, deviations between the size of the shrinking filament and that of the original

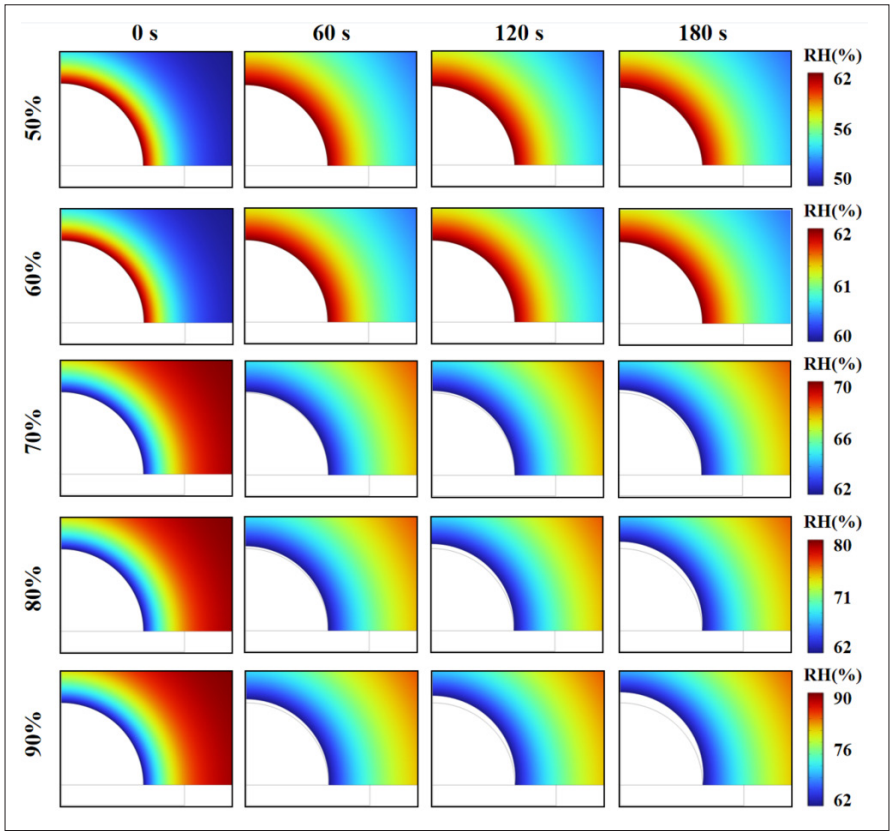

Figure 6. Humidity distribution in the ambient air with a filament diameter of 0.4 mm, illustrating the geometric variation of the printed filament under various relative humidity (RH) conditions.

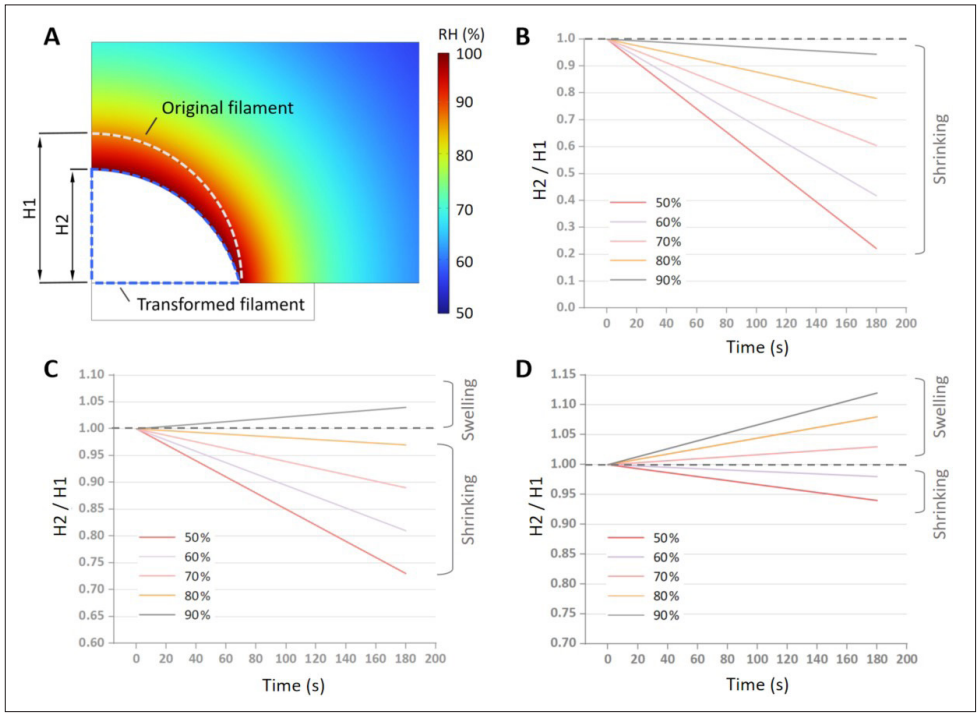

Figure 7. Quantitative comparison of the geometric variation of the printed filaments. (A) Schematic diagram of the transformed filament in the finite element method model. (B–D) Geometric variation curves of the printed filaments with various diameters: (B) 0.2 mm, (C) 0.3 mm, and (D) 0.4 mm.

filament should be minimized. To identify the optimal RH levels for hydrogel 3D printing, horizontal dashed lines corresponding to an H2/H1 of 1 are included in Figure 7B–D. The geometric variation of the 0.2 mm filament reaches the greatest moderation at 90% RH. For the 0.3 mm filament, both the curves of the 80 and 90% RHs demonstrate lower deviations from the dashed line. Similarly, for the 0.4 mm filament, the geometric variation presents the lowest alleviation at 60 and 70% RHs.

In practice, the challenges posed by humidity-driven swelling are more severe than those of humidity-driven shrinking. During the layer-by-layer deposition process, well-arranged hydrogel filaments in adjacent layers fuse, creating an architecture with a larger volume. When the RH is too low, shrinking filaments reduce structural density and slightly weaken the mechanical properties of the manufactured 3D structure. However, due to the fusion of hydrogel filaments, the moisture transfer between adjacent filaments can partially moderate the impact of moisture loss. In contrast, when the RH is excessively high, swelling filaments reduce the spacing between adjacent filaments, lowering the pore size within the 3D architecture. This can not only cause uncontrolled mechanical properties but also lead to poor breathability, limiting the applicability of the biomimetic structure in cell culturing or tissue engineering.

Therefore, based on the deformation trends obtained from the simulations, the RH level corresponding to the minimal deviation from an H2/H1 of 1 was selected as the optimal RH for each filament diameter. According to the calculation results, the optimal RH levels for the 3D printing process of the 0.2, 0.3, and 0.4 mm hydrogel filaments were 90, 80, and 60%, respectively.

3.2. Experimental validation of the simulation results

As demonstrated in Figure 8A, the height of the 3D-printed F-127 filament was measured from the captured micrographs. By calculating the H2-to-H1 ratio based on the micrographs, the geometric variation curves of 0.2, 0.3, and 0.4 mm F-127 filaments were plotted (Figure 8B–D). When compared with the simulation results in Figure 6, although the experimental curves do not perfectly match the simulated data, the overall trends show strong agreement. To measure the deviation of the experimental results from the simulated data, absolute errors (ε) between the simulated and the experimental geometric variation curves were calculated at several time points (Table 2).

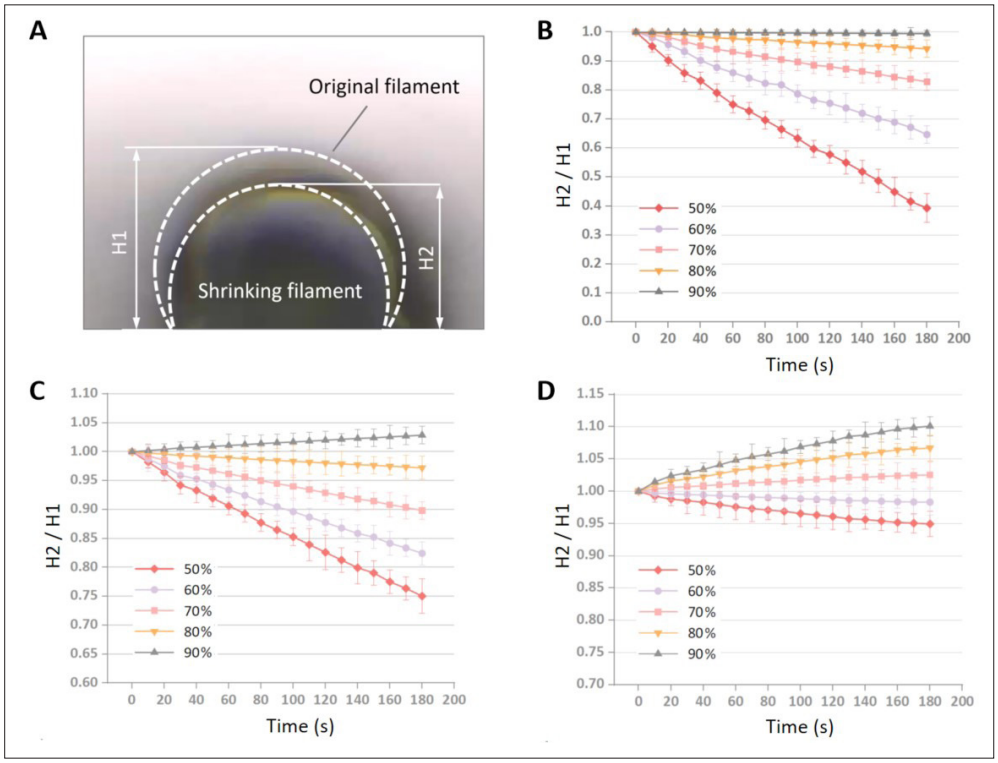

Figure 8. Geometric variation curves of the 3D-printed hydrogel filaments. (A) Schematic diagram of the measurement of filament diameters. (B–D) Geometric variation curves of hydrogel filaments with various diameters: (B) 0.2 mm, (C) 0.3 mm, and (D) 0.4 mm.

Compared with the simulated curves in Figure 6, the variation of each experimental curve in Figure 8 is not strictly linear. Instead, all experimental curves exhibit a decreasing rate of descent over time, resulting in increasing deviation between the experimental and simulation data. This phenomenon can be attributed to the unique internal structure of hydrogel materials, which consists of a fluid phase (water) and a solid phase (crosslinked polymer network). During moisture loss, the polymer network remains within the filament, playing the role of load-bearing and shape-retaining. At the beginning of evaporation, the polymer network constitutes a small volume of the hydrogel filament and thus has little impact on geometric variation. However, as water content in the material decreases, the proportion of the solid phase increases. Consequently, the influence of moisture loss on geometric shrinkage is gradually alleviated as H2/H1 decreases, eventually leading to a greater ε. Nevertheless, although neglecting the polymer network causes a gentle increase in ε, the simulation results still match the experimental data well in most cases. As shown in Table 2, the maximum absolute error (ε_{Max}) across geometric variation curves is limited to 0.228, supporting the reliability of the FEM simulation results.

3.3. 3D printing trial for hydrogel filaments under optimal humidity

Due to the remarkable humidity-driven swelling–shrinking behavior of hydrogels, inappropriate RH levels within the printing space can severely affect the layer-by-layer deposition of complex 3D architectures. To address this issue, the present method aims to identify optimal RH levels for 3D printing hydrogel filaments and to alleviate the collapse or shrinkage of multilayered constructs. According to the FEM simulation result, the optimal RH levels for the 0.2, 0.3, and 0.4 mm hydrogel filaments are 90, 80, and 60%, respectively. To validate the feasibility of these conditions, 3D hydrogel architectures were manufactured using the 3D printer shown in Figure 1, and the corresponding results are presented in this section.

Figure 9A–C demonstrates 3D-printed ear models of small, medium, and large sizes, respectively, fabricated

Table 2. The absolute error and the maximum absolute error between the simulated data and the experimental results across multiple time points

d (mm)	RH (%)	ε									ε_{Max}
		20 s	40 s	60 s	80 s	100 s	120 s	140 s	160 s	180 s	
0.2	50	0.024	0.015	0.015	0.015	0.040	0.076	0.110	0.134	0.171	0.171
	60	0.012	0.017	0.035	0.062	0.091	0.127	0.162	0.202	0.228	0.228
	70	0.019	0.030	0.050	0.076	0.103	0.133	0.164	0.193	0.224	0.224
	80	0.015	0.027	0.043	0.064	0.080	0.101	0.122	0.143	0.162	0.162
	90	0.005	0.010	0.015	0.021	0.027	0.033	0.039	0.045	0.051	0.051
0.3	50	0.008	0.010	0.008	0.007	0.002	0.002	0.006	0.013	0.021	0.021
	60	0.006	0.007	0.006	0.005	0.002	0.001	0.004	0.009	0.014	0.014
	70	0.003	0.004	0.003	0.003	0.001	0.001	0.002	0.005	0.008	0.008
	80	0.001	0.001	0.001	0.001	0.001	0.002	0.005	0.002	0.002	0.005
	90	0.001	0.001	0.002	0.003	0.005	0.006	0.007	0.009	0.011	0.011
0.4	50	0.006	0.004	0.004	0.003	0.002	0.001	0.003	0.005	0.009	0.009
	60	0.002	0.002	0.002	0.001	0.001	0.001	0.001	0.002	0.003	0.003
	70	0.003	0.002	0.002	0.001	0.001	0.003	0.001	0.002	0.005	0.005
	80	0.007	0.005	0.006	0.004	0.002	0.001	0.003	0.006	0.012	0.012
	90	0.011	0.008	0.009	0.005	0.003	0.001	0.005	0.009	0.019	0.019

Abbreviations: *d*:, diameter; RH, relative humidity.

under optimal RH conditions of 90, 80, and 60%. Under these conditions, the constructs maintained splendid shape throughout the 3D printing process. The well-arranged F-127 filaments provided stable support for adjacent layers and exhibited smooth, uniform shapes. In contrast, Figure 9D–F presents ear models printed under inappropriate ambient RH conditions of 80, 70, and 50% for the small, medium, and large sizes, respectively. Although the F-127 hydrogel filaments initially appeared continuous upon deposition, as printing proceeded, a gradual shrinkage and even collapse occurred due to inappropriate ambient RH. This compromised the capability to support the upper layers and resulted in irregular holes within the 3D-printed architectures. At the edges of each model, an evident moisture loss occurred, as demonstrated in the micrographs. These fragile structures often fail to provide the mechanical or biological properties required for medical applications.

The observed phenomena can be explained as follows. The medical-grade biodegradable hydrogel used in this study consists of hydrophilic polymer networks that retain plenty of water and exhibit pronounced humidity-driven swelling–shrinking behavior. As illustrated in Figure 6, to minimize moisture loss and geometric variation of the hydrogel filaments, specific RH levels were selected as the optimal RH for each filament diameter. Since the ear models (Figure 9A–C) were printed under these selected RH conditions, the shape of each hydrogel filament was maintained throughout the manufacturing process. On the contrary, when the ambient RH was inappropriate (Figure 9D–F), the moisture loss led to geometric shrinkage.

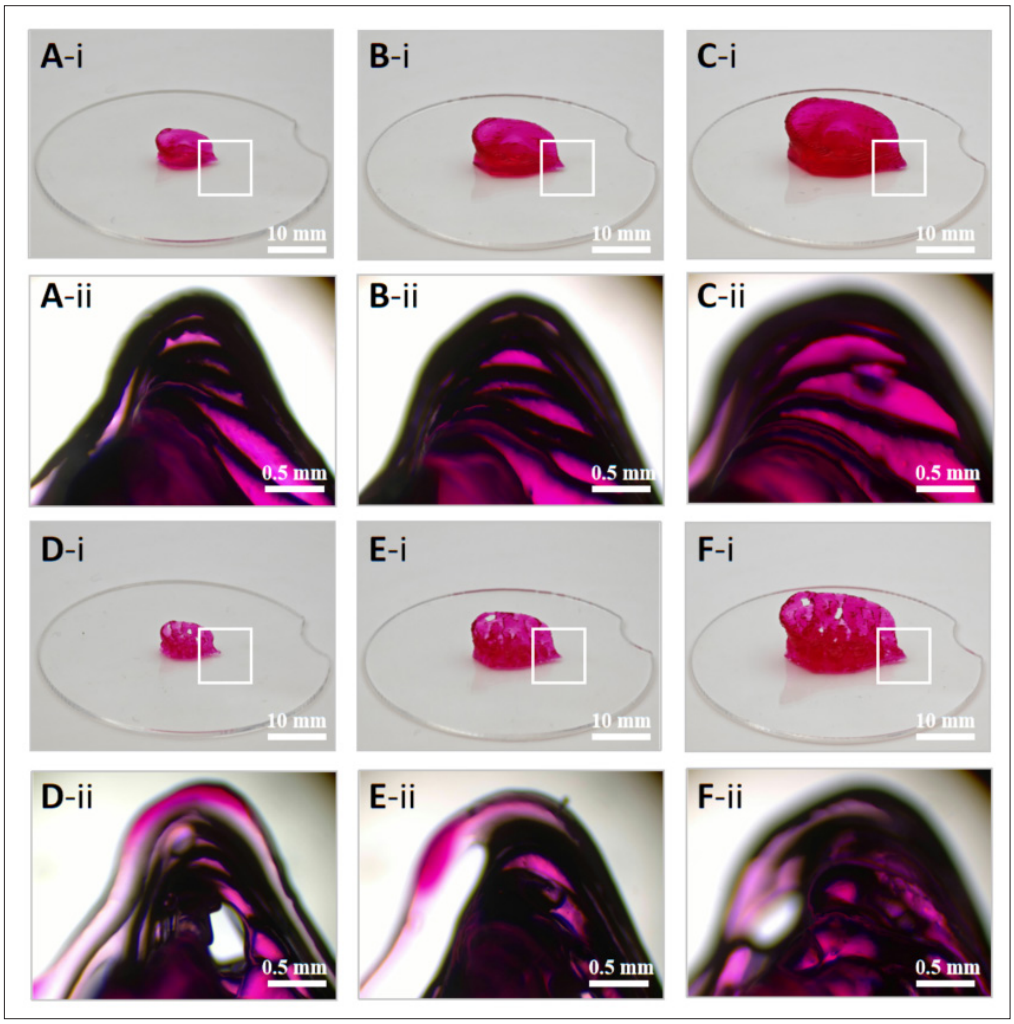

Figure 9. Photographs and micrographs of the 3D-printed ear models. (A–C) Ear models printed with filament diameters of (A) 0.2 mm, (B) 0.3 mm, and (C) 0.4 mm under optimal ambient humidity conditions. (D–F) Corresponding models printed under relatively low ambient humidity conditions, showing structural deformation. Scale bar for all upper panels: 10 mm; Magnification: 8×. Scale bar for all lower panels: 0.5 mm; Magnification: 64×.

To provide a quantitative basis for evaluating the printing quality of the hydrogel constructs under different RH conditions, the overall height of each printed structure was measured as a representative indicator of structural integrity. Given the complexity of the ear-shaped geometry, conventional image analysis techniques, such as edge detection, contour extraction, or pixel-wise segmentation, were not feasible for consistent quantitative assessment. Therefore, vertical height was selected as a measurable and reproducible metric that reflects the degree of structural collapse or swelling caused by humidity-driven deformation. The height of each sample was obtained from side-view images and is presented in Table 3. The results demonstrate that samples printed under optimal RH conditions exhibited significantly greater structural retention compared to those printed under inappropriate RH conditions.

Currently, numerous studies have explored 3D printing using F-127 materials. However, a majority of these printed structures exhibit shrinkage and collapse during the extrusion process due to inappropriate ambient RH. Moisture loss significantly limits the fabrication of large-scale 3D architectures with complex structures. Table 4 compares the 3D-printed F-127 architectures of various sizes in existing studies. It demonstrates that the effective lengths and widths of recently proposed structures usually fall within the range of 5–10 mm, with effective heights generally not higher than 8 mm. Meanwhile, the shapes of these architectures are not complex enough to meet the requirements of medical applications. In contrast, in this study, a 3D-printed ear model with an effective size of 20 mm (length) × 10 mm (width) × 10 mm (height) is successfully generated. This outcome confirms that 3D printing with optimal RH conditions can alleviate moisture loss and enhance the structural fidelity of 3D architectures.

F-127 was selected as the model hydrogel in this study due to its pronounced and stable geometric deformation under varying RH conditions, along with its excellent printability and reproducibility. These characteristics made it suitable for controlled investigation of humidity-driven swelling–shrinking mechanisms and for quantitative FEM modeling. However, it is important to note that the proposed finite element framework—including two-phase flow modeling, water vapor transport simulation, and RH–geometry coupling—is not limited to the specific material properties of F-127. The model is designed to be generalizable and can be applied to other widely used hydrogel-based inks, such as GelMA with tunable crosslinking density, ionically crosslinked alginate, and photopolymerizable PEG-DA, provided that key physical parameters (e.g., swelling ratio, viscosity, and diffusion coefficient) are available. These hydrogels are extensively used in tissue engineering and bioprinting, indicating the strong applicability and scalability of our model in practical biomanufacturing settings.

4. Conclusion

In this study, the humidity-driven swelling–shrinking behavior of hydrogel filaments during 3D printing was investigated through numerical simulations and experimental validation. A novel FEM coupling field simulation model was developed to identify optimal

Table 3. Overall heights of printed structures with various humidity levels

Figure	Filament diameter (mm)	Ambient humidity (%)	Overall height (mm)
A	0.2	90	5.4
D		80	4.5
B	0.3	80	8.5
E		70	7.6
C	0.4	60	10.0
F		50	8.8

Table 4. Results of printed F-127 structures in recent studies

Reference	Structure	Filament diameter (mm)	Effective size (length × width × height, mm^3)
[41]	Reticulate structure	0.5	8×8×1
[42]		0.2	10×10×5
[43]	Cube structure	0.4	5×5×5
	Pyramid structure		10×10×8

ambient RH conditions for hydrogel extrusion. Printing trials were conducted to validate the effectiveness of the proposed approach in mitigating geometric shrinkage in 3D-printed architectures. The main conclusions are summarized as follows:

(i) A FEM thermal–humidity–multiphase flow coupling field simulation model was proposed and experimentally validated, successfully predicting the geometric variation of hydrogel filaments under a variety of ambient RH conditions.

(ii) The optimal RH conditions for 3D printing of hydrogel filaments with diameters of 0.2, 0.3, and 0.4 mm were identified as 90, 80, and 60%, respectively.

(iii) Printing trials using F-127 hydrogel materials demonstrated that higher ambient RH effectively prevents both uncontrollable geometric swelling and shrinkage during the 3D printing process.

(iv) Under optimized RH conditions for hydrogel filaments, 3D architectures of the human ear were successfully manufactured with an effective size of 20 mm (length) × 10 mm (width) × 10 mm (height).

It should be noted that the humidity-driven swelling–shrinking behavior discussed in this study is specific to hydrogel-based biomaterials, such as F-127 and GelMA. These materials possess high water content and strong moisture responsiveness under ambient conditions. In contrast, thermoplastic biocompatible polymers, such as polycaprolactone and polypropylene, are largely unaffected by humidity due to their hydrophobic nature and low water uptake. Therefore, the findings of this study are not intended to generalize across all biocompatible printing materials.

Although the present study provides a quantitative understanding of humidity-driven deformation in single-layer hydrogel filaments, the current model is limited to 2D cross-sectional simulations and does not fully capture the 3D deposition dynamics of multilayer structures. In practice, interlayer moisture transport, filament fusion behavior, and cumulative deformation significantly impact the final geometry and functionality of printed biomimetic constructs. Due to the absence of robust theoretical models for describing layer-by-layer coupling and time-dependent structural evolution, accurate simulation of full 3D architectures remains a challenge. Future work will focus on developing a comprehensive, multi-physics 3D FEM framework that incorporates interlayer interactions and global deformation mechanisms. This will further enhance the predictive capability and practical value of the proposed approach in large-scale hydrogel biomanufacturing.

Acknowledgments

None.

Funding

The authors deeply acknowledge the financial support from the Key Research and Development Plan Project of Heilongjiang Province (grant no. 2022ZX02C22); the Science and Technology Innovation Talent Project on Manufacturing Industry of Harbin (grant no. 2023HBRCGD011, 2022CXRCGD029); the Interdisciplinary Research Foundation of HIT (grant no. IR2021223); and the Natural Science Foundation of Chongqing (grant no. CSTB2023NSCQ-MSX0822).

Conflict of interest

Dr. Swee Leong Sing serves as the Editorial Board Member of the journal, but did not in any way involve in the editorial and peer-review process conducted for this paper, directly or indirectly. Other authors declare they have no competing interests.

Author contributions

Conceptualization: Qiang Gao
Data curation: Qiang Gao
Formal analysis: Lihua Lu
Funding acquisition: Wei Zhang
Investigation: Peng Zhang
Methodology: Min Zhu
Project administration: Lihua Lu
Resources: Le Xu
Software: Kaicheng Yu
Supervision: Yifeng Yao
Validation: Swee Leong Sing
Visualization: Wei Zhang
Writing–original draft: Kaicheng Yu
Writing–review and editing: Kaicheng Yu

Ethics approval and consent to participate

Not applicable.

Consent for publication

Not applicable.

Availability of data

The datasets generated and analyzed during the current study are available from the corresponding author upon reasonable request.

Reference

1 Kühl J, Gorb S, Kern M, et al. Extrusion-based 3D printing of osteoinductive scaffolds with a spongiosa-inspired structure. *Front Bioeng Biotechnol*. 2023;11:1268049. doi: 10.3389/fbioe.2023.1268049.

2. Dutta SD, An JM, Hexiu J, et al. 3D bioprinting of engineered exosomes secreted from M2-polarized macrophages through immunomodulatory biomaterial promotes in vivo wound healing and angiogenesis. *Bioact Mater.* 2025;45:345-362. doi: 10.1016/j.bioactmat.2024.11.026.

3. Daly AC, Prendergast ME, Hughes AJ, Burdick JA. Bioprinting for the biologist. *Cell*. 2021;184(1):18-32. doi: 10.1016/j.cell.2020.12.002.

4. Wang H, Guo K, Zhang L, et al. Valve-based consecutive bioprinting method for multimaterial tissue-like constructs with controllable interfaces. *Biofabrication*. 2021;13:035001. doi: 10.1088/1758-5090/abdb86.

5. Zhao Z, Xiang Y, Koellhoffer EC, et al. 3D bioprinting cowpea mosaic virus as an immunotherapy depot for ovarian cancer prevention in a preclinical mouse model. *Mater Adv*. 2024;5(4):1480-1486. doi: 10.1039/D3MA00899A.

6. Weng T, Zhang W, Xia Y, et al. 3D bioprinting for skin tissue engineering: current status and perspectives. *J Tissue Eng*. 2021;12:1758518878. doi: 10.1177/20417314211028574.

7. Ng WL, An J, Chua CK. Process, material, and regulatory considerations for 3D printed medical devices and tissue constructs. *Engineering*. 2024;36:146-166. doi: 10.1016/j.eng.2024.01.028.

8. Namazi AM, Aghajanzadeh MS, Imani R. Optimizing a self-healing gelatin/aldehyde-modified xanthan gum hydrogel for extrusion-based 3D printing in biomedical applications. *Mater Today Chem*. 2024;40:102208. doi: 10.1016/j.mtchem.2024.102208.

9. Ijeoma P, Ridel AF, Parkar H. Digital protocol for the bioprinting of a three-dimensional acellular dermal scaffold. Biomedical visualization. In: *How to use 3D Printing Innovations and Digital Storage to Democratize Anatomy Education*. Biomedical Visualization, Springer, Cham. 2024:99-113. doi: 10.1007/978-3-031-68501-9_5.

10. Li W, Wang M, Ma H, Chapa-Villarreal FA, Lobo AO, Zhang YS. Stereolithography apparatus and digital light processing-based 3D bioprinting for tissue fabrication. *iScience*. 2023;26(2):106039. doi: 10.1016/j.isci.2023.106039.

11. Liu J, Xu C. Improving uniformity of cell distribution in post-inkjet-based bioprinting. *J Manuf Sci Eng*. 2024;146(1):014501. doi: 10.1115/1.4063134.

12. Bozek J, Kurchakova O, Michel J, et al. Pneumatic conveying inkjet bioprinting for the processing of living cells. *Biofabrication*. 2025;17:025003. doi: 10.1088/1758-5090/ada8e2.

13. Zhang P, Gao Q, Yu K, Yao Y, Lu L. Investigation on the temperature control accuracy of a print head for extrusion 3D printing and its improved design. *Biomedicines*. 2022;10(6):1233. doi: 10.3390/biomedicines10061233.

14. Gao Q, Yu K, Chen F, Lu L, Zhang P. Investigation on the temperature distribution uniformity of an extrusion-based 3D print head and its temperature control strategy. *Pharmaceutics*. 2022;14(10):2108. doi: 10.3390/pharmaceutics14102108.

15. Ji S, Guvendiren M. Complex 3D bioprinting methods. *APL Bioeng*. 2021;5(1):11508. doi: 10.1063/5.0034901.

16. Wang X, Jiang J, Yuan C, et al. 3D bioprinting of GelMA with enhanced extrusion printability through coupling sacrificial carrageenan. *Biomater Sci*. 2024;12(3):738-747. doi: 10.1039/D3BM01489D.

17. Burns N, Rajesh A, Manjula-Basavanna A, Duraj-Thatte A. 3D extrusion bioprinting of microbial inks for biomedical applications. *Adv Drug Deliv Rev.* 2025;217:115505. doi: 10.1016/j.addr.2024.115505.

18. Iyer KS, Bao L, Zhai J, et al. Microgel-based bioink for extrusion-based 3D bioprinting and its applications in tissue engineering. *Bioact Mater*. 2025;48:273-293. doi: 10.1016/j.bioactmat.2025.02.003.

19. Yuce-Erarslan E, Tutar R, Izbudak B, et al. Photo-crosslinkable chitosan and gelatin-based nanohybrid bioinks for extrusion-based 3D-bioprinting. *Int J Polym Mater.* 2021;72(1):1-12. doi: 10.1080/00914037.2021.1981322.

20. Lima TDPL, Canelas CADA, Concha VOC, Costa FAMD, Passos MF. 3D bioprinting technology and hydrogels used in the process. *J Funct Biomater.* 2022;13(4):214. doi: 10.3390/jfb13040214.

21. Shie M, Shen Y, Astuti SD, et al. Review of polymeric materials in 4D printing biomedical applications. *Polymers*. 2019;11(11):1864. doi: 10.3390/polym11111864.

22. Chang CC, Boland ED, Williams SK, Hoying JB. Direct-write bioprinting three-dimensional biohybrid systems for future regenerative therapies. *J Biomed Mater Res B Appl Biomater*. 2011;98B(1):160-170. doi: 10.1002/jbm.b.31831.

23. Lv C, Sun X, Xia H, et al. Humidity-responsive actuation of programmable hydrogel microstructures based on 3D printing. *Sens Actuators B Chem*. 2018;259:736-744. doi: 10.1016/j.snb.2017.12.053.

24. Dai C, Li Z, Li Z, et al. Direct-printing hydrogel-based platform for humidity-driven dynamic full-color printing and holography. *Adv Funct Mater*. 2023;33(9):2212053. doi: 10.1002/adfm.202212053.

25. Sun S, Xu Y, Maimaitiyiming X. 3D printed carbon nanotube/polyaniline/gelatin flexible NH3, stress, strain, temperature multifunctional sensor. *React Funct Polym*. 2023;190:105625. doi: 10.1016/j.reactfunctpolym.2023.105625.

26. Yu K, Gao Q, Lu L, Zhang P. A process parameter design method for improving the filament diameter accuracy of extrusion 3D printing. *Materials*. 2022;15(7):2454. doi: 10.3390/ma15072454.

27. Zhao L, Wang P, Tian J, et al. A novel composite hydrogel for solar evaporation enhancement at air-water interface. *Sci Total Environ*. 2019;668:153-160. doi: 10.1016/j.scitotenv.2019.02.407.

28. Park JH, Jang J, Lee J, Cho D. Current advances in three-dimensional tissue/organ printing. *Tissue Eng Regen Med*. 2016;13:612-621. doi: 10.1007/s13770-016-8111-8.

29. Search J, Mahjoubnia A, Chen AC, et al. 3D-printing of selectively porous, freestanding structures via humidity-induced rapid phase change. *Addit Manuf*. 2023;68:103514. doi: 10.1016/j.addma.2023.103514.

30. Matamoros M, Gómez-Blanco JC, Sánchez ÁJ, et al. Temperature and humidity PID controller for a bioprinter atmospheric enclosure system. *Micromachines*. 2020;11(11):999. doi: 10.3390/mi11110999.

31. Yu K, Gao Q, Yao Y, Lin Z, Zhang P, Lu L. Investigation of the humidity control in the printing space for the material extrusion of medical biodegradable hydrogel. *Addit Manuf*. 2024;93:104452. doi: 10.1016/j.addma.2024.104452.

32. Yu K, Gao Q, Xu J, et al. Computational investigation of a 3D-printed skin substitute with orthotropy in mechanical property. *Comput Biol Med*. 2023;166:107536. doi: 10.1016/j.compbiomed.2023.107536.

33. Scotti C, Wirz D, Wolf F, et al. Engineering human cell-based, functionally integrated osteochondral grafts by biological bonding of engineered cartilage tissues to bony scaffolds. *Biomaterials*. 2010;31(8):2252-2259. doi: 10.1016/j.biomaterials.2009.11.110.

34. Cubo N, Garcia M, Del CJ, Velasco D, Jorcano JL. 3D bioprinting of functional human skin: production and in vivo analysis. *Biofabrication*. 2016;9:15006. doi: 10.1088/1758-5090/9/1/015006.

35. Cahn JW, Hilliard JE. Free energy of a nonuniform system. I. Interfacial free energy and free energy of a nonuniform system. III. Nucleation in a two-component incompressible fluid. *J Chem Phys*. 1959;31:688-699. doi: 10.1002/9781118788295.ch3.

36. Gao Q, Lu L, Zhang R, Song L, Huo D, Wang G. Investigation on the thermal behavior of an aerostatic spindle system considering multi-physics coupling effect. *Int J Adv Manuf Technol*. 2019;102:3813-3823. doi: 10.1007/s00170-019-03509-4.

37. Fick A. On liquid diffusion. *J Membr Sci*. 1995;100(1):33-38. doi: 10.1016/0376-7388(94)00230-V.

38. Shu S, Zhan Z, Xu J, Huang Y, Huang W, Lin Y. Three-dimensional numerical simulation and experiment of moisture condensation mechanism inside high voltage switchgear. *Int J Electr Power Energy Syst*. 2023;151:109129. doi: 10.1016/j.ijepes.2023.109129.

39. Naghieh S, Chen X. Printability–a key issue in extrusion-based bioprinting. *J Pharm Anal*. 2021;11(5):564-579. doi: 10.1016/j.jpha.2021.02.001.

40. Schwab A, Levato R, D Este M, Piluso S, Eglin D, Malda J. Printability and shape fidelity of bioinks in 3D bioprinting. *Chem Rev*. 2020;120(19):11028-11055. doi: 10.1021/acs.chemrev.0c00084.

41. Lee J, Kim G. Three-dimensional hierarchical nanofibrous collagen scaffold fabricated using fibrillated collagen and pluronic F-127 for regenerating bone tissue. *ACS Appl Mater Interfaces*. 2018;10(42):35801-35811. doi: 10.1021/acsami.8b14088.

42. Boonlai W, Hirun N, Suknuntha K, Tantishaiyakul V. Development and characterization of pluronic F127 and methylcellulose based hydrogels for 3D bioprinting. *Polym Bull*. 2023;80:4555-4572. doi: 10.1007/s00289-022-04271-6.

43. Fu Z, Angeline V, Sun W. Evaluation of printing parameters on 3D extrusion printing of pluronic hydrogels and machine learning guided parameter recommendation. *Int J Bioprint*. 2021;7(4):434. doi: 10.18063/ijb.v7i4.434.

ACCSCIENCE PUBLISHING

International Journal of Bioprinting

RESEARCH ARTICLE

3D-bioprinted osteocytes expressing Wnt7b protect osteoblast differentiation from microgravity

Jinling Zhang[1†], Pengtao Wang[1†], Xiaoling Chen[1], Saima Khan[1], Haiping Ouyang[2], Yangxi Liu[2], Bo He[2], Xian Li[3], Xing Liu[2*], and Xiaolin Tu[1*]

[1]Laboratory of Skeletal Development and Regeneration, Key Laboratory of Clinical Laboratory Diagnostics (Ministry of Education), College of Laboratory Medicine, Chongqing Medical University, Chongqing, China

[2]Department of Orthopedics, Ministry of Education Key Laboratory of Child Development and Disorders, National Clinical Research Center for Child Health and Disorders, Children's Hospital of Chongqing Medical University, Chongqing, China

[3]College of Medical Informatics, Chongqing Medical University, Chongqing, China

Abstract

Maintaining bone formation in microgravity/weightless environments remains a major challenge. Under weightless conditions, osteocytes act as mechanosensors to inhibit Wnt canonical signaling and bone formation by secreting sclerostin. This study explores whether osteocytic Wnt7b can counteract microgravity-induced bone loss through Wnt non-canonical signaling. Unlike previous bioprinting studies that focused on structural scaffolds or generic cell types, a novel bioprinted scaffold consisting of polycaprolactone (supportive) and osteocyte (functional) hydrogels was constructed in this study. Osteocytes overexpressing Wnt7b were co-cultured with bone marrow stromal cells (ST2) in a 3D biomimetic weightless biomicroenvironmental system (3D-BWBM) to assess osteogenic and lipogenic differentiation. The results indicated that osteocytic Wnt7b enhanced osteogenic differentiation and mineralization of ST2 cells via the Wnt non-canonical pathway PKCδ, while suppressing the expression of lipogenic markers (*Pparg*, *Cebpa*) and adipogenesis. Reverse transcription quantitative polymerase chain reaction (RT-qPCR) analysis revealed elevated expression of *Sost* and *Mef2c*, downregulation of the Wnt target gene *Opg*, and elevated expression of pro-osteoclastogenic cytokine *Rankl* and pro-inflammatory cytokines *Tnfa* and *Il1b*, thus validating the microgravity effect. Unlike conventional 2D culture of RCCS™ cells, the 3D hydrogels were printed with tunnels (500 μm) for efficient nutrient/metabolite exchange, resulting in good cell growth, high cell viability (97%), and a six-fold increase in proliferative activity within 7 days. Wnt7b osteocytes were still able to maintain the osteogenic differentiation of ST2 cells, as evidenced by elevated alkaline phosphatase activity, mineralization (1.8-fold increase), and a decrease in osteoblast marker genes (*Alpl, Runx2, Col1a1*). In conclusion, Wnt7b-PCKδ signaling counteracts microgravity-induced bone loss, and further *in vivo* studies on osteocytic Wnt7b are warranted to confirm this causal relationship.

Keywords: 3D bioprinting; Microgravity; Osteogenic differentiation; Wnt7b; Wnt noncanonical signaling

[†]These authors contributed equally to this work.

***Corresponding authors:**
Xiaolin Tu
(xtu@cqmu.edu.cn)

Xing Liu
(400269@hospital.cqmu.edu.cn)

Citation: Zhang J, Wang P, Chen X, *et al.* 3D-bioprinted osteocytes expressing Wnt7b protect osteoblast differentiation from microgravity. *Int J Bioprint.* 2025;11(4):426-445. doi: 10.36922/IJB025240238

Received: June 12, 2025
Accepted: July 3, 2025
Published Online: July 3, 2025

Copyright: © 2025 Author(s). This is an Open Access article distributed under the terms of the Creative Commons Attribution License, permitting distribution and reproduction in any medium, provided the original work is properly cited.

Publisher's Note: AccScience Publishing remains neutral with regard to jurisdictional claims in published maps and institutional affiliations.

1. Introduction

Bone loss in microgravity remains a significant challenge for astronauts, with bone mineral density (BMD) of the lumbar spine and hip joint decreasing by 1–1.5% per month,[1–3] mainly due to suppressed osteoblast activity and increased osteoclast-based osteolysis.[4,5] Current countermeasures, including physical exercise, nutritional supplementation, and pharmacological protection, have limited effectiveness, potential risks, and side effects.[6] A promising alternative is to target osteocytes, the mechanosensory cells in the skeleton that regulate osteoblast/osteoclast activity through Wnt signaling.[7,8] However, the loss of mechanical loads, such as prolonged bed rest, paralysis, or space flight,[9] upregulates osteocyte sclerostin (gene: *Sost*), which blocks the binding of Wnt ligand to its coreceptor Lrp5/6. This, in turn, inhibits the Wnt/β-catenin canonical signaling pathway,[10] leading to a decrease in osteoblast differentiation.[11,12]

Wnt7b, a ligand that activates the non-canonical Wnt pathway, has emerged as a potential solution. In contrast to Wnt/β-catenin signaling, Wnt7b-PKCδ is sclerostin independent and promotes osteogenesis in mice.[13,14] We recently observed that mice with osteocyte-specific Wnt/β-catenin activation (daβcat^{Ot}) exhibit elevated Wnt7b expression (Figure 1A) and are protected from weightlessness-induced bone loss. This led us to hypothesize that osteocytic Wnt7b creates a microenvironment conducive to osteogenesis even under microgravity conditions.

The cost of conducting research under actual microgravity conditions is high, resulting in limited research opportunities. Various types of bone tissue engineering (BTE) scaffolds are widely used in microgravity environments.[15] Although scaffolds may provide temporary physical support for cell attachment, proliferation, and differentiation, the microgravity environment confers a unique mechanical environment with profound effects on cell fate.[16] Therefore, cell culture in microgravity environments could inspire greater potential for scaffold-based BTE. The use of biomaterials combined with a simulated weightlessness device for *in vitro* 3D culture provides a platform that closely mimics *in vivo* conditions, thereby supporting tissue and cell regeneration.[17,18]

Recent advances in 3D bioprinting have enabled the fabrication of bone-mimicking scaffolds with customized mechanical and biochemical properties.[19] However, most studies have focused on structural optimization (e.g., porosity, stiffness) or general effector cell (e.g., mesenchymal stem cells, osteoblasts) encapsulation, without utilizing mechanosensitive cell sources as functionalized agents to actively counteract microgravity-induced bone loss. Recent research has developed microgravity-compatible bioprinted constructs but relied on passive scaffold designs that lacked innate osteoinductive signaling.[20]

Herein, we present two key innovations: (i) bioprinting of functionalized osteocytes and (ii) a 3D biomimetic weightless biomicroenvironment (3D-BWBM) as a bionic microgravity platform. We designed Wnt7b-expressing osteocytes (MLO-Y4) as a bioactive cell source to bypass sclerostin-mediated Wnt inhibition. Unlike previous studies using undifferentiated cells, Wnt7b-activated osteocytes promoted osteogenic differentiation of undifferentiated cells via the non-canonical Wnt-PKCδ pathway while inhibiting adipogenic differentiation—a dual mechanism that is not possible with conventional scaffolds or growth factors. Likewise, by combining a 3D bioprinted polycaprolactone (PCL)-gelatin methacryloyl (GelMA) scaffold with NASA's rotating cell culture system (RCCS™), we have created 3D-BWBM that goes beyond traditional 2D RCCS™ cultures. Our system features multi-scale tunnels (500 μm) for enhanced nutrient/metabolite transport. Intercellular crosstalk is maintained by printing osteocyte-ST2 co-cultures for long-term osteogenic function under simulated microgravity conditions.

This study combines, for the first time, mechanosensitive cell customization with a 3D-bioprinted exoskeleton for microgravity applications, providing a scalable solution for disuse osteoporosis. By expanding the scope of bioprinting to realize biological functions in extreme environments, this study establishes a critical link between biomanufacturing and space medicine.

2. Materials and methods

2.1. Materials

Puromycin (10 mg/mL stock solution), Rottlerin (PKCδ inhibitor, dissolved in dimethyl sulfoxide [DMSO], stored at 10 mM), rapamycin (mTORC inhibitor, dissolved in DMSO, stored at 50 mM), and iCRT-14 (Wnt canonical signaling inhibitor, dissolved in DMSO, stored at 50 mM) were purchased from MedChemExpress (China). The BCIP/NBT Alkaline Phosphatase Color Development kit, modified Oil Red O staining kit, calcein/PI cell viability/cytotoxicity assay kit, alkaline phosphatase (AP) assay kit, phenylmethanesulfonyl fluoride (PMSF), RIPA lysis buffer, the nuclear and cytoplasmic protein extraction kit, phosphatase inhibitors, and DAPI staining solutions were obtained from Beyotime Biotechnology (China). TRizol reagent, Evo M-MLV reverse transcription premix kit, and SYBR Green Premix Pro Taq HS qPCR kit were obtained

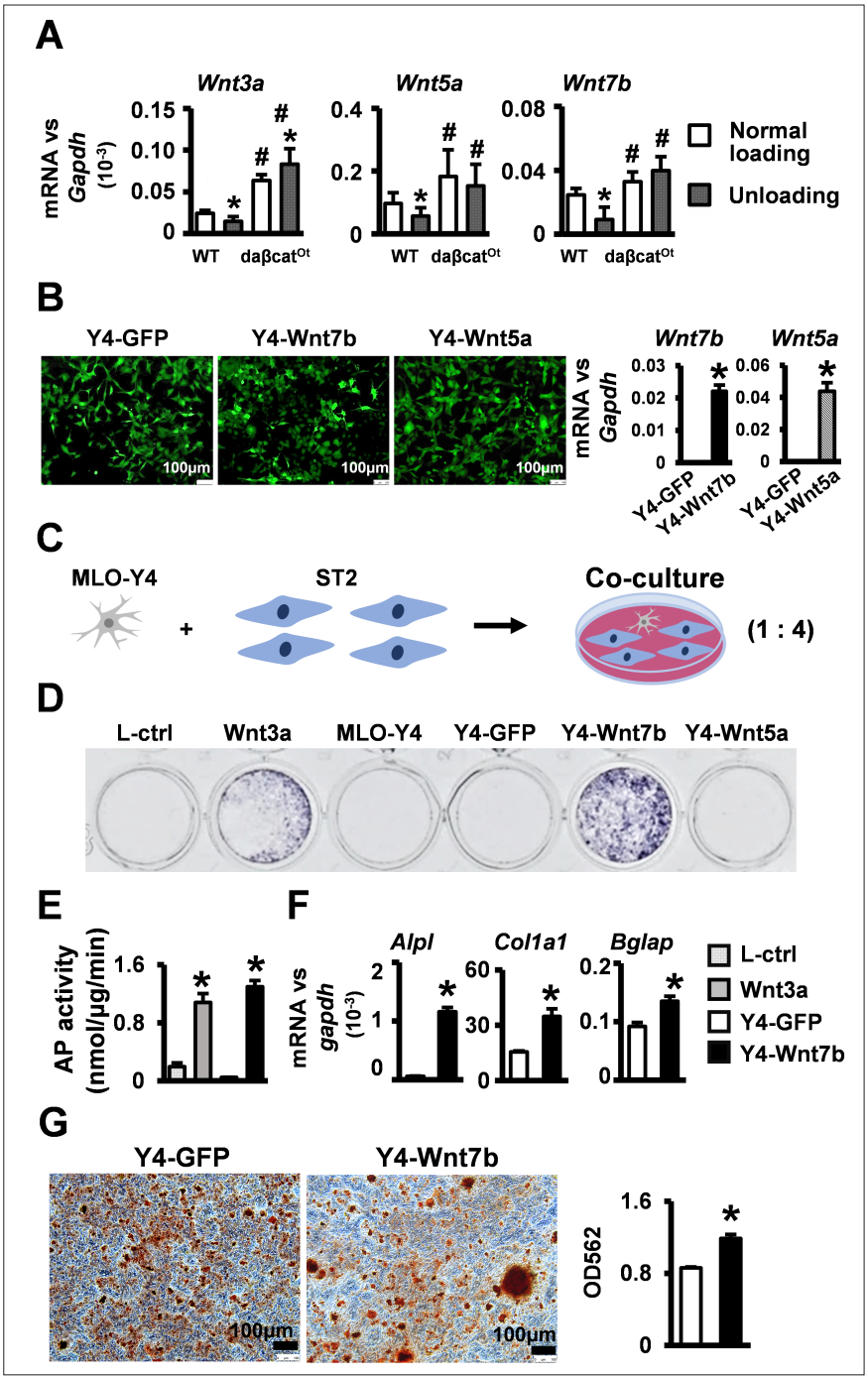

Figure 1. Effect of osteocytic Wnt7b on the osteogenic differentiation of ST2 cells. (A) Expression levels of Wnt ligands (Wnt3a, Wnt5a, Wnt7b) in the tibia and femur of 16-week-old daβcat^{Ot} mice and WT controls after 14 days of tail suspension, measured by RT-qPCR. Data are presented as mean ± standard deviation; *$p < 0.05$ versus normal loading; #$p < 0.05$ versus WT, by Two-Way ANOVA, $n = 5–7$. (B) Images and gene expression of the osteocytic cell line MLO-Y4 cells infected by lentiviruses expressing Wnt7b, Wnt5a, and their control GFP, respectively. Scale bar = 100 μm. (C) Schematic of the co-culture model: MLO-Y4 osteocytes and ST2 bone marrow stromal cells were co-cultured at a 1:4 ratio. (D) AP staining after 3 days of co-culture. L-ctrl and Wnt3a groups represent MLO-Y4 cells treated with control or Wnt3a-conditioned medium, respectively. MLO-Y4, Y4-GFP, Y4-Wnt7b, and Y4-Wnt5a represent co-culture of ST2 cells with the corresponding MLO-Y4 osteocytes. (E) AP biochemical activity assay of the co-culture as indicated. (F) Expression of osteoblast marker genes (*Alpl*, *Col1a1*, *Ibsp*, *Bglap*) of the co-culture as indicated. (G) Alizarin Red S staining and quantification of mineralization nodules of the co-culture of Y4-GFP and Y4-Wnt7b. Scale bar: 100 μm. *$p < 0.05$, compared with Y4-GFP or L-ctrl by Student's *t*-test, $n = 3$ for panels B, E, F, and G. Abbreviations: AP, alkaline phosphatase; daβcat^{Ot}, mice with daminantly active Wnt/β-catenin in osteocytes; GFP, green fluorescent protein; mRNA, messenger ribonucleic acid; RT-qPCR, reverse transcription quantitative polymerase chain reaction; WT, wide type.

from Accurate Biotechnology (China). Lyophilized GelMA and photo-crosslinking agent lithium phenyl-2,4,6-trimethylbenzoylphosphinate (LAP) were obtained from Sunp Biotech (China). Hydrocortisone, 3-isobutyl-1-methylxanthine (IBMX), indomethacin, PCL, and polybrene were obtained from Sigma (United States of America [USA]). The quantitative polymerase chain reaction (qPCR) primers were synthesized by Sangon Biotech (China). Alizarin Red S (ARS), β-glycerophosphate disodium salt solution, and L-ascorbic acid were obtained from Solarbao Biotechnology (China). The Cell Counting Kit-8 (CCK-8) was obtained from Yeasen Biotechnology (China). Phosphate-buffered saline (PBS) and SDS-PAGE gels were obtained from Epizyme Biotech (China).

Rabbit polyclonal anti-mouse β-catenin antibody, Lamin B1 polyclonal antibody, MARCKS polyclonal antibody, and phospho-MARCKS (Ser159/163) polyclonal antibody were purchased from Proteintech (China). Cy3-labeled goat anti-rabbit IgG (H+L) was obtained from Beyotime Biotechnology (China). Polyclonal anti-Gapdh antibody and secondary antibody goat anti-rabbit IgG H&L (HRP) were obtained from ZENBIO (China).

Alpha modified eagle's minimum essential medium (α-MEM) and Dulbecco's modified eagle (DMEM) medium were purchased from Gibco (USA). The penicillin-streptomycin solution (100×) was obtained from Beyotime Biotechnology (China). Fetal bovine serum (FBS) was obtained from Biological Industries (Israel).

2.2. Cell lines and cell culture

The osteocytic cell line (MLO-Y4) was provided by Professor Lynda Bonewald, Indiana University School of Medicine, and the ST2 cells were provided by Dr. Steve Teitelbaum, Washington University. Both cell lines were cultured in α-MEM growth medium supplemented with 10% FBS and 1% penicillin-streptomycin. Wnt3a-expressing cells (Wnt3a) and their control cells (L-ctrl) were purchased from the American Type Culture Collection (ATCC, USA) and cultured in DMEM growth medium containing 10% FBS and 1% penicillin-streptomycin. All cells were cultured in an incubator with 5% CO_2 at 37°C.

MLO-Y4 cells stably transfected with lentivirus expressing green fluorescent protein (GFP) (control), Wnt7b, and Wnt5a were labeled as Y4-GFP, Y4-Wnt7b, and Y4-Wnt5a, respectively. For co-culture experiments, Y4 (1×10^4 cells/well) and ST2 cells (4×10^4 cells/well) were seeded together in 24-well plates and cultured for 3 days or as otherwise indicated. Osteogenic differentiation was assessed by AP staining after co-culturing MLO-Y4 and ST2 at 1:2, 1:4, 1:6, and 1:8 ratios, respectively.

2.3. Isolation of long bones of tail-suspended mice for RNA extraction

Mice with dominantly active β-catenin in osteocytes (daβcat^{Ot}) and wild-type control mice (WT) were generated as previously reported.[21] Briefly, DMP1-8kb-Cre mice expressing Cre recombinase in osteocytes were crossed with Catnb$^{lox(ex3)/lox(ex3)}$ mice, in which exon 3 of the β-catenin gene (encoding the degradation domain) is flanked by LoxP sites. All animal procedures were approved by the Institutional Animal Care and Use Committee of Chongqing Medical University and conducted in accordance with relevant guidelines (IACUC-CQMU-2024-0277).

The 14-week-old daβcat^{Ot} and WT mice underwent suspension for 14 days.[22] Following euthanasia, tibiae and femurs were dissected, and soft tissue (skin, muscle) was meticulously removed. After clipping the femoral epiphysis, the bone marrow was flushed three times with α-MEM containing 1% FBS. The cleaned long bone shafts were immediately snap-frozen in liquid nitrogen and stored in –80°C until RNA extraction.

2.4. Stable transfection of MLO-Y4 with lentivirus

MLO-Y4 cells overexpressing Wnt7b or Wnt5a were generated via stable lentiviral transduction, as previously described.[23] Lentiviruses expressing Wnt7b, Wnt5a, and GFP were purchased from GENECHEM (China). MLO-Y4 cells were transfected at a multiplicity of infection (MOI) of 100 in the presence of 7 μg/mL polybrene. Transfection efficiency was assessed 48 h post-infection by GFP fluorescence intensity. Transfected cells were selected and maintained in culture medium containing 0.5 μg/mL puromycin for at least 1 week to eliminate non-transfected cells.

2.5. RNA extraction and quantitative real-time PCR

Total RNA was extracted from long bone shafts or cultured cells using TRIzol reagent according to the manufacturer's instructions, as previously described.[23] Complementary DNA (cDNA) was synthesized using the Evo M-MLV reverse transcription premix kit, and qPCR was performed using the SYBR Green Premix Pro Taq HS qPCR kit in the CFX Connect Real-Time PCR Detection System (Bio-Rad Laboratories, USA). All primer sequences are listed in Table 1. All qPCR reactions were performed three times. The relative mRNA expression levels were calculated using the $2^{-\triangle CT}$ method, with the housekeeping gene glyceraldehyde-3-phosphate dehydrogenase (*Gapdh*) as the reference gene.

2.6. Alkaline phosphatase staining

Alkaline phosphatase (AP) staining was performed as described previously.[23] Cells were washed with 1× PBS and fixed with 3.7% formaldehyde (Chongqing Chuandong Chemical Group, China) for 5 min at room temperature. Fixed cells were then incubated with staining solution from the BCIP/NBT Alkaline Phosphatase Color Development Kit according to the manufacturer's protocol for 30 min at room temperature. For the PCL and cell-integrated 3D-printed (PCI3D) modules, staining was performed after 7 and 14 days of culture, with the staining duration extended to ≥4 h. Stained samples were imaged using a standard digital camera.

2.7. Alkaline phosphatase biochemical activity assay

The AP biochemical activity assay was quantified as previously described.[23] Briefly, cells were washed with PBS and lysed in 300 μL of 10 mM Tris/HCl (pH 7.4) per well. Lysates were scraped, sonicated on ice, and centrifuged at 13,000 rpm for 3 min at 4°C. The supernatant was collected, and AP activity was measured using the AP assay kit following the manufacturer's instructions. Absorbance at 405 nm was recorded using a VarioskanTM LUX multimode microplate reader (Thermo Fisher Scientific, USA).

2.8. Mineralization assay

Mineralized matrix deposition was assessed by ARS staining, as previously described.[23] Osteocytes and ST2 cells were seeded in 24-well plates or PCI3D modules and cultured in growth medium for 3 or 7 days, respectively. Osteogenic differentiation was then induced by culturing the cells for 14 days in osteogenic medium consisting of growth medium supplemented with 10 mM β-glycerophosphate disodium and 50 μg/mL L-ascorbic acid. Cells or modules were fixed with 3.7% formaldehyde for 3 min and stained with 0.4% ARS solution (pH 4.2) for 30 min. Stained samples were imaged under a microscope. To quantify mineralization, the ARS stain was eluted with 10% cetylpyridinium chloride (CPC) for 1 h. The eluent was collected, and absorbance was measured at 562 nm to quantify the mineralization status.

2.9. Western blotting

Western blotting was conducted following standard procedures.[24] Total proteins were extracted by lysing cells in RIPA lysis buffer containing PMSF and phosphatase inhibitors. Cytoplasmic and nuclear protein fractions were isolated using a nuclear and cytoplasmic protein extraction kit. Protein samples (20 μg per lane) were separated by 10% SDS-PAGE and transferred onto 0.22 μm polyvinylidene fluoride (PVDF) membranes (Boster

Table 1. Sequences of primers used for qPCR

Gene	Primer sequence (5'–3')	
	Forward	Reverse
Gapdh	GCACAGTCAAGGCCGAGAAT	GCCTTCTCCATGGTGGTGAA
Wnt3a	CTTAGTGCTCTGCAGCCTGA	GAGTGCTCAGAGAGGAGTACTGG
Wnt5a	TTGGCCACGTTTTTCTCC	TGGCTGCAGAGAGGCTGT
Wnt7b	GCCTCATGAACCTTCACAAC	AACTTAGGTAGCGTGGTCCA
Alpl	TTCGCTATCTGCCTTGCCTG	AGTCTGTGTCTTGCCTGCC
Runx2	CCGTGGCCTTCAAGGTTGT	TTCATAACAGCGGAGGCA
Col1a1	TCAACCCCGTCTACTTCCCT	TTCAACAGTCCAAGAACCCCAT
Bglap	GCCTACAAACGCATCTACGG	GAGAGAGAGGACAGGGAGGA
Sp7	GCCCCCTGGTGTTCTTCATT	CTTCCCCCTTCTTGGCACTC
Ibsp	CAGAGGAGGCAAGCGTCACT	GCTGTCTGGGTGCCAACACT
Axin2	TGAGCGGCAGAGCAAGTCCAA	GGCAGACTCCAATGGGTAGCT
Pparg	AGCCCTTTACCACAGTTGATTTCTCC	GCAGGTTCTACTTTGATCGCACTTTG
Cebpa	TGGACAAGAACAGCAACGAG	TCACTGGTCAACTCCAGCAC
Mef2c	AAGCCTCAGCATCAAGTCAGAAC	GCGTGGTGTGTTGTGGGTATC
Sost	GTGCCTCATCTGCCTACTTGTG	CGGTTCATGGTCTGGTTGTTCTC
Tnfa	CACGCTCTTCTGTCTACTGAACTTC	CTTGGTGGTTTGTGAGTGTGAGG
Il1b	TCGCAGCAGCACATCAACAAG	TCCACGGGAAAGACACAGGTAG
Il8	GAGCACTCCATAAGGCACAAA	ATGGTTCCTTCCGGTGGT

Biological Technology, China). Membranes were blocked with 5% bovine serum albumin (BSA) for 2 h, and then incubated overnight at 4°C with primary antibodies: β-catenin antibody (1:2000), Lamin B1 antibody (1:2000), Gapdh antibody (1:2000), MARCKS antibody (1:2000), or phospho-MARCKS (Ser159/163) (1:2000). After washing with PBST, membranes were incubated with the secondary antibody goat anti-rabbit IgG H&L (HRP) (1:5000) for 1.5 h at room temperature. Protein bands were visualized using enhanced chemiluminescence (ECL) reagent (Abbkine Scientific, China) and imaged using an ECL imager (CLINX Qinxiang Scientific, China). Band intensities were quantified using ImageJ and normalized to loading controls.[13]

2.10. Immunofluorescence detection of β-catenin nuclear translocation

Nuclear translocation of β-catenin was detected by immunofluorescence, as described.[25] Y4-GFP and Y4-Wnt7b cells were cultured in a 24-well plate for 24 h. Cells were fixed with 3.7% formaldehyde solution at room temperature for 3 min, permeabilized with 0.25% Triton X-100 for 30 min, and blocked with 1% BSA for 30 min. Cells were then incubated overnight at 4 °C with β-catenin antibody (1:100). After washing three times with PBS, cells were incubated with Cy3-labeled goat anti-rabbit IgG secondary antibody (1:200) for 60 min in the dark. Nuclei were counterstained with DAPI solution (200 μL per well) for 3 min. Images were acquired using a fluorescence microscope (Leica, Germany).

2.11. Induction of adipogenic differentiation

Adipogenic differentiation was induced as previously described.[24] Briefly, Y4-GFP or Y4-Wnt7b cells were cultured with ST2 cells at a 1:4 ratio in 12-well plates. Upon reaching confluency (typically after 3 days), the growth medium was replaced with adipogenic induction medium (DMEM supplemented with 10% FBS, 0.5 μM hydrocortisone, 0.5 mM IBMX, and 60 μM indomethacin). Cells were maintained in this medium for up to 7 days, with half of the medium replaced every 3 days, until lipid droplets were observed microscopically. Adipogenesis was visualized for 30 min using the Oil Red O staining kit according to the manufacturer's instructions. Lipid droplets were imaged using an inverted microscope (Nikon, Japan).

2.12. PCI3D module preparation

The PCI3D modules were biofabricated using a dual-nozzle 3D bioprinter (Sunpbiotech, China), incorporating PCL as structural support and cell-laden hydrogels containing functional MLO-Y4 and ST2 cells, as previously detailed.[23] Briefly, lyophilized GelMA was dissolved in α-MEM to prepare a 20% (w/v) GelMA solution containing 0.5% (w/v) LAP. A cell suspension containing 2×10^5 MLO-Y4 cells and 8×10^5 ST2 cells in 0.5 mL α-MEM was mixed with an equal volume of GelMA/LAP solution, resulting in a final bioink containing 10% (w/v) GelMA, 0.25% (w/v) LAP, and cells. The cell-laden bioink was loaded into a cooled syringe and printed using a cell-printing nozzle.

Simultaneously, PCL pellets were melted at 95°C for 30 min in a separate printing nozzle designed for thermoplastics. Melted PCL was printed at a speed of 2 mm/s to form a framework with a diameter of 400 μm and a spacing of 1100 μm. The cell-laden GelMA bioink was printed alongside the PCL strands at a speed of 5 mm/s (strand diameter: 300 μm; spacing: 500 μm). After printing each layer, the GelMA hydrogel was crosslinked under 405 nm blue light for 10 s. Printing was performed sequentially in three layers, with the PCL and cell-laden GelMA strands oriented perpendicularly between adjacent layers. The fabricated PCI3D modules were transferred to 6-well plates containing growth medium and cultured at 37°C with 5% CO_2.

2.13. Cell viability within PCI3D modules

Cell viability within PCI3D modules was quantified at Days 1, 4, and 7 of culture using a Calcein/ Propidium Iodide (PI) cell viability and cytotoxicity detection kit, as described previously.[23] Modules were washed with PBS and incubated in staining solution (prepared by diluting Calcein AM and PI stock solutions in assay buffer according to the kit instructions) for 30 min at 37 °C in the dark. Calcein AM stains live cells green, while PI stains dead cells red. Immediately after staining, the modules were imaged using an inverted fluorescence microscope (Leica, Germany). Cell viability was quantified using ImageJ software (64-bit, v1.46).

2.14. Cell proliferative activity within PCI3D modules

Cell proliferation in PCI3D modules was evaluated on Days 1, 4, and 7 using the CCK-8 assay kit, according to the manufacturer's instructions.[23] The PCI3D module was first washed with PBS, then cut into four pieces and placed in a 96-well plate. Subsequently, 90 μL of PBS and 10 μL of CCK-8 solution were added to each well and incubated for 2 h. The supernatant was then transferred to a new 96-well plate, and the absorbance was measured at 450 nm using the multi-function microplate reader (Thermo Fisher Scientific, USA).

2.15. 3D-BWBM system

The 3D-BWBM system was established to evaluate the protective effect of osteocytic Wnt7b against microgravity-impaired osteoblast differentiation. This system integrates the PCI3D system, which prints PCI3D modules[23] containing the biological microenvironment (Wnt7b-

overexpressing osteocytes in this study), with the R-approved microgravity-simulation system, RCCS™. The 3D-BWBM was set up in a CO_2 incubator.

In order to rapidly evaluate the effect of osteocytic Wnt7b on osteogenic differentiation under microgravity in a 3D environment closely resembling *in vivo* conditions,[26,27] we printed the PCI3D module and cut it into small modules about 5 × 5 mm^2 with optional compartments, allowing for installation within the high-aspect rotating vessel (HARV™) of the RCCS™. The HARV™ was filled with growth medium, carefully degassed to remove air bubbles, sealed with a plug at the filling port, and subsequently mounted onto the rotating base. To ensure clear experimental effects, prevent cell dislodgement, and maintain the module suspended at the center of the vessel, a rotational speed of 20–30 rpm/min was optimized for this experiment to simulate microgravity and low shear stress conditions.[28] Finally, RCCS™ was placed in a CO_2 incubator to culture the modules for 7 days, during which the medium was changed once.

2.16. Statistical analysis

GraphPad Prism 8.0.1 software was used for statistical analysis. Each experiment was repeated three times. Data were expressed as mean ± standard deviation. Differences in data between two groups were analyzed by *t*-test; differences between multiple groups were analyzed by one-way analysis of variance (ANOVA); and differences between groups with two or more independent variables were analyzed by two-way ANOVA. A *p*-value less than 0.05 indicates statistical significance.

3. Results

3.1. Osteocytic Wnt7b induces osteogenic differentiation of ST2 cells

We observed that mice with osteocyte-specific Wnt/β-catenin activation (daβcatOt) exhibited resistance to the induced bone loss in a tail suspension model simulating weightlessness. To investigate this phenomenon, we analyzed the expression of Wnt ligands in the long bones of daβcatOt mice and their cohort control mice (WT). We found that the expression levels of *Wnt3a*, *Wnt5a*, and *Wnt7b* were positively correlated with bone loss and bone protection in the microgravity environment (Figure 1A). To determine whether these three Wnt ligands possess a protective function against microgravity-induced bone loss in osteocytes, we established stable osteocyte cell line MLO-Y4 expressing Wnt5a, Wnt7b, and GFP (control), namely Y4-Wnt5a, Y4-Wnt7b, and Y4-GFP, respectively. RT-qPCR analysis revealed that Y4-Wnt5a and Y4-Wnt7b overexpressed their respective *Wnt5a* and *Wnt7b* mRNAs (Figure 1B). MLO-Y4 treated with Wnt3a-conditioned medium exhibited enhanced osteogenic differentiation-promoting activity.[29]

The prepared osteocyte cell lines were used as functional cells and co-cultured with effector cells, specifically bone marrow mesenchymal cells ST2, for 3 days (Figure 1C), followed by an assessment of their osteogenic differentiation activity. The co-culture cell ratio of MLO-Y4 to ST2 at 1:4 was selected (Figure S1, Supporting Information), consistent with previous reports indicating that osteogenic factors from osteocytes promote ST2 osteogenic differentiation through activation of the canonical Wnt signaling pathway.[25,30,31] Osteogenic differentiation, assessed by AP staining, displayed significantly increased staining intensity in the co-culture of Wnt3a-treated MLO-Y4 and Y4-Wnt7b groups, but no significant increase was observed in the Y4-Wnt5a co-culture group (Figure 1D). The Y4-GFP co-culture group exhibited no significant difference compared to the MLO-Y4 co-culture group treated with the Wnt3a control medium (L-ctrl). Consistent with the staining results, Y4-Wnt7b and Y4-Wnt3a significantly promoted osteogenic differentiation, with robust increases in AP biochemical activity compared to their respective controls, Y4-GFP and Y4-L-ctrl (Figure 1E).

However, given that the osteogenic activity of Wnt3a can be inhibited by the Wnt/β-catenin antagonist ICG-001[32] and that sclerostin produced by microgravity also inhibits the canonical Wnt signaling pathway, we focused on Wnt7b as a potential strategy to bypass sclerostin inhibition under microgravity conditions. Furthermore, RT-qPCR analysis revealed that the Y4-Wnt7b co-culture group significantly upregulated the expression of osteoblast marker genes (*Alpl, Col1a1, Ibsp,* and *Bglap*) in ST2 cells (Figure 1F). To verify whether the osteocyte-mediated osteogenic differentiation of ST2 cells in the co-culture system was exclusively derived from ST2 cells, we then examined the AP expression of Y4-GFP and Y4-Wnt7b cells, respectively. The AP staining results showed that the intensity of AP staining of Y4-Wnt7b itself and Y4-GFP cells was significantly weaker than that in the ST2 cells cocultured with L-ctrl medium-treated MLO-Y4 and Y4-GFP (Figure S2A, Supporting Information). Also, the mRNA levels of osteoblast marker genes *Alpl*, *Ibsp*, and *Bglap* were comparable to those of Y4-GFP cells in Y4-Wnt7b cells (Figure S2B, Supporting Information), suggesting that Wnt7b hardly altered the expression of osteoblast marker genes in MLO-Y4 cells. Finally, we assessed the effect of osteocyte Wnt7b on mineralization. ARS staining demonstrated that the mineralized nodules formed in the Y4-Wnt7b co-culture group were larger, denser, and had 1.4 times more calcium deposition than those in the Y4-GFP co-culture group (Figure 1G).

Therefore, we will conduct further studies on the force-sensitive and functional bone cell Wnt7b, which actively counteracts microgravity-induced impairment of osteoblast differentiation.

3.2. Osteocytic Wnt7b activates the PKCδ pathway of Wnt noncanonical signaling to promote osteogenic differentiation

To determine whether osteocytic Wnt7b signals through the canonical Wnt pathway, we assessed β-catenin protein levels in Y4-Wnt7b cells, as β-catenin is a central mediator of canonical signaling.[13] Western blot analysis of cytoplasmic and nuclear fractions revealed no significant difference in β-catenin levels compared to Y4-GFP controls (Figure 2A). Furthermore, immunofluorescence staining with an anti-β-catenin antibody demonstrated no observable translocation of β-catenin from the cytoplasm to the nucleus in Y4-Wnt7b cells relative to Y4-GFP cells (Figure 2B). Moreover, at concentrations below 10 μM, iCRT-14 (the canonical Wnt signaling antagonist) did not attenuate Y4-Wnt7b-induced osteoblast differentiation of ST2 cells, as measured by AP staining and its biochemical activity assays (Figure S3A and B, Supporting Information). Similarly, iCRT-14 did not alter the expression of the canonical Wnt target gene *Axin2* compared to the DMSO control (Figure S3C, Supporting Information). These findings indicate that osteocytic Wnt7b does not activate the canonical Wnt signaling pathway.

Given our previous reports that Wnt7b activates noncanonical pathways involving mTORC1[14] and PKCδ[13] in osteoblasts to promote bone formation, we next investigated these possibilities in our osteocyte model. Treatment with the mTORC1-specific inhibitor rapamycin[33] in the co-culture of Y4-Wnt7b and ST2 cells for 3 days displayed no significant inhibition of AP activity. In contrast, rapamycin effectively inhibited osteoblast differentiation induced by Wnt3a-treated MLO-Y4 cells (Figure S4, Supporting Information). This suggests that mTORC1 signaling is not essential for osteocytic Wnt7b-mediated osteogenesis.

Finally, we tested the involvement of PKCδ signaling using its selective inhibitor Rottlerin.[34] Firstly, we tested the effect of different concentrations of Rottlerin on Wnt7b-induced osteogenic differentiation. AP staining revealed that treatment with 1 μM Rottlerin significantly reduced the differentiation function of Y4-Wnt7b cells (Figure 2C). Furthermore, Rottlerin inhibited the phosphorylation of the myristoylated alanine-rich C-kinase substrate (MARCKS), which is a well-established marker of PKC activation.[35] Western blot analysis demonstrated that Y4-Wnt7b cells exhibited increased levels of p-MARCKS (Ser159/163) compared to controls. Treatment of Y4-Wnt7b cells with 1 μM Rottlerin significantly reduced p-MARCKS levels (Figure 2D). Functionally, 1 μM Rottlerin completely inhibited osteoblast differentiation in ST2 cells co-cultured with Y4-Wnt7b cells, as observed in AP staining and its biochemical activity assays (Figure 2E and F), significant downregulation of osteoblast marker genes (*Alpl, Col1a1, Ibsp*) via qPCR (Figure 2G), and a marked 1.4-fold reduction in osteocytic Wnt7b-induced mineralization by ARS staining (Figure 2H).

Collectively, these results demonstrate that osteocytic Wnt7b promotes osteogenic differentiation of ST2 cells primarily through activation of the PKCδ-mediated noncanonical Wnt signaling pathway, rather than through canonical Wnt or mTORC1 signaling.

3.3. Osteocytic Wnt7b-PKCδ pathway inhibits adipogenic differentiation

To investigate whether osteocytic Wnt7b inhibits adipogenic differentiation, we co-cultured Y4-Wnt7b and ST2 cells (1:4 ratio) in adipogenic medium for 7 days. While abundant lipid droplets formed in ST2 cells co-cultured with Y4-GFP controls, visualized by Oil Red O staining (Figure 3A), significantly fewer droplets were observed in the Y4-Wnt7b group. Furthermore, osteocytic Wnt7b downregulated the expression of key adipogenic transcription factors PPARγ (*Pparg*) and C/EBPα (*Cebpa*) (Figure 3B).

Next, we investigated whether inhibition of PKCδ signaling could restore the adipogenic differentiation of ST2 cells by using Rottlerin in the co-culture system. After 7 days of adipogenic induction, lipid droplet accumulation increased with Rottlerin concentration, largely reaching control (Y4-GFP) levels at 1 μM (Figure 3A). However, the lipid droplets were smaller and denser, which may be due to the continued inhibition of Wnt7b-PKCδ signaling by Rottlerin, thereby preventing the formation of larger lipid droplets. Consistent with this observation, 2 μM Rottlerin restored *Pparg* and *Cebpa* expression to control levels (Figure 3B).

The above results indicated that Rottlerin reverses the osteocytic Wnt7b-mediated inhibition of adipogenesis, suggesting that the Wnt7b-PKCδ signaling axis in osteocytes plays an important role in the negative regulation of adipogenesis.

3.4. Construction of Y4-Wnt 7b PCI3D modules

We fabricated 3D scaffolds using our in-house developed PCI3D system,[23] simultaneously printing PCL frameworks and cell-laden hydrogel bundles containing either Y4-GFP or Y4-Wnt7b cells mixed with ST2 cells at a 1:4 ratio (Figure 4A). GelMA hydrogel served as the bioink for the cell bundles. Utilizing its temperature-dependent viscosity, GelMA was uniformly extruded at 25°C using a

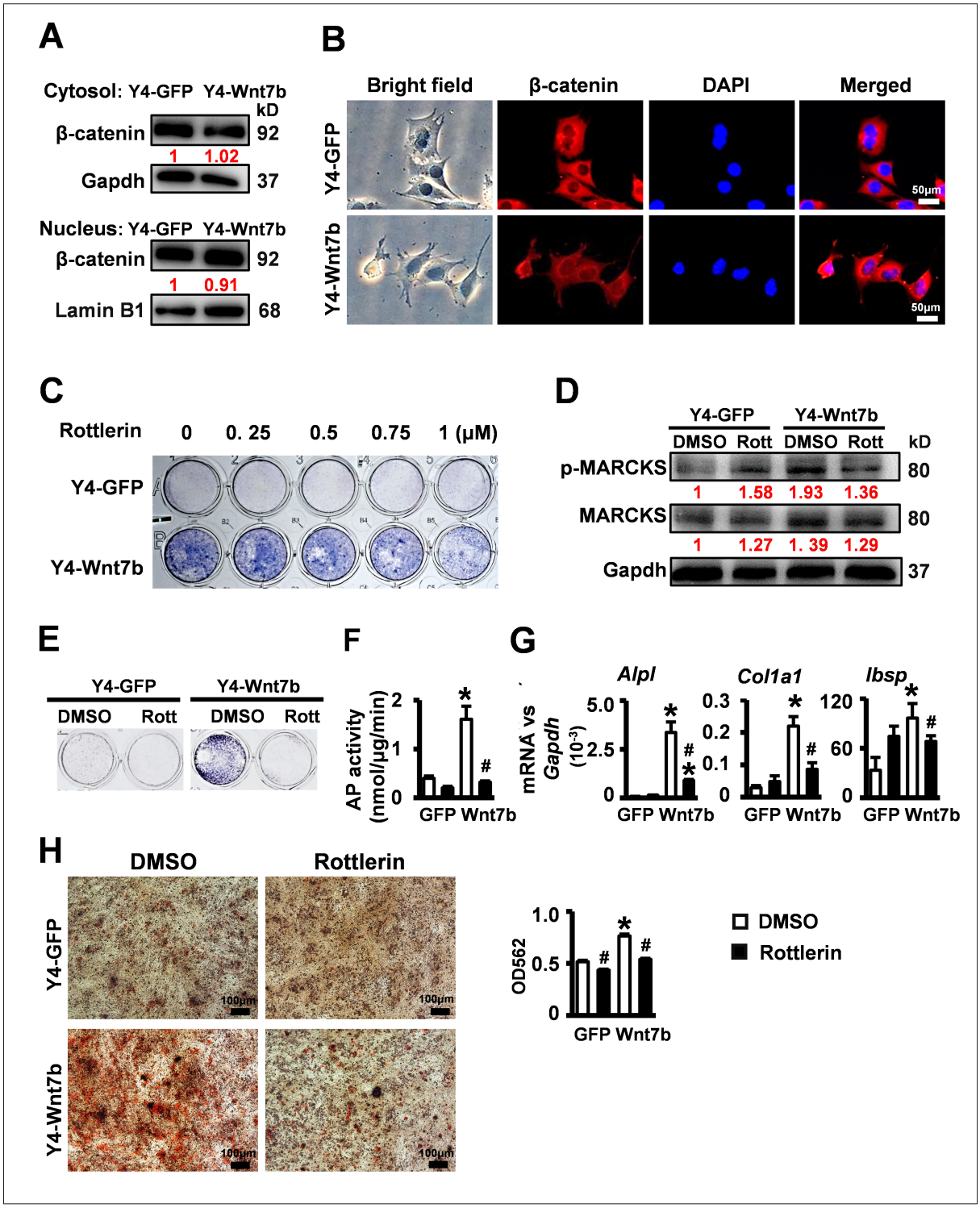

Figure 2. Osteocytic Wnt7b activates the PKCδ pathway to promote osteogenic differentiation. (A) Western blot analysis of β-catenin levels in cytoplasmic and nuclear extractions of Y4-Wnt7b and Y4-GFP cells. (B) Immunofluorescence staining of β-catenin (red) and nuclei (DAPI, blue) in Y4-Wnt7b cells. Scale bar = 50 μm. (C) AP staining in ST2 cells co-cultured with Y4-Wnt7b in different concentrations of Rottlerin. (D) Western blot analysis of phospho-MARCKS in the lysates of Y4-Wnt7b and Y4-GFP cells. (E–G) The effect of PKCδ signaling on osteocytic Wnt7b-induced osteoblast differentiation of ST2 cells was examined by AP staining (E), AP biochemical activity assay (F), and qPCR of osteoblast marker genes (G). (H) Alizarin Red S staining of mineralized nodulesof PKCδ signaling on the mineralization of osteocytic Wnt7b-induced osteoblast. Scale bar = 100 μm. *$p < 0.05$ versus Y4-GFP, #$p < 0.05$ versus DMSO control ($n = 3$) for panels F, G, H. Abbreviations: Bright field; DMSO, dimethyl sulfoxide.

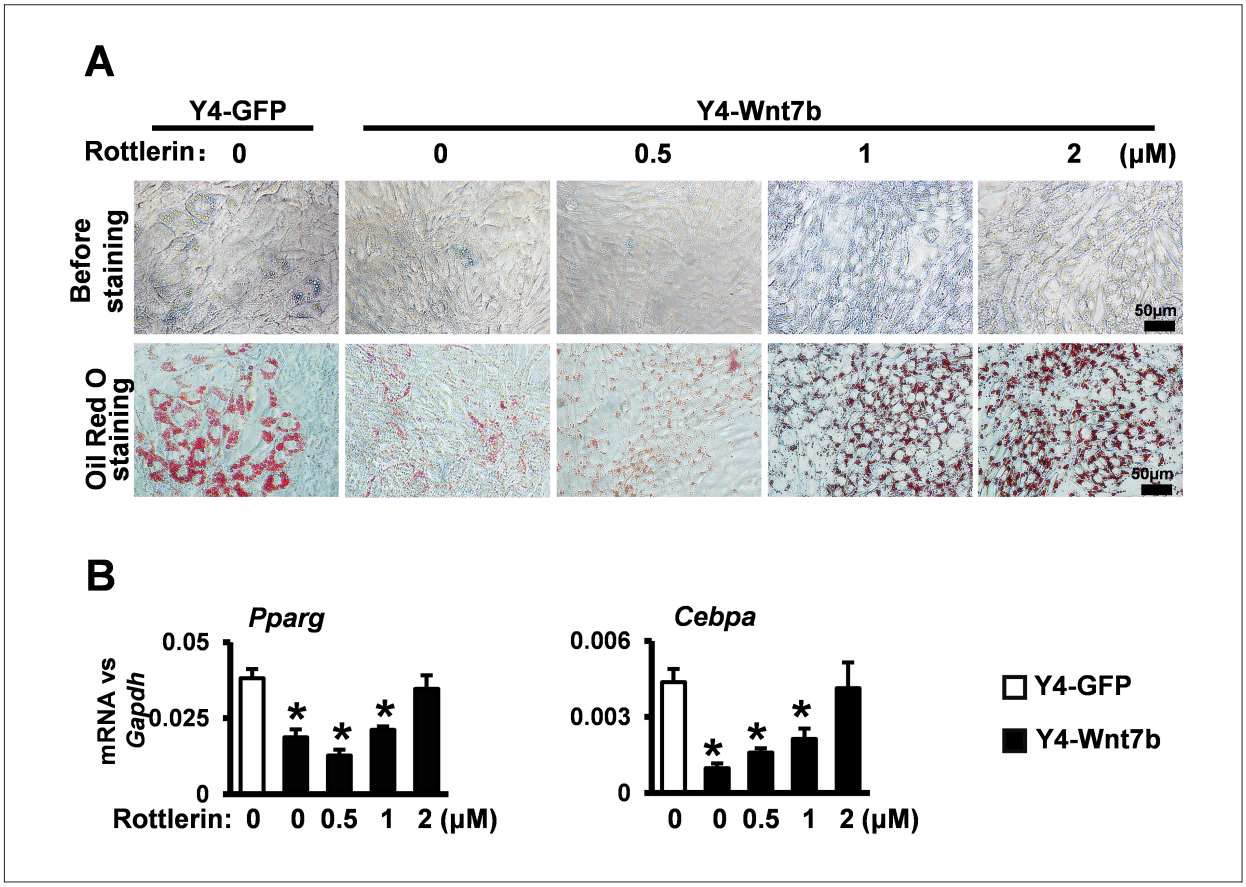

Figure 3. Osteocytic Wnt7b inhibits adipogenic differentiation via PKCδ. (A) Light microscopy and Oil Red O staining of lipid droplets in ST2 cells co-cultured with Y4-Wnt7b, with or without Rottlerin treatment (0.5–2 μM) for 7 days in adipogenic medium. Scale bars: 50 μm. (B) Expression of adipogenic transcription factors (*Pparg*, *Cebpa*) ($n = 3$); $^*p < 0.05$ versus Y4-GFP.

pneumatic syringe with a 300-μm nozzle diameter. PCL bundles and hydrogel bundles were printed in parallel with interconnecting 400-μm tunnels to facilitate nutrient transport and metabolite exchange. Y4-Wnt7b modules were fabricated by alternating printing cycles with blue-light crosslinking. The resulting modules exhibited stable mechanical support and interconnected pore architecture conducive to mass transport.

We first assessed the impact of Y4-Wnt7b on cell viability and proliferation within the PCI3D modules. Calcein AM/PI staining performed after 1, 4, and 7 days of culture revealed high cell viability over time (Figure 4B). Quantitative analysis (ImageJ) confirmed cell survival rates exceeding 97% in both Y4-GFP and Y4-Wnt7b groups throughout the 7-day period (Figure 4C). CCK-8 proliferation assays demonstrated steady cell growth within the modules. Notably, the Y4-Wnt7b group exhibited significantly higher proliferative activity compared to the Y4-GFP control group at Days 4 and 7 (Figure 4D). These results indicate that the PCI3D modules provide a supportive microenvironment for sustained cell survival and proliferation.

3.5. Osteocytic Wnt7b promotes osteogenic differentiation of ST2 cells in PCI3D modules

To assess the function of osteocytic Y4-Wnt7b in promoting osteogenic differentiation within a simulated *in vivo* 3D environment, we utilized PCI3D modules seeded with ST2 cells. Y4-Wnt7b- or Y4-GFP-expressing PCI3D modules were co-cultured with ST2 cells in growth medium for 7 or 14 days. Compared to the Y4-GFP controls, the Y4-Wnt7b group exhibited increased AP staining intensity (Figure 5A) and significantly enhanced AP activity (Figure 5B), indicating that Wnt7b potently augmented ST2 cell osteogenic differentiation within the 3D modules. Consistent with this, qPCR analysis revealed that Y4-Wnt7b significantly upregulated the expression of key osteogenic marker genes (*Alpl*, *Col1a1*, *Runx2*) at both

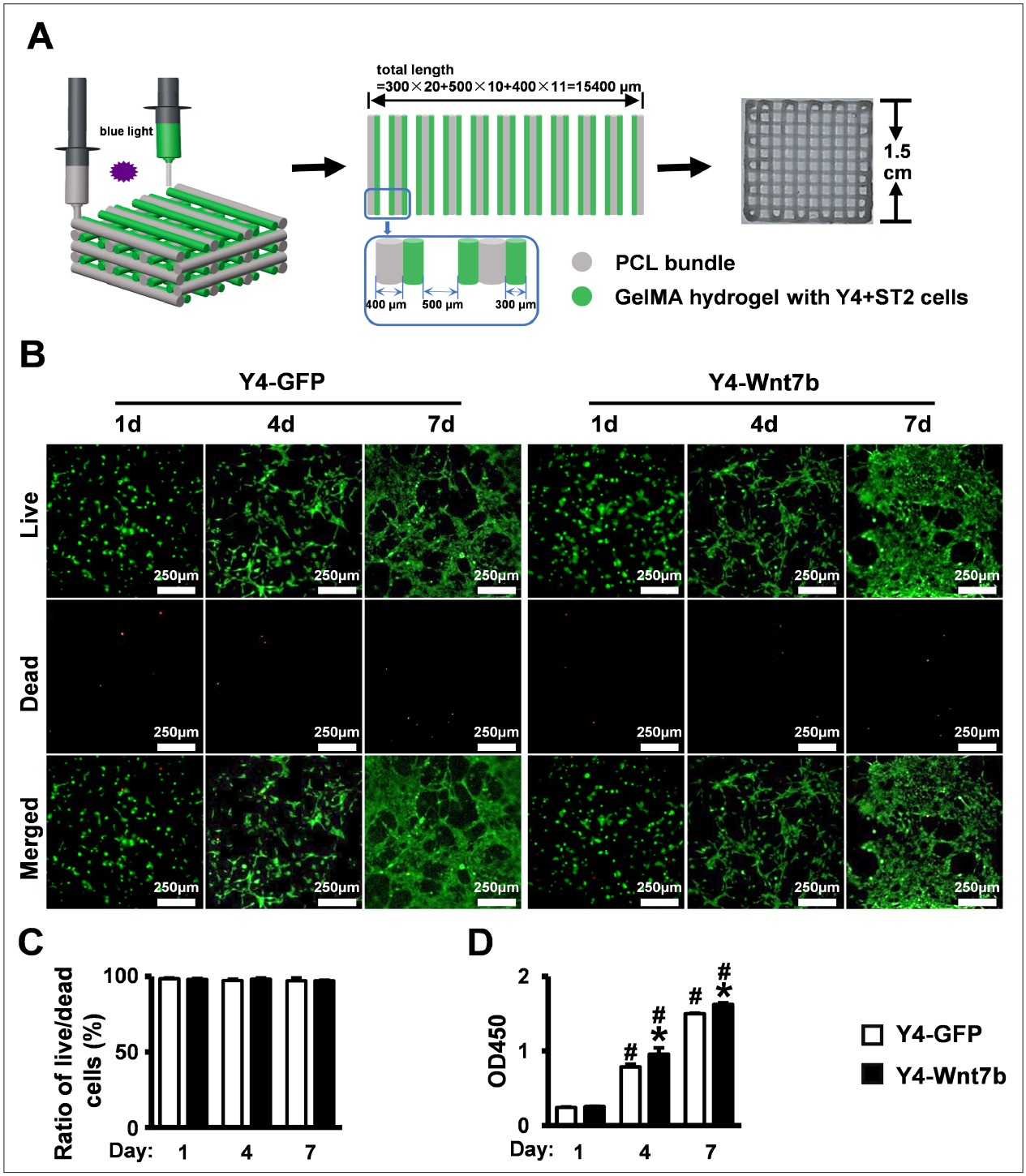

Figure 4. Cell viability and proliferation in 3D-printed PCI3D modules. (A) Schematic of PCI3D module fabrication: PCL bundles (gray) and cell-laden GelMA hydrogels (green) were alternately printed. (B) Calcein AM (live, green)/PI (dead, red) staining of Y4-Wnt7b and ST2 cells after 1, 4, and 7 days of co-culture. Scale bar: 250 μm. (C) Live/dead cell ratio was analyzed by ImageJ. (D) CCK-8 assay for proliferative activity. *$p < 0.05$ versus Y4-GFP; #$p < 0.05$ versus Day 1 by two-way ANOVA ($n = 3$). Abbreviations: ANOVA, analysis of variance; Calcein AM, calcein acetoxymethyl ester; GelMA, gelatin methacryloyl; PCL, poly-ε-caprolactone; PI, propidium iodide.

time points, with expression levels further elevated at Day 14 (Figure 5C).

We next evaluated the effect of Y4-Wnt7b on mineralization within the PCI3D modules. Following 7 days in growth medium, the modules were cultured in osteogenic medium containing ascorbic acid and β-glycerophosphate disodium for an additional 14 days. ARS staining demonstrated a marked increase in mineralized nodule formation in the Y4-Wnt7b modules compared to Y4-GFP controls, with a corresponding 1.8-fold increase in calcium deposition (Figure 5D). This further confirmed the potent role of osteocytic Wnt7b in driving osteogenic differentiation and matrix mineralization within the 3D environment.

Furthermore, analysis of adipogenic potential revealed that Y4-Wnt7b significantly downregulated the expression of adipogenic transcription factors (*Pparg*, *Cebpa*, *Fabp4*) compared to controls (Figure 5E). This suggests that Wnt7b may also inhibit adipogenic differentiation within the simulated *in vivo* environment provided by the PCI3D modules.

3.6. Osteocytic Wnt7b promotes osteoblast differentiation independent of microgravity-induced sclerostin production

We found that osteocytic Wnt7b significantly promotes ST2 cell osteogenic differentiation and mineralization through the Wnt noncanonical signaling pathway in both 2D and 3D cultures. To test whether this mechanism functions in weightless environments, we built the 3D-BWBM system that simulates a microgravity biological microenvironment using RCCS™ (Figure 6A). The system enables rapid examination of the effects of simulated *in vivo* Wnt7b on osteoblast differentiation within a 3D-printed scaffold. After 7 days of cultivation in HARV™, MLO-Y4 cells expressed higher levels of myocyte enhancer factor 2C (*Mef2c*), which can activate the expression of *Sost*, leading to sclerostin production.[36] The qPCR results demonstrated that the mRNA levels of both *Sost* and *Mef2c* were significantly upregulated (Figure 6B), indicating that the microgravity conditions were successfully simulated in osteocytes.

Mechanosensory osteocytes upregulate the expression of *Sost*/sclerostin under mechanical unloading[11,37,38] and downregulate it under mechanical loading,[11,37] respectively. Sclerostin is known to bind to Lrp5/6 and inhibit the Wnt canonical signaling pathway,[39] thereby suppressing bone formation both *in vitro* and *in vivo*. We placed PCI3D modules into HARV™ and suspended them for 7 days. Meanwhile, under microgravity conditions, osteocytic Wnt7b significantly maintained and even enhanced osteoblast differentiation of ST2 cells, as observed by AP staining and activity assays, compared to Y4-GFP controls (Figure 7A and B). The qPCR results revealed that Y4-Wnt7b significantly upregulated the expression of osteoblast marker genes *Alpl*, *Ibsp*, *Col1a1*, *Bglap*, and *Sp7* (Figure 7). These data confirm that osteocytic Wnt7b continues to promote osteogenic differentiation of ST2 cells under microgravity conditions, suggesting a strong protective effect of Wnt7b against weightlessness-induced bone loss.

However, osteocytic Wnt7b had the least effect on adipogenesis compared with the Y4-GFP group, with no significant difference in the expression of adipogenic transcription factors *Pparg*, *Cebpa*, or *Fabp4*, all of which tended to decrease under microgravity conditions (Figure 7D).

4. Discussion

Our study demonstrated that osteocyte-derived Wnt7b effectively promotes osteogenic differentiation of bone marrow stromal cells (ST2) and protects against microgravity-induced impairment of osteogenesis. This protective effect stems from Wnt7b's unique ability to activate the sclerostin-independent Wnt noncanonical PKCδ signaling pathway. We further established a functionalized 3D-bioprinted osteocyte niche (PCI3D module) and integrated it with a simulated microgravity platform (3D-BWBM) to validate Wnt7b's efficacy under conditions mimicking spaceflight.

The impetus for this investigation arose from our observation that elevated Wnt7b expression correlates with preserved bone mass in osteocyte-specific β-catenin activated (daβcat^{Ot}) mice subjected to tail suspension, a model of disuse osteoporosis and simulated microgravity. We mechanistically demonstrated that osteocytic Wnt7b potently induces osteoblast differentiation and mineralization in co-cultured ST2 cells, while concurrently suppressing adipogenesis by downregulating key adipogenic transcription factors *Pparg* and *Cebpa*. Critically, the specific PKCδ inhibitor Rottlerin inhibited Wnt7b-induced osteogenesis and reversed its inhibition of adipogenesis in ST2 cells (Figure 7E), unequivocally establishing the PKCδ pathway as the central mediator of Wnt7b's dual function. This positions Wnt7b as a potent intrinsic physiological osteogenic microenvironmental factor (POME) and a compelling candidate for BTE applications.

Beyond sclerostin upregulation, our gene expression analysis within the 3D-BWBM system confirmed a comprehensive microgravity response. We observed the expected upregulation of *Sost* and its transcriptional

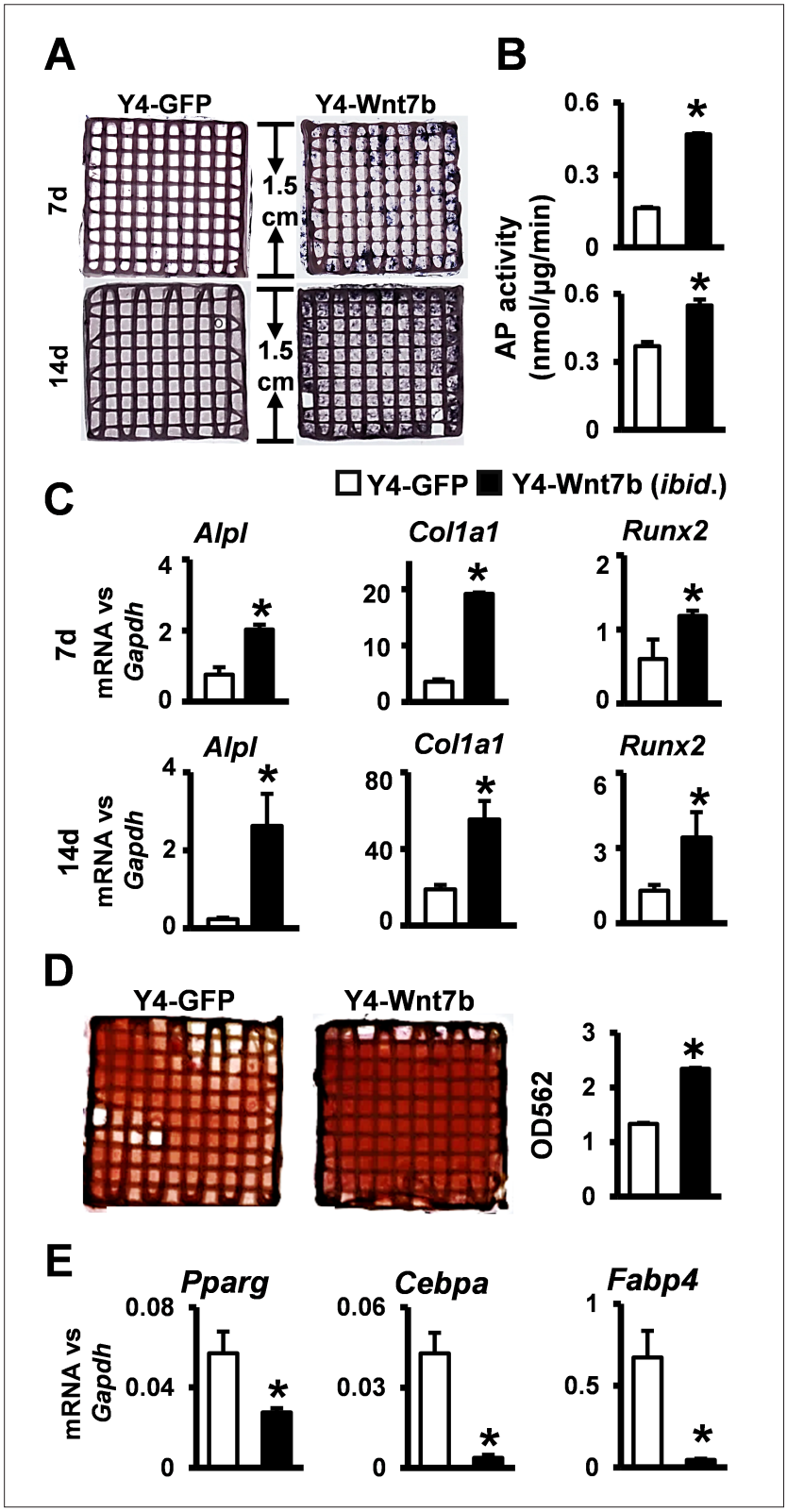

Figure 5. Osteogenic and anti-adipogenic effects of osteocytic Wnt7b in 3D modules. (A–C) AP staining (A), AP activity (B), and osteoblast marker gene expression (C) of Y4-Wnt7b on osteoblast differentiation of ST2 cells in PCI3D modules cultured for 7 and 14 days. (D) Alizarin Red S staining of mineralization. (E) Adipogenic gene expression (*Pparg, Cebpa, Fabp4*). *$p < 0.05$ versus Y4-GFP by Student's *t*-test; $n = 3$.

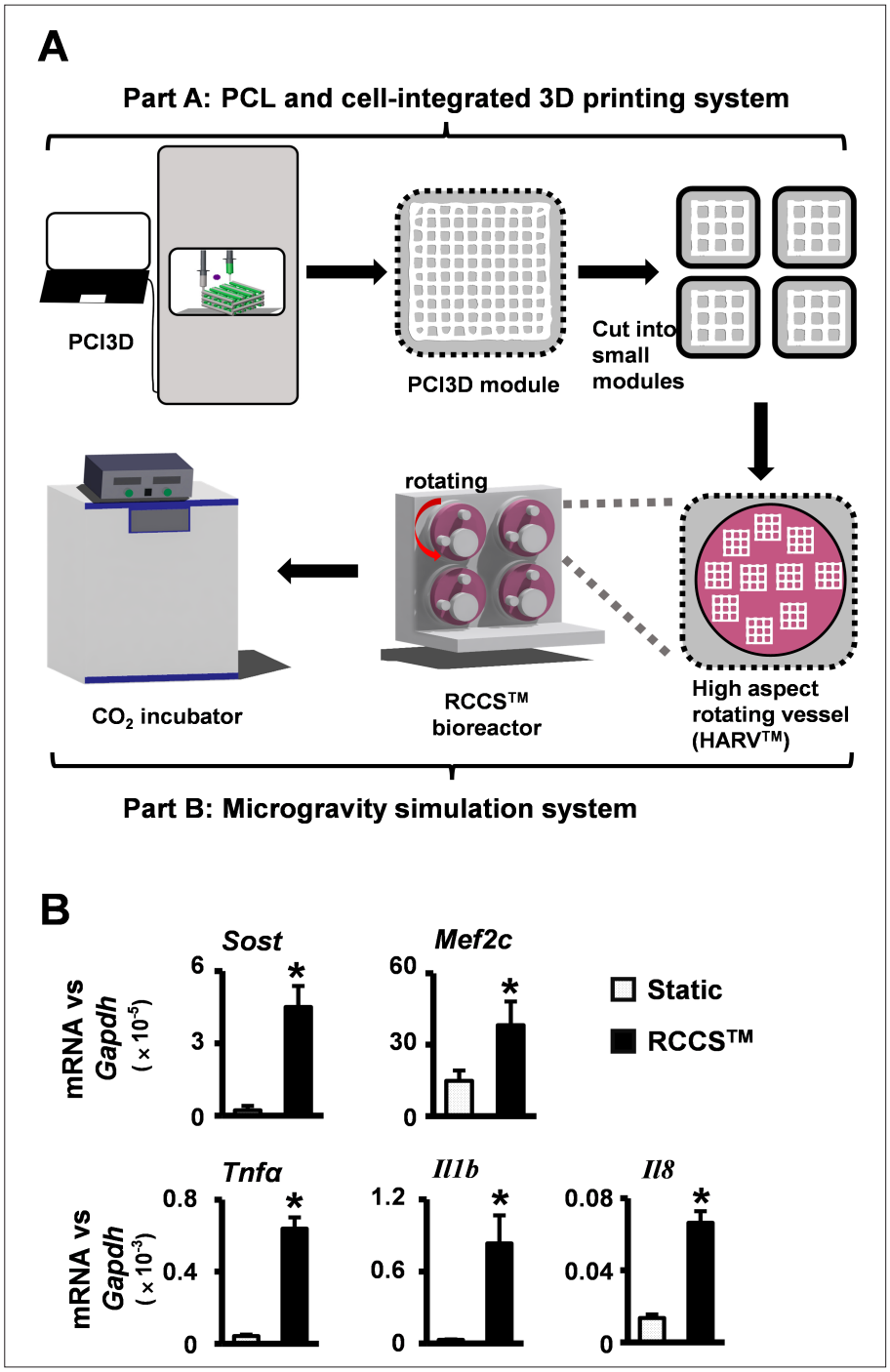

Figure 6. The 3D-BWBM system for microgravity simulation. (A) Diagram of the 3D-BWBM system combining PCI3D printing (Part A) and NASA's RCCS™ bioreactor (Part B). (B) Reverse transcription quantitative polymerase chain reaction (RT-qPCR) results of Sost (sclerostin), Mef2c, Il1b, Tnfa, and Il8 in PCI3D modules under static or microgravity conditions. *$p < 0.05$ versus Y4-GFP by Student's *t*-test; $n = 3$. Abbreviations: 3D-BWBM, 3D biomimetic weightless bio-microenvironmental system; NASA, National Aeronautics and Space Administration; PCI3D, PCL and cell-integrated 3D-printed; RCCS™, Rotary Cell Culture System; RT-qPCR, reverse transcription quantitative polymerase chain reaction.

regulator *Mef2c*.[36] Furthermore, elevated pro-inflammatory cytokines (*Tnfa*, *Il1b*) are consistent with the inflammatory and catabolic state triggered by microgravity,[40] potentially contributing to enhanced osteoclastogenesis, as evidenced by an increased *Rankl/Opg* ratio. The disruption of mechanotransduction cascades in microgravity likely impairs normal osteocyte function, biasing stromal cell fate towards adipogenesis at the expense of osteogenesis.[41] Thus, the 3D-BWBM system robustly recapitulates key

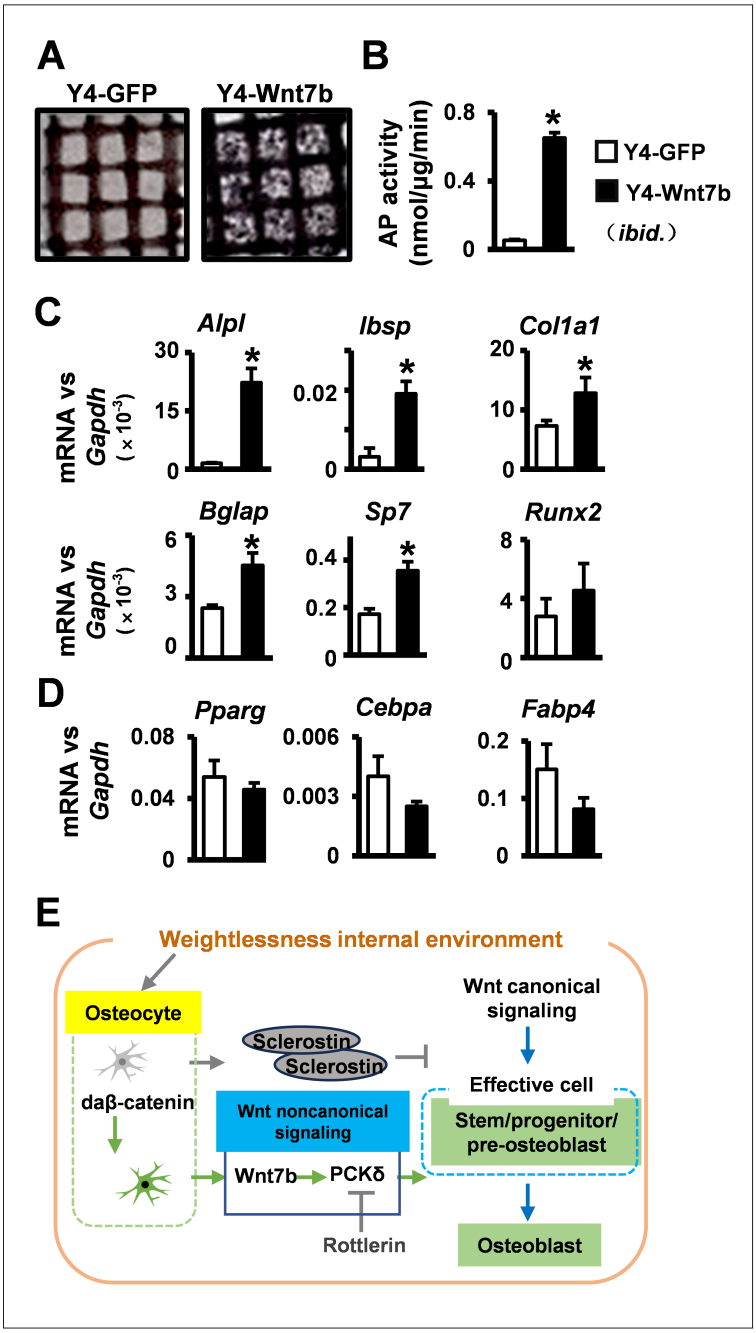

Figure 7. Osteocytic Wnt7b protects osteogenesis under microgravity. (A–C) Alkaline phosphatase (AP) staining (A), AP activity (B), and osteoblast marker gene expression (C) in PCI3D modules cultured in 3D-BWBM for 7 days. (D) Adipogenic gene expression under microgravity conditions. (E) Proposed model: Wnt7b-PKCδ signaling bypasses sclerostin-mediated inhibition of canonical Wnt to promote osteogenesis. *$p < 0.05$ vs. Y4-GFP; $n = 3$. Abbreviation: 3D-BWBM, 3D biomimetic weightless biomicroenvironmental system.

pathophysiological features of weightlessness-induced bone loss.

Osteocytic Wnt7b represents a novel POME acting through the Wnt noncanonical PKCδ pathway, distinguishing it from our previous reports on osteogenic microenvironments, such as osteocyte-activated canonical Wnt signaling,[25,30,31] decellularized matrix,[29] Dll4,[23] and BMP7,[42] all of which operate through different mechanisms. Importantly, Wnt7b-PKCδ signaling bypasses sclerostin-mediated inhibition of the canonical Wnt pathway, a major limitation of current anabolic strategies like Romosozumab (sclerostin antibody) and potentially Teriparatide (parathyroid hormone, PTH1-34).[43] While the anabolic mechanism of abaloparatide (parathyroid hormone-related protein, PTHrP) remains unclear, our findings highlight Wnt noncanonical signaling—particularly via osteocytic Wnt7b-PKCδ—as a previously unexplored and highly promising target for counteracting disuse osteoporosis. Currently, no therapies specifically target Wnt noncanonical signaling for weightlessness-induced bone loss, nor utilize osteocytes engineered with this pathway as functional cells within 3D constructs to promote osteogenesis under microgravity.

While our data robustly support Wnt7b's protective role against microgravity-impaired osteogenesis via sclerostin-independent PKCδ activation, definitive proof of causality necessitates further *in vivo* studies. Conditional knockout of Wnt7b specifically in the osteocytes of daβcat^{Ot} mice, or its neutralization via antibodies, will establish whether Wnt7b is indispensable for the observed bone-sparing effects. We are currently designing these experiments using tail-suspended mouse models. Additionally, testing if osteocyte-specific Wnt7b overexpression alone (without concomitant β-catenin activation) replicates the protective phenotype in wild-type mice will further isolate its intrinsic therapeutic potential.

Both Wnt/β-catenin and noncanonical pathways (especially the Wnt-Ca^{2+} pathway) generally promote osteoblastogenesis while inhibiting adipogenesis.[44] PKC isoforms exhibit complex, sometimes opposing, roles in adipogenesis.[45–47] Fleming et al.[48] demonstrated that PKC-α, -δ, and -μ inhibit adipogenesis, while PKC-ε promotes it. Our results demonstrate that osteocytic Wnt7b inhibits adipogenesis by downregulating the transcription of the adipogenic transcription factors *Pparg* and *Cebpa* through PKCδ signaling under 2D and simulated 3D conditions. Although microgravity typically enhances adipogenesis in human mesenchymal stem cells,[34] the expression of adipogenic factors tended to decrease in our 3D-BWBM system containing Wnt7b osteocytes. This suggests that the dual function of the Wnt7b-PKCδ axis—of promoting osteogenesis while suppressing adipogenesis—may be particularly well-suited for preventing the skewed lineage commitment characteristic of weightlessness-induced bone loss.

Interestingly, unlike Wnt canonical signaling, osteocytic Wnt7b did not significantly alter the expression of osteoclast regulators (*Rankl, Opg,* and *Rankl/Opg* ratio) under static culture. However, microgravity itself robustly increased the *Rankl/Opg* ratio. Intriguingly, osteocytic Wnt7b further elevated this ratio to control Y4-GFP under microgravity (Figure S5, Supporting Information), suggesting that Wnt7b may paradoxically enhance osteoclast differentiation in disuse conditions. While counterintuitive for an anabolic process, enhanced bone resorption could potentially contribute to bone remodeling by recruiting mesenchymal stem cells to resorption sites, ultimately promoting subsequent bone formation.[49] The net effect *in vivo* warrants further investigation.

Current countermeasures against spaceflight bone loss, including exercise, nutrition,[50] and drugs (e.g., PTH[51]), face significant challenges in terms of their efficacy and practicality in microgravity. Antibodies targeting sclerostin displayed promise but can only partially mitigate bone loss in partially weight-bearing mice.[52] Crucially, sclerostin production persists during prolonged spaceflight or bed rest, raising concerns about the long-term efficacy and potential side effects of continuous antibody administration. Clinically effective PTH exhibits region-specific and load-dependent responses under weightlessness conditions,[51] and an ultra-high dose (80 μg/kg/day) of PTH was required for protection in one study,[39] posing osteosarcoma risks.[53] PTHrP promotes bone formation but may not directly drive osteogenic differentiation of progenitor cells.[54] Therefore, novel anabolic strategies are urgently needed. Wnt7b, acting independently of *Sost*/sclerostin and effectively promoting osteogenesis even in its presence, emerges as a highly promising candidate for protecting weightlessness-induced bone loss.

The 3D-BWBM system represents a significant technological innovation, integrating our in-house PCI3D bioprinting with the established RCCS™ bioreactor. This system enables rapid assessment of potential bone homeostasis regulators under simulated microgravity within a biomimetic 3D microenvironment. Current microgravity tissue engineering models, whether 2D[55] or 3D,[56–59] often lack the interconnected tunnel structures essential for efficient nutrient/oxygen/metabolite exchange, limiting cell viability, and function deep within constructs. Unlike conventional BTE scaffolds, where cell activity is often confined to surfaces,[60] our PCI3D module features precisely printed, uniform tunnels

(~500 μm diameter), facilitating excellent nutrient/metabolite transport, and closely mimicking the *in vivo* physiological conditions.[23] The RCCS™ rotation provides simulated microgravity while ensuring sufficient mass transport for 3D tissue culture.[59] Using this advanced system, we confirmed that osteocytic Wnt7b robustly promotes osteogenic differentiation of stromal cells under microgravity, consistent with our *in vivo* finding of increased lumbar BMD in protected mice.

Furthermore, advances in BTE and 3D printing enable precise control over implant shape and structure.[61,62] Integrating bioactive microenvironments with printing materials is key to enhancing implant functionality.[63,64] Bioprinting combined with specific cellular microenvironments offers a powerful strategy for creating "smart" constructs that mimic the microenvironment to support stem cell proliferation, migration, and differentiation.[65] Our approach of co-printing Wnt7b-expressing osteocytes with stromal cells within a PCL-GelMA scaffold not only ensured excellent cell survival and proliferation but also effectively supported osteogenic differentiation and mineralization. This underscores the significant potential of osteocytic Wnt7b as a molecular target and bioactive component for: (i) reconstructing bone integrity in astronauts, long-term bedridden patients, or those with paralysis to prevent disuse osteoporosis; and (ii) serving as a novel bioactive material for repairing critical-sized bone defects.

5. Conclusion

In this study, we demonstrated that osteoblast-derived Wnt7b effectively counteracted microgravity-induced bone loss by activating the sclerostin-independent PKCδ pathway, which promotes osteogenesis while inhibiting adipogenesis in bone marrow stromal cells. Through innovative 3D bioprinting technology, we developed a functionalized osteocyte niche (PCI3D) and validated its efficacy in a simulated microgravity system (3D-BWBM), confirming that Wnt7b exerts a protective effect towards weightlessness-induced bone loss. Our findings highlight Wnt7b-PKCδ signaling as a novel target for the treatment of disuse osteoporosis and establish a scalable bioengineering strategy for bone regeneration in extreme environments. Future *in vivo* studies will further elucidate its translational potential in spaceflight and clinical applications.

Acknowledgments

The authors are grateful to Lynda Bonewald for kindly providing the MLO-Y4 cell line.

Funding

This work was supported by the National Natural Science Foundation of China (grant numbers: 82471909, 81672118, and 32101053) and the Chongqing Natural Science Foundation (grant numbers: CSTB2022NSCQ-LZX0048 and CSTB2023NSCQ-MSX0424).

Conflict of interest

The authors declare they have no competing interests.

Author contributions

Conceptualization: Xing Liu, Xiaolin Tu
Formal analysis: Jinling Zhang, Pengtao Wang, Xiaoling Chen, Yangxi Liu, Bo He
Investigation: Jinling Zhang, Pengtao Wang, Xiaoling Chen, Saima Khan, Haiping Ouyang
Methodology: Jinling Zhang, Pengtao Wang
Writing–original draft: Jinling Zhang, Pengtao Wang, Xing Liu
Writing–review & editing: Jinling Zhang, Pengtao Wang, Xian Li, Xing Liu, Xiaolin Tu

Ethics approval and consent to participate

All animal procedures were approved by the Institutional Animal Care and Use Committee of Chongqing Medical University (IACUC-CQMU-2024-0277).

Consent for publication

Not applicable.

Availability of data

Data presented in this study are available upon request from the corresponding authors.

Further disclosure

This study was presented orally by Jinling Zhang at the 2023 China Biomaterials Conference in October 2023.

References

1. McCarthy ID. Fluid shifts due to microgravity and their effects on bone: a review of current knowledge. *Ann Biomed Eng.* 2005;33:95-103.
doi: 10.1007/s10439-005-8967-6

2. Lang T, LeBlanc A, Evans H, Lu Y, Genant H, Yu A. Cortical and trabecular bone mineral loss from the spine and hip in long-duration spaceflight. *J Bone Miner Res.* 2004;19:1006-1012.
doi: 10.1359/jbmr.040307

3. Durnova G, Kaplansky A, Morey-Holton E. Histomorphometric study of tibia of rats exposed aboard American spacelab life sciences 2 shuttle mission. *J Gravit Physiol.* 1996;3:80-81.

4. Carmeliet G, Bouillon R. The effect of microgravity on morphology and gene expression of osteoblasts in vitro. *Faseb J.* 1999; 13(Suppl):S129-S134. doi: 10.1096/fasebj.13.9001.s129

5. Smith SM, Wastney ME, O'Brien KO, et al. Bone markers, calcium metabolism, and calcium kinetics during extended-duration space flight on the mir space station. *J Bone Miner Res.* 2005; 20:208-218. doi: 10.1359/jbmr.041105

6. Vico L, Hargens A. Skeletal changes during and after spaceflight. *Nat Rev Rheumatol.* 2018;14: 229-245. doi: 10.1038/nrrheum.2018.37

7. Robling AG, Bonewald LF. The osteocyte: new insights. *Annu Rev Physiol.* 2020;82:485-506. doi: 10.1146/annurev-physiol-021119-034332

8. Delgado-Calle J, Bellido T. The osteocyte as a signaling cell. *Physiol Rev.* 2022;102:379-410. doi: 10.1152/physrev.00043.2020

9. Spatz JM, Wein MN, Gooi JH, et al. The Wnt inhibitor sclerostin is up-regulated by mechanical unloading in osteocytes in vitro. *J Biol Chem.* 2015;290:16744-16758. doi: 10.1074/jbc.M114.628313

10. Lin C, Jiang X, Dai Z, et al. Sclerostin mediates bone response to mechanical unloading through antagonizing Wnt/beta-catenin signaling. *J Bone Miner Res.* 2009;24:1651-1661. doi: 10.1359/jbmr.090411

11. Tu X, Rhee Y, Condon KW, et al. Sost downregulation and local Wnt signaling are required for the osteogenic response to mechanical loading. *Bone.* 2012;50:209-217. doi: 10.1016/j.bone.2011.10.025

12. Bloomfield SA, Martinez DA, Boudreaux RD, Mantri AV. Microgravity stress: bone and connective tissue. *Compr Physiol.* 2016;6:645-686. doi: 10.1002/cphy.c130027

13. Tu X, Joeng KS, Nakayama KI, et al. Noncanonical Wnt signaling through G protein-linked PKCdelta activation promotes bone formation. *Dev Cell.* 2007;12:113-127. doi: 10.1016/j.devcel.2006.11.003

14. Chen J, Tu X, Esen E, et al. WNT7B promotes bone formation in part through mTORC1. *PLoS Genet.* 2014;10:e1004145. doi: 10.1371/journal.pgen.1004145

15. Cui Y, Liu W, Zhao S, Zhao Y, Dai J. Advances in microgravity directed tissue engineering. *Adv Healthc Mater.* 2023;12:e2202768. doi: 10.1002/adhm.202202768

16. Bradbury P, Wu H, Choi JU, et al. Modeling the impact of microgravity at the cellular level: implications for human disease. *Front Cell Dev Biol.* 2020;8;96. doi: 10.3389/fcell.2020.00096

17. Silvani G, Basirun C, Wu H, et al. A 3D-bioprinted vascularized glioblastoma-on-a-chip for studying the impact of simulated microgravity as a novel pre-clinical approach in brain tumor therapy. *Adv Ther.* 2021;4:2100106. doi: 10.1002/adtp.202100106

18. Van Ombergen A, Chalupa-Gantner F, Chansoria P, et al. 3D bioprinting in microgravity: opportunities, challenges, and possible applications in space. *Adv Healthc Mater.* 2023;12:e2300443. doi: 10.1002/adhm.202300443

19. Kang HW, Lee SJ, Ko IK, et al. A 3D bioprinting system to produce human-scale tissue constructs with structural integrity. *Nat Biotechnol.* 2016;34:312-319. doi: 10.1038/nbt.3413

20. Mochi F, Scatena E, Rodriguez D, Ginebra M-P, Del Gaudio C. Scaffold-based bone tissue engineering in microgravity: potential, concerns and implications. *NPJ Microgravity.* 2022;8:45. doi: 10.1038/s41526-022-00236-1

21. Tu X, Delgado-Calle J, Condon KW, et al. Osteocytes mediate the anabolic actions of canonical Wnt/β-catenin signaling in bone. *Proc Natl Acad Sci USA.* 2015;112:E478-E486. doi: 10.1073/pnas.1409857112

22. Morey-Holton ER, Globus RK. Hindlimb unloading of growing rats: a model for predicting skeletal changes during space flight. *Bone.* 1998;22:83S-88S. doi: 10.1016/S8756-3282(98)00019-2

23. Wang P, Wang X, Wang B, Li X. 3D printing of osteocytic Dll4 integrated with PCL for cell fate determination towards osteoblasts in vitro. *Bio-Design Manuf.* 2022;5: 497-511. doi: 10.1007/s42242-022-00196-1

24. Gong W, Li M, Zhao L, et al. Sustained release of a highly specific GSK3β inhibitor SB216763 in the PCL scaffold creates an osteogenic niche for osteogenesis, anti-adipogenesis, and potential angiogenesis. *Front Bioeng Biotechnol.* 2023;11:1215233. doi: 10.3389/fbioe.2023.1215233

25. Liu Y, Ruan X, Li J, et al. The osteocyte stimulated by Wnt agonist SKL2001 is a safe osteogenic niche improving bioactivities in a polycaprolactone and cell integrated 3d module. *Cells.* 2022;11:831. doi: 10.3390/cells11050831

26. Yuste I, Luciano FC, González-Burgos E, Lalatsa A, Serrano DR. Mimicking bone microenvironment: 2D and 3D in vitro models of human osteoblasts. *Pharmacol Res.* 2021;169:105626. doi: 10.1016/j.phrs.2021.105626

27. Zhou Z, Pang Y, Ji J, et al. Harnessing 3D in vitro systems to model immune responses to solid tumours: a step towards improving and creating personalized immunotherapies. *Nat Rev Immunol.* 2024;24:18-32.

doi: 10.1038/s41577-023-00896-4

28. Hammond TG, Hammond JM. Optimized suspension culture: the rotating-wall vessel. *Am J Physiol Renal Physiol.* 2001;281:F12-F25.
doi: 10.1152/ajprenal.2001.281.1.F12

29. Wang X, Tu X, Ma Y, et al. Wnt3a-induced ST2 decellularized matrix ornamented PCL scaffold for bone tissue engineering. *Biocell.* 2022;46:2089-2099.
doi: 10.32604/biocell.2022.020069

30. Luo Y, Liu Y, Wang B, Tu X. CHIR99021-treated osteocytes with Wnt activation in 3D-printed module form an osteogenic microenvironment for enhanced osteogenesis and vasculogenesis. *Int J Mol Sci.* 2023;24:6008.
doi: 10.3390/ijms24066008

31. Zhang J, Zhang Y, Chen J, Gong W, Tu X. The osteocyte with SB216763-activated canonical Wnt signaling constructs a multifunctional 4D intelligent osteogenic module. *Biomolecules.* 2024;14:354.
doi: 10.3390/biom14030354

32. Liu G, Chen J, Wang X, Liu Y, Ma Y, Tu X. Functionalized 3D-printed ST2/gelatin methacryloyl/polcaprolactone scaffolds for enhancing bone regeneration with vascularization. *Int J Mol Sci.* 2022;23:8347.
doi: 10.3390/ijms23158347

33. Abraham RT. Identification of TOR signaling complexes: more TORC for the cell growth engine. *Cell.* 2002;111:9-12.
doi: 10.1016/s0092-8674(02)01009-7

34. Gschwendt M, Muller HJ, Kielbassa K, et al. Rottlerin, a novel protein kinase inhibitor. *Biochem Biophys Res Commun.* 1994;199:93-98.
doi: 10.1006/bbrc.1994.1199

35. Aderem A. The MARCKS brothers: a family of protein kinase C substrates. *Cell.* 1992;71:713-716.
doi: 10.1016/0092-8674(92)90546-o

36. Leupin O, Kramer I, Collette NM, et al. Control of the SOST bone enhancer by PTH using MEF2 transcription factors. *J Bone Miner Res.* 2007;22:1957-1967.
doi: 10.1359/jbmr.070804

37. Robling AG, Niziolek PJ, Baldridge LA, et al. Mechanical stimulation of bone in vivo reduces osteocyte expression of Sost/sclerostin. *J Biol Chem.* 2008;283:5866-5875.
doi: 10.1074/jbc.M705092200

38. Spatz JM, Fields EE, Yu EW, et al. Serum sclerostin increases in healthy adult men during bed rest. *J Clin Endocrinol Metab.* 2012;97:E1736-E1740.
doi: 10.1210/jc.2012-1579

39. Uda Y, Azab E, Sun N, Shi C, Pajevic PD. Osteocyte mechanobiology. *Curr Osteoporos Rep.* 2017;15:318-325.
doi: 10.1007/s11914-017-0373-0

40. Metzger CE, Anand Narayanan S, Phan PH, Bloomfield SA. Hindlimb unloading causes regional loading-dependent changes in osteocyte inflammatory cytokines that are modulated by exogenous irisin treatment. *NPJ Microgravity.* 2020;6:28.
doi: 10.1038/s41526-020-00118-4

41. Lau P, Vico L, Rittweger J. Dissociation of bone resorption and formation in spaceflight and simulated microgravity: potential role of myokines and osteokines? *Biomedicines.* 2022;10:342.
doi: 10.3390/biomedicines10020342.

42. Zhang Y, Zhao Y, Xie Z, Li M, Liu Y, Tu X. Activating Wnt/β-catenin signaling in osteocytes promotes osteogenic differentiation of BMSCs through BMP-7. *Int J Mol Sci.* 2022;23:16045.
doi: 10.3390/ijms232416045

43. Sapir-Koren R, Livshits G. Osteocyte control of bone remodeling: is sclerostin a key molecular coordinator of the balanced bone resorption-formation cycles? *Osteoporos Int.* 2014;25:2685-2700.
doi: 10.1007/s00198-014-2808-0

44. Yuan Z, Li Q, Luo S, et al. PPARγ and Wnt signaling in adipogenic and osteogenic differentiation of mesenchymal stem cells. *Curr Stem Cell Res Ther.* 2016;11:216-225.
doi: 10.2174/1574888x10666150519093429

45. Borner C, Guadagno SN, Fabbro D, et al. Expression of four protein kinase C isoforms in rat fibroblasts. Differential alterations in ras-, src-, and fos-transformed cells. *J Biol Chem.* 1992; 267:12900-12910.
doi: 10.1016/S0021-9258(18)42360-5

46. Ohno S, Akita Y, Hata A, et al. Structural and functional diversities of a family of signal transducing protein kinases, protein kinase C family; two distinct classes of PKC, conventional cPKC and novel nPKC. *Adv Enzyme Regul.* 1991;31:287-303.
doi: 10.1016/0065-2571(91)90018-h

47. Hug H, Sarre TF. Protein kinase C isoenzymes: divergence in signal transduction? *Biochem J.* 1993;291(Pt 2): 329-343.
doi: 10.1042/bj2910329

48. Fleming I, MacKenzie SJ, Vernon RG, et al. Protein kinase C isoforms play differential roles in the regulation of adipocyte differentiation. *Biochem J.* 1998;333(Pt 3):719-727.
doi: 10.1042/bj3330719

49. Tang Y, Wu X, Lei W, et al. TGF-beta1-induced migration of bone mesenchymal stem cells couples bone resorption with formation. *Nat Med.* 2009;15:757-765.
doi: 10.1038/nm.1979

50. Smith SM, Heer MA, Shackelford LC, et al. Benefits for bone from resistance exercise and nutrition in long-duration spaceflight: evidence from biochemistry and densitometry. *J Bone Miner Res.* 2012;27:1896-1906.
doi: 10.1002/jbmr.1647

51. Halloran BP, Bikle DD, Harris J, et al. Regional responsiveness of the tibia to intermittent administration of parathyroid

hormone as affected by skeletal unloading. *J Bone Miner Res.* 1997;12:1068-1074.
doi: 10.1359/jbmr.1997.12.7.1068

52. Spatz JM, Ellman R, Cloutier AM, et al. Sclerostin antibody inhibits skeletal deterioration in mice exposed to partial weight-bearing. *Life Sci Space Res (Amst).* 2017;12: 32-38.
doi: 10.1016/j.lssr.2017.01.001

53. Barbehenn EK, Lurie P, Wolfe SM. Osteosarcoma risk in rats using PTH 1-34. *Trends Endocrinol Metab.* 2001; 12:383.
doi: 10.1016/s1043-2760(01)00489-1

54. Hildreth BE, 3rd, Werbeck JL, Thudi NK, et al. PTHrP 1-141 and 1-86 increase in vitro bone formation. *J Surg Res.* 2010;162:e9-e17.
doi: 10.1016/j.jss.2010.02.023

55. Costa-Almeida R, Granja PL, Gomes ME. Gravity, tissue engineering, and the missing link. *Trends Biotechnol.* 2018;36:343-347.
doi: 10.1016/j.tibtech.2017.10.017

56. Artegiani B, Clevers H. Use and application of 3D-organoid technology. *Hum Mol Genet.* 2018;27:R99-R107.
doi: 10.1093/hmg/ddy187

57. He J, Zhang X, Xia X, et al. Organoid technology for tissue engineering. *J Mol Cell Biol.* 2020;12:569-579.
doi: 10.1093/jmcb/mjaa012

58. Yi SA, Zhang Y, Rathnam C, Pongkulapa T, Lee KB. Bioengineering approaches for the advanced organoid research. *Adv Mater.* 2021;33:e2007949.
doi: 10.1002/adma.202007949

59. Hwang YS, Cho J, Tay F, et al. The use of murine embryonic stem cells, alginate encapsulation, and rotary microgravity bioreactor in bone tissue engineering. *Biomaterials.* 2009;30:499-507.
doi: 10.1016/j.biomaterials.2008.07.028

60. Avitabile E, Fusco L, Minardi S, et al. Bioinspired scaffold action under the extreme physiological conditions of simulated space flights: osteogenesis enhancing under microgravity. *Front Bioeng Biotechnol.* 2020;8:722.
doi: 10.3389/fbioe.2020.00722

61. Hann SY, Cui H, Esworthy T, et al. Dual 3D printing for vascularized bone tissue regeneration. *Acta Biomater.* 2021;123:263-274.
doi: 10.1016/j.actbio.2021.01.012

62. Zhou F, Hong Y, Liang R, et al. Rapid printing of bio-inspired 3D tissue constructs for skin regeneration. *Biomaterials.* 2020;258:120287.
doi: 10.1016/j.biomaterials.2020.120287

63. Zhang W, Shi W, Wu S, et al. 3D printed composite scaffolds with dual small molecule delivery for mandibular bone regeneration. *Biofabrication.* 2020;12:035020.
doi: 10.1088/1758-5090/ab906e

64. Chen S, Shi Y, Zhang X, Ma J. Evaluation of BMP-2 and VEGF loaded 3D printed hydroxyapatite composite scaffolds with enhanced osteogenic capacity in vitro and in vivo. *Mater Sci Eng C Mater Biol Appl.* 2020;112:110893.
doi: 10.1016/j.msec.2020.110893

65. West-Livingston LN, Park J, Lee SJ, Atala A, Yoo JJ. The role of the microenvironment in controlling the fate of bioprinted stem cells. *Chem Rev.* 2020; 120:11056-11092.
doi: 10.1021/acs.chemrev.0c00126

ACCSCIENCE PUBLISHING

International Journal of Bioprinting

RESEARCH ARTICLE

3D printing of the keloid scar using tunable GelMA-based bioinks for skin fibrosis modeling

Laurensia Danis Anggradita[1,2†], Murugaiyan Manimohan[3†], Sung Sik Hur[1†], Taekyun Kim[1,2], Wonjong Seon[1,2], Mohamed Aboobucker Sithique[3], Seung Min Nam[4*], and Yongsung Hwang[1,2*]

[1]Department of Integrated Biomedical Science, Soonchunhyang Institute of Medi-bio Science (SIMS), Soonchunhyang University, Cheonan, Chungnam 31151, Republic of Korea

[2]Department of Integrated Biomedical Science, Soonchunhyang University, Cheonan, Chungnam 31151, Republic of Korea

[3]PG & Research Department of Chemistry, Islamiah College, Thiruvalluvar University, Vaniyambadi, Tamil Nadu 635752, India.

[4]Department of Plastic and Reconstructive Surgery, Soonchunhyang University College of Medicine, Soonchunhyang University Bucheon Hospital, Bucheon, Gyeonggi 14584, Republic of Korea

(This article belongs to the *Special Issue: Intelligent 3D Bioprinting Strategies for Future Regenerative Medicine*)

Abstract

The development of mechanically tunable and cytocompatible hydrogels is critical for advancing three-dimensional (3D) bioprinting in tissue engineering. Here, we report a composite bioink composed of gelatin methacrylate (GelMA), methylcellulose, sodium alginate, and laponite-RDS. This formulation supports extrusion-based printing without ionic crosslinkers, mimics the extracellular matrix (ECM), and maintains stable viscoelasticity under physiological conditions (37°C, pH 7.4). Electrostatic and hydrogen bonding interactions among the charged polymers enhance pre-gel viscosity, shear-thinning behavior, and print fidelity. To evaluate its potential in disease modeling, patient-derived keloid fibroblasts were encapsulated in 3D-bioprinted constructs using two GelMA-based formulations with different stiffness levels, such as soft (G4A1M1R1, 2.1 kPa) and stiff (G5A1M1R1, 7.9 kPa), chosen to replicate the mechanical properties of normal dermis and keloid tissue, respectively. Both constructs exhibited excellent cell viability after three days, confirming cytocompatibility. Furthermore, matrix stiffness significantly regulated fibrotic gene expression. The stiffer hydrogel induced higher expression of *COL1*, *MMP2*, and *IL6*, suggesting enhanced myofibroblast activation and ECM remodeling. Immunofluorescence staining further confirmed elevated protein levels of α-SMA, FSP1, and actin stress fibers (F-actin) in the stiff construct, consistent with keloid pathology. Taken together, these results demonstrate that the GelMA-based bioink enables stiffness-dependent modulation of fibrotic responses, offering a simplified yet relevant 3D model of fibrotic skin. This platform may provide a useful basis for future studies on keloid progression and preliminary antifibrotic drug screening.

Keywords: Bioinks; Bioprinting; Keloid; Shape fidelity; Skin fibrosis; Viscoelastic properties

[†]These authors contributed equally to this work.

***Corresponding authors:**
Seung Min Nam (zodiac1003@schmc.ac.kr)

Yongsung Hwang (yshwang0428@sch.ac.kr)

Citation: Anggradita LD, Manimohan M, Hur SS, *et al.* 3D printing of the keloid scar using tunable GelMA-based bioinks for skin fibrosis modeling. *Int J Bioprint*. 2025;11(4):446-461. doi: 10.36922/IJB025160154

Received: April 19, 2025
1st revised: July 8, 2025
2nd revised: July 23, 2025
Accepted: July 23, 2025
Published Online: July 23, 2025

Copyright: © 2025 Author(s). This is an Open Access article distributed under the terms of the Creative Commons Attribution License, permitting distribution, and reproduction in any medium, provided the original work is properly cited.

Publisher's Note: AccScience Publishing remains neutral with regard to jurisdictional claims in published maps and institutional affiliations.

1. Introduction

Three-dimensional (3D) bioprinting has emerged as a transformative technology in tissue engineering and regenerative medicine, enabling the fabrication of artificial tissues and organ-like constructs that replicate native biological structure and function.[1,2] Among the various techniques, extrusion-based bioprinting allows for the precise deposition of cell-laden hydrogels within predesigned architectures to generate biomimetic platforms for tissue-specific applications.[3] Central to the success of this approach is the development of suitable bioinks—composite materials that integrate living cells with tunable biomaterials—to ensure high print fidelity, mechanical stability, and cytocompatibility throughout the printing and maturation processes.

A range of natural polymers and nanomaterials have been explored as bioink constituents, including gelatin methacrylate (GelMA), alginate, methylcellulose (MC), and laponite-RDS.[4,5] GelMA, a photo-crosslinkable gelatin derivative, is widely used for its cytocompatibility, cell-adhesive motifs, and tunable mechanical properties, which can be modulated by its concentration and the degree of methacrylation.[6–8] Alginate, a non-toxic polysaccharide, offers excellent printability through ion-induced gelation with divalent cations such as Ca^{2+}.[9] When blended with GelMA, it has been shown to enhance mechanical properties and improve matrix support for cell attachment.[10] However, excessive crosslinking or increased polymer density can hinder extrusion, prompting the need for rheological modulators.

MC serves as one such modifier. As a thermoresponsive polymer, MC enhances viscoelasticity and contributes to bioink cohesion by undergoing a sol–gel transition via hydrophobic interactions and reduced hydrogen bonding upon heating.[11–13] Its incorporation enables improved extrusion performance and structural fidelity at ambient temperatures. Laponite-RDS, a synthetic nanoclay, forms electrostatic interactions with charged polymers, thereby increasing viscosity, enhancing shear-thinning behavior, and modulating pore structure within the hydrogel matrix.[14] Beyond its physical reinforcement, laponite-RDS has demonstrated the ability to support a range of biological functions, including stem cell differentiation, migration, and neural regeneration, making it a promising additive in bioactive bioinks.[15–17]

Keloids are pathological fibrotic scars characterized by excessive collagen deposition, tissue stiffening, and abnormal extracellular matrix (ECM) remodeling. These lesions extend beyond the original wound site and are driven by aberrant fibroblast activation—primarily through TGF-β1 signaling—which leads to increased migratory activity, matrix production, and upregulation of fibrosis-related genes, including the members of MMP, LOX, and LOXL gene families.[18] The development of reliable *in vitro* models that recapitulate the keloid microenvironment is essential for understanding disease mechanisms and screening antifibrotic therapies. While several natural polymers such as collagen, gelatin, alginate, chitosan, and fibrin have been used to construct skin models,[19] the need remains for bioinks that are both biocompatible and mechanically tunable—particularly for modeling stiffness-sensitive fibrotic phenotypes.

Recent advances in 3D bioprinting have enabled the fabrication of stiffness-tunable artificial keloid constructs capable of supporting cell viability, mimicking keloid-like ECM architecture, and recapitulating relevant signaling pathways.[20] Building upon these advances, we developed a composite bioink system comprising GelMA, sodium alginate, MC, and laponite-RDS, designed to replicate the fibrotic microenvironment of keloid tissue through mechanical tuning and cell-instructive matrix design.

In this study, we systematically evaluated the contributions of each bioink component to matrix stiffness, viscosity, viscoelasticity, degradation behavior, and cell compatibility. Using patient-derived keloid fibroblasts encapsulated in these hydrogels, we established a 3D-bioprinted keloid model that supports cell viability and fibrosis-associated gene expression. This platform offers a robust and modular approach for engineering disease-specific skin models and lays the groundwork for future applications in personalized medicine and antifibrotic drug screening.

2. Materials and methods

2.1. Bioink preparation

GelMA was synthesized as previously reported.[21] Briefly, 10% (w/v) gelatin (cat# G1890, Sigma-Aldrich, St. Louis, USA) was dissolved in deionized water under continuous stirring at 60°C. Next, 8 mL of methacrylic anhydride (# 276685, Sigma-Aldrich, USA) was added dropwise while stirring. After 2 h of reaction, deionized water was added, which was maintained for another 30 min. Subsequently, the solution was dialyzed using a dialysis membrane (MWCO; approximately 12–14 kDa; Spectrum Laboratories, USA) at 55°C for 7 days. Following dialysis, the solution was filtered and lyophilized.

To prepare a bioink blend, lyophilized GelMA was dissolved in phosphate-buffered saline (PBS) and incubated at 60°C for 1 h to ensure proper GelMA dilution. Next, MC powder (cat# M7027-250G, Sigma-Aldrich, USA), alginate (cat# J61887-30, Alfa Aesar, USA), and laponite-RDS (cat# LAPONITE-RDS, BYK, Germany) were added

to the GelMA solution. To induce photocrosslinking of the bioink after printing, 0.5% (w/v) Irgacure 2959 (cat# 55047962; BASF, Germany) was added to the bioink blend. The final mixture was stirred at 25°C using a magnetic stirrer for 4 h at 120 rpm. This process yielded a composite bioink composed of GelMA (G), alginate (A), MC (M), and laponite-RDS (R), referred to as G*x*A*x*M*x*R*x*. The "*x*" determines the concentration (w/v) as described in Table S1.

2.2. Rheology testing of uncrosslinked hydrogel

The viscosity and viscoelasticity of the uncrosslinked bioinks were determined using a Kinexus rheometer (Kinexus Ultra+, Malvern Panalytical, England). First, the pre-gel of the bioink was loaded onto the rheometer plate, and the gap between the upper geometry and the plate was set to 0.5 mm. The sample was equilibrated to 37°C before testing. Viscosity was measured using a cone-plate geometry, with shear rates ranged from 0.1 to 2 s^{-1} across a logarithmic scale with 20 intervals. Viscoelasticity was determined by amplitude and frequency sweeps using a parallel-plate cone. For the amplitude sweep, the applied shear strain ranged from 0.01 to 5%, at a constant oscillation frequency of 1 Hz, with a sampling density of 20 points per logarithmic decade. The frequency sweep was measured from 0.01 to 50 Hz at a constant strain of 2%.

2.3. Mechanical testing of crosslinked hydrogel

Mechanical properties were measured using an Instron device (EZ-SX; SHIMADZU, Japan) in compressive mode. Digital calipers were used to measure the diameters and heights of the hydrogels. Compression was applied from 0 to 70% strain at a rate of 1 mm/min at room temperature. Data were recorded when the ramp head contacted the hydrogel and registered a force of 0.01 N. Testing was terminated when the hydrogel broke. To calculate the Young's modulus (E), we used the linear region of the stress–strain curve with 10% strain. For each formulation, the average Young's modulus was calculated from three replicates. Data analysis was performed using MATLAB (MathWorks, USA). A two-degree polynomial interpolation was used to determine the Young's moduli at intermediate concentrations. Table S1 lists Young's moduli measured at different concentrations. The Young's moduli for each group are summarized in Figure S1. Table S4 summarizes the mechanical properties of each group, including toughness, stress, and strain at break.

2.4. Shape fidelity

The hydrogels were printed using the Inkredible+ Bioprinter (CellInk, Göteborg, Sweden) at room temperature. A square grid pattern (13.5 × 13.5 mm with 3 × 3 = 9 pores) was printed on Petri dish. For printing, 2 mL of bioink solution was added to the cartridge. Printing was performed using 22G blunt conical bioprinting nozzles (ID: 410 μm). The applied pressure ranged from 3 to 6 kPa, depending on the bioink formulation, as described in Table S2. The printing process was performed at a feed rate of 1500 mm/min and a layer height of 0.8 mm. After printing, the hydrogels were polymerized under ultraviolet (UV) light (365 nm; Blak-Ray XX-15L; UVP, Upland, USA) for 5 min. The hydrogels were then equilibrated in PBS for 24 h. Shape fidelity was assessed by comparing the measured pore size with the designed pore size using the following formula[22]:

$$\text{Shape fidelity} = \left(\frac{a \times b}{a' \times b'} \right) \times 100\% \quad \text{(I)}$$

where a and b are the designed dimensions of the pore base, and a' and b' are the corresponding dimensions of the actually printed pore base.

Detailed information on the calculation of shape fidelity is provided in Figure S2 and Table S6.

2.5. *In situ* hydrogel

Patient-derived keloid tissue was obtained from the Soonchunhyang University of Bucheon Hospital, according to the protocols approved by the Institutional Review Board of Soonchunhang University Bucheon Hospital (SCHBC_IRB_2017-08-010). This study was conducted in accordance with the 1964 Declaration of Helsinki and its subsequent amendments. The dermal layer was separated, and keloid dermal fibroblasts were isolated following a previous protocol.[18] The cells were cultured in Dulbecco's modified Eagle's medium (10-013-CV, Corning, USA) supplemented with 10% fetal bovine serum (cat# 35-015-CV, Corning, USA), 1% l-glutamine (200 mM; cat# 25030081, Gibco-BRL, USA), and 1% penicillin–streptomycin (15140122, Life Technologies, USA). The bioinks were prepared in PBS at 80% of the total volume. Next, the cell pellet was resuspended in PBS at 10% of the total hydrogel volume and added to the bioink blend. For hydrogel encapsulation, cells were suspended at a density of 1 × 10^6 cells/mL for real-time polymerase chain reaction (qPCR) analysis and at 2 × 10^6 cells/mL for immunofluorescence staining and live/dead assays to enhance signal detection and cell representation. The solution was stirred for 15 min. This formed a cell-laden hydrogel with a total dissolved volume of 90%. Considering the 10% volume loss during hydrogel blending, we dissolved the *in situ* hydrogel in 90% of the total volume of PBS to prevent further dilution upon cell addition. The hydrogel was printed as a grid-like structure and subsequently exposed to UV light (365 nm; Blak-

Ray XX-15L; UVP, USA) for 5 min for crosslinking. The hydrogel was kept in the growth medium for 3 days before further experiments.

2.6. Live/dead cell viability assay

Cell viability was assessed three days after the printing process using the Live/Dead Viability/Cytotoxicity Kit (cat# 3 L-3224, Invitrogen, USA), following the manufacturer's instructions. After staining, the hydrogel was washed with PBS and imaged using a THUNDER Imager (Leica Microsystem, Germany) with 5× objective lens (N Plan; NA, 0.12; Cat# 11506303, Leica Microsystem, Germany) and an EVOS M700 imaging system (Thermo Fisher Scientific, Waltham, USA) equipped with a 10× water immersion objective lens (Fluorite; NA, 0.30), utilizing a stitching function to generate complete images of the hydrogel.

2.7. Real-time polymerase chain reaction

Total RNA was isolated from the hydrogel using TRIzol reagent (Cat# 15596018, Ambion, USA), and cDNA synthesis was performed using ReverTra Ace qPCR RT Master Mix with gDNA Remover (Cat# KMM-101, TOYOBO, Japan), following the manufacturer's instructions. Subsequently, qPCR was performed using a QuantStudio 1 Real-Time PCR System (Applied Biosystems, Foster City, USA) and SYBR Green Real-time PCR Master Mix (Cat# 4472918, TOYOBO, Japan). Table S3 lists the primers used for the qPCR. All experiments were performed in triplicate for each group. Glyceraldehyde 3-phosphate dehydrogenase (*GAPDH*) served as a housekeeping gene. The ΔC_t values were determined as $Ct^{target} - Ct^{GAPDH}$, and relative fold changes were calculated using the $2^{-\Delta\Delta Ct}$ method.[23]

2.8. Immunofluorescence

In situ hydrogels were fixed in 4% paraformaldehyde (PFA, Cat# CNP015-0500, CellNest, Korea) for 30 min and permeabilized with 0.3% Triton X-100 (Cat# TRX777.500, Bioshop, Canada) solution for 30 min at room temperature. Subsequently, hydrogels were blocked in a solution of 5% BSA for 30 min at room temperature. Hydrogels were then incubated in primary antibodies for 48 h at 4°C, followed by secondary antibodies for 24h at 4°C. Antibodies are listed in Table S4. Confocal imaging was performed using an LSM 710 microscope (Carl Zeiss, Germany) at the Soonchunhyang Biomedical Research Core Facility of Korea Basic Science Institute with a 10× objective lens (Plan-Apochromat; NA, 0.45; Cat# 420640-9900-000, Carl Zeiss, Germany). Tiled images were acquired using a THUNDER Imager (Leica Microsystem, Germany) with a 5× objective lens (N Plan; NA, 0.12; Cat# 11506303, Leica Microsystem, Germany).

2.9. Statistical analysis

Data were analyzed using GraphPad Prism version 10.3 (GraphPad Software, Inc., USA). Bar graphs represent mean values, with error bars indicating standard deviations. The statistical significance between two groups was assessed using Student's *t*-test, while comparisons among multiple groups were conducted using one-way analysis of variance followed by Tukey's post hoc test. Statistical significance was set at $^{*}p < 0.05$, $^{**}p < 0.01$, and $^{***}p < 0.001$.

3. Results and discussion

3.1. GelMA concentration as a biocompatible crosslinker

The G*x*A*x*M*x*R*x* bioink system was formulated through polyelectrolyte complexation and covalent crosslinking among GelMA (G), alginate (A), MC (M), and laponite-RDS (R), as illustrated in Figure 1. The variable "*x*" denotes the respective concentrations used (Table S1). Each component serves a distinct role: GelMA acts as a biocompatible crosslinker offering structural integrity and cell-adhesive moieties, while alginate, MC, and laponite-RDS modulate viscoelasticity and printability.

GelMA is an ampholytic polymer carrying both negative and positive charges. At acidic pH values below its isoelectric point, its amine groups are protonated, rendering it positively charged and enabling electrostatic interactions with the negatively charged MC to form polyelectrolyte complexes.[24] Concurrently, alginate contributes to the polymer network through nucleophilic attack by its carboxylic acid groups on the hydroxyl functionalities of MC, leading to ring-opening of the pyranose structure and formation of aldehyde intermediates.[25] These intermediates react with GelMA's amine groups, generating nitrogen-containing intermediate rings. Additionally, primary amines on GelMA can form stable amide bonds with carboxylic or ester groups on alginate, enhancing both intra- and inter-molecular crosslinking and improving hydrogel stability.[26] Furthermore, alginate and MC primarily interact with GelMA through physical entanglement and hydrogen bonding, which increase viscosity and enhance viscoelasticity. These interactions also promote shear-thinning behavior, thereby improving the printability of the hydrogel system.[27]

Laponite-RDS, a synthetic nanoclay composed of disc-like platelets (~15 nm diameter, ~1 nm thickness), features alternating trioctahedral and tetrahedral layers with interspersed magnesium and lithium ions surrounded by negatively charged silicate surfaces. This high charge density and surface area render it suitable for biomedical applications. In bioink formulations, laponite-RDS enhances mechanical stiffness, shear-thinning behavior,

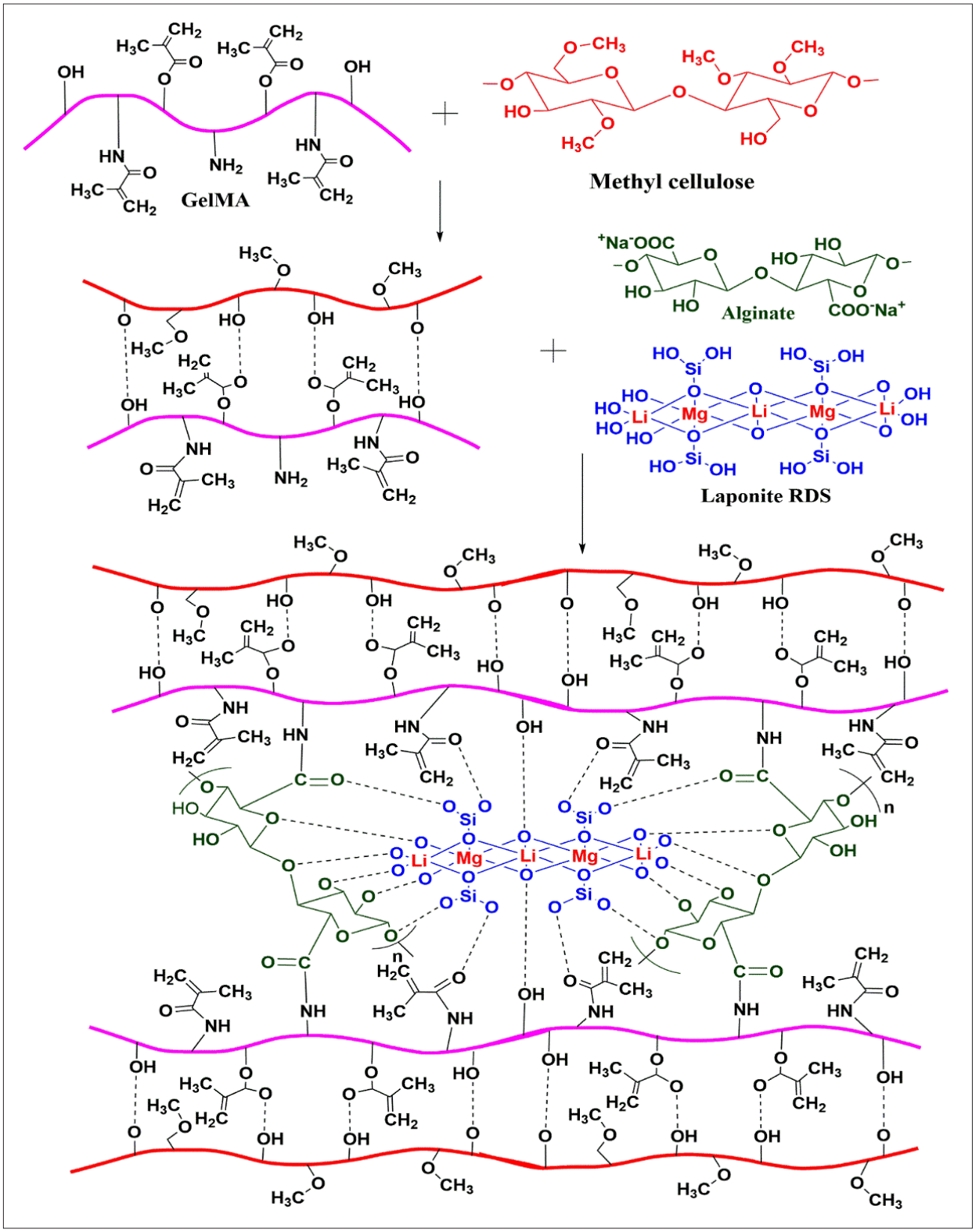

Figure 1. Preparation of gelatin methacrylate (GelMA), methylcellulose (M), alginate (A), and laponite-RDS (R) blended bioink (GxMxAxRx).

and surface roughness through interparticle interactions and water intercalation.[28] Its negatively charged surfaces can form ionic interactions with the positively charged amine groups of GelMA, thereby improving network stability and mechanical reinforcement.[29]

To investigate GelMA's role as a mechanical crosslinker, we compared bioinks with 4% (G4A1M1R1) and 5% (G5A1M1R1) GelMA content, representing soft and stiff hydrogels, respectively (Figure 2A). Despite the 25% increase in GelMA concentration, no statistically significant differences in viscosity or viscoelastic moduli were observed between the groups (Figure 2B–G). Both exhibited typical non-Newtonian, shear-thinning behavior, with viscosity decreasing as shear rate increased (Figure 2B–C). This property supports extrusion-based bioprinting, where low viscosity under shear facilitates flow and high viscosity post-extrusion maintains structural fidelity.[30] Frequency sweep analysis indicated stable viscoelastic behavior across both groups (Figure 2D, G), but compression testing revealed significantly higher stiffness in G5A1M1R1, with a Young's modulus of 7.9 ± 1.3 kPa compared to 2.1 ± 0.92 kPa in G4A1M1R1 (Figure 2H–I). These findings suggest that mechanical reinforcement primarily arises from enhanced GelMA crosslinking, rather than bulk rheological differences. Since GelMA relies on chemical crosslinking via photopolymerization rather than ionic or physical interactions, the resulting hydrogel remains stable under physiological ionic conditions, which might otherwise affect electrostatic interactions and compromise structural integrity (Figure 2J–K). Furthermore, slower degradation was observed in G5A1M1R1 (Figure S1C), indicative of a denser and more stable polymer network. Enhanced mechanical resilience and matrix stability are likely due to the increased density of covalent and non-covalent crosslinks formed at higher GelMA concentrations.[24,31] In summary, increasing GelMA concentration improves the mechanical performance, degradation resistance, and printability of the hydrogel, which are essential for supporting cellular viability and long-term culture in

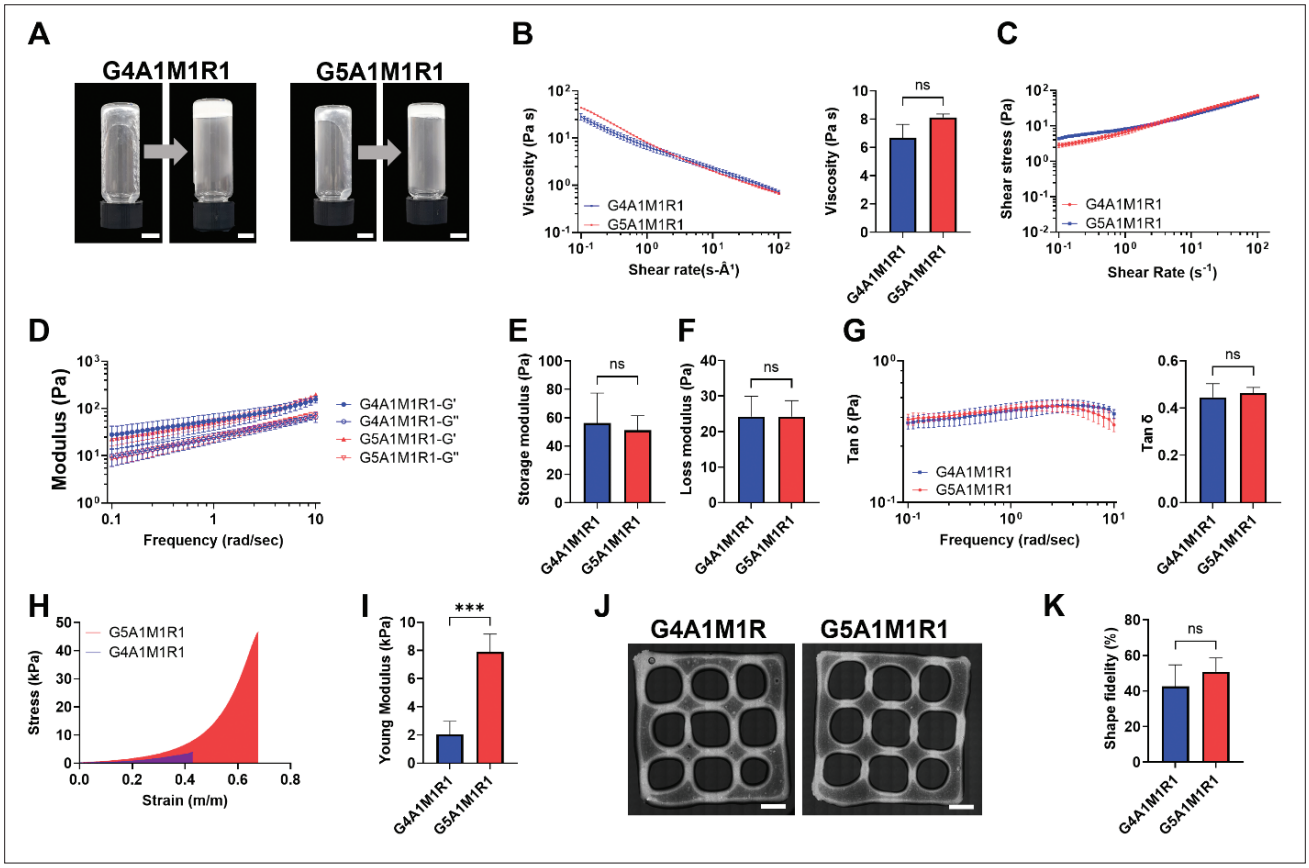

Figure 2. Effect of GelMA as a crosslinker on the rheological and mechanical properties of bioink. (A) Crosslinked hydrogel blend consists of GelMA (4 and 5% w/v), alginate (1% w/v), methylcellulose (MC) (1% w/v), and laponite-RDS (1% w/v). Scale bar: 5 mm. (B) Viscosity and (C–G) rheological properties of hydrogel blends with varying concentrations of GelMA. (H–I) Higher mechanical properties observed with higher crosslinker concentration. $^{*}p < 0.05$, $^{***}p < 0.001$. (J–K) Printability and structural shape fidelity of a hydrogel blend. Scale bar: 2.5 mm.

3D-bioprinted constructs. Although higher GelMA content can hinder extrusion due to nozzle clogging, this limitation can be overcome by co-formulating with alginate, MC, and laponite-RDS to preserve flow characteristics while maintaining structural fidelity.

3.2. Alginate as an elasticity enhancer

In extrusion-based bioprinting, viscosity and shear-thinning behavior are critical for achieving high-resolution structures while maintaining mechanical stability during and after deposition. Building on previous studies, we investigated the role of alginate as a viscoelasticity enhancer by comparing formulations containing different alginate concentrations: 0.5% (G5A0.5M1R1) and 1% (G5A1M1R1), without the use of multivalent cation crosslinkers (Figure 3A). As expected, the bioink with higher alginate concentration exhibited a substantial increase in viscosity (~76%) and more pronounced shear-thinning behavior (Figure 3B–C). This increase in viscosity reflects alginate's concentration-dependent chain entanglement, which improves printability by supporting controlled extrusion and better shape retention. Higher viscosity also enables faster structural recovery post-printing, a key parameter for high-fidelity bioprinting.

Both formulations displayed solid-like viscoelastic characteristics, with storage modulus (G′) consistently exceeding loss modulus (G″) over increasing frequencies (Figure 3D). Notably, the G′ of the 1% alginate group (G5A1M1R1: 50.17 ± 8.59 Pa) was more than twice that of the 0.5% group (G5A0.5M1R1: 19.50 ± 12.52 Pa), suggesting a significant enhancement in network stiffness (Figure 3D–E). This finding supports the role of alginate as a structural modifier that promotes stronger elastic responses within the composite hydrogel. Although the increase in G″ was not statistically significant (Figure 3F), it followed a similar upward trend.

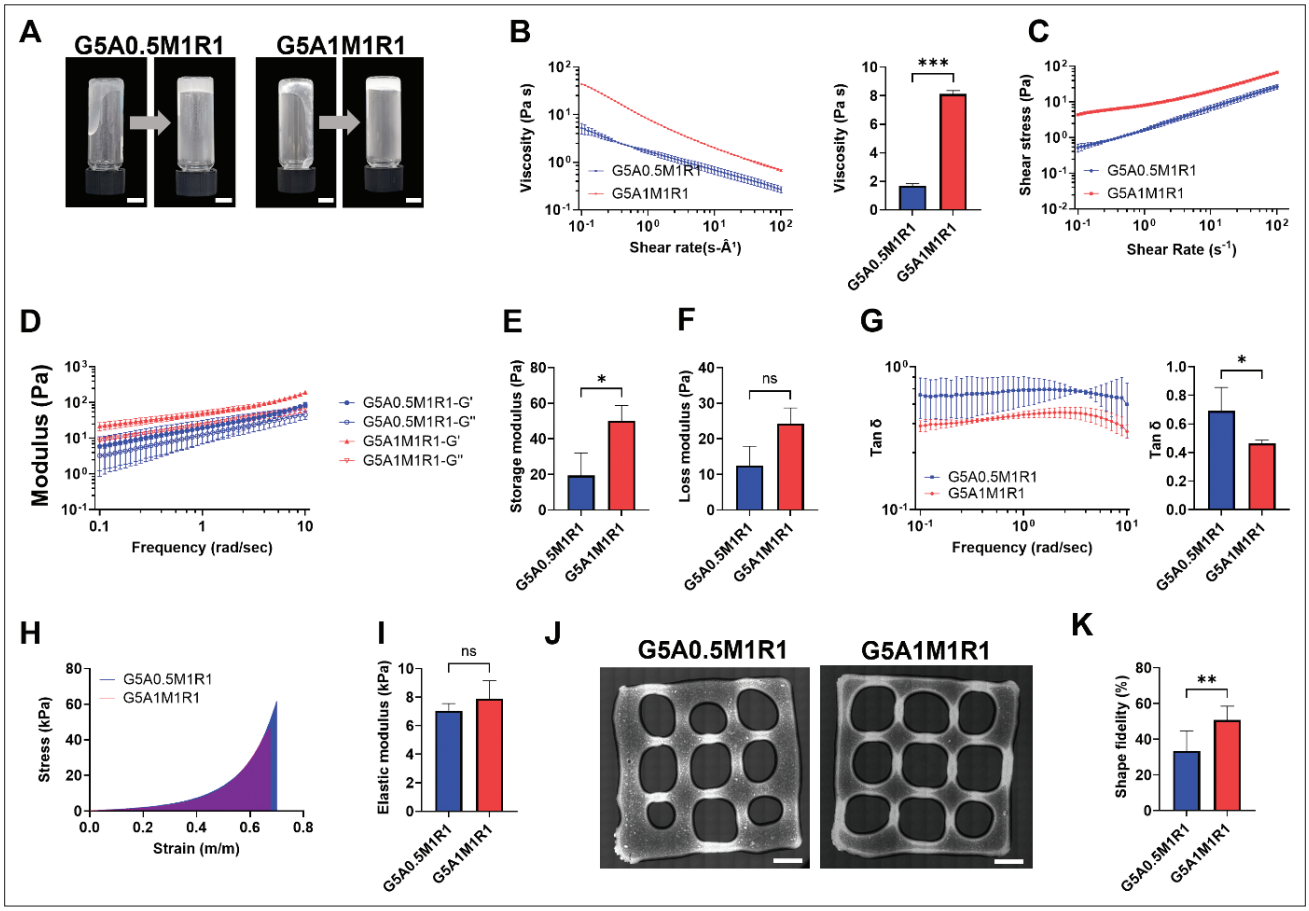

Figure 3. Role of alginate as a viscoelasticity enhancer. (A) Crosslinked hydrogel blend consists of GelMA (5% w/v), alginate (0.5 and 1% w/v), MC (1% w/v), and laponite-RDS (1% w/v). Scale bar: 5 mm. (B) Viscosity and (C–G) rheological properties of hydrogel blends with varying alginate concentrations. (H–I) Mechanical properties with varying concentration of alginate. *$p < 0.05$, **$p < 0.01$, ***$p < 0.001$. (J–K) Printability and shape structural fidelity of a hydrogel blend. Scale bar: 2.5 mm.

The damping factor (tan δ), defined as G″/G′, decreased in the G5A1M1R1 group (Figure 3G), indicating reduced viscous dissipation and a more dominant elastic component. This aligns with previous studies suggesting that gelatin–alginate hydrogels with tan δ values between 0.25 and 0.45 yield optimal print fidelity.[32] Interestingly, mechanical testing revealed slightly higher toughness in the lower alginate concentration group (Figure 3H, Table S5). This may be attributed to more efficient integration of alginate into the polymer matrix at lower concentrations, enhancing the load distribution within the hydrogel network. Although the difference in Young's modulus between groups was not statistically significant (Figure 3I), a slight increase was observed with higher alginate content, consistent with steric hindrance and chain entanglement effects.

In the absence of ionic crosslinkers, alginate's influence appears to arise primarily from physical entanglement with GelMA and MC chains, rather than stable ionic or covalent interactions. This physical contribution nonetheless improved the structural fidelity and reduced the degradation rate of the hydrogel, likely by shielding gelatin cleavage sites from enzymatic degradation (Figure S1C). Bioprinting trials demonstrated that incorporating 1% alginate, along with GelMA, MC, and laponite-RDS, enabled the formation of robust, well-defined structures at 25°C (Figure 3J), producing better printability properties (Figure 3K). These results confirm that alginate serves as an effective viscosity and elasticity enhancer, contributing to the mechanical performance, printability, and biological utility of the G*x*A*x*M*x*R*x* bioink formulation.

3.3. Enhancing viscosity by methylcellulose

One of the key limitations in extrusion-based bioprinting is the need to balance high-resolution printing with minimal shear-induced cellular damage. MC, a hydrophilic cellulose derivative, is widely used to increase viscosity and improve print fidelity while supporting cell viability. To evaluate the role of MC in our bioink system, we compared two concentrations—0.5% (G5A1M0.5R1) and 1% (G5A1M1R1)—while maintaining constant concentrations of GelMA, alginate, and laponite-RDS (Figure 4A).

Although increasing the MC concentration led to a 33% increase in viscosity, this enhancement was modest compared to that observed with alginate (Figure 4B). Both formulations retained a clear shear-thinning profile, which is critical for facilitating bioink flow during extrusion and maintaining structural integrity post-deposition.

Rheological analysis demonstrated improved viscoelasticity in the higher MC concentration group, though the changes were not statistically significant (Figure 4C–G). The increase in G′ and G″ suggests that MC modulates the hydrogel's mechanical response under deformation. Unlike previous reports that have described a Newtonian plateau at low to intermediate shear rates in MC-only solutions,[33] our composite formulation exhibited continuous shear-thinning behavior across all shear rates. This likely results from the combined effects of GelMA, alginate, and laponite-RDS, which modify the microstructural dynamics of the hydrogel network.

The 1% MC formulation also demonstrated enhanced mechanical integrity, as shown by a steeper stress–strain curve (Figure 4H) and improved toughness (Table S5). Moreover, the elastic modulus increased from 5.53 ± 1.03 kPa (G5A1M0.5R1) to 7.91 ± 1.26 kPa (G5A1M1R1), a 1.4-fold enhancement (Figure 4I). These improvements reflect the role of MC in reinforcing the hydrogel network and increasing resistance to deformation. In addition, the degradation rate was slower in the higher MC group (Figure S1C), which is consistent with MC-induced steric hindrance that reduces enzymatic accessibility to cleavage sites.

However, increased MC concentration could reduce the printability (Figure 4K) as the MC controlled shape fidelity and reduced spreading observed in the 1% MC group (Figure 4J). The combination of MC with alginate and GelMA allows for controlled deposition of even low-viscosity formulations by modulating the composite's viscoelastic response. Furthermore, MC is known to alter the hydrogel's microstructure and act as a rheological modifier, thereby slowing release rates and improving long-term stability.[34] Overall, increasing MC concentration enhanced viscosity, mechanical stiffness, and structural integrity, without compromising biocompatibility. The addition of MC also increased the loss modulus and yield stress of the hydrogel blend,[35] contributing to the robustness of printed constructs—especially when fine structural features and cell protection during printing are required.

3.4. Laponite-RDS controls rheological properties

Rapid degradation of hydrogels remains a key limitation for long-term applications in tissue engineering. To address this, laponite-RDS—a synthetic, discotic nanoclay—was incorporated into the bioink formulation to enhance rheological and mechanical properties. Laponite-RDS consists of alternating silicate layers with embedded magnesium and lithium ions, forming a charged, plate-like structure (~15 nm in diameter, ~1 nm in thickness) that imparts thixotropic behavior and high surface reactivity.[36]

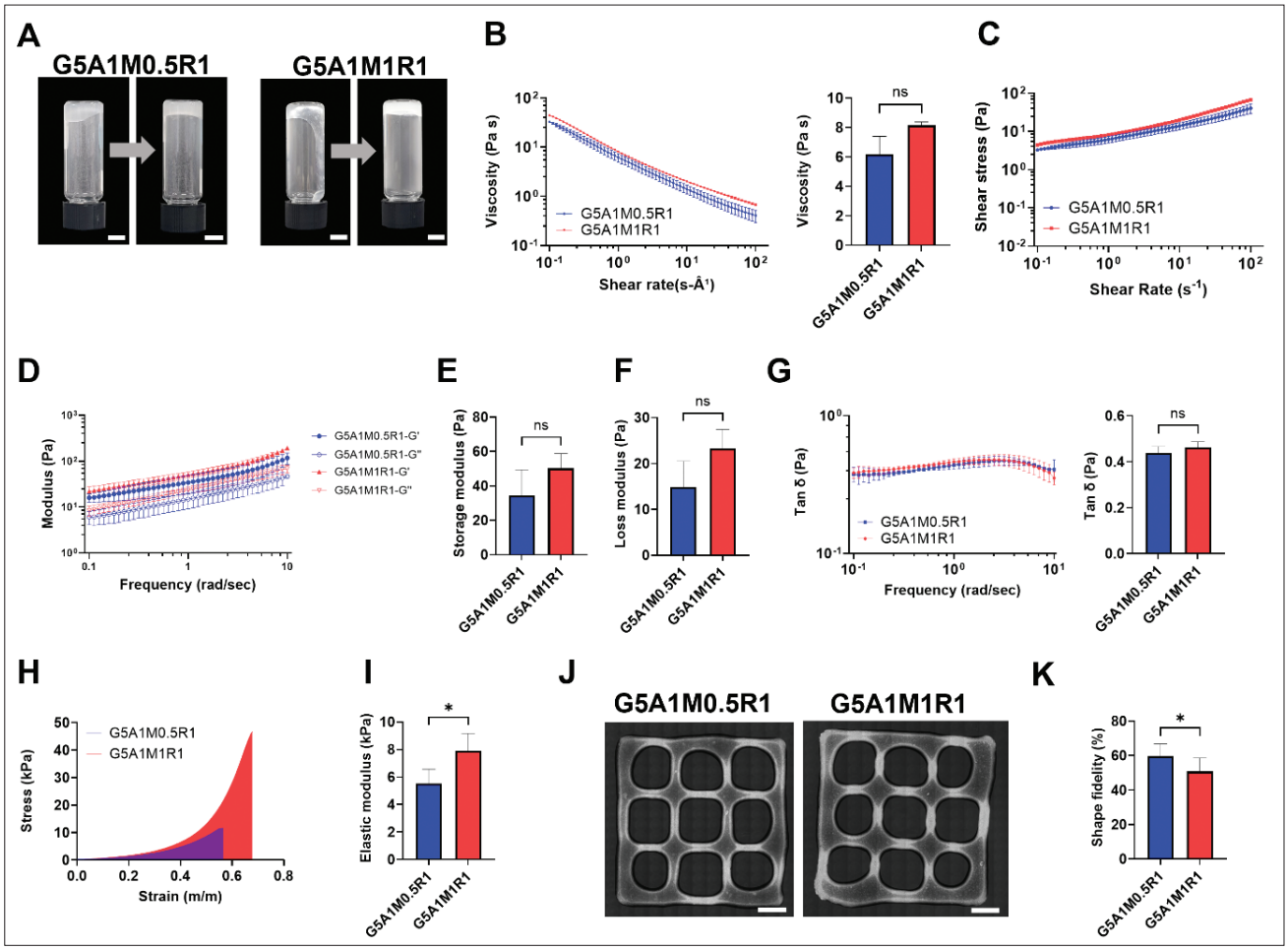

Figure 4. Tuning the viscoelasticity by increasing MC concentration. (A) Crosslinked hydrogel blend consists of GelMA (5% w/v), alginate (1% w/v), MC (0.5 and 1% w/v), and laponite-RDS (1% w/v). Scale bar: 5 mm. (B) Viscosity and (C–G) viscoelastic properties of hydrogel blends with varying concentrations of MC. (H–I) Increased viscoelasticity with a higher concentration of MC content. *$p < 0.05$. (J–K) Printability and structural shape fidelity of a hydrogel blend. Scale bar: 2.5 mm.

To evaluate its contribution, we compared formulations with (G5A1M1R1) and without (G5A1M1) laponite-RDS (Figure 5A). The inclusion of laponite-RDS increased viscosity by approximately 75%, contributing to the formation of a thicker and more cohesive bioink (Figure 5B). Both groups exhibited clear shear-thinning behavior, but the addition of laponite-RDS enhanced this effect, facilitating improved extrusion performance during printing.

Rheological profiling showed increased storage (G′) and loss (G″) moduli in the presence of laponite-RDS, with 62 and 47% increases, respectively (Figure 5C–G). Although the enhancement in elastic behavior was modest, the overall viscoelastic balance shifted toward greater rigidity. These effects are attributed to electrostatic interactions between the cationic amine groups of GelMA and the negatively charged silicate surfaces of laponite-RDS.[29] The disc-shaped laponite particles possess a net negative charge on their faces due to exposed silicate (SiO_4^{4-}) groups, while their edges carry a slight positive charge from divalent cations such as Mg^{2+} and monovalent Li^+. These charge distributions enable reversible ionic interactions with the amphoteric side chains of GelMA, contributing to increased pre-gel viscosity and enhanced network stabilization prior to photopolymerization. Interestingly, while the impact of laponite-RDS on G′ and G″ was consistent, the differences did not reach statistical significance (Figure 5G), suggesting that its primary function may be to fine-tune rather than drastically alter bulk viscoelasticity. Nevertheless, mechanical testing revealed a lower stress response and reduced toughness in the absence of laponite-RDS (Figure 5H, Table S5), indicating compromised structural integrity. The degradation rate was also higher in laponite-RDS-free

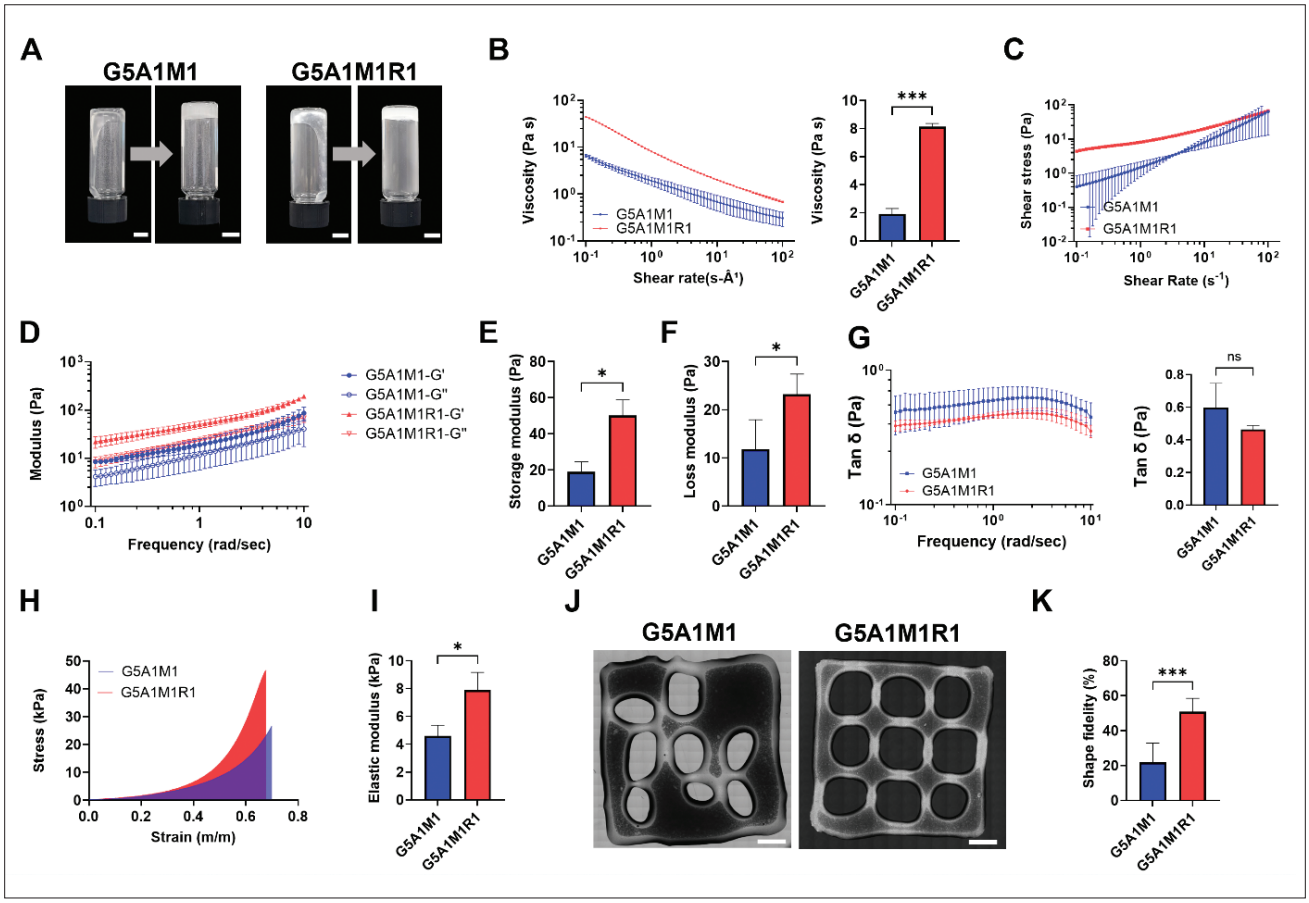

Figure 5. Incorporation of laponite-RDS enhances printability of bioink. (A) Crosslinked hydrogel blend consists of GelMA (5% w/v), alginate (1% w/v), MC (1% w/v), and laponite-RDS (0 and 1% w/v). Scale bar: 5 mm. (B) Viscosity and (C–G) rheological properties of hydrogel blends with and without laponite-RDS. (H–I) Laponite-RDS increases mechanical properties and (J–K) the structural shape fidelity of the hydrogel blend as a bioink. *$p < 0.05$, ***$p < 0.001$. Scale bar: 2.5 mm.

bioinks (Figure S1C), supporting the role of laponite in stabilizing the hydrogel network.

Laponite's contribution to mechanical reinforcement is further supported by Young's modulus measurements, which increased from 4.59 ± 0.79 kPa in the laponite-free group (G5A1M1) to 7.91 ± 1.26 kPa in the laponite-containing group (G5A1M1R1) (Figure 5I). These findings confirm that laponite-RDS enhances the elastic modulus, likely through increased crosslinking density and network entanglement.[37] Finally, printing performance analysis showed that laponite-RDS improved print fidelity by minimizing spreading and maintaining the printed geometry post-extrusion (Figure 5J–K). This improvement is attributed to physical crosslinking effects that influence key mechanical and rheological properties—including elastic modulus, swelling behavior, viscosity, and flowability—through electrostatic interactions, hydrogen bonding, hydrophobic interactions, and van der Waals forces. The locally charged polymers in the bioink—GelMA, MC, and alginate—can also interact with charged biomolecules such as antifibrotic drugs, potentially modulating cell behavior depending on the net surface charge.[38,39] Similarly, alginate (rich in COO– groups) and carboxymethylated MC interact with GelMA via hydrogen bonding and ionic entanglement involving amine and hydroxyl side chains.[35,40] While weaker than covalent crosslinking, these interactions contribute to shear-thinning behavior, increased yield stress, and enhanced pre-gel viscosity.

Upon UV-induced photopolymerization of GelMA, covalent crosslinks become the dominant contributors to the hydrogel's structural integrity. Nevertheless, pre-existing physical interactions such as hydrogen bonding, electrostatic entanglement, and polymer chain entanglement among GelMA, alginate, and MC remain important for modulating the viscoelastic behavior,

particularly under physiological conditions (pH 7.4, 37°C).[27,41,42] The hydrogel system exhibits rapid gelation, high yield stress, and prolonged stress relaxation, enabling efficient transitions between flow and solid states. These properties contribute to reliable extrusion, improved print fidelity, and stable construct formation during 3D bioprinting.

Collectively, these multiscale interactions, including ionic bonding, hydrogen bonding, and polymer network entanglement, synergistically regulate the rheological performance of the bioink. This cooperative behavior enhances the pre-print stability and post-print mechanical integrity, enabling the formation of cell-laden constructs with clinically relevant stiffness. Prior studies involving GelMA–clay–alginate systems have demonstrated similar synergistic effects,[43-45] supporting the design rationale and functional benefits of our composite formulation.

3.5. Biocompatibility of G*x*A*x*M*x*R*x* as a keloid skin model

Keloids are fibrotic skin disorders characterized by excessive ECM deposition, particularly collagen types I, and abnormal fibroblast behavior, leading to stiff, nodular lesions that extend beyond the original wound. A hallmark of keloid pathology is the activation of dermal fibroblasts into myofibroblasts, marked by elevated expression of fibrosis-related proteins such as α-SMA and FSP-1.[18,46] To model this pathophysiology *in vitro*, we encapsulated patient-derived keloid dermal fibroblasts within two GelMA-based bioink formulations: G4A1M1R1 (soft) and G5A1M1R1 (stiff). These compositions represented the lowest and highest stiffness values among all tested hydrogels (Figure S1A), enabling us to assess the impact of matrix stiffness on keloid fibroblast behavior. Importantly, the concentrations of MC, alginate, and laponite-RDS were held constant across both groups to minimize compositional variability and isolate stiffness as the primary variable. The selected formulations were specifically chosen to closely match the microscale elastic moduli of normal dermis (~2.4 ± 1.0 kPa) and keloid tissue (~14.2 ± 1.0 kPa), as previously reported.[47] Thus, this design allowed us to mimic physiologically relevant mechanical cues and assess mechanotransduction in a 3D-printed skin fibrosis model.

Live/dead assays performed 3 days post-encapsulation showed strong calcein-AM fluorescence, confirming high cell survival within the 3D-printed constructs (Figure 6A). These findings demonstrate the low cytotoxicity and excellent biocompatibility of the G*x*A*x*M*x*R*x* hydrogel system. Notably, key functional motifs such as RGD sequences and MMP-sensitive linkages are preserved during GelMA photopolymerization, facilitating cell adhesion and matrix remodeling.[8] Furthermore, the natural origin and known biocompatibility of alginate and MC, along with laponite-RDS at non-toxic concentrations, support the formulation's safety for tissue engineering. The consistent cell viability also suggests the stability of the hydrogel under physiological ionic conditions. Thus, despite the presence of charged polymers such as GelMA, MC, and alginate, no detrimental effects on cell viability were observed.

We next characterized fibrotic responses of the encapsulated keloid fibroblasts. Compared to normal dermal fibroblasts, patient-derived keloid fibroblasts showed significantly higher expression of ECM remodeling genes (*COL1*, *MMP2*, *LOX*), myofibroblast markers (ACTA2, Vimentin), the fibrosis-associated marker FSP1, and the inflammatory cytokine IL6 (Figure S3A and B). To assess the potential of the G*x*A*x*M*x*R*x* bioink for modeling fibrotic skin, we further examined gene expression responses to matrix stiffness. The stiffer G5A1M1R1 formulation induced markedly higher expression of *COL1* (~90%), *MMP2* (~70%), and *IL6* (~85%) compared to the softer G4A1M1R1 formulation (Figure 6B), demonstrating that even modest differences in stiffness can enhance the fibrotic and inflammatory phenotype of keloid fibroblasts in 3D culture. Additional upregulation of *FSP1* (~18%) and *LOX* (~20%) was also observed in G5A1M1R1, consistent with fibroblast activation and increased ECM crosslinking activity. These findings are consistent with prior reports that increased matrix stiffness promotes mechanosensitive signaling, fibroblast-to-myofibroblast differentiation, and excessive ECM remodeling, which are the hallmarks of fibrotic tissue pathology.[18,48,49]

To confirm these changes at the protein level, we performed immunofluorescence staining on single square-shaped 3D-printed constructs (adapted from a 3 × 3 grid pattern; Figure S2A). Positive expression of MTS1 (*FSP1*), F-actin, and α-SMA was observed in encapsulated keloid fibroblasts (Figure 6C–D), with substantially stronger signal intensity and greater cell aggregation in G5A1M1R1. These findings support the activation of myofibroblasts under stiff microenvironmental conditions. The transition of fibroblasts to myofibroblasts is a hallmark of skin fibrosis, characterized by elevated expression of α-SMA and FSP1, along with prominent actin stress fiber formation (F-actin).[50] Together, these findings suggest that the G*x*A*x*M*x*R*x* bioink provides a mechanically tunable and biocompatible platform for constructing simplified 3D models that recapitulate key features of fibrotic skin tissue. By integrating GelMA, alginate, MC, and laponite-RDS, we developed a structurally stable scaffold that supports cell viability and enables stiffness-dependent modulation of fibrotic gene expression. While preliminary, this system

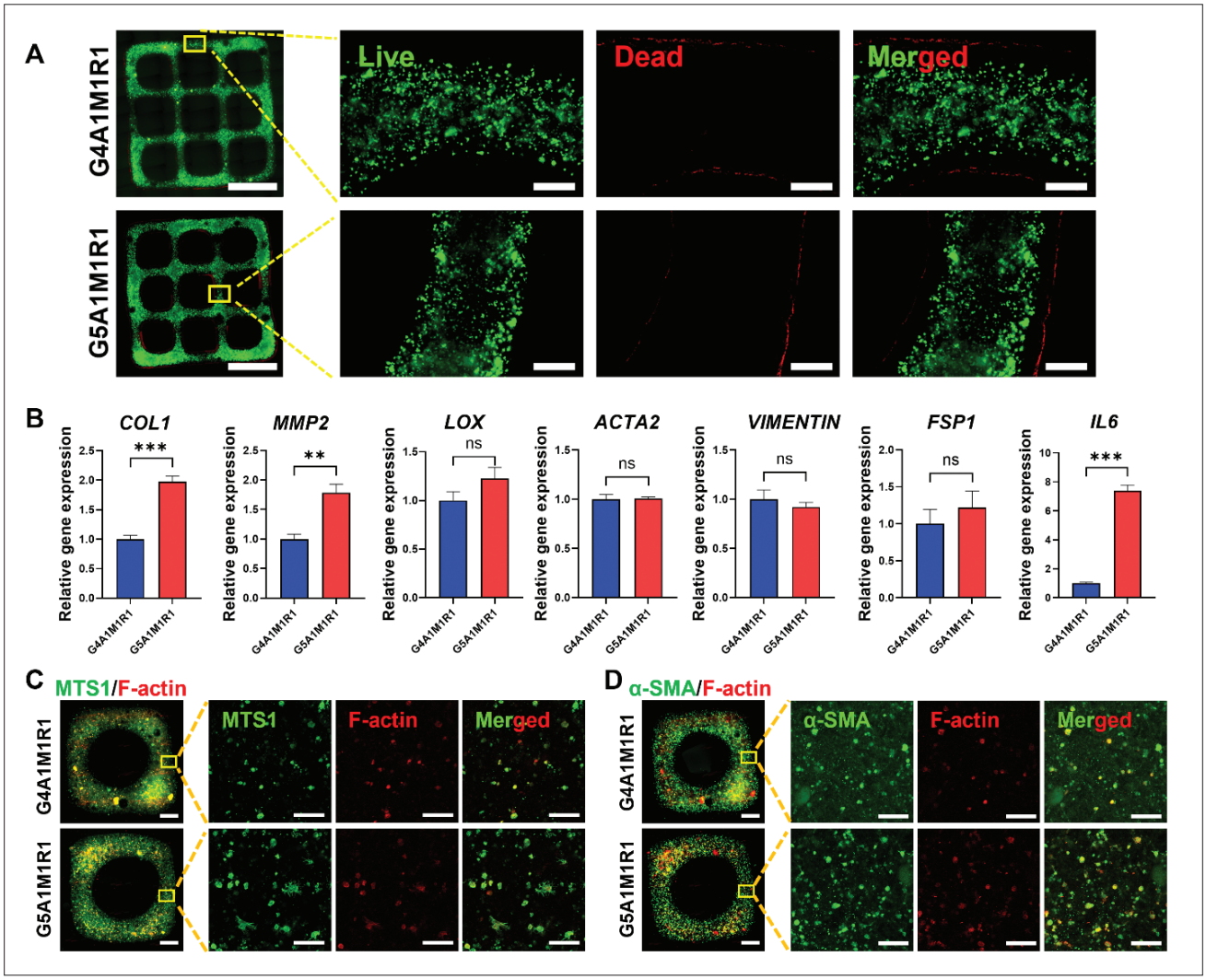

Figure 6. Fabrication of a keloid biomimetic disease model via encapsulation of keloid dermal fibroblasts in stiffness-controlled bioinks. (A) The biocompatibility of the hydrogel blend, comprising GelMA (4 and 5% w/v), alginate (1% w/v), MC (1% w/v), and laponite-RDS (1% w/v), is demonstrated by high cell viability, as indicated by Calcein-AM staining. Scale bars: 5 mm (magnified: 200×). (B) Keloid dermal fibroblasts remain functionally active when encapsulated in the hydrogel blend, maintaining their characteristic behavior. $n = 3$. $^{**}p < 0.01$, $^{***}p < 0.001$. (C, D) Pro-fibrotic response of keloid dermal fibroblasts was demonstrated by elevated expression of MTS1, α-SMA, and F-actin, as shown by immunofluorescence staining. Scale bars: 1 mm (magnified: 200×).

offers a foundational tool for future *in vitro* studies of keloid-associated fibroblast behavior. With further development, it may be adapted to include additional skin-resident cell types, such as keratinocytes, for the fabrication of more complex, multilayered tissue constructs.[51]

Although the current study focuses on the development and characterization of a mechanically tunable GelMA-based bioink for modeling fibrotic skin, the translational potential of this system could be further expanded through its drug delivery capability. GelMA hydrogels have been widely reported as promising platforms for localized and sustained drug release due to their tunable mesh size, physicochemical properties, and biocompatibility.[52,53] For instance, a GelMA-based drug delivery system has been shown to encapsulate albumin-bound paclitaxel (Abraxane®) with high efficiency (up to 96%) and achieve sustained release over several weeks by modulating GelMA concentration and enzymatic degradation kinetics, without compromising mechanical integrity.[54] Furthermore, systematic studies have demonstrated that drug loading, ionic strength, and environmental pH can significantly influence water states and hydrogel mesh size, thereby tuning drug retention and release behavior.[26] These findings suggest that the rheological and

crosslinking features of GelMA, well-preserved in our G*x*A*x*M*x*R*x* formulation, could support incorporation of antifibrotic therapeutics in future applications. Additionally, the high batch-to-batch reproducibility and controllability of GelMA production further enhance its clinical feasibility for biofabrication and drug screening platforms.[55] Therefore, while drug delivery was not directly addressed in this study, our bioink formulation may offer a dual-function system for stiffness-regulated disease modeling and therapeutic testing, warranting further investigation. Moreover, although degradation rates were evaluated and found to differ modestly across formulations (Figure S1C), other potentially influential parameters, including porosity and mesh size, which may impact both cellular responses and drug loading or release behavior, were not quantitatively characterized and should be systematically explored in future work.

Despite these promising results, several limitations should be acknowledged. First, the biological effects of individual bioink components, including alginate, MC, and laponite-RDS, were not independently assessed under stiffness-matched conditions, and thus compositional influences beyond mechanical cues cannot be fully excluded. Second, although the bioink formulation includes electrostatic interactions among charged polymers, its structural stability is primarily governed by GelMA photopolymerization. The impact of physiological ions or charged biomolecules, especially in the context of long-term culture or drug screening, remains to be investigated. Lastly, as this study focused on short-term fibrotic responses, future work should investigate long-term ECM remodeling, protein-level signaling pathways, and the incorporation of co-culture systems to more accurately model the complex pathophysiology of keloid disease. In particular, the current model is limited to fibroblast-only constructs, and future studies incorporating additional skin-resident cell types, such as keratinocytes, will be essential to more faithfully replicate the cellular heterogeneity and structural complexity of fibrotic skin tissue.

4. Conclusion

The 3D bioprinting has emerged as a transformative technology for fabricating complex, functional, and biomimetic tissue constructs by integrating living cells with tailored biomaterials and biochemical cues. In this study, we developed a composite bioink composed of GelMA, alginate, MC, and laponite-RDS, designed to achieve tunable mechanical properties, robust printability, and high biocompatibility. GelMA served as the primary crosslinkable backbone, forming stable networks upon UV exposure and providing cell-adhesive motifs essential for tissue integration. While alginate is conventionally used as an ionically crosslinked matrix, we leveraged it here as a viscoelasticity enhancer, demonstrating its utility even in the absence of calcium. The addition of MC improved mechanical resilience and contributed to the formation of a cohesive hydrogel network, while laponite-RDS, a nanoclay with high surface reactivity, significantly enhanced the rheological profile by boosting viscosity, shear-thinning behavior, and elastic modulus. This work establishes a mechanically tunable and cytocompatible bioink capable of supporting 3D bioprinting of keloid-like fibrotic tissue constructs. By maintaining constant bioink composition and modulating stiffness via GelMA concentration, we demonstrated that matrix mechanics alone can significantly influence the activation of patient-derived keloid fibroblasts. The platform holds promise for disease modeling and future applications in drug screening and regenerative medicine. While this study demonstrates proof-of-concept for stiffness-regulated fibrosis modeling, further work is needed to explore long-term culture responses, matrix remodeling, and the independent biological roles of individual hydrogel components under stiffness-matched conditions. Additionally, the impact of physiological ions or charged therapeutic molecules on bioink stability and drug-release behavior warrants investigation in future applications.

Acknowledgments

We thank the Soonchunhyang Biomedical Research Core-Facility of the Korea Basic Science Institute (KBSI) for providing access to essential instrumentation and technical support throughout this study.

Funding

This work was supported by the Soonchunhyang University Research Fund and the National Research Foundation of Korea funded by the Ministry of Science and ICT (MSIT) (grant numbers: RS-2019-NR040068, RS-2023-00284258, and 2017R1D1AB03029770).

Conflict of interest

The authors declare they have no competing interests.

Author contributions

Conceptualization: Laurensia Danis Anggradita, Seung Min Nam, Yongsung Hwang

Formal analysis: Laurensia Danis Anggradita, Sung Sik Hur, Taekyun Kim, Wonjong Seon,

Mohammed Aboobucker Sithique, Seung Min Nam, Yongsung Hwang

Funding acquisition: Seung Min Nam, Yongsung Hwang

Investigation: Laurensia Danis Anggradita, Seung Min Nam, Yongsung Hwang
Methodology: Laurensia Danis Anggradita, Seung Min Nam, Yongsung Hwang
Project administration: Seung Min Nam, Yongsung Hwang
Writing – original draft: Laurensia Danis Anggradita, Murugaiyan Manimohan, Sung Sik Hur,
Seung Min Nam, Yongsung Hwang
Writing – review & editing: Laurensia Danis Anggradita, Murugaiyan Manimohan,
Seung Min Nam, Yongsung Hwang
All authors have read and agreed to the published version of the manuscript.

Ethics approval and consent to participate

The study was conducted according to the guidelines of the Declaration of Helsinki and approved by the Institutional Review Board of Soonchunhyang University Bucheon Hospital (SCHBC_IRB_2017-08-010). Informed consent was obtained from all individual participants included in the study.

Consent for publication

Not applicable.

Availability of data

The data that support the findings of this study are available from the corresponding author upon reasonable request.

References

1. Gu BK, Choi DJ, Park SJ, Kim MS, Kang CM, Kim C-H. 3-Dimensional bioprinting for tissue engineering applications. *Biomater Res*. 2016;20(1):12. doi: 10.1186/s40824-016-0058-2
2. Choi K, Park CY, Choi JS, *et al*. The effect of the mechanical properties of the 3D printed gelatin/hyaluronic acid scaffolds on hMSCs differentiation towards chondrogenesis. *Tissue Eng Regen Med*. 2023;20(4):593-605. doi: 10.1007/s13770-023-00545-w
3. Rossi A, Pescara T, Gambelli AM, *et al*. Biomaterials for extrusion-based bioprinting and biomedical applications. *Front Bioeng Biotechnol*. 2024;12:1393641. doi: 10.3389/fbioe.2024.1393641
4. Chen XB, Fazel Anvari-Yazdi A, Duan X, *et al*. Biomaterials/bioinks and extrusion bioprinting. *Bioact Mater*. 2023;28:511-536. doi: 10.1016/j.bioactmat.2023.06.006
5. Yoon J, Han H, Jang J. Nanomaterials-incorporated hydrogels for 3D bioprinting technology. *Nano Converg*. 2023;10(1):52. doi: 10.1186/s40580-023-00402-5
6. Nath R, Thomas J, Janardanan A, *et al*. An insight into synthesis, properties and applications of gelatin methacryloyl hydrogel for 3D bioprinting. *Mater Adv*. 2023;22:5496-5529. doi: 10.1039/D3MA00715D
7. Wu Y, Xiang Y, Fang J, *et al*. The influence of the stiffness of GelMA substrate on the outgrowth of PC12 cells. *Biosci Rep*. 2019;39(1):BSR20181748. doi: 10.1042/BSR20181748
8. Piao Y, You H, Xu T, *et al*. Biomedical applications of gelatin methacryloyl hydrogels. *Eng Regen*. 2021;2:47-56. doi: 10.1016/j.engreg.2021.03.002
9. Axpe E, Oyen ML. Applications of alginate-based bioinks in 3D bioprinting. *Int J Mol Sci*. 2016;17(12):1976. doi: 10.3390/ijms17121976
10. Aldana AA, Valente F, Dilley R, Doyle B. Development of 3D bioprinted GelMA-alginate hydrogels with tunable mechanical properties. *Bioprinting*. 2021;21:e00105. doi: 10.1016/j.bprint.2020.e00105
11. Contessi N, Altomare L, Filipponi A, Farè S. Thermo-responsive properties of methylcellulose hydrogels for cell sheet engineering. *Mater Lett*. 2017;207:157-160. doi: 10.1016/j.matlet.2017.07.023
12. Chang C, Zhang L. Cellulose-based hydrogels: present status and application prospects. *Carbohydr Polym*. 2011;84(1):40-53. doi: 10.1016/j.carbpol.2010.12.023
13. Contessi Negrini N, Bonetti L, Contili L, Farè S. 3D printing of methylcellulose-based hydrogels. *Bioprinting*. 2018;10:e00024. doi: 10.1016/j.bprint.2018.e00024
14. Ma Z, He H, Deng C, *et al*. 3D bioprinting of proangiogenic constructs with induced immunomodulatory microenvironments through a dual cross-linking procedure using laponite incorporated bioink. *Compos B Eng*. 2022;229:109399. doi: 10.1016/j.compositesb.2021.109399
15. Choi D, Heo J, Aviles Milan J, *et al*. Structured nanofilms comprising Laponite® and bone extracellular matrix for osteogenic differentiation of skeletal progenitor cells. *Mater Sci Eng C Mater Biol Appl*. 2021;118:111440. doi: 10.1016/j.msec.2020.111440
16. Li C, Hou Y, He M, *et al*. Laponite lights calcium flickers by reprogramming lysosomes to steer DC migration for an effective antiviral CD8(+) T-cell response. *Adv Sci (Weinh)*. 2023;10(30):e230300. doi: 10.1002/advs.202303006.
17. Wang Y, Zhao T, Jiao Y, *et al*. Silicate nanoplatelets promotes neuronal differentiation of neural stem cells and restoration of spinal cord injury. *Adv Healthc Mater*. 2023;12(19):e2203051. doi: 10.1002/adhm.202203051.

18. Kim H, Anggradita LD, Lee SJ, *et al*. Ameliorating fibrotic phenotypes of keloid dermal fibroblasts through an epidermal growth factor-mediated extracellular matrix remodeling. *Int J Mol Sci*. 2021;22(4):2198. doi: 10.3390/ijms22042198

19. Olejnik A, Semba JA, Kulpa A, Dańczak-Pazdrowska A, Rybka JD, Gornowicz-Porowska J. 3D bioprinting in skin related research: recent achievements and application perspectives. *ACS Synth Biol*. 2022;11(1):26-38. doi: 10.1021/acssynbio.1c00547

20. Kwon SH, Lee J, Yoo JA-O, Jung YA-O. Artificial keloid skin models: understanding the pathophysiological mechanisms and application in therapeutic studies. *Biomater Sci*. 2024;25(13):3321-3334. doi: 10.1039/d4bm00005

21. Kang H, Shih Y-RV, Hwang Y, *et al*. Mineralized gelatin methacrylate-based matrices induce osteogenic differentiation of human induced pluripotent stem cells. *Acta Biomater*. 2014;10(12):4961-4970. doi: 10.1016/j.actbio.2014.08.010.

22. Temirel M, Dabbagh SR, Tasoglu S. Shape fidelity evaluation of alginate-based hydrogels through extrusion-based bioprinting. *J Funct Biomater*. 2022;13(4):225. doi: 10.3390/jfb13040225

23. Livak KJ, Schmittgen TD. Analysis of relative gene expression data using real-time quantitative PCR and the 2(-Delta Delta C(T)) method. *Methods*. 2001;25(4):402-8. doi: 10.1006/meth.2001.1262. PMID: 11846609.

24. Wang K-Y, Jin X-Y, Ma Y-H, *et al*. Injectable stress relaxation gelatin-based hydrogels with positive surface charge for adsorption of aggrecan and facile cartilage tissue regeneration. *J Nanobiotechnol*. 2021;19(1):214. doi: 10.1186/s12951-021-00950-0

25. Vigata M, Meinert C, Bock N, Dargaville BL, Hutmacher DW. Deciphering the molecular mechanism of water interaction with gelatin methacryloyl hydrogels: role of ionic strength, pH, drug loading and hydrogel network characteristics. *Biomedicines*. 2021;9(5):574. doi: 10.3390/biomedicines9050574

26. Xiao S, Zhao T, Wang J, *et al*. Gelatin methacrylate (GelMA)-based hydrogels for cell transplantation: an effective strategy for tissue engineering. *Stem Cell Rev Rep*. 2019;15(5):664-679. doi: 10.1007/s12015-019-09893-4.

27. Fang W, Yang M, Wang L, *et al*. Hydrogels for 3D bioprinting in tissue engineering and regenerative medicine: current progress and challenges. *Int J Bioprint*. 2023;9(5):759. doi: 10.18063/ijb.759. PMID: 37457925

28. Stealey ST, Gaharwar AK, Zustiak SP. Laponite-based nanocomposite hydrogels for drug delivery applications. *Pharmaceuticals*. 2023;16(6):821. doi: 10.3390/ph16060821

29. de Barros NR, Gomez A, Ermis M, *et al*. Gelatin methacryloyl and Laponite bioink for 3D bioprinted organotypic tumor modeling. *Biofabrication*. 2023;15(4):045005. doi: 10.1088/1758-5090/ace0db

30. Ashammakhi N, Ahadian S, Xu C, *et al*. Bioinks and bioprinting technologies to make heterogeneous and biomimetic tissue constructs. *Mater Today Bio*. 2019;1:100008. doi: 10.1016/j.mtbio.2019.100008

31. Muthuramalingam K, Lee HA-O. Effect of GelMA hydrogel properties on long-term encapsulation and myogenic differentiation of C(2)C(12) spheroids. *Gels*. 2023;9(12):925. doi: 10.3390/gels9120925.

32. Gao T, Gillispie GJ, Copus JS, *et al*. Optimization of gelatin-alginate composite bioink printability using rheological parameters: a systematic approach. *Biofabrication*. 2018;10(3):034106. doi: 10.1088/1758-5090/aacdc7.

33. Moreira R, Chenlo F, Silva C, Torres MD. Rheological behaviour of aqueous methylcellulose systems: effect of concentration, temperature and presence of tragacanth. *LWT*. 2017;84:764-770. doi: 10.1016/j.lwt.2017.06.050

34. Schütz K, Placht A-M, Paul B, Brüggemeier S, Gelinsky M, Lode A. Three-dimensional plotting of a cell-laden alginate/methylcellulose blend: towards biofabrication of tissue engineering constructs with clinically relevant dimensions. *J Tissue Eng Regen Med*. 2017;11(5):1574-1587. doi: 10.1002/term.2058

35. Rastin H, Ormsby RT, Atkins GJ, Losic DA-OX. 3D bioprinting of methylcellulose/gelatin-methacryloyl (MC/GelMA) bioink with high shape integrity. *ACS Appl Bio Mater*. 2020;3(3):1815-1826. doi: 10.1021/acsabm.0c00169

36. Afghah F, Altunbek M, Dikyol C, Koc B. Preparation and characterization of nanoclay-hydrogel composite support-bath for bioprinting of complex structures. *Sci Rep*. 2020;10(1):5257. doi: 10.1038/s41598-020-61606-x

37. Mignon A, Pezzoli D, Prouvé E, *et al*. Combined effect of laponite and polymer molecular weight on the cell-interactive properties of synthetic PEO-based hydrogels. *React Funct Polym*. 2019;136:95-106. doi: 10.1016/j.reactfunctpolym.2018.12.017

38. Aazmi A, Zhang D, Mazzaglia C, *et al*. Biofabrication methods for reconstructing extracellular matrix mimetics. *Bioact Mater*. 2023;31:475-496. doi: 10.1016/j.bioactmat.2023.08.018.

39. GhavamiNejad A, Ashammakhi N, Wu XY, Khademhosseini A. Crosslinking strategies for 3D bioprinting of polymeric hydrogels. *Small*. 2020;16(35):2002931. doi: 10.1002/smll.202002931

40. Karaca MA, Khalili V, Ege D. Highly flexible methyl cellulose/gelatin hydrogels for potential cartilage tissue engineering applications. *Biopolymers*. 2025;116(1):e23641. doi: 10.1002/bip.23641

41. Šebenik U, Lapasin R, Krajnc M. Rheology of aqueous dispersions of laponite and TEMPO-oxidized nanofibrillated cellulose. *Carbohydr Polym*. 2020;240:116330. doi: 10.1016/j.carbpol.2020.116330

42. Yue K, Trujillo-de Santiago G, Alvarez MM, Tamayol A, Annabi N, Khademhosseini A. Synthesis, properties, and biomedical applications of gelatin methacryloyl (GelMA) hydrogels. *Biomaterials*. 2015;73:254-271. doi: 10.1016/j.biomaterials.2015.08.045

43. Li H, Chen S, Dissanayaka WL, Wang M. Gelatin methacryloyl/sodium alginate/cellulose nanocrystal inks and 3D printing for dental tissue engineering applications. *ACS Omega*. 2024;9(49):48361-48373. doi: 10.1021/acsomega.4c06458

44. Xu L, Zhang Z, Jorgensen AM, *et al*. Bioprinting a skin patch with dual-crosslinked gelatin (GelMA) and silk fibroin (SilMA): an approach to accelerating cutaneous wound healing. *Mater Today Bio*. 2023;18:100550. doi: 10.1016/j.mtbio.2023.100550

45. Zeimaran E, Pourshahrestani S, Röder J, Detsch R, Boccaccini AR. 3D printing of photocrosslinked alginate dialdehyde-gelatin hydrogels reinforced with cobalt-containing mesoporous bioactive glass nanoparticles for developing skin wound dressings. *Adv Mater Interfaces*. 2025;12(11):2400913. doi: 10.1002/admi.202400913

46. Limandjaja GC, Niessen FB, Scheper RJ, Gibbs S. The Keloid disorder: heterogeneity, histopathology, mechanisms and models. *Front Cell Dev Biol*. 2020;8:360. doi: 10.3389/fcell.2020.00360.

47. Hsu CK, Lin HH, Harn HI, *et al*. Caveolin-1 controls hyperresponsiveness to mechanical stimuli and fibrogenesis-associated RUNX2 activation in keloid fibroblasts. *J Invest Dermatol*. 2018;138(1):208-218. doi: 10.1016/j.jid.2017.05.041

48. Saraswati S, Marrow SMW, Watch LA, Young PP. Identification of a pro-angiogenic functional role for FSP1-positive fibroblast subtype in wound healing. *Nat Commun*. 2019;10(1):3027. doi: 10.1038/s41467-019-10965-9

49. Camman M, Nieswic N, Joanne P, *et al*. Fibrotic-like collagen matrices as innovative 3D in vitro models for investigating the impact of pathological ECM on muscle regeneration in muscular dystrophies. *bioRxiv*. 2024. doi: 10.1101/2024.12.23.630059

50. Tai Y, Woods EL, Dally J, *et al*. Myofibroblasts: function, formation, and scope of molecular therapies for skin fibrosis. *Biomolecules*. 2021;11(8):1095. doi: 10.3390/biom11081095

51. Lee W, Debasitis JC, Lee VK, *et al*. Multi-layered culture of human skin fibroblasts and keratinocytes through three-dimensional freeform fabrication. *Biomaterials*. 2009;30(8):1587-1595. doi: 10.1016/j.biomaterials.2008.12.009

52. Jang Y, Jang J, Kim BY, Song YS, Lee DY. Effect of gelatin content on degradation behavior of PLLA/gelatin hybrid membranes. *Tissue Eng Regen Med*. 2024;21(4):557-569. doi: 10.1007/s13770-024-00626-4

53. Lee YJ, Oh JH, Park S, *et al*. The application of L-serine-incorporated gelatin sponge into the calvarial defect of the ovariectomized rats. *Tissue Eng Regen Med*. 2025;22(1):91-104. doi: 10.1007/s13770-024-00686-6

54. Vigata M, Meinert C, Pahoff S, Bock N, Hutmacher DW. Gelatin methacryloyl hydrogels control the localized delivery of albumin-bound paclitaxel. *Polymers*. 2020;12(2):501. doi: 10.3390/polym12020501

55. Zhu M, Wang Y, Ferracci G, Zheng J, Cho NJ, Lee BH. Gelatin methacryloyl and its hydrogels with an exceptional degree of controllability and batch-to-batch consistency. *Sci Rep*. 2019;9(1):6863. doi: 10.1038/s41598-019-42186-x

Our Journals

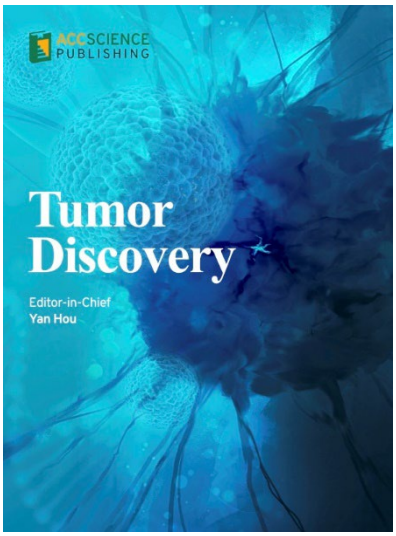

Tumor Discovery is a peer-reviewed and open-access journal that aims to present new cancer research with strong emphasis on fundamental and translational studies. *Tumor Discovery* covers topics, including but not limited to the following:

- Etiology and pathogenesis of cancer
- Mechanisms and molecular pathways underlying cancer initiation and progression
- Tumor metastasis
- Tumor evolution and heterogeneity
- Tumor microenvironment and tumor-host interactions
- Cancer genetics and genomics
- Cancer characterization using omics approaches
- Discovery and validation of cancer biomarker
- Discovery of new therapeutic targets
- New approaches of diagnostic and treatment modalities
- Statistical methods in cancer research

Global Translational Medicine is a quarterly journal that focuses on medicine, biological sciences, and biomaterials engineering. The goal of *Global Translational Medicine* is to provide a platform to researchers for showcasing their latest research works in translational medicine so as to advance the field towards the betterment of human health. Despite the advancement of omics and new technologies, the process of transforming these technologies and scientific research results into effective therapies and putting them into clinical use still has a long way to go. *Global Translational Medicine* provides a platform to fill the gaps in preclinical and inter-disciplinary research, to promote clinical translation of scientific research results, and to contribute to the conception of new and improved preventive measures as well as diagnostic and therapeutic techniques of diseases.

Global Translational Medicine covers the following themes: cardiovascular disease, metabolism/diabetes/obesity, neuroscience/neurology, cancer, biomaterials and their applications in medicine, proteomics/metabolomics, pharmacogenomics, biomarkers, bioinformatics and data mining, animal and clinical research, and medical methods arising from interdisciplinary crossover.

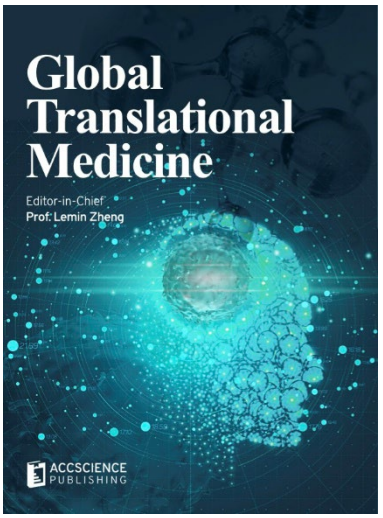

Start a new journal

Write to us via email if you are interested to start a new journal with AccScience Publishing. Please attach your CV, professional profile page and a brief pitch proposal in your email. We shall inform you of our decision whether we are interested to collaborate in starting a new journal.

Contact: info@accscience.com

https://accscience.com/journal/IJB



Contact
www.accscience.com
9 Raffles Place, Republic Plaza 1 #06-00 Singapore 048619
Email: editorial@accscience.com
Phone: +65 8182 1586